

Final Report
on

“Hydrogen-Assisted IC Engine Combustion as a Route to
Hydrogen Implementation”

October 1, 2004 – September 30, 2008

Andre L. Boehman and Daniel C. Haworth

Report Issue Date:
February 2009

Instrument Number: DE-FC26-04NT42233

The Pennsylvania State University
The Energy Institute
University Park, PA 16802

Table of Contents

Disclaimer.....	3
Abstract	4
Executive Summary	5
Approach	6
Results	7
Task 1.1: Combustion & Emissions Impacts and Lubricant Challenges of HCNG.....	8
Task 1.2: Numerical Simulation of SI Engine Comb. with HCNG Fueling.....	42
Task 1.3: Field Vehicle Instrumentation and Combustion Analysis	43
Task 1.4: Examination of Selective NOx Recirc. (SNR) in HVNG-Fueled Engines	44
Task 2.1: Hydrogen Assisted Combustion Studies in a CI Engine.....	45
Task 2.2: Simulation of HCCI-SCCI Combustion	61
Task 2.3: Examination of SNR during H ₂ -Assisted Diesel Combustion	62
Conclusion and Milestones.....	71
Appendices	75
Appendix A-1.2: MS Thesis by Saket Priyadarshi	76
Appendix A-1.3: MS Thesis by Jamie Clark.....	206
Appendix A-2.1.A: MS Thesis by Greg Lilik	308
Appendix A-2.1.B: PhD Thesis by Elana Chapman	485
Appendix A-2.2.B: MS Thesis by Bryan Nese.....	826

Disclaimer

This report was prepared as an account of work sponsored by an agency of the United States Government. Neither the United States Government nor any agency thereof, nor any of their employees, makes any warranty, express or implied, or assumes any legal liability or responsibility for the accuracy, completeness, or usefulness of any information, apparatus, product, or process disclosed, or represents that its use would not infringe privately owned rights. Reference herein to any specific commercial product, process, or service by trade name, trademark, manufacturer, or otherwise does not necessarily constitute or imply its endorsement, recommendation, or favoring by the United States Government or any agency thereof. The views and opinions of authors expressed herein do not necessarily state or reflect those of the United States Government or any agency thereof.

Abstract

The “Freedom Car” Initiative announced by the Bush Administration has placed a significant emphasis on development of a hydrogen economy in the United States. While the hydrogen-fueled fuel-cell vehicle that is the focus of the “Freedom Car” program would rely on electrochemical energy conversion, and despite the large amount of resources being devoted to its objectives, near-term implementation of hydrogen in the transportation sector is not likely to arise from fuel cell cars. Instead, fuel blending and “hydrogen-assisted” combustion are more realizable pathways for wide-scale hydrogen utilization within the next ten years. Thus, a large potential avenue for utilization of hydrogen in transportation applications is through blending with natural gas, since there is an existing market for natural-gas vehicles of various classes, and since hydrogen can provide a means of achieving even stricter emissions standards. Another potential avenue is through use of hydrogen to “assist” diesel combustion to permit alternate combustion strategies that can achieve lower emissions and higher efficiency.

This project focused on developing the underlying fundamental information to support technologies that will facilitate the introduction of coal-derived hydrogen into the market. Two paths were envisioned for hydrogen utilization in transportation applications. One is for hydrogen to be mixed with other fuels, specifically natural gas, to enhance performance in existing natural gas-fueled vehicles (e.g., transit buses) and provide a practical and marketable avenue to begin using hydrogen in the field. A second is to use hydrogen to enable alternative combustion modes in existing diesel engines, such as homogeneous charge compression ignition, to permit enhanced efficiency and reduced emissions.

Thus, this project on hydrogen-assisted combustion encompassed two major objectives: (1) Optimization of hydrogen-natural gas mixture composition and utilization through laboratory studies of spark-ignition engine operation on H₂-NG and numerical simulation of the impact of hydrogen blending on the physical and chemical processes within the engine; and (2) Examination of hydrogen-assisted combustion in advanced compression-ignition engine processes. To that end, numerical capabilities were applied to the study of hydrogen assisted combustion and experimental facilities were developed to achieve the project objectives.

Executive Summary

This project on hydrogen-assisted combustion encompassed two major objectives. Optimization of hydrogen-natural gas mixture composition and utilization through laboratory studies of spark-ignition engine operation on H₂-NG and numerical simulation of the impact of hydrogen blending on the physical and chemical processes within the engine. Examination of hydrogen-assisted combustion in advanced compression-ignition engine processes. To that end, numerical capabilities are being applied to the study of hydrogen assisted combustion and experimental facilities are being developed to achieve the project objectives.

During the period of performance, we performed experimental studies of compressed natural gas (CNG) and hydrogen-enriched natural gas (HCNG) in a spark ignition engine and a field vehicle and performed experimental studies of hydrogen-assisted compression ignition combustion in a turbodiesel engine via fumigation of the intake air with hydrogen. The gaseous fuels for both experiments were obtained from the DOE sponsored Hydrogen Fueling Station at Penn State which was built by Air Products and Chemicals, Inc. and dispenses the HCNG and H₂ fuels used in these studies. A fuel delivery system for the engine test stands was designed and built for this program with technical guidance from Air Products. Overall, the key observations regarding HCNG combustion are that the role of the hydrogen is to increase the burning rate of CNG, which permits significant retardation of spark timing. However, the impact of the hydrogen on spark timing to achieve maximum brake torque (MBT) is no more significant than the effect of increasing swirl within the engine. Overall, the key observations regarding H₂ on diesel combustion are that thermal efficiency and emissions are not strongly affected by the substitution of diesel fuel by fumigated hydrogen, which can be seen as a way of displacing diesel fuel usage, but that there is a dramatic increase in the relative proportion of NO₂ to NO in the NO_x emissions from the engine as hydrogen substitution is increased.

During the period of performance, numerical methods were developed and applied to provide a fundamental understanding of how hydrogen influences the spark-ignition combustion of natural gas and the compression ignition combustion of *n*-heptane. In particular, we have performed calculations examining the flame speed enhancement with hydrogen addition to methane, the interaction between an *n*-heptane spray and a uniform mixture of air and hydrogen, and the NO_x emissions and the shift between NO and NO₂, which was observed in the experiments, to examine what chemical reactions are responsible for this shift.

Approach

The experimental approach to achieving the project objectives involves the application of a Ricardo Hydra single cylinder research engine for the SI studies and of a VM Motori 2.5L turbodiesel engine for the CI studies. Also, a service van from Penn State's Office of Physical Plant is being used for field vehicle testing and for assessing lubricant compatibility with HCNG operation.

Ricardo Hydra Engine

The Ricardo Hydra engine, a single-cylinder four valves per cylinder SI engine presently is configured for port fuel injection of gasoline. The engine has been outfitted with an intake fuel/air mixer to provide CNG and HCNG fueling capabilities. The engine is being used to study the combustion enhancements provided by hydrogen assist.

VM Motori 2.5L Turbodiesel Engine

The VM Motori 2.5L turbodiesel engine is a state-of-the-art electronically controlled common rail injection engine, with electronically controlled cooled EGR. This engine represents current technology, passenger car diesel technology. The engine has been instrumented with a multi-cylinder combustion analysis, rail pressure sensing and needle lift sensing. The engine includes an interface to the electronic controls providing the ability to change operating parameters on-the-fly.

Numerical Simulations

CHEMKIN (homogeneous reactor models, steady one-dimensional laminar flame models); XSenkplot (a graphical postprocessor for CHEMKIN that facilitates the analysis of detailed chemical mechanisms); GMTEC (a research unstructured three-dimensional time-dependent CFD code for computing in-cylinder aero-thermo-fluids processes); and STAR-CD (a commercial unstructured three-dimensional time-dependent CFD code for computing in-cylinder aero-thermo-fluids processes).

Results

The discussion of results is organized by task, according to the task structure in the SOPO. For the purpose of presenting the overall results from the entire project and capturing the entirety of the excellent work done by the group of graduate students who have contributed to the project, appendices with the complete theses are included. For a task where one or more students primarily performed their thesis research on that task, a brief Executive Summary of key findings is included under the heading of that task along with a reference to the appropriate appendix and thesis for the full results from that task. Under two tasks (1.1 and 2.3), a completed graduate thesis on the work under that task is either in progress (1.1) or the work was not broad enough to encompass an entire graduate thesis (2.3). In these two cases, a complete report is provided within the body of the report for that task.

Task 1.1 *Combustion and Emissions Impacts and Lubricant Challenges of HCNG*

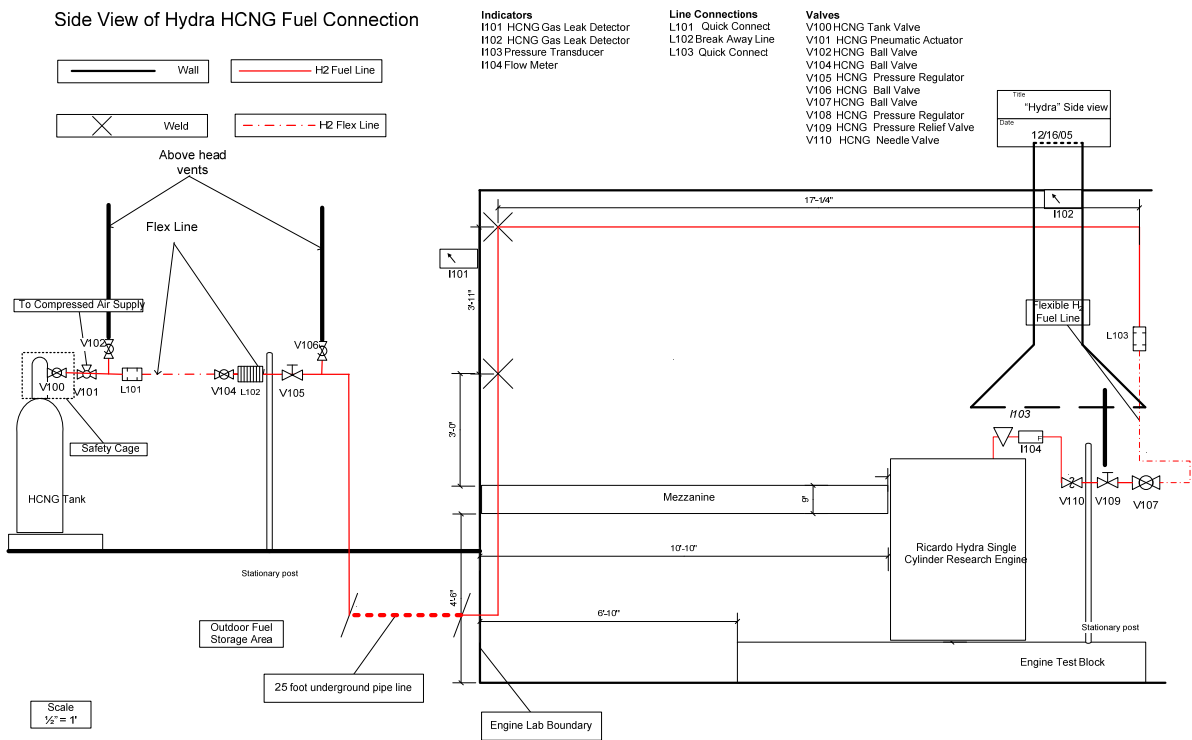
Experimental

In Year 1, the work focused on engine and fueling system development for the Ricardo Hydra test stand. In Year 2, construction of the hydrogen fueling system was largely completed, a temporary hydrogen delivery system was put in place and some preliminary data for hydrogen assisted gasoline combustion were obtained. In Years 3 and 4, the studies of CNG and HCNG combustion were performed.

A 3600 psi glass-wrapped steel storage tank is refueled on campus at the DOE/PSU/Air Products hydrogen fueling station. An Impco gaseous air-fuel mixer has been integrated to ensure homogeneous preparation of the air-fuel mixture entering the engine. Stoichiometry is controlled with a metering valve inline with a mass flow sensor, upstream the mixer.

The gaseous fueling system comprises stainless steel components, including a regulator, pressure relief device (PRD), and manual shut off valves. Fuel flow will be controlled from the LabView interface. When fueling is requested (by the user), a digital circuit is powered, opening a solenoid valve to send compressed air to a pneumatic valve at the storage tank, allowing fuel to flow. The storage tank is located outside of the laboratory, where pressure will be reduced from 3600 psi to 200 psi prior to entering the building. A PRD downstream the regulator prevents high pressure from entering the building in case the regulator fails. Components inside the building are rated for 5000 psi, for safety.

Electronic, explosion proof hydrogen leak detectors are mounted near regions of the fueling system where mechanical connections exist. Upon detection of a hydrogen leak, the digital circuit powers off, preventing fuel flow from the storage vessel. The engine ignition is cut as well, but the engine is motored to empty the fuel line. A fume hood located directly above the test stand draws any leaked fuel from the laboratory.



Ricardo Hydra engine test stand

The Ricardo Hydra engine test stand configured with advanced control system and dynamometer with absorbing and motoring capabilities was acquired for the hydrogen assisted combustion project, Figure 2. The Hydra is a 0.5 L, single-cylinder, 4-valve, naturally aspirated, port-injected, spark ignition engine. The control system allows the user independent control of RPM (or torque), load, stoichiometry, and spark timing.



Figure 2: Ricardo Hydra Research Engine

The associated data acquisition system comprises thermocouples, pressure transducers, shaft encoder, lambda sensor, mass flow controller, and sensors for in-cylinder flame sensing, Figure 3. All are integrated into a LabView PXI system, using a SCXI chassis. LabView version 7 was used to create a data monitoring and collection system, complete with MFB calculations, and heat release code. A laminar flow element and plenum chamber were integrated for accurate charge airflow measurement.

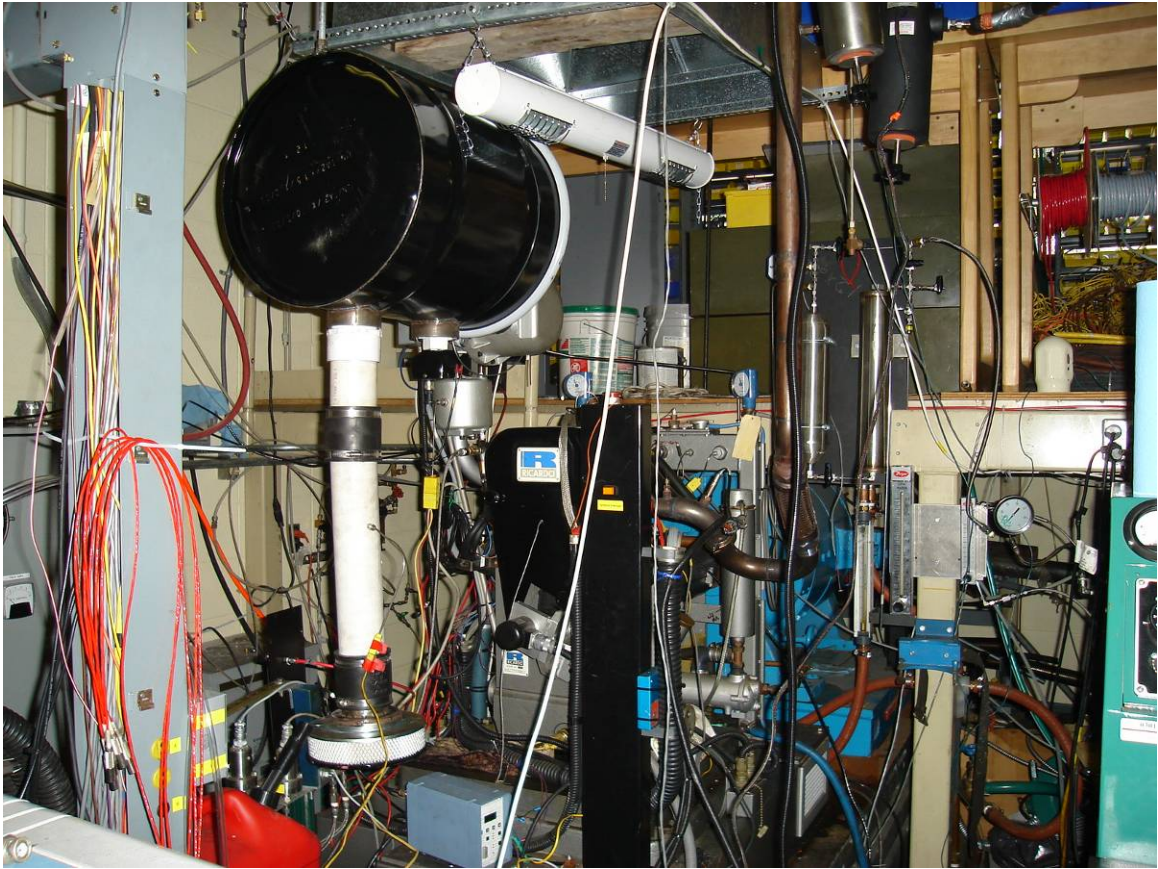


Figure 3: Engine Test Stand Instrumentation

Emissions measurement

The Hydra exhaust is outfitted with a heated canister filter coupled to a heated sample line, both temperature controlled to 190°C, in order to preserve emissions in their gaseous state as they travel to analytical equipment. Emissions analysis was achieved using an AVL emissions rack, comprising analyzers for CO, CO₂, NO_x, HC (low and high) and O₂, with the ability to verify AFR as well, Figure 4.

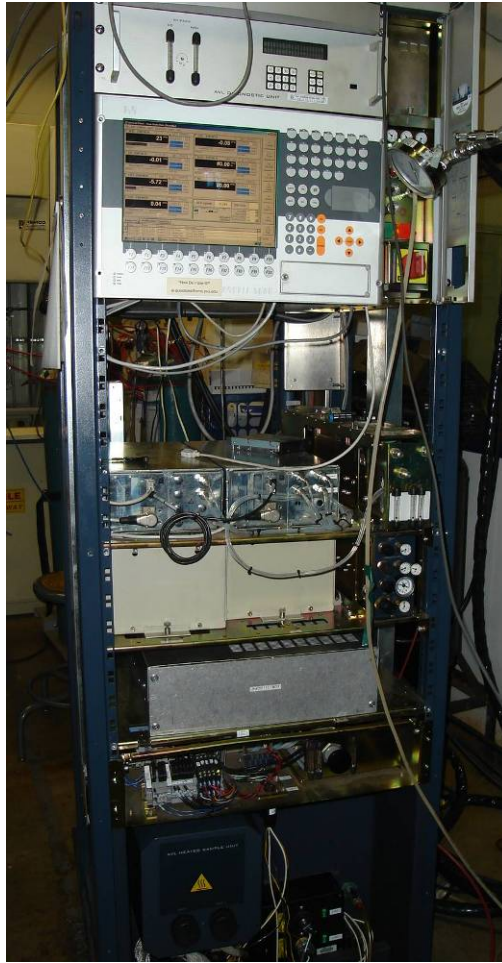


Figure 4: AVL Emissions Bench

Speciation of engine exhaust was achieved with a gas chromatograph, calibrated for low range HC's and hydrogen, Figure 5



Figure 5: Gas Chromatograph (GC) for HC Speciation of Exhaust Gas

A thermophoretic sampling unit enables extraction of soot samples from the exhaust stream, to provide qualitative information about the morphology of the soot via transmission electron microscopy (TEM) imaging of the samples.

The exhaust was routed through a chiller to remove water condensate, and then drawn through a DNPH cartridge via vacuum pump, in order to collect samples for analysis with high pressure liquid chromatography (HPLC). This analysis provides concentrations of the following oxygenated species:

- formaldehyde
- acrolein
- acetaldehyde
- acetone
- propional
- crotonal
- methylethylketone
- methacrolein
- butyral
- benzal
- valeral
- tolual
- hexanal

Components for intake-induced swirl generation

The Hydra possesses a quiescent combustion chamber. Components have been fabricated and employed to partially or fully block on of the intake ports to generated intake-induced swirl. An internally threaded aluminum component was manufactured to press into one of the intake ports, to accept components to partially or fully block the intake port. These blockage components are shown in Figure 6. Figure 7 shows one port opened and one port fully blocked.



Figure 6: Swirl Components

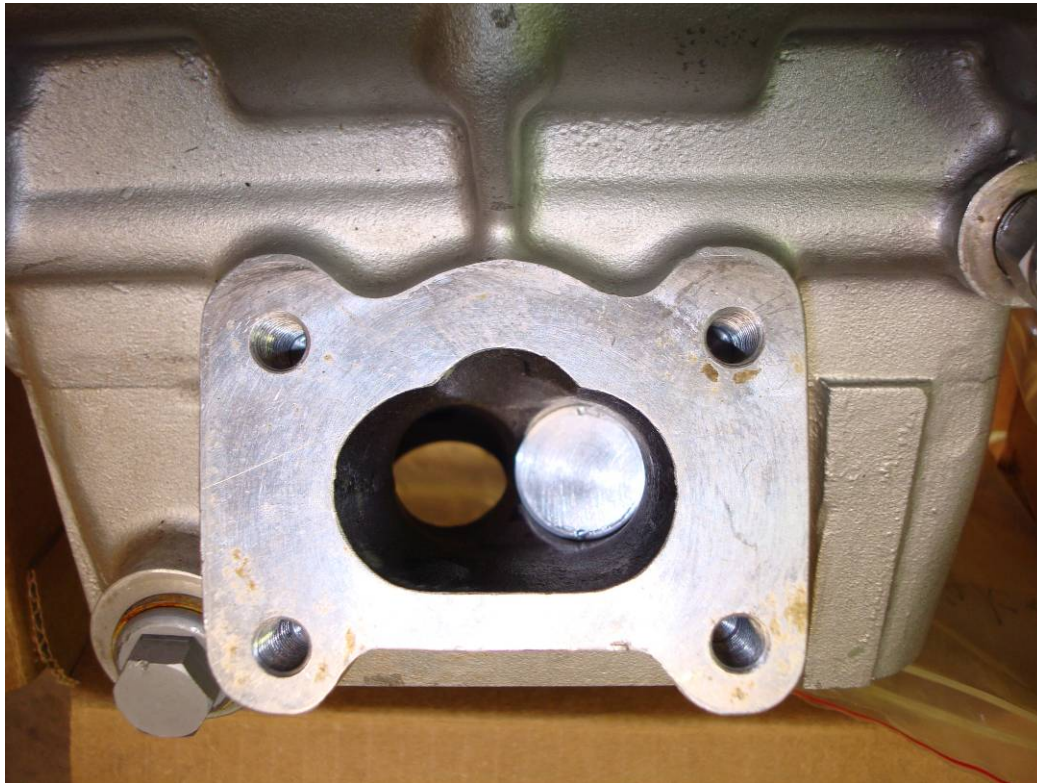


Figure 7: Intake Port Blockage Components

The Hydra head was tested on a flow bench at General Motor's Tech Center to quantify swirl numbers for the head without blockages, and also for the head with one port fully blocked.

Flame development instrumentation

The two devices designed for studying the flame propagation in SI engine have been obtained. A head gasket equipped with 6 ion probes (Figure 8) has been designed and fabricated for the Hydra engine which enables detecting the flame arrival along the plane of head gasket. Signal conditioning is accomplished with a circuitry developed in-house and the signals are processed with a high speed multiple channel data acquisition board.

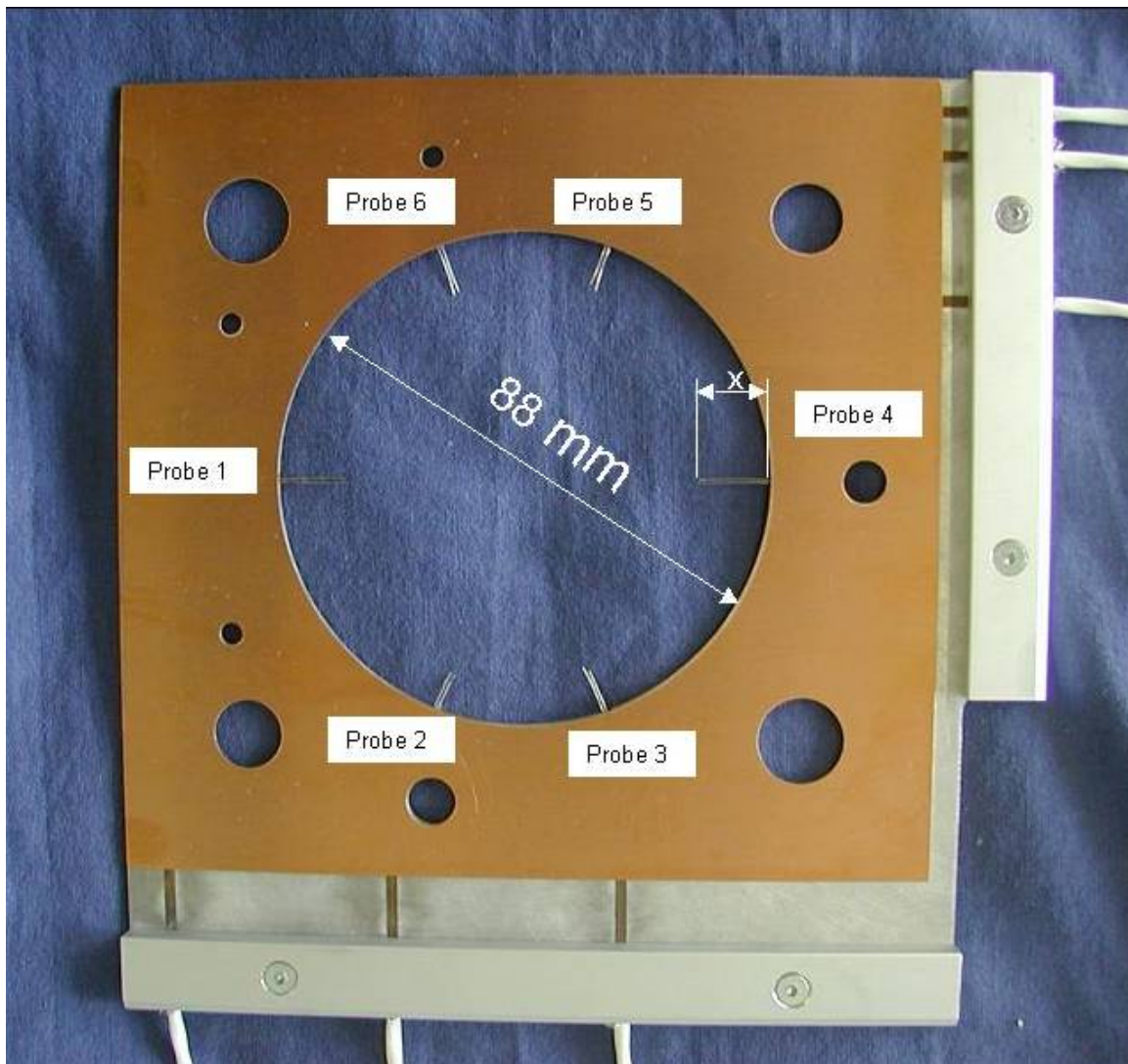


Figure 8: Ion Probe Head Gasket

Another in-cylinder flame detector, optical sensor equipped spark plug, has also been obtained (Figure 9, Figure 10) which allows the flame detection on the top of the combustion chamber.

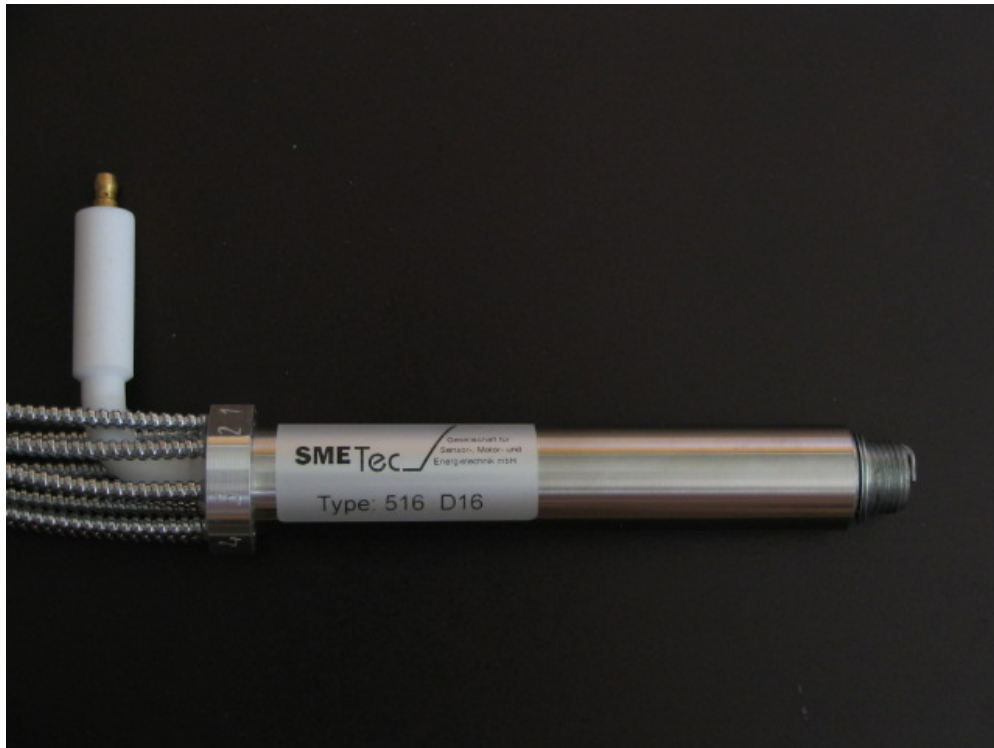


Figure 9: Fiber Optic Spark Plug

The signals generated from the ion sensors and fiber optic sensors will be analyzed and portrayed via radar graphs, to provide a visual representation of the flame (being sensed) within the cylinder.



Figure 10: Fiber-Optic Spark Plug

Novel gaseous fueling system

A gaseous fueling system was designed, fabricated, and employed, according to relevant fuel system guidelines. In order to introduce gaseous natural gas and hydrogen into the engine safely, Figure 11. The system comprises a 3600 psi, glass wrapped steel cylinder with an 80L capacity. The tank comprises manual shut-off valves on each end of the tank. One valve is also outfitted with a fueling receptacle, Figure 12. The other valve is fitted with quick disconnects, to easily and safely detach the tank from the fueling system, so that the tank can be transported to the hydrogen fueling station on campus. The quick disconnect is attached to a hose, which is connected to a break-away line that was installed for safety, to protect the system if the tank should be moved without first disconnecting the tank.



Figure 11: Gaseous Fuel Storage Tank, 3600 PSI

The break-away enters a pneumatic valve, which is opened to allow fuel to flow from the tank into the building when a solenoid valve is switched on to permit compressed air to flow outside to the pneumatic valve. A pressure regulator sits inline downstream the pneumatic valve, and drops the pressure from 3600 psi down to 200 psi so that low-pressure fuel is entering the fueling system into the building. The outlet of the pressure regulator has a pressure relief device to ensure low-pressure delivery to the laboratory, in the event that the pressure regulator fails or becomes damaged.



Figure 12: HCNG Fueling Receptacle

The pressure of the gaseous fuel is regulated down to 75psi once it reaches the engine test stand, and then enters a mass flow controller for accurate mass control and measurement. A vent hood is positioned above the engine, and is outfitted with a hydrogen sensor. A schematic of the fueling system is shown in Figure 1.

Experiments: Baseline

The data collected in this phase of research are generalized into four sets: CNG combustion, with and without swirl; HCNG combustion, with and without swirl. All baseline tests were conducted at 2000 RPM. Stoichiometry and spark timing were swept at a given load for each data set. This process was repeated for 3 different load conditions. Performance, combustion statistics, flame development, and emissions data were measured and calculated.

The Model Based Calibration tool in Matlab was used for design of experiments, in order to reduce the number of data points required to portray the trends of various responses from the engine, under various conditions. The preliminary data was used to develop correlations, and those correlations were considered in selecting future data points.

Results and Discussion

The following studies were conducted at 1.5 bar BMEP at stoichiometric AFR and MBT spark timing without intake induced swirl. The fueling rates for those conditions were held constant as throttle was opened incrementally to vary stoichiometry, and ST adjusted to MBT at each new AFR. The same fueling rates were adopted for the cases where intake-induced swirl was introduced via full blockage of one intake port; the same process was employed to adjust AFR & MBT timing as described above. The starting point of 1.5 bar BMEP was used in both 2000 RPM and 2750 RPM cases.

Additional tests were conducted at constant spark timing for the 2000 RPM case. The spark timing required to attain MBT at stoichiometric AFR and 1.5 bar BMEP for both non-swirl CNG & HCNG cases was held constant as a function of stoichiometry.

The results for each experiment are described in the following sections. The term quiescent is used to describe the engine head without any modifications; this configuration yields no intake-induced turbulence, and is denoted in the data label suffix as “nS.” Swirl is used to describe the configuration where one intake port is blocked fully, generating some amount of intake-induced swirl, and denoted as “s” in the data label suffix. (i.e. CNGns, CNGs, HCNGns, HCNGs).

Comparison of CNG & HCNG Combustion Characteristics at 2000 RPM, MBT Timing.

Figure 13 shows that hydrogen addition enables retarded spark timing, as expected from the results in the literature. The ability for HCNG to achieve MBT with reduced spark advance compared to neat CNG, provides evidence of the increased burn rate of hydrogen compared to natural gas.

Figure 14 shows that HCNG can be burned at stoichiometries significantly leaner than CNG, before the COV% of IMEP increases to undesirable levels (regarding noise considerations and engine wear, etc.). This data corresponds well with much of the data found in literature supporting that hydrogen addition to natural gas extends the lean limit of combustion.

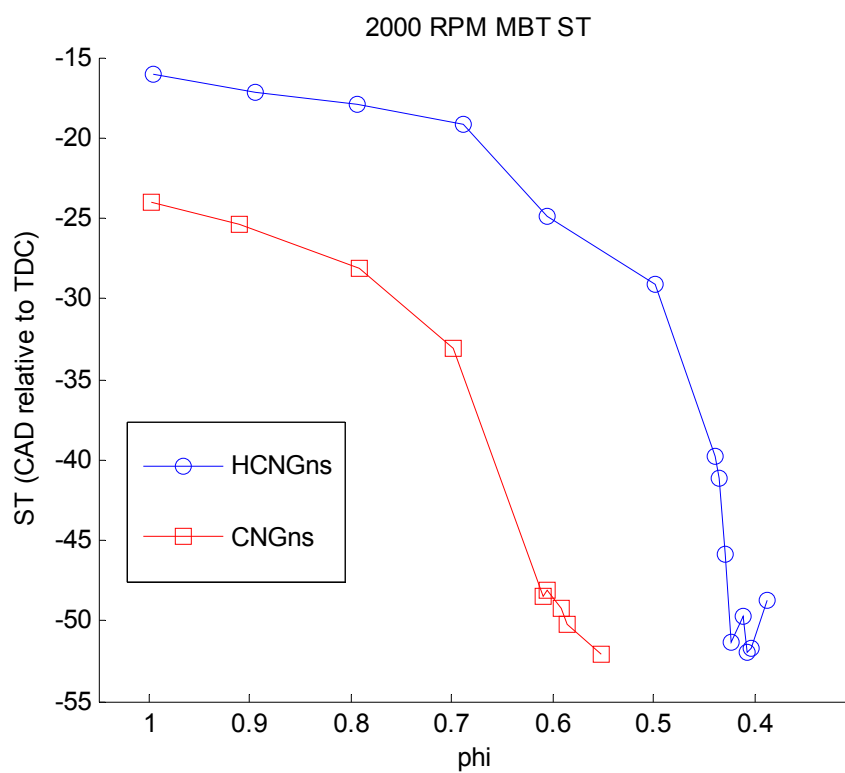


Figure 13: MBT spark timing shows that the addition of hydrogen to natural gas enables more retarded spark timings, due to a reduction in ignition delay.

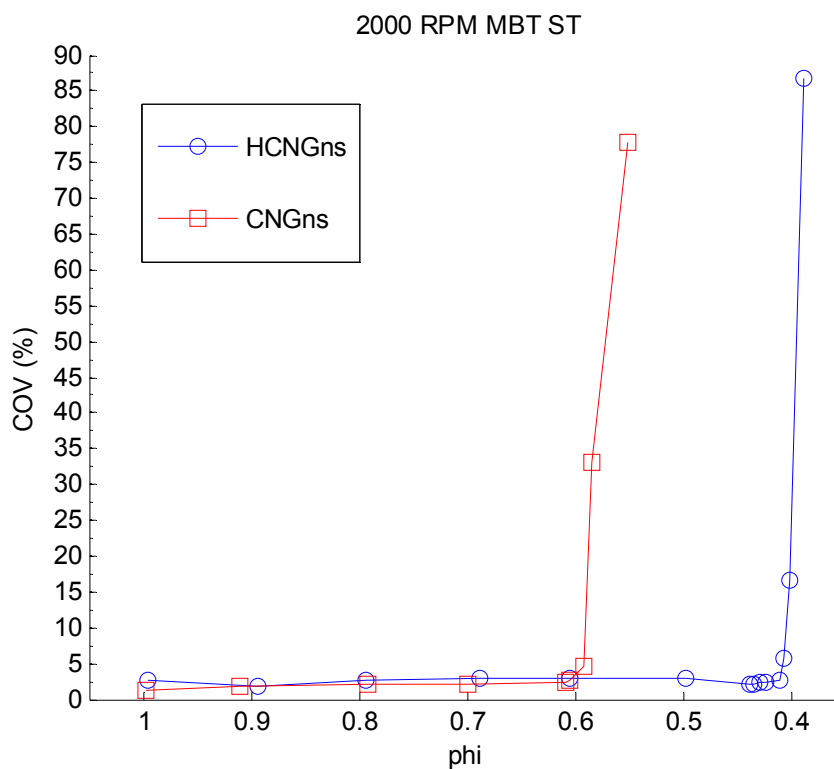


Figure 14: Coefficient of variance as a function of fuel equivalence ratio for CNG and HCNG combustion without swirl at MBT spark timing.

While the lean limit is extended with HCNG compared to CNG alone, it is important to note that COV% of IMEP in the range of $0.1 \geq \Phi \geq 0.6$ is greater or the same for HCNG compared to CNG (Figure 15). This means that the influence of hydrogen on stabilizing combustion is evident when the ignition character of CNG is weak, i.e., only under very lean conditions.

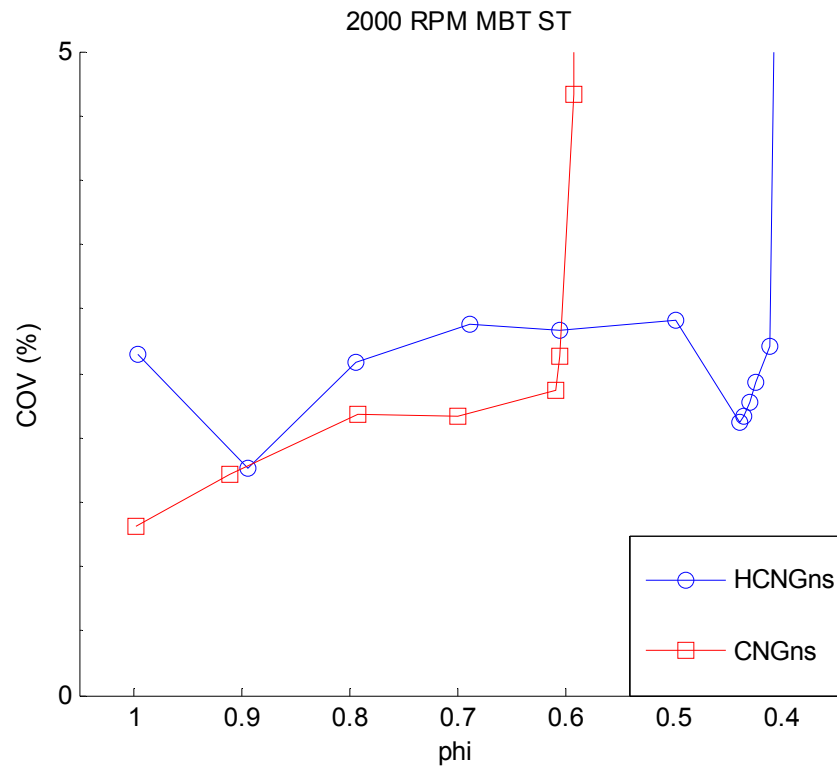


Figure 15: Coefficient of variance as a function of fuel equivalence ratio for CNG and HCNG combustion without swirl at MBT spark timing, with narrowed scale for COV.

Figure 16 shows that performance enhancements are achieved when adding hydrogen to natural gas, and combustion is sustained at leaner stoichiometries than can be achieved with natural gas. That higher torque output is observed with HCNG arises from the delayed spark timing, which reduces pumping losses associated with early combustion.

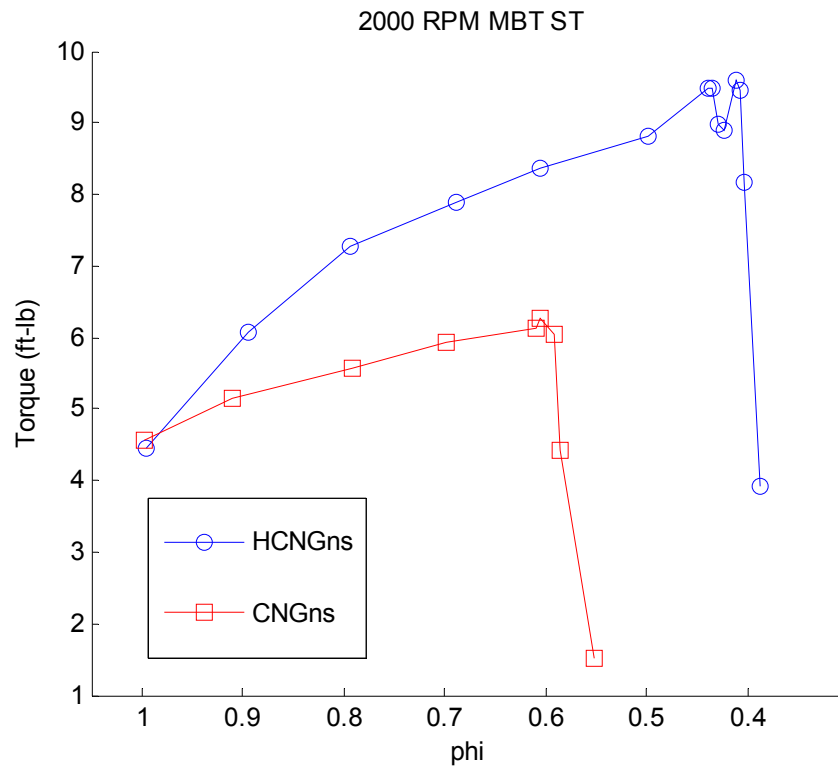


Figure 16: Trends of torque as a function of equivalence ratio show that hydrogen assisted combustion of natural gas provides ability to sustain combustion performance at more lean stoichiometry and provides the means to achieve higher output.

Figure 17 shows that with HCNG the combustion duration is shorter, as a consequence of the faster burn rate provided by hydrogen addition.

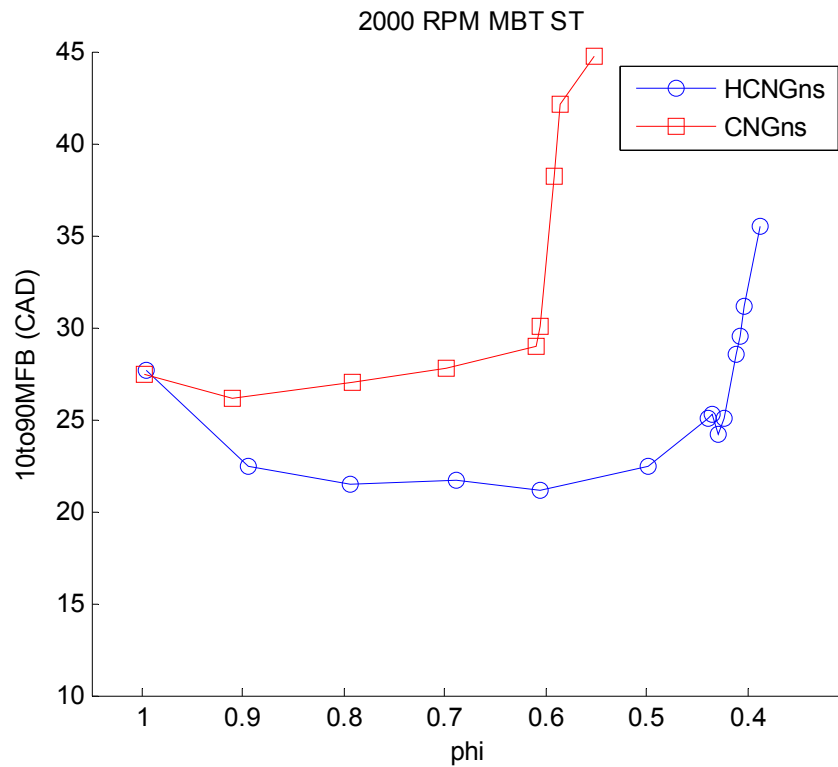


Figure 17: Burn duration as a function of fuel equivalence ratio. The burn duration of CNG and HCNG is the same at stoichiometric AFR, but is significantly shorter for HCNG particularly under lean conditions..

Figure 18 shows the variation of NO_x emissions with stoichiometry for CNG and HCNG and displays the well known trend for SI combustion, which includes a peak in NO_x emissions near stoichiometric ($\phi=1$) conditions and falling off rapidly as combustion becomes more and more lean.

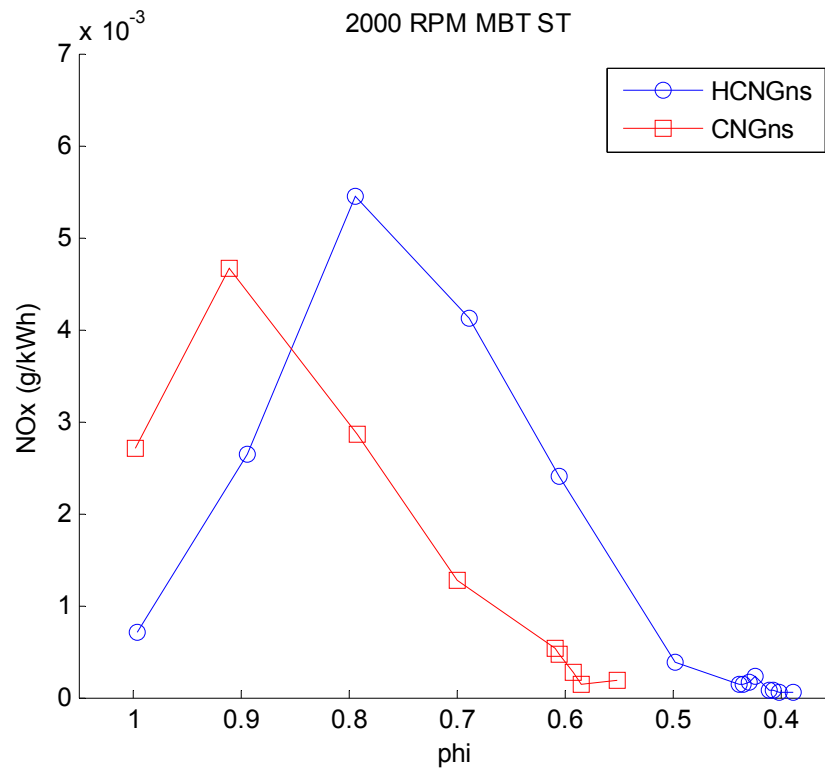


Figure 18: Nox emissions as a function of fuel equivalence ratio.

Effects of Swirl on CNG & HCNG Combustion at 2000 RPM, MBT Timing.

The previous section showed results that coincided with the general findings in the current literature regarding hydrogen assisted combustion of natural gas. However, the published work to date does not attempt to explain the source of the enhancements provided by hydrogen, aside from the notion that the diffusivity of hydrogen is greater than that of CNG in air. The aim of this work is to uncover a scientific explanation for the enhancements of CNG combustion when hydrogen is added.

Starting with the understanding that the diffusivity of hydrogen in air is greater than that of CNG (or methane, for simplicity) in air, and combining this concept with that of the rate of combustion is dependent upon the mixedness of the oxidizer and fuel, the effects of turbulence on the combustion processes of CNG/air and HCNG/air become important.

Figure 18 shows the factors that influence burn rate. The set of experiments at 2000 RPM, MBT timing account for AFR as stoichiometry is swept for both fuels, both with and without intake-induced swirl. The combustion phasing is accounted for, as MBT timing was met for each fuel, in each swirl scenario, at each equivalence ratio. The mixing is a function of the diffusivity of the constituents of air & fuel, the intake temperature, and the swirl. The level of intake-induced swirl is fixed for both CNG and HCNG, but the intake air temperatures may vary depending on the day of testing, and the diffusivities clearly change given the fuel. Heat transfer varies with the energy content of the fuel, and energy required to break the fuel bonds, the resistance at the spark gap associated with the given air fuel mixture, and the composition of the exhaust gases and the relative heat capacities of each.

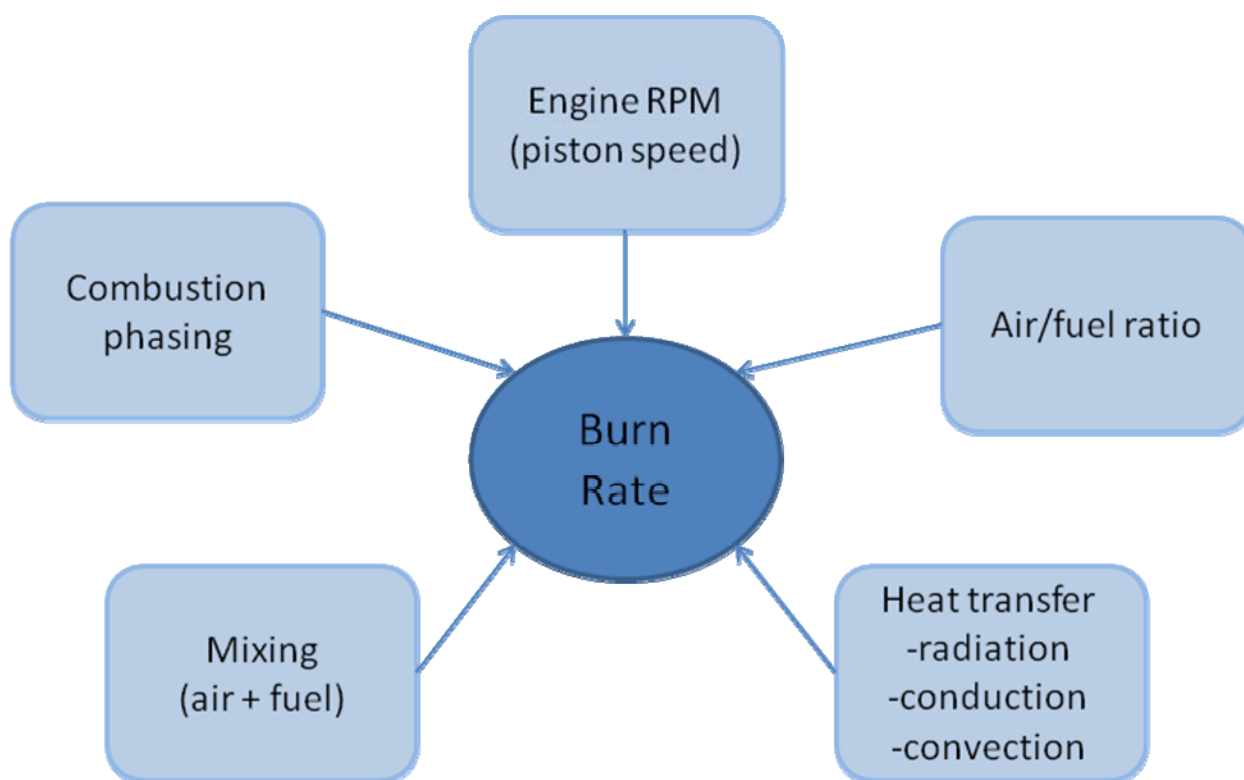


Figure 19: Pictorial view of factors that influence burn rate.

Heywood showed that burn rate of the reactants increases as a function of engine speed [Heywood, 1998]. Additionally, introducing swirl increases the in-cylinder gas velocity, hence increasing engine RPM and introducing intake-induced swirl will increase the burn rate more than increasing RPM or increasing turbulence alone.

This section provides the results and discussion for engine operation at 2000 RPM with MBT spark timing for both CNG and HCNG combustion at various equivalence ratios, with and without intake-induced swirl (via complete blockage of one intake port).

Figure 20 shows that spark timing trends as a function of ϕ for each fuel and swirl condition and shows that swirl enables retarded spark timings. Note that the MBT timing for CNG with intake-induced swirl in the stoichiometric range aligns closely with those for HCNG without swirl – this shows that (regarding MBT timing) hydrogen supplants swirl for CNG. This data also shows that the swirl effects CNG more significantly than HCNG in terms of enabling retarded spark timings, particularly for equivalence ratios richer than 0.7.

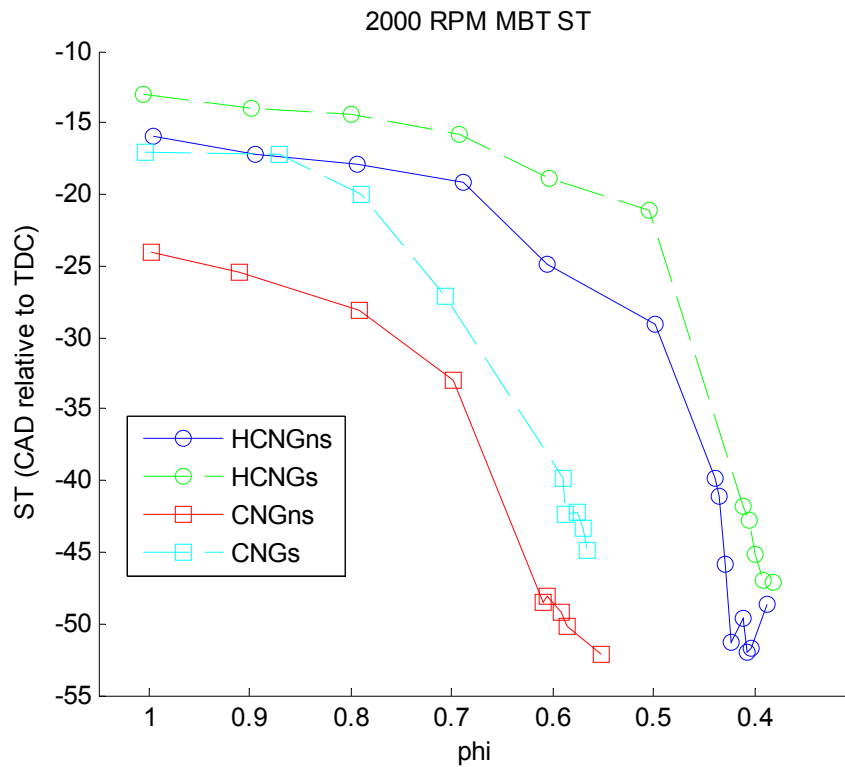


Figure 20: MBT spark timing as a function of equivalence ratio for each fuel in each swirl scenario.

Figure 21 shows the COV% as a function of equivalence ratio for CNG and HCNG without and with swirl. The effect of swirl is to stabilize combustion out to slightly more lean combustion conditions for either CNG or HCNG, but that hydrogen addition along permits the engine to sustain combustion at far more lean conditions than the addition of swirl.

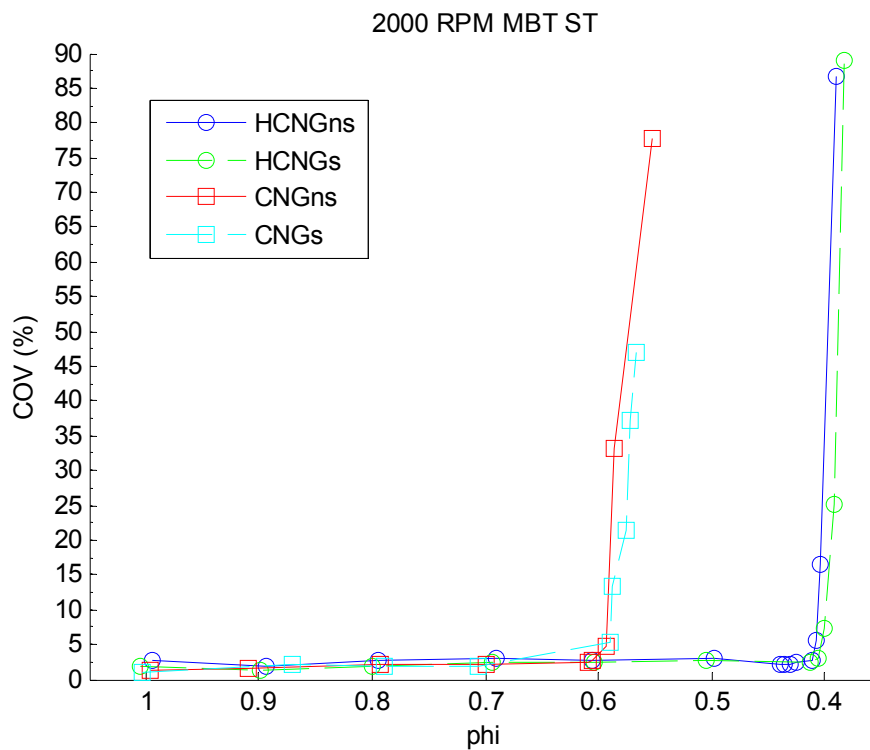


Figure 21: Coefficient of variance as a function of fuel equivalence ratio for CNG and HCNG combustion without and with swirl at MBT spark timing.

Figure 22 shows how the start of combustion varies with stoichiometry for CNG and HCNG without and with swirl. The start of combustion (at MBT spark timing) is more retarded with swirl and for CNG with swirl is similar to that for HCNG without or with swirl. This is evidence that the influence of swirl is as large or larger than the influence of hydrogen addition.

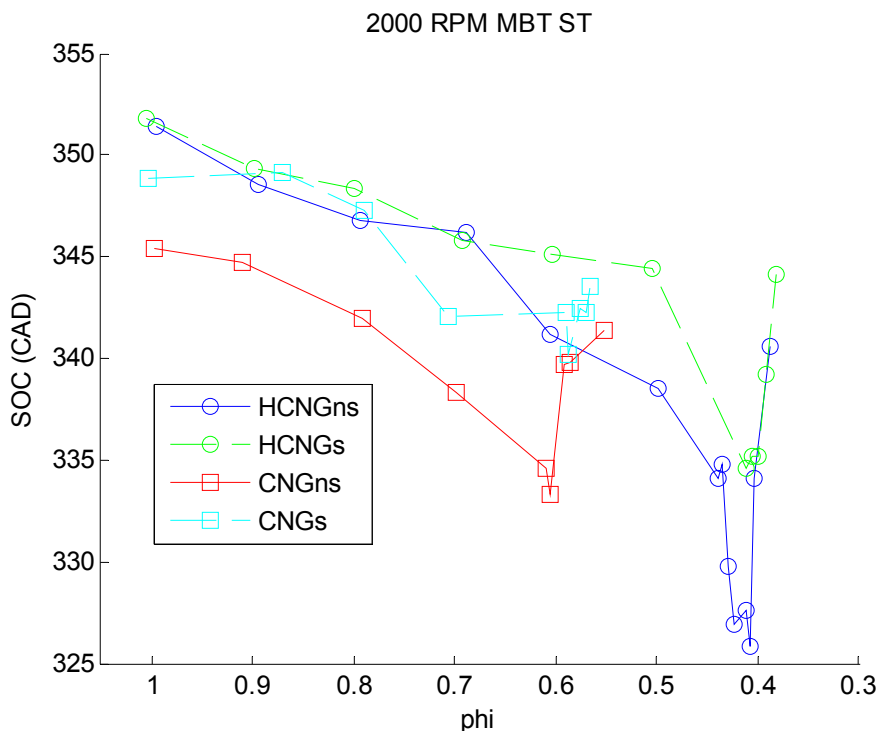


Figure 22: Start of combustion as a function of equivalence ratio for CNG and HCNG without and with swirl. The SOC is retarded when swirl is present, for both fuels, but more significantly so for CNG. The main improvement for HCNG (with swirl) is in the lean range.

Figure 23 shows combustion duration as a function of stoichiometry for CNG and HCNG combustion without and with swirl and indicates that burn duration is decreased with intake-induced swirl for both CNG & HCNG combustion. The trend is generally more significant for CNG than for HCNG. Between $\phi = 0.9$ and $\phi = 0.6$, the burn duration for CNG with swirl is about the same as for HCNG without swirl. The fastest burn durations occur for HCNG with swirl, and are significantly faster than the other three cases. At 2000 RPM, hydrogen and swirl both contribute to the combustion process in terms of increasing the burn rate. Figure 22 also shows that while swirl shortens the burn duration for CNG as much as hydrogen addition does, addition of swirl to CNG does not extend combustion to lean conditions in the manner that hydrogen addition does.

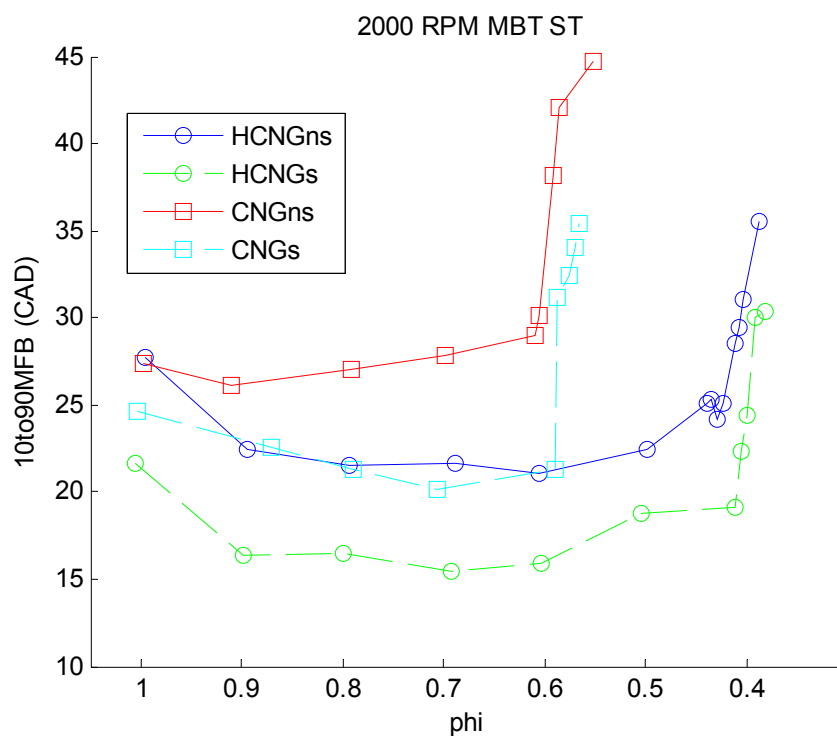


Figure 23: Burn duration (10-90% mass fraction burned) as a function of equivalence ratio for each fuel with and without the presence of intake-induced swirl.

Figure 24 shows the behavior of torque as a function of equivalence ratio. The highest torque output achieved is for HCNG with swirl. HCNG produces more torque than CNG as a function of stoichiometry. And swirl barely improves the torque output for CNG combustion. Coupling this data with the burn duration (Figure 23), burn rate alone does not explain the torque enhancement for HCNG over CNG, neither does SOC.

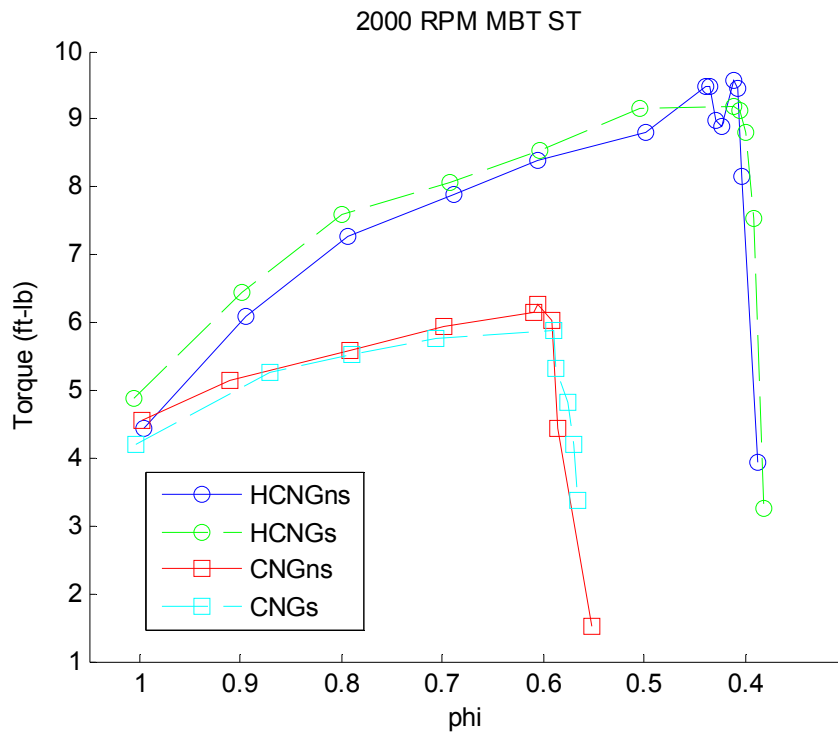


Figure 24: Output torque as a function of equivalence ratio for each fuel and each swirl scenario.

Comparison of the Combustion Characteristics of CNG & HCNG with intake-induced swirl at 2750 RPM, MBT Timing.

In order to further examine the relative impacts of swirl and hydrogen addition on the combustion of CNG, experiments were performed at an elevated engine speed. The SOC occurs closer to top dead center when intake-induced swirl is present for each fuel, as depicted in Figure 25. The effect is more dramatic for CNG compared to HCNG. The trends for both fuels with and without swirl are very similar in nature to those for ST, more so than in the 2000 RPM case.

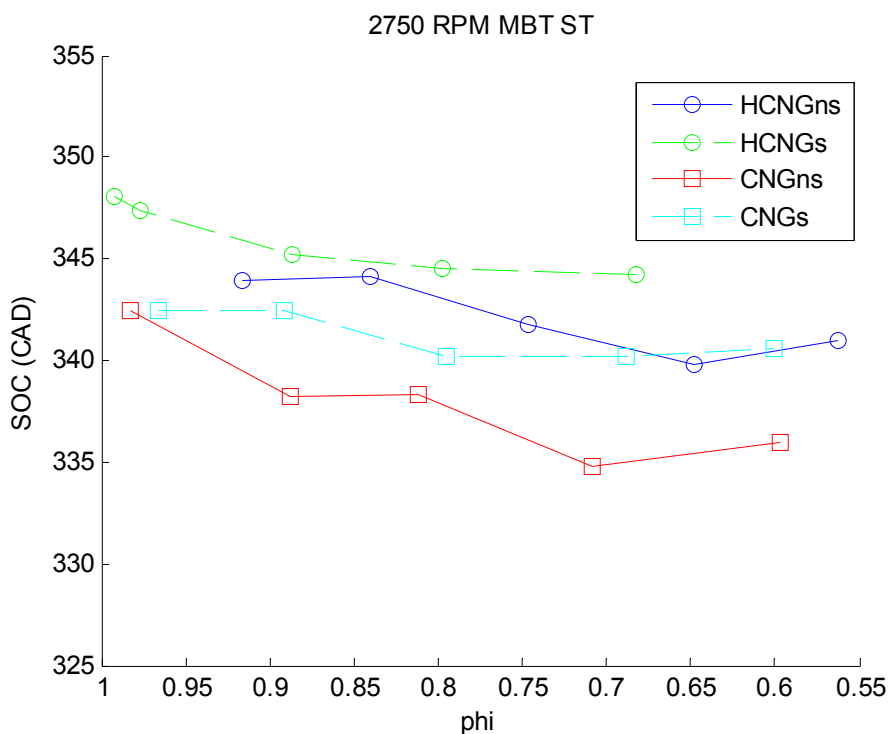


Figure 25: Start of combustion as a function of equivalence ratio.

Swirl decreases the combustion duration for both fuels, as shown in Figure 26. The burn duration is basically the same for CNG and HCNG without swirl. This was not true in the 2000 RPM case. It seems that the contribution that hydrogen had on the burn rate of CNG (without swirl) is not realized at 2750 RPM. The trend diverges (for the no swirl cases) as CNG nears its lean limit. Also, the difference between the burn rates at a given phi is less significant (with swirl) in this case than for 2000 RPM.

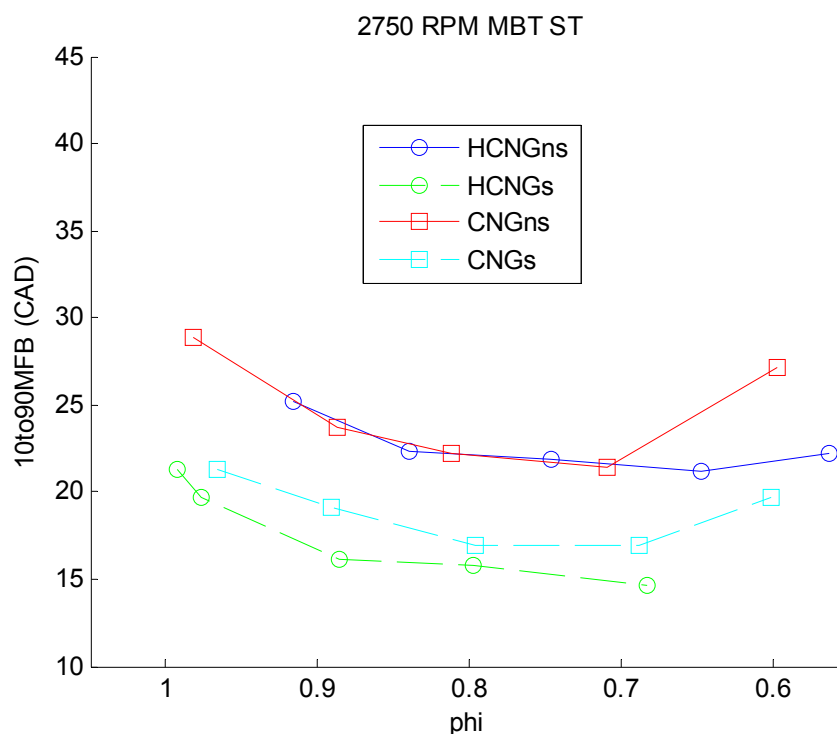


Figure 26: Burn duration (10 to 90% mass fraction burned) as a function of equivalence ratio for CNG and HCNG without and with swirl at MBT spark timing.

Comparison of the Combustion Characteristics of CNG & HCNG with intake-induced swirl at 2000 RPM, with Constant Spark Timing

The results in the previous section showed that swirl combined with faster piston speeds (higher engine RPM of 2750 compared to 2000) resulted in an overall smaller disparity between CNG and HCNG regarding burn rate. However, those results were obtained using MBT spark timing. In order to fully ascertain the effects of swirl and engine speed (piston speed), the affect of combustion phasing should be removed. Hence, the following studies were conducted at constant spark timing as a function of equivalence ratio. The spark timing used for CNG and for HCNG were determined at stoichiometric conditions for each fuel, at a common output condition (1.5 bar BMEP). The spark timing positions (15 CAD BTDC for HCNG and 27 CAD BTDC for CNG) were used for both swirl and non-swirl scenarios. Figure 27 shows the constant spark timings measured from the ST control circuit. The testing methodology required that the load condition be the same for each fuel, at $\phi = 1$, with no intake-induced swirl. The fueling rate for each fuel was held constant for both the no swirl and the intake-induced swirl cases.

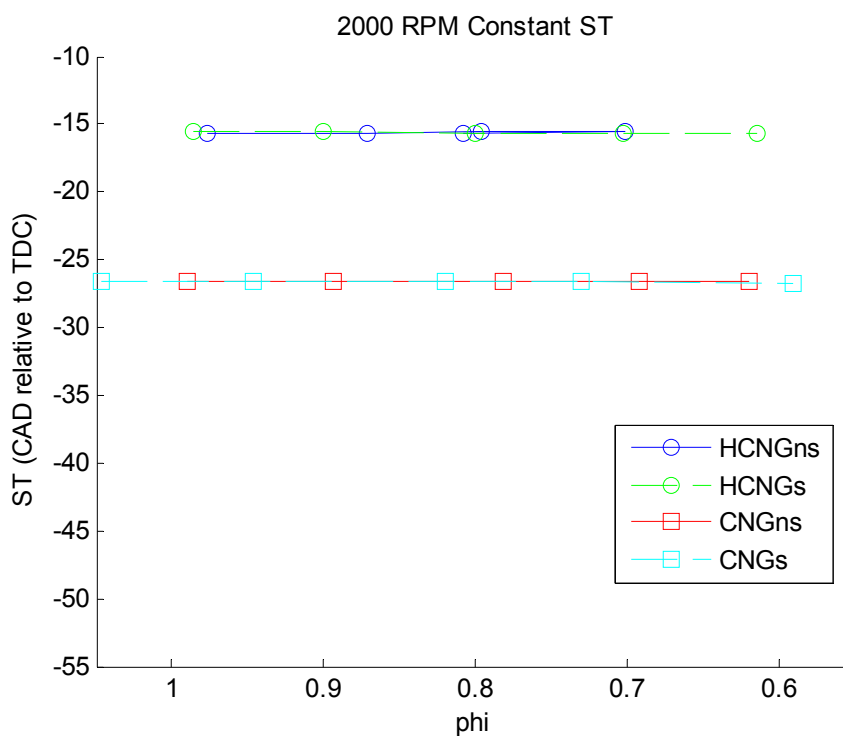


Figure 27: MBT spark timing as a function of equivalence ratio, as determined for the non-swirl case.

The start of combustion (SOC) at constant spark timing is influenced by stoichiometry when ST is held constant (Figure 28). These profiles also show that swirl improves SOC for both fuels, and suggest that the effect of swirl on SOC is more significant for CNG than for HCNG.

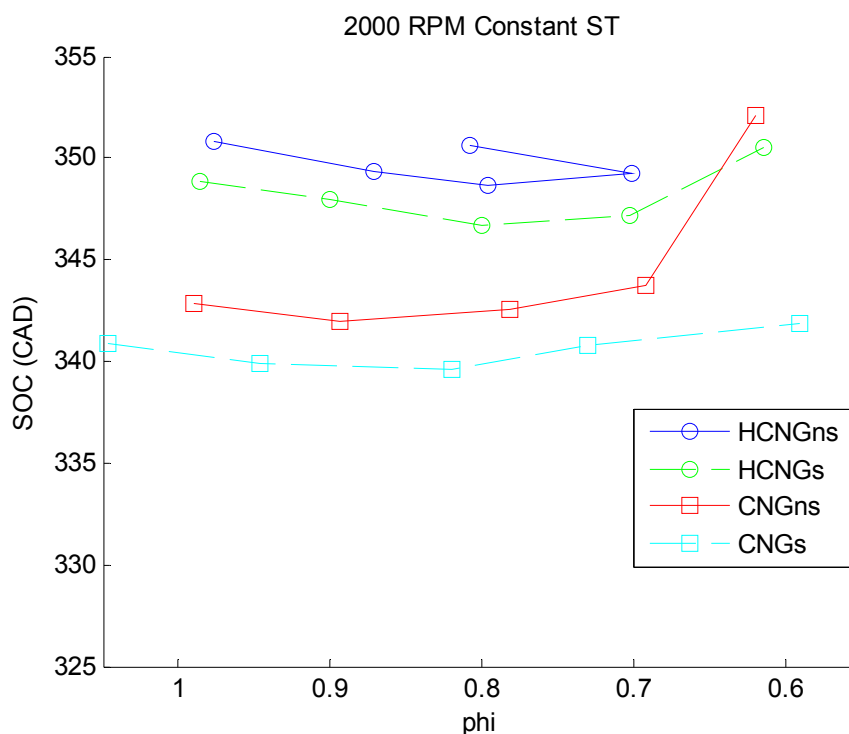


Figure 28: Start of combustion, for spark timing set at MBT spark timing from the non-swirl case, as a function of equivalence ratio.

The data shown in Figure 29 show that swirl increases the heat release-derived fuel burn duration for both fuels at constant spark timing. CNG and HCNG have similar burn rates without swirl, indicative that hydrogen alone does not enhance the burn rate at constant spark timing. Recall that the spark timing was chosen based on 1.5 bar BMEP at stoichiometric for each fuel without intake-induced swirl. CNG with swirl burns faster (slightly) than HCNG with swirl. [Note that the 10-90% MFB values for CNGs & HCNGs at $\phi = 0.6$ are not shown but are near 116 CAD].

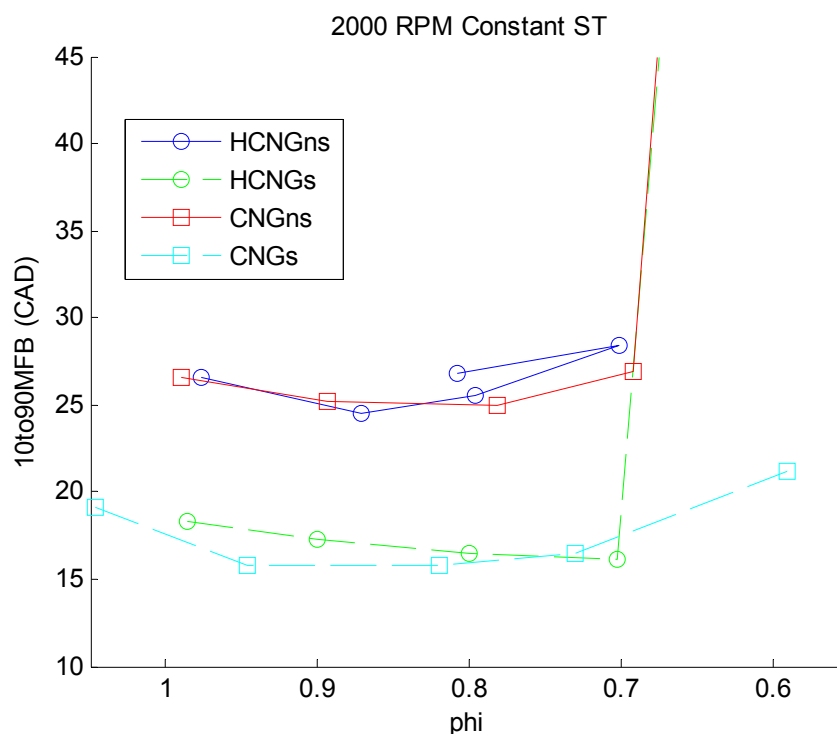


Figure 29: Combustion duration, for spark timing set at MBT spark timing from the non-swirl case, as a function of equivalence ratio.

Swirl improves the start of combustion, but does not increase the burn rate for either fuel. Hydrogen both improves the start of combustion and the burn rate compared to both cases with CNG.

High-level examination of the influence of intake-induced swirl and hydrogen on the combustion kinetics of CNG (2000 RPM, MBT Timing, lean stoichiometries)

Figure 30 shows that there is a significant difference in MBT timing for CNG with and without swirl, and practically no difference for HCNG with and without swirl, in this lean stoichiometric range.

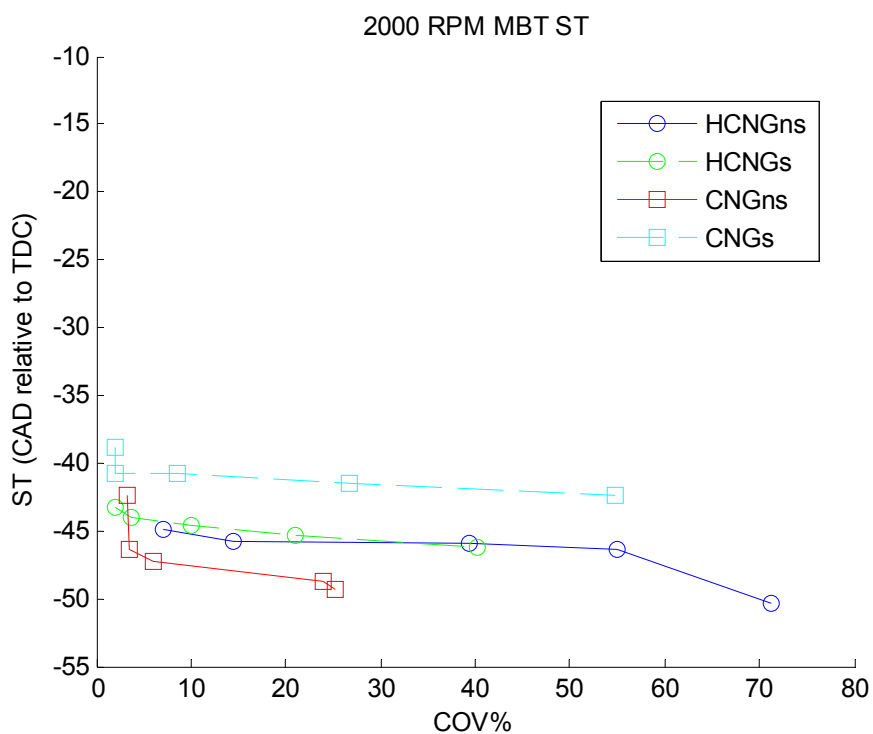


Figure 30: Spark timing versus coefficient of variance for CNG and HCNG without and with swirl with spark timing set to the MBT timing for combustion without swirl.

Figure 31 shows that CNG without swirl experiences the most significant delay between ST and SOC, and that CNG combustion experiences the greatest change with the addition of swirl, for this spark timing approach.

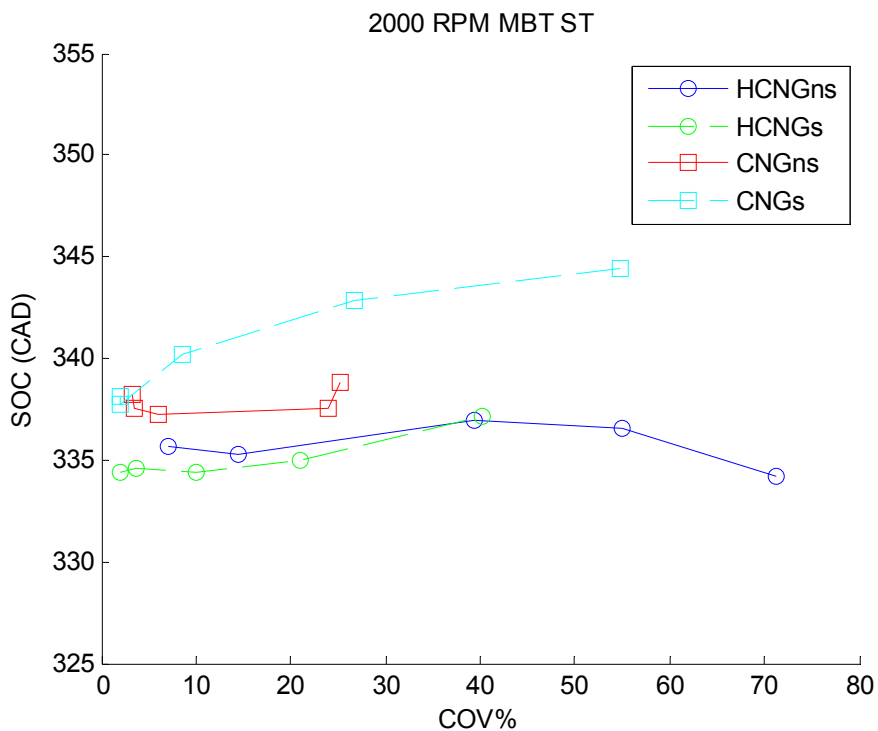


Figure 31: Start of combustion for CNG and HCNG without and with swirl with spark timing set to the MBT timing for combustion without swirl.

Figure 32 shows that the burn rates for CNG and HCNG are quite similar without swirl, until the COV exceeds 25%. The burn duration is significantly faster for both swirl when swirl is present. HCNG with swirl improves burn rate over CNG with swirl. This as well as the trends in Figure 23 seem to suggest a synergetic behavior when both hydrogen and swirl are present.

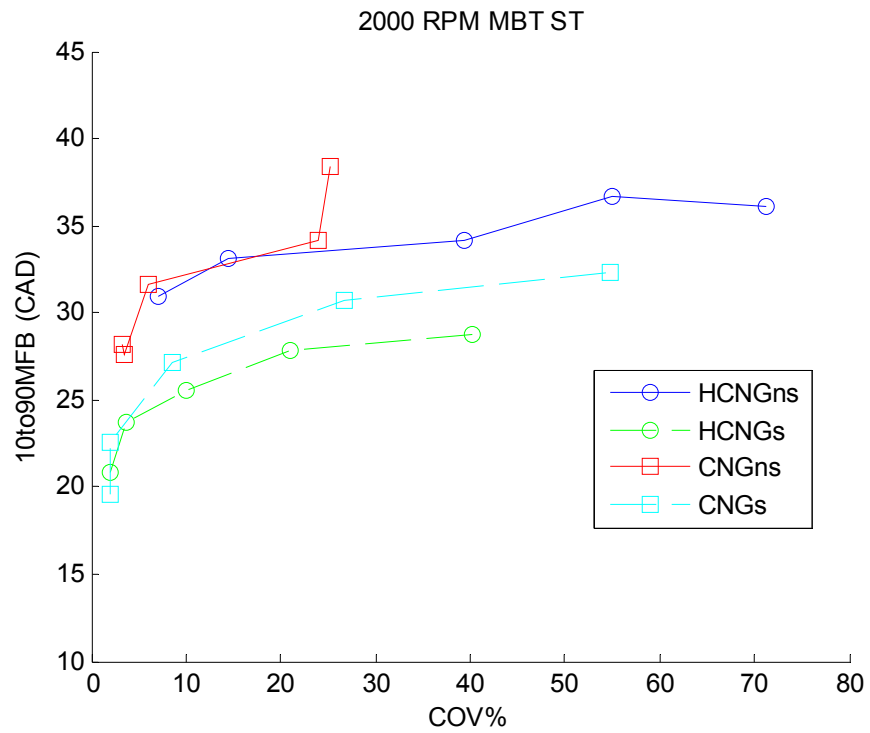


Figure 32: Combustion duration versus coefficient of variance for CNG and HCNG without and with swirl with spark timing set to the MBT timing for combustion without swirl.

Task 1.2 Numerical Simulation of SI Engine Comb. with HCNG Fueling

Executive Summary

In the work under this task, the influence of hydrogen addition to premixed, steady - state, one - dimensional methane/air flames under spark ignition engine conditions is discussed. Three basic studies were performed: changes in the flame structure due to the change in the hydrogen concentration for a fixed equivalence ratio, influence of the diffusion coefficient of hydrogen on flame structure and exhaust - gas recirculation. For the first study, in general, there has been an earlier occurrence of the reaction zone, earlier and higher peaks for key intermediate species and reduction in the NO_x with hydrogen enrichment. Intermediate species OH, O and H have been considered to be important in the rate of reactions $\text{OH} + \text{CH}_4 \rightarrow \text{CH}_3 + \text{H}_2\text{O}$ and $\text{O} + \text{CH}_4 \rightarrow \text{CH}_3 + \text{OH}$. For the second study, little influence of the low diffusion coefficient of hydrogen on the flame has been observed for this configuration. For the third study, it was observed that there has been a reduction in the peak temperature, delay in the occurrence of the reaction zone and reduction and delayed occurrence in the peaks of key intermediate species with EGR addition. The reduction in peak temperature and delay in the occurrence of the reaction zone prevents the formation of thermal NO and hence NO_x reduces. In this thesis, a computational approach is applied to investigate autoignition and NO_x emissions for hydrogen-hydrocarbon fuel blends with air or air-EGR blends. It is hypothesized that ignition timing might be controlled via a pilot injection of diesel fuel into a premixed hydrogen/air/EGR mixture.

The outcome of this work resulted in the MS Thesis of Saket Priyadarshi, which is included is included in this report as Appendix A-1.2

Task 1.3 Field Vehicle Instrumentation and Combustion Analysis

Executive Summary

While hydrogen fuel-cell vehicles have been the focus of recent media attention, near term implementation of hydrogen as a combustion enhancer is a more reliable pathway for wide-scale hydrogen utilization within the next ten years. Through combustion analysis, hydrogen addition to natural gas has shown to increase thermal efficiency and reduce CO, NO and hydrocarbon emissions (UHC) in studies on stationary test cell engines. On-road vehicle studies testing hydrogen-natural gas blends show emissions benefits and increase in fuel economy. However, on-road tests lack exhaustive combustion analysis to explain what is occurring in the cylinder. In this study, the effect of a 33 percent volumetric blend of hydrogen (HCNG) on natural gas combustion was investigated in a 5.4L spark-ignited engine in a Ford E-250 van. In-cylinder combustion analyses were performed and untreated exhaust emissions were measured at 15 and 30 mph with road loads of 10, 20 and 30 horsepower. Hydrogen increased the flame speed reducing time for flame kernel development and combustion duration. However, the hotter burn lost more heat to the surroundings and thermal efficiency of HCNG was lower than natural gas. Increasing engine speeds magnified reduction in combustion duration created by hydrogen. As load on the engine increased, hydrogen-influenced reduction on burn time was reduced. Heat and throttling losses reduced the thermal efficiency of the combustion. More complete combustion with hydrogen reduced carbon based emissions and bulk cylinder temperature increase drove increased NO formation.

The outcome of this work resulted in the MS Thesis of Jamie Clark, which is included is included in this report as Appendix A-1.3.

Task 1.4 Examination of Selective NOx Recirc.(SNR) in HCNG-Fueled Engines

Under this task, we began preparation of the hardware needed to dispense NO to the intake air of the engine test stands, but delayed the start of work while students completed their theses and their thesis defenses. The experimental apparatus was put into place and was ready for these experiments in FY08Q4, but the Hydrogen Fueling Station had an equipment failure which to date has not been repaired. Without the station, we could not refill our HCNG tank. Thus, this task could not be completed this quarter.

Task 2.1 Hydrogen Assisted Combustion Studies in a CI Engine

Executive Summary

Under this task, experimental studies were performed on the combustion of diesel fuel under conventional CI engine operation and under advanced combustion operation, without and with the addition of hydrogen to the intake air. Additional work was performed for comparison with the hydrogen addition studies that included addition of dimethyl ether and methane to the intake air of the diesel engine to consider the influence of cetane number of the fumigated fuel on the behavior of the engine.

First, the effect of hydrogen assisted diesel combustion on conventional and advanced combustion modes was investigated on a DDC/VM Motori 2.5L, 4- cylinder, turbocharged, common rail, direct injection light-duty diesel engine, with exhaust emission being the main focus. Hydrogen was substituted for diesel fuel on a percent energy basis of 0%, 2.5%, 5%, 7.5%, 10% and 15%. The conventional combustion modes studied consisted of four engine combinations of speed and load (1800 rpm at 25% of maximum output, 1800 rpm at 75% of maximum output, 3600 rpm at 25% of maximum output, and 3600 rpm at 75% of maximum output). A significant retarding of injection timing by the diesel fuel injection timing map in the engine's electronic control unit (ECU) was observed during the increased aspiration of hydrogen. The retarding of injection timing resulted in significant emission reductions, however, the same emission reductions were achieved without aspirated hydrogen by manually retarding the injection timing. Subsequently, hydrogen assisted diesel combustion was conducted, with the pilot and main injection timings locked, to study the effects caused directly by hydrogen addition. Hydrogen assisted diesel combustion resulted in a modest increase of NO_x emissions and a NO / NO₂ trade-off in which NO emissions decreased and NO₂ emissions increased, with NO₂ becoming the dominate NO_x component in some circumstances. Increased aspiration of hydrogen resulted in PM, and HC emissions which fluctuated with speed and load. Predominantly, CO and CO₂ decreased with the increase of hydrogen. The aspiration of hydrogen into the engine modestly decreased fuel economy due to the reduction of oxygen in the cylinder charge. In the advanced combustion portion of the study, the engine was operated under a partially-premixed charge compression ignition PCCI mode known as high efficiency clean combustion (HECC), in which NO_x and PM emissions dramatically decreased while fuel economy was maintained. Hydrogen assisted diesel combustion was performed while the engine operated in the HECC mode, which resulted in emissions and combustion impacts similar to those observed in the conventional combustion modes.

Second, The second study investigated the NO_x reductions which could be achieved with a mixed mode combustion process utilizing a fumigated fuel and a pilot injection of diesel fuel. In this research, the fumigated fuel was dimethyl ether (DME) and DME/Methane blends, while the pilot injection fuel was ULSD. Several sets of experiments were performed to study the ignition of the fumigated fuel, and its impact on the NO_x emissions. In the first set of experiments, the DME concentration was spanned over a range of 15 to 44% energy equivalent of the total fuel requirement. An approximately 20% reduction in NO_x emissions

was observed up to 35% DME energy equivalent. As the energy equivalent increased above 35%, the NO_x emissions began to increase with the increase in the peak of the high temperature heat release (HTHR). While the NO_x emissions decreased, there was also a significant shift in the NO to NO₂ conversion for all DME fumigation test conditions in comparison to the baseline diesel cases. For 25% DME energy equivalent, the injection timing of the pilot diesel was retarded and a reduction in the NO_x emissions was observed. The low temperature heat release (LTHR) and the HTHR remained constant in magnitude and timing while the injection timing of the pilot diesel was retarded. The peak pressure for the premixed and diffusion portions merged, with increasing premixed DME combustion. With retarded injection timing, NO_x reduction occurred as a result of the decrease in the bulk cylinder temperature and in the combustion duration before cylinder quenching from the exhaust stroke. In the second set of experiments, the intake air temperature was increased to study the impact on NO_x and the mixed mode combustion process. While the amount of DME residual in the exhaust decreased along with the total hydrocarbon and CO emissions, the NO_x emissions increased with increasing bulk cylinder temperature. For the speed and load used in this experiment, there was enough fuel and compression to combust most of the fuel, yet not enough to complete the combustion of the unburned hydrocarbons and CO. While air heating shifted the stoichiometry of the fuel and air mixture by reducing the density of air, the heating led to increased NO_x with reduction in the NO to NO₂ conversion. This may indicate that the system was above the low temperature range for this conversion to occur. In the third set of experiments, a small amount of Methane was introduced into the system to study the impact on the cetane number of the fumigated fuel. On a brake specific power basis, the Methane addition reduced the NO_x emissions more than with only DME, however the NO to NO₂ conversion was lower. NO_x emissions were further reduced by retarding the injection timing, but increased with increasing intake air temperature. Through the use of the intake air heating, it was observed that the ignition of the DME/Methane blend was advanced with a smaller LTHR and a higher HTHR. While NO_x emissions increased with the increase in bulk cylinder temperature, only the NO emissions increased while NO₂ remained constant. Gaseous emissions analysis showed that the heating caused greater conversion of the Methane and DME during combustion.

The primary outcomes of the work under this task resulted in the MS Thesis of Greg Lilik and a portion of the PhD Thesis of Elana Chapman, which are included in this report as Appendix A-2.1.A and Appendix A-2.1.B, respectively. Dr. Chapman's thesis included two separate studies, organized around a theme of using combustion strategy and fuel formulation to reduce NO_x emissions.

Addendum

Through the review of the thesis work completed under this task, we determined some follow up experiments to perform, specifically in which we removed EGR to more exclusively probe the impact of hydrogen. We also considered the possibility of optimizing the timing of diesel injection when hydrogen is being fumigated, which yielded some evidence that at retarded injection timing the benefits of hydrogen are more significant than at the normal (baseline programming for our engine) injection timing.

Also, with our industrial partner, Asemblon, we continue looking at options for incorporating direct injection of hydrogen along with the direct injection of diesel fuel. This may permit higher levels of hydrogen utilization.

Below are results from these experiments described above, for hydrogen assist without EGR, hydrogen assist with single injection and “optimization” of injection timing when using hydrogen assist. These experiments were performed in collaboration with and with input from our partner Asemblon. We have referred to these tests as Phase 2 (where our DOE program plan represented Phase 1) and Test 0 (sticking with intake fumigation with H₂). Under Phase 2, Test 1 and Test 2 will involve direct injection of hydrogen.

Test 0.1

Hydrogen assisted diesel combustion, without EGR and unbound injection timing

Hydrogen assisted diesel combustion was conducted on the DDC 2.5L at the EMS Energy Institute, without EGR, but with floating injection timing at 1800 at 25% of maximum torque, 1800 at 75% of maximum torque, 3600 at 25% of maximum torque, and 3600 at 75% of maximum torque.

Table: Injection timings induced by the addition of fuel energy at 0%, 2.5%, 7.5% and 15% on the energy basis.

	1800 @ 25%		1800 @ 75%		3600 @ 25%		3600 @ 75%	
H2%	Main (ATDC)	Pilot (ATDC)	Main (ATDC)	Pilot (ATDC)	Main (ATDC)	Pilot (ATDC)	Main (ATDC)	Pilot (ATDC)
0	2.88	-17.41	-6.15	-38.25	-12.25	-56.78	-13.57	-58.07
2.5	2.88	-17.41	-5.76	-37.27	-12.11	-56.61	-13.57	-58.07
7.5	3.00	-17.30	-3.10	-32.06	-12.05	-56.55	-14.50	-59.00
15	3.11	-17.18	-1.10	-26.40	-11.90	-56.40	-14.60	-59.10

The effect of hydrogen aspiration on injection timing shift was most prominent at 1800 rpm at 75% maximum torque. This is because the injection timing map of the DDC 2.5L was programmed to have the most variation at 1800 rpm, which is the speed of the maximum rated torque of the engine. Given so, a small change in fuel quantity for this speed was programmed to have larger steps in timing change. The screen shot below shows the actual injection timing map of the main injection of the DDC 2.5L engine. The horizontal axis of the map is engine speed in rpm and the vertical axis is fuel injection volume in mm³.

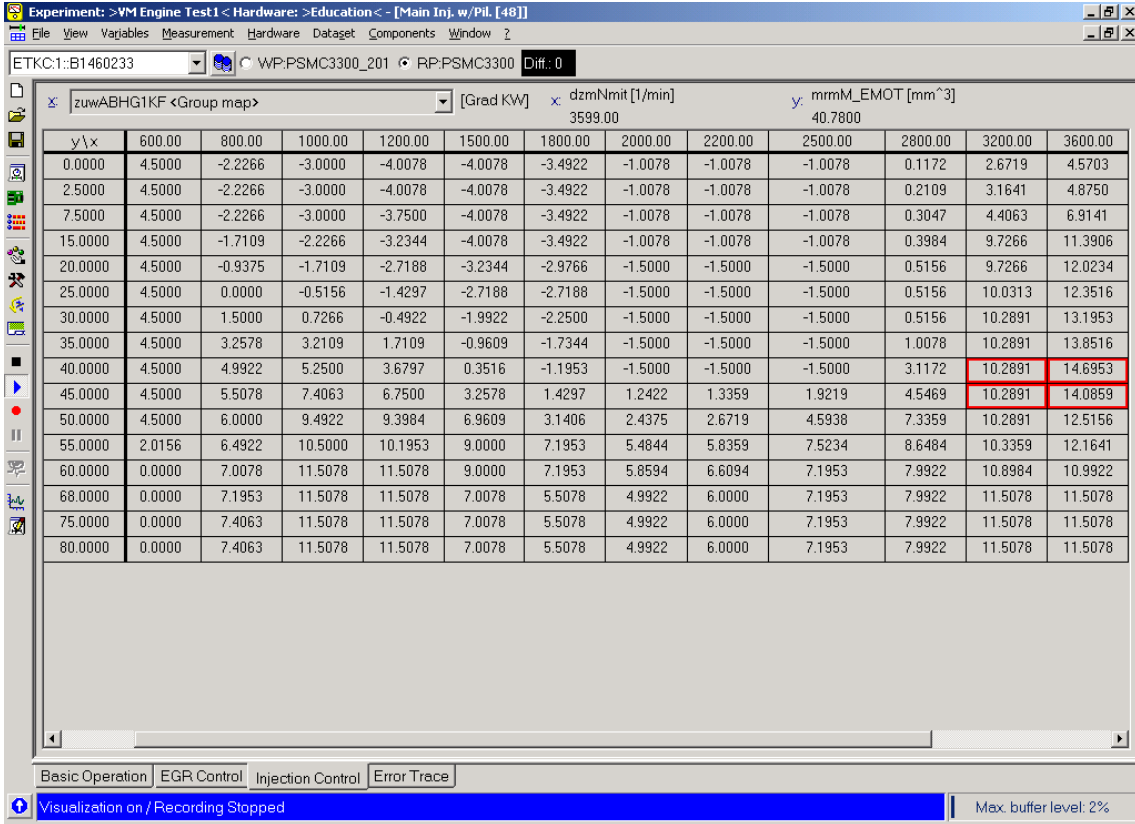


Figure 1: Screen shot of DDC 2.5L engine while operating at 3600 rpm at 75% of torque.

NO_x Emissions

NO _x [g/kW.h]				
H2%	1800 @ 25%	1800 @ 75%	3600 @ 25%	3600 @ 75%
0	2.84	5.22	5.35	4.83
2.5	3.04	5.03	5.41	4.96
7.5	3.16	4.19	5.56	5.27
15	3.26	3.65	5.46	5.60

NOX Percent Difference				
H2%	1800 @ 25%	1800 @ 75%	3600 @ 25%	3600 @ 75%
0	N/A	N/A	N/A	N/A
2.5	6.79	-3.64	1.19	2.65
7.5	10.79	-21.76	3.87	8.75
15	13.76	-35.38	1.98	14.83

NO Emissions

NO [g/kW.h]				
H2%	1800 @ 25%	1800 @ 75%	3600 @ 25%	3600 @ 75%
0	2.14	5.05	3.25	4.67
2.5	1.74	4.67	2.69	4.56
7.5	1.51	3.77	2.36	4.67
15	1.48	3.27	1.98	4.96

NO Percent Difference				
H2%	1800 @ 25%	1800 @ 75%	3600 @ 25%	3600 @ 75%
0	N/A	N/A	N/A	N/A
2.5	-20.53	-7.70	-18.81	-2.53
7.5	-34.19	-28.90	-31.76	-0.04
15	-36.16	-42.65	-48.22	5.99

NO₂ Emissions

NO2 [g/kW.h]				
H2%	1800 @ 25%	1800 @ 75%	3600 @ 25%	3600 @ 75%
0	0.70	0.17	2.11	0.16
2.5	1.30	0.36	2.73	0.40
7.5	1.65	0.42	3.21	0.60
15	1.78	0.38	3.47	0.64

NO2 Percent Difference				
H2%	1800 @ 25%	1800 @ 75%	3600 @ 25%	3600 @ 75%
0	N/A	N/A	N/A	N/A
2.5	59.69	71.12	25.75	88.10
7.5	80.58	84.91	41.46	117.32
15	86.66	75.37	49.05	121.54

HC Emissions

HC [g/kW.h]				
H2%	1800 @ 25%	1800 @ 75%	3600 @ 25%	3600 @ 75%
0	0.80	0.12	1.19	0.23
2.5	0.79	0.10	1.29	0.22
7.5	0.78	0.07	1.30	0.22
15	0.73	0.07	1.31	0.24

HC Percent Difference				
H2%	1800 @ 25%	1800 @ 75%	3600 @ 25%	3600 @ 75%
0	N/A	N/A	N/A	N/A
2.5	-1.36	-21.11	8.06	-4.53
7.5	-2.22	-46.34	9.28	-3.71
15	-9.58	-56.78	10.07	6.21

CO₂ Emissions

CO ₂ [g/kW.h]				
H2%	1800 @ 25%	1800 @ 75%	3600 @ 25%	3600 @ 75%
0	2.49	2.32	13.74	0.74
2.5	2.38	2.31	13.47	0.71
7.5	2.22	2.49	12.30	0.66
15	1.88	1.75	11.28	0.51

CO ₂ Percent Difference				
H2%	1800 @ 25%	1800 @ 75%	3600 @ 25%	3600 @ 75%
0	N/A	N/A	N/A	N/A
2.5	-4.50	-0.58	-1.99	-3.55
7.5	-11.48	7.23	-11.07	-11.68
15	-28.08	-27.93	-19.65	-36.73

CO Emissions

CO [g/kW.h]				
H2%	1800 @ 25%	1800 @ 75%	3600 @ 25%	3600 @ 75%
0	867.54	789.28	1030.97	773.87
2.5	852.33	777.94	1009.32	758.94
7.5	821.94	759.08	982.63	726.33
15	778.98	717.13	910.51	649.78

CO Percent Difference				
H2%	1800 @ 25%	1800 @ 75%	3600 @ 25%	3600 @ 75%
0	N/A	N/A	N/A	N/A
2.5	-1.77	-1.45	-2.12	-1.95
7.5	-5.40	-3.90	-4.80	-6.34
15	-10.76	-9.58	-12.41	-17.43

Brake specific fuel consumption

BSFC [g/kW.h]				
H2%	1800 @ 25%	1800 @ 75%	3600 @ 25%	3600 @ 75%
0	10.71	8.98	14.25	10.15
2.5	10.79	9.11	14.44	10.16
7.5	11.03	9.42	14.59	10.12
15	11.21	9.65	14.82	9.95

BSFC Percent Difference				
H2%	1800 @ 25%	1800 @ 75%	3600 @ 25%	3600 @ 75%
0	N/A	N/A	N/A	N/A
2.5	0.82	1.42	1.31	0.16
7.5	3.01	4.70	2.36	-0.22
15	4.56	7.16	3.87	-1.98

Particulate emissions

PM [g/kW.h]				
H2%	1800 @ 25%	1800 @ 75%	3600 @ 25%	3600 @ 75%
0	0.39	0.15	0.49	0.16
2.5	0.38	0.14	0.56	0.15
7.5	0.39	0.21	0.57	0.13
15	0.37	0.25	0.54	0.12

PM Percent Difference				
H2%	1800 @ 25%	1800 @ 75%	3600 @ 25%	3600 @ 75%
0	N/A	N/A	N/A	N/A
2.5	-0.56	-7.66	13.00	-3.71
7.5	0.03	33.79	13.39	-19.30
15	-3.94	51.08	8.08	-30.46

To summarize the data, the 1800 rpm at 75% of maximum torque was the only mode to show significant injection timing shift due to hydrogen aspiration. A significant retardation of injection timing resulted in emissions and fuel consumption rates which are typical of late injection strategies. Heat release data, pressure trace data and needle lift data for this Test 0.1 were recorded and are available, however they are not displayed in this document because they are not informative.

Test 0.2

Effect of Pilot injection on hydrogen aspiration

This section explains the reasoning being diesel injection optimization for hydrogen aspiration being focused on single pulse injection. Dual pulse diesel injection is the injection strategy used for currently manufactured diesel engines. The use of a pilot injection reduces the rapid increase of pressure in the cylinder by adding fuel to the cylinder over a gradual period of time with two injections. This strategy reduces engine noise and reduces NO_x emissions.

The figure below displays the rate of heat release and needle lift with hydrogen substitution spanning from 0% to 50% on an energy basis. The injection timing was unlocked. The needle lift sensor is inherently noisy at low speed and low load operation, however it can be seen that the injection timing was not significantly shifted by hydrogen substitution. The main injection peak at 50% hydrogen substitution is noticeably decreased, reflecting a decrease in diesel injection. The significance of this plot is observed in the rate of heat release. As seen in previous work, the addition of hydrogen via aspiration increases the heat release in the pilot injection and decreases the rate of heat release in the main injection. With the majority of the heat release occurring at the early injection timing of the pilot injection, large quantities of hydrogen, in essence, act to advance injection timing. Advanced injection timing is known to increase NO_x emissions and decrease PM emissions in terms of the NO_x-PM trade-off associated conventional diesel combustion.

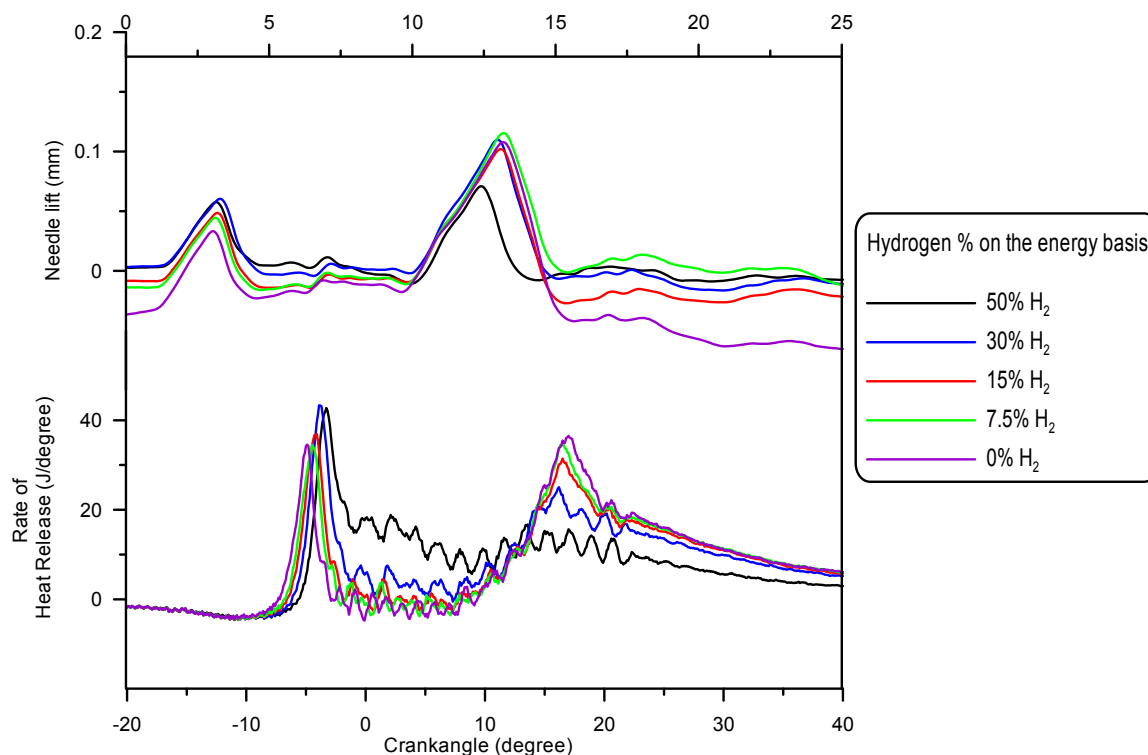


Figure 2: Dual injection at 1800 rpm at 25% torque with energy substitution at 0%, 7.5%, 15%, 30% and 50% on the energy basis.

NO_x:

NOX [g/kW.h]	
H2%	1800 @ 25%
0	2.84
2.5	3.04
7.5	3.16
10	3.16
15	3.26
30	3.58
50	4.12

NOX Percent Difference	
H2%	1800 @ 25%
0	N/A
2.5	6.79
7.5	10.79
10	10.66
15	13.76
30	23.20
50	36.97

NO [g/kW.h]	
H2%	1800 @ 25%
0	2.14
2.5	1.74
7.5	1.51
10	1.45
15	1.48
30	1.66
50	2.61

NO Percent Difference	
H2%	1800 @ 25%
0	N/A
2.5	-20.53
7.5	-34.19
10	-38.24
15	-36.16
30	-24.79
50	20.01

NO2 [g/kW.h]	
H2%	1800 @ 25%
0	0.70
2.5	1.30
7.5	1.65
10	1.71
15	1.78
30	1.92
50	1.51

NO2 Percent Difference	
H2%	1800 @ 25%
0	N/A
2.5	59.69
7.5	80.58
10	83.44
15	86.66
30	92.81
50	73.29

HC [g/kW.h]	
H2%	1800 @ 25%
0	0.80
2.5	0.79
7.5	0.78
10	0.76
15	0.73
30	0.63
50	0.62

HC Percent Difference	
H2%	1800 @ 25%
0	N/A
2.5	-1.36
7.5	-2.22
10	-4.54
15	-9.58
30	-23.18
50	-25.91

CO [g/kW.h]	
H2%	1800 @ 25%
0	2.49
2.5	2.38
7.5	2.22
10	2.11
15	1.88
30	1.22
50	0.58

CO Percent Difference	
H2%	1800 @ 25%
0	N/A
2.5	-4.50
7.5	-11.48
10	-16.37
15	-28.08
30	-68.57
50	-124.67

CO2 [g/kW.h]	
H2%	1800 @ 25%
0	867.54
2.5	852.33
7.5	821.94
10	799.25
15	778.98
30	647.63
50	414.56

CO2 Percent Difference	
H2%	1800 @ 25%
0	N/A
2.5	-1.77
7.5	-5.40
10	-8.19
15	-10.76
30	-29.03
50	-70.66

BSFC [g/kW.h]	
H2%	1800 @ 25%
0	10.71
2.5	10.79
7.5	11.03
10	10.96
15	11.21
30	11.29
50	10.76

BSFC Percent Difference	
H2%	1800 @ 25%
0	N/A
2.5	0.82
7.5	3.01
10	2.32
15	4.56
30	5.28
50	0.55

H2 Flow Rate [g/s]	
H2%	1800 @ 25%
0	0.00
2.5	0.01
7.5	0.03
10	0.04
15	0.06
30	0.12
50	0.21

In summary, dual diesel injection strategies resulted in an advancement of the rate of heat release which negatively effected NO_x emissions. Fuel efficiency is observed to be reduced with the advancement of heat release, due to early combustion which works against the compression stroke of the engine. An NO-NO₂ shift was observed with an increase of hydrogen from 2.5% to 30%. At 50% hydrogen substitution an anomaly occurs where the NO-NO₂ shift did not occur and fuel efficiency returned to near base levels. The anomaly could indicate that 50% hydrogen had induced the engine to operate in an advance combustion mode. Addition data points are required to verify the trend.

In this data set, carbon emissions of incomplete combustion (CO and HC) are observed to dramatically decrease with the increased addition of hydrogen. This occurred for two plausible reasons: a decrease of carbon fuel and an increased residence time for complete combustion of fuel. However, it should be noted that CO and HC are less worrisome diesel emissions, as they can be removed in after treatment.

Single injection locked at default injection timing

In further exploration, large quantities of hydrogen were aspirated into the engine at 1800 rpm and 25% of maximum torque at the default single injection timing given by the engines ESU.

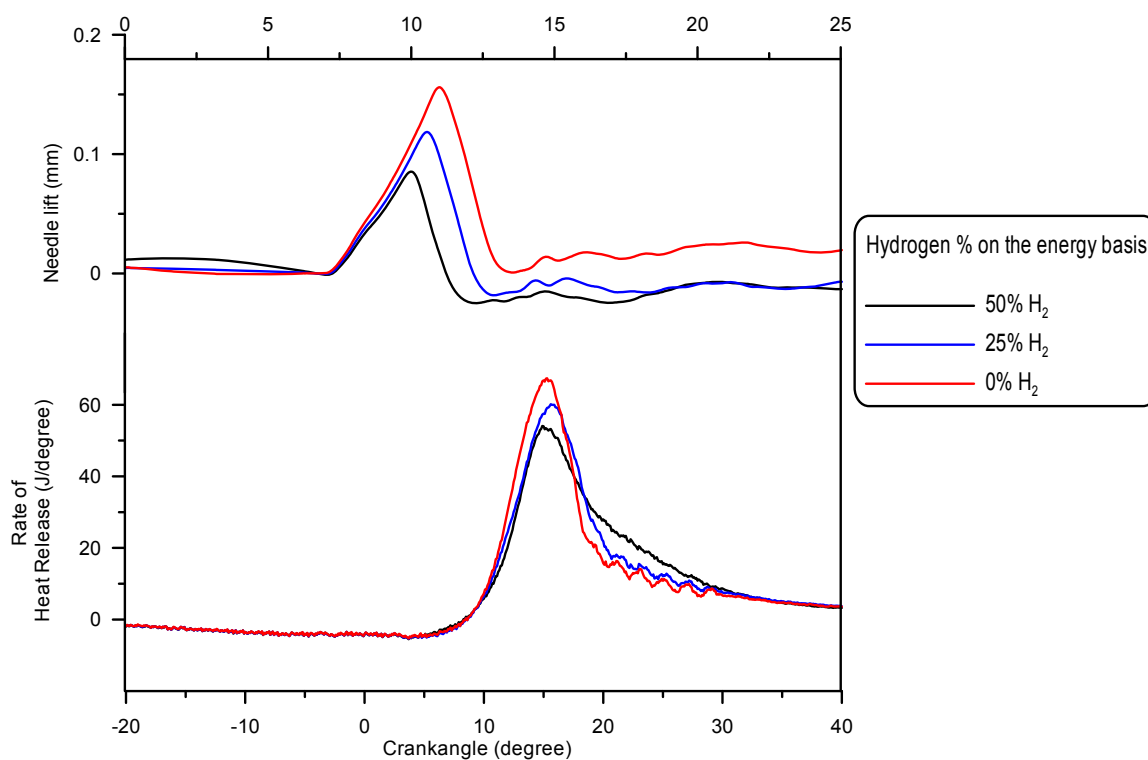


Figure 3: Rate of Heat Release and Needle lift for 1800 rpm at 25% of torque with 0% 25% and 50% hydrogen substitution on the energy basis

NOX [g/kW.h]	
H2%	1800 @ 25%
0	4.44
25	4.79
50	4.27

NOX Percent Difference	
H2%	1800 @ 25%
0	N/A
25	7.44
50	-4.07

NO [g/kW.h]	
H2%	1800 @ 25%
0	3.09
25	2.47
50	2.52

NO Percent Difference	
H2%	1800 @ 25%
0	N/A
25	-22.26
50	-20.49

NO2 [g/kW.h]	
H2%	1800 @ 25%
0	1.35
25	2.31
50	1.75

NO2 Percent Difference	
H2%	1800 @ 25%
0	N/A
25	52.56
50	25.66

HC [g/kW.h]	
H2%	1800 @ 25%
0	1.49
50	0.75

HC Percent Difference	
H2%	1800 @ 25%
0	N/A
50	-65.52

CO [g/kW.h]	
H2%	1800 @ 25%
0	5.20
50	1.48

CO Percent Difference	
H2%	1800 @ 25%
0	N/A
50	-111.30

CO2 [g/kW.h]	
H2%	1800 @ 25%
0	866.38
50	436.47

CO2 Percent Difference	
H2%	1800 @ 25%
0	N/A
50	-66.00

BSFC [g/kW.h]	
H2%	1800 @ 25%
0	10.67
25	11.17
50	10.91

BSFC Percent Difference	
H2%	1800 @ 25%
0	N/A
25	4.53
50	2.21

In summary, NO_x emissions of the single injection strategy are noticeably lower than that of dual injection strategy when utilizing hydrogen aspiration. The aspiration of 50% hydrogen seems to induce the engine to operate in an advanced combustion mode. NO_x emissions at 25% hydrogen increased, but at 50% hydrogen were observed to modestly decrease. Fuel efficiency was also observed to recover at 50% hydrogen. In this test set, the aspiration of large quantities of hydrogen was seen to lower emissions from incomplete combustion, though slightly less than that observed during dual injection.

Single injection optimization for hydrogen assisted diesel combustion

The original test matrix of this experiment compared the gaseous emissions observed from an array of injection timings with and without hydrogen. During testing the matrix was expanded to include increased quantities of hydrogen at injection timing where hydrogen induced a reduction in NO_x. The default injection timing of the engine with single engine at 1800 rpm and 75% of maximum torque is -7.5° ATDC. Injection timing was not significantly advanced to an early timing, because doing so would cause combustion before top-dead-center which is damaging to the engine and reduces fuel efficiency.

NOX [g/kw.h]				
ATDC	0% H2	7.5% H2	15% H2	25% H2
-10.5	6.19	6.15		
-9	5.71	5.73		
-7.5	5.34	5.35		
-3	4.43	4.36	4.38	
1	3.72	3.66	3.54	3.16
4	3.39	3.31	3.20	2.87

NOX Percent Difference				
ATDC	0% H2	7.5% H2	15% H2	25% H2
-10.5	N/A	-0.64		
-9	N/A	0.39		
-7.5	N/A	0.21		
-3	N/A	-1.61	-1.08	
1	N/A	-1.53	-4.84	-16.41
4	N/A	-2.36	-5.59	-16.66

NO [g/kw.h]				
ATDC	0% H2	7.5% H2	15% H2	25% H2
-10.5	5.92	5.61		
-9	5.49	5.21		
-7.5	5.14	4.87		
-3	4.32	3.98	3.95	
1	3.62	3.39	3.19	2.86
4	3.28	3.10	2.91	2.60

NO Percent Difference				
ATDC	0% H2	7.5% H2	15% H2	25% H2
-10.5	N/A	-5.37		
-9	N/A	-5.21		
-7.5	N/A	-5.40		
-3	N/A	-8.26	-8.89	
1	N/A	-6.52	-12.61	-23.20
4	N/A	-5.67	-11.96	-23.38

NO2 [g/kw.h]				
ATDC	0% H2	7.5% H2	15% H2	25% H2
10.5	0.27	0.54		
9	0.22	0.52		
7.5	0.20	0.48		
3	0.11	0.38	0.43	
-1	0.11	0.28	0.36	0.29
-4	0.10	0.21	0.29	0.27

NO2 Percent Difference				
ATDC	0% H2	7.5% H2	15% H2	25% H2
10.5	N/A	66.67		
9	N/A	81.47		
7.5	N/A	82.08		
3	N/A	111.52	119.46	
-1	N/A	89.85	109.11	94.16
-4	N/A	66.18	94.90	89.28

BSFC [g/kw.h]				
ATDC	0% H2	7.5% H2	15% H2	25% H2
10.5	8.90	9.22		
9	8.92	8.99		
7.5	8.88	9.02		
3	9.01	9.21	9.49	
-1	9.39	9.51	9.67	9.77
-4	9.72	9.83	10.10	10.13

BSFC Percent Difference				
ATDC	0% H2	7.5% H2	15% H2	25% H2
10.5	N/A	3.48		
9	N/A	0.74		
7.5	N/A	1.63		
3	N/A	2.20	5.13	
-1	N/A	1.34	2.94	4.00
-4	N/A	1.11	3.84	4.10

CO2 [g/kw.h]				
ATDC	0% H2	7.5% H2	15% H2	25% H2
10.5	792.40	747.13		
9	794.47	746.77		
7.5	795.97	747.27		
3	800.89	765.46	716.56	
-1	830.67	792.68	743.72	645.60
-4	859.68	811.67	768.51	677.54

CO2 Percent Difference				
ATDC	0% H2	7.5% H2	15% H2	25% H2
10.5	N/A	-5.88		
9	N/A	-6.19		
7.5	N/A	-6.31		
3	N/A	-4.52	-11.11	
-1	N/A	-4.68	-11.05	-25.07
-4	N/A	-5.74	-11.20	-23.70

CO [g/kw.h]				
ATDC	0% H2	7.5% H2	15% H2	25% H2
10.5	3.75	3.92		
9	3.10	2.70		
7.5	2.17	1.89		
3	0.57	0.53	0.52	
-1	0.57	0.59	0.61	0.71
-4	1.00	0.97	0.99	1.02

CO Percent Difference				
ATDC	0% H2	7.5% H2	15% H2	25% H2
10.5	N/A	4.39		
9	N/A	-14.04		
7.5	N/A	-14.06		
3	N/A	-6.54	-7.91	
-1	N/A	4.54	8.27	22.74
-4	N/A	-3.20	-1.86	1.58

HC [g/kw.h]				
ATDC	0% H2	7.5% H2	15% H2	25% H2
10.5	0.09	0.08		
9	0.09	0.08		
7.5	0.10	0.08		
3	0.10	0.08	0.07	
-1	0.09	0.08	0.06	0.06
-4	0.09	0.07	0.06	0.05

HC Percent Difference				
ATDC	0% H2	7.5% H2	15% H2	25% H2
10.5	N/A	-12.76		
9	N/A	-16.28		
7.5	N/A	-20.74		
3	N/A	-18.66	-36.07	
-1	N/A	-15.92	-41.13	-44.19
-4	N/A	-20.34	-34.96	-50.54

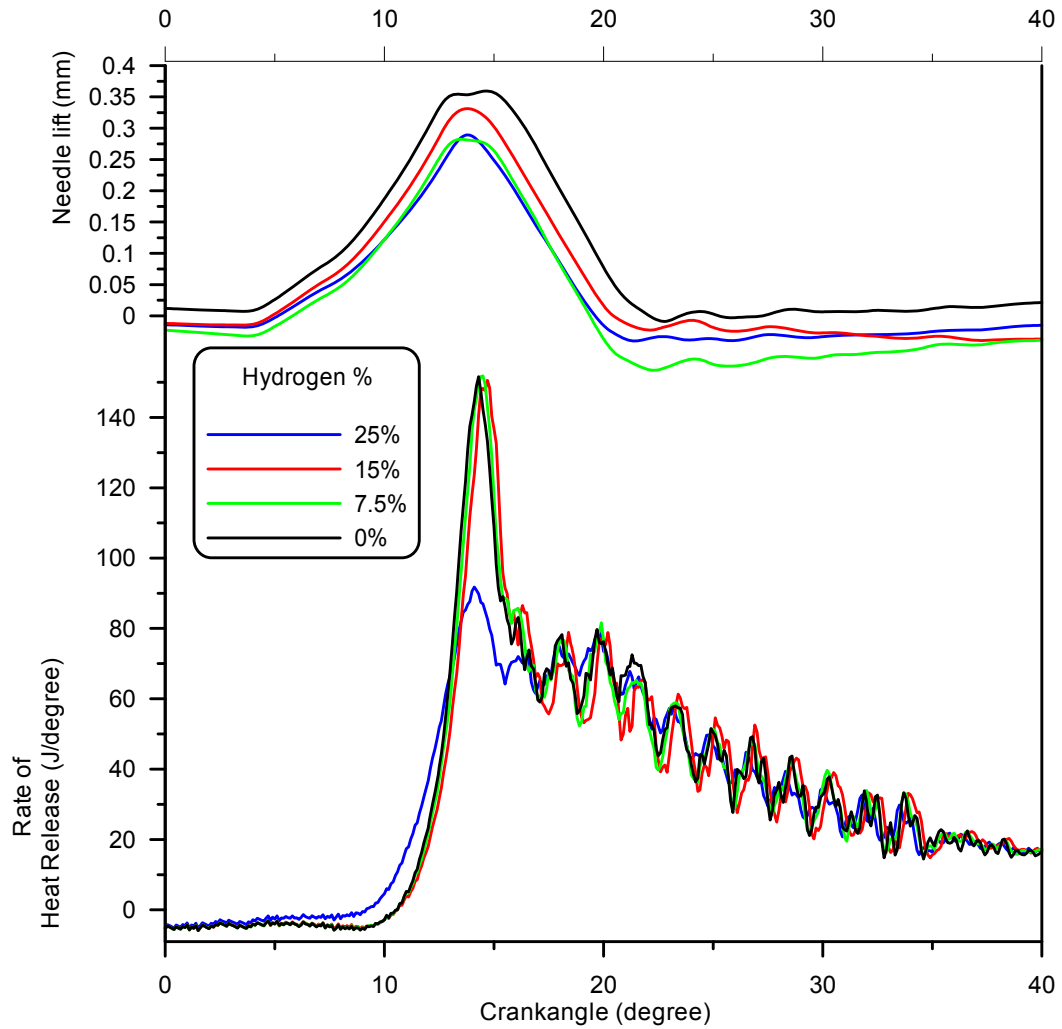


Figure 4: Rate of Heat Release and Needle lift for 1800 rpm at 75% of torque with 0%, 7.5, 15% and 25% hydrogen substitution on the energy basis at a locked injection timing of 4° ATDC.

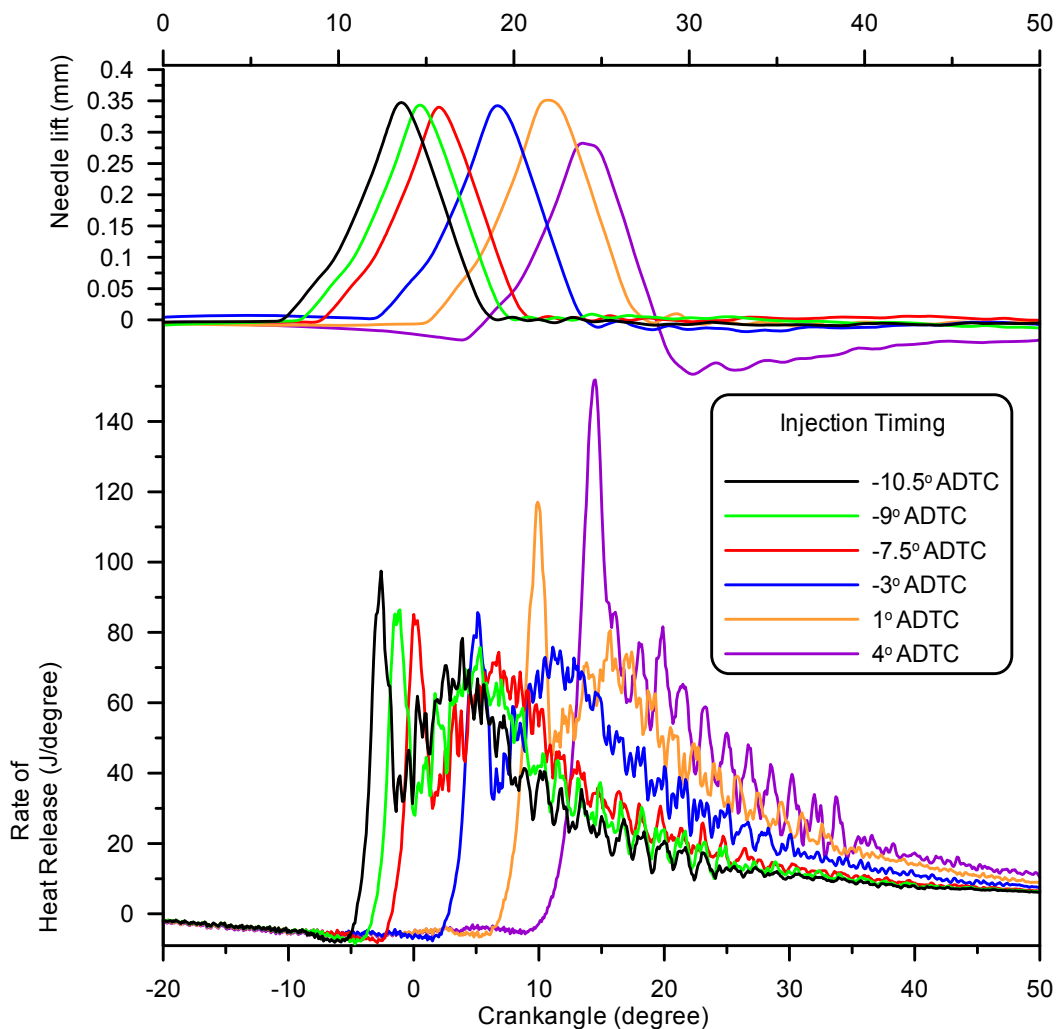


Figure 5: Rate of Heat Release and Needle lift for 1800 rpm at 75% of torque 7.5% hydrogen substitution on the energy basis at injection timings of -10.5° ATDC, -9° ATDC, -7.5° ATDC, -3° ATDC, 1° ATDC and 4° ATDC.

In summary, a single pulse injection strategy coupled with early injection produced the lowest observed emissions from hydrogen aspiration. With this strategy a notable reduction of NO_x emissions was observed, along with significant reduction in the other emissions. However, a slight fuel efficiency penalty was observed with hydrogen aspiration as the injection timing was shifted away from the optimum heat release position near top-dead-center.

Task 2.2 Simulation of HCCI-SCCI Combustion

Executive Summary

In this task, a computational approach is applied to investigate autoignition and NO_x emissions for hydrogen-hydrocarbon fuel blends with air or air-EGR blends. It is hypothesized that ignition timing might be controlled via a pilot injection of diesel fuel into a premixed hydrogen/air/EGR mixture.

Two levels of modeling are applied: a zero-dimensional time-dependant reactor model, and a three-dimensional time-dependant computational fluid dynamics (CFD) model. Because thermochemistry plays a crucial role in HCCI autoignition and NO_x emissions, significant effort has been devoted to selection and validation of the chemical mechanisms for representative single-component hydrocarbon fuels and for NO_x formation.

The primary outcome of this work resulted in the MS Thesis of Bryan Nese, which is included is included in this report as Appendix A-2.2

In continuing work since the completion of the work by Bryan Nese, CFD runs have been made to explore the effect of H₂ substitution on engine-out NO and NO₂ levels. Six cases were run with 0% to 15% H₂: 1800 r/min, 25% peak load; 1800 r/min, 75% peak load; 3600 r/min, 25% peak load; 3600 r/min, 75% peak load; 1800 r/min, 25% peak load, LTC mode; and 1800 r/min, 25% peak load, HECC mode. Detailed geometry and fuel-injector information were not available for the experimental engine, so there are considerable differences between the experimental engine configuration and the modeled engine configuration. Nevertheless, the computed percentage changes in NO and NO₂ with H₂ addition match the experimentally measured changes quite well for the two light-load, conventional-diesel cases. Quantitative agreement is not as good for the other cases. The CFD results show increasing levels of in-cylinder HO₂ with increasing H₂. This had been hypothesized to explain the observed decrease in NO and increase in NO₂ with increasing H₂.

Task 2.3 Examination of SNR during H₂-Assisted Diesel Combustion

Under this task, we dispensed NO to the intake air of the engine test stand, using the same injection point as used for the hydrogen. Below is a summary of our observations. The guiding measurements for this work are found in several SAE papers, two by Daimler Benz (982592 and 982593) and a later paper by our group (SAE 2006-01-3369). In particular, for diesel combustion we observed the following results in the past work.

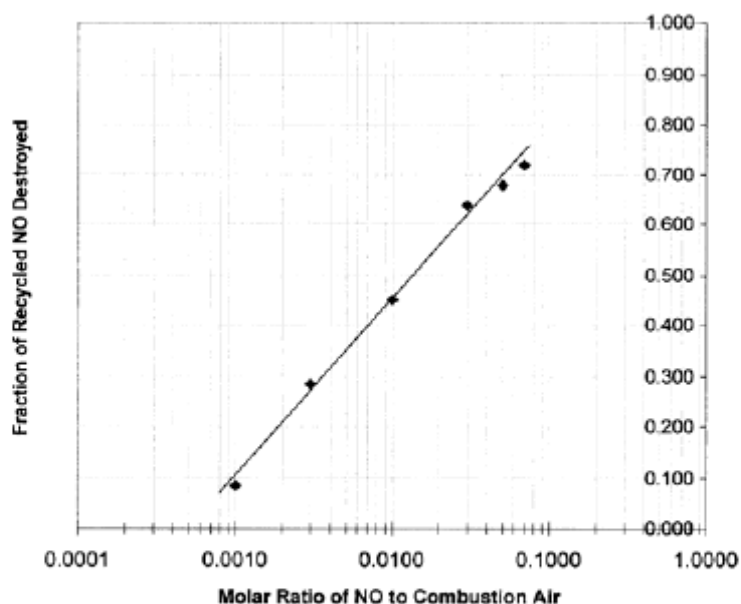


Figure 6: Fraction of Recycled NO Destroyed by Diesel Combustion on a Yanmar TS180, Single-Cylinder Engine.

(from SAE 2006-01-3369)

Selective NO_x Recirculation (SNR) was conducted at the EMS Energy Institute's combustion lab on a highly instrumented DDC 2.5L, common rail, diesel engine in the presence of hydrogen assisted diesel combustion. Chemically pure (99%) NO was delivered from 500 psi lab bottles and was aspirated into the intake of the engine, post inter-cooler at 0, 0.0005, 0.001, 0.005 and 0.01 NO/Air molar ratios. The molar ratios were based on previous work conducted by Flynn at the same facilities¹. The upper limit of the molar ratio was based on the calibration span gas and ECO-Physics NO_x analyzer which were limited to 4800ppm. A manifold of four Matheson rotameters were used to measure the required flow rate of NO. The given molar ratios NO/Air were tested at 0% and 7.5% hydrogen substitution on the energy basis, which was likewise aspirated into the engine post intercooler, as used in previous studies². The injection time of the pilot and main injection were electronically fixed to the base condition injection timing, to limit the effect of additional variables. Testing was conducted at 1800 rpm at 25% and 75% of maximum torque.

Table: Testing matrix

NO/Air (Molar Ratio)	1800rpm @ 25%		1800rpm @ 75%	
	0% H2	7.5% H2	0% H2	7.5% H2
0				
0.0005				
0.001				
0.005				
0.01				

In the literature, the effectiveness of SNR is calculated based on destruction percent of the intake and exhaust, which is calculated by ¹:

$$\text{Destruction(\%)} = \frac{(\text{Baseline NO Emission}) + [\text{Injected NO} * (\text{N}_{\text{air}}/\text{N}_{\text{total}})] - (\text{NO Emission Output}) * 100}{[\text{Injected NO} * (\text{N}_{\text{air}}/\text{N}_{\text{total}})]}$$

where N_{air} , and N_{total} are the number of moles of air and the total number of moles of products consecutively.

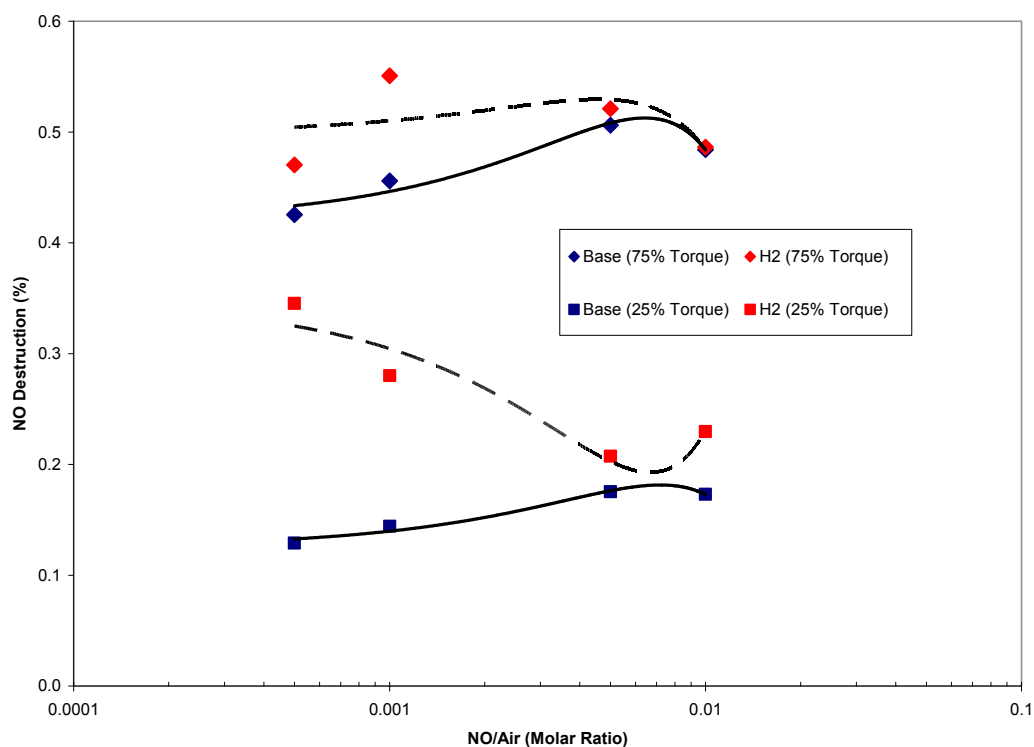


Figure 7: NO Destruction (%) vs. NO/Air (molar Ratio) with 0% and 7.5% hydrogen substitution on the energy basis at 1800 rpm at 25% and 75% of maximum output.

The base conditions without hydrogen yield NO destruction % similar to that produced by Flynn for the same NO/Air molar ratios ¹. Hydrogen increased the percent of NO destruction in both high load and low load conditions. At the lower NO/Air molar ratios tested, hydrogen was observed to have a greater increase of percent of NO destruction.

Table: Gaseous exhaust emissions and brake specific energy consumption for 1800 rpm at 25% maximum torque with 0% hydrogen substitution on the energy bases, for 0, 0.0005, 0.001, 0.005 and 0.01 NO/Air molar ratios.

NO/Air (Molar Ratio)	Ex. NO _x (g/kW.h)	Ex. NO (g/kW.h)	Ex. NO ₂ (g/kW.h)	Ex. THC (g/kW.h)	Ex. CO (g/kW.h)	Ex. CO ₂ (g/kW.h)	Ex. O ₂ (g/kW.h)	BSFC (MJ/kW.h)
0	2.94	2.34	0.60	0.76	2.34	836	775	10.85
0.0005	6.46	5.57	0.89	0.72	1.85	839	779	10.77
0.001	10.58	9.58	1.00	0.75	1.80	826	763	10.90
0.005	38.87	36.40	2.47	0.83	1.83	817	761	10.69
0.01	58.80	54.25	4.55	0.87	2.30	814	769	10.77

Table: Gaseous exhaust emissions and brake specific energy consumption for 1800 rpm at 25% maximum torque with 7.5% hydrogen substitution on the energy bases, for 0, 0.0005, 0.001, 0.005 and 0.01 NO/Air molar ratios.

NO/Air (Molar Ratio)	Ex. NO _x (g/kW.h)	Ex. NO (g/kW.h)	Ex. NO ₂ (g/kW.h)	Ex. THC (g/kW.h)	Ex. CO (g/kW.h)	Ex. CO ₂ (g/kW.h)	Ex. O ₂ (g/kW.h)	BSFC (MJ/kW.h)
0	3.21	1.63	1.58	0.92	2.05	771	753	11.00
0.0005	6.82	3.74	3.08	0.81	1.73	778	746	11.01
0.001	11.58	7.82	3.76	0.78	1.64	775	742	10.87
0.005	38.85	33.72	5.12	0.84	1.54	766	736	10.95
0.01	57.30	47.63	9.67	1.09	1.98	765	739	10.97

At low load, an increase in NO_x was observed for both the base and hydrogen cases with increasing NO/Air molar ratio. Slight increase of NO_x and a NO to NO₂ was observed with the introduction of hydrogen, as seen in previous work². THC and CO emissions fluctuated with increasing NO/Air molar ratios. These fluctuation in emissions correspond to the fluctuations observed in the start of combustion (SOC), given in the apparent rate of heat release plots below. An early start of combustion results in lowered THC and CO emissions and a delayed SOC results in increased emissions. The same trend was observed for BSFC. The emission effects caused by hydrogen are comparable to base operation and reflect observations made in previous work².

Table: Gaseous exhaust emissions and brake specific energy consumption for 1800 rpm at 75% maximum torque with 0% hydrogen substitution on the energy bases, for 0, 0.0005, 0.001, 0.005 and 0.01 NO/Air molar ratios.

NO/Air (Molar Ratio)	Ex. NO _x (g/kW.h)	Ex. NO (g/kW.h)	Ex. NO ₂ (g/kW.h)	Ex. THC (g/kW.h)	Ex. CO (g/kW.h)	Ex. CO ₂ (g/kW.h)	Ex. O ₂ (g/kW.h)	BSFC (MJ/kW.h)
0	6.05	5.66	0.39	0.11	1.87	753	166	8.93
0.0005	6.75	6.61	0.14	0.10	2.51	758	165	9.11
0.001	7.83	7.66	0.17	0.09	2.50	755	163	9.00
0.005	14.70	14.21	0.49	0.10	2.79	751	165	8.99
0.01	23.34	22.04	1.30	0.11	2.13	743	169	8.93

Table: Gaseous exhaust emissions and brake specific energy consumption for 1800 rpm at 75% maximum torque with 7.5% hydrogen substitution on the energy bases, for 0, 0.0005, 0.001, 0.005 and 0.01 NO/Air molar ratios.

NO/Air	Ex. NOx	Ex. NO	Ex. NO2	Ex. THC	Ex. CO	Ex. CO2	Ex. O2	BSFC
(Molar Ratio)	(g/kW.h)	(g/kW.h)	(g/kW.h)	(g/kW.h)	(g/kW.h)	(g/kW.h)	(g/kW.h)	(MJ/kW.h)
0	5.72	5.32	0.40	0.07	3.44	722	154	9.29
0.0005	6.60	6.15	0.44	0.07	4.24	727	155	9.25
0.001	7.59	7.02	0.57	0.07	4.48	722	153	9.35
0.005	14.74	13.60	1.14	0.08	4.25	715	154	9.35
0.01	23.64	21.76	1.88	0.09	2.76	696	158	9.14

At high loads, the THC and CO emissions fluctuations were the reverse of that observed at low loads with increasing NO/Air molar ratios. All other effects are similar to those observed for low load operations.

As mentioned earlier, fluctuations in the apparent rate of heat release with increase NO/Air molar ratio were observed and were unexpected. The plots below for the low load and high load cases with and without hydrogen, all reflect the same trend in SOC per given NO/Air molar ratios. The SOC and timing of the maximum pilot heat release of each NO/Air molar ratio are consistent for the multiple trace samples taken for each mode. However, the maximum heat release of the pilot was observed to vary greatly per trace of a given mode. Thus, during SNR, the magnitude of the pressure peaks fluctuations, was also represented in high coefficient of variance of IMEP.

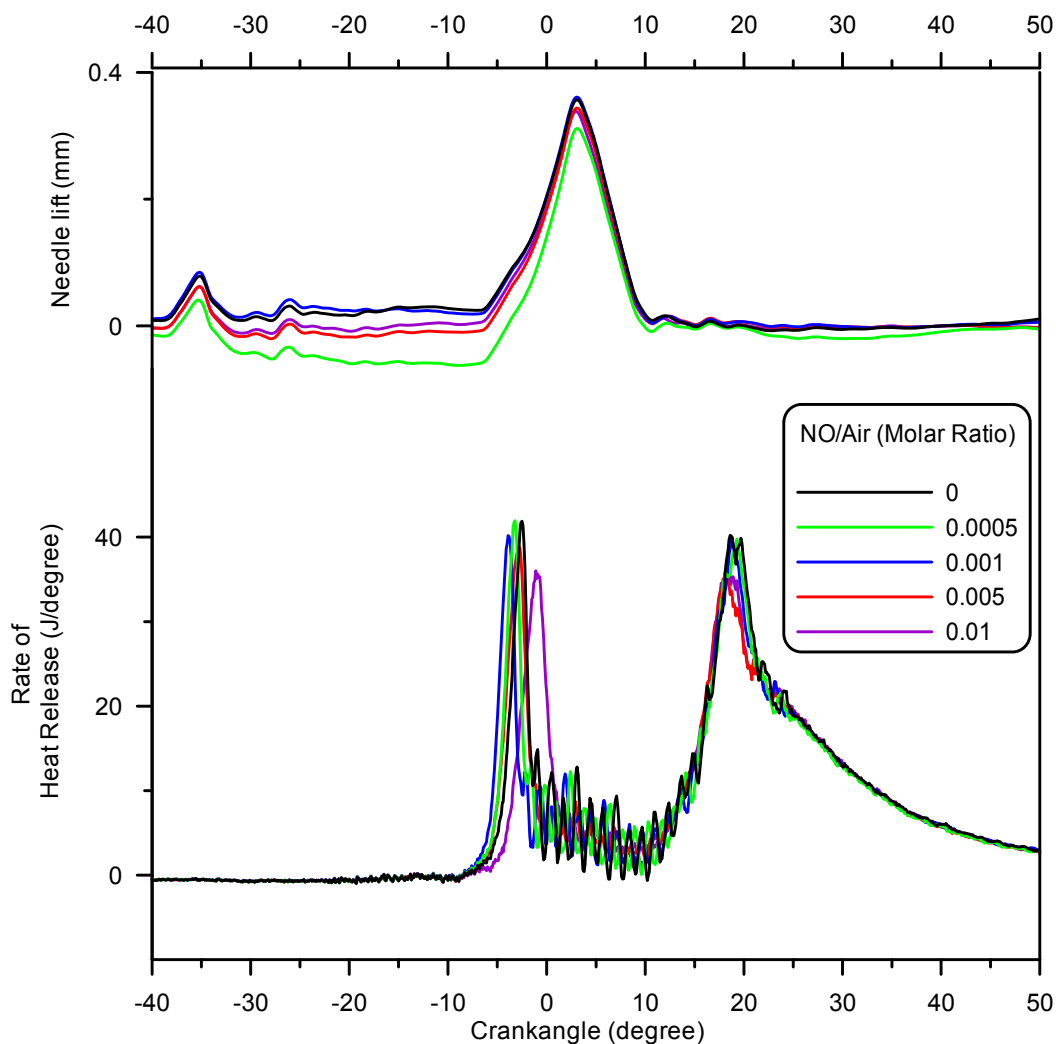


Figure 8: 1800 rpm at 25% of maximum torque with 0% hydrogen on the energy basis

Table: Key timing and parameters for 1800 rpm at 25% maximum torque with 0% hydrogen substitution on the energy bases, for 0, 0.0005, 0.001, 0.005 and 0.01 NO/Air molar ratios.

NO/Air (Molar Ratio)	Destruction (%)	Incr. of NOx (%)	Pilot Inj. (BTDC)	SOC (BTDC)	Pilot Max. RORH (J/degree)	Pilot Max. RORH (BTDC)	Pilot Inj. Delay (degree)
0	1	199.8	-17.41	-8.37	41.88	-2.50	9.04
0.0005	0.14	44.1	-17.41	-8.38	41.93	-3.20	9.03
0.001	0.15	14.0	-17.41	-8.53	40.17	-3.90	8.88
0.005	0.17	-13.4	-17.41	-8.36	38.86	-2.80	9.05
0.01	0.16	-15.7	-17.41	-8.36	30.01	-1.10	9.05

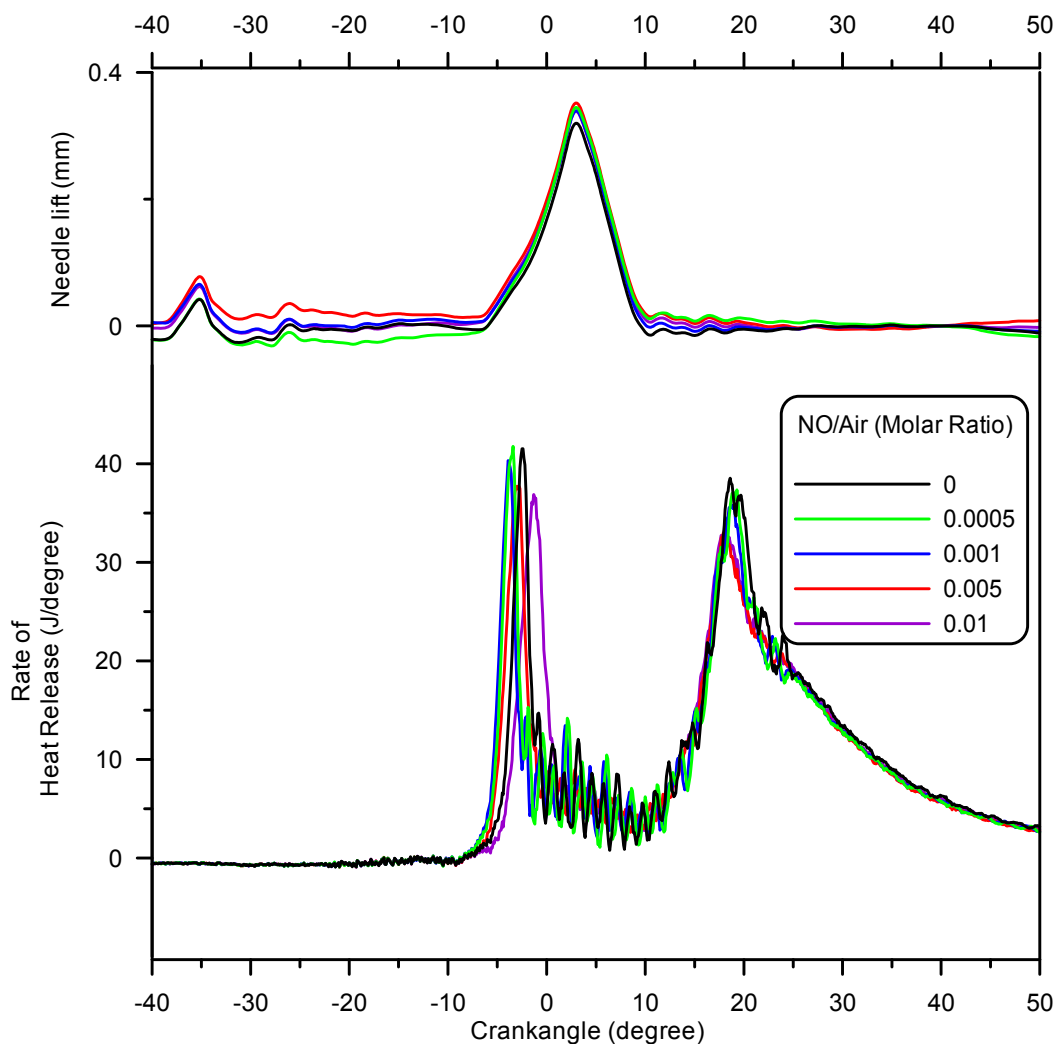


Figure 9: 1800 rpm at 25% of maximum torque with 7.5% hydrogen on the energy basis

Table: Key timing and parameters for 1800 rpm at 25% maximum torque with 7.5% hydrogen substitution on the energy bases, for 0, 0.0005, 0.001, 0.005 and 0.01 NO/Air molar ratios.

NO/Air (Molar Ratio)	Destruction (%)	Incr. of NOx (%)	Pilot Inj. (BTDC)	SOC (BTDC)	Pilot Max. RORH (J/degree)	Pilot Max. RORH (BTDC)	Pilot Inj. Delay (degree)
0	1.00	194.1	-17.41	-7.99	41.5	-2.45	9.42
0.0005	0.35	49.6	-17.41	-8.4	41.7	-3.40	9.01
0.001	0.27	15.2	-17.41	-8.52	40.3	-3.90	8.89
0.005	0.19	-13.3	-17.41	-8.37	37.7	-3.00	9.04
0.01	0.23	-19.8	-17.41	-7.98	36.9	-1.30	9.43

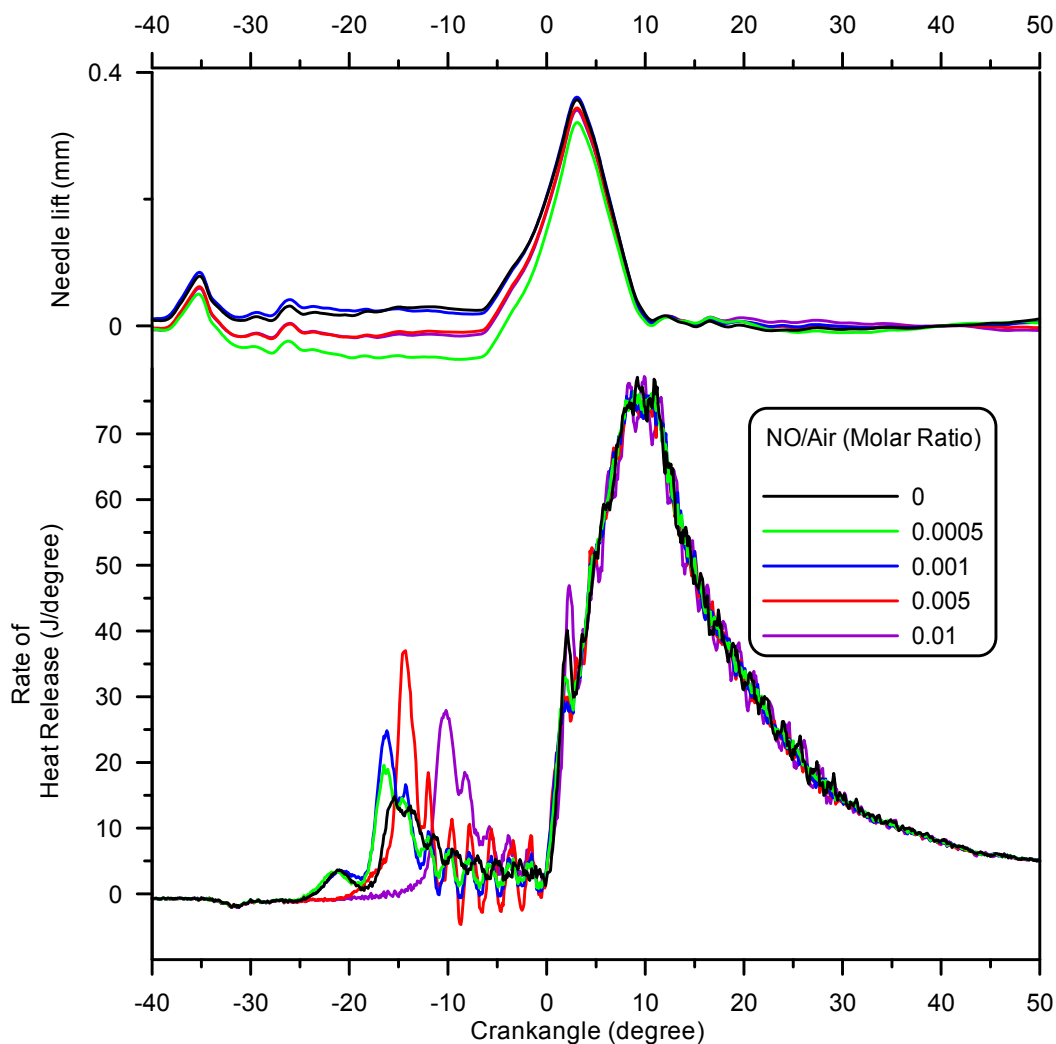


Figure 10: 1800 rpm at 75% of maximum torque with 0% hydrogen on the energy basis

Table: Key timing and parameters for 1800 rpm at 75% maximum torque with 7.5% hydrogen substitution on the energy bases, for 0, 0.0005, 0.001, 0.005 and 0.01 NO/Air molar ratios.

NO/Air (Molar Ratio)	Destruction (%)	Incr. of NOx (%)	Pilot Inj. (BTDC)	SOC (BTDC)	Pilot Max. RORH (J/degree)	Pilot Max. RORH (BTDC)	Pilot Inj. Delay (degree)
0	1	197.6	-38.3	-23.52	14.82	-15.40	14.78
0.0005	0.43	115.5	-38.3	-24.034	19.67	-16.50	14.266
0.001	0.46	62.5	-38.3	-23.74	24.83	-16.20	14.56
0.005	0.51	-29.2	-38.3	-19.73	37.01	-14.30	18.57
0.01	0.48	-46.2	-38.3	-14.92	27.92	-10.20	23.38

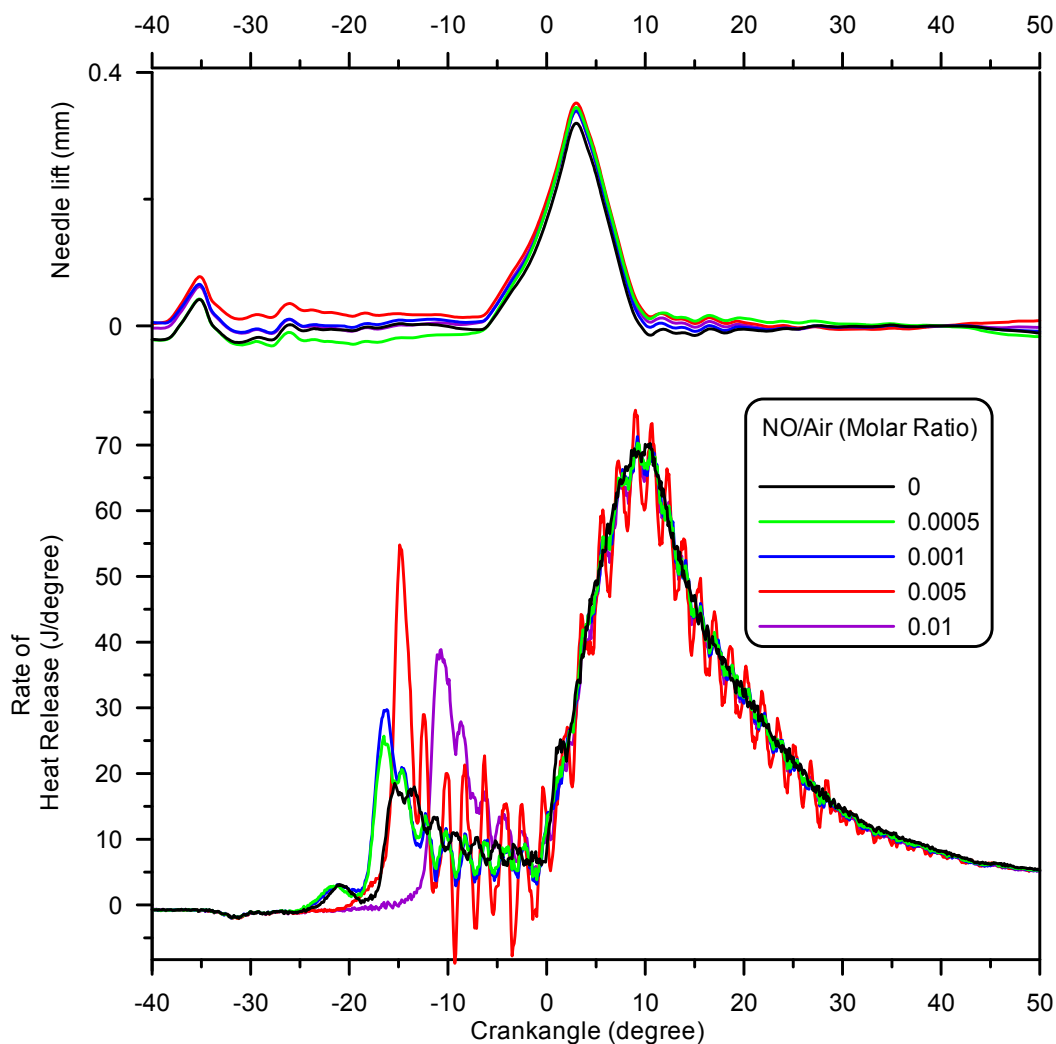


Figure 11: 1800 rpm at 75% of maximum torque with 7.5% hydrogen on the energy basis

Table: Key timing and parameters for 1800 rpm at 75% maximum torque with 7.5% hydrogen substitution on the energy bases, for 0, 0.0005, 0.001, 0.005 and 0.01 NO/Air molar ratios.

NO/Air (Molar Ratio)	Destruction (%)	Incr. of NOx (%)	Pilot Inj. (BTDC)	SOC (BTDC)	Pilot Max. RORH (J/degree)	Pilot Max. RORH (BTDC)	Pilot Inj. Delay (degree)
0	1.00	194.9	-38.3	-23.106	18.49	-15.40	15.194
0.0005	0.46	112.2	-38.3	-24.04	25.7	-16.50	14.26
0.001	0.54	58.5	-38.3	-23.92	29.72	-16.20	14.38
0.005	0.51	-26.9	-38.3	-19.79	54.8	-14.90	18.51
0.01	0.48	-44.7	-38.3	-14.95	38.86	-10.70	23.35

The non linear progression of SOC timing with increasing NO/Air molar ratios is an interesting effect that warrants further investigation. SNR with a single pulse injection would be the next logical step in studying the effect of NO on SOC.

References

1. Flynn, P. J. Destruction of Nitric Oxide via Selective NO_x Recirculation during Lean Combustion The Pennsylvania State University, University Park, 2003.
2. Lilik, G. K. Hydrogen Assisted Diesel Combustion. The Pennsylvania State University, University Park, 2008.

Conclusions and Milestones

Milestones

For FY08 quarter #4 the chief milestone was:

Complete examination of impact of hydrogen addition on selective NO_x recirculation (SNR) in SI combustion with HCNG.

This planned milestone was not completed, due to delays in getting the compressed cylinders of pure NO and then by the failure of the Hydrogen Fuel Station at Penn State, which prevented refilling of our fuel tank with HCNG.

However, all other tasks were completed as outlined in the original project plan.

Conclusions

The chief overall conclusions to be drawn from the body of work presented in this report are as follows:

1. Hydrogen promotes the enhancement of burning rate and flame speed in the SI combustion of natural gas, and stabilizes combustion at the lean limit of combustion thereby broadening the equivalence ratio range over which an SI engine can be operated.
2. With proper choice of spark timing to account for the faster burn rate and shorter combustion duration (i.e., with spark timing retard), emissions and performance benefits relative to conventional natural gas combustion can be realized.
3. Hydrogen assisted diesel combustion does not provide any significant improvement in emissions or efficiency, in sharp contrast to many unfounded claims made by commercial entities promoting the use of hydrogen “boosting.” Even attempts to optimize the combustion process for the presence of hydrogen do little to improve emissions or efficiency.
4. However, hydrogen assisted combustion can displace significant amounts of diesel fuel usage with little or no penalty, in these tests up to as much as 15% substitution on an energy basis across the full speed and load range. The only anomalous effect is a sharp rise in the percentage of NO₂ in the total NO_x emissions from the engine.

Acknowledgment

The authors wish to thank the National Energy Technology Laboratory for their support of this work under Instrument No. DE-FC26-04NT42233. We are also grateful to Keith Cavellini and Ryan Harrier (formerly) of CAV Engineering for assistance with providing repair parts, tools and technical assistance for our 2.5L turbodiesel test engine. In addition, we are grateful to Carl Hensman and Pat Quarles of Asemblon for their support of this work.

DE-FC26-04NT42233			DOE Obligation		Recipient Share		Cumulative	
Quarter	From	To	Approved Budget	Actual Costs	Approved Budget	Actual Costs	Approved Budget	Actual Costs
1Q04	Start	12/31/04	52,175	1,474	18,231	-	70,406	1,474
2Q05	1/1/05	3/31/05	52,175	27,711	18,231	8,908	70,406	36,619
3Q05	4/1/05	6/30/05	52,175	33,160	18,231	20,177	70,406	53,336
4Q05	7/31/05	9/30/05	52,175	86,691	18,231	16,468	70,406	103,159
1Q06	10/1/05	12/31/05	47,241	37,789	19,603	17,396	66,844	55,185
2Q06	1/1/06	3/31/06	47,241	51,453	19,603	17,396	66,844	68,849
3Q06	4/1/06	6/30/06	47,241	66,421	19,603	17,294	66,844	83,715
4Q06	7/31/06	9/30/06	47,241	66,207	19,603	14,146	66,844	80,353
1Q07	10/1/06	12/31/06	-	24,353	25,471	20,097	25,471	44,450
2Q07	1/1/07	3/31/07	48,598	35,445	25,471	25,384	74,069	60,829
3Q07	4/1/07	6/30/07	48,599	62,140	25,471	16,923	74,070	79,062
4Q07	7/31/07	9/30/07	48,598	48,021	25,471	8,742	74,069	56,762
1Q08	10/1/07	12/31/07	48,598.00	18,774	\$0.00	75,479	48,598	94,254
2Q08	1/1/08	3/31/08	-	20,728	\$3,334.00	29,468	3,334	50,196
3Q08	4/1/08	6/30/08	-	-	\$3,333.00	30,545	3,333	30,545
4Q08	7/1/08	9/30/08	-	11,689	\$3,333.00	-	3,333	11,689
			592,055	592,055	263,220	318,421	855,275	910,476

Update: 10/31/2008

PLEASE NOTE: During the period 1/1/2008-3/31/2008 there where changes to be made to the Task Schedule.

Task: (MILESTONES)	Quarters:													
	Dec	Jan	Feb	Mar	Apr	May	Jun	Jul	Aug	Sep	Oct	Nov	Dec	
1														
1.1 Combustion/Emissions Impact	Anticipated/Actual									Start				
1.2 Numerical Simulation	Anticipated/Actual													
1.3 Field Vehicle Analysis	Anticipated/Actual													
1.4 Examination of Recirculation	Anticipated/Actual													
2														
2.1 Hydrogen Studies	Anticipated/Actual													
2.2 Simulation of HCCI-SCCI	Anticipated/Actual													
2.3 Examination of SNR	Anticipated/Actual													

* Install Combustion Analysis Instrumentation on Ricardo Research Engine - Completed 12/31/04
 ** Complete Installation of Instrumentation (Diesel Engine) for pilot-ignited homogeneous combustion - 3/31/05

Appendices

The appendices included with this report are each a completed graduate thesis from a student working under a particular subtask.

- Appendix A-1.2: MS Thesis in Mechanical Engineering by Saket Priyadarshi
- Appendix A-1.3: MS Thesis in Energy & Geo-Environmental Engineering by Jamie Clark
- Appendix A-2.1.A: MS Thesis in Energy & Geo-Environmental Engineering by Greg Lilik
- Appendix A-2.1.B: PhD Thesis in Fuel Science by Elana Chapman
- Appendix A-2.2.B MS Thesis in Mechanical Engineering by Bryan Nese

Appendix A-1.2: MS Thesis in Mechanical Engineering by Saket Priyadarshi

33 S. Mann Ave.
Yeagertown, PA - 17099

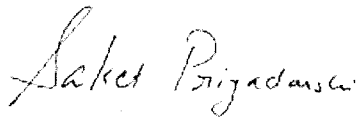
January 14, 2009

National Energy Technology Laboratory
U.S. Department of Energy
626 Cochran Mill Road
P.O. Box 10940
Pittsburgh, PA 15236-0940

Dear U.S. Department of Energy:

I hereby grant the U.S. Department of Energy permission to use my thesis in the Final Technical Report for Award Number DE-FC26-04NT42233, "Hydrogen-Assisted IC Engine Combustion as a Route to Hydrogen Implementation." My thesis was written with support of the U.S. Department of Energy under this award and copyright for the thesis lies with me.

Sincerely,

A handwritten signature in cursive script that reads "Saket Priyadarshi".

(Saket Priyadarshi)

The Pennsylvania State University

The Graduate School

Department of Mechanical Engineering

EFFECTS OF HYDROGEN ENRICHMENT ON METHANE/AIR

PREMIXED LAMINAR FLAMES

UNDER

SI ENGINE CONDITIONS

A Thesis in

Mechanical Engineering

by

Saket Priyadarshi

© 2006 Saket Priyadarshi

Submitted in Partial Fulfillment
of the Requirements
for the Degree of

Master of Science

May 2006

I grant The Pennsylvania State University the nonexclusive right to use this work for the University's own purposes and to make single copies of the work available to the public on a not-for-profit basis if copies are not otherwise available.

Saket Priyadarshi

The thesis of Saket Priyadarshi was reviewed and approved* by the following:

Dr. Dan Haworth
Professor of Mechanical Engineering
Thesis Advisor

Dr. Stephen R. Turns
Professor of Mechanical Engineering

Dr. H. Joseph Sommer III
Professor of Mechanical Engineering
Head of the Department of Mechanical and Nuclear Engineering

*Signatures are on file in the Graduate School

ABSTRACT

In this study, the influence of hydrogen addition to premixed, steady - state, one - dimensional methane/air flames under spark ignition engine conditions is discussed. Three basic studies were performed: changes in the flame structure due to the change in the hydrogen concentration for a fixed equivalence ratio, influence of the diffusion coefficient of hydrogen on flame structure and exhaust - gas recirculation. For the first study, in general, there has been an earlier occurrence of the reaction zone, earlier and higher peaks for key intermediate species and reduction in the NO_x with hydrogen enrichment. Intermediate species OH, O and H have been considered to be important in the rate of reactions $\text{OH} + \text{CH}_4 \rightarrow \text{CH}_3 + \text{H}_2\text{O}$ and $\text{O} + \text{CH}_4 \rightarrow \text{CH}_3 + \text{OH}$. For the second study, little influence of the low diffusion coefficient of hydrogen on the flame has been observed for this configuration. For the third study, it was observed that there has been a reduction in the peak temperature, delay in the occurrence of the reaction zone and reduction and delayed occurrence in the peaks of key intermediate species with EGR addition. The reduction in peak temperature and delay in the occurrence of the reaction zone prevents the formation of thermal NO and hence NO_x reduces.

TABLE OF CONTENTS

LIST OF FIGURES	vii
LIST OF TABLES	xii
ACKNOWLEDGEMENTS	xiii
Chapter 1 Introduction	1
1.1 Background	1
Chapter 2 Literature Review	4
2.1 Introduction	4
2.1.1 Engine Experiments and Modeling	4
2.1.1.1 Exhaust Emission and Energy Consumption Effects from Hydrogen Supplementation of Natural Gas (Catellan and Wallace, 1995)	5
2.1.1.2 NO _x Emissions and Efficiency of Hydrogen, Natural Gas and Hydrogen/ Natural Gas Blended Fuels (Hoekstra et al., 1996)	8
2.1.1.3 Knock in Spark Ignition Hydrogen Engines (Li and Karim, 2004)	10
2.1.1.4 The Addition of Hydrogen to a Gasoline Fuelled SI Engine (Andrea et al., 2004)	15
2.1.1.5 Emission Results from the New Development of a Dedicated Hydrogen – Enriched Natural Gas Heavy Duty Engine (Collier et al., 2005)	19
2.1.1.6 Effects of Hydrogen Enhancement on Efficiency and NO _x Emissions of Lean and EGR - Diluted Mixtures in a SI Engine (Ivanic et al., 2005)	20
2.1.2 Fundamental Combustion Experiments and Modeling	23
2.1.2.1 Hydrogen/Oxygen Additives Influence on Premixed Iso- Octane/Air Flame (Sobiesiak et al., 2002)	23
2.1.2.2 Nitric Oxide Detection in Turbulent Premixed Methane/Air Flames (Herrmann and Boulouchos, 2005)	25
2.1.3 Present Work	27
Chapter 3 Computational Tools	29
3.1 CHEMKIN	29
3.1.1 chem.inp	31
3.1.2 therm.dat	32
3.1.3 tran.dat	34

3.2	Application Codes	35
3.2.1	PREMIX	35
3.3	XSenkplot	40
Chapter 4 Combustion Conditions and Cases Studied		43
4.1	Thermochemical Conditions.....	43
4.1.1	Pressure and Temperature	43
4.1.2	Reactant Composition	44
4.2	Chemical Mechanisms.....	44
4.3	Molecular Diffusivity	47
4.4	Exhaust Gas Recirculation (EGR).....	48
4.5	Computational Issues.....	49
4.5.1	CHEMKIN Version.....	50
4.5.2	TFIX	51
4.5.3	Flame Domain	51
4.6	Run Matrix.....	51
4.6.1	Varying Hydrogen Fraction For Fixed Equivalence Ratio.....	52
4.6.2	Molecular Diffusion Studies.....	53
4.6.3	EGR Studies	54
Chapter 5 Results		56
5.1	Comparison Among Chemical Mechanisms	56
5.1.1	Temperature Profiles	57
5.1.2	CH ₄ , CH ₃ and OH.....	58
5.1.3	NO	64
5.1.4	NO ₂	65
5.1.5	H ₂	68
5.2	Variation in Hydrogen Fraction.....	70
5.2.1	Temperature.....	71
5.2.2	CH ₄ and H ₂ Mole Fractions.....	72
5.2.3	OH radicals.....	76
5.2.4	O Radicals	78
5.2.5	H radicals.....	79
5.2.6	O ₂ Mole Fraction	80
5.2.7	NO Mole Fraction.....	81
5.2.8	NO ₂ Mole Fraction	83
5.3	Diffusion of Hydrogen.....	87
5.3.1	Laminar Flame Speed.....	88
5.3.2	Temperature.....	88
5.3.3	CH ₄ and CH ₃	89
5.3.4	OH	91
5.3.5	NO and NO ₂ mole fractions	92
5.3.6	H ₂ and H mole fractions	95

5.4 EGR Studies.....	97
5.4.1 Laminar Flame Speed.....	98
5.4.2 Temperature profile.....	98
5.4.3 CH ₄ and CH ₃ Mole Fraction Profiles	99
5.4.4 OH Mole Fraction.....	100
5.4.5 O Mole Fraction Profile.....	101
5.4.6 H ₂ and H Mole Fraction Profile.....	102
5.4.7 NO and NO ₂ mole fraction	104
Chapter 6 Conclusions and Future Work.....	108
6.1 Conclusions.....	108
6.2 Future Work.....	110
References.....	111

LIST OF FIGURES

Fig. 2-1: Knocking region as a function of ϕ and compression ratio for pure H ₂ . Source: Li and Karim, 2004.....	11
Fig. 2-2: K.L.E.R. variation with compression ratio under unthrottled operation in a CFR engine. Source: Li and Karim, 2004.....	13
Fig. 2-3: Indicated power production and indicated power production efficiency as a function of compression ratio. Source: Li and Karim, 2004.	14
Fig. 2-4: Variation of K.L.C.R. as a function of fraction CH ₄ and CO in a fuel. Source: Li and Karim, 2004.....	14
Fig. 2-5: Variation of K.L.E.R. as a function of fraction CH ₄ and CO in a fuel. Source: Li and Karim, 2004.....	15
Fig. 2-6: Change in NO concentration with change in 90% burn duration due to H ₂ addition. Source: Andrea et al., 2004.	18
Fig. 2-7: NO _x vs equivalence ratio for different H ₂ /CH ₄ mixtures. Source: Collier et al., 2005	19
Fig. 2-8: NO distribution for different ϕ and constant turbulence. Source: Herrmann and Boulouchos, 2005	26
Fig. 2-9: NO _x concentration variation under different turbulence conditions and constant equivalence ratio. Source: Herrmann and Boulouchos, 2005	27
Fig. 3-1: Basic structure of CHEMKIN (Source: Kee et al., 1996).....	30
Fig. 3-2: Sample chem.inp file.....	32
Fig. 3-3: Sample therm.dat file.	32
Fig. 3-4: Sample tran.dat file.	35
Fig. 3-5: PREMIX schematic.....	37
Fig. 3-6: Output screen from XSenkplot post processing.....	41
Fig. 3-7: Reaction pathways plot from XSenkplot	41
Fig. 5-1: Compared laminar flame speeds for H ₂ /CH ₄ mixtures using the GRI Mech 3.0 mechanism, P = 8 atm, T = 598 K.....	57

Fig. 5-2: Temperature profile comparison for different reaction mechanisms. $P = 8$ atm, $T = 598$ K, $\phi = 1.0$, $\Psi = 0.3$.	58
Fig. 5-3: CH ₄ profile comparison for different reaction mechanisms. $P = 8$ atm, $T = 598$ K, $\phi = 1.0$, $\Psi = 0.3$.	59
Fig. 5-4: CH ₃ profile comparison for different reaction mechanisms. $P = 8$ atm, $T = 598$ K, $\phi = 1.0$, $\Psi = 0.3$.	59
Fig. 5-5: Reaction rate profile comparison for different reaction mechanisms. $P = 8$ atm, $T = 598$ K, $\phi = 1.0$, $\Psi = 0.3$.	61
Fig. 5-6: OH profile comparison for different reaction mechanisms. $P = 8$ atm, $T = 598$ K, $\phi = 1.0$, $\Psi = 0.3$.	62
Fig. 5-7: Reaction rate profile comparison for different reaction mechanisms. $P = 8$ atm, $T = 598$ K, $\phi = 1.0$, $\Psi = 0.3$.	63
Fig. 5-8: Reaction rate profile comparison for different reaction mechanisms. $P = 8$ atm, $T = 598$ K, $\phi = 1.0$, $\Psi = 0.3$.	63
Fig. 5-9: NO mole fraction comparison for different reaction mechanisms. $P = 8$ atm, $T = 598$ K, $\phi = 1.0$, $\Psi = 0.3$.	64
Fig. 5-10: Reaction zone NO mole fraction profiles for different reaction mechanisms. $P = 8$ atm, $T = 598$ K, $\phi = 1.0$, $\Psi = 0.3$.	65
Fig. 5-11: NO ₂ mole fraction profiles for different reaction mechanisms. $P = 8$ atm, $T = 598$ K, $\phi = 1.0$, $\Psi = 0.3$.	66
Fig. 5-12: Reaction zone NO ₂ mole fraction profiles for different reaction mechanisms. $P = 8$ atm, $T = 598$ K, $\phi = 1.0$, $\Psi = 0.3$.	66
Fig. 5-13: Reaction rate comparison for different reaction mechanisms. $P = 8$ atm, $T = 598$ K, $\phi = 1.0$, $\Psi = 0.3$.	67
Fig. 5-14: H ₂ mole fraction profiles for different reaction mechanisms. $P = 8$ atm, $T = 598$ K, $\phi = 1.0$, $\Psi = 0.3$.	68
Fig. 5-15: Reaction rate profiles for different reaction mechanisms. $P = 8$ atm, $T = 598$ K, $\phi = 1.0$, $\Psi = 0.3$.	69
Fig. 5-16: Reaction rate profiles for different reaction mechanisms. $P = 8$ atm, $T = 598$ K, $\phi = 1.0$, $\Psi = 0.3$.	70
Fig. 5-17: Temperature profiles for different Ψ . $P = 8$ atm, $T = 598$ K, $\phi = 0.7$, reaction mechanism - GRI Mech 3.0.	71

Fig. 5-18 : CH ₄ mole fraction profiles for different Ψ . $P = 8$ atm, $T = 598$ K, $\phi = 0.7$, reaction mechanism - GRI Mech 3.0.....	72
Fig. 5-19 : H ₂ mole fraction profiles for different Ψ . $P = 8$ atm, $T = 598$ K, $\phi = 0.7$, reaction mechanism - GRI Mech 3.0.....	73
Fig. 5-20 : Reaction rate profiles for reaction [5-2] for different Ψ . $P = 8$ atm, $T = 598$ K, $\phi = 0.7$, reaction mechanism - GRI Mech 3.0.	74
Fig. 5-21 : Reaction rate profiles for reaction [5-1] for different Ψ . $P = 8$ atm, $T = 598$ K, $\phi = 0.7$, reaction mechanism - GRI Mech 3.0.	75
Fig. 5-22 : Reaction rate profiles for different Ψ . $P = 8$ atm, $T = 598$ K, $\phi = 0.7$, reaction mechanism - GRI Mech 3.0.....	75
Fig. 5-23 : OH mole fraction profiles for different Ψ . $P = 8$ atm, $T = 598$ K, $\phi = 0.7$, reaction mechanism - GRI Mech 3.0.....	76
Fig. 5-24 : O mole fraction profiles for different Ψ . $P = 8$ atm, $T = 598$ K, $\phi = 0.7$, reaction mechanism - GRI Mech 3.0.....	78
Fig. 5-25 : H mole fraction profiles for different Ψ . $P = 8$ atm, $T = 598$ K, $\phi = 0.7$, reaction mechanism - GRI Mech 3.0.....	80
Fig. 5-26 : O ₂ mole fraction profiles for different Ψ . $P = 8$ atm, $T = 598$ K, $\phi = 0.7$, reaction mechanism - GRI Mech 3.0.....	81
Fig. 5-27 : NO mole fraction profiles for different Ψ . $P = 8$ atm, $T = 598$ K, $\phi = 0.7$, reaction mechanism - GRI Mech 3.0.....	82
Fig. 5-28 : Reaction rate profiles for different Ψ . $P = 8$ atm, $T = 598$ K, $\phi = 0.7$, reaction mechanism - GRI Mech 3.0.....	83
Fig. 5-29 : Reaction - zone NO ₂ mole fraction profiles for different Ψ . $P = 8$ atm, $T = 598$ K, $\phi = 0.7$, reaction mechanism - GRI Mech 3.0.....	84
Fig. 5-30 : NO ₂ mole fraction profiles for different Ψ . $P = 8$ atm, $T = 598$ K, $\phi = 0.7$, reaction mechanism - GRI Mech 3.0.....	85
Fig. 5-31 : Reaction rate profiles for different Ψ . $P = 8$ atm, $T = 598$ K, $\phi = 0.7$, reaction mechanism - GRI Mech 3.0.....	86
Fig. 5-32 : Reaction rate profiles for different Ψ . $P = 8$ atm, $T = 598$ K, $\phi = 0.7$, reaction mechanism - GRI Mech 3.0.....	86
Fig. 5-33 : Reaction rate profiles for different Ψ . $P = 8$ atm, $T = 598$ K, $\phi = 0.7$, reaction mechanism - GRI Mech 3.0.....	87

Fig. 5-34: Temperature profiles for three diffusion cases. $P = 8$ atm, $T = 598$ K, $\phi = 0.7$, $\Psi = 0.3$, reaction mechanism - GRI Mech 3.0.	89
Fig. 5-35: CH ₄ mole fraction profiles for three diffusion cases. $P = 8$ atm, $T = 598$ K, $\phi = 0.7$, $\Psi = 0.3$, reaction mechanism - GRI Mech 3.0.	90
Fig. 5-36: CH ₃ mole fraction profiles for three diffusion cases. $P = 8$ atm, $T = 598$ K, $\phi = 0.7$, $\Psi = 0.3$, reaction mechanism - GRI Mech 3.0.	91
Fig. 5-37: OH mole fraction profiles for three diffusion cases. $P = 8$ atm, $T = 598$ K, $\phi = 0.7$, $\Psi = 0.3$, reaction mechanism - GRI Mech 3.0.	92
Fig. 5-38: NO mole fraction profiles for three diffusion cases. $P = 8$ atm, $T = 598$ K, $\phi = 0.7$, $\Psi = 0.3$, reaction mechanism - GRI Mech 3.0.	93
Fig. 5-39: Reaction - zone NO mole fraction profiles for three diffusion cases. $P = 8$ atm, $T = 598$ K, $\phi = 0.7$, $\Psi = 0.3$, reaction mechanism - GRI Mech 3.0.	93
Fig. 5-40: NO ₂ mole fraction profiles for three diffusion cases. $P = 8$ atm, $T = 598$ K, $\phi = 0.7$, $\Psi = 0.3$, reaction mechanism - GRI Mech 3.0.	94
Fig. 5-41: Reaction - zone NO ₂ mole fraction profiles for three diffusion cases. $P = 8$ atm, $T = 598$ K, $\phi = 0.7$, $\Psi = 0.3$, reaction mechanism - GRI Mech 3.0.	95
Fig. 5-42: H ₂ mole fraction profiles for three diffusion cases. $P = 8$ atm, $T = 598$ K, $\phi = 0.7$, $\Psi = 0.3$, reaction mechanism - GRI Mech 3.0.	96
Fig. 5-43: H mole fraction profiles for three diffusion cases. $P = 8$ atm, $T = 598$ K, $\phi = 0.7$, $\Psi = 0.3$, reaction mechanism - GRI Mech 3.0.	96
Fig. 5-44: Temperature profiles for EGR and normal flames. $P = 8$ atm, $T = 598$ K, $\phi = 0.7$, $\Psi = 0.7$, reaction mechanism - GRI Mech 3.0.	98
Fig. 5-45: CH ₄ mole fraction profiles for EGR and normal flames. $P = 8$ atm, $T = 598$ K, $\phi = 0.7$, $\Psi = 0.7$, reaction mechanism - GRI Mech 3.0.	99
Fig. 5-46: CH ₃ mole fraction profiles for EGR and normal flames. $P = 8$ atm, $T = 598$ K, $\phi = 0.7$, $\Psi = 0.7$, reaction mechanism - GRI Mech 3.0.	100
Fig. 5-47: OH mole fraction profiles for EGR and normal flames. $P = 8$ atm, $T = 598$ K, $\phi = 0.7$, $\Psi = 0.7$, reaction mechanism - GRI Mech 3.0.	101
Fig. 5-48: O mole fraction profiles for EGR and normal flames. $P = 8$ atm, $T = 598$ K, $\phi = 0.7$, $\Psi = 0.7$, reaction mechanism - GRI Mech 3.0.	102
Fig. 5-49: H ₂ mole fraction profiles for EGR and normal flames. $P = 8$ atm, $T = 598$ K, $\phi = 0.7$, $\Psi = 0.7$, reaction mechanism - GRI Mech 3.0.	103

Fig. 5-50 : H mole fraction profiles for EGR and normal flames. $P = 8$ atm, $T = 598$ K, $\phi = 0.7$, $\Psi = 0.7$, reaction mechanism - GRI Mech 3.0.	103
Fig. 5-51 : NO mole fraction profiles for EGR and normal flames. $P = 8$ atm, $T = 598$ K, $\phi = 0.7$, $\Psi = 0.7$, reaction mechanism - GRI Mech 3.0.	104
Fig. 5-52 : NO mole fraction profiles for EGR and normal flames for the reaction zone. $P = 8$ atm, $T = 598$ K, $\phi = 0.7$, $\Psi = 0.7$, reaction mechanism - GRI Mech 3.0.	105
Fig. 5-53 : NO ₂ mole fraction profiles for EGR and normal flames for the reaction zone. $P = 8$ atm, $T = 598$ K, $\phi = 0.7$, $\Psi = 0.7$, reaction mechanism - GRI Mech 3.0.	106
Fig. 5-54 : NO ₂ mole fraction profiles for EGR and normal flames. $P = 8$ atm, $T = 598$ K, $\phi = 0.7$, $\Psi = 0.7$, reaction mechanism - GRI Mech 3.0.	107

LIST OF TABLES

Table 3-1: Contents of “therm.dat” file.	33
Table 3-2: Keywords for PREMIX file premix.inp.	38
Table 3-3: Steps to compile and run a CHEMKIN application on a UNIX system. ...	39
Table 4-1: Reaction mechanisms considered	45
Table 4-2: Reactant composition for fixed ϕ and constant energy.	53
Table 4-3: Cases for molecular diffusion study.	53
Table 4-4: Cases for EGR study.	54
Table 4-5: Reactant composition for EGR study.	55
Table 5-1: Important reactions in the consumption of CH_4 (GRI Mech 3.0, $\phi = 0.7$ and $\Psi = 0.3, 0.7$)	60
Table 5-2: Important reactions in the consumption of H_2 for $P = 8$ atm, $T = 598\text{K}$, $\phi = 1.0$, $\Psi = 0.3$	69
Table 5-3: Important reactions for the production of OH (OH mole fraction / sec) ...	77
Table 5-4: Important reactions for the production of O (O mole fractions / sec).....	78
Table 5-5: Important reactions involving production of H (H mole fractions/sec).....	79
Table 5-6: Important reactions involved in the production and consumption of NO (NO mole fraction / sec).	82
Table 5-7: Important reactions in the production and destruction of NO_2 (NO_2 mole fractions / sec).....	84

ACKNOWLEDGEMENTS

This project is supported by DOE Grant # DE-FC25-04NT42233. The research was conducted under the supervision of, and with the contribution from, Dr. Daniel C. Haworth. I would like to thank Dr. Stephen R. Turns for his suggestions and comments. Finally I would like to thank my family and friends for their continuing support throughout the decisions and challenges of my educational career.

Chapter 1

Introduction

1.1 Background

Hydrocarbon - based fuels such as gasoline, diesel and natural gas are important sources of energy. But these resources are limited in quantity on earth. Moreover these energy sources are a major source for the release of pollutants. Some of the pollutants are CO_2 , NO , NO_2 , SO_2 and particulate matter. CO_2 is a green house gas that leads to global warming and associated complexities. SO_2 causes acid rain. NO and NO_2 lead to formation of photochemical smog. In addition to these particulate matter can lead to different respiratory problems. A potential solution for these pollutants is to replace carbon - based fuels with alternatives and hydrogen is an important fuel in this respect. An important source of mechanical power for transportation and other applications is the internal combustion (IC) engine. Hydrogen can be accommodated in IC engines with relatively modest modifications. Natural gas typically contains more than 95% CH_4 and it is considered to be an important alternative to gasoline and diesel fuel as it is very abundant in quantity and not expensive. Natural gas also can be used in existing IC engines with little modification as the energy content of natural gas is similar to that of other hydrocarbon fuels.

However, there are important issues involved with the use of hydrogen. Hydrogen has very low mass density and the energy per unit mole for hydrogen is much lower

compared with hydrocarbon fuels. To prevent energy loss from an IC engine, the size of the engine has to be increased significantly. This problem can be countered with boosting (e.g. turbo charging). Hydrogen is also very expensive. The most economical method of hydrogen production currently is 2.2 times more expensive than the cheapest method for natural gas production (Akansu et al., 2004). This makes it economically difficult to use hydrogen as a stand - alone fuel. An alternative is to use hydrogen as a blend with existing hydrocarbon fuels like diesel, gasoline and natural gas. This replaces some of the carbon with hydrogen, thereby decreasing carbon dioxide emissions in favor of water. Moreover, some of the unique properties of hydrogen such as high molecular diffusivity and low ignition energy can lead to engine performance improvements. With hydrogen, the engine can be run at lower equivalence ratios and there is less residual fuel in the exhaust. NO_x emissions also can be reduced as the combustion can be carried out at lower equivalence ratio and hence lower temperature. Lower temperature reduces the formation of thermal NO which helps in reducing the engine - out NO_x.

Hydrogen can be used in electrochemical engines (fuel cells) as well as in IC engines. In electrochemical systems hydrogen is used to produce electric current which can be used to drive an electric motor. Internal - combustion engines are more widespread currently, and use the combustion of hydrogen with oxygen to release energy which is used to drive the piston to generate mechanical power.

Several fundamental hypotheses regarding the use of hydrogen in IC engines will be examined in this thesis. These include chemical kinetic effects resulting from hydrogen enrichment and molecular transport effects. The propagation of steady one-

dimensional laminar premixed flames of hydrogen/CH₄ gas blends is studied numerically under conditions that are relevant to combustion in spark - ignition IC engines.

Chapter 2

Literature Review

2.1 Introduction

Hydrogen has been the focus of research for a number of years. The use of H₂ as a fuel for IC engines dates to 1820, when Reverend Cecil in England used H₂ as a fuel (Akansu et al., 2004). Erren et al. in the 1930s first emphasized the importance of H₂ in reducing air pollution (Aslan et al., 1991). Unique properties of H₂ that make it beneficial for engine operation have long been recognized. The efficiency and emission levels of a H₂/methanol - fueled engine have been studied in detail by Adt and Swain (1974). They observed that the brake thermal efficiency of an engine operated with H₂ as an additive with methanol was higher compared to engine operation with methanol alone. NO_x emissions also were reduced. Tianshen et al. (1985) observed that supplying H₂ together with methanol to spark - ignition (SI) engines improved the combustion characteristics: flame propagation improved, ignition delay was reduced and thermal efficiency improved.

2.1.1 Engine Experiments and Modeling

In this section previous work related to engine experiments and modeling using H₂ as a fuel or as an additive is reviewed. This is done by summarizing salient results from several papers.

2.1.1.1 Exhaust Emission and Energy Consumption Effects from Hydrogen Supplementation of Natural Gas (Catellan and Wallace, 1995)

Experiments for exhaust emissions and energy consumption effects due to addition of hydrogen in natural gas (NG) have been studied in this work. Most of the experiments were on the rich side of stoichiometric. From the experiments it was found that hythane (contains up to 20% H₂ by volume in a H₂/NG fuel mixture) fuelling leads to greater efficiency at low - load conditions compared to NG. The addition of hydrogen increases the laminar flame speed of mixture. Changes in laminar flame speed have the largest effect on the flame initiation part of the combustion process. Therefore the addition of H₂ reduces burn time, especially at low speed and light load conditions where combustion duration is largest. A reduction in pumping loss with hythane also leads to a larger efficiency: manifold absolute pressure was higher with hythane fuelling by 0-3% in the experiment.

Brake-specific NO_x emissions (BSNO_x) were 10-40% higher with hythane fuelling. This results from an earlier start of combustion and higher temperature over a longer time. Once formed, NO_x does not have time to re - equilibrate to N₂ and O₂ as cylinder temperature decreases as the exhaust valve opens.

At higher loads there is little difference between the brake specific total hydrocarbon (BSTHC) emissions for the two fuels. This is significant, since NG has higher carbon content than hythane. Engine out hydrocarbon emissions in SI engines are dominated by fuel trapped in crevices that is not oxidized. Higher temperature in the cylinder can allow the oxidation of this fuel and hence reduce unburned hydrocarbons in the exhaust. The actual level depends on the rate of oxidation of crevice hydrocarbons

which are returned to the combustion chamber late in the expansion stroke. This can be reasoned using relation [2-1] provided by Thomson and Wallace (2002), between exhaust gas total hydrocarbons and exhaust gas temperature at constant equivalence ratio, ϕ :

$$\ln\left(\frac{N}{[THC]^a}\right) \propto \left(-\frac{1}{T_{ex}}\right) \text{ for constant } \phi. \quad [2.1]$$

Increased exhaust temperature leads to a reduction in the emissions. Here, exhaust temperature is defined as the temperature just before the burned gases reach the catalytic converter. For hythane fuelling it was found that the exhaust temperature was lower than for NG fueling. This leads to a reduced burning of fuel from the crevices and thus an increased THC emission.

Brake-specific carbon monoxide (BSCO) emissions are higher for NG combustion compared to hythane for all speed and load conditions. CO is formed by three processes in an engine cylinder. At low loads, slow flame propagation can cause CO concentration to freeze at high proportions before complete oxidation is allowed to take place. During combustion a high NO_x formation rate will displace oxygen, thus allowing less carbon oxidation to reach completion. Also the brief combustion of returning fuel from crevices can lead to CO formation. So under NG fueling higher CO emission was due to incomplete post combustion oxidation of returning fuel as there is higher post combustion of returning gases under NG conditions while there is a higher NO_x production under hythane fueling.

Brake-specific hydrogen (BSH₂) emissions are higher with hythane fueling than with NG. BSH₂ emissions were found to be more dependent on the combustion process than on the concentration of hydrogen in the fuel.

The effects of spark timing on efficiency and emissions were also studied. With advanced spark timing the peak pressure occurred close to top-dead-center and the combustion process occurred earlier in the cylinder. However, too much advance can lead to occurrence of peak pressure earlier than top-dead-center and hence a loss of efficiency. With an advancement of spark timing, combustion begins earlier and hence the gases are exposed to a higher temperature for a longer duration and this leads to an increase in NO_x emission. Advanced timing has the same effect for both fuels on BSTHC. An advance in spark timing means there will be a reduction in the exhaust gas temperature and hence there would be reduced post combustion of returning fuel from the crevices leading to a higher BSTHC. Emission differences between fuels were higher at 1800 rpm than at 1200 rpm. The lower exhaust temperatures at 1200 rpm prohibit post oxidation, so higher relative temperatures under natural gas fueling are less important in the post-combustion oxidation of hydrocarbons. At 1800 rpm temperature difference plays a more important role in the process. Hence, BSTHC emissions are higher for hythane than NG fueling. CO emission is not affected by the spark timing.

With an increase in ϕ THC emissions increased as there is a reduction in the amount of available oxygen. Also THC emissions are higher for hythane fuelling than for NG. In the case of hythane fuelling there is a preferential oxidation of returning (from crevices) H₂ compared to CH₄ and hence more unburned CH₄ is left. BSNO_x emission decreased as ϕ increased as there is a reduction in temperature with an increase in ϕ and also there is less oxygen available for NO_x formation with richer mixtures. The heat capacity of methane is 13% higher than H₂ on a volumetric basis. So as ϕ increases, the

heat absorption of the additional fuel could cause the temperature to decrease more quickly under natural gas fuelling.

2.1.1.2 NO_x Emissions and Efficiency of Hydrogen, Natural Gas and Hydrogen/ Natural Gas Blended Fuels (Hoekstra et al., 1996)

NO_x emissions and efficiency of engines using H₂, NG and H₂/NG blends are discussed in this paper. The study was conducted to meet the equivalent zero emission vehicle (EZEV) standard set by the California Air Resource Board (California Air Resource Board, 1995). The authors performed engine dynamometer testing of a homogeneous-charge, spark-ignition, lean-burn engine fueled by NG, H₂ or H₂/NG blends. Hydrogen/compressed natural gas blends were explored due to the higher energy density of H₂/CH₄ blends and lower cost compared to pure H₂. A compilation of the different methods of production of hydrogen and NG and associated cost has been published by Akansu et al. (2004). The most economical method of hydrogen production (steam reforming) is 2.2 times more expensive than the production of NG (Basye and Swaminathan, 1997).

For the experiments, Hoekstra used a spark - ignited V8 engine with a 9:1 compression ratio. A chemiluminescent detector was used to detect NO_x emissions. To reduce the heat loss at top-dead-center, the engine was designed to produce minimum swirl. The H₂ used was 99.9% pure and the NG composition was 93.6% CH₄, 3.6% ethane, 1% propane, 0.7% CO₂, 0.5% N₂ and 0.4% butane. Cycle-to-cycle variation in the indicated mean effective pressure (IMEP) was analyzed and the coefficient of variation (COV) of IMEP was defined as the ratio of standard deviation to the mean. A COV of

10% was used to define the lean limit of engine operation; COV above 10% is perceived as a poor running condition. The experiments were done at 12.7 kW of power output to simulate a full - sized passenger car or light truck running at highway cruise.

From the experiments it was observed that there was an increase in NOx emissions with increasing hydrogen content at constant equivalence ratio. As the equivalence ratio decreased, there was a reduction in NOx emissions as the amount of air in the combustion chamber increased. At a fixed equivalence ratio, the COV was lower for higher hydrogen content in the fuel mixture. The lean limit of operation based on COV = 0.1 varied from $\phi = 0.7$ for NG to $\phi = 0.58$ for 30% hydrogen. Ignition timing was found to have a strong impact on NOx emissions. As equivalence ratio increases, the effect of spark timing on NOx emissions increases, with an advance in spark timing leading to an increase in the NOx emissions.

Tests were also conducted to determine the minimum equivalence ratio for the operation of the engines. The minimum was found to be $\phi = 0.2$ for pure hydrogen, $\phi = 0.48$ for 30% H₂ and $\phi = 0.62$ for 100% NG. The effects of spark advance on emissions and efficiency were analyzed and it was found that with 100% hydrogen, the EZEVE standard was not satisfied for operation below $\phi = 0.4$. Similar results were found for 100% NG fueling. In that case, the EZEVE standard was not satisfied for operation at $\phi = 0.62$, and at this point the operation was erratic. When ϕ was increased the operation became smooth but the EZEVE standard was not satisfied. When the same type of analysis was done for 30% H₂ and 70% NG fueling, operation at $\phi = 0.52$ lead to a large efficiency penalty but the EZEVE standard was satisfied. Operation near minimum advance for best torque (MBT) spark timing with hydrogen at $\phi = 0.4$ and with 30%

hydrogen at $\phi = 0.52$ gave similar NO_x results. The mixed fuel took 35% longer to burn, leading to a drop of 6% in efficiency for 30% hydrogen compared to 100% hydrogen as fuel. The pure hydrogen case was most sensitive to spark timing, with 30% hydrogen in between, and NG being the least sensitive. Moreover, results from a multi - cylinder engine at 9:1 compression ratio indicated that NO_x levels of less than 10 ppm are possible at steady - state, part - throttle ($\phi = 0.65$) operation with 30% hydrogen as fuel with negligible efficiency penalty relative to MBT efficiency.

2.1.1.3 Knock in Spark Ignition Hydrogen Engines (Li and Karim, 2004)

The phenomenon of knock is an important concern as it limits the engine compression ratio. Knock in SI engines is acknowledged as a barrier to the further improvement of efficiency, increased power and use of wider range of fuels. Knock causes high vibration and it can damage engine components. Knock behavior of hydrogen in spark - ignition engines has been discussed in this paper. The authors modified a knock prediction model developed for SI methane engine applications. For this purpose a knock criterion, K_n , is defined. Knock occurred when this quantity exceeded a certain critical value. The criterion is a time-varying function defined as the “calculated temporal variation in the accumulated energy released due to pre-ignition chemical reaction activity within the temporally diminishing in size end gas per instantaneous value of the cylinder volume.” This energy release is normalized relative to the total amount of energy that is released through normal flame propagation per unit swept volume of cylinder:

$$K_n = \frac{\frac{\text{total energy released due to end gas reactions up to time } t}{\text{cylinder volume}|_t}}{\frac{\text{total energy of the whole charge to be released by flame propagation}}{\text{cylinder volume}|_0}} \quad [2.2]$$

The function K_n is dimensionless, and it also represents “the fractional increase in total cylinder pressure due to the pre-flame oxidation reaction activity of the instantaneous size of the diminishing end gas relative to the mean effective combustion pressure.” Mean effective combustion pressure is defined as the average increase in cylinder pressure due to normal combustion. This modeling approach was successful in CH_4 SI engines. With hydrogen, there is a much wider range of operation on either side of stoichiometric where there can be knock, as shown in Fig 2-1.

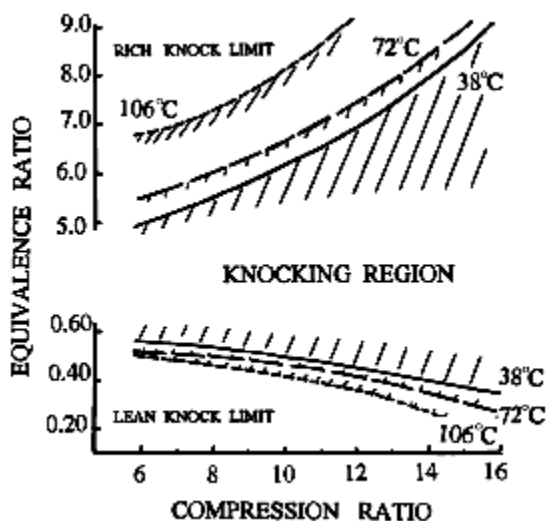


Fig. 2-1: Knocking region as a function of ϕ and compression ratio for pure H_2 . Source: Li and Karim, 2004.

To account for this difference, K_n has been modified so that total energy release for any mixture is further normalized relative to the stoichiometric mixture. The combustion

duration is normalized relative to a constant value such as that observed with a common fuel like methane. The modified equation is:

$$K_n = \frac{h_{sp} - h_f}{\Delta h_o} \times \frac{m_u}{m_o} \times (CR - 1) \times \frac{\Delta h_o}{(\Delta h_o)_{stoich}} \times \frac{\Delta \theta_{c,ref}}{\Delta \theta_{c,f.c}}. \quad [2.3]$$

Here h_{sp} and h_t are specific enthalpies of the unburned end gas at spark passage and at time instant t , respectively, Δh_o is effective heating value of the fresh charge, m_u is the remaining mass of the end gas at time t and m_o is the mass of the initial fresh charge.

In this work the onset of knock was recorded using a transducer on the cylinder. Onset of knock was accompanied by the typical knocking sound and also the appearance of high - frequency pressure oscillations near the beginning of the expansion stroke. There was good agreement between the experimental and predicted values when knock - limited equivalence ratio (KLER) was plotted against compression ratio (CR). There was a difference between the predicted and experimental values at low CR and low intake temperatures. Fig 2-2 shows the effect of changing CR and intake temperature over the knock limits.

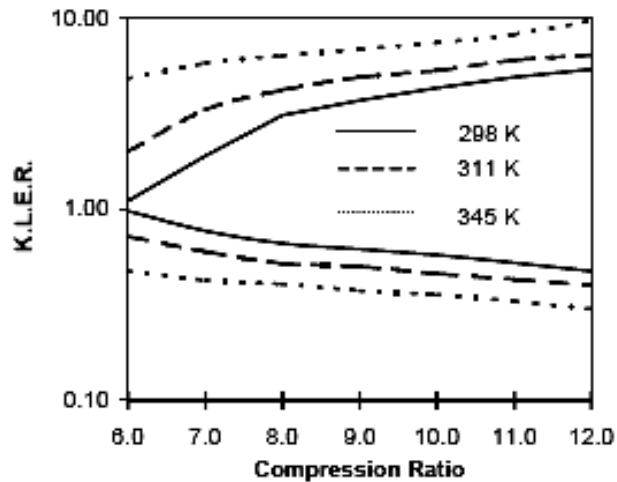


Fig. 2-2: K.L.E.R. variation with compression ratio under unthrottled operation in a CFR engine. Source: Li and Karim, 2004.

With an advance in spark timing the knock region widened by a very small amount. The knocking region tends to widen and the operational region tends to narrow with increasing temperature and increasing CR.

Fig 2-3 shows that the engine achieves a power production peak at moderate CR, while high efficiency values are achieved at high compression ratios. Increasing the compression ratio leads to an increase in the power production efficiency. Reducing the equivalence ratio helps in higher utilization of the available fuel.

The fuel used in this study was natural gas, which contains many gases other than CH_4 . The impact of these gases on knock was also studied using hydrogen as fuel. A number of experiments were performed and both KLCR and KLER were established for CH_4 and CO. These are shown in Figures 2-4 and 2-5 respectively. Pure CH_4 and CO have better knock resistance than hydrogen in air. CH_4 improves the knock resistance while CO has little benefit on the H_2/NG blend, even though pure CO has the best knock

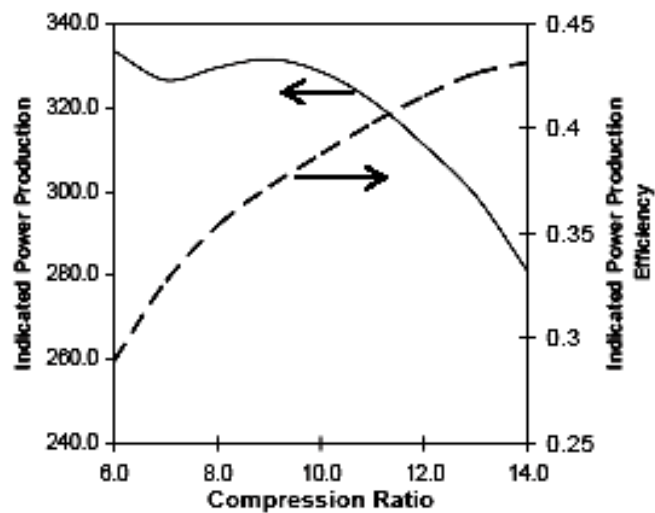


Fig. 2-3: Indicated power production and indicated power production efficiency as a function of compression ratio. Source: Li and Karim, 2004.

resistance out of the three. This is due to the enhanced oxidation rate of CO in the presence of H₂. The better knock resistance of CO comes into play only when the concentration of CO is very high.

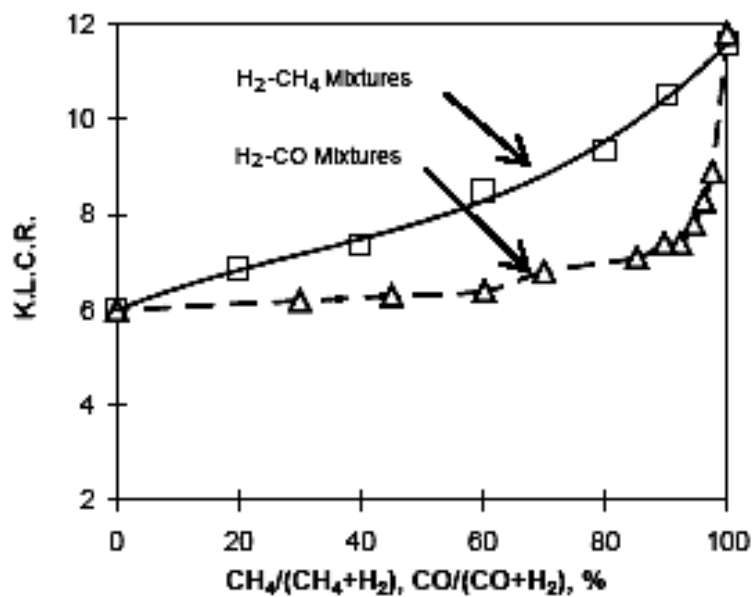


Fig. 2-4: Variation of K.L.C.R. as a function of fraction CH₄ and CO in a fuel. Source: Li and Karim, 2004.

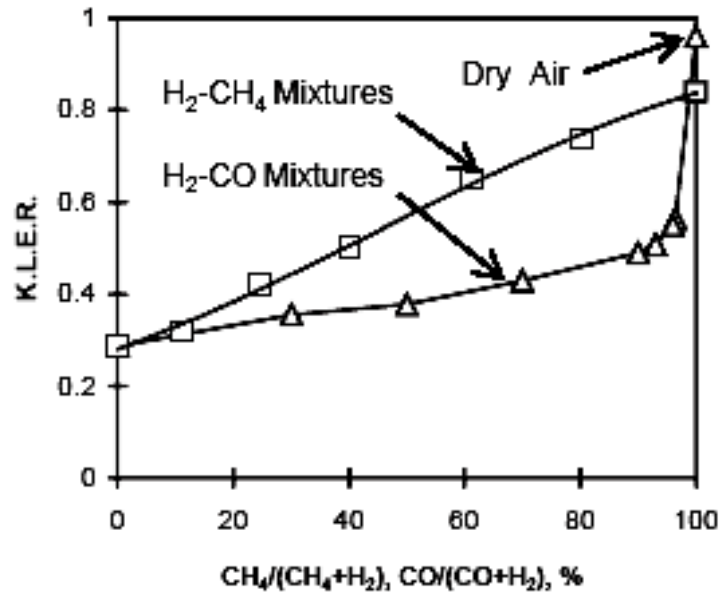


Fig. 2-5: Variation of K.L.E.R. as a function of fraction CH₄ and CO in a fuel. Source: Li and Karim, 2004.

2.1.1.4 The Addition of Hydrogen to a Gasoline Fuelled SI Engine (Andrea et al., 2004)

There have also been efforts to use hydrogen with other fuels including gasoline. Andrea et al. (2004) have made an experimental study of the use of hydrogen with gasoline in IC engines. They used a 20 HP, four-stroke, V – twin engine; and the spark plug was fitted with a pressure transducer to measure the engine pressure. The equivalence ratio defined by Yu et al. (1986), has been used:

$$\phi = \frac{Q_G / \{Q_{Air} - Q_H / (C_H / C_{Air})_{st}\}}{(C_G / C_{Air})_{st}} \quad [2.4]$$

Here Q represents the flow rate and C is the concentration of gasoline (subscript G), hydrogen (subscript H) or air (subscript air). $(C_H/C_{Air})_{st}$ is the stoichiometric fuel/air ratio for hydrogen, and $Q_H / (C_H/C_{Air})_{st}$ represents the amount of air needed to oxidize hydrogen completely. This is subtracted from total amount of air, producing the amount that is left for the oxidation of the hydrocarbon.

From the experiments, it was observed that there was very little effect of hydrogen addition on engine torque if the equivalence ratio $\phi > 0.85$. With the addition of 2% hydrogen there was an improvement in torque of only 1 Nm while for $\phi < 0.85$, there was an improvement of 5 Nm. For 1% H_2 addition the results are in between those of no hydrogen and those of 2% addition. Here addition of hydrogen has been done on a volumetric basis. The results can be separated into two groups based on equivalence ratio. For $\phi > 0.85$ there is no difference in crank angle degree (CAD) where the peak burn rate occurred with hydrogen addition. No change was seen in the 2-10%, 10-90% and 50-90% burn duration periods with hydrogen addition in the mixtures for $\phi > 0.85$, with the differences falling within the limits of uncertainty. For $\phi < 0.85$, on average the period necessary to burn 2-10% of mass decreased by 5 CAD with addition of 2% hydrogen and an average reduction of 3 CAD was seen with the addition of 1% hydrogen in air. All the differences were larger than experimental uncertainty of 2 CAD. The trend of decrease continued for the 10 – 90% burn duration period. An average decrease of 20 CAD with addition of 2% H_2 and 9 CAD with the addition of 1% H_2 in air was seen.

The COV in the IMEP (COV_{IMEP}) was calculated in order to quantify cycle-to-cycle variation. From the results it was evident that with 2% H_2 addition, the engine almost always operated in an acceptable range of less than 10% COV_{IMEP} and the

COV_{IMEP} began to increase above 10% for mixtures with $\phi < 0.65$. Addition of hydrogen reduced the cyclic variability. Without hydrogen addition, COV_{IMEP} was above 10% for charges leaner than $\phi = 0.85$. In some cases with the hydrogen addition, there was a reduction in COV_{IMEP} by 30% when compared to operating without any addition. So hydrogen addition reduced the cyclic variation when the operation otherwise would become unstable due to the low equivalence ratio. No effect of hydrogen addition is seen near stoichiometric burning as the engine operation is already stable. The authors have reasoned that fluctuations in the early stage of the combustion process have a large impact on cycle – to - cycle variability, as the flame is small at the start of combustion and it is not able to average out any inhomogeneity in the fuel-air mixture. This inconsistency in the spark kernel is carried as the flame grows. The decrease in cycle-to-cycle variability (as indicated by COV_{IMEP}) with the addition of hydrogen was attributed to the decrease in burn duration.

Formation of NO was studied through the experiments. It was observed that while operating close to stoichiometric conditions the addition of hydrogen has little impact on the NO concentration. However, for $\phi < 0.8$ the formation of NO increased with increasing hydrogen. The increase in NO emissions with the addition of hydrogen is correlated to the faster burn rate as shown in Fig 2-6.

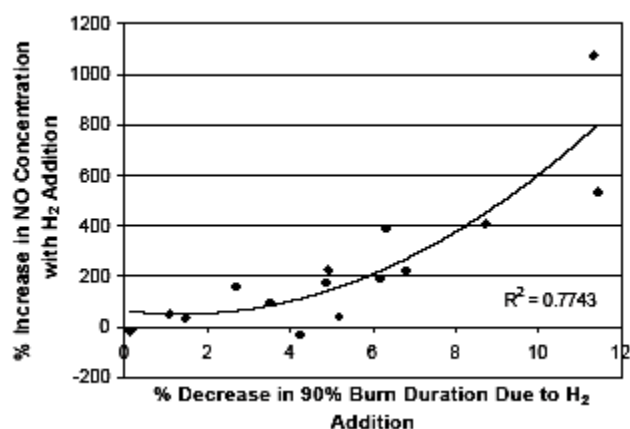


Fig. 2-6: Change in NO concentration with change in 90% burn duration due to H₂ addition. Source: Andrea et al., 2004.

With the addition of hydrogen, earlier burn occurred thereby increasing the cylinder pressure and temperature, leading to an increase in NO. Higher temperature rise favors the formation of NO over NO₂ and also increases the rate of formation of NO.

Experiments were also carried out to determine the feasibility of a hydrogen-producing unit onboard. The device produced 6.7 ml/s of hydrogen from an electrical power input of 169 W. If this device is scaled up to produce H₂ in the amount required for 1% H₂ addition (80 ml/s) and 2% H₂ addition (130 ml/s), the resultant power consumption would be 2000 W and 3000 W respectively. The corresponding increase in power from the engine would be 500 – 1800 W for 1% H₂ addition and 200 – 3500 W for 2% H₂ addition. Even if the efficiency loss is ignored, the energy required to generate hydrogen is more than the energy produced from its use as a blend with gasoline.

2.1.1.5 Emission Results from the New Development of a Dedicated Hydrogen – Enriched Natural Gas Heavy Duty Engine (Collier et al., 2005)

NOx emission benefits from the use of H₂ have been observed by Collier et al. (2005). One of the major mechanisms for reducing NOx from engines is through charge dilution. This can be done by exhaust gas recirculation (EGR) or by lean burning of the mixture. The problem in either case is misfire beyond a certain limit. The addition of hydrogen to a hydrocarbon fuel does not reduce NOx directly. In fact, NOx emissions increase with the addition of H₂ for the same overall stoichiometry. The benefit of H₂ is to extend the lean limit or dilute limit of operation, thereby reducing the combustion temperature and hence reducing NOx.

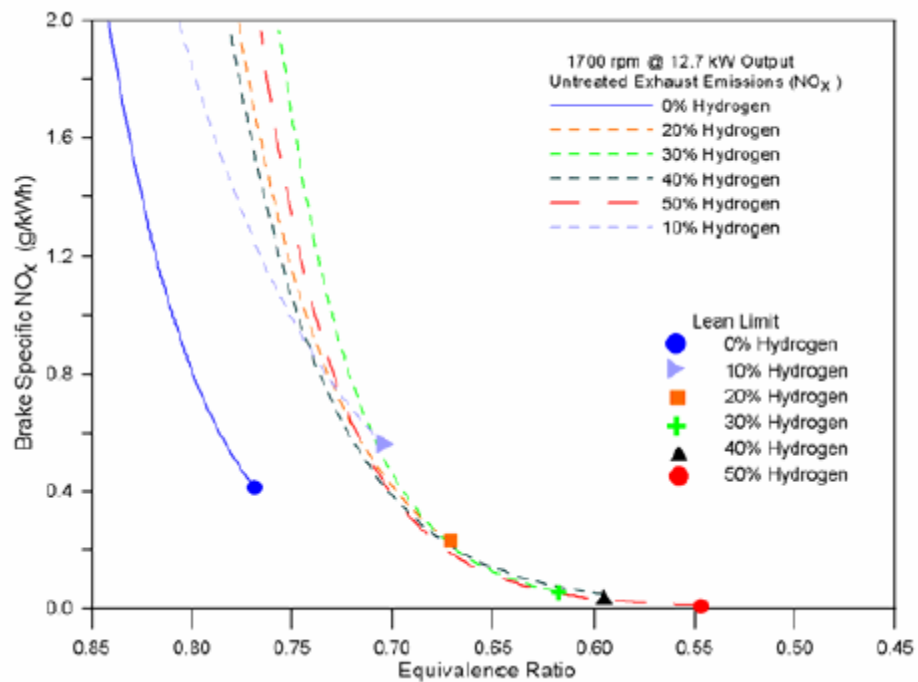


Fig. 2-7: NOx vs equivalence ratio for different H₂/CH₄ mixtures. Source: Collier et al., 2005

From Fig 2-7 it is evident that with increased H₂ addition the lean burn limit (reducing ϕ) has been extended. The benefits of lean burn for reducing NO_x emissions diminish for very low values of ϕ . This “knee of the NO_x curve” decreases with increasing H₂ fraction. Fig 2-7 shows that 30% of H₂ addition by volume is optimum in the sense that higher levels of H₂ do not yield significant additional reductions in NO_x. Here the engine was operated at constant torque and rpm and the charge was diluted with excess air until there was a misfire to determine the lean burn limit. Misfire was determined by in-cylinder pressure measurements.

From the experiments they also hypothesized that in the combustion of NG, the rate-controlling reaction is:



Once CH₃ is formed, other reactions proceed quickly. Conversion of CH₄ to CH₃ radical via the OH- radical is also a fast reaction. In the presence of H₂, OH radicals are produced very quickly and these are instrumental in removing the first H atom from the CH₄ molecule and thus creating the CH₃ radical.

2.1.1.6 Effects of Hydrogen Enhancement on Efficiency and NO_x Emissions of Lean and EGR - Diluted Mixtures in a SI Engine (Ivanic et al., 2005)

Ivanic et al. (2005) observed experimentally the benefits of using H₂ as an additive with indolene fuel. It was found that lowered combustion temperatures reduce NO_x emissions. Reducing the intake manifold throttling lowers pumping losses leading to higher net efficiency. With the increased presence of air there was an increase in the

ratio of specific heats that increases the expansion work by allowing the burned gases to expand through a larger temperature ratio prior to exhaust. The combustion efficiency was increased because of the increased amount of fuel that was burned. However, these advantages are offset by reduced combustion speed of the dilute fuel-air mixture which can lead to cycle-to-cycle variation. Hydrogen addition also allowed higher dilution, accelerating the combustion process and thus extending the dilution limit.

For this study H_2 was produced through a gasoline reformer called a plasmatron. For this purpose a thermal diffusion parameter (TDP) was defined as:

$$TDP = \frac{\Delta T_{stoichiometric}}{\Delta T}$$

$$\Delta T = \frac{\sum_{i=1}^5 m_{xi} Q_{LHV,xi}}{\sum_{j=1}^9 m_{xj} C_{v,xj}} \quad [2.6]$$

$$xi \in (C_7H_{14}, H_2, CO, CH_4, C_2H_2)$$

$$xj \in (H_2O, H_2, CO, CO_2, N_2, C_7H_{14}, C_2H_2, O_2, CH_4)$$

Here ΔT is the chemical energy released during combustion per constant value heat capacity of the unburned cylinder charge, Q_{LHV} is the lower heating value, m is the mass of the species in consideration and C_v is the heat capacity of the species in consideration. The basis for the TDP is the thermal capacity of the diluent. It is used to normalize data with different diluents and compare them on a common basis. Since TDP accounts for heat capacities for all diluents present in the charge mixture, EGR dilution levels that correspond to particular air dilution can be determined, since they result in the same TDP value.

From the experiments it was observed that under partial load conditions, lean dilution improves efficiency by 12% while EGR improves efficiency by 8%. Either form of dilution reduces NO_x by 98% when the engine is operated close to its dilution limit. Lean dilution caused NO_x levels to peak near a relative air – fuel ratio of 1.1 and then decline out to the dilution limit, while increased EGR dilution always reduced the NO_x emissions. By comparing the TDP parameter, it was found that the effect of EGR, at equal dilution, on NO_x was more than the dilution by excess air.

2.1.2 Fundamental Combustion Experiments and Modeling

In this section previous work related to combustion experiments and modeling using H₂ as a fuel or as an additive is reviewed. Salient results are summarized from two important papers.

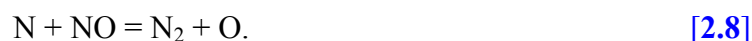
2.1.2.1 Hydrogen/Oxygen Additives Influence on Premixed Iso-Octane/Air Flame (Sobiesiak et al., 2002)

Numerical methods have also been employed to study the impact of hydrogen addition on the performance of different fuels. Sobiesiak et al. studied the behavior of premixed flames for different compositions of iso - octane/ air using CHEMKIN and a detailed chemical mechanism provided by Peters (1994) along with the GRI Mech 3.0 (Smith et al.) NO_x mechanism. The final mechanism consists of 308 reactions and 75 species. Calculations were performed with different amounts of O, H, H₂ and O₂ and with equivalence ratios varying from 0.6 to 1.3. A larger increase in laminar flame speed with H₂ addition was found for lean-burning compared to stoichiometric - burning cases. For stoichiometric burning with 5% and 10% addition of H₂, flame speed increased 1% and 5% respectively, while for an equivalence ratio of 0.6, 10% hydrogen addition yielded a 10% increase in flame speed. This results from the combined effect of the higher burning velocity of hydrogen and enriched oxygen concentration. There also was an increase in reaction rate with addition of atomic hydrogen. For the stoichiometric case the increase was similar to that for H₂ addition at 5% and 10% levels, but for lean and rich mixtures

the increase was twice that for addition of H₂. The most significant increase in burning velocity was for the case of addition of H and O simultaneously. For all additives there was an earlier rise in temperature in the preheat region, but later in the reaction zone the temperature fell below that of pure isooctane case. Finally, the higher reaction rates in the recombination zone resulted in higher flame temperatures. Hydrogen/oxygen additives have a small effect on the induction time, but the increase in reaction rates resulting in higher flame temperature result in higher burning velocity with additives. CO emissions were found to be related to the OH radical concentration. In general there was an increase in the CO oxidation in the zone where there was an increase in OH concentration. The reaction involving consumption of CO is:



NO concentration was found to increase for higher adiabatic flame temperatures. The addition of oxygen results in increased concentration of O and also of the adiabatic flame temperature leading to an increase in NO concentration. This was evident from the study of pure H₂/O₂ flames near stoichiometry, where 90% of the NO produced was in the post - flame region. The single most influential reaction observed was:



In the flame region 10% of NO was produced from the following six important reactions:





NO₂ emissions were higher for all the cases with different additives. However the increase in NO_x was smaller if the additives were used in lean mixtures.

2.1.2.2 Nitric Oxide Detection in Turbulent Premixed Methane/Air Flames (Herrmann and Boulouchos, 2005)

An experimental study of nitric oxide formation in turbulent premixed flames has been done by Herrmann and Boulouchos (2005) to determine the impact of turbulence and equivalence ratio. NO production in hydrocarbon/air mixtures occurs through two principal mechanisms. Thermal NO is produced at high temperatures by the Zeldovich mechanism. In the prompt NO or Fenimore mechanism, the CH radicals react with the nitrogen in air to form HCN and N, eventually leading to NO. In the experiment the flame front was defined by the presence of OH radicals. The threshold for the OH concentration was determined by the inflection point in the signal histogram within the reaction zone. Laminar premixed flame speed calculations show that this position corresponds to highest CH radical concentration and hence the highest heat - release rate. Variations in NO concentration with varying equivalence ratio are shown in Fig 2-8. With increasing distance downstream in the flame, there is a homogenization of NO concentration. As a consequence of the optimal combination of temperature and oxygen concentration, the highest NO concentration appears at $\phi = 0.91$. For leaner mixtures NO

concentration decreases as the post - flame temperature reduces so that the contribution of the Zeldovich mechanism reduces.

Fig 2-9 shows the NO distribution along the symmetric axis for constant equivalence ratios and different turbulence conditions. In the reaction zone, the profiles for near stoichiometric flames show a steeper slope. There is a small influence of turbulence on NO formation. At higher turbulence levels, NO formation increases due to higher turbulent burning speed, a shorter flame is formed and the reaction zone is located closer to the burner.

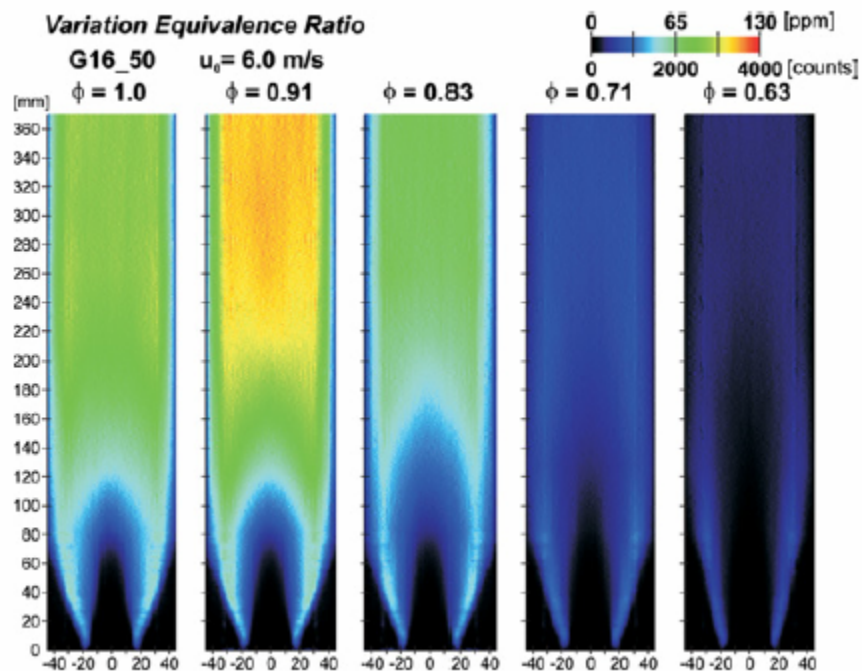


Fig. 2-8: NO distribution for different ϕ and constant turbulence. Source: Herrmann and Boulouchos, 2005

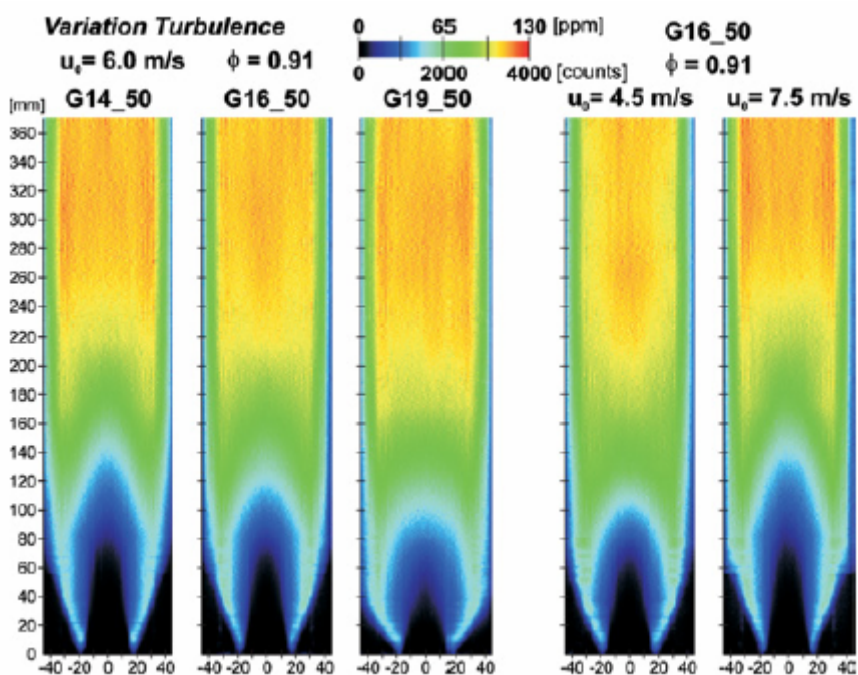


Fig. 2-9: NO_x concentration variation under different turbulence conditions and constant equivalence ratio. Source: Herrmann and Boulouchos, 2005

2.1.3 Present Work

In this study, the influence of hydrogen addition to premixed, steady - state, one - dimensional methane flames is examined. Three basic studies were performed: changes in the flame structure due to changes in the hydrogen/methane ratio for a fixed equivalence ratio; influence of the diffusion coefficient of hydrogen on flame structure; and the influence of exhaust - gas recirculation. For the investigation of hydrogen content, energy content of the fuel mixture has been kept constant to isolate thermal effects from kinetic and transport effects. For the investigation of molecular diffusion effects, two schemes were adopted: in the first scheme the diffusion coefficient of hydrogen is set equal to that for methane while in second scheme the Lewis number has

been set to unity for all the species in the reacting mixture. Exhaust - gas recirculation is an important method for reducing NO_x production in IC engines. For the EGR study, 20% by volume of intake mixture has been considered to be products of combustion and its influence on reducing the NO_x has been studied.

Chapter 3

Computational Tools

3.1 CHEMKIN

The major computational tools used for the present study are CHEMKIN II (Kee et al. 1989) and CHEMKIN 4.0 (Reaction Design, 2004). CHEMKIN is a software suite developed by Sandia National Laboratories beginning in the 1970s; it is used for microelectronics, combustion and chemical processing applications. CHEMKIN incorporates complex chemical kinetics and realistic thermochemical properties. There is a large collection of programs and subroutine libraries that work together to facilitate the formation, solution and interpretation of problems involving gas - phase and heterogeneous reacting systems.

The basic structure of CHEMKIN is shown in Fig 3-1. The CHEMKIN package is basically composed of two blocks of FORTRAN code and two input files. The two codes are the “CHEMKIN Interpreter” and the “Gas – Phase Subroutine Library,” and the input files are the thermodynamic database (therm.dat) and the gas-phase reactions (chem.inp). The “chem.inp” input file consists of lists of elements, species and reactions. The thermodynamic data, “therm.dat,” contains thermodynamic properties for each species mentioned in the form of polynomial coefficients (Kee et al., 1989). Thermodynamic data for all the species mentioned in the input file must be present. The user needs to run the

interpreter, which reads the symbolic description of the reaction mechanism and thermodynamic properties from the thermodynamic database.

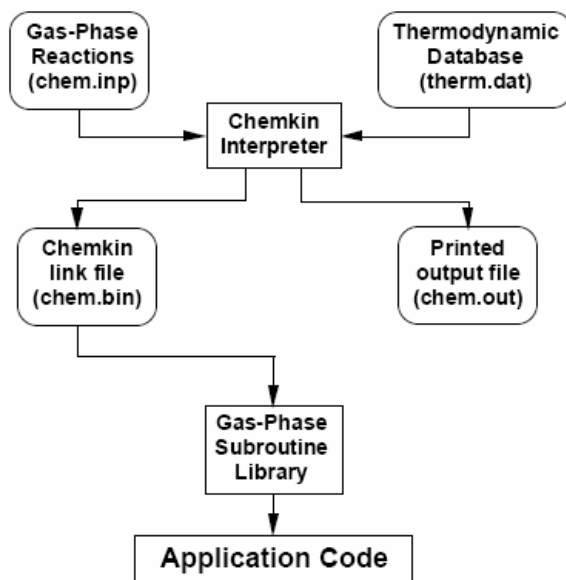


Fig. 3-1: Basic structure of CHEMKIN (Source: Kee et al., 1996)

The linking file that is produced is called “chem.bin” and can either be in binary or ASCII format as desired. There is also an output file called “chem.out” that echoes a detailed list of elements, species, reactions and errors, if any. The linking file contains the information for all the species, reactions and thermodynamic properties which are later used by the calls from other CHEMKIN subroutines in the application code. The application code calls the subroutines contained in the Gas – Phase Subroutine Library to obtain information on molar production rates and other quantities. The routines in the Gas – Phase Subroutine Library derive the necessary information from the linking file and process it to give the desired results. The inputs for the subroutines in the Gas – Phase Subroutine Library typically are temperature, pressure and species composition. Before calling any other CHEMKIN subroutine in the Gas – Phase Subroutine library, it is

necessary to call subroutine CKINIT which fills the work arrays ICKWRK, RCKWRK and CCKWRK. These work arrays are related to integer, floating point and character space, respectively, and are filled when the linking file is read by the CKINIT subroutine. The dimension for the work arrays are specified by the user; if the size of data that is required is larger than the size of the arrays an error message is printed asking for an increase in the array dimension. Next a brief description of the input files for CHEMKIN is provided.

3.1.1 chem.inp

This input file to the CHEMKIN interpreter contains the names of the elements and species that are involved. Input is restricted to an 80 - column format. The input for elements and species is format free with blank space separating the names. In addition there is a description of the elementary reactions that are involved. The elements and species are specified in a symbolic form and must be in the list of elements that CHEMKIN can accept. In the case of isotopes, the molecular weights must follow the symbolic name. After the elements and the species, there is a list of elementary reactions in symbolic form. The reactions must involve only those species that have been included in the species list. Each reaction is followed by three Arrhenius coefficients: a pre-exponential factor A , temperature exponent β and activation energy E_A . The forward rate coefficient for each reaction is presumed to follow equation 3-1:

$$k_f = AT^\beta \exp\left(\frac{-E_A}{RT}\right) \quad [3.1]$$

where R is the universal (molar) gas constant.

Enhanced third - body efficiencies for selected species may be specified in the line following any reaction that contains an arbitrary third body M . Comments are indicated by exclamation marks. A sample of the interpreter input file is shown in Fig 3-2. CHEMKIN uses C. G. S. units by default.

```

ELEMENTS
H O AR
END
SPECIES
H2 O2 H O OH HO2 H2O2 H2O AR
END
REACTIONS
H2+O2=OH+OH          1.7E13  0.0  47780.
H+O2+M=HO2+M        2.1E18  -1.0   0. !SLACK
  H2O/21./ H2/3.3/ O2/0.0/
H2O2+H=HO2+H2        1.6E12  0.0   3800.
H2O2+OH=H2O+HO2      1.0E13  0.0   1800.
END

```

Fig. 3-2: Sample chem.inp file.

3.1.2 therm.dat

Each species listed in the “chem.inp” file must have associated thermodynamic properties in the thermodynamic data file “therm.dat.” A sample thermodynamic data file is shown in Fig 3-3.

```

THERMO
  300.000 1000.000 5000.000
O          L 1/900 1          G 200.000 3500.000 1000.000          1
2.5692078E+00-8.59741137E-05 4.19484589E-08-1.00177799E-11 1.22833691E-15  2
2.9275791E+04 4.7843864E+00 3.16826710E+00-3.27931884E-03 6.64306396E-06  3
-6.1280624E-09 2.11265971E-12 2.91222592E+04 2.05193346E+00          4
END

```

Fig. 3-3: Sample therm.dat file.

The format for “therm.dat” file must follow the rules (Kee et al., 1996) that are given in Table 3-1. Polynomial coefficients $a_{1k} \rightarrow a_{7k}$ for each species k corresponding to species specific heat, enthalpies and entropies as follows:

Table 3-1: Contents of “therm.dat” file.

Line Number	Contents	Format	Column
1	THERMO	Free	Any
2	Temperature ranges for two sets of coefficients: lowest temperature, common temperature and highest temperature	3F10.0	1 to 30
3	Species name which must start in column 1	18A1	1 to 18
	Date	6A1	19 to 24
	Atomic symbols and formulas	4(2A1, I3)	25 to 44
	Phase of species: S, L or G.	A1	45
	Low temperature	E10.0	46 to 55
	High temperature	E10.0	56 to 65
	Common temperature if needed	E8.0	66 to 73
	Atomic symbols and formulas	2A1, I3	74 to 78
	The integer 1	I1	80
4	Coefficients a_{1k} to a_{5k} for upper temperature interval calculation using equations [3.2] through [3.4].	5(E15.0)	1 to 75
	The integer 2	I1	80
5	Coefficients a_{6k} , a_{7k} for upper temperature interval and a_{1k} , a_{2k} , a_{3k} for lower temperature interval calculation	5(E15.0)	1 to 75
	The integer 3	I1	80
6	Coefficients a_{4k} , a_{5k} , a_{6k} , a_{7k} for lower temperature interval	4(E15.0)	1 to 60
	The integer 4	I1	80

$$\frac{C_{p,k}^o}{R} = a_{1k} + a_{2k}T_k + a_{3k}T_k^2 + a_{4k}T_k^3 + a_{5k}T_k^4 \quad [3.2]$$

$$\frac{H_k^o}{RT_k} = a_{1k} + \frac{a_{2k}}{2}T_k + \frac{a_{3k}}{3}T_k^2 + \frac{a_{4k}}{4}T_k^3 + \frac{a_{5k}}{5}T_k^4 + \frac{a_{6k}}{T_k} \quad [3.3]$$

$$\frac{S_k^o}{R} = a_{1k} \ln T_k + a_{2k}T_k + \frac{a_{3k}}{2}T_k^2 + \frac{a_{4k}}{3}T_k^3 + \frac{a_{5k}}{4}T_k^4 + a_{7k} \quad [3.4]$$

Other thermodynamic properties are given in terms of C_p^o , H^o and S^o .

3.1.3 tran.dat

In the case of flame calculations it is also necessary to specify multicomponent viscosities, thermal conductivities, diffusion coefficients and thermal diffusion coefficients. There are separate subroutines for each of these calculations, and they are contained in the CHEMKIN program tranlib.f. Molecular transport properties are specified in a third input file named “tran.dat.” The contents of this file are the symbolic name for each of the species listed in the “chem.inp” file. The species name is followed by an index indicating whether the species is monoatomic (0), linear (1) or non-linear geometry (2). The remaining entries for each row are: the Lennard – Jones potential well depth in Kelvin, Lennard – Jones collision diameter in Angstroms, dipole moment in Debye, the polarizability in cubic angstroms and the rotation relaxation collision number

at 298 K. After the last number a comment can be added. A sample tran.dat file is shown in Fig 3-4.

```

AR      0 136.500 3.330 0.000 0.000 0.000
C       0  71.400 3.298 0.000 0.000 0.000
C2      1  97.530 3.621 0.000 1.760 4.000
C2O     1 232.400 3.828 0.000 0.000 1.000
CN2     1 232.400 3.828 0.000 0.000 1.000
C2H     1 209.000 4.100 0.000 0.000 2.500

```

Fig. 3-4: Sample tran.dat file.

3.2 Application Codes

Application codes solve conservation equations for mass, momentum and energy for a specified configuration. Each application code calls appropriate subroutines from the gas - phase subroutine library. For example, the mixture mass density may be calculated from given temperature, pressure and mass fraction using equation 3.5 by calling subroutine CKRHOY:

$$\rho = \sum_{k=1}^K [X_k] W_k. \quad [3.5]$$

```
CALL CKRHOY (P, T, Y, ICKWRK, RCKWRK, RHO) .
```

3.2.1 PREMIX

The application code generally is provided by the user. However, for several standard configurations application codes are available (e.g. an adiabatic reactor,

premixed flame, compression - ignition engines, etc) with the standard CHEMKIN package. PREMIX (Kee et. al., 1996) is the name of the application code for steady, one - dimensional, freely propagating laminar premixed flames.

PREMIX computes the flame species and temperature profiles as well as the laminar flame speed. The calculation involves multi-component molecular transport properties (Kee et. al., 1989) and finite-rate chemical kinetics. PREMIX solves the system of ordinary differential equations governing the steady one-dimensional flame structure using implicit finite-difference methods including both time-dependent and steady-state methods. It employs automatic solution adaptive mesh refinement to refine the grids in the region of steep gradients.

Two flame configurations can be solved using PREMIX. The first is a burner-stabilized flame with known mass flow rate. Here there are two variants: one where the temperature profile is known (only the species quantities are solved) and one where the temperature profile is determined from the energy conservation equation.

The second flame configuration is a freely propagating flame. This configuration is appropriate when the reactant temperature and pressure are known and there are no heat losses from the flame (adiabatic). The temperature profile is obtained from solving the energy equation and the mass flow rate (or laminar flame speed) is an output of the calculation. CHEMKIN uses the boundary-value solver TWOPNT to perform the solution.

A schematic showing the PREMIX computation steps is shown in Fig 3-5.

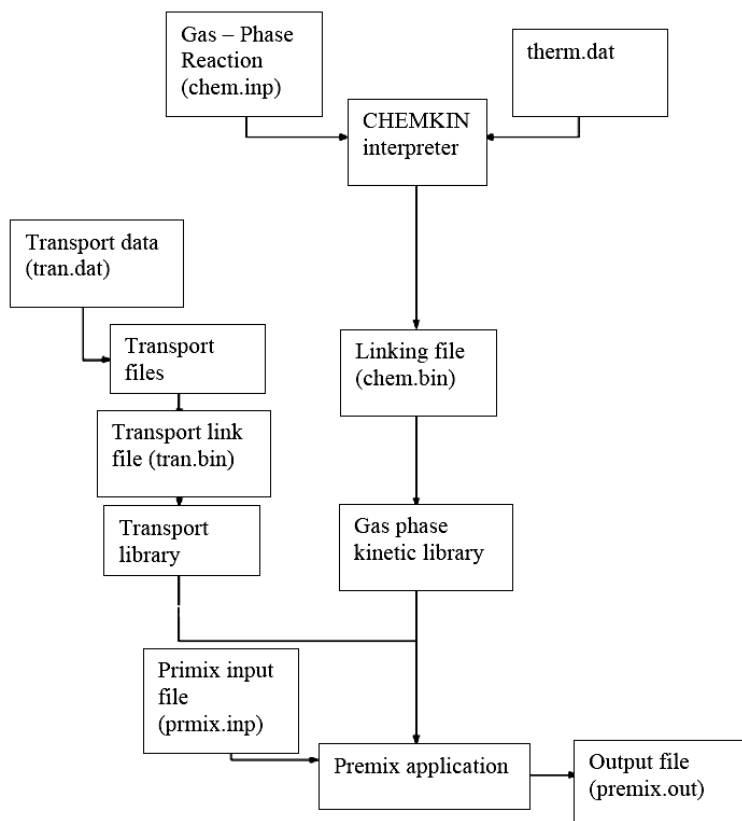


Fig. 3-5: PREMIX schematic.

The molecular transport properties for each of the species listed in the “chem.inp” file are specified in the “tran.dat” file, as discussed earlier. The tran.dat file is processed by tranlib.f to generate a transport linking file, “tran.bin.” The transport linking file tran.bin, CHEMKIN linking file chem.bin and user input file premix.inp are the three inputs to PREMIX. The user input file, premix.inp, uses (Table 3-2) a keyword format. Each line has an identifying keyword. Some of the keywords require numerical input while others do not. Table 3-2 gives a brief description of the keywords. Some of the keywords can give the user better control over the numerical solution, but the default values have been found to be adequate in most cases.

Table 3-2: Keywords for PREMIX file premix.inp.

Keywords	Description
ENRG	Solution is obtained from a coupled energy and species equation. Given temperature profile is used as an initial guess.
FREE	Freely propagating will be solved for, and hence flame speed determined.
MIX	Transport properties are calculated using mixture-averaged formulas.
VCOR	Ensures mass conservation of gas mixture.
FLRT	Initial estimated mass flow rate of the reactants.
PRES	Pressure (constant).
TFIX	A boundary condition that fixes the temperature at one point in the flame. It is required as the problem is posed in a flame-fixed coordinate system.
TEMP	The initial guessed temperature profile.
CURV	Adaptive mesh parameter, which controls the number of grid points inserted in regions of high curvature. Smaller values yield finer meshes.
GRAD	Adaptive mesh parameter, which controls the number of grid points inserted in regions of high gradient. Smaller values yield finer meshes.
NPTS	The number of initial mesh points. For lower values of GRAD and CURV, higher values are required to ensure convergence.
WMIX	An estimated width of the flame zone.
XCEN	An estimated location for the center of the flame.
XEND	An estimated location for the end point (product side) of the flame.
INTM	The mole fractions of the intermediate species.
MOLE	Calculations will be done in the terms of mole fraction (versus mass fractions).
PROD	Estimated mole fractions for the products.
REAC	Moles of reactant species.
ATIM	Absolute tolerance for the convergence of Newton iterations in time-stepping procedure.
ATOL	Absolute tolerance for the convergence of Newton iterations.
RTIM	Relative tolerance for the convergence of Newton iterations in time-stepping procedure.
RTOL	Relative tolerance for the convergence of Newton iterations.
TIME	Time step to be used if Newton method fails.
TIM2	Same as TIME except that it is used for the energy equation.
WDIF	Upwind differencing is to be used on the convective terms.
PRNT	Printing of the intermediate solution.
CNTN	Use for a continuation run so that the program expects keywords after "END."
END	Signifies the end of input.

The UNIX commands required to compile and run an application code using the CHEMKIN II package are shown in Table 3-3.

Table 3-3: Steps to compile and run a CHEMKIN application on a UNIX system.

UNIX command	Meaning
<code>ifc -o chem.exe ckinterp.f</code> (ifc- Intel FORTAN compiler)	Compile and link the interpreter using IFC compiler and get the executable chem.exe.
<code>./chem.exe</code>	Execute the interpreter. The interpreter will open the files chem.inp and therm.dat. These files are opened as logical units 5 and 17, respectively. The interpreter creates the binary linking file chem.bin and the ASCII output file chem.out. These files use units 25 and 6, respectively.
<code>ifc -c cklib.f</code>	Compile the CHEMKIN Gas-Phase Subroutine library.
<code>ifc -c sample_user.f</code>	Compile the user's FORTRAN program sample-user.f.
<code>ifc -o sample_user.exe sample_user.o cklib.o</code>	Link the user's FORTRAN program with the CHEMKIN Gas-Phase Subroutine Library.
<code>./sample.exe<sample_user.inp>sample_user.out</code>	Execute the user's program, reading 'sample_user.inp' as unit 5 for the user's input and creating 'sample_user.out' on unit 6 for the user's output.

3.3 XSenkplot

XSenkplot (NIST XSenkplot, 1996) is a graphical post - processor for CHEMKIN application codes. It helps to sort through and display species and reaction information obtained from the CHEMKIN calculations. XSenkplot reads the mechanism (chem.bin) and solution (save.bin) files from a CHEMKIN application run and uses the CHEMKIN subroutine library CKLIB Version 4.9 for the interactive display of information from the solution file. There are two versions of the program: Senkplot (uses SGI GL Graphics call) and XSenkplot (uses X Windows and OSF/Motif Graphics calls that are supported on UNIX workstations). XSenkplot has been modified to work on LINUX workstations as part of the present work.

XSenkplot allows variety of analyses of time/temperature dependent species and reaction information, including: species concentration (mole fractions), species - steady state analysis, individual reaction rates and net production/destruction rates, reaction equilibrium analysis and time/temperature history analysis of the system. An interactive analysis of independent and dependent species and reaction pathways and pathway flowchart construction can also be performed. Figure 3.6 shows examples of plots obtained from XSenkplot for a CH_4/O_2 , adiabatic, steady - state and one - dimensional system using PREMIX. Similar analyses can be performed for other CHEMKIN application codes. Figure 3.7 shows the reaction pathways plot.

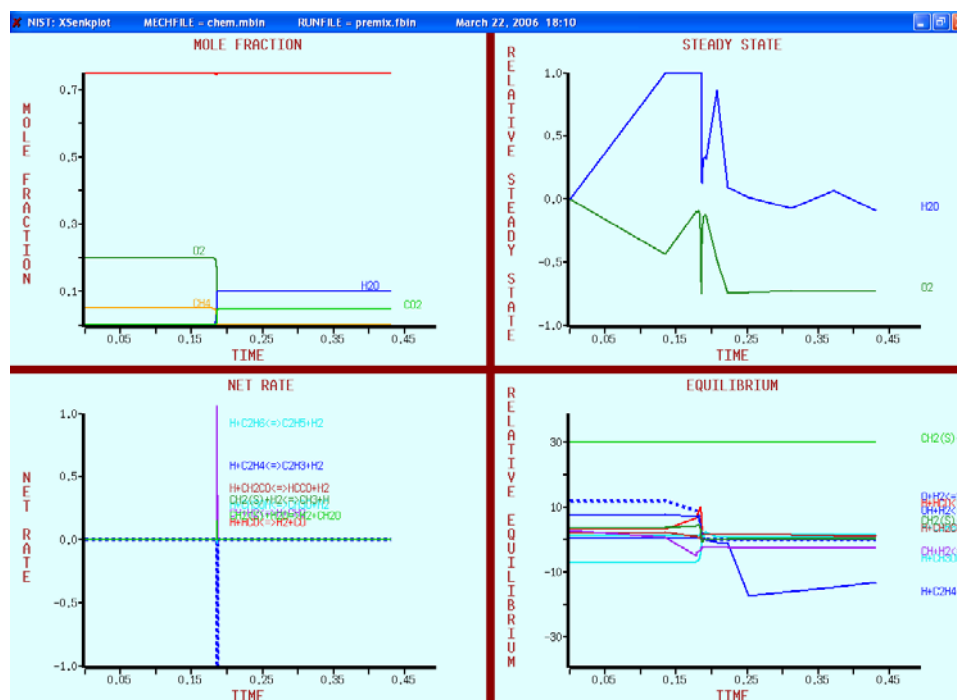


Fig. 3-6: Output screen from XSenkplot post processing

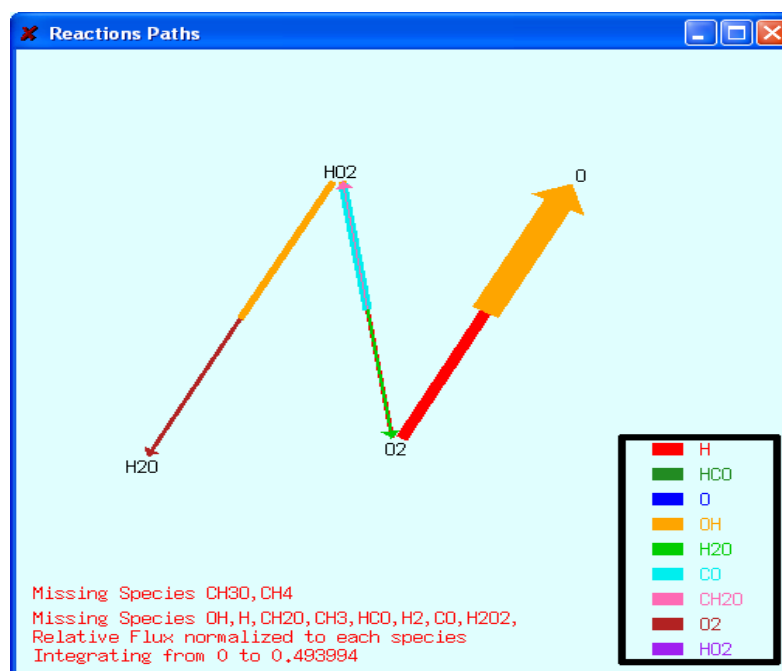


Fig. 3-7: Reaction pathways plot from XSenkplot

The reaction pathways window displays selected species in the reacting system and the reaction paths that connect them. Each reaction is indicated by an arrow from reactant to the product. The base of the arrow represents the reactants while the point of the arrow represents the products. The length of the arrow is insignificant; however, the thickness of the arrows represents the relative rates of the reactions, and the color of the arrow represents the reaction partner. A legend on the lower right - hand corner of the plot lists the associated partners in the reactions based on the color. Unimolecular reactions (no reaction partner) are represented by black arrows.

Chapter 4

Combustion Conditions and Cases Studied

Three basic studies have been performed: comparison of the flame structure for varying hydrogen fraction in CH₄/H₂ fuel mixtures, study of the influence of molecular diffusivities and study of the effect of EGR. In this chapter, discussions of thermochemical conditions, chemical mechanisms, molecular diffusivity models and exhaust gas recirculation (EGR) methodology are presented. Computational issues are discussed and a run matrix is developed.

4.1 Thermochemical Conditions

4.1.1 Pressure and Temperature

Typical in-cylinder temperature and pressure at the time of ignition (~ 20 – 40 degrees before top-dead-center) in a SI engine range from 500 – 700 K and 8 – 10 atm respectively. Hence a reactant temperature of 598 K (325 °C) and pressure of 8 atm has been used for all simulations. The conclusions that are drawn regarding the effects of variations in reactant composition, chemical mechanism and molecular diffusivity are expected to remain valid over the range of temperatures and pressures that would be encountered in a practical engine.

4.1.2 Reactant Composition

Fuel-lean to stoichiometric mixtures are of interest. Lean mixtures are of particular interest for their higher thermal efficiency and lower combustion temperatures; the latter reduce the engine - out NO_x. Thermal NO reactions become important at temperatures above 1800 K, so it is desired to keep the maximum temperature below that level. Lower equivalence ratio can be achieved with a higher percentage of hydrogen in H₂/CH₄ fuel blends. For pure CH₄ the lowest equivalence ratio for stable combustion is approximately 0.6. In the presence of hydrogen lower equivalence ratios of 0.3 can be achieved. Hydrogen fractions (Ψ defined as ratio of moles of H₂ to total number of moles of H₂ and CH₄) of 0.0, 0.3, 0.7 and 1.0 have been studied here. The value $\Psi = 0.3$ is of particular interest, as this is the value that has been identified by Collier et al. (2005) as yielding the lowest BSNO_x in experimental studies of H₂/natural gas-fueled SI engines.

4.2 Chemical Mechanisms

Numerous methane and/or natural gas mechanisms are available in CHEMKIN format. Each mechanism has been optimized for different temperature and pressure ranges, equivalence ratios and combustion regimes (e.g. premixed flame propagation, auto-ignition, etc.).

The mechanisms considered for the present study are summarized in Table 4-1. These have been selected based on the requirement of simulating methane and/or natural gas premixed flames under IC - engine conditions, with particular emphasis on NO_x emissions.

Table 4-1: Reaction mechanisms considered

Mechanism	Number of species	Number of reactions
GRI Mech 2.11 (Bowman et al.)	49	279
GRI Mech 3.0 (Smith et al.)	53	325
Glarborg (Glarborg et al., 1998)	71	447
ARM (based on GRI Mech 2.11) (Pope et al.)	19	16

The GRI Mech mechanisms are available from University of California, Berkley (Gregory et al., 2003). GRI Mech is a list of elementary chemical reactions and associated rate constants that have been optimized for natural gas/hydrogen flames. GRI Mech 2.11 is an older release while GRI Mech 3.0 is a newer version that has been optimized further for methane and natural gas combustion including NO_x emissions. The GRI Mech mechanisms are not intended be used for higher hydrocarbon species as a primary fuel in spite of the presence of C₂ and C₃ species in the system. The mechanisms are suitable for a pressure range of 1000 torr to 10 atm, temperature range of 1000 to 2500 K and equivalence ratios from 0.1 to 5.0 for premixed systems. The GRI mechanisms have been adopted widely as “full” methane and/or natural gas mechanisms in the combustion modeling community and as the basis for much reduced mechanism development.

Glarborg et al. (1998) used GRI Mech 2.11 as the basis for the development of advanced NO_x chemistry. The Glarborg mechanism includes several species and reactions aimed at improved NO_x prediction. In particular, pathways for the reaction of species pairs HCCO, CH₃ and CH₃, NO have been modified from the GRI Mech 2.11

mechanism. The Glarborg mechanism is considered to be one of the most detailed mechanisms for the study of NO_x chemistry.

GRI Mech 2.11, GRI Mech 3.0 and Glarborg are detailed mechanisms that are intended to provide a complete description of the elementary (molecular level) reactions that occur in the system. Many of the species and reactions are not necessary for normal calculations but have been included for radiation and ionization studies, for example, where rarer reactions and low-concentration species become important. Large mechanisms are computationally expensive, difficult to analyze in detail using reaction pathways analysis and not necessary in many situations. Computational efficiency is important in the engine combustion studies which are the eventual target of the present research. Hence there is a need for smaller or reduced mechanisms that capture the global behavior of the system. Augmented reduced mechanisms (ARM's) are mechanisms that have been derived from detailed mechanisms that eliminate the reactions and species that are not important for normal combustion studies. There are many versions of ARM's available. An ARM obtained from GRI Mech 2.11 has been used for the present study (Pope et al). The number of species and reactions has been reduced from 49 and 279 in GRI Mech 2.11 to 19 and 16, respectively, in the ARM considered. Here, however, the ARM lacks detailed NO_x chemistry; NO₂ is not considered, for example.

To create a reduced mechanism from a detailed mechanism, several systematic steps are followed. First a skeletal mechanism is created from the detailed mechanism. This is done by eliminating reactions with rates that are small compared to other reactions. Reactions also can be eliminated if the flux of a species through the reaction is less than a pre-determined value. For every reaction that is eliminated a comparison

analysis with the original detailed mechanism is done to avoid the elimination of important reactions. Hence, a skeletal reaction set is obtained that has a reduced number of elementary reactions and species. From the skeletal mechanisms, quasi-steady-state (QSS) analysis and other algebraic methods as discussed by Chen (1987) are applied to identify QSS species. QSS species are those species whose concentrations remain low with respect to the product concentration. QSS analysis results in a non-linear algebraic equation set that expresses the concentration of QSS species in terms of other retained species. The QSS species and the corresponding reactions that are linked to QSS species thus can be eliminated from the reaction mechanism. The resulting global reaction set no longer corresponds to an elementary reaction set, and the chemical production rates do not fit the standard CHEMKIN template (see Section 3.1). Therefore, it is necessary to provide a customized replacement for the CHEMKIN subroutine CKWYP that provides molar production and destruction rates for each species. Computer-assisted reduced mechanism (CARM) code can also be used to get the final reduced mechanisms in the form of a FORTRAN code that can be read in by CHEMKIN (Sung et al., 2001)

4.3 Molecular Diffusivity

The molecular diffusivity of H_2 is almost three times that of methane (Andrea et al., 2004). It has been proposed that hydrogen's high molecular diffusivity improves the homogeneity of the charge and increases turbulence thereby leading to improved combustion (Andrea et al., 2004). Here the influence of molecular diffusivity on steady, one-dimensional, laminar premixed flames has been investigated using two different

approaches. In the first scheme the diffusion coefficient of H₂ was set equal to that of CH₄, and in the second scheme the Lewis numbers (Le) of all the species in the reacting mixture were set to unity. The following equations pertain:

$$Le = \frac{\alpha}{D}, \quad [4.1]$$

$$\alpha = \frac{k}{\rho C_p}, \quad [4.2]$$

where α is the mixture thermal diffusivity, ρ is the mixture density, k is the mixture conductivity and C_p is the mixture specific heat.

For this purpose changes were made in the CHEMKIN subroutines MCADIF, MCMDIF and MCSDIF that deal with the mixture-averaged diffusion coefficient, multicomponent diffusion coefficient and binary diffusion coefficient of the mixture, respectively. In all the cases Soret effect has been neglected by setting to zero the thermal diffusion coefficients calculated from subroutines MCATDR and MCMCDT. The baseline flame structure with species-dependent molecular diffusivities and Lewis numbers then is compared to the flame structures obtained with the modified transport coefficients.

4.4 Exhaust Gas Recirculation (EGR)

One method employed to reduce engine-out NO_x emissions in an actual engine is to recirculate a portion of the exhaust gas back in the intake manifold. EGR reduces NO_x by acting as an inert gas that absorbs some of the heat released in the combustion process, thereby lowering the temperature. Lower temperature reduces the thermal NO and that in

turn reduces the NO_2 that is formed from the oxidation of NO . The EGR rate is controlled as a function of engine load and speed to ensure, for example, that there is no rough performance of the engine during the start-up or hard acceleration when the fuel is burned at close to stoichiometric conditions. In a production engine, up to 30% EGR (by volume) may be employed. In the present study, 20% of the intake mixture has been considered to be recirculated exhaust gas on a volumetric basis.

An iterative process is necessary to determine the reactant composition that corresponds to a specified level of EGR. The product composition for 0% EGR is determined first; 20% by volume of that composition is added to the original fuel – air mixture. This results in a new product composition, and the reactant composition is revised accordingly. This process is continued until the product composition and temperature become constant; typically 5-6 iterations are required. The amount of exhaust gas that is required to be used for EGR is described in detail in section 4.6.3. Radicals have not been considered for EGR as their concentration is very low compared to other components of exhaust like CO_2 , H_2O , NO , NO_2 , etc.

4.5 Computational Issues

In this section three computational issues are discussed briefly: the choice of CHEMKIN version, the value of TFIX (see Table 3-2), and the length of the computational domain.

4.5.1 CHEMKIN Version

CHEMKIN II (Kee et al., 1996) and CHEMKIN 4.01 (Reaction Design, 2005) have been used for the present study. CHEMKIN II is the pre-commercial version developed by Sandia National Laboratory and CHEMKIN 4.01 is the current commercial version from Reaction Design. CHEMKIN II was preferred, as the output file “save.bin” produced by CHEMKIN II is compatible with XSENKPLOT while that from CHEMKIN 4.01 is not compatible. Moreover, source code is available for CHEMKIN II. However, convergence problems were encountered in some cases with CHEMKIN II. CHEMKIN 4.01 has been used for cases where there have been convergence problems using CHEMKIN II. In particular it was difficult to refine the mesh beyond GRAD and CURV values of 0.2 each with CHEMKIN-II. With these values of CURV and GRAD, the results from the PREMIX calculations sometimes were not consistent with the results from an EQUIL calculation (adiabatic flame temperature and equilibrium composition). With CHEMKIN 4.01, the CURV and GRAD values could be reduced to values as low as 0.01. Here it has been confirmed that the product composition and temperature from the PREMIX calculations were within 0.6% of the values obtained using EQUIL.

For the studies where the molecular transport coefficients were altered, it was possible to obtain accurate results with the higher CURV and GRAD values. In these cases only CHEMKIN II has been used.

4.5.2 TFIX

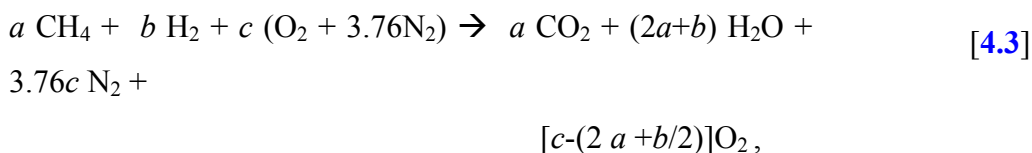
The baseline reactant conditions for the flame study are 598 K and eight atmospheres pressure. Under these conditions TFIX has been set to 600 K, slightly higher than the reactant temperature of 598 K. This is an appropriate choice as it is preferred to set the value of TFIX to be close to the reactant inlet temperature. It has been confirmed that results are not sensitive to the choice of TFIX.

4.5.3 Flame Domain

The computational domain extended from -0.5 cm to 10 cm in all cases. The large domain ensures that results are insensitive to the extent of computational domain and that even very slow reactions (e.g. those leading to formation of NO and NO₂) approach equilibrium at the outflow boundary.

4.6 Run Matrix

In the present study flame structure has been compared for different compositions of fuel. The fuel composition has been varied by replacing CH₄ molecules with H₂ molecules while keeping the energy content of the fuel mixture constant. Here the energy of the fuel mixture has been calculated based on lower heating values of CH₄ and H₂. The energy content has been kept constant to ensure a fair comparison for the IC engine application and to clearly separate thermal effects from kinetic and transient effects. The following equations are used to establish the global mixture stoichiometry (for $\phi \leq 1$):



$$c = (1/\phi)*(2a + b/2). \quad [4.4]$$

Here, ϕ is the equivalence ratio, and a , b and c denote moles of CH_4 , H_2 , and air ($\text{O}_2 + 3.76 \text{ N}_2$) respectively. The lower heating values for H_2 and CH_4 are respectively: 286 kJ/mole and 802 kJ/mole (Andrea et al., 2005). Therefore, to keep the energy content of the fuel mixture constant while replacing CH_4 with H_2 , the following equation pertains:

$$802 a + 286 b = 6416. \quad [4.5]$$

Here an arbitrary value for 'a' has been taken ($a = 8$) with $b = 0$.

Reactant compositions for each of the three basic studies are presented in the following subsections.

4.6.1 Varying Hydrogen Fraction For Fixed Equivalence Ratio

Table 4-2 shows the equivalence ratios that have been investigated and the corresponding moles of each reactant. The study was done for each of four chemical mechanisms: ARM, GRI Mech 2.11, GRI Mech 3.0 and Glarborg.

Table 4-2: Reactant composition for fixed ϕ and constant energy.

Equivalence Ratio, ϕ	a (CH ₄)	b (H ₂)	c (O ₂)	$3.76c$ (N ₂)	Hydrogen Fraction, $\Psi = b/(b+a)$
1	8.0000	0.0000	16.0000	60.1600	0
	6.9390	2.9740	15.3658	57.7757	0.3
	4.3666	10.1887	13.8275	51.9917	0.7
0.7	8.0000	0.0000	22.8570	85.9428	0
	6.9390	2.9740	21.9512	82.5367	0.3
	4.3666	10.1887	19.7536	74.27389	0.7
0.5	8.0000	0.0000	32.0000	120.3200	0
	6.9390	2.9740	30.7317	115.5514	0.3
	4.3660	10.1887	27.6551	103.9834	0.7

4.6.2 Molecular Diffusion Studies

The influence of molecular diffusion has been investigated using two schemes, as described in Section 4.3. The equivalence ratios and corresponding hydrogen fractions for this study are shown in Table 4.3. The exact fuel – air composition can be obtained from Table 4.2. For each of these cases the flame structure with modified diffusion coefficients has been compared to the flame structure with the baseline multi-component diffusion model.

Table 4-3: Cases for molecular diffusion study.

Reaction Mechanism	Equivalence Ratio (ϕ)	Hydrogen Fraction (Ψ)
GRI Mech 3.0	1.0	0.7
GRI Mech 2.11	0.3	0.3
Glarborg	0.5	0.7
ARM	0.7	0.7

4.6.3 EGR Studies

For the EGR study equations [4.3] through [4.5] are augmented with the following equations:

$$d = \varepsilon n, \quad [4.6]$$

$$d + e = n. \quad [4.7]$$

Here, n is the total reactant moles input in the system, including EGR, d is the number of moles of exhaust gas that are input in the reactants for EGR on a molar basis, e is the number of reactant moles in the absence of EGR and ε is the fraction of input moles to be supplied as EGR. For the present study an EGR rate of 20% ($\varepsilon = 0.20$) has been considered.

The EGR study included variation in the reaction mechanism, equivalence ratio ϕ and hydrogen fractions Ψ as shown in Table 4-4 (for 20% EGR).

Table 4-4: Cases for EGR study.

Reaction Mechanism	Equivalence Ratio (ϕ)	Hydrogen Fraction (Ψ)
GRI Mech 3.0	1	0.3
	0.7	0.7
Glarborg	0.7	0.7

The number of moles of fuel, air and EGR are shown in Table 4-5. These calculations have been done using the equations [4.6] and [4.7]. The composition of EGR has been determined iteratively as discussed in Section 4.4.

Table 4-5: Reactant composition for EGR study.

ϕ	$\Psi = b/(b+a)$	a (CH ₄)	b (H ₂)	c (O ₂)	$3.76c$ (N ₂)	total moles, e	moles of EGR, d
1	0.3	6.939	2.974	15.3658	57.7757	83.055	20.7637
0.7	0.7	4.3666	10.188	19.753	74.2738	108.582	27.1457

Chapter 5

Results

5.1 Comparison Among Chemical Mechanisms

Several chemical mechanisms available for use with CHEMKIN have been compared using PREMIX for flame structure characteristics and flame speed. The focus has been on key species including OH, CH₃, H, NO, NO₂, CH₄, H₂ and on temperature profiles. The chemical mechanisms that have been considered are: Glarborg, GRI-Mech 2.11, GRI-Mech 3.0 and ARM; these have been discussed in detail in Section 4.2.

Two important quantities associated with premixed flames are laminar flame speed and flammability limits. Laminar flame speed is defined as the velocity at which the reactants enter the stationary flame. The unburned gas is assumed to enter the flame in a direction normal to the flame sheet. Laminar flame speeds for a typical SI engine range from 50 cm/s to 100 cm/s (Heywood, 1988). For the present study, flammability limit has been defined empirically as the equivalence ratio where the laminar flame speed falls to 10 cm/s as lower values would correspond to unacceptably low combustion rates in IC engines. Fig 5-1 shows the laminar flame speed versus ϕ and Ψ using the Glarborg mechanism. For $\phi \geq 0.5$, the flame speed exceeds 10 cm/s for all Ψ . For $\phi < 0.5$, the flame speed falls below 10 cm/s at lower values of Ψ .

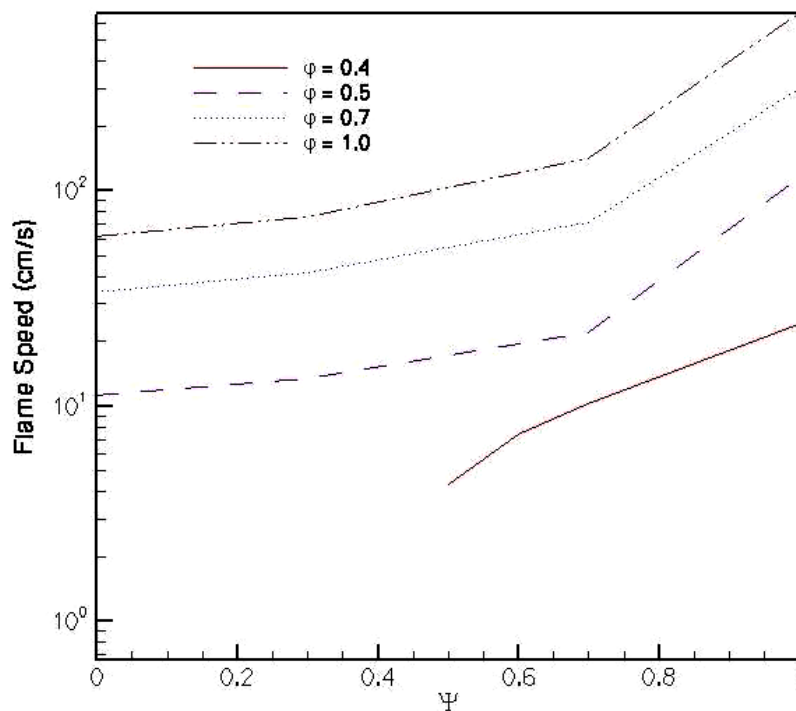


Fig. 5-1: Computed laminar flame speeds for H_2/CH_4 mixtures using the GRI Mech 3.0 mechanism, $P = 8 \text{ atm}$, $T = 598 \text{ K}$.

5.1.1 Temperature Profiles

Fig 5-2 shows the temperature profiles obtained from the four different reaction mechanisms. There are no significant changes in the temperature profiles among the reaction mechanisms. The reaction zone occurs earliest for the Glarborg mechanism and latest for GRI Mech 3.0; GRI Mech 2.11 and ARM are in between. The peak product temperature depends only on the thermodynamic properties, and is essentially the same for all mechanisms.

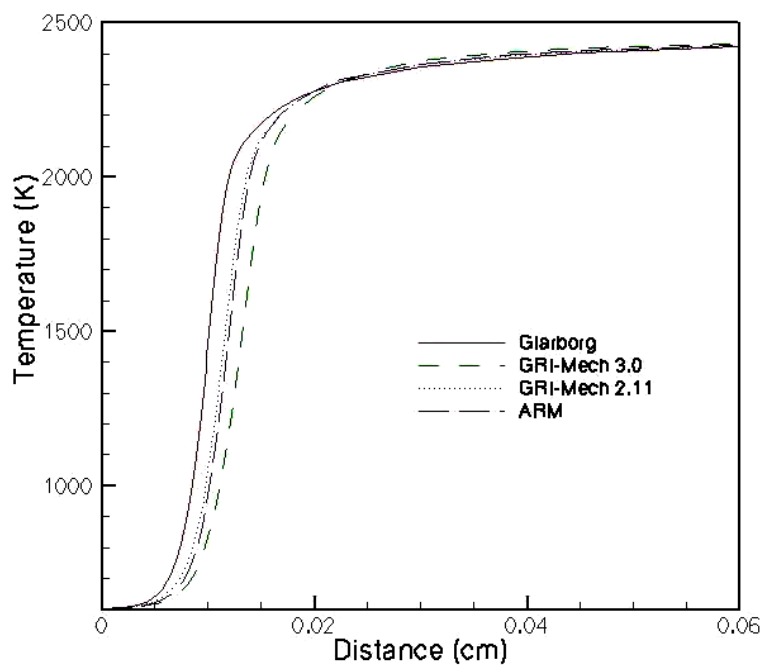


Fig. 5-2: Temperature profile comparison for different reaction mechanisms. $P = 8$ atm, $T = 598$ K, $\phi = 1.0$, $\Psi = 0.3$.

5.1.2 CH₄, CH₃ and OH

Fig 5-3 shows comparison of CH₄ profiles from different mechanisms. There is an increased consumption of CH₄ for the Glarborg mechanism that is consistent with the earlier occurrence of the reaction zone for the Glarborg mechanism as indicated by Fig 5-2. GRI Mech 3.0 shows the slowest chemistry. GRI Mech 2.11 and ARM mechanisms are again in between Glarborg and GRI Mech 3.0.

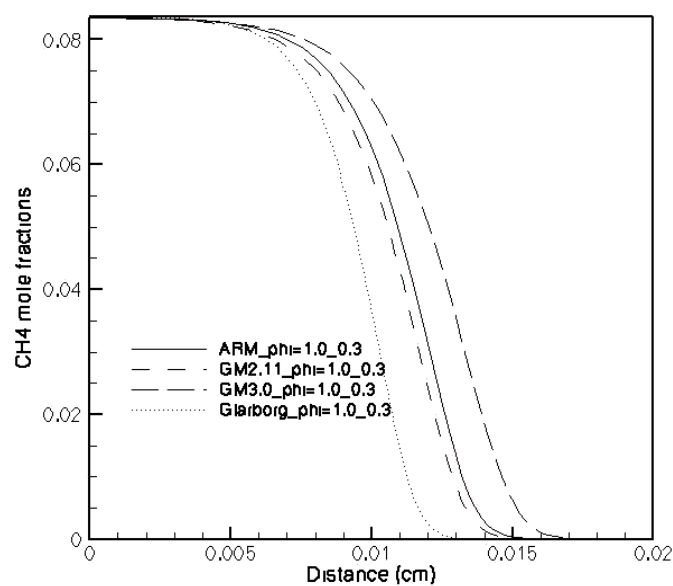


Fig. 5-3: CH₄ profile comparison for different reaction mechanisms. $P = 8$ atm, $T = 598$ K, $\phi = 1.0$, $\Psi = 0.3$.

The earlier consumption of CH₄ for the Glarborg mechanism leads to an earlier peak in CH₃ concentration as shown in Fig 5-4.

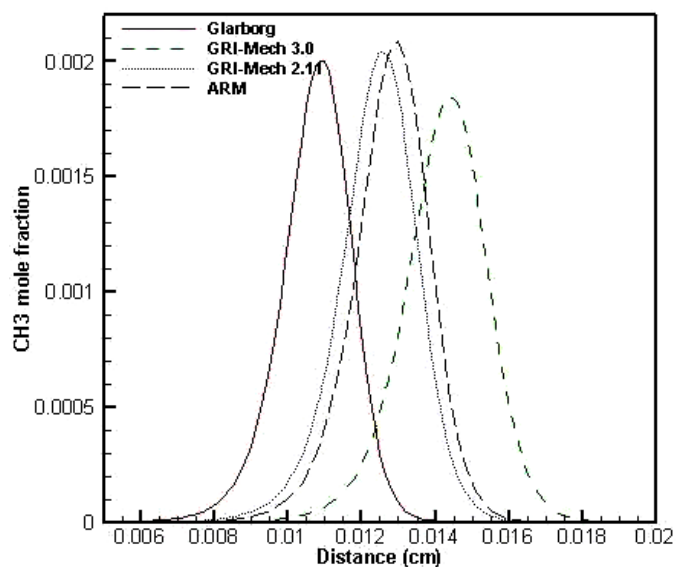


Fig. 5-4: CH₃ profile comparison for different reaction mechanisms. $P = 8$ atm, $T = 598$ K, $\phi = 1.0$, $\Psi = 0.3$.

It has been suggested that the rate - controlling step in the combustion of CH₄ (Collier et al., 2005) is:



However, this is not necessarily true as observed from Table 5-1 that compares the destruction flux of CH₄ for two reactions.

Table 5-1: Important reactions in the consumption of CH₄ (GRI Mech 3.0, $\phi = 0.7$ and $\Psi = 0.3, 0.7$)

	$\Psi = 0.3$ (CH ₄ mole fractions / sec)	$\Psi = 0.7$ (CH ₄ mole fractions / sec)
OH+CH ₄ <=>CH ₃ +H ₂ O	-2.80E-02	-4.13E-02
O+CH ₄ <=>OH+CH ₃	-9.70E-03	-1.19E-02
H+CH ₄ <=>CH ₃ +H ₂	-8.78E-03	-9.88E-03

Fig 5-5 shows the consumption rate of CH₄ through the first reaction in Table 5-1:



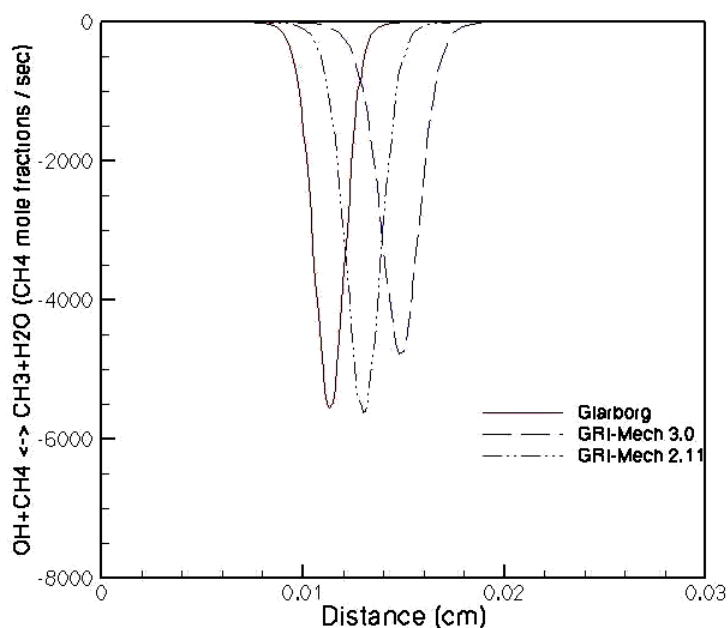


Fig. 5-5: Reaction rate profile comparison for different reaction mechanisms. $P = 8$ atm, $T = 598$ K, $\phi = 1.0$, $\Psi = 0.3$.

The reactions [5-1] and [5-2] have both been considered as controlling the consumption rate for CH_4 . The higher OH levels from the Glarborg mechanism as shown in Fig 5-6 manifests itself in a higher rate for reactions [5-2] as shown in Figure 5-5. So, there is a higher and earlier consumption of CH_4 to produce CH_3 radicals for the Glarborg mechanism compared to GRI Mech 2.11, GRI Mech 3.0 and ARM.

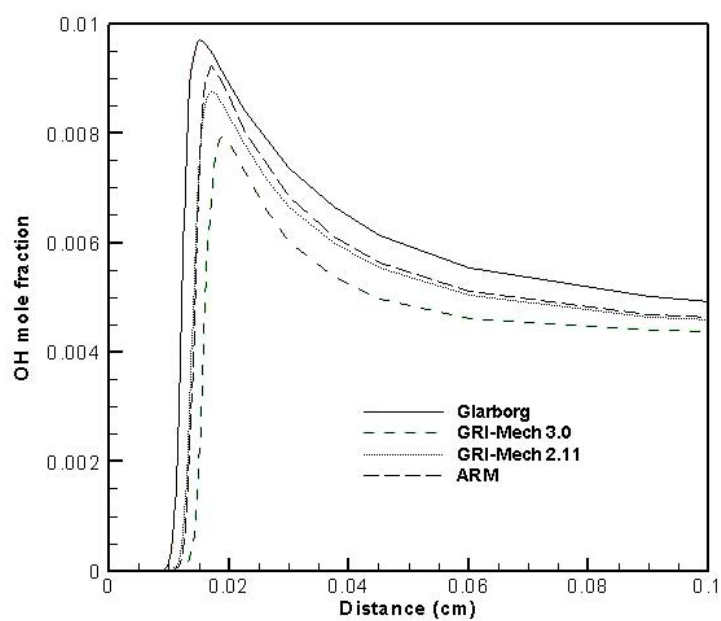


Fig. 5-6: OH profile comparison for different reaction mechanisms. $P = 8$ atm, $T = 598$ K, $\phi = 1.0$, $\Psi = 0.3$.

Figure 5-8 shows the consumption rate from three different mechanisms for CH_4 through the third reaction from Table 5-1.

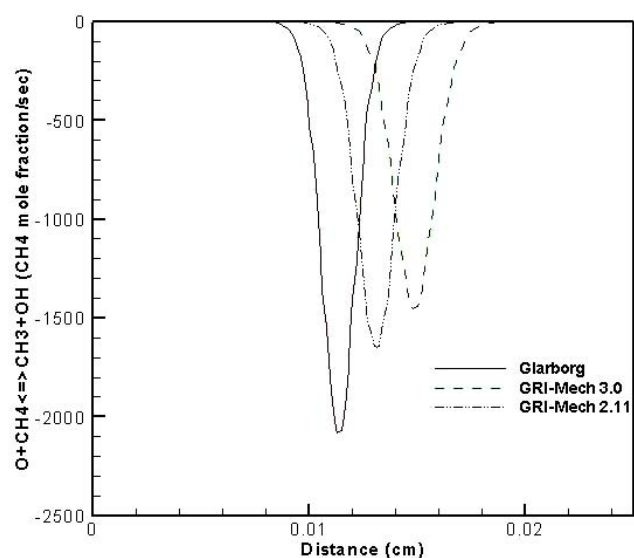


Fig. 5-7: Reaction rate profile comparison for different reaction mechanisms. $P = 8$ atm, $T = 598$ K, $\phi = 1.0$, $\Psi = 0.3$.

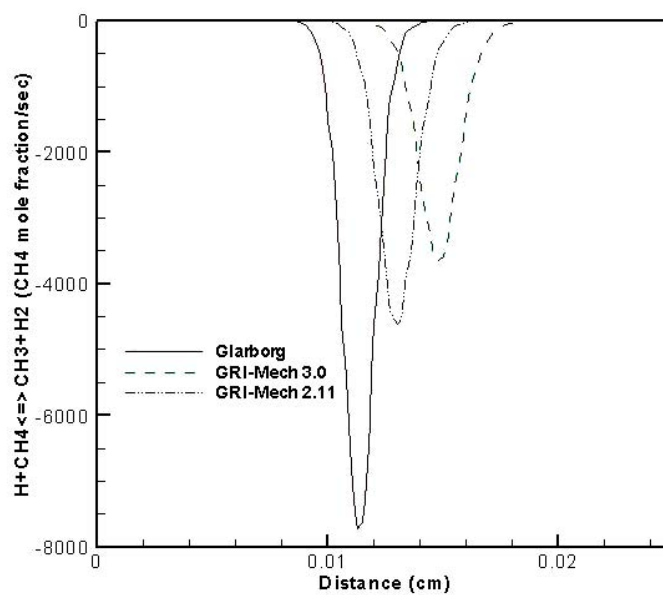


Fig. 5-8: Reaction rate profile comparison for different reaction mechanisms. $P = 8$ atm, $T = 598$ K, $\phi = 1.0$, $\Psi = 0.3$.

5.1.3 NO

Fig 5-9 shows the NO mole fraction profiles obtained from four reaction mechanisms. NO mole fractions are highest for the Glarborg mechanism although the differences are small in all cases. Fig 5-10 shows the NO mole fraction profiles through the reaction zone from the different reaction mechanisms. It can be seen that the reaction-zone mole fraction is also highest initially for the Glarborg mechanism. The NO prediction from ARM is higher compared to the GRI-Mech 2.11 and GRI-Mech 3.0.

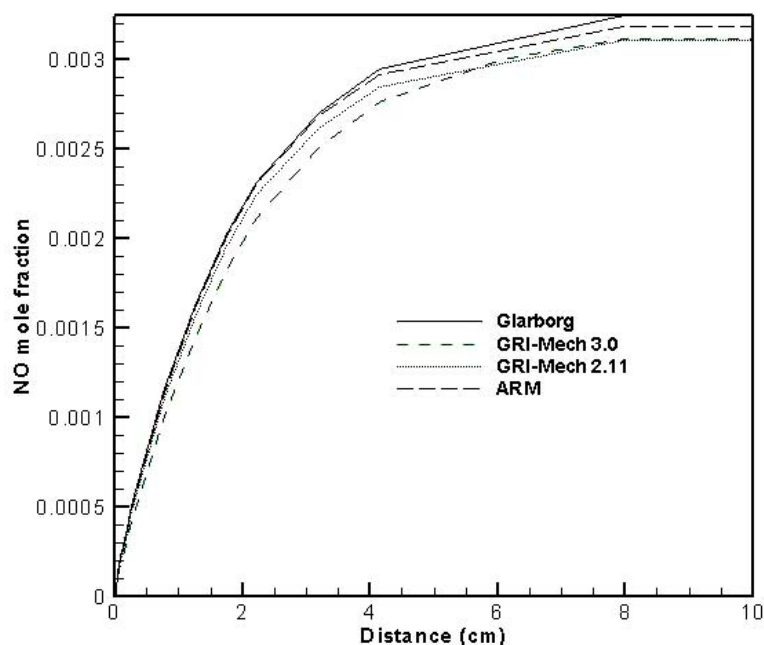


Fig. 5-9: NO mole fraction comparison for different reaction mechanisms. $P = 8$ atm, $T = 598$ K, $\phi = 1.0$, $\Psi = 0.3$.

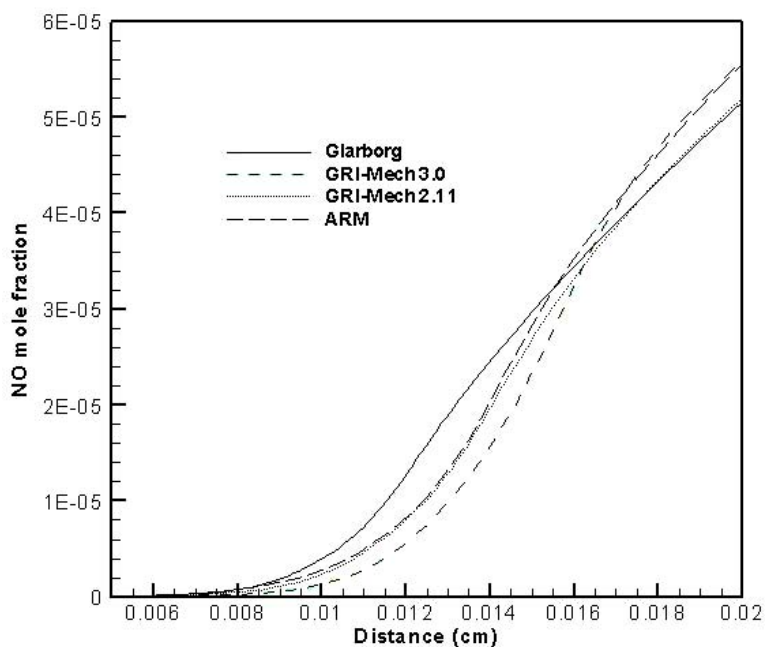


Fig. 5-10: Reaction zone NO mole fraction profiles for different reaction mechanisms. $P = 8$ atm, $T = 598$ K, $\phi = 1.0$, $\Psi = 0.3$.

5.1.4 NO₂

Fig 5-11 compares the NO₂ mole fraction profiles for three different reaction mechanisms. It can be seen that the Glarborg mechanism gives the lowest NO₂ mole fraction while GRI-Mech 3.0 gives the largest mole fraction. Fig 5-12 shows the NO₂ mole fraction profile through the reaction zone for three mechanisms. Again, the NO₂ mole fraction is lowest for the Glarborg mechanism. The ARM mechanism doesn't include NO₂ chemistry; hence it is absent from Figures 5-11 and 5-12.

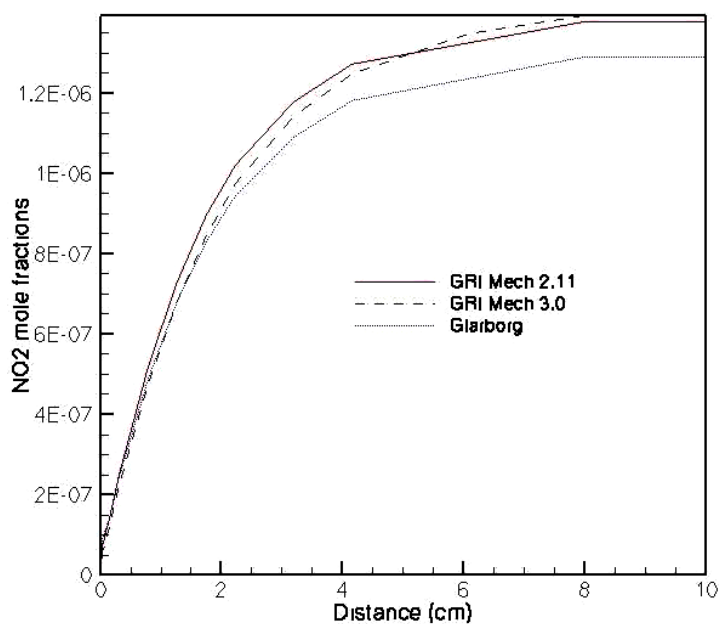


Fig. 5-11: NO_2 mole fraction profiles for different reaction mechanisms. $P = 8$ atm, $T = 598$ K, $\phi = 1.0$, $\Psi = 0.3$.

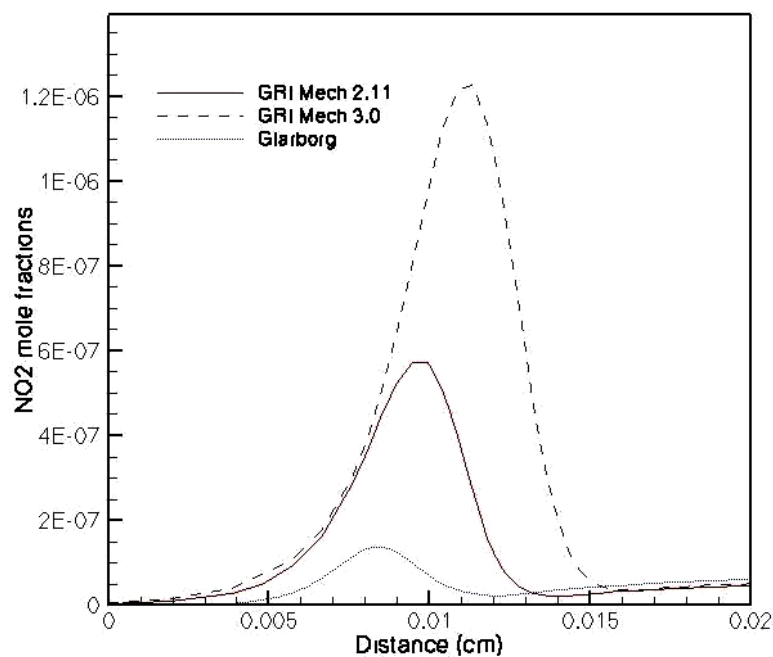


Fig. 5-12: Reaction zone NO_2 mole fraction profiles for different reaction mechanisms. $P = 8$ atm, $T = 598$ K, $\phi = 1.0$, $\Psi = 0.3$.

The lower NO_2 mole fraction from the Glarborg mechanism is consistent with the higher destruction rate of NO_2 through the reactions [5-3] and [5-4]:



Figure 5-13 shows the comparison of destruction rates of NO_2 through reaction [5-3] for three reaction mechanisms. It can be seen that the destruction rate is highest for the Glarborg mechanism. Similar behavior is seen for the other reactions involved in the destruction of NO_2 . It has been observed for the Glarborg mechanism that there has also been an increase in the reactions producing NO_2 , but the net production of NO_2 is dominated by the reactions consuming NO_2 . Similar behavior is seen in the profile for reaction [5-4].

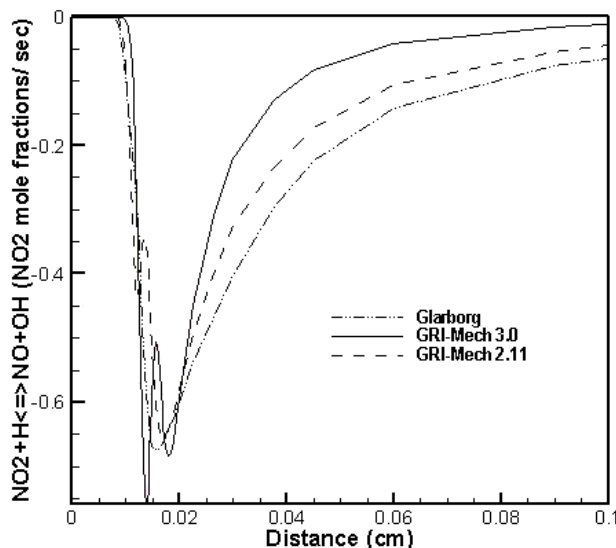


Fig. 5-13: Reaction rate comparison for different reaction mechanisms. $P = 8$ atm, $T = 598$ K, $\phi = 1.0$, $\Psi = 0.3$.

5.1.5 H₂

Fig 5-14 shows the H₂ mole fraction profiles for the four different reaction mechanisms. Consumption initially is highest for the Glarborg mechanism, is lower for GRI Mech 2.11, and is lowest for GRI Mech 3.0 to a point, after which the trend reverses.

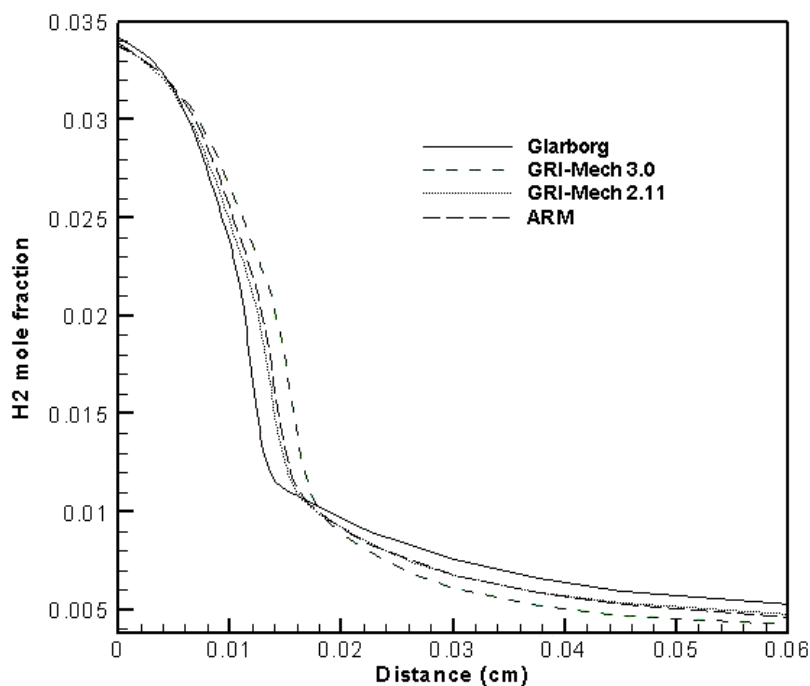
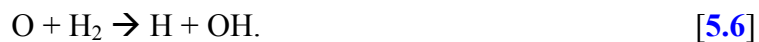


Fig. 5-14: H₂ mole fraction profiles for different reaction mechanisms. $P = 8$ atm, $T = 598$ K, $\phi = 1.0$, $\Psi = 0.3$.

The mole fraction profiles for H₂ can be understood from the reaction rates for the reactions:



Reactions [5-5] and [5-6] are the most important reactions for the consumption of H_2 (Table 5-2). The relative reaction rates have the same trend for all four reaction mechanisms considered. Other reactions that consume H_2 have rates which are even smaller.

Table 5-2: Important reactions in the consumption of H_2 for $P = 8$ atm, $T = 598$ K, $\phi = 1.0$, $\Psi = 0.3$.

Reactions	Rates (mole fractions/sec)
$OH+H_2 \rightleftharpoons H+H_2O$	-8.42E-02
$O+H_2 \rightleftharpoons H+OH$	-3.36E-02
$CH_2(S)+H_2 \rightleftharpoons CH_3+H$	-3.67E-05

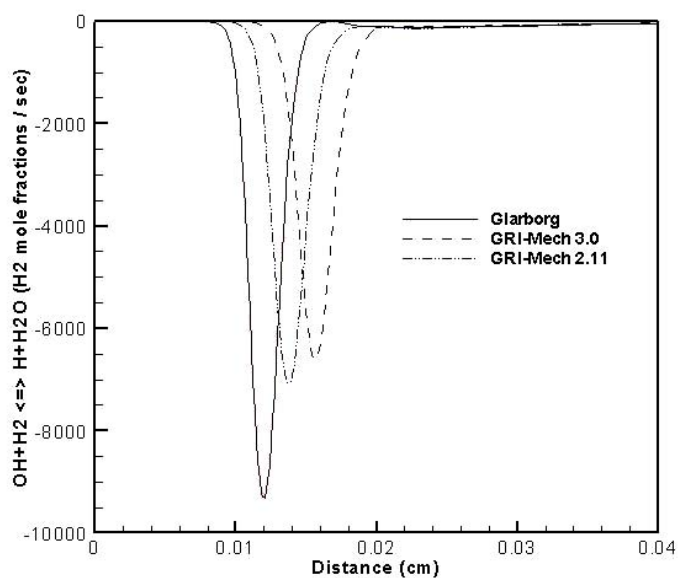


Fig. 5-15: Reaction rate profiles for different reaction mechanisms. $P = 8$ atm, $T = 598$ K, $\phi = 1.0$, $\Psi = 0.3$.

Reaction [5-5] is completed earlier for Glarborg compared to GRI Mech 2.11 and GRI Mech 3.0 (Fig 5-15). This accounts for the different H_2 mole fractions from the different reaction mechanisms. The pattern is same for reaction [5-6] (Fig 5-16). The ARM mechanism doesn't include the elementary reaction [5-6] so it has not been included in Figures 5-15 and 5-16.

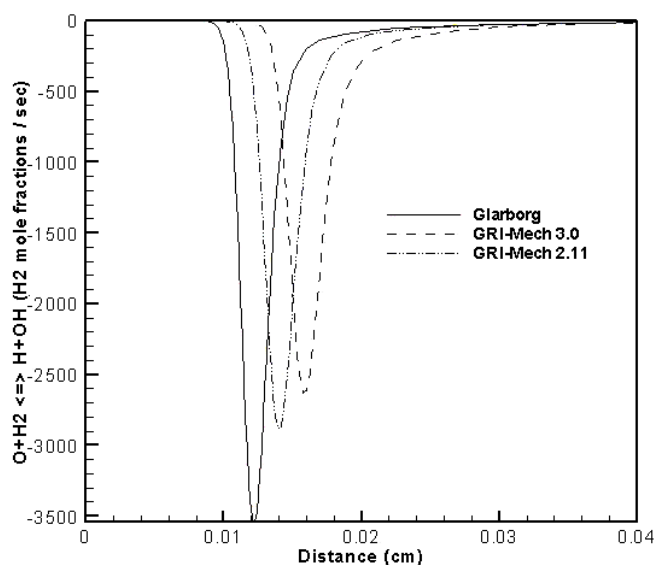


Fig. 5-16: Reaction rate profiles for different reaction mechanisms. $P = 8$ atm, $T = 598$ K, $\phi = 1.0$, $\Psi = 0.3$.

Similar behavior was observed for other equivalence ratios and for other ratios of CH_4 to H_2 when the different mechanisms were compared.

5.2 Variation in Hydrogen Fraction

The approach has been described in detail in Section 4.6.1. Comparisons have been done for the four reaction mechanisms described in Section 4.2. For these mechanisms, the

compositions considered were $\Psi = 0.0, 0.3$ and 0.7 for each of $\phi = 1, 0.7$ and 0.5 . Here results are presented for $\phi = 0.7$, $\Psi = 0, 0.3$ and 0.7 using GRI Mech 3.0. For other mechanisms and equivalence ratios the character of the curves is similar.

5.2.1 Temperature

The temperature profiles for different Ψ are shown in Fig 5-17.

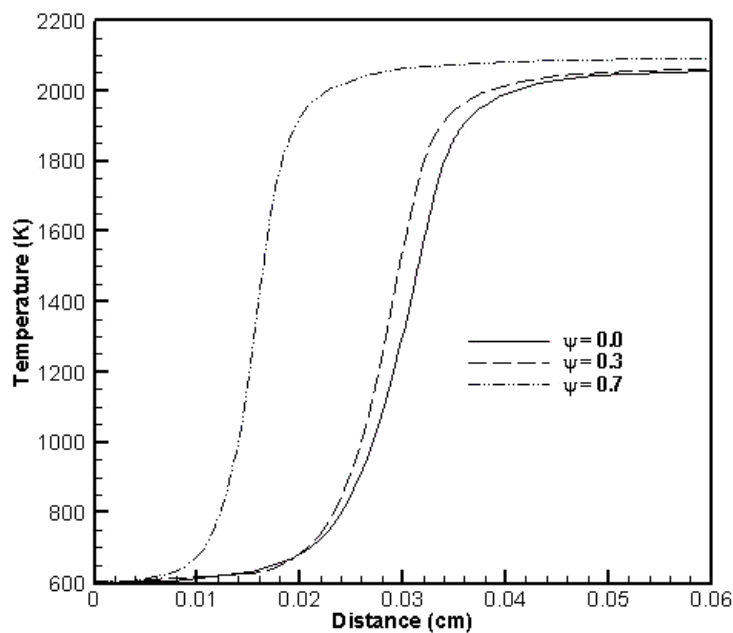


Fig. 5-17: Temperature profiles for different Ψ . $P = 8$ atm, $T = 598$ K, $\phi = 0.7$, reaction mechanism - GRI Mech 3.0.

The peak temperature occurs earlier for higher Ψ implying an earlier occurrence of the reaction zone with an increase in the hydrogen content of the fuel mixture. The peak temperature, however, remains the same as the energy content is the same for all values of Ψ .

5.2.2 CH₄ and H₂ Mole Fractions

Figures 5-18 and 5-19 show the CH₄ and H₂ mole fraction profiles for different Ψ . There is an earlier and faster consumption of CH₄ and H₂ with increasing Ψ , which is consistent with the earlier occurrence of the reaction zone that was noted in Fig 5-17.

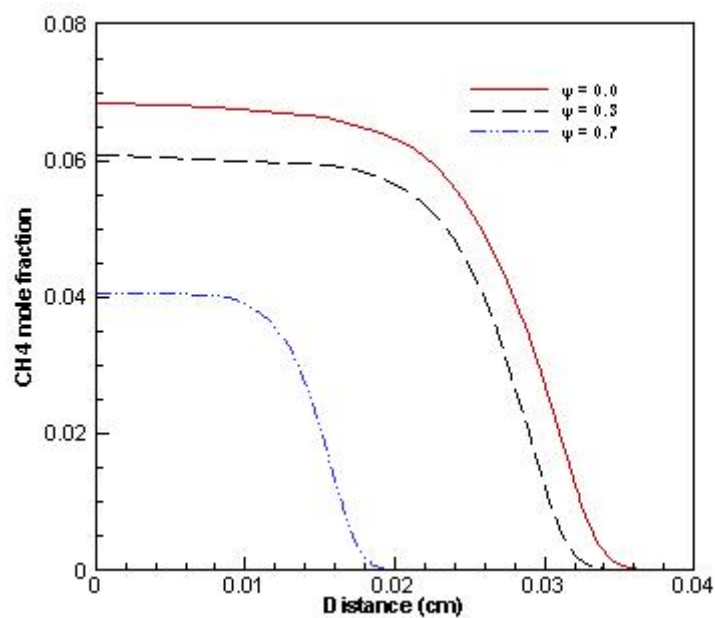


Fig. 5-18: CH₄ mole fraction profiles for different Ψ . $P = 8$ atm, $T = 598$ K, $\phi = 0.7$, reaction mechanism - GRI Mech 3.0.

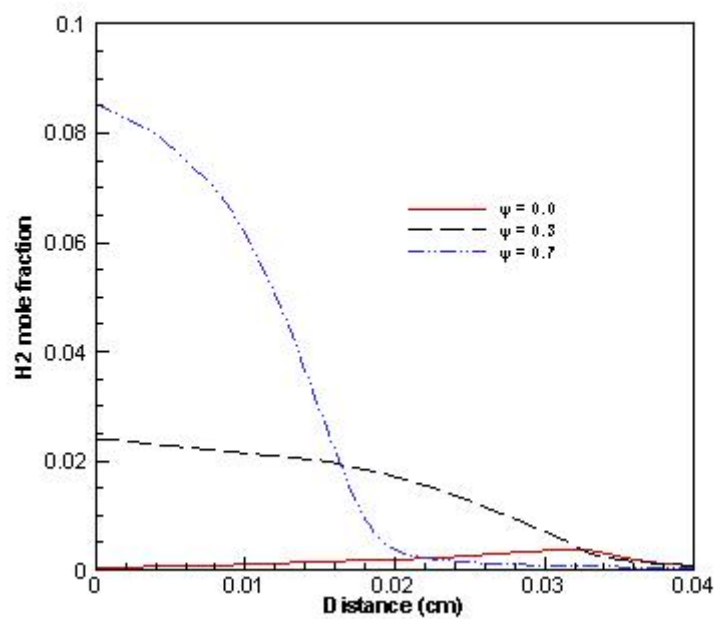


Fig. 5-19: H₂ mole fraction profiles for different Ψ . $P = 8$ atm, $T = 598$ K, $\phi = 0.7$, reaction mechanism - GRI Mech 3.0.

The reaction steps that control the rate of consumption of CH₄ are reactions [5-1] and [5-2]. The reaction rates for these reactions for different Ψ are plotted in Fig 5-20 and Fig 5-21.

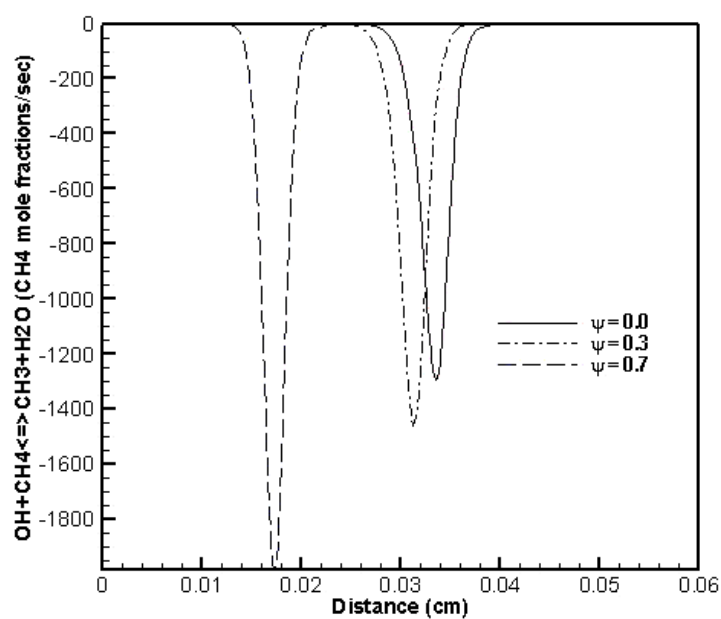


Fig. 5-20: Reaction rate profiles for reaction [5-2] for different Ψ . $P = 8$ atm, $T = 598$ K, $\phi = 0.7$, reaction mechanism - GRI Mech 3.0.

The peak reaction rates are higher and the reactions occur earlier with increasing Ψ . This explains the increase in consumption rate of CH_4 with higher H_2 content. Similarly, there has been an increase in the rate of other reactions involved in the consumption of CH_4 as shown in Figures 5-21 and 5-22.

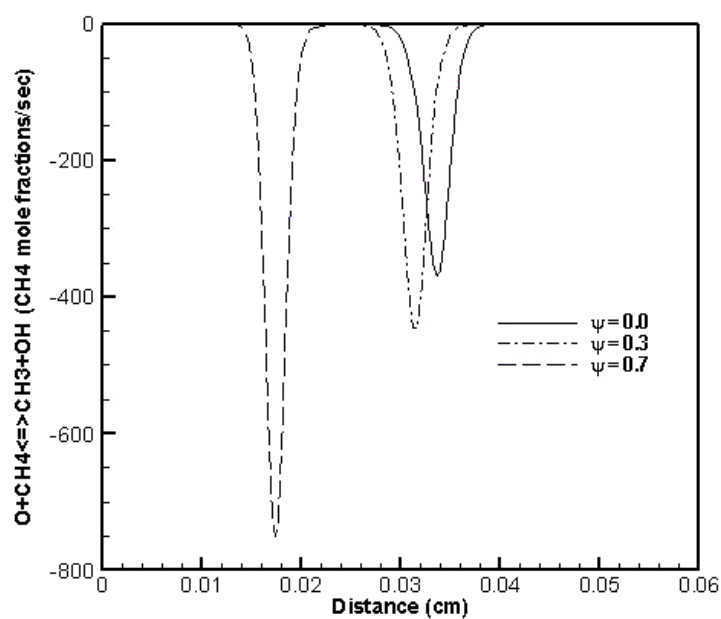


Fig. 5-21: Reaction rate profiles for reaction [5-1] for different Ψ . $P = 8$ atm, $T = 598$ K, $\phi = 0.7$, reaction mechanism - GRI Mech 3.0.

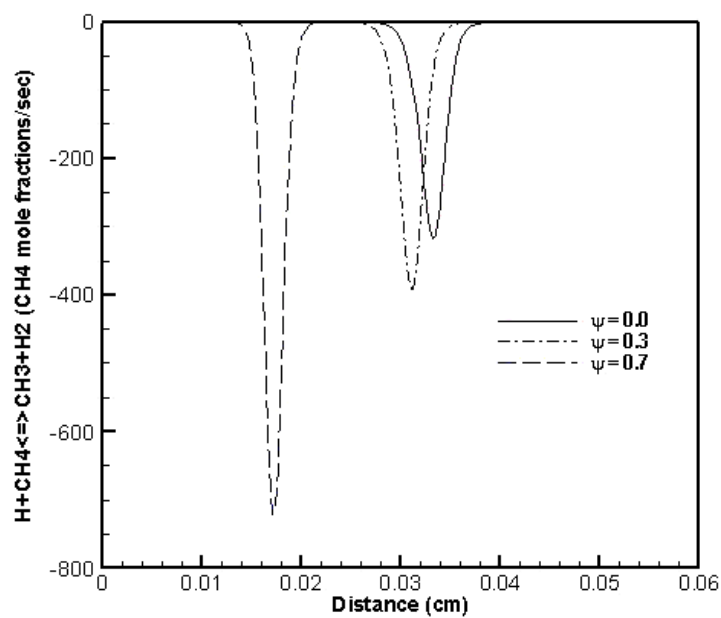


Fig. 5-22: Reaction rate profiles for different Ψ . $P = 8$ atm, $T = 598$ K, $\phi = 0.7$, reaction mechanism - GRI Mech 3.0.

5.2.3 OH radicals

Reaction [5-2] shows the significance of OH in the consumption of CH_4 . OH mole fraction profiles for different Ψ are shown in Fig 5-23.

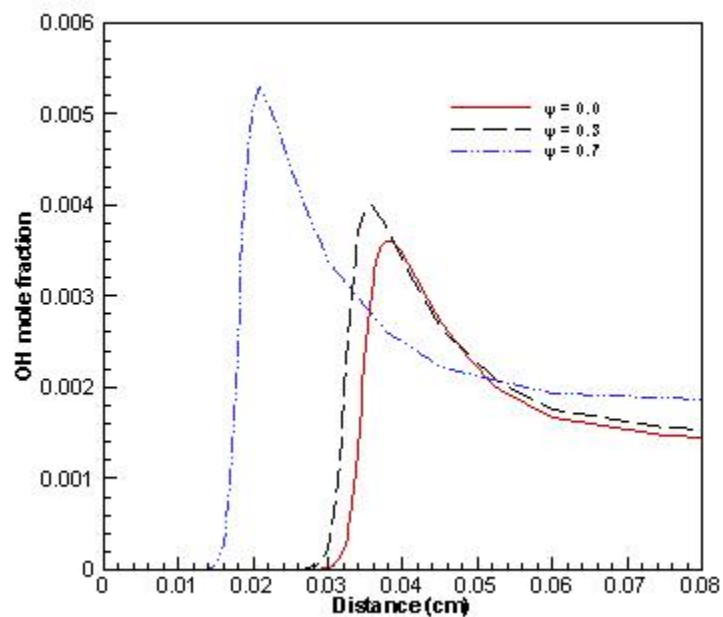


Fig. 5-23: OH mole fraction profiles for different Ψ . $P = 8$ atm, $T = 598$ K, $\phi = 0.7$, reaction mechanism - GRI Mech 3.0.

The relative flux of OH for different reactions is shown in Table 5-3 for $\Psi = 0.3$ and 0.7.

Table 5-3: Important reactions for the production of OH (OH mole fraction / sec)

	$\Psi = 0.3$	$\Psi = 0.7$
$\text{H} + \text{O}_2 \rightleftharpoons \text{O} + \text{OH}$	1.05E-01	1.11E-01
$\text{H} + \text{HO}_2 \rightleftharpoons 2\text{OH}$	1.86E-02	3.17E-02
$\text{O} + \text{H}_2 \rightleftharpoons \text{H} + \text{OH}$	1.40E-02	2.82E-02
$\text{O} + \text{CH}_4 \rightleftharpoons \text{OH} + \text{CH}_3$	1.19E-02	9.70E-03
$\text{HO}_2 + \text{CH}_3 \rightleftharpoons \text{OH} + \text{CH}_3\text{O}$	1.10E-02	7.19E-03
$\text{O} + \text{HO}_2 \rightleftharpoons \text{OH} + \text{O}_2$	3.57E-03	-
$\text{O} + \text{CH}_2\text{O} \rightleftharpoons \text{OH} + \text{HCO}$	3.28E-03	-
$\text{CH}_2 + \text{O}_2 \rightleftharpoons \text{OH} + \text{H} + \text{CO}$	3.03E-03	-

From Table 5-3 it can be concluded that there has been a factor of two increase in the production of OH radicals with an increase in Ψ from 0.3 to 0.7 through the reaction:



The relative flux of OH has reduced for some reactions but these reductions are compensated by the increase in the flux through reaction [5-7]. The increase in OH leads to earlier and faster break up of CH_4 molecules to produce CH_3 through reaction [5-2], and hence the reaction zone occurs earlier for higher Ψ .

5.2.4 O Radicals

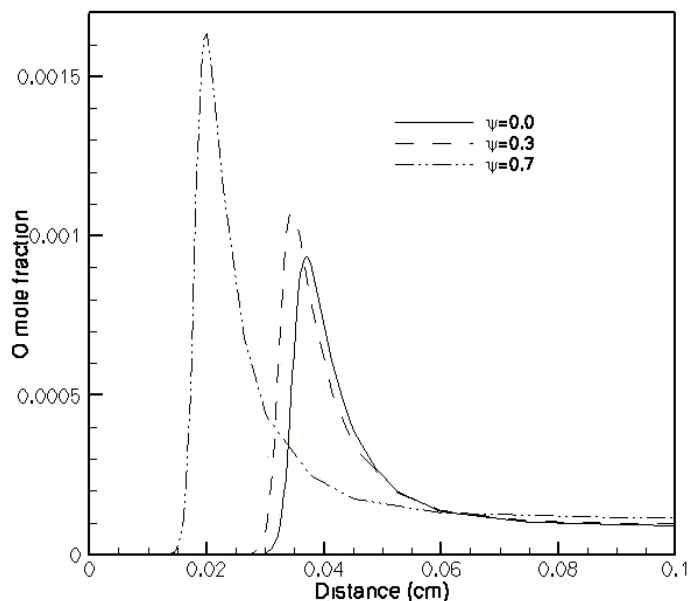


Fig. 5-24: O mole fraction profiles for different Ψ . $P = 8$ atm, $T = 598$ K, $\phi = 0.7$, reaction mechanism - GRI Mech 3.0.

Fig 5-24 shows the O mole fractions profiles for different Ψ . There is an increase in O mole fraction with increasing Ψ .

Table 5-4 shows the relative flux of O for different reactions for three values of Ψ .

Table 5-4: Important reactions for the production of O (O mole fractions / sec)

	$\Psi = 0.0$	$\Psi = 0.3$	$\Psi = 0.7$
$\text{H} + \text{O}_2 \rightleftharpoons \text{O} + \text{OH}$	1.70E-03	1.05E-01	1.11E-01
$\text{CH}_2 + \text{O}_2 \rightleftharpoons \text{O} + \text{CH}_2\text{O}$	1.05E-01	1.45E-03	-

The relative flux of O increases 100 times as Ψ increases from 0.0 to 0.7 due to the reaction:



Therefore, the increase in the O mole fraction can be attributed to the increase in the significance of the reaction [5-8].

5.2.5 H radicals

Table 5-5 shows the relative flux for production of H radicals for different Ψ .

Table 5-5: Important reactions involving production of H (H mole fractions/sec)

	$\Psi = 0.0$	$\Psi = 0.3$	$\Psi = 0.7$
$\text{OH} + \text{CO} \rightleftharpoons \text{H} + \text{CO}_2$	6.81E-02	6.62E-02	5.02E-02
$\text{OH} + \text{H}_2 \rightleftharpoons \text{H} + \text{H}_2\text{O}$	3.00E-02	5.00E-02	1.05E-01
$\text{O} + \text{CH}_3 \rightleftharpoons \text{H} + \text{CH}_2\text{O}$	1.36E-02	1.31E-02	1.10E-02
$\text{H} + \text{CH}_2\text{O} (+\text{M}) \rightleftharpoons \text{CH}_3\text{O} (+\text{M})$	1.11E-02	1.00E-02	6.25E-03
$\text{HCO} + \text{H}_2\text{O} \rightleftharpoons \text{H} + \text{CO} + \text{H}_2\text{O}$	1.07E-02	9.83E-03	6.99E-03
$\text{HCO} + \text{M} \rightleftharpoons \text{H} + \text{CO} + \text{M}$	1.04E-02	8.99E-03	5.49E-03
$\text{O} + \text{H}_2 \rightleftharpoons \text{H} + \text{OH}$	9.64E-03	1.40E-02	2.82E-02
$\text{O} + \text{CH}_3 \rightleftharpoons \text{H} + \text{H}_2 + \text{CO}$	9.04E-03	8.71E-03	7.33E-03
$\text{CH}_2 + \text{O}_2 \rightleftharpoons 2\text{H} + \text{CO}_2$	8.21E-03	7.03E-03	4.19E-03
$\text{CH}_2 + \text{O}_2 \rightleftharpoons \text{OH} + \text{H} + \text{CO}$	3.54E-03	3.03E-03	
$\text{CH}_2(\text{S}) + \text{O}_2 \rightleftharpoons \text{H} + \text{OH} + \text{CO}$	2.75E-03	2.43E-03	
$\text{H} + \text{C}_2\text{H}_4 (+\text{M}) \rightleftharpoons \text{C}_2\text{H}_5 (+\text{M})$	2.16E-03		

The increase in OH radical concentration increases the production of H radicals through reaction $\text{OH} + \text{H}_2 \rightarrow \text{H} + \text{H}_2\text{O}$ (Table 5-5). This increase in H radical (Fig 5-25) can further accelerate the production of OH radicals through the reactions $\text{H} + \text{O}_2 \rightarrow \text{O} + \text{OH}$ and $\text{H} + \text{HO}_2 \rightarrow 2\text{OH}$. The increase in O radicals further accelerates OH production through $\text{O} + \text{H}_2 \rightarrow \text{H} + \text{OH}$. Higher OH and O lead to more rapid consumption of CH_4

through reactions [5-1] and [5-2]. This process is self-supporting and becomes stronger for higher H_2 levels.

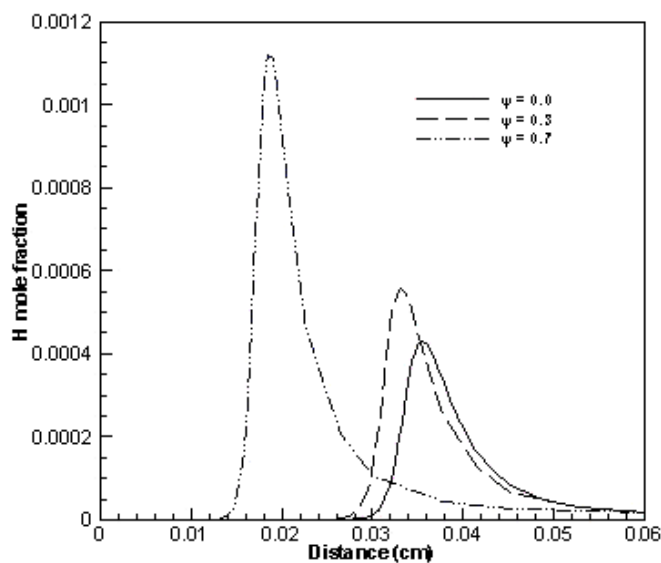


Fig. 5-25: H mole fraction profiles for different Ψ . $P = 8$ atm, $T = 598$ K, $\phi = 0.7$, reaction mechanism - GRI Mech 3.0.

5.2.6 O_2 Mole Fraction

O_2 mole fraction profiles for different Ψ are shown in Fig 5-26. The earlier O_2 consumption with increasing Ψ is consistent with the earlier production of O radicals and the earlier occurrence of the reaction zone for higher Ψ .

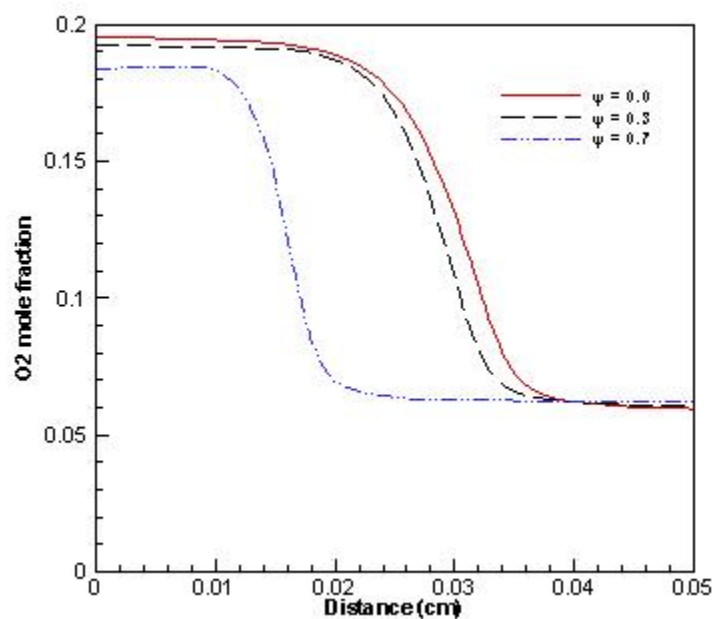


Fig. 5-26: O₂ mole fraction profiles for different Ψ . $P = 8$ atm, $T = 598$ K, $\phi = 0.7$, reaction mechanism - GRI Mech 3.0.

5.2.7 NO Mole Fraction

Fig 5-27 shows NO mole fraction profiles for different Ψ . The horizontal portion of the curve at the location 8 cm refers to the equilibrium concentration of NO. The equilibrium concentration is different for different Ψ . The straight - line nature of the curve can be attributed to the coarse grid structure near the boundary.

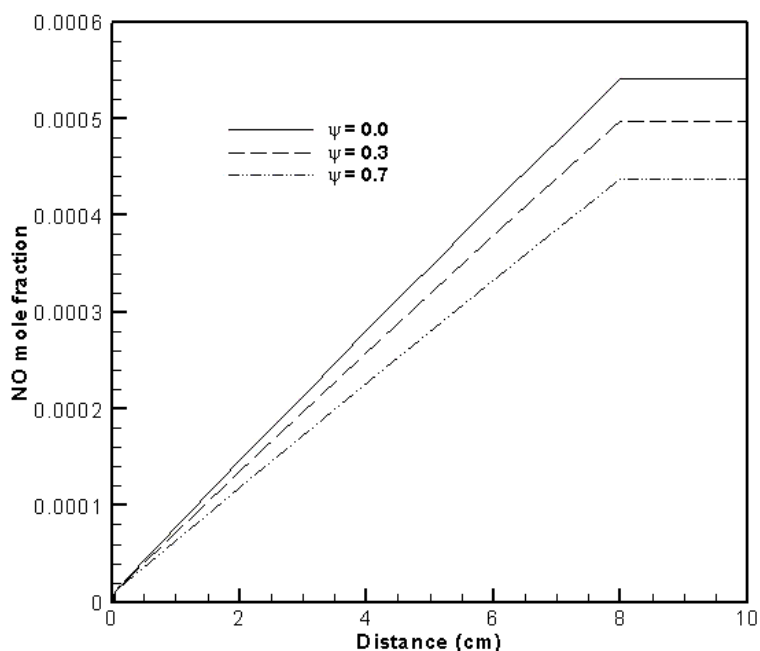


Fig. 5-27: NO mole fraction profiles for different Ψ . $P = 8$ atm, $T = 598$ K, $\phi = 0.7$, reaction mechanism - GRI Mech 3.0.

The relative importance of different reactions in NO formation and destruction is shown in Table 5-6.

Table 5-6: Important reactions involved in the production and consumption of NO (NO mole fraction / sec).

Production		Consumption	
$N+O_2 \rightleftharpoons NO+O$	2.30E-04	$N+NO \rightleftharpoons N_2+O$	-2.84E-04
$N_2O+O \rightleftharpoons 2NO$	5.23E-05	$NH+NO \rightleftharpoons N_2O+H$	-1.82E-05
$N+OH \rightleftharpoons NO+H$	4.37E-05	$NO+O+M \rightleftharpoons NO_2+M$	-8.76E-06
$NO_2+H \rightleftharpoons NO+OH$	1.35E-05	$HO_2+NO \rightleftharpoons NO_2+OH$	-7.43E-06
$N+CO_2 \rightleftharpoons NO+CO$	1.31E-05	$H+NO+M \rightleftharpoons HNO+M$	-5.71E-07
		$CH_2+NO \rightleftharpoons H+HNCO$	-4.70E-07
		$HCCO+NO \rightleftharpoons HCNO+CO$	-2.55E-07

($\phi = 0.7$, $\Psi = 0.3$, reaction mechanism – GRI

These reactions occur earlier and faster for higher Ψ . But the increase in rates of reactions producing NO with increasing Ψ is dominated by the increase in the rates of reactions

consuming NO resulting in a net drop in the NO mole fraction. Among the most significant consumption reactions is the increase in the rate of:



This is shown in Fig 5-28.

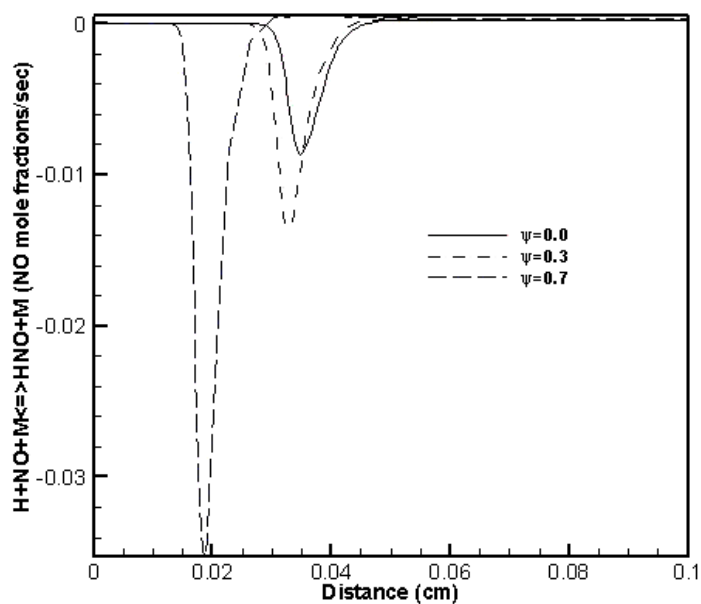


Fig. 5-28: Reaction rate profiles for different Ψ . $P = 8$ atm, $T = 598$ K, $\phi = 0.7$, reaction mechanism - GRI Mech 3.0.

5.2.8 NO₂ Mole Fraction

Reactions involved in the production and destruction of NO₂ are shown in Table 5-7.

Table 5-7: Important reactions in the production and destruction of NO₂ (NO₂ mole fractions / sec).

	$\Psi = 0.7$	$\Psi = 0.3$	$\Psi = 0$
Creation			
NO+O+M \rightleftharpoons NO ₂ +M	6.82E-06	8.38E-06	8.76E-06
HO ₂ +NO \rightleftharpoons NO ₂ +OH	4.21E-06	6.50E-06	7.43E-06
Destruction			
NO ₂ +H \rightleftharpoons NO+OH	-9.10E-06	-1.24E-05	-1.35E-05
NO ₂ +O \rightleftharpoons NO+O ₂	-6.11E-07	-9.14E-07	-1.03E-06

There is no change in the relative importance of the reactions for different Ψ . However, NO₂ mole fraction reduces with increasing Ψ as shown in Figs 5-29 and 5-30.

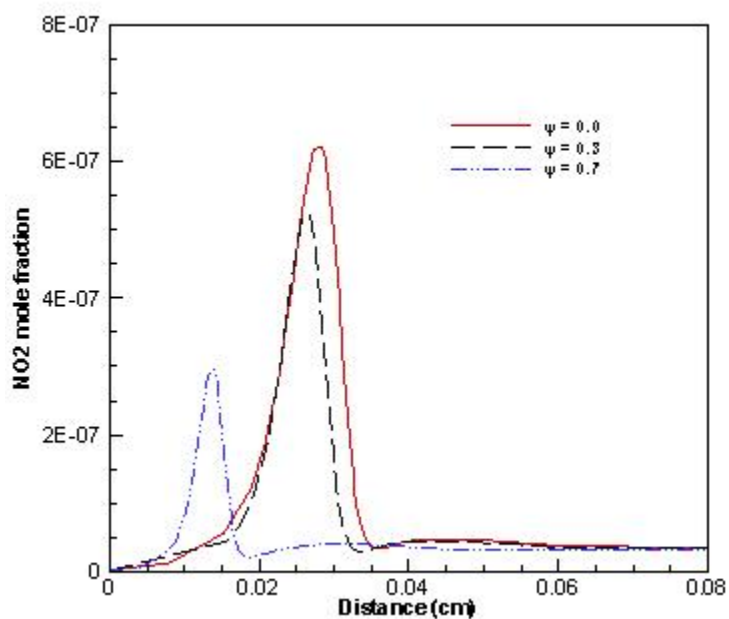


Fig. 5-29: Reaction - zone NO₂ mole fraction profiles for different Ψ . $P = 8$ atm, $T = 598$ K, $\phi = 0.7$, reaction mechanism - GRI Mech 3.0.

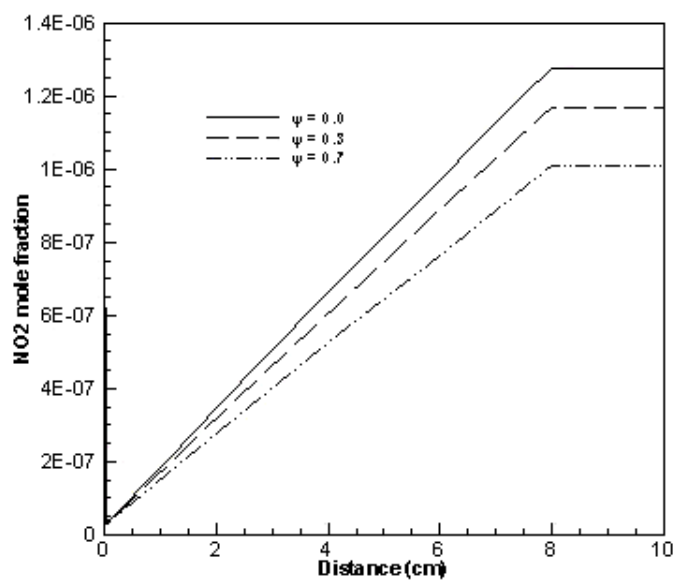


Fig. 5-30: NO₂ mole fraction profiles for different Ψ . $P = 8$ atm, $T = 598$ K, $\phi = 0.7$, reaction mechanism - GRI Mech 3.0.

In Fig 5-30 the horizontal portion of the curve at location 8 cm refers to the equilibrium concentration of NO₂. The discontinuous nature of the curve is due to the coarse grid near the outflow boundary.

Figures 5-31 through 5-33 show several reactions involved in the production and destruction of NO₂.

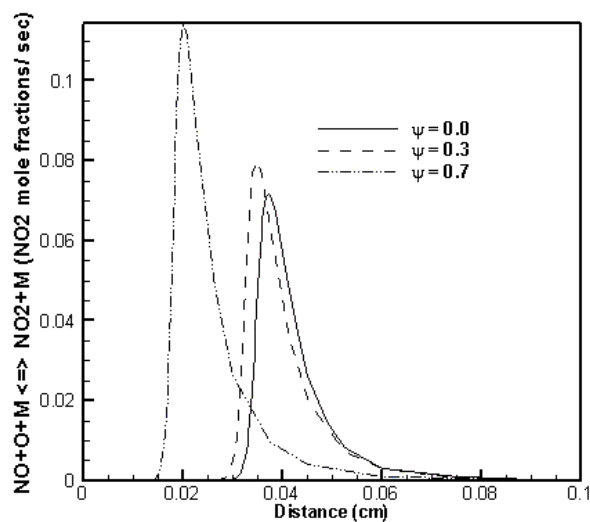


Fig. 5-31: Reaction rate profiles for different Ψ . $P = 8$ atm, $T = 598$ K, $\phi = 0.7$, reaction mechanism - GRI Mech 3.0.

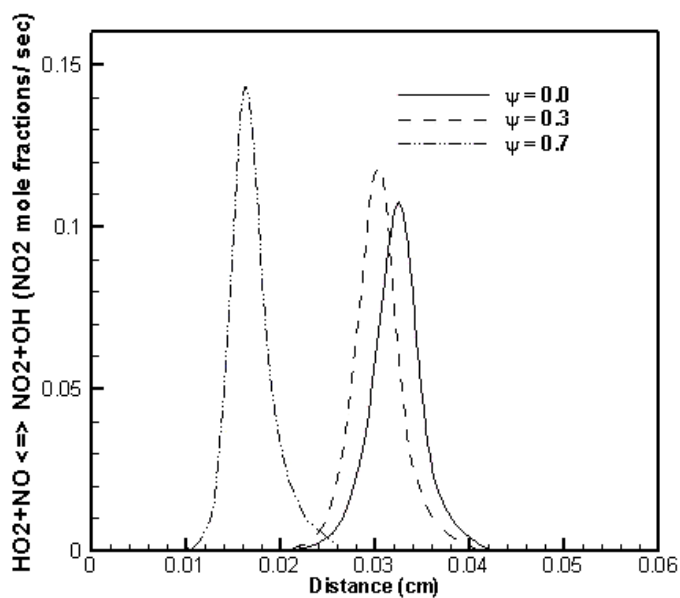


Fig. 5-32: Reaction rate profiles for different Ψ . $P = 8$ atm, $T = 598$ K, $\phi = 0.7$, reaction mechanism - GRI Mech 3.0.

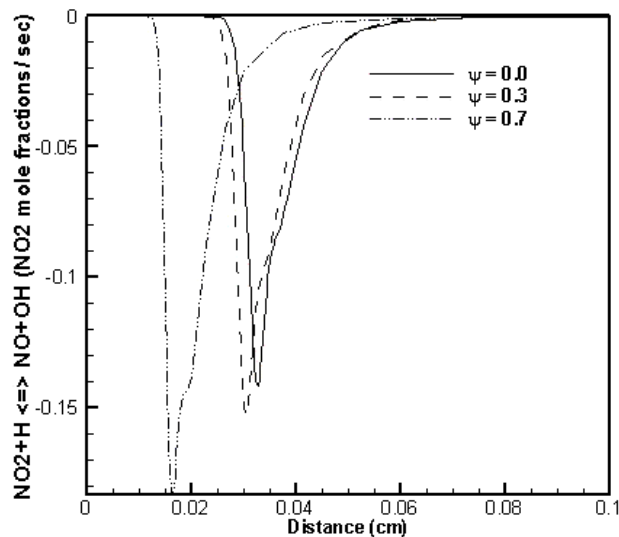


Fig. 5-33: Reaction rate profiles for different Ψ . $P = 8$ atm, $T = 598$ K, $\phi = 0.7$, reaction mechanism - GRI Mech 3.0.

There is an increase in the rate of reactions producing and consuming NO_2 with increasing Ψ , but the net result is lower NO_2 with increasing Ψ .

5.3 Diffusion of Hydrogen

The molecular diffusion coefficient of hydrogen is higher than that for hydrocarbons (Andrea et al., 2004) and changes in flame character in the presence of hydrogen have been attributed to its high diffusivity (Glassman, 1996; Sobiesiak, et al., 2002). In this section the effect of hydrogen's high molecular diffusivity on premixed, steady, one-dimensional laminar flames is discussed. Two cases having modified transport coefficients (Section 4.3) are compared to a baseline ("normal") flame with the standard CHEMKIN/TRANSPORT multicomponent diffusion model. The diffusion

coefficient of hydrogen is reduced by 71.03% when its Lewis number (and all others) is set to unity while it is reduced by 70.02% when set equal to the diffusion coefficient of CH₄. Here results are presented for reaction mechanism GRI Mech 3.0 with $\phi = 0.7$ and $\Psi = 0.3$. For other reaction mechanisms and compositions the conclusions are essentially the same. The results from PREMIX calculations in principle should be same as the EQUIL results but due to numerical error, the final solution has error up to 1% when compared to the EQUIL calculations.

5.3.1 Laminar Flame Speed

There was no significant change in the laminar flame speed when the diffusion coefficient for the species has been changed. The laminar flame speed remained 41.52 cm/s when the diffusion coefficient of H₂ was set equal to the diffusion coefficient of CH₄. However, when the Le has been set to unity for all the species the laminar speed increases to 45.91 cm/s.

5.3.2 Temperature

Fig 5-34 shows the temperature profiles for flames with modified diffusion coefficients compared to the normal flame. There is no noticeable change in the temperature profile when the diffusion coefficient of hydrogen is set equal to that for methane. When the Lewis numbers are set to unity for all species, the reaction zone occurs earlier but there is no other significant difference.

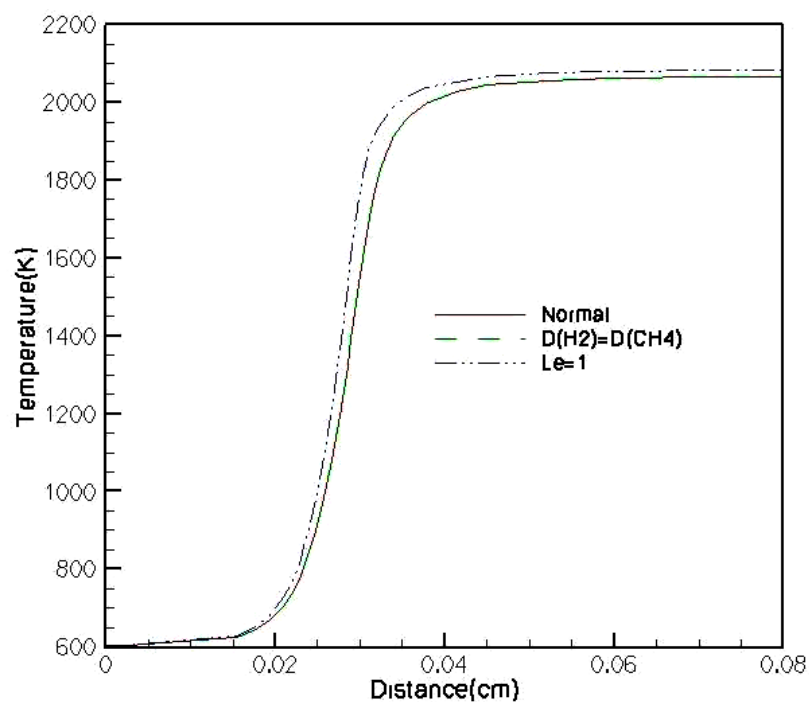


Fig. 5-34: Temperature profiles for three diffusion cases. $P = 8$ atm, $T = 598$ K, $\phi = 0.7$, $\Psi = 0.3$, reaction mechanism - GRI Mech 3.0.

5.3.3 CH₄ and CH₃

Figure 5-35 shows the CH₄ mole fraction profiles for the three cases considered.

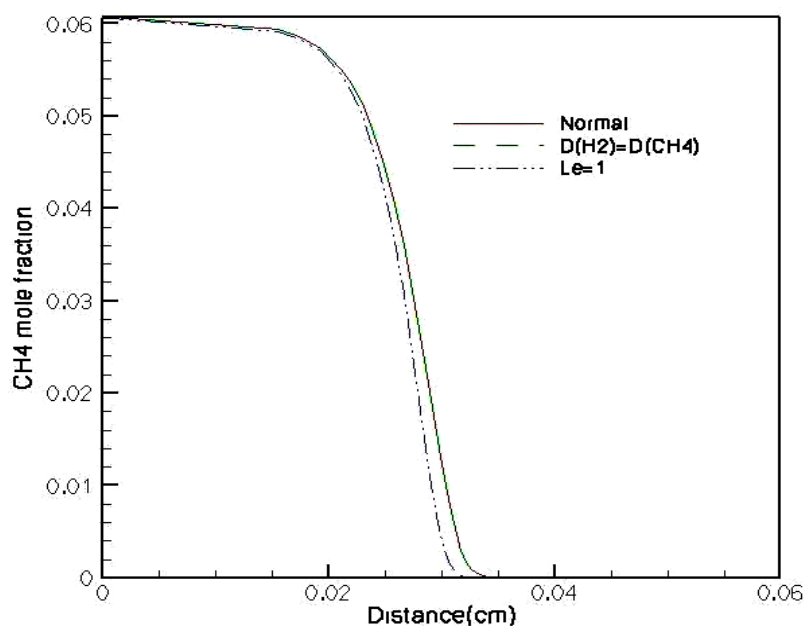


Fig. 5-35: CH₄ mole fraction profiles for three diffusion cases. $P = 8$ atm, $T = 598$ K, $\phi = 0.7$, $\Psi = 0.3$, reaction mechanism - GRI Mech 3.0.

There are no significant differences in the mole fraction profiles when the diffusion coefficient of hydrogen is set equal to that of methane. When the Lewis numbers are set to unity, the reaction zone occurs earlier but the change is not large. Similar behavior is seen for CH₃ in Fig 5-36. There is a small increase in CH₃ mole fraction when the Lewis number is set to unity for all species.

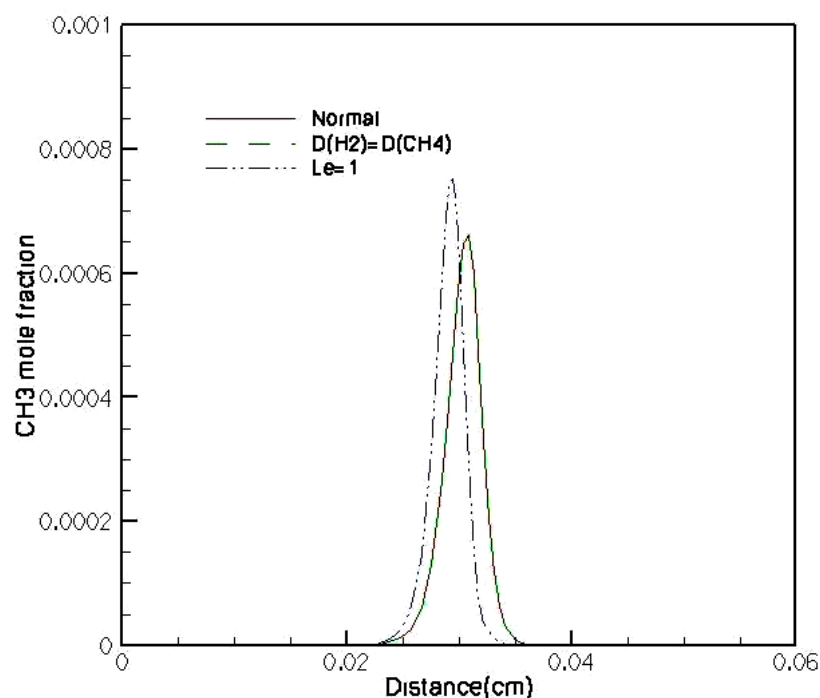


Fig. 5-36: CH_3 mole fraction profiles for three diffusion cases. $P = 8 \text{ atm}$, $T = 598\text{K}$, $\phi = 0.7$, $\Psi = 0.3$, reaction mechanism - GRI Mech 3.0.

5.3.4 OH

Figure 5-37 shows the OH mole fraction profiles for the three cases. There is no change in the OH mole fraction by setting the diffusion coefficient of hydrogen equal to the diffusion coefficient of methane. OH mole fraction increases and the peak occurs earlier when the Lewis numbers are set to unity for all species. However, the change is not significant.

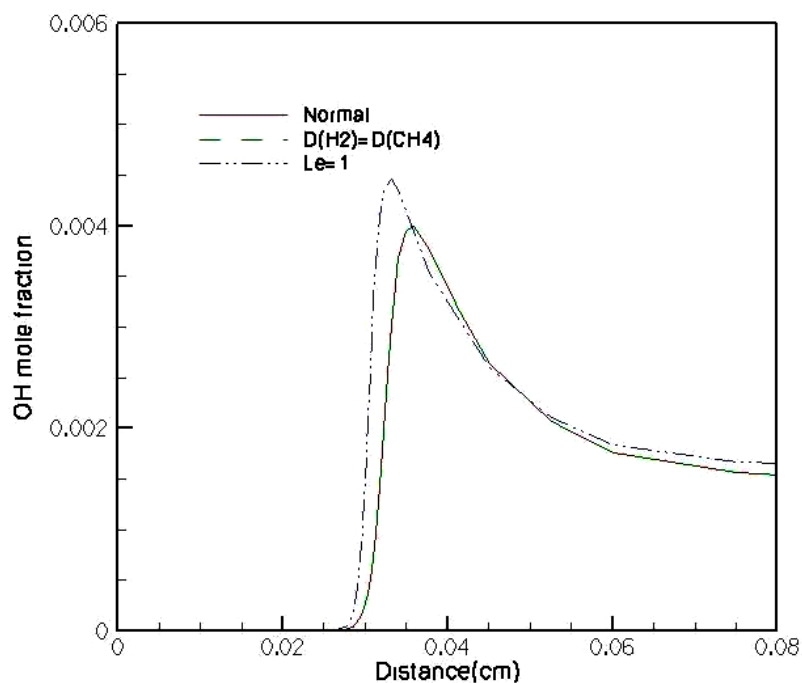


Fig. 5-37: OH mole fraction profiles for three diffusion cases. $P = 8$ atm, $T = 598$ K, $\phi = 0.7$, $\Psi = 0.3$, reaction mechanism - GRI Mech 3.0.

5.3.5 NO and NO₂ mole fractions

Figure 5-38 compares the NO mole fraction profiles for the three molecular diffusion cases over the entire computation domain. The NO mole fractions are slightly higher when the Lewis numbers are unity for all species compared to the baseline case and to the case where the diffusion coefficient of hydrogen is set equal to that for methane. The horizontal part of the curve at the location 8-10 cm indicates the equilibrium mole fraction. The discontinuity in the curve is due to the coarse grid at the boundary.

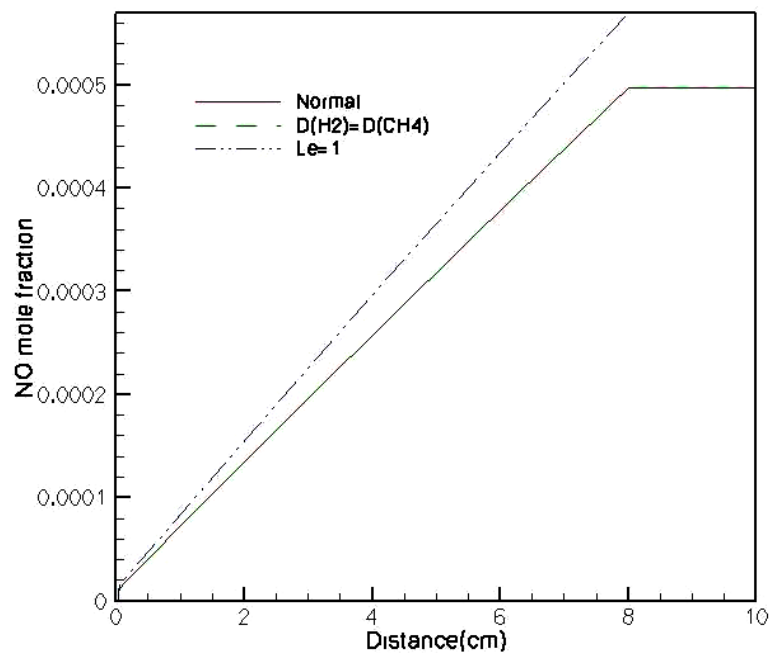


Fig. 5-38: NO mole fraction profiles for three diffusion cases. $P = 8$ atm, $T = 598$ K, $\phi = 0.7$, $\Psi = 0.3$, reaction mechanism - GRI Mech 3.0.

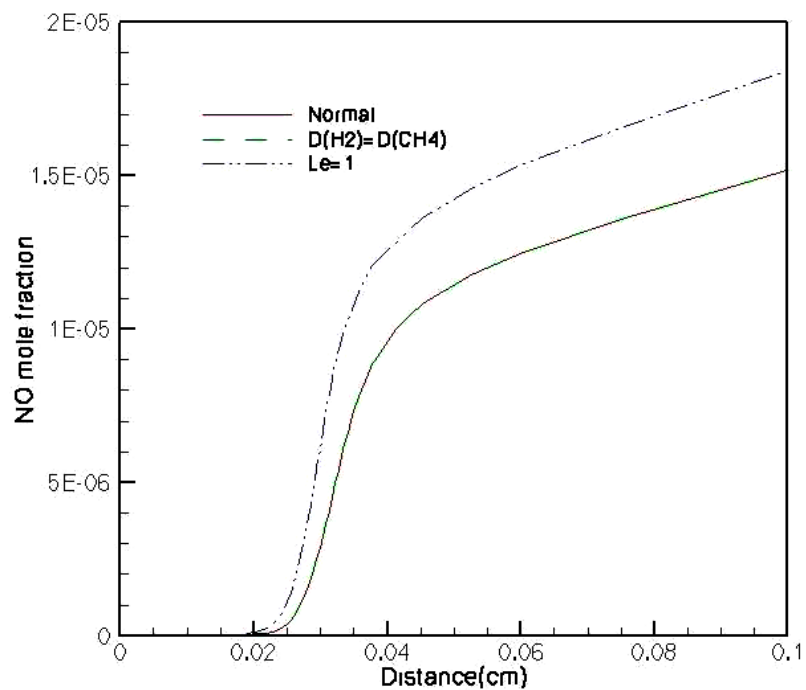


Fig. 5-39: Reaction - zone NO mole fraction profiles for three diffusion cases. $P = 8$ atm, $T = 598$ K, $\phi = 0.7$, $\Psi = 0.3$, reaction mechanism - GRI Mech 3.0.

Figure 5-39 shows the NO mole fraction profiles in the reaction zone. Again, there is no noticeable change in the NO mole fraction profile when the diffusion coefficient of hydrogen is set equal to that for methane. When the Lewis numbers are set to unity, the NO mole fraction increases but the increase is not large.

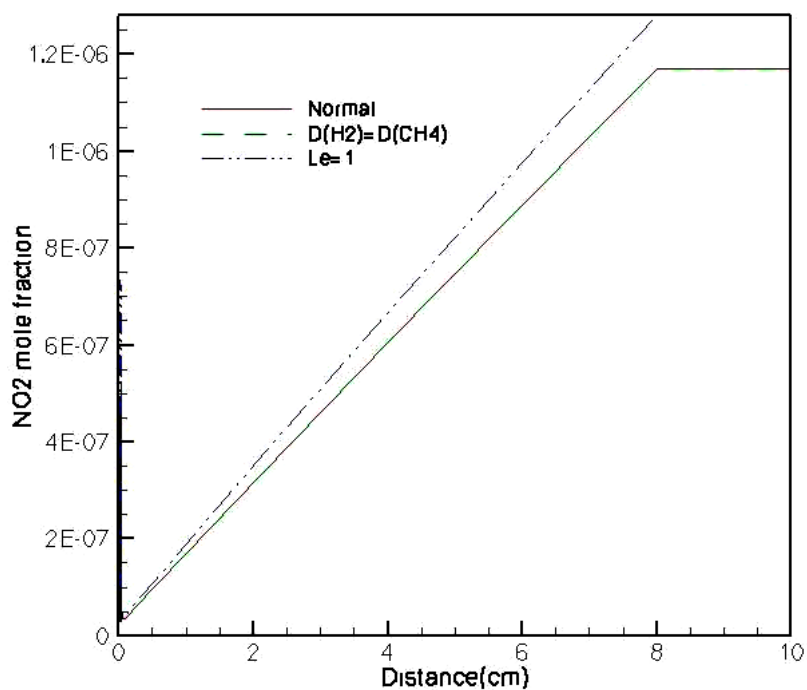


Fig. 5-40: NO₂ mole fraction profiles for three diffusion cases. $P = 8$ atm, $T = 598$ K, $\phi = 0.7$, $\Psi = 0.3$, reaction mechanism - GRI Mech 3.0.

Figures 5-40 and 5-41 show the NO₂ mole fraction profiles. The NO₂ mole fraction is larger for cases where the diffusion coefficient of hydrogen has been reduced through the two schemes discussed earlier compared to the normal case, but the increase is not significant.

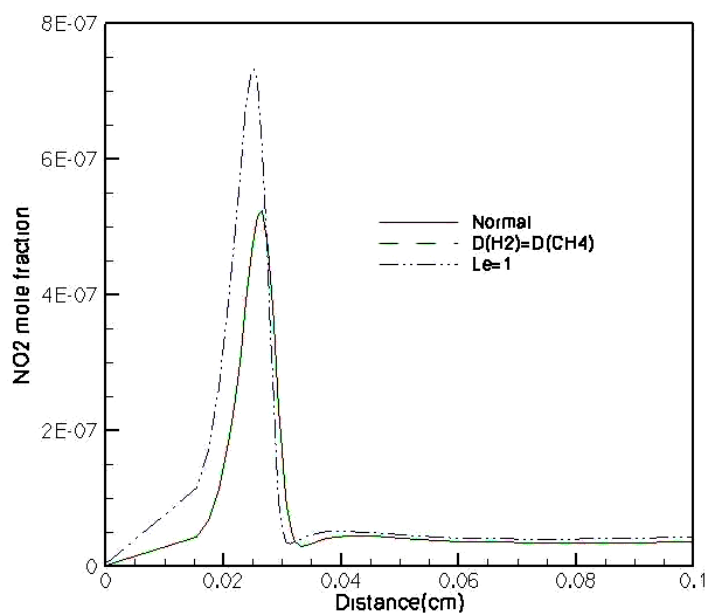


Fig. 5-41: Reaction - zone NO_2 mole fraction profiles for three diffusion cases. $P = 8 \text{ atm}$, $T = 598\text{K}$, $\phi = 0.7$, $\Psi = 0.3$, reaction mechanism - GRI Mech 3.0.

5.3.6 H_2 and H mole fractions

H_2 mole fraction profiles for the three cases are shown in Fig 5-42. The initial rate of consumption is higher for the baseline case. However, the overall consumption pattern remains the same.

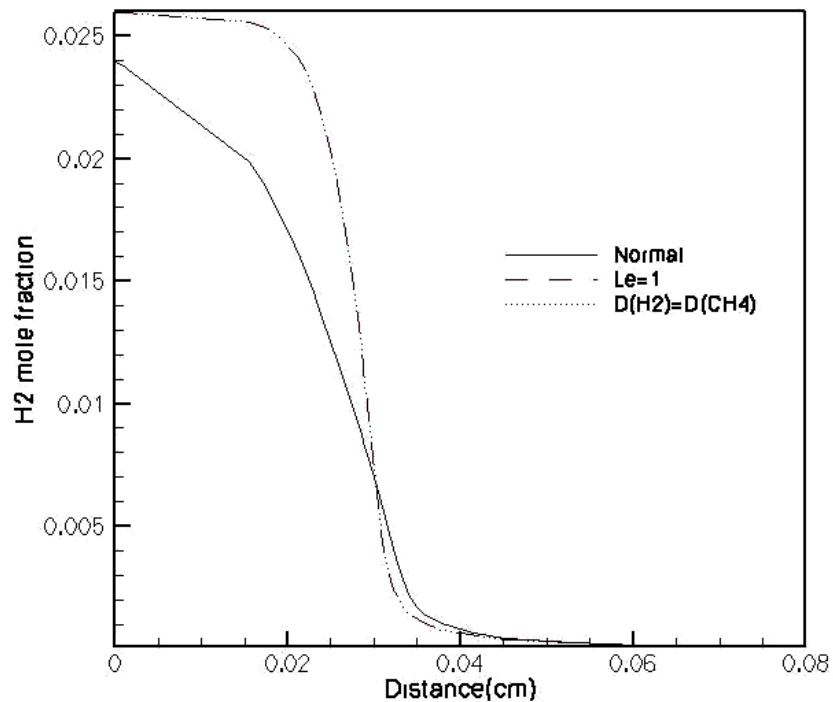


Fig. 5-42: H_2 mole fraction profiles for three diffusion cases. $P = 8$ atm, $T = 598$ K, $\phi = 0.7$, $\Psi = 0.3$, reaction mechanism - GRI Mech 3.0.

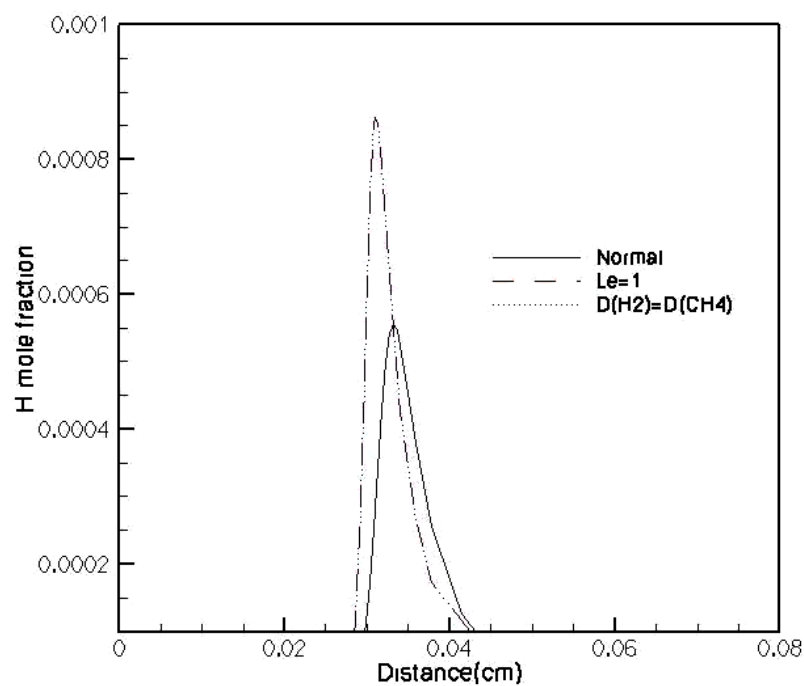


Fig. 5-43: H mole fraction profiles for three diffusion cases. $P = 8$ atm, $T = 598$ K, $\phi = 0.7$, $\Psi = 0.3$, reaction mechanism - GRI Mech 3.0.

Figure 5-43 shows the H mole fraction profiles for three cases. There is increased production of H radicals when the diffusion coefficient of H₂ is reduced through either of the two schemes discussed earlier.

From these results, it can be concluded that there is no significant change in the reaction zone structure when the diffusion coefficient of hydrogen is reduced through either of the two schemes discussed earlier. However, different conclusions can be expected for unsteady and multi-dimensional flames (Glassman, 1996).

5.4 EGR Studies

NO_x emissions from an actual engine can be reduced by recirculating some of the exhaust gas back into the intake manifold. Exhaust gas is chemically nonreactive and acts as a diluent for the fuel-air mixture. It absorbs some of the heat that is released and also effectively reduces the equivalence ratio of the reactant mixture (depending on how it is introduced). The reduced temperature reduces the formation of thermal NO and hence the engine-out NO_x decreases with EGR.

A number of test cases were performed for different ϕ and Ψ . Here detailed results are shown for $\phi = 0.7$, $\Psi = 0.7$ using GRI Mech 3.0. The EGR flame is compared to a baseline flame with no EGR (“normal”). Qualitatively similar results are found for the other mechanisms and thermochemical conditions.

5.4.1 Laminar Flame Speed

For the case of $\phi = 0.7$ and $\Psi = 0.7$ using GRI Mech 3.0, the laminar flame speed reduces from 71.64 cm/s to 25.94 cm/s when 20% of intake is considered to be exhaust gas. Similarly, the laminar flame speed is reduced for other combinations of Ψ and ϕ using reaction mechanisms GRI Mech 2.11, Glarborg and ARM, when 20% of intake was considered to be exhaust gas.

5.4.2 Temperature profile

Figure 5-44 shows the temperature profiles for EGR and normal flames.

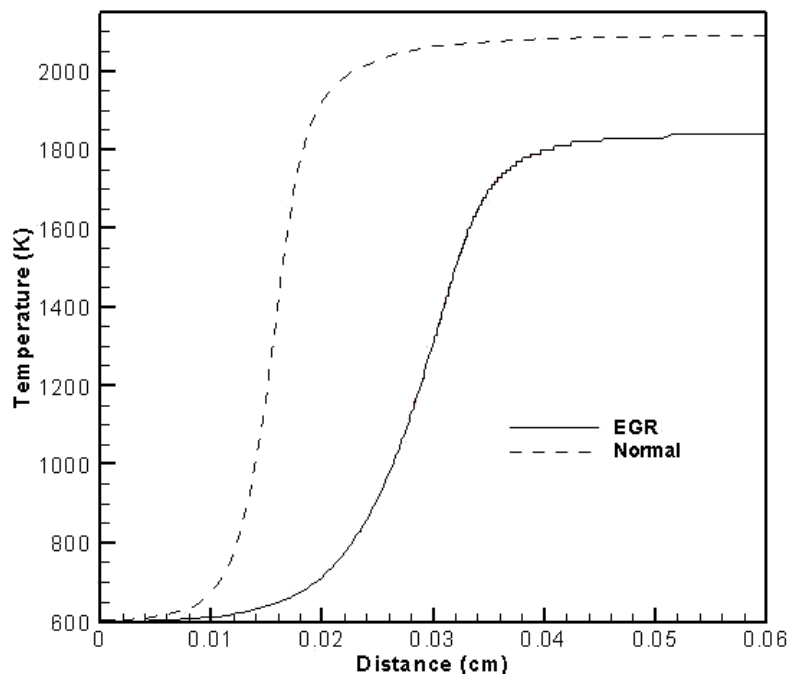


Fig. 5-44: Temperature profiles for EGR and normal flames. $P = 8$ atm, $T = 598$ K, $\phi = 0.7$, $\Psi = 0.7$, reaction mechanism - GRI Mech 3.0.

The peak temperature drops and the reaction zone is delayed for the EGR flame.

5.4.3 CH₄ and CH₃ Mole Fraction Profiles

Figures 5-45 and 5-46 show the mole fraction profiles for CH₄ and CH₃. Because of the delay in the occurrence of the reaction zone with EGR, the consumption of CH₄ is delayed, and hence the formation of CH₃, with EGR.

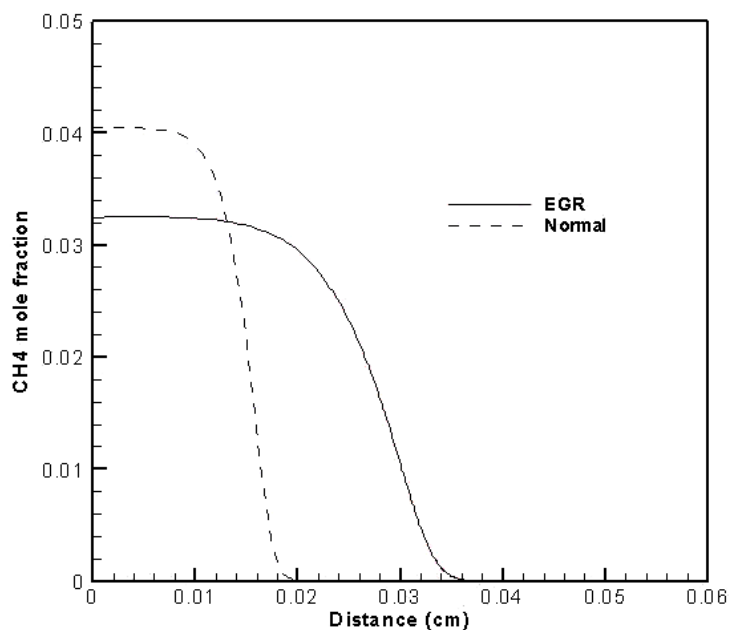


Fig. 5-45: CH₄ mole fraction profiles for EGR and normal flames. $P = 8$ atm, $T = 598$ K, $\phi = 0.7$, $\Psi = 0.7$, reaction mechanism - GRI Mech 3.0.

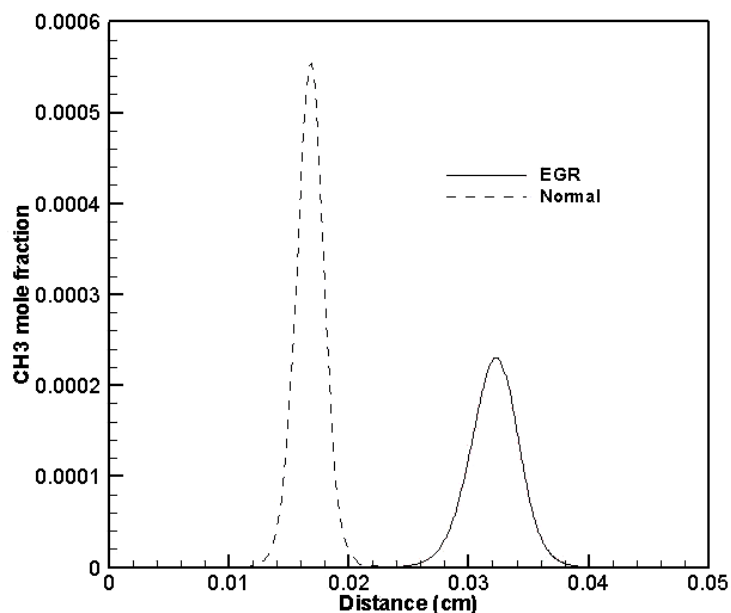


Fig. 5-46: CH_3 mole fraction profiles for EGR and normal flames. $P = 8 \text{ atm}$, $T = 598 \text{ K}$, $\phi = 0.7$, $\Psi = 0.7$, reaction mechanism - GRI Mech 3.0.

5.4.4 OH Mole Fraction

OH mole fraction profiles are shown for EGR and normal flames in Fig 5-47. Because of the delay in the reaction zone with EGR, the occurrence of OH radical in the flame is delayed. The peak OH mole fraction is also lowered with EGR. Delayed and reduced mole fraction of OH slows down the rate-controlling reaction [5-2] involved in the consumption of CH_4 , consistent with Fig 5-45.

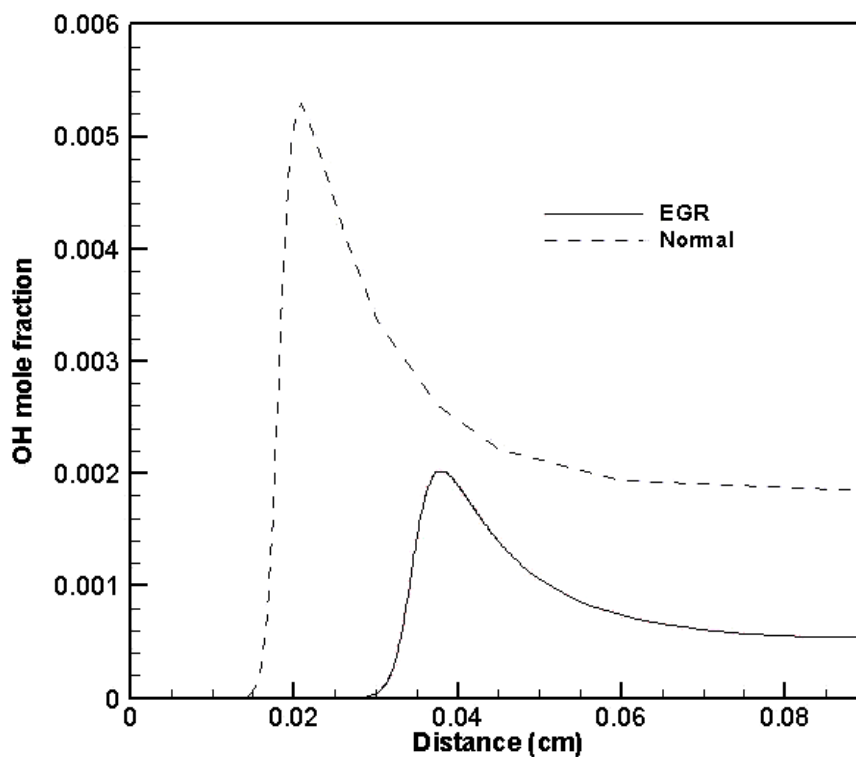


Fig. 5-47: OH mole fraction profiles for EGR and normal flames. $P = 8$ atm, $T = 598$ K, $\phi = 0.7$, $\Psi = 0.7$, reaction mechanism - GRI Mech 3.0.

5.4.5 O Mole Fraction Profile

Figure 5-48 shows the O mole fraction profiles for the normal and EGR flames. The peak for the EGR profile is lower compared to the normal flame. Oxygen atoms are important in the consumption of CH_4 through reaction [5-1], producing CH_3 . Due to reduction in the O mole fraction the consumption rate of CH_4 is reduced as shown in Fig 5-45. Hence the mole fraction of CH_4 and CH_3 flames is reduced as shown in Fig 5-45 and 5-46.

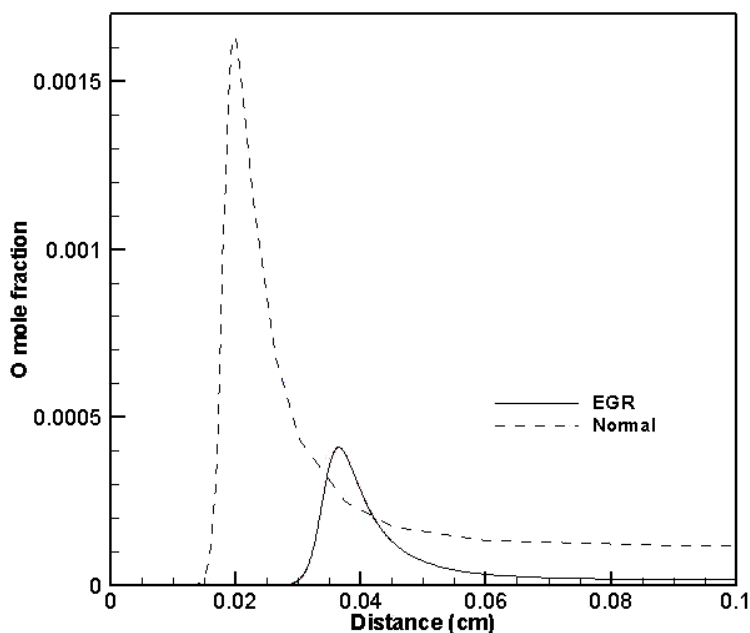


Fig. 5-48: O mole fraction profiles for EGR and normal flames. $P = 8$ atm, $T = 598$ K, $\phi = 0.7$, $\Psi = 0.7$, reaction mechanism - GRI Mech 3.0.

5.4.6 H₂ and H Mole Fraction Profile

Figures 5-49 and 5-50 show the H₂ and H mole-fraction profiles for normal and EGR flames. From Table 5-2, it is seen that reactions important in the consumption of H₂ involve the presence of OH and O radicals. Hence a reduction in OH and O mole fractions leads to a lower consumption rate of H₂ as shown in Fig 5-49.

Another result of the reduction in OH mole fraction is reduced production of H through the important reaction $\text{OH} + \text{H}_2 \rightarrow \text{H} + \text{H}_2\text{O}$ and hence the EGR flame has lower H mole fraction compared to the normal flame, as shown in Fig 5-50.

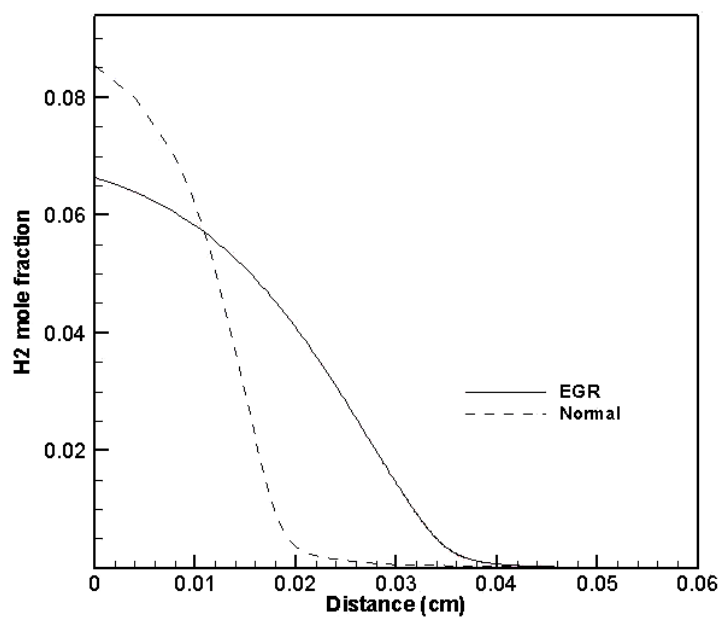


Fig. 5-49: H₂ mole fraction profiles for EGR and normal flames. $P = 8$ atm, $T = 598$ K, $\phi = 0.7$, $\Psi = 0.7$, reaction mechanism - GRI Mech 3.0.

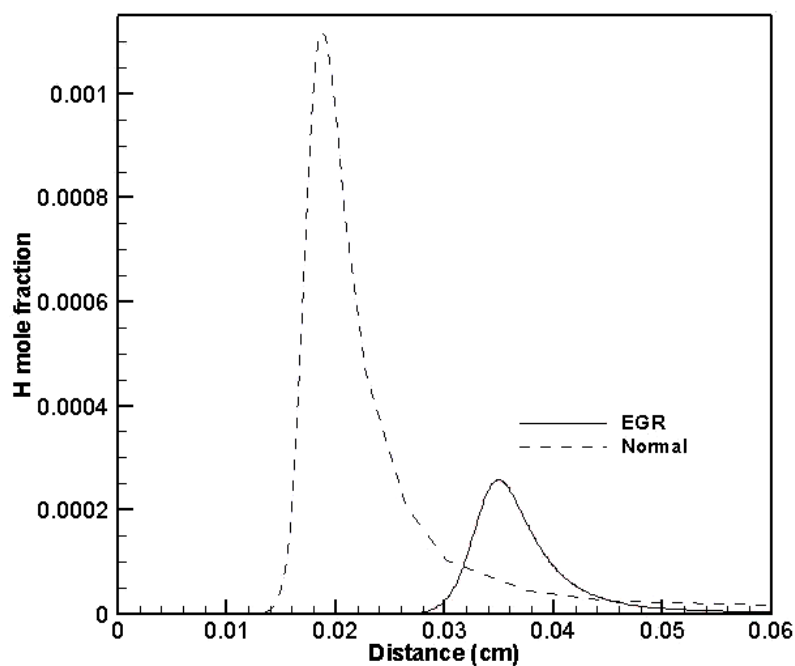


Fig. 5-50: H mole fraction profiles for EGR and normal flames. $P = 8$ atm, $T = 598$ K, $\phi = 0.7$, $\Psi = 0.7$, reaction mechanism - GRI Mech 3.0.

5.4.7 NO and NO₂ mole fraction

Figures 5-51 and 5-52 show the NO mole fraction profiles for EGR and normal flames. EGR causes a reduction in the flame temperature (Fig 5-44) and this leads to a reduction in thermal NO.

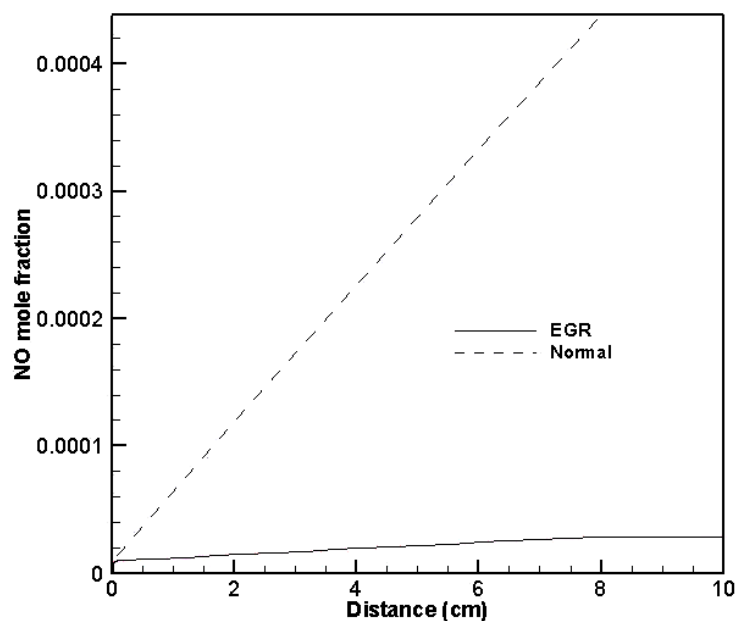


Fig. 5-51: NO mole fraction profiles for EGR and normal flames. $P = 8$ atm, $T = 598$ K, $\phi = 0.7$, $\Psi = 0.7$, reaction mechanism - GRI Mech 3.0.

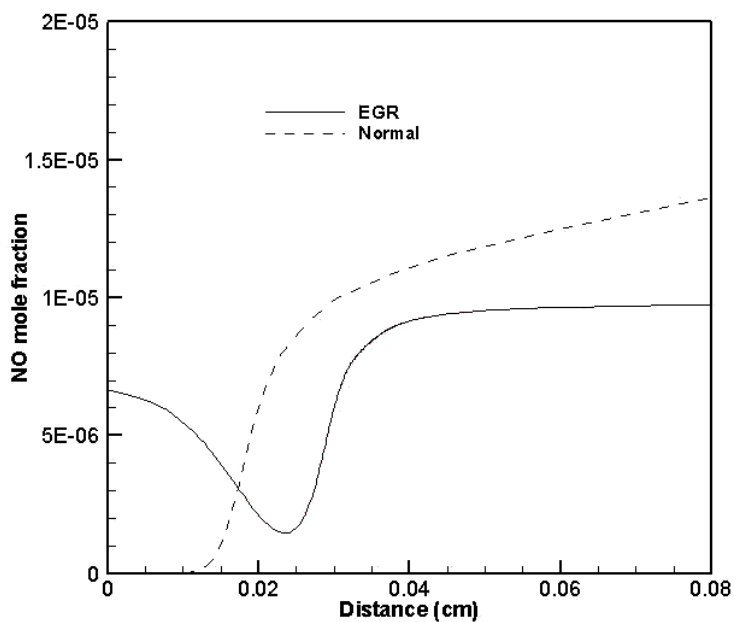


Fig. 5-52: NO mole fraction profiles for EGR and normal flames for the reaction zone. $P = 8$ atm, $T = 598$ K, $\phi = 0.7$, $\Psi = 0.7$, reaction mechanism - GRI Mech 3.0.

Fig 5-52 shows the NO concentration in the reaction zone. NO concentration for the EGR flame is higher initially, as some NO is present in the reactants through the EGR. However, there is a sudden reduction in the NO mole fraction for the EGR flame, due to the oxidation of NO to NO_2 . This causes an increase in the NO_2 mole fraction as shown in Fig 5-53.

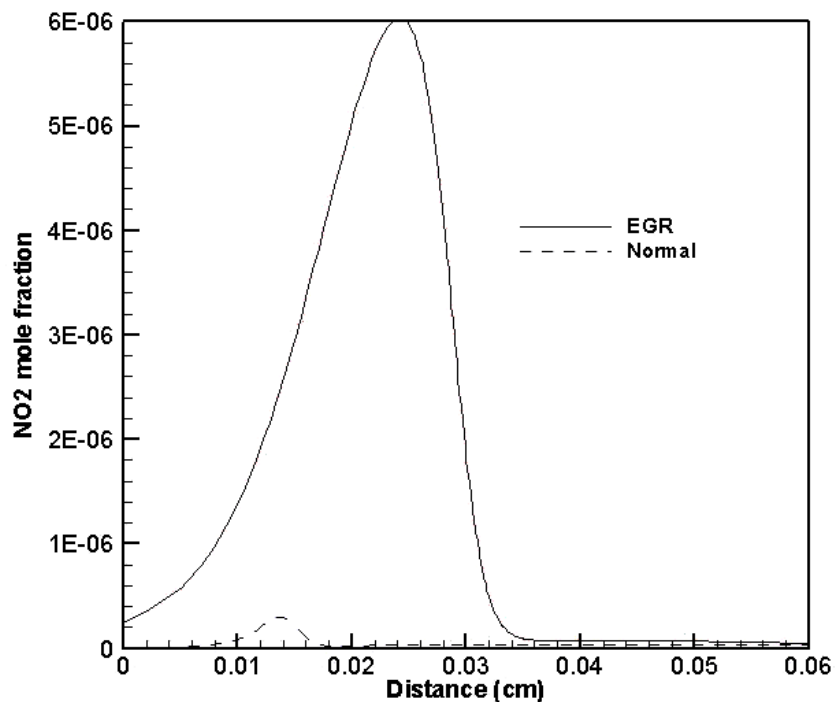


Fig. 5-53: NO₂ mole fraction profiles for EGR and normal flames for the reaction zone. $P = 8$ atm, $T = 598$ K, $\phi = 0.7$, $\Psi = 0.7$, reaction mechanism - GRI Mech 3.0.

Fig 5-54 shows the NO₂ mole-fraction profiles comparison for EGR and normal flames over the entire flame. The final NO₂ mole fraction is lower for the EGR flame. As discussed in Section 5.1.4, production of NO₂ is through oxidation of NO. Hence, the reduction in NO mole fraction (Fig 5-51) causes a reduction in NO₂ mole fraction.

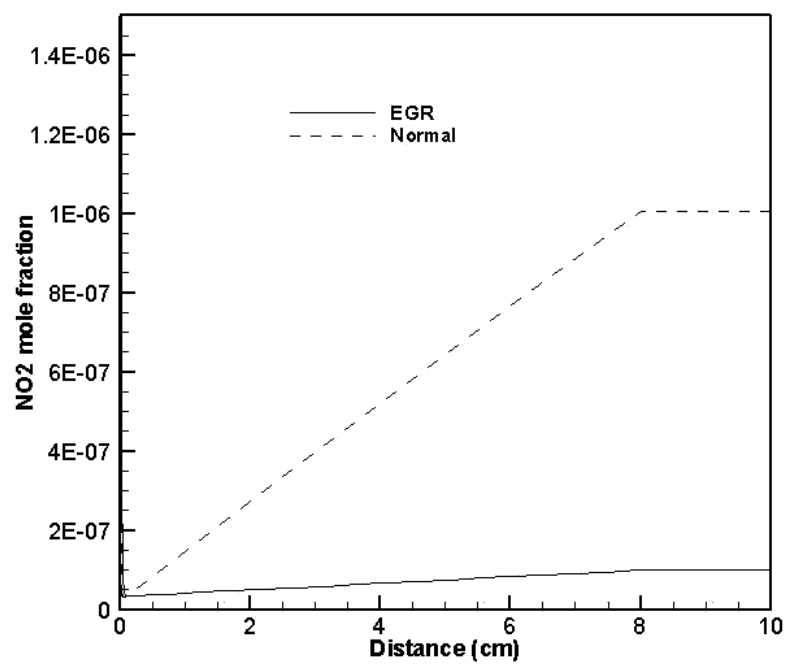


Fig. 5-54: NO₂ mole fraction profiles for EGR and normal flames. $P = 8$ atm, $T = 598$ K, $\phi = 0.7$, $\Psi = 0.7$, reaction mechanism - GRI Mech 3.0.

Chapter 6

Conclusions and Future Work

6.1 Conclusions

In this work, CHEMKIN and PREMIX have been used to study one - dimensional, premixed, laminar and steady - state flames under IC - engine conditions ($P = 8 \text{ atm}$ and $T = 598 \text{ K}$). The basic aim of the study has been to understand the behavior of flames with varying levels of H_2 in H_2/CH_4 fuel mixtures. For this study the energy content of the fuel mixture has been kept constant to ensure a fair comparison for IC - engine applications and to clearly separate the thermal effects from kinetic and transport effects.

Three basic studies have been performed. In the first, laminar flame structures from four different reaction mechanisms have been compared. The reaction mechanisms considered are Glarborg, GRI Mech 2.11, GRI Mech 3.0 and ARM. The peak temperature remains the same for all the four mechanisms but the reaction zone occurs earliest for Glarborg mechanism and latest for GRI Mech 3.0. GRI Mech 2.11 and ARM have reaction zones at intermediate locations. Similarly, the consumption of CH_4 and H_2 and the formation of intermediate species occur earliest for the Glarborg mechanism and latest for GRI Mech 3.0 with ARM and GRI Mech 2.11 in between. NO formation is similar for the four reaction mechanisms while NO_2 formation is highest with GRI Mech 3.0. NO_2 formation is lowest with the Glarborg mechanism and is intermediate for GRI Mech 2.11. ARM does not incorporate NO_2 chemistry.

In the second study, the fraction of H₂ in H₂/CH₄ fuel blends (Ψ) has been varied while keeping the energy content and equivalence ratio (ϕ) constant. It has been observed that for higher Ψ , the reaction zone occurs earlier. So, under higher concentration of H₂ in the fuel mixture there is an increased rate for the consumption of CH₄. Thus key intermediate species form earlier for higher Ψ , and CH₄ consuming reactions [5-1] and [5-2] have an increased rate and occur earlier for higher Ψ . It has been found that in addition to the reaction [5-2] that has been proposed by Collier et al. (2005) as the rate - controlling reaction in the consumption of CH₄, reaction [5-1] becomes rate - controlling for higher Ψ . While the ratio of several different reactions contributing to the production and consumption of NO increase with increasing Ψ , the increased rate for consumption reaction [5-9] dominates resulting in a net decrease in the mole fraction of NO with increasing Ψ .

The third study focused on the high molecular diffusivity of hydrogen. For this study two schemes were adopted. In the first scheme the diffusion coefficient of H₂ was set equal to the diffusion coefficient of CH₄. In the second scheme the Lewis numbers were set to unity for all the species in the reaction mixture. No significant changes in the flame structure were observed when the diffusion coefficients of the species were changed according to the two schemes. However, the conclusions are expected to be different for unsteady and/or multidimensional flames.

In the fourth study, the impact of exhaust - gas recirculation was investigated. Here 20% of the intake mixture was considered to be the products of combustion. EGR changed the flame structure and reduced the peak temperature. The consumption rates of CH₄ and H₂ were reduced with EGR and the concentrations of intermediate species OH,

CH_3 and O were reduced and there was a delayed occurrence of their peaks. NO_x formation was also reduced with EGR. NO formation reduced as a result of the lower temperature. NO_2 mole fractions initially were higher in the reaction zone due to the oxidation of NO in the reactants with EGR, but final NO_2 values were lower with EGR.

6.2 Future Work

The present work focused on laminar, one - dimensional, premixed, steady - state flames under IC - engine conditions. However, IC engine flames are turbulent, multi dimensional and unsteady. Future work should move towards unsteady and/or multidimensional premixed flames. Eventually, the outcomes of these fundamental flame studies must be distilled into models that can be applied to multidimensional CFD for realistic engine configurations. There it will not be feasible to account explicitly for detailed chemical kinetics and molecular transport.

References

- Adt, R. R. and M. R. Swain (1974). The hydrogen/methanol–air breathing automobile engine. *The Hydrogen Economy Miami Energy Conference*, p.S10-38–48.
- Akansu, S.O., Z. Dulger, N. Kahraman and T. N. Veziroglu (2004). Internal combustion engines fueled by natural gas – hydrogen mixtures. *International Journal of Hydrogen Energy*, 29: 1527 – 1539.
- Andrea, T. D., P. F. Henshaw and D. S. K. Ting (2004). The addition of hydrogen to a gasoline fuelled SI engine. *International Journal of Hydrogen Energy*, 29:1541-1552.
- Aslan, E., M. Ergeneman and C. Sorusbay (1991). Use of hydrogen in internal combustion engine as fuel. PhD Thesis. Istanbul Technical University, Istanbul.
- Bailey, P. S. (1980). Assessment of potential future markets for the production of hydrogen from water in Canada. International Energy Agency Report, 1980.
- Basye L and S. Swaminathan (1997). Hydrogen production costs - a survey. Sentech, Inc., Report, DOE/GD/10170/778, US,1997.
- Bowman, C. T., R. K. Hanson, D. F. Davidson, W. C. Gardiner, Jr., V. Lissianski, G.P. Smith, D.M. Golden, M. Frenklach and M. Goldenberg in http://www.me.berkeley.edu/gri_mech/.
- California Air Resource Board (CARB) (1995). Proposed equivalent zero emission vehicle standards. *IEEE Spectrum*, page 72, September 1995.
- Cattelan, A. and J. Wallace (1995). Exhaust emission and energy consumption effects from hydrogen supplementation of natural gas. *SAE Paper No. 952497*.
- Chen, J. Y. (1987). A general procedure for constructing reduced reaction mechanisms with given independent reactions. *Sandia National Laboratories Report SAND87-8782*.
- Collier, K., R. L. Hoekstra, N. Mulligan, C. Jones and D. Hahn (1996). Untreated exhaust emissions of a hydrogen-enriched CNG production engine conversion. *SAE Paper No. 960858*.
- Collier, K., N. Mulligan, S. Dongsung and S. Brandon (2005). Emission results from the new development of a dedicated hydrogen – enriched natural gas heavy duty engine, *SAE Paper No. 2005-01-0235*.

- Glarborg, P., M. U. Alzueta, K. Johansen and J. A. Miller (1998). Kinetic modeling of hydrocarbon/ nitric oxide interactions in a flow reactor. *Combustion and Flame*, 115:1-27.
- Glassman, I. (1996). *Combustion*, Academic Press, San Diego.
- Gregory, P. S., D. M. Golden, M. Frenklach, N. W. Moriarty, B. Eiteneer, M. Goldenberg, C. T. Bowman, R. K. Hanson, S. Song, W. C. Gardiner, V. V. Lissianski, and Z. Qin. (2003). **GRI-Mech 3.0**. Available at http://www.me.berkeley.edu/gri_mech/
- Herrmann, K. and K. Boulouchos (2005). Nitric oxide detection in turbulent premixed methane/ air flames, *Proceedings of the Combustion Institute*, 30:1517 – 1525.
- Hoekstra, R. L., P. V. Blarigan and N. Mulligan (1996). NOx emissions and efficiency of hydrogen, natural gas and hydrogen/ natural gas blended fuels. *SAE Paper No. 961103*.
- Heywood, J.B (1988). *Internal Combustion Engine Fundamentals*, Mc Graw Hill Book Company, p. 409, Fig 9-28(d).
- Ivanic, Z., F. Ayala and J. B. Heywood (2005). Effects of hydrogen enhancement on efficiency and NOx emissions of lean and EGR - diluted mixtures in a SI engine. *SAE Paper No. 2005-01-0253*.
- Kee, R. J., F. M. Rupley and J. A. Miller (1989) Chemkin-II: A FORTRAN chemical kinetics package for the analysis of gas phase chemical kinetics, *Sandia National Laboratories Report SAND89-8009*.
- Kee, R. J., F. M. Rupley and J. A. Miller (1996) Chemkin-III: A FORTRAN chemical kinetics package for the analysis of gas phase chemical kinetics, *Sandia National Laboratories Report SAND96-8216*.
- Li, H. and Karim, G. A. (2004) Knock in spark ignition hydrogen engines. *International Journal of Hydrogen Energy*, 29: 859 – 865.
- NIST XSenkplot (1996): <http://www.csl.nist.gov/div836/836.03/xsenkplot/index.html>
- Pope et al. <http://www.ca.sandia.gov/TNF/chemistry.html>
- Peters, N. (1994) <http://www.itv.rwth-aachen.de/Downloadarea/DFG-Abschlussbericht/DFG-Abschlussbericht.pdf>
- Reaction Design (2004): <http://www.reactiondesign.com/lobby/open/index.html>

- Smith, G. P., Golden, D. M., Frenklach, M., Moriarty, N. W., Eiteneer, B., Goldenberg, M., Bowman, C. T., Hanson, R. K., Song, S., Gardiner, W. C., Vitali, J., Lissianski, V. and Q, Zhiwei in http://www.me.berkeley.edu/gri_mech/
- Sobiesiak, A., C. Uykur and D. S-K. Ting (2002). Hydrogen/oxygen additives influence on premixed iso - octane/air flame, *SAE Paper No. 2002-01-1710*.
- Sung, C. J., C. K. Law and J. Y. Chen (2001). Augmented reduced mechanisms for NO emission in methane oxidation. *Combust Flame*, 125:906 - 919.
- Tiashen D, L. Jingding and L. Yingqing (1985). Combustion-supporting fuel for methanol engines: hydrogen. The International Symposium on Hydrogen Systems, Beijing, China, 7–11 May, 1985. p. 105–13.
- Thompson, N. D. and J. S. Wallace (1994). Effect on engine operating variables and piston and ring parameters on crevice hydrocarbon emissions, *SAE Paper No 940480*.
- Yu, G., C. K. Law and C. K. Wu (1986). Laminar fame speeds of hydrocarbon + air mixtures with hydrogen addition. *Combust Flame*, 63:339–47.

**Appendix A-1.3: MS Thesis in Energy & Geo-Environmental Engineering
by Jamie Clark**

Jamie Clark
744 Coleman Ave
Apt L
Menlo Park, CA 94025

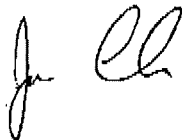
February 4, 2009

National Energy Technology Laboratory
U.S. Department of Energy
626 Cochrans Mill Road
P.O. Box 10940
Pittsburgh, PA 15236-0940

Dear U.S. Department of Energy:

I hereby grant the U.S. Department of Energy permission to use my thesis in the Final Technical Report for Award Number DE-FC26-04NT42233, "Hydrogen-Assisted IC Engine Combustion as a Route to Hydrogen Implementation." My thesis was written with support of the U.S. Department of Energy under this award and copyright for the thesis lies with me.

Sincerely,



Jamie Clark
R&D Engineer

The Pennsylvania State University
The Graduate School
The College of Earth and Mineral Science

**THE EFFECTS OF HYDROGEN ADDITION ON A SPARK-IGNITED
COMPRESSED NATURAL GAS VEHICLE**

A Thesis in
Energy and Geo-Environmental Engineering

by
Jamie Michael Clark

Submitted in Partial Fulfillment
of the Requirements
for the Degree of

Master of Science

May 2008

The thesis of Jamie Michael Clark was reviewed and approved* by the following:

André L. Boehman
Professor of Fuel Science and Materials Science and Engineering
Thesis Advisor

Sarma V. Pisupati
Associate Professor Energy and Mineral Engineering

Joel R. Anstrom
Research Associate, Pennsylvania Transportation Institute

Yaw D. Yeboah
Professor of Energy and Mineral Engineering
Head of the Department of Energy and Mineral Engineering

*Signatures are on file in the Graduate School

ABSTRACT

The “Freedom Car” Initiative enacted by the Bush Administration has placed significant emphasis on the development of a hydrogen economy in the United States. While hydrogen fuel-cell vehicles have been the focus of recent media attention, near term implementation of hydrogen as a combustion enhancer is a more reliable pathway for wide-scale hydrogen utilization within the next ten years. Through combustion analysis, hydrogen addition to natural gas has shown to increase thermal efficiency and reduce CO, NO and hydrocarbon emissions (UHC) in studies on stationary test cell engines. On-road vehicle studies testing hydrogen-natural gas blends show emissions benefits and increase in fuel economy. However, on-road tests lack exhaustive combustion analysis to explain what is occurring in the cylinder. In this study, the effect of a 33 percent volumetric blend of hydrogen (HCNG) on natural gas combustion was investigated in a 5.4L spark-ignited engine in a Ford E-250 van. In-cylinder combustion analyses were performed and untreated exhaust emissions were measured at 15 and 30 mph with road loads of 10, 20 and 30 horsepower. Hydrogen increased the flame speed reducing time for flame kernel development and combustion duration. However, the hotter burn lost more heat to the surroundings and thermal efficiency of HCNG was lower than natural gas. Increasing engine speeds magnified reduction in combustion duration created by hydrogen. As load on the engine increased, hydrogen-influenced reduction on burn time was reduced. Heat and throttling losses reduced the thermal efficiency of the combustion. More complete combustion with hydrogen reduced carbon-based emissions and bulk cylinder temperature increase drove increased NO formation.

TABLE OF CONTENTS

LIST OF FIGURES.....	vii
LIST OF TABLES.....	ix
ACKNOWLEDGEMENTS.....	x
Chapter 1 Introduction	1
1.1 Motivation.....	1
1.2 Objectives of Research	3
1.3 Summary of Tasks	4
Chapter 2 Literature Review and Background.....	5
2.1 Outline	5
2.2.1 Hydrogen Production.....	7
2.3 Fundamentals of Combustion in Spark-ignited Engines	8
2.3.1 Spark-Ignited Stoichiometric Combustion of Hydrocarbons	9
2.3.2 Flame Kernel Development.....	10
2.3.3 Combustion Kinetics	11
2.3.4 Methane Oxidation Kinetics	11
2.3.5 Hydrogen Oxidation Kinetics	12
2.4 Measuring Combustion Performance	13
2.4.1 Mass Fraction Burned.....	13
2.4.2 Ignition Delay	15
2.4.3 Combustion Duration	15
2.5 Hydrogen Benefits to Combustion	16
2.5.1 Increased Cycle Efficiency	16
2.5.2 Increased Flame Speed	17
2.5.3 Rate-Limiting Factors.....	18
2.5.4 Experimental Research on HCNG flames	20
2.5.5 Spark Timing Adjustments for Optimization	21
2.6 Emissions	22
2.6.1 Oxides of Nitrogen	22
2.6.2 CO Formation	23
2.6.3 Unburned Hydrocarbons	23
2.7 HCNG in Test Cell Engines	24
2.7.1 Part Load Condition HCNG	24
2.7.2 Swirl Addition to HCNG.....	26
2.7.3 Hydrogen-Natural Gas Studies	26
2.7.4 Emissions Testing.....	27
2.8 Hydrogen Addition in On-Road Performance	28
2.8.1 Vehicle Operating Conditions	29

2.8.2 Pressure Sensors in Vehicles	30
2.8.3 Vehicle Loads	31
2.8.4 HCNG Vehicle Literature.....	32
Chapter 3 Experimental Set-up	34
3.1 Outline	34
3.2 Test Engine and Fueling	34
3.3 Engine Instrumentation and Data Acquisition System	36
3.4 Fuel Analysis	39
3.5 Semtech-DS Emissions Equipment	40
3.6 Testing Procedure	41
3.7 Heat Release Analysis	42
3.8 Calculating Air-Fuel Ratio	47
3.9 Test Plan	48
Chapter 4 Results and Discussion.....	50
4.1 Introduction.....	50
4.2 Engine and Fuel Conditions.....	50
4.2.1 Air-Fuel Ratio.....	51
4.2.2 Spark Advance.....	52
4.3 Characteristics of Hydrogen Combustion.....	54
4.3.1 Pressure.....	54
4.3.2 Apparent Heat Release	56
4.3.2 Fuel Burning Rates	58
4.3.3 Calculated In-Cylinder Temperature	61
4.3.4 Heat Transfer	63
4.3.4 Coefficient of Variance	66
4.4 Combustion Trends.....	67
4.4.1 Combustion Duration	67
4.4.2 Flame Development Angle	70
4.4.3 Indicated Thermal Efficiency	72
4.5 Emissions Results	73
4.5.1 Carbon Dioxide	73
4.5.2 Carbon Monoxide Emissions	74
4.5.3 Oxides of Nitrogen	75
4.6 Vehicle Speed	76
Chapter 5 Conclusions and Future Work.....	78
5.1 Conclusions.....	78
5.2 Future Work.....	79

Bibliography	80
Appendix A Fuel Properties.....	83
A.1 Natural Gas Composition.....	83
A.2 Hydrogen-Natural Gas Composition	83
A.3 Calculated Fuel Characteristics	84
Appendix B Matlab Heat Release Code	85
B.1 Matlab Code programmed in version 2007b.....	85

LIST OF FIGURES

Figure 2-1: Pathways to Hydrogen Production [7]	7
Figure 2-2: Normalized Heat Release and Mass fraction burned [13]	14
Figure 2-3: Ideal cycle efficiency as a function of gamma and compression ratio[15]	17
Figure 2-5: OH Signal Intensity in Natural Gas and 20 Percent HCNG[20].....	21
Figure 3-1: Crankshaft Pulley Adapter to Crank Angle Encoder	37
Figure 3-2: Pressure Transducer Set-Up.....	38
Figure 3-3: 200 Cycle Averaged Cylinder Pressure Trace	45
Figure 3-4: Instantaneous Heat Release Rate	46
Figure 4-1: Air-Fuel Ratio for HCNG testing.....	51
Figure 4-2: Air-Fuel Ratio for CNG testing	52
Figure 4-3: 200 Cycle Averaged Pressure Trace, 1350 RPM, 10 horsepower road load	55
Figure 4-4: 200 Cycle Averaged Pressure Trace, 1370 RPM, 30 horsepower road load	56
Figure 4-5: Heat Release Rate 1350 RPM, 10 horsepower Road Load.....	57
Figure 4-6: Heat Release Rate 1370 RPM, 30 horsepower Road Load.....	58
Figure 4-7: Normalized Heat Release 1350 RPM, 30 hp Road Load.....	59
Figure 4-8: Normalized Heat Release 1370 RPM, 30 hp Road Load.....	60
Figure 4-9: Peak Heat Release Rate at 1350, 1360 and 1370 RPM, 30 mph	61
Figure 4-10: Bulk Cylinder Temperature 1350 RPM, 10 hp Road Load	62
Figure 4-11: Bulk Cylinder Temperature 1370 RPM, 30 hp Road Load	63
Figure 4-12: Net Heat Release and Heat Transfer 1350 RPM, 10 hp Road Load	65
Figure 4-13: Net Heat Release and Heat Transfer 1370 RPM, 30 hp Road Load	66

Figure 4-14: Combustion Duration at 1350, 1360 and 1370 RPM.....	69
Figure 4-15: Combustion Duration at 3700, 3750, 3800 RPM.....	69
Figure 4-16: Flame Development Angle at 1350, 1360 and 1370 RPM	71
Figure 4-17: Flame Development Angle at 3700, 3750, 3800 RPM	71
Figure 4-18: Indicated Thermal Efficiency at 1350, 1360 and 1370 RPM	73
Figure 4-19: CO ₂ at 1350, 1360 and 1370 RPM.....	74
Figure 4-20: CO at 1350, 1360 and 1370 RPM.....	75
Figure 4-21: NO at 1350, 1360 and 1370 RPM.....	76

LIST OF TABLES

Table 2-1: Hydrogen and Methane Fuel Properties [1]	6
Table 3-1: Test Engine Specifications	35
Table 3-2: Summary of Exhaust Species and Measuring Techniques.....	41
Table 3-3: Test Matrix	49
Table 4-1: Spark Advance Timings	53
Table 4-2: Road Load at Low Speed Test Settings.....	77
Table A-1: Natural Gas Composition	83
Table A-2: HCNG Composition	83
Table A-3: Calculated Fuel Characteristics	84

ACKNOWLEDGEMENTS

I would like to thank my thesis adviser, Dr. André Boehman, for offering me the opportunity to join his group. I greatly appreciated his support, guidance and patience throughout the process of this study. I would also like to thank my committee members, Dr Anstrom, Dr. Pisupati and Dr. Yeboah, for reviewing my thesis.

I would like to give special thanks to Vince Zello for his technical help on the engine instrumentation. Without his assistance my data would never have been collected or been correct. Dr. Joel Anstrom, Sam Entz, and the mechanics of the PTI garage have given me great support in vehicle technology. Thanks to Jim Flanagan for letting me use his work vehicle. Also, Semtech-DS deserves thanks for performing an emissions measurement demonstration and giving me the emissions results.

I would like to thank Yu Zhang, Dr. Octavio Armas, and Dr. Thomas Litzinger for their support in troubleshooting heat release calculations. I would also like to thank Dr. Kirk Collier for his support in understanding the control of and changes to the van. Thanks also to Jeff Saxton for his help in signal processing. I'm grateful for Jim Szybist and Peter Perez for building the foundation of the LabVIEW heat release program. I am also grateful for everyone else not mentioned from the Diesel Combustion and Emissions Lab at the Energy Institute for their help and collaboration.

I am also grateful for the Government Automotive Transportation Education program for providing me financial support through my entire graduate school education.

Finally I would like to thank my wife and parents for their continued support for me and my life aspirations.

Chapter 1

Introduction

1.1 Motivation

Over the past decades natural gas has become a popular alternative fuel for the growing transportation sector. Light-duty vehicles running on natural gas represent a maturing technology, while natural gas heavy-duty transit vehicles are popular in urban areas. As a fuel source for large scale for transportation needs, natural gas provides advantages in automotive technology because of its emissions benefits in comparison with diesel and gasoline engines. The chemical structure of the fuel is advantageous as the carbon-hydrogen bonds in methane reduce carbon dioxide emissions per unit of energy compared diesel and gasoline.

However, there are several drawbacks with natural gas engines, particularly in efficiency and emissions as engines must meet increasingly stringent U.S. government-mandated requirements. Among hydrocarbons, methane, the main component in natural gas, has the slowest flame speed [1]. This reduces thermal efficiency by increasing energy losses due to heat transfer. Because of less efficient burning, significant amounts of methane remain in the exhaust after a combustion cycle is completed. The unburned methane expelled to the atmosphere can negate the fuels reduction in carbon dioxide emissions because it has 21 times the global warming potential [2] of carbon dioxide. Another issue in natural gas engines is maintaining proper engine control with varying

fuel composition. Hydrocarbon content in natural gas can vary, with the volumetric content of methane ranging from 70 to 96 percent. The Electronic Control Unit (ECU) adjusts the intake composition and spark timing based on an incorrect assumption of fuel energy, creating combustion conditions that reduce engine efficiency.

Other conditions which the natural gas vehicle industry must deal with include fuel storage, distribution, and safety issues. Fuel storage tanks require aggressive safety features such as stainless steel or carbon fiber tanks, which increase vehicle weight. Lack of appropriate gaseous fuel infrastructure prevents effective distribution to the entire population. Safety considerations sway public opinion which slows steps in research and development of this technology [3].

Despite these drawbacks and hindrances, some advances are being made in advocating the development of natural gas and alternative fuels. The “FreedomCAR (Cooperative Automotive Research)” initiative enacted in January 2002, as well as the Hydrogen Fuel Initiative announced by the Bush Administration in January 2003, places a significant emphasis on the development of the hydrogen economy (developing fuel cells and designing the necessary infrastructure for producing, storing, and distributing hydrogen) in the United States. While current technology and infrastructure does not lend itself to a commercial hydrogen economy, “hydrogen-assisted” combustion is a more realizable pathway for large-scale hydrogen utilization in the near future.

Despite the large amount of resources currently being devoted to hydrogen technology research, near-term implementation of hydrogen in the transportation sector is not yet a reality. To further research in this area and as part of The Pennsylvania State University’s initiative towards a hydrogen economy, a partnership between the

university, Air Products, and Collier Technologies has resulted in the creation of hydrogen and hydrogen-compressed natural gas vehicles and a fueling station for use in university transportation and for research needs.

The potential of hydrogen to increase indicated thermal efficiency and reduce emissions in natural gas combustion has been investigated for several reasons. First, natural gas and hydrogen blend uniformly because they are both in a gaseous state at standard temperature and pressure. Hydrogen has a higher stoichiometric laminar flame speed in air than methane. Literature states [4] that an increase in laminar flame speed has been shown to reduce the flame initiation stage of combustion. This effect is even more pronounced at light-load conditions, where combustion duration is the longest. Another advantage of hydrogen is that it increases the stability of combustion at leaner burn mixtures, a characteristic that has been extensively researched in natural gas combustion. Finally, hydrogen and methane mixtures have been shown to slightly reduce pumping losses in the engine increasing the [5].

1.2 Objectives of Research

The objective of this research is to determine the in-cylinder combustion performance of natural gas and a hydrogen-natural gas blend in a vehicle equipped to operate using either fuel. The plan calls for the research vehicle to be run at a set vehicle speed and varying load conditions. The resulting combustion performance is measured to determine the effect of hydrogen on natural gas combustion. Hydrogen addition has been shown to have a positive effect on combustion and emissions in the literature, and

correlations will be drawn that evaluate if these hold true in the data obtained in this study. The hypothesis of this research is that, like in test cell engine research, hydrogen will decrease the combustion duration, increasing the indicated thermal efficiency of the engine, while reducing carbon monoxide and unburned hydrocarbons emissions. Increased gas temperatures will increase NO output.

1.3 Summary of Tasks

Due to the compactness of the efficient modern day vehicle, data acquisition instrumentation hardware had to be built around tightly packaged engine components. Hardware to measure in-cylinder pressure and crank angle position were purchased, designed, fabricated, and mounted onto the vehicle. The vehicle itself was mounted on a chassis dynamometer and run at set speeds and loads using compressed natural gas (CNG) and a 33 percent blend of hydrogen with compressed natural gas (HCNG). A data acquisition program was written in LabVIEW to record real-time cylinder pressures, while emissions data were simultaneously recorded using Sensors Inc.'s Semtech-DS emissions analyzer. Using a heat release calculation program written in Matlab, the combustion and emissions data were analyzed to determine combustion performance across all test points.

Chapter 2

Literature Review and Background

2.1 Outline

To gain insight into how hydrogen affects natural gas combustion in an internal combustion engine, it is essential to have a clear understanding of the fuel structure and properties of methane and hydrogen, as well as of spark-ignition combustion principles, differences in kinetic interactions, and vehicle loading. In this chapter, a description of the chemical structure and properties of methane and hydrogen is given, followed by an overview of the spark-ignited engine combustion process, combustion propagation mechanisms, and the quantitative ways in which combustion is measured. Finally, previous research on hydrogen's effect on natural gas combustion in engines and vehicles is reviewed.

2.2 Chemical Structure and Properties of Methane and Hydrogen Fuels

Natural gas is a light hydrocarbon composed of methane (CH_4) and from 0 to 20 percent of ethane (C_2H_6) and propane (C_3H_8). Nitrogen, helium, and carbon dioxide are also found in trace amounts. Natural gas has the highest ignition temperature of any commonly used hydrocarbon fuel, and is the slowest burning as well [6].

While engine manufacturers have produced engines that run on compressed natural gas (CNG), a more recent development is conversion of engines to operate on a

hydrogen-natural gas blend fuel, which is commonly known as hydrogen enriched compressed natural gas, or HCNG. By displacing some natural gas with hydrogen, scientists and engineers have been attempting to improve combustion performance and extend the lean-burn limit of methane, by blending 1 to 30 volume percent hydrogen in natural gas. This process has generated enough interest that one company, Hythane Company LLC, has patented a 20 volume percent blend of hydrogen with natural gas labeled “Hythane”.

Hydrogen addition has been shown to increase thermal efficiency and reduce carbon monoxide and unburned hydrocarbons by increasing the combustion quality of natural gas [5]. Table 2-1 compares the fuel characteristics of hydrogen and methane:

Table 2-1: Hydrogen and Methane Fuel Properties [1]

	Hydrogen (H ₂)	Methane (CH ₄)
Equivalence Ratio ignition lower limit	0.10	0.53
Mass Lower Heating Value	119,930	50,020
Density of gas at STP (kg/m ³)	0.083764	0.65119
Volumetric Lower heating Value at STP (kJ/m ³)	10,046	32,573
Stoichiometric Air/Fuel Ratio	34.20	17.19
Volumetric Lower Heating Value in air at stoichiometric conditions (kJ/m ³)	2913	3088
Hydrogen to Carbon Ratio	0.00	0.25

Because of hydrogen’s highly reactive nature, it burns faster and more completely than methane. While this property makes hydrogen a prime candidate for increasing overall efficiency and reducing emissions, hydrogen is also less dense. Its displacement of natural gas in the fuel reduces the in-cylinder energy content, reducing power in a

volumetrically equivalent charge of natural gas. The very low volumetric energy density of hydrogen is one of hydrogen's major drawbacks.

2.2.1 Hydrogen Production

Hydrogen is a common element found in many naturally occurring substances, yet diatomic hydrogen (H_2) is not found naturally on earth. Hydrocarbon fuels (C_xH_y) and water (H_2O) are the primary sources for hydrogen production. Through a variety of energy intensive processes, primary energy sources such as coal, petroleum, and natural gas are refined into synthesis gas, as shown as in Eq. 2-1, to produce hydrogen. Another method used to produce pure hydrogen is to pass electric current through water to separate its hydrogen and oxygen atoms. Hydrogen offers an advantage over fossil fuels because there are multiple pathways for hydrogen production.

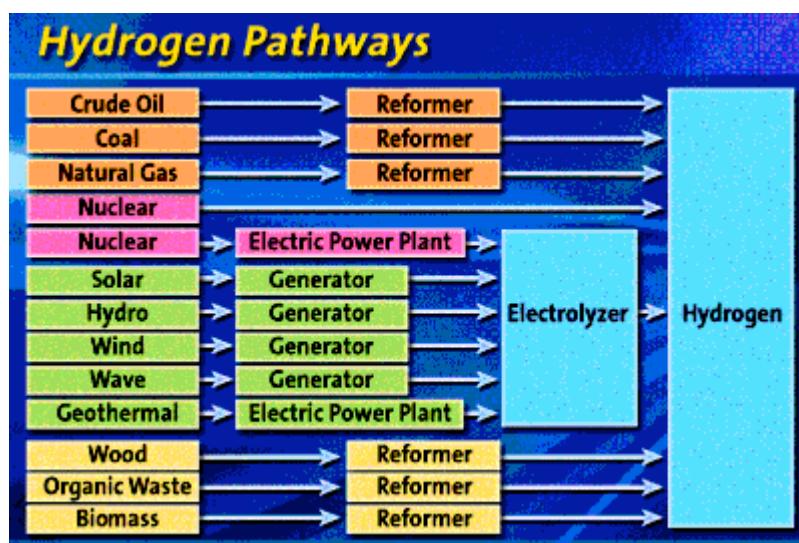
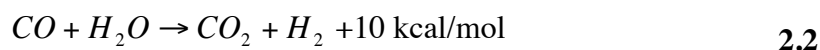
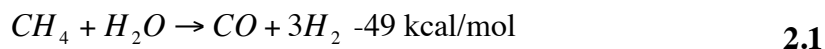


Figure 2-1: Pathways to Hydrogen Production [7]

The most mature technology used to produce hydrogen is steam reforming of natural gas. Steam methane reforming (SMR) involves passing steam and natural gas over a nickel catalyst at temperatures above 500°C. The two reversible reactions responsible for hydrogen production are as follows.



During the process, steam is added in excess of the stoichiometric requirement so that Eq. 2.2 will shift right to form hydrogen and carbon dioxide [8]. The Pennsylvania State University uses a variant of this hydrogen-production strategy. This advanced steam methane reformer is the most cost-effective hydrogen producer for small-scale applications.

A pressure swing absorption (PSA) unit purifies the resulting gas to 99.99 percent pure hydrogen, which is compressed and stored [9]. The purified hydrogen is then recombined with unrefined natural gas to produce HCNG. In comparison to the price of pure natural gas, the cost of 80/20 and 90/10 blends of natural gas and hydrogen is 8 percent and 15 percent greater, respectively[10].

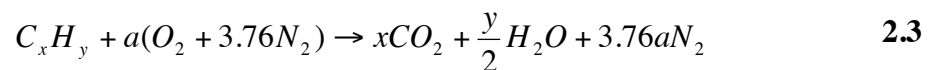
2.3 Fundamentals of Combustion in Spark-ignited Engines

In order to better understand the role that hydrogen plays in combustion, it is necessary to review the fundamentals of combustion in spark-ignited engines. In general, the natural gas spark-ignited engine combustion process can be summarized as follows.

At a suitable time during the intake stroke, gaseous fuel is introduced at a high pressure into the engine cylinder by the fuel injection system through small orifices. The fuel then mixes with throttled air coming in through the intake manifold. A few crank angle degrees of rotation before the piston reaches the top dead center (TDC) position, the air-fuel mixture ignites when the spark plug initiates combustion in the cylinder, causing the cylinder pressure and temperature to increase rapidly. As the piston moves further into the expansion stroke, the cylinder pressure and temperature begin to decrease. The combustion reactions are quenched as the cylinder temperature drops during the expansion stroke. Details of the spark-ignited engine combustion process are introduced in the following sections.

2.3.1 Spark-Ignited Stoichiometric Combustion of Hydrocarbons

Combustion is a rapid chemical reaction between radicals that converts chemical energy in the fuel to thermal energy via oxidation [6]. Assuming that only major products are formed, hydrocarbon fuels combust following the basic formula under stoichiometric conditions.



The stoichiometric air-fuel ratio can be found by taking the ratio of the mass of air to fuel using Eq. 2.4 with Eq. 2.3.

$$(A/F)_{stoich} = \frac{4.76a}{1} \frac{MW_{air}}{MW_{fuel}} \quad 2.4$$

When the mass of fuel and air is adjusted, the mixture can be considered fuel lean or fuel rich, and the change is indicated by the equivalence ratio. The equivalence ratio is the ratio between the stoichiometric air-fuel ratio and the actual air-fuel ratio.

$$\Phi = \frac{(A/F)_{stoich}}{(A/F)_{actual}} \quad 2.5$$

2.3.2 Flame Kernel Development

Before combustion can take place, a source of energy must first be introduced. In a spark-ignited engine, a spark plug initiates combustion, which develops the initial flame kernel. The energy input is enough to sustain a propagating flame, which in the first few crank angle degrees exhibits characteristics of a laminar flame. This smooth, spherical flame, which contains only minor irregularities, surrounds the spark plug gap.

Because of the smooth shape of the flame, the flame kernel development is highly sensitive to variations in laminar flame speed and mixture composition. Reduction in the flame speed causes heat to be lost by conduction to the surroundings, which leads to cooler flame temperatures. With lower flame temperatures, the flame kernel development process approaches the point of extinction and increased formaldehyde formation [11].

As the flame grows, it interacts with the turbulent flow field near the spark plug. Because of distinct, uncontrollable variations in the turbulence, the flame rarely propagates the same way in each cycle, causing cycle-to-cycle variation. Repetitive variation in the cylinder can lead to early flame quenching and reduced combustion performance. Once the flame kernel has developed into a turbulent flame, the most

significant parameter controlling the remaining flame propagation is the turbulent-kinetic energy in the cylinder [12].

2.3.3 Combustion Kinetics

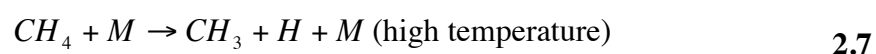
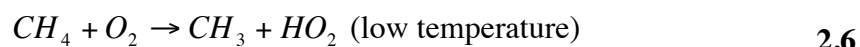
Combustion is governed by radical intermediates when reacted with air. Radicals require high temperature to form. These temperatures are maintained during the reaction by heat produced by combustion. Radicals initiate a chain reaction, propagating the radical formation throughout the system. The first step in the combustion reaction is the chain-initiating step in which two stable molecules collide to form a stable molecule and two radicals. Next, chain propagating and branching steps involve the collision between a radical and stable molecules resulting in the formation of one or two radicals. Combustion is terminated when the radical pool is depleted by interactions of the radicals with the wall or through recombination. The next sections will explore the kinetics involved in methane and hydrogen combustion, to get an idea of why hydrogen benefits combustion on a molecular level.

2.3.4 Methane Oxidation Kinetics

In HCNG combustion, the two primary types of oxidation reactions involve methane and hydrogen. This section will explore the theories behind the changes in oxidation process.

The first step in the combustion of methane and air is the cleavage of a carbon-hydrogen bond, resulting in the creation of a hydrogen radical and a hydrocarbon radical.

The carbon-hydrogen bond in methane has approximately 40 kilojoules more energy than the same bond in long-chain hydrocarbons, leading to difficulty in methane-air ignition. More energy is required to break the first bond in the molecule, to initiate the reaction. The chain initiation reactions for combustion, shown below, are classified as either low-temperature or high-temperature reactions [6].

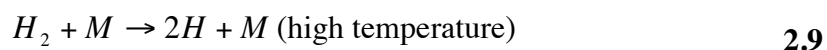


2.3.5 Hydrogen Oxidation Kinetics

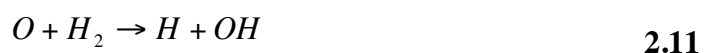
In the hydrogen-oxygen reaction system, the dissociation energy of hydrogen is lower than that of oxygen. In hydrogen oxidation, early forming H radicals advance combustion in the early stages of the burn. The literature [6] suggests that the chain-initiating step for hydrogen combustion, is the following:



It is argued that because of its high energy requirement, 435 kJ/mol, hydrogen will react only at high temperatures during a collision with another molecule, as in Eq. 2.9.



The pool of O, H, and OH radicals builds quickly through a series of chain reactions:



These chain-branching reactions have very low activation energy, which advances combustion rapidly at lower temperatures.

2.4 Measuring Combustion Performance

Combustion statistics can be computed from the in-cylinder pressure measurements. Such statistics are useful in comparing combustion performance regardless of engine size, conditions, or as in the subject of this study, fuel.

Measured cylinder pressure in an internal combustion engine is a function of cylinder volume change, combustion, heat transfer to the cylinder walls, flow in and out of crevice regions, and flow past the piston rings. Pressure measurements are used to determine the approximate heat released in the cylinder during the four-stroke cycle. These data allow trends in the combustion process to be determined.

This section will describe the approach used to analyze the cylinder pressure and its use in determining the speed at which combustion occurs in the cylinder.

2.4.1 Mass Fraction Burned

Using pressure trace analysis to determine the fraction of the fuel burned in the cylinder as a function of crank angle allows for the characterization of the various stages of the combustion process and to compare rates of oxidation [11]. While a popular method to determine mass fraction burned is to use the Weibe function, it is also possible to approximate the fraction of fuel burned by using the normalized values of cumulative heat release. It must be taken into account that normalized heat release at stoichiometric

or rich conditions begins to deviate from the actual mass fraction burned, as shown in the modeled data in Figure 2-2.

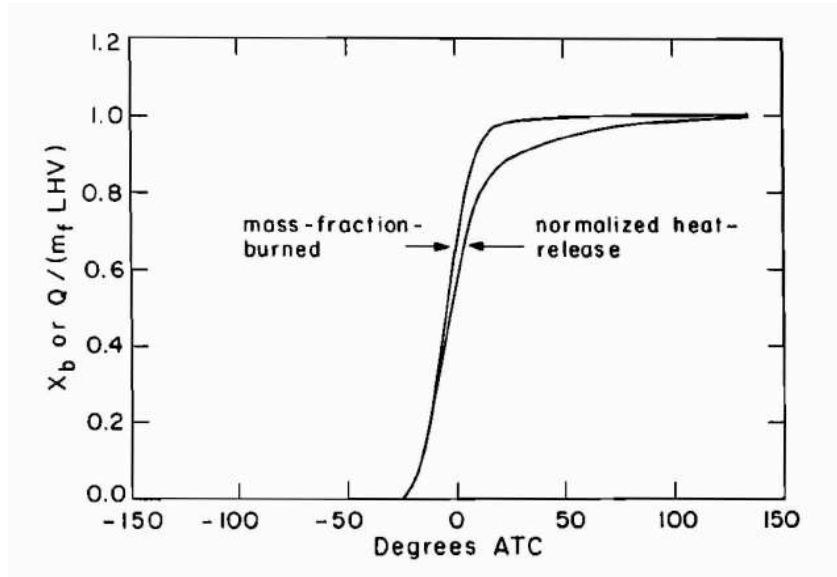


Figure 2-2: Normalized Heat Release and Mass fraction burned [13]

Not all of the chemical energy of the burned fuel is released because of dissociation and limited oxygen availability, at high temperature and pressure conditions, resulting in the discrepancy shown above. The unconverted chemical energy is approximated by the enthalpy of CO and H₂ within the cylinder. Chun et al. [13] state that in real-time pressure data, normalized heat release is a reasonable estimate of mass fraction burned because the dissociation level will be smaller due to the effects of heat transfer and crevice losses on peak temperature. For the purposes of this study, the normalized heat release determined by the heat release data will equal the percent mass fraction burned of the fuel.

2.4.2 Ignition Delay

In a combustion chamber, ignition delay is governed by the chemistry of the fuel, the geometry of the combustion chamber, the air-fuel ratio, and cycle-to-cycle variations of combustion. Engine geometry and spark plug position dictate the flame front surface area. The larger the area, the more fresh charge can enter and propagate the combustion reaction. Also known as flame development angle, ignition delay is the crank angle interval from spark discharge to when a significant amount of fuel chemical energy has released. This quantity is usually 10 percent of fuel mass fraction burned, but can also be taken as 1 or 5 percent [11].

Heat release is computed using the derivative of pressure trace as a function of crank angle. Small oscillations in pressure data can cause significant errors in heat release analysis. These oscillations are exacerbated at low rates of heat release. To reduce the effect of noise, the crank angle interval from spark timing to 10 percent mass fraction burned is defined as the flame development angle as used in Swain et al. [4].

2.4.3 Combustion Duration

Combustion duration is the crank angle interval of during which the fuel burns in the cylinder. This measurement is the interval between 10 to 90 percent of the fuel mass fraction burned. From a thermodynamic standpoint, the highest efficiency is achieved if all of the chemical energy was released when the piston was at top dead center. However, achieving such a combustion rate is not only impractical, but also would cause irreparable damage to the engine. Manipulating engine conditions to decrease combustion duration is

advantageous because it reduces heat losses in the engine. Engine speed is a major factor in combustion duration: a four-fold increase in speed will increase the combustion duration by a factor of 1.6 at stoichiometric conditions [11].

2.5 Hydrogen Benefits to Combustion

In the following section, the benefits of hydrogen addition to combustion of natural gas are reviewed. Hydrogen fuel chemistry, composition, and properties lend itself to an increased efficiency, flame speed, and radical formation over those of methane during combustion.

2.5.1 Increased Cycle Efficiency

The theoretical maximum of a constant volume cycle conversion of fuel energy to usable energy is called the ideal cycle efficiency and is calculated by Eq. 2.13.

$$\eta_{i,CV} = 1 - \frac{1}{r_c^{\gamma-1}} \quad 2.13$$

Ideal cycle efficiency is a function of compression ratio and specific heat ratio (γ). Specific heat ratio is a measurement of the degrees of freedom of a molecule—the more degrees of motion in the molecule, the larger the number of degrees of freedom. A diatomic molecule, like hydrogen (H_2), will have a higher ratio of specific heats at the same temperature and pressure than a 5-atom molecule, like methane (CH_4) [14]. Hydrogen at standard temperature and pressure has a ratio of specific heats of 1.4, while the ratio for methane is 1.3. The ideal cycle efficiency would be expected as more

hydrogen is added to the charge, based on Eq. 2.13. Efficiency of an internal combustion engine is shown in Figure 2-3 as a function of gamma and compression ratio.

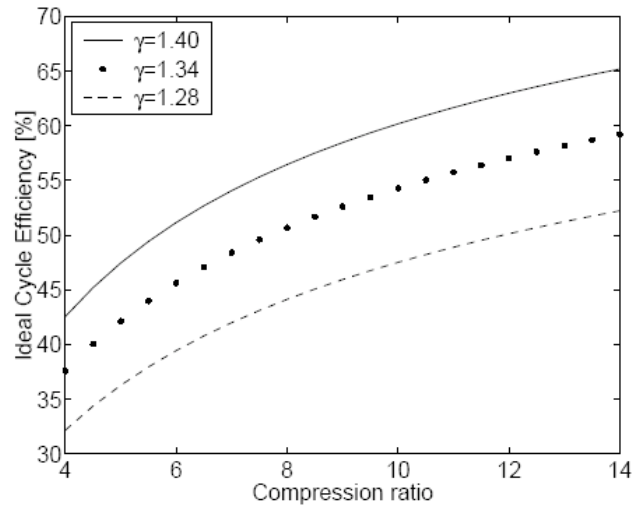


Figure 2-3: Ideal cycle efficiency as a function of gamma and compression ratio[15]

One of the main sources of inefficiency in a spark-ignited engine is throttling of the intake airflow coming into the cylinder. Throttling results in less inducted air mass and an increased pressure drop as the air is drawn into the cylinder during the intake stroke. This reduces thermal efficiency because of a reduction in peak pressure attained during combustion. However, it has been shown [5] that a mixture of 20 percent hydrogen in natural gas when hydrogen blends are used, such pumping losses are reduced contributing to a higher thermal efficiency.

2.5.2 Increased Flame Speed

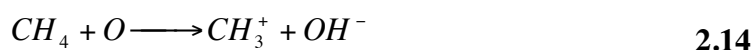
Quicker burn time reduces heat transfer from the hot in-cylinder gases to the surroundings, resulting in efficiency gains. During the faster combustion that occurs with

hydrogen and air, the thermal energy lost is only 17 to 25 percent of the total energy released. Methane air combustion loses 22 to 33 percent of its energy through the same convective heat transfer through the cylinder walls. The slower propagating flame speed of stoichiometric methane combustion in air is 40 cm/s while an identical hydrogen and air flame propagates at a rate between 265 and 325 cm/s [1]. Yu et al. [16] studied the effect of hydrogen addition to the flame speed of natural gas and found a linear correlation between the addition of hydrogen and the increase of the methane-hydrogen-air flame speed.

2.5.3 Rate-Limiting Factors

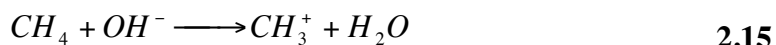
Because the process of combustion depends on the formation of radicals in order to accelerate flame propagation, a larger pool of radicals increases flame speed. However, some radical reactions have a slow reaction rate that governs the speed of combustion in the system. This reaction is known as the rate-limiting step because it controls how fast the overall reaction occurs.

It has been hypothesized by Collier et al. [17] that the rate-limiting step in the combustion of natural gas is:



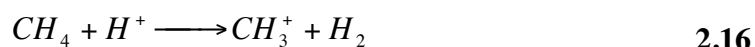
It is further hypothesized that once CH_3 is formed, the remaining major reactions completing combustion to CO_2 and H_2O proceed rapidly. In contrast to methane combustion, hydrogen and air combustion produces hydroxyl radicals rapidly at low

temperatures. The formation of the hydroxyl radicals can help bypass the rate-limiting step by the reaction [17]:



The addition of hydrogen to methane increases the number of hydroxyl radicals available to strip the first hydrogen atom from the methane molecule. Bypassing the rate-limiting step causes combustion to occur more rapidly.

This idea was investigated further by Priyadarshi [18] in his master's thesis. By using computer modeling of the entire reaction system, he showed that methane combustion in 30 volume percent HCNG combustion is limited by Eq. 2.16:



His findings confirm that the hydroxyl reaction with methane is a rapid reaction. This result suggests that a higher concentration of hydroxyl radicals increases the speed of combustion.

Detailed kinetic modeling in a jet stirred reactor was done by Dagaut et al. [19] using modeling software. The group modeled the kinetics involved in both natural gas–oxygen combustion, and hydrogen–natural gas–oxygen combustion at an equivalence ratio of 0.3. Their study showed that in both cases, methane oxidation is completed via reaction with OH radicals 72 percent of the time. Concurrently, H and O radicals oxidize methane 14 and 10 percent of the time, respectively. With 1.75 percent volumetric addition of hydrogen, the percentage of methane oxidized by OH is unchanged. From this, it can be theorized that OH is the most important reactant in methane oxidation.

Modeling also showed hydrogen addition increases the importance of the reaction below.



Increased activity of Eq. 2.17 [19] increases OH present in the system. The modeled 1.75 percent addition of hydrogen increases the presence of OH radicals by 17 percent. Because of their earlier stated importance to methane combustion, the increased availability of these radicals increases flame propagation.

2.5.4 Experimental Research on HCNG flames

H, O, and OH radicals are of extreme importance in propagating the combustion reaction. The increase in radical formation seen in modeling has also been observed experimentally. Schefer [20] characterized flame structure using OH planar laser-induced fluorescence. A comparison of natural gas flame and 20 percent hydrogen and natural gas flame on a burner produced the graph in Figure 2-4. The figure shows that increased hydrogen in the fuel increases the surface area of the OH radicals in the flame, allowing more air-fuel mixture to oxidize. The increase in OH concentration in the outer flame was 20 percent. OH radicals reduced 20 percent in concentration in the inner flame. The increased radical availability increases the flame stability, allowing it to run at leaner conditions.

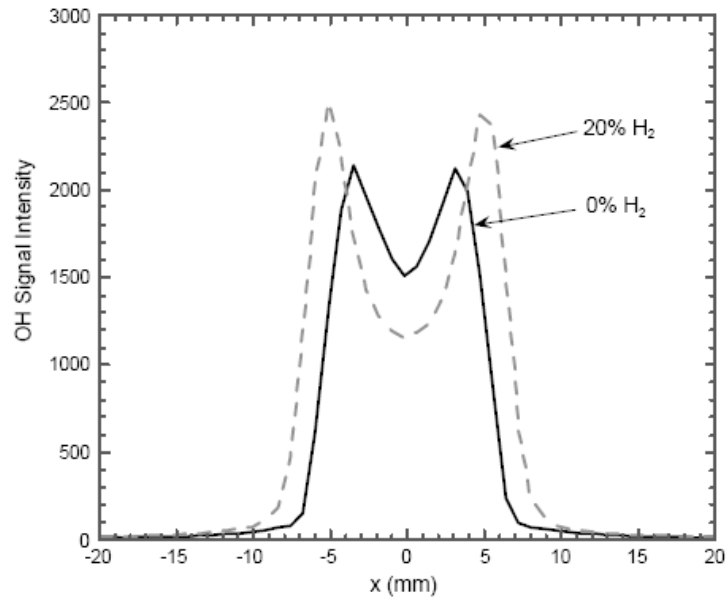


Figure 2-5: OH Signal Intensity in Natural Gas and 20 Percent HCNG[20]

2.5.5 Spark Timing Adjustments for Optimization

While HCNG mixtures offer an advantage of combustion over CNG, fuels cannot simply be interchanged to obtain optimal efficiency. Researchers have blamed poor performance of HCNG on their failure to reprogram fuel and spark timing maps designed to optimize natural gas utilization in the engine [21].

Nagalingam et al. [22] showed that faster-burning hydrogen produces optimum torque an average of 20 crank angle degrees before that of natural gas. They also reported retardation in optimal spark advance with HCNG due to faster combustion in a research engine running at 1200 rpm. At this point, peak engine power could no longer reach the same level as with natural gas alone. Later research by Collier et al. [23] showed that optimal spark timing reduces from 40 degrees before top dead center (BTDC) to 36

degrees BTDC when hydrogen is added to methane. Reduced combustion duration requires retarded ignition timing to optimize engine output.

2.6 Emissions

Government-mandated emissions regulations are becoming increasingly stringent worldwide. Emissions levels of vehicles used on the road today already require high-cost, complex technology to maintain current emission regulations. To meet the stricter emissions regulations of the future, hydrogen addition is another option for vehicle manufacturers.

Environmentally harmful emissions measured in this study were nitrogen oxide (NO), nitrogen dioxide (NO₂), and carbon monoxide (CO). By changing the fuel composition in the cylinder, some pathways of formation will increase, while others decrease. This section explores how these emissions are formed.

2.6.1 Oxides of Nitrogen

The principal source of nitrogen in nitrogenous oxides (NO, NO₂) is air. It is generally accepted in the scientific community that for stoichiometric air-fuel mixtures, the Zeldovich mechanism governs the production of nitrogen oxide. NO is formed in the flame and postflame gases. The engine compression stroke compresses the burned gases released during the early stages of combustion, increasing their temperature. This temperature increase drives the mechanism to form more NO.

NO_2 is produced in much smaller quantities than NO during normal combustion. It is formed when NO reacts with a hydroperoxyl radical to form a hydroxyl radical and NO_2 . More prevalent in light-load diesel combustion, NO_2 is formed when it mixes with cooler fluid, preventing the conversion of NO_2 to NO . In a spark-ignition engine, NO_2 is highest in concentration in a slightly fuel-rich mixture. [11]

2.6.2 CO Formation

Carbon monoxide (CO) emissions are a result of incomplete oxidation. The amount of CO emitted increases with a reduction of excess fuel. CO formation can be summarized by the following reaction [11], in which the R group is the rest of the hydrocarbon.



The CO is then converted into CO_2 through the slower reaction of CO and an OH radical.



It is generally accepted that at peak cylinder temperature, the carbon-oxygen-hydrogen system is equilibrated. As the combustion gases cool, the temperature and pressure gradients within the gas cause uneven CO oxidation, resulting in CO emissions [11].

2.6.3 Unburned Hydrocarbons

Hydrocarbon emissions are the consequence of the incomplete combustion of hydrocarbon fuel. While methane in the exhaust is not a regulated hydrocarbon because

of its inert characteristics, pyrolysis and synthesis of methane that occurs during combustion forms other harmful gasses. The resulting oxygenates, carbonyls, and aldehydes contribute to pollution. Unburned hydrocarbons are formed when they are not exposed to the flame front to allow the oxidation reaction to occur. They can be found in crevices on the surface of the cylinder or blow by piston rings, only to reappear in the cylinder after combustion has completed [11].

2.7 HCNG in Test Cell Engines

This study is an attempt to bridge the gap between HCNG test cell research and vehicle testing by determining what happens inside the cylinder during vehicle driving conditions. This section will detail the results researchers obtained using constant speed and load testing on an engine test stand. The following section will review issues related to real driving conditions and look at hydrogen-natural gas testing in the literature. The results will explore correlations between the two.

2.7.1 Part Load Condition HCNG

Spark-ignited engines require a constantly adjusted amount of fuel, proportional to the energy required by the engine to produce the required power output. The throttle valve restricts air coming through the intake to maintain the correct stoichiometry of the air-fuel mixture. Light-load conditions are plagued by incomplete combustion, which decreases thermal efficiency and increases emissions. These conditions compose a large portion of the Federal Driving Cycle [4], which is representative of normal vehicle

operation. Therefore, it is of utmost importance for the vehicle to perform effectively at these conditions.

Engines running at low speed and loads have been found to have slower flame speeds than those running at wide-open throttle. Light-load conditions result in an increased burn time in the cylinder because of lower turbulence. But the slower combustion speed is also a result of a higher concentration of residuals remaining in the cylinder. Such conditions increase the severity of flame initiation and propagation problems.

In order to investigate the relationship between load and burn time, low road loads were tested, by Cattelan et al. [5], who evaluated the brake-specific energy consumption (BSEC) as a function of engine load for Hythane and natural gas. At low loads of 5 and 30 N-m, benefit from the addition of hydrogen was indicated by a decrease in specific energy consumption (BSEC). However, at loads greater than 30 N-m, the difference in BSEC became negligible.

Testing was done on a closed-loop, three-way catalyst engine that controlled the equivalence ratio to 1.0 by Swain et al. [4]. At an equivalence ratio of 1.0, there was only a rise in NO formation from 4.5 to 5.5 g/hp-hr. The smaller increase in BSNO_x was attributed to the 4 percent to 5 percent increase in thermal efficiency. Higher loads attenuated thermal efficiency gains when less exhaust gas remained in the cylinder. A reduction in BSCO and BSHC was also observed at low load stoichiometric conditions.

2.7.2 Swirl Addition to HCNG

Swirl is an effective technique to increase mixing of the air-fuel mixture which improves combustion performance. At wide-open throttle conditions, throttling losses are reduced. Other important factors like in-cylinder flow velocity become a more important factor in combustion progress. Using a natural gas engine with hydrogen blends of 0 to 20 percent, Andersson [15] analyzed the difference in combustion between different induced flow velocities. Using the more turbulence inducing quartette head, he found there was no benefit from hydrogen addition.

Stoichiometric combustion of natural gas with hydrogen addition in a high swirl case showed no reduction in ignition delay. At the same conditions with high turbulence, combustion duration did not reduce with addition of hydrogen. The author concluded that during periods of high turbulence the other engine conditions could assist combustion, negating benefits of hydrogen addition.

2.7.3 Hydrogen-Natural Gas Studies

Using cylinder pressure data, Swain et al. [4] tested methane and Hythane burn durations at lean conditions using computer modeling. Two graphs from their results show distinctly different trends. While the testing is only done only for equivalence ratios from 0.65 to 0.80, extrapolated data project the effects of hydrogen at stoichiometric conditions. At stoichiometric conditions, the measure of combustion duration in crank angle degrees converges, indicating that hydrogen has no benefit on stoichiometric methane combustion at 1000 rpm, 1 bar BMEP. However, HCNG and CNG show linear,

parallel trends in flame development angle over the measured equivalence ratios. This indicates that at an equivalence ratio of 1.0, hydrogen reduces the flame development angle.

Karim et al. [24] increased the amount of hydrogen in natural gas and subsequently derived relevant combustion statistics for a variety of equivalence ratios. Hydrogen increased the peak pressure in each cylinder 1 bar for every 10 percent volume hydrogen added. By increasing the concentration of hydrogen in the fuel mixture, a reduction in the length of ignition delay and combustion duration was observed. These results reflect the speeding up of both flame initiation and propagation rates.

2.7.4 Emissions Testing

The latter part of the study will compare emissions data from stationary engine testing and vehicle testing.

Stationary engine testing with producer gas addition, a 33 percent blend of hydrogen with inert gases, was performed by Jensen et al. [25]. Their research explored the change in combustion performance when producer gas was added to natural gas. A statistically significant drop in unburned hydrocarbons was detected. It was determined that combustion enhancement is caused by post oxidation, which is less sensitive to cyclic variations. The lower level of unburned hydrocarbons suggests a more complete combustion, which can be attributed to the faster burning rate of hydrogen. In this instance, hydrogen seems to be a dominating factor in the consumption of hydrocarbons, despite the addition of inert gases as the remaining components in the producer gas like

CO₂, and N₂, which retard flame propagation. The reduction in unburned hydrocarbons suggests a more complete combustion of the fuel in the cylinder.

NO emissions increase when hydrogen is added to the natural gas mixture at the same operating air-fuel ratio because hydrogen drives the flame temperature higher. Collier et al. [23] studied the untreated emissions leaving the HCNG engine. NO emissions increased 5 percent at stoichiometric conditions. However when ignition timing was retarded in a lean burn engine with 70:30 HCNG mixture, NO_x emissions were controlled to low levels over a range of speed and loads. The spark timing maps on the ECU were installed by Collier technologies that retard spark timing in efforts to reduce NO production from the hotter burning HCNG. More information regarding emissions data across hydrogen-natural gas blends in engine combustion can be found in Akansu's work [10].

2.8 Hydrogen Addition in On-Road Performance

It is impossible for engine manufacturers to predict all the conditions an engine will experience during its lifetime and so engine settings are based on testing done on isolated engine test stands. In these tests, the electronic control unit (ECU) controls engine parameters such as spark ignition, air intake, and fuel injection using data such as temperatures and exhaust composition to optimize engine performance. However, with varying external conditions that occur when the vehicle is on the road, engine loads will fluctuate unpredictably, and the engine can experience in-cylinder combustion variations from cycle to cycle that reduce indicated thermal efficiency. In this final section, issues

related to vehicle performance are reviewed. Next, the background of pressure sensors is explored followed by fundamentals of engine loading.

2.8.1 Vehicle Operating Conditions

Current government standards require engine and vehicle manufacturers to meet specific requirements, which have become more stringent over time. Catalytic converters were first used in commercial gasoline vehicles in 1975 as a way to help meet the mandated emissions requirements. Three different reactions take place in the standard catalytic converter. Two are the oxidation reactions in which unburned hydrocarbons and carbon monoxide are converted to carbon dioxide. A third reaction reduces NO using a platinum-based catalyst to reduce NO to N_2 and O_2 .

To catalytically convert these emissions effectively, three-way catalytic converters require that the engine run at stoichiometric conditions. If the fuel mixture is too lean, the oxidation reactions are favored; if it is too rich, the reduction reactions are favored. These results have been shown by Pede et al. [26] in testing on a lean burn HCNG vehicle running the New European Drive Cycle (NEDC). They found that lean operating conditions resulted in higher concentrations of harmful exhaust emissions such as NO_x , CO, and UHC's than would be expected under stoichiometric conditions. The different mole fractions inhibit the formation of N_2 and CO_2 in the catalytic converters, minimizing the effect of the lean burn.

2.8.2 Pressure Sensors in Vehicles

While there are few published studies studying heat release through pressure sensors on an actual vehicle, pressure signals do provide important information that can be processed to optimize thermal conversion efficiency. Detection of knock and combustion conditions from the pressure data allows the ECU to finely tune individual cylinder parameters.

A majority of engines on production vehicles are closed loop systems that determine the amount of fuel and air required in the cylinder to produce the appropriate amount of power at the smallest cost to fuel economy and emissions. In the closed loop system, temperature and exhaust information is fed back via the oxygen sensor and thermocouples, and the ECU uses a pre-determined engine map to determine appropriate engine settings. However, exhaust temperature and oxygen content are inaccurate measures of combustion performance. Cylinder pressure sensors give the ECU a better picture of the quality of combustion inside the cylinder. Because the cost of pressure sensors can run into the thousands of dollars, resulting benefits in combustion performance do not justify their use in mass produced vehicles as yet.

Over the past 20 years, in-cylinder pressure sensors have dramatically reduced in cost. To further improve performance and efficiency, engineers have looked at ways to use data for real-time cylinder pressure. Rather than determining combustion performance through sensors external to the combustion process, engineers can look at the signature of combustion through the pressure trace. Using in-cylinder pressure measurements as a feedback sensor, in the place of an oxygen sensor, to control the amount of EGR and the air-fuel ratio is the latest in numerous attempts of engine control

[27]. With the development of more accurate combustion prediction, increased fuel economy and decreased emissions have been achieved. For instance, it is possible to operate the engine at minimum spark advance in order to create conditions for maximum brake torque (MBT), thereby compensating for burn rate and spark requirement differences between cylinders. Cylinder-pressure based control can be adapted for environmental factors, manufacturing variations, component wear, and degradation of various types.

Having a pressure sensor located in the cylinder of a vehicle has been shown to allow a variety of improvements in the vehicle's combustion performance. In the mid-1970s, Hubbard et al. [28] were able to achieve brake-mean effective pressure and fuel economy within 0.1 percent of the theoretical optimum. The pressure sensor in the cylinder enabled the ECU to better understand the combustion in the cylinder. The current study will produce high quality combustion analysis using pressure sensor data.

2.8.3 Vehicle Loads

Propelling a vehicle forward requires the engine to provide energy to the wheels overcoming the load applied from the vehicle surroundings. The instantaneous motion resistance power (P_v) that a vehicle has to overcome to travel at a given speed is a function of speed (v), rolling resistance (R_r), grade resistance (R_g), aerodynamic resistance (R_a) and inertial forces in the vehicle ($\gamma_m ma$). It can be modeled using the following equation [29]:

$$P_v = v(R_r + R_g + R_a + \gamma_m ma) \quad 2.20$$

Other factors that reduce the power available from the engine are accessories loads (P_{ac}) such as air conditioning or interior lighting. Transmission efficiency (η_{tr}) is the energy that will be lost through the transmission. The power equation then becomes [29]:

$$\eta_{tr}(P - P_{ac}) = (R_r + R_g + R_a + \gamma_m ma) \quad 2.21$$

The vehicle powertrain transfers power from the crankshaft in the engine to the wheels. This system includes the transmission, driveshaft, differential, and the final drive. Losses that occur among these interlocking elements are due to vibration, friction, and rotation.

2.8.4 HCNG Vehicle Literature

In order to verify that the engine tests performed in a lab applied to actual testing conditions, Pede et al. [26] tested a 3500 kg truck powered by a 2.8L natural gas engine. Fuel economy and emissions that occurred using HCNG blends of 0, 10, and 15 percent were compared. Primary studies were done on stoichiometric combustion in efforts to reduce tailpipe NOx emissions.

It was found that at the same conditions, retarding the spark timing reduced the levels of NOx dramatically without significantly reducing the output of the engine. In all stoichiometric test cases, the HCNG blends showed reductions in tailpipe hydrocarbons, NOx, and CO₂, when compared to natural gas. The amount of CO emissions decreased with 10 percent hydrogen added, yet increased with 15 percent added. There was a positive linear correlation between fuel economy and quantity of hydrogen. Indicated

thermal efficiency followed a positive linear correlation with hydrogen addition and increased 5 percent with the 15 percent HCNG blend.

Don Karner et al. [21] studied a Dodge Ram Wagon to evaluate fuel and emissions with CNG and HCNG fueling during actual and simulated driving conditions. While in service running on compressed natural gas, the vehicle fuel economy was 13.2 miles-per-gallon equivalent (gge). When running on a 15 percent HCNG blend, the same vehicle ran at a more efficient fuel economy of 14.7 miles per gge. When the vehicle was run on the FTP-75 road test, reductions in unburned hydrocarbons, carbon monoxide, and carbon dioxide were seen. A 90 percent increase in NO_x was attributed to the fact that the engine was not tuned to optimize HCNG conditions.

While the current study does not focus on emissions, the decrease in fuel economy and increase in NO_x emissions should not be as severe because the ECU has been reprogrammed to optimize for HCNG combustion.

Chapter 3

Experimental Set-up

3.1 Outline

The following section begins with an explanation of the engine modification and set-up required for this study. Next, hardware modifications required for this study and the testing procedure are explained. Then the data acquisition system and data analysis methods are discussed. Finally, the engine testing plan is introduced.

3.2 Test Engine and Fueling

In 2004, the Pennsylvania State University purchased a number of fleet vehicles to provide mobility for employees at the Office of the Physical Plant. As part of an initiative to use alternative fuels, Penn State's order included a number of natural gas vans. The vehicle involved in this study is one of those compressed natural gas (CNG) dedicated vehicles, a 2004 Ford E-Series E-250 Van. The stock vehicle meets the van wagon SULEVII emissions standards. Its fuel economy is 18.5 miles per gas gallon equivalent (gge), and it has a range of 280 mi, based on a slow fueling of the tank to 3600 psi [30]. Detailed engine specifications are listed in Table **3-1**.

Table 3-2: Test Engine Specifications

Engine	SOHC 5.4-Liter, V8, Natural Gas Engine
Displacement	5.4 L
Bore	90 mm
Stroke	106 mm
Compression Ratio	11.0
Connecting Rod Length	169.1 mm
Rated Power	194 kW @ 4500 rpm
Peak Torque	474 Nm @ 2500 rpm
Injection System	Electronically controlled common-rail injection system
Valve Train	2 valves/cylinder

Air Products and Chemicals, Inc. installed a hydrogen fueling station on campus in December of 2005 that dispenses neat hydrogen and HCNG. Together with Collier Technologies, the Pennsylvania State University has developed hydrogen-blend HCNG vehicles on campus to use this station. In these vehicles, Collier Technologies reprogrammed the fuel and spark maps to optimize burning of HCNG, and, to increase power output in the engine, added an Eaton M90 supercharger. A Dynetek carbon fiber reinforced aluminum tank replaced the stock stainless steel fuel tank which is susceptible to hydrogen embrittlement. To allow for switching fuels, interchangeable CNG and HCNG nozzles have been mounted to the fuel port on the side of the vehicle. Fueling is done just like a typical gasoline or diesel pump.

3.3 Engine Instrumentation and Data Acquisition System

While running the vehicle, data were collected on a Dell Dimension desktop computer with a National Instruments PCI-MIO-16E-4 data acquisition card, which has a 333 kilo-samples per second maximum sampling rate. The board reads three signals: a pulse signal every 0.1 crank-angle degree, a pulse signal every 360 crank-angle degrees from the crank angle encoder, and a voltage signal returned from the transducer. The three signals were processed through a data acquisition program written in LabVIEW 7.1 and recorded to a data file.

The piston position and speed were measured using a Model 725 Accu-Coder optical shaft encoder. Every 0.1 change in crank angle degree, a pulse signal was sent to the computer and a cylinder pressure value was recorded. The crank angle encoder was connected to the crankshaft pulley by a custom-made mounting bracket. A grooved aluminum adaptor was bolted inside the crankshaft pulley and attached to a belt that drove the crank angle encoder. Figure 3-1 shows the crank angle encoder set-up mounted on the engine.

A second signal referenced the position of the piston by sending a pulse every 360-degree rotation. Top dead center was determined by using an indicator suspended above the cylinder. This point was confirmed by marking 20 degrees before and after top dead center on the crankshaft adapter at the halfway point. This position was marked on the crankshaft adapter using a scribe. The referencing signal was set to pulse when the piston reached this mark.

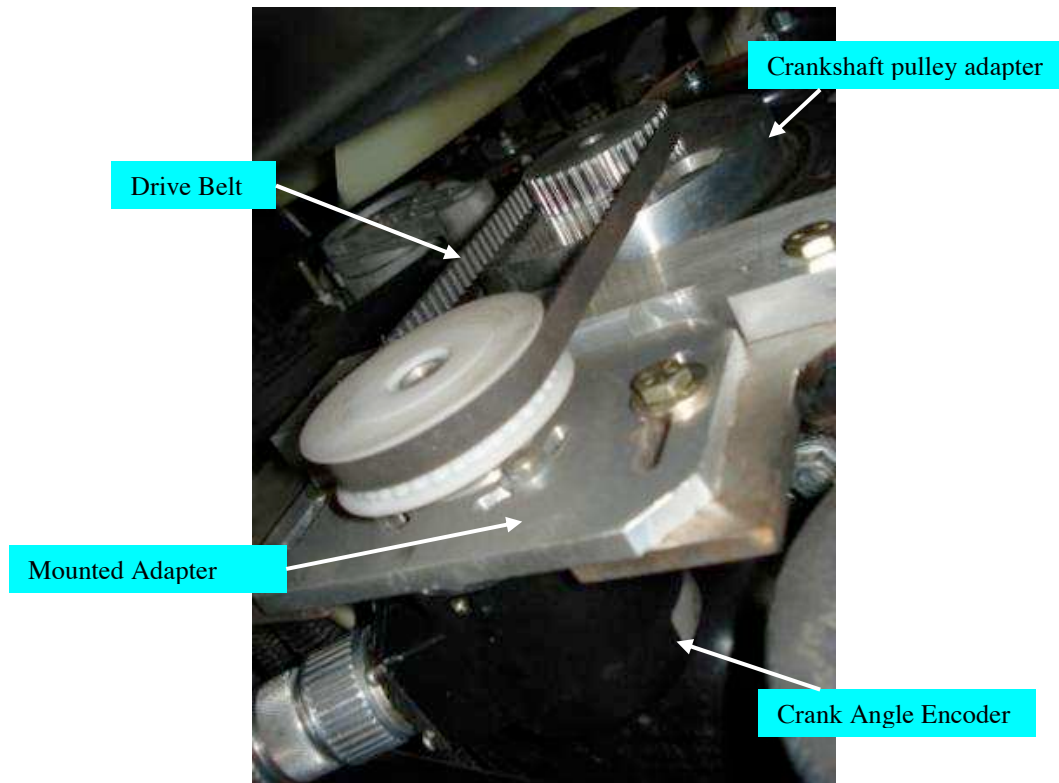


Figure 3-1: Crankshaft Pulley Adapter to Crank Angle Encoder

Pressure signal measurements were performed using a Kistler Type 6117BCD27 measurement spark plug with an integrated pressure transducer. The working spark plug was removed from cylinder 7 and the Kistler spark plug was inserted in its place. The crystal in the transducer creates an electric charge in picocoulombs as a function of in-cylinder pressure. This charge is passed through a Kistler 5010B charge amplifier, which generates a proportional voltage. The voltage value is recorded using the data acquisition system. Set-up of the pressure transducer system is shown in Figure 3-2.

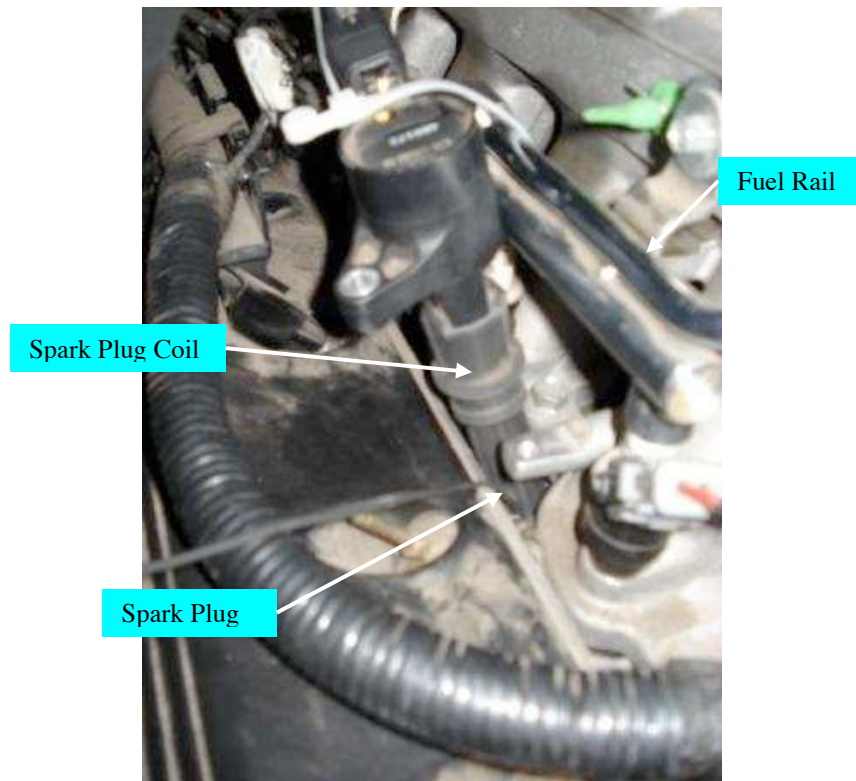


Figure 3-2: Pressure Transducer Set-Up

In order to obtain steady-state engine conditions, the van was operated on a Clayton Industries model VVT chassis dynamometer, which absorbs energy through large rollers on either side of the rear wheels. These rollers are vehicle-speed limited, and load is controlled by the operator. Testing procedures were set by a test matrix to determine combustion performance at controlled speed and load conditions. Standard driving cycles such as the Federal Transit Protocol (FTP) cycle, etc., were not followed since during such transient test cycles variable pressure conditions occur during combustion preventing steady-state combustion analysis. Instead, steady speed and load conditions were used as the basis for the test procedure. Once the vehicle reaches the pre-

set speed, a driver applied the throttle further with his or her foot to maintain the road load setting. Load conditions are specified in the test matrix.

During testing, engine settings were recorded from the ECU using a scan tool. A series of cables were attached to a laptop running Ford Integrated Diagnostic System (IDS) software, which allowed the user to select individual parameters to read from the engine. Real-time intake air flow and temperature, throttle position, and spark advance were recorded during the test period.

3.4 Fuel Analysis

A gas chromatograph (GC) was used to determine the composition of the two test fuels [31]. Because the gas used in the vehicle could not be sampled readily from the vehicles fuel tank or during the fueling procedure, natural gas was sampled over multiple days and the data averaged to determine the average compositions of the natural gas and the hydrogen-natural gas mixture.

The procedure used to determine fuel composition was as follows: Gaseous fuel was collected in a gas sample bag. A 50-microliter fuel sample was extracted with a syringe, and injected into the GC. The sample port volume was 1mL, made up of the 50 microliter sample along with 950 microliters of argon (carrier gas). This procedure was executed twice, once for the flame ionization detector (for low molecular weight hydrocarbons), and then for the thermal conductivity detector (for hydrogen and nitrogen).

The gas chromatograph was calibrated for methane, ethylene, ethane, propylene, propane, butylene, butane, and hydrogen, for the ranges typically found in natural gas. The chromatogram provided the mole fraction of each constituent. That mole fraction was then multiplied by 20 to bring the mole fractions up to the 1-microliter basis.

3.5 Semtech-DS Emissions Equipment

Emissions data from the test vehicle were collected externally using a Semtech-DS, which is an onboard emissions testing system produced by Sensors, Inc., Saline, Michigan. The Semtech-DS uses a combination of methods, including Flame Ionization Detection (FID) with Non-Dispersive Infrared (NDIR) and Non-Dispersive Ultraviolet (NDUV). These methods allow for direct comparisons in test cell measurements for THC, CO, CO₂, NO, and NO₂ in compliance with CFR-40, 1065 Subpart J. A distinct advantage of this technology is its ability to absorb high shock or vibration, while providing accuracy, and resolution in a short response time. In these tests, the FID was not operational and no hydrocarbon data were recorded.

The following system was used to obtain exhaust gas for analysis: Immediately after exiting the exhaust manifold, a portion of the exhaust gases passed through a one-quarter-inch hole drilled into the exhaust pipe. A Swagelok weld fitting was attached to the exhaust pipe through which the exhaust sample flowed into a foot-long steel tube designed to protect the heated lines of the emissions analyzer. Exhaust gas continued through to a 190 °C heated line into the Semtech-DS to be analyzed.

Using an exhaust flowmeter linked to the vehicle's on-board computer, the user could instantaneously measure emissions data as a function of engine performance in g/km, g/kg fuel, or g/bhp-hr. In addition, the testing block had communications and global positioning system modules. Data could be provided over cellular or Internet links in addition to on-board collection and storage. Since the vehicle was operated on a chassis dynamometer rather than over the road, this communications technology was not utilized.

The CO, CO₂, O₂, NO, and NO₂ concentrations were recorded on both a wet and dry sample basis. For the purposes of this report, they are reported on a dry sample basis.

Table 3-3 is a summary of the measurement techniques used by the Semtech-DS.

Table 3-3: Summary of Exhaust Species and Measuring Techniques

Measure Gaseous Species (units)	Measurement Technique
CO (volume percent)	NDIR
CO ₂ (ppm)	NDIR
O ₂ (volume percent)	Paramagnetic detector
NO (ppm)	NDUV resonant absorption spectroscopy
NO ₂ (ppm)	NDUV resonant absorption spectroscopy

3.6 Testing Procedure

The testing took place on the chassis dynamometer located adjacent to the Pennsylvania Transportation Institute at University Park, Pennsylvania. The pressure sensor and crank angle encoder were installed and connected to the data acquisition system. Exhaust gas recirculation (EGR) was prevented from entering the intake by disconnecting the EGR control valve connected to the throttle. Finally, it was verified

that the referencing signal from the crank angle encoder was being sent when the piston reached top dead center. The vehicle was prepared to run once the instruments needed to run the experiment and record data were set up.

The engine was then turned on and warmed up until the coolant temperature held a constant reading on the dashboard. Because there was no passive cooling of the engine, a large fan drew fresh air into the laboratory from outside the building. To run the test, the driver applied the throttle to bring the vehicle to the chassis dynamometer limited vehicle speeds of 15 or 30 miles per hour. The driver would then increase throttle position to maintain a road load of 10, 20, or 30 horsepower. At each road load setting, an averaged 200 cycle pressure trace was saved to a file using LabVIEW. Updated scan tool data were read by the emissions system and saved to a separate file.

3.7 Heat Release Analysis

To investigate the effect of hydrogen on natural gas combustion, apparent heat-release rate calculations for both fuels were performed. Heat release rate data allow for comparison of combustion performance for the two fuels. In this study a zero-dimensional single zone model for the apparent heat release rate calculation [11] was used. This model is based on the following assumptions. First, the mixture is distributed homogeneously and has uniform properties throughout the cylinder. Second, the calculated ratio of specific heats of the in-cylinder gas mixture is assumed to be the same as that of air. Finally, the heat release due to combustion is considered to be heat addition to the cylinder.

The apparent heat release rate was calculated based on the cylinder pressure data using the first law of thermodynamics as described by Heywood [11]. The in-cylinder pressure changes as a result of cylinder volume, combustion, heat transfer effects, flow into crevices, and leakage. The most significant contributors to pressure increase are volume change and combustion.

Heywood defines the chemical heat release rate, or gross heat release rate as shown in Eq. 3.1. Literally, the gross heat release rate is the “chemical energy” of the fuel that is released by combustion.

$$\partial Q_{ch} = dU_s + \partial Q_{ht} + \partial W + \sum h_i dm_i \quad 3.1$$

The apparent heat release rate, also known as the net heat release rate, is the chemical heat release rate minus the losses incurred by heat transfer to the walls and crevice volume losses, as shown in Eq. 3.2. Because proper instrumentation to determine blow-by and crevice volume was restricted due to space considerations, the model used assumed heat transfer and crevice effects to be zero.

$$dQ_{ch} = dQ_n - \partial Q_{ht} - \sum h_i dm_i \quad 3.2$$

Net work and sensible energy of the charge determine the apparent heat release rate in Eq. 3.3. The equation for net heat release that includes measured variables is shown in Eq. 3.4. Differentiating the ideal gas law gives Eq. 3.5.

$$\frac{dQ_n}{dt} = \frac{dU_s}{dt} + \frac{dW}{dt} \quad 3.3$$

$$\frac{dQ_n}{dt} = mc_v \frac{dT}{dt} + p \frac{dV}{dt} \quad 3.4$$

$$PdV + VdP = mRdT \quad 3.5$$

Substituting the ideal gas law into Eq. 3.4 gives Eq. 3.6.

$$\frac{dQ_n}{dt} = \left(1 + \frac{c_v}{R}\right) * P \frac{dV}{dt} + \frac{c_v}{R} V \frac{dP}{dT} \quad 3.6$$

The value for the C_v/R term is found using the ratio of specific heats as is found in Heywood as Eq. 3.7, and will give Eq. 3.8 when substituted into Eq. 3.6.

$$\frac{c_v}{R} = \frac{1}{\gamma - 1} \quad 3.7$$

$$\frac{dQ_n}{dt} = \frac{\gamma}{\gamma - 1} P \frac{dV}{dt} + \frac{1}{\gamma - 1} V \frac{dP}{dt} \quad 3.8$$

The ratio of specific heats for the mixture is calculated using the equations below. For bulk cylinder temperatures less than 1000 degrees Kelvin, Eq. 3.9 is used. For temperatures greater than 1000 degrees Kelvin, Eq. 3.10 is used [32].

$$\gamma = 1.3 + 6.0 * 10^{-5} * T - 1.5 * 10^{-7} * T^2 - 5.6 * 10^{-11} * T^3 + 9.2 * 10^{-14} * T^4 \quad 3.9$$

$$\gamma = 1.4 - 2.5 * 10^{-4} * T + 1.4 * 10^{-7} * T^2 - 3.7 * 10^{-11} * T^3 + 3.7 * 10^{-15} * T^4 \quad 3.10$$

Calculation of the bulk cylinder temperature was performed using Eq. 3.11, rearranged and with respect to crank angle position. The integral in Eq. 3.12 gives the bulk cylinder temperature.

$$\frac{dT}{d\theta} = \frac{1}{(m_{air} + m_{fuel})c_v} * \left(\frac{dQ_n}{d\theta} - p \frac{dV}{d\theta}\right) \quad 3.11$$

$$T(\theta_i) = \int \frac{dT}{d\theta} d\theta \quad 3.12$$

In order for heat release calculations to be accurate, pressure data must meet four criteria: First, the correct reference pressure must be used to convert pressure signals to absolute pressures. Second, the pressure versus crank angle degree phasing is accurate to

within 0.2 crank angle degrees. Third, clearance volume is estimated with sufficient accuracy. And finally, transducer temperature variations due to wall heat flux are held to a minimum.

Pressure measurements were averaged over 200 cycles with 0.1 crank angle degree resolution. Figure 3-3 is a 200-cycle average pressure trace of natural gas combustion at a high speed and load.

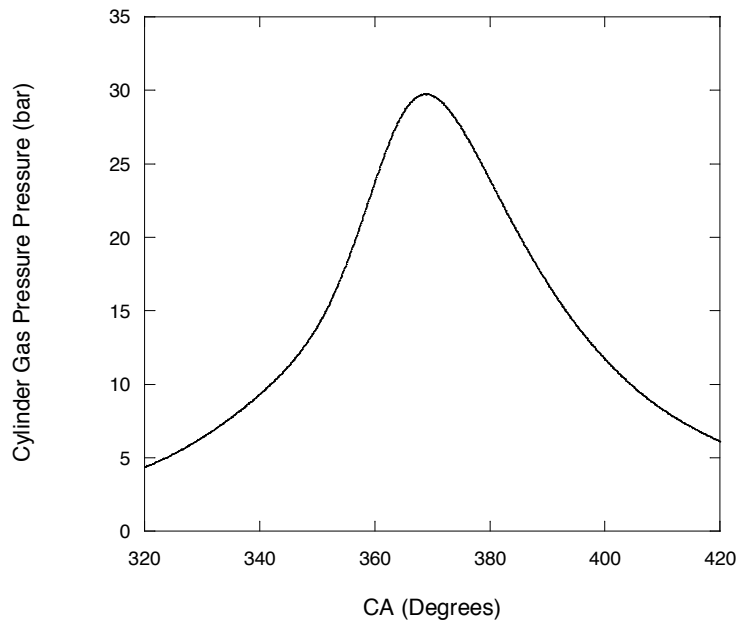


Figure 3-3: 200 Cycle Averaged Cylinder Pressure Trace

In order to perform the heat release rate calculations, two derivative terms are needed, $dV/d\theta$ and $dP/d\theta$. The derivative of volume can be calculated using the first order central difference scheme shown in Eq. 3.13. Any noise in the pressure signal can be detrimental to the heat release calculations. This is because the heat release is a derivative of the pressure trace, and any noise will be magnified. To reduce this problem, a fourth

order central finite difference is used to calculate the derivative of pressure, as shown in Eq. 3.14.

$$\frac{dV_i}{d\theta} = \frac{V_{i+1} - V_{i-1}}{2 * \Delta\theta} \quad 3.13$$

$$\frac{dP_i}{d\theta} = \frac{P_{i-2} - 8 * P_{i-1} + 8 * P_{i+1} - P_{i+2}}{12 * \Delta\theta} \quad 3.14$$

An example of an instantaneous heat release graph is given in Figure 3-4.

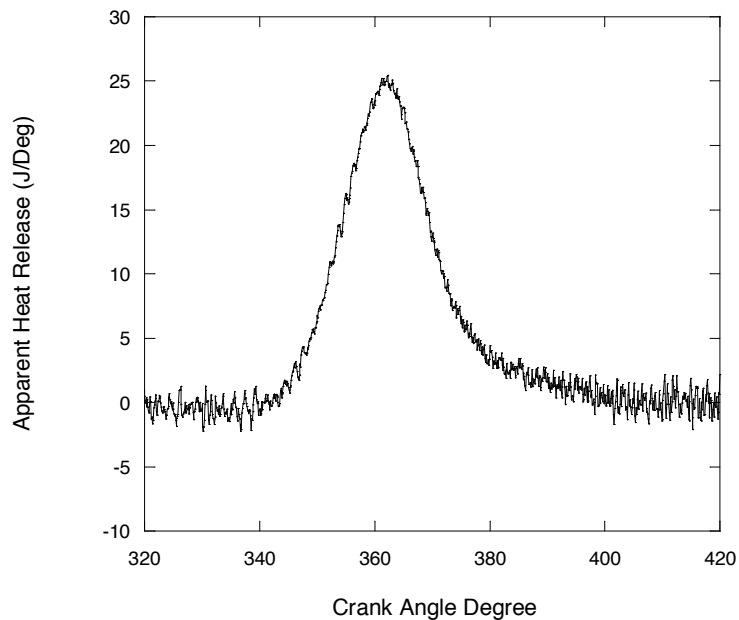


Figure 3-4: Instantaneous Heat Release Rate

The cumulative heat release is calculated by integrating the apparent heat release rate, as shown in Eq. 3.15. To determine the mass fraction burned, heat release is converted into a percentage relative to maximum cumulative heat release. For each crank angle degree after the start of combustion, the percentage of maximum cumulative heat release is calculated using Eq. 3.16. For the purposes of this study, the percentage of heat released is equal to the percentage of mass fraction burned.

$$Q(\theta_i) = \int_{\theta_{soc}}^{\theta_i} \frac{dQ_n}{d\theta} d\theta \quad 3.15$$

$$Q\% = \frac{Q_i}{Q_{max}} \quad 3.16$$

3.8 Calculating Air-Fuel Ratio

Heat release calculations require accurate determination of the mass of air and fuel inside the instrumented cylinder. The mass of air in the cylinder is calculated using the air flow rate entering the intake manifold. Mass of fuel is calculated using the air-fuel ratio determined by emissions data.

The method used to determine air-fuel ratio comes from work by Spindt [33]. In the Spindt method, the air-fuel ratio can be determined from the ratios of the wet exhaust components CO₂, CO, O₂, and unburned hydrocarbons. Because unburned hydrocarbon values were not recorded due to the inoperable FID, they were assumed to be equivalent to the baseline test in Cattelan et al. [5]. The fraction of hydrogen and carbon in the fuel are found using Eq. 3.17 and Eq. 3.18 based on the C_xH_y composition of the fuel.

$$F_c = \frac{12.01 * x}{12.01 * x + 2.016 * y} \quad 3.17$$

$$F_h = \frac{2.016 * y}{12.01 * x + 2.016 * y} \quad 3.18$$

Ratios of the exhaust products are determined from the mole fractions of O₂, CO₂, CO and HC in Eq. 3.19, Eq. 3.20 and Eq. 3.21.

$$Q = \frac{P_{O_2}}{P_{CO_2}} \quad 3.19$$

$$R = \frac{P_{CO}}{P_{CO_2}} \quad 3.20$$

$$F_b = \frac{P_{CO} + P_{CO_2}}{P_{CO} + P_{CO_2} + P_{HC}} \quad 3.21$$

These relationships are used in Eq. 3.22 to determine the approximate air-fuel ratio of the intake charge.

$$(A/F)_{ratio} = F_b \left(11.492 * F_c \left(\frac{1 + R/2 + Q}{1 + R} \right) + \left(\frac{120 * F_h}{3.5 + R} \right) \right) \quad 3.22$$

3.9 Test Plan

The objective of this study was to determine the effects of hydrogen on natural gas combustion under a variety of test conditions in order to determine how hydrogen benefits the efficiency of natural gas combustion in vehicles.

Fuels used in this study were compressed natural gas (CNG) and a 33 percent hydrogen-compressed natural gas (HCNG) blend, with hydrogen representing 9 percent of the energy of the fuel in the HCNG. The natural gas source was the same for each test, and the hydrogen was generated by the Air Products and Chemicals, Inc. fueling station via steam reforming of methane, which was then blended with natural gas. Detailed fuel composition information can be found in Appendix A.

Hydrogen was expected to increase combustion performance at low-speed and load conditions. Each fuel was tested at identical vehicle conditions. Normal operation was tested with the transmission in the “D” position. To evaluate fuel changes at high

engine speeds, the automatic transmission was placed in position D1. Table 3-4 details the test conditions used in investigating the effect of hydrogen on combustion during various driving conditions.

Table 3-4: Test Matrix

Fuel: CNG

Road Load (horsepower)	10	20	30
Transmission Position	D/D1		
Vehicle Speed (miles/hour)	15/30		

Fuel: HCNG

Road Load (horsepower)	10	20	30
Transmission Position	D/D1		
Vehicle Speed (miles/hour)	15/30		

Chapter 4

Results and Discussion

4.1 Introduction

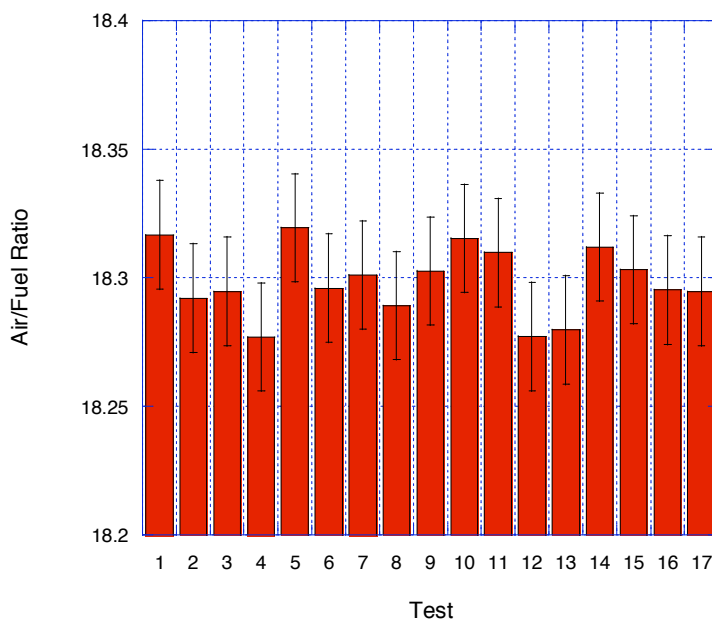
This chapter is divided into five parts. In the first section, the calculations and data read from the vehicle are evaluated. The second section reviews the measures of combustion performance, including ignition delay, combustion duration, and coefficient of variance, as a function of fuel. In the third part, the effect of engine speed and vehicle load on combustion for both fuels is investigated. Next, emissions performance with hydrogen addition to natural gas is investigated. Finally, how the combustion performance in the cylinder changes as a function of vehicle speed is reviewed.

4.2 Engine and Fuel Conditions

In this section, the fuel and engine conditions necessary for analyzing engine performance were recorded and calculated. The air-fuel ratio was calculated using emissions data. Because of the lack of instrumentation on the vehicle, the air-fuel ratio had to be calculated using raw exhaust data. Spark timing was determined by the electronic control unit, which controls the beginning of combustion in the spark-ignited engine.

4.2.1 Air-Fuel Ratio

The air-fuel ratios for HCNG, which were calculated using the Spindt method, appear in Figure 4-1. The same method was used to calculate CNG air-fuel ratios, which are given in Figure 4-2. Because equipment limitations did not provide all variables required to compute air-fuel ratio, stoichiometric hydrocarbon results from Cattelan et al. [5] were used. The error bars on the graph were the result of the 95 percent confidence interval of CO on the air-fuel ratio calculation.



4-1: Air-Fuel Ratio for HCNG testing

The average HCNG air-fuel ratio calculated using the Spindt method is 18.29. Air-fuel ratio values for CNG combustion averaged 17.38. Using the methane and hydrogen components measured in the gas chromatograph, stoichiometric HCNG and CNG combustion with air have air-fuel ratios of 18.10 and 17.18, respectively. These values are close to those in Figure 4-1 and Figure 4-2, where air-fuel ratios recorded

fluctuations of less than 1 percent. For the purposes of this study, it can be assumed that engine control is fine-tuned to stoichiometric conditions.

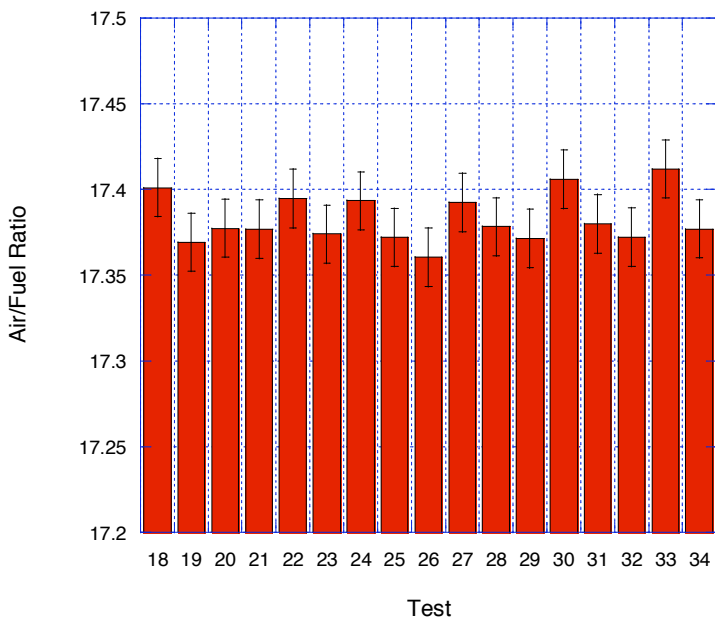


Figure 4-2: Air-Fuel Ratio for CNG testing

4.2.2 Spark Advance

Spark-ignited engines use an electrically generated charge to begin the combustion process in the cylinder. In the vehicle used in this research, spark timing maps optimized performance by controlling the engine to “learn” the most efficient HCNG spark timing. These map data points were read off of the scan tool during the testing, at vehicle speeds of 15 miles per hour and 30 miles per hour. The average values for spark advance timings using CNG and HCNG are found in Table 4-1. While there

was some variation in spark advance at the same speed and load, this was probably a result of the highly sensitive nature of the throttle which was difficult to control. This data shows that spark advance is a function of throttle position and unaffected by fuel composition.

Table 4-1: Spark Advance Timings

Vehicle Speed: 15 MPH

<u>Transmission Position D (low speed)</u>	CNG Spark Advance (BTDC)	HCNG Spark Advance (BTDC)
10 hp	23	23.5
20 hp	22.5	22.5
30 hp	22	22
<u>Transmission Position D1 (high speed)</u>	CNG Spark Advance (BTDC)	HCNG Spark Advance (BTDC)
10 hp	27.5	27.5
20 hp	25	25.5
30 hp	24	24.5

Vehicle Speed: 30 MPH

<u>Transmission Position D (low speed)</u>	CNG Spark Advance (BTDC)	HCNG Spark Advance (BTDC)
10 hp	22.5	22.5
20 hp	20.5	21
30 hp	19.5	19.5
<u>Transmission Position D1 (high speed)</u>	CNG Spark Advance (BTDC)	HCNG Spark Advance (BTDC)
10 hp	32	32.5
20 hp	31	31
30 hp	29.5	30.5

4.3 Characteristics of Hydrogen Combustion

Combustion characterization describes how the air-fuel charge inside the cylinder is burned. In the next section, the effect of 33 percent hydrogen on natural gas combustion in the spark-ignition engine at 1350 RPM, 40 percent wide-open throttle and 1370 RPM, 67 percent wide-open throttle are compared. This section shows the pressure measurements, heat release trends, and combustion duration, as well as temperature and coefficient of variance.

4.3.1 Pressure

Pressure measurements are useful tools for indicating variations in the phasing and duration of combustion. They are also used to calculate the apparent heat release rate.

Under identical speed and load conditions, pressure during combustion of HCNG was greater than that of neat natural gas. Two examples of pressure during a combustion cycle from the 30 miles-per-hour test are found in Figure 4-3 and Figure 4-4. Karim et al. [24] observed an increase of pressure of 1 bar per 10 percent hydrogen addition during lean burn conditions. In this study, at stoichiometric conditions, a larger increase in peak pressure is seen. A 5 bar increase in peak pressure with HCNG is observed, equivalent to a 1.5 bar increase per 10 percent hydrogen addition.

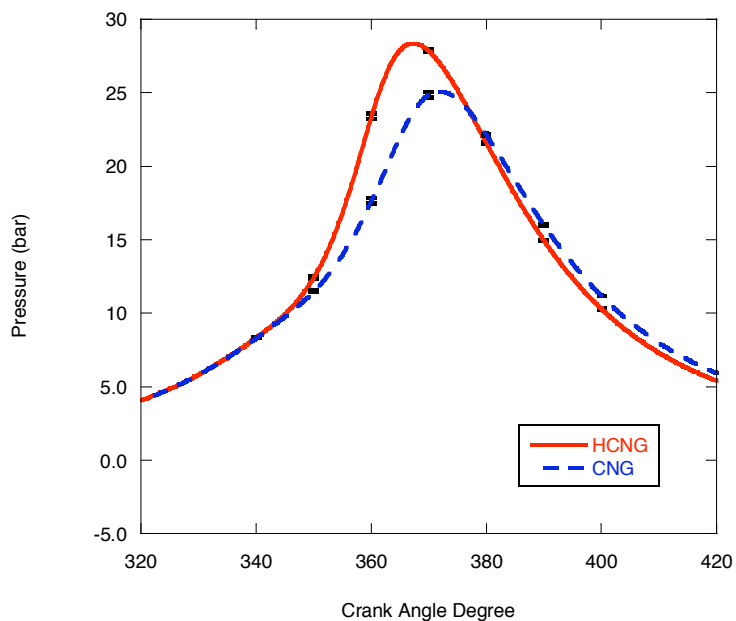


Figure 4-3: 200 Cycle Averaged Pressure Trace, 1350 RPM, 10 horsepower road load

Volume change and combustion have the largest effects on cylinder pressure [11]. Since there are no volumetric changes in the cylinder, the pressure increases that occur in the cylinder are a result of the HCNG combustion process. As Figure 4-3 and Figure 4-4 show, HCNG increases the pressure at a much more rapid pace than CNG, peaking close to top dead center. Pressure after spark discharge is indicative of heat release of the fuel during combustion. Peak pressure occurring closer to top dead center more closely resembles the Otto cycle, which indicates an increase in the thermal efficiency of the combustion.

Error bars show the 95 percent confidence interval on the pressure data during areas of high uncertainty. Because the pressure is used to calculate the rest of the combustion statistics in this section, it is assumed the characteristics of combustion are statistically significant.

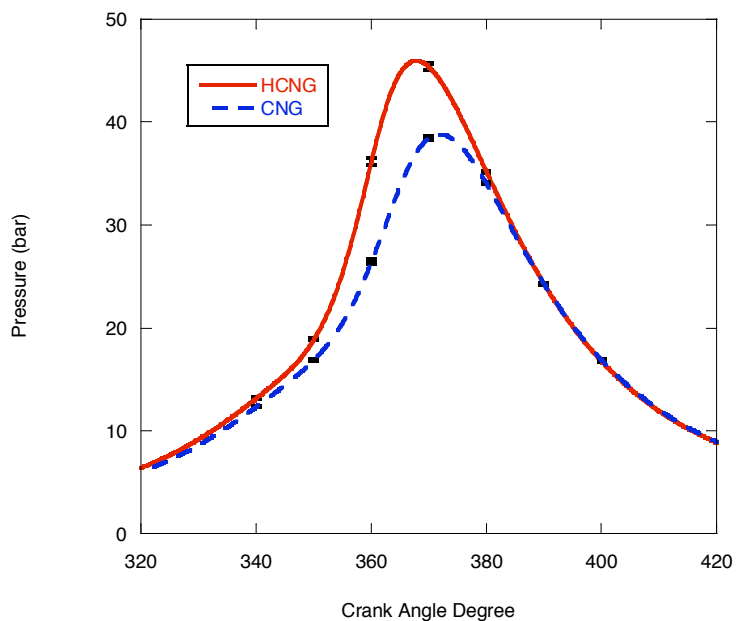


Figure 4-4: 200 Cycle Averaged Pressure Trace, 1370 RPM, 30 horsepower road load

4.3.2 Apparent Heat Release

To study the effect of fuel on bulk combustion characteristics, heat release analyses were performed at all testing conditions. The heat release rates were different between the two fuels, as shown in Figure 4-5 and Figure 4-6. These figures showed that hydrogen addition resulted in a faster release of fuel energy, when compared with CNG. The results also indicated that HCNG combustion peak heat release rate increases 25 percent and occurs 9 crank angle degrees before that of CNG.

Increased heat release early in the power stroke puts extra stress on the structural integrity of the cylinder, and increases NO formation, but it also allows for best indicated thermal efficiency. In Figure 4-5 and Figure 4-6 HCNG releases more than half of the

energy during the compression stroke, before top dead center. Energy released when the volume of the cylinder is decreasing works against the motion of the piston decreasing indicated work, which causes a decrease in the power output of the cylinder. These are considerable throttling losses that detract from the thermal efficiency of the combustion process with HCNG.

The heat release characteristics in this study exhibit non-ideal combustion. Heywood [11] states that addition of exhaust gas recirculation (EGR) increases the burn duration in the cylinder. In the case study, EGR of 20 percent increases the flame development angle and combustion duration 50 percent. If the exhaust gas recirculation valve was connected, it would retard heat release, reducing losses in indicated work.

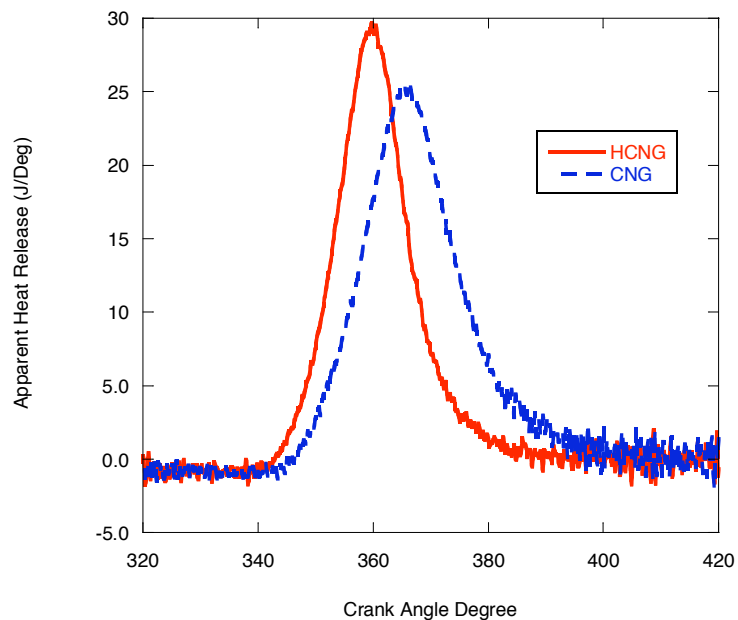


Figure 4-5: Heat Release Rate 1350 RPM, 10 horsepower Road Load

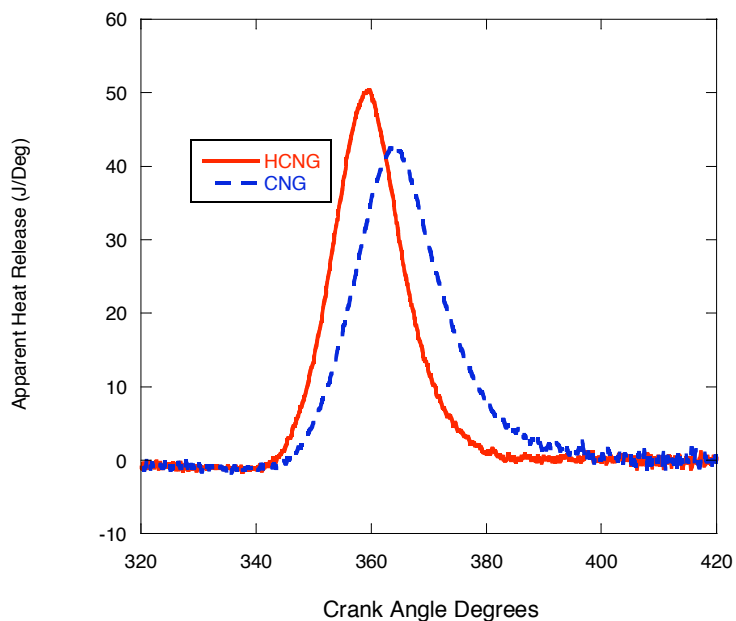


Figure 4-6: Heat Release Rate 1370 RPM, 30 horsepower Road Load

4.3.2 Fuel Burning Rates

The computed mass fraction burned approximates the burned mass inside the cylinder and are an indicator of combustion performance within the cylinder. Normalized heat release is representative of the mass fraction burned in the cylinder. Figure 4-7 and Figure 4-8 show the normalized cumulative heat release that occurred at 1350 and 1370 RPM, both at 30 hp road load.

It is advantageous to characterize different stages of combustion by the duration in crank angle degrees. The crank angle degrees covered during each stage of combustion are indicative of the combustion process. Figure 4-7 and Figure 4-8 show that compared with natural gas, hydrogen addition decreases the flame development angle and

combustion duration. Hydrogen also causes more fuel to burn before top dead center. This early burn of the fuel releases energy during the compression stroke, which results in a decrease in thermal efficiency.

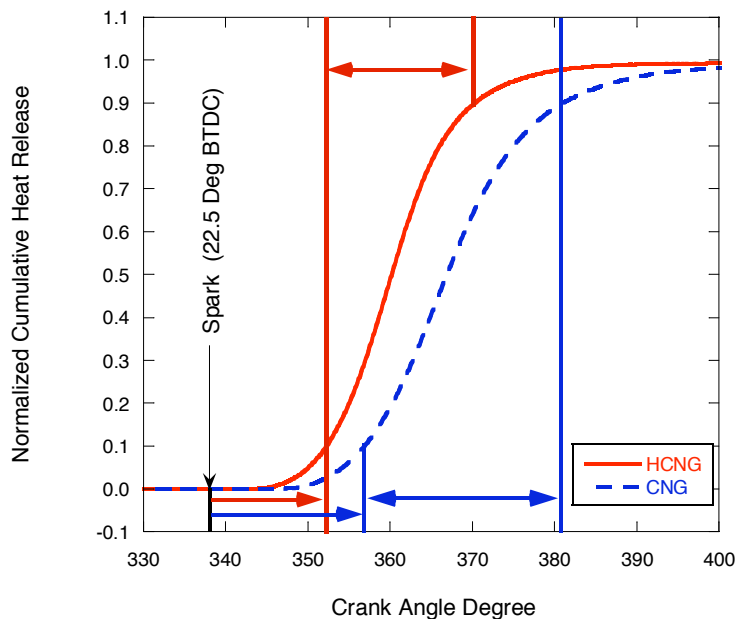


Figure 4-7: Normalized Heat Release 1350 RPM, 10 hp Road Load

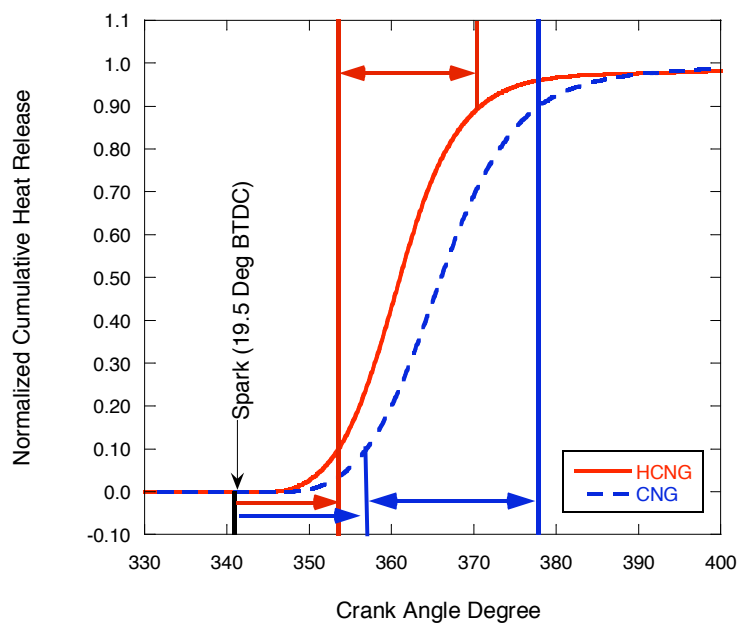
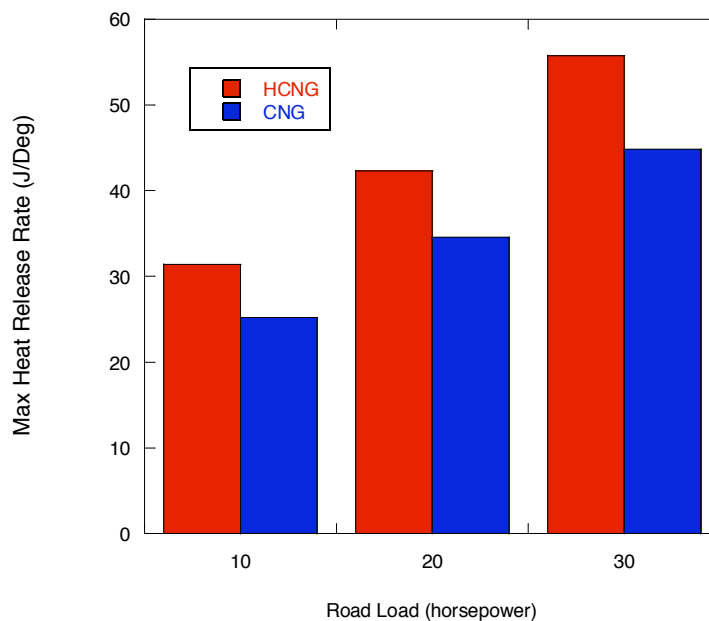


Figure 4-8: Normalized Heat Release 1370 RPM, 30 hp Road Load

The quicker burn reduces the amount of time during the combustion cycle that the gases are at high temperature, which results in a reduction in heat transfer losses. The slope of the line in Figures 4-7 and Figure 4-8 during the combustion duration is indicative of the speed of the fuel burn. While both fuels begin combustion at the same time, the HCNG combustion reaction progresses much faster.

Figure 4-9 shows the peak heat release rate for the tests run at 30 miles per hour. A higher heat release rate indicates a larger mass of fuel being burned per crank angle degree. As this figure shows, the addition of hydrogen to natural gas increases the peak burn rate of the fuel and is independent of load. At all testing conditions, HCNG increases the maximum burn rate of the fuel by 25 percent, compared with CNG.



4-9: Peak Heat Release Rate at 1350, 1360 and 1370 RPM, 30 mph

4.3.3 Calculated In-Cylinder Temperature

An increase in bulk cylinder temperature contributes to heat loss to the surroundings and drives NO formation. The temperatures calculated using the pressure data show that the rapid combustion of HCNG increase the bulk cylinder temperature.

In this study, an increase in temperatures from 7 to 10 percent was observed with hydrogen addition. Figure 4-10 and Figure 4-11 show the single-zone analysis of bulk cylinder temperature at 1350 and 1370 RPM. It must be noted that during normal operation, the vehicle as modified by Collier Technologies employed a significant amount of supplemental exhaust gas recirculation in order to lower combustion temperatures and prevent NO_x formation.

The peak temperature for HCNG combustion occurs closer to top dead center, when the volume of the cylinder is the smallest. Intense heat at this stage in combustion increases the transfer of heat to the combustion chamber surfaces, which reduces the pressure of the system. Increased temperature is sustained across a longer period during HCNG combustion than with CNG. The more time HCNG spends at high temperature, the more NO formation occurs.

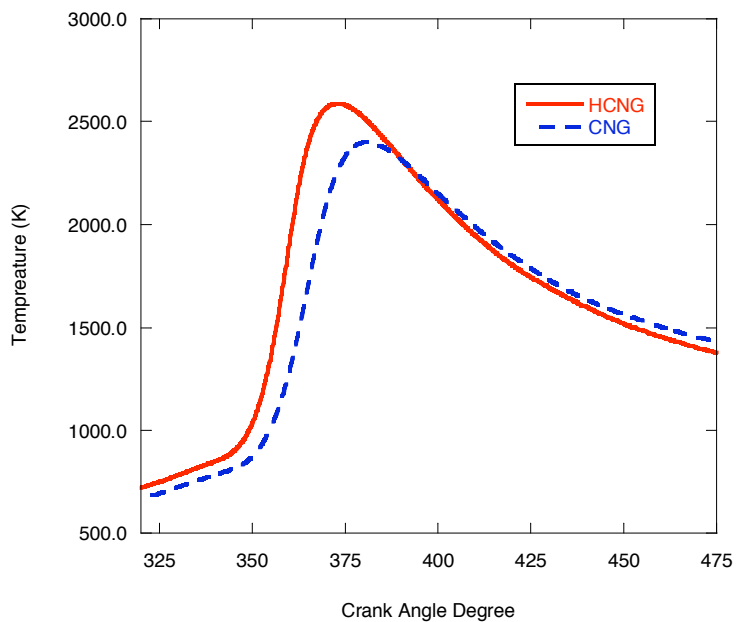
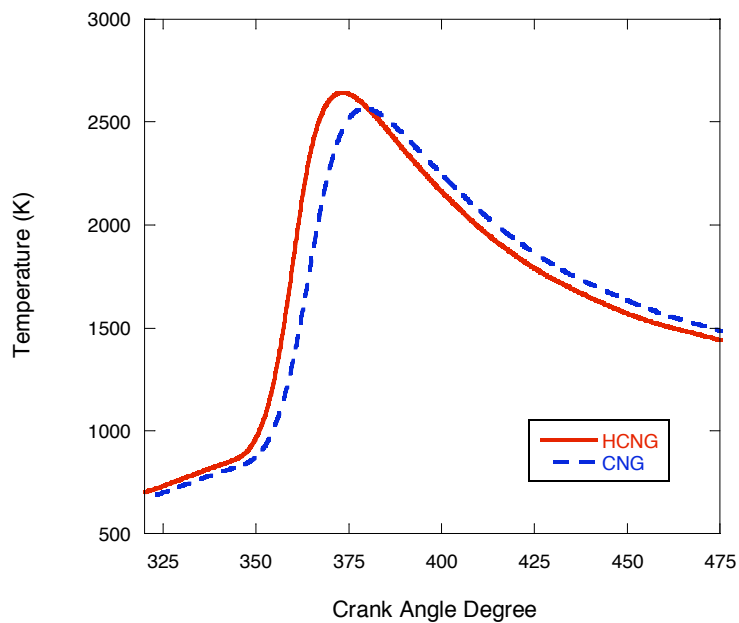


Figure 4-10: Bulk Cylinder Temperature 1350 RPM, 10 hp Road Load



4-11: Bulk Cylinder Temperature 1370 RPM, 30 hp Road Load

4.3.4 Heat Transfer

Reducing the heat loss to the surroundings can increase the thermal efficiency of combustion. Previous findings [1] have attributed increased thermal efficiency in HCNG combustion, when compared to CNG combustion, to a faster burn time. This increased efficiency with HCNG occurs because lower combustion duration reduces the time for which the cylinder is at high temperatures, losing heat to the surroundings. In this study, the amount of heat lost to the outer walls and carried away by the coolant was calculated using the Woschni heat transfer correlation.

The expansion stroke is where the most significant heat transfer losses occur. There, the heat transfer will cause the gas pressure in the cycle to fall below isentropic

expansion as the volume increases, resulting in a decrease in thermal efficiency. Figure 4-12 and Figure 4-13 show the Net Heat Release and Heat Transfer at 1350 and 1370 RPM. The figures indicate the cumulative heat transferred as net work on the system, Q_n , and heat transferred to the surroundings, Q_{ht} .

More heat is transferred to the surroundings because of elevated combustion temperatures with HCNG combustion. While previous published work has stated that HCNG's decrease in combustion duration would reduce the heat transfer to the surroundings, an earlier start of combustion and higher bulk cylinder temperatures result in greater transfer of energy to the cylinder wall.

It is interesting to note that as much as 50 percent of the energy available in the cylinder is lost to the coolant. While this number appears to be high, low speed and load conditions for a six-cylinder spark-ignited engine at the same engine speed were found by Ament et al. [34] to lose 50 percent of the fuel heating value to the coolant load. This validates the high heat transfer rates for HCNG and CNG combustion found in this study.

Net heat release is equal to the sensible energy change and work transfer to the piston [11]. Since these two traces are run at the same operating conditions, it can be assumed that the work transferred to the piston is equal. Net natural gas combustion has a higher net heat release than HCNG because of the increased losses via heat transfer to the surroundings.

As the engine load increases, the difference in energy losses between the HCNG and CNG is reduced. As the engine load increases, a higher percentage of fuel energy is converted to work on the piston, with only 40 percent of energy lost to the surroundings.

During the increase engine load, combustion is more complete which reduces the impact of the hydrogen.

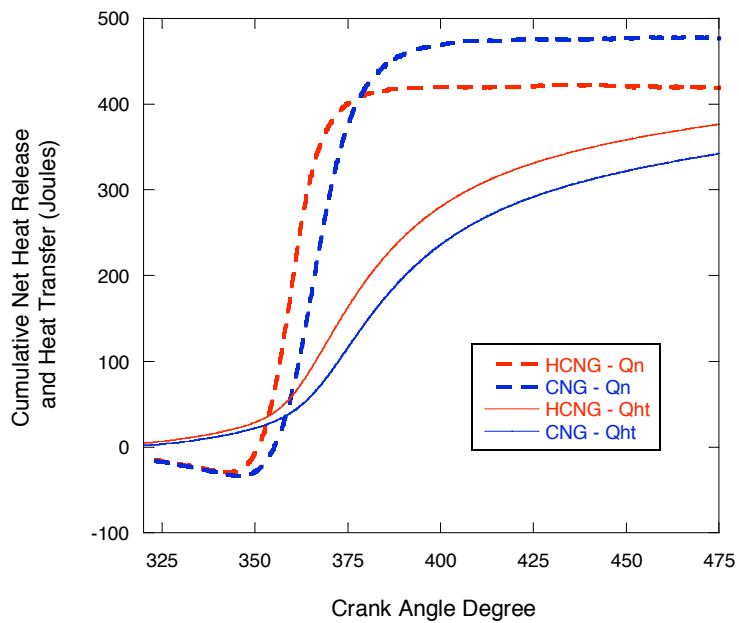


Figure 4-12: Neat Heat Release and Heat Transfer 1350 RPM, 10 hp Road Load

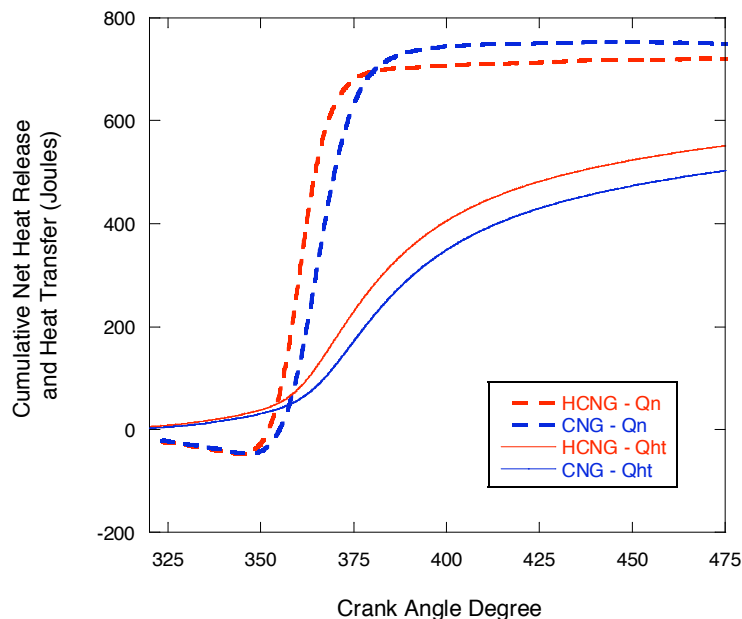


Figure 4-13: Net Heat Release and Heat Transfer 1370 RPM, 30 hp Road Load

4.3.4 Coefficient of Variance

Reduction in coefficient of variance of indicated mean effective pressure (COV) is one of the main advantages of hydrogen addition to natural gas. This study recorded the values of COV at all test conditions. All values fell within the acceptable limits of engine stability. All conditions reported a COV of less than 2.5. The data shows that there is no advantage of COV with HCNG under these near stoichiometric combustion conditions. Any variance in combustion was probably due to cylinder residuals, which fluctuated in composition and quantity, or because of poor throttle control by the driver during the testing sequence. Low coefficient of variance of around 1 percent has been

reported in the literature [15] during stoichiometric combustion of HCNG and CNG. The investigation in the COV of HCNG and CNG combustion is of interest for lean combustion conditions. With increasing the excess air, combustion stability decreases. Hydrogen has been shown to increase combustion stability at these conditions, but its effect is negated during stoichiometric combustion.

4.4 Combustion Trends

Hydrogen has been shown to assist combustion at lower loads and reduce combustion performance at higher loads [5, 15]. This section discusses combustion performance, which was evaluated at 30 miles per hour at various speeds and loads. The goal was to determine the effect of hydrogen on natural gas combustion under varying conditions. Three test points were acquired at transmission position “D” and “D1,” at road loads of 10, 20, and 30 horsepower.

4.4.1 Combustion Duration

Increased load on the vehicle increases the load on the engine. Road load increases can be from uphill conditions, accessory loads, or road conditions. As the load increases, the rate of combustion increases rapidly because more fuel must be burned in the combustion cycle to produce the same power output. To produce the same amount of output from the cylinder, the engine must increase injection time in order to inject more fuel into the cylinder. Hydrogen content of 33 percent in natural gas represents only 9

percent of the fuel energy, which means some power is lost when using HCNG due to the reduction of volumetric energy content.

Figure **4-14** demonstrates the effects of hydrogen during a significant load increase on the engine. As the engine load increases, overall combustion duration decreases. According to scan tool data, the load on the engine during a road load of 10, 20 and 30 horsepower is 40, 57 and 66 percent, respectively, of wide-open throttle. As the load on the engine increases significantly from 40 to 67 percent throttle, reduction in combustion duration with hydrogen addition is reduced.

Figure **4-15** shows high-speed tests in which HCNG reduces combustion duration. High engine speed maximizes HCNG speed reduction [11]. Hydrogen addition at these high combustion duration points reduces the crank angle interval covered by 25 percent. The engine load conditions at this transmission position are 35, 40 and 43 percent wide-open throttle. At these small engine load increases, the combustion duration does not change significantly.

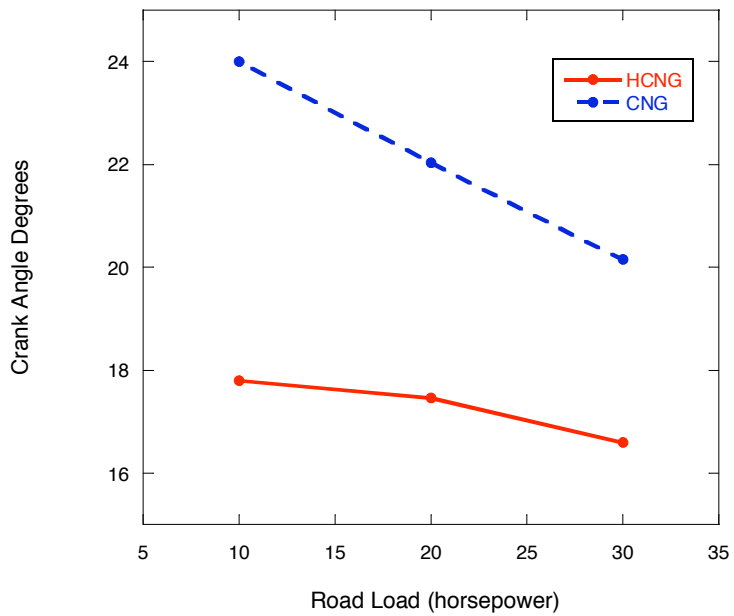


Figure 4-14: Combustion Duration at 1350, 1360 and 1370 RPM

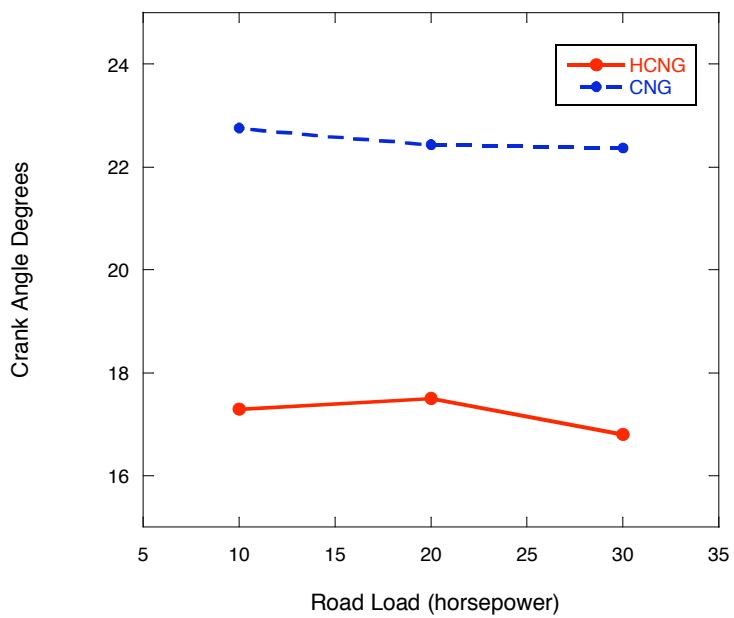


Figure 4-15: Combustion Duration at 3700, 3750, 3800 RPM

4.4.2 Flame Development Angle

The flame development angle is the distance from the spark to when 10 percent of the mass of the fuel has burned [11]. Increasing hydrogen addition has proven to decrease the flame development angle in the literature [4]. This early stage of combustion features a mostly laminar flame that forms a spherical flame kernel around the spark plug gap. The flame interacts with the surrounding turbulent flow increasing the surface area of the flame, which increases the propagation speed of the flame. When hydrogen enters the flame kernel, its reaction with the flame front increases the speed at which the reaction zone propagates. Across all testing conditions, HCNG showed a reduction in flame development angle.

Figure 4-16 shows the decrease in flame development angle that occurred in these tests. As the engine load nears 67 percent of wide-open throttle, at a road load of 40 horsepower, the effects of hydrogen are reduced.

As with combustion duration, during high-speed conditions a decrease in the flame development angle is observed during HCNG combustion. This is shown in Figure 4-17. For both indications of combustion speed, the effect of hydrogen addition in reducing flame development angle is more pronounced at higher speeds.

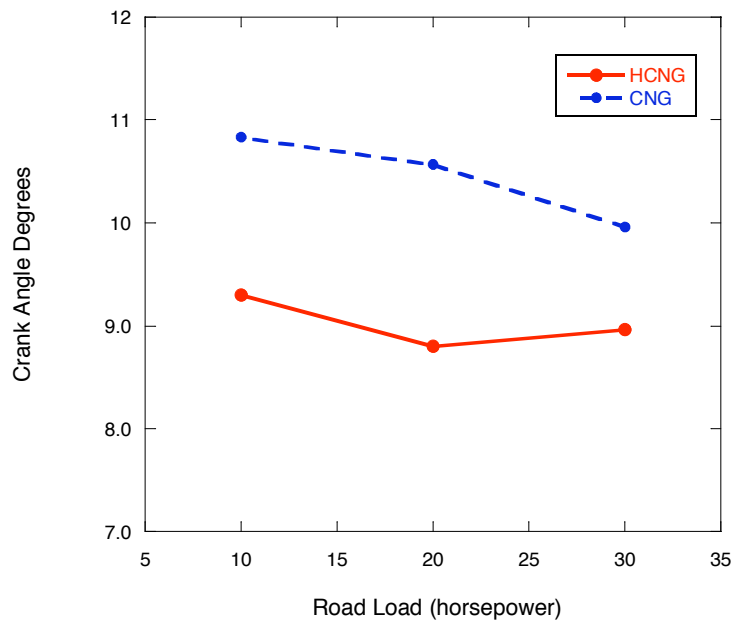


Figure 4-16: Flame Development Angle at 1350, 1360 and 1370 RPM

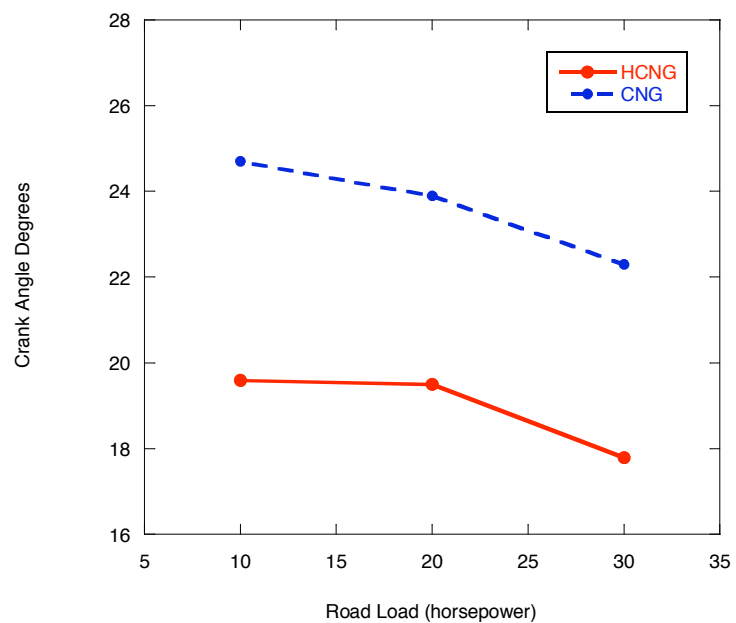


Figure 4-17: Flame Development Angle at 3700, 3750, 3800 RPM

4.4.3 Indicated Thermal Efficiency

Spark-ignition engines use a throttle plate to control engine power. As the throttle plate closes, intake pressure and fuel flow are reduced, resulting in lower intake pressures. These lower pressures contribute to combustion inefficiencies. This effect is clearly seen in Figure 4-18, which illustrates how load increases the thermal efficiency of the engine. The values obtained for indicated thermal efficiency in natural gas engines range from 33 to 38 percent, which is 10 percent higher than that obtained in gasoline spark-ignited engines. The main factor accounting for this discrepancy is that natural gas engines tend to have a higher compression ratio, which increases the thermal efficiency, and inaccuracy of mass measurements from instrumentation can reduce the theoretical energy available.

Many papers cite hydrogen addition as increasing the indicated thermal efficiency of natural gas [4, 35], however Figure 4-18 shows that compressed natural gas has a higher thermal efficiency than HCNG at all loads. While the data shows a deviation from expected thermal efficiency results, it is similar to results found by Bauer et al. [1] when testing an engine running at 700 and 900 rpm. The reduced thermal efficiency observed in this study is a result of the extra heat lost during high temperature combustion of HCNG and increased losses in indicated work due to early combustion. Improvement in thermal efficiency would be observed if EGR was reconnected or spark timing was retarded.

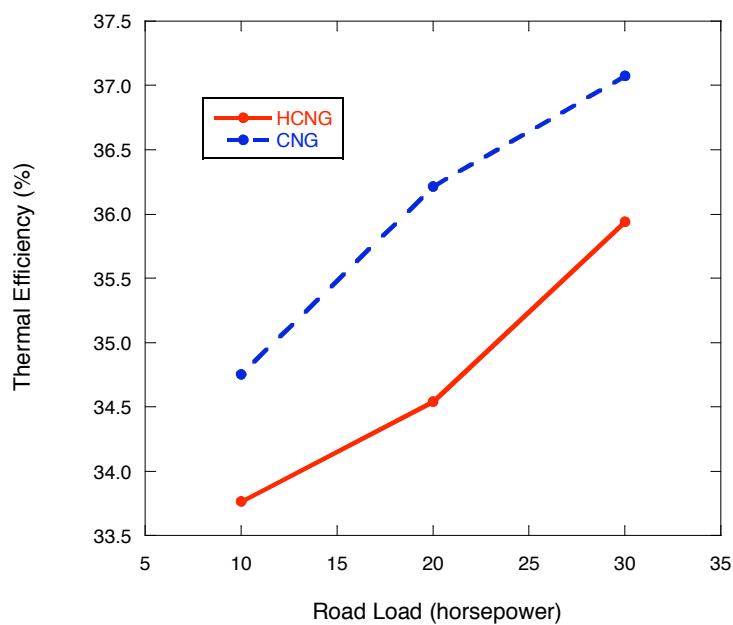


Figure 4-18: Indicated Thermal Efficiency at 1350, 1360 and 1370 RPM

4.5 Emissions Results

The reduction of regulated pollutants is one of the main motivations for HCNG research. In this study, the engine-out exhaust measurements were recorded to determine the pre-catalyst effect of hydrogen addition on natural gas combustion. It was not possible to accurately record the actual load on the engine so the results can only be compared at the same testing conditions.

4.5.1 Carbon Dioxide

Carbon dioxide (CO₂) is a product of complete combustion. Figure 4-19 shows the CO₂ emissions present in the exhaust during this study. It was found that a reduction

of carbon-based fuel in the charge reduces the CO₂ formation by 10 percent. Reductions in CO₂ were independent of increased load. Natural gas fuel contains approximately 7.2 percent more carbon per unit energy than the HCNG used in the study. The engine-out CO₂ differences between the fuels corresponded with the amount of carbon oxidized in the combustion process.

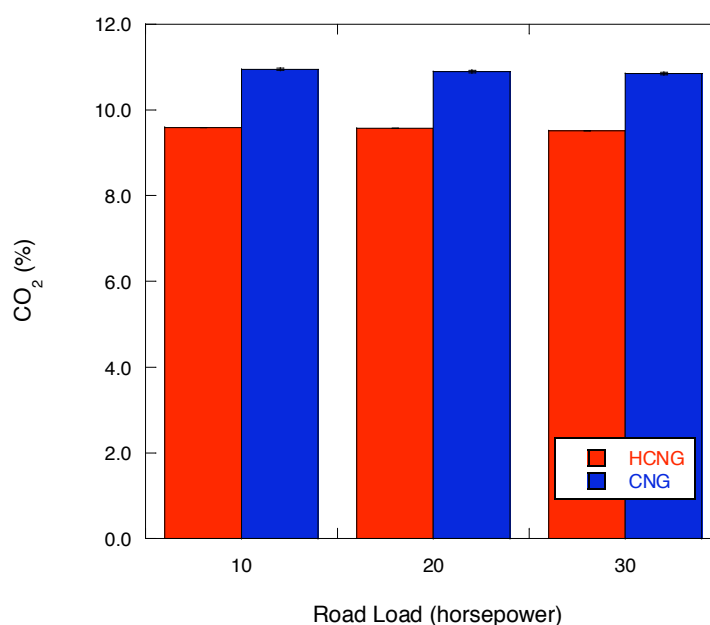


Figure 4-19: CO₂ at 1350, 1360 and 1370 RPM

4.5.2 Carbon Monoxide Emissions

Carbon monoxide (CO) emissions are produced in high amounts during part load conditions due to incomplete oxidation. Decreased CO emissions have been observed by Andersson [15] at stoichiometric conditions. Figure 4-20 shows the carbon monoxide emissions produced over increasing loads. CO oxidation was enhanced by the higher

temperatures of the postflame gases during HCNG combustion. While reductions in CO concentration are seen with hydrogen addition, the results are statistically insignificant due to the range covered by the error bars. Therefore no conclusions can be drawn.

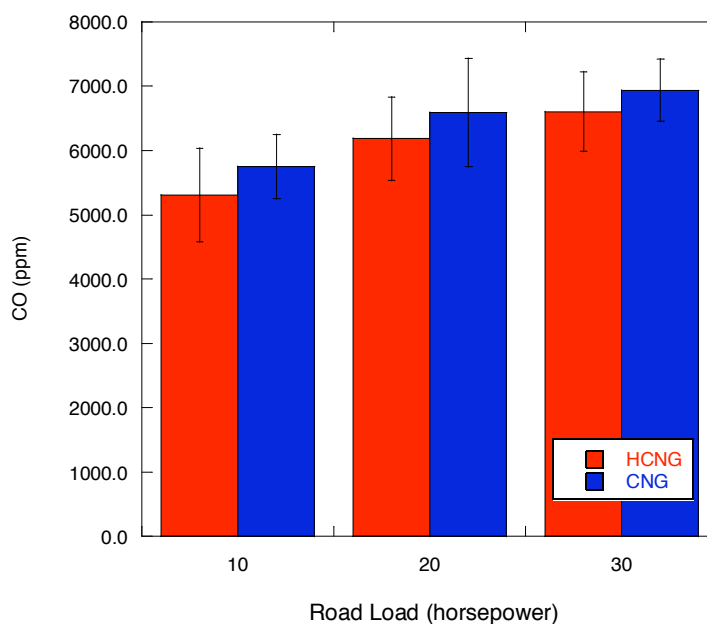


Figure 4-20: CO at 1350, 1360 and 1370 RPM

4.5.3 Oxides of Nitrogen

High temperatures that occur during combustion are the main contributor to nitric oxide (NO) formation. In this study, the test vehicle controlled the air-fuel ratio to run stoichiometrically, which increased peak temperatures over lean-burn combustion. These higher temperatures were amplified by the hydrogen addition. Increased exposure to these post-combustion temperatures drove NO production, as shown in Figure 4-21. An

increase in engine-out oxides of nitrogen emissions with HCNG has also been observed in the literature [5, 15, 22].

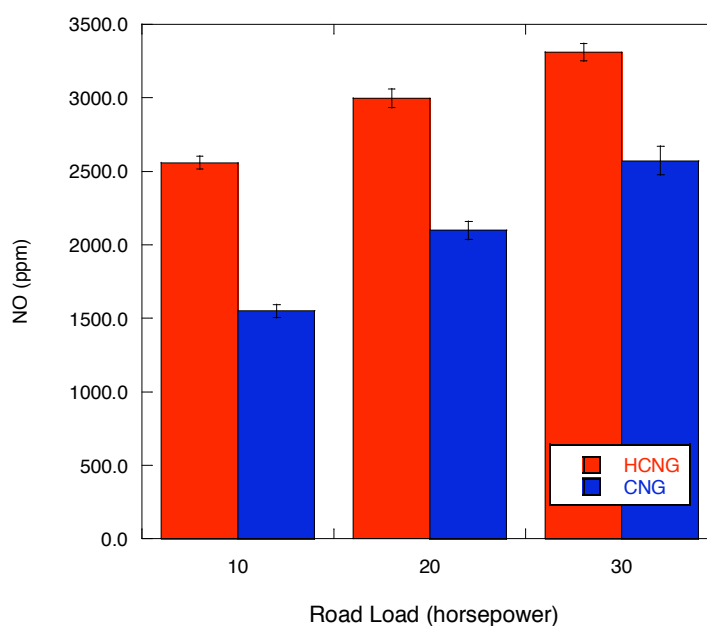


Figure 4-21: NO at 1350, 1360 and 1370 RPM

4.6 Vehicle Speed

Two different vehicle speeds of 15 and 30 miles per hour were measured to determine the effect that speed has on combustion performance. After all of the calculations were performed, combustion performance in the cylinder when the vehicle is traveling at 15 miles per hour is nearly identical to when it is travelling at 30 miles per hour. Table 4-2 shows the engine load as a percentage of wide open throttle according to the ECU. Vehicle tests run at 15 miles per hour have a slightly lower load than the tests run at 30 miles per hour. Combustion trends are very similar at the same load

positions. The trends observed during increased loading conditions already have been addressed during this study and are not reported in detail in this section.

Table 4-2: Road Load at Low Speed Test Settings

Road Load (hp)	15 mph Load (%)	30 mph Load (%)
10	38.00	42.00
20	53.00	57.00
30	58.00	65.00

Chapter 5

Conclusions and Future Work

5.1 Conclusions

Based on engine testing and simulation results, the following conclusions were drawn:

1. Stoichiometric combustion of HCNG reduces ignition delay and creates conditions conducive for a faster burn.
2. HCNG reacts faster than natural gas, producing a decrease in combustion duration. Apparent heat release rates are advanced which work against the motion of the piston.
3. Bulk cylinder temperatures of HCNG increase energy losses to the surroundings.
4. Work against the piston and heat transfer to the surroundings reduces thermal efficiency of HCNG compared with CNG.
5. The effects of hydrogen addition, (i.e., decreased flame development angle and combustion duration, increased temperatures, increased heat loss), decrease as the load on the engine increases.
6. At the same road load, changes in vehicle speed only slightly reduce the load on the engine, resulting in similar combustion performance.

5.2 Future Work

During this study, combustion performance was measured in the vehicle with no modifications except for fuel to determine the effect of hydrogen in natural gas combustion in a vehicle. Limits due to insufficient resources prevented measurement of fully functional combustion performance in the vehicle. For a more in-depth study, the following suggestions for future work are proposed.

1. Reprogram the ECU to optimize the engine to run based on the test fuel for combustion comparison.
2. Increase measuring equipment on the vehicle to measure actual operating conditions including EGR, fuel rail pressures to understand in-cylinder combustion processes better.

Bibliography

- [1] C. G. Bauer and T. W. Forest, "Effect of hydrogen addition on the performance of methane-fueled vehicles. Part I: effect on S.I. engine performance," *International Journal of Hydrogen Energy*, vol. 26, pp. 55-70, 2001.
- [2] P. Forster and V. Ramaswamy, "Changes in Atmospheric Constituents and in Radiative Forcing," in *Changes in Atmospheric Constituents and in Radiative Forcing. In: Climate Change 2007: The Physical Science Basis. Contribution of Working Group I to the Fourth Assessment Report of the Intergovernmental Panel on Climate Change*: Cambridge University Press, Cambridge, United Kingdom and New York, NY, USA., 2007.
- [3] T. Truett, "Literature Review for the Baseline Knowledge Assessment of the Hydrogen, Fuel Cells, and Infrastructure Technologies Program," O. R. N. Laboratory, Ed., 2003.
- [4] M. R. Swain, M. J. Yusef, Z. Dulger, and M. N. Swain, "The Effects of Hydrogen on Natural Gas Engine Operation," *Society of Automotive Engineers Paper No. 932775*, 1993.
- [5] A. Cattelan and J. Wallace, "Exhaust Emission and Energy Consumption Effects from Hydrogen Supplementation of Natural Gas," in *Fuel & Lubricants Meeting & Exposition Toronto, Ontario: Society of Automotive Engineers Paper No. 960858*, 1995.
- [6] I. Glassman, *Combustion*, 3rd ed.: Academic Press, Inc, 1996.
- [7] "Hydrogen Commerce," <http://www.hydrogencommerce.com>, Accessed January, 2008.
- [8] A. L. Dicks, "Hydrogen Generation from Natural Gas for the Fuel Cell Systems of Tomorrow," *Journal of Power Sources*, vol. 61, pp. 113-124, 1996.
- [9] D. Guro, "Development of a Turnkey H2 Refueling Station," Air Products and Chemicals, Inc, Allentown, PA 2006.
- [10] S. O. Akansu, Z. Dulger, N. Kahraman, and T. N. Veziroglu, "Internal combustion engines fueled by natural gas-hydrogen mixtures," *International Journal of Hydrogen Energy*, vol. 29, pp. 1527-1539, 2004.
- [11] J. Heywood, *Internal Combustion Engine Fundamentals*: McGraw-Hill, Inc., 1988.
- [12] P. M. Najt and T. Kuo, "An Experimental and Computational Evaluation of Two Dual-Intake-Valve Combustion Chambers," *Society of Automotive Engineers Paper No. 902140*, 1990.
- [13] K. M. Chun and J. Heywood, "Estimating Heat-Release and Mass-of-Mixture Burned from Spark-Ignition Engine Pressure Data," *Combustion Science and Technology*, vol. 54, pp. 133-143, 1987.
- [14] M. J. Zucrow, *Gas Dynamics* vol. 1. New York: John Wiley & Sons, 1976.
- [15] T. Andersson, "Hydrogen Addition for Improved Lean Burn Capability on Natural Gas Engine," Lund Institute of Technology 2002.

- [16] G. Yu, C. K. Law, and C. K. Wu, "Laminar Flame Speeds of Hydrocarbon + Air Mixtures with Hydrogen Addition," *Combustion and Flame*, pp. 339-347, 1985.
- [17] K. Collier, N. Mullian, D. Shin, and S. Brandon, "Emission Results from the New Developments of a Dedicated Hydrogen-Enriched Natural Gas Heavy Duty Engine," Society of Automotive Engineers, 2005.
- [18] S. Priyadarshi, "Effects of Hydrogen Enrichment on Methane/Air Premixed Laminar Flames Under SI Engine Conditions," in *Mechanical and Nuclear Engineering*. vol. Master of Science State College: The Pennsylvania State University, 2006, p. 128.
- [19] P. Dagaut and A. Nicolle, "Experimental and detailed kinetic modeling study of hydrogen-enriched natural gas blend oxidation over extended temperature and equivalence ratio ranges," *Proceedings of the Combustion Institute*, vol. 30, pp. 2631-2638, 2005.
- [20] R. W. Schefer, "Hydrogen Enrichment for improved lean flame stability," *International Journal of Hydrogen Energy*, vol. 28, pp. 1131-1141, 2003
- [21] D. Karner and J. Francfort, "Dodge Ram Wagon Van – Hydrogen/CNG Operations Summary," U. S. D. o. Energy, Ed.: Idaho National Engineering and Environmental Laboratory, 2003.
- [22] B. Nagalingam, F. Duebel, and K. Schmillen, "Performance Study Using Natural Gas, Hydrogen-Supplemented Natural Gas and hydrogen in AVL Research Engine," *International Association for Hydrogen Energy*, vol. 8, pp. 715-520, 1983.
- [23] K. Collier, R. L. Hoekstra, N. Mulligan, C. Jones, and D. Hahn, "Untreated Exhaust Emissions of a Hydrogen-Enriched CNG Production Engine Conversion," in *International Congress & Exposition* Detroit, Michigan: Society of Automotive Engineers, 1996.
- [24] G. A. Karim, I. Wierzba, and S. Boon, "Some Considerations of the Lean Flammability Limits of Mixtures Involving Hydrogen," *International Journal of Hydrogen Energy*, vol. 10, pp. 117-123, 1985.
- [25] T. K. Jensen and J. Schramm, "Hydrocarbon Emissions from Combustion of Mixtures of Natural Gas and Hydrogen Containing Producer Gas in a SI Engine," *Society of Automotive Engineers Paper No. 2001-01-3532*, 2001.
- [26] G. Pede, E. Rossi, M. Chiesa, and F. Ortenzi, "Test of Blends of Hydrogen and Natural Gas in a Light-Duty Vehicle," *Society of Automotive Engineers Paper No. 2007-01-2045*, 2007.
- [27] C. Anastatia and G. Pestana, "A Cylinder Pressure Sensor for Closed Loop Engine Control," *Society of Automotive Engineers Paper No. 870288*, 1987.
- [28] M. Hubbard, P. D. Dobson, and J. D. Powell, "Closed Loop Control of Spark Advance Using a Cylinder Pressure Sensor," *Journal of Dynamics Systems*, 1976.
- [29] J. Y. Wong, *Theory of Ground Vehicles*, Second ed., Wily-Interscience, 1993.
- [30] "U.S. DOE Energy Efficiency and Renewable Energy Home Page," <http://www.do.gov>, Accessed January 2008.
- [31] Melanie Fox, personal communication, 2008.

- [32] T. K. Hayes, L. D. Savage, and S. C. Sorenson, "Cylinder Pressure Data Acquisition and Heat Release Analysis on a Personal Computer," *Society of Automotive Engineers Paper No. 860029*, 1986.
- [33] R. Spindt, "Air-Fuel Ratios From Exhaust Gas Analysis," *Society of Automotive Engineers Paper No. 650507*, 1965.
- [34] F. Ament, D. J. Patterson, and A. Mueller, "Heat Balance Provides Insight into Modern Engine Fuel Utilization," *SAE paper 770221*, 1977.
- [35] R. Sierens and E. Rosseel, "Variable Composition Hydrogen/Natural Gas Mixtures for Increased Engine Efficiency and Decreased Emissions," *Journal of Engineering for Gas Turbines and Power*, vol. 122, pp. 135-140, 2000.

Appendix A
Fuel Properties

A.1 Natural Gas Composition

Table A-1: Natural Gas Composition

Natural Gas Constituents	% Volume
CH ₄	89.94
C ₂ H ₆	5.26
C ₃ H ₈	0.66
C ₄ H ₁₀	0.05
H ₂	0.00
N ₂	4.08

A.2 Hydrogen-Natural Gas Composition

Table A-2: HCNG Composition

HCNG Constituents	% Volume
CH ₄	60.26
C ₂ H ₆	3.53
C ₃ H ₈	0.44
C ₄ H ₁₀	0.04
H ₂	33.00
N ₂	2.74

A.3 Calculated Fuel Characteristics

Table A-3: Calculated Fuel Characteristics

	CNG	HCNG
Density (g/L)	0.7822	0.5538
LHV (kJ/kg)	46402	50358
Stoichiometric Air Fuel Ratio	17.18	18.10

Appendix B

Matlab Heat Release Code

B.1 Matlab Code programmed in version 2007b

```
% Program written by Jamie Clark, September 2007
% Updated February 1, 2008

% Program reads Pressure and Volume Data from pressure traces

% Data is taken to calculate heat release profile

clc
clear all

% read data files
input = dlmread ('C:\Documents and Settings\Jamie\Desktop\Tests
9_7_07\33', '\t', 1);

%test properties
speed = 1350; %speed in rpms
intakeAir = 110; %intake air degF
massair = 42.7; %mass flow of air in g/s

% fuel specific properties
afratio = 17.18; %air/fuel ratio of the mixture in cylinder
LHV = 46402; %lower heating value of fuel in kJ/kg
eqrat = 1.0; %equivalent ratio

%CALCULATIONS

% store the data from file in usable matrices
for i = 1:7200
    degCA(i) = input(i,1) + 0.1; % Crank angle position
    CylPres(i) = input (i,2); % In-cylinder Pressure
end

% engine properties
cyl = 8; %number of cylinders in the engine
bore = .09; % m
stroke = .106; % m
cr = 11; % compression ratio
conrod = .1691; % m - connecting rod length
crankrad = .053; % m
```

```

%DAQ properties
delCA = 0.1; %frequency of pressure measurements in degrees

% fuel specific initial conditions
gamma = 1.35; %initialized gamma
Cv = .897; %initialize Cv

% unit conversions
umassair = massair * 60 / 1000; %mass airflow conversion to kg/min
mair = umassair/cyl/(speed/2); % mass flow of air in kg
Tin = ((intakeAir - 32) * 5/9) + 273.15; %convert temp to Kelvin
R = 8.314/29*1000; %initialize R - J/kgK
rps = speed / 60; %engine speed in radians
sp = 2*stroke*rps; %mean piston speed
f = conrod/crankrad; % for heat transfer
mfuel = mair/afratio; %calculate mass of fuel

% Heat Transfer Calcs
C1 = 2.28; %constant c1 from Heywood
w = C1 * sp; % average flow velocity inside the cylinder for
compression and expansion - can add "+ C2*Vd*Tr/prVr*(Pcyl-Pmotored)"
Twall = 450; %assumed wall temperature in Kelvin

%Engine Volume calculations
Vd = pi*bore^2*stroke/4; %swept volume, displaced volume
Vc = Vd/(cr-1);%clearance volume

for i = 1:7200
    radCA(i) = degCA(i)*pi/180; % convert crank angle position to
radians
    cylVol(i) = Vc + (pi/4 * bore^2) * (crankrad*(1-
cos(radCA(i))+crankrad/(4*conrod)*(1-cos(2*radCA(i))))); %find volume
of cylinder
end

for i = 2:7199 %intermediate pressure smoothing and Net IMEP
    IntPres(i) = (CylPres(i-1) + CylPres(i+1))/2;
    dv(i) = (cylVol(i+1)-cylVol(i-1))/(2*delCA); %calculate dv
(m^3/deg)

    nimep(i) = (CylPres(i)+CylPres(i+1)) * dv(i);
    Nimep = sum(nimep)/2/Vd/10;

    if (i > 1800) && (i < 5400)
        gimep(i) = (CylPres(i)+CylPres(i+1))*dv(i);
        Gimep = sum(gimep)/2/Vd/10;
    end

    ica(i)=degCA(i);
end

for i = 3:7198

```

```

    Pres(i) = ((IntPres(i-1) + IntPres(i) + IntPres(i+1))/3); %smoothed
pressure trace
    Pres(i) = Pres(i)*100000; % convert bar to Pa
    kPres(i)= Pres(i)/1000; %Pressures in kPa
    pca(i) = degCA(i);
end

for i = 5:7195
    dp(i) = (-Pres(i+2)+8*Pres(i+1)-8*Pres(i-1)+Pres(i-2))/(12*delCA);
%calculate dp (Pa/deg)
    ppca(i) = degCA(i);
end

% Calc net IMEP

%initialize dq, T and Q
for i = 3:5436
    dq(i)= 0.0;
    Q(i)= 0.0;
    T(i)= Tin;
    T2(i) = Tin;
    tg(i) = Tin;
    Qtot = 0;
    done10 = 0;
    done50 = 0;
    done90 = 0;
    donesoc = 0;
    pair(i) = 0;
    Re(i) = 0;
    mu(i) = 0;
    Aw(i) = 0;
    hc(i) = 0;
    dQwall(i) = 0;
    Qwall(i) = 0;
    dQw(i) = 0;
    mb(i)=0;
    startmfb=0;
end

% temperature measurements
for i = 2000:5436

    % Calculate Heat Release
    if (i >= 3000) && (i <= 4950)
        dq(i) = (1/(gamma-1))*(gamma*Pres(i)*dv(i)+cylVol(i)*dp(i));
%solve Instantaneous Heat release J/deg
        Q(i) = dq(i)* delCA + Q(i-1); %Cumulative heat Release in J
    end

    % first temperature calculation
    dt(i) = 1/ ((mair + mfuel)*Cv)*((dq(i)/1000)-kPres(i)*dv(i));
%calculate change in temperature
    T(i) = dt(i) * delCA + T(i-1); %intergrate temp

```



```

% second temperature calculation
dt2(i) = 1/ ( (mair + ((Q(i)/1000)/LHV))*Cv)*(dq(i)/1000 - kPres(i)
* dv(i));
T2(i) = dt2(i) * delCA + T2(i-1);

% third Temperature Calculation
tg(i) = (Pres(i) * cylVol(i)) / (R * (mair + mfuel)) ; % ideal gas
law temperature calculation, gives highest #

% Woschni heat transfer
Aw(i) = (pi * bore ^ 2 / 2) + ((pi * bore * stroke / 2) * (f + 1 -
cos(radCA(i)) + (f ^ 2 - (sin(radCA(i))) ^ 2) ^ 0.5)); % area of wall
exposed unit of m2
%pair(i) = Pres(i)/(R*tg(i)); % density of air
%mu(i) = 3.3 * 10^-7 * tg(i) ^ 0.7/(1 + 0.027 * egrat); %kg/msK
%Re(i) = pair(i) * sp * bore / mu(i); %Renyolds number
hc(i) = 3.26 * bore^-0.2 * (Pres(i)/1000)^0.8 * tg(i)^-0.55 *
w^0.8; % heat transfer coefficient in W/m2K pressure in kPa
dQw(i) = hc(i) * Aw(i) * (T(i) - Twall) ; %J/s
dQwall(i) = dQw(i) * (1/(360*rps)); % convert Watt to J/deg
Qwall(i) = dQwall(i) * delCA + Qwall(i-1); % cumulative heat
transfer

% recalculate gamma
if T(i) > 1000
    gamma = 1.485 - 0.00025527 * T(i) + 1.3911e-7 * T(i)^2 -
3.6506e-11 * T(i)^3 + 3.6966e-15 * T(i)^4;
else
    gamma = 1.3966 + 6.0455e-5 * T(i) - 1.5686e-7 * T(i)^2 -
5.6788e-11 * T(i)^3 + 9.2994e-14 * T(i)^4;
end

%crank angle referencing for plotting
ca(i)=degCA(i);

% recalculate Cv
Cv = .287 / (gamma - 1);

% calculate gross HR
dQgross(i) = dq(i) + dQwall(i); %J/deg
dmb(i) = dQgross(i)/(LHV*1000); % fuel burn rate kg/deg

% Computation of total fraction burned (kg/deg)
mb(i) = dmb(i) * delCA + mb(i-1);

% Integrate to get total heat release
Qgross(i) = Q(i) + Qwall(i);
end

%calculate MFB

for i = 3200:5000

```

```

% convert Q to %
maxQ = max(Q);
minQ = min(Q);
perQ(i) = (Q(i)-minQ) / (maxQ-minQ) * 100;

%determine CA and Pressure at SOC, 10, 50 and 90% mfb
if (perQ(i) == 0)
    startmfb = 1;
end
if (startmfb == 1)
    if (perQ(i) > 0) && (donesoc == 0)
        CASoc = i/10;
        Psoc = kPres(i);
        donesoc = 1;
    elseif (perQ(i) >=10) && (done10 == 0)
        CAMfb10 = i/10;
        Pmfb10 = kPres(i);
        done10 = 1;
    elseif (perQ(i) >= 50) && (done50 == 0)
        CAMfb50 = i/10;
        Pmfb50 = kPres(i);
        done50 = 1;
    elseif (perQ(i) >= 90) && (done90 == 0)
        CAMfb90 = i/10;
        Pmfb90 = kPres(i);
        done90 = 1;
    end
end
mca(i)=degCA(i);
end

% combustion characteristics

tento90 = CAMfb90 - CAMfb10; %10 - 90 mfb
FDA = CAMfb10 - CASoc; % flame development angle

% FDA = CAMfb10 - CASoc; % flame development angle
%efficiencies

% DATA STORAGE & OUTPUT
% save values in matrix form

out(1,1) = max(Q); %J
out(2,1) = max(T); %K
out(3,1) = CASoc; %CAD
out(4,1) = Psoc; %kPa
out(5,1) = CAMfb10; %CAD
out(6,1) = Pmfb10; %kPa
out(7,1) = CAMfb50; %CAD
out(8,1) = Pmfb50; %kPa
out(9,1) = CAMfb90; %CAD

```

```
out(10,1) = Pmfb90; %kPa
out(11,1) = FDA; %flame development angle, total CAD
out(12,1) = tento90; %total CAD
out(13,1) = max(dq); %J/deg
out(14,1) = max(dmb); %kg/deg
out(15,1) = Gimep; %kPa
out(16,1) = Nimep; %kPa

%output(18,1) = combeff;

dlmwrite('output.txt',out)
```

**Appendix A-2.1.A: MS Thesis in Energy & Geo-Environmental
Engineering by Greg Lilik**

The Energy Institute
C211 Coal Utilization Laboratory
University Park, PA 16802

January 29, 2009

National Energy Technology Laboratory
U.S. Department of Energy
626 Cochran's Mill Road
P.O. Box 10940
Pittsburgh, PA 15236-0940

Dear U.S. Department of Energy:

I hereby grant the U.S. Department of Energy permission to use my thesis in the Final Technical Report for Award Number DE-FC26-04NT42233, "Hydrogen-Assisted IC Engine Combustion as a Route to Hydrogen Implementation." My thesis was written with support of the U.S. Department of Energy under this award and copyright for the thesis lies with me.

Sincerely,

A handwritten signature in black ink that reads "Gregory K Lilik". The signature is written in a cursive style with a large initial 'G'.

Gregory K. Lilik
Graduate Research Assistant

The Pennsylvania State University
The Graduate School
The Department of Energy and Geo-Environmental Engineering

HYDROGEN ASSISTED DIESEL COMBUSTION

A Thesis in
Energy and Geo-Environmental Engineering

by
Gregory K. Lilik

© 2008 Gregory K. Lilik

Submitted in Partial Fulfillment
of the Requirements
for the Degree of

Master of Science

May 2008

The thesis of Gregory K. Lilik was reviewed and approved* by the following:

André L. Boehman
Professor of Fuel Science and Materials Science and Engineering
Thesis Advisor

Harold Schobert
Professor of Fuel Science

Angela Lueking
Assistant Professor of Energy and Geo-Environmental Engineering

Daniel C. Haworth
Professor of Mechanical Engineering

Yaw D. Yeboah
Professor of Energy and Mineral Engineering
Head of the Department of Energy and Mineral Engineering

*Signatures are on file in the Graduate School

ABSTRACT

In this study, the effect of hydrogen assisted diesel combustion on conventional and advanced combustion modes was investigated on a DDC/VM Motori 2.5L, 4-cylinder, turbocharged, common rail, direct injection light-duty diesel engine, with exhaust emission being the main focus. Hydrogen was substituted for diesel fuel on a percent energy basis of 0%, 2.5%, 5%, 7.5%, 10% and 15%. The conventional combustion modes studied consisted of four engine combinations of speed and load (1800 rpm at 25% of maximum output, 1800 rpm at 75% of maximum output, 3600 rpm at 25% of maximum output, and 3600 rpm at 75% of maximum output). A significant retarding of injection timing by the diesel fuel injection timing map in the engine's electronic control unit (ECU) was observed during the increased aspiration of hydrogen. The retarding of injection timing resulted in significant emission reductions, however, the same emission reductions were achieved without aspirated hydrogen by manually retarding the injection timing. Subsequently, hydrogen assisted diesel combustion was conducted, with the pilot and main injection timings locked, to study the effects caused directly by hydrogen addition.

Hydrogen assisted diesel combustion resulted in a modest increase of NO_x emissions and a NO / NO_2 trade-off in which NO emissions decreased and NO_2 emissions increased, with NO_2 becoming the dominate NO_x component in some circumstances. Increased aspiration of hydrogen resulted in PM , and HC emissions which fluctuated with speed and load. Predominantly, CO and CO_2 decreased with the increase of

hydrogen. The aspiration of hydrogen into the engine modestly decreased fuel economy due to the reduction of oxygen in the cylinder charge.

In the advanced combustion portion of the study, the engine was operated under a partially-premixed charge compression ignition PCCI mode known as high efficiency clean combustion (HECC), in which NO_x and PM emissions dramatically decreased while fuel economy was maintained. Hydrogen assisted diesel combustion was performed while the engine operated in the HECC mode, which resulted in emissions and combustion impacts similar to those observed in the conventional combustion modes.

TABLE OF CONTENTS

LIST OF FIGURES	viii
LIST OF TABLES	xiv
NOMENCLATURE	xix
ACKNOWLEDGEMENTS	xxi
Chapter 1 Introduction	1
1.1 Motivation.....	1
1.2 Objective and Hypothesis	2
Chapter 2 Literature Review	3
2.1 Diesel Combustion.....	3
2.2 Nitrogen Oxide Emissions	11
2.3 Particulate Matter Emissions	13
2.4 Carbon Monoxide Emissions.....	16
2.5 Carbon Dioxide Emissions	17
2.6 Unburned Hydrocarbon Emissions.....	18
2.14 Hydrogen	19
2.8 Diesel Pilot Ignited Hydrogen Combustion.....	22
2.7 Engine Gas Recirculation	28
2.8 Homogeneous Charge Compression Ignition	29
2.9 Partially-premixed Charge Compression Ignition	31
2.10 Low Temperature Combustion	32
2.11 Smokeless Locally Rich Diesel Combustion.....	33
2.12 Modulated Kinetics.....	34
2.13 High Efficiency Clean Combustion.....	36
2.16 Research Objective Identified via the Literature Review	38
Chapter 3 Experimental Setup	39
3.1 Engine Test Stand	39
3.2 Data Acquisition	40
3.3 Electronic Control Unit Modification.....	41
3.4 EGR Operation	41
3.5 Hydrogen Flow Rate Monitoring and Control.....	44
3.6 Diesel Fuel Flow Rate	46
3.7 Gaseous Emissions: AVL Combustion Emissions Bench II	46
3.8 Gaseous Emissions: GC.....	47
3.9 Particulate Matter Emissions: BG-1	47

3.10 Particulate Matter Emissions: SMPS.....	48
3.11 Cylinder Pressure Trace Analysis.....	49
3.12 Test Plan	50
Chapter 4 Discussion and Results of Conventional Combustion Modes with Hydrogen Substitution.....	52
4.1 Introduction.....	52
4.2 Mode Parameters	53
4.3 Hydrogen Substitution.....	53
4.4 Needle Lift.....	54
4.5 Pressure Trace.....	57
4.6 Apparent Heat Release Rate	61
4.7 Bulk Cylinder Gas Temperature.....	65
4.8 Exhaust Temperature	66
4.9 Equivalence Ratio.....	67
4.10 Gaseous Emissions	69
4.11 Erroneous NO _x Emissions Measurements	69
4.12 Gaseous Emissions: NO _x	71
4.13 Gaseous Emissions: NO	73
4.14 Gaseous Emissions: NO ₂	75
4.15 Gaseous Emissions: HC.....	79
4.16 Gaseous Emissions: Unburned Hydrogen	81
4.17 Gaseous Emissions: CO.....	81
4.18 Gaseous Emissions: CO ₂	83
4.19 Gaseous Emissions: Particulate Matter	85
4.20 Brake Specific Fuel Consumption.....	87
4.21 Summary.....	88
Chapter 5 Discussion and Results of Advanced Combustion Modes with Hydrogen Substitution.....	90
5.1 Introduction.....	90
5.2 Exhaust Gas Recirculation.....	92
5.3 Mode Parameters	95
5.4 Needle Lift.....	96
5.5 Pressure Trace.....	99
5.6 Coefficient of Variance.....	103
5.7 Apparent Heat Release Rate	104
5.8 Equivalence Ratio.....	109
5.9 Exhaust Temperature	110
5.10 Gaseous Emissions: NO _x	112
5.11 Gaseous Emissions: NO	114
5.12 Gaseous Emissions: NO ₂	116
5.13 Gaseous Emissions: HC.....	119

5.14 Gaseous Emissions: CO.....	121
5.15 Gaseous Emissions: CO ₂	123
5.16 Particulate Matter Emissions: BG-1	125
5.17 Particulate Matter Emissions: SMPS.....	127
5.18 Brake Specific Fuel Consumption.....	132
5.19 Summary.....	134
Chapter 6 Conclusion.....	137
6.1 Conclusion.....	137
6.2 Future Work.....	139
Bibliography	142
Appendix A Brake Specific Calculations	147
A.1 Brake Specific Calculations.....	147
Appendix B Error Analysis.....	149
B.1 Error Analysis	149
Appendix C Repeatability Study	153
C.1 Repeatability Study.....	153

LIST OF FIGURES

Figure 2.1: Pressure–volume diagram of an ideal Diesel cycle. [2]	4
Figure 2.2: Four-stroke engine cycle [4].....	5
Figure 2.4: A model of CI diesel jet generated from laser diagnostic testing [8].....	11
Figure 2.5: Schematic of Diesel Particles and Vapor Phase Compounds, redrawn by Hess [12].....	13
Figure 2.6: Soot formation process from gas phase to solid agglomerated particles [13].....	15
Figure 2.7: EPA heavy duty on-highway engine emissions standards [14].	16
Figure 2.8: Fuel stages for energy and technology types for hydrogen production [21].....	21
Figure 2.9: Fuel stages for energy and technology types for hydrogen production -continued [21].....	22
Figure 2.10: 3D-CFD model of local equivalence ratio vs. local temperature [36]. ...	33
Figure 2.11: Smokeless Locally Rich Diesel Combustion (SRDC) Combustion [42].....	34
Figure 2.12: Schema of Modulated Kinetics (MK) Combustion[27].....	35
Figure 2.13: Concept map of various LTC modes.....	37
Figure 3.1: DDC 2.5L common rail diesel engine set up [1].....	40
Figure 3.2: Instrumented air intake/EGR Y-pipe.....	42
Figure 3.3: DDC 2.5L EGR/H2 flow diagram.....	43
Figure 3.4: Custom intake air manifold aspiration system.	44
Figure 3.5: Diagram of the hydrogen delivery system.	45
Figure 4.1: Actual hydrogen percentage energy substitution for the four modes tested, with □ 0%, ■ 2.5%, ■ 5%, ■ 7.5%, ■ 10% and ■ 15% hydrogen substitution on an energy basis.....	54
Figure 4.2: Repeatability study of needle lift at 1800 rpm at 25% maximum outputs, of. ————Trial 1, - - - Trial 2 and - - - -Trial 3.....	55

Figure 4.3: Needle lift at 1800 rpm at 25% maximum output, with ———0%, — — 2.5%, - - - -7.5% and · · · · ·15%.hydrogen substitution on an energy basis.	56
Figure 4.4: Needle lift at 1800 rpm at 75% maximum output, with ———0%, — — 2.5%, - - - -7.5% and · · · · ·15% hydrogen substitution on an energy basis.	56
Figure 4.5: Comparison between pressure traces from the four cylinders of the Detroit Diesel 2.5L TD DI-4V Automotive Diesel Engine at 1800 rpm at 25% maximum output for ———Cylinder 1, — — Cylinder 2, - - - - Cylinder 3 and · · · · ·Cylinder 4.	58
Figure 4.6: Pressure trace at 1800 rpm at 25% maximum output, with ———0%, — — 2.5%, - - - -7.5% and · · · · ·15%.hydrogen substitution on an energy basis.....	59
Figure 4.7: Pressure trace at 1800 rpm at 75% maximum output, with ———0%, — — 2.5%, - - - -7.5% and · · · · ·15%.hydrogen substitution on an energy basis.....	60
Figure 4.8: Pressure trace at 3600 rpm at 25% maximum output, with ———0%, — — 2.5%, - - - -7.5% and · · · · ·15%.hydrogen substitution on an energy basis.....	60
Figure 4.9: Pressure trace at 3600 rpm at 75% maximum output, with ———0%, — — 2.5%, - - - -7.5% and · · · · ·15%.hydrogen substitution on an energy basis.....	61
Figure 4.10: Apparent heat release rate at 1800 rpm at 25% maximum output, with ———0%, — — 2.5%, - - - -7.5% and · · · · ·15%.hydrogen substitution on an energy basis.....	63
Figure 4.11: Apparent heat release rate at 1800 rpm at 75% maximum output, with ———0%, — — 2.5%, - - - -7.5% and · · · · ·15% hydrogen substitution on an energy basis.....	63
Figure 4.12: Apparent heat release rate at 3600 rpm at 25% maximum output, with ———0%, — — 2.5%, - - - -7.5% and · · · · ·15%.hydrogen substitution on a energy basis.....	64
Figure 4.13: Apparent heat release rate at 3600 rpm at 75% maximum output, with ———0%, — — 2.5%, - - - -7.5% and · · · · ·15%.hydrogen substitution on an energy basis.....	64

Figure 4.14: Maximum bulk cylinder gas temperature of the four modes tested, with 0%, 2.5%, 7.5%, and 15% hydrogen substitution on an energy basis.	65
Figure 4.15: Exhaust temperature of the four modes tested, with 0%, 2.5%, 5%, 7.5%, 10% and 15% hydrogen substitution on an energy basis....	67
Figure 4.16: Equivalence ratio of the four modes tested, with 0%, 2.5%, 5%, 7.5%, 10% and 15% hydrogen substitution on an energy basis.....	68
Figure 4.17: Brake specific NO _x emissions at 1800 rpm at 75% maximum output when injection timing is allowed to drift and when injection timing is locked down, with 0%, 2.5%, 5%, 15%, 25% and 30% hydrogen substitution on an energy basis.....	70
Figure 4.18: Needle lift at 1800 rpm at 75% maximum output, when injection timing is not locked, with 0%, 15%, and 30% hydrogen substitution on an energy basis.....	71
Figure 4.19: Brake specific NO _x emissions of the four modes tested, with 0%, 2.5%, 5%, 7.5%, 10% and 15% hydrogen substitution on an energy basis.	72
Figure 4.20: Brake specific NO emissions of the four modes tested, with 0%, 2.5%, 5%, 7.5%, 10% and 15% hydrogen substitution on an energy basis.	74
Figure 4.21: Brake specific NO ₂ emissions of the four modes tested, with 0%, 2.5%, 5%, 7.5%, 10% and 15% hydrogen substitution on the energy basis.	76
Figure 4.22: Brake specific NO _x , NO and NO ₂ emissions vs. energy percent from hydrogen fuel for 3600rpm at 25% of maximum output.	78
Figure 4.23: Brake specific HC emissions of the four modes tested, with 0%, 2.5%, 7.5% and 15% hydrogen substitution on an energy basis.	79
Figure 4.24: Brake specific H ₂ emissions of the four modes tested, with 0%, 2.5%, 7.5%, and 15% hydrogen substitution on an energy basis.	81
Figure 4.25: Brake specific CO emissions of the four modes tested, with 0%, 2.5%, 5%, 7.5%, 10% and 15% hydrogen substitution on an energy basis.	82

Figure 4.26: Brake specific CO ₂ emissions of the four modes tested, with □ 0%, ■ 2.5%, ■ 5%, ■ 7.5%, ■ 10% and ■ 15% hydrogen substitution on an energy basis.	84
Figure 4.27: Brake specific PM emissions of the four modes tested, with □ 0%, ■ 2.5%, ■ 7.5% and ■ 15% hydrogen substitution on an energy basis.	86
Figure 4.28: Brake specific fuel consumption of the four modes tested, with □ 0%, ■ 2.5%, ■ 5%, ■ 7.5%, ■ 10% and ■ 15% hydrogen substitution on an energy basis.	87
Figure 5.2: Needle Lift comparison of the baseline mode, LTC mode and HECC mode with 0% of hydrogen. ———baseline, — — LTC and · · · · ·HECC....	97
Figure 5.3: Needle lift of baseline mode, with ———0%, — — 2.5%, - - - -7.5% and · · · · ·15% hydrogen substitution on an energy basis.	98
Figure 5.4: Needle lift of LTC mode, with ———0%, — — 2.5%, - - - -7.5% and · · · · ·15% hydrogen substitution on an energy basis.	98
Figure 5.5: Needle lift of HECC mode, with ———0%, — — 2.5%, - - - -7.5% and · · · · ·15% hydrogen substitution on an energy basis.	99
Figure 5.6: Pressure trace comparison of the baseline mode, LTC mode and HECC mode with 0% of hydrogen. ———baseline, — — LTC and · · · · ·HECC.	100
Figure 5.7: Pressure trace of baseline mode, with ———0%, — — 2.5%, - - - -7.5% and · · · · ·15% hydrogen substitution on an energy basis.	101
Figure 5.8: Pressure trace of LTC mode, with ———0%, — — 2.5%, - - - -7.5% and · · · · ·15% hydrogen substitution on an energy basis.	101
Figure 5.9: Pressure trace of HECC mode, with ———0%, — — 2.5%, - - - -7.5% and · · · · ·15% hydrogen substitution on an energy basis.	102
Figure 5.10: Apparent heat release rate comparison of the baseline mode, LTC mode and HECC mode with 0% of hydrogen. ———baseline, — — LTC and · · · · ·HECC.	106

Figure 5.11: Apparent heat release rate of baseline mode, with ———0%, — — 2.5%, - - - -7.5% and · · · · ·15% hydrogen substitution on an energy basis.	107
Figure 5.12: Apparent heat release rate of LTC mode, with ———0%, — — 2.5%, - - - -7.5% and · · · · ·15% hydrogen substitution on an energy basis.	108
Figure 5.13: Apparent heat release rate of HECC mode, with ———0%, — — 2.5%, - - - -7.5% and · · · · ·15% hydrogen substitution on an energy basis.	109
Figure 5.15: Exhaust temperature of the three modes tested, with □ 0%, ■ 2.5%, ■ 5%, ■ 7.5%, ■ 10% and ■ 15% hydrogen substitution on an energy basis....	111
Figure 5.17: Brake specific NO emissions of the three modes tested, with □ 0%, ■ 2.5%, ■ 5%, ■ 7.5%, ■ 10% and ■ 15% hydrogen substitution on an energy basis.	115
Figure 5.18: Brake specific NO ₂ emissions of the three modes tested, with □ 0%, ■ 2.5%, ■ 5%, ■ 7.5%, ■ 10% and ■ 15% hydrogen substitution on an energy basis.	117
Figure 5.19: Brake specific HC emissions of the three modes tested, with □ 0%, ■ 2.5%, ■ 5%, ■ 7.5%, ■ 10% and ■ 15% hydrogen substitution on an energy basis.	120
Figure 5.20: Brake specific CO emissions of the three modes tested, with □ 0%, ■ 2.5%, ■ 5%, ■ 7.5%, ■ 10% and ■ 15% hydrogen substitution on an energy basis.	122
Figure 5.21: Brake specific CO ₂ emissions of the three modes tested, with □ 0%, ■ 2.5%, ■ 5%, ■ 7.5%, ■ 10% and ■ 15% hydrogen substitution on an energy basis.	124
Figure 5.22: Brake specific PM emissions of the three modes tested, with □ 0%, ■ 2.5%, ■ 7.5%, and ■ 15% hydrogen substitution on an energy basis.	126
Figure 5.23: SMPS Bypass comparison of the baseline mode, LTC mode and HECC mode with 0% of hydrogen. ———baseline, — — LTC and · · · · ·HECC.	129
Figure 5.24: SMPS thermal denuder at 30°C of the baseline mode, LTC mode and HECC mode with 0% of hydrogen. ———baseline, — — LTC and · · · · ·HECC.	130

- Figure 5.25: SMPS Thermal Denuder at 300°C at 0% hydrogen. — baseline, — LTC and ····HECC..... 131
- Figure 5.26: HECC mode exploration at 1800 rpm, 4.2 bmep and 50% EGR with rail pressure at 490 bars. —○— TD 30°C at 2 BTDC, —□— TD 300°C at 2 BTDC, —●— TD 30°C at 4 BTDC and —■— TD 300°C at 4 BTDC..... 132
- Figure 5.27: Brake specific fuel consumption of the four modes tested, with □ 0%, ■ 2.5%, ■ 5%, ■ 7.5%, ■ 10% and ■ 15% hydrogen substitution on an energy basis. 133

LIST OF TABLES

Table 2.1: General Motors Reactivity Scale (0-100). Based on the NO ₂ formation rate for hydrocarbon relative to the NO ₂ formation rate for 2,3-dimethyl-2-butene[5, 18].	18
Table 2.2: Qualitative results given in the literature on hydrogen assisted diesel combustion. Where + indicates an increase and - indicates a decrease in the given emission species or parameter.	27
Table 3.1: DDC 2.5L Engine Specification.	39
Table 3.2: Test matrix for conventional hydrogen assisted diesel combustion on the basis of fuel energy percent.	50
Table 3.3: Test matrix for conventional combustion modes with hydrogen substitution on the basis of fuel energy percent, in which the maximum % hydrogen limit was found.	51
Table 3.4: Test matrix for advanced combustion modes with hydrogen assisted diesel combustion on the basis of fuel energy percent.	51
Table 4.1: Parameters of baseline operations for the four test modes.	53
Table 4.2: Percent difference of brake specific NO _x emissions from the baseline at 1800 rpm at 75% maximum output with 0%, 2.5%, 5%, 15%, 25% and 30% hydrogen substitution on an energy basis. Positive values indicate an increase and negative values indicate a decrease from the baseline.	70
Table 4.3: Percent difference of brake specific NO _x emissions from the baseline at the four modes tested with 0%, 2.5%, 5%, 7.5%, 10% and 15% hydrogen substitution on an energy basis. Positive values indicate an increase and negative values indicate a decrease from the baseline.	73
Table 4.4: Percent difference of brake specific NO emissions from the baseline at the four modes tested with 0%, 2.5%, 5%, 7.5%, 10% and 15% hydrogen substitution on an energy basis. Positive values indicate an increase and negative values indicate a decrease from the baseline.	75
Table 4.5: Percent difference of brake specific NO ₂ emissions from the baseline at the four modes tested with 0%, 2.5%, 5%, 7.5%, 10% and 15% hydrogen substitution on an energy basis. Positive values indicate an increase and negative values indicate a decrease from the baseline.	77
Table 4.6: Percent difference of brake specific HC emissions from the baseline at the four modes tested with 0%, 2.5%, 5%, 7.5%, 10% and 15% hydrogen	

substitution on an energy basis. Positive values indicate an increase and negative values indicate a decrease from the baseline.....	80
Table 4.7: Percent difference of brake specific CO emissions from the baseline at the four modes tested with 0%, 2.5%, 5%, 7.5%, 10% and 15% hydrogen substitution on an energy basis. Positive values indicate an increase and negative values indicate a decrease from the baseline.....	83
Table 4.8: Percent difference of brake specific CO ₂ emissions from the baseline at the four modes tested with 0%, 2.5%, 5%, 7.5%, 10% and 15% hydrogen substitution on an energy basis. Positive values indicate an increase and negative values indicate a decrease from the baseline.....	84
Table 4.9: Percent difference of brake specific HC emissions from the baseline at the four modes tested with 0%, 2.5%, 5%, 7.5%, 10% and 15% hydrogen substitution on an energy basis. Positive values indicate an increase and negative values indicate a decrease from the baseline.....	86
Table 4.10: Percent difference of brake fuel consumption from the baseline at the four modes tested with 0%, 2.5%, 5%, 7.5%, 10% and 15% hydrogen substitution on an energy basis. Positive values indicate an increase and negative values indicate a decrease from the baseline.....	88
Table 5.1: 0% parameters of advanced combustion mode hydrogen assisted diesel combustion. All modes were run at 1800 rpm at 25% maximum of output.....	95
Table 5.2: Percent difference of maximum pressure from 0% hydrogen substitution at the three modes tested with 2.5%, 7.5% and 15% hydrogen substitution on an energy basis. Positive values indicate an increase and negative values indicate a decrease from the baseline.....	102
Table 5.3: Percent difference of maximum pressure from the baseline mode to the LT mode and HECC mode with 0%, 2.5%, 7.5% and 15% hydrogen substitution on an energy basis. Positive values indicate an increase and negative values indicate a decrease from the baseline.....	103
Table 5.4: Coefficient of variance for all four cylinders baseline mode, LTC mode and HECC mode with 0%, 2.5%, 7.5% and 15% hydrogen substitution on an energy basis.	104
Table 5.5: Percent difference of exhaust temperature from 0% hydrogen to 2.5%, 5%, 7.5%, 10% and 15% hydrogen substitution on an energy basis for the baseline mode, LTC mode and HECC mode. Positive values indicate an increase and negative values indicate a decrease from the baseline.....	112

Table 5.6: Percent difference of exhaust temperature comparing the baseline mode to LTC mode and baseline mode to HECC mode. Positive values indicate an increase and negative values indicate a decrease from the baseline.	112
Table 5.7: Percent difference of brake specific NO _x emissions from 0% hydrogen to 2.5%, 5%, 7.5%, 10% and 15% hydrogen substitution on an energy basis for the baseline mode, LTC mode and HECC mode. Positive values indicate an increase and negative values indicate a decrease from the baseline.	114
Table 5.8: Percent difference of brake specific NO _x emissions comparing baseline mode to LTC mode and baseline mode to HECC mode. Positive values indicate an increase and negative values indicate a decrease from the baseline.	114
Table 5.9: Percent difference of brake specific NO emissions from 0% hydrogen to 2.5%, 5%, 7.5%, 10% and 15% hydrogen substitution on an energy basis for the baseline mode, LTC mode and HECC mode. Positive values indicate an increase and negative values indicate a decrease from the baseline.	115
Table 5.10: Percent difference of brake specific NO emissions comparing baseline mode to LTC mode and baseline mode to HECC mode. Positive values indicate an increase and negative values indicate a decrease from the baseline.	116
Table 5.11: Percent difference of brake specific NO ₂ emissions from the baseline at the four modes tested with 0%, 2.5%, 5%, 7.5%, 10% and 15% hydrogen substitution on an energy basis. Positive values indicate an increase and negative values indicate a decrease from the baseline.	118
Table 5.12: Percent difference of brake specific NO ₂ emissions comparing baseline to LTC and baseline to HECC. Positive values indicate an increase and negative values indicate a decrease from the baseline.	118
Table 5.13: Percent difference of brake specific HC emissions from the baseline at the four modes tested with 0%, 2.5%, 5%, 7.5%, 10% and 15% hydrogen substitution on an energy basis. Positive values indicate an increase and negative values indicate a decrease from the baseline.	121
Table 5.14: Percent difference of brake specific HC emissions comparing baseline to LTC and baseline to HECC. Positive values indicate an increase and negative values indicate a decrease from the baseline.	121
Table 5.15: Percent difference of brake specific CO emissions from the baseline at the four modes tested with 0%, 2.5%, 5%, 7.5%, 10% and 15% hydrogen	

substitution on an energy basis. Positive values indicate an increase and negative values indicate a decrease from the baseline.....	123
Table 5.16 : Percent difference of brake specific CO emissions comparing baseline to LTC and baseline to HECC. Positive values indicate an increase and negative values indicate a decrease from the baseline.....	123
Table 5.17 : Percent difference of brake specific CO ₂ emissions from the baseline at the four modes tested with 0%, 2.5%, 5%, 7.5%, 10% and 15% hydrogen substitution on an energy basis. Positive values indicate an increase and negative values indicate a decrease from the baseline.....	124
Table 5.18 : Percent difference of brake specific CO ₂ emissions comparing baseline to LTC and baseline to HECC. Positive values indicate an increase and negative values indicate a decrease from the baseline.....	125
Table 5.19 : Percent difference of brake specific PM emissions from the baseline at the four modes tested with 0%, 2.5%, 5%, 7.5%, 10% and 15% hydrogen substitution on an energy basis. Positive values indicate an increase and negative values indicate a decrease from the baseline.....	127
Table 5.20 : Percent difference of brake specific PM emissions comparing baseline to LTC and baseline to HECC. Positive values indicate an increase from the baseline, while negative values indicate a decrease.....	127
Table 5.21 : Percent difference of brake fuel consumption from the baseline at the four modes tested with 0%, 2.5%, 5%, 7.5%, 10% and 15% hydrogen substitution on an energy basis. Positive values indicate an increase and negative values indicate a decrease from the baseline.....	133
Table 5.22 : Percent difference of brake specific fuel consumption comparing baseline to LTC and baseline to HECC. Positive values indicate an increase and negative values indicate a decrease from the baseline.....	134
Table 5.23 : Major operational parameters and emissions result of the three modes tested.....	135
Table B.1 : Major sources of instruments error which affect gaseous emission results in percent error.	151
Table B.2 : Major sources of instruments errors which affect PM emission results in percent error.....	151
Table B.3 : Major sources of systematic error which affect gaseous and PM emission results in percent error.....	151

Table C.1: Repeatability study of the DDC 2.5L engine operating at 1800 rpm and 25% of maximum output on three different trials presented by standard deviation.	153
Table C.2: Comparison of the DDC 2.5L engine at 1800 rpm and 25% of maximum output with 0% and 15% hydrogen substitution on an energy basis by standard deviation.	154

NOMENCLATURE

Acronym	Description
BSU	Bosch smoke unit
CFD	Computational fluid dynamics
CI	Compression ignition
COV	Coefficient of variance
CPC	Condensation particle counter
CRT	Continuously regenerating trap
DMA	Differential mobility analyzer
ECU	Electronic control unit
EGR	Engine gas recirculation
EOI	End of injection
ϕ	Equivalence ratio
FID	Flame ionization detector
GC	Gas chromatograph
HC	Unburned hydrocarbon
HCCI	Homogeneous charge compression ignition
HECC	High efficiency clean combustion
HSDI	High speed direct injection
IC	Internal combustion
IMEP	Indicated mean effective pressure
LTC	Low temperature combustion

Acronym	Description
MK	Modulated kinetics
NMHC	Non-methane hydrocarbons
PAH	Polycyclic aromatic hydrocarbons
PCCI	Premixed charge compression ignition
PM	Particulate matter
PPM	Part-per-million
RCM	Rapid compression machine
RPM	Rotation per minute
RSS	Root-sum-square
SI	Spark ignited
SMPS	Scanning mobility particle sizer
SOF	Soluble organic fraction
SOI	Start of injection
SRDC	Smokeless locally rich diesel combustion
TCD	Thermal conductivity detector
TDC	Top-dead-center

ACKNOWLEDGEMENTS

I would first like to thank Dr. Andre Boehman, my advisor, who took a risk and gave me this opportunity to learn. I would like to thank my committee, Dr. Harold Schobert, Dr. Angela Lueking and Dr. Daniel Haworth for their time and effort reviewing my thesis.

A special thanks to Yu Zhang, who graciously and patiently trained me in the use of the DDC 2.5L test stand. I would also like to thank Elana Chapman for her guidance as a graduate student. Thank you to Jamie Clark in his help debugging the data acquisition system. Thank you to Mel Fox for her aid in developing the hydrogen fueling system. Countless thanks to Vince Zello, for his super human patience and willingness to fix anything that the graduate students brake.

Thank you to Dr. James Hansel, formerly of Air Products, who gave excellent council in the design and safety aspects of the hydrogen fueling system. Thank you to Keith Cavallini of CAV Engineering for his ongoing hardware support of the DDC 2.5L engine.

A special thanks to José Martín Herreros Arellano, a visiting student from University of Castilla-La Mancha, for his aid in engine testing and friendship.

Most of all, thank you to my parents, Kenneth and Karen Lilik, and my brother Chris, for their on going support and encouragement throughout my education and career.

Chapter 1

Introduction

1.1 Motivation

Fears of dwindling oil reserves and new regulations on diesel engine emissions have driven research to focus on the use of alternative fuels. The utilization of alternative fuel diminishes the reliance on petroleum based fuel which is a step towards energy security. In this thesis, hydrogen was used as a supplemental fuel in a production diesel engine and thus replaced a portion of the diesel fuel demanded to produce engine output. The engine exhaust emissions, produced when hydrogen fuel was substituted for diesel, were of primary interest. By changing the fuel used to power an engine, the resulting engine-out emissions will change. However, as in the case of NO_x emissions from bio-diesel, the emissions resulting from alternative fuels may not be beneficial [1].

The literature review, presented in Chapter 2, on diesel pilot hydrogen ignition, indicates that hydrogen substitution is a promising method of reducing undesired exhaust emissions, especially at high rates of hydrogen substitution. The literature reports studies exclusively performed on small or single cylinder diesel engines. The hydrogen assisted diesel combustion studies in this thesis were performed on a DDC/VM Motori 2.5L, 4-cylinder, turbocharged, common rail, direct injection light-duty diesel engine. This engine was available in the European version of the Jeep Cherokee and Chrysler Voyager.

Advanced combustion modes, such as homogeneous charge compression ignition (HCCI) and premixed charge compression ignition (PCCI), are currently of interest to further reduce diesel emissions, specifically NO_x and particulate matter (PM). As presented in the literature review of Chapter 2, HCCI and PCCI modes induce the engine to combust the fuel in the pre-mixed phase, resulting in a fuel lean charge and lowered combustion temperature, and thus, resulting in an engine operation away from zones of NO_x and PM formation. In this thesis, the DDC 2.5L engine was operated on a particular PCCI mode, high efficiency clean combustion (HECC), developed by Wagner, Sluder and coworkers at Oak Ridge National Laboratory. This study represents the first published operation of the HECC mode outside of Oak Ridge National Laboratory. In novel experimentation, the DDC 2.5L engine was operated in the HECC mode while hydrogen assisted diesel combustion was performed, in hopes to further reduce NO_x and PM emissions and reduce cycle-to-cycle variations, common to advanced combustion modes which rely on high percentages of exhaust gas recirculation EGR.

1.2 Objective and Hypothesis

The objectives of this work are to test the following hypotheses.

- A production diesel engine can utilize gaseous hydrogen fuel, via aspiration, in combination with diesel fuel with minimal modifications to the engine.
- The aspiration of hydrogen into a diesel engine will increase the pre-mixed combustion phase of a diesel engine, reducing NO_x and PM emissions.

- Small quantities of aspirated hydrogen will have little effect on engine performance and emission.
- The HECC mode can be achieved using a production DDC/VM Motori 2.5L, 4-cylinder, turbocharged, common rail, direct injection light-duty diesel engine. While operating in the HECC mode, the addition of hydrogen to the combustion chamber will smooth-out the combustion process, quantified by the coefficient of variance (COV) of the indicated mean effective pressure (IMEP) and further reduce NO_x and PM emissions.

Chapter 2

Literature Review

2.1 Diesel Combustion

Diesel engines are of interest due their higher efficiency in comparison to spark ignited (SI) engines. The diesel engine is named after Rudolph Diesel who first invented the engine in 1897. The diesel engine, also known as the compression ignition (CI) engine, operates under the basis of the diesel cycle. The idealized diesel cycle is a constant pressure heat addition cycle, which differs from the idealized Otto cycle of the SI engine in which heat addition occurs at a constant volume. Figure 2.1 displays the ideal diesel cycle.

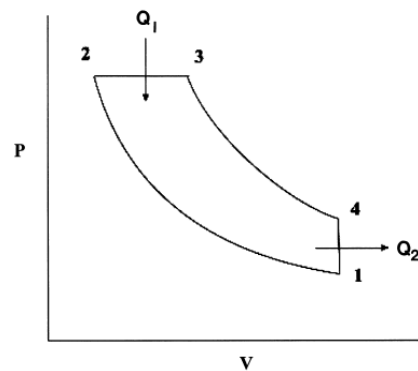


Figure 2.1: Pressure–volume diagram of an ideal Diesel cycle. [2]

The four processes of the diesel cycle shown in Figure 2.1 are [3]:

- 1 to 2 isentropic compression
- 2 to 3 constant pressure heat addition
- 3 to 4 isentropic expansion
- 4 to 1 constant volume heat rejection

The four processes of the diesel cycle are related to the four strokes (or stages) of the diesel engine given in Figure 2.2. However, for every four strokes of a diesel engine, there are two complete revolutions of the engine. During the intake stroke the piston moves down at which time, the intake valves are open, drawing air into the cylinder. During the compression stroke, the intake valves close and the piston travels to its apex known as top-dead-center (TDC), where the air undergoes isentropic compression. According to the ideal gas law, increased pressure causes an increase in temperature. The cylinder now contains compressed hot air. Diesel fuel is then injected into the cylinder. As the diesel fuel enters the cylinder it autoignites due to the high temperature and pressurized air. The combustion of the diesel fuel increases the in-cylinder temperature

and pressure which pushes the piston down during the expansion (or power) stroke. The piston then moves to the bottom of the cylinder. At this point the exhaust valves open as the cylinder moves back up to TDC forcing the exhaust gases out of the cylinder, for the exhaust stroke.

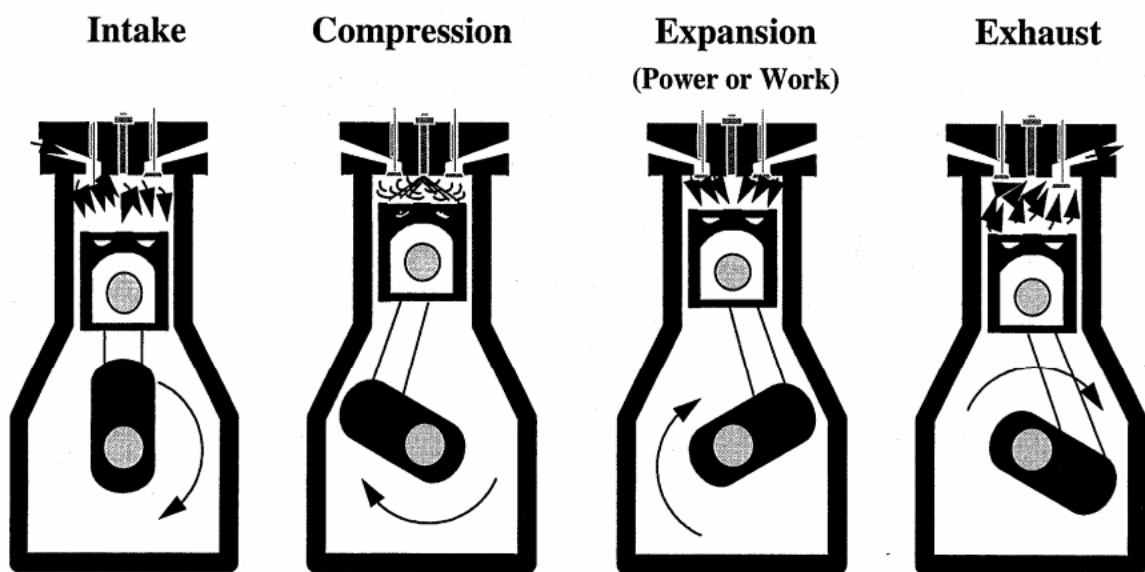


Figure 2.2: Four-stroke engine cycle [4].

A key thermodynamic concept of the internal combustion (IC) engine is that air is the working fluid. An IC engine is an air pump. Thus, the torque and power rating of an IC engine are governed by the amount of air which can be forced into the cylinders. Therefore, turbochargers are used to increase the mass of the air charge in a diesel engine. In comparison to the SI engine, a CI engine operates at low RPM (rotation per minute). Thus, a CI engine at a given cylinder displacement will have a lower power rating than an SI engine of similar displacement.

Typically, hydrocarbon fuels have been used to fuel IC engines. Complete combustion of hydrocarbon fuel occurs under stoichiometric conditions. The stoichiometric air-fuel ratio is the ratio of air to fuel where there is just enough of both for complete oxidation of the fuel. The value of the stoichiometric air-fuel ratio is unique to every hydrocarbon fuel. In the generic formula for diesel fuel, $C_{10.8}H_{18.7}$, the stoichiometric air fuel ratio is 14.33 g-air/g-fuel. Under stoichiometric combustion the maximum heat release for a given fuel is achieved [5]. Equation **2.1** and **2.2** display the generic formula for hydrocarbon combustion [6]. In this equation, complete combustion is assumed. The only products are CO_2 and H_2O . To a first approximation, N_2 in the air does not react but merely acts as an inert diluent.



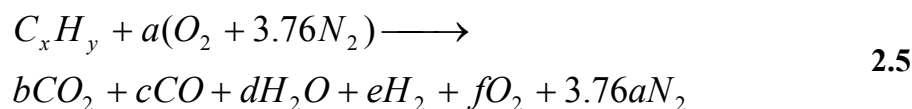
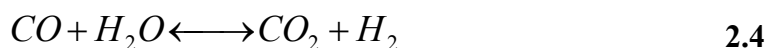
$$a = x + y/4 \quad \mathbf{2.2}$$

Complete combustion, shown in Eq. **2.1**, in which only CO_2 , H_2O and N_2 are the products, never occurs in reality. Intermediate products are formed and incomplete combustion occurs due to the air-fuel mixture not being stoichiometric. Globally the air-fuel ratio of a CI engine is lean, but in local regions where combustion principally occurs, the ratio is rich. There will also be pockets of lean and stoichiometric combustion occurring. The equivalence ratio (ϕ), defined in Eq. **2.3** [6], is used to express whether a mixture is rich or lean. Equivalence ratio is the ratio of the calculated stoichiometric air-fuel ratio over the actual air-fuel ratio.

$$\phi = \frac{\left(\frac{A}{F}\right)_{stochastic}}{\left(\frac{A}{F}\right)_{actual}} = \frac{\left(\frac{F}{A}\right)_{actual}}{\left(\frac{F}{A}\right)_{stochastic}} \quad 2.3$$

Different products of incomplete combustion are created as the equivalence ratio locally shifts from lean to rich [6]. Equation 2.1 can be expanded to include products of incomplete combustion by adding the water-gas shift reaction, Eq. 2.4, to the equation.

The result is Eq. 2.5, in which no dissociation to minor species is assumed.

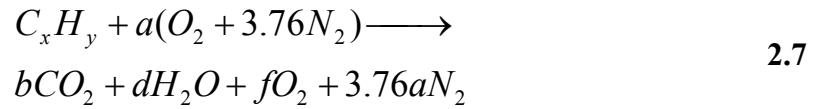


$$a = \frac{x + y/4}{\phi} \quad 2.6$$

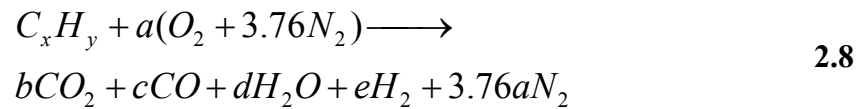
Equation 2.5 is only a simple model, since an abundance of minor species are actually formed from the combustion of a hydrocarbon fuel. However, a more complex model requires computer software to account for the conditions such as pressure, temperature, and localized equivalence ratio along with the reactions that occur between all the intermediate species.

Equation 2.7 and Eq. 2.8 are derived from the simple model of Eq. 2.5. The equations display the different products of the reaction, which occur when the equivalence ratio is fuel lean and when the equivalence ratio is fuel rich (i.e., $\phi > 1$).

For ϕ lean or stoichiometric:



For ϕ rich or stoichiometric:



The conventional CI combustion process can be further explained by Figure 2.3, in which the rate of heat release from a directly injected diesel fuel is examined vs. crank angle. The diesel combustion process can be broken up into four different phases: ignition delay period, premixed combustion phase, mixing-controlled combustion phase, and the late combustion phase. The ignition delay period begins at the start of injection (SOI). During the ignition delay period, the rate of heat release drops below zero due to the fuel absorbing heat while vaporizing [1]. Next is the premixed combustion phase where a rapid rate of heat release occurs. The portion of the fuel which has mixed with air forms a combustible mixture and ignites. After all of the premixed air-fuel charge is consumed, the mixing controlled combustion phase begins. Here the combustion transitions from a premixed flame to diffusion flame. The rate of combustion is controlled by the fuel vaporization and mixing, in contrast to the fast burn of the kinetics-driven premixed flame. During the mixing-controlled combustion phase, the end of injection (EOI) occurs. In the late combustion phase, unburned fuel seeks oxygen as it is turbulently mixing throughout the cylinder [5].

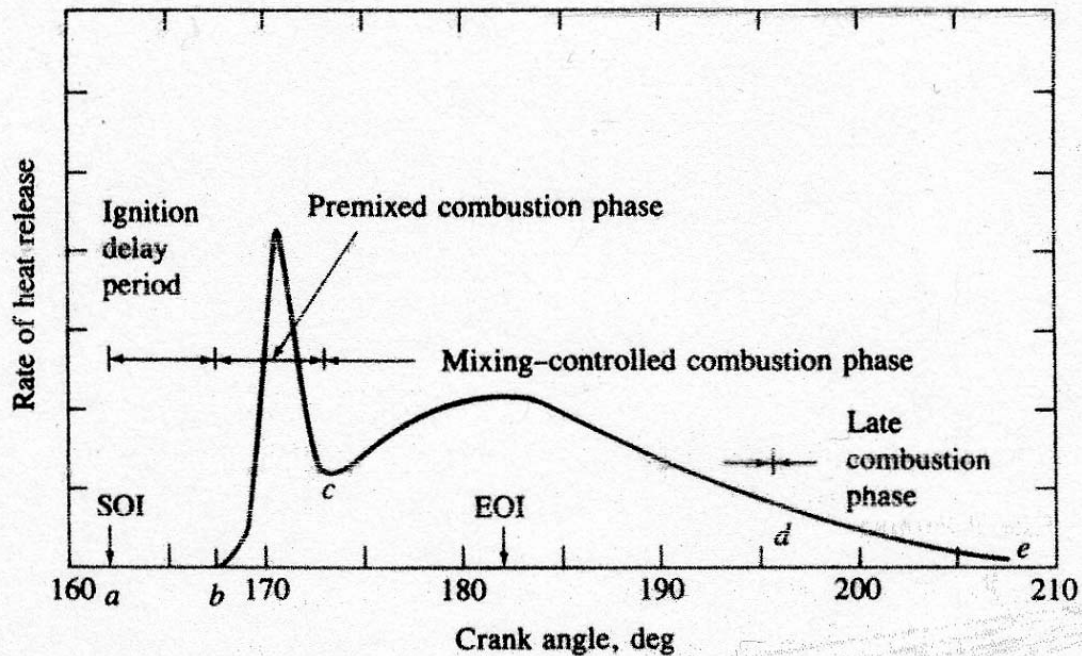


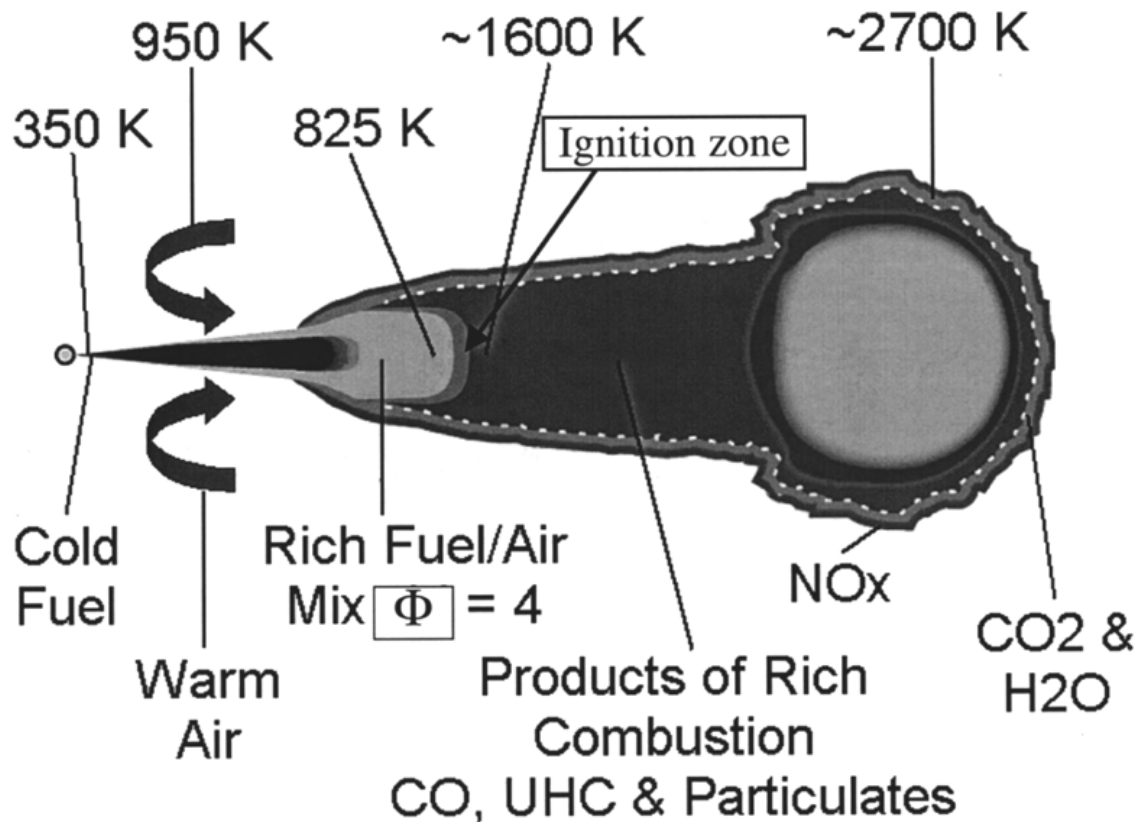
Figure 2.3: Conventional DI diesel rate of heat release vs. crank angle of the major phases of the diesel combustions process [5].

Figure 2.3 indicates that, in conventional diesel operation, the majority of the heat release occurs during the mixing-controlled combustion phase and thus most emissions will be created in the mixing controlled phase. Dec furthered the understanding of the mixing-control combustion phase, in a sequence of laser diagnostic studies [7]. Dec developed a generalized explanation for the behavior of the combusting diesel jet. He described the structure of the diffusion flame, indicating the layers by equivalence ratio and concentration of soot which varies throughout the combusting diesel jet.

Westbrook later added detail to the generalized depiction of the diesel spray flame, Figure 2.4, to include approximate temperatures and indicated the regions in which NO_x , CO_2 , H_2O , CO and UHC are produced [8]. This generalized description of

the diesel spray flames provides an excellent framework to explain the experimental observation of the diesel combustion process. The cold fuel enters the cylinder where it is vaporized by the hot compressed air. The fuel and air mix reach a combustible equivalence ratio at ~ 4 and reach autoignition at $\sim 650\text{K}$ [9]. Temperature builds as equivalence ratio drops and oxidation increases. The inner region of the jet indicates incomplete combustion due to lack of oxygen, and the formation of soot precursors. The outer layers of the jet have near-stoichiometric equivalence ratios and generate high combustion temperatures as a consequence. The emissions generated in the diffusion flame, seen in Figure 2.4 are undesired products of incomplete combustion, and other pollutant formation pathways.

Temperatures



Chemistry

Figure 2.4: A model of CI diesel jet generated from laser diagnostic testing [8].

2.2 Nitrogen Oxide Emissions

Oxides of nitrogen, known as NO_x, are of concern due to their health and environmental effects. NO_x is a blanket term which refers to nitric oxide (NO) and nitrogen dioxide (NO₂). 95% of engine emitted NO_x is NO [5]. In the atmosphere, NO oxidizes into NO₂. Unburned hydrocarbons and sunlight increase the rate of oxidation of

NO into NO₂. NO₂ is poisonous to the respiratory system causing both lung infection and respiratory allergies. NO₂ is toxic in levels greater than 0.05 ppm. [10]

NO₂ is also harmful to the environment. NO₂ affects the photochemistry of both the troposphere and stratosphere. Photochemical smog is formed in high traffic areas. NO_x mixes with OH* and HO₂ radicals to form HNO₂ which forms acid rain [10].

NO usually accounts for the majority of the NO_x produced from IC engines. NO can be formed by three different mechanisms which are the thermal or Zeldovich mechanism, the Fenimore or prompt mechanism, and the N₂O intermediate mechanism. [3] The Zeldovich mechanism produces the majority of NO in diesel engines. It occurs due to high combustion temperatures. The extended Zeldovich mechanism is given as:



Equation **2.9** is endothermic and has activation energy of +75.0 kcal.

Equation **2.10** is exothermic and has an activation energy of +31.8 kcal. Equation **2.11** is exothermic and has an activation energy of +49.4 kcal.

NO_x is formed in regions of the flame where there is enough energy for nitrogen to oxidize. NO_x formation is thus governed by temperature and the availability of oxygen. Unfortunately, diesel engines operate under fuel lean conditions and produce high temperatures from diffusion flame combustion.

2.3 Particulate Matter Emissions

PM along with NO_x are the most problematic diesel emissions. Particulate matter (PM) is of concern due to its effects on health. PM that has a diameter of $0.10\mu\text{m}$ can permeate through the lungs and cause numerous health problems. PM causes cancer, autoimmune disorders, alteration in blood coagulability and increased cardiovascular disorders [11].

PM is made of two main components: a solid carbon fraction, or soot, and a soluble organic fraction (SOF). Lubrication oils and water bound sulfates compose minor contributions to the total PM [12]. Figure 2.5 depicts the general layout of the components of PM.

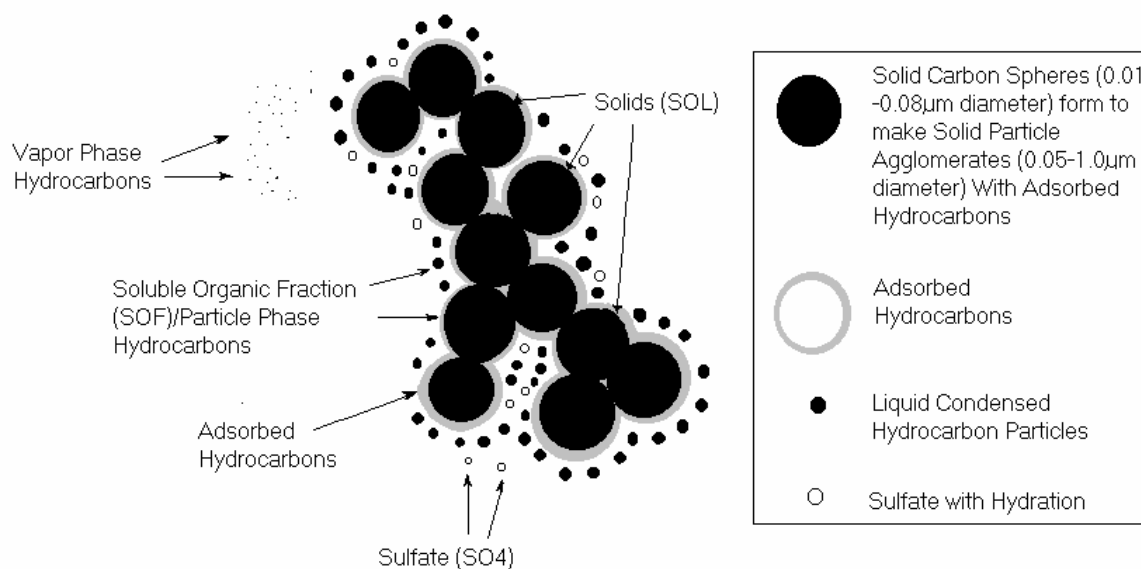


Figure 2.5: Schematic of Diesel Particles and Vapor Phase Compounds, redrawn by Hess [12].

The organic fraction is made of unburned hydrocarbons that are absorbed by the soot or condense onto the soot along with lube oil and sulfates. Sulfates, however, are less of a concern with the recent mandate towards low sulfur fuels. Soot is produced in the locally fuel rich zones of a flame. The production of soot is a competition between formation and oxidation. Total particulate matter is a product of an incomplete combustion path. The PM formation path is a complex process in which the following steps are generally accepted: first aromatic ring (soot growth), polycyclic aromatic hydrocarbons growth (growth due to SOF), particle nucleation, and particle growth (growth due to SOF, lube oils and sulfates) [12].

In a recent review paper, Tree and Svensson discussed the current understanding of the soot formation process, which can be broken up into 6 steps: pyrolysis, nucleation, coalescence, surface growth, agglomeration and oxidation. In this process, liquid or vapor phase hydro-carbons form solid soot particles [13].

Oxidation of carbon can occur during any of the 5 formation steps, in that, once a carbon atom is partially oxidized, it will no longer be able to form soot. The pyrolysis step forms soot precursors known as polycyclic aromatic hydrocarbons (PAH), via a competition between fuel pyrolysis and oxidation of fuel, which both occur at high temperatures. Because of this competition, a diffusion flame will produce more soot than a premixed flame in which oxygen is readily available to mix with the fuel.

In the nucleation step, particles form from gas phase reactants. In this process, the precursor aromatic rings grow in the presence of acetylene to develop into particle nuclei. Surface growth is the process in which the nuclei soot particles gain mass by absorbing gaseous hydrocarbons. The size to which the soot particles grow is dependent on the

residence time of the particles. The final step of soot formation involves the agglomeration of the spherical soot particle. In this process the primary particles formed during surface growth combine together to form chains of particles [13].

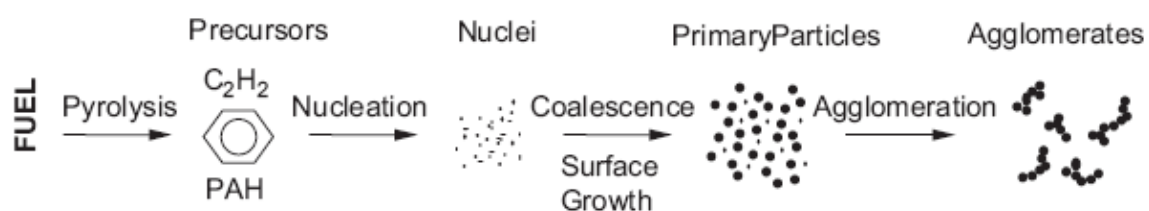


Figure 2.6: Soot formation process from gas phase to solid agglomerated particles [13].

New regulations for diesel engine emissions have driven a shift in focus to advanced combustion modes and use of alternative fuels. The emission restrictions on NO_x and PM have exponentially increased since the 1970's. Figure 2.7 show the EPA heavy duty highway engine emissions standard from the 1970's to present.

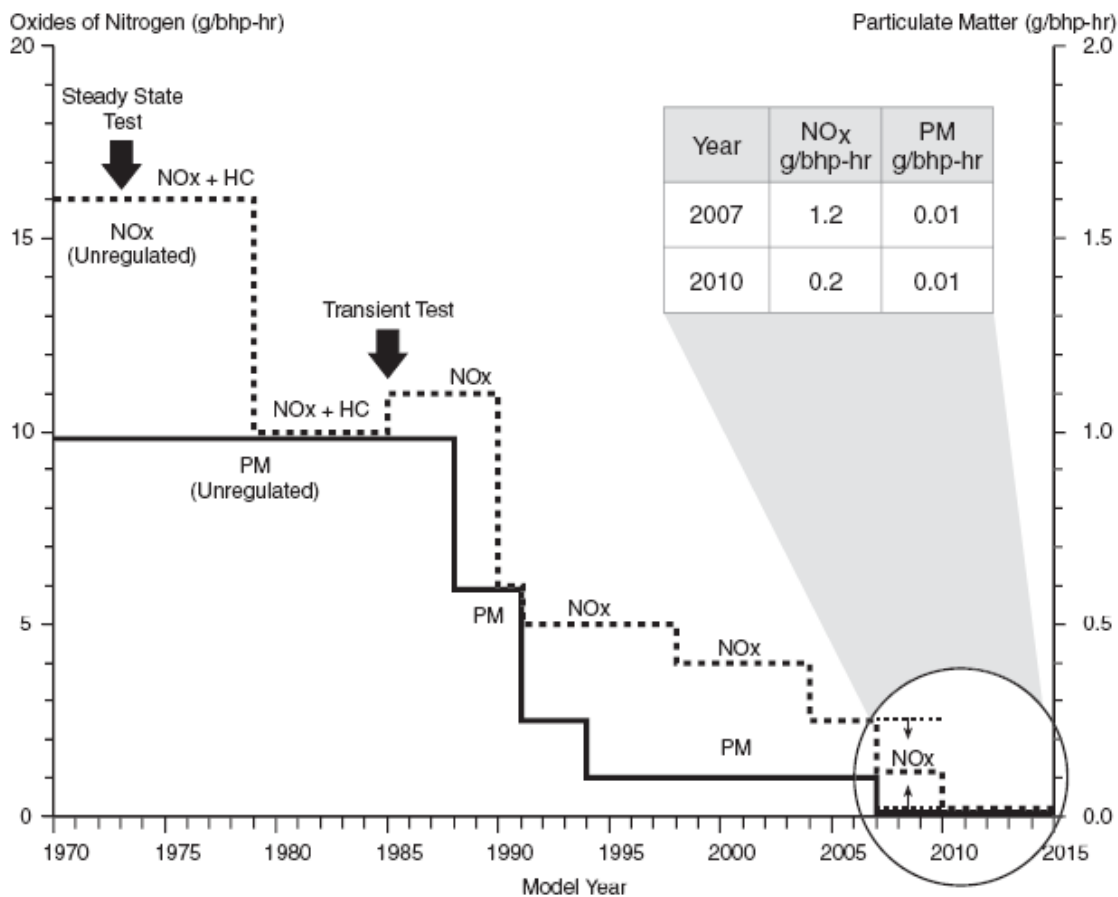


Figure 2.7: EPA heavy duty on-highway engine emissions standards [14].

2.4 Carbon Monoxide Emissions

Carbon monoxide (CO) is of concern because it is poisonous to humans. CO enters the blood stream via the lungs through respiration. In the blood stream CO forms carboxyhemoglobin with the hemoglobin in the blood. The presence of

carboxyhemoglobin reduces the amount of oxygen available in the blood resulting in hypoxia and at high levels can cause death [15].

CO is directly linked to the air-fuel ratio. It is usually generated when there is a lack of oxygen. Diesel engines operate under a globally lean stoichiometry; however, there are still locally rich regions in the diffusion flame. The principal formation path of CO is given by Eq. 2.12, where R is the hydrocarbon radical [5].



CO emissions, like PM, are a result of a competition between formation and oxidation. However, the oxidation of CO has a slower reaction; the formation will win out under rich charge conditions. The oxidation of CO is given in Eq. 2.13.



In addition, Dec and Sjoberg have shown that CO emissions at low loads increase as the equivalence ratio is lowered to between 0.1 to 0.12 [16]. This is logical since incomplete combustion occurs when the air-fuel charge is overly lean as well as overly rich.

2.5 Carbon Dioxide Emissions

Carbon dioxide (CO₂) is of concern because it is a green house gas. However, it is also a direct product of hydrocarbon fuel combustion [5]. Rather than a pollutant emission due to incomplete combustion, CO₂ is a representation of fuel conversion

efficiency when viewed on a brake specific basis (per unit of net energy output) and represent the most desired final products, along with H₂O, from hydrocarbon combustion.

2.6 Unburned Hydrocarbon Emissions

Unburned hydrocarbon (HC) emissions are of concern because of their effect on health and the environment. Recall that some HC emissions contributed to the organic fraction of PM and are carcinogenic when absorbed by the body. HC emissions are broken into two categories, methane (CH₄) and non-methane hydrocarbons (NMHC). CH₄ has 21 times the greenhouse gas potential of CO₂ [17]. The NMHC are very reactive in the atmosphere and produce photochemical smog, which is an irritant to the respiratory system. Table 2.1 lists the reactivity of specific HCs [5].

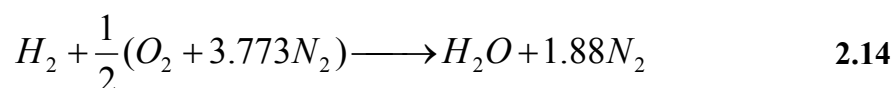
Table 2.1: General Motors Reactivity Scale (0-100). Based on the NO₂ formation rate for hydrocarbon relative to the NO₂ formation rate for 2,3-dimethyl-2-butene [5, 18].

Hydrocarbon	Relative reactivity
C1-C4 paraffins Acetylene Benzene	0
C4 and higher molecular weight paraffins Monoalkyl benzenes Ortho- and para-dialkyl benzenes Cyclic paraffins	2
Ethylene Meta-dialkyl benzenes Aldehydes	5
1-Olefins (except ethylene) Diolefins Tri- and tetraalkyl benzenes	10
Internally bonded olefins	30
Internally bonded olefins with substitution at the double bond Cycloolefins	100

HC emissions are due to incomplete combustion and occur from four main sources. Fuel can disperse into regions of the cylinder where it is so locally fuel lean and/or cool that combustion cannot occur. A charge can be overly fuel rich and thus will not combust. Fuel can be trapped in the fuel injector and come out when it is too late to combust. Finally the fuel spray can penetrate to the cylinder wall where it penetrates crevices and mixes with the lubricating oil. On the cylinder wall, combustion of the fuel can be quenched by the cool temperature of the cylinder wall [3, 5].

2.7 Hydrogen

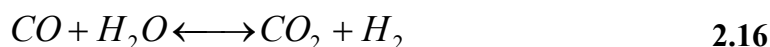
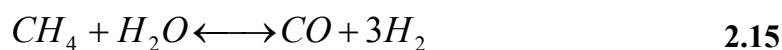
Hydrogen is of interest as a transportation fuel because it is a promising replacement to fossil hydrocarbons. The burning of hydrogen does not produce any carbon emissions, depending upon the source of the hydrogen. The zero emission combustion potential of hydrogen is displayed in, for stoichiometric combustion of hydrogen [5].



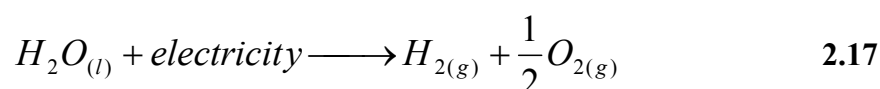
Unfortunately, pure diatomic hydrogen (H_2) is not found in nature. Rather energy must be consumed to generate diatomic hydrogen out of hydrogen containing molecules. For this reason hydrogen is often referred to as an energy carrier rather than a fuel [19].

Hydrogen can be produced by either reforming a hydrocarbon-based fuel or electrolysis. Methane, CH_4 , is the primary hydrocarbon fuel for reforming due to its high hydrogen content. Steam reforming of CH_4 accomplished by the reaction in Eq. 2.15.

The water gas shift reaction, Eq. **2.16**, is then used to produce CO₂ and hydrogen from the product CO [20].



Electrolysis, Eq. **2.17**, produces hydrogen from electricity and water [21].



Hydrogen production from steam methane reforming and electrolysis are not emission free. CO₂ is produced during methane reforming. The electricity used in electrolysis must be generated, which produces emissions depending on the fuel source.

Chui and coworkers conducted a life cycle analysis study to compare the possible pathways to produce hydrogen, based on steam methane reforming and electrolysis [21]. The 11 pathways to hydrogen production are given in Figure **2.8** and Figure **2.9**. The life cycle analysis showed electrolysis with hydroelectric power to be the preferred path to hydrogen production.

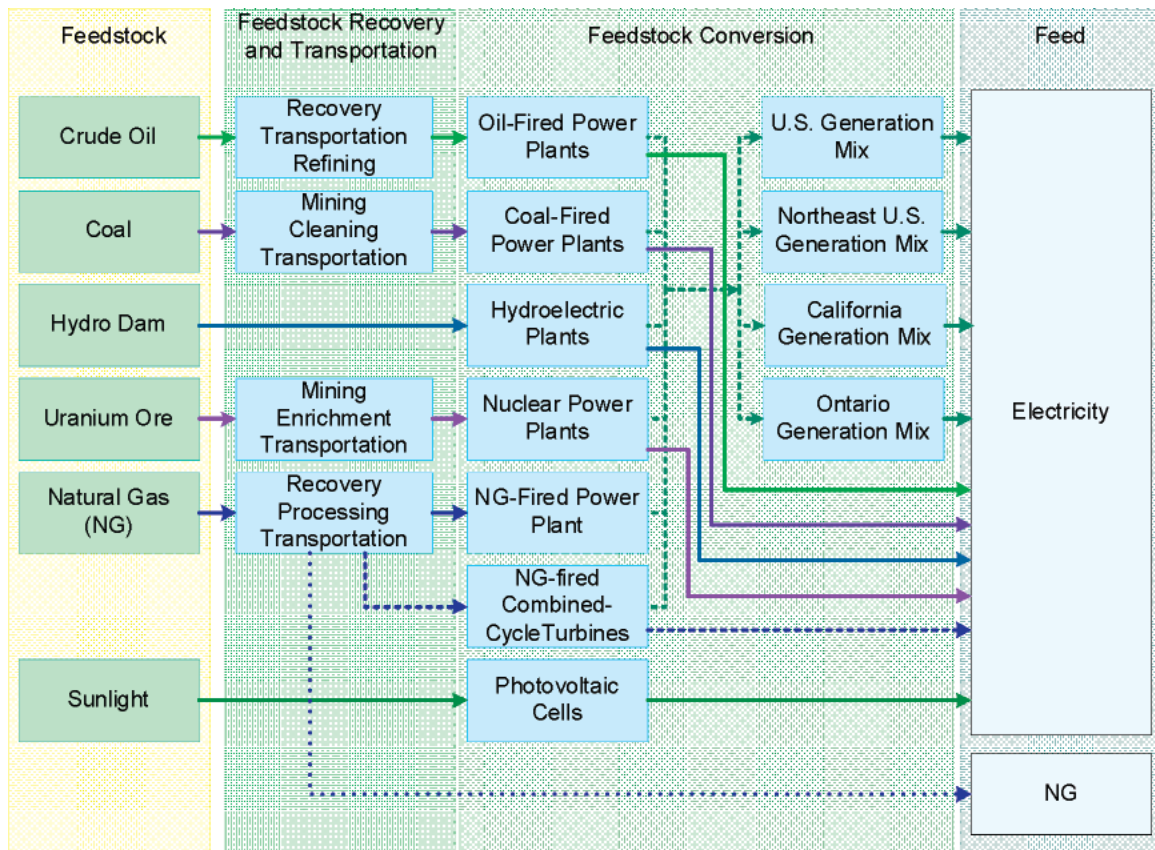


Figure 2.8: Fuel stages for energy and technology types for hydrogen production [21].

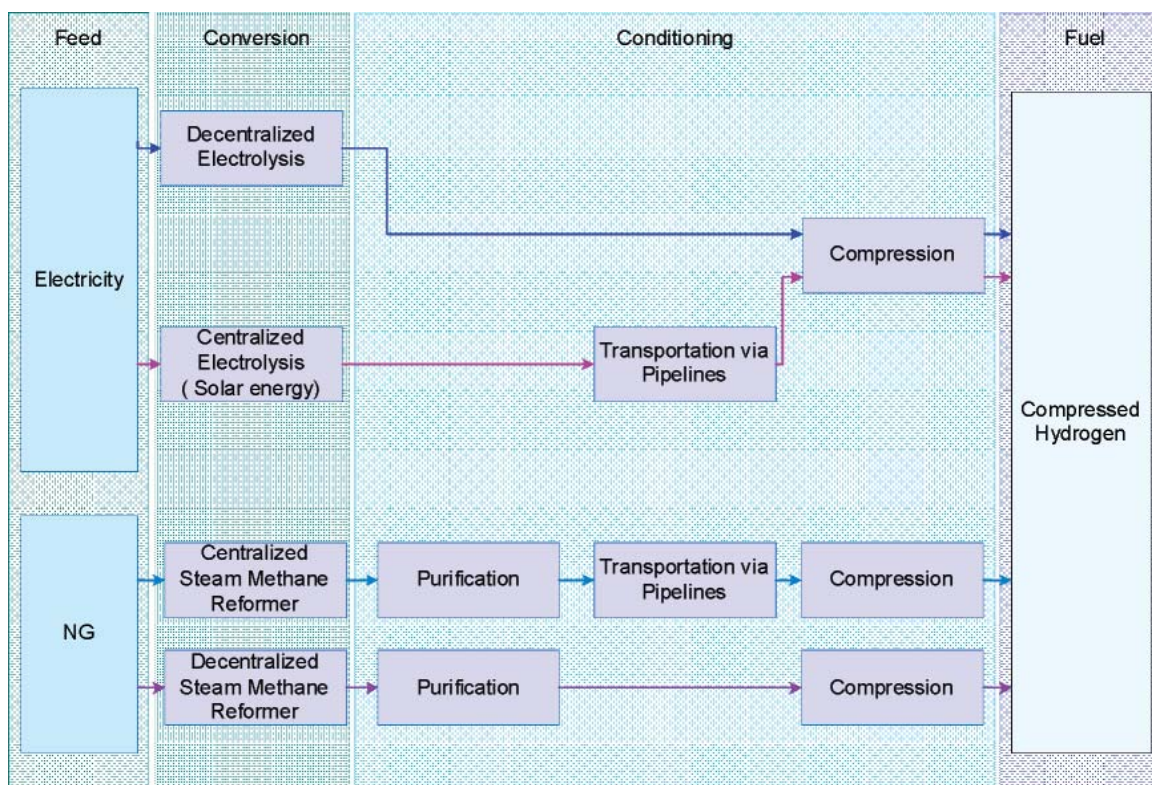


Figure 2.9: Fuel stages for energy and technology types for hydrogen production -continued [21].

2.8 Diesel Pilot Ignited Hydrogen Combustion

Hydrogen has an autoignition temperature of 858K requiring an ignition source to combust in an IC engine [22]. Diesel fuel which has an autoignition temperature of 525K can be used as a pilot to ignite hydrogen. The literature contains a body of work in which hydrogen was used in conjunction with diesel fuel to power CI engines. This dual-fuel combustion is often called diesel pilot-ignited hydrogen combustion. Diesel pilot-ignited hydrogen combustion at low quantities of hydrogen is beneficial since the diesel fuel is being replaced by hydrogen, which may stretch the supply of hydrocarbon fuels.

There is a range of emissions results reported on diesel pilot hydrogen combustion. This literature must be examined critically. The size, power output and rotational speed of the engine used in the studies skew these emission results. Lower emissions are achievable at the cost of de-rating an engine, to the point of unusable road performance.

Varde and Varde conducted some of the earliest work on hydrogen substitution [23]. The work was conducted on a 4.75 kW, single cylinder direct injection, naturally aspirated diesel engine. A pilot injection of diesel fuel was fixed at 22° BTDC and engine speed was fixed at 2400 RPM. The hydrogen was fumigated into the air intake. In this work, propane, natural gas and hydrogen were compared in “dual-fuel” combustion. The flows of the gases were reported by an H/C ratio, which included the diesel fuel. In the case of hydrogen, 15% of the total fuel energy was used as the maximum flow rate. A reduction of smoke was reported when hydrogen was introduced at a full rated load. A 50% reduction of smoke was reported at part load when 15% of the total fuel energy was hydrogen. Increasing the hydrogen at part load past 15% of total fuel energy was shown to increase soot levels, due to insufficient oxygen. NO_x was seen to increase with hydrogen substitution at both part and full load. An increase of 30% NO_x was reported at full rated load with 15% of the total fuel energy being hydrogen. HC levels were also seen to increase with increased flow rates of hydrogen at part and full load.

Lambe and Watson conducted a study in which they optimized a CI engine for hydrogen combustion with a diesel pilot [22]. A Petter PH1W, 6kW open chamber, naturally aspirated, direct injection, diesel engine was used in the study. A delayed port admission system was used to supply hydrogen. The system administered hydrogen via a secondary valve that allowed the flow of hydrogen into the cylinder when the intake

valve opened. Under high loads, an atomized water jet was administered to prevent curve knock. Hydrogen comprised 65% to 95% of the fuel energy. To accomplish such high fuel substitution levels, a minimum pilot diesel fuel quantity was first found. At low loads, lower efficiency was achieved running in a dual-fuel mode compared to running with diesel alone. At higher loads of 75% of maximum output the dual-fuel operation was more efficient than the diesel-only operation. Exhaust emissions were taken at 1000 RPM and 1500 RPM at unclear quantities of hydrogen (somewhere between 65% and 95%) and were compared to diesel-only combustion. At 1000 RPM and full load, smoke was reported to be reduced by 82% with dual-fuel combustion. At 1500 RPM and full load, smoke was reported to be reduced by 20%. NO_x tended to increase at 1000 RPM under light loads, with dual-fuel combustion. At 1500 RPM NO_x increased under dual-fuel combustion. CO_2 emissions decreased for all loads under dual-fuel combustion. At 1000 RPM, CO_2 decreased by 20%. At 1500 RPM, CO_2 decreased by 85%. For both speeds, CO emissions decreased overall. HC emissions increased for both speeds. Nitrogen oxides were reduced by up to 70% in some cases. It was observed that combustion under dual-fuel operation is controlled by flame propagation rather than autoignition.

Tomita and coworkers investigated diesel and hydrogen dual-fuel combustion using a four-stroke, single cylinder, diesel engine with a single cylinder [24]. Injection timing was altered over a wide range of crank angles from 67.7 BTDC to 3.2 ATDC. Testing was conducted at 1000 RPM. The hydrogen was aspirated into the air intake. A pilot injection of diesel was used to ignite the hydrogen. Hydrogen flow rate was quantified in two ways, the total equivalence ratio and as the ratio of the hydrogen equivalence ratio over the total equivalence ratio. The equivalence ratio of diesel-only

and dual-fuel were made equal for comparison. Smoke was seen to decrease to near zero levels at all injection timings and at all equivalence ratios of hydrogen. NO_x emissions dropped to zero at injection timings of 40° BTDC and earlier for all equivalence ratios of hydrogen. However, at timings later than 40° BTDC, NO_x emissions increased over diesel-only combustion. HC emissions made only modest decrease with increasing hydrogen. CO₂ emissions decreased with increasing levels of hydrogen. Thermal efficiency was found to increase significantly at injection timings of 30° BTDC and earlier.

Kumar and Nagalingam investigated the performance increase of hydrogen on vegetable oil in a CI engine [25]. In this work, hydrogen-diesel combustion was also studied for comparison. The study was conducted on a Kirloskar AV1, single cylinder, four-stroke CI engine with a power rating of 3.7kW at 1500 RPM. The tests were conducted at 1500 RPM at 80% and 100% of maximum output. The diesel fuel was injected at 27 BTDC. The hydrogen was inducted into the air intake. Hydrogen flow rate was reported as “hydrogen mass share” given in equation Eq. 2.18.

$$\text{Hydrogen mass share} = \frac{m_{H_2}}{m_{H_2} + m_f} \quad 2.18$$

The hydrogen mass share used in their testing ranged between 0% and 30%, with 5% reported to be the optimum hydrogen mass share. Justification for this was unclear. Brake thermal efficiency increased by 1.7% at 100% of maximum output. At 40% maximum output, 5% hydrogen mass share caused a 1.5% reduction of brake thermal efficiency. The lower efficiency at 40% of maximum output was reported to be due to insufficient diesel fuel to ignite the hydrogen. The smoke reduced from 3.9 BSU (Bosch

smoke unit) to 2.7 BSU at 5% mass share and at 100% of maximum output. At 40% of maximum output, smoke dropped from 1.5 BSU to 1 BSU at 5% of hydrogen mass share. HC emissions reduced from 100 ppm to 70 ppm at 100% of maximum output at 5% hydrogen mass share. At 40% of maximum output, HC emissions decreased from 30 ppm to ~25 ppm, at 5% hydrogen mass share. CO emissions reduced from 20% to 0.14% at 100% of maximum output and 5% hydrogen mass share. At 40% of maximum output, CO emissions decreased from 0.9% to 0.6 %, at 5% hydrogen mass share. NO emissions increased from ~775 ppm to ~895% at 100% of maximum output and 5% hydrogen mass share. At 40% of maximum output, NO showed no significant variation at 5% hydrogen mass share.

In a fundamental study, Lu and coworkers conducted spectral analysis and chemiluminescence imaging hydrogen addition to a HSDI engine under conventional and low-temperature combustion [26]. The work was conducted on a rapid compression machine (RCM) with optical access, which operated at ~1000 RPM. Hydrogen was supplied to the cylinder along with the air. Hydrogen was added at a rate of 0%, 5%, 10% and 15% of the energy released. The LTC mode was based on 25% and 50% EGR and late injection timing. They reported that under mixing-controlled diesel combustion, small amounts of hydrogen had no significant effects on soot temperature, soot concentration or peak pressure. Under LTC, 15% hydrogen fuel energy led to increased soot concentration and soot temperature. The study also examined the OH radical to determine if it would burn part of the soot formed during early combustion. At 10% energy release from hydrogen, in LTC condition, the OH radical was found to further reduce soot concentration due to long residence timings.

The diesel pilot ignited hydrogen combustion literature varies in emissions results from study to study. Given the literature, diesel pilot ignited hydrogen combustion appears to be a promising method to reduce petroleum fuel consumption while achieving emissions reduction. However, these results must be qualified on a full size automotive diesel engine to validate the benefits associated with diesel pilot-ignited hydrogen combustion.

The findings in the published literature on hydrogen assisted diesel combustion are qualitatively presented in Table 2.2. The table indicates inconsistent results from the aspiration of hydrogen into a diesel engine, though it should be noted that the published studies consisted of a broad variation in testing conditions and parameters. A definitive study is thus necessary to clarify these inconsistent results.

Table 2.2: Qualitative results given in the literature on hydrogen assisted diesel combustion. Where + indicates an increase and - indicates a decrease in the given emission species or parameter.

	<i>Varde, 1984</i> [23]	<i>Lambe, 1993</i> [22]	<i>Tomita, 2001</i> [24]	<i>Kumar, 2003</i> [27]	<i>Lu, 2004</i> [26]
<i>No_x</i>	+	-	-	+	+
<i>Soot</i>	-	-	-	-	+
<i>HC</i>	-	+	-	-	
<i>CO</i>		-	-	-	
<i>CO₂</i>		-	-		
<i>Brake thermal efficiency</i>			-	+	
<i>Ignition delay</i>			+	+	
<i>Peak cylinder pressure</i>				+	

2.9 Engine Gas Recirculation

Engine gas recirculation (EGR) is a technique used to reduce NO_x emissions in compression ignition engines. EGR is accomplished by looping exhaust gas back into the intake manifold. The EGR level is controlled by a valve in the loop before the exhaust gas enters the turbocharger. The pressure differential between the exhaust and intake will limit the percent of EGR possible [28].

Engine gas recirculation reduces NO_x emissions in two ways. CO₂ a major product of combustion and has a high specific heat. The high CO₂ content of EGR gas acts as a heat sink to reduce adiabatic flame temperature and thus reduce NO_x. Secondly, circulation of EGR into the air intake dilutes the O₂ content of air. This reduces combustion temperatures and provides less O₂ to combine with N₂ to form NO_x. However, the reduction in O₂ content, moreover, the shift of air-fuel charge to a fuel rich ratio, increases PM production [5, 28, 29].

Exhaust gas recirculation percentage (EGR%) can be quantified based on the volume percent of CO₂ in the ambient air intake air, and exhaust, as given in Eq. 2.19[29].

$$EGR\% = \frac{CO_{2Intake} (vol\%) - CO_{2Ambient} (vol\%)}{CO_{2Exhaust} (vol\%) - CO_{2Ambient} (vol\%)} \quad 2.19$$

EGR decreases engine efficiency. Pump losses increase as EGR rates increase. The indicated work decreases as incomplete combustion increases, in the form of increased CO and HC emissions. Also, indicated work suffers from the reduced cylinder

temperatures. EGR is cooled using engine coolant to recover and prevent the loss of volumetric efficiency caused by fumigating the intake charge with excessively hot gases. However, cooling the EGR increases the losses from heat rejection [30].

Simulated EGR is also used in laboratory settings when large quantities of EGR rates are required. Bottled CO₂ typically is used to simulate EGR. However, results achieved from simulated EGR are somewhat skewed due to the lack of water vapor and combustible species present in actual EGR gas. Studies have been conducted to compare actual EGR to simulated EGR [28].

Large rates of EGR increase cylinder to cylinder variation [31]. Under high EGR conditions, individual cylinders do not receive uniform charges of EGR. This is due to the short mixing length between the point where the EGR meets the intake and a given cylinder. This will result in varying emissions from cylinder to cylinder [32].

2.10 Homogeneous Charge Compression Ignition

Homogeneous charge compression ignition (HCCI) combustion is an advanced combustion mode of interest due to its potential for low NO_x and PM emissions while achieving high efficiency. HCCI utilizes advantages associated with spark ignition engines and compression ignition engines [33]

HCCI combines a homogeneous charge with a compression ignition combustion process. The homogenous mixture of HCCI is fuel lean and/or dilute. Combustion of the charge occurs globally without a propagating flame, resulting in combustion with local hotspots [34]. Fuel lean mixtures produce less PM due to the high rate of oxidization

occurring in the locally lean charges. The locally lower temperatures of HCCI produce less NO_x . In contrast, the stratified diffusion flame, conventionally used in compression ignition engines, has layers of fuel rich zones where PM is created. Also, at the periphery of these fuel rich zones pockets of high temperature are present, which generate thermal NO_x .

The stated efficiency of HCCI is higher than that of SI engines but equivalent to CI engines. The high efficiency derives from the reduction of pumping losses which are present when the intake air is throttled, such as in the case of stoichiometric SI engines [33]

Some obstacles still remain before HCCI will be realized in production applications. The largest problem facing HCCI is the requirement for an ignition control system with varying speeds and loads. The ignition timing is based on fueling rate and in-cylinder temperature. This is difficult to control in a transient state with varying power demands. Another challenge for HCCI is its lack of ability to operate in high load. At high loads HCCI combustion occurs rapidly causing increased levels of NO_x , noise and possibly damage to the mechanical components of the engine. HCCI also does not work properly under cold start operation. The cold cylinder walls absorb the heat of compression preventing an HCCI engine from firing. HCCI produces excess amounts of CO and HC, which is an issue because catalyst technology does not work properly at low exhaust temperatures [35].

2.11 Partially-premixed Charge Compression Ignition

HCCI can be approximated in a CI engine by early fuel injection combined with high EGR. The acronym PCCI has been used in the literature on advanced combustion with multiple meanings. Neely and coworkers used PCCI to refer to premixed controlled compression ignition combustion, having an increased, advanced pilot injection, and a retarded main injection [36]. Kanda [37] and Araki[38] refer to PCCI as premixed charge compression ignition, in which diesel fuel is injected early. Sluder and coworkers refer to PCCI as partially-premixed charge compression ignition [39]. No matter what the PCCI acronym stands for, PCCI commonly refers to an advanced combustion process that allows for a large premixed burn. In PCCI, fuel is injected early into the cylinder, during which an ignition delay occurs until cylinder conditions are right for autoignition. During the ignition delay atomized diesel fuel mixes with air, creating a locally fuel lean charge. If injection of diesel fuel continues past the point of autoignition, the burn will transition from a premixed burn to a diffusion burn.

The contrast between HCCI and PCCI should be noted. The air-fuel charge in HCCI is homogeneous when it enters the cylinder. In PCCI, advanced injection of fuel leads to an extended premix-combustion phase. PCCI can be seen as an intermediate step between conventional diesel combustion and HCCI. The charge in PCCI is not mixed as well, thus there will be more hot spots. Also, since PCCI injects fuel via the diesel fuel injector, the long ignition delay may result in diesel fuel penetration to the cylinder walls, resulting in incomplete combustion. Like HCCI, PCCI suffers from increased HC and CO emissions related to the overly lean combustion conditions. However, PCCI permits

a practical route to approximate HCCI, because injection timing and EGR level can be used in concert to control ignition timing.

2.12 Low Temperature Combustion

Low temperature combustion (LTC) is a generic term that refers to an engine condition which operates below that required for the formation of NO_x ($\phi < 2.5$, $2000\text{K} < T$) and/or PM ($\phi > \sim 2.5$, $1700\text{K} < T < 2400\text{K}$) [40]. Combustion temperature can be lowered by introducing EGR or by altering the combustion process to be locally fuel lean. These techniques can be used in tandem. EGR is used as a thermodynamic “dead weight” to reduce the rate of heat release in the cylinder. EGR is introduced into the cylinder by displacing the intake air. Thus, O_2 is reduced, which successfully reduces NO_x . However, PM emissions increase due to the reduction in oxygen and the resulting inhibition of soot oxidation. HCCI-like conditions are coupled with EGR to reduce PM emissions. A well mixed air-fuel charge is locally fuel lean. A fuel lean charge will produce less heat and have more O_2 locally available to oxidize PM or prevent formation of PM.

The concept of LTC is best presented by a 3D-CFD model originally developed by Akihama and coworkers [40]. This map plots local equivalence ratio versus local flame temperature. The map provides insight into the NO_x -PM trade off which is at the heart of diesel engine emissions. Figure 2.10 displays an updated version of Akihama and coworkers’ model.

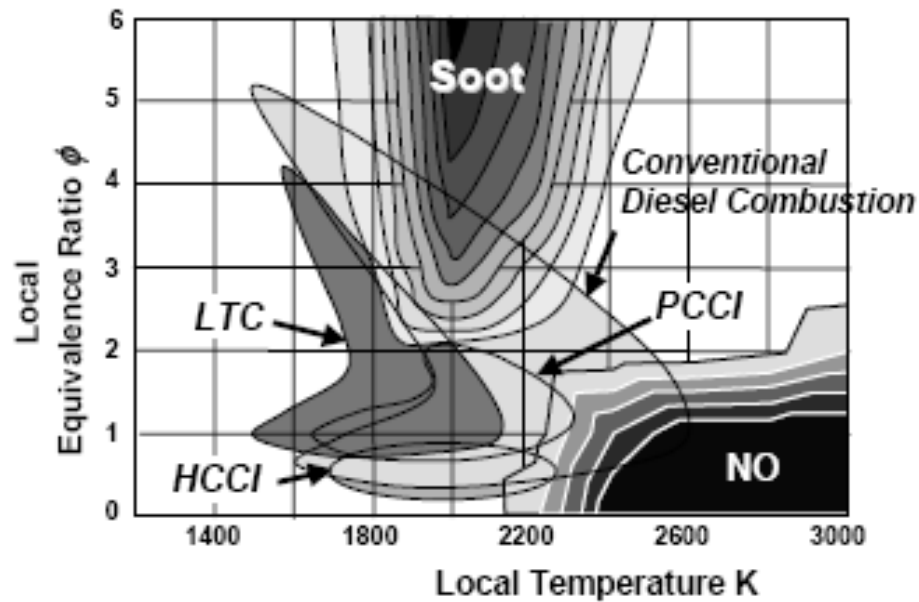


Figure 2.10: 3D-CFD model of local equivalence ratio vs. local temperature [36].

LTC has been heavily explored with the recent onset of strict diesel emissions regulation. Here the most pertinent variations of LTC are discussed.

2.13 Smokeless Locally Rich Diesel Combustion

Smokeless locally rich diesel combustion (SRDC) was developed by Toyota [41]. The mode is entered by introducing extremely large amounts of cooled EGR (~60%). This lowers the air-fuel ratio to stoichiometric levels (~20 A/F ratio). However, the EGR decreases the local combustion temperature below the PM formation temperature. [40] [42] The concept of SRDC emissions reduction is summarized in Figure 2.11.

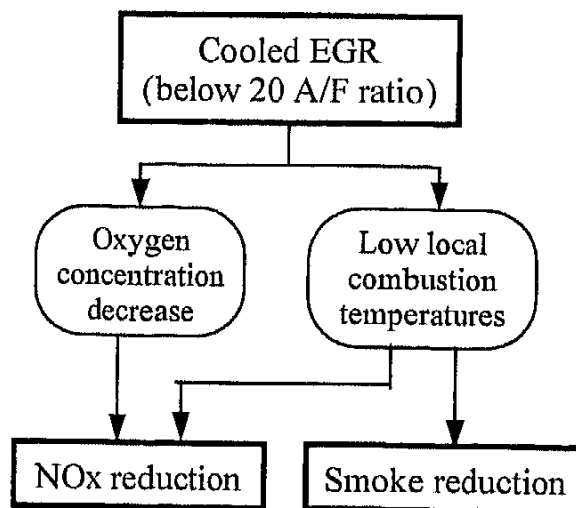


Figure 2.11: Smokeless Locally Rich Diesel Combustion (SRDC) Combustion [42]

2.14 Modulated Kinetics

Modulated kinetics (MK) was developed by Nissan [27]. The MK condition is achieved by using single pulse fuel injection, retarding fuel injection after TDC, utilizing moderate levels of EGR (~30%) and increasing swirl [43]. The results of these modifications are increased ignition delay causing increased mixing of fuel and air. The concept of MK's emissions reductions is summarized in Figure 2.12.

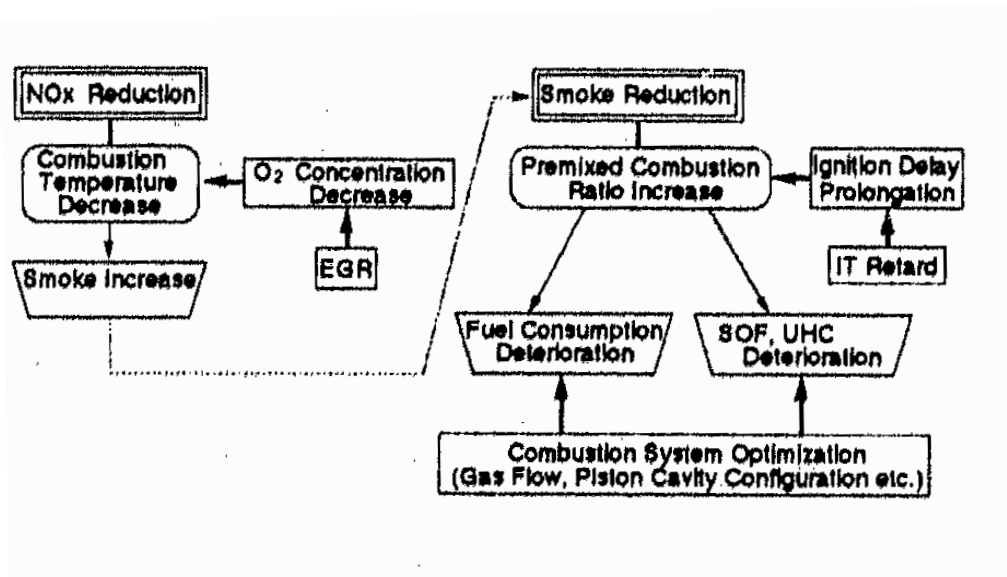


Figure 2.12: Schema of Modulated Kinetics (MK) Combustion[27].

Modulated kinetics is stated to reduce NO_x by the formerly mentioned methods [42]. EGR reduces the O_2 content and slows the heat release rate. Smoke or PM will increase with decreased levels of O_2 . PM is reduced via the premixed charge coupled with retarded injection timing and low temperatures to inhibit PM formation. MK is reported to produce increased levels of HC emission, SOF emissions and increased fuel consumption which are associated with HCCI-like modes. To combat these increases in some emissions, MK utilizes swirl which is augmented by piston configuration and fuel injection pressure [42].

Singh and coworkers conducted a study in which SRDC and MK were compared on a single cylinder high speed direct injection (HSDI) turbocharged engine. The study found that both SRDC and MK did reduce NO_x and PM. However significant disadvantages offset the emission reductions. The MK mode neared the misfiring limit of the engine. HC emission and fuel consumption were found to be high due to late

combustion. The main disadvantage of SRDC is the high EGR requirement, which resulted in a fuel economy penalty. The study also found that increases in swirl and injection pressure could be used to further reduce NO_x and PM. However these decreases would be offset by a penalty in fuel consumption [42].

2.15 High Efficiency Clean Combustion

High efficiency clean combustion (HECC) was developed at Oak Ridge National Laboratory. HECC, formally known as Efficient-LTC, is accomplished by a combination of single pulse injection, EGR (50%), early injection timing, and increased injection pressure. The EGR reduces NO_x emissions and increases PM emissions. The early injection allows time for the diesel fuel to mix with air before combustion. Thus, an extended premixed combustion phase occurs, accompanied by a shorted mixing-controlled combustion phase. The premixed air and fuel are locally fuel lean, thus decreasing PM. As the premixed air-fuel charge is consumed, the combustion transitions to a diffusion burn. Increasing the injection pressure decreases the injection duration, which causes more fuel to be premixed and burned during the premixed combustion phase. The HECC mode provides a decrease in NO_x emissions and PM emissions while maintaining or even increasing fuel efficiency. However, the HECC mode results in increased HC and CO emissions, which is common with HCCI-like modes [39, 44-49].

In a recent study Wagner, Sluder and coworkers, who developed the HECC mode at Oak Ridge National Laboratory, have shown the HECC mode to be operable at 1500 RPM at 1.0 bar IMEP, 1500 RPM at 2.6 bar IMEP, 2000 RPM at 2.0 bar IMEP and 2300

RPM and 4.2 bar IMEP. The tests were conducted on a modified Mercedes 1.7-liter, direct-inject diesel engine with cooled EGR. In all four of the engine conditions, NO_x was reduced by more than 80% compared to the baseline. PM decreased between 30% - 50% and was even further decreased from 85% -100% when the fuel injector nozzles were replaced to further increase atomization. HC levels doubled at the lowest speed and only slightly increased at the highest speed. The CO emissions double in three of the four conditions. The fuel consumption remained the same as the baseline for all four conditions. Figure 2.13 is a concept map that summarizes the techniques used to achieve the SRDC, MK and HECC LTC modes.

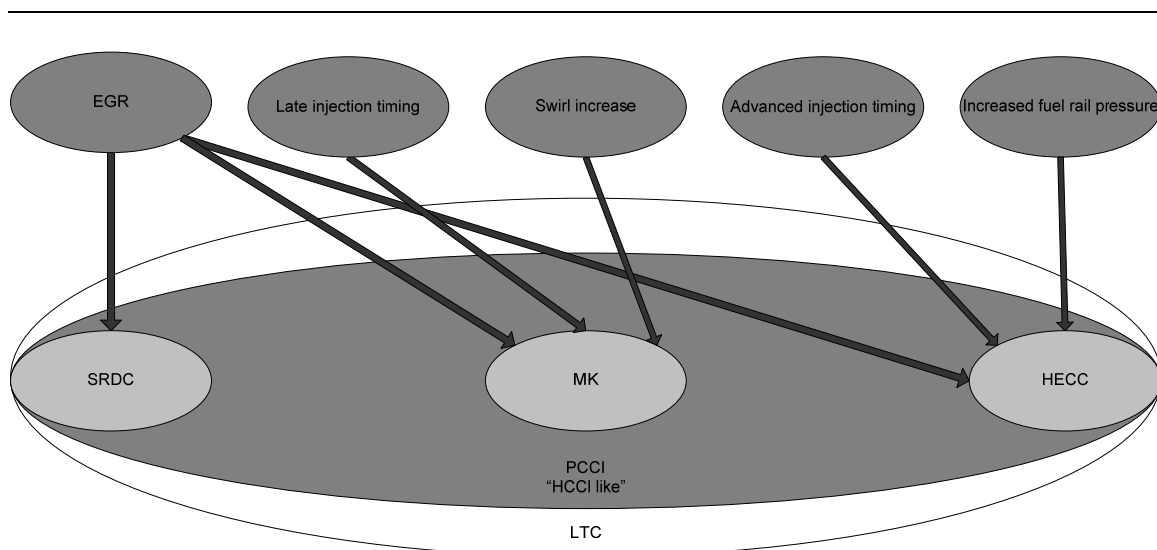


Figure 2.13: Concept map of various LTC modes.

2.16 Research Objective Identified via the Literature Review

The literature to date on the topics of hydrogen assisted diesel combustion and HECC contains gaps which require further experimental research. The gaps in the literature aimed to be filled by the work in thesis are as follows:

- To perform hydrogen assisted diesel combustion on a light-duty production diesel engine under laboratory conditions.
- To verify that the aspiration of hydrogen into a diesel engine will increase the pre-mixed combustion phase, decreasing NO_x and PM emissions.
- To verify that small quantities of aspirated hydrogen will have little effect on engine performance and emissions
- To demonstrate that the HECC mode can be achieved using a production DDC/VM Motori 2.5L, 4-cylinder, turbocharged, common rail, direct injection light-duty diesel engine.
- To demonstrate that while operating in the HECC mode, the addition of hydrogen to the combustion chamber will smooth-out the combustion process, quantified by the coefficient of variance (COV) of the indicated mean effective pressure (IMEP) and further reduce NO_x and PM emissions.

Chapter 3

Experimental Setup

3.1 Engine Test Stand

A heavily instrumented DDC/VM Motori 2.5L, 4-cylinder, turbocharged, common rail, direct injection light-duty diesel engine was used for steady-state testing. Engine specifications are given in Table 3.1 and the general engine layout is given in Figure 3.1.

Table 3.1: DDC 2.5L Engine Specification.

Engine	DDC 2.5L TD DI-4V Automotive Diesel Engine
Displacement	2.5L
Bore	92 mm
Stroke	94 mm
Compression Ratio	17.5
Connecting Rod Length	159 mm
Rated Power	103KW@4000 RPM
Peak Torque	340Nm@1800 RPM
Injection System Bosch	electronically controlled common-rail injection system
Valve Train	4 valves/cylinder

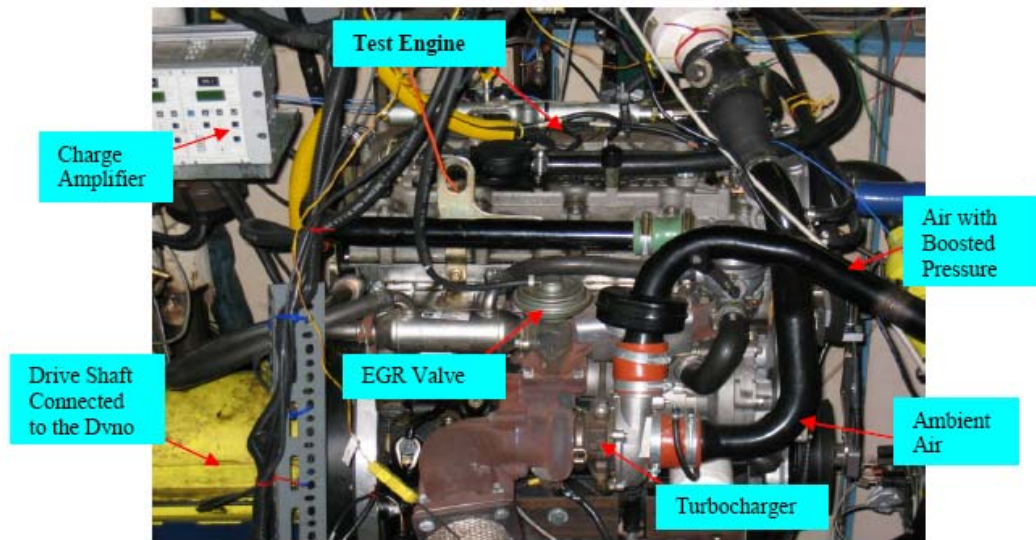


Figure 3.1: DDC 2.5L common rail diesel engine set up [1].

A 250HP Eaton eddy current water-cooled dynamometer was coupled to the 2.5L DDC engine to generate load. The engine and dynamometer were controlled by a Digalog Testmate control unit.

3.2 Data Acquisition

Time-based data acquisition was managed using a custom programmed National Instruments LabView VI. Analog signals from pressure transducers, thermocouples, mass flow meters, and emissions data were read by a series of National Instruments FieldPoint modules, including a FP-2015, a FP-AO-210, a FP-DO-403, a FP-AI-102, a FP-AI-112 and three FP-TC-120 modules. The data collected by the FieldPoint modules were saved every 10 seconds during 15 minutes of sampling per test.

3.3 Electronic Control Unit Modification

The electronic control unit (ECU) is the computer that controls engine operation. An unlocked ECU was used to modify and control main injection and pilot injection timings, as well as, EGR valve position, and fuel rail pressure. The unlocked ECU was connected to an ETAS MAC 2 unit via an ETK connection. The MAC 2 unit was connected to a PC running ETAS INCA v5.0 software. INCA managed the ECU modifications in real-time.

3.4 EGR Operation

The DDC 2.5L engine regulates EGR rates using an ECU map based on engine speed and injection volume. The ECU map dictates the flow rate by varying the amplitude of the signal sent to a proportional pneumatic valve. The stock DDC 2.5L engine then introduces EGR to the intake manifold via a Y-pipe. The Y-pipe was modified to include a stainless steel tube which extended into the engine's intake manifold, as given in Figure 3.2. CO₂ emissions were sampled from this tube, thus providing an accurate indication of CO₂ levels in the intake manifold charge.



Figure 3.2: Instrumented air intake/EGR Y-pipe.

It was necessary to aspirate simulated EGR into the engine's air intake to achieve a well-mixed and high concentration of EGR charge (~50%). Bone-dry CO₂ with a purity of 99.8% was used as simulated EGR. The flow rate of the simulated EGR was monitored and regulated using an array of Matheson model 605 rotameters. The simulated EGR was aspirated after the charge air cooler, as seen in Figure 3.3.

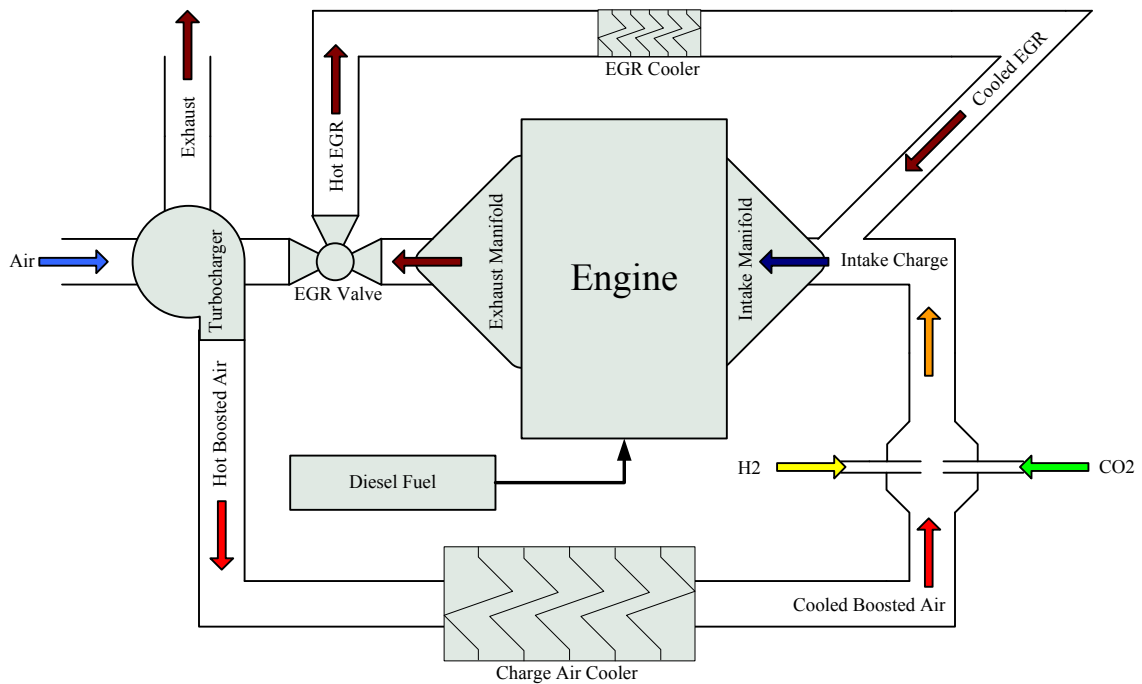


Figure 3.3: DDC 2.5L EGR/H₂ flow diagram.

The simulated EGR was dispersed and mixed with the boosted air using a custom built mixing manifold. The manifold consisted of four porous metal (Hastelloy) filters, customarily used as spargers, placed on the radial of the manifold. Two of the porous metal filters were used to inject simulated EGR. The other two porous metal filters were used to inject hydrogen gas. The manifold is seen in Figure 3.4.



Figure 3.4: Custom intake air manifold aspiration system.

3.5 Hydrogen Flow Rate Monitoring and Control

Hydrogen was supplied to the engine from a Structural Composites Industries 5000 psi 87.99L tank, which was located outdoors, adjacent to the testing facility. A diagram of the hydrogen delivery system is given in Figure 3.5. While the system was designed to withstand 2000 psi of hydrogen, only a 150 psi flow was necessary to achieve the required flow demands. The hydrogen delivery system was designed with redundant safety features, such as two pressure relief valves, and indoor and outdoor iTrans Fixed Point Monitors for hydrogen leak detection. This system also included a pneumatic tank

shut-off valve, which would automatically close in the case of engine failure.

Stainless steel (304) tubing and fittings were used to construct the hydrogen delivery system, which featured Swagelok fittings and valves. To prevent indoor leaks, weld connections were implemented when possible. Indoors, a fume hood was placed above the mechanical connections of the system to collect any leaking hydrogen.

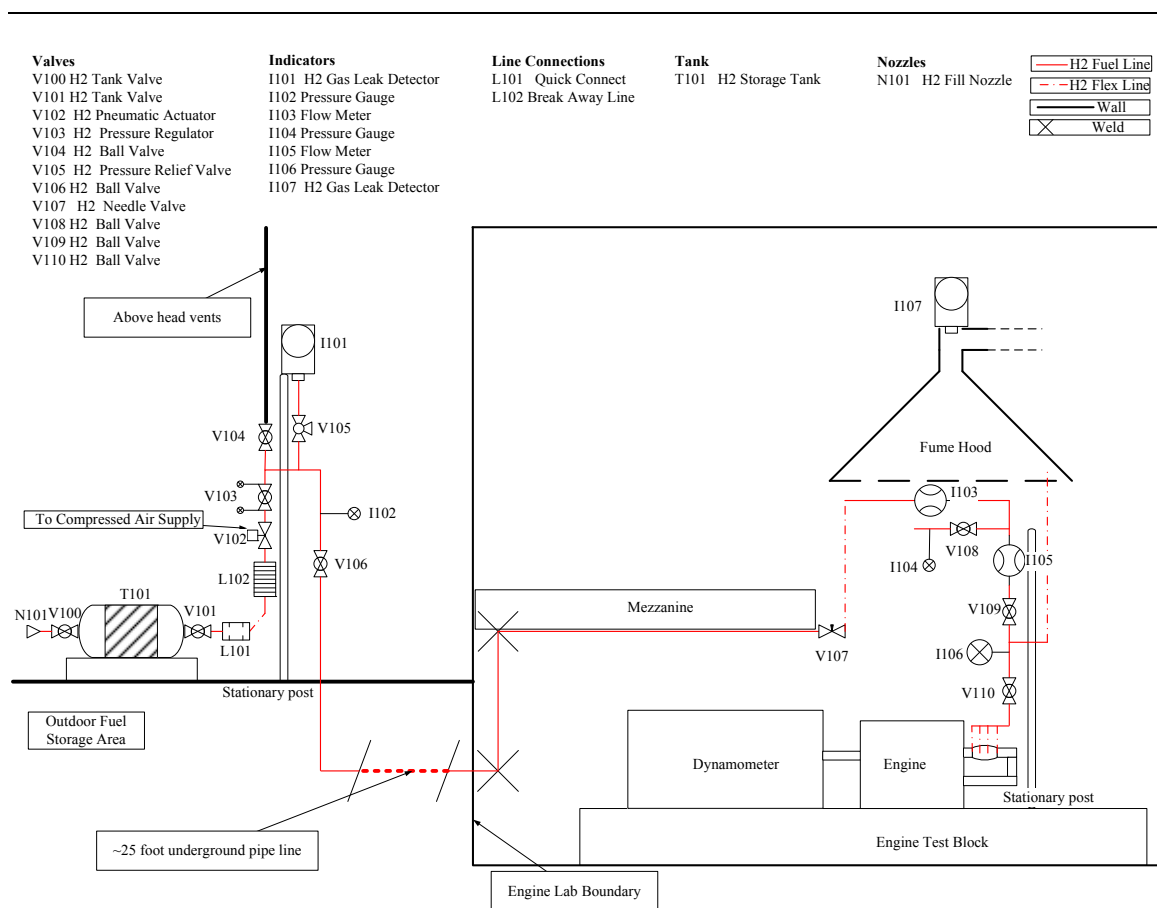


Figure 3.5: Diagram of the hydrogen delivery system.

A regulator and a needle valve were used to control the flow rate of hydrogen to the engine. Since the test plan called for a wide range of hydrogen flow rates, two mass flow meters of different ranges, were used to monitor the hydrogen. While a Sierra

Instruments Toptrak model 820 mass flow meter monitored flows between 0-50slpm, a Teledyne Hastings Nall-P mass flow meter monitored flows between 50-200 slpm. The hydrogen was aspirated into the engine using the same method described for simulated EGR aspiration in Figure 3.3 and Figure 3.4.

3.6 Diesel Fuel Flow Rate

Diesel fuel consumption was measured using a Sartorius electronic microbalance. The custom LabView VI calculated diesel fuel consumption rates based on 100 measurements of fuel tank mass, tracking the small change in mass over 60 seconds.

3.7 Gaseous Emissions: AVL Combustion Emissions Bench II

An AVL Combustion Emissions Bench II was used to measure gaseous emissions. The bench was composed of six gas specific analyzers. Hot exhaust gases were sampled from the engine's exhaust pipe by head-line filters, and then fed through heated lines kept at a constant temperature of 190 °C. NO_x and NO were measured using an EcoPhysics chemiluminescence analyzer. NO₂ was assumed to be the value of NO subtracted from NO_x. Total hydrocarbons and methane were measured by using two separate ABB Flame Ionization detectors. CO and CO₂ were measured by two separate Rosemount infrared analyzers, and O₂ was measured by using a Rosemount paramagnetic analyzer. The hot exhaust sample going to the CO, CO₂ and O₂ analyzers was first chilled to reduce moisture.

3.8 Gaseous Emissions: GC

The hydrogen content of the exhaust gas was measured using a HP 6890 gas chromatograph (GC). The GC included a thermal conductivity detector (TCD) and a flame ionization detector (FID). Exhaust gas was supplied to the GC via a headline filter and heated sample line, kept at a constant 190°C. A 10ft (for TCD) and a 36ft (for FID) HayeSep D packed stainless steel, 100/125 mesh, 1/8" diameter column were used to concurrently analyze on-line permanent gases, water, and hydrocarbons. A factory set analysis method was used to examine exhaust samples. Argon was used as the carrier gas to pass the exhaust gas through the system, and flowed at 30 mL per minute for 16 minutes. The argon flow then ramped up to a rate of 60 mL per minute for 19 minutes. The GC initiated analysis at an oven temperature of -15 °C for 17 minutes, and increased at a rate of 30 °C per minute for 8 minutes. The GC then held to 255 °C for 10 minutes, with a total sampling time of 35 minutes.

3.9 Particulate Matter Emissions: BG-1

Particulate matter was measured using a Sierra Instruments BG-1 Micro-Dilution test stand. The samples were taken at a dilution ratio of 10, a total flow rate of 110 slpm and a sample flow rate of 10 slpm over 5 minutes. The particulate matter samples were collected on Pallflex 90mm Filters, Type EMFAB TX40HI20-WW. The filters were weighed on a Sartorius M5P electronic microbalance, before and after sampling. The scale was located in an environmental chamber set at 25°C, with 45% relative humidity. The filters were placed in the environmental chamber 48 hours prior to mass analysis.

Five sample filters were taken per mode and the four sample filters having the lowest standard deviation were averaged to represent the mass produced at a given mode.

3.10 Particulate Matter Emissions: SMPS

A TSI 3936 Scanning Mobility Particle Sizer (SMPS) was used to analyze the size distribution of the particulate matter. The SMPS instrument included a TSI series 3080 Electrostatic Classifier with a Differential Mobility Analyzer (DMA), a series 3776 Condensation Particle Counter (CPC), and a series 3065 Thermal Denuder. A PC running Aerosol Instrument Manager Software collected and managed the sampled data.

The BG-1 was used to draw and dilute samples from the exhaust. The BG-1 drew samples at a dilution ratio of 10, a total flow rate of 108.6 slpm and a sample flow rate of 100 slpm. The SMPS drew samples from the BG-1 at a rate of 1.4 slpm. The SMPS measurements were conducted using three different sample methods: passing the samples through the Thermal Denuder, passing the samples through the Thermal Denuder at 300°C and having the samples by-passing the Thermal Denuder. The sampling methods affected the content of the volatile hydrocarbon present on the particulate matter. A large number of samples (~6) should have been taken on the SMPS to correct for and average out the inconsistent residence timing of the exhaust samples in the dilution chamber of the BG-1. Unfortunately, due to the limited test time possible before the hydrogen tank emptied, only three SMPS data samples were taken during this study at each operating condition.

3.11 Cylinder Pressure Trace Analysis

Pressure traces were measured using AVL GU12P pressure transducers, which replaced the glow plug in each of the four cylinders. The pressure trace voltages from the pressure transducers were amplified by a set of Kistler type 5010 dual mode amplifiers. The amplified voltages were read by an AVL Indimodul 621 data acquisition system. Needle lift data were collected from a Wolff Controls Inc. Hall-effect needle lift sensor, which was placed on the injector of Cylinder 1. The needle lift signal was also collected by the Indimodul, which was triggered by a crank angle signal from an AVL 365C angle encoder placed on the crankshaft. The pressure traces and needle lift data were recorded at a resolution of 0.1 crank angle degrees, and were averaged over 200 cycles. The real-time Indimodul data were transferred to a PC, which ran AVL Indicom 1.3 and Concerto 3.90 to calculate the apparent heat release rate.

The apparent rate of heat release for each of the four cylinders was calculated from the volume and pressure trace data. The calculation is a built-in feature of Indicom/Concerto and is based on cylinder pressure. The algorithm neglects losses and assumes a polytropic coefficient of 1.37 for diesel fuel. The apparent rate of heat release algorithm is given in Eq. 3.1 [50].

$$Q_i = \frac{K}{\kappa - 1} [\kappa \cdot P_i \cdot (V_{i+n} - V_{i-n}) + V_i \cdot (P_{i+n} - P_{i-n})] \quad 3.1$$

Where:

n is the interval (0.1 degree)

κ is the polytropic coefficient ($\kappa = \frac{c_p}{c_v}$ where c_p is the temperature at a constant

pressure and c_v is the temperature at a constant volume of the fuel)

P is the cylinder pressure

V is the volume

3.12 Test Plan

This thesis contains two different studies, which both utilized hydrogen assisted diesel combustion. In the first study, hydrogen assisted diesel combustion was explored under four conventional steady-state operation modes, which are given in Table 3.2.

Table 3.2: Test matrix for conventional hydrogen assisted diesel combustion on the basis of fuel energy percent.

3600 rpm (75% load)				
3600 rpm (25% load)				
1800 rpm (75% load)				
1800 rpm (25% load)				
	0% H ₂	2.5% H ₂	7.5% H ₂	15% H ₂

These four modes were chosen to provide a range of high and low loads at high and low speeds to examine the effect of hydrogen substitution on emissions and combustion behavior. In this study, the maximum rate of aspirated hydrogen substitution at a given mode was discovered, as seen in Table 3.3.

Table 3.3: Test matrix for conventional combustion modes with hydrogen substitution on the basis of fuel energy percent, in which the maximum % hydrogen limit was found.

1800 rpm (75% load)								
	0% H ₂	2.5% H ₂	7.5% H ₂	15% H ₂	25% H ₂	30% H ₂	35% H ₂	...% H ₂

The second study examined the effect of hydrogen assisted diesel combustion on advanced combustion modes, given in the test matrix of Table 3.4. In this study, it was necessary to first locate an engine specific “HECC” mode, which was defined as providing simultaneous a reduction of NO_x and PM while maintaining or increasing fuel efficiency. The criteria for the HECC mode were based on work by Wagner, Sluder and coworkers. A HECC operation mode is entered at a single pulse injection by advancing injection timing, increasing rail pressure, and increasing EGR to ~50%. The definition of “LTC” operation mode was also based on Wagner, Sluder and coworkers’ work, i.e. a ~50% EGR without any other modification from the Baseline mode at the same speed and load as the HECC mode. The Baseline mode was defined as the same speed and load as the HECC mode without any modifications.

Table 3.4: Test matrix for advanced combustion modes with hydrogen assisted diesel combustion on the basis of fuel energy percent.

~50% EGR "HECC"				
~50% EGR "LTC"				
Baseline				
	0% H ₂	2.5% H ₂	7.5% H ₂	15% H ₂

Chapter 4

Discussion and Results of Conventional Combustion Modes with Hydrogen Substitution

4.1 Introduction

In this section the results of experimentation on hydrogen substitution of conventional diesel combustion modes are discussed. The hydrogen for diesel substitution rate was defined on the percentage energy basis. In an exploratory search, the maximum possible rate of hydrogen substitution was found for a given mode. For the 1800 rpm at 75% maximum output mode, 30% hydrogen substitution was found to be the operable limit. At 35% the engine simply shut down from being choked. There were no significant reductions in emission trends past the 15% substitution point, thus 15% hydrogen substitution was marked as the limit for rigorous testing.

Hydrogen was substituted for diesel in a span up to 15% on a fuel energy basis, in four unique modes. A level of 15% hydrogen substitution was also chosen because it is below the lower explosion limit of hydrogen in air, 4.1% volume, for all modes tested. Furthermore, increasing the hydrogen substitution past 15% would have required an excessive flow rate of hydrogen, rates nearing 200 slpm in high load modes.

Results of each of the four baseline test modes are compared on the basis of parameter change. The effect of hydrogen substitution is then reported and explained. Hydrogen substitution caused only modest changes in emissions. Many of the effects on

emissions were mode dependent. Though hydrogen caused a modest reduction in emissions, hydrogen can be substituted for diesel with out penalty.

4.2 Mode Parameters

Table 4.1 lists the parameters of the modes explored in this study. These parameters are for the baseline mode (0% hydrogen on the fuel energy basis). Hydrogen substitution caused small changes to the EGR %, intake manifold gas temperature and the exhaust gas temperature parameters. The injection timing was electronically held constant by reprogramming the engine's ECU. Speed and load were held constant by using a combination of dynamometer and engine controllers.

Table 4.1: Parameters of baseline operations for the four test modes.

Mode	Load (kW)	EGR (%)	Boost (bar)	Intake Manifold Gas (°C)	Exhaust Gas (°C)	Pilot Inj. (°ATDC)	Main Inj. (°ATDC)
1800 rpm @ 25% Max. Ouput	15.7	10.5	0.2	56.3	332.5	-17.4	2.9
1800 rpm @ 75% Max. Ouput	46.5	0.7	0.7	42.0	476.9	-38.3	-6.2
3600 rpm @ 25% Max. Ouput	26.1	1.4	0.9	70.3	247.9	-56.8	-12.3
3600 rpm @ 75% Max. Ouput	78.2	1.0	1.1	76.5	476.4	-58.1	-13.6

4.3 Hydrogen Substitution

Figure 4.1 displays the actual values of hydrogen substitution. The flow rate of hydrogen to be used for substitution was calculated from the diesel flow rate, which varies and shifts with the operation of the engine, even at steady state. There is slight variation of hydrogen percentage at the given points between modes. However, this

variation is small and the step changes in hydrogen percentage are large enough to ignore this discrepancy.

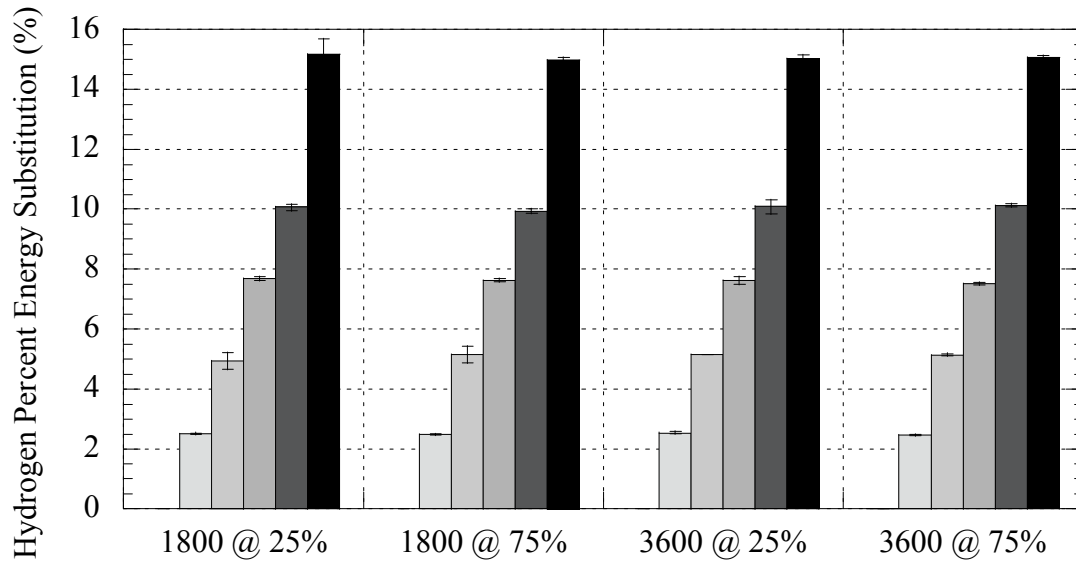


Figure 4.1: Actual hydrogen percentage energy substitution for the four modes tested, with □ 0%, ■ 2.5%, ■ 5%, ■ 7.5%, ■ 10% and ■ 15% hydrogen substitution on an energy basis.

4.4 Needle Lift

The needle lift provides an indication of the injection timing and duration. The needle lift also indicated whether the injection timing had shifted. Three needle lift traces were taken at 1800 rpm at 25% maximum output without the addition of hydrogen.

These three repeated needle lift traces are given in Figure 4.2.

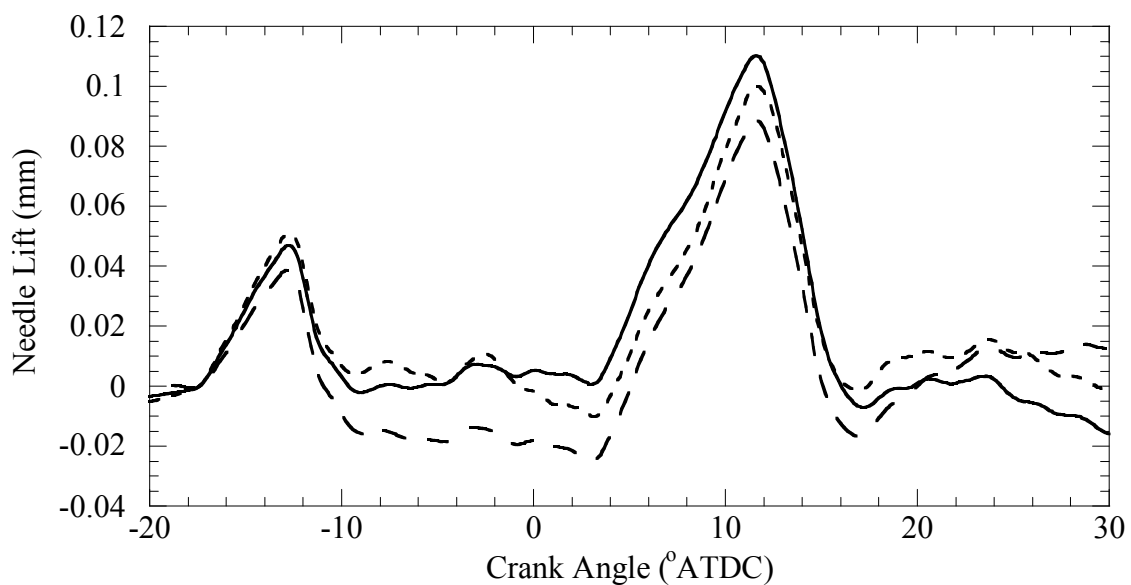


Figure 4.2: Repeatability study of needle lift at 1800 rpm at 25% maximum outputs, of. — Trial 1, - - Trial 2 and - - - Trial 3.

Figure 4.2 indicates that the injection timing is indeed locked down. Though, the needle lift trials share a common profile, they vary in starting height. Figure 4.3 and Figure 4.4 are needle lift profiles with hydrogen substitution. Hydrogen substitution causes the absolute height of the needle lift to reduce. This indicates smaller volume of diesel fuel passes through the fuel injectors as hydrogen substitution increases. It is important to note that hydrogen substitution did not cause a shift in injection timing or injection duration.

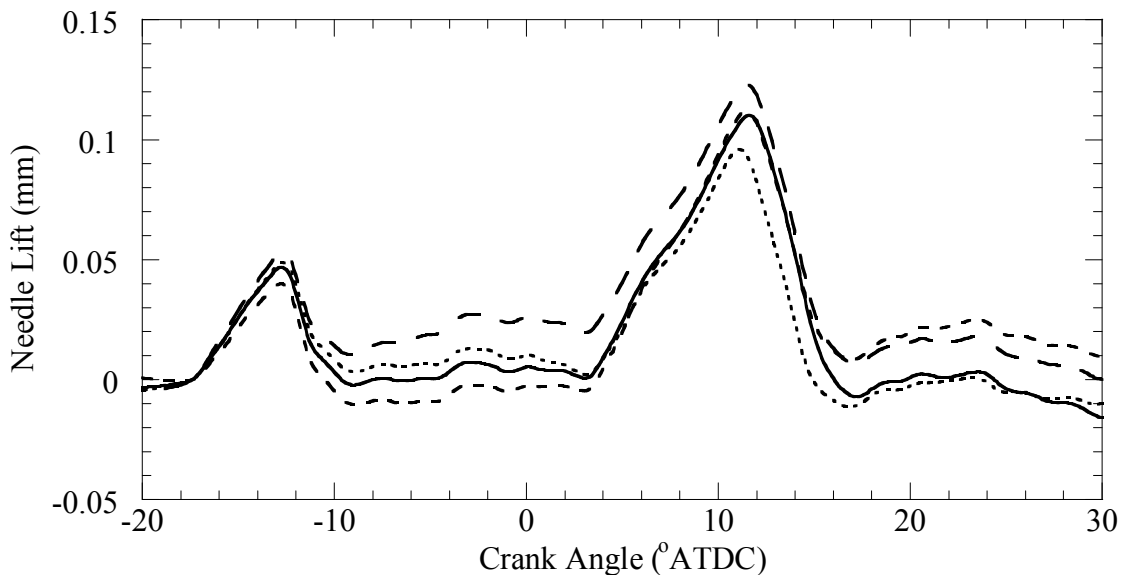


Figure 4.3: Needle lift at 1800 rpm at 25% maximum output, with — 0%, — — 2.5%, - - - - 7.5% and · · · · · 15% hydrogen substitution on an energy basis.

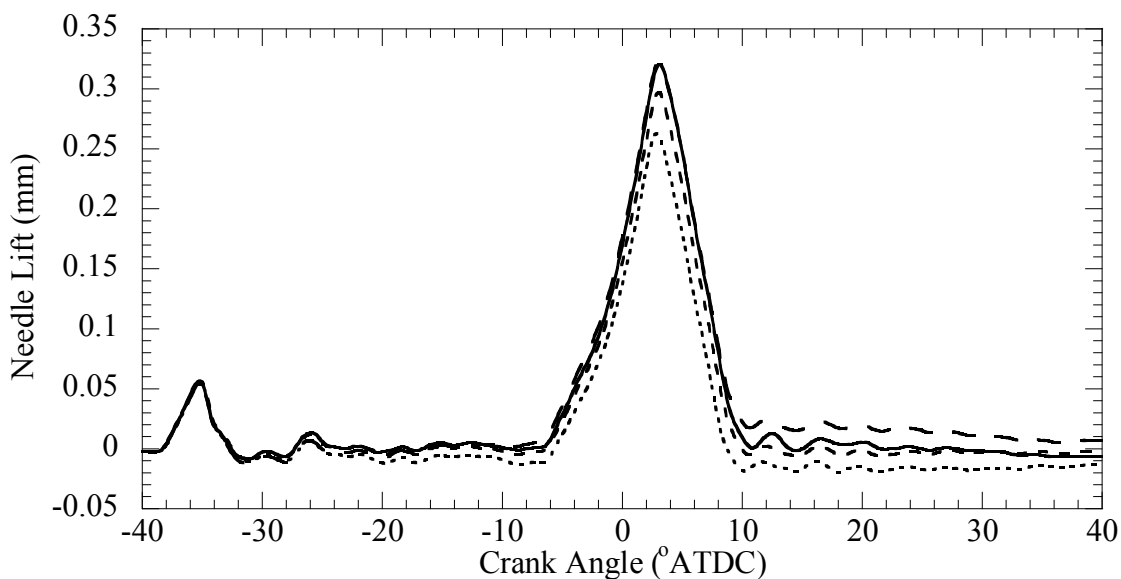


Figure 4.4: Needle lift at 1800 rpm at 75% maximum output, with — 0%, — — 2.5%, - - - - 7.5% and · · · · · 15% hydrogen substitution on an energy basis.

4.5 Pressure Trace

Pressure traces were measured on all four cylinders. Apparent heat release rates for each cylinder were calculated from the pressure traces. Historically, there has been variation in pressure traces between the four cylinders of Penn State's Detroit Diesel 2.5L TD DI-4V Automotive Diesel Engine. Mainly, the difference is due to the condition of individual piston rings of each cylinder. Piston rings prevent combustion gases from blowing by the pistons into the crank case. If the high pressure combustion gases pass by the piston rings, the pressure traces and the calculated apparent heat release rate will be affected.

As a result of the difference in cylinder pressure held by the piston rings, the completeness of combustion will vary from cylinder to cylinder. Incomplete combustion from a cylinder will increase emissions such as hydrocarbons, carbon monoxide and particulate matter. This incomplete combustion is further exacerbated when large amounts of EGR are introduced. The EGR will absorb energy released from the combustion process, reducing the rate of oxidation.

A variation in cylinder to cylinder pressure is to be expected. Figure 4.5 is the plot of the pressure trace for all four cylinders. Cylinder 3 is seen in this plot and others to be the representative average of pressure trace and thus of the heat release. Cylinder 3 will be used in plots when mode to mode comparisons are made.

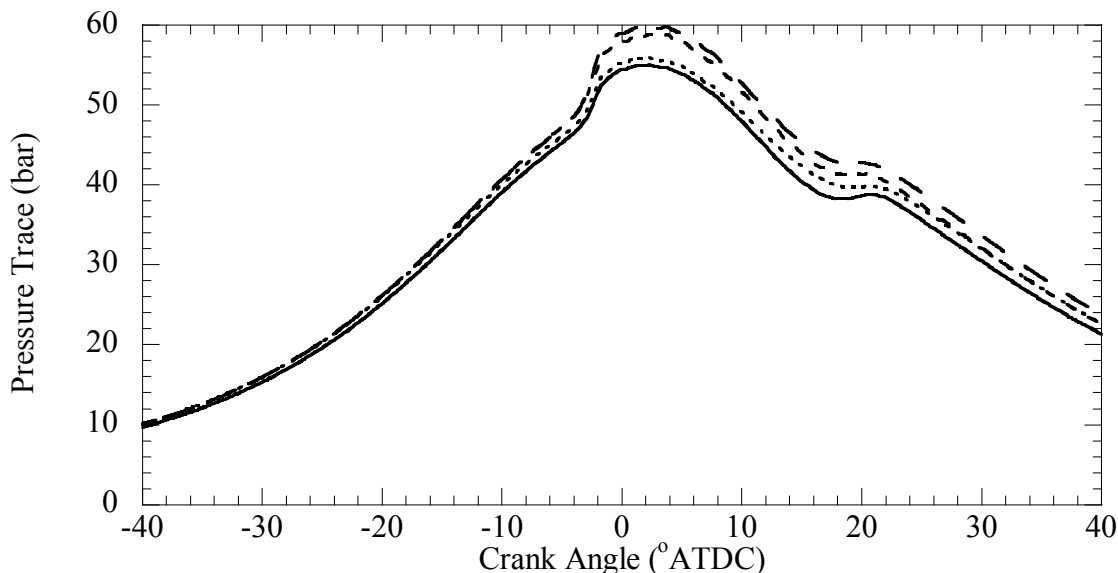


Figure 4.5: Comparison between pressure traces from the four cylinders of the Detroit Diesel 2.5L TD DI-4V Automotive Diesel Engine at 1800 rpm at 25% maximum output for — Cylinder 1, - - Cylinder 2, - - - - Cylinder 3 and · · · · · Cylinder 4.

Pressure traces indicate the in-cylinder pressure caused by combustion and volume change. Figure 4.6 to Figure 4.9 display the pressure traces from the four test modes, with hydrogen substitution. In general an increase of speed, and even more so, an increase in load will increase the combustion pressure. The maximum in cylinder pressure is desired to occur after top dead center so that energy from combustion will be released during the power stroke.

Optimum power release does not occur in the low speed modes, but does in the two high speed modes. The 1800 rpm at 25% maximum output mode has its maximum pressure peak occurring at top dead center. This means that there is a large pressure increase occurring before top dead center, which is fighting the piston's travel during the compression stroke. The 1800 rpm at 75% maximum output condition has a delay in

pressure release. This too will cause a drop in efficiency. The pressure is being delayed from creating power during the power stroke.

Hydrogen causes the maximum in-cylinder pressure to increase in all four modes. The effect is greater in the high load modes, where more complete combustion of the fuel occurred. Also, in the high load modes, hydrogen causes the maximum pressure peak to occur earlier. The substitution of hydrogen for diesel fuel decreases the amount of diesel fuel injected in both the pilot and main injections. Hydrogen combusts as the premixed fuel is ignited by the diesel pilot injection. A large amount of fuel and thus pressure is released during the pilot injection. This pressure accumulates with the pressure from the main injection and leads to a higher maximum pressure.

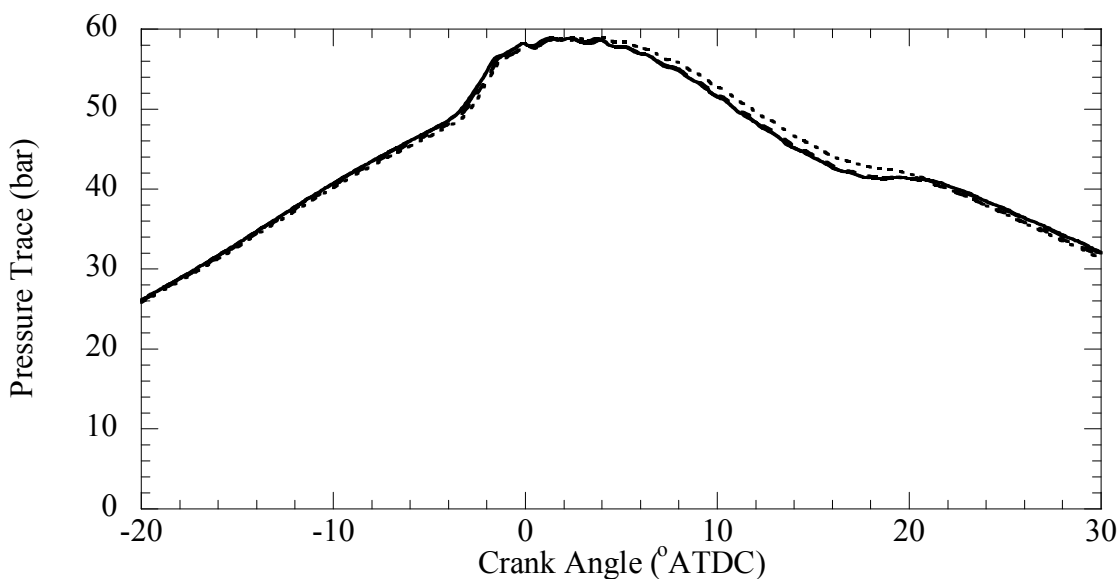


Figure 4.6: Pressure trace at 1800 rpm at 25% maximum output, with — 0%, - - 2.5%, - - - 7.5% and · · · · 15% hydrogen substitution on an energy basis.

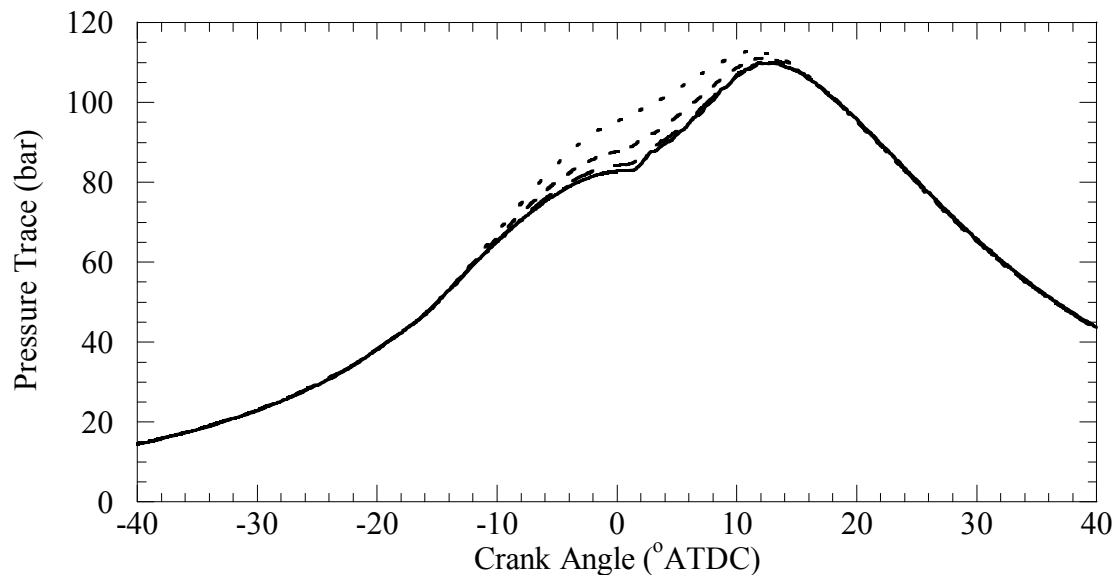


Figure 4.7: Pressure trace at 1800 rpm at 75% maximum output, with — 0%, - - 2.5%, ···· 7.5% and · · · · 15% hydrogen substitution on an energy basis.

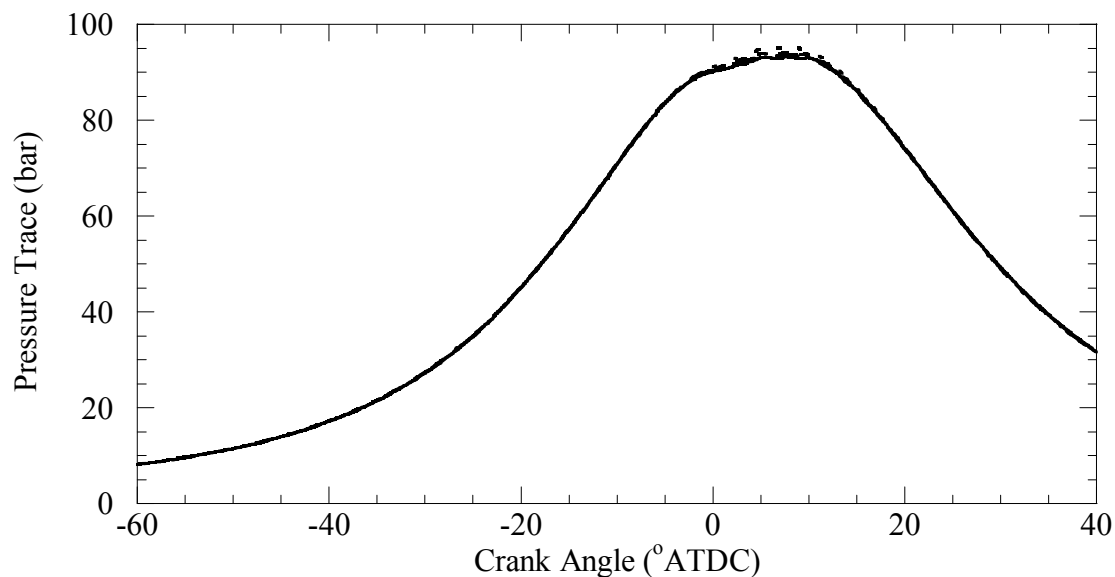


Figure 4.8: Pressure trace at 3600 rpm at 25% maximum output, with — 0%, - - 2.5%, ···· 7.5% and · · · · 15% hydrogen substitution on an energy basis.

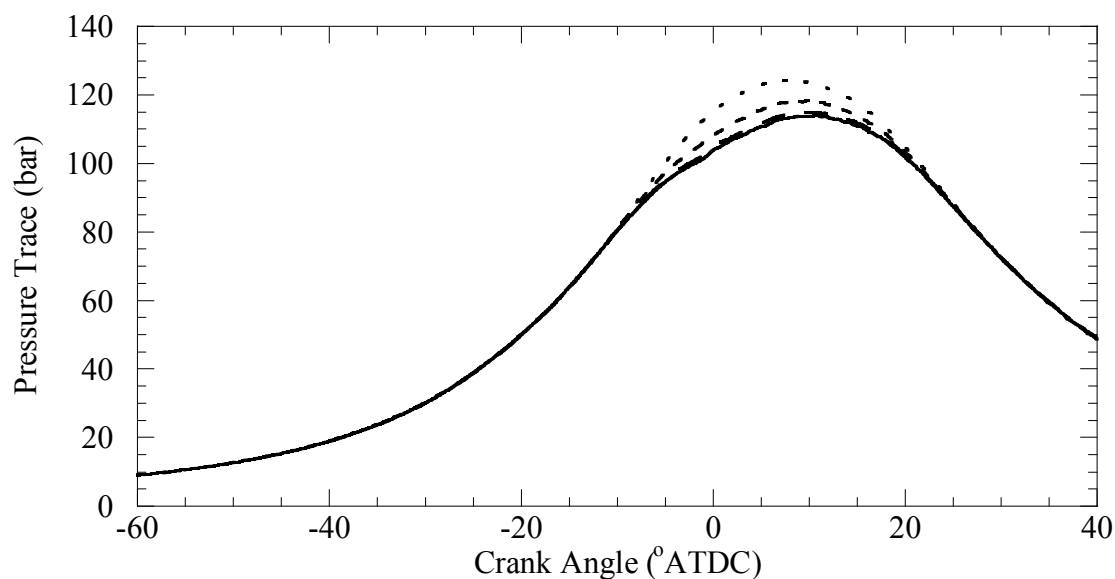


Figure 4.9: Pressure trace at 3600 rpm at 75% maximum output, with — 0%, - - - 2.5%, - . - . 7.5% and 15% hydrogen substitution on an energy basis.

4.6 Apparent Heat Release Rate

Figure 4.10 through Figure 4.13 display the apparent heat release rates of the four test modes with hydrogen substitution. The baseline apparent heat release rate of each of the four modes is different due to the load, speed and injection timing of the modes. In the case of the low speed modes a well defined apparent heat release rate from the pilot injection was seen. The combustion of the pilot injection fuel is known as the premixed combustion phase [5]. Here heat release is caused by the combustion of a premixed flame. Since the hydrogen is introduced into the cylinder during the intake stroke, no further hydrogen is available for combustion after the intake valve shuts. The bulk of the hydrogen is burned in the premixed combustion phase of the pilot injection. GC exhaust

data indicated an increase of hydrogen in the exhaust as fumigated levels of hydrogen increase. This however is a small amount of unburned hydrogen which is analogous to unburned hydrocarbons seen in exhaust.

Figure 4.10 and Figure 4.11 show slight ignition delay in the premixed combustion phase, with increased levels of hydrogen. The diesel fuel acts as a pilot to ignite the hydrogen, since hydrogen has a lower cetane number than diesel fuel. Increasing levels of hydrogen slightly increase the apparent heat release rate of the premixed combustion phase. With the increase in hydrogen, less diesel fuel is injected. Thus, less heat is absorbed during the fuel vaporization phase between the premixed combustion phase and the mixing-control combustion phase of the main injection [5]. The heat release during the mixing-controlled combustion phase is decreased with the increase of hydrogen substitution. This is because less diesel fuel is injected during the main injection phase when hydrogen substitution occurs. Overall, the introduction of hydrogen has modest effects on the apparent heat release rates.

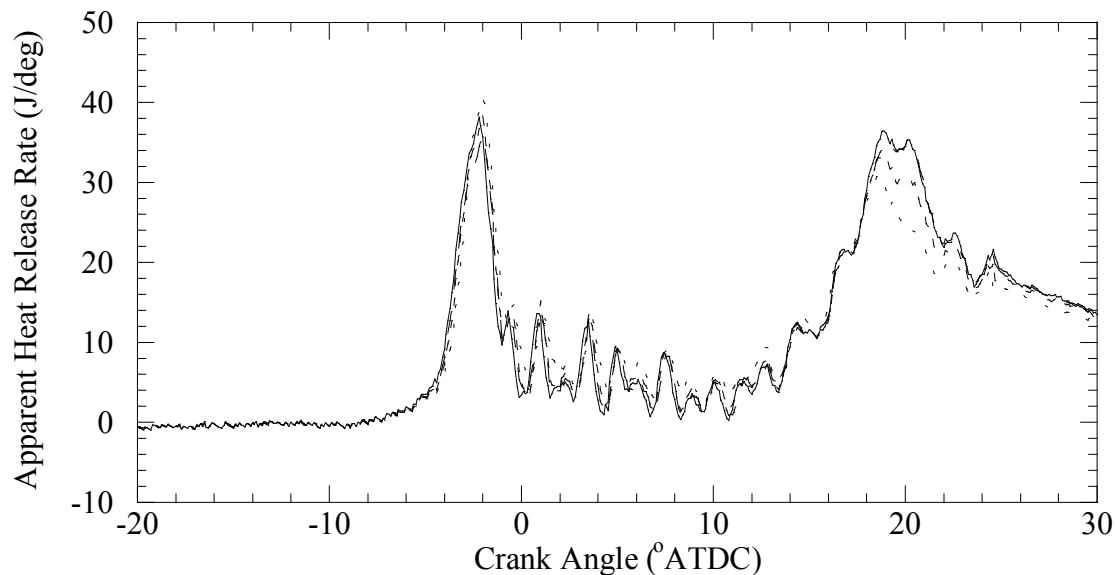


Figure 4.10: Apparent heat release rate at 1800 rpm at 25% maximum output, with — 0%, - - - 2.5%, - - - - 7.5% and - · - · 15% hydrogen substitution on an energy basis.

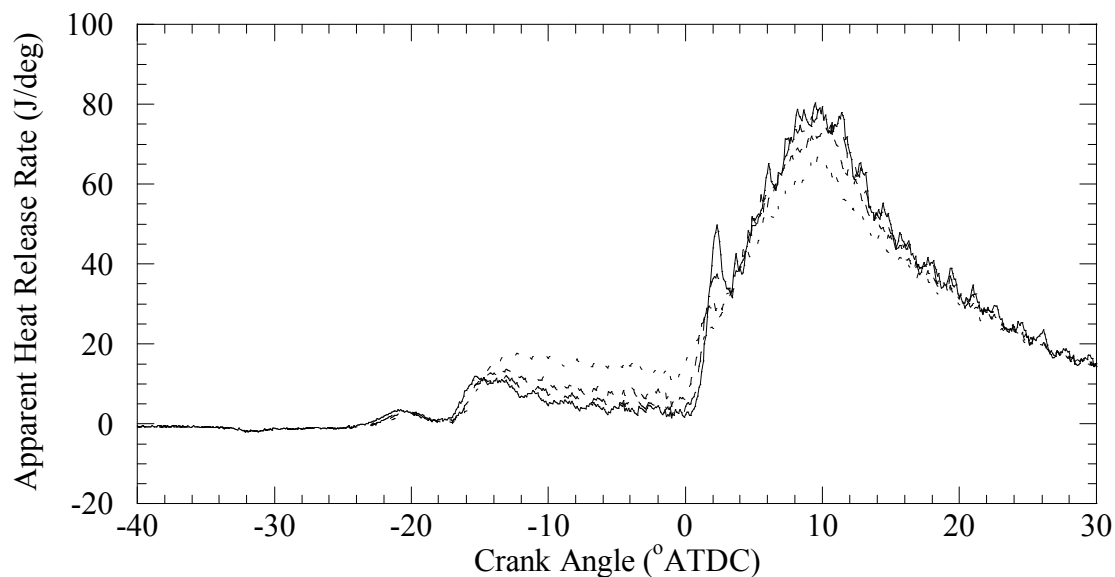


Figure 4.11: Apparent heat release rate at 1800 rpm at 75% maximum output, with — 0%, - - - 2.5%, - - - - 7.5% and - · - · 15% hydrogen substitution on an energy basis.

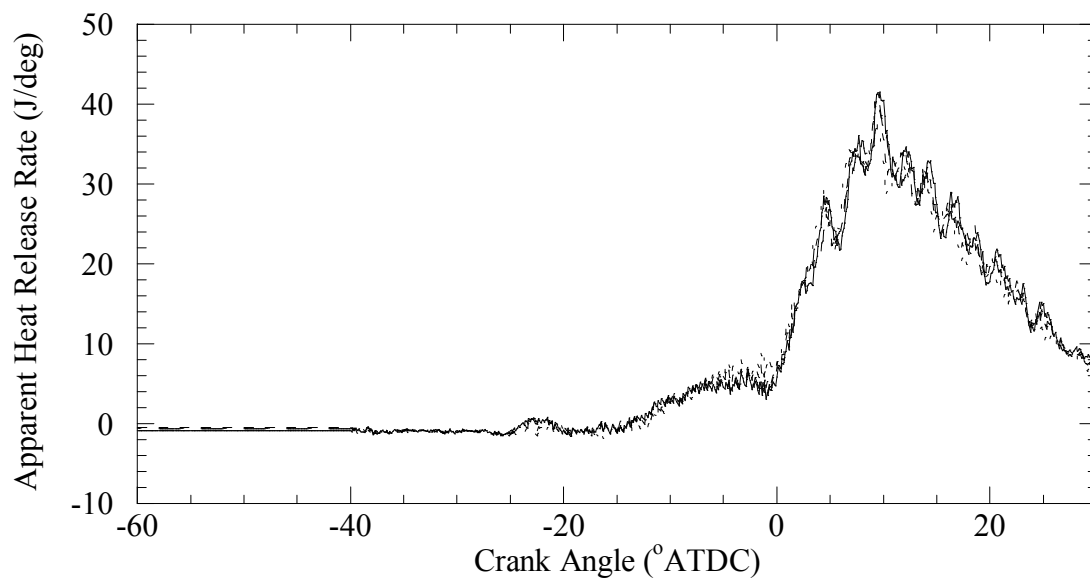


Figure 4.12: Apparent heat release rate at 3600 rpm at 25% maximum output, with — 0%, - - - 2.5%, - . - . 7.5% and 15% hydrogen substitution on an energy basis.

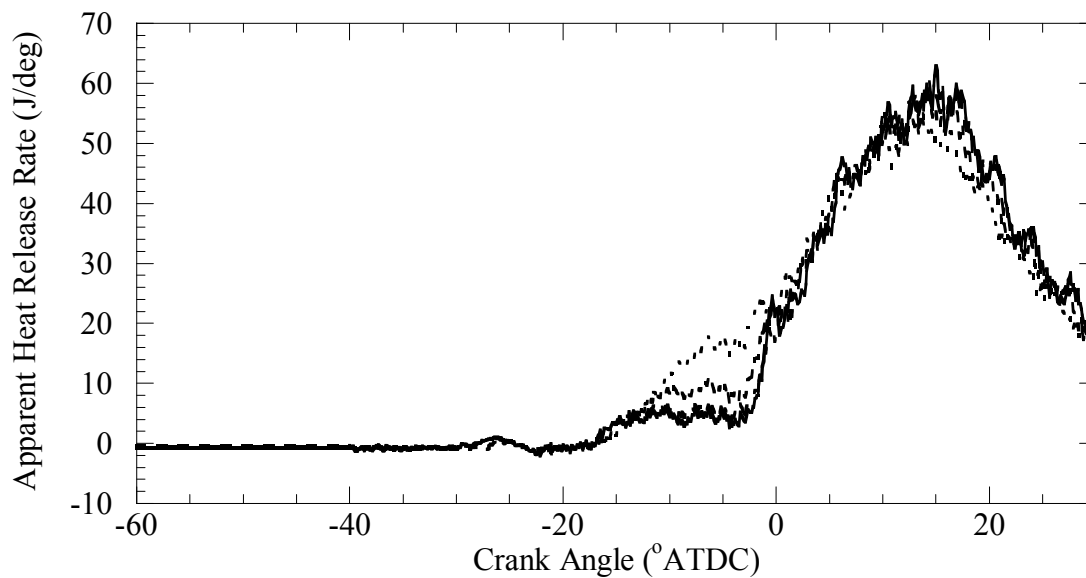


Figure 4.13: Apparent heat release rate at 3600 rpm at 75% maximum output, with — 0%, - - - 2.5%, - . - . 7.5% and 15% hydrogen substitution on an energy basis.

4.7 Bulk Cylinder Gas Temperature

The temperature of the bulk cylinder gas was calculated from the pressure traces using the ideal gas law. Figure 4.14 displays the maximum in cylinder gas temperature for all four modes with 0%, 2.5%, 7.5% and 15% hydrogen substitution.

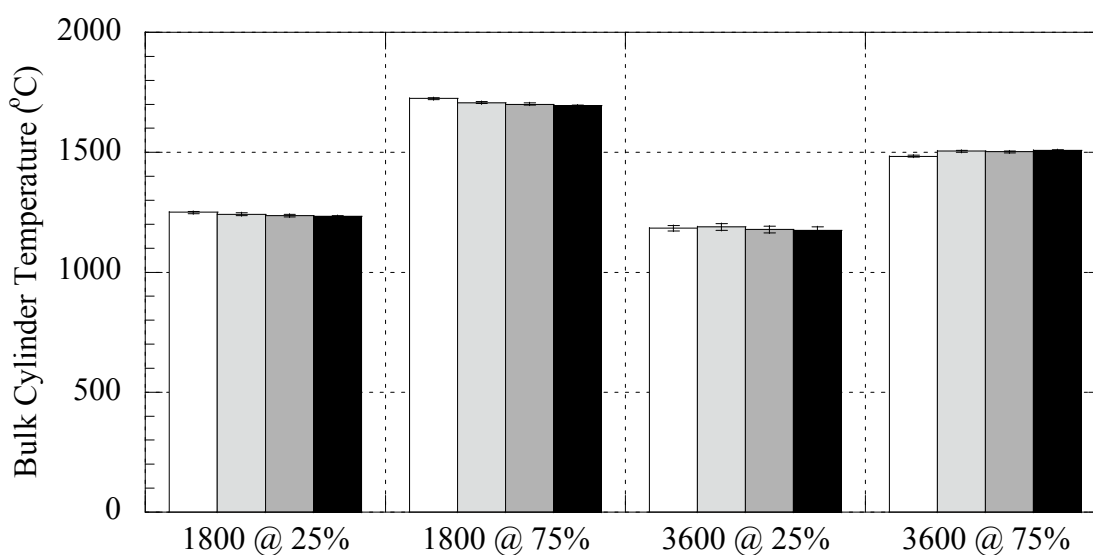


Figure 4.14: Maximum bulk cylinder gas temperature of the four modes tested, with 0%, 2.5%, 7.5%, and 15% hydrogen substitution on an energy basis.

The 1800 rpm at 25% maximum output mode has a bulk cylinder gas temperature nearing that of the other three modes even though it utilizes ~10% EGR, where the other modes utilize less than 2% EGR. The 1800 rpm at 25% maximum output mode would be expected to have a lower temperature since EGR lowers combustion temperatures [6]. Jacobs et al. explain that in the presence of EGR the bulk gas temperature will increase due to the increase in temperature of the intake charge and the decreasing of trapped mass

[30]. Further more, Jacobs, et al. go on to say that flame temperature would therefore be a more accurate predictor of NO_x formation then that of bulk gas temperature.

According to Figure 4.14, hydrogen makes less than a 0.5% difference in bulk cylinder temperature even at 15% energy input. According to the calculation of the cylinder bulk gas temperature, hydrogen makes relatively little change. To further understand what is occurring in the cylinder, adiabatic flame temperature must be considered. A complex model, outside the scope of this work, is necessary to calculate the adiabatic flame temperature, due to the consumption of the hydrogen fuel during the combustion of the pilot injected diesel fuel.

4.8 Exhaust Temperature

The exhaust temperature is examined in Figure 4.15. The exhaust temperature provides an indirect representation of the global combustion temperature. Enthalpy is removed from the exhaust gases by the turbocharger and EGR loop resulting in a reduced exhaust gas temperature. However, exhaust temperature will provide an indication of major alteration in combustion conditions and the engine's mode of operation, which is useful to ensure repeatability of engine operation.

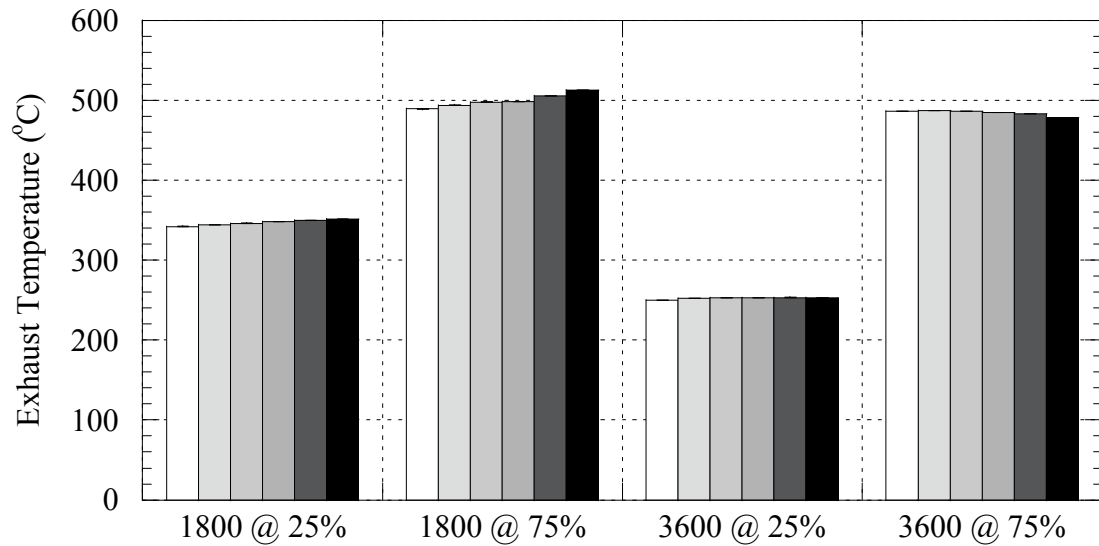


Figure 4.15: Exhaust temperature of the four modes tested, with \square 0%, \blacksquare 2.5%, \blacksquare 5%, \blacksquare 7.5%, \blacksquare 10% and \blacksquare 15% hydrogen substitution on an energy basis.

4.9 Equivalence Ratio

The equivalence ratio is defined as:

$$\phi = \frac{\left(\frac{F}{A}\right)_{actual}}{\left(\frac{F}{A}\right)_{stoichiometric}} \quad 4.1$$

Where $\left(\frac{F}{A}\right)_{actual}$ is the actual fuel-air ratio and $\left(\frac{F}{A}\right)_{stoichiometric}$ is the stoichiometric fuel-air ratio. The actual fuel-air ratio was calculated in real-time based on flow rates of hydrogen, diesel and air.

The high load modes utilize a larger amount of fuel, which leads to a higher equivalence ratio. Also, the high speed modes have increased levels of air density, via the turbo charger. These reasons explain why each of the four modes have the baseline

equivalence ratio given in Figure 4.16. For example the low amount of fuel and high level of boost air in 3600 rpm at 25% maximum output mode, produces a noticeably lower equivalence ratio compared to the other modes.

The equivalence ratio is used to provide insight into the gaseous exhaust emissions. Increased levels of hydrogen cause an increasing trend in equivalence ratio. The increase in equivalence ratio is because the hydrogen is introduced into the engine via the air intake. By doing so, some portion of intake air must be displaced to give way to the hydrogen. In the 3600 rpm at 75% maximum output mode hydrogen is seen to decrease the equivalence ratio. This is due to the large level of boosted air, that has a greater effect on lowering the equivalence ratio than hydrogen does on increasing the equivalence ratio when hydrogen substitution occurs.

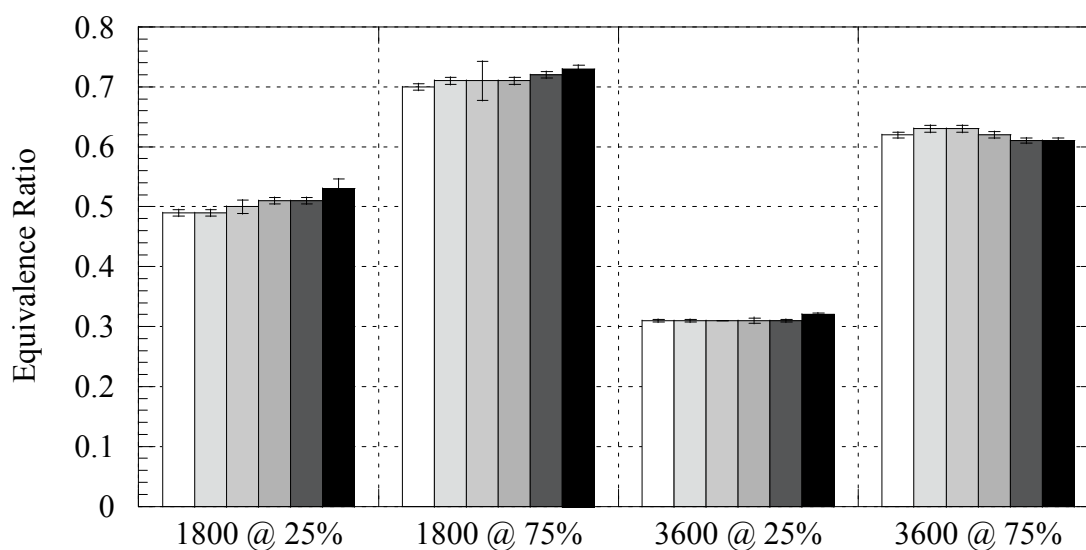


Figure 4.16: Equivalence ratio of the four modes tested, with \square 0%, \square 2.5%, \square 5%, \square 7.5%, \blacksquare 10% and \blacksquare 15% hydrogen substitution on an energy basis.

4.10 Gaseous Emissions

Gaseous emissions are presented in brake specific units ($\text{g/kW}_{\text{Output-hr}}$). They were also calculated in fuel energy specific units ($\text{g/kW}_{\text{Fuel energy in-hr}}$). The fuel energy specific unit values yield plots with similar trends as those of the brake specific emission plots. Thus, the brake specific emission plots are presented.

4.11 Erroneous NO_x Emissions Measurements

Injection timing was locked down during fuel substitution to prevent the engine's ECU from shifting injection strategies. Locking down the injection timing is important because of the engine's response to fuel substitution. During testing, the speed and load were held at constant values. As hydrogen levels increased, the engine throttled back diesel fuel to maintain a constant speed. The ECU's injection strategy is based on engine speed and diesel fuel injection volume. The injection timing was manually held constant to prevent the injection strategy from moving to a later injection, when injected diesel fuel volume decreased. A shift in injection strategies will cause erroneous emissions and de-rate the engine.

Erroneous NO_x emissions measurements due to a shift in injection timing are displayed in Figure 4.17. These erroneous emissions, with timing drift, are compared to the emissions with the injection timing locked. Brake specific NO_x emissions are greatly reduced as hydrogen substitution increases and injection timing is allowed to drift to a late injection strategy. These large NO_x emission reductions are not caused by the combustion of hydrogen. The emission reductions caused by the shift in injection timing

were recreated, without hydrogen substitution, by varying the injection timing to the same shifted injection timing observed with hydrogen substitution. Figure 4.18 displays the needle lift caused by the hydrogen substitution, when injection timing is not locked.

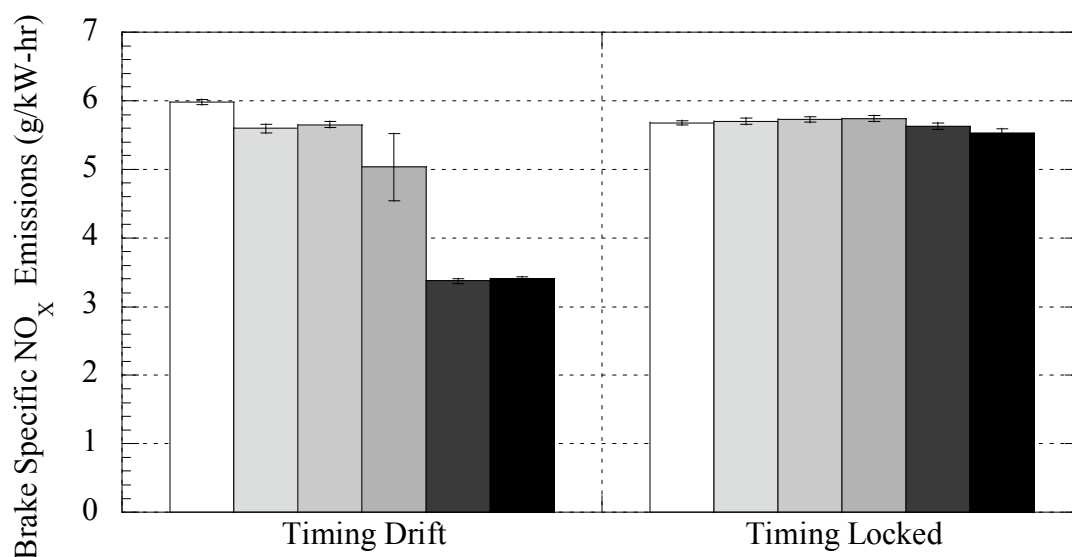


Figure 4.17: Brake specific NO_x emissions at 1800 rpm at 75% maximum output when injection timing is allowed to drift and when injection timing is locked down, with □ 0%, ■ 2.5%, ■ 5%, ■ 15%, ■ 25% and ■ 30% hydrogen substitution on an energy basis.

Table 4.2: Percent difference of brake specific NO_x emissions from the baseline at 1800 rpm at 75% maximum output with 0%, 2.5%, 5%, 15%, 25% and 30% hydrogen substitution on an energy basis. Positive values indicate an increase and negative values indicate a decrease from the baseline.

	1800 @ 75% with Timing Drift	1800 @ 75% with Timing Locked
0 % Diff.	n/a	n/a
2.5 % Diff.	-6.6	0.4
5 % Diff.	-5.7	0.8
15 % Diff.	-17.2	1.1
25 % Diff.	-55.7	-0.9
30 % Diff.	-54.8	-2.7

Large reductions in NO_x emission, reported in the literature to be caused by hydrogen substitution, are not due to hydrogen. The emissions reductions are from a shift in injection timing along the engine's injection timing map. Thus, it would be necessary to reprogram a vehicle's ECU to properly utilize hydrogen substitution with de-rating the engine when retrofitting a vehicle.

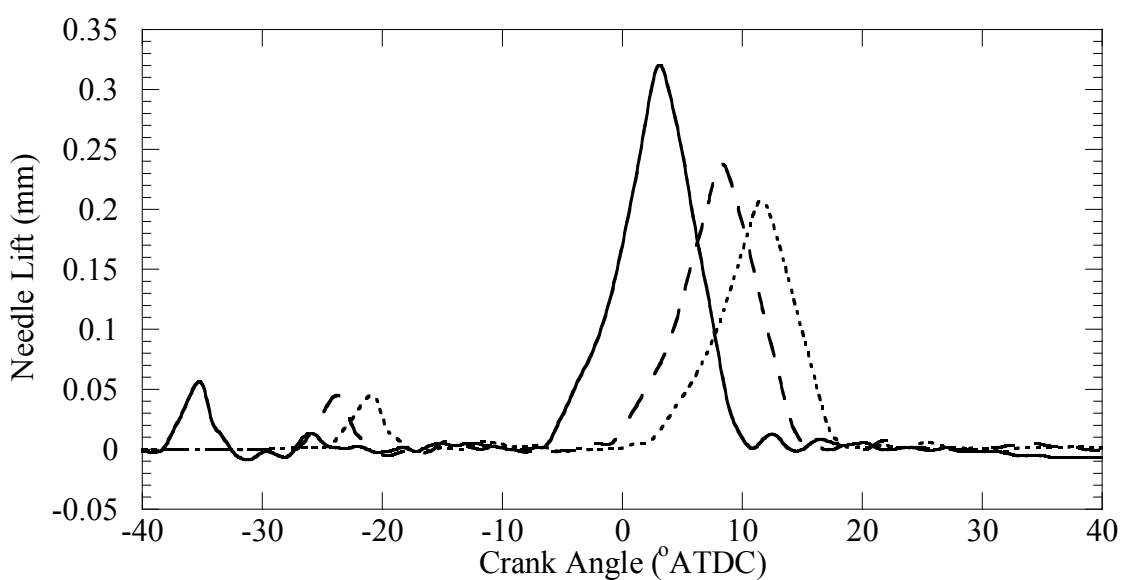


Figure 4.18: Needle lift at 1800 rpm at 75% maximum output, when injection timing is not locked, with — 0%, - - 15%, and · · · · 30% hydrogen substitution on an energy basis.

4.12 Gaseous Emissions: NO_x

The 1800 rpm at 25% maximum torque mode has lower base levels of brake specific NO_x due to the mode's use of ~10% EGR. The other modes utilize less than 2% EGR, which accounts for the difference in base NO_x levels. NO_x emission increased slightly in all four modes with the introduction of hydrogen. Hydrogen substitution has its

greatest effect on the low load modes. In the high load modes, the increase caused by hydrogen is small and falls within the error bars. The largest increase of NO_x occurs in the 3600 rpm at 25% maximum output mode. This mode sees an increase of 9% from the baseline with the substitution of 15% hydrogen. NO and NO_2 must be examined to further explain and understand the NO_x emissions.

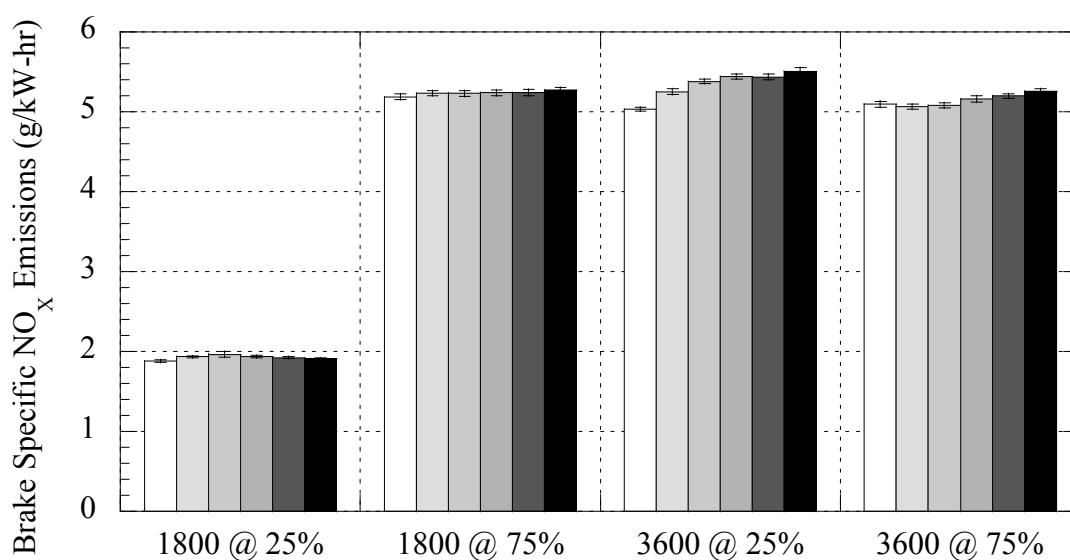


Figure 4.19: Brake specific NO_x emissions of the four modes tested, with \square 0%, \blacksquare 2.5%, \blacksquare 5%, \blacksquare 7.5%, \blacksquare 10% and \blacksquare 15% hydrogen substitution on an energy basis.

Table 4.3: Percent difference of brake specific NO_x emissions from the baseline at the four modes tested with 0%, 2.5%, 5%, 7.5%, 10% and 15% hydrogen substitution on an energy basis. Positive values indicate an increase and negative values indicate a decrease from the baseline.

	1800 @ 25%	1800 @ 75%	3600 @ 25%	3600 @ 75%
0 % Diff.	n/a	n/a	n/a	n/a
2.5 % Diff.	3.0	0.9	4.3	-0.6
5 % Diff.	4.6	0.8	6.6	-0.3
7.5% Diff.	3.4	1.0	7.8	1.3
10 % Diff.	2.5	1.0	7.7	2.0
15 % Diff.	1.8	1.6	9.0	3.1

4.13 Gaseous Emissions: NO

NO classically accounts for the largest contribution of NO_x. Figure 4.20 displays the brake specific NO emissions from the modes tested. In comparison between the two high load modes and the two low load modes, the high load modes produce higher levels of NO. The increased levels of NO are thermal NO, produced from the increased heat release that occurs at high load conditions.

The two high load modes and two low load modes have similar magnitudes and trends, respectively. However, there is a slight discrepancy between the two low load modes. The 1800 rpm at 25% maximum output mode has a lower magnitude of NO compared to that of the 3600 at 25% maximum outputs. This again can be explained by the ~10% EGR used in the 1800 rpm at 25% maximum output mode.

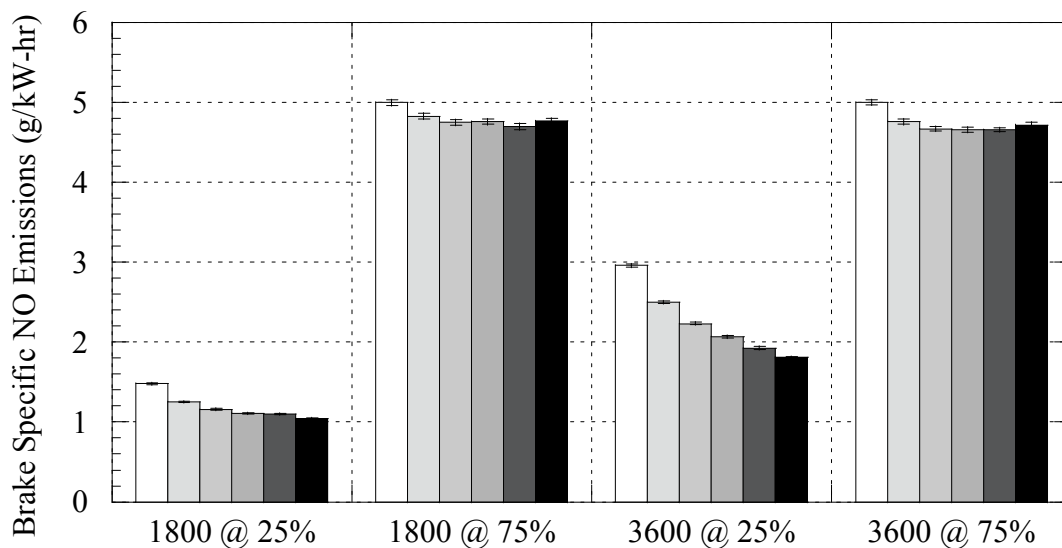


Figure 4.20: Brake specific NO emissions of the four modes tested, with \square 0%, \blacksquare 2.5%, \blacksquare 5%, \blacksquare 7.5%, \blacksquare 10% and \blacksquare 15% hydrogen substitution on an energy basis.

Figure 4.20 shows a general trend of decreasing levels of NO with the increase of hydrogen. The decrease is more pronounced and even outside of the error bars in the case of the two low load modes. The higher load modes show a less significant decreasing trend that falls within the error bars after 2.5% hydrogen substitution.

Table 4.4 show that in the low loads modes, 2.5% of hydrogen substitution can reduce brake specific NO by 17%. Table 4.4 also points out that higher speeds are affected more by hydrogen substitution, than lower speeds.

Table 4.4: Percent difference of brake specific NO emissions from the baseline at the four modes tested with 0%, 2.5%, 5%, 7.5%, 10% and 15% hydrogen substitution on an energy basis. Positive values indicate an increase and negative values indicate a decrease from the baseline.

	1800 @ 25%	1800 @ 75%	3600 @ 25%	3600 @ 75%
0 % Diff.	n/a	n/a	n/a	n/a
2.5 % Diff.	-16.9	-3.4	-17.1	-5.0
5 % Diff.	-24.2	-5.2	-28.5	-6.9
7.5% Diff.	-28.7	-4.8	-35.7	-7.0
10 % Diff.	-29.7	-6.0	-42.1	-7.1
15 % Diff.	-35.0	-4.7	-48.5	-5.7

4.14 Gaseous Emissions: NO₂

As with the case of brake specific NO emissions, the high speed modes produce similar magnitudes of brake specific NO₂ emissions. However, the low speed modes again produce a dissimilar amount NO₂. To explain this discrepancy the production of NO₂ must be examined.

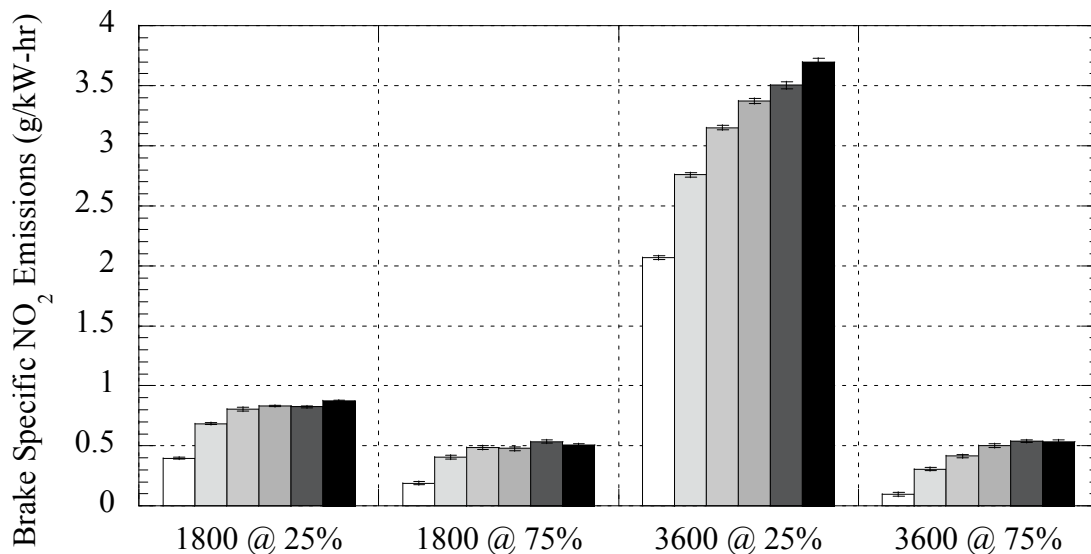


Figure 4.21: Brake specific NO₂ emissions of the four modes tested, with □ 0%, ■ 2.5%, ■ 5%, ■ 7.5%, ■ 10% and ■ 15% hydrogen substitution an the energy basis.

The major path in the production of NO₂ is from NO [51]. This path is given in

Eq. 4.2.



The HO₂ is produced from the increased levels of hydrogen. Glassman states that the most probable initial step in the combustion of oxygen and hydrogen is [52]:



With the path from NO to NO₂ in mind, the difference in magnitude between the low load conditions can again be explained by the ~10% of EGR used in the 1800 rpm at 25% maximum output mode. There is more NO available in the 3600 rpm at 25% maximum output mode to be converted to NO₂.

Table 4.5: Percent difference of brake specific NO₂ emissions from the baseline at the four modes tested with 0%, 2.5%, 5%, 7.5%, 10% and 15% hydrogen substitution on an energy basis. Positive values indicate an increase and negative values indicate a decrease from the baseline.

	1800 @ 25%	1800 @ 75%	3600 @ 25%	3600 @ 75%
0 % Diff.	n/a	n/a	n/a	n/a
2.5 % Diff.	53.3	72.1	28.6	105.1
5 % Diff.	68.0	87.1	41.5	124.9
7.5% Diff.	70.8	85.8	47.9	135.4
10 % Diff.	70.2	94.8	51.5	139.6
15 % Diff.	74.8	90.2	56.6	139.1

Table 4.5 displays the percent difference of the increase of NO₂ caused by the hydrogen substitution. Since the baseline values of NO₂ are initially very low, the effect caused by hydrogen is quite dramatic. Figure 4.22 shows the transition from NO being the dominant contributor to NO_x, to NO₂ being the dominant contributor to NO_x, due to hydrogen substitution, in the case of 3600 rpm at 25% of maximum output. A shift in NO_x species also occurs in the 1800 rpm at 25% of maximum output mode; however the NO₂ does not overcome the NO, as in the case presented in Figure 4.22. This is due to the EGR in the 1800 rpm at 25% of maximum output mode. A slight shift in NO_x species occurs in the high load modes as well, but this shift is small compared to that of the low load modes.

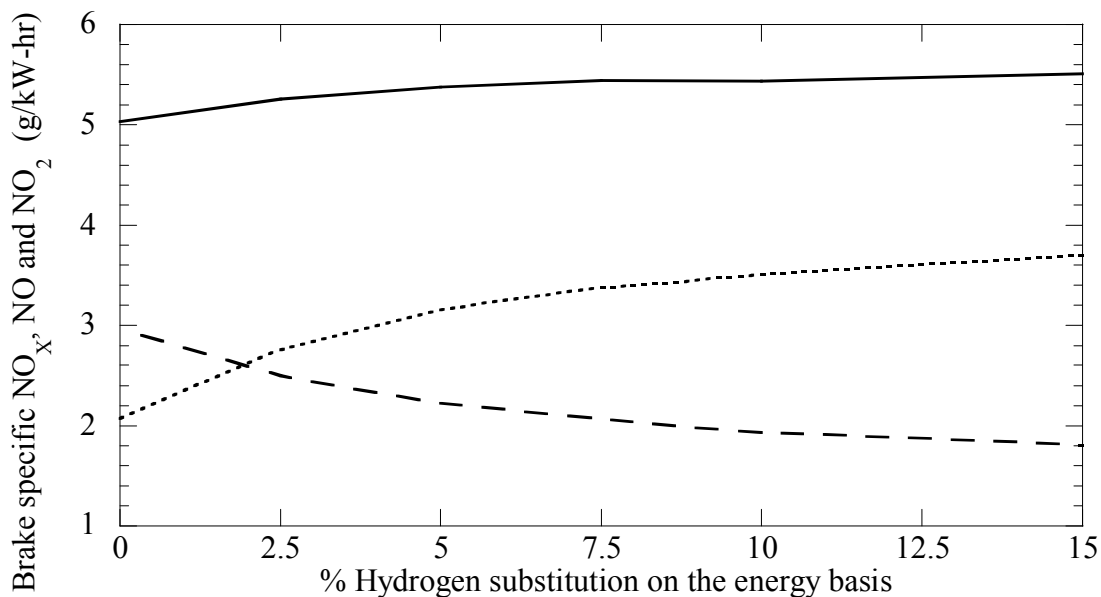


Figure 4.22: Brake specific NO_x , NO and NO_2 emissions vs. energy percent from hydrogen fuel for 3600rpm at 25% of maximum output.

The conversion from NO to NO_2 , due to hydrogen substitution, is beneficial even though NO_x levels increase. NO_2 is used as the oxidizer in Continuously Regenerating Trap (CRT) systems, which are used to reduce particulate matter emissions [53]. If NO_2 is not present in large enough quantities, it is necessary to oxidize NO into NO_2 , to enable passive regeneration in the CRT [54]. The oxidation of NO to NO_2 would require an oxidation catalyst to be placed upstream of the CRT. The increased production of NO_2 from hydrogen substitution would reduce the need for NO oxidation catalysts in the CRT system.

4.15 Gaseous Emissions: HC

HC emissions are difficult to sample. They tend to drop out of the heated exhaust sample and condense if they encounter cold spots in the sampling apparatus. This is reflected in the 1800 rpm at 25% maximum output mode seen in Figure 4.23.

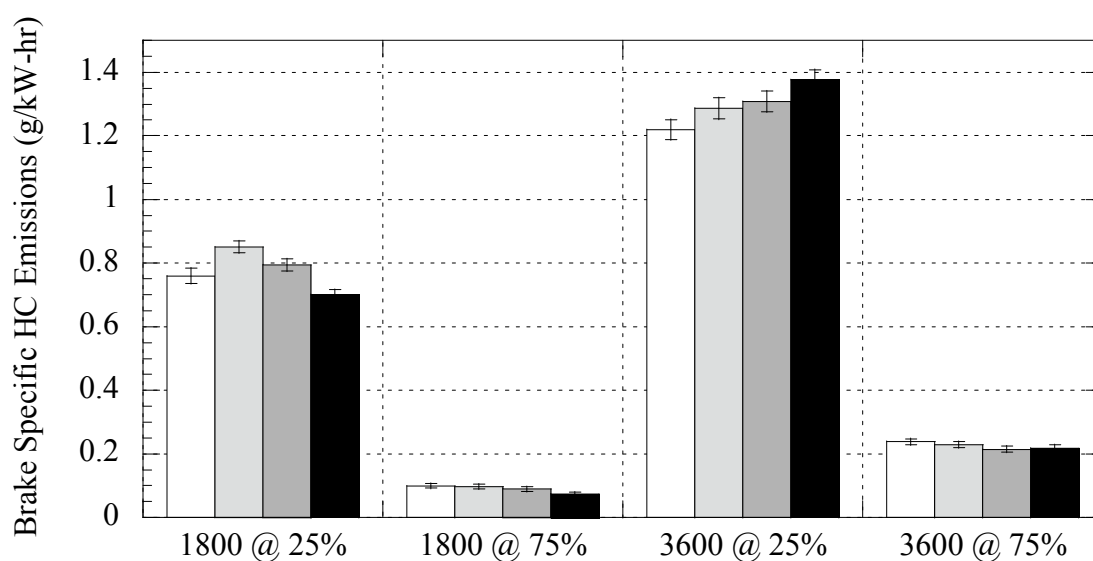


Figure 4.23: Brake specific HC emissions of the four modes tested, with \square 0%, \blacksquare 2.5%, \blacksquare 7.5% and \blacksquare 15% hydrogen substitution on an energy basis.

HC emissions are products of incomplete combustion. Incomplete combustion can occur when the in cylinder temperature and pressure are not high enough to completely combust the injected fuel. HC emissions will also occur, if injected diesel fuel penetrates past the flame front and reaches the cylinder walls. Also, atomized fuel may also seep into the crevices of the cylinder, excluding it from combustion.

The low load modes have increased levels of brake specific HC emissions. This is due to the incomplete combustion that occurs at low load. The 3600 rpm at 25%

maximum output mode has a larger degree of incomplete combustion. This is due to this mode's overly lean equivalence ratio.

Both of the high load modes have low levels of HC emission. The 3600 rpm at 25% maximum output mode has higher levels of HC emission, due to the cycle speed of the mode, which reduces the time for the fuel to completely combust.

At high loads, hydrogen substitution reduces brake specific HC emissions. This is because there is less diesel fuel in the main injection that can be lost to incomplete combustion by either hiding in a crevice or gathering on the cylinder walls. However, in the low load modes, brake specific HC emissions increase due to hydrogen substitution. In the low load modes the heat release is much lower than that of the high load modes. When hydrogen substitution occurs there is less diesel fuel injected during the main injection, which further reduces the heat release. This reduction in heat release acts to further increase the amount of HC released from incomplete combustion.

Table 4.6: Percent difference of brake specific HC emissions from the baseline at the four modes tested with 0%, 2.5%, 5%, 7.5%, 10% and 15% hydrogen substitution on an energy basis. Positive values indicate an increase and negative values indicate a decrease from the baseline.

	1800 @ 25%	1800 @ 75%	3600 @ 25%	3600 @ 75%
0 % Diff.	n/a	n/a	n/a	n/a
2.5 % Diff.	11.4	-1.7	5.3	-4.2
5 % Diff.	32.6	36.7	13.6	4.5
7.5% Diff.	4.4	-9.7	7.0	-10.7
10 % Diff.	-4.0	-25.5	17.6	-11.4
15 % Diff.	-8.2	-30.4	12.1	-8.8

4.16 Gaseous Emissions: Unburned Hydrogen

Unburned HC emissions can be correlated directly to the unburned hydrogen seen in Figure 4.24. There is very little unburned hydrogen. Levels of unburned hydrogen increase with low load modes that suffer from incomplete combustion. Unburned hydrogen also increases as the substitution percent increases.

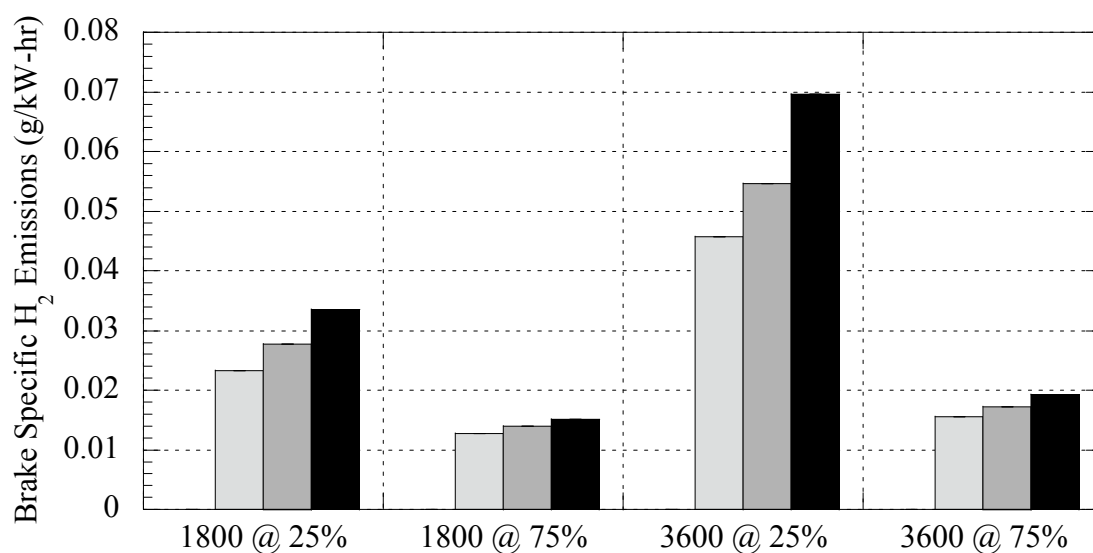


Figure 4.24: Brake specific H₂ emissions of the four modes tested, with □ 0%, ■ 2.5%, ■ 7.5%, and ■ 15% hydrogen substitution on an energy basis.

4.17 Gaseous Emissions: CO

CO emissions correlate with and are primarily controlled by air fuel ratio. Heywood states that a diesel engine operates in fuel lean conditions and thus CO emissions are unimportant and do not need to be discussed [5]. Nonetheless, the

formation of CO is directly linked to the availability of HC. The principal CO formation is based on the hydrocarbon combustion mechanism[51].

The mechanism is summarized by:



The R stands for a hydrocarbon radical.

In the case of 3600 rpm at 25% of maximum output mode, the brake specific CO levels are higher than those of the other modes. At this mode, the turbo-charger is active, increasing the density of the charged air, while the low load is demanding little fuel.

Hence the equivalence ratio is lean as seen in Figure 4.16. Even though this mode is lean, there is a large amount of CO. The large CO content is due to incomplete combustion which is redetected in the increased levels of brake specific hydrocarbon at this mode.

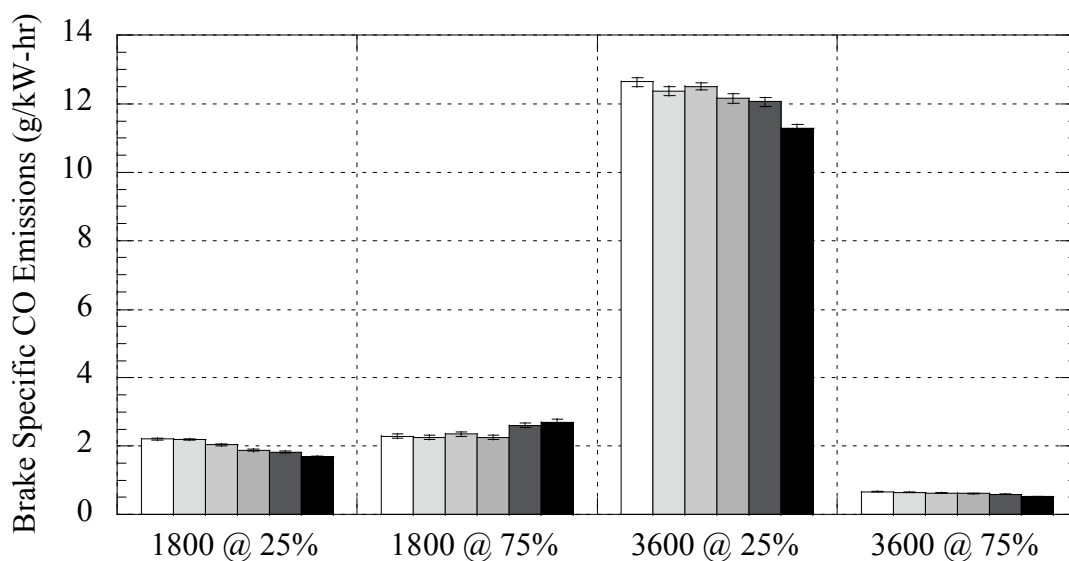


Figure 4.25: Brake specific CO emissions of the four modes tested, with \square 0%, \square 2.5%, \square 5%, \blacksquare 7.5%, \blacksquare 10% and \blacksquare 15% hydrogen substitution on an energy basis.

Table 4.7: Percent difference of brake specific CO emissions from the baseline at the four modes tested with 0%, 2.5%, 5%, 7.5%, 10% and 15% hydrogen substitution on an energy basis. Positive values indicate an increase and negative values indicate a decrease from the baseline.

	1800 @ 25%	1800 @ 75%	3600 @ 25%	3600 @ 75%
0 % Diff.	n/a	n/a	n/a	n/a
2.5 % Diff.	-0.3	-2.1	-2.1	-3.0
5 % Diff.	-8.2	2.3	-1.0	-6.5
7.5% Diff.	-16.4	-1.8	-3.8	-8.1
10 % Diff.	-18.8	13.0	-4.7	-12.3
15 % Diff.	-26.0	16.6	-11.3	-23.6

4.18 Gaseous Emissions: CO₂

Carbon dioxide is one of the main products of combustion when burning hydrocarbon fuels. Reducing hydrocarbon fuel will reduce the amount of carbon dioxide formed during combustion. This is accomplished during hydrogen substitution.

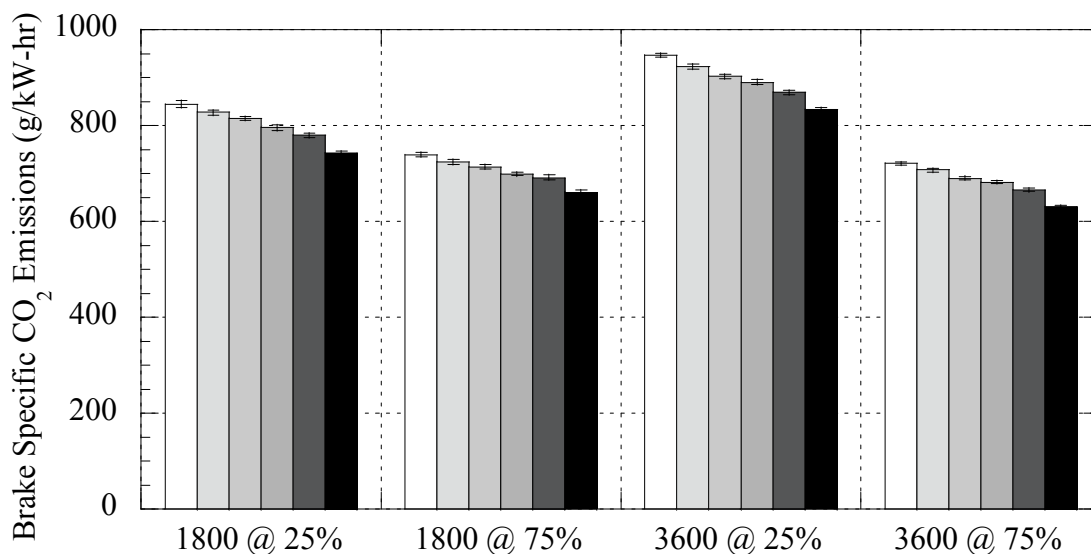


Figure 4.26: Brake specific CO₂ emissions of the four modes tested, with □ 0%, ■ 2.5%, ■ 5%, ■ 7.5%, ■ 10% and ■ 15% hydrogen substitution on an energy basis.

Table 4.8: Percent difference of brake specific CO₂ emissions from the baseline at the four modes tested with 0%, 2.5%, 5%, 7.5%, 10% and 15% hydrogen substitution on an energy basis. Positive values indicate an increase and negative values indicate a decrease from the baseline.

	1800 @ 25%	1800 @ 75%	3600 @ 25%	3600 @ 75%
0 % Diff.	n/a	n/a	n/a	n/a
2.5 % Diff.	2.1	2.0	2.6	2.0
5 % Diff.	3.6	3.4	4.9	4.4
7.5% Diff.	6.0	5.6	6.2	5.6
10 % Diff.	8.0	6.6	8.7	8.0
15 % Diff.	12.9	11.2	12.8	13.6

There is an increased level of brake specific CO₂ in the 3600 rpm at 25% maximum output mode. The excess CO₂ is coming from the high levels of CO in this mode. CO converts to CO₂ in the path given in Eq. 4.5 [52].



In general, the introduction of hydrogen causes an almost 1 to 1 reduction of CO₂. As the fraction of hydrogen increases, the quantity of diesel fuel decreases. Hence there are less HC radicals available to form CO.

4.19 Gaseous Emissions: Particulate Matter

The majority of particulate will be created in the diffusion flame during the mixing control burn phase, where fuel pyrolysis occurs. The creation of particulate is a competition between formation and oxidation [5]. In conditions where higher temperatures occur, particulate will be oxidized and emitted levels will decrease.

A correlation between levels of brake specific particulate emissions and apparent heat release rate can be made. In the apparent heat release rate plots above, the high load modes had higher rates of heat release. Below in Figure 4.26 the high load modes have lower levels of brake specific particulate emissions, than those of the low load modes. The higher apparent heat release rates signify a higher rate of oxidation occurred in the high load modes.

Hydrogen substitution appears to reduce brake specific particulate emissions at high speeds and increase brake specific particulate emissions at slow speeds. These trends can be explained by again looking at the apparent heat release rates of the modes. In the case of the low speed modes hydrogen decreases the apparent heat release rates of the low speed modes, reducing oxidation. In the high speed modes there is a slight decrease in apparent heat release rates, but the decrease of hydrocarbon fuel levels during hydrogen substitution reduces the amount of carbon available to form particulate.

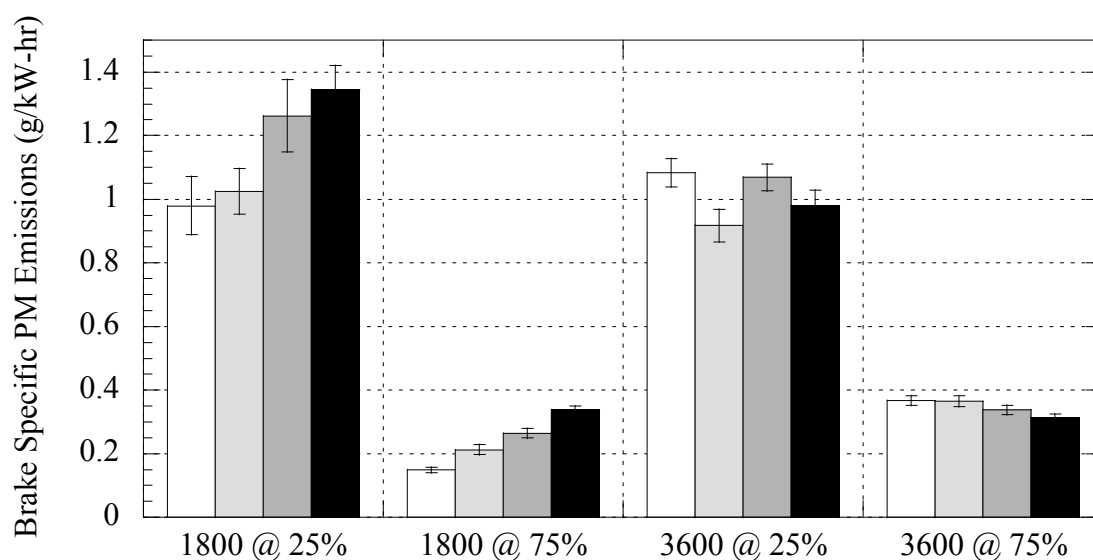


Figure 4.27: Brake specific PM emissions of the four modes tested, with \square 0%, \blacksquare 2.5%, \blacksquare 7.5% and \blacksquare 15% hydrogen substitution on an energy basis.

Table 4.9: Percent difference of brake specific HC emissions from the baseline at the four modes tested with 0%, 2.5%, 5%, 7.5%, 10% and 15% hydrogen substitution on an energy basis. Positive values indicate an increase and negative values indicate a decrease from the baseline.

	1800 @ 25%	1800 @ 75%	3600 @ 25%	3600 @ 75%
0 % Diff.	n/a	n/a	n/a	n/a
2.5 % Diff.	4.5	35.4	-16.5	-0.8
7.5% Diff.	25.2	56.1	-1.3	-8.5
15 % Diff.	31.4	77.7	-9.8	-16.0

4.20 Brake Specific Fuel Consumption

The brake specific fuel consumption was calculated based on the consumption of both diesel and hydrogen fuel. Internal combustion engines are most efficient at high loads. This is reflected in Figure 4.27. The 3600 rpm at 25% maximum output mode, has the poorest efficiency of all the modes. This is due to the large amount of incomplete combustion which occurs in this mode.

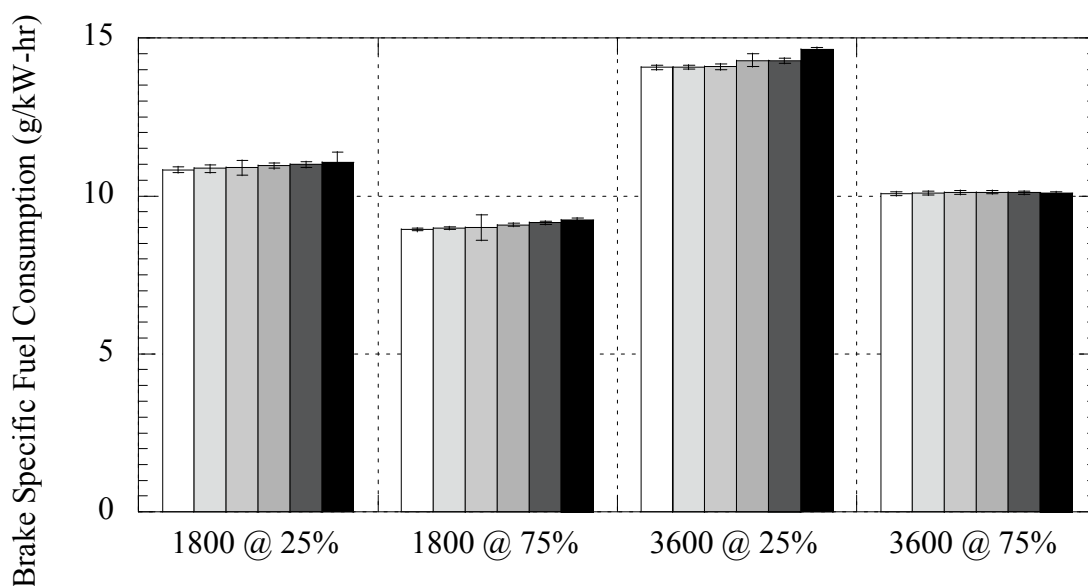


Figure 4.28: Brake specific fuel consumption of the four modes tested, with \square 0%, \blacksquare 2.5%, \blacksquare 5%, \blacksquare 7.5%, \blacksquare 10% and \blacksquare 15% hydrogen substitution on an energy basis.

Hydrogen substitution decreased the brake specific fuel efficiency of the modes due to the reduction of air. Fumigation of hydrogen into the air intake displaces air for fuel in the form of hydrogen. Air is the working fluid of an engine, thus a reduction in air will reduce the output of an engine. Brake specific fuel efficiency losses experienced when hydrogen is fumigated into the air intake, would be recovered by direct injection of hydrogen into the combustion cylinder.

Table 4.10: Percent difference of brake fuel consumption from the baseline at the four modes tested with 0%, 2.5%, 5%, 7.5%, 10% and 15% hydrogen substitution on an energy basis. Positive values indicate an increase and negative values indicate a decrease from the baseline.

	1800 @ 25%	1800 @ 75%	3600 @ 25%	3600 @ 75%
0 % Diff.	n/a	n/a	n/a	n/a
2.5 % Diff.	0.3	0.4	0.1	0.2
5 % Diff.	0.6	0.6	0.1	0.4
7.5% Diff.	1.1	1.7	1.6	0.5
10 % Diff.	1.4	2.5	1.5	0.3
15 % Diff.	2.0	3.6	4.0	0.2

4.21 Summary

The benefits of hydrogen for diesel fuel substitution are more modest than those reported from anecdotal reports. The cause of the emission reductions seen in anecdotal reports are from injection timing shifts, not hydrogen combustion.

However, hydrogen substitution does yield modest emissions reduction with limited penalty. The foremost benefit is the reduction in hydrogen carbon fuel during substitution for hydrogen. Fumigation of hydrogen into the air intake was seen to displace up to 30% of the diesel fuel energy required to run a compression ignition engine at a high load. Also carbon dioxide was reduced by at a nearly a one to one percentage reduction on the basis of fuel energy.

Hydrogen substitution causes a dramatic shift of the NO_x species, from NO dominance to NO₂ dominance. This NO_x shift has the potential to be coupled with CRTs to oxide soot.

The benefits of hydrogen substitution are significant, since these results show that substitution of the diesel fuel with hydrogen can be accomplished with little or no detrimental effect. Thus, substantial quantities of diesel fuel can be “displaced” through hydrogen utilization via substitution. The practicality of vehicles utilizing hydrogen substitution is limited by the feasibility of equipment cost versus the cost benefits from the modest emission reductions.

Chapter 5

Discussion and Results of Advanced Combustion Modes with Hydrogen Substitution

5.1 Introduction

In this section, the results of hydrogen assisted combustion under advanced combustion modes are presented. Though an in-depth study of hydrogen assisted combustion under advanced combustion modes is novel, the ability to reproduce the advanced combustion modes on a stock production engine is equally fascinating. The advanced combustion modes used in this study are based on work done by Wagner, Sluder and coworkers at Oak Ridge National Laboratory [39, 44-49].

Wagner, Sluder and coworkers developed an advanced combustion mode known as High Efficiency Clean Combustion (HECC). The HECC mode is an efficient LTC/PCCI mode, which reduces NO_x and PM while improving brake specific fuel efficiency. An LTC mode is typically classified as a mode in which NO_x and PM are reduced via high concentrations of EGR. In this study, like the work done at Oak Ridge, an LTC mode is presented as an intermediate step to the HECC mode.

Wagner, Sluder and coworkers performed their study on a modified Mercedes 1.7L direct-injection diesel engine. This study was conducted on a Detroit Diesel 2.5L TD DI-4V engine. The differences between the two engines made it impossible to repeat the exact conditions performed at Oak Ridge National Laboratory. However, Wagner, Sluder and coworkers have shown it possible to achieve HECC at a broad range of speeds

and loads [39]. There were also variations in the NO_x and PM reduction due to the range of speed and load conditions which Wagner, Sluder and coworkers used to achieve the HECC mode.

In this study, a HECC mode was located at 1800 rpm at 25% of maximum output because of its normally high concentrations of EGR. The high EGR concentration is due to the mode's low speed, which utilizes little boost. High exhaust pressure and low manifold pressure allow EGR to readily overcome the positive pressure of the intake manifold. The HECC mode listed in this study shares trends with Wagner, Sluder and coworkers' HECC modes. The HECC mode used in this study achieved a 71% brake specific NO_x reduction, an 80% brake specific PM reduction, a 4% brake specific fuel consumption reduction, a 73% brake specific HC increase, and a 106% CO increase.

The results of hydrogen substitution for diesel fuel on the basis of energy percent are presented below in the baseline mode, LTC mode and HECC mode. Hydrogen substitution was done at 0%, 2.5% 5% 7.5% 10% and 15%, of the fuel energy. Hydrogen substitution in advanced modes caused modest emission reductions, which were similar to emission reductions seen during hydrogen substitution for conventional combustion modes. A 15% hydrogen substitution was achieved in the advanced combustion modes without significant penalty on emissions or performance.

5.2 Exhaust Gas Recirculation

The key parameter used to enter the HECC mode is a high concentration of EGR, ~50%. EGR% was defined as [29]:

$$EGR\% = \frac{CO_{2Intake}(vol\%) - CO_{2Ambient}(vol\%)}{CO_{2Exhaust}(vol\%) - CO_{2Ambient}(vol\%)} \quad 5.1$$

On the Detroit Diesel 2.5L TD DI-4V engine there is an EGR valve that diverts exhaust gas into the intake manifold. This valve is controlled by the engine's ECU. With the EGR valve fully open, the volumetric flow rate of EGR supplied into the intake manifold from the exhaust manifold was dependent on the gradient between the exhaust manifold pressure and the intake manifold pressure. Engine modes that utilize boost pressure from the turbocharger can not achieve high concentrations of EGR because the boost pressure in the intake manifold is too great for the exhaust gas to overcome.

There are two methods to force large levels of exhaust into the intake manifold via the EGR loop. The first method is to increase the back-pressure on the exhaust. This is accomplished by causing a flow restriction downstream of the EGR loop. A valve on the exhaust pipe can be used as a restriction. In this method, exhaust is forced into the EGR loop due to the downstream restriction. Because an internal combustion engine is an air pump, this method is inherently problematic, ultimately de-rating the engine by preventing the engine from achieving its maximum air throughput.

In the second method, the intake air is choked by a restriction upstream of the intake manifold and EGR loop. A valve can be used to create a restriction, choking the intake air and causing exhaust to be pulled through the EGR loop. Unlike the case of the back pressure method, this intake choking method does not cause the engine to derate

from a pumping restriction. The second method, however, will derate the engine due to the exchange of air (the working fluid of an engine) for EGR.

The choking EGR method was initially used in attempts to enter the HECC mode. Unfortunately, the Detroit Diesel 2.5L TD DI-4V engine was found to produce exorbitant levels of CO emissions and HC emissions at 50% EGR. These high emissions were due to incomplete combustion, with levels varying per cylinder. This incomplete combustion is reflected in the apparent rate of heat release seen in Figure 5.1.

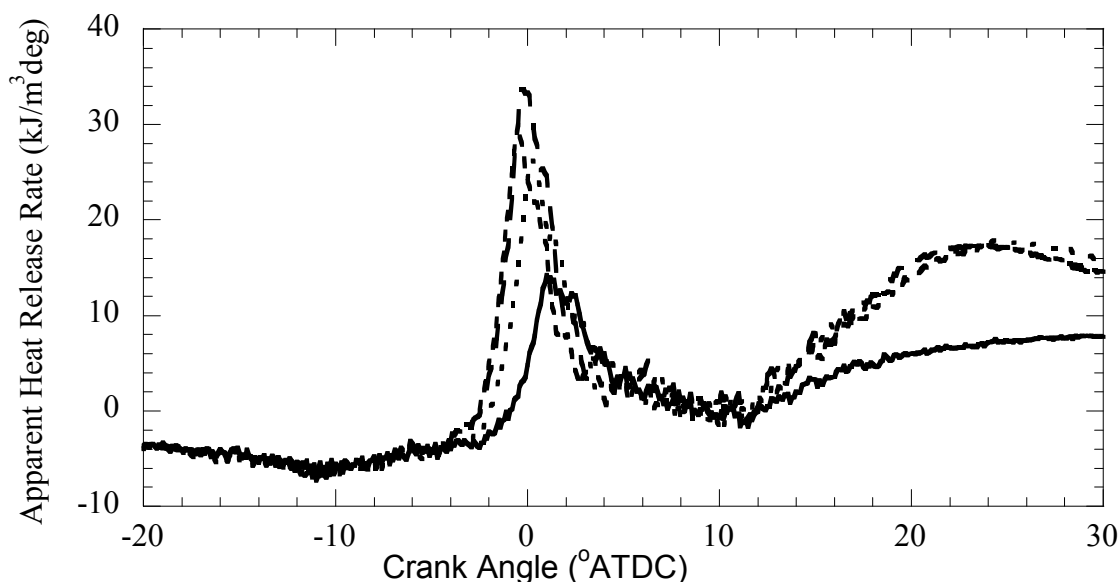


Figure 5.1: In complete combustion seen in Apparent Heat Release Rate in cylinders for 1800 rpm at 20 ft-torque. Pilot injection at -17ATDC and the main injection is at -2.9 ATDC. EGR ~50%. ———dQ1, - - -dQ2, - - - -dQ3 and · · · · ·dQ4.

The incomplete combustion was most pronounced in Cylinder 1, which was caused by poor mixing of the EGR and intake air. Since the EGR loop connects to the air intake directly before the air actually enters the intake manifold there is little time for the EGR and air to mix. The phenomenon of high EGR concentrations increasing the cylinder to cylinder variation was noted by Zheng and coworkers [31].

To eliminate the high levels of incomplete combustion, simulated EGR was used to achieve a HECC mode. Bone-dry CO₂ with a purity of 99.8% was used as simulated EGR, which was aspirated into the engine air intake downstream of the turbocharger at the same location as hydrogen aspiration. At this point of aspiration the simulated EGR was assumed to be well mixed.

In conjunction with simulated EGR, the Detroit Diesel 2.5L TD DI-4V engine's EGR valve was set to full open. At 1800 rpm, 25% of maximum output, and with the EGR valve fully open, the engine will produce ~16% EGR. With the engine-produced EGR and simulated EGR added together, the EGR requirement of the HECC mode was met. The method of using simulated EGR reduced the level of incomplete combustion observed during the exploration for the HECC mode.

Wagner, Sluder and coworkers cooled their EGR with a heat exchanger to prevent damaging the plastic intake manifold on their Mercedes 1.7L engine [49]. Cooled EGR is preferable since it will recover the volumetric efficiency of the engine that would otherwise be lost if intake air is hot. The Detroit Diesel 2.5L TD DI-4V engine cools its EGR with a heat exchanger cooled by the circulating engine coolant. The simulated EGR was warmed to room temperature before entering the engine. It should be noted that a small error was introduced by using room temperature simulated EGR (~25°C) compared to using engine exhaust cooled by actual EGR (~50°C).

5.3 Mode Parameters

Table 5.1 lists the parameters of the modes explored in this study. These parameters reflect the operating modes for 0% hydrogen on a fuel energy basis. Hydrogen substitution caused small changes to the EGR %, intake manifold gas temperature, and the exhaust gas temperature parameters. The injection timing was electronically held constant by reprogramming the engine's ECU. Speed and load were held constant by using a combination of dynamometer and engine controllers.

Table 5.1: 0% parameters of advanced combustion mode hydrogen assisted diesel combustion. All modes were run at 1800 rpm at 25% maximum of output.

Mode	Speed (rpm)	Load (kW)	EGR (%)	Simulated EGR (%)	Total EGR (%)	Boost (bar)	Rail Pressure (bar)	Intake Manifold Gas (°C)	Exhaust Gas (°C)	Pilot Inj. (°ATDC)	Main Inj. (°ATDC)
Baseline	1800	15.7	11	0	11	0.17	450	59	342	-17.4	2.9
LTC	1800	15.7	16	32	48	0.14	450	70	357	-17.4	2.9
HECC	1800	15.7	16	34	50	0.18	490	75	336	N/A	-4.0

The baseline mode utilized the engine's default diesel fuel injection strategy for the given speed and load based on the engine's ECU maps. The LTC mode uses the same locked injection timing as the baseline mode, as well as with the maximum engine produced EGR and aspirated simulated EGR. The HECC mode utilizes a single pulse injection and advanced main injection timing. And in addition to the rail pressure was increased from a default pressure of 450 bar to 490 bar. The HECC mode also uses the maximum engine-generated EGR along with simulated EGR.

5.4 Needle Lift

The needle lift data indicated the crank angle at which fuel is injected, as well as the duration of injection and needle lift height of fuel injected. Figure 5.2 displays the comparison of needle lift for the baseline, LTC, and HECC modes under 0% hydrogen. Predictably, the baseline mode and the LTC mode, had similar start of injection and injection durations. This is due to the injection timing being locked at -17.4°ATDC for the pilot injection, and 2.9°ATDC for the main injection timing in both modes. The HECC mode had a single injection that was set at -4°ATDC . The HECC mode also had higher needle lift since the mode utilized only a single injection and must inject all the required fuel during this single injection. The area under the injection peaks represents the quantity of fuel injected during the actuation of the fuel injector. It is important to note that this HECC mode also utilized increased rail pressure, thus a large quantity of fuel was injected for the given injection duration and needle lift height.

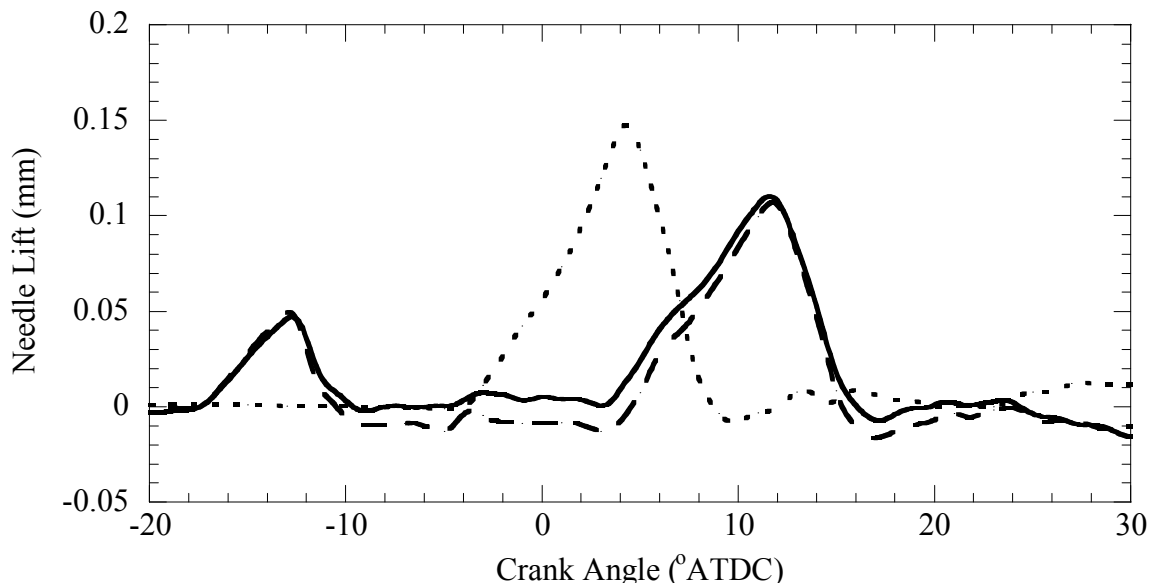


Figure 5.2: Needle Lift comparison of the baseline mode, LTC mode and HECC mode with 0% of hydrogen. — baseline, - - LTC and · · · · HECC.

Figures 5.3 through Figure 5.5 are the needle lift of the baseline mode, LTC mode, and HECC mode with hydrogen substitution. The needle lift signal contains noise from external sources. A majority of the noise was filtered out by averaging 200 samples. The needle lift signals' reluctance to return to zero height after injection was caused by a combination of signal noise and oscillation inherent to a fast-acting spring system. The oscillation observed in the main injection was caused by the preceding pilot injection. As to be expected, the pilot injections in Figure 5.3 and Figure 5.4 overlap. Because of the noise, and the oscillations shifting the height of the injection, the main injection is difficult to analyze. Figure 5.5 reflects the HECC mode, which utilized a single injection. Note that the needle lift signal in Figure 5.5 clearly shows that the increasing rate of hydrogen substitution decreases the height, and thus the quantity of diesel fuel introduced by the injector.

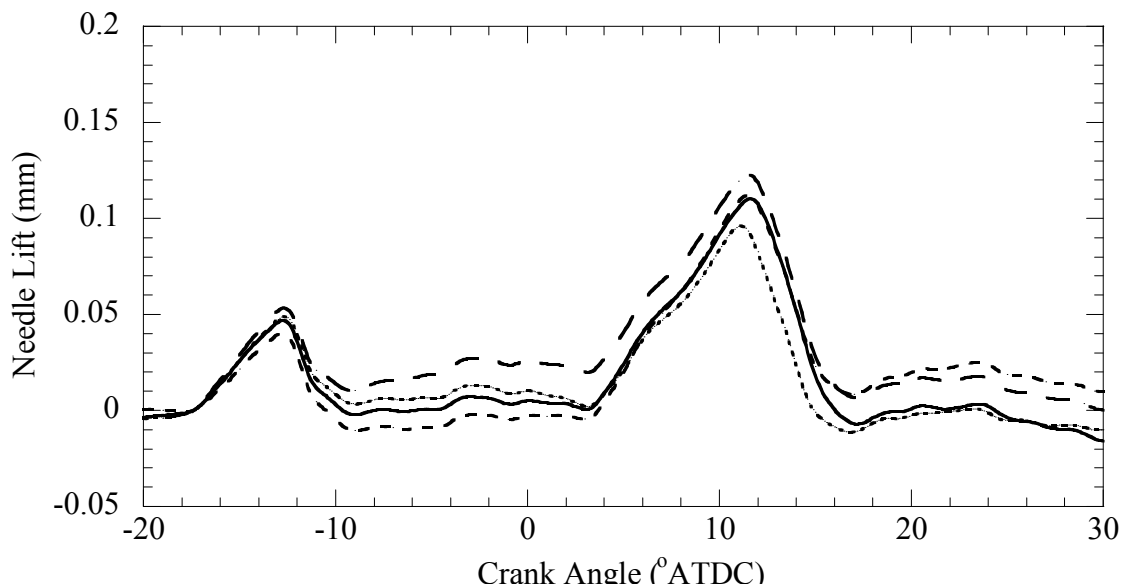


Figure 5.3: Needle lift of baseline mode, with — 0%, - - 2.5%, - · - 7.5% and · · · · 15% hydrogen substitution on an energy basis.

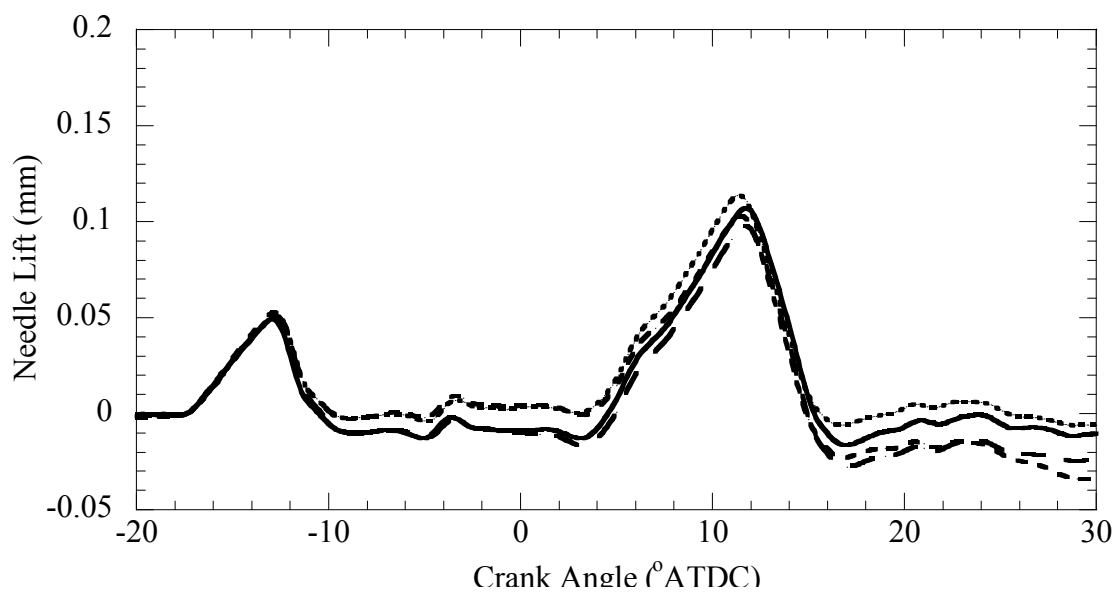


Figure 5.4: Needle lift of LTC mode, with — 0%, - - 2.5%, - · - 7.5% and · · · · 15% hydrogen substitution on an energy basis.

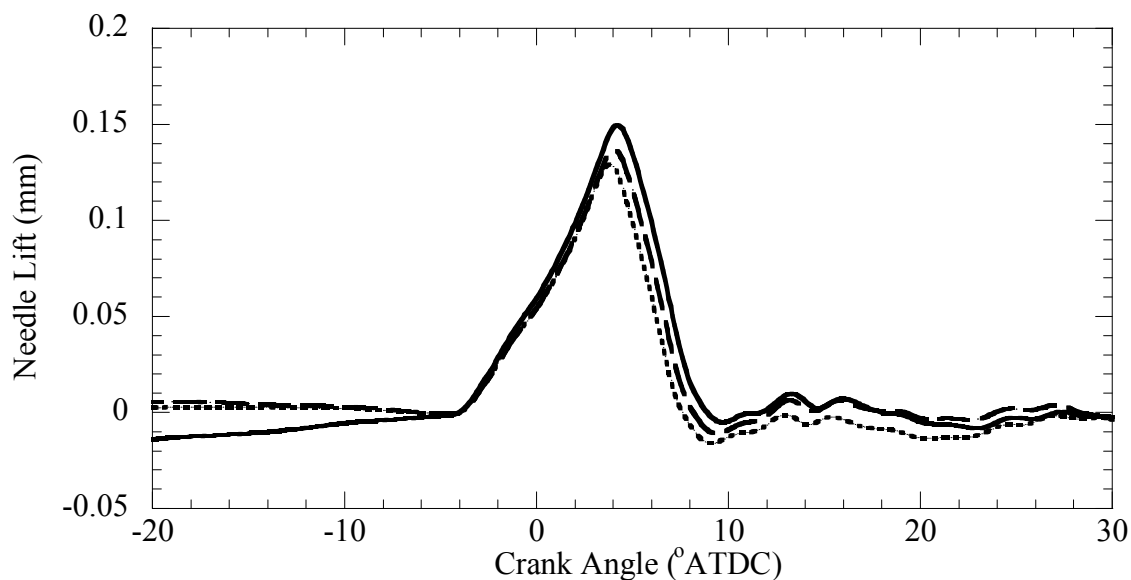


Figure 5.5: Needle lift of HECC mode, with — 0%, - - 2.5%, - · - · 7.5% and · · · · 15% hydrogen substitution on an energy basis.

5.5 Pressure Trace

The pressure traces indicate the pressure due to cylinder volume reduction from the piston's travel, as well as the pressure created from hot product gases. The baseline mode and the LTC mode have similar pressure traces due to their similar parameters. In Figure 5.6 a 2.7% decrease in maximum pressure occurs in the LTC mode compared to the baseline. The reduction in maximum pressure seen in the pressure traces is due to the LTC mode's high level of EGR. The EGR absorbs released heat, lowering the adiabatic flame temperature [1]. An increase in EGR levels also leads to a reduction in oxygen, oxidizer need to burn the fuel. Thus, the maximum pressure of the LTC mode is reduced. The maximum pressure produced in the HECC mode with 0% hydrogen substitution was

21% lower than that of the baseline mode, due to the large degree of pre-mixed combustion which occurred in the HECC mode. The second pressure peak of the HECC mode is due to the mode's transition to mixing-controlled combustion, which is further explained by the apparent heat release rate.

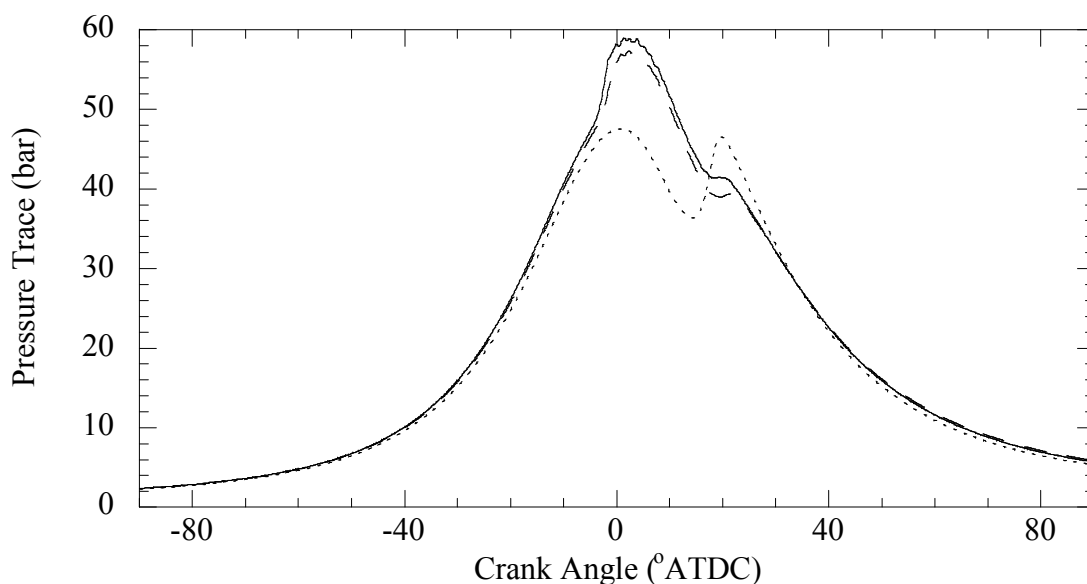


Figure 5.6: Pressure trace comparison of the baseline mode, LTC mode and HECC mode with 0% of hydrogen. — baseline, - - LTC and - · - · HECC.

Figures 5.7 to 5.9 show the pressure traces of the baseline mode, LTC mode and HECC mode with 0%, 2.5%, 5% and 15% hydrogen substitutions. Increasing levels of hydrogen caused a slight increase in maximum pressure. Table 5.2 compares the increase of peak pressure caused by hydrogen.

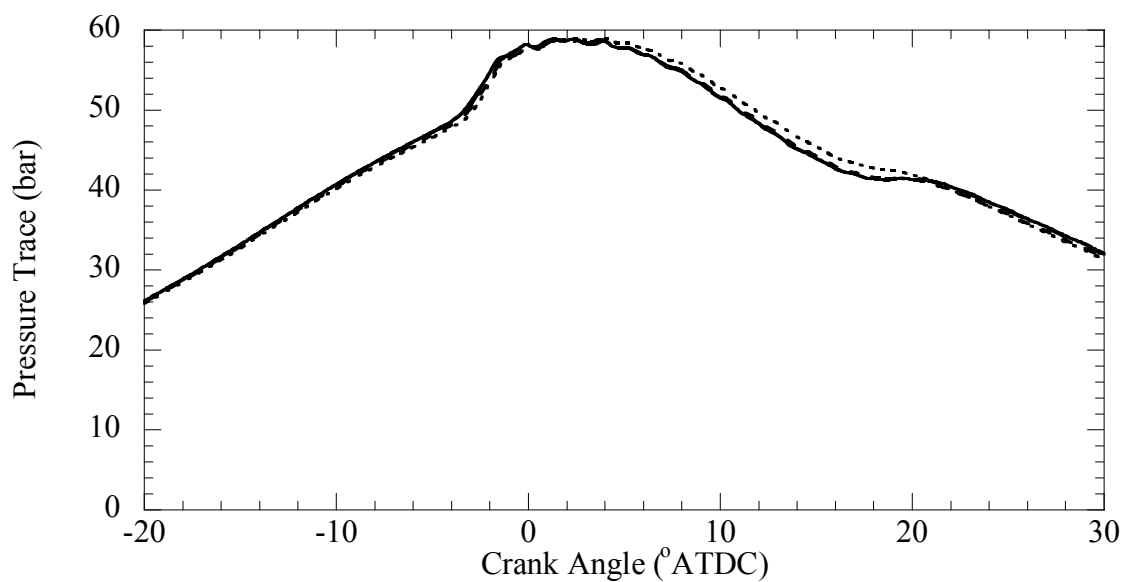


Figure 5.7: Pressure trace of baseline mode, with — 0%, - - 2.5%, - - - 7.5% and · · · · 15% hydrogen substitution on an energy basis.

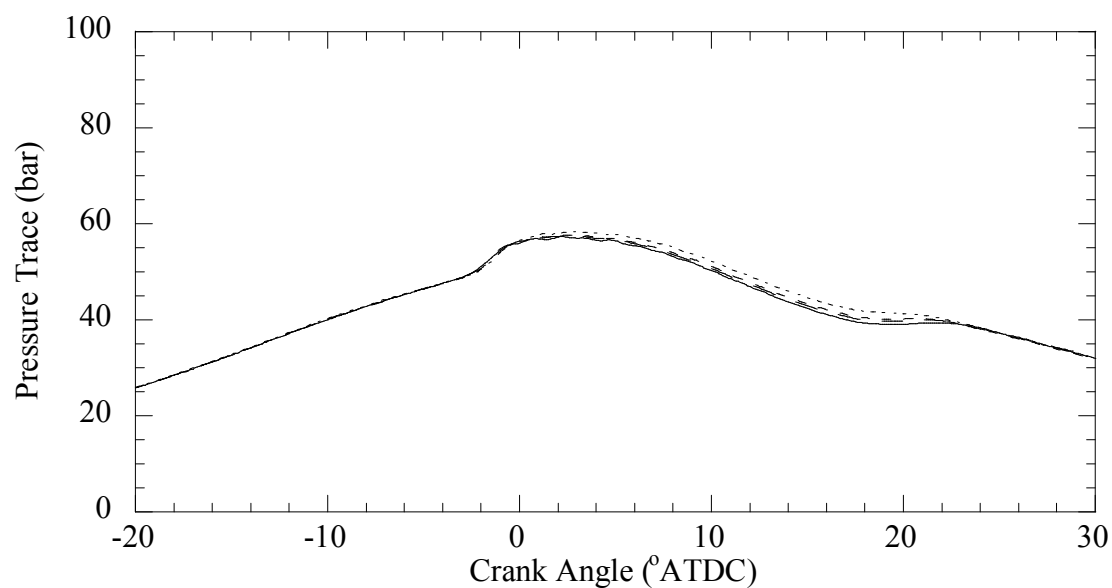


Figure 5.8: Pressure trace of LTC mode, with — 0%, - - 2.5%, - - - 7.5% and · · · · 15% hydrogen substitution on an energy basis.

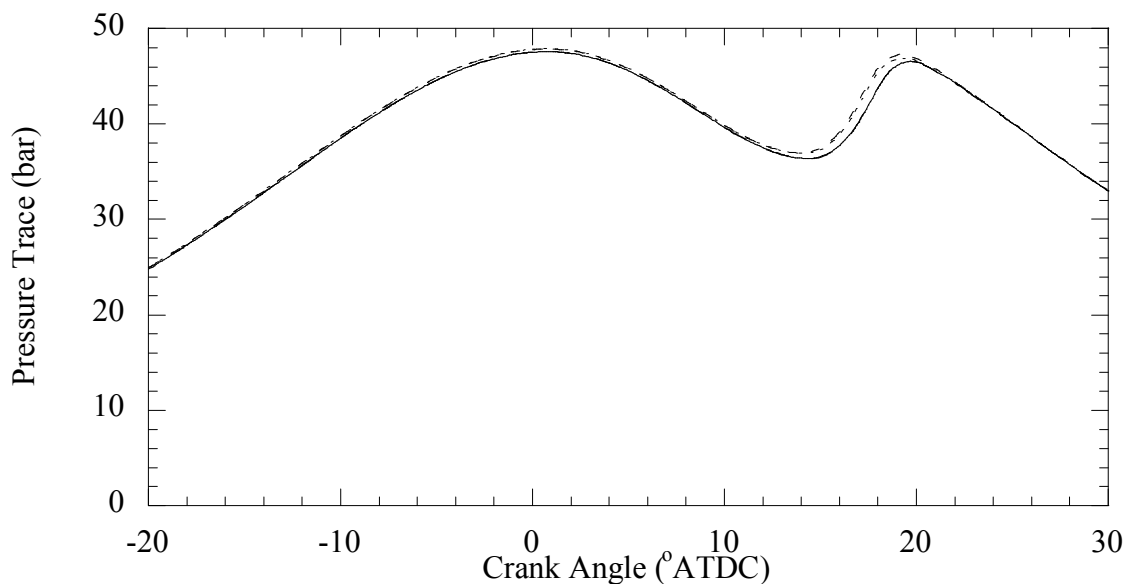


Figure 5.9: Pressure trace of HECC mode, with — 0%, - - 2.5%, - · - · 7.5% and · · · · 15% hydrogen substitution on an energy basis.

Table 5.2: Percent difference of maximum pressure from 0% hydrogen substitution at the three modes tested with 2.5%, 7.5% and 15% hydrogen substitution on an energy basis. Positive values indicate an increase and negative values indicate a decrease from the baseline.

	Baseline	LTC	HECC
0% Diff.	n/a	n/a	n/a
2.5% Diff.	-0.2	0.7	0.0
7.5% Diff.	-0.3	0.7	0.6
15% Diff.	0.1	1.7	0.7

Table 5.3 compares the increase of maximum pressure of the baseline mode compared to the LTC mode and the baseline mode compared to the HECC mode. The LTC mode decreases slightly in maximum pressure compared to the LTC mode by 2.7%

at 0% hydrogen substitution. The HECC mode, however, displays a 21.3% decrease in maximum pressure.

Table 5.3: Percent difference of maximum pressure from the baseline mode to the LT mode and HECC mode with 0%, 2.5%, 7.5% and 15% hydrogen substitution on an energy basis. Positive values indicate an increase and negative values indicate a decrease from the baseline.

	Baseline to LTC	Baseline to HECC
0% Diff.	-2.7	-21.3
2.5% Diff.	-1.7	-21.1
7.5% Diff.	-1.7	-20.4
15% Diff.	-1.1	-20.8

5.6 Coefficient of Variance

The coefficient of variance is a measure used to quantify cycle-to-cycle variation based on the in-cylinder indicated mean effective pressure (IMEP). Heywood defines the coefficient of variance as given in Eq. 5.2 [5].

$$COV_{imep} = \frac{\sigma_{imep}}{imep} \cdot 100\% = \frac{\sigma}{\mu} \cdot 100\% \quad 5.2$$

The mean (μ) and the standard deviation (σ) of the coefficient of variance were calculated from 200 cycles of pressure traces. A $COV_{imep} > 1$ indicates increased variation between cycles. Table 5.4 displays the coefficient of variance of all four cylinders of the baseline mode, LTC mode, and HECC mode with hydrogen substitution.

Table 5.4: Coefficient of variance for all four cylinders baseline mode, LTC mode and HECC mode with 0%, 2.5%, 7.5% and 15% hydrogen substitution on an energy basis.

Baseline					LTC				HECC			
H2%	<i>Cyl. 1</i>	<i>Cyl. 2</i>	<i>Cyl. 3</i>	<i>Cyl. 4</i>	<i>Cyl. 1</i>	<i>Cyl. 2</i>	<i>Cyl. 3</i>	<i>Cyl. 4</i>	<i>Cyl. 1</i>	<i>Cyl. 2</i>	<i>Cyl. 3</i>	<i>Cyl. 4</i>
0	5.5	5.2	5.6	4.6	6.4	3.0	3.0	3.3	3.6	2.9	3.8	3.2
2.5	5.6	5.0	5.2	4.6	4.6	3.2	3.4	3.2	3.5	3.0	3.6	3.3
7.5	5.6	4.8	5.7	4.5	7.1	3.3	3.1	3.4	3.5	3.3	4.1	3.5
15	5.4	4.4	5.9	4.4	10.2	3.7	4.3	4.2	3.6	3.0	3.6	3.0

When compared to the baseline mode at 0% hydrogen substitution, the LTC mode overall displayed less cycle-to-cycle variation, except in Cylinder 1. The pressure traces show that the 2.5 L DDC engine's Cylinder 1 performed poorly due to inadequate mixing of the intake charge. The HECC mode also displayed less cycle-to-cycle variation over the baseline mode at 0% hydrogen substitution. The decreased cycle-to-cycle variation of the LTC mode and HECC mode can be attributed to the high EGR content used in these modes. High EGR, however, is reported to increase cycle-to-cycle variation, not decrease it [5, 31]. The hydrogen substitution does not create any appreciable trends in coefficient of variation. A repeatability study with 0% hydrogen has confirmed the lack of a trend in the coefficient of variance seen in table 5.4.

5.7 Apparent Heat Release Rate

Figure 5.10 displays the apparent heat release rate of the baseline mode, LTC mode, and HECC with 0% hydrogen substitution. The start of combustion of the pilot injection (-7.9TDC) of the LTC mode are delayed compared to the start of combustion of the pilot injection (-8.7 °ATDC) for the baseline mode. The delay in start of combustion observed for the LTC mode is due to the mode's high concentration of EGR, which

absorbs the heat produced by the in-cylinder compression, requiring further time to achieve ignition. Since its injection timing is different, the HECC mode's start of combustion (7.1°ATDC) cannot be compared to that of the other modes.

The apparent heat release rate profiles of the baseline mode and LTC mode appear generic, corresponding to the four diesel combustion phases given by Heywood [5]. The HECC mode has a unique apparent heat release rate profile. Diesel fuel is injected into this mode at -4°ATDC , but combustion does not start until 7.1°ATDC . The HECC mode has an 11.1° ignition delay. This extended start of combustion is due to the large concentration of EGR ($\sim 50\%$) used in the mode, as well as, an advanced injection timing. This mode is unique as it utilizes only three of the four diesel combustion phases given by Heywood, including a longer than usual ignition-delay phase. The single injection of the HECC mode ends at 8.7°ATDC and the start of combustion begins at HECC (7.1°ATDC). By the time combustion begins almost all of the fuel is injected into the cylinder, thus causing almost all of the fuel to be consumed in a pre-mixed combustion phase. Indicated by the end of injection and start of combustion overlapping, a small quantity of fuel was burned in the mixing-controlled combustion phase. However, the apparent heat release rate plot, given in Figure 5.10, does not indicate the presence of a mixing-controlled combustion phase peak. Rather it indicates the heat release's transition directly from a pre-mixed combustion phase to a late combustion phase, which is the trailing trace in the HECC mode's apparent heat release rate plot. The apparent heat release rate plot of the HECC mode provides verification that the mode is a PCCI combustion mode.

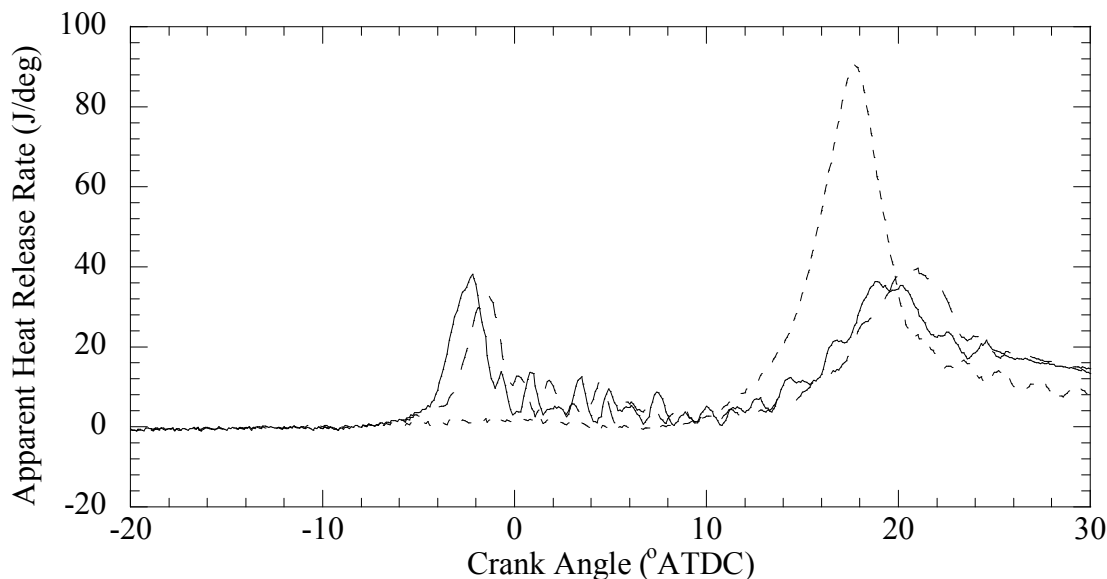


Figure 5.10: Apparent heat release rate comparison of the baseline mode, LTC mode and HECC mode with 0% of hydrogen. — baseline, - - LTC and · · · · HECC.

Figures 5.11 through 5.13 show the apparent heat release rates of the baseline mode, LTC mode and HECC mode with 0%, 7.5% and 15% hydrogen substitution. Hydrogen substitution caused similar apparent heat release rate plots for both the baseline mode and the LTC mode. Hydrogen substitution caused the premixed combustion phase of the baseline mode and the LTC mode to have a higher peak as hydrogen substitution increased. The peaks of the mixing-controlled combustion phase of both the baseline mode and LTC mode decrease as hydrogen substitution increases. Both the increase of the pre-mixed combustion phase peak and the decrease in the mixing-controlled combustion phase peak are caused by the method in which hydrogen is injected into the engine. The hydrogen is aspirated into the engine along with the intake air. Thus, once the intake valve of a cylinder closes, hydrogen can no longer be added. After the pilot

injection of diesel consumes the hydrogen, there is no more hydrogen available to be burned during the main injection. The engine injected less diesel fuel into the cylinder when hydrogen substitution was increased because the engine was set to a fixed load.

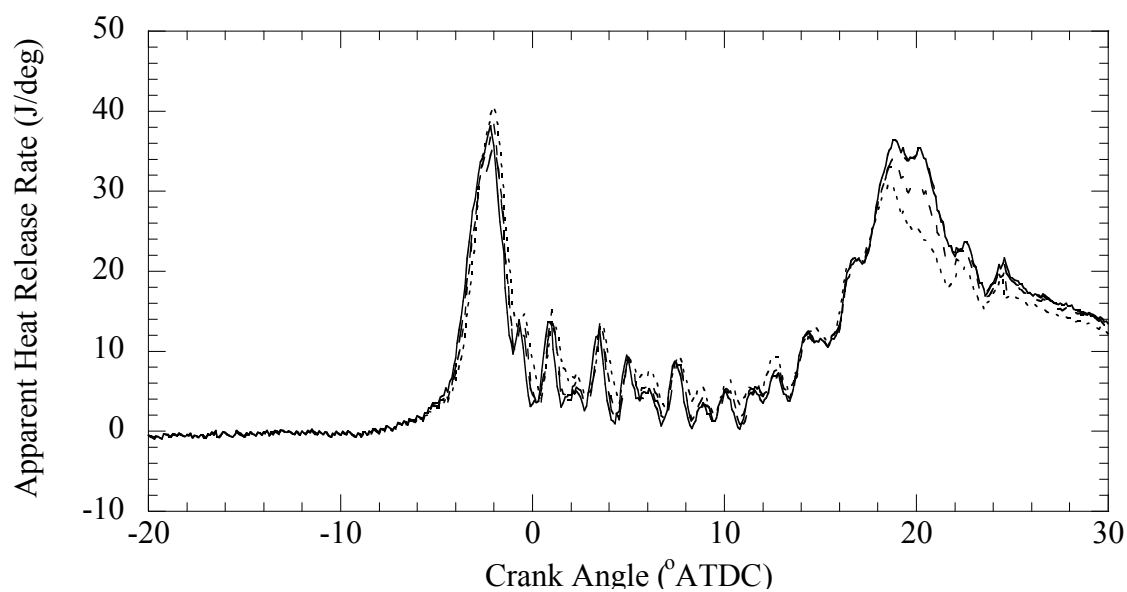


Figure 5.11: Apparent heat release rate of baseline mode, with — 0%, - - - 2.5%, - · - · 7.5% and · · · · 15% hydrogen substitution on an energy basis.

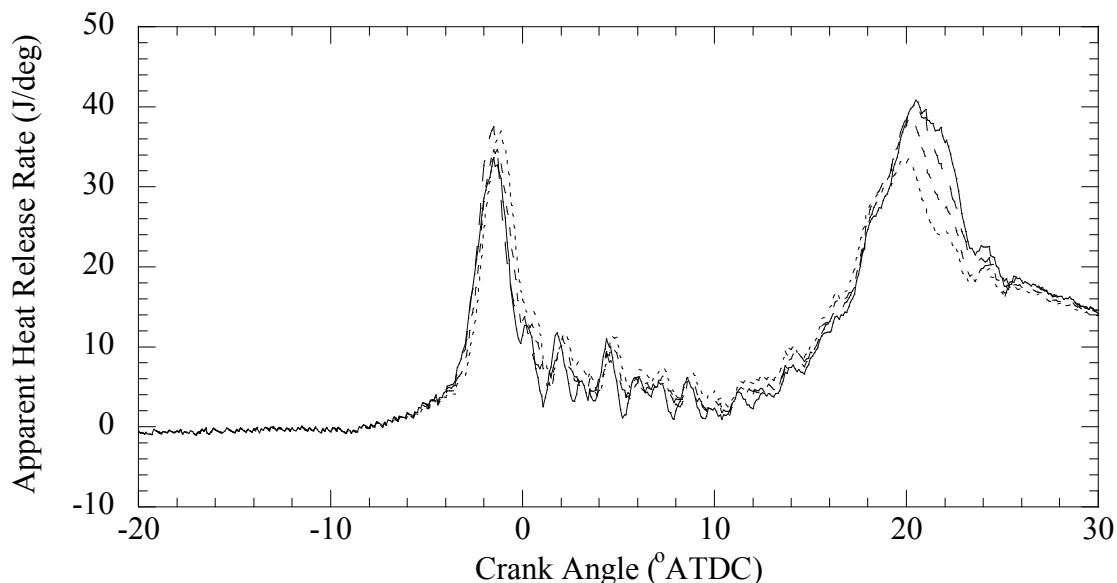


Figure 5.12: Apparent heat release rate of LTC mode, with — 0%, - - - 2.5%, - - - - 7.5% and · · · · 15% hydrogen substitution on an energy basis.

Figure 5.13 displays the apparent heat release rate of the HECC mode with hydrogen substitution. The increased substitution of hydrogen did not create appreciable trends in maximum apparent heat release rate. The addition of hydrogen did, however, advance the crank angle of the maximum heat release from 15.2°ATDC at 0% hydrogen to 14.9°ATDC at 15% hydrogen substitution. This shift in maximum apparent heat release rate is due to the increased presence of hydrogen, causing greater portions of the fuel to be premixed at an earlier crank angle.

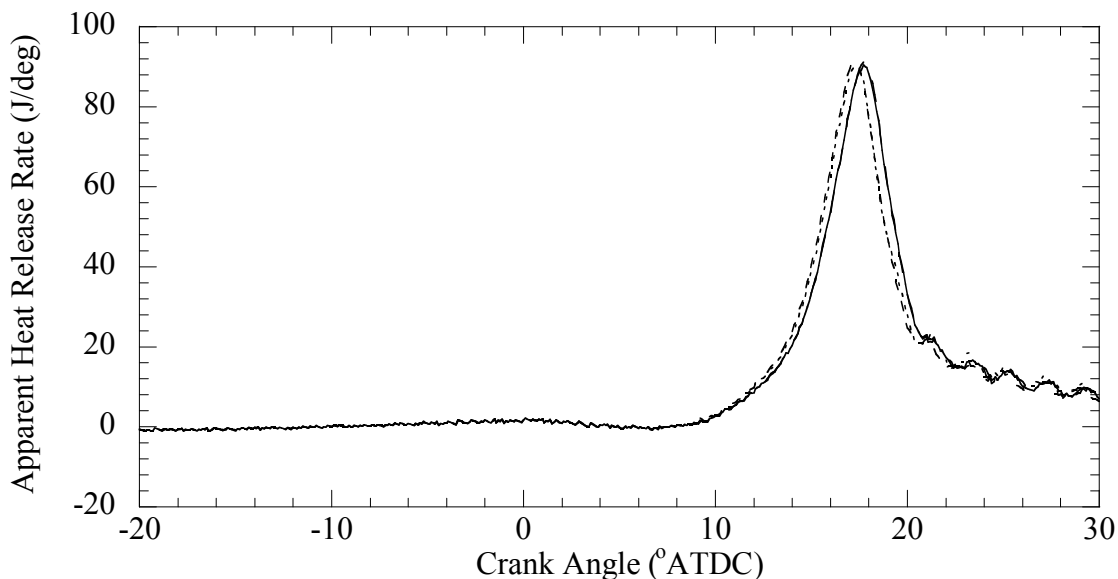


Figure 5.13: Apparent heat release rate of HECC mode, with — 0%, - - - 2.5%, - - - - 7.5% and · · · · 15% hydrogen substitution on an energy basis.

5.8 Equivalence Ratio

Figure 5.14 displays the global equivalence ratio of the three modes tested. The equivalence ratios of the modes are fuel lean. The apparent heat release rate indicated that the baseline mode and LTC mode consist mainly of mixing-controlled combustion phases, thus, combustion takes place as a diffusion flame with an array of locally fuel lean regions and locally fuel rich regions. According to the apparent heat release rate data, the HECC mode is mainly composed of a pre-mixed combustion phase, which indicates that the equivalence ratio is likely locally fuel lean through the air-fuel charge. The difference between the local equivalence ratios of the modes is used to explain exhaust emissions.

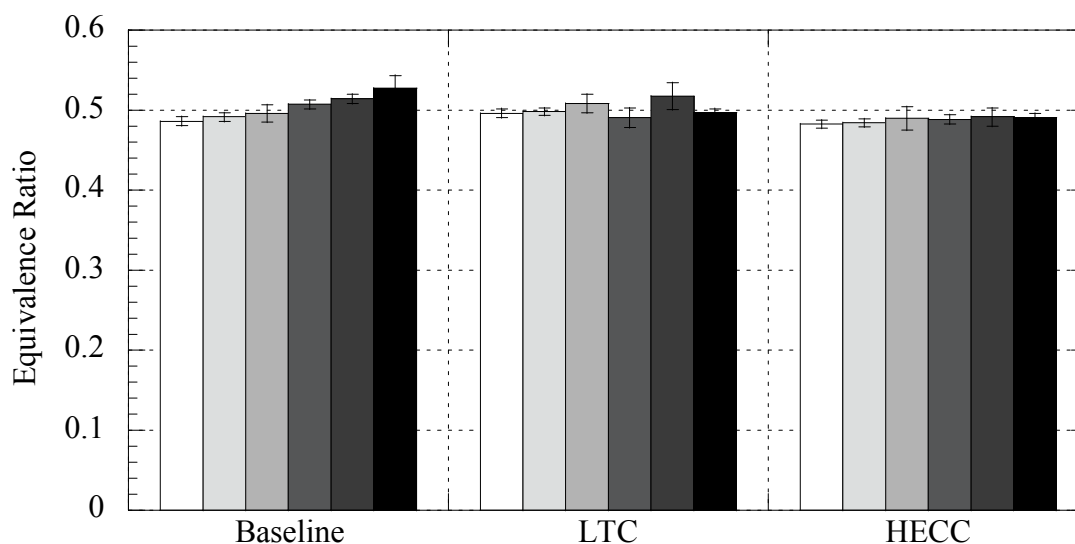


Figure 5.14: Equivalence Ratio of the three modes tested, with \square 0%, \blacksquare 2.5%, \blacksquare 5%, \blacksquare 7.5%, \blacksquare 10% and \blacksquare 15% hydrogen substitution on an energy basis.

The equivalence ratios of the three modes with 0% hydrogen are practically the same when error is taken into consideration. All three modes show a trend of increasing equivalence ratio with increasing hydrogen substitution. This trend is to be expected, since aspirated hydrogen addition will displace intake air, decreasing the air-fuel ratio.

5.9 Exhaust Temperature

Figure 5.15 displays the exhaust temperatures of the three modes tested. Exhaust temperature provides only an indirect indication of the global in-cylinder temperature. A bulk cylinder temperature based on the ideal gas law was not used to calculate temperature because the high levels of EGR used in the modes would result in erroneously high calculated temperatures, due to the increase in temperature of the intake charge and the decreasing of trapped mass [30]. Computational Fluid Dynamics (CFD)

modeling, which is outside the scope of this work, would provide the best indication of the combustion temperatures.

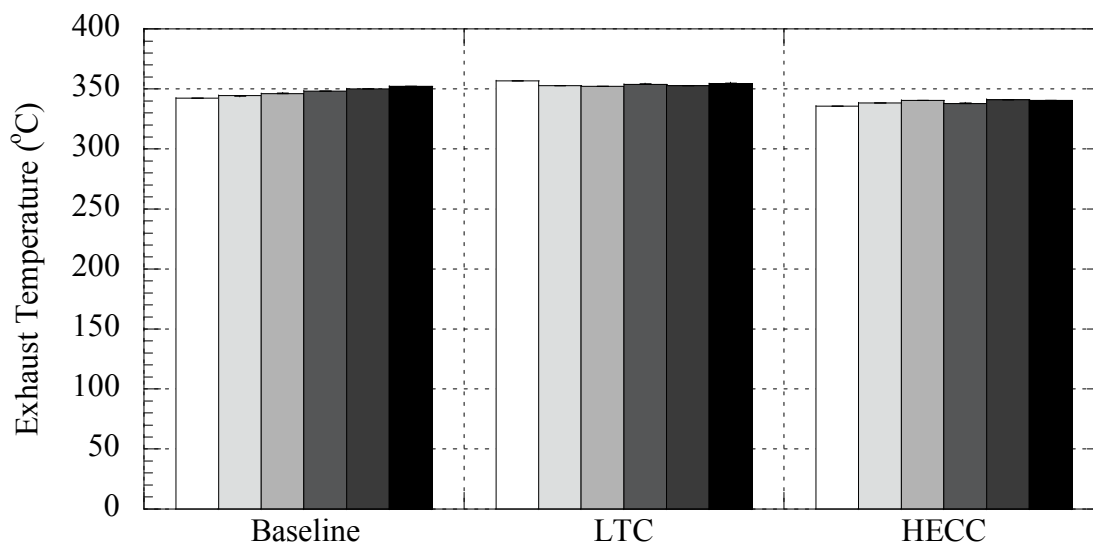


Figure 5.15: Exhaust temperature of the three modes tested, with \square 0%, \square 2.5%, \square 5%, \square 7.5%, \blacksquare 10% and \blacksquare 15% hydrogen substitution on an energy basis.

Tables 5.5 and 5.6 compare the three modes with and without hydrogen substitution. Hydrogen substitution clearly increased the exhaust temperature of the baseline mode and the HECC mode. LTC mode however, showed a modest decrease in exhaust temperature, which can be attributed to a shift in laboratory conditions.

Table 5.5: Percent difference of exhaust temperature from 0% hydrogen to 2.5%, 5%, 7.5%, 10% and 15% hydrogen substitution on an energy basis for the baseline mode, LTC mode and HECC mode. Positive values indicate an increase and negative values indicate a decrease from the baseline.

	Baseline	LTC	HECC
0% Diff.	n/a	n/a	n/a
2.5% Diff.	0.6	-1.1	0.8
5% Diff.	1.2	-1.3	1.5
7.5% Diff.	1.8	-0.7	0.8
10% Diff.	2.2	-1.1	1.7
15% Diff.	2.9	-0.5	1.5

Table 5.6: Percent difference of exhaust temperature comparing the baseline mode to LTC mode and baseline mode to HECC mode. Positive values indicate an increase and negative values indicate a decrease from the baseline.

	Baseline to LTC % Diff.	Baseline to HECC % Diff.
0%	4.1	-2.0
2.5%	2.5	-1.8
5%	1.7	-1.7
7.5%	1.6	-3.0
10%	0.8	-2.6
15%	0.7	-3.4

5.10 Gaseous Emissions: NO_x

The high levels of EGR used in the advanced combustion mode lowered the combustion temperature, quenching the production of thermal NO, thus reducing NO_x. The LTC mode decreased NO_x emissions by 89.5% compared to the baseline mode with 0% hydrogen substitution. The NO_x reduction of the HECC mode was less than that of the LTC mode, with a 71.2% NO_x reduction from the baseline with 0% hydrogen substitution. The HECC mode used on the DDC 2.5L engine was not optimized to

produce low NO_x emissions alone, but was rather optimized for simultaneously low NO_x emissions, low PM emissions and high thermal efficiency. Rail pressure, injection timing and EGR% were the variables adjusted in the HECC mode optimization process.

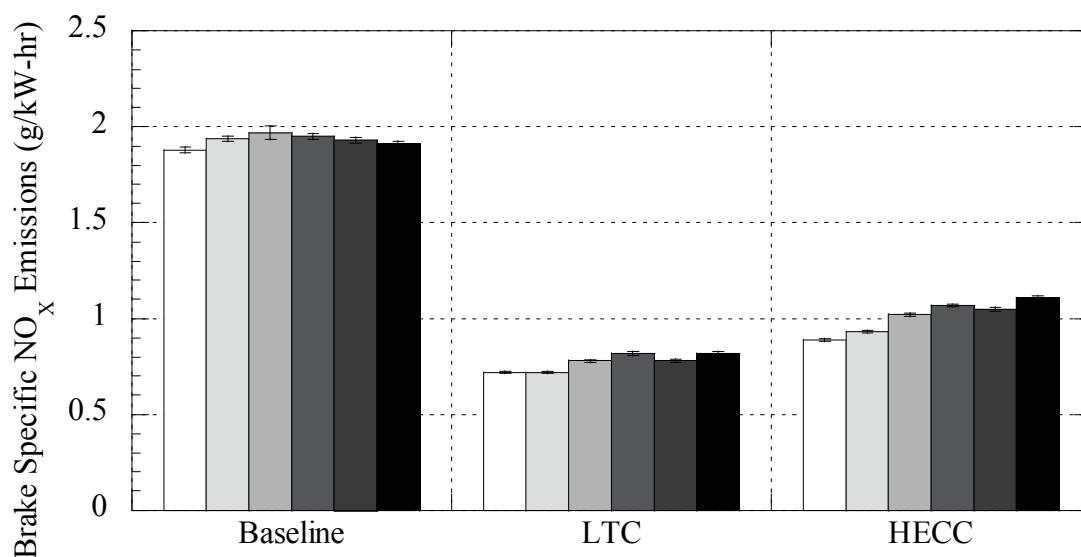


Figure 5.16: Brake specific NO_x emissions of the three modes tested, with □ 0%, ■ 2.5%, ■ 5%, ■ 7.5%, ■ 10% and ■ 15% hydrogen substitution on an energy basis.

The addition of hydrogen produced modest increases in NO_x emissions for the baseline mode, although hydrogen caused NO_x emissions for the LTC mode and HECC mode to more significantly increase on the percent difference basis, as given in Table 5.7. The high levels of EGR used in the LTC mode and the HECC mode dramatically reduced NO_x emissions from the baseline mode; hydrogen, however, still increased NO_x emissions independently of the reductions caused by high levels of EGR. The effect of hydrogen on the LTC mode and the HECC mode can be further explained by examining the NO emissions and the NO₂ emissions independently.

Table 5.7: Percent difference of brake specific NO_x emissions from 0% hydrogen to 2.5%, 5%, 7.5%, 10% and 15% hydrogen substitution on an energy basis for the baseline mode, LTC mode and HECC mode. Positive values indicate an increase and negative values indicate a decrease from the baseline.

	Baseline	LTC	HECC
0% Diff.	n/a	n/a	n/a
2.5% Diff.	3.0	-0.1	4.0
5% Diff.	4.6	8.7	13.6
7.5% Diff.	3.4	13.5	18.0
10% Diff.	2.5	8.7	15.7
15% Diff.	1.8	13.2	21.6

Table 5.8: Percent difference of brake specific NO_x emissions comparing baseline mode to LTC mode and baseline mode to HECC mode. Positive values indicate an increase and negative values indicate a decrease from the baseline.

	Baseline to LTC % Diff.	Baseline to HECC % Diff.
0%	-89.5	-71.2
2.5%	-92.0	-70.4
5%	-86.2	-63.2
7.5%	-81.2	-58.0
10%	-84.4	-59.3
15%	-80.1	-53.2

5.11 Gaseous Emissions: NO

According to Figure 5.17 and Table 5.10, the LTC mode and the HECC mode reduced NO emissions by ~83% compared to the baseline mode at 0% hydrogen substitution. The NO_x and NO emissions together indicate that the HECC mode did not decrease NO₂ emissions as significantly as the LTC mode. As seen in Table 5.9,

hydrogen substitution did not appreciably effect the advanced combustion modes' NO emissions.

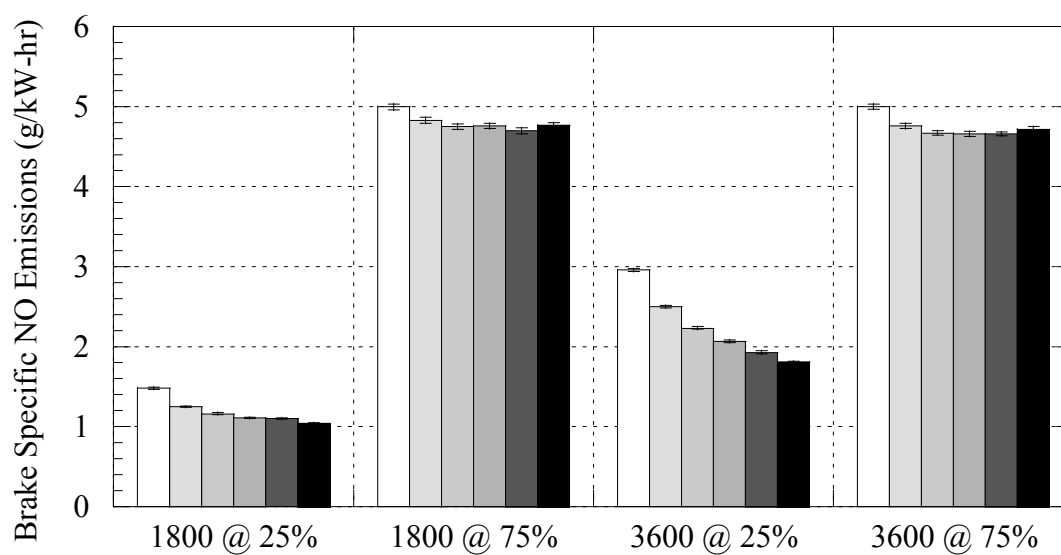


Figure 5.17: Brake specific NO emissions of the three modes tested, with \square 0%, \blacksquare 2.5%, \blacksquare 5%, \blacksquare 7.5%, \blacksquare 10% and \blacksquare 15% hydrogen substitution on an energy basis.

Table 5.9: Percent difference of brake specific NO emissions from 0% hydrogen to 2.5%, 5%, 7.5%, 10% and 15% hydrogen substitution on an energy basis for the baseline mode, LTC mode and HECC mode. Positive values indicate an increase and negative values indicate a decrease from the baseline.

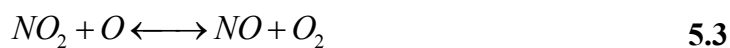
	Baseline	LTC	HECC
0% Diff.	n/a	n/a	n/a
2.5% Diff.	-16.9	-5.2	-1.5
5% Diff.	-24.2	1.5	1.8
7.5% Diff.	-28.7	-8.0	1.8
10% Diff.	-29.7	-3.2	-0.4
15% Diff.	-35.0	-7.1	2.9

Table 5.10: Percent difference of brake specific NO emissions comparing baseline mode to LTC mode and baseline mode to HECC mode. Positive values indicate an increase and negative values indicate a decrease from the baseline.

	Baseline to LTC % Diff.	Baseline to HECC % Diff.
0%	-82.5	-83.3
2.5%	-72.5	-70.1
5%	-59.9	-60.6
7.5%	-64.4	-56.5
10%	-59.2	-57.5
15%	-57.7	-49.4

5.12 Gaseous Emissions: NO₂

Figure 5.18 and Table 5.12 indicate that the LTC mode reduced NO₂ emissions by 119.2%, while the HECC mode only reduced NO₂ emissions 33.8%, in comparison to the baseline mode at 0% hydrogen substitution. The appearance of higher level of NO₂ emissions produced in the HECC mode over the LTC mode is not expected. While the major pathway to NO₂ formation is the oxidation of NO, the LTC and HECC modes both produced similar values of brake specific NO emissions. Upatnieks, Mueller and Martin conducted a study on an optically-accessible, heavy-duty DI diesel engine in which intake oxygen was diluted via nitrogen as simulated EGR, which resulted in an increased NO₂ to NO ratio. The increase of NO₂ and decrease of NO was attributed to an increased quenching of the NO₂-to-NO reaction (Eq. 5.3) due to decreasing flame temperatures [55].



The observation reported by Upatnieks, Mueller and Martin correspond to the NO and NO₂ emissions of LTC and HECC modes of this study, although CO₂ was used instead of nitrogen. The extended pre-mixed combustion phase of the HECC mode can be assumed to have lower flame temperature than that of the LTC mode, which has majority mixing-controlled combustion phase. This assumed lower flame temperatures of the HECC mode will then further quenching of the NO₂-to-NO reaction, thus HECC mode produced higher NO₂ emissions.

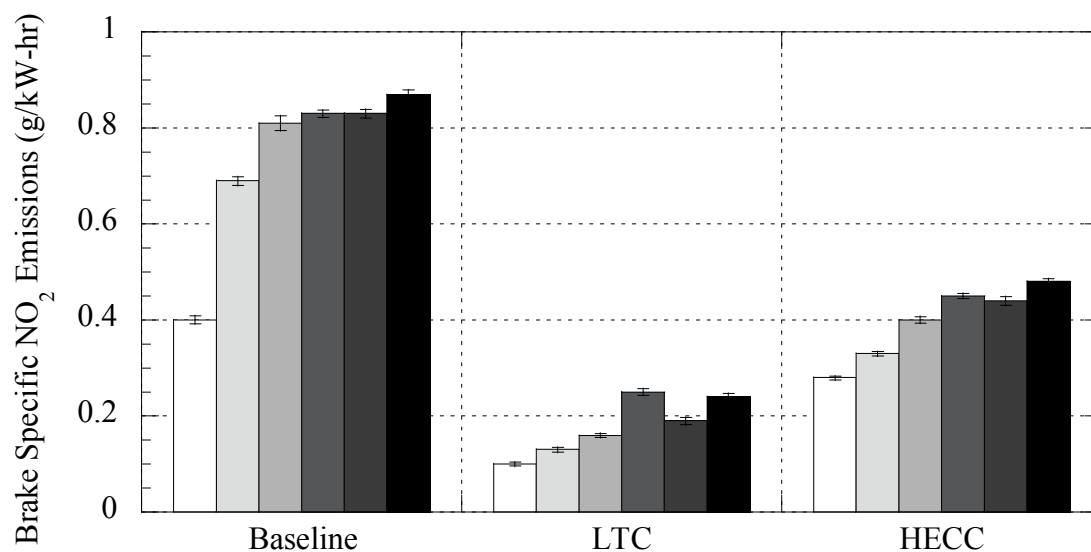


Figure 5.18: Brake specific NO₂ emissions of the three modes tested, with □ 0%, ■ 2.5%, ■ 5%, ■ 7.5%, ■ 10% and ■ 15% hydrogen substitution on an energy basis.

Table 5.11: Percent difference of brake specific NO₂ emissions from the baseline at the four modes tested with 0%, 2.5%, 5%, 7.5%, 10% and 15% hydrogen substitution on an energy basis. Positive values indicate an increase and negative values indicate a decrease from the baseline.

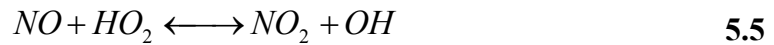
	Baseline	LTC	HECC
0% Diff.	n/a	n/a	n/a
2.5% Diff.	53.3	26.3	14.7
5% Diff.	68.0	43.2	34.8
7.5% Diff.	70.8	85.9	45.3
10% Diff.	70.2	59.5	43.0
15% Diff.	74.8	83.4	52.0

Table 5.12: Percent difference of brake specific NO₂ emissions comparing baseline to LTC and baseline to HECC. Positive values indicate an increase and negative values indicate a decrease from the baseline.

	Baseline to LTC % Diff.	Baseline to HECC % Diff.
0%	-119.2	-33.8
2.5%	-135.9	-70.8
5%	-135.2	-67.1
7.5%	-107.1	-60.1
10%	-126.6	-61.8
15%	-112.4	-57.8

Hydrogen substitution caused an increase of NO₂ emissions in all three modes. The increased NO₂ in both LTC and HECC modes, however, is counterintuitive since NO₂'s main creation path is from NO and there was no NO increase measured in advanced combustion mode. The most likely explanation is that the hydrogen present caused localized increases in flame temperature, which then created thermal NO. The NO emissions were not measured in the exhaust because the presence of HO₂, created by hydrogen (see Eq. 4.3) reacted with the NO to form NO₂, as given in Eq. 4.2. Kinetic and

CFD modeling is necessary to further explain the discrepancies between the NO_2 emissions of the advanced combustion modes, with and without hydrogen substitution.



5.13 Gaseous Emissions: HC

The advanced combustion modes increased the HC emissions compared to the baseline mode. The HC emissions of the LTC mode increased by 33% compared to the baseline mode, while the HECC mode's HC emissions experienced a significant 73% increase. HC emissions are reported to increase in PCCI mode, like the HECC mode, caused by overly lean combustion conditions. Wagner, Sluder and coworkers reported increased HC when the HECC mode operated at low engine speed and a decrease in HC emission under high engine speeds. While the cause for the increase in hydrocarbon was not explored by Wagner, Sluder and coworkers the increase was attributed to the mixing timescale of the low speed engine operation [39].

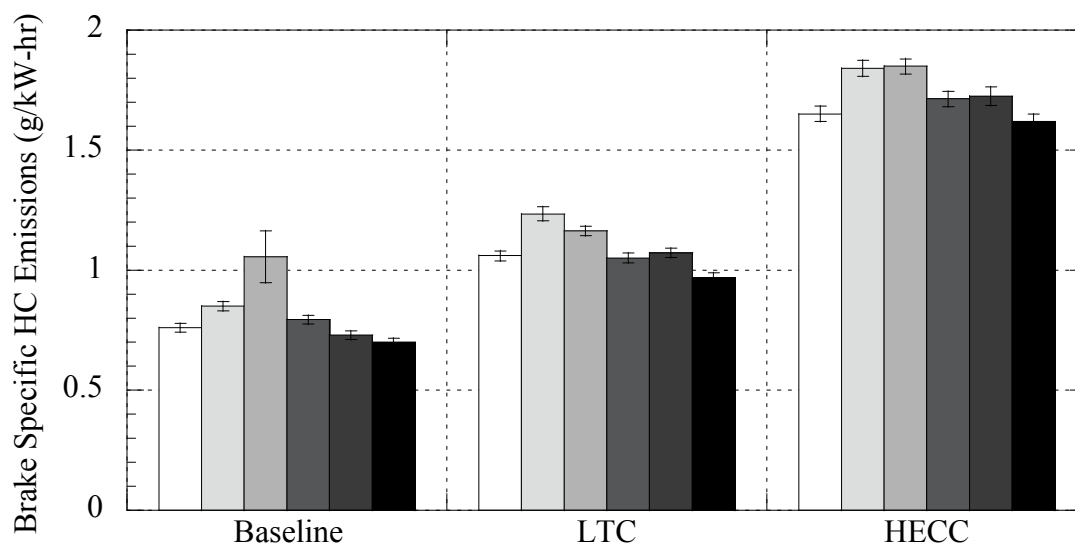


Figure 5.19: Brake specific HC emissions of the three modes tested, with \square 0%, \blacksquare 2.5%, \blacksquare 5%, \blacksquare 7.5%, \blacksquare 10% and \blacksquare 15% hydrogen substitution on an energy basis.

The baseline mode's HC emissions data appears to contain error in sampling at 5% hydrogen substitution data. HC emission equipment is sensitive to cold spots in the sampling line, which can cause the hydrocarbons to condense and thus result in erroneous emissions. Hydrogen substitution, however, caused an increase of HC emissions at 2.5% and 5% of hydrogen substitution for all three of the modes tested. At 7.5% of hydrogen substitution, the HC emissions decreased. Intuitively, an increase of hydrogen fuel and a decrease in hydrocarbon fuel should reduce HC emissions. Nonetheless, low percentages of hydrogen substitution increased the level of incomplete combustion, thus producing unburned hydrocarbon emissions.

Table 5.13: Percent difference of brake specific HC emissions from the baseline at the four modes tested with 0%, 2.5%, 5%, 7.5%, 10% and 15% hydrogen substitution on an energy basis. Positive values indicate an increase and negative values indicate a decrease from the baseline.

	Baseline	LTC	HECC
0% Diff.	n/a	n/a	n/a
2.5% Diff.	11.4	15.2	10.9
5% Diff.	32.6	9.5	11.3
7.5% Diff.	4.4	-0.7	3.7
10% Diff.	-4.0	1.2	4.4
15% Diff.	-8.2	-9.0	-1.9

Table 5.14: Percent difference of brake specific HC emissions comparing baseline to LTC and baseline to HECC. Positive values indicate an increase and negative values indicate a decrease from the baseline.

	Baseline to LTC % Diff.	Baseline to HECC % Diff.
0%	33.0	73.9
2.5%	36.8	73.5
5%	9.9	54.7
7.5%	28.0	73.3
10%	38.0	81.0
15%	32.2	79.3

5.14 Gaseous Emissions: CO

Figure 5.20 shows the HECC mode CO emissions increased by 105% compared to the baseline mode at 0% hydrogen substitution. The LTC mode CO emissions increased by 50% compared to the baseline mode at 0% hydrogen substitution. The dramatic increase in CO emissions, specifically in the HECC mode, can be attributed to incomplete combustion. The HECC mode operates in a locally fuel lean condition. Overly fuel lean combustion will lead to incomplete combustion [16]. High levels of EGR also compound the degree of incomplete combustion [30]. The increased level of

CO emissions in the LTC mode was also caused by incomplete combustion due to the high levels of EGR.

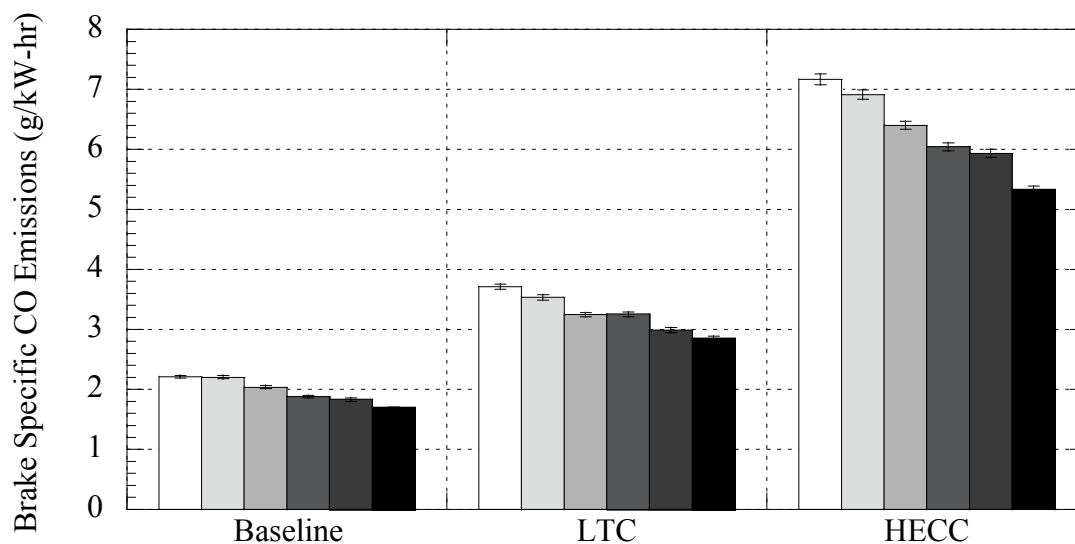


Figure 5.20: Brake specific CO emissions of the three modes tested, with \square 0%, \blacksquare 2.5%, \blacksquare 5%, \blacksquare 7.5%, \blacksquare 10% and \blacksquare 15% hydrogen substitution on an energy basis.

Hydrogen substitution caused a significant decrease in CO emissions in all three modes tested, as can be seen in Tables 5.15 and 5.16. The increased levels of hydrogen may have formed HO_2 radicals, which in turn attacked the CO. The reduction of air due to hydrogen aspiration decreases the amount of localized air-fuel pockets which are overly fuel lean leading to incomplete combustion and CO formation.

Table 5.15: Percent difference of brake specific CO emissions from the baseline at the four modes tested with 0%, 2.5%, 5%, 7.5%, 10% and 15% hydrogen substitution on an energy basis. Positive values indicate an increase and negative values indicate a decrease from the baseline.

	Baseline	LTC	HECC
0% Diff.	n/a	n/a	n/a
2.5% Diff.	-0.3	-4.9	-3.7
5% Diff.	-8.2	-13.4	-11.3
7.5% Diff.	-16.4	-13.0	-17.0
10% Diff.	-18.8	-21.4	-18.8
15% Diff.	-26.0	-25.9	-29.4

Table 5.16: Percent difference of brake specific CO emissions comparing baseline to LTC and baseline to HECC. Positive values indicate an increase and negative values indicate a decrease from the baseline.

	Baseline to LTC % Diff.	Baseline to HECC % Diff.
0%	50.5	105.7
2.5%	46.2	103.2
5%	45.6	103.4
7.5%	53.7	105.3
10%	48.1	105.7
15%	50.6	103.2

5.15 Gaseous Emissions: CO₂

CO₂ emissions increased in the advanced combustion modes over the baseline modes, due to the increased levels of CO₂ added in the form of EGR. The CO₂ emissions of both LTC and HECC modes nearly overlap, as can be seen in Table 5.18. Even though both of the advanced combustion modes utilized ~50% EGR, the overlap is unexpected because the carbon emissions pathways and the modes' fuel efficiencies are different.

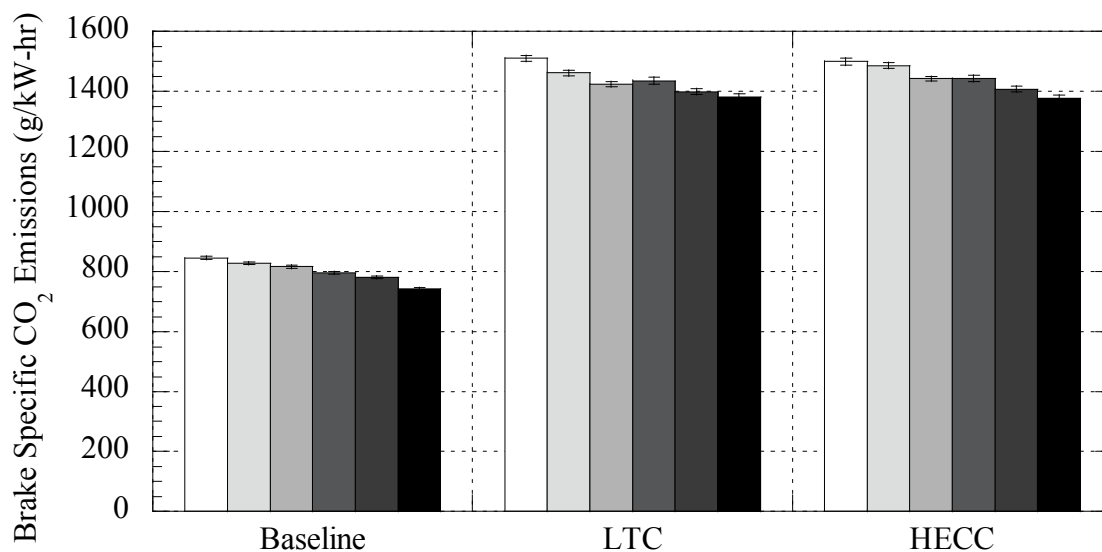


Figure 5.21: Brake specific CO₂ emissions of the three modes tested, with □ 0%, ■ 2.5%, ■ 5%, ■ 7.5%, ■ 10% and ■ 15% hydrogen substitution on an energy basis.

Hydrogen substitution reduces brake specific CO₂ emissions in all three modes.

The substitution of hydrogen fuel for hydrocarbon fuel reduces the availability of carbon to produce CO₂. Table 5.17 shows that CO₂ is reduced more aggressively in the baseline mode as the EGR level was much lower than the advanced combustion modes.

Table 5.17: Percent difference of brake specific CO₂ emissions from the baseline at the four modes tested with 0%, 2.5%, 5%, 7.5%, 10% and 15% hydrogen substitution on an energy basis. Positive values indicate an increase and negative values indicate a decrease from the baseline.

	Baseline	LTC	HECC
0% Diff.	n/a	n/a	n/a
2.5% Diff.	-2.1	-3.3	-0.9
5% Diff.	-3.6	-5.9	-4.0
7.5% Diff.	-6.0	-5.1	-3.9
10% Diff.	-8.0	-7.7	-6.4
15% Diff.	-12.9	-8.8	-8.5

Table 5.18: Percent difference of brake specific CO₂ emissions comparing baseline to LTC and baseline to HECC. Positive values indicate an increase and negative values indicate a decrease from the baseline.

	Baseline to LTC % Diff.	Baseline to HECC % Diff.
0%	56.5	55.9
2.5%	55.4	57.0
5%	54.4	55.5
7.5%	57.3	57.8
10%	56.8	57.4
15%	60.2	59.9

5.16 Particulate Matter Emissions: BG-1

Particulate matter is mainly created in the diffusion flame of the mixing-controlled combustion phase, as is the case with the baseline mode in Figure 5.22. The PM is formed in fuel-rich zones of the flame, where fuel is pyrolyzed. The LTC mode uses the same injection strategy as the baseline combustion mode, thus the LTC mode's combustion is also dominated by the mixing-controlled combustion phase. However, the LTC mode utilizes ~50% EGR, which lowers the combustion temperature by absorbing heat. The reduction in combustion temperature lowers the rate at which the PM is oxidized. Furthermore, the reduction of oxygen with the increase of EGR reduced the oxygen available to oxidize soot formed in the diffusion flame. Thus, the PM in the LTC mode is 46% higher than the baseline mode.

The combustion of the HECC mode is dominated by the pre-mixed combustion phase. The pre-mixed air-fuel charge combusts locally fuel-lean at lower temperatures compared to a diffusion flame. The HECC mode also utilizes ~50% EGR, which

decreases combustion temperatures further. The low combustion temperatures and the low fuel equivalence ratio of the HECC mode shifts the mode outside of the PM formation peninsula of Akihama and coworkers' local equivalence ratio vs. local temperature model [40]. The rate of oxidation is reduced by lowered combustion temperatures, but so little PM is formed that the HECC mode yields lower PM than the baseline or LTC modes.

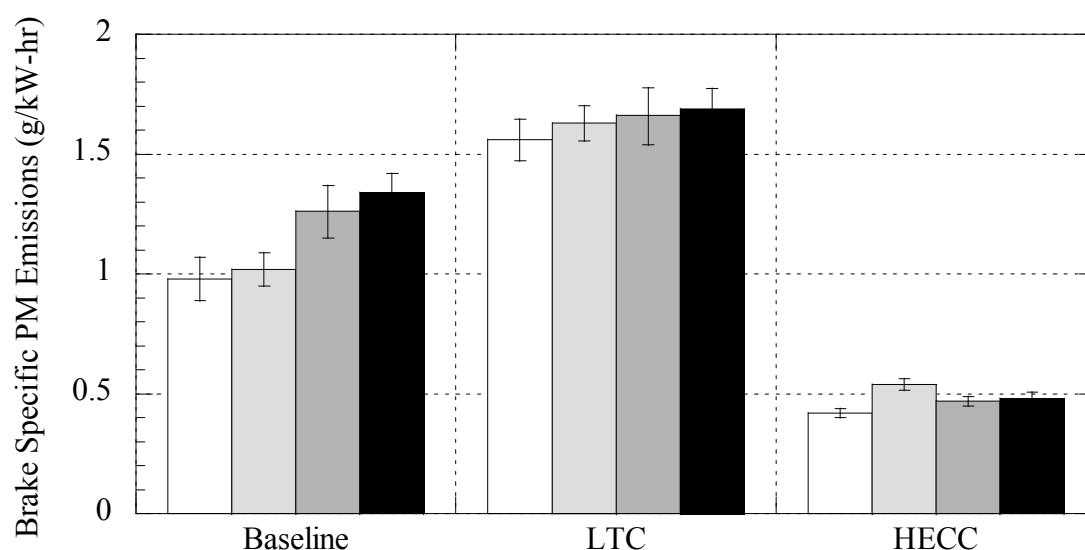


Figure 5.22: Brake specific PM emissions of the three modes tested, with \square 0%, \blacksquare 2.5%, \blacksquare 7.5%, and \blacksquare 15% hydrogen substitution on an energy basis.

Hydrogen caused an increase of PM in the three modes tested. The aspiration of hydrogen reduced the oxygen intake to the engine, thus reducing the oxygen available to oxidize the soot formed in the rich spray flame of the baseline mode and LTC mode. The increase of PM in the HECC mode was less substantial, as seen in Table 5.19. The long ignition delay in the HECC mode allowed the hydrogen more time to mix with the

diesel fuel and air. The premixed charge contained lower concentrations of localized hydrogen, thus reducing the spike in local temperatures.

Table 5.19: Percent difference of brake specific PM emissions from the baseline at the four modes tested with 0%, 2.5%, 5%, 7.5%, 10% and 15% hydrogen substitution on an energy basis. Positive values indicate an increase and negative values indicate a decrease from the baseline.

	Baseline	LTC	HECC
0% Diff.	n/a	n/a	n/a
2.5% Diff.	4.5	3.9	25.5
7.5% Diff.	25.2	5.9	11.6
15% Diff.	31.4	7.8	14.2

Table 5.20: Percent difference of brake specific PM emissions comparing baseline to LTC and baseline to HECC. Positive values indicate an increase from the baseline, while negative values indicate a decrease.

	Baseline to LTC	Baseline to HECC
0% Diff.	46.0	-80.7
2.5% Diff.	45.4	-62.3
7.5% Diff.	27.2	-91.9
15% Diff.	22.8	-94.7

5.17 Particulate Matter Emissions: SMPS

The SMPS was used to further analyze the PM emissions. The SMPS data compares the concentration in number of PM particles by volume to the diameter of the sampled particles. The SMPS data was taken using three different settings: sampling by

bypassing the thermal denuder, sampling through the thermal denuder at 30°C, and sampling through the thermal denuder at 300°C.

The advanced combustion modes at 0% hydrogen substitution were not limited by hydrogen expenditure and were more thoroughly studied using the SMPS. Figure 5.23, Figure 5.24 and Figure 5.25 compare the baseline mode, LTC mode and HECC mode when sample bypassed the thermal denuder and flowed through the thermal denuder at 30°C and at 300°C. The diluted exhaust sample contained PM made up of a solid carbon fraction (soot) and organic fraction.

The organic fraction is composed of unburned hydrocarbons that conglomerated on the soot particles. The LTC mode and the HECC mode had increased levels of unburned hydrocarbons, which could indicate higher levels of organic fraction on the soot. Figure 5.23 shows that when the sample bypasses the thermal denuder, the LTC mode yields a higher concentration of particles than the baseline mode and the HECC mode's concentrations are quite reduced. The mass based PM data provides the same trend.

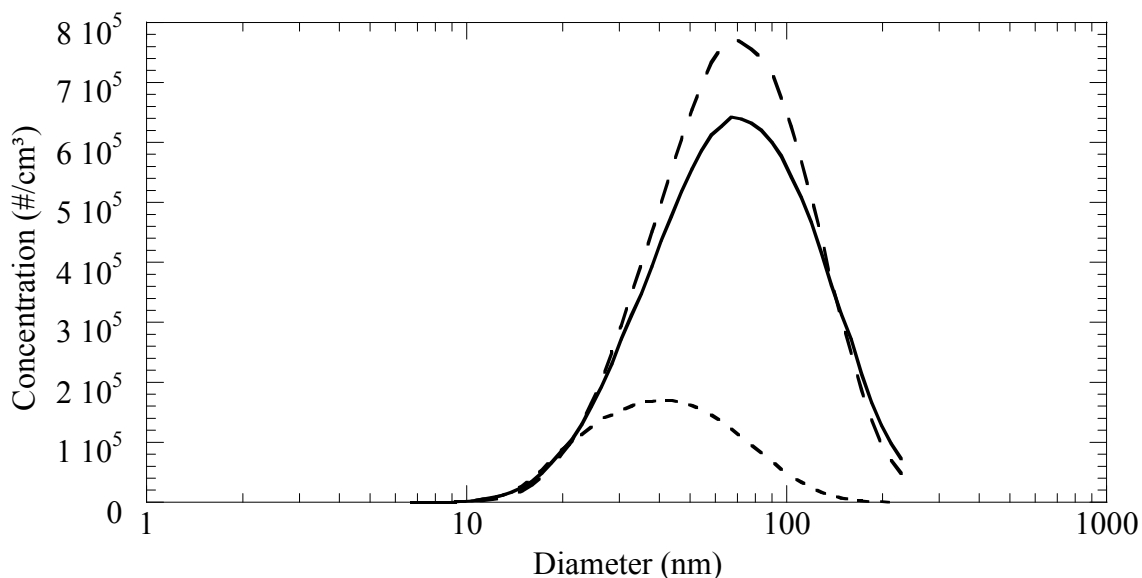


Figure 5.23: SMPS Bypass comparison of the baseline mode, LTC mode and HECC mode with 0% of hydrogen. — baseline, - - LTC and - · - · HECC.

Figure 5.24 shows data for samples flowing through the thermal denuder at 30°C for 0% hydrogen substitution. The concentration of particles is significantly reduced with the sample flowing through the thermal denuder. The baseline mode's concentration unexpectedly increased over the LTC mode when the sample passed through the 30°C thermal denuder, which is set at that temperature to avoid removing the organic fraction. The thermal denuder is, however, a cylinder full of activated carbon which filters and absorbs the organic fraction from the PM. The LTC mode contained a larger organic fraction of PM than that of baseline mode, which accounts for the shift in concentration seen in Figure 5.24.

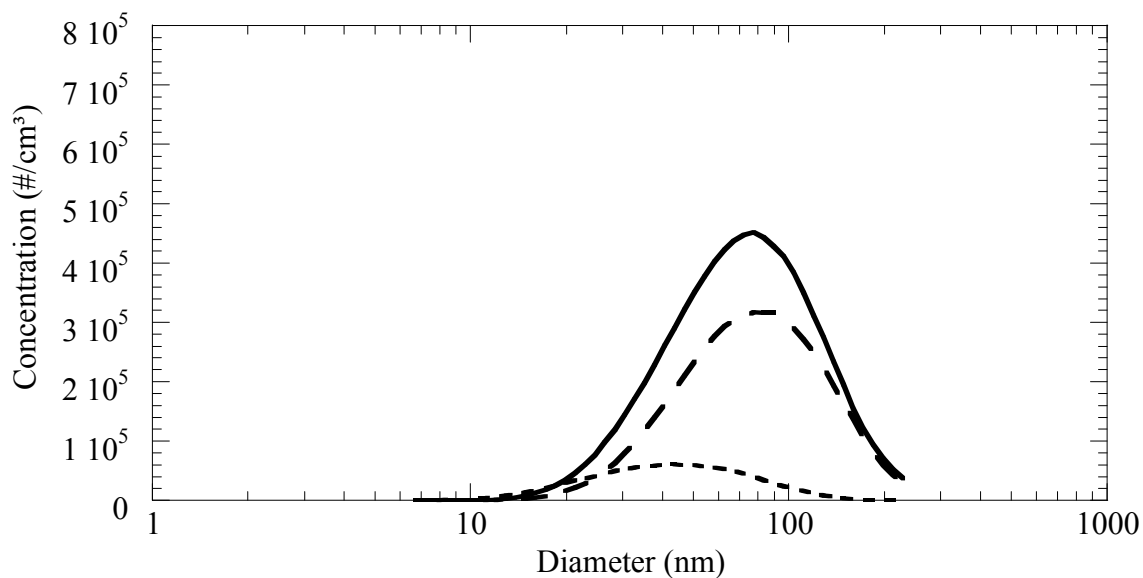


Figure 5.24: SMPS thermal denuder at 30°C of the baseline mode, LTC mode and HECC mode with 0% of hydrogen. — baseline, - - LTC and · · · · HECC.

Figure 5.25 displays the PM concentrations of the three modes tested, with the sample flowing through the thermal denuder at 300°C for 0% hydrogen substitution. The organic fraction of the PM is completely stripped away and only soot remains, due to the thermal denuder being set to 300°C. Note that the concentrations of all three of the modes are dramatically reduced.

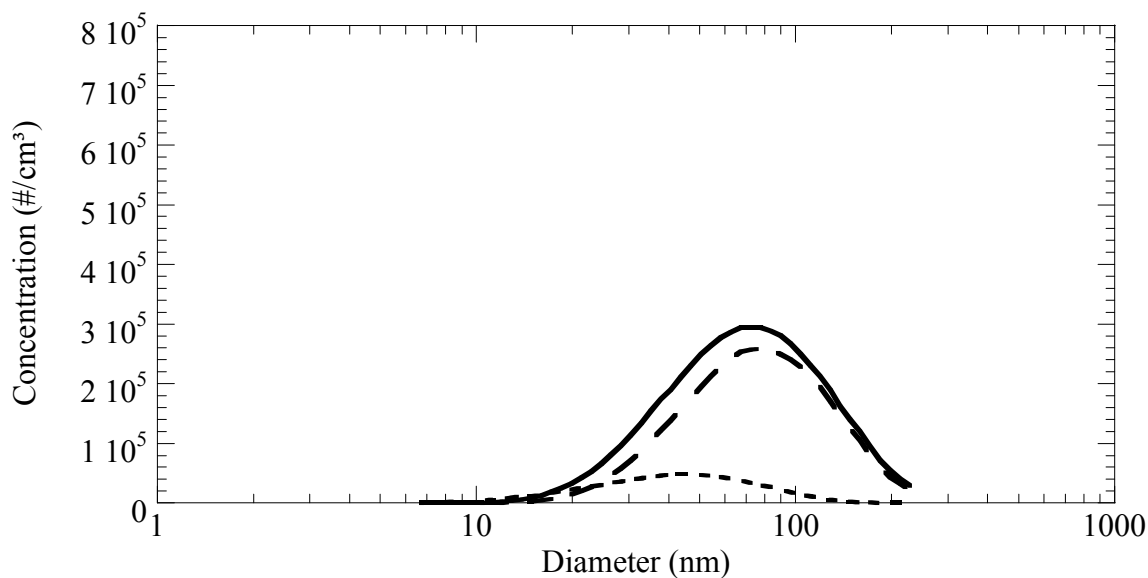


Figure 5.25: SMPS Thermal Denuder at 300°C at 0% hydrogen. — baseline, - - LTC and · · · · HECC.

While the HECC mode was being explored on the DDC 2.5L engine, the SMPS was used to generate expedient PM data. In the exploration process, the injection timing was adjusted to locate where the engine operated at simultaneously low NO_x emissions and low PM emissions while also maintaining fuel economy. In the exploration process, the engine was found to produce large quantities of nano-particles at 2° BTDC.

Figure 5.26 compares the HECC mode used at 4° BTDC to the mode that produced the nano-particles at 2° BTDC. The PM nano-particles are entirely composed of the organic fraction. As can be seen in Figure 5.26, the thermal denuder removes the nano-particles and an ultra-low soot concentration remains. These findings are intended to be explored in future work.

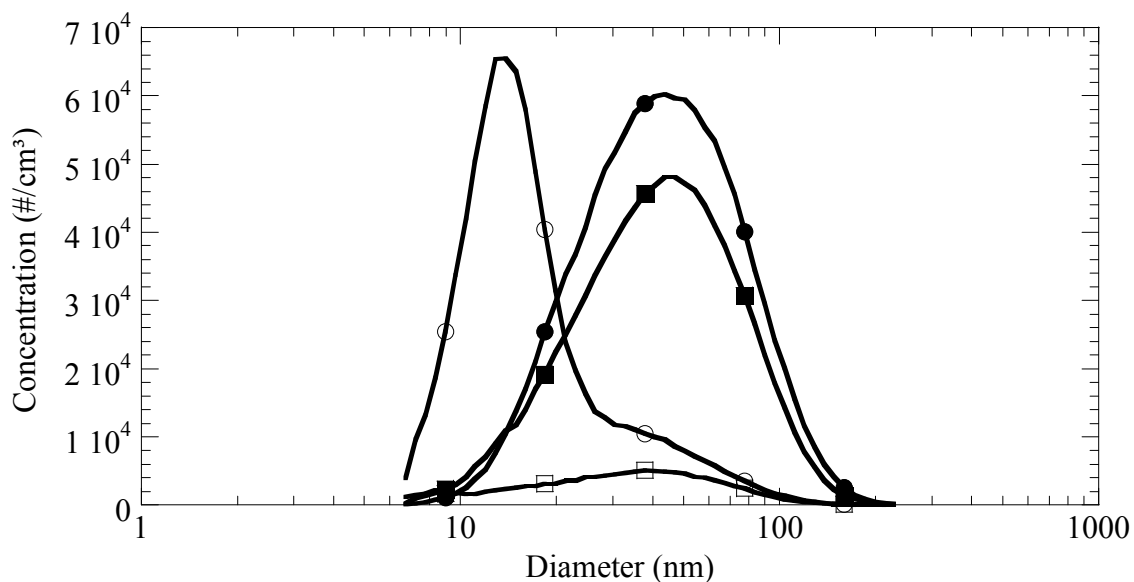


Figure 5.26: HECC mode exploration at 1800 rpm, 4.2 bmep and 50% EGR with rail pressure at 490 bars. —○— TD 30°C at 2 BTDC, —□— TD 300°C at 2 BTDC, —●— TD 30°C at 4 BTDC and —■— TD 300°C at 4 BTDC.

5.18 Brake Specific Fuel Consumption

Brake specific fuel consumption of the LTC mode compared to the baseline mode increased by an 0.2%. The fuel efficiency of the HECC mode, however, increased by 3.6% over the baseline. Brake specific fuel consumption increased in all three of the tested modes with an increase of hydrogen substitution. It should be noted that the aspiration of hydrogen into the air intake displaced air. Diminution in air, the working fluid of the engine, will reduce volumetric efficiency and fuel economy.

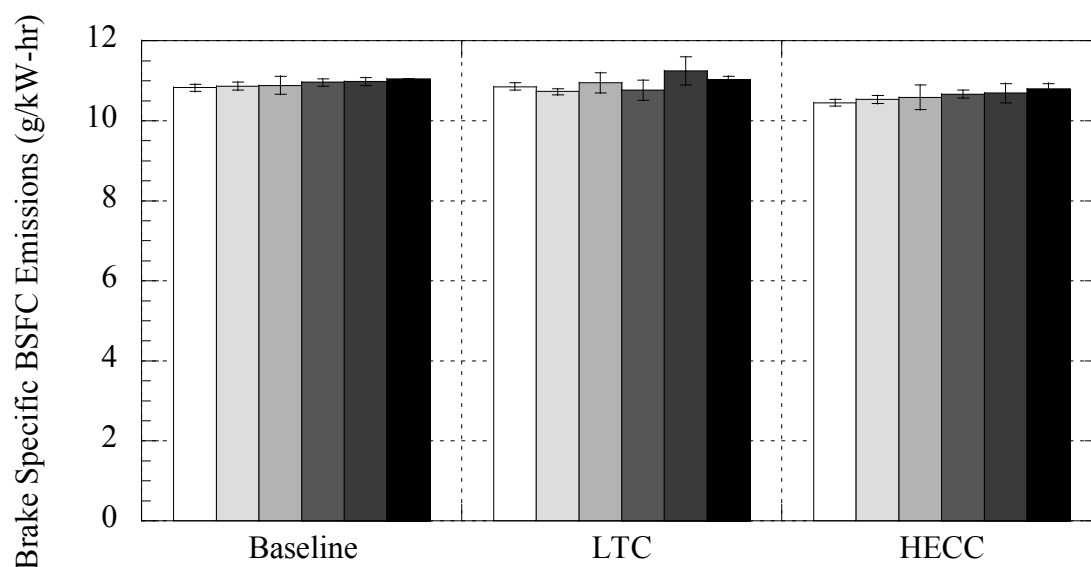


Figure 5.27: Brake specific fuel consumption of the four modes tested, with \square 0%, \blacksquare 2.5%, \blacksquare 5%, \blacksquare 7.5%, \blacksquare 10% and \blacksquare 15% hydrogen substitution on an energy basis.

Table 5.21: Percent difference of brake fuel consumption from the baseline at the four modes tested with 0%, 2.5%, 5%, 7.5%, 10% and 15% hydrogen substitution on an energy basis. Positive values indicate an increase and negative values indicate a decrease from the baseline.

	Baseline	LTC	HECC
0% Diff.	n/a	n/a	n/a
2.5% Diff.	0.3	-1.1	0.8
5% Diff.	0.6	0.8	1.3
7.5% Diff.	1.1	-0.8	2.1
10% Diff.	1.4	3.6	2.4
15% Diff.	2.0	1.6	3.4

Table 5.22: Percent difference of brake specific fuel consumption comparing baseline to LTC and baseline to HECC. Positive values indicate an increase and negative values indicate a decrease from the baseline.

	Baseline to LTC % Diff.	Baseline to HECC % Diff.
0%	0.2	-3.6
2.5%	-1.2	-3.1
5%	0.5	-2.9
7.5%	-1.7	-2.6
10%	2.3	-2.6
15%	-0.2	-2.2

5.19 Summary

The DDC 2.5L engine operated in a PCCI mode referred to here as HECC. The mode was found at 1800 rpm at 25% of maximum output, with a single injection that was set at -4° ATDC, $\sim 50\%$ of combined engine produced EGR and simulated EGR and a common rail pressure of 490 bar. Along with the HECC mode, an intermediate mode (LTC mode) utilized $\sim 50\%$ EGR, with all other operation parameters studied held at default. Compared to the default baseline operation at the given speed and load, the HECC mode reduced brake specific NO_x emissions by 72.1%, reduced brake specific NO emissions by 83.2%, reduced brake specific NO_2 emissions by 33.8%, increased brake specific HC emissions by 73.9%, increased brake specific CO emissions by 105.6%, increased brake specific CO_2 emissions by 55.9%, reduced brake specific PM emissions by 80.7%, and reduced brake specific fuel consumption by 3.6%. These results correspond to those achieved by Wagner, Sluder and coworkers at Oak Ridge Nationals Laboratory, where the HECC mode was developed. Major operational parameters and emissions results of the three modes tested are given in Table 5.23.

Table 5.23: Major operational parameters and emissions result of the three modes tested.

	Baseline	LTC	HECC
EGR Total (%)	11	48	50
Engine produce EGR (%)	11	16	16
Simulated EGR (%)	none	32	34
BSFC (g/kW.hr)	253	253	244
NO _x (g/kW.hr)	1.74	0.68	0.79
PM (g/kW.hr)	0.98	1.57	0.42
THC (g/kW.hr)	0.76	1.06	1.65
Intake Temp (C)	59	70	75
ExhTemp (C)	342	357	336
Main Timing (°BTDC)	-2.9	-2.9	4.0
Pilot Timing (°BTDC)	17.4	17.4	none
Rail Pressure (bar)	450	450	490

On an energy basis, hydrogen was substituted for diesel fuel at 0%, 2.5%, 5%, 7.5%, 10%, and 15% by aspirating the hydrogen into the engine's intake air, after the turbocharger. The effect of hydrogen substitution on the advanced combustion mode, HECC, was similar in results to the study in which hydrogen was substituted for diesel fuel in conventional combustion modes. In general, the effect of hydrogen substitution on the HECC mode was to increase brake specific NO_x emissions from 4.0% to 21.6%, which was a result of the increase in combustion temperature caused by hydrogen. Hydrogen had little effect on the brake specific NO emissions of the HECC mode unlike in the conventional modes where an increase of hydrogen was seen to decrease NO. The brake specific NO₂ emissions increased trend from 14.7% to 52.0%, with an increase of hydrogen. The brake specific HC emissions first increased with 2.5% and 5% then decreased from 7.5% to 15% hydrogen substitution. The brake specific CO emissions decreased trend from 3.7% to 29.4%, with an increase of hydrogen, due to more complete

combustion. The brake specific CO₂ emissions had a decreasing trend from 0.9% to 8.5%, with an increase of hydrogen, due to a decrease of hydrocarbon input to the engine. The brake specific PM emissions had an increasing trend from 25.5% to 14.2%, with an increase of hydrogen, due to the increase in localized combustion temperature. The brake specific fuel consumption had an increasing trend from 0.8 % to 3.4%, with an increase of hydrogen, due to the reduction of intake air.

Hydrogen increased the amount of premixed fuel added to the HECC mode, which was hoped to further enhance this PCCI mode. The reductions on the HECC modes emissions with hydrogen substitution were modest. As legislative emission restrictions on diesel engines increase advanced combustion modes will continue to be studied as a part of a solution. In this study, hydrogen substitution has been demonstrated in an engine running an advanced combustion mode up to 15% hydrogen fuel substitution, without penalty. Further benefits can be projected when hydrogen is utilized in an engine optimized for PCCI combustion.

Chapter 6

Conclusion

6.1 Conclusion

The aim of the studies presented in this Thesis were to examine the benefits of aspirating small quantities of hydrogen gas into the air intake of a diesel engine, while the engine was running in conventional combustion modes and advanced combustion modes. The following conclusions were drawn from the experimental work conducted on the conventional combustion modes.

- Aspirating hydrogen into the air intake of an unmodified diesel engine will result in retarded injection timing, based on the engine's ECU injection timing map, given the reduction of diesel fuel. Significant changes in emissions will occur due to the retarding of injection timing which can be repeated by manually retarding the injection timing without aspirating hydrogen.
- Depending on engine operation parameters, up to 30% of the fuel energy demand of a diesel engine can be from aspirated hydrogen. At 35%, the engine will choke from lack of oxygen.
- Hydrogen substitution for diesel fuel, by aspiration, resulted in a modest increase in brake specific NO_x emissions. However, hydrogen substitution results in a significant decrease of brake specific NO emissions and a significant increase of brake specific

NO₂ emissions. The NO/NO₂ trade off caused directly from hydrogen substitution can be advantageously used in after treatment systems.

- Hydrogen substitution for diesel fuel, by aspiration, resulted in a modest decrease in brake specific CO emissions.
- Hydrogen substitution for diesel fuel, by aspiration, resulted in a modest decrease in brake specific CO₂ emissions.
- Hydrogen substitution for diesel fuel, by aspiration, resulted in a modest decrease in brake specific HC emissions at high load operation and a modest increase at low load operation.
- Hydrogen substitution for diesel fuel, by aspiration, resulted in a decrease in brake specific PM emissions at high speed operation and an increase at low speed operation.
- Hydrogen substitution for diesel fuel, by aspiration, resulted in an increase in brake specific fuel consumption. This increase is inherently due to the reduction of air via hydrogen substitution.

The following conclusions can be drawn from the experimental work conducted on the advanced combustion modes.

- The advanced operation condition known as HECC was achieved on Penn State's Detroit Diesel 2.5L TD DI-4V using simulated EGR. The resulting emissions corresponded to those of Wagner, Sluder and coworkers at Oak Ridge National Laboratory.

- The coefficient of variance of the indicated mean effective pressure was not affected by the substitution of hydrogen, beyond what can be achieved through a repeatability study without using hydrogen.
- The high concentration of EGR used in the advanced combustion modes reduced the brake specific NO emissions, such that hydrogen substitution had no reducing effect.
- Hydrogen substitution for diesel fuel, by aspiration, resulted in an increase in brake specific NO₂ emissions, resulting in an overall increase of NO_x.
- Hydrogen substitution, by aspiration, for the advanced combustions modes caused trends similar to the conventional combustion modes for the brake specific HC, CO, CO₂ and PM emissions at low speed and low load conditions.

6.2 Future Work

The studies reported in this Thesis have generated questions to be answered in future work. The following areas of future work are recommended based on experimental worked conducted conventional combustion modes.

- In this study, the injection timing of diesel fuel was not optimized for the addition of hydrogen through aspiration. The engine was operated with the engine's default injection timing locked. Increased emission benefits may be possible through the optimization of diesel injection timing.

- Aspiration of hydrogen into the air intake of a diesel engine is an inexpensive and simple method to retrofit an engine to combust hydrogen. This study has shown hydrogen substitution, via aspiration, to be limited to 30% hydrogen on an energy basis, before the engine is choked by lack of oxygen. Direct injection of pressurized hydrogen into the engine cylinders would allow for the majority of the fuel energy needed to operate a CI engine to come from hydrogen. A minimal amount of diesel fuel would be required to ignite the hydrogen as a pilot fuel. According to literature, higher percentages of hydrogen substitution yield emissions benefits.

The following recommendations for future work are based on experimental work conducted on the advanced combustion modes.

- Combustion simulation and Computational Fluid Dynamics (CFD) modeling would provide insight into the localized concentrations of hydrogen in the pre-mixing combustion phase of the HECC mode. Furthermore, such modeling would provide accurate indication of local combustion temperatures which would aid in the explanation of the resulting emissions.
- The SMPS indicated the formation of nano-particles formed from the organic fraction of PM. The nano-particles were found while searching for the HECC mode at -2 °ATDC. When the thermal denuder was used to burn off the organic fraction of PM, trace levels of soot remained. This data indicates the possibility of nearly eliminating soot in a further optimized HECC mode.

- Simulated EGR constituted the majority of the EGR concentration needed to operate in the advanced combustion modes. Refinement of the EGR loop and a rebuild of the engine should allow the engine to run in the advanced combustion modes using actual EGR. A comparison between the emissions of the HECC mode entered using simulated EGR and actual EGR would be insightful.

Bibliography

1. Zhang, Y., *EFFECTS OF BIODIESEL ON ENGINE PERFORMANCE AND NOX EMISSIONS IN A COMMON RAIL DIESEL ENGINE*, in *The Department of Energy and Geo-Environmental Engineering*. 2006, The Pennsylvania State University: State College.
2. Bhattacharyya, S., *Optimizing an irreversible Diesel cycle - fine tuning of compression ratio and cut-off ratio*. *Energy Conversion & Management*, 2000. **41**: p. 847-854.
3. Ferguson, C.R. and A.T. Kirkpatrick, *Internal Combustion Engines, Applied Thermosciences*, ed. 2nd. 2000: John Wiley & Sons, Inc. .
4. Khair, M., *Diesel Engine Technology*, in *Society of Automotive Engineers Seminar Series*. 1998, SAE: Warrendale, PA.
5. Heywood, J.B., *Internal Combustion Engine Fundamentals*. 1988, New York: McGraw-Hill Book Company. 930.
6. Turns, S.R., *An introduction to Combustion*. 2nd ed. 2000: McGraw-Hill
7. Dec, J.E., *A Conceptual Model of DI Diesel Combustion Based on Laser-Sheet Imaging*. SAE, 1997. **97-0873**.
8. WESTBROOK, C.K., *CHEMICAL KINETICS OF HYDROCARBON IGNITION IN PRACTICAL COMBUSTION SYSTEMS*. Proceedings of the Combustion Institute., 2000. **28**: p. 1563–1577.
9. Szybist, J.P., *FUEL COMPOSITION IMPACTS ON PROCESSES IN COMPRESSION IGNITION ENGINES*, in *The Department of Energy and Geo-Environmental Engineering*. 2005, The Pennsylvania State University.
10. Fritz, A. and V. Pitchon, *Review: The current state of research on automotive lean NOx catalysis*. *Applied Catalysis B: Environmental* 1997. **13**: p. 1-25.
11. Sydbom, A., et al., *Health effects of diesel exhaust emissions*. *Eur Respir J*, 2001. **17**: p. 733-746.

12. Hess, H.S.I., *THE IMPACT OF OXYGENATED FUELS ON DIESEL COMBUSTION AND EMISSIONS*, in *Department of Energy and Geo-Environmental Engineering*. 2002 The Pennsylvania State University: State College, PA.
13. Tree, D.R. and K.I. Svensson, *Soot processes in compression ignition engines*. *Progress in Energy and Combustion Science*, 2007. **33**: p. 272–309.
14. McGeehan, J.A., et al., *On The Road to 2010 Emissions: Field Test Results and Analysis with DPF-SCR System and Ultra Low Sulfur Diesel Fuel*. SAE, 2005. **2005-01-3716**.
15. Raub, J.A., *Health effects of exposure to ambient carbon monoxide*. *Chemosphere: Global Change Science*, 1999. **1**: p. 331-351.
16. Dec, J.E. and M. Sjöberg, *A Parametric Study of HCCI Combustion – the Sources of Emissions at Low Loads and the Effects of GDI Fuel Injection*. Society of Automotive Engineers, 2003. **2003-01-0752**.
17. Hayes, R.E., *Catalytic solutions for fugitive methane emissions in the oil and gas sector*. *Chemical Engineering Science*, 2004. **59**: p. 4073-4080.
18. Patterson, D.J. and N.A. Henein, *Emissions From Combustion Engines and Their Controls*. 1972, Ann Arbor, Michigan: Ann Arbor science publishers inc.
19. WINTER, C.-J., H. KLAIB, and J. NITSCH, *HYDROGEN AS AN ENERGY CARRIER: WHAT IS KNOWN? WHAT DO WE NEED TO LEARN?* *Int. J. Hydrogen Energy*, 1990. **15**(2): p. 79-91.
20. Wang, Y.-N. and A.E. Rodrigues, *Hydrogen production from steam methane reforming coupled with in situ CO₂ capture: Conceptual parametric study*. *Fuel*, 2005. **84**: p. 1778–1789.
21. Chui, F., A. Elkamel, and M. Fowler, *An Integrated Decision Support Framework for the Assessment and Analysis of Hydrogen Production Pathways*. *Energy & Fuels*, 2006. **20**: p. 346-352.
22. Lambe, S.M. and H.C. Watson, *Optimizing the design of a hydrogen engine with pilot diesel fuel ignition*. *International Journal of Vehicle Design*, 1993. **14**(4): p. 370-389.
23. Varde, K.S. and L.K. Varde. *Reduction of soot in diesel combustion with hydrogen and different H/C gaseous fuels*. in *5th World Hydrogen Energy*. 1984. Toronto, Canada.

24. Tomita, E., et al., *Hydrogen Combustion and Exhaust Emissions Ignited with Diesel Oil in a Dual Fuel Engine*. Society of Automotive Engineers, 2001. **No: 2001-01-3503**.
25. Kumar, M.S., A. Ramesh, and B. Nagalingam, *Use of hydrogen to enhance the performance of a vegetable oil fuelled compression ignition engine*. International Journal of Hydrogen Energy, 2003(28): p. 1143-1154.
26. Lu, P.-H., X.-b. Xie, and M.-C. Lai, *Spectral Analysis and Chemiluminescence Imaging of Hydrogen Addition to HSDI Diesel Combustion Under Conventional and Low-Temperature Conditions*. SAE, 2004. **2004-01-2919**.
27. Kimura, S., et al., *Ultra-Clean Combustion Technology Combining a Low-Temperature and Premixed Combustion Concept for Meeting Future Emission Standards*. Society of Automotive Engineers, 2001. **2001-01-0200**.
28. Zheng, M., G.T. Reader, and J.G. Hawley, *Diesel engine exhaust gas recirculation- a review on advanced and novel concepts*. Energy Conversion and Management, 2004. **45**: p. 883-900.
29. Lapuerta, M., J. Hernandez, and F. Gimenez, *Evaluation of exhaust gas recirculation as a technique for reducing diesel engine NOx emissions*. Proc Instn Mech Engrs, 2000. **214 Part D**.
30. Jacobs, T., D. Assanis, and Z. Filipi, *The Impact of Exhaust Gas Recirculation on Performance and Emissions of a Heavy-Duty Diesel Engine*. SAE, 2003. **2003-01-1068**.
31. Zheng, M. and G. Reader, *Preliminary investigation of cycle to cycle variation in a nonair-breathing Diesel engine*. J Energy Resour Technol, 1995. **117**: p. 24-8.
32. Edwards, K.D., et al., *A Hybrid 2-Zone/WAVE Engine Combustion Model for Simulating Combustion Instabilities During Dilute Operation*. SAE, 2005. **2005-01-3801**
33. Yao, M., et al., *Experimental Study on Homogeneous Charge Compression Ignition Combustion with Primary Reference Fuel*. Combust. Sci. and Tech., 2007. **2539–2559**: p. 2539–2559.
34. Szybist, J.P. and B.G. Bunting, *Cetane Number and Engine Speed Effects on Diesel HCCI Performance and Emissions* SAE, 2005(2005-01-3723).
35. Epping, K., et al., *The Potential of HCCI Combustion for High Efficiency and Low Emissions*. Society of Automotive Engineers, 2002. **2002-01-1923**.

36. Neely, G.D., et al., *New Diesel Emission Control Strategy to Meet US Tier 2 Emissions Regulations* SAE, 2005. **2005-01-1091**
37. Kanda, T., et al., *PCCI Operation with Early Injection of Conventional Diesel Fuel*. SAE, 2005. **2005-01-0378**.
38. Araki, M., et al., *Effects of Compression Ratio on Characteristics of PCCI Diesel Combustion with a Hollow Cone Spray* SAE, 2005. **2005-01-2130**
39. Sluder, C.S. and R.M. Wagner, *An Estimate of Diesel High-Efficiency Clean Combustion Impacts on FTP-75 Aftertreatment Requirements*. SAE, 2006. **2006-01-3311**.
40. Akihama, K., Y. Takatori, and K. Inaga, *Mechanism of the Smokeless Rich Diesel Combustion by Reducing Temperature*. Society of Automotive Engineers, 2001. **2001-01-0655**.
41. Sasaki, S., T. Ito, and S. Iguchi. *Smoke-less Rich Combustion by Low Temperature Oxidation in Diesel Engines*. in *Aachen Colloquium Automobile and Engine Technology 2000*. 2000.
42. Singh, J., et al., *An Investigation of The Low Temperature Combustion Regime (LTC) in a Small Bore HSDI Diesel Engine*. ASME, 2005. **ICES2005-1033**: p. 217-224.
43. Aceves, S.M. and D.L. Flowers, *A Detailed Chemical Kinetic Analysis of Low Temperature Non-Sooting Diesel Combustion*, in *UCRL-CONF-206985*. 2004.
44. Sluder, C.S., et al., *Low Temperature Urea Decomposition and SCR Performance*. Society of Automotive Engineers, 2005. **2005-01-1858**.
45. Sluder, C.S., et al., *A Thermal Conductivity Approach for Measuring Hydrogen in Engine Exhaust*. Society of Automotive Engineers, 2004. **2004-01-2908**.
46. Sluder, C.S., et al., *Implications of Particulate and Precursor Compounds Formed During High-Efficiency Clean Combustion in a Diesel Engine*. Society of Automotive Engineers, 2005. **2005-01-3844**.
47. Wagner, R.M., et al., *Simultaneous Low Engine-Out NO_x and Particulate Matter with Highly Diluted Diesel Combustion*. Society of Automotive Engineers, 2003. **2003-01-0262**.
48. Wagner, R.M., et al., *Extending Exhaust Gas Recirculation Limits in Diesel Engines*, Oak Ridge National Laboratory: Oak Ridge.

49. Wagner, R.M., et al. *Combustion Mode Switching for Improved Emissions and Efficiency in Diesel Engine*. in *Proceeding of the 4th Joint Technical Meeting of the U.S. Sections of the Combustion Institute*. 2005. Philadelphia, Pa.
50. AVL, *AVL Concerto SoftVersion 3.9 Software Guide*. 2006.
51. Kuo, K.K.-y., *Principles of Combustion*. 2 edition ed. 2005: Wiley-Interscience.
52. Glanssman, I., *Combustion*. 3rd ed. 1996, San Diego: Academic Press. 631.
53. Setiabudi, A., M. Makkee, and J.A. Moulijn, *The role of NO₂ and O₂ in the accelerated combustion of soot in diesel exhaust gases*. *Applied Catalysis B: Environmental* 50, 2004: p. 185–194.
54. Walker, A.P., et al., *Controlling particulate emissions from diesel vehicles*. *Topics in Catalysi*, 2004. **28**.
55. Upatnieks, A., C.J. Mueller, and G.C. Martin, *The Influence of Charge-Gas Dilution and Temperature on DI Diesel Combustion Processes Using a Short-Ignition-Delay, Oxygenated Fuel* SAE, 2005. **2005-01-2088**.
56. Boehman, A.L., *CATALYTIC OXIDATION OF CARBON MONOXIDE IN A LARGE SCALE PLANAR ISOTHERMAL PASSAGE*, in *The Department of Mechanical engineering*. 1992, Stanford University.

Appendix A

Brake Specific Calculations

A.1 Brake Specific Calculations

In subsequent equations the method used to convert from part-per-million (ppm) emissions into brake specific emissions for the cases of CO is given. The NO_x, NO, CO₂, NO₂, HC and PM emissions were converted to brake specific units using an identical method.

$$\text{CO} \frac{\text{g}}{\text{kW}\cdot\text{h}} = \frac{\text{CO} \frac{\text{g}}{\text{hr}}}{(\text{load}\cdot\text{kW})} \quad \text{A.1}$$

Where:

$$\text{CO} \frac{\text{g}}{\text{hr}} = \left(\text{CO}_{\text{density}} \frac{\text{kg}}{\text{m}^3} \right) \left(\text{Exhaust_flow}_{\text{volumetric}} \frac{\text{L}}{\text{hr}} \right) \quad \text{A.2}$$

$$\left(\text{CO}_{\text{density}} \frac{\text{kg}}{\text{m}^3} \right) = \frac{(\text{CO}\text{-ppm})}{1000000} \cdot \frac{(101325\text{Pa})}{\left(\frac{8314 \frac{\text{Pa}\cdot\text{m}^3}{\text{mol}\cdot\text{K}}}{\text{CO}_{\text{MW}}} \right) \cdot [(273\text{K}) + \text{Exhaust}_{\text{temp}}\cdot\text{C}]} \quad \text{A.3}$$

$$\left(\text{Exhaust_flow}_{\text{volumetric}} \frac{\text{L}}{\text{hr}} \right) = \frac{\left[\left(\text{Air}_M \frac{\text{g}}{\text{hr}} \right) + \left(\text{Fuel}_M \frac{\text{g}}{\text{hr}} \right) \right]}{\text{ExhaustDensity} \frac{\text{kg}}{\text{m}^3}} \quad \text{A.4}$$

$$\left(\text{ExhaustDensity} \frac{\text{kg}}{\text{m}^3} \right) = \frac{[300^\circ\text{C} \cdot (\text{ExhaustDensity_at_300C})]}{(\text{Exhaust_temp} \cdot \text{C} + 273\text{-K})} \quad \mathbf{A.5}$$

$$\text{ExhaustDensity_at_300C} = 1.2 \frac{\text{kg}}{\text{m}^3} \quad \mathbf{A.6}$$

Appendix B

Error Analysis

B.1 Error Analysis

The error analysis method used in this Thesis was based on the error analysis method used by Hess[12]. Error is characterized in four main classes, instrument measurement errors, systematic errors, personal errors and random errors. Instrument measurement errors, also referred to as zeroth order uncertainty, are associated with the uncertainty that arises from the precision of measurement equipment. Systematic errors, also referred to as first order uncertainty, are associated with the uncertainty that arises from the accuracy of measurement equipment. Personal error is due to the judgment of an observer while recording the data. Random error is the error that remains after the instrument measurement errors, systematic errors, and personal errors are accounted for. The overall combination of all error is characterized as the N^{th} order uncertainty which can be quantified as the root-sum-square of the fore mentioned uncertainties [12, 56].

The value of error can be reported as absolute error, relative error or percentage error. The absolute error is the value given by the difference between the measured results and the actual results. The relative error is calculated by dividing the absolute error by the mean of the measured value. The percentage error is defined by multiplying the relative error by 100%.

Data acquisition was conducted under steady-state, with instrumentation measuring speed, load, temperatures, pressures, mass air flow, fuel mass, and emissions from the AVL bench, over a 15 minute sampling period, with a data point taken every 10 seconds. Though the engine operated at steady state, the AVL emission bench was placed in a standby mode until data sampling was enabled. The individual analyzers which comprise the bench often required an unpredictable period of time to stabilize. Thus, selections of 25 sequential data points were selected, those points having the lowest standard deviation of the recorded data. The points were then analyzed using the Student t-test to calculate the error between the 25 data points sampled at steady-state, as given in Eq. **B.1**. The Student t-test multiple used was 1.96, due to the 25 samples taken, based on a 95% confidence interval.

$$\text{Percentage Error}_{\text{Student}} = \frac{t_{\alpha/2, v} \cdot \sigma}{\sqrt{n} \cdot \bar{\chi}} \cdot 100\% \quad \text{B.1}$$

Where:

$t_{\alpha/2, v}$, Student t-test multiplier (1.96)

n, number of data pints (25)

$\bar{\chi}$, Mean

σ , Standard deviation

The gaseous and PM emissions were the data of most concern in this Thesis. All other data have been taken used to better explain the resulting gaseous and PM emissions results. Thus, the gaseous and PM emissions data points were rigorously analyzed and

presented with error bars. The instrumental and systematic errors which affected gaseous and PM emissions measurements are presented in Table **B.1**, Table **B.2** and Table **B.3**.

Table **B.1**: Major sources of instruments error which affect gaseous emission results in percent error.

Abbreviation	Equipment	Percent error [%]
HC%_Inst	HC analyzer error of linearization	1.570
NO _x %_Inst	NO _x analyzer error of linearization	0.308
NO%_Inst	NO analyzer error of linearization	0.308
NO ₂ %_Inst	NO ₂ analyzer error of linearization	0.308
CO%_Inst	CO analyzer error of linearization	0.909
CO ₂ %_Inst	CO ₂ analyzer error of linearization	0.714
FCE%_Inst	Fuel scale	0.136
RME%_Inst	Engine rotational speed measurement	0.111

Table **B.2**: Major sources of instruments errors which affect PM emission results in percent error.

Abbreviation	Equipment	Percent error [%]
BME%_Inst	BG-1 measurement	3.441
PSE%_Inst	PM scale	0.001
FCE%_Inst	Fuel scale	0.136
RME%_Inst	Engine rotational speed measurement	0.111

Table **B.3**: Major sources of systematic error which affect gaseous and PM emission results in percent error.

Abbreviation	Measurements	Percent error [%]
ERSM%_sys	Engine rotational speed measurement	0.032
ELM%_sys	Engine load measurement	0.227
MAFM%_sys	Mass air flow measurement	0.739
FM%_sys	Fuel measurement	0.812

Hess explains that the proper method for combining instrument and systematic errors for brake specific calculations in which multiplication occurs is to root-sum-square (RSS) the error in the percent error form. By doing so only large values of error are necessary to consider, since the RSS calculation will not be affected by errors which are 5 times smaller [12]. An example of the RSS calculation for gaseous NO_x is given in Eq. **B.2**.

$$RSS_{Percent} = (\%Error_{student}^2 + NO_x_Inst^2 + FCE\%_Intr^2 + RME\%_Inst^2 + ERSM\%_sys^2 + ELM\%_sys^2 + MAFA\%_sys^2 + FM\%_sys^2)^2 \quad \mathbf{B.2}$$

The resulting percent error value was then divided by 100% to be converted back to a relative error value, as in Eq. **B.3**

$$Error_{Relative} = RSS_{Percent} / 100\% \quad \mathbf{B.3}$$

The error bars were then finally calculated by converting the relative error into absolute error by multiplying by the mean value of the given brake specific value, as in Eq. **B.4**.

$$ErrorBar = \bar{\chi} \cdot Error_{Relative} \quad \mathbf{B.4}$$

Appendix C

Repeatability Study

C.1 Repeatability Study

To confirm the integrity and reliability of the data presented in the thesis, a repeatability study was performed. The repeatability study consisted of three separate operations of the DDC 2.5L engine at 1800 rpm at 25% of maximum output with out hydrogen aspiration. Exhaust, intake air and oil temperatures noted in the data to confirm the consistency of engine operation condition. The indicators of the repeatability study are the gaseous emissions data in brake specific units, which are presented in Table C.1.

Table C.1: Repeatability study of the DDC 2.5L engine operating at 1800 rpm and 25% of maximum output on three different trials presented by standard deviation.

Trial	Speed (rpm)	Power (Kw)	Exhaust (°C)	Intake Air (°C)	Oil (°C)	HC (g/kW.h)	NO _x (g/kW.h)	NO (g/kW.h)	NO ₂ (g/kW.h)	CO (g/kW.h)	CO ₂ (g/kW.h)	
7/2/2007	12pm	1798.09	15.66	332.52	22.40	93.07	-	1.93	1.51	0.42	2.16	844.97
8/14/2007	8am	1805.27	15.67	339.47	21.48	91.47	0.83	1.93	1.50	0.42	2.28	838.26
8/14/2007	5pm	1805.14	15.66	342.30	21.89	91.70	0.76	1.88	1.48	0.40	2.21	845.21
Standard Deviation	4.11	0.01	5.04	0.46	0.87	0.05	0.03	0.01	0.01	0.06	3.94	

The repeatability study confirms the repeatability of the data in this thesis by comparing the standard deviation of the three trials to the standard deviation of the engine operating at 1800 rpm and 25% of maximum output with 0% and 15% hydrogen substitution on an energy basis, given in Table C.2.

Table C.2: Comparison of the DDC 2.5L engine at 1800 rpm and 25% of maximum output with 0% and 15% hydrogen substitution on an energy basis by standard deviation.

Hydrogen	Speed (rpm)	Power (Kw)	Exhaust (°C)	Intake Air (°C)	Oil (°C)	HC (g/kW.h)	NO _x (g/kW.h)	NO (g/kW.h)	NO ₂ (g/kW.h)	CO (g/kW.h)	CO ₂ (g/kW.h)
0%	1805.14	15.66	342.30	21.89	91.70	0.76	1.88	1.48	0.40	2.21	845.21
15%	1,806.14	15.69	352.21	21.49	91.67	0.70	1.91	1.04	0.87	1.70	742.79
STD	0.70	0.02	7.01	0.29	0.02	0.04	0.02	0.31	0.34	0.36	72.42

The 15% increase of hydrogen substitution seen in Table C.2 indicates an increase in the standard deviation compared to the standard deviation of the repeatability study, in all emission except for HC. The difficulties in recording HC emissions were discussed in the results sections of this thesis. The repeatability study shown here added confidence to the data presented in this thesis, even though hydrogen substitution resulted in modest changes in emission data.

Appendix A-2.1.B: PhD Thesis in Fuel Science by Elana Chapman

January 13, 2009

National Energy Technology Laboratory
U.S. Department of Energy
626 Cochrans Mill Road
P.O. Box 10940
Pittsburgh, PA 15236-0940

Dear U.S. Department of Energy:

I hereby grant the U.S. Department of Energy permission to use my thesis in the Final Technical Report for Award Number DE-FC26-04NT42233, "Hydrogen-Assisted IC Engine Combustion as a Route to Hydrogen Implementation." My thesis was written with support of the U.S. Department of Energy under this award and copyright for the thesis lies with me.

Sincerely,



1/13/2009

Elana Chapman
Project Engineer- GM Powertrain (current employment)
Previous Graduate Research Assistant at Penn State University

The Pennsylvania State University
The Graduate School
Department of Energy and Mineral Engineering

**NO_x REDUCTION STRATEGIES FOR
COMPRESSION IGNITION ENGINES**

A Dissertation in
Fuel Science

by

Elana M. Chapman

Submitted in Partial Fulfillment
of the Requirements
for the Degree of

Doctor of Philosophy

May 2008

The dissertation of Elana M. Chapman was reviewed and approved* by the following:

André L. Boehman
Professor of Fuel Science and Materials Science and Engineering
Dissertation Advisor
Chair of Committee

Alan W. Scaroni
Professor of Fuel Science
Associate Dean for Graduate Education and Research, College of Earth
and Mineral Sciences

Angela D. Lueking
Assistant Professor of Energy and Geo-Environmental Engineering

Thomas A. Litzinger
Professor of Mechanical Engineering

Daniel C. Haworth
Professor of Mechanical Engineering

Yaw D. Yeboah
Professor of Energy and Mineral Engineering
Head, Department of Energy and Mineral Engineering

*Signatures are on file in the Graduate School

ABSTRACT

The scope of this investigation is to explore strategies to reduce NO_x emissions from compression ignition engines. Two methods are presented in this collection of studies: 1) NO_x reduction accomplished through a change in fuel formulation, specifically through a change in the saturated fuel carbon chains of biodiesel; and 2) NO_x reduction accomplished through a mixed mode combustion process utilizing a fumigated fuel and a pilot injection of diesel fuel.

In the first study, a light duty diesel engine was used to investigate the change in saturation of a biodiesel fuel and its impact on NO_x emissions. Previous studies have shown that a reduction in the iodine value of a biodiesel fuel produces a reduction in NO_x emissions. The iodine value of the fuel is reduced through the saturation of the C18 molecules via hydrogenation of biodiesel fuel. Experiments were performed at several speeds and loads without exhaust gas recirculation (EGR), and a NO_x reduction with the hydrogenated diesel fuel was observed. For all the modes studied, the NO_x emission was higher for the biodiesel and lower for the hydrogenated biodiesel in comparison to the ultra low sulfur diesel (ULSD) fuel. Results from the calculation of the adiabatic flame temperature shows that the results could be explained by the difference in adiabatic flame temperature of the fuel, thus influencing the prompt NO_x contribution in addition to the thermal contribution. Since the adiabatic flame temperatures are similar for the hydrogenated biodiesel and the ULSD, yet the NO_x reduction with the hydrogenated biodiesel is much lower than the ULSD levels, another explanation for the reduction is suggested: the additional prompt NO_x contribution from the change in fuel chemistry.

The second study investigated the NO_x reductions which could be achieved with a mixed mode combustion process utilizing a fumigated fuel and a pilot injection of diesel fuel. In this research, the fumigated fuel was dimethyl ether (DME) and DME/Methane blends, while the pilot injection fuel was ULSD. Several sets of experiments were performed to study the ignition of the fumigated fuel, and its impact on the NO_x emissions. In the first set of experiments, the DME concentration was spanned over a range of 15 to 44% energy equivalent of the total fuel requirement. An approximately 20% reduction in NO_x emissions was observed up to 35% DME energy equivalent. As the energy equivalent increased above 35%, the NO_x emissions began to increase with the increase in the peak of the high temperature heat release (HTHR). While the NO_x emissions decreased, there was also a significant shift in the NO to NO₂ conversion for all DME fumigation test conditions in comparison to the baseline diesel cases. For 25% DME energy equivalent, the injection timing of the pilot diesel was retarded and a reduction in the NO_x emissions was observed. The low temperature heat release (LTHR) and the HTHR remained constant in magnitude and timing while the injection timing of the pilot diesel was retarded. The peak pressure for the premixed and diffusion portions merged, with increasing premixed DME combustion. With retarded injection timing, NO_x reduction occurred as a result of the decrease in the bulk cylinder temperature and in the combustion duration before cylinder quenching from the exhaust stroke. In the second set of experiments, the intake air temperature was increased to study the impact on NO_x and the mixed mode combustion process. While the amount of DME residual in the exhaust decreased along with the total hydrocarbon and CO emissions, the NO_x emissions increased with increasing bulk cylinder temperature. For

the speed and load used in this experiment, there was enough fuel and compression to combust most of the fuel, yet not enough to complete the combustion of the unburned hydrocarbons and CO. While air heating shifted the stoichiometry of the fuel and air mixture by reducing the density of air, the heating led to increased NO_x with reduction in the NO to NO₂ conversion. This may indicate that the system was above the low temperature range for this conversion to occur. In the third set of experiments, a small amount of Methane was introduced into the system to study the impact on the cetane number of the fumigated fuel. On a brake specific power basis, the Methane addition reduced the NO_x emissions more than with only DME, however the NO to NO₂ conversion was lower. NO_x emissions were further reduced by retarding the injection timing, but increased with increasing intake air temperature. Through the use of the intake air heating, it was observed that the ignition of the DME/Methane blend was advanced with a smaller LTHR and a higher HTHR. While NO_x emissions increased with the increase in bulk cylinder temperature, only the NO emissions increased while NO₂ remained constant. Gaseous emissions analysis showed that the heating caused greater conversion of the Methane and DME during combustion.

TABLE OF CONTENTS

LIST OF FIGURES	x
LIST OF TABLES	xxii
ACKNOWLEDGMENTS	xxiv
Chapter 1 Introduction	1
Chapter 2 Literature Review	4
2.1 Motivation	4
2.2 Compression Ignition Engines and the Autoignition Process	7
2.2.1 Low Temperature Heat Release	10
2.3 Diesel Emissions	15
2.3.1 Diesel Combustion Conceptual Model	15
2.3.2 NO _x Emissions	17
2.3.3 Particulate Matter Emissions	22
2.4 Emissions Reduction Strategies	23
2.4.1 Pre-Combustion Strategies for Emissions Reduction	25
2.4.1.1 Dimethyl Ether	26
2.4.1.2 Biodiesel	31
2.4.1.3 Iodine Value of Biodiesel Fuels	34
2.4.1.4 Theories about Biodiesel and NO _x	35
2.4.2 In-Cylinder Combustion	40
2.4.2.1 Homogeneous Charge Compression Ignition (HCCI)	42
2.4.2.2 Variables involved in HCCI process	43
2.4.2.3 Types of Fuel Mixture Preparation for Compression Ignition Combustion	45
2.4.2.4 HCCI engine and Dual Mode Processes	46
2.4.2.5 Mixed Mode Combustion	46
2.4.2.6 Ignition Delay	48
2.4.3 Post Combustion	49
2.4.3.1 NO _x Aftertreatment Devices	49
2.4.3.2 Particulate Matter Aftertreatment Devices	51
Chapter 3 Experimental Setup	53
3.1 Introduction	53
3.2 Engine Description	53
3.3 Engine Test Stand Data Acquisition	55
3.4 Diesel Fuel Flow Rate	56
3.5 Engine Control Unit	56
3.6 Exhaust Gas Recirculation	57

3.7 Gaseous Emissions Equipment Description	57
3.7.1 Gaseous Emissions: AVL Combustion Emissions Bench II (CEB II).....	57
3.7.2 Gas Chromatography (GC).....	58
3.7.3 Fourier Transform Infrared (FTIR) Spectroscopy.....	60
3.8 Particulate Matter Emissions Equipment Description	61
3.8.1 Particulate Emissions: Gravimetric Filters	61
3.8.2 Particulate Emissions: Tapered Element Oscillating Microbalance (TEOM).....	63
3.8.3 Particulate Matter Emissions: Scanning Mobility Particle Sizer (SMPS)	64
3.9 Fuel Injection Needle Lift and Cylinder Pressure Data Collection and Analysis: AVL IndiCom.....	66
3.10 Description of Experimental Tests	68
3.11 Repeatability Study of Engine	69
 Chapter 4 NO _x Reduction through Fuel Modification: Hydrogenated Biodiesel	 71
4.1 Preface	71
4.2 Introduction.....	72
4.3 Background.....	73
4.3.1 Biodiesel Processing.....	73
4.3.2 Hydrogenation Processing.....	74
4.3.3 Iodine Value and NO _x Emissions	76
4.4 Initial Experimental Tests and Data	77
4.5 Second Set of Experimental Tests	81
4.6 Fuel Property Tests and Results	82
4.6.1 Cetane number by Ignition Quality Tester (IQT).....	82
4.6.2 Compound analysis	85
4.6.3 Cloud Point and Pour Point.....	85
4.6.4 Viscosity	87
4.6.5 Higher Heating Value.....	88
4.6.6 Boiling Range Distribution.....	89
4.7 Engine Tests Results and Data Analysis	90
4.7.1 Fuel Tests over various Engine Modes	91
4.7.2 Pressure Trace and Heat Release Analysis.....	101
4.7.3 Needle Lift.....	112
4.7.4 Bulk Cylinder Temperature.....	117
4.8 Discussion.....	124
4.8.1 Discussion of Biodiesel NO _x Theories	124
4.8.2 Fuel Injection Strategy on NO _x emissions.....	134
4.9 Conclusions.....	145
 Chapter 5 NO _x Reduction through Mixed Mode Combustion.....	 148

5.1 Preface	148
5.2 Introduction.....	149
5.3 DME and Mixed Mode Combustion Process	152
5.4 Design and Testing of the DME Gaseous Fueling System.....	156
5.5 Test Results from a Navistar 7.3L Heavy Duty Turbocharged Diesel Engine.....	160
5.6 DDC 2.5L Light Duty Turbocharged Diesel Engine Tests	169
5.7 Description of Experimental Set-up	170
5.8 Results from a DDC 2.5L Turbo Diesel Engine.....	171
5.8.1 Increasing Dimethyl Ether Concentrations in Intake Air	171
5.8.1.1 Sierra Instruments BG-2 Gravimetric Particulate Matter Data ..	200
5.8.1.2 Tapered Element Oscillating Microbalance (TEOM) and Scanning Mobility Particle Sizer (SMPS) Data	204
5.8.2 Impact of Intake Air Heating.....	210
5.8.3 Impact of Change in Cetane Number of the Fumigated Fuel.....	229
5.9 Discussion.....	247
5.9.1 DME Ignition and Reaction Kinetics	247
5.9.2 Explanation for shift in NO to NO ₂ emissions	250
5.9.3 Chemkin Modeling of DME HCCI	253
5.9.4 Injection Timing and Heated Intake Air Effect.....	257
5.9.5 Influence of High Temperature Heat Release from DME.....	258
5.9.6 Hydrocarbons in Exhaust Species	259
5.9.7 Effect of Methane Addition.....	262
5.9.8 Effect of Mixed Mode Combustion on particulate matter.....	263
5.10 Conclusions.....	265
Chapter 6 Summary, Conclusions, and Suggestions for Future Work	269
6.1 Summary.....	269
6.2 Observations and Conclusions.....	269
6.2.1 NO _x Reduction through fuel modification: Hydrogenated Biodiesel ..	270
6.2.2 NO _x Reduction through Mixed Mode Combustion	271
6.3 Suggestions for Future Work.....	275
6.3.1 NO _x Reduction through fuel modification: Hydrogenated Biodiesel ..	275
6.3.2 NO _x Reduction through Mixed Mode Combustion	277
Bibliography	280
Appendix A TEOM Instrument File Configuration and User Configuration.....	300
A.1 Instrument File Configuration	300
A.2 User File Configuration	302
Appendix B Biodiesel and Ultra Low Sulfur Diesel Fuel Specification Reports.....	304
B.1 Biodiesel Fuel Specification	304

B.2 Hydrogenated Biodiesel Fuel Specification..... 308
B.3 BP 15 Ultra Low Sulfur Diesel Fuel Certificate of Analysis..... 312

LIST OF FIGURES

Figure 2.1: United States and European Union PM Regulations [7].....	5
Figure 2.2: United States and European Union NO _x Emissions Regulations with trends in NO _x reduction technology [6, 7]	6
Figure 2.3: Typical Direct Injection engine heat-release-rate diagram identifying different diesel combustion phases [11]	10
Figure 2.4: Overall reaction scheme for dimethyl ether oxidation [24]	14
Figure 2.5: Schematic of the conceptual model of DI diesel Combustion [29].....	16
Figure 2.6: Summary of the fuel burning process [19].....	17
Figure 2.7: NO production associated with the Fenimore prompt mechanism [32, 33].....	19
Figure 2.8: Schematic of Diesel Particles and Vapor Phase Compounds [46].....	23
Figure 2.9: Emissions Control Strategies for Compression Ignition Engines [49].....	24
Figure 2.10: Average emissions impacts of biodiesel for heavy-duty highway engines [53]	33
Figure 2.11: Iodine Value vs. NO _x [99]	34
Figure 2.12: LTC and PCCI concept on Φ - T map [134]	42
Figure 2.13: Definition of the combustion parameters [140]	44
Figure 3.1: Detroit Diesel Corporation 2.5L Engine	54
Figure 3.2: Engine Rating of the 2.5L Detroit Diesel/ VM Motori Engine [172]	54
Figure 3.3: Sierra Instruments BG-2 Micro-Dilution Test Stand [176].....	61
Figure 3.4: DDC 2.5 L Engine Test Specification for NO _x Reduction with Fuel Modification Experiments: Hydrogenated Biodiesel	68
Figure 3.5: Repeatability Study Test NO _x (g/kWh) Emissions Data: 1800 rpm and 61 ft-lb torque and at a fuel injection timing of 7° BTDC.....	70
Figure 4.1: Iodine Value vs. NO _x emissions[99].	77
Figure 4.2: NO _x (g/kg fuel) vs AVL 8 mode test. [179]	78

Figure 4.3: BSFC (g/kWh) vs AVL 8 mode test [179].....	79
Figure 4.4: CO (g/kg fuel) vs AVL 8 mode test [179].....	80
Figure 4.5: Photograph of the Ignition Quality Tester (IQT) at the Penn State Energy Institute.....	83
Figure 4.6: Sample data readout from the IQT. Needle lift is displayed in yellow and combustion pressure in blue.....	84
Figure 4.7: Pour Point (°C) by fuel type (B percentage is the blend percentage in the fuel).....	86
Figure 4.8: Cloud Point (°C) by fuel type (B percentage is the blend percentage in the fuel).....	87
Figure 4.9: NO _x Emissions (g/kg fuel) for DDC 2.5L engine, Mode 1= 1500 rpm/50 ft-lb, Mode 2= 1500 rpm/100 ft-lb, Mode 3= 1660 rpm/75 ft-lb, Mode 4= 1660rpm/125 ft-lb, with pilot and main injection, without EGR, for various biodiesel blends in comparison to baseline diesel fuel ULSD (BP15)	93
Figure 4.10: CO ₂ Emissions (g/kg fuel) for DDC 2.5L engine, Mode 1= 1500 rpm/50 ft-lb, Mode 2= 1500 rpm/100 ft-lb, Mode 3= 1660 rpm/75 ft-lb, Mode 4= 1660rpm/125 ft-lb, with pilot and main injection, without EGR, for various biodiesel blends in comparison to baseline diesel fuel ULSD (BP15)	94
Figure 4.11: Hydrocarbon Emissions (g/kg fuel) for DDC 2.5L engine, Mode 1= 1500 rpm/50 ft-lb, Mode 2= 1500 rpm/100 ft-lb, Mode 3= 1660 rpm/75 ft-lb, Mode 4= 1660rpm/125 ft-lb, with pilot and main injection, without EGR, for various biodiesel blends in comparison to baseline diesel fuel ULSD (BP15)	95
Figure 4.12: CO Emissions (g/kg fuel) for DDC 2.5L engine, Mode 1= 1500 rpm/50 ft-lb, Mode 2= 1500 rpm/100 ft-lb, Mode 3= 1660 rpm/75 ft-lb, Mode 4= 1660rpm/125 ft-lb, with pilot and main injection, without EGR, for various biodiesel blends in comparison to baseline diesel fuel ULSD (BP15)	96
Figure 4.13: Fuel Consumption (g/hr) for DDC 2.5L engine, Mode 1= 1500 rpm/50 ft-lb, Mode 2= 1500 rpm/100 ft-lb, Mode 3= 1660 rpm/75 ft-lb, Mode 4= 1660rpm/125 ft-lb, with pilot and main injection, without EGR, for various biodiesel blends in comparison to baseline diesel fuel ULSD (BP15)	97
Figure 4.14: Brake Specific Fuel Consumption (g/kWh) for DDC 2.5L engine, Mode 1= 1500 rpm/50 ft-lb, Mode 2= 1500 rpm/100 ft-lb, Mode 3= 1660 rpm/75 ft-lb, Mode 4= 1660rpm/125 ft-lb, with pilot and main injection, without EGR, for various biodiesel blends in comparison to baseline diesel fuel ULSD (BP15)	98

Figure 4.15: Brake Specific Energy Consumption (MJ/kWh) for DDC 2.5L engine, Mode 1= 1500 rpm/50 ft-lb, Mode 2= 1500 rpm/100 ft-lb, Mode 3= 1660 rpm/75 ft-lb, Mode 4= 1660rpm/125 ft-lb, with pilot and main injection, without EGR, for various biodiesel blends in comparison to baseline diesel fuel ULSD (BP15).....	100
Figure 4.16: Exhaust Temperature (°C) for DDC 2.5L engine, Mode 1= 1500 rpm/50 ft-lb, Mode 2= 1500 rpm/100 ft-lb, Mode 3= 1660 rpm/75 ft-lb, Mode 4= 1660rpm/125 ft-lb, with pilot and main injection, without EGR, for various biodiesel blends in comparison to baseline diesel fuel ULSD (BP15)	101
Figure 4.17: Mode 1 Pressure Trace Plot for DDC 2.5L engine, Mode 1= 1500 rpm/50 ft-lb, with pilot and main injection, without EGR, for various biodiesel blends in comparison to baseline diesel fuel ULSD (BP15).....	103
Figure 4.18: Mode 2 Pressure Trace Plot for DDC 2.5L engine, Mode 2= 1500 rpm/100 ft-lb, with pilot and main injection, without EGR, for various biodiesel blends in comparison to baseline diesel fuel ULSD (BP15).....	104
Figure 4.19: Mode 3 Pressure Trace Plot for DDC 2.5L engine, Mode 3= 1660 rpm/75 ft-lb, with pilot and main injection, without EGR, for various biodiesel blends in comparison to baseline diesel fuel ULSD (BP15).....	105
Figure 4.20: Mode 4 Pressure Trace Plot for DDC 2.5L engine, Mode 4= 1660rpm/125 ft-lb, with pilot and main injection, without EGR, for various biodiesel blends in comparison to baseline diesel fuel ULSD (BP15).....	107
Figure 4.21: Mode 1 Rate of Heat Release Plot for DDC 2.5L engine, Mode 1= 1500 rpm/50 ft-lb, with pilot and main injection, without EGR, for various biodiesel blends in comparison to baseline diesel fuel ULSD (BP15).....	108
Figure 4.22: Mode 2 Rate of Heat Release Plot for DDC 2.5L engine, Mode 2= 1500 rpm/100 ft-lb, with pilot and main injection, without EGR, for various biodiesel blends in comparison to baseline diesel fuel ULSD (BP15).....	109
Figure 4.23: Mode 3 Rate of Heat Release Plot for DDC 2.5L engine, Mode 3= 1660 rpm/75 ft-lb, with pilot and main injection, without EGR, for various biodiesel blends in comparison to baseline diesel fuel ULSD (BP15).....	110
Figure 4.24: Mode 4 Rate of Heat Release Plot for DDC 2.5L engine, Mode 4= 1660rpm/125 ft-lb, with pilot and main injection, without EGR, for various biodiesel blends in comparison to baseline diesel fuel ULSD (BP15).....	111
Figure 4.25: Mode 1 Needle Lift Plot for DDC 2.5L engine, Mode 1= 1500 rpm/50 ft-lb, with pilot and main injection, without EGR, for various biodiesel blends in comparison to baseline diesel fuel ULSD (BP15).....	113

Figure 4.26: Mode 2 Needle Lift Plot for DDC 2.5L engine, Mode 2= 1500 rpm/100 ft-lb, with pilot and main injection, without EGR, for various biodiesel blends in comparison to baseline diesel fuel ULSD (BP15).....	114
Figure 4.27: Mode 3 Needle Lift Plot for DDC 2.5L engine, Mode 3= 1660 rpm/75 ft-lb, with pilot and main injection, without EGR, for various biodiesel blends in comparison to baseline diesel fuel ULSD (BP15).....	115
Figure 4.28: Mode 4 Needle Lift Plot for DDC 2.5L engine, Mode 4= 1660rpm/125 ft-lb, with pilot and main injection, without EGR, for various biodiesel blends in comparison to baseline diesel fuel ULSD (BP15).....	116
Figure 4.29: Mode 1 Bulk Cylinder Temperature Plot for DDC 2.5L engine, Mode 1= 1500 rpm/50 ft-lb, with pilot and main injection, without EGR, for various biodiesel blends in comparison to baseline diesel fuel ULSD (BP15)	118
Figure 4.30: Mode 2 Bulk Cylinder Temperature Plot for DDC 2.5L engine, Mode 2= 1500 rpm/100 ft-lb, with pilot and main injection, without EGR, for various biodiesel blends in comparison to baseline diesel fuel ULSD (BP15)	120
Figure 4.31: Mode 3 Bulk Cylinder Temperature Plot for DDC 2.5L engine, Mode 3= 1660 rpm/75 ft-lb, with pilot and main injection, without EGR, for various biodiesel blends in comparison to baseline diesel fuel ULSD (BP15)	122
Figure 4.32: Mode 4 Bulk Cylinder Temperature Plot for DDC 2.5L engine, Mode 4= 1660rpm/125 ft-lb, with pilot and main injection, without EGR, for various biodiesel blends in comparison to baseline diesel fuel ULSD (BP15)	123
Figure 4.33: Adiabatic Flame Temperature of fuels at a pressure of 50 bar vs. Phi (ϕ)	127
Figure 4.34: NO _x (g/kg fuel) for DDC 2.5L engine, 1800 rpm and 61 ft-lb with single injection timing of 7° BTDC, without EGR, comparing ULSD (BP15) to 20% soy-based biodiesel to 20% hydrogenated soy-based biodiesel.....	139
Figure 4.35: NO _x (g/kWh) for DDC 2.5L engine, 1800 rpm and 61 ft-lb with single injection timing of 7° BTDC, without EGR, comparing ULSD (BP15) to 20% soy-based biodiesel to 20% hydrogenated soy-based biodiesel.....	140
Figure 4.36: Pressure (bar) per crank angle degree for DDC 2.5L engine, 1800 rpm and 61 ft-lb with single injection timing of 7° BTDC, without EGR, comparing ULSD (BP15) to 20% soy-based biodiesel to 20% hydrogenated soy-based biodiesel.....	141

Figure 4.37: Heat Release (J/deg) for DDC 2.5L engine, 1800 rpm and 61 ft-lb with single injection timing of 7° BTDC, without EGR, comparing ULSD (BP15) to 20% soy-based biodiesel to 20% hydrogenated soy-based biodiesel ..	142
Figure 4.38: Bulk Cylinder Temperature (K) for DDC 2.5L engine, 1800 rpm and 61 ft-lb with single injection timing of 7° BTDC, without EGR, comparing ULSD (BP15) to 20% soy-based biodiesel to 20% hydrogenated soy-based biodiesel.....	143
Figure 4.39: Needle Lift (mm) for DDC 2.5L engine, 1800 rpm and 61 ft-lb with single injection timing of 7° BTDC, without EGR, comparing ULSD (BP15) to 20% soy-based biodiesel to 20% hydrogenated soy-based biodiesel.....	144
Figure 5.1: Custom intake air manifold aspiration system	157
Figure 5.2: DME fuel tank with heaters.....	158
Figure 5.3: DME tank pressure and temperature monitoring system	159
Figure 5.4: NO _x emissions in gram NO _x per kg fuel (Test Condition = Speed (rpm)/Load (ft-lbs)) ; Baseline is ULSD diesel fuel.....	162
Figure 5.5: NO emissions (gram NO /hour) (Test Condition = Speed (rpm)/Load (ft-lbs)) ; Baseline is ULSD diesel fuel.	163
Figure 5.6: NO ₂ emissions (gram NO ₂ /hour) (Test Condition = Speed (rpm)/Load (ft-lbs)) ; Baseline is ULSD diesel fuel.....	164
Figure 5.7: Brake Specific Energy Consumption (MJ/ hp-hr) ; Baseline is ULSD diesel fuel.....	165
Figure 5.8: Heat Release data for 876 rpm and 84 ft-lb torque with increasing DME concentration in comparison to the baseline diesel operation.	167
Figure 5.9: Heat Release data for 1000 rpm and 150 ft-lb torque with increasing DME concentration in comparison to the baseline diesel operation	168
Figure 5.10: Layout of intake air heating system before installation on the DDC 2.5L engine stand.....	170
Figure 5.11: NO _x (g/kg fuel) for mixed mode combustion at 1800 rpm and 61 ft-lb torque with increasing DME concentration fumigated in the intake air.....	172
Figure 5.12: NO _x (g/kWh) for mixed mode combustion at 1800 rpm and 61 ft-lb torque with increasing DME concentration fumigated in the intake air.....	173

Figure 5.13: NO (g/kg fuel) for mixed mode combustion at 1800 rpm and 61 ft-lb torque with increasing DME concentration fumigated in the intake air.....	174
Figure 5.14: NO ₂ (g/kg fuel) for mixed mode combustion at 1800 rpm and 61 ft-lb torque with increasing DME concentration fumigated in the intake air.....	175
Figure 5.15: Brake Specific Fuel Consumption (g/kWh) for mixed mode combustion at 1800 rpm and 61 ft-lb torque with increasing DME concentration fumigated in the intake air	176
Figure 5.16: Brake Specific Energy Consumption (MJ/kWh) for mixed mode combustion at 1800 rpm and 61 ft-lb torque with increasing DME concentration fumigated in the intake air	177
Figure 5.17: CO (g/kg fuel) for mixed mode combustion at 1800 rpm and 61 ft-lb torque with increasing DME concentration fumigated in the intake air.....	178
Figure 5.18: Total Hydrocarbons (g/kg fuel) for mixed mode combustion at 1800 rpm and 61 ft-lb torque with increasing DME concentration fumigated in the intake air	179
Figure 5.19: GC Data: BP15 in comparison to mixed mode combustion with increasing energy equivalent percent DME concentration at 7° BTDC.....	180
Figure 5.20: CO ₂ (g/kg fuel) for mixed mode combustion at 1800 rpm and 61 ft-lb torque with increasing DME concentration fumigated in the intake air.....	181
Figure 5.21: Methane (ppm) for mixed mode combustion at 1800 rpm and 61 ft-lb torque with increasing DME concentration fumigated in the intake air.....	182
Figure 5.22: Exhaust Temperatures (°C) for mixed mode combustion at 1800 rpm and 61 ft-lb torque with increasing DME concentration fumigated in the intake air	183
Figure 5.23: Cylinder Pressure Traces (bar) for BP15 in comparison to mixed mode combustion with increasing energy equivalent percent DME concentration at 7° BTDC	184
Figure 5.24: Heat Release Rate (J/deg) for BP15 in comparison to mixed mode combustion with increasing energy equivalent percent DME concentration at 7° BTDC	185
Figure 5.25: Bulk Cylinder Temperature (K) for BP15 in comparison to mixed mode combustion with increasing energy equivalent percent DME concentration at 7° BTDC	186

Figure 5.26: NO _x (g/kg fuel) for mixed mode combustion at 1800 rpm and 61 ft-lb torque with 25% energy equivalent DME concentration fumigated in the intake air at various injection timings.....	187
Figure 5.27: NO _x (g/kWh) for mixed mode combustion at 1800 rpm and 61 ft-lb torque with 25% energy equivalent DME concentration fumigated in the intake air at various injection timings.....	188
Figure 5.28: NO (g/kg fuel) for mixed mode combustion at 1800 rpm and 61 ft-lb torque with 25% energy equivalent DME concentration fumigated in the intake air at various injection timings.....	189
Figure 5.29: NO ₂ (g/kg fuel) for mixed mode combustion at 1800 rpm and 61 ft-lb torque with 25% energy equivalent DME concentration fumigated in the intake air at various injection timings.....	190
Figure 5.30: Methane (ppm) for mixed mode combustion at 1800 rpm and 61 ft-lb torque with 25% energy equivalent DME concentration fumigated in the intake air at various injection timings.....	191
Figure 5.31: GC Data: 25% energy equivalent DME concentration at varying pilot injection timings: 7°, 5°, 3° BTDC	192
Figure 5.32: Brake Specific Fuel Consumption (g/kWh) for mixed mode combustion at 1800 rpm and 61 ft-lb torque with 25% energy equivalent DME concentration fumigated in the intake air at various injection timings.....	193
Figure 5.33: Brake Specific Energy Consumption (MJ/kWh) for mixed mode combustion at 1800 rpm and 61 ft-lb torque with 25% energy equivalent DME concentration fumigated in the intake air at various injection timings.....	194
Figure 5.34: Fuel Consumption (g/hr) for mixed mode combustion at 1800 rpm and 61 ft-lb torque with 25% energy equivalent DME concentration fumigated in the intake air at various injection timings	195
Figure 5.35: Cylinder Pressure (bar) for mixed mode combustion at 1800 rpm and 61 ft-lb torque with 25% energy equivalent DME concentration fumigated in the intake air at various injection timings	196
Figure 5.36: Heat Release Rate (J/deg) for mixed mode combustion at 1800 rpm and 61 ft-lb torque with 25% energy equivalent DME concentration fumigated in the intake air at various injection timings	197
Figure 5.37: Bulk Cylinder Temperature (K) for mixed mode combustion at 1800 rpm and 61 ft-lb torque with 25% energy equivalent DME concentration fumigated in the intake air at various injection timings	199

Figure 5.38: BP-15 1800 rpm 61 ft-lbs: 3°, 5°, 7°, 9° BTDC (left to right)	200
Figure 5.39: BP-15 with 25% energy equivalent DME: 1°, 3°, 7° BTDC (left to right)	201
Figure 5.40: BP-15 with 40% energy equivalent DME: 2°, 3°, 5°, 7° BTDC (left to right)	202
Figure 5.41: BP-15 with 40% energy equivalent DME: 7° BTDC (left)	203
Figure 5.42: BP-15 1800 rpm 61 ft-lbs torque: 3° BTDC (top left), 7° BTDC (bottom left); BP-15 with 25% energy equivalent DME : 3° BTDC (top right), 7° BTDC (bottom right).....	204
Figure 5.43: TEOM data for mixed mode combustion at 1800 rpm and 61 ft-lb torque with increasing DME concentration fumigated in the intake air.....	205
Figure 5.44: TEOM data for mixed mode combustion at 1800 rpm and 61 ft-lb torque with 25% energy equivalent DME concentration fumigated in the intake air at various fuel injection timings	206
Figure 5.45: SMPS Data: BP-15 1800vrpm 61 ft-lbs comparing with the Thermal Denuder at 40°C and 350°C	207
Figure 5.46: SMPS Data: BP-15 1800 rpm 61 ft-lbs comparing with the Thermal Denuder at 40°C and 350°C and SMPS Data: BP-15 with 25% energy equivalent DME 1800vrpm 61 ft-lbs comparing with the Thermal Denuder at 40°C and 350°C	208
Figure 5.47: SMPS Data: BP-15 with 25% energy equivalent DME 1800 rpm 61 ft-lbs comparing with the Thermal Denuder at 40°C and 350°C at 7° BTDC and SMPS Data: BP-15 with 25% energy equivalent DME 1800 rpm 61 ft-lbs comparing with the Thermal Denuder at 40°C and 350°C at 3° BTDC	209
Figure 5.48: NO _x (g/kg fuel) for mixed mode combustion at 1800 rpm and 61 ft-lb torque with 25% energy equivalent DME concentration fumigated in the intake air at various intake air temperatures compared to BP15, all at 3° BTDC fuel injection timing.....	211
Figure 5.49: NO _x (g/kWh) for mixed mode combustion at 1800 rpm and 61 ft-lb torque with 25% energy equivalent DME concentration fumigated in the intake air at various intake air temperatures compared to BP15, all at 3° BTDC fuel injection timing.....	212
Figure 5.50: NO (g/kg fuel) for mixed mode combustion at 1800 rpm and 61 ft-lb torque with 25% energy equivalent DME concentration fumigated in the	

intake air at various intake air temperatures compared to BP15, all at 3° BTDC fuel injection timing.....	213
Figure 5.51: NO ₂ (g/kg fuel) for mixed mode combustion at 1800 rpm and 61 ft-lb torque with 25% energy equivalent DME concentration fumigated in the intake air at various intake air temperatures compared to BP15, all at 3° BTDC fuel injection timing.....	214
Figure 5.52: Brake Specific Fuel Consumption (g/kWh) for mixed mode combustion at 1800 rpm and 61 ft-lb torque with 25% energy equivalent DME concentration fumigated in the intake air at various intake air temperatures compared to BP15, all at 3° BTDC fuel injection timing.....	215
Figure 5.53: Brake Specific Energy Consumption (MJ/kWh) for mixed mode combustion at 1800 rpm and 61 ft-lb torque with 25% energy equivalent DME concentration fumigated in the intake air at various intake air temperatures compared to BP15, all at 3° BTDC fuel injection timing.....	216
Figure 5.54: CO (g/kg fuel) for mixed mode combustion at 1800 rpm and 61 ft-lb torque with 25% energy equivalent DME concentration fumigated in the intake air at various intake air temperatures compared to BP15, all at 3° BTDC fuel injection timing.....	217
Figure 5.55: CO ₂ (g/kg fuel) for mixed mode combustion at 1800 rpm and 61 ft-lb torque with 25% energy equivalent DME concentration fumigated in the intake air at various intake air temperatures compared to BP15, all at 3° BTDC fuel injection timing.....	218
Figure 5.56: Methane (ppm) for mixed mode combustion at 1800 rpm and 61 ft-lb torque with 25% energy equivalent DME concentration fumigated in the intake air at various intake air temperatures compared to BP15, all at 3° BTDC fuel injection timing.....	219
Figure 5.57: Total Hydrocarbons (g/kg fuel) for mixed mode combustion at 1800 rpm and 61 ft-lb torque with 25% energy equivalent DME concentration fumigated in the intake air at various intake air temperatures compared to BP15, all at 3° BTDC fuel injection timing.....	220
Figure 5.58: Exhaust Temperature (°C) for mixed mode combustion at 1800 rpm and 61 ft-lb torque with 25% energy equivalent DME concentration fumigated in the intake air at various intake air temperatures compared to BP15, all at 3° BTDC fuel injection timing.....	221
Figure 5.59: GC Data: BP15 in comparison to mixed mode combustion with 25% energy equivalent DME concentration at 3° BTDC with increasing temperature.....	222

Figure 5.60: Cylinder Pressure (bar) for mixed mode combustion at 1800 rpm and 61 ft-lb torque with 25% energy equivalent DME concentration fumigated in the intake air at various intake air temperatures compared to BP15, all at 3° BTDC fuel injection timing	223
Figure 5.61: Heat Release Rate (J/deg) for mixed mode combustion at 1800 rpm and 61 ft-lb torque with 25% energy equivalent DME concentration fumigated in the intake air at various intake air temperatures compared to BP15, all at 3° BTDC fuel injection timing.....	224
Figure 5.62: Bulk Temperature (K) for mixed mode combustion at 1800 rpm and 61 ft-lb torque with 25% energy equivalent DME concentration fumigated in the intake air at various intake air temperatures compared to BP15, all at 3° BTDC fuel injection timing.....	226
Figure 5.63: TEOM data for mixed mode combustion at 1800 rpm and 61 ft-lb torque with 25% energy equivalent DME concentration fumigated with increasing intake air temperature.....	227
Figure 5.64: SMPS Data: BP-15 with 25% energy equivalent DME at 1800 rpm and 61 ft-lbs compared with the Thermal Denuder at 40°C and 350°C at 3° BTDC with an Intake Air Temperature of 25°C and SMPS Data for BP-15 with 25% energy equivalent DME at 1800 rpm and 61 ft-lbs compared with the Thermal Denuder at 40°C and 350°C at 3° BTDC with Intake Air Temperature at 70°C.....	228
Figure 5.65: NO _x (g/kg fuel) for mixed mode combustion at 1800 rpm and 61 ft-lb torque with 25% DME energy equivalent with and without 5 SLPM (6.5% energy equivalent) Methane fumigated in the intake air at various intake air temperatures compared to BP15, at 7 and 1 ° BTDC fuel injection timing	230
Figure 5.66: NO _x (g/kWh) for mixed mode combustion at 1800 rpm and 61 ft-lb torque with 25% DME energy equivalent with and without 5 SLPM (6.5% energy equivalent) Methane fumigated in the intake air at various intake air temperatures compared to BP15, at 7 and 1 ° BTDC fuel injection timing	231
Figure 5.67: NO (g/kg fuel) for mixed mode combustion at 1800 rpm and 61 ft-lb torque with 25% DME energy equivalent with and without 5 SLPM (6.5% energy equivalent) Methane fumigated in the intake air at various intake air temperatures compared to BP15, at 7 and 1 ° BTDC fuel injection timing	232
Figure 5.68: NO ₂ (g/kg fuel) for mixed mode combustion at 1800 rpm and 61 ft-lb torque with 25% DME energy equivalent with and without 5 SLPM (6.5% energy equivalent) Methane fumigated in the intake air at various intake air temperatures compared to BP15, at 7 and 1 ° BTDC fuel injection timing	233

Figure 5.69: Brake Specific Fuel Consumption (g/kWh) for mixed mode combustion at 1800 rpm and 61 ft-lb torque with 25% DME energy equivalent with and without 5 SLPM (6.5% energy equivalent) Methane fumigated in the intake air at various intake air temperatures compared to BP15, at 7 and 1 ° BTDC fuel injection timing.....	234
Figure 5.70: Brake Specific Energy Consumption (MJ/kWh) for mixed mode combustion at 1800 rpm and 61 ft-lb torque with 25% DME energy equivalent with and without 5 SLPM (6.5% energy equivalent) Methane fumigated in the intake air at various intake air temperatures compared to BP15, at 7 and 1 ° BTDC fuel injection timing.....	235
Figure 5.71: CO (g/kg fuel) for mixed mode combustion at 1800 rpm and 61 ft-lb torque with 25% DME energy equivalent with and without 5 SLPM (6.5% energy equivalent) Methane fumigated in the intake air at various intake air temperatures compared to BP15, at 7 and 1 ° BTDC fuel injection timing	236
Figure 5.72: Total Hydrocarbons (g/kg fuel) for mixed mode combustion at 1800 rpm and 61 ft-lb torque with 25% DME energy equivalent with and without 5 SLPM (6.5% energy equivalent) Methane fumigated in the intake air at various intake air temperatures compared to BP15, at 7 and 1 ° BTDC fuel injection timing.....	237
Figure 5.73: CO ₂ (g/kg fuel) for mixed mode combustion at 1800 rpm and 61 ft-lb torque with 25% DME energy equivalent with and without 5 SLPM (6.5% energy equivalent) Methane fumigated in the intake air at various intake air temperatures compared to BP15, at 7 and 1 ° BTDC fuel injection timing	238
Figure 5.74: Methane (ppm) for mixed mode combustion at 1800 rpm and 61 ft-lb torque with 25% DME energy equivalent with and without 5 SLPM (6.5% energy equivalent) Methane fumigated in the intake air at various intake air temperatures compared to BP15, at 7 and 1 ° BTDC fuel injection timing	239
Figure 5.75: Exhaust Temperature (°C) for mixed mode combustion at 1800 rpm and 61 ft-lb torque with 25% DME energy equivalent with and without 5 SLPM (6.5% energy equivalent) Methane fumigated in the intake air at various intake air temperatures compared to BP15, at 7 and 1 ° BTDC fuel injection timing.....	240
Figure 5.76: GC Data: BP15 in comparison to mixed mode combustion with 25% energy equivalent DME concentration and with 25% energy equivalent DME concentration at various injection timing and with increasing temperature	241
Figure 5.77: Cylinder Pressure (bar) for mixed mode combustion at 1800 rpm and 61 ft-lb torque with 25% DME energy equivalent with and without 5 SLPM	

(6.5% energy equivalent) Methane fumigated in the intake air at various intake air temperatures compared to BP15, at 7 and 1 ° BTDC fuel injection timing.....	242
Figure 5.78: Heat Release Rate (J/deg) for mixed mode combustion at 1800 rpm and 61 ft-lb torque with 25% DME energy equivalent with and without 5 SLPM (6.5% energy equivalent) Methane fumigated in the intake air at various intake air temperatures compared to BP15, at 7 and 1 ° BTDC fuel injection timing.....	244
Figure 5.79: Bulk Temperature (K) for mixed mode combustion at 1800 rpm and 61 ft-lb torque with 25% DME energy equivalent with and without 5 SLPM (6.5% energy equivalent) Methane fumigated in the intake air at various intake air temperatures compared to BP15, at 7 and 1 ° BTDC fuel injection timing.....	246
Figure 5.80: Overall reaction scheme for dimethyl ether oxidation [24]	249
Figure 5.81: Chemkin simulation of 25% energy equivalent DME HCCI, A/F ratio of 138.1 and $\Phi = .065$, with various species (Initial Temperature 25 °C, Pressure 1 atm, Heat Loss 0.0 cal/sec)	254
Figure 5.82: Chemkin model of 25% energy equivalent DME HCCI, A/F ratio of 138.1 and $\Phi = .065$, with HO ₂ in comparison to other species (Initial Temperature 25 °C, Pressure 1 atm, Heat Loss 0.0 cal/sec).....	255
Figure 5.83: Chemkin model of 25% (A/F ratio of 138.1 and $\Phi = .065$), 35% (A/F ratio of 101.3 and $\Phi = .088$), and 44% (A/F ratio of 89.3 and $\Phi = .100$) energy equivalent DME HCCI showing increasing HO ₂ species (Initial Temperature 25 °C, Pressure 1 atm, Heat Loss 0.0 cal/sec).....	256
Figure 5.84: GC Trace for 25% DME energy equivalent mixed mode combustion at 7° BTDC: FID trace in the later retention time (x-axis) region at 225°C.....	261

LIST OF TABLES

Table 2.1: U.S. Heavy-Duty Diesel Engine Emission Standards [1, 8-10]	6
Table 2.2: Physical Properties of DME [57, 61, 68, 69].....	28
Table 3.1: DDC 2.5L Engine Specifications	55
Table 3.2: AVL Combustion Emissions Bench II Analyzer Ranges.....	58
Table 3.3: SMPS Property configuration for data collection.....	65
Table 3.4: Repeatability Study Engine Test Data: 1800 rpm and 61 ft-lb torque and at a fuel injection timing of 7° BTDC.....	69
Table 3.5: Repeatability Study Test Emissions Data: 1800 rpm and 61 ft-lb torque and at a fuel injection timing of 7° BTDC	69
Table 4.1: Chemical properties of and Fatty Acid content of the Hydrogenated Soy Biodiesel (GCMS from supplier)	75
Table 4.2: AVL 8-mode test for the DDC 2.5L turbodiesel engine [179].....	78
Table 4.3: DDC 2.5L Engine Test Specification	81
Table 4.4: Derived Cetane Number (DCN).....	84
Table 4.5: Cloud Point and Pour Point	86
Table 4.6: Viscosity (cSt) for the various fuels and blends at (40°C).....	88
Table 4.7: Calorific Value (BTU/lb) of the Fuels.....	89
Table 4.8: Boiling Range Distribution (°C) of the Fuels	90
Table 4.9: Percent Change in Emissions in Comparison to Conventional Diesel fuel for Fuel Consumption (g/hr), Brake Specific Fuel Consumption (g/kWh), and Brake Specific Energy Consumption (MJ/kWh).....	99
Table 4.10: Mode 1 Maximum Pressure (bar).....	102
Table 4.11: Mode 2 Maximum Pressure (bar).....	103
Table 4.12: Mode 3 Maximum Pressure (bar).....	105
Table 4.13: Mode 4 Maximum Pressure (bar).....	106

Table 4.14: Mode 1 Maximum Bulk Temperature (K).....	118
Table 4.15: Mode 2 Maximum Bulk Temperature (K).....	120
Table 4.16: Mode 3 Maximum Bulk Temperature (K).....	122
Table 4.17: Mode 4 Maximum Bulk Temperature (K).....	124
Table 4.18: Methyl Esters physical data and composition	126
Table 4.19: Comparison between the B100 and H100 chemical composition (B100 here is the AGP #1 in Appendix C.).....	126
Table 4.20: Elemental ratios for the biodiesel fuels (C=carbon, H=hydrogen, O=oxygen)	132
Table 5.1: Properties of dimethyl ether (DME) [212].....	153
Table 5.2: Description of Initial Engine Test Plan (ULSD= Ultra Low Sulfur Diesel; DME= Dimethyl Ether).....	161
Table 5.3: Breakdown of fueling and injection conditions (Negative Dynamic Injection Timing indicates before TDC).....	166

ACKNOWLEDGMENTS

This Ph.D dissertation is not only a product of my scholarly research, endless hours spent in the engine lab, and data analysis, but also because of the guidance, support, and help of many individuals who were there encouraging me to persevere when I was ready to give up and resign. I would like to briefly acknowledge those people who cheered me on to the finish line.

I would like give special thanks to my advisor Dr. André L. Boehman who gave me significant freedom to explore my own research projects, and guided me toward ideas which enhanced my research. Through him, I've learned that a good researcher must expect the unexpected, and be willing to find other routes to explore their research problems.

I also appreciate the insights and guidance from the members of my dissertation committee: Dr. Alan W. Scaroni, Dr. Angela D. Lueking, Dr. Thomas A. Litzinger, and Dr. Daniel C. Haworth. I thank them for illuminating the bigger picture of my research work and for helping me focus on the research topic. Our many discussions helped me better understand my experimental data and improve its analysis.

In addition, I would like to thank the following people for their help with various topics and support in our research lab as we worked together to build our experiments: Vince Zello, Greg Lilik, Stephen Kirby, Glen Decker, Hibiki Koga, Shirish Bhide, Jennifer Erich, Jim Szybist, Scott Pflumm, Eugene Kung, the remainder of my research group and the many others who assisted me with my research work.

I would like to especially thank many family members who have provided me the anchored moral support I needed to persevere with my research and finish this dissertation. In particular, my mother, Martha Chapman, was a very instrumental part of my successful completion of this research work. She nursed me to health during the difficult times when I broke my leg, and supported me when my father died. I appreciate her assistance in copying and archiving scholarly articles. I am thankful for her constant moral support and cheering me to the finish line. My father, James Chapman, also supported me with the construction of a portion of my research experimental bench.

So many friends buoyed me as I swam the ocean of graduate school, but in particular, I deeply appreciate the encouragement, coaching and humor of two friends who remained confident in my abilities to navigate academia and continue to succeed: Joanna Rogalski and Kathy Wiedeman.

Finally, I would like to acknowledge the sponsors and industrial supporters of my research work:

Chapter 4: Hydrogenated Biodiesel

Steve Achenbach from Twin River Technologies for providing the hydrogenated biodiesel

AGP for providing biodiesel samples

Mike Haas USDA for providing technical services

Chapter 5: Mixed Mode Combustion with Dimethyl Ether

DOE Hydrogen Assisted Combustion Program Grant No. DE-FC26-04FT42233

DOE Refinery Integration Program Grant No. DE-FC26-04NT41828

Dupont for providing the Dymel A (Dimethyl Ether)

My experiences at Penn State University have made me a careful researcher, an inquisitive scholar, a more innovative automotive engineer, and a better person.

Chapter 1

Introduction

The reduction of oxides of nitrogen emission (NO_x) from compression ignition engines is an important objective due to environmental and human health concerns particularly in areas that are ozone non-attainment zones (e.g., Philadelphia, Houston). In addition, NO_x emissions from engines and vehicles are legislated and regulated around the world, with the emissions regulations continually tightening in the upcoming years. Thus, many methods that can reduce those emissions from in-use compression ignition engines and vehicles are being considered as options.

There are various methods that can be used to reduce NO_x emissions from a compression ignition engine. Two of these methods were studied as a collection of research presented in this thesis. In particular, NO_x reductions can be achieved: 1) through a change in the formulation of biodiesel fuel by hydrogenation of the fuel, and 2) through a change in the mode of combustion with the use of a fumigated fuel. Some of these studies have been previously published, and are contained within this thesis in part or in whole.

The first study involves the effect of biodiesel fuel formulation on NO_x emissions. Specifically, a NO_x increase has been demonstrated widely when using a soy-based biodiesel as a fuel in a compression ignition engine. In the literature, it is suggested that NO_x emissions from different types of biodiesel are related to a change in the iodine value of the fuel. The hypothesis of this research is that the reduction in iodine

value of the fuel, which in turn is a change in the saturation of the C18 chain of the fuel, leads to a reduction in NO_x emissions. A set of tests were performed in a light duty diesel engine running with its normal fuel injection timing and without EGR over various engine speed and load points. In total, 2 engine speeds and 2 different loads were tested. The normal fuel injection timing includes a pilot injection prior to a main injection. Based on the preliminary studies, it was expected that the hydrogenated biodiesel would show a reduction in the NO_x emissions from this particular engine, but it was unclear what the magnitude would be because the previous work had been completed with the EGR present. This research provides new insight into the impact on exhaust emissions from a change in the chemical composition of the biodiesel fuel while using a pilot and main fuel injection strategy in a light duty diesel engine. It would be beneficial to be able to use an alternative fuel in a diesel engine that would produce less NO_x emissions than diesel fuel, which would enhance the motivation to move to non-petroleum sources of fuel.

The second study involved modifying the combustion process by introducing a gaseous fuel into the intake air system. This method is being defined as a “mixed mode” combustion. The engine is allowed to operate in its usual fashion with a diesel fuel pilot injection while another gaseous fuel is being fumigated into the intake air system. For this research, the fumigation fuel was dimethyl ether (DME). The engine was operated at a single speed and load, while the feedrate of the fumigated fuel was varied to study the effect of the fumigated fuel on the combustion process and thus the gaseous emissions. The engine test stand was modified to include an intake air heating system to study the effect of temperature on the ignition behavior of the fuels. The hypothesis of

this research is that a fumigated low ignition temperature fuel can modify the typical NO_x formation paths in diesel combustion and thus reduce the total NO_x emissions. The studies involved several experiments at one specific engine speed and load. First, the DME concentration in the engine mode was explored to determine the minimum NO_x emissions that could be achieved at a particular single pulse injection timing. In addition, injection timing was modified at this particular fuel concentration to observe the effect of combustion timing on the emissions. Next, intake air heating was used to further study the ignition effect of the DME on the overall combustion process and exhaust emissions. Finally, a short study was performed to blend Methane into the fumigated DME concentration and to determine if further NO_x reductions could be achieved with this configuration, and how the ignition behavior of the charge was altered. Based on the preliminary study, it was expected that there would be some NO_x reduction with the DME fumigated into the engine. The intake air heating is expected to further enhance the ignition of the DME and demonstrate how an engine configuration could be changed (i.e. higher compression) to better utilize DME in the engine. While utilization of natural gas and Methane in a compression ignition engine is highly desired because of its wide availability, mixing it with DME and testing it in the engine provides insight into the impact of ignition behavior in reducing the NO_x emission in the mixed mode combustion system, which is presently unclear.

Chapter 2

Literature Review

2.1 Motivation

The motivation for researching NO_x reduction strategies stems from several factors. Primarily, governments worldwide, including the United States, are setting new standards for emissions from new compression ignition engines and vehicles. This is being done for the benefit of human health and the environment, via significant reductions of particulate matter and NO_x emissions. NO_x emissions are the precursors to smog that is produced through photochemical reactions in the atmosphere [1-4]. NO and NO₂ also readily dissolve into water, and thus form nitric acid, the major contributor to acid rain [4]. In a report to the World Health Organization, the health effects of diesel particulate matter emissions exposure were reviewed and shown through epidemiological studies to give higher incidences of cancer in animals, as well as higher incidence of lung cancer in people who experience high concentrations of diesel exhaust [5].

The target for accepted NO_x emissions in the US has been tightened over the last 25 years by the U.S. Environmental Protection Agency (EPA). Between 1997 and 2000, the EPA set new Federal emission standards for on-road diesel vehicles that dramatically reduced allowable nitrogen oxide (NO_x) and particulate matter (PM) emissions. Under these new standards, model year 2004 (MY2004) NO_x emissions from on-road heavy-duty diesel engines were half those required under MY1998 standards (2.5 g/KW-hr in

MY2004). Starting with MY2007, new on-road heavy-duty diesel engines needed to achieve PM levels and phased-in NO_x (starting from 2007, ending in 2010) that are only 10% of MY2004 levels [6]. As a result, diesel engine and vehicle manufacturers needed to implement exhaust after-treatment control devices to meet the MY2007 and later (MY2007+) requirements. These standards were implemented in conjunction with Federal ultra-low-sulfur diesel (<15-ppm sulfur) production requirements, facilitating the introduction of low-emission technologies that would otherwise be compromised by high sulfur levels in the diesel engine exhaust. Figure 2.1 and Figure 2.2 show a historical perspective of the regulations for diesel engines in Europe and the US. Table 2.1 shows the current challenging state of US emissions regulations for Heavy-Duty Diesel Engines.

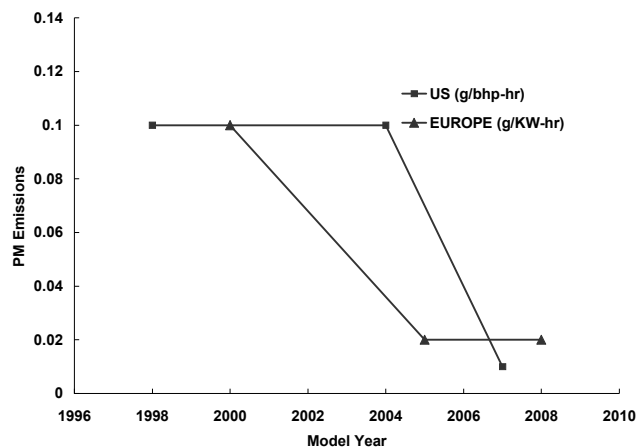


Figure 2.1: United States and European Union PM Regulations [7]

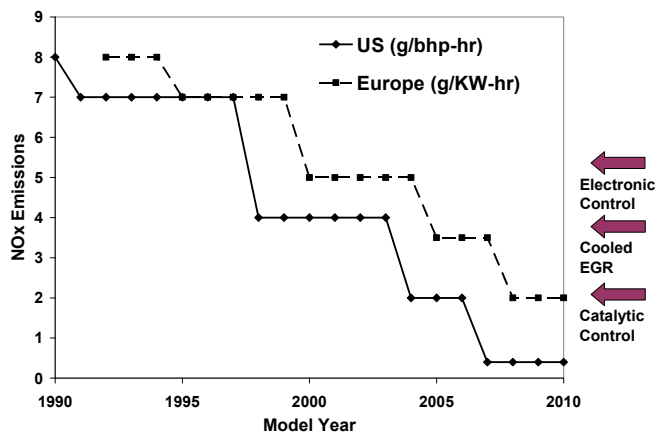


Figure 2.2: United States and European Union NO_x Emissions Regulations with trends in NO_x reduction technology [6, 7]

Table 2.1: U.S. Heavy-Duty Diesel Engine Emission Standards [1, 8-10]

Emissions Type	Current Regulation	2004 (gm/bhp-hr)	2007(gm/bhp-hr)	2010(gm/bhp-hr)
NO _x	4		.2 (50% of fleet sales)	.2
HC	1.3		.14 (NMHC) (50% of fleet sales)	.14 (NMHC)
NO _x and HC		2.4		
PM	.1		.01	.01

*Required on-board diagnostics (OBD) systems for vehicles between 8500 and 14000 lbs to be phased-in, beginning in 2005

NO_x- Nitrogen Oxides ; HC- Hydrocarbons; PM- Particulate Matter

In addition to the health effects issues, the US is focused on integrating fuels from non-petroleum feedstocks into the fuel inventory for US commercial and consumer use.

Some of the fuels being considered have been shown to increase certain emissions that

are under regulatory control. The introduction of these alternative fuels into the inventory is of great importance to the US economy and security, and thus research and development to minimize the exhaust emissions is required.

However, what is not clear is how to meet these regulations with diesel and alternative fuels. Researchers are pursuing many options, including pre-combustion, in-cylinder and post combustion technologies, and combinations of each. To meet 2007 particulate matter emissions regulations, diesel engine manufacturers are pursuing exhaust after-treatment devices since the technology is available. To meet 2010 emissions regulations, researchers are focusing on exhaust after-treatment devices and in-cylinder methods of emissions control, including homogeneous charge compression ignition engines and other low temperature combustion strategies. The research proposed includes a combination of these options to meet the aggressive NO_x emissions reductions: exhaust after treatment technologies, modifying the chemical properties of the compression ignition fuel, and induction of a mixture of fuel and air into a compression ignition engine while using a diesel fuel pilot to ignite the fuel-air mixture.

2.2 Compression Ignition Engines and the Autoignition Process

The words “compression ignition” refer to the engine classification based on the method of fuel ignition. The compression ignition (CI) process is used in conventional diesel engines by pilot injection of diesel fuel. In this type of engine, air is inducted into the cylinder, and compressed. Just before the combustion process is to start, the fuel is injected into the engine. For a given engine speed, the air flow is essentially constant,

and engine load can be adjusted by increasing the amount of fuel injected for each cycle. There are several variations on the type of CI engine including the working cycle (2 or 4 stroke), method of air preparation (naturally aspirated or turbocharged), and method of fueling (indirect or direct injection) [11].

The compression of the fuel and air mixture causes the mixture to autoignite. As Heywood describes it, autoignition is defined as a rapid combustion reaction which is not initiated by an external ignition source [11]. In the literature about basic combustion research, this kind of autoignition is described as an explosion. However, to the engine combustion researcher, the term autoignition is preferred over thermal explosion [11].

A fuel's autoignition tendency is described by its cetane number. Compression ignition engines require a fuel to have a cetane number of at least 40 or higher. Normal ULSD (Ultra Low Sulfur Diesel) has a cetane number of around 50, according to fuel certificate of analysis.

The autoignition of the fuel and air is a complex reacting system where the chemical mechanisms consist of a large number of simultaneous and interdependent reactions or chain reactions [11]. It occurs when the energy being released by the reacting system overcomes the required heat loss to the surroundings. Modern autoignition combustion is described through the use of the chain reaction processes: initiating reactions, propagation reactions, and termination reactions. There are some propagating reactions that produce two radical molecules for each radical that is consumed in the reaction, referred to as a chain branching reaction. When the chain branching reactions occur very rapidly, the term chain branching explosion is used to describe the system [11, 12]. Pfahl and coworkers have described the self-ignition

behavior of diesel-relevant fuels in a homogeneous mixture to have a two-step self ignition, with the first step considered a cool flame, followed by a deflagrative phase (negative temperature coefficient), then by a secondary explosion [13].

The compression ignition combustion process is typically described as having three main phases: 1) ignition delay, 2) premixed or kinetically controlled combustion, and 3) diffusion, or mixing controlled combustion. First, after the fuel is injected, there is some ignition delay as the fuel and air mix together, the fuel droplets are vaporized, and a combustible mixture is created. The ignition delay period ends when autoignition occurs. Second, upon autoignition, a premixed phase of combustion occurs where the fuel and air that are mixed during the ignition delay period are consumed. This results in a high rate of pressure rise and heat release. Finally, the diffusion phase of combustion occurs. During this phase, a diffusion flame front surrounds the fuel spray. At the flame front, stoichiometric mixtures of the fuel and air are present. The rate of reactions and thus the rate of heat release are controlled by the rate of mixing of the fuel and air. Figure 2.3 shows an example of a heat release diagram and each of these three phases represented [11].

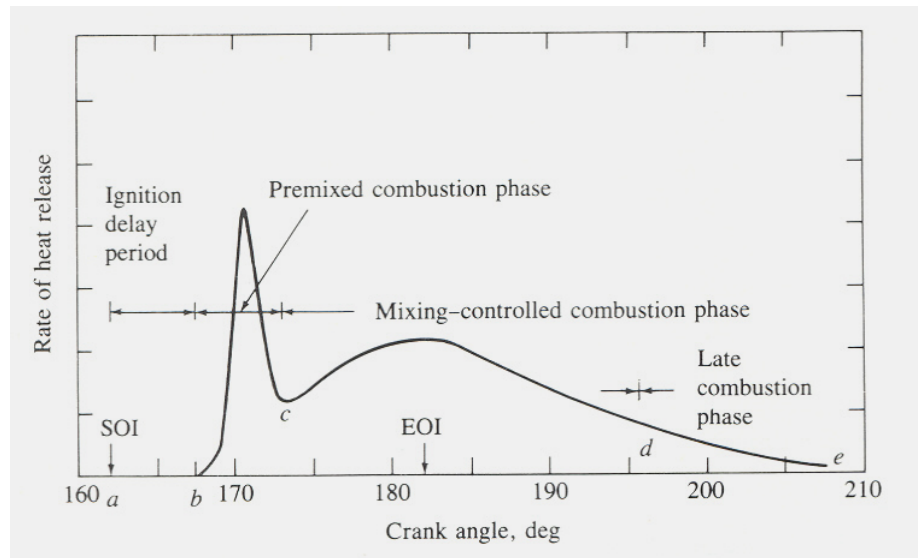


Figure 2.3: Typical Direct Injection engine heat-release-rate diagram identifying different diesel combustion phases [11]

2.2.1 Low Temperature Heat Release

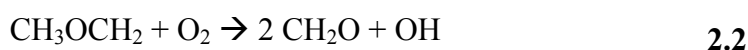
Low temperature heat release has been shown to occur during the first stage of ignition in the low temperature chemical kinetic reactions of the hydrocarbon oxidation [14]. Higgins and coworkers observed a two stage ignition process while running a heavy duty diesel engine at moderate load [14]. The low temperature chemistry exhibited a slow rise in pressure and is shown in the chemiluminescence of the spray [14]. Earlier work by Dec and Espey also showed evidence of the pre-ignition cool flame characteristics [15].

The low temperature reactions would occur below approximately 760K, which is the temperature at which there is a decrease in the reactivity of the system, labeled as

NTC (negative temperature coefficient) behavior and demonstrated by Curran and coworkers as being caused by the competition between two decomposition pathways that provide lower reactivity [16, 17]. Curran and coworkers elucidated the reaction mechanisms for n-heptane and iso-octane ignition, and thus differentiated the low temperature and high temperature regions and their reaction steps [16, 18].

Flynn and coworkers showed that the first stage ignition can cause an increase in the temperature of the reaction zone by 200-300 °C [19]. However, the magnitude of this behavior is dependent on the fuel properties and whether the fuel exhibits some low temperature heat release [20].

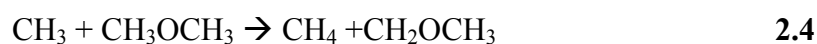
Of interest to the present research are the low temperature reactions and heat release of dimethyl ether (CH₃OCH₃). Through the early research on the chemical kinetics of DME oxidation, it has been demonstrated that the radical reactions during the propagation phase of the combustion process of dimethyl ether include OH, H and CH₃ [21]. With the presence of the OH radical, the ignition quality is enhanced by making the fuel mixture more reactive, thereby shortening the ignition delay and increasing oxidation rates. When the OH radical was present and DME was provided, the reaction continued. The proposed reaction channels for the presence of the OH radical are given in Eq. 2.1 and Eq. 2.2 [22]:



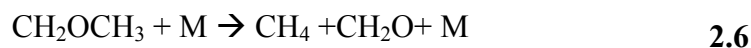
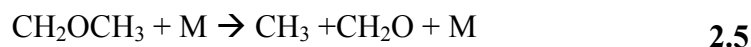
From other work, the proposed decomposition reactions include the following chain reaction in Eq. 2.3 [21]:



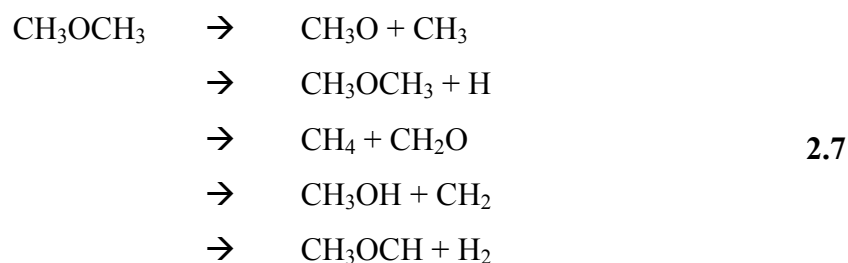
Then, a CH_3 radical abstracts a hydrogen atom from a second molecule of dimethyl ether by the reaction Eq. 2.4 :



The resulting CH_2OCH_3 radical then decomposes to formaldehyde and methyl radical, and then finally to formaldehyde and Methane, according to the following reactions Eq. 2.5 and Eq. 2.6 [21]:



Within this study, the author proposed and concluded the following competitive reactions through an ab initio calculation, given in Eq. 2.7 :



A focus on experiments to confirm portions and proposed mechanisms of DME kinetics in the low, intermediate and high temperature regions has yielded a better understanding of the oxidation mechanisms [23-25]. A schematic presentation of those mechanisms is shown in Figure 2.4 [24]. At low temperatures, the methoxymethyl radical (CH_3OCH_2) adds to molecular oxygen and forms the methoxymethyl-peroxy radical ($\text{CH}_3\text{OCH}_2\text{O}_2$) [24]. After an intramolecular H isomerization, this radical proceeds through a reaction scheme shown in Figure 2.4. In the ranges of temperatures from 550-600 K, chain branching is due to the reaction pathway leading through the carbonyl-hydroperoxide ($\text{HO}_2\text{CH}_2\text{OCHO}$) with the formation of two hydroxyl radicals. As the temperature increases above 600 K, the beta (β) scission of the hydroperoxy-methoxymethyl radical ($\text{CH}_2\text{OCH}_2\text{O}_2\text{H}$) increases [24]. This path produces one hydroxyl radical and 2 molecules of formaldehyde, decreasing the reactivity of the system and leading to the NTC region between 600-725K. When the temperature reaches above 730 K, the hydrogen peroxide (H_2O_2) dissociates into two hydroxyl radicals leading to the rapid consumption of the rest of the DME fuel [24].

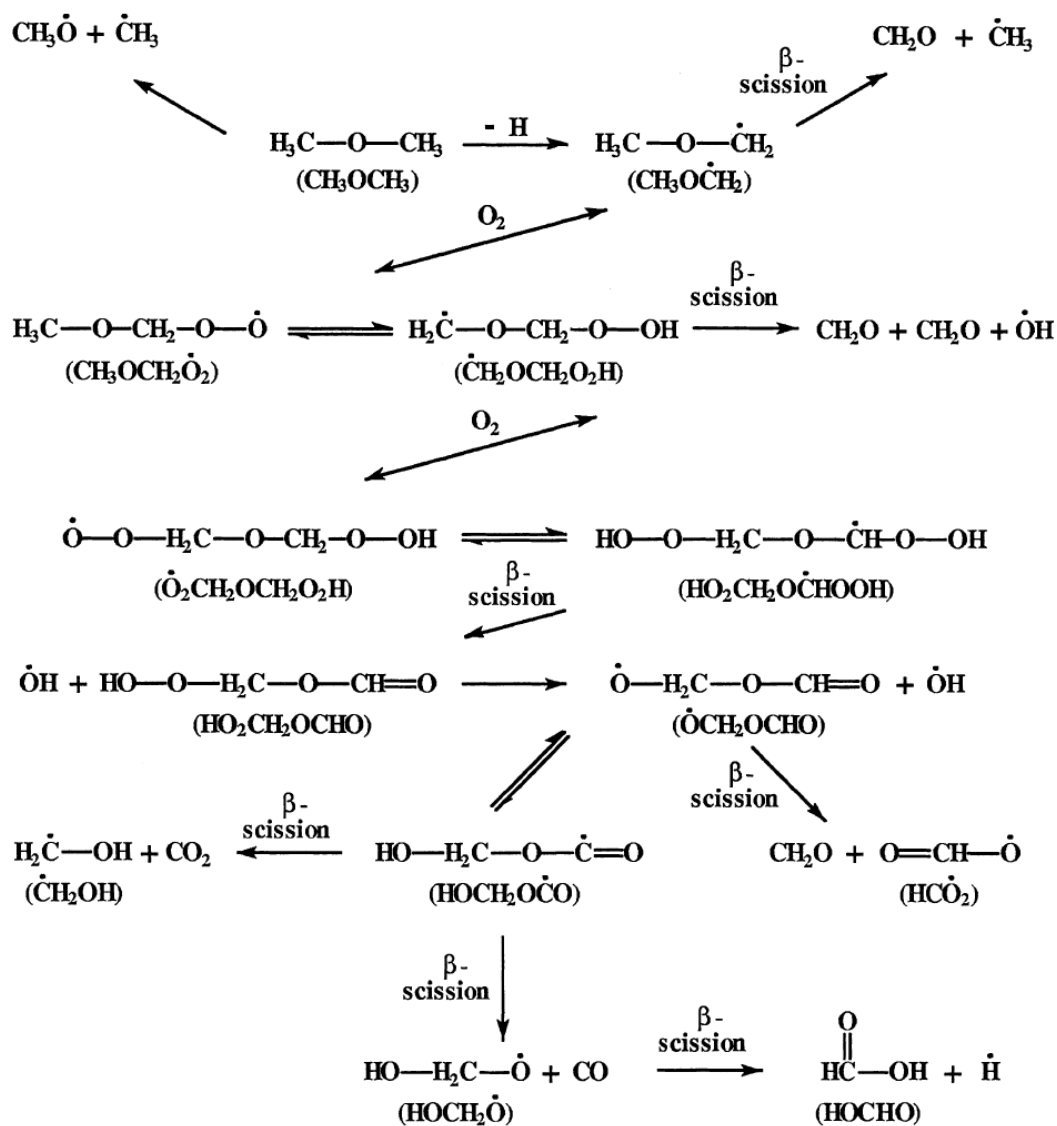


Figure 2.4: Overall reaction scheme for dimethyl ether oxidation [24]

Dagaut and coworkers performed experimental and detailed kinetic modeling studies of the low temperature oxidation of DME with NO to determine the sensitivity of the reactions of DME in the presence of NO [26]. It was shown that above 600K, NO enhanced the oxidation of DME and yielded methyl formate, and the NO was oxidized to NO₂ [26]. Below the 600K, the oxidation of DME was inhibited by the NO [26]. They

present a detailed chemical kinetic mechanism and go on to explain the reactions that inhibit DME oxidation below 600K [26].

Pfahl and coworkers' research confirmed that DME exhibits the typical two stage heat release characteristic of some hydrocarbons, that has since been shown in research from Dec and Flynn [13].

2.3 Diesel Emissions

The previously described combustion process results in some emissions that are undesirable. Diesel engines have been traditionally high emitters of NO_x and particulate emissions. Other pollutants include carbon monoxide (CO) and unburned hydrocarbons (HC). These are typically very low for a diesel engine since the air –fuel mixture is lean of stoichiometric [11, 27]. The following sections will focus on the two major pollutants from a diesel engine, NO_x and particulate matter.

2.3.1 Diesel Combustion Conceptual Model

Several researchers have developed and expanded on the conceptual model of diesel combustion [28, 29]. Figure 2.5 shows the most currently accepted model for the diesel fuel spray and flame developed from laser-based measurements [29]. As the liquid fuel leaves the nozzle and travels out as a jet, it rapidly entrains hot air in the cylinder thus initiating fuel vaporization [19]. This leads to the formation of a boundary of fuel-vapor and air mixture in the shear layer along the sides of the fuel jet. The beginning part

of the fuel oxidation process takes place as the fuel-vapor and air mixture enters the jet. The final oxidation process takes place around the edges of the jet. Figure 2.5 shows this 2 stage fuel oxidation process. The region of this fuel-vapor and air mixture can have an equivalence ratio from 2-4. In Dec's research, the NO_x emissions are produced in the thin layer around the diffusion burning interface. This interface is identified by a thin layer of OH fluorescence [19].

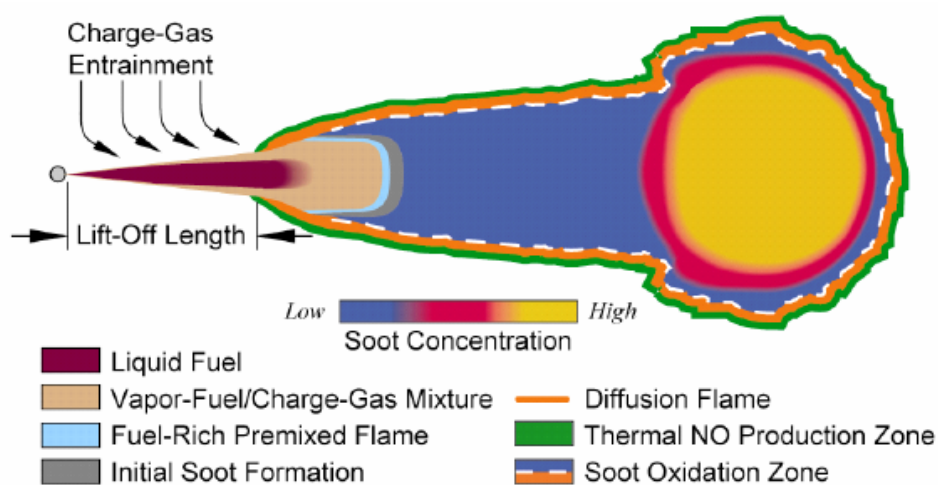


Figure 2.5: Schematic of the conceptual model of DI diesel Combustion [29]

Figure 2.6 provides additional detail on the thermal and chemical variations inside the burning fuel spray plume. Cold liquid fuel enters the warm air supplying the reactants of a rich premixed zone that feeds the interior of the plume. The rich combustion products are oxidized at the surface of the diffusion flame. It is believed that no free oxygen is available inside the diffusion flame layer. The diffusion flame layer has the constituents and temperature for the formation of diesel particulate [19].

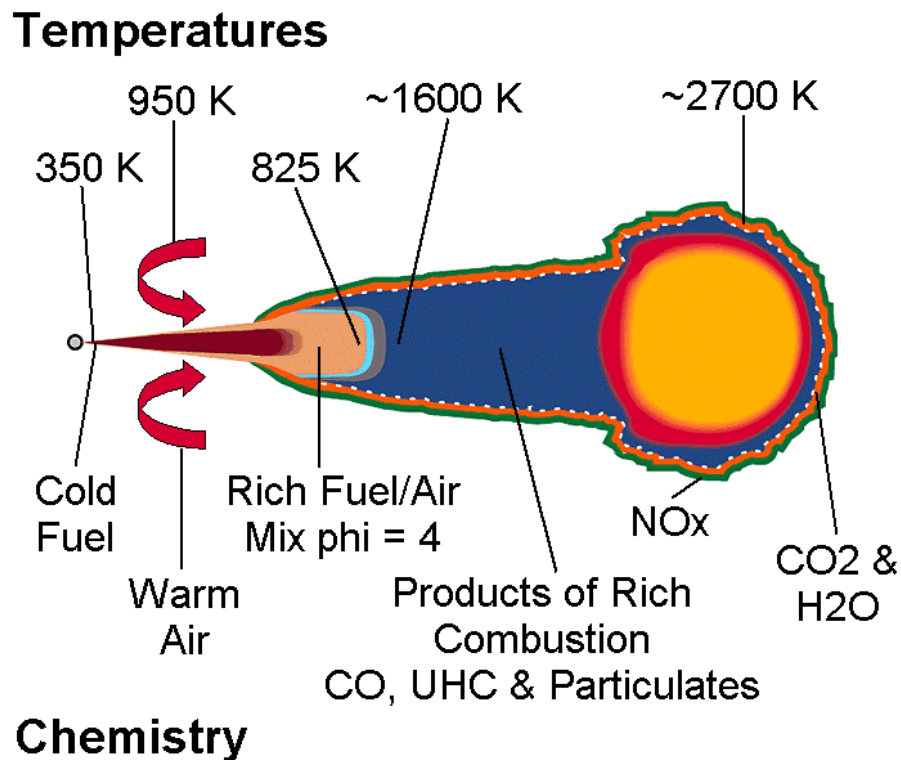


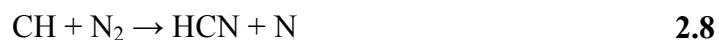
Figure 2.6: Summary of the fuel burning process [19]

2.3.2 NO_x Emissions

Oxides of nitrogen (NO_x) are formed as a result of the combustion process. NO_x includes NO and NO₂. Diesel engines produce significant amounts of NO_x, depending on the load conditions of the engine. Of the 100 to 2000 ppm which is produced, the majority of this (greater than 80%) is nitric oxide (NO), with the balance being NO₂ [11]. There are several mechanisms for the formation of NO_x: Fuel NO, Thermal NO, Prompt NO, and NO₂.

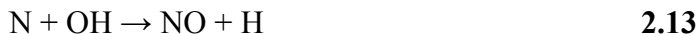
Fuel NO comes from the oxidation of fuel-bound nitrogen to an oxide of nitrogen. However, the fuels used in this research have little or no fuel bound nitrogen. While the initial fuel bound nitrogen is not present, there are fuel radical-bound nitrogen reactions that play a role in the formation of NO. Those postulated reactions, also typically called the fuel reburn reactions, are shown in Figure 2.7 and act in the same manner as the prompt NO mechanisms.

The amount of prompt NO typically is considerably smaller than the amount formed by the thermal NO mechanism. The prompt NO mechanism (or sometimes called the Fenimore mechanism) occurs as a result of hydrocarbon species (CH or C₂) and atmospheric nitrogen in the flame zone and occurs very rapidly [30]. Their reaction in the flame zone could make nitrogen available for oxidation in addition to CN and HCN, and thus leads to NO production. The Fenimore reactions that are the main focus are shown in Eq. 2.8 and Eq. 2.9, where Eq. 2.8 is the primary reaction and rate limiting [31, 32].



When the equivalence ratio is less than 1.2, the reactions proceed from hydrogen cyanide (HCN) according to the following chain sequence Eq. 2.10, Eq. 2.11, Eq. 2.12 and Eq. 2.13 [31]:





Eq. 2.13 is also a reaction involved in the thermal NO mechanism, as well.

The main reactions for zones where the equivalence ratio is above 1.2 are shown in Figure 2.7, where the NO is recycled to HCN in a slower reaction scheme and where NO is actually destroyed [31-33].

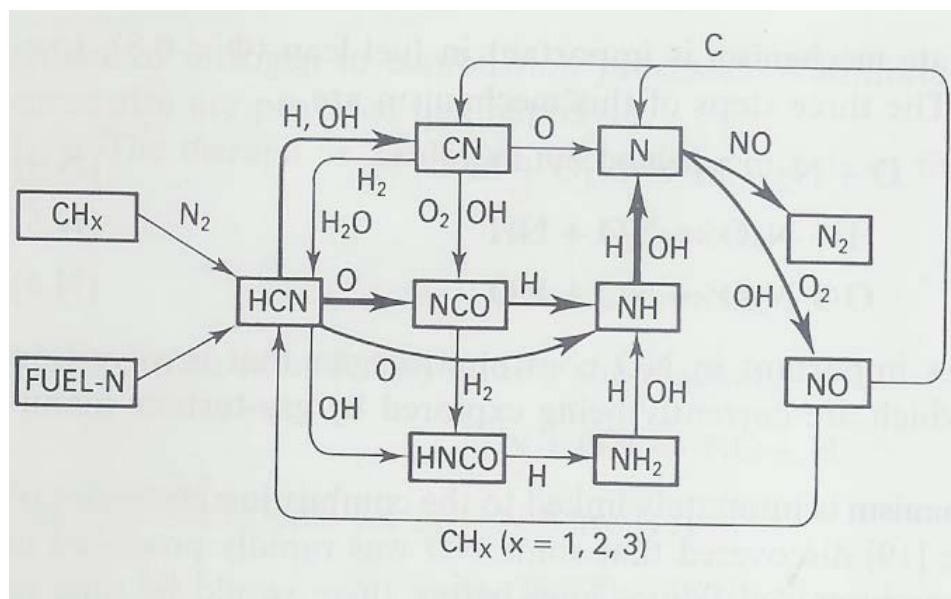


Figure 2.7: NO production associated with the Fenimore prompt mechanism [32, 33]

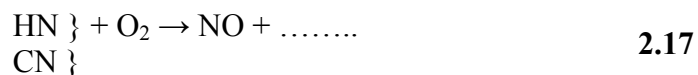
In the case of the diesel engine, the most significant mechanism is the extended Zeldovich mechanism, also known as the thermal NO mechanism in which NO is typically found and formed in the post flame zone at a slower rate than the prompt NO.

The extended Zeldovich mechanism consists of the following three reactions, Eq. 2.14 , Eq. 2.15, and, Eq. 2.16 .



NO formation is strongly dependent on temperature [11]. It is typically formed during the first 20 degrees of crank angle, after the start of combustion. Therefore, emission reduction strategies target this time period, and aim to reduce the combustion temperatures [34].

NOx also includes NO₂ emissions. Glassman discusses briefly the literature on contributions to NO₂ emissions reported in exhaust gases and in flames [12]. He notes that these results seem surprising since kinetic models have indicated that NO₂ formation and reduction can be neglected in practical devices. Merryman and Levy examined NOx formation in a flat flame burner operated near stoichiometric conditions [35]. They postulated a series of reactions that represent their findings, shown below in Eq. 2.17, Eq. 2.18, and Eq. 2.19 :





In the low temperature regions of the visible flames, they measured large concentrations of HO₂ that can react with the NO in the high temperature regions and diffuse back to the lower temperature regions of the flame [35]. They also found that NO₂ is consumed rapidly in the near post flame zone, where the NO concentration also rose. The significant reaction is represented by Eq. **2.18** [35]. Glassman suggests that the NO₂ formation is further supported by the fact that Eq. **2.18** is two orders of magnitude faster than Eq. **2.19** [12]. Cernansky and Sawyer also concluded from their experiments with turbulent diffusion flames that the high levels of NO₂ were a result of the HO₂ reaction with NO and O atoms [36]. Hilliard and Wheeler also showed the presence of NO₂ in engine exhaust [37].

More recent research has focused on the hydrocarbons in the turbulent diffusion flame [38-41]. Hori has investigated low concentrations of various hydrocarbons below C₄H₁₀ and their effect on NO₂ conversion between 600 K and 1100 K. Meunier and coworkers focused on the formation and destruction of NO in a propane diffusion flame. They showed that the prompt NO_x mechanism was a dominant route, in addition to the reactions between NO and hydrocarbon radicals such as HCN in what is typically described as fuel reburn. Cheng, Mueller and coworkers have also shown the increase in NO₂ emissions with the decrease in NO emissions in a dilute mixing controlled combustion in an optical direct injection diesel engine [42-44].

2.3.3 Particulate Matter Emissions

Particulate matter can be defined as the combination of soot, condensed hydrocarbons, sulfates, oil, and water that attach to agglomerated soot particles in the exhaust stream [45]. Soot formation takes place in an environment in the engine that is 1000 to 2800 K and at pressures from 50 to 100 atmospheres [11]. Particulate matter can also be divided into two separate groups, the soluble and the insoluble fraction [46]. The insoluble fraction is comprised mainly of the elemental carbon formed in the diffusion flame that agglomerates into soot. The soluble portion of the particulate matter emissions are the hydrocarbon species that condense and adsorb on the insoluble portion. The aerosol of solid phase particles in the exhaust gas are further described by the total amount of the condensed phase per unit volume of the exhaust gas, and the number of soot particles per unit volume with a specific size diameter characteristic range of the total group [11]. For particle sizing, the particles are typically assumed to be spherical, while TEM photos show that this is not the case. Figure 2.8 is a representation of the various types of compounds present in particulate matter emissions.

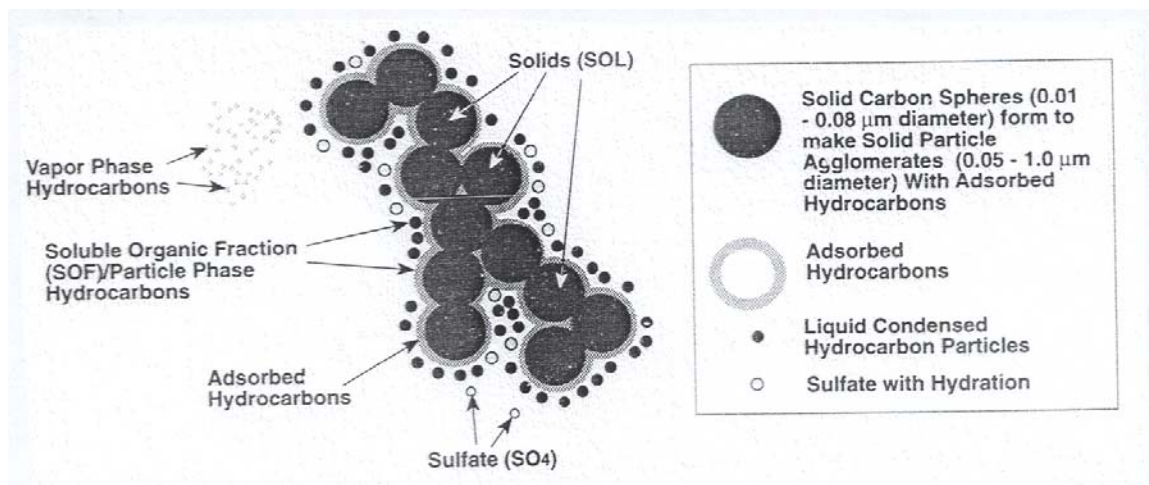


Figure 2.8: Schematic of Diesel Particles and Vapor Phase Compounds [46]

Detailed modeling and experiments have been conducted to try to understand the soot formation process in different types of flame structures and in flames of various fuels [47]. It has been established that several classes of hydrocarbons, namely polycyclic aromatic hydrocarbons (PAH) and acetylene (C₂H₂), are important precursors to soot formation and are created in fuel-rich conditions [11, 48]. From the initial formation of a benzene ring, the soot particle increases in size through the addition of acetylene [48]. The adsorption and condensation of the hydrocarbons occurs after the soot leaves the cylinder and begins to cool in the exhaust gas stream [11].

2.4 Emissions Reduction Strategies

Emission control strategies can be divided into three categories: pre-combustion, in-cylinder, and post-combustion [49, 50]. A list of common approaches for each area can be found below in Figure 2.9 [49]. For many years, diesel engines have escaped the

necessity of post-combustion controls because of modifications which could be made to fuel or to the engine to meet any new set of emissions regulations. However, an important requirement for implementation of many post-combustion technologies is the reduction of the sulfur content of the fuel, i.e. , the pre-combustion area. This was just accomplished with the introduction of the ultra low sulfur diesel fuel (ULSD) in October of 2006 mandated by the EPA [8, 10]. The following discussion will focus on the pre-combustion, in-cylinder, and post –combustion strategies of controlling NO_x emissions and particulate matter emissions.

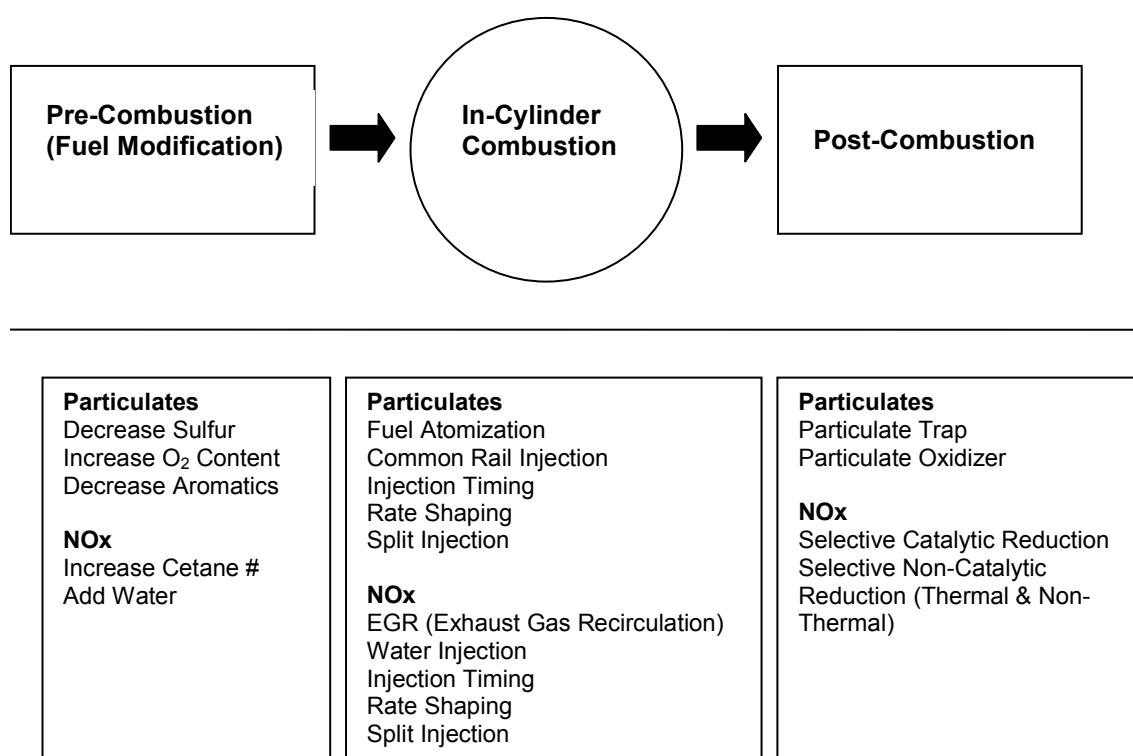


Figure 2.9: Emissions Control Strategies for Compression Ignition Engines [49]

2.4.1 Pre-Combustion Strategies for Emissions Reduction

Many researchers have shown that the properties of diesel fuels in combination with engine technology can greatly affect the engine out emissions [51]. With the current research focus shifting to demonstrating alternative compression ignition fuels from non-petroleum sources in diesel engines, much research is bringing to light ways to reduce exhaust emissions, including particulate matter emissions, through changes in fuel formulation.

To enable the implementation of particulate and NO_x control technologies, the US EPA has mandated that ultra-low-sulfur fuels be available to enable advanced aftertreatment strategies, which can be highly sulfur sensitive [52]. Modification of diesel fuel composition, for example, by blending with oxygenated fuels, also can contribute to reducing emissions. The addition of biomass-derived fuels and synthetic fuels to diesel fuel base stocks is a means of producing a cleaner burning diesel fuel. Blending with oxygenated or zero sulfur fuels can lead to particulate emissions reductions by interfering with the soot formation process and by decreasing the formation of sulfates. However, in the case of biodiesel fueling (e.g., “B20”, a blend of 20 vol.% methyl soyate in diesel fuel) there is a well documented increase of 2-4% in NO_x emissions [53].

Hess showed that there could be 10% brake specific particulate matter reduced with just 2% oxygen addition in the fuel [54]. Hess used such oxygenates as monoglyme and diglyme, from the family of glycol ethers. Hess’s work also showed that with each 1% of oxygen blended above 2%, the improvement of the particulate matter reduction

decreases until approximately 7% oxygen blended into the fuel, and yields about 7% brake specific particulate matter reduction.

The recent requirement for fuel sulfur reduction to allow for the use of exhaust catalysts also gave way to the added benefit of particulate reduction [9, 10, 55]. Fuel sulfur has been shown to contribute to a total particulate matter mass in the form of sulfates [56].

Other alternative compression ignition fuels from non-petroleum sources are of significant interest and have been shown to reduce or increase exhaust emissions. Two of these fuels for compression ignition engines will be discussed as they are used in this research: Dimethyl Ether and Biodiesel.

2.4.1.1 Dimethyl Ether

Dimethyl ether (DME) has been considered for use as a fuel in compression ignition engines since the early 1990s. Fleisch and coworkers demonstrated a Navistar diesel engine meeting the California ULEV emissions while operating on DME [57]. The exciting results have suggested that the DME is a potential fuel for the future that can meet the stringent emissions. The following section gives a brief overview of DME.

DME is a compound that has been targeted for future use as a fuel, in several countries around the world, including Japan, China, and Sweden [58-60]. Motivation to use DME exists for several reasons. There has been confirmation that the fuel yields low particulate emissions and possibly lower NO_x emissions [57, 61, 62]. In addition, DME

can be made from a variety of feedstocks including coal, biomass, and natural gas via the synthesis gas process, which can support the use of alternative energy resources [63, 64].

Compounds in which two hydrocarbon groups are bonded to one oxygen, represented as R-O-R', are called ethers. The organic groups bounded to the ether may be alkyl, aryl, or vinylic, and the oxygen can either be in an open chain or ring configuration [65]. Ethers commonly observed in long chain structures are referred to as linear ethers. As compared to alkanes of similar carbon number, the boiling points of ethers are higher [65]. This class of oxygenated compounds have high cetane numbers and excellent cold flow properties [66].

Simply stated, dimethyl ether is an ether with a methyl group on each side of an oxygen atom. Today, it is predominantly used as an aerosol propellant because it is not harmful to the ozone layer, in contrast to the chlorofluorocarbons used previously [64]. Also, it is virtually non-toxic and is easily degraded in the upper atmosphere [67]. It can be represented by the symbol: CH₃-O-CH₃. The physical properties of DME are shown in Table 2.2 along with some other fuels for comparison [57, 61, 68, 69].

Table 2.2: Physical Properties of DME [57, 61, 68, 69]

Property	DME	Diesel	Propane
Chemical Formula	C ₂ H ₆ O	C _{10.8} H _{18.7}	C ₃ H ₈
Mole Weight	46.07	148.6	44.11
Critical Temperature- °C	127	-	95.6
Boiling Point- °C	-24.9	71-193	-42.1
Vapor Pressure at 20 °C-kg/m ²	5.1	<0.01	8.4
Critical Pressure-bar	53.7	-	43
Liquid Viscosity- cP	.15	2-4	.10
Liquid Density at 20 °C-kg/m ³	668	800-840	501
Bulk Modulus (N/m ²)	6.37E+08	1.49E+09	
Specific Density, gas	1.59	-	1.52
Solubility in H ₂ O at 20 °C g/l	70	Negligible	.12
Lower Heating Value- kJ/kg	28430	42500	46360
Heat of vaporization- kJ/kg 20°C	410	233	426
Explosion limit in air- vol%	3.4-17	1.0-6.0	2.1-9.4
Ignition temperature at 1 atm- °C	235	250	470
Cetane Number	55-60	40-55	-

The cetane number describes the ignition quality of the fuel. The shorter the ignition delay the better the ignition quality of the fuel, and thus, the higher the cetane number. Since DME has a higher cetane number than conventional diesel fuel, it will ignite readily and burn more completely.

The viscosity of DME, as a liquid, is much lower than that of diesel fuels. This offers an advantage in that the fuel will be easier to deliver into the engine cylinder than diesel fuel during cold weather conditions. However, some studies have shown that DME leaks from the fuel injectors [70, 71]. In addition, using neat DME within an engine creates some lubricating problems because of the low viscosity. Researchers are now understanding that the fuels used in automotive fuel injection systems have inherent

lubricating traits which are a very significant factor, especially when additives and alternative fuels are being considered [72-75].

The boiling point of DME is another important advantage for its use as a fuel. Again, it proves to have better characteristics for cold starting conditions, which is a key factor in engine development.

The vapor pressure of DME is a concern. Since the fuel is a gas at atmospheric pressure, to use it as a liquid one would need to mix the fuel with a lubricity additive and inject the fuel as a liquid with the entire fuel system pressurized [76]. This leads to other complications with fuel delivery, although the technology to do this is similar in nature to LPG (Liquid Propane Gas) because LPG is also moderately pressurized to keep it in a liquid state [77].

Another important aspect of combustion emissions from a diesel engine fueled on DME versus diesel fuel, is the reduction and elimination of particulate emissions. Particulate emissions can be observed as a black smoke emitted out the tailpipe. The oxygen content of a fuel blend with DME (at roughly 40 to 100 wt.%), allows for the emissions to be smokeless, as shown in the literature [57, 61, 69, 78-81]. DME has a 34.8% oxygen content as a neat fuel. Nabi and coworkers showed “smokeless” engine operation from a diesel fuel with an oxygen content at around 38 wt. % [78]. However, work by Chen and coworkers confirms that even with 80 wt.% DME addition to diesel fuel, some smoke will be produced at high engine loads, even though it is a small amount [81].

The heating value of DME is a concern, because the heating value of diesel is roughly 1.7 times that of DME. This results in the need for more volume of fuel to produce the same output from combustion. By altering injection amounts to the cylinders, the amount can be compensated to counteract the decreased heating value and prevent “de-rating” of engine output.

Dimethyl Ether (DME) has been shown to reduce PM and NO_x emissions [57, 82-86]. Not only has DME been demonstrated theoretically and experimentally to exhibit rapid reaction chemistry, but also DME has been shown to reduce NO and CO emissions in premixed flames [87]. In comparing DME with propane and butane in a fuel equivalence ratio range of 0.6 to 3.2, DME demonstrated reduced CO emissions, and less striking, NO reduction over the other two fuels. As a result of finding higher equilibrium NO concentration with DME, it was determined that this was due to a higher adiabatic flame temperature over the entire stoichiometric range in comparison to propane and n-butane[87]. However, Frye concedes that in all comparisons made on the NO emissions, DME gave at worst the same result as propane and n-butane[87].

The US does not currently have in place facilities for the manufacture of DME on a fuel production scale or the infrastructure available for the use and distribution of the fuel. This fuel has been considered in many economic models and studied as a fuel to achieve tripled fuel economy, but it is not currently a fuel being considered for use in US vehicles, and thus no on-road vehicles are in trials or production [88-92]. It has been reported that DME acts similarly as LPG fuel and the LPG fuel transport lines could be used to transport and distribute DME in a more widespread capacity [93, 94].

The research discussed in Chapter 5 uses DME as the fumigated fuel in a Mixed Mode Combustion process. That research exploits the unique low temperature ignition quality of DME.

2.4.1.2 Biodiesel

Biodiesel has received rapidly growing interest as a fuel to blend with existing diesel fuels. Biodiesel is an alternative diesel fuel created by the conversion of oils, fats and fatty acids to methyl and ethyl esters via esterification processes [95]. A variety of vegetable oils and animal fats provide the source of the triglyceride fats and oils [96]. Continuous feedstock growth and livestock production provide a constant supply of source material allowing biodiesel to be a renewable source of fuel, which can be created domestically [97].

Additionally, biodiesel is miscible with petroleum-based diesel and works in any diesel engine with little or no modifications as pure biodiesel or as a blend with any other diesel fuel. In fact, biodiesel contains a higher oxygen (~ 11 wt. %) content resulting in a more complete combustion of the fuel, reducing emissions of particulate matter, unburned hydrocarbons and carbon monoxide. Sharp and coworkers' research showed a 40% reduction in CO emissions using neat biodiesel in modern diesel engines, while hydrocarbon emissions were eliminated [98]. They also tested a 20% biodiesel blend and found a comparable and proportional trend in the emissions [98].

While there are many benefits to biodiesel, studies have shown that engine emissions using biodiesel fuels typically increases emissions of oxides of nitrogen (NO_x)

[53, 97]. This compiled data from the US EPA is shown in Figure **2.10** [53]. For a 20% blend of biodiesel in diesel fuel, on average, a 2% increase in NO_x emissions is observed. However, this EPA study was the culmination of much research on heavy duty diesel engines that have various types of diesel engine injection equipment. Research is now focused on the fuel property aspects of the biodiesel and how this affects the resultant NO_x emissions. The EPA study also prompted more research into the effect of biodiesel on Light Duty Diesel engines, as this was missing from the initial review. Duffield, Shapouri, Grabowski, McCormick, and Wilson's report, "U.S. Biodiesel Development: New Markets for Conventional and Genetically Modified Agricultural Products", has also prompted further research into improving biodiesel in the areas of NO_x emissions, viscosity, and oxidative stability to allow biodiesel to become a commercially acceptable fuel [97].

One approach to improving the properties of biodiesel fuels is to increase the degree of saturation of the ester molecules contained in the biodiesel. The saturation of the biodiesel fuel is often measured and reported as the iodine value. McCormick and coworkers showed a correlation between the iodine value and NO_x emission from various biodiesel feedstocks [99]. Figure **2.11** shows the correlation developed by McCormick and coworkers between the iodine value of biodiesel from various feedstocks and the resulting NO_x emissions from the use of the fuel. Researchers are pursuing modifying the soybean oil through genetic engineering of the soy plant to increase the oleic acid content [100]. Increased saturation can also be achieved by hydrogenation of the biodiesel fuel. Chapter 4 of this research presents a study of the emissions characteristics from a light duty diesel engine from the blending of a hydrogenated soy based biodiesel

with low sulfur diesel. In this research, the EGR is removed so that the NO_x reduction effect of the EGR does not complicate the actual reductions or increases achieved by the fuel.

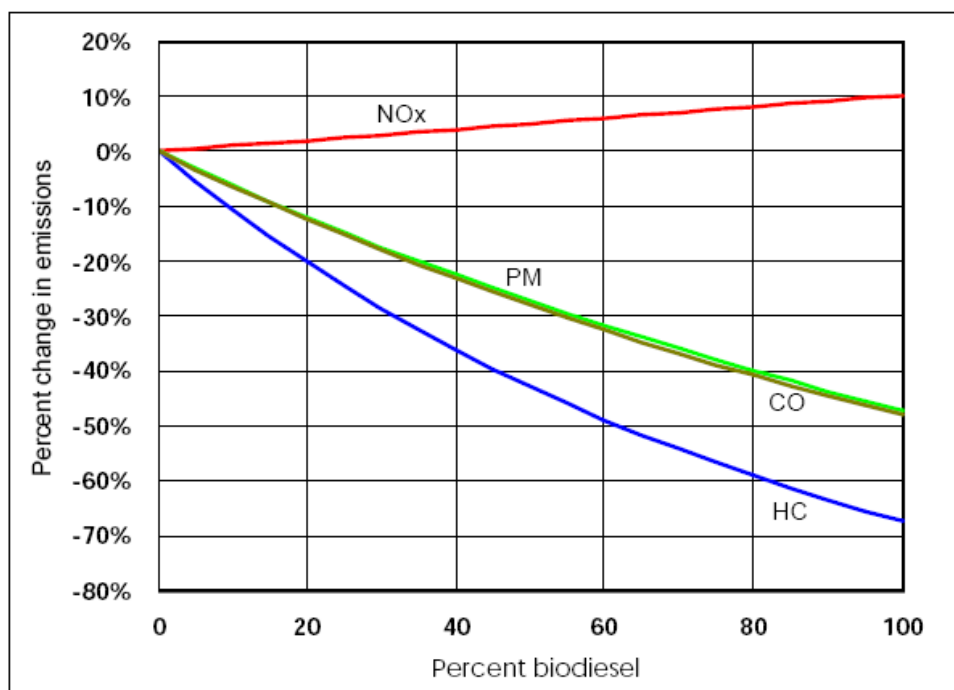


Figure 2.10: Average emissions impacts of biodiesel for heavy-duty highway engines [53]

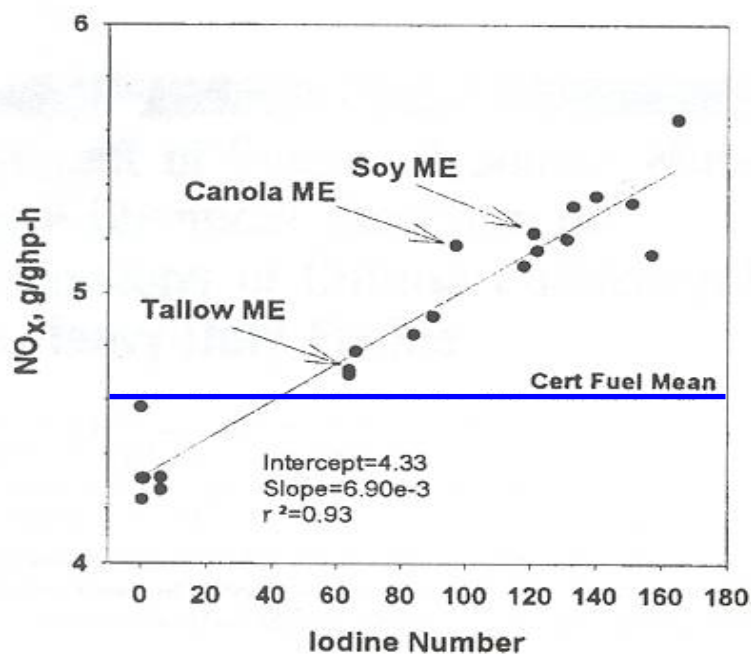


Figure 2.11: Iodine Value vs. NO_x [99]

2.4.1.3 Iodine Value of Biodiesel Fuels

The iodine number is a measure of the degree of unsaturation of the esters within biodiesel fuels [95, 99]. A fuel containing a higher degree of unsaturated esters will have more double bonds within the fatty acid chain than that of a fuel with a lower degree of saturation. According to McCormick and coworkers, a lower iodine number results in less nitrogen oxide emissions than a biodiesel fuel with a higher iodine number [99]. This correlates with his other observations because a biodiesel fuel with a higher iodine number will have a lower cetane number and a higher density [101, 102]. However, McCormick and co-workers observed that a higher degree of saturation decreased the

boiling point and viscosity of the biodiesel fuels that were tested resulting in poor cold flow properties [99].

Thus, fuel properties are very interrelated with each other and with engine performance. The fuel properties and their relationship to the combustion of the hydrogenated and normal soy based biodiesel fuel are further investigated in Chapter 4.

2.4.1.4 Theories about Biodiesel and NO_x

The increase of NO_x emissions as a result of the use of biodiesel in an engine has not clearly been understood. Recent reviews of the emissions results are clearly showing increases and reductions of NO_x emissions depending upon engine size, fuel injection type, fuel injection strategy, and engine testing strategy. Researchers have given various explanations [103-106]. This section will explore the current explanations given for the biodiesel NO_x effect. The current theories include: 1) Adiabatic Flame Temperature, 2) Flame Radiation, 3) Mixing, 4) Prompt NO_x, 5) Fuel Injection Timing, 6) Cetane Number, 7) Mixture Stoichiometry at the Lift-Off Length, 8) Oxygen Content of the Fuel, 9) Fuel spray characteristics, such as droplet size and air entrainment.

Adiabatic Flame Temperature: The conceptual model of the diffusion or mixing controlled phase of diesel combustion suggests that NO_x is formed on the lean side of the flame [29]. Dec also confirmed this model through laser based measurements [107]. Thus, the flame temperature in the diffusion zone in close proximity to the NO_x formation zone has an influence on the thermal NO_x formation. Some authors state that the adiabatic flame temperature of the fuel is higher for biodiesel fuels [108-110], while

others state that it is higher for diesel fuels [111, 112]. Cheng and coworkers found no significant difference between methyl oleate and a primary reference fuel in calculations for the stoichiometric conditions representative of those in the diffusion flame [42].

Flame Radiation: The flame radiation theory relates to the reduction of soot volume fraction as a result of using a biodiesel fuel or fuel blends. Musculus showed that soot radiation from the flame zone may cool down the diffusion flame temperature and thus lead to a reduction in NO_x emissions [113, 114]. Since there is less soot in the diffusion flame region during the combustion of biodiesel, this can lead to a reduction of soot radiation from the flame region and result in higher flame temperatures [113, 114]. Cheng and coworkers used spatially integrated natural luminosity (SINL) in an optically accessible single cylinder Caterpillar 3176 engine to view the change in the luminosity of the soot radiation with different fuels [42]. In their research, the timing of the start of combustion for each fuel was matched to keep the overall combustion timing the same. Their research shows that there is less luminosity for biodiesel in comparison to the reference fuel with increasing engine load, suggesting that the reduction in flame radiation may be increasing the peak flame temperature and thereby NO_x emissions [42].

Mixing: In the literature, a connection between the premixed-burn fraction and NO_x emissions has been demonstrated [113]. Musculus has shown that as the premixed-burn fraction increases, NO_x emissions increase. The timing of the premixed-burn fraction can be a function of the injection timing, or more importantly the ignition delay of the fuel. A smaller premixed-burn fraction would be attributed to a shorter ignition delay.

Prompt NO: Prompt NO is formed by reaction of radical HC species with nitrogen, leading to the formation of NO [33]. It can account for a significant portion of the NO_x formation [33]. Researchers have suggested that prompt NO (also known as Fenimore NO) is the reason for the increase in NO_x emissions, and not the Zeldovich mechanism (thermal NO) [99, 115]. They speculate that during combustion of the biodiesel fuel, the double bounded molecules cause higher levels of certain hydrocarbon radicals in the fuel-rich zone of the diesel combustion spray [110]. Ban-Weiss and coworkers used numerical simulations of methyl butanoate to show that the Fenimore mechanism contributes to 13% of the overall NO_x emissions [110]. They also confirmed with a comparison to methyl trans-2-butenoate that the double bond produces an increase in the flame temperature of 14 K, which resulted in a 21% increase in the NO_x emissions [110].

Fuel Injection Timing: An advance of the start of injection due to the physical property differences between diesel fuel and biodiesel fuel has been proposed and shown to be a contributor to the NO_x emissions increase [103]. Szybist and coworkers showed that this trend of injection timing advance directly correlated to a NO_x increase, and explained this was due to the elevated bulk modulus of compressibility of the biodiesel fuel [116]. This work was performed with a pump-line-nozzle fuel injection system. This advance is also seen as a result of a change in the throttle position as a result of the additional biodiesel fuel required due to the reduced heating value of biodiesel [117]. While Boehman and coworkers established a relationship between the bulk modulus of the fuel and fuel injection timing [118], Szybist and coworkers concluded that the dominant effect for the particular engine being tested was the timing of maximum heat

release and maximum cylinder temperature[119, 120]. Recent work performed with a light duty diesel engine equipped with a common rail injection system showed that the system exhibited no measurable injection timing shift when biodiesel blends were used [121]. However, biodiesel blends exhibited higher maximum needle lifts, longer injection durations, and higher rail pressures to deliver the required fuel as a result of the change in heating value with biodiesel [121].

Other researchers have studied how the impact of multiple injection strategy affects NO_x emissions when using biodiesel fuels. Choi and coworkers showed that at high load, a split injection strategy had no effect on NO_x emissions, but at low load, NO_x decreased and the effect seemed to be dependant upon the start of injection [122]. Utilization of a pilot injection is becoming important in modern diesel engines as a means to reduce the combustion noise level. The pilot injection decreases the premixed-burn fraction intensity of the combustion process. Zhang studied the pilot injection effect in a 4 cylinder DI diesel engine [123]. While his studies showed that the NO_x emissions could be reduced with the use of EGR and without pilot, there was an increasing amount of smoke emissions with the pilot injection and a slight increase in the NO_x emissions [123]. Zhang looked at the change in the interval between the pilot and the main injection and saw little change in the NO_x emission level, showing that this can be used to reduce combustion noise and have no effect on NO_x emissions [123]. Senatore and coworkers showed in their work that “by varying injection start advance and EGR percentage” for biodiesel, these were effective measures to produce the same NO_x emissions produced from a EURO IV Common Rail Diesel Engine [124].

Cetane Number: Biodiesel fuel tends to have a higher cetane number than diesel fuels. Based on this data, it would be expected that biodiesel would reduce the NO_x emissions since it would produce a shorter ignition delay and thus a shorter premixed-burn fraction [42]. Hence, cetane number alone may not be an effective measure of the ignition behavior of the fuel.

Mixture Stoichiometry at the Lift-Off Length: Cheng and coworkers suggest that the mixture stoichiometry at the lift-off length of the fuel from the injector nozzle may be different between diesel and biodiesel and thus plays a role in the NO_x increase, but the mechanisms for this are unknown [42]. Choi and Reitz showed through numerical simulation that the spray tip penetration and fuel mass injections increase with biodiesel blended in diesel fuel [125].

Oxygen Content of the Fuel: Some researchers suggest that the higher oxygen availability in the combustion chamber as a result of the oxygen in the fuel contributes to the NO formation process [126, 127]. Schmidt and coworkers showed that enriching the intake air with oxygen led to the same NO_x increase exhibited with the increase in oxygen of the biodiesel fuel. Iida and coworkers also showed an increase in NO_x emissions with an increase in the oxygen in the intake air. Song and coworkers showed that both the enrichment of the intake air and the oxygenated fuel gave an increase in the NO_x emissions [128]. The increase was higher for the enriched intake air than for the use of the oxygenated fuel. Other researchers argue against the presence of oxygen in the fuel as an explanation of the NO_x increase. Lupuerta and coworkers made this conclusion because the diffusion combustion is occurring in regions of stoichiometric oxygen-fuel ratio, and thus the oxygen in the fuel is not enough to make a difference in

the flame chemistry [108, 129]. Yuan and coworkers tried to find a correlation between NO_x and fuel oxygen content, but were unsuccessful [130].

Fuel Spray Characteristics: The fuel spray characteristics, including droplet size distribution, droplet inertia, air entrainment, penetration in cylinder, evaporation rate, and heat dissipation are affected by the various fuel properties [95]. These fuel properties include viscosity, surface tension, cetane number, and the boiling range temperature of the fuels [95]. These physical phenomena have some influence on the ignition delay time, and thus on the premixed-burn fraction/ diffusion combustion ratio and in turn on the NO formation process [103]. If cetane number is not an effective measure of the ignition behavior of the fuel, then there are other fuel properties that would affect the premixed-burn fraction of the fuel and increase the NO_x emissions, in spite of the higher cetane number of the biodiesel fuel [42]. As mentioned previously, Choi and Reitz showed through numerical simulation that blends of biodiesel fuel require higher fuel mass injection rates and thus produce increased spray tip penetration in the cylinder [125]. This effect of mixing of a biodiesel fuel type and spray penetration into the cylinder was also shown by Yuan and coworkers [130].

2.4.2 In-Cylinder Combustion

There are several techniques which can aid in reducing NO_x emissions in the cylinder during the combustion process. These include exhaust gas recirculation (EGR), injection timing control, and fuel injection rate shaping [131-133]. The goal of these three techniques is to reduce the peak flame temperature which leads to thermal NO_x or

to reduce the time for the thermal NO reaction while still achieving the best BSFC for the particular engine condition. However, these techniques also have drawbacks. In altering the fuel injection timing to the cylinder, power decreases and fuel consumption increases. Also, reducing the peak flame temperature causes an increase in the level of soot emissions, due to the reduced kinetic rate for soot oxidation [49].

There are several new techniques being explored to simultaneously reduce the soot and NO_x emissions from the combustion process. These include Low Temperature Combustion (LTC), Homogeneous Charge Compression Ignition (HCCI), Premixed Controlled Compression Ignition (PCCI). Both LTC and PCCI have been shown to give high NO_x reduction and low particulate emissions [134]. PCCI differs from HCCI in that a direct injection of fuel prior to the main injection achieves air/fuel mixture gradients that are not truly homogeneous as in HCCI [135]. High levels of EGR are also associated with LTC and PCCI modes. Hardy and Reitz combined the effects of PCCI and diffusion-controlled diesel combustion to achieve emissions levels below the 2010 emission standards [135]. A map of the local combustion temperature and local equivalence ratio shows the range characteristics of the different combustion modes [134]. This map is shown in Figure **2.12**.

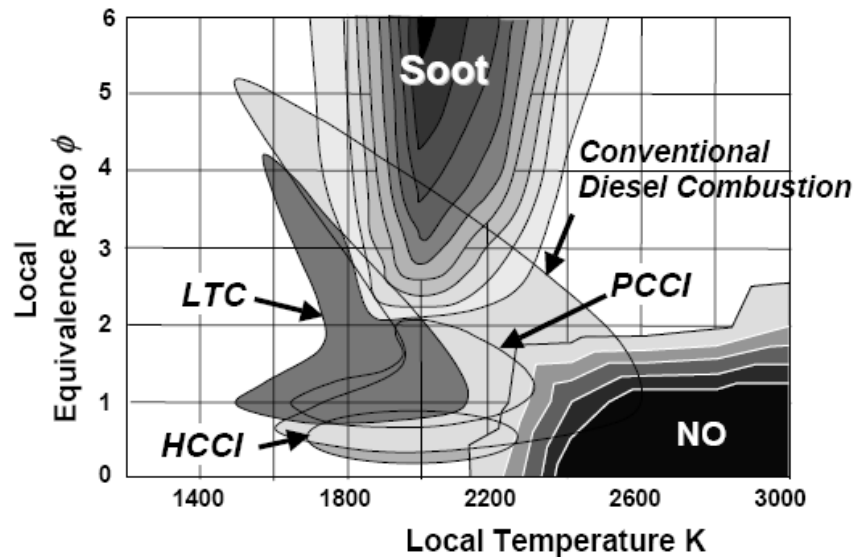


Figure 2.12: LTC and PCCI concept on Φ - T map [134]

2.4.2.1 Homogeneous Charge Compression Ignition (HCCI)

Homogeneous Charge Compression Ignition (HCCI) combustion occurs when a mixture of air and fuel, and sometimes recycled combustion products, is compressed until it autoignites [136]. The result is heat releasing reactions that initiate simultaneously at multiple sites in the combustion chamber. In contrast to diesel (diffusion –controlled) combustion, HCCI reactions are not limited by the mixing rate at the interface between the jet of fuel and the surrounding oxidizer. HCCI combustion differs from spark-ignited combustion because it has no discernible flame front and it has no localized high temperature reaction region [137].

For the purpose of the research involved in this project, the following definitions are introduced. Induction of a fuel and air mixture into an engine cylinder during the

intake stroke, and the compression of that mixture to ignition is referred to as homogenous charge compression ignition or HCCI. When using a diesel pilot as the ignition source for the homogeneous charge, the combination of combustion strategies is referred to as mixed mode combustion.

2.4.2.2 Variables involved in HCCI process

HCCI combustion displays a particular heat release curve with two distinct stages. The first stage of the heat release is associated with low temperature kinetic reactions (cool and/or blue flame) [136]. The time delay between the first and the main heat release is attributed to the negative temperature coefficient regime of the reactions [138, 139]. An example of the combustion parameter diagram is shown below in Figure **2.13** [140]. Research has shown that HCCI combustion initiates simultaneously in multiple locations in the cylinder and that there is no discernable flame propagation [138]. Most researchers believe that HCCI heat release is purely controlled by chemical reactions [136]. Since the reactions are not initiated by spark ignition and not limited by traditional flame sheet physics, leaner mixtures can be used in HCCI combustion [136].

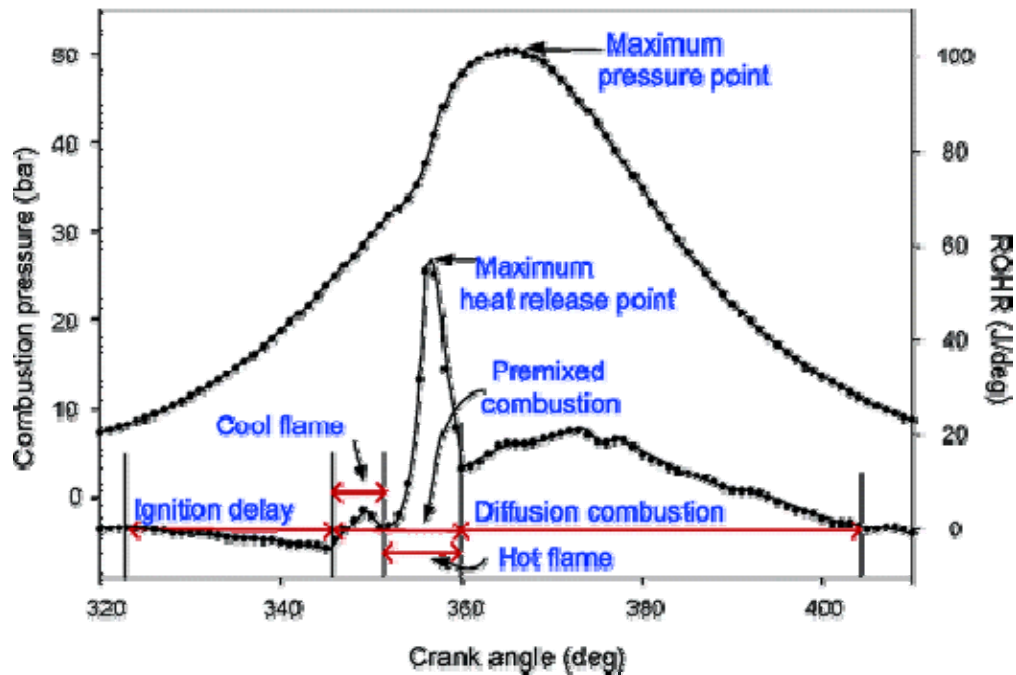


Figure 2.13: Definition of the combustion parameters [140]

Management of HCCI combustion in a practical system is a function of controlling the autoignition of the fuel which is dictated by the location of the low temperature reactions which then function to generate the high temperature reactions in the main heat release. Therefore, it is important to control the low temperature reactions [141]. Researchers have offered several methods to accomplish this, which include controlling the intake air temperature, modify the fuel blending, or turbocharging/supercharging the intake air charge [142, 143]. These are specific methods to modify the initial temperature of the fuel and air charge, without significant modifications to the engine, as would be required to implement variable compression ratio or variable valve timing [136, 144].

2.4.2.3 Types of Fuel Mixture Preparation for Compression Ignition Combustion

Throughout the development of the HCCI concept, there have been limitations discovered with the process. These include the increase in hydrocarbon and carbon monoxide emissions, the limitation on engine load that can be achieved both on the low end of operation (speed and load that operate the engine below 2.0 bar IMEP) and the high end of operation (speed and load the operate the engine above 3.5 bar IMEP) [145], and the ability to control ignition of various fuel types. Therefore, researchers have tried to resolve the issues with different types of fuel mixture preparation for compression ignition combustion which include HCCI –like concepts and testing with various fuels:

- Fuels (liquid and gaseous): Gasoline, diesel, naphtha, natural gas, butane, propane
- Fuel introduction: micro-atomization in air induction, fumigation, direct injection in cylinder
- Mixing: Homogeneous, partial mixed [135, 146]
- Ignition initiation: Through the compression of the fuel, initiated by a spark, initiated by a pilot injection

Though there have been many researchers working on the same issues over the last 10-15 years, some of the same questions still remain. Most importantly, the kind of fuel appropriate for the HCCI process and how to control the ignition behavior of the fuel [145, 147, 148]. Additionally, the benefits for emissions reductions have not always been successfully demonstrated across all engine platforms, lending further support for continued research.

2.4.2.4 HCCI engine and Dual Mode Processes

A suggested method to increase the operating range of an engine operating with the HCCI process is to prepare it to run in a dual mode process. This can mean two things: 1) that the engine operates with two different combustion processes over the entire range of operation of the engine, and 2) that the engine operates in HCCI with a pilot injection, as a dual fuel engine, with the injection occurring inside the intake air system just prior to entry into the cylinder or directly into the cylinder. Stanglmaier and coworkers at Southwest Research Institute developed a dual fuel natural gas engine to operate in HCCI mode at idle to mid range operation to improve fuel efficiency and reduce NO_x emissions [149]. Although the goal of the experimentation was achieved, higher levels of HC and CO emissions were also observed [149]. Park and coworkers at West Virginia University developed a dual fuel engine based on the Navistar T444E [150]. The engine was fumigated with natural gas, and the diesel injection system was operated to bring in diesel fuel at a different timing scheme than the original engine [150]. Although they were successful in reducing NO_x and particulate matter emissions, the HC and CO emissions increased substantially over the diesel-only levels [150].

2.4.2.5 Mixed Mode Combustion

There is also another style of combustion that is being explored. In the literature, some researchers call it the dual fuel engine, whether those fuels are gaseous or liquid or a combination of both [151-154]. In each of these researchers' work, diesel or biodiesel fuel was used as a "pilot" fuel, a gaseous fuel is inducted or injected into the cylinder,

and a pre-mixed gaseous fuel and air mixture is compressed. While this may sound similar in nature to conventional pilot and main fuel injection in a diesel engine, the benefits of a dual fuel engine are only now being researched and understood. Karim has postulated a schematic representation of the energy release rate for this type of combustion strategy [151]. In his schematics for both a light load and a heavy load condition, he shows three phases of the energy release: 1) phase one is due to the combustion of the pilot fuel, 2) phase 2 is due to the combustion of the gaseous fuel that is in the immediate vicinity of the pilot combustion, and 3) phase 3 is due to any preignition reactions and the turbulent flame propagation within the lean mixture [151]. Karim's research focused on using primarily propane, hydrogen, and methane as the gaseous fuel, with the primary focus on methane, and emissions characteristics and combustion analysis [151].

Chapter 5 of this thesis focuses on a similar kind of dual fuel engine, referred to here as a mixed mode combustion process. In this research, DME is the fuel being inducted into the engine and diesel is the pilot fuel. In this process, a low temperature combustion mode is initially achieved with a secondary diffusion mode of diesel combustion. However, the low temperature combustion was not achieved with the aid of high levels of EGR or cooled EGR. It is hypothesized that, through the use of the ignition properties of the fuel and early low temperature heating in the cylinder, a reduction in NO_x emissions can be achieved.

2.4.2.6 Ignition Delay

An important property of the fuel is its ignition delay, or the time from which the fuel begins to be injected into the cylinder until some detectable heat release occurs. Time is required to sufficiently mix the fuel and air present in the cylinder, and then chain initiation reactions take place so that the chemical explosion begins to occur and the chain propagation reactions begin to increase in number [11]. Researchers have tried to understand the factors that affect the ignition delay so that this could be used to better control the combustion process regardless of fuel type [11]. The standard equation used to describe ignition delay is shown in Eq. 2.20. In this equation, τ_{id} is the ignition delay, E_A is the apparent activation energy for the fuel autoignition process, \tilde{R} is the universal gas constant, p is pressure, and A and n are constants dependent on the fuel, fuel injection, and air flow characteristics [11]. Heywood goes on to explain that there are many factors that affect the ignition delay, including mixture temperature, pressure, and equivalence ratio. This is the typical equation used for data from combustion bombs and flow reactors [11].

$$\tau_{id} = Ap^{-n} \exp\left(\frac{E_A}{\tilde{R}T}\right) \quad 2.20$$

Other correlations for predicting ignition delays have been prepared based on empirical formulas and give good agreement over a wide range of engine conditions. One developed by Hardenburg and Hase predicts the ignition delay based on the cetane number of the fuel and the temperature and pressure during the delay at top dead center (TDC) conditions [155]. This equation from Hardenburg and Hase along with a

refinement from Prakash and coworkers [156] provided Garnier and coworkers an equation that was able to model the ignition delay for a syngas dual fueled engine above a 30% substitution of the fuel [157]. The authors claim good agreement at 30% and above, but their figures show a margin of 1 crank angle degree above 50% substitution of the fuel between the experimental and predicted ignition delay, which indicated good agreement within a margin of 1 crank angle degree [157].

Karim has shown in his research the effect of the fuel and air mixture on the start of combustion timing in a dual fuel engine mode for various fuels [151]. While methane and hydrogen exhibited little change in the start of combustion timing over the various stoichiometric ratios, the start of combustion timing for ethylene and propane over various stoichiometric ratios varied widely [151].

2.4.3 Post Combustion

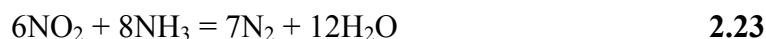
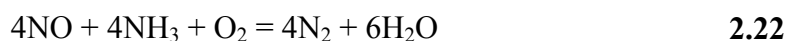
2.4.3.1 NO_x Aftertreatment Devices

The general method which exists for controlling NO_x via post-combustion techniques involves some type of catalytic reaction, chemical reaction or a combination of both. There are two types of catalytic reduction: Selective Catalytic Reduction (SCR), and Selective Non-Catalytic Reduction (SNCR), both thermal and non-thermal [50]. The method that is most widely being considered is the SCR method, also most commonly known as DeNO_x Catalysis. In this method, a zeolite catalyst is used to absorb NO_x molecules. A reagent is injected into the exhaust stream to chemically reduce the NO_x.

Previously, the typical reagent used was the fuel itself, which reduces the efficiency of the vehicle. However, it is common now to use urea. It should be noted that this process works in a small temperature band (200-250 °C for precious metal zeolites and 400-450 °C for base metal zeolites), and for vehicles the NO_x reduction is low and selectivity is poor [158].

The predominant method of selective catalytic reduction uses ammonia or urea as the reductant [159]. Studies with these types of catalyst applications have shown 90% reduction and higher can be achieved with an SCR catalyst and urea as the reductant [160, 161]. Testing has been completed using SCR, EGR, and intensive engine mapping which resulted in dramatic reduction of NO_x emissions [162].

The following reactions, Eq. 2.21 through Eq. 2.25, describe the primary chemical reactions that occur in the ammonia SCR system. All of these reactions are occurring in the catalyst to reduce NO_x down to elemental nitrogen and water. Reaction Eq. 2.22 is the dominant mechanism for NO reduction [163].





Current research is focusing on the use of SCR with urea as the reductant and Lean NOx traps (LNTs) to meet emissions in Europe for 2009 and beyond, with technology which can also be applied to vehicles in the US market [164]. For vehicle aftertreatment, a combination of LNTs and SCRs is also being considered, with the LNT being used to provide ammonia to the SCR during rich regenerations [164]. For heavy duty engines, exhaust temperatures are high enough to provide the heat necessary for the urea to hydrolyze to ammonia and for reactions to take place. However, in light duty diesel engine applications, exhaust temperatures are too low for appropriate operation of the NOx reduction with either a LNT or SCR in conjunction with particulate matter reduction over the catalyst [165, 166]. To achieve ULEV II standards (.05 g/mi NOx), Tennison and coworkers used a fast warm up routine with the engine to gain the required light off temperature for the SCR within the first 100 seconds of operation [167]. Ogunwumi and coworkers are working on in-situ methods via an ammonia generating catalyst to generate ammonia so that urea is not required as an added on board reductant [168].

2.4.3.2 Particulate Matter Aftertreatment Devices

Diesel particulate emissions pose a significant potential health hazard. Control of diesel particulate emissions is an issue requiring the attention of the fuels, engine and aftertreatment industries. To achieve the reductions in particulate emissions mandated by

the US Environmental Protection Agency in 2007, use of diesel particulate filters (DPF) will be a necessity [169].

There are two groups of diesel exhaust aftertreatment devices: particulate traps and diesel oxidation catalysts. Diesel particulate traps, which are primarily filters, control diesel particulate matter emissions by physically trapping the particulates. The major challenge in the design of a diesel particulate trap system is to regenerate the trap by oxidizing the collected particulate matter in a reliable and cost-effective manner [170]. A critical requirement for implementation of diesel particulate filters on diesel-powered vehicles is having a low “break even temperature”, or balance point temperature, defined as the temperature at which particulate deposition on the filter is balanced by particulate oxidation on the filter and indicated by exhaust restriction. This balance point needs to occur at sufficiently low temperatures to fit within the exhaust temperature range of a typical diesel vehicle’s duty cycle. Catalytic coating on the diesel particulate filter, use of a fuel-borne catalyst and oxidation catalysts placed upstream of the particulate filter can all reduce this balance point temperature [171].

Chapter 3

Experimental Setup

3.1 Introduction

This chapter provides details of the experimental set up and the methods used for this research. First, the general engine system used for both experiments will be described. Further detail on modification to the engine systems for each experiment are contained in the respective chapters. Then, a detailed description of the equipment used for the collection of the experimental data will be provided in additional sections. A review of the engine and emissions equipment repeatability will be discussed.

3.2 Engine Description

A Detroit Diesel Corporation (DDC) 2.5 L 4-cylinder turbocharged direct injection engine (built by VM Motori, Italy) was used for both experiments described in the Chapters 4 and 5. The engine, made for the European market by VM Motori, was purchased by DDC and was sold to Chrysler for inclusion in their Jeep Cherokee CJ vehicles for the European and South American markets. The engine is configured with a Bosch common rail fuel injection system. It is shown below coupled with the 5 speed manual transmission in Figure 3.1. The performance curve of the engine is shown in Figure 3.2.



Figure 3.1: Detroit Diesel Corporation 2.5L Engine

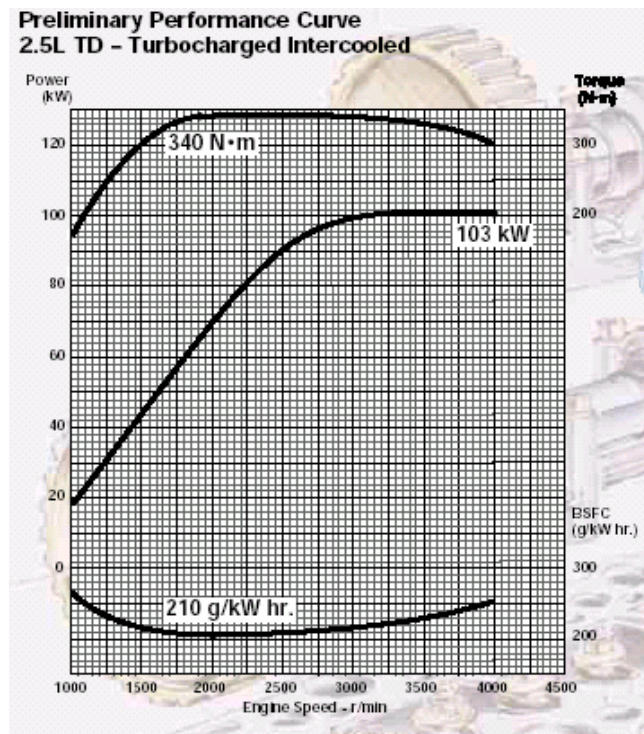


Figure 3.2: Engine Rating of the 2.5L Detroit Diesel/ VM Motori Engine [172]

The DDC 2.5L engine is described in Table 3.1. The standard fuel injection strategy is comprised of a pre-injection followed by a main injection to reduce emissions and engine noise.

Table 3.1: DDC 2.5L Engine Specifications

Engine	DDC 2.5L TD DI-4V automotive diesel engine
Displacement	2.5L
Bore	92mm
Stroke	94mm
Compression Ratio	17.5
Connecting rod length	159mm
Rated Power	103KW@4000 RPM
Peak Torque	340Nm@1800 RPM
Injection system	Electronically controlled common-rail (Bosch)
Valve train	4 valves/cylinder
Intake Valve Opens	15.6° ATDC
Intake Valve Closes	64.4° ABDC
Exhaust Valve Opens	66° BBDC
Exhaust Valve Closes	32° ATDC

A 250HP Eaton eddy current water-cooled dynamometer was coupled to the 2.5L DDC engine to generate load. The engine and dynamometer were controlled by a Digalog Testmate control unit.

3.3 Engine Test Stand Data Acquisition

A time based data acquisition program was managed using a custom programmed National Instruments Labview virtual instrument (VI). The data acquisition program was set up to collect the steady state operational data from the engine's operation. The VI was created to capture the engine and exhaust status via analog signals from pressure

transducers, thermocouples, and serial communication from the fuel scale and emissions equipment. The signal inputs were located on a series of external computer modules, which were a collection of National Instrument Field Point Modules connected to a command module (FP-2015) to run the VI, and save the data. The data collected by the Field Point Modules was saved every 10 seconds during 20 minutes of sampling per test. Information regarding fuel consumption by the engine was collected by this program via serial communication. Gaseous emissions measurements from the ALV CEB II were collected via serial communication and also recorded.

3.4 Diesel Fuel Flow Rate

The engine fuel consumption was measured using a Sartorius model EA60EDE-IOUR precision scale that has an accuracy of ± 2 g. The custom LabView VI calculated the diesel or biodiesel fuel consumption rates based on 100 measurements of fuel tank mass, tracking the small change in mass over 60 seconds.

3.5 Engine Control Unit

The electronic control unit (ECU) is the computer that controls engine operation. An unlocked ECU was used to modify and control main injection and pilot injection timings, as well as, EGR valve position, and fuel rail pressure. The unlocked ECU was connected to an ETAS MAC 2 unit via an ETK connection. The MAC 2 unit was

connected to a PC running ETAS INCA v5.0 software. INCA managed the ECU modifications in real-time.

3.6 Exhaust Gas Recirculation

The DDC 2.5L engine regulates exhaust gas recirculation (EGR) rates using an ECU map based on engine speed and injection volume. The ECU map dictates the flow rate by varying the amplitude of the signal sent to a proportional pneumatic valve. The stock DDC 2.5L engine then introduces EGR to the intake manifold via a Y-pipe. When EGR was used in the experiment, the ECU was allowed to control the EGR per the ECU map. When the EGR was not used, the EGR signal to the proportional pneumatic valve was disconnected.

3.7 Gaseous Emissions Equipment Description

3.7.1 Gaseous Emissions: AVL Combustion Emissions Bench II (CEB II)

Gaseous emissions were measured using analyzers integrated into an AVL Combustion Emissions Bench II (CEB II) emissions bench. Exhaust gases were kept at a constant temperature of 190°C with a heated sample line. NO_x emissions were measured without exhaust cooling using an EcoPhysics chemiluminescence analyzer. A portion of the sample gas was chilled to remove moisture from the sample before being analyzed with Rosemount CO (IR), CO₂ (IR), and O₂ (paramagnetic) detectors. NO₂

emissions were determined by subtracting the NO result from the total NO_x result. Total hydrocarbons and methane were also collected on separate ABB Flame Ionization Detector (FID) analyzers. All gaseous emissions were sampled continuously throughout the testing and measurements were automatically logged by the data acquisition system every 10 seconds via serial communication.

Each analyzer has a separate calibration range. Those are shown in Table 3.2. Each analyzer has a 1% of full scale instrument error, in addition to an R2 % error in the calibration curve of the instrument.

Table 3.2: AVL Combustion Emissions Bench II Analyzer Ranges

Species	Range
THC (Total Hydrocarbons)	930 ppm
O ₂	24 %
CH ₄	9920 ppm
CO ₂	19.10 %
CO- Low	2451 ppm
NO _x	4557
NO	4557

3.7.2 Gas Chromatography (GC)

Gas chromatography is a type of chromatography in which the mobile phase is the carrier gas, such as helium, and the stationary phase is a microscopic layer of liquid or polymer on an inert solid support, inside a glass or metal tubing, called a column [173]. The chemical constituents of the sample gas pass in the carrier gas stream at different rates depending on their various chemical and physical properties and their interaction with the specific column filling. As the chemicals exit the end of the column, they are detected

and identified electronically by the calibrations that have been made in the software based on retention time, and detector response. The stationary phase in the column functions to separate different components that pass through the column and exit at a different time, which marks the retention time of the species [174].

Gaseous emissions were collected in a HP 6890 Series GC that was configured with 2 Haysep D packed columns (stainless steel, 100/125 mesh size, 1/8" diameter) with different lengths (10 and 36 ft) for both the flame ionization detector (FID) and the thermal conductivity detector (TCD). The shorter column was used in conjunction with the FID for analysis of hydrocarbons, while the longer column was used with the TCD for analysis of permanent gases and water.

The GC method used for this testing involved cooling the system to -15°C with liquid nitrogen, and then collecting data for 17 minutes at this temperature. Next, the GC went through a ramp stage from -15°C to 225°C at 30°C per minute for a period of 7 minutes. Then, at the 25 minute mark, the system was at 225°C , and continued at this temperature for 10 minutes. At the 35 minute mark, the testing was complete. The inert carrier gas used was argon (30 ml/min for the first 16 minutes, and 60 ml/min for the remainder of the test). The GC method used was configured for previous research and worked for this particular testing. Although it was not the goal of this research to improve the existing method, the method provided information about this research, specifically the amount of DME left in the exhaust emissions.

The GC chromatograms from the FID can give an indication of the change in the type of light hydrocarbons in the exhaust emissions for the C1-C6 range or species with a molecular weight less than or equal to a C6 compound [175]. In contrast, the AVL CEB

II gives bulk hydrocarbon concentrations for all hydrocarbons that are in the gaseous exhaust stream and that do condense below 190° C.

3.7.3 Fourier Transform Infrared (FTIR) Spectroscopy

Exhaust gas analyses was completed using a Nicolet Magna 550 Fourier Transform Infrared (FTIR) Spectrometer. The FTIR spectrometer was calibrated to analyze for a range of 0-200 ppm of N₂O. The spectrometer cell temperature was maintained at approximately 132 ± 5 °C to prevent water from condensing from the exhaust gas. The spectrometer cell pressure was maintained at approximately 680 ± 5 mm Hg with a vacuum system and bypass balance valve.

Throughout testing, the spectrum background was updated approximately every 60 minutes. Spectrum background sampling provided a reference point in terms of both the ambient and spectrometer operating conditions. Spectrum background updates consisted of purging the FTIR cell with N₂ for two minutes and then collecting a background spectrum.

For each RPM/engine load data point, three spectrum traces were recorded. The gaseous emissions concentrations obtained from each of the three sample traces were then averaged to obtain a representative concentration value for the particular RPM/engine load value.

3.8 Particulate Matter Emissions Equipment Description

3.8.1 Particulate Emissions: Gravimetric Filters

Particulate matter data was collected using a Sierra Instruments BG-2 Micro-Dilution Test Stand, shown in Figure 3.3 [176]. A probe collects a sample of exhaust to be analyzed. From the probe, the exhaust travels to a dilution tunnel that contains channels through which shop air is forced to quench the exhaust and dilute the particulate matter. The quenched sample is then deposited onto a filter. Finally, the exhaust gas is routed into the stand to determine other parameters such as temperature and mass flow [176].

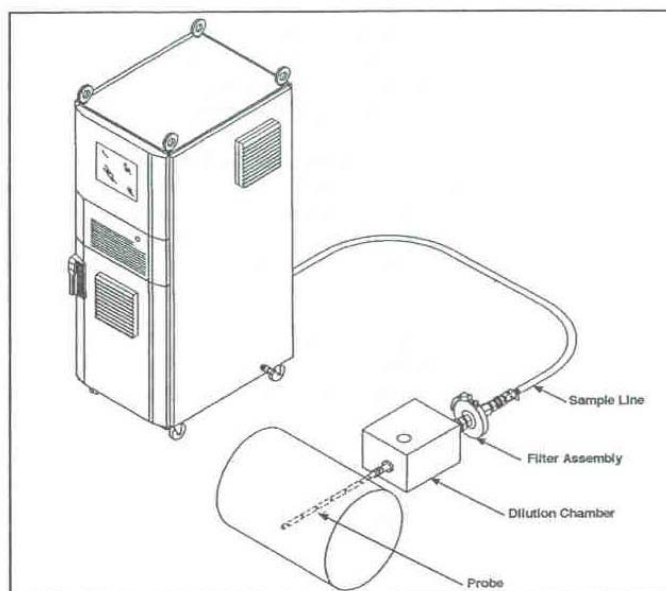


Figure 3.3: Sierra Instruments BG-2 Micro-Dilution Test Stand [176]

The type of filter used is a Pallflex 90 mm membrane filter. Each one is weighed and placed in a humidity chamber with a constant temperature, set at 25°C and 45% RH, for at least 24 hours before it is used. After a sample is collected, the filter is placed back into the chamber for another 24 hours and weighed again. From these measurements, the mass emissions of the particulate matter can be determined.

The BG-2 test stand must be set up before each day of testing. This includes a 20-minute computer warm up period and a 60-minute continuous purge of the sample line to clear out any debris from a previous day's sampling. A normalization filter is then used before taking actual data to clear out any residual debris from the line [176].

Setting up the dilution ratio is crucial to how much particulate matter is deposited onto the filter. Too low a ratio and not enough particulate matter will be deposited to reach an accurately measurable quantity, and vice versa. This ratio ensures at least 100 milligrams will be accumulated on the filter.

The engine must reach steady-state conditions (exhaust temperature stabilization) before taking a data point to ensure a fair reading. The exhaust is sampled for seven minutes, after which the BG-2 line valves are closed to protect the filter from any sudden pressure increase that could damage the filter and ruin the data point [76].

For the testing described in this thesis, particulate matter (PM) emissions were measured by sampling the exhaust using a Sierra Instruments BG-2 mini-dilution tunnel with a constant dilution air/sample flow ratio of 6:1, and a total flow of 60 L/min for a period of 7 minutes. Filters were collected from the sampling for gravimetric analysis and visual inspection. For each condition, only two filters were collected, weighed and analyzed accordingly. While this provides an indication of the change in particulate

mass, it is not meant to give statistically significant results which would require 6 or more filters per test.

3.8.2 Particulate Emissions: Tapered Element Oscillating Microbalance (TEOM)

Particulate matter (PM) emissions were measured by sampling the exhaust using a Sierra Instruments BG-2 mini-dilution tunnel with a constant dilution air/sample flow ratio of 6:1, and a total flow of 60 L/min. A portion of the diluted exhaust gas (3 L/min) was passed to a Rupprecht & Patashnick Tapered Element Oscillating Microbalance (TEOM) Series 1105 PM analyzer which measures the real-time particulate mass concentration (mg/m^3). PM is collected on a Teflon filter # TX40/57-007224-0020 sold by Thermo (formerly Rupprecht & Patashnick). The software collects data on mass every half second as mass concentration (mg/m^3) and translates that data into mass rate (g/sec) and total mass (g). The analyzer includes an inertial balance that directly measures the mass that is collected on a filter cartridge. The instrument monitors the change in the natural oscillating frequency of a tapered element over time as mass is collected on the filter. The instrument is set to 3 L/min flow for exhaust gas, with the mass transducer temperature, internal head, and heated sample tube temperatures set at 50°C . Data is collected every 0.1 sec for mass rate and mass concentration averaging, with total mass being averaged at every 10 seconds. The instrument can be used for transient and steady state PM emissions PM measurements. Configuration files of the equipment and software are found in Appendix A.

3.8.3 Particulate Matter Emissions: Scanning Mobility Particle Sizer (SMPS)

The TSI 3936 scanning mobility particle sizer (SMPS) spectrometer measures particle size and number density from .0025 to 1.0 μm , and from 1 to 10^8 particles/ cm^3 , respectively. The data is collected and displayed in up to 167 actual channels, or 64 channels per decade. The SMPS system includes the TSI series 3080 Electrostatic Classifier with a Differential Mobility Analyzer (DMA) and a series 3776 Condensation Particle Counter (CPC). Aerosol Instrument Manager software is provided to simplify set up of the system, operation, data collection and analysis. The SMPS has also been coupled with a Dekati series 3065 Thermal Denuder.

Before the sample enters the SMPS, it passes through the thermal denuder. Depending on the temperature setting of the instrument, hydrocarbons that have agglomerated on the particulate matter are volatilized off of the particles as the sample passes through the packed carbon bed. When entering the SMPS system, the sample initially passes through a single stage impactor to remove large particles outside the measurement range. Next, the sample passes through a bipolar ion neutralizer to create a high level of positive and negative ions. The charged and neutral particles then enter the DMA in which the particles are separated according to their electrical mobility. Neutral particles exit the DMA with the excess air. Particles with negative charges are repelled towards and deposit on the outer wall of the DMA. Particles with positive charges are attracted towards the inner electrode. Particles within a narrow range of electrical mobility have the ability to pass through a narrow slit opening near the bottom of the DMA. After the aerosol particles exit the DMA, they enter the CPC and are counted.

Through the ramping of the voltage of the inner electrode exponentially over a selected period of time defined by the test, the entire particle size distribution and number concentration are measured.

The particular instrument configuration used to collect the data in this experiment is shown in Table 3.3 . The SMPS was connected to the exhaust system of the DDC engine in combination with the Sierra Instruments BG-2. The BG-2 provided the vacuum to deliver the appropriate sample to the SMPS, and was adjusted to provide a 6:1 dilution ratio across the dilution tunnel filter system. Four samples were collected for each data point. The first two samples were discarded, and the remaining two points were averaged for the data presented in the figures.

Table 3.3: SMPS Property configuration for data collection

Hardware Setting	Value	Units	Comment
Impactor Type	0.071	cm	For Flow rate between 1.0-2.2 lpm
Sheath Flow	14	lpm	
Aerosol Flow	1.4	lpm	Set below maximum of 1.5 lpm; BG-2 set to compensate for this flow at a dilution ratio of 6:1
Size Range	6.26 - 237.1	nm	
Voltage Range	11 - 9848	V	
Scan Up time	90	sec	
Scan Retrace time	30	sec	
Scheduling			
Scans per Sample	1		Manual Triggering
Number of Samples	4		
Total Sample Time	8	min	
Physical Properties			
Particle Density	1.2	g/cc	
Gas Viscosity	1.32 e-05	kg/(m s)	
Mean Free Path	6.65 e-08	m	

3.9 Fuel Injection Needle Lift and Cylinder Pressure Data Collection and Analysis: AVL IndiCom

Pressure traces were collected from each cylinder at .1 crank angle resolution with an AVL GU12P pressure transducer connected to a Kistler 5010 Dual Mode charge amplifier. The pressure transducers were located in the glow plug hole for each cylinder. The amplifier signal was collected by an AVL 621 IndiModul, which is a high speed data acquisition system that records the data in real time. An AVL 365C Crank Angle Encoder is connected to the engine crank as a means to synchronize the pressure trace to the crank angle degree and top dead center. The final data from the Indimodul is sent to a PC connected to the system. The real-time data file can then be saved by the AVL IndiCom 1.3 software with Concerto 3.90 as a set of pressure traces and as an averaged file.

For this research, a set of 200 pressure traces was collected and then saved. The set of 200 traces were then averaged into one single trace and then saved. With the IndiCom software, the pressure traces can be analyzed for many pieces of information of interest from the combustion process, including heat release.

IndiCom uses the first law of thermodynamics for calculating the rate of heat release from the volume and pressure data collected by the Indimodule. Losses are neglected. The ratio of specific heats, γ , used in the equation for the heat release in the IndiCom equation is 1.37 for a diesel engine. The apparent rate of heat release algorithm is given in Eq. 3.1, with further explanation referenced from the AVL IndiCom manual and found in [177].

$$Q_i = \frac{K}{\kappa - 1} [\kappa \cdot P_i \cdot (V_{i+n} - V_{i-n}) + V_i \cdot (P_{i+n} - P_{i-n})] \quad 3.1$$

Where:

n is the interval (0.1 degree)

κ is the polytropic coefficient ($\kappa = \frac{c_p}{c_v}$ where c_p is the temperature at a constant

pressure and c_v is the temperature at a constant volume of the fuel)

P is the cylinder pressure

V is the volume

As Heywood explains, a typical range of values for gamma for diesel heat release analysis is 1.3 to 1.35 [11]. However, the gamma will change values based on the constituents that are in the cylinder at a particular time during the compression and expansion strokes [11]. Heywood goes on to say that the appropriate value for gamma that will give the most accurate heat release is not well defined [11].

A Hall-effect needle lift sensor provided by Wolff Controls Inc. was used to obtain the injector needle lift of Cylinder 1. This signal was brought into the AVL 621 Indimodul, which was triggered by a crank angle signal from the AVL 365C angle encoder placed on the crankshaft. The real-time Indimodul data was transferred to the PC with the AVL IndiCom 1.3 software and Concerto 3.90 for further analysis.

3.10 Description of Experimental Tests

The detailed descriptions of each experiment and engine test conditions are given within the chapter for each experiment. However, a brief description of the testing will be reviewed. Each experiment had a different set of engine testing conditions, in addition to some changes to the base engine configuration, or change in fuel injection strategy for the testing. Fuel property information is found in Appendix C.

For the research performed in Chapter 4 with the hydrogenated biodiesel, the first set of experiments was performed without Exhaust Gas Recirculation over 4 operating modes with the following test conditions shown in Figure 3.4 :

Mode Number	Speed (rpm)	Load (ft-lbs)
1	1500	50
2	1500	100
3	1660	75
4	1660	125

Figure 3.4: DDC 2.5 L Engine Test Specification for NO_x Reduction with Fuel Modification Experiments: Hydrogenated Biodiesel

The second set of tests with the hydrogenated biodiesel were performed at one engine mode: 1800 rpm and 61 ft-lbs of torque with a single pulse injection at 7° BTDC and without Exhaust Gas Recirculation.

For the research performed in Chapter 5 with the mixed mode combustion process, the tests were performed at one engine mode: 1800 rpm and 61 ft-lbs of torque with a single pulse injection at various timings BTDC and without Exhaust Gas Recirculation.

3.11 Repeatability Study of Engine

The engine was operated over a period of days to perform a repeatability study. The test condition outlined in Chapter 5, 1800 rpm and 61 ft-lb torque and at a fuel injection timing of 7° BTDC, was used for the study. As shown in Table 3.4, the study was performed over three days, with the test data being collected between 10 am and 12 pm (noon) on the various days. The intake air temperatures were within 2 degrees over the tests. The average speed was recorded within 3 rpm for a series of 60 data points. The load was recorded within 0.09 ft lbs for the same series of 60 data points.

Table 3.4: Repeatability Study Engine Test Data: 1800 rpm and 61 ft-lb torque and at a fuel injection timing of 7° BTDC

Date	Time	Speed (rpm)	Load (ft-lbs)	Exhaust Temp (C)	Boost Air Temp (C)
11/6/2007	11:53 AM	1801.6	60.91	287.9	27.3
11/8/2007	10:22 AM	1800.8	60.89	285.8	27.6
10/9/2007	11:05 AM	1802.5	60.96	277.5	25.5

The data for the tests is shown below in Table 3.5. The emissions data error was computed to determine standard deviations for a series of 60 data points. With the standard deviation and average, the error bars were computed to be within a range of 1 to 2 % for the emissions data.

Table 3.5: Repeatability Study Test Emissions Data: 1800 rpm and 61 ft-lb torque and at a fuel injection timing of 7° BTDC

Date	BSFC (g/kWh)	BSEC (MJ/kWh)	CO ₂ (g/kWh)	CO (g/kWh)	NOx (g/kWh)	Hydrocarbons (g/kWh)
11/6/2007	241.84	11.07	908.13	3.18	5.41	1221.19
11/8/2007	243.73	11.15	907.26	3.07	5.30	1005.90
10/9/2007	237.54	10.87	913.78	3.71	5.10	1248.15

The NO_x (g/kWh) data for the tests is shown in Figure 2.1 with error bars. The variation between the data points shows a 5.7% difference over the three days.

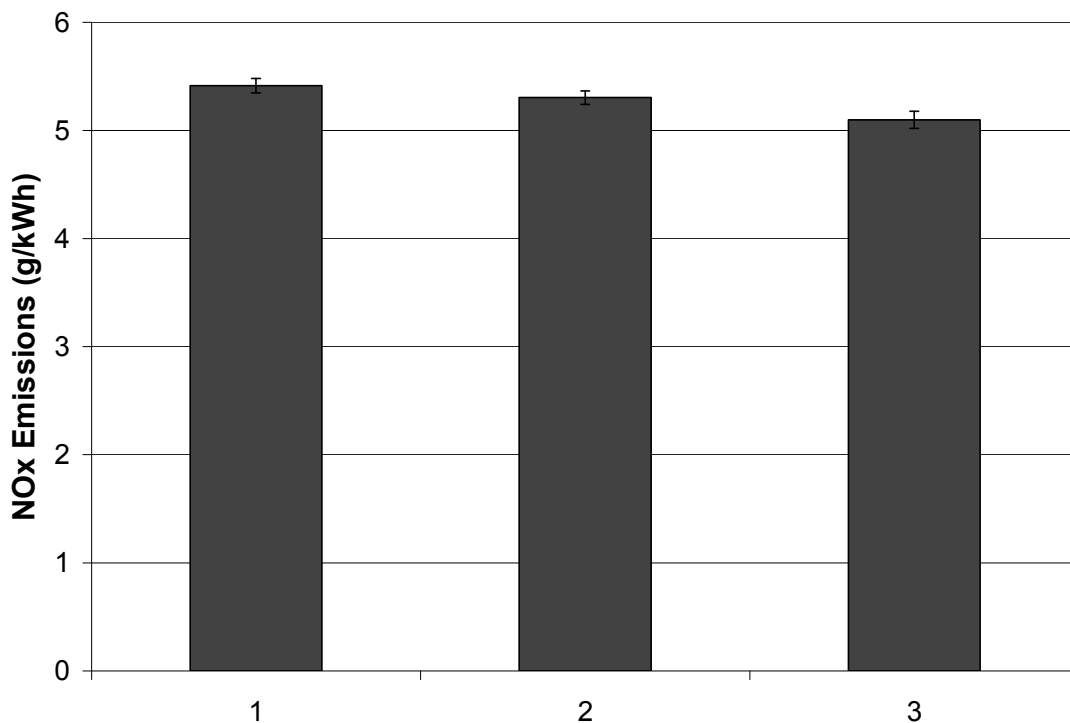


Figure 3.5: Repeatability Study Test NO_x (g/kWh) Emissions Data: 1800 rpm and 61 ft-lb torque and at a fuel injection timing of 7° BTDC

Chapter 4

NO_x Reduction through Fuel Modification: Hydrogenated Biodiesel

4.1 Preface

This chapter presents some new data and some previously published data from two American Chemical Society pre-prints [178, 179]. The initial project began with the assignment of a team of students from the class Fuel Science 504 : Problems in Fuels Engineering to address the biodiesel NO_x effect. The author has extended the research by finding a commercial hydrogenated biodiesel fuel and performing a series of engine tests and fuel property tests with the fuel. There were several contributing authors to the current body of work. The author's contributions to this work include the engine tests and the viscosity tests. Stephen R. Kirby contributed by measuring the derived cetane number in the Ignition Quality Tester and the calorific values of the fuels. José Rodríguez-Fernández contributed by performing the Cloud Point and Pour Point tests. A hydrogenated biodiesel fuel has a lower iodine value and is more saturated, and thus has a different percentage of the chemical compounds than would normally be found in soy-based biodiesel. In the tests, the fuel properties of the hydrogenated biodiesel are compared neat and in blends to the normal soy based biodiesel. The engine tests involve fixing certain engine parameters to study their effect on the production of NO_x from the combustion of the fuel.

4.2 Introduction

Biodiesel is an alternative diesel fuel created by the conversion of oils, fats and fatty acids to methyl and ethyl esters via esterification processes [95]. A variety of vegetable oils, typically soybean oil in the United States, and animal fats provide the source of the triglyceride fats and oils [96]. Continuous feedstock growth and livestock production provide a constant supply of source material allowing biodiesel to be a renewable source of fuel, which can be created domestically.

Additionally, biodiesel is miscible with petroleum-based diesel and works in any diesel engine with little or no modifications as pure biodiesel or as a blend with any other diesel fuel. But, the Engine Manufacturers Association recommends no more than 5% blends of biodiesel[180]. Biodiesel is a cleaner burning fuel and reduces most harmful emissions such as particulate matter, unburned hydrocarbons and carbon monoxide [53, 98].

However, a few issues need to be resolved before biodiesel fuels can be a prominent alternative fuel. The economics of providing an appropriate source material and of producing an affordable final product to create acceptable biodiesel fuels must be favorable. At present, there are significant quality control issues in the biodiesel industry[181-183]. Moreover, engine emissions of oxides of nitrogen typically increase when using biodiesel fuels [53].

One approach to combat this “biodiesel NO_x effect” is to increase the degree of saturation of the ester molecules contained in the biodiesel. This degree of saturation is measured as the iodine value of the fuel. This report investigates a potential option that

may be used to achieve a higher degree of saturation: hydrogenation of soybean oil prior to transesterification of the biodiesel fuel. This research explored the approach of achieving a more saturated biodiesel fuel and observing its effects on NO_x emissions in various fuel blends. A hydrogenated soy methyl ester was mixed with an ultra low sulfur diesel fuel and tested in a light duty diesel engine. This hydrogenated fuel has a higher percentage of oleic acid methyl ester, and a reduction in the linoleic and linolenic methyl esters (yielding a fuel similar to that studied by Szybist et al. [119]). Previous engine and emissions testing on a light duty diesel engine revealed decreased NO_x levels for some engine modes and an increase for other modes [178, 179].

4.3 Background

4.3.1 Biodiesel Processing

Vegetable oils and animal fats are mostly made up of triacylglycerols (TAG), which are often referred to as triglycerides. The TAG are esters of fatty acids with glycerol as the backbone of the structure [184]. The fatty acids contained in the oil vary in the length of the carbon chains, as well as the number of unsaturated (double) bonds [185]. In order to be used as a diesel substitute, the vegetable oil triglycerides must be converted to methyl or ethyl esters. This is accomplished through the process of transesterification [185]. In the transesterification process, the oil is reacted with a catalyst and an alcohol (usually methanol) to form the ester groups (usually methyl

esters) from the fatty acids that are found in the original oil[184]. Glycerine is a byproduct of this reaction and must be removed before the material can be used as a fuel.

4.3.2 Hydrogenation Processing

Hydrogenation is, “the addition of hydrogen to a double or triple bond to yield a saturated product” [65]. This option of saturation of the molecules is particularly attractive as the process of hydrogenation is already being conducted on an industrial scale and is a well established technology for edible fats and oils processing. The reasons to hydrogenate a fat or oil are to change the physical form for functionality use, or to improve the oxidative stability [186]. The typical analytical evaluations for control of a hydrogenation batch are refractive index, iodine value, and melting points [186]. For this project, hydrogenated soy methyl ester was available commercially and was used in the engine testing.

According to the supplier of the hydrogenated biodiesel, the product is made by the typical hydrogenation process. Once at their facility, they further change the product by the following process. Refined and bleached (RB) soybean oil is purchased from their supplier. The RB process is aimed primarily at removing the impurities that come in with the crude vegetable oils. Then, the RB soybean oil is combined with methanol and sodium methoxide (catalyst) in a reactor/settler that allows glycerine to settle out. The processor drives the reaction through the addition of excess methanol and removal of glycerine. The crude methyl ester is flashed to remove excess methanol, washed with water to remove soap, catalyst, glycerin, and methanol. There is a final drying stage to

remove any water and methanol that is left over. Finally, atypical to the industry, the processor distills the product to create a water white methyl ester product, separating it from heavy impurities such as un-reacted glycerides [187].

Table 4.1 lists the chemical properties of a hydrogenated soy biodiesel used in the previous research [179] and this study. The fuel reports are also found in Appendix E. It is important to note the shift in the methyl oleate (C18-1) composition of the fuel from a typical soy methyl ester.

Table 4.1: Chemical properties of and Fatty Acid content of the Hydrogenated Soy Biodiesel (GCMS from supplier)

Property	Value
% C12	0.0
% C14	0.0
% C16	12.3
% C18	87.2
Iodine Value	90
Methanol	0.0
Acid Value	0.14
GC Compound	% Composition
C16	12.31%
C18	7.81%
C18-1	58.17%
C18-2	20.24%
C18-3	0.92%
C22	0.53%

4.3.3 Iodine Value and NO_x Emissions

Iodine Value is an analytical technique used to measure the amount of unsaturated fatty acids present in an oil. The Iodine Value, according to AOCS Method Cd 1-25, is obtained by reacting a fat with a known amount of halogen, iodine, or iodine chloride [186]. Through the reduction of the excess halogen with KOH and titration with a standard sodium thiosulfate using a starch solution as the indicator of the free iodine, the amount of iodine consumed by the fat is determined [186]. The final value is represented as the percent of iodine absorbed. A higher number means that a higher degree of unsaturated fatty acids are present [186].

According to Figure 4.1 from McCormick and coworkers [99], as the iodine value of the fuel decreases, the NO_x level will decrease as well. Biodiesel from soy typically gives an Iodine Value of 130. Since the hydrogenated biodiesel has an iodine value of 90, there should be less NO_x emissions from the engine in grams NO_x per gram horsepower-hour. Diesel fuel is typically given an iodine value of 10.

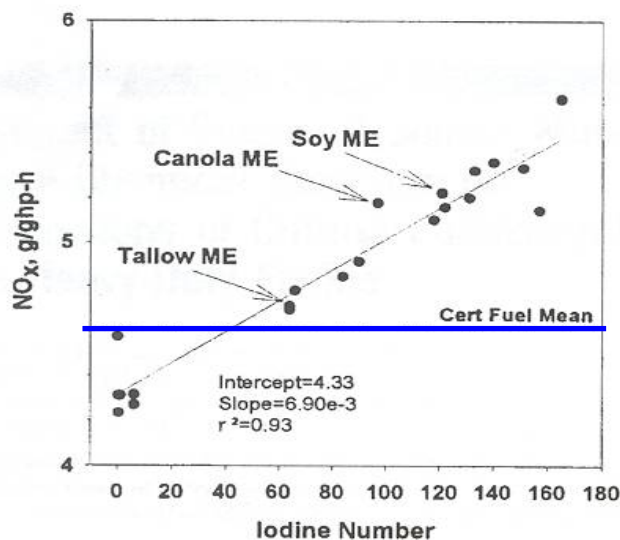


Figure 4.1: Iodine Value vs. NO_x emissions[99].

4.4 Initial Experimental Tests and Data

The intent of the project is to decrease the NO_x emissions from biodiesel combustion through the saturation of the biodiesel methyl esters, specifically methyl esters made from soybean oil. Data previously reported by the author involved the use of an ultra low sulfur diesel (ULSD) (British Petroleum 15ppm sulfur content fuel- BP15) as the base fuel and the hydrogenated soy methyl ester was blended at 50 vol% (B50)[179]. The data was collected from a Detroit Diesel Corporation (DDC) 2.5L 4-cylinder turbodiesel engine, configured with a Bosch common rail fuel injection system.

The fuel injection strategy is comprised of a pre-injection followed by a main injection to reduce emissions and engine noise. For these tests, the engine was allowed to operate as it was calibrated for normal vehicle operation. The experimental tests

followed the prescribed AVL 8-mode testing conditions as outlined in Table 4.2 below for this particular engine.

Table 4.2: AVL 8-mode test for the DDC 2.5L turbodiesel engine [179]

Mode	Speed (rpm)	Load (ft-lbs)
1	1000	0
2	1330	51.7
3	1630	148.7
4	1960	210.5
5	4000	39.8
6	3850	91.5
7	3850	157.8
8	3670	224.2

Based on the data presented in Figure 4.2 , there is a NO_x reduction for 5 of the 8 modes for this particular engine. However, there is an increase in NO_x for the three low speed modes for the engine, which is where the engine might operate for 1/3 of the time, in a typical duty cycle for a light duty vehicle.

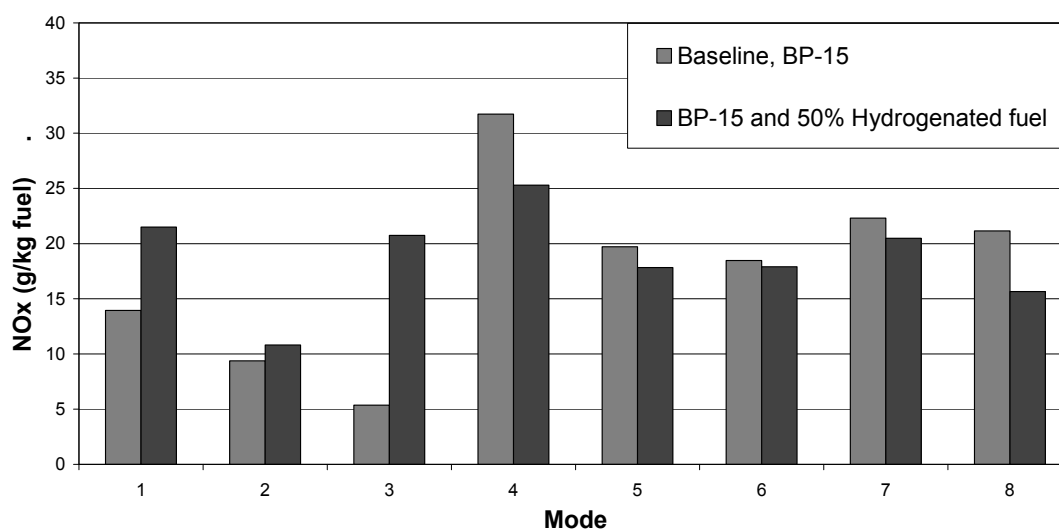


Figure 4.2: NO_x (g/kg fuel) vs AVL 8 mode test. [179]

The Brake Specific Fuel Consumption (BSFC), shown in Figure 4.3, is higher for the biodiesel blend due to the decrease of the lower heating value from the biodiesel portion of the fuel. Therefore, the engine required more fuel to achieve the speed and load condition.

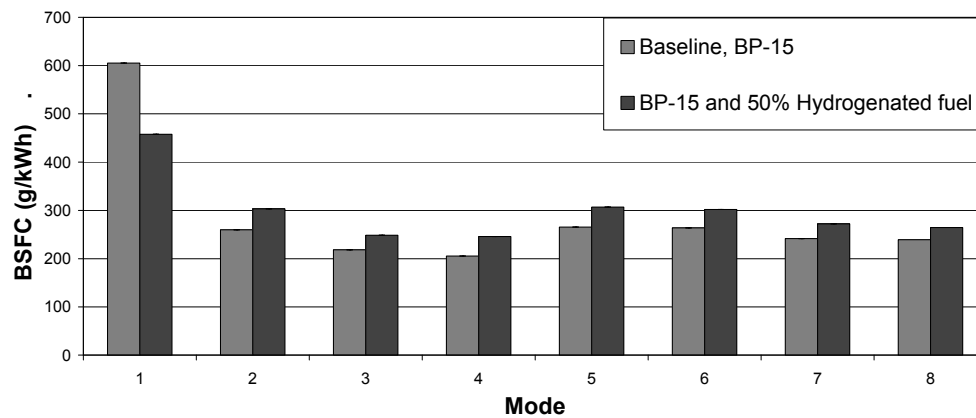


Figure 4.3: BSFC (g/kWh) vs AVL 8 mode test [179]

There is an increase in CO emissions which is not consistent across the modes, presented in Figure 4.4. At high speeds, this difference becomes small between the fuels.

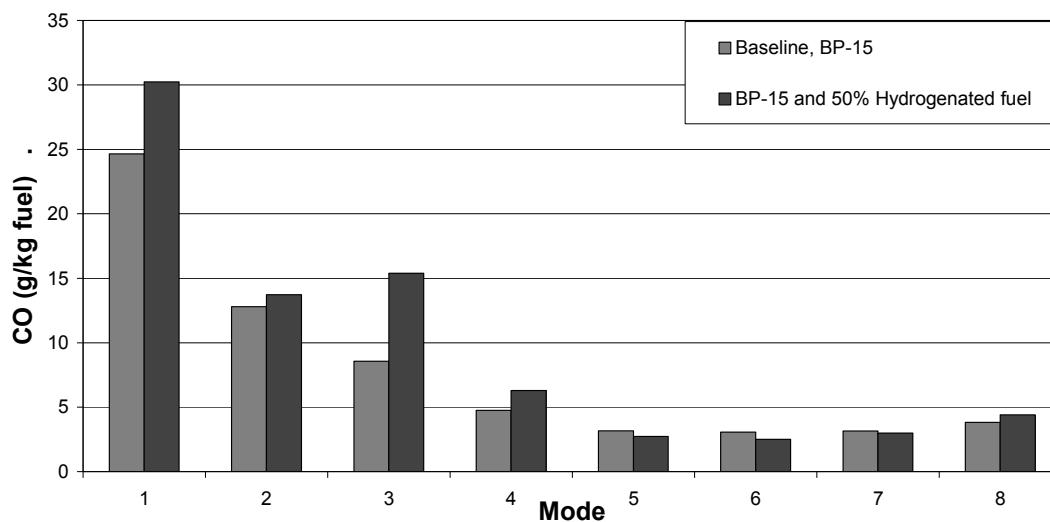


Figure 4.4: CO (g/kg fuel) vs AVL 8 mode test [179]

The data collected was an average of two data points for each fuel, which is insufficient to obtain a measure of the statistical significance of the results. Additionally, the engine was not equipped at the time with the ability to collect pressure traces which would enhance the analysis to include the ignition delay of the fuels, as well as the effect of the pilot and main injections on the heat release.

After reviewing this initial data, a significant change in NO_x emissions was not observed as expected. It was concluded that the effect of the EGR and of the injection timing may be impacting the outcome. Therefore, another set of engine tests was performed to study the impact of the blending of the fuel on the NO_x emissions, without the use of EGR. This second study was conducted to gather more information about how the engine's fuel injection system was operating, and to gather pressure traces and heat release information. The set of experiments involved running the engine at the lower

speeds and loads and varying the blend levels of both the hydrogenated biodiesel and a conventional soy based biodiesel.

4.5 Second Set of Experimental Tests

A set of engine tests was performed with the hydrogenated biodiesel fuels, to compare to a conventional biodiesel fuel. The tests were performed with no engine EGR, but with the normal pilot and main fuel injection pulse, but not held to a fixed timing via the INCA/ETAS system. Fuel property tests were also conducted.

Engine conditions for this set of tests were limited due to complications with the engine driveshaft. Although the goal was to span engine speed and load while using the engine as it was normally programmed to operate, that was not possible. The test conditions are shown in Table 4.3 . Four engine modes were tested, with no EGR applied and with the normal pilot and main fuel injection pulse. Emissions data and TEOM PM data were collected. The emission data was collected through a labview program that was connected to the AVL CEB II. The engine operating data was collected with a Leeds & Northrup MicroMax data system.

Table 4.3: DDC 2.5L Engine Test Specification

Mode Number	Speed (rpm)	Load (ft-lbs)
1	1500	50
2	1500	100
3	1660	75
4	1660	125

4.6 Fuel Property Tests and Results

To understand the physical changes that arise in the fuel based on a change in the chemical composition of the fuel (in this case via the hydrogenation of the fuel), some tests were conducted on the fuels to identify the change in properties. The tests and the results are described in the following sections. When the normal biodiesel fuel is shown in a table, a capital B is used. For the hydrogenated biodiesel, a capital H is used. When the biodiesel is mixed with the diesel fuel in a blended amount, the amount is designated by a number following the capital letter. For example, B20 represents 20% conventional biodiesel blended in diesel fuel.

4.6.1 Cetane number by Ignition Quality Tester (IQT)

The derived cetane number (DCN) for each of the fuel blends was measured in accordance with ASTM D6890-07a [188]. A correlation has been developed to convert the measured ignition delay into a DCN, which is correlated with the CN measured by ASTM D613 (CFR Cetane Rating engine). The ignition delay (defined as the elapsed time from injection to where the chamber pressure reaches $P_{\text{initial}} + 50$ psi) under specified conditions is measured using the Ignition Quality Tester (IQT). The instrument also calculates a standard deviation of the derived cetane number based on the number of sample repetitions. The instrument is shown in Figure 4.5. The system is fully automated and an experiment consists of 15 pre-injections (to equilibrate system temperatures) followed by 32 injections. The reported DCNs are the averages of these 32 injections of pre-filtered fuels. A sample of data from a single injection is presented as a

screen shot in Figure 4.6. Table 4.4 shows the cetane number for the fuels based on ASTM D6890-07a. As is shown in the table, the biodiesel fuel has a higher cetane number and thus a shorter ignition delay. The hydrogenated biodiesel has a higher cetane number than the normal soy-based biodiesel. Knothe and coworkers showed the cetane number associated with the specific fatty acid chain lengths [101]. Thus, an increase in the methyl oleate composition of the biodiesel fuel will increase the cetane number. In previous work, Knothe coworkers also showed that the pre-combustion compounds formed with unsaturated fatty compounds had a lower cetane number, thus explaining the low cetane number for unsaturated biodiesel fuels [189].

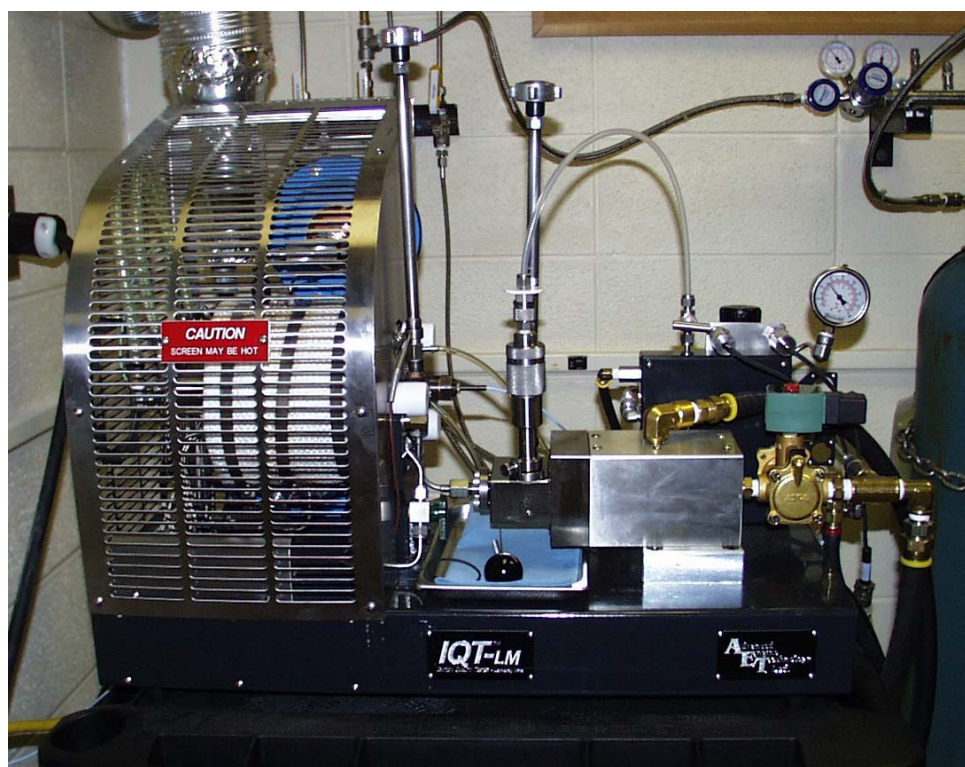


Figure 4.5: Photograph of the Ignition Quality Tester (IQT) at the Penn State Energy Institute

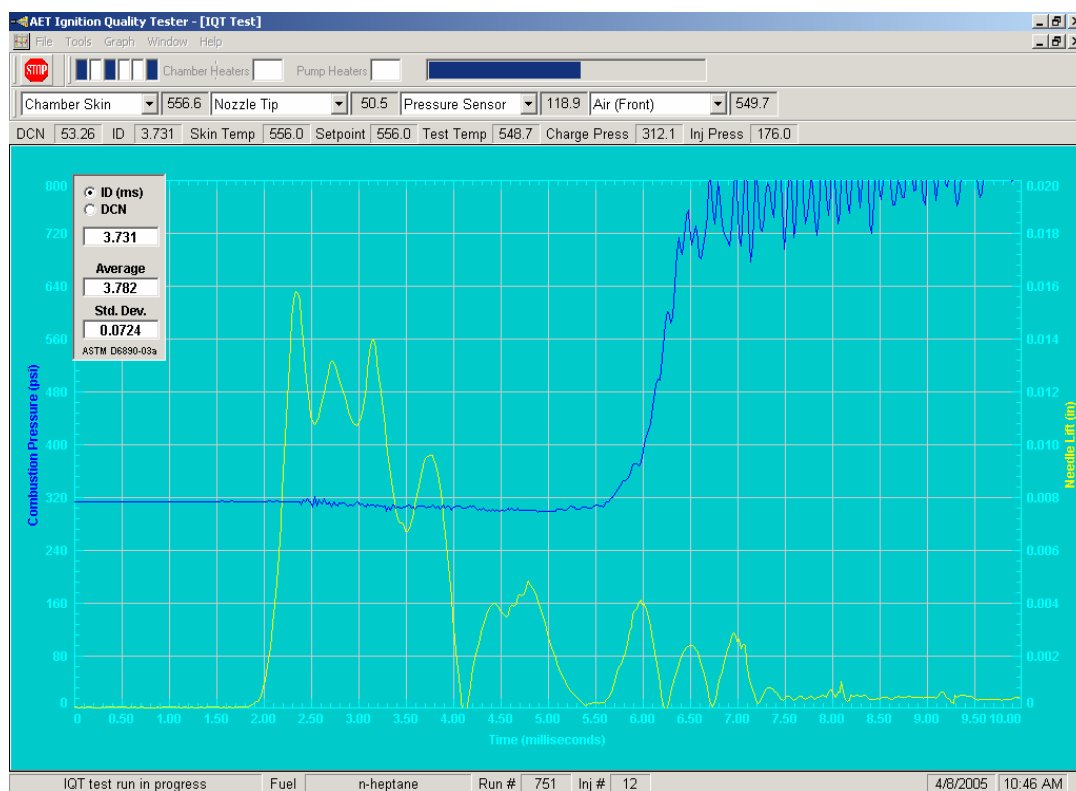


Figure 4.6: Sample data readout from the IQT. Needle lift is displayed in yellow and combustion pressure in blue

Table 4.4: Derived Cetane Number (DCN)

Sample	Ignition Delay (ms)	DCN	Standard Deviation of DCN
ULSD (BP15)	4.231	47.0	0.85
B20	4.106	48.4	1.09
B40	3.983	49.9	1.26
B100	3.907	50.8	1.97
H20	3.888	51.1	1.07
H40	3.726	53.3	0.96
H100	3.114	65.1	2.25
B100- same batch/ different barrel	3.723	53.4	2.16

4.6.2 Compound analysis

The hydrogenated biodiesel was analyzed with GCMS method by the company supplying the sample. The data is used to gain information on the compound composition of the fuel. The biodiesel from AGP was analyzed by the USDA Agricultural Research Service with a similar GCMS method [190]. The reports are provided in Appendix E. The sample reports from AGP are also provided in Appendix E.

4.6.3 Cloud Point and Pour Point

Cloud Point and Pour Point tests are described by ASTM D 2500-99 and D 97-96a, respectively [191, 192]. The intent of the tests was to evaluate the cloud and pour point of the fuels according to ASTM D 2500-99 and D 97-96a, but that was impossible because of the available equipment. Just as ASTM rules show, different baths would have been necessary at 0, -18, -33, ... °C, but only one was available [191, 192]. In addition, the lowest temperature reached, even with two external coolers, was only -24 °C, so it was necessary to place the test jars directly into the cooling medium to perform the tests.

Raw numbers observed for Cloud Point (CP) and Pour Point (PP) are shown in Table 4.5. Pour Point is plotted in Figure 4.7 by fuel type. Cloud Point is plotted by fuel in Figure 4.8. Each sample was tested twice, and the identical values were measured. One of the major problems associated with biodiesel is the low cloud point and pour point [102]. Therefore, it is important to know the effect of the saturation on these properties. As can be seen, both cloud and pour point increase with increasing percentage of biodiesel in the fuel, either with normal biodiesel or hydrogenated

biodiesel. The more saturated hydrogenated biodiesel showed higher cloud and pour points (poorer cold flow properties) as it is widely reported in the literature [193, 194].

Table 4.5: Cloud Point and Pour Point

	ULSD (BP15)	B20	H20	B40	H40	B100	H100
Cloud Point (°C)	-12	-10	-10	-9	-8	0	5
Pour Point (°C)	-21	-18	-12	-12	-12	-6	0

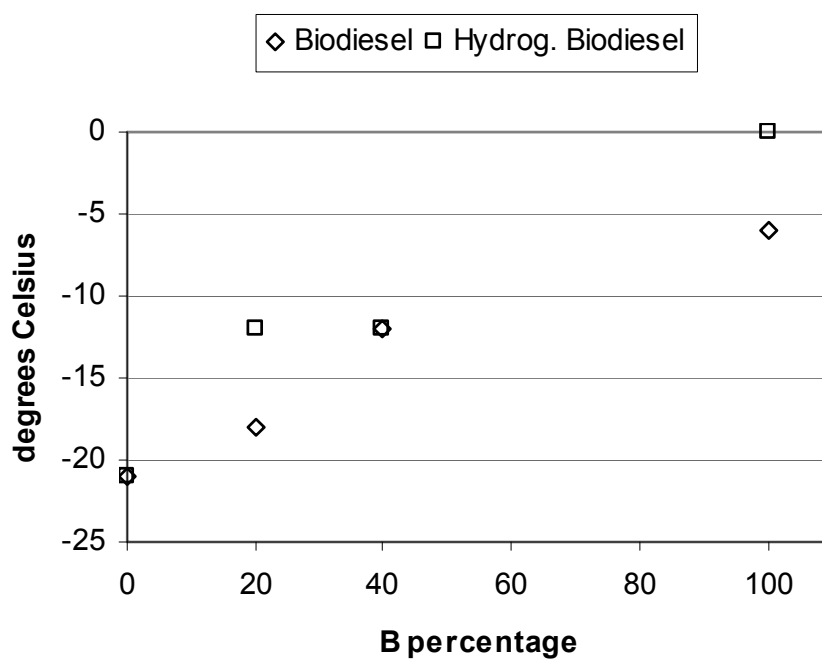


Figure 4.7: Pour Point (°C) by fuel type (B percentage is the blend percentage in the fuel)

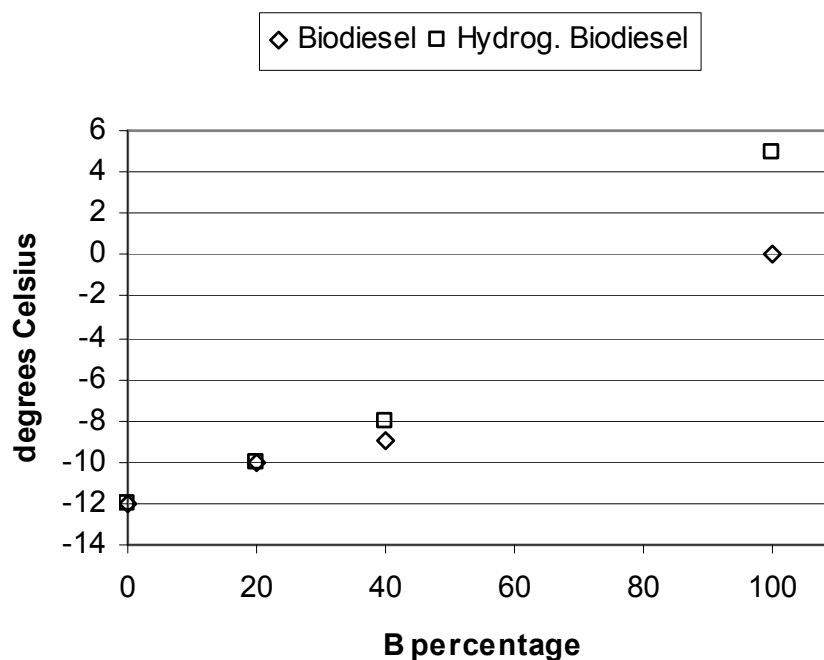


Figure 4.8: Cloud Point (°C) by fuel type (B percentage is the blend percentage in the fuel)

4.6.4 Viscosity

Viscosity is determined by using a timed method through the use of a capillary viscometers described in ASTM D 446-07 [195]. The procedure is described in ASTM D 445-06 [196]. A Modified Oswald Viscometer was used, numbered R201. For these tests, the fluid was placed in the viscometer bath set at 40° C for 30 minutes before the timed test. A sample size of 10-15 measurements were collected and averaged. The data is shown below in Table 4.6. As shown by Knothe and coworkers, the kinematic viscosity of methyl esters is higher than petroleum diesel fuel, and the viscosity increases

as the C18 molecule becomes more saturated [102, 197]. Thus, the hydrogenated biodiesel fuel will have a higher viscosity than the conventional soy-based biodiesel.

Table 4.6: Viscosity (cSt) for the various fuels and blends at (40°C)

Fuel	Viscosity (cSt)
ULSD (BP15)	2.52
B20	2.68
B100	3.96
H20	2.80
H100	4.61

4.6.5 Higher Heating Value

This test is performed per ASTM D5865-07 and is used to determine the calorific value of the component with a bomb calorimeter [198]. The results of the tests of the fuels are shown in Table 4.7. As seen in the table, the heating value of the two biodiesel fuels is less than that of the diesel. The heating value of the hydrogenated biodiesel is slightly higher than for the conventional biodiesel as a result of the saturation. Knothe shows in his work that the heating value for methyl oleate is higher than the heating value for methyl linoleate and methyl linolenate [102]. Even with a change in the chemical composition of the biodiesel fuels, they have similar heating values.

Table 4.7: Calorific Value (BTU/lb) of the Fuels

Fuel	Calorific Value (Btu/lb)
ULSD (BP15)	19671
B20	19177
B40	18615
B100	17115
H20	19200
H40	18715
H100	17138

4.6.6 Boiling Range Distribution

The test for boiling range distribution is performed per ASTM D 2887 [199]. The boiling range distribution of petroleum fractions are determined by Gas Chromatography. The test is limited to samples with a boiling range greater than 55 °C and a final boiling point of 538 °C, and having a vapor pressure sufficiently low to permit sampling at ambient temperatures. The three neat fuels boiling ranges were tested, and the results are shown in Table 3.2. Boiling range distribution provides information about the volatility of the fuel, and particular end points have shown trends with exhaust emissions, as for example T90 has trended with particulate matter mass. As is shown in the table, the range for the ULSD is much broader than for the biodiesel fuels. The two biodiesel fuels have similar boiling ranges.

Table 4.8: Boiling Range Distribution (°C) of the Fuels

% Off	ULSD (BP15) BP(°C)	B100 BP(°C)	H100 BP(°C)
IBP	115.0	326.9	326.4
5	165.3	328.3	327.9
10	184.7	333.3	328.9
15	198.5	350.3	350.1
20	210.9	350.9	350.9
25	220.7	351.3	351.5
30	230.8	351.6	351.9
35	239.4	351.9	352.3
40	249.3	352.1	352.6
45	257.5	352.3	352.9
50	266.7	352.5	353.2
55	275.6	352.7	353.4
60	285.1	352.9	353.7
65	293.6	353.1	353.9
70	301.0	353.3	354.1
75	311.7	353.4	354.4
80	321.2	353.6	354.6
85	333.1	353.8	354.9
90	348.3	354.0	355.3
95	368.3	354.8	355.9
FBP	429.0	360.6	361.4

4.7 Engine Tests Results and Data Analysis

The following sections show the data that has been analyzed and plotted. The set of tests involve examination of the fuel blends being over various engine speeds and loads without EGR.

4.7.1 Fuel Tests over various Engine Modes

The set of data represents the fuels and their blends being tested over various engine modes. Gaseous emissions and particulate matter data were collected. Emissions results are shown in Figure 4.9 - Figure 4.12. Fuel consumption results are shown in Figure 4.13 - Figure 4.15. Exhaust Temperatures are shown in Figure 4.16.

As shown in Figure 4.9 and detailed in previous literature, NO_x increases with the addition of 20% soy-based biodiesel to the diesel fuel in comparison to the conventional diesel fuel. Over the various modes, the increase in NO_x emissions is different: Mode 1- 20.2 % increase, Mode 2- 4.6 % increase, Mode 3- 2.3 % increase, and Mode 4- 10.8 % increase. However, previous research has suggested a 1% increase in NO_x emissions for a 10% increase in biodiesel blended in diesel fuel [53]. The data in this research with a light duty diesel engine refutes the given general trend for heavy duty diesel engines over the past 40 years collected in older engine equipment and in various engine test cycles. As shown in this research and by other researchers, the NO_x emissions increase with load, as shown quite clearly in Modes 2 and 4 in comparison to Modes 1 and 3[122, 200]. Therefore, it is clear that the general trend with biodiesel and NO_x emissions does not take into account the change in engine testing conditions and engine equipment, although this new data suggests that it does not adequately represent the trend.

This data also shows a difference in the NO_x data shown by Zhang in his work with the same engine and with a B40 blend. Mode 3 is the comparable point. Zhang showed that with the B40 blend, there was a slight reduction in NO_x emissions (brake specific – g/kWh) with the double injection strategy [121]. However, the injection

strategy in this research, as shown later in the needle lift data, was different. The pilot injection was not as advanced as in Zhang's research [121]. This indicates that phasing of the pilot injection to the main injection can have some significant impact on NOx emissions.

For the 40% soy-based biodiesel addition, a decrease in NOx emissions over conventional diesel was observed: Mode 1- 11.7% decrease, Mode 2- 13.8 % decrease, Mode 3- 14.3% decrease, Mode 4- 3.3% decrease. As suggested by the literature, hydrogenated biodiesel gives lower NOx emissions [99], and that is shown in this data set. The addition of 20% and 40% of the hydrogenated biodiesel fuel gave similar NOx emissions, and these were similar to the 40% soy-based biodiesel. At this point, there are two explanations that are apparent: 1) there is some change in the chemistry of the fuels with the B40 and then H20 and H40 blends that reduced the NOx emissions, and 2) this change in fuel chemistry along with the injection strategy of pilot and main timing led to this decrease.

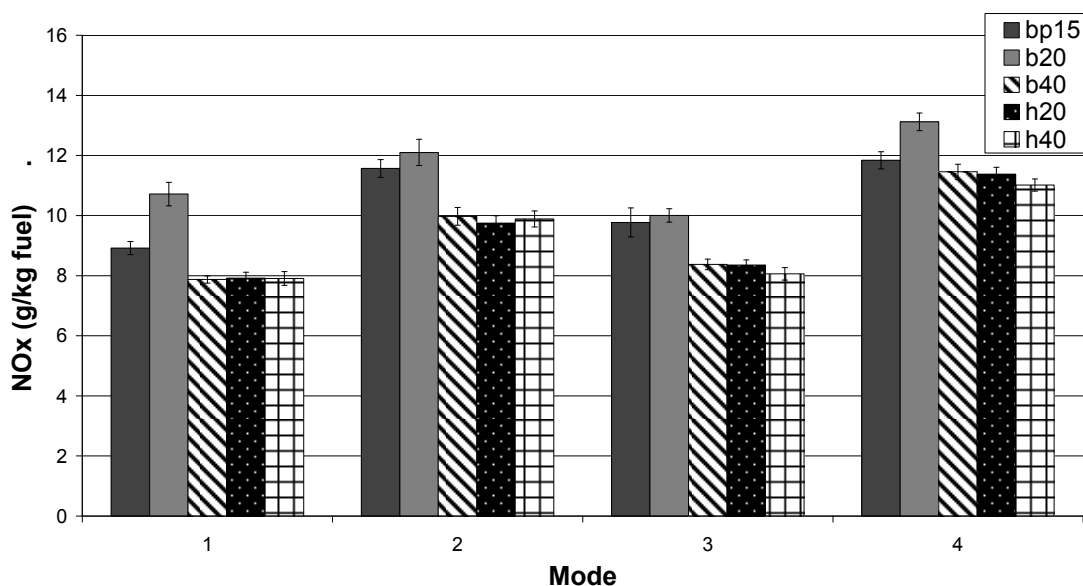


Figure 4.9: NO_x Emissions (g/kg fuel) for DDC 2.5L engine, Mode 1= 1500 rpm/50 ft-lb, Mode 2= 1500 rpm/100 ft-lb, Mode 3= 1660 rpm/75 ft-lb, Mode 4= 1660rpm/125 ft-lb, with pilot and main injection, without EGR, for various biodiesel blends in comparison to baseline diesel fuel ULSD (BP15)

CO₂ emissions are shown in Figure 4.10 . The data for all 4 modes show CO₂ emissions in the approximate same range taking into account the error bars. Mode 1 shows an increase of 4.7% in the CO₂ emissions for B20 with a decrease of 6.5 % for B40 in comparison to the baseline diesel fuel. The H20 and H40 are similar to the baseline diesel, showing a decrease of .8 % and 3.1% respectively. Mode 2 shows a similar trend as Mode 1. Mode 3 shows relatively the same CO₂ emissions for all fuels. Mode 4 shows an increase in CO₂ emissions for the biodiesel fuels, with B20 an 8.3% increase, B40 an 8% increase, H20 a 7.8% increase, and H40 a 4.5% increase.

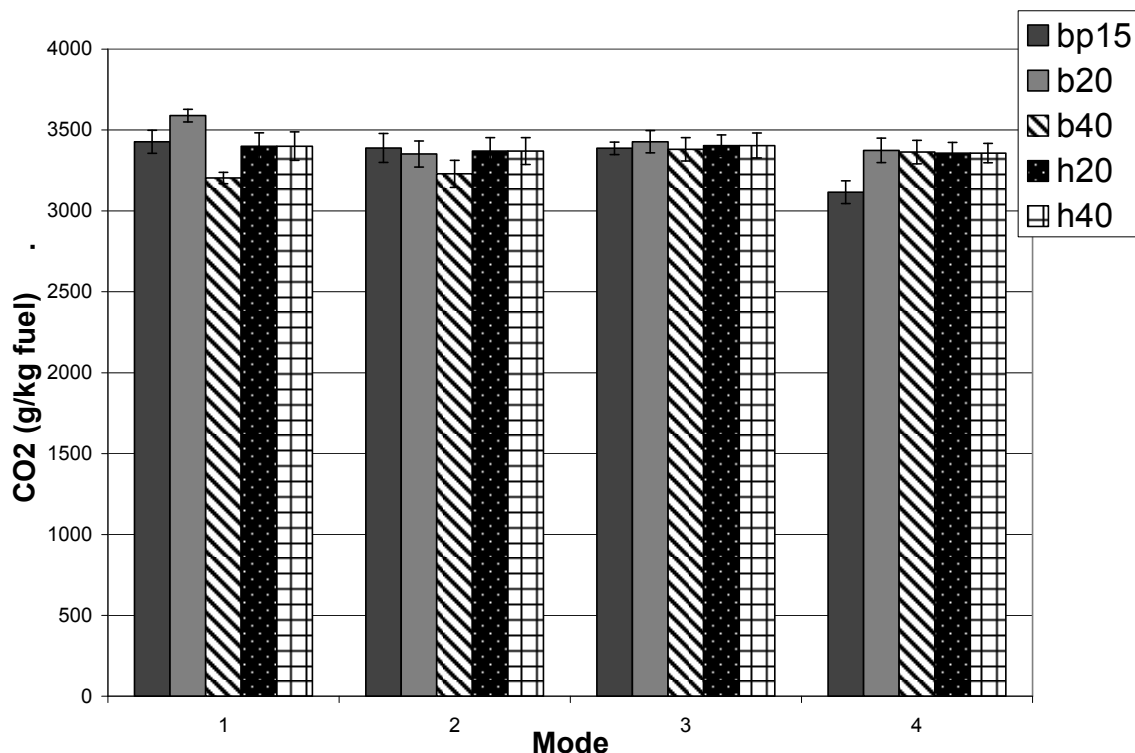


Figure 4.10: CO₂ Emissions (g/kg fuel) for DDC 2.5L engine, Mode 1= 1500 rpm/50 ft-lb, Mode 2= 1500 rpm/100 ft-lb, Mode 3= 1660 rpm/75 ft-lb, Mode 4= 1660rpm/125 ft-lb, with pilot and main injection, without EGR, for various biodiesel blends in comparison to baseline diesel fuel ULSD (BP15)

Hydrocarbon emissions are shown in Figure 4.11 . As shown in the figure, hydrocarbon emissions decrease with increasing load. Also, shown in all modes, but more pronounced in Mode 1, as the biodiesel blend is increased from 20 to 40 %, the hydrocarbon emissions decrease. The hydrogenated biodiesel gives a reduction of hydrocarbons over all modes, and with the increasing % of blend in the baseline diesel. For the H20 blend, the percent reduction in hydrocarbons in comparison to the conventional diesel fuel are: Mode 1- 35.6%, Mode 2- 29.6%, Mode 3- 22.3%, Mode 4- 23.6%.

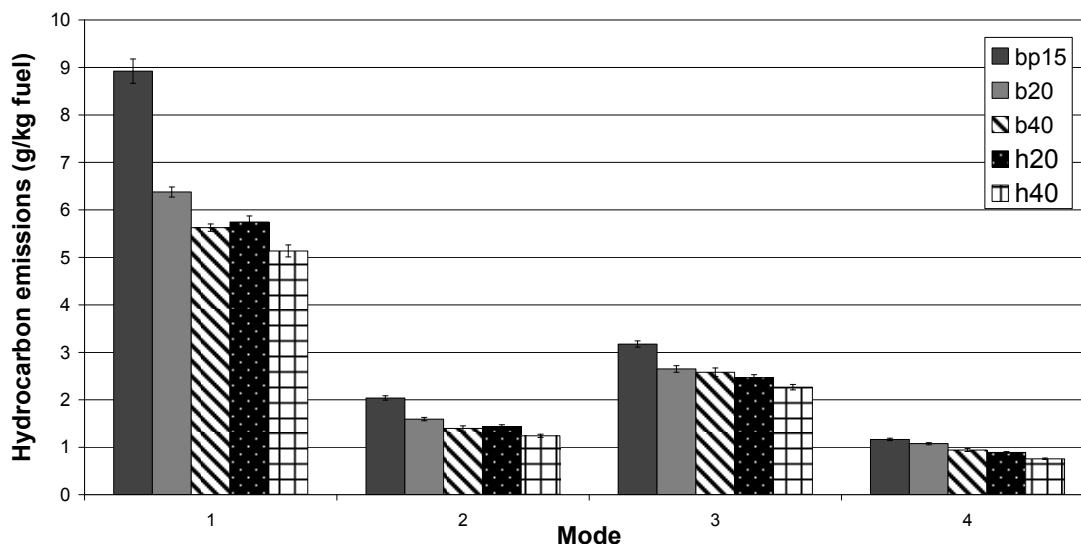


Figure 4.11: Hydrocarbon Emissions (g/kg fuel) for DDC 2.5L engine, Mode 1= 1500 rpm/50 ft-lb, Mode 2= 1500 rpm/100 ft-lb, Mode 3= 1660 rpm/75 ft-lb, Mode 4= 1660rpm/125 ft-lb, with pilot and main injection, without EGR, for various biodiesel blends in comparison to baseline diesel fuel ULSD (BP15)

CO emissions are shown in Figure 4.12 . For Mode 1, an increase of 4.8% in CO is seen for the B20 blend, but decreases shown for all other biodiesel blends: B40 – 1.0%, H20-6.5%, and H40-9.7%. For Mode 2, a decrease is shown for all biodiesel blends: B20 – 7.1%, B40 - 12.0%, H20 – 9.3%, and H40 – 17.2%. For Mode 3, an increase of 1.0 % in CO is seen for the B40 blend, but decreases shown for all other biodiesel blends: B20 - 4.8%, H20 - 8.6%, and H40 - 12.3%. For Mode 4, a decrease is shown for all biodiesel blends: B20- .7%, B40 - 4.6%, H20 - 6.1%, and H40 - 12.9%.

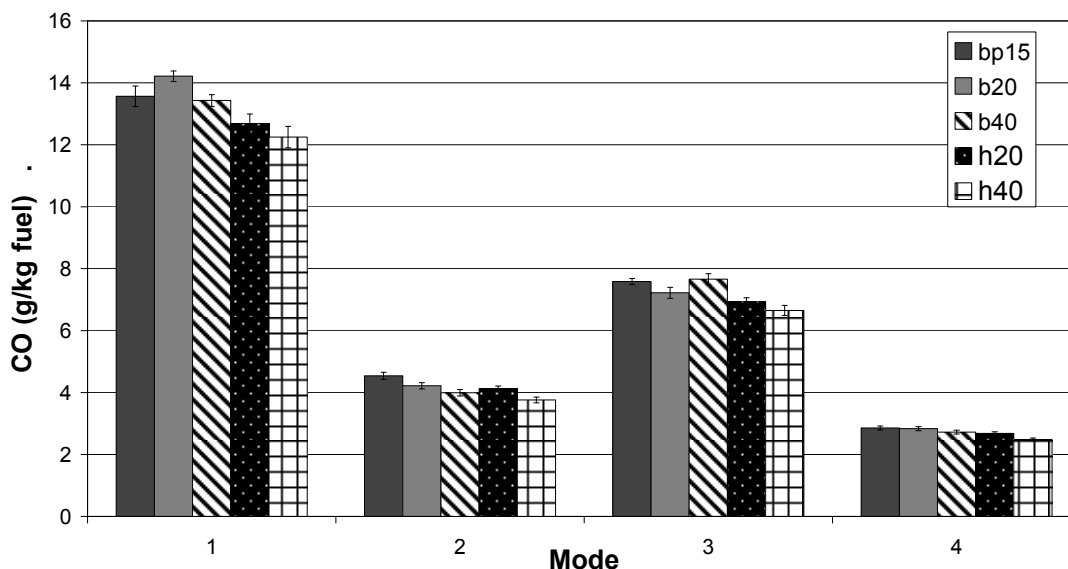


Figure 4.12: CO Emissions (g/kg fuel) for DDC 2.5L engine, Mode 1= 1500 rpm/50 ft-lb, Mode 2= 1500 rpm/100 ft-lb, Mode 3= 1660 rpm/75 ft-lb, Mode 4= 1660rpm/125 ft-lb, with pilot and main injection, without EGR, for various biodiesel blends in comparison to baseline diesel fuel ULSD (BP15)

Fuel consumption is shown in Figure 4.13 . As shown in the data, the fuel consumption error bars make it difficult to determine a change in the actual consumption. However, it would be expected that as the soy-based biodiesel and hydrogenated biodiesel are blended into diesel fuel, more fuel would be required since the calorific values of both fuels are lower than diesel. It should also be noted that the fuel injector delivery operates on a volume fuel injection, and the density of the soy-based biodiesel and hydrogenated biodiesel are similar, and higher than the convention diesel fuel. Therefore, as the engine would need to adjust to inject more of the biodiesel fuel to compensate for the lower calorific value, it would also be adjusting to deliver less volume to compensate for the change in density. Table 4.9 shows the percent change in fuel consumption (g/hr) in comparison to conventional diesel fuel.

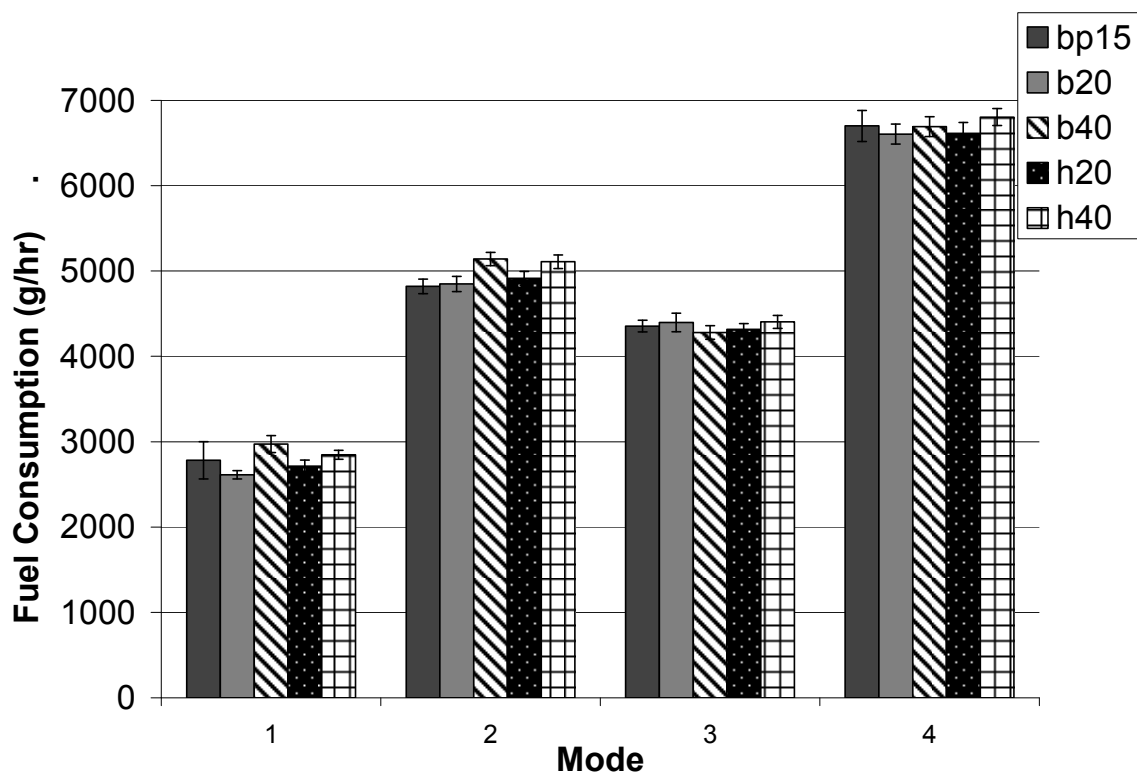


Figure 4.13: Fuel Consumption (g/hr) for DDC 2.5L engine, Mode 1= 1500 rpm/50 ft-lb, Mode 2= 1500 rpm/100 ft-lb, Mode 3= 1660 rpm/75 ft-lb, Mode 4= 1660rpm/125 ft-lb, with pilot and main injection, without EGR, for various biodiesel blends in comparison to baseline diesel fuel ULSD (BP15)

Brake Specific Fuel Consumption (BSFC) is shown in Figure 4.14 . The fuel consumption based on the power delivery by the engine shows that slightly more hydrogenated biodiesel was needed for Mode 1 and 2, but approximately the same for the other modes. The engine required the same soy-based biodiesel in comparison to the baseline diesel fuel for all 4 modes. Table 4.9 shows the percent change in BSFC (g/kWh) in comparison to conventional diesel fuel.

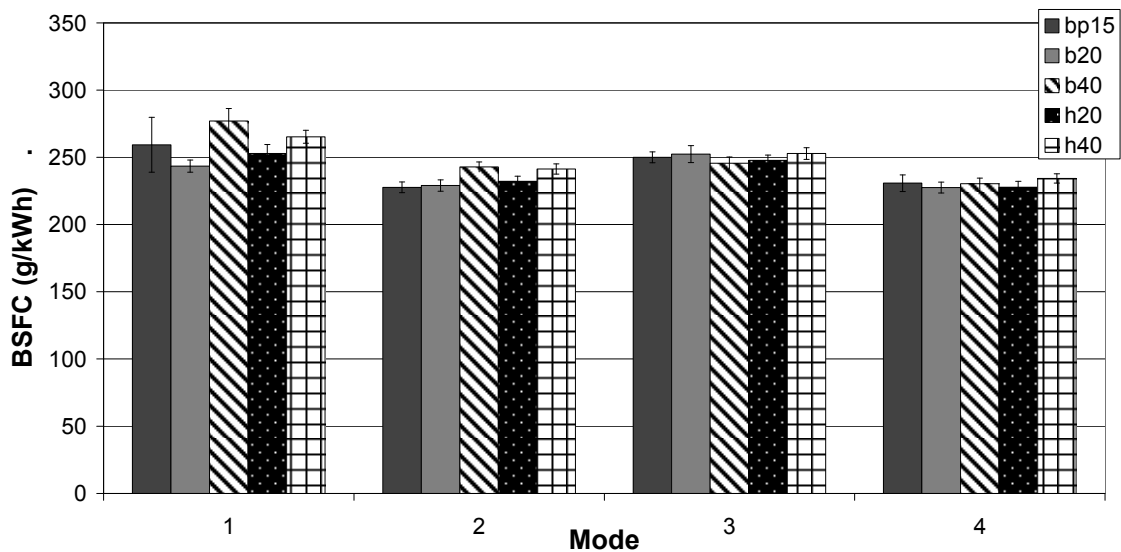


Figure 4.14: Brake Specific Fuel Consumption (g/kWh) for DDC 2.5L engine, Mode 1= 1500 rpm/50 ft-lb, Mode 2= 1500 rpm/100 ft-lb, Mode 3= 1660 rpm/75 ft-lb, Mode 4= 1660rpm/125 ft-lb, with pilot and main injection, without EGR, for various biodiesel blends in comparison to baseline diesel fuel ULSD (BP15)

Table 4.9: Percent Change in Emissions in Comparison to Conventional Diesel fuel for Fuel Consumption (g/hr), Brake Specific Fuel Consumption (g/kWh), and Brake Specific Energy Consumption (MJ/kWh)

	Fuel (g/hr)	BSFC (g/kWh)	BSEC(MJ/kWh)
b20			
m1	-6.1	-6.1	-8.5
m2	0.6	0.6	-1.9
m3	1.0	1.0	-1.6
m4	-1.4	-1.4	-3.9
b40			
m1	6.8	6.8	1.1
m2	6.7	6.7	0.9
m3	-1.7	-1.7	-7.0
m4	-0.1	-0.1	-5.5
h20			
m1	-2.5	-2.5	-4.8
m2	2.0	2.0	-0.5
m3	-0.9	-0.9	-3.3
m4	-1.3	-1.3	-3.7
h40			
m1	2.3	2.3	-2.7
m2	6.0	6.0	0.8
m3	1.1	1.1	-3.8
m4	1.6	1.6	-3.4

Brake Specific Energy Consumption (BSEC) is shown in Figure 4.15. This figure is based on the heating value of the fuel divided by the power output from the engine for the particular fuel. Mode 1 and 2 show that more hydrogenated biodiesel is required for the same power output, but that the soy-based biodiesel and baseline fuels are relatively similar. The Mode 1 soy-based biodiesel requirement for less fuel is not consistent with what would have been expected. For Mode 3 and 4, the energy equivalent basis shows

the same fuel requirement for each fuel compared. Again, this would not be expected since the fuels for this figure are adjusted for the difference in calorific value of the fuel.

Table 4.9 shows the percent change in BSEC (MJ/kWh) in comparison to conventional diesel fuel.

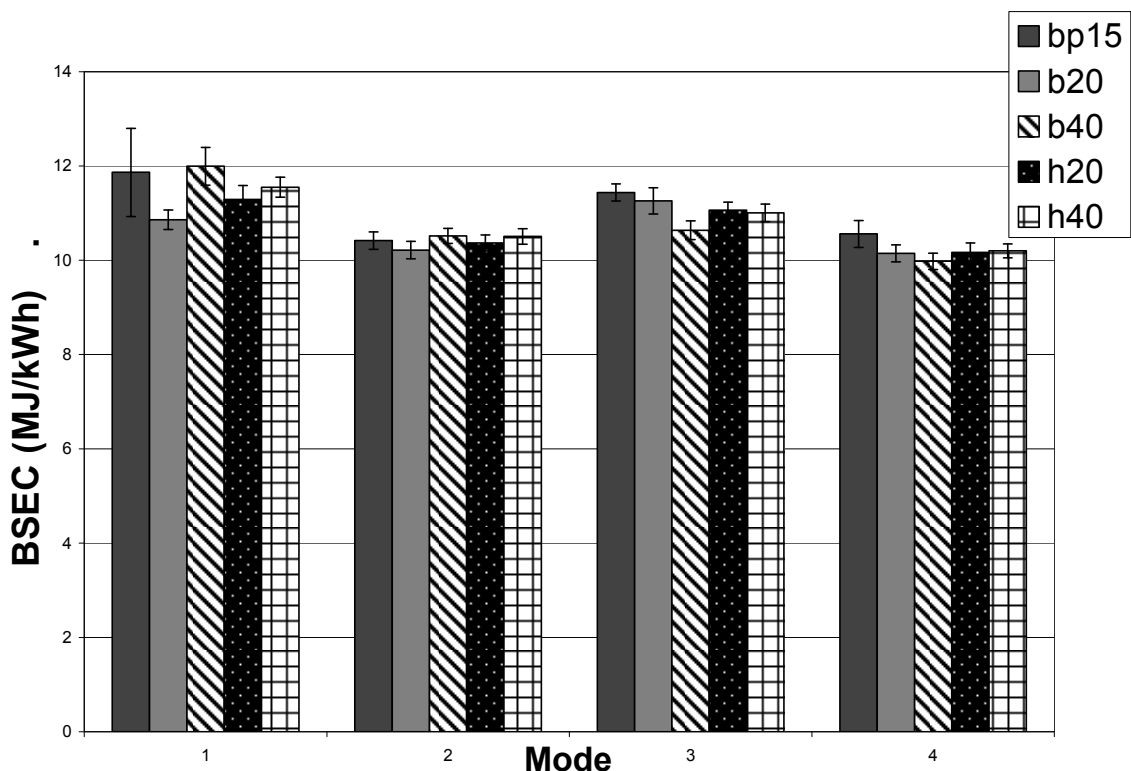


Figure 4.15: Brake Specific Energy Consumption (MJ/kWh) for DDC 2.5L engine, Mode 1= 1500 rpm/50 ft-lb, Mode 2= 1500 rpm/100 ft-lb, Mode 3= 1660 rpm/75 ft-lb, Mode 4= 1660rpm/125 ft-lb, with pilot and main injection, without EGR, for various biodiesel blends in comparison to baseline diesel fuel ULSD (BP15)

Exhaust temperatures for each fuel are shown in Figure 4.16 . These are downstream exhaust temperatures taken at the same exhaust point for each test. As shown in the figure, Mode 1 shows an increase in the exhaust temperature for each biodiesel fuel blend, and with a slight increase for the 40% blend. Mode 2 shows an

increase in the temperature for the B40, H20, and H40 blends. In Mode 3 and 4, the exhaust temperature is the same or slightly above the baseline diesel temperature for the soy-based biodiesel, but a definite increase is shown for the hydrogenated blends.

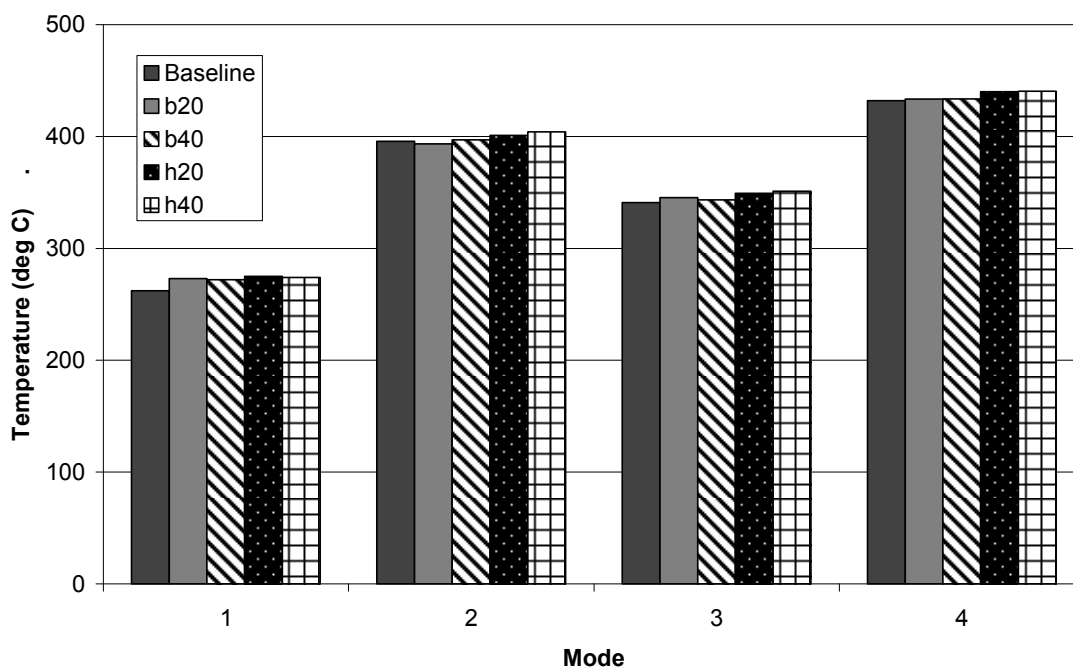


Figure 4.16: Exhaust Temperature ($^{\circ}\text{C}$) for DDC 2.5L engine, Mode 1= 1500 rpm/50 ft-lb, Mode 2= 1500 rpm/100 ft-lb, Mode 3= 1660 rpm/75 ft-lb, Mode 4= 1660rpm/125 ft-lb, with pilot and main injection, without EGR, for various biodiesel blends in comparison to baseline diesel fuel ULSD (BP15)

4.7.2 Pressure Trace and Heat Release Analysis

The following figures show the pressure trace and heat release analysis from the testing. A set of 200 pressure cycles were collected for each cylinder. In this group of figures, the data from cylinder 3 is represented as an averaged cycle from the 200 traces.

Pressure trace data from Mode 1 for the test fuels are shown in Figure 4.17 . The plot shows similar pressure curves for each fuel. The premixed and diffusion phases are pronounced and distinct in the plot. Table 4.10 shows the maximum pressure achieved by each fuel.

Table 4.10: Mode 1 Maximum Pressure (bar)

Fuel Type	bp15	b20	b40	h20	h40
Maximum Pressure (bar)	55.9	55.7	54.9	54.7	54.3

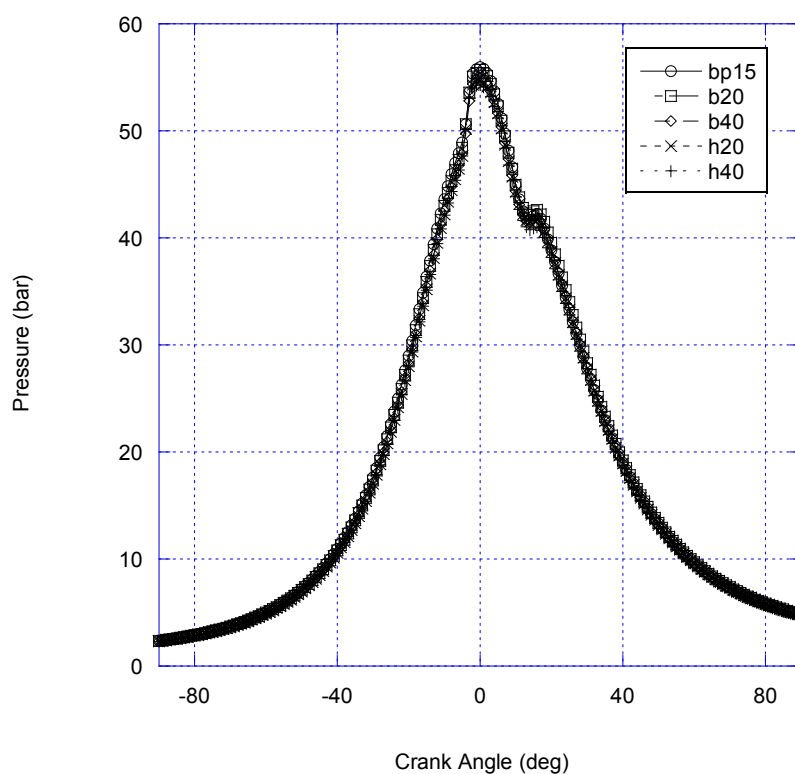


Figure 4.17: Mode 1 Pressure Trace Plot for DDC 2.5L engine, Mode 1= 1500 rpm/50 ft-lb, with pilot and main injection, without EGR, for various biodiesel blends in comparison to baseline diesel fuel ULSD (BP15)

Pressure trace data from Mode 2 for the test fuels are shown in Figure 4.18 . The plot shows similar pressure curves for each fuel. The premixed and diffusion phases are pronounced and distinct in the plot. Table 4.11 shows the maximum pressure achieved by each fuel.

Table 4.11: Mode 2 Maximum Pressure (bar)

Fuel Type	bp15	b20	b40	h20	h40
Maximum Pressue (bar)	67.0	66.4	64.9	65.4	65.1

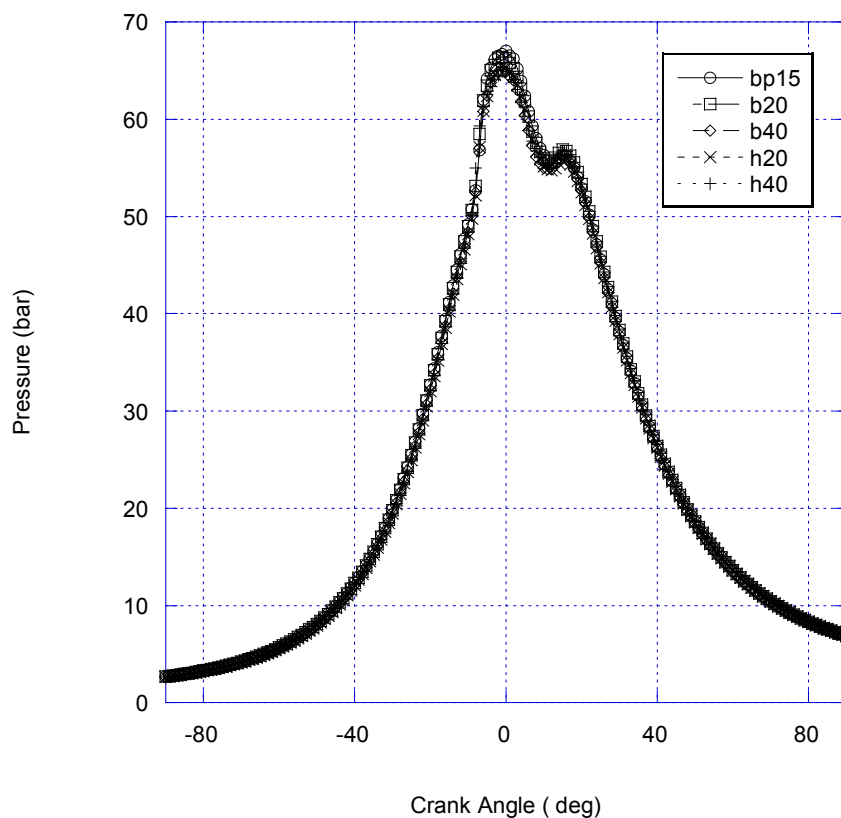


Figure 4.18: Mode 2 Pressure Trace Plot for DDC 2.5L engine, Mode 2= 1500 rpm/100 ft-lb, with pilot and main injection, without EGR, for various biodiesel blends in comparison to baseline diesel fuel ULSD (BP15)

Pressure trace data from Mode 3 for the test fuels are shown in Figure 4.19 . The plot shows similar pressure curves for each fuel. The premixed and diffusion phases are pronounced and distinct in the plot. Table 4.12 shows the maximum pressure achieved by each fuel.

Table 4.12: Mode 3 Maximum Pressure (bar)

Fuel Type	bp15	b20	b40	h20	h40
Maximum Pressue (bar)	66.0	65.4	62.9	63.6	63.4

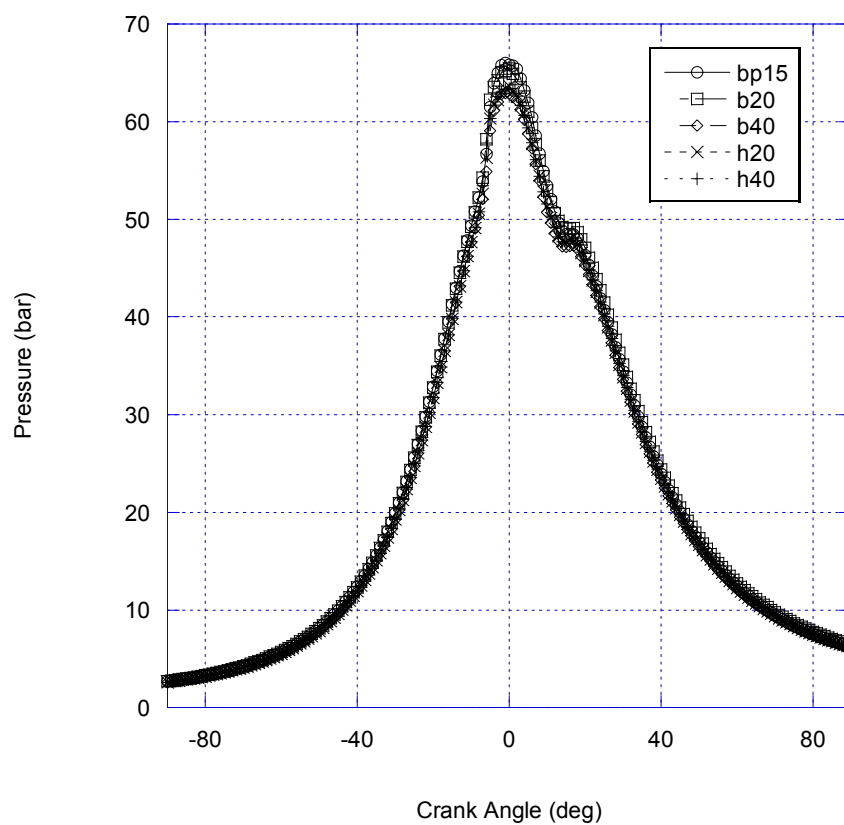


Figure 4.19: Mode 3 Pressure Trace Plot for DDC 2.5L engine, Mode 3= 1660 rpm/75 ft-lb, with pilot and main injection, without EGR, for various biodiesel blends in comparison to baseline diesel fuel ULSD (BP15)

Pressure trace data from Mode 4 for the test fuels are shown in Figure 4.20 . The plot shows similar pressure curves for each fuel. The premixed and diffusion phases are pronounced and distinct in the plot. Table 4.13 shows the maximum pressure achieved by each fuel.

Table 4.13: Mode 4 Maximum Pressure (bar)

Fuel Type	bp15	b20	b40	h20	h40
Maximum Pressue (bar)	75.8	73.9	72.9	72.7	72.7

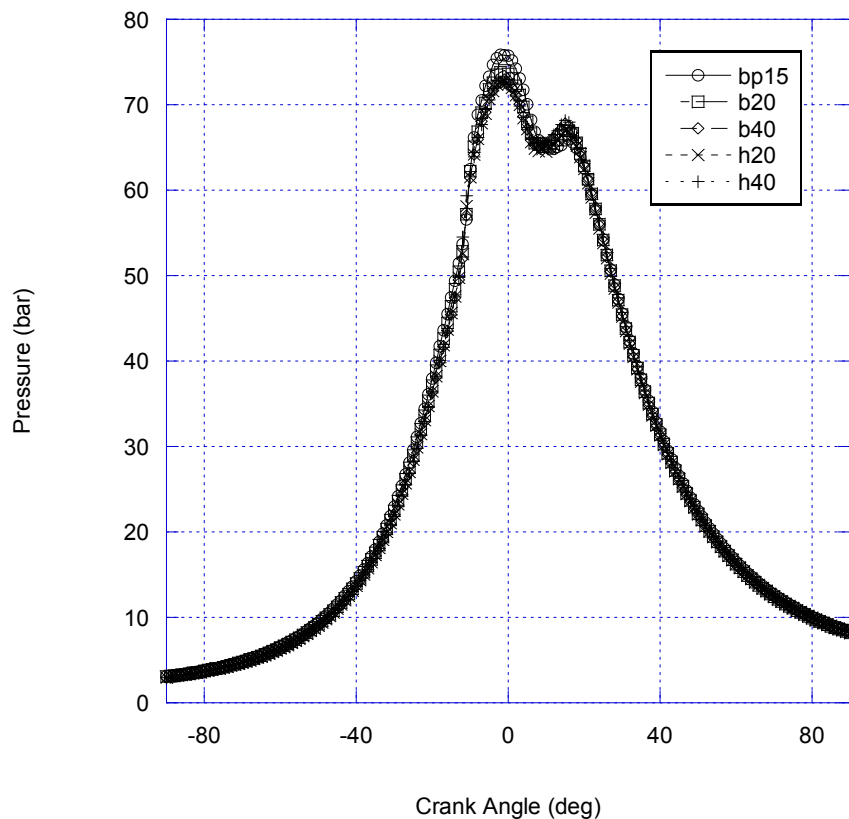


Figure 4.20: Mode 4 Pressure Trace Plot for DDC 2.5L engine, Mode 4= 1660rpm/125 ft-lb, with pilot and main injection, without EGR, for various biodiesel blends in comparison to baseline diesel fuel ULSD (BP15)

Heat release data from Mode 1 through Mode 4 for the test fuels are shown in Figures 4.21 through 4.24. All heat release data plots shows similar rate of heat release curves for each fuel in each specific mode. Based on the needle lift data plots for the pilot and main injection, the heat release data plots show a heat release for the each injection pulse.

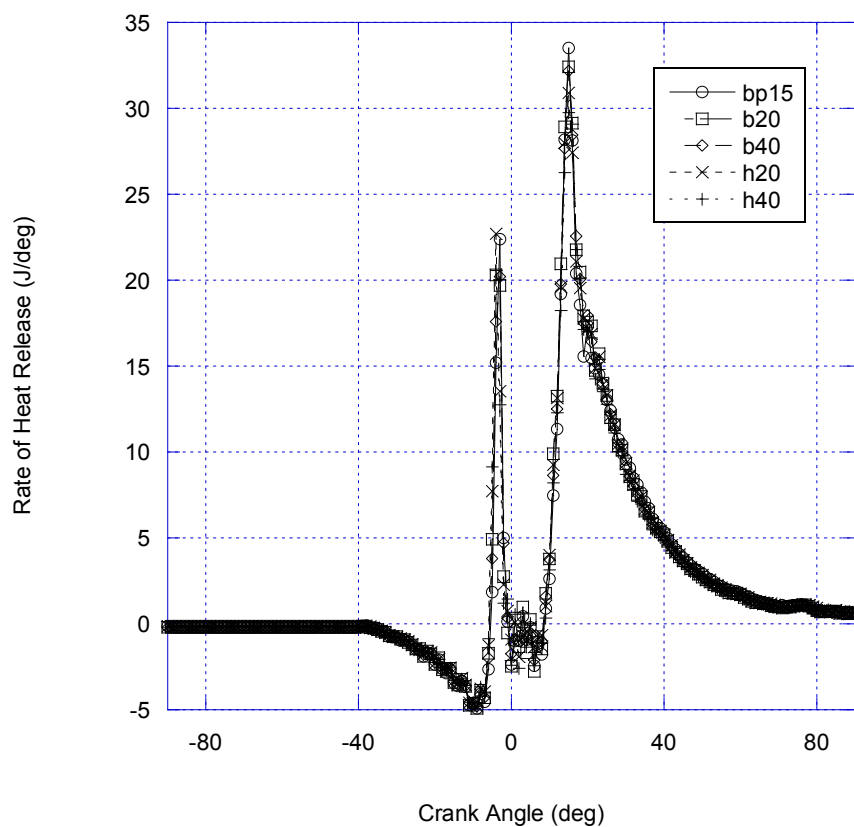


Figure 4.21: Mode 1 Rate of Heat Release Plot for DDC 2.5L engine, Mode 1= 1500 rpm/50 ft-lb, with pilot and main injection, without EGR, for various biodiesel blends in comparison to baseline diesel fuel ULSD (BP15)

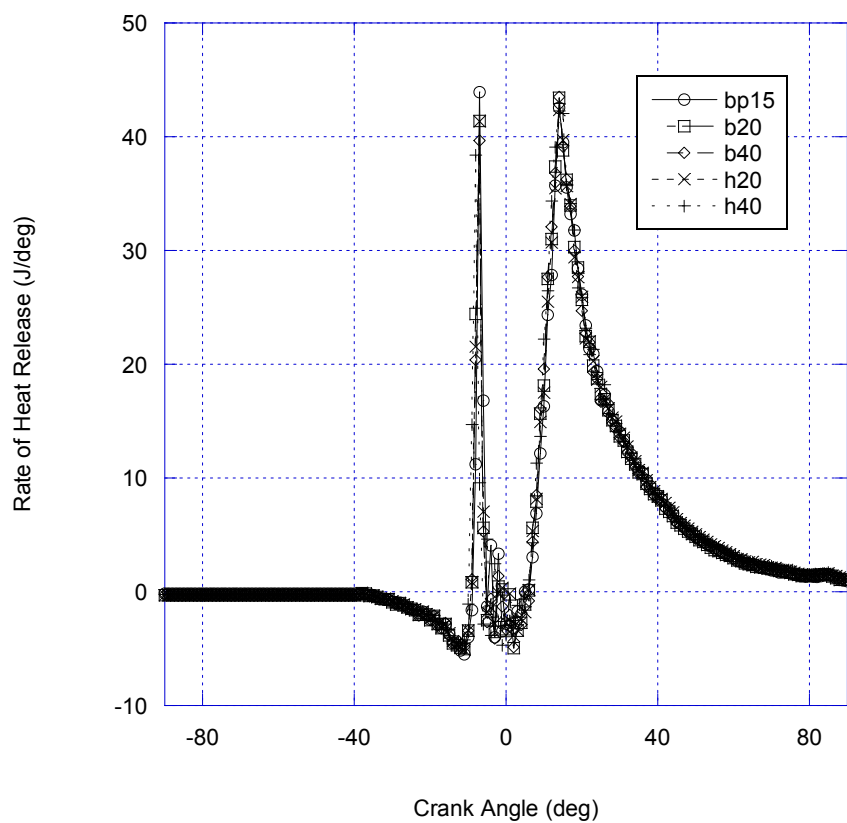


Figure 4.22: Mode 2 Rate of Heat Release Plot for DDC 2.5L engine, Mode 2= 1500 rpm/100 ft-lb, with pilot and main injection, without EGR, for various biodiesel blends in comparison to baseline diesel fuel ULSD (BP15)

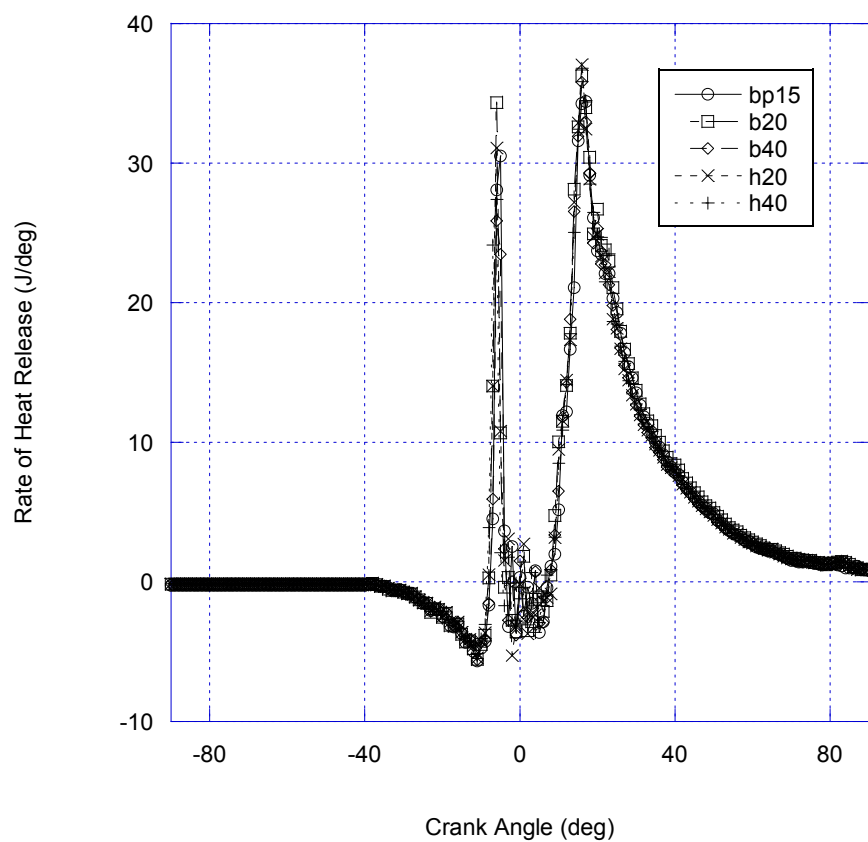


Figure 4.23: Mode 3 Rate of Heat Release Plot for DDC 2.5L engine, Mode 3= 1660 rpm/75 ft-lb, with pilot and main injection, without EGR, for various biodiesel blends in comparison to baseline diesel fuel ULSD (BP15)

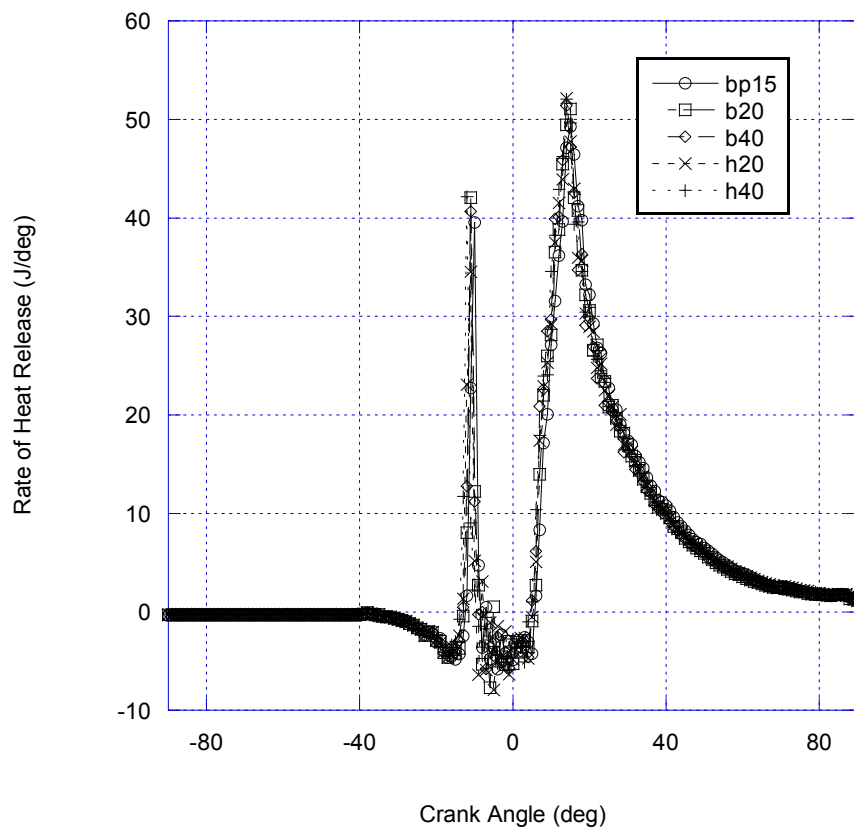


Figure 4.24: Mode 4 Rate of Heat Release Plot for DDC 2.5L engine, Mode 4= 1660rpm/125 ft-lb, with pilot and main injection, without EGR, for various biodiesel blends in comparison to baseline diesel fuel ULSD (BP15)

4.7.3 Needle Lift

The following figures show the fuel injector needed lift analysis. A set of 200 needle lift cycles were collected for each cylinder. In this group of figures, the data from the needle lift sensor applied in cylinder 1 is represented as an averaged cycle from the 200 traces.

Needle Lift data from Mode 1 through Mode 4 for the test fuels are shown in Figures 4.25 through 4.28. The needle lift data plots show similar needle lift curves for each fuel in each specific mode.

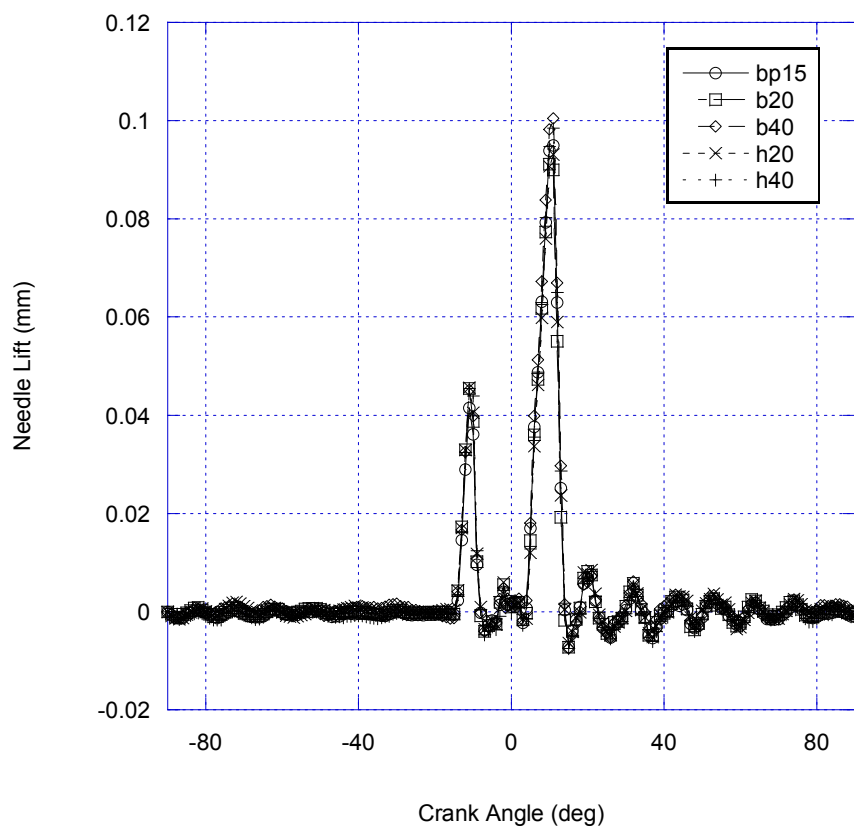


Figure 4.25: Mode 1 Needle Lift Plot for DDC 2.5L engine, Mode 1= 1500 rpm/50 ft-lb, with pilot and main injection, without EGR, for various biodiesel blends in comparison to baseline diesel fuel ULSD (BP15)

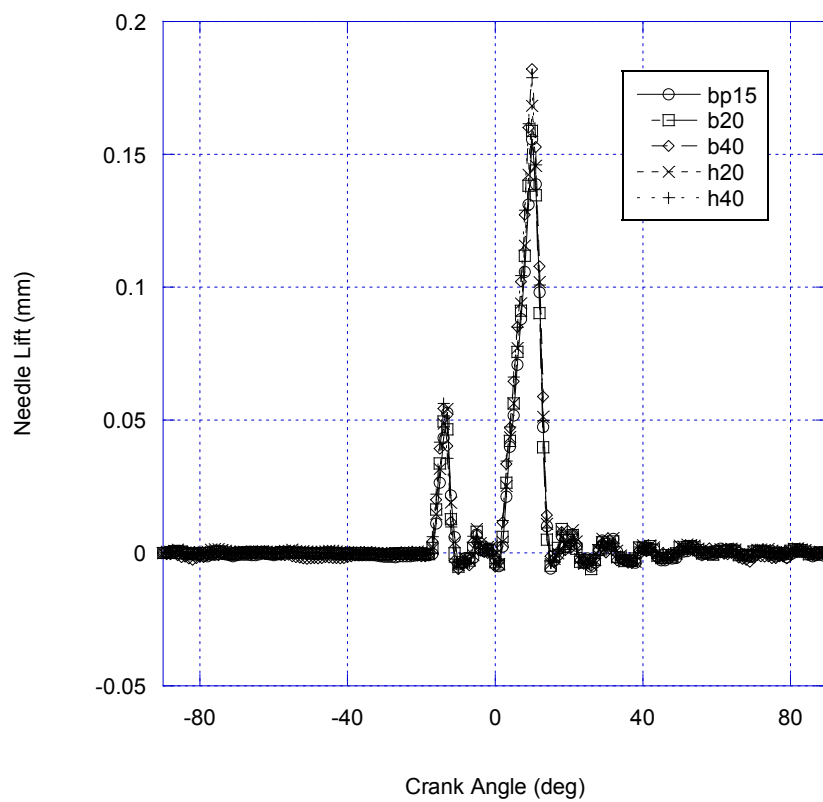


Figure 4.26: Mode 2 Needle Lift Plot for DDC 2.5L engine, Mode 2= 1500 rpm/100 ft-lb, with pilot and main injection, without EGR, for various biodiesel blends in comparison to baseline diesel fuel ULSD (BP15)

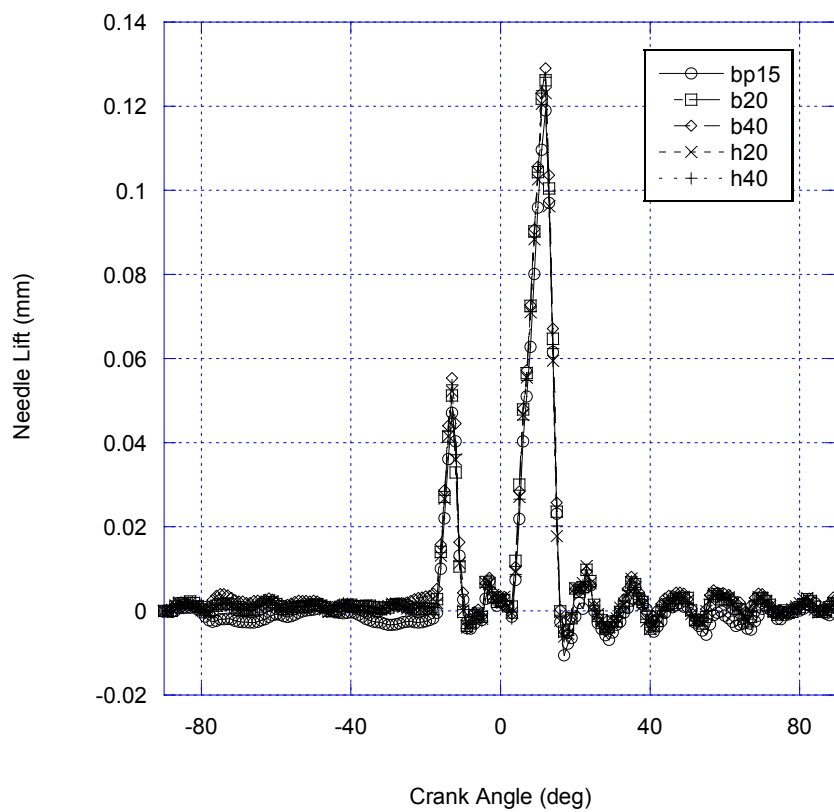


Figure 4.27: Mode 3 Needle Lift Plot for DDC 2.5L engine, Mode 3= 1660 rpm/75 ft-lb, with pilot and main injection, without EGR, for various biodiesel blends in comparison to baseline diesel fuel ULSD (BP15)

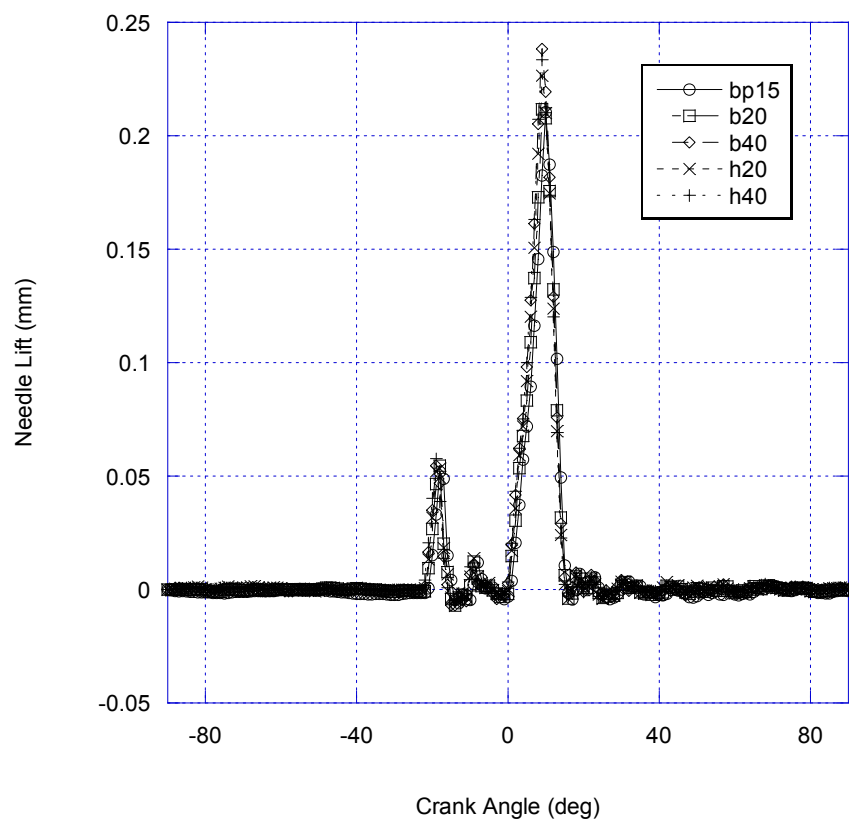


Figure 4.28: Mode 4 Needle Lift Plot for DDC 2.5L engine, Mode 4= 1660rpm/125 ft-lb, with pilot and main injection, without EGR, for various biodiesel blends in comparison to baseline diesel fuel ULSD (BP15)

4.7.4 Bulk Cylinder Temperature

The following figures show the bulk cylinder temperature analysis from the testing. A set of 200 pressure cycles were collected for each cylinder and bulk cylinder temperature was calculated. In this group of figures, the data from cylinder 3 is represented as an averaged cycle from the 200 traces.

Bulk cylinder temperature data from Mode 1 for the test fuels are shown in Figure 4.29 . The plot shows similar bulk temperature for each fuel, but with varying maximum temperatures. Table 4.14 shows the maximum bulk temperature achieved. As is shown in the table, the bulk temperature is higher for the biodiesel blends than for the diesel fuel. The higher biodiesel blend does not produce a higher bulk cylinder temperature.

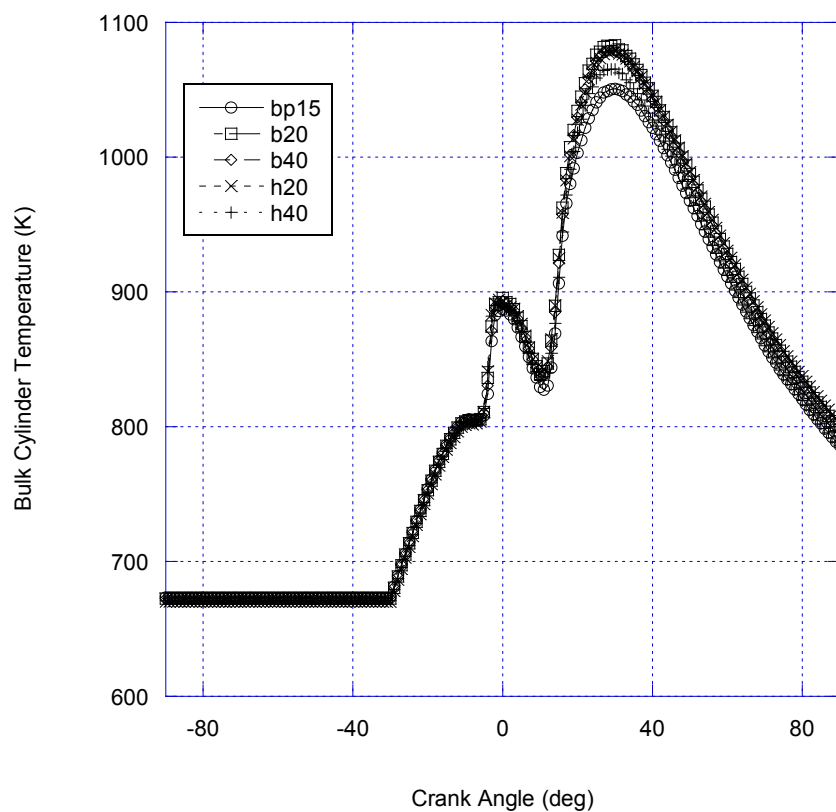


Figure 4.29: Mode 1 Bulk Cylinder Temperature Plot for DDC 2.5L engine, Mode 1= 1500 rpm/50 ft-lb, with pilot and main injection, without EGR, for various biodiesel blends in comparison to baseline diesel fuel ULSD (BP15)

Table 4.14: Mode 1 Maximum Bulk Temperature (K)

Fuel Type	bp15	b20	b40	h20	h40
Maximum Bulk Temperature (K)	1050.7	1082.9	1079.2	1079.3	1065.3

Bulk cylinder temperature data from Mode 2 for the test fuels are shown in Figure 4.30 . The plot shows similar bulk temperature for each fuel, but with varying maximum temperatures. Table 4.15 shows the maximum bulk temperature achieved. As is shown in the table, the bulk temperature is higher for the biodiesel blends than for the diesel fuel. The higher biodiesel blend does produce a higher bulk cylinder temperature with all cases.

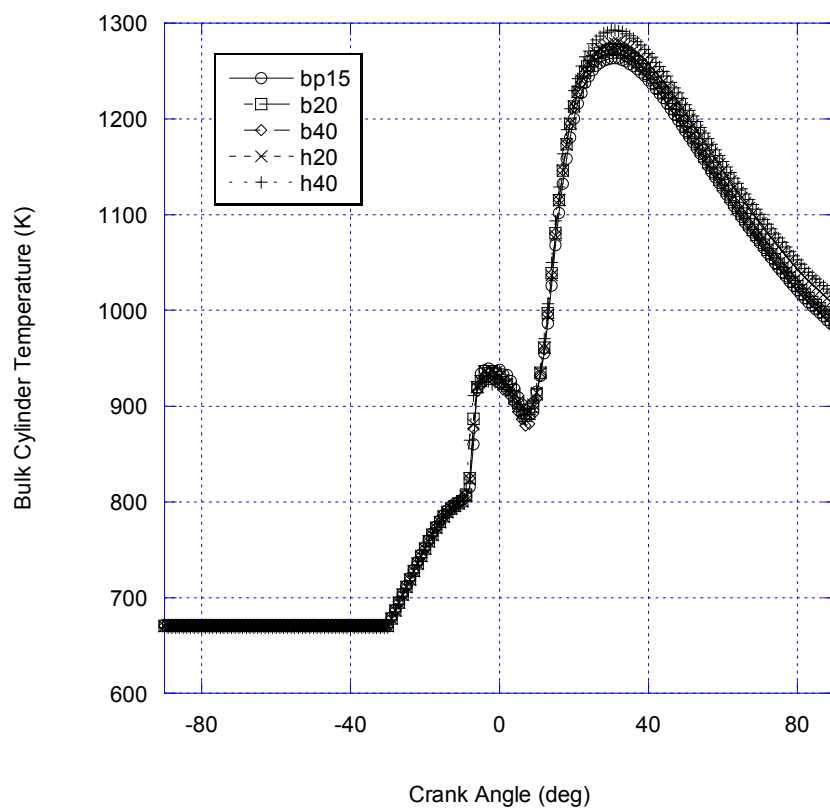


Figure 4.30: Mode 2 Bulk Cylinder Temperature Plot for DDC 2.5L engine, Mode 2= 1500 rpm/100 ft-lb, with pilot and main injection, without EGR, for various biodiesel blends in comparison to baseline diesel fuel ULSD (BP15)

Table 4.15: Mode 2 Maximum Bulk Temperature (K)

Fuel Type	bp15	b20	b40	h20	h40
Maximum Bulk Temperature (K)	1263.6	1272.9	1273.6	1280	1292.8

Bulk cylinder temperature data from Mode 3 for the test fuels are shown in Figure 4.31 . The plot shows similar bulk temperature for each fuel, but with varying maximum temperatures. Table 4.16 shows the maximum bulk temperature achieved. As is shown in the table, the bulk temperature is higher for the biodiesel blends than for the diesel fuel. The higher biodiesel blend does not produce a higher bulk cylinder temperature in all cases.

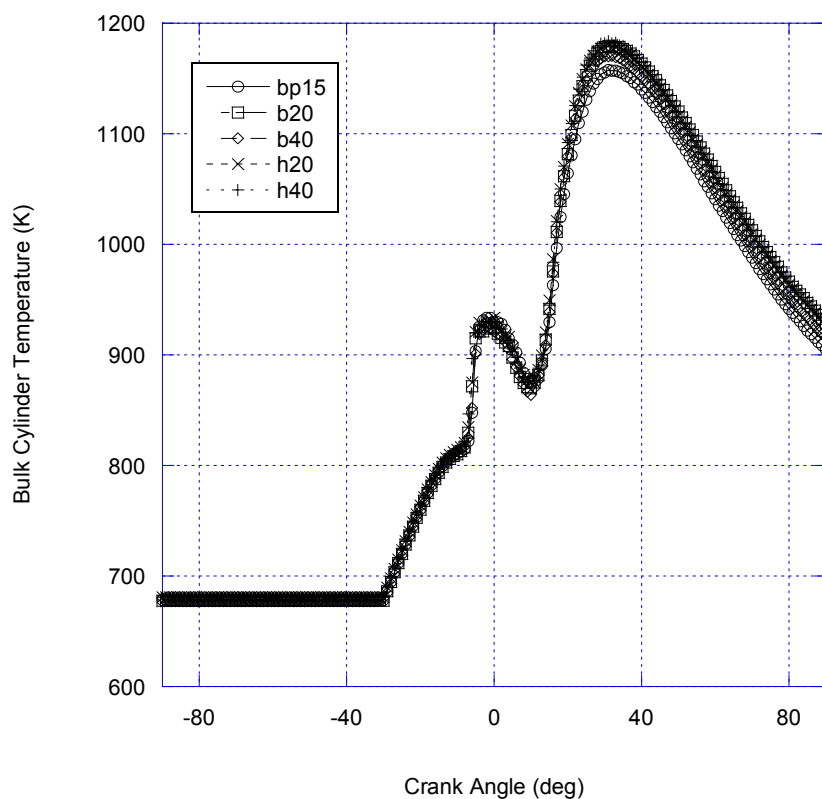


Figure 4.31: Mode 3 Bulk Cylinder Temperature Plot for DDC 2.5L engine, Mode 3= 1660 rpm/75 ft-lb, with pilot and main injection, without EGR, for various biodiesel blends in comparison to baseline diesel fuel ULSD (BP15)

Table 4.16: Mode 3 Maximum Bulk Temperature (K)

Fuel Type	bp15	b20	b40	h20	h40
Maximum Bulk Temperature (K)	1157.6	1179.4	1170.5	1179.5	1183.7

Bulk cylinder temperature data from Mode 4 for the test fuels are shown in Figure 4.32. The plot shows similar bulk temperature for each fuel, but with varying maximum temperatures. Table 4.17 shows the maximum bulk temperature achieved. As is shown in the table, the bulk temperature is higher for the biodiesel blends than for the diesel fuel. The higher biodiesel blend does produce a higher bulk cylinder temperature.

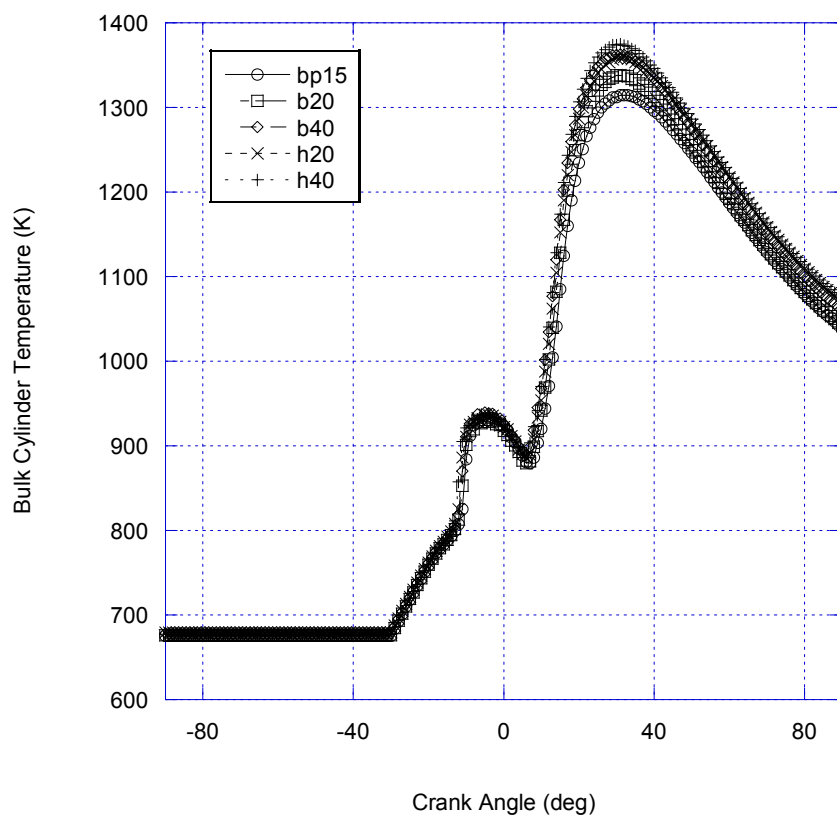


Figure 4.32: Mode 4 Bulk Cylinder Temperature Plot for DDC 2.5L engine, Mode 4= 1660rpm/125 ft-lb, with pilot and main injection, without EGR, for various biodiesel blends in comparison to baseline diesel fuel ULSD (BP15)

Table 4.17: Mode 4 Maximum Bulk Temperature (K)

Fuel Type	bp15	b20	b40	h20	h40
Maximum Bulk Temperature (K)	1314.5	1337.6	1362.7	1359.2	1374.8

4.8 Discussion

There are two aspects to the data that deserve discussion. First, the current theories for the biodiesel NO_x effect will be reviewed while discussing the results of this set of experiments previously presented. The nine theories follow with a brief discussion of each in relation to the data. Second, the fuel injection strategy of this engine, with a pilot pulse and a main injection, provided an interesting set of results, but with a complicated set of mechanisms acting.

4.8.1 Discussion of Biodiesel NO_x Theories

Adiabatic Flame Temperature

From a general review of the calculation for the adiabatic flame temperature, it seems that one must know the enthalpy of formation for the specific fuel. While some data on the methyl esters of biodiesel is available, there is not much data available on the specific carbon chain species that would allow an exact adiabatic flame temperature to be calculated [102]. However, a simple calculation was performed by Zhang comparing methyl oleate and a diesel surrogate fuel [201]. There is some thermophysical data

available in the NASA CEA to make this calculation. As seen in Zhang's results, the methyl oleate gave a lower adiabatic flame temperature for both the low load and high load conditions, and across various stoichiometries [201]. At stoichiometric conditions, the temperature difference was 20 K [201]. Zhang concluded that the adiabatic flame temperature difference could not explain the NO_x emissions increase seen with biodiesel.

In comparing Zhang's calculation to the fuel property data for this research, it should be noted that the actual NO_x emissions from Zhang's work was based on a biodiesel fuel that had about 22% methyl oleate composition, which is the same soy-based normal biodiesel used in this work. Those samples are represented as AGP#1 and AGP#2 in Appendix B. The hydrogenated biodiesel had an approximate 69% methyl oleate composition, which more closely matches the calculation variable that Zhang used, assuming 100% methyl oleate. Making this assumption, this data could explain the change seen in the reduction of the NO_x for the hydrogenated biodiesel.

Ban-Weiss and coworkers suggest that the higher flame temperature for biodiesel is related to the higher flame temperature seen with molecules that have double bonds [110]. Therefore, saturated molecules will have lower flame temperatures. The hydrogenated biodiesel has 3 times more methyl oleate than the soy-based biodiesel, and as a result has a lower number of double bonded molecules. This is also a good argument for explaining the reduction in NO_x shown in Figure 4.9, which is then due to a reduction in the number of double bonded molecules in the fuel composition. Table 4.18 shows the description of the methyl esters and their composition. Table 4.19 shows the change in the composition to the fuel and how this affects the carbon, hydrogen, and oxygen composition, in addition to the number of double bonds available in the fuel.

Table 4.18: Methyl Esters physical data and composition

Methyl Esters	MW	Carbon	Hydrogen	Oxygen	# Double Bonds	Carbon Chain
Myristic	228	14	28	2	0	14:00
Palmitic	256	16	32	2	0	16:00
Steric	284	18	36	2	0	18:00
Oleic	282	18	34	2	1	18:01
Linoleic	280	18	32	2	2	18:02
Linolenic	278	18	30	2	3	18:03
Arachidic	312	20	40	2	0	20:00
Behenic	340	22	44	2	0	22:00

Table 4.19: Comparison between the B100 and H100 chemical composition (B100 here is the AGP #1 in Appendix B.)

Carbon Chain	B100	Carbon	Hydrogen	Oxygen	# Double Bonds	H100	Carbon	Hydrogen	Oxygen	# Double Bonds
14:00						0.07	0.0002	0.0004	0.0000	
16:00	10.7	0.0348	0.0696	0.0050		11	0.0353	0.0705	0.0044	
18:00	4.5	0.0147	0.0294	0.0018		0	0.0000	0.0000	0.0000	
18:01	22.6	0.0743	0.1486	0.0083	0.2311	68.76	0.2296	0.4337	0.0255	0.6888
18:02	52.3	0.1783	0.3367	0.0198	1.0695	18.44	0.0639	0.1137	0.0071	0.3694
18:03	7.4	0.0454	0.0454	0.0030	0.2270	0.87	0.0031	0.0052	0.0003	0.0261
20:00	0.3	0.0010	0.0020	0.0001		0.62	0.0020	0.0040	0.0002	
22:00						0.07	0.0002	0.0005	0.0000	
Total	97.8	0.3485	0.6317	0.0380	1.5276	99.83	0.3344	0.6280	0.0376	1.0843

A calculation of the adiabatic flame temperature was made based on the higher heating value of the fuel to investigate whether the NO_x increase with the soy based biodiesel, and the NO_x decrease with the hydrogenated biodiesel could be attributed to the difference in temperature. With the available compound information for the fuels, the enthalpy of formation was calculated from the balanced stoichiometric equation for the fuel. Since the direct heat of vaporization information was not available, for simplicity,

an assumption was made that this was constant across the three fuels. With the enthalpy of formation and through the use of HP Flame, a computer tool developed by Turns [31] and based on the Olikara and Borman routines [202], the adiabatic flame temperature was determined for varying stoichiometries at a pressure of 50 bar. Figure 4.33 shows the results based on the calculations. The ULSD and the H100 trend in a similar manner, while the B100 is higher by approximately 100K at $\phi=1$. This data supports the theory that the higher NO_x emissions shown for the B20 version are due to the higher adiabatic flame temperature for B100.

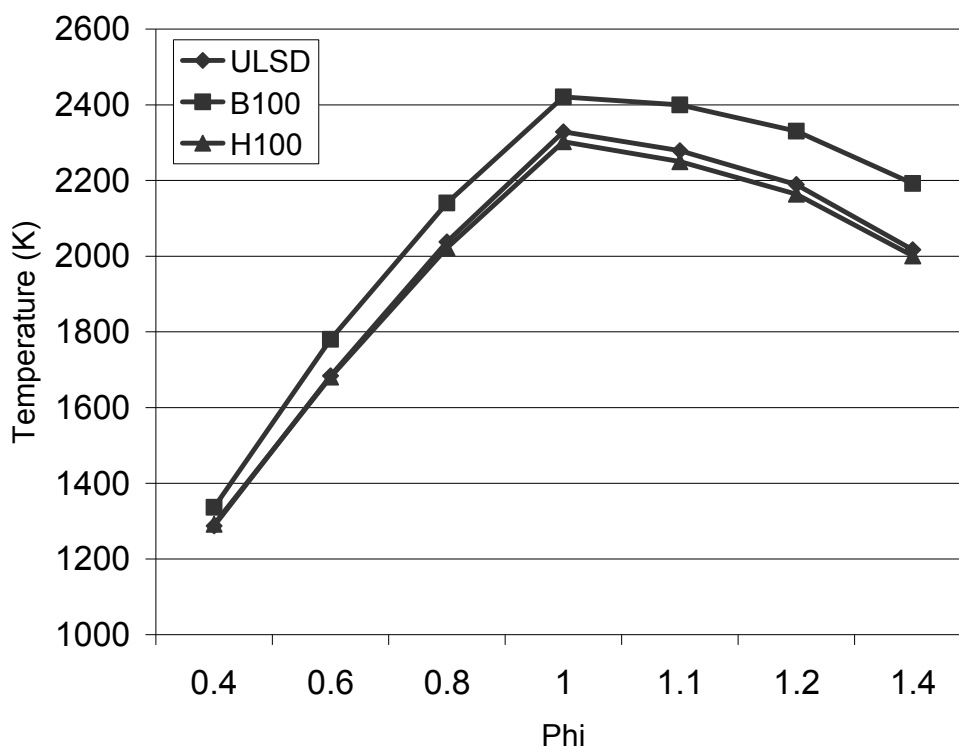


Figure 4.33: Adiabatic Flame Temperature of fuels at a pressure of 50 bar vs. Phi (ϕ)

The adiabatic flame temperature data presented here follows the trend shown by the modeling by Ban-Weiss and coworkers [110], that a more saturated compound will have a lower peak temperature than its comparable unsaturated compound, thus producing lower NO_x emissions. Cheng and coworkers also computed adiabatic flame temperature with modified version of the EQUIL module of the CHEMKIN software package [42]. Their modified version accounts for the mixing and vaporization of the fuel at the engine coolant's conditions at the calculated motored TDC temperature and pressure to properly account for differences in the adiabatic flame temperature due to differences in the latent heat of vaporization of the fuels. This yielded differences in the charge gas temperature after the fuels were vaporized [42]. They compared methyl oleate to a primary reference fuel for diesel for various stoichiometries and found that the adiabatic flame temperatures were the same up to $\phi = 1.5$. Above this, the adiabatic flame temperature of the primary reference fuel was higher. And, data presented by Zhang shows that the adiabatic flame temperature of methyl oleate is lower than a surrogate diesel fuel by 20K based on modeling with the NASA CEA chemical equilibrium code [203]. The adiabatic flame temperature data for methyl oleate from Zhang, and Chen and coworkers is similar in trends to the data presented here for the adiabatic flame temperature because the H100 fuel composition is approximately 60% methyl oleate.

Flame Radiation

Again, the theory about soot and flame radiation claims that the reduction in soot concentration reduces the soot radiation in the flame zone and thus the diffusion flame

temperature is higher and thus thermal NO_x formation increases [113, 114]. There was no data collected in this research to verify or refute this theory, although the sooting tendency of the B20 and H20 fuels should have been similar, ruling out the effect of shifts in flame radiation causing the NO_x effect.

Mixing

Musculus showed that as the pre-mixed burn fraction increases, the NO_x emissions increase [113]. The pressure traces from this research, Figures 4.17 through 4.20, show a consistent premixed and diffusion burn for each fuel and for each speed and load condition.

Prompt NO

Researchers have suggested that a change in the fuel chemistry, specifically the change in the number of double bonds in the biodiesel fuel, could be the reason for the increase in NO_x emissions, via the prompt NO mechanism [110]. The data shown in this research would support the theory that a reduction in the number of double bounds produces a reduction in the NO_x emissions, as shown in Figure 4.9 and Table 4.19. When the hydrogenated biodiesel fuel was used, a reduction in NO_x emissions over the conventional biodiesel was achieved.

Fuel Injection Timing

The advance of injection timing with biodiesel fuel due to the physical property differences between diesel fuel and biodiesel fuel has been proposed and shown to be a

contributor to the NO_x emission increase [103]. In this research, the needle lift data from fuel injector #1 was collected for each fuel and for each mode. As shown in Figures 4.25 through 4.28, the needle lift for each fuel had a pilot and a main pulse which did not change timing regardless of fuel. This corresponds with the data previously for this engine and observations regarding common rail engines [121, 201]. The common rail engine seems to be less affected by a change in the fuel composition with regard to fuel injection timing. However, as shown in the needle lift figures, there were some changes in the needle lift for the biodiesel fuels, indicating an increase in pressure to increase the height of the needle, thus allowing more fuel to enter the cylinder in a fixed timing.

Cetane Number

Previously, it has been expected that higher cetane number fuels will produce shorter pre-mixed burn fractions and thus lower NO_x emissions [42]. In this research, the hydrogenated biodiesel has a higher cetane number and lower NO_x emissions, as shown in Table 4.9 and Figure 4.9. While this fits the stated theory, the soy-based biodiesel also has a cetane number higher than diesel fuel and lower than the hydrogenated biodiesel fuel. As shown in the NO_x emissions results, Figure 4.9, the soy-based biodiesel produced NO_x emissions higher than the diesel, while the hydrogenated biodiesel produced NO_x emissions at the same rate as the diesel fuel or lower than the diesel fuel.

Mixture Stoichiometry at Lift Off Length

Cheng and coworkers suggest that the mixture stoichiometry at the lift-off length of the fuel from the injector nozzle may be different between diesel and biodiesel and

thus plays a role in the NO_x increase, but the mechanisms for this are unknown [42]. In Cheng and coworker's research, the fuel spray penetration lengths were used to adjust the actual start of injection for each fuel to be able to exactly match the start of combustion by knowing the ignition delay [42]. While some experimental information is provided, it is unclear what changes were made in either the injection timing delay or pressure. However, their research provides insight that the spray, droplet break up, and fuel vaporization at the lift-off length are unknowns. The research in this thesis does not support or refute this theory. Injection pressure was allowed to vary with respect to the injection timing. It is unknown if higher injection pressures produce longer lift-off lengths.

Oxygen Content of the Fuel

Some researchers suggest that the higher oxygen availability in the combustion chamber as a result of the oxygen in the fuel contributes to the NO formation process [126, 127]. This research compared two different biodiesel fuels with similar blend concentrations in diesel fuel. After calculating the oxygen content by methyl ester carbon chain lengths, it was found that the oxygen content of the fuels is similar, as shown in Table 4.19. Table 4.20 shows the ratios between carbon, hydrogen and oxygen for the two fuels. The carbon to oxygen ratio is essentially the same for each fuel. While the oxygen concentrations are similar, the NO_x reductions are not, and thus no correlation can be made. Therefore, the fuel bound oxygen would not be attributed to be a contributing factor in the NO_x effect.

 Table 4.20: Elemental ratios for the biodiesel fuels (C=carbon, H=hydrogen, O=oxygen)

Ratio	B100	H100
H/C	1.81287	1.87809
C/H	0.55161	0.53246
C/O	9.17032	8.88758

Fuel Spray Characteristics

The fuel spray characteristics, including droplet size distribution, droplet inertia, air entrainment, penetration in cylinder, evaporation rate, and heat dissipation are affected by the various fuel properties [95]. These fuel properties include viscosity, surface tension, cetane number, and the boiling range temperature of the fuels [95].

In a recent article by Boulanger and coworkers, the liquid properties of the C18 methyl ester were compared to a C12 alkane representing diesel fuel to gain some insight into the change in physical properties of the fuel and how they affect NO_x emissions [204]. For this simulation, C12 and C7 alkanes were chosen to serve as the reference case (n-dodecane for the liquid properties and n-heptane for the gaseous phase combustion properties). The model compound to represent biodiesel was methyl linoleate. The differences in the fuel properties and behavior were divided into 4 groupings: 1) vapor pressure, heat of vaporization, and surface tension; 2) thermal conductivity within the droplet and heat capacity of the liquid; 3) density and viscosity changes, split into two sub-groups to separate the effect of dynamic viscosity from density; 4) full set of biodiesel properties [204]. Some interesting points from their findings:

- It is expected that combustion takes longer for biodiesel and needs more time to vaporize as a result of the higher volatility, higher viscosity, and surface tension. The higher viscosity and surface tension diminish the break-up efficiency of the fuel, thus favoring the diffusion mode of combustion.
- Weaker fuel spray break-up due to higher viscosity of the fuel alone with no change in spray density advances the onset of heat release. Their data suggests this, but they could not give an explanation for it.
- Slower vaporization produces higher temperatures that last longer in the combustion cycle.
- It was believed that momentum due to larger density helped to maintain droplet velocity and break-up in the long term.
- A larger kinematic viscosity tends to lead to larger droplet size (Sauter mean diameter).
- Because of slower evaporation, peak temperature occurs later during the expansion stroke and tends to be lower, but is higher during the end of the cycle.
- The pressure traces of their research show that combustion phasing is governed by physical properties.
- They conclude from their work that biodiesel NO_x is a result of lower vaporization rate causing a longer spray penetration, the evaporating droplets sweeping a larger volume which cause fuel release into a larger ignitable zone, due directly to the lower volatility of the fuel. The

volume of the reaction zone increases with higher temperatures. This wider ignitable zone is suspected to contribute to the NO_x increase.

- When the kinematic viscosity and density of the fuel increase, the high temperature zone volume is not well developed and thus the maximum temperature is lower.

As is seen from the fuel property data for this research, section 4.7, the B100 and the H100 have higher kinematic viscosities than diesel fuel. Thus, the advance in the start of combustion for the B100 and higher NO_x could be attributed to the increased kinematic viscosity. However, the in-cylinder data does not show any effect of advance in start of combustion with the biodiesel fuels. From an analysis of the density of the fuels used, the densities of both the B100 and H100 are comparable, and slightly higher than the diesel fuel (BP15 .8339 g/ml; B100 .87785 g/ml; H100 .87276 g/ml). Volatility information for the fuels is not available for comparison. Therefore, it is unclear if Boulanger and coworkers theory that the higher density and lower volatility both produce a longer vaporization and larger droplets spray field zone, thus causing higher NO_x emissions, would provide a good explanation for the emissions seen in this research.

4.8.2 Fuel Injection Strategy on NO_x emissions

Several researchers have studied the effect of the multiple pulse injection and its impact on the combustion characteristics and emissions from diesel engines both with diesel and biodiesel fuels [122, 123, 200, 205]. The following section discusses their findings and relates them to the current body of research.

Choi and coworkers tested the effect of biodiesel fuels blends and multiple injections in a diesel engine [122]. In their high load condition, they showed that the NO_x emissions between the base diesel and multiple pulse diesel fuel were roughly the same over various start of injection timings. However, when comparing the B20 and B40 blends with multiple injection of biodiesel to diesel fuel, the B20 blend produced more NO_x emissions regardless of injection timing, where the B40 blend produced the same or less NO_x emissions than diesel fuel. At the low load condition, the double injection with the diesel fuel produced less NO_x emissions as the start of injection timing was retarded, producing lower NO_x at -1CA ATDC [122]. The impact of the injection timing was also seen in the biodiesel data. As the injection timing was retarded, the multiple pulse biodiesel blends produced less NO_x than the single injection of the diesel and biodiesel blends, and less than the double injection of the diesel [122]. The effect of multiple fuel injections on fuel consumption was more significant in the high load than the low load, with increase seen as a function of start of injection timing [122].

Zhang's work showed how the interval of the pilot from the main fuel pulse could lower the emissions at his low load condition (1600 rpm /58.9 ft-lb) even further than with a single injection without the use of EGR [123]. While smoke emissions are impacted without the use of EGR, the NO_x emissions can be managed well without an EGR if a pilot injection is used [123]. He also showed how the size, or the amount of fuel in the pilot, made an impact on NO_x emissions.

Tennison and workers showed multiple injections and injection pressure affected the smoke and NO_x from an engine [206]. At the same injection pressure, a single injection had a better impact on NO_x than a double injection, while smoke emissions

were significantly reduced [206]. In a second study on the pilot timing, as the pilot time was retarded, the NO_x decreased and the soot increases. However, as the pilot was advanced closer to the main injection, the NO_x increased and the soot decreased [206]. This study definitely showed how low NO_x emissions can go with an increase in injection pressure [206]. They also concluded that ignition delay of the pilot quantity was dependent on a chemical delay and not a physical mixing delay, based on the data that showed that the point of ignition for the pilot injection was at the same crank angle regardless of the pilot timing [206].

Carlucci and coworkers studied the effect of the pilot injection on the main fuel injection and then added a third injection called an “early” injection before the pilot injection [205]. With this strategy, they were able to successfully reduce smoke and NO_x emissions over various engine conditions [205]. The early pilot strategy of injection of a quantity of fuel very advanced with respect to top dead center allows for the formation of a locally lean mixture in the engine cylinder. This fuel is ignited by the pilot injection. By coupling the two injections, there was a weak heat release produced. An increase in this early duration leads to a main combustion event that has a lower ignition delay and a premixed peak [205]. The experimental results showed that a short early injection coupled with the pilot injection was effective in reducing fuel consumption, NO_x and soot levels [205].

As evidenced by the needle lift traces, the injection strategy of the engine for this research involved a pilot and main injection. With that strategy, two distinct heat release peaks were shown in the heat release plot for all 4 engine modes. As indicated by Carlucci’s literature review, the pilot ignition combustion causes a reduction in the

ignition delay of the main injection, and as a consequence, a decrease in the rising rate of the cylinder pressure during the main combustion [205]. As he described it, the pilot injection decreases the ignition delay of the main injection thus reducing the fuel fraction burned during the premixed phase, leading to a reduction in the combustion temperature peak [205]. However, in this research comparing the diesel fuel with the biodiesel fuel blends, there is an observation of NO_x emissions reduction with the hydrogenated biodiesel fuel, while there is a NO_x increase with the soy-based biodiesel fuel in comparison with the diesel fuel. This would lead one to conclude that while the pilot injection is playing a role in reducing the ignition of the main injection, there is not a consistent NO_x emission given for each of the fuels. Thus, there are fuel chemistry differences that must also be playing a role in the changes seen in the NO_x emissions.

It should be mentioned that there has been some research with a hydrogenated-like biodiesel. Knothe and coworkers tested a technical grade methyl oleate in a 2003 DDC series 60 diesel engine with direct injection and electronic control [105]. The engine was fitted with high pressure electronic unit injectors, with EGR and an EGR cooler. In their CFR 40 Part 86 Subpart N testing, they showed a 6% increase in the NO_x emissions when methyl oleate was used while the biodiesel fuel used showed a 12% increase over diesel emissions [105]. It is unclear from their paper if there was any kind of unique fuel injection strategy during the engine operation. A more recent set of experiments was performed by Tat and coworkers with a biodiesel made from high-oleic soybeans [207]. In their testing, a John Deere 4045T 4.5L 4 cylinder turbocharged direct injection diesel engine was used. In their work, they showed a decrease in NO_x emissions as compared to the soy-based biodiesel, but still an increase in NO_x compared

with the diesel fuel [207]. The data in their paper indicate that this engine has a single injection pulse, and that the two biodiesel fuels were operating with a start of injection slightly retarded as a result of the isentropic bulk modulus change of the fuels [207]. It is suggested that these two groups of researchers found an increase in the NO_x emissions for the high oleic biodiesel in an engine with a single injection pulse. However, what is not clear is the impact of the EGR on the combustion process and on the results of the research.

To clarify the fuel injection strategy question on NO_x emissions, an additional test was performed in the DDC 2.5L engine at 1800 rpm and 61 ft lbs torque, at a fixed single injection timing of 7° BTDC. Figure 4.34 shows the NO_x data from the single injection case based on the fuel used. The figure shows an increase with the B20 blend over the ULSD, and a decrease with the H20 blend.

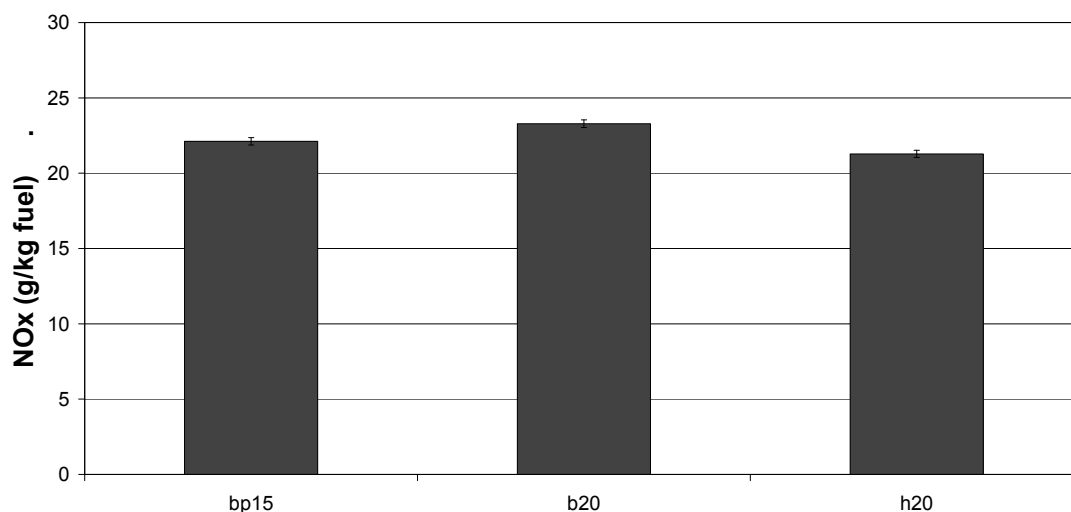


Figure 4.34: NO_x (g/kg fuel) for DDC 2.5L engine, 1800 rpm and 61 ft-lb with single injection timing of 7° BTDC, without EGR, comparing ULSD (BP15) to 20% soy-based biodiesel to 20% hydrogenated soy-based biodiesel

On a power basis, the NO_x emissions for each biodiesel fuel are observed to be lower than the ULSD diesel fuel, as shown in Figure 4.35. However, the small changes for the B20 are within the error bars for the data points, so nothing definitive can be stated about the difference. The difference between the H20 and the ULSD are significant based on the error bars.

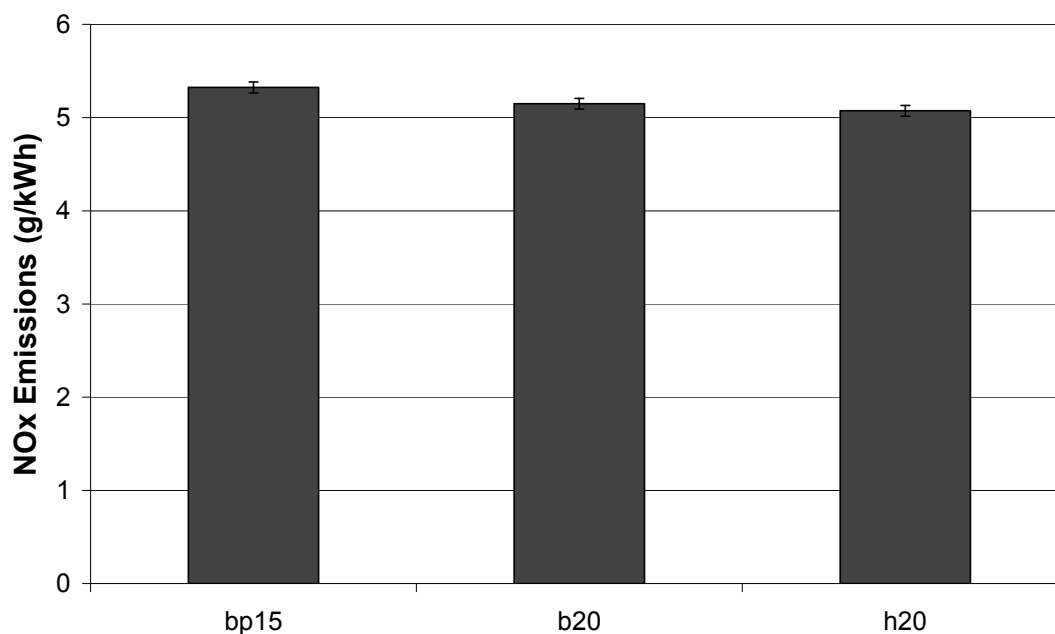


Figure 4.35: NO_x (g/kWh) for DDC 2.5L engine, 1800 rpm and 61 ft-lb with single injection timing of 7° BTDC, without EGR, comparing ULSD (BP15) to 20% soy-based biodiesel to 20% hydrogenated soy-based biodiesel

Based on the previous two figures, it could be concluded that the fuel injection strategy plays no role in the change in NO_x emissions between the fuels. Testing with the neat fuels may increase the differences seen in the emissions, and thus show a clearer trend.

Pressure data is shown in Figure 4.36. The data has a 0.1 crank angle resolution. The pressure traces are similar for each fuel.

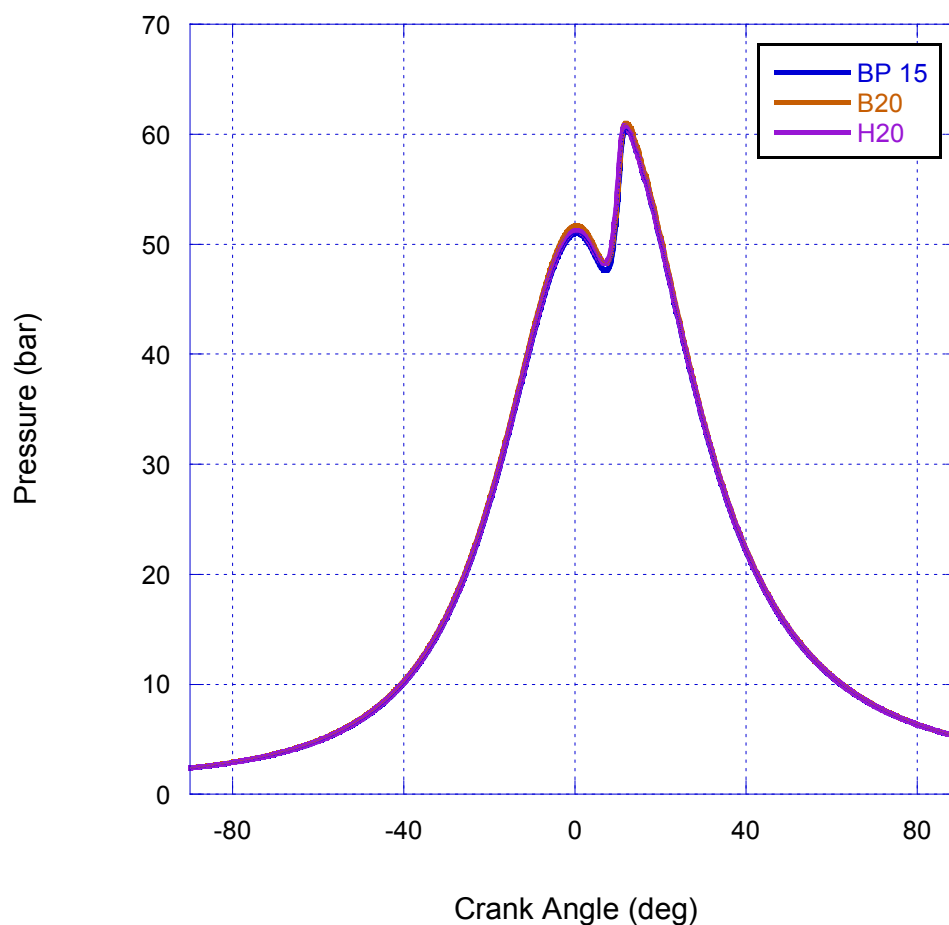


Figure 4.36: Pressure (bar) per crank angle degree for DDC 2.5L engine, 1800 rpm and 61 ft-lb with single injection timing of 7° BTDC, without EGR, comparing ULSD (BP15) to 20% soy-based biodiesel to 20% hydrogenated soy-based biodiesel

Heat Release data is shown in Figure 4.37. As is shown, the heat release for the BP 15 diesel is the highest. The peak duration lasts for an additional crank angle degree over the H20 peak duration. B20 is slightly higher than H20, but follows the same trend in duration as the BP 15 diesel.

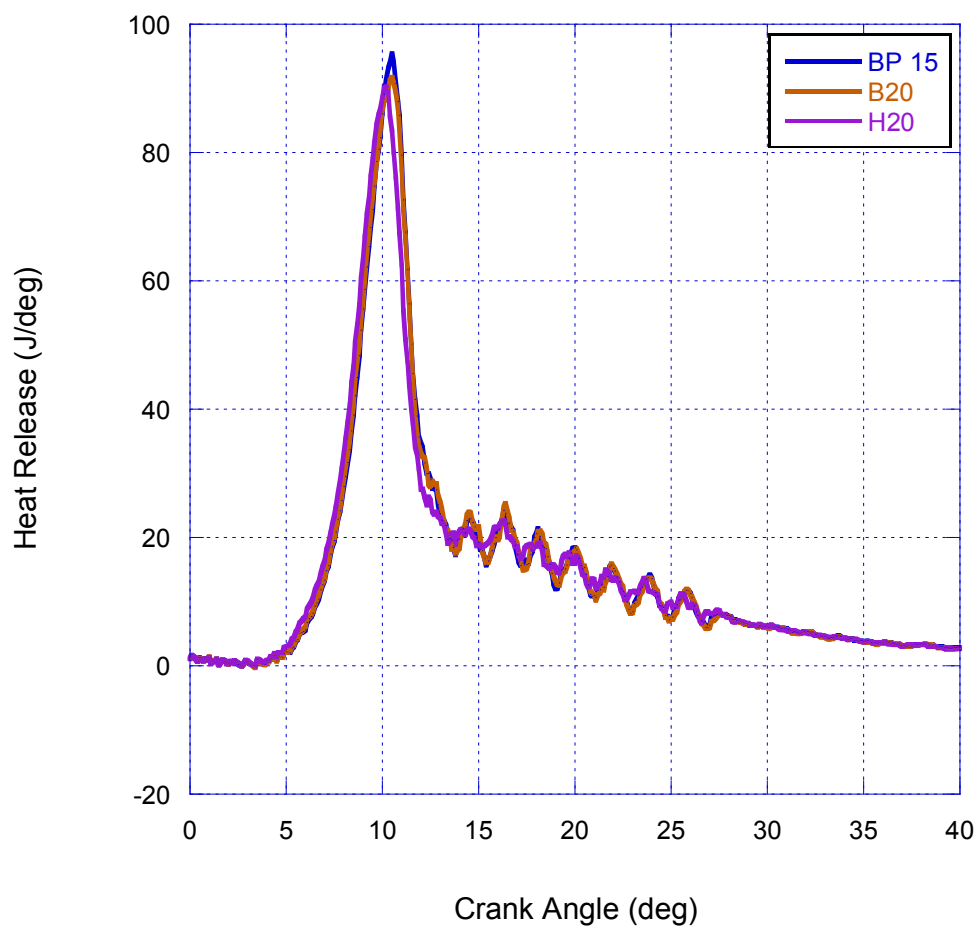


Figure 4.37: Heat Release (J/deg) for DDC 2.5L engine, 1800 rpm and 61 ft-lb with single injection timing of 7° BTDC, without EGR, comparing ULSD (BP15) to 20% soy-based biodiesel to 20% hydrogenated soy-based biodiesel

Bulk Cylinder Temperature data is shown in Figure 4.38 . The temperatures calculated are similar for each fuel.

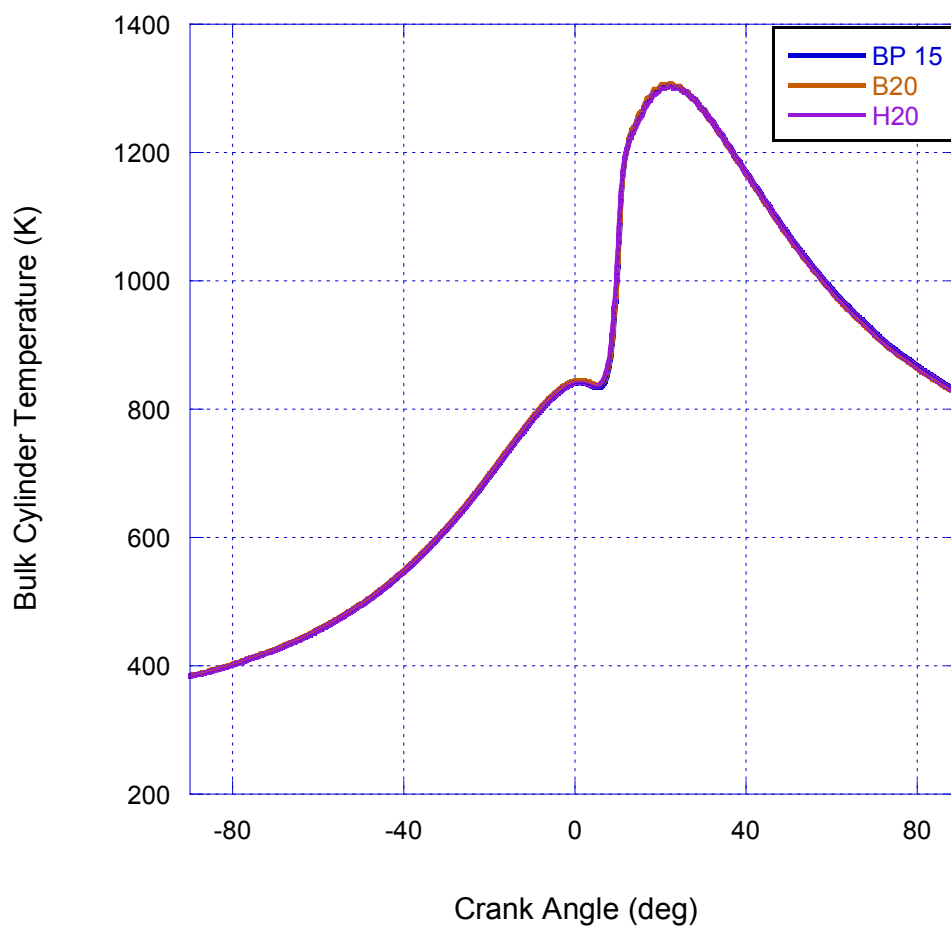


Figure 4.38: Bulk Cylinder Temperature (K) for DDC 2.5L engine, 1800 rpm and 61 ft-lb with single injection timing of 7° BTDC, without EGR, comparing ULSD (BP15) to 20% soy-based biodiesel to 20% hydrogenated soy-based biodiesel

Needle Lift data from the instrumented fuel injector is shown in Figure 4.39.

Because the needle lift sensor does not reset to the same location with each injection, the zero axis is normalized for each needle lift trace. As is seen in the figure, the fuel injection starts at -7° BTDC. The B20 and H20 needed lift traces rise faster than the BP

15 diesel, indicating a higher pressure on the needle to deliver the appropriate quantity of fuel to meet the same power requirement. More fuel would be required for the B20 and H20 blends as the energy density of the biodiesel is less than that of the BP 15 diesel fuel.

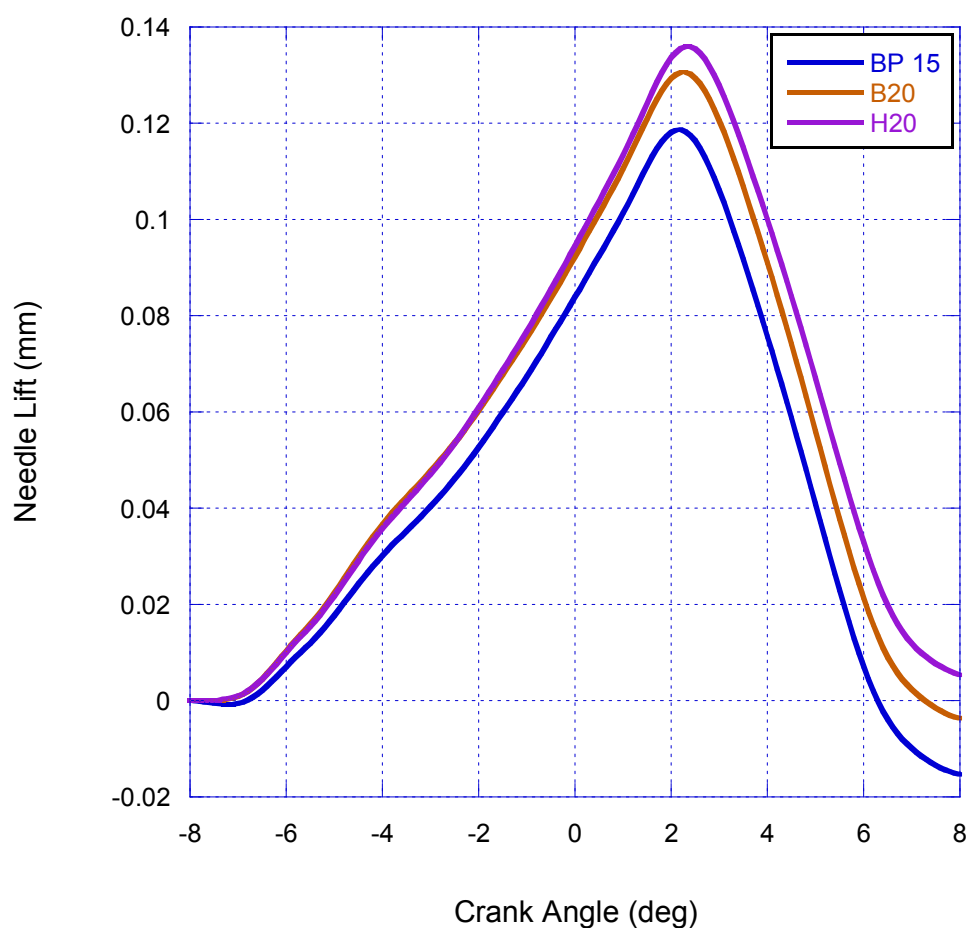


Figure 4.39: Needle Lift (mm) for DDC 2.5L engine, 1800 rpm and 61 ft-lb with single injection timing of 7° BTDC, without EGR, comparing ULSD (BP15) to 20% soy-based biodiesel to 20% hydrogenated soy-based biodiesel

Based on the combustion data plots presented, the slightly higher and longer duration heat release for the BP 15 diesel fuel could explain the higher NO_x emissions. However, the needle lift trace shows a shorter (1° in comparison to the B20 and 2° in comparison to the H20) duration of fueling, which indicates a longer duration of fuel spray. With a longer duration of fuel spray, there would be a shorter time for NO emissions, thus a lower amount of NO_x. On a fuel basis, the B20 NO_x emissions were higher than the BP 15 diesel fuel. Thus, this increase cannot be explained by the needle lift data.

4.9 Conclusions

A study was performed to test the effect of NO_x reduction from a compression ignition engine by reducing the iodine value of a biodiesel fuel by hydrogenating it, and thus changing the fuel properties by increasing the hydrogen content, reducing the double bonds of the fuel, and increasing its cetane number. The current research presented here focuses on the emissions from an engine that had the EGR shut off and used a pilot and main injection strategy. Engine tests were performed to compare this hydrogenated fuel with a soy-based biodiesel fuel. Two blend concentrations were prepared: a 20% blend and a 40% blend. The fuels were tested in 4 engine modes, and compared to an ultra low sulfur diesel fuel. The 20% soy-based biodiesel showed increases in NO_x emissions across the 4 engine modes. The 40% soy-based biodiesel and both hydrogenated biodiesel blends showed NO_x reductions for all 4 engine modes, and in all cases below the emissions levels for the ultra low sulfur diesel fuel.

From the review of the theories for the NO_x increase associated with biodiesel, the following can be said about the data:

- If a higher adiabatic flame temperature indicates an increase in the NO_x emissions as a result of the number of double bonds in the biodiesel fuel, then a decrease in those double bonds would lead to a decrease in the NO_x emissions. This data and the adiabatic flame temperature calculation support this conclusion.
- Fuel injection pressure increased as the needle lifted higher to deliver the required fuel in the same timing. This increase in pressure and its affect on the NO_x emission is unknown.
- It may also be possible that the chemistry of the fuel affects the physical properties of the fuel as it is delivered into the cylinder. Specifically, that the higher density and lower volatility both produce a longer vaporization and a larger droplet spray field zone, thus causing higher NO_x emissions. However, the density of the B100 and H100 are similar, which does not explain the reduction in NO_x result for the H20 and H40 fuel blends. The boiling range information for the neat fuels shows that the volatility of the biodiesel fuels are similar, and with higher volatility than the BP 15 diesel fuel. Thus, the higher volatility and shorter vaporization would lead to lower NO_x emissions. Heat Release data showed similar vaporization, and yet lower NO_x emissions with the H20 fuel.

Based on the discussion regarding the theories for the biodiesel NO_x effect, the results seen in the NO_x emission data would have to be explained by the increase in adiabatic flame temperature for the soy-based biodiesel and the Prompt NO_x effect as a result of the change in the biodiesel fuel properties between the soy-based biodiesel and the hydrogenated biodiesel.

Chapter 5

NO_x Reduction through Mixed Mode Combustion

5.1 Preface

This chapter presents new data that has not been previously published. Initial research was performed by the author on a Navistar 7.3L heavy duty turbocharged diesel engine. The data from the initial study is presented here. Because the engine's fuel injection system (Caterpillar's HEUI fuel injectors- hydraulic electronic unit injectors) produced a multiple pulse (split-shot) injection at the low engine speed and load condition, it was unclear in the heat release data when the dimethyl ether (DME) ignition was occurring and when the diesel fuel ignition was occurring. However, the emissions data from the initial study did suggest a NO_x reduction benefit from the DME in a mixed mode combustion system. A second study was then performed in an engine which had fuel injection control and where the impact of the fuel injection timing on the combustion process could be studied more easily during mixed mode combustion. A Detroit Diesel Corporation (DDC) 2.5L light duty turbocharged diesel engine was used in this second study. The engine intake air system was modified to incorporate an air heating system so that the impact of intake air heating on the low temperature heat release ignition could be probed.

5.2 Introduction

Rising fuel prices and government regulated reductions of exhaust emissions continue to pressure engine and vehicle manufacturers to make improvements in efficiency and emissions. Those improvements can be made through changing the fuel, modifying how energy is stored and used on a vehicle, and through improvements in the engine combustion process.

This research plan addresses the issue of reducing emissions while maintaining or improving diesel-like fuel efficiency through a homogeneous fumigated fueling scheme in a turbo diesel engine. In this work, the theoretical concepts of combustion efficiency and emissions of a homogeneous fumigated charge compression ignition process (HCCI) initiated by a pilot fuel injection, or what may be better described as a mixed mode combustion scheme, will be explored.

Dimethyl ether (DME) is a gaseous material used commonly as a propellant in aerosol cans. Also, it has been found to be an effective fuel for use in compression ignition engines due to its high cetane number and smokeless combustion [208]. DME is seen to be an important fuel for worldwide use due to its flexibility for use in home heating, engines, and stationary power, as well as its various potential feedstocks: coal, biomass and natural gas [209]. With the increase in the cost of a barrel of oil, the financial prospects for DME have improved sufficiently to make it a more viable fuel for US interests. Researchers in other countries have been studying the use of DME in HCCI engines [210, 211]. However, the control of ignition timing and combustion duration over a wide range of engine speeds and loads remains a hindrance to the use of HCCI [211].

Therefore, understanding what may affect the ignition and combustion process in an HCCI engine and how it affects the process is a significant need in harnessing HCCI for practical use.

The theme of this research was to explore if a mixed mode combustion system with DME as the gaseous fuel could reduce NO_x emissions from a compression ignition engine. A set of initial experiments with DME inducted into the intake of an engine and coupled with a diesel fuel pilot injection were performed. These initial experiments showed that NO_x emissions could be reduced with this “mixed-mode” combustion strategy. Engine hardware did not allow for all aspects of the pilot fuel injection timing to be explored, and competing effects of multiple injections skewed some data. The experiments did not completely address how low the NO_x emission could go, or how to achieve minimal NO_x emissions.

The hypothesis being tested is that through the improvement of the ignition quality of a mixed mode DME/diesel pilot injection compression ignition engine, control of the homogeneous ignition process at the low speed and low load conditions will simultaneously yield lower NO_x emissions and similar or improved efficiency. Using the high ignition quality of DME via its low ignition temperature reactions, control of the homogeneous ignition process can be achieved by controlling the reaction rate of the fuel and air mixture.

The reaction rate of the cylinder charge is a function of several variables including intake air temperature, heat addition through compression of the cylinder charge, heat addition through introduction of exhaust gases in the intake charge, cetane number of the pilot fuel injection, cetane number of fuel and gases in the intake air, and

the air/fuel ratio in the cylinder charge. The homogeneous charge fuel for these experiments will consist of DME and mixtures of DME with Methane to study the effect of changes in the cetane number of the cylinder charge. The pilot fuel injections will consist of an ultra low sulfur diesel fuel. An intake air heater will be used to vary the charge temperature as a way to model the impact of adjusting compressive heating and intake air heating effect on the autoignition of the charge.

The research work that will be discussed included several aspects. Those include:

1. Design and test the fueling system on the Navistar 7.3L and the DDC 2.5L engines to introduce the homogeneous mixture into the engine intake port. Show that the engine can be operated at a steady state condition.
2. Perform a series of tests with the Navistar 7.3L to study the effects of varying the concentrations of DME and air in the intake charge. Perform another set of tests with the DDC 2.5L engine to study the effect of varying timing of the pilot injection of the diesel fuel by varying 1) the cetane number of the intake charge with DME and blends of DME and Methane, and 2) the intake temperature of the charge.
3. Explain the behavior of the system through various methods which include:
 - Use the AVL CEB (Combustion Emissions Bench) II to measure the emissions of the process and compare to normal mode operation. With this equipment, changes in NO_x, CO, CO₂, Methane and hydrocarbon emissions will be measured. Use a Nicolet FTIR spectrometer to collect exhaust to confirm the N₂O emissions. Use gas chromatography to collect information on the amount of DME and other C1-C6 carbon compounds found in the

exhaust gases. Collect particulate matter emissions to confirm the magnitude of reduction from this mixed mode system.

- Use the pressure trace analysis software to analyze the bulk fuel burning and heat release of the mixed mode process. The data will provide information on the ignition quality of the fuel and the burning rate.

5.3 DME and Mixed Mode Combustion Process

The proposed research involves a direct injection diesel engine, operating through the use of DME (dimethyl ether) and Methane blends fumigated in the intake air and ignited through the use of the diesel fuel pilot injection. Therefore, literature relevant to this subject would include any dual fuel concept using DME and diesel pilot injection, in addition to a combination of DME and other gases fumigated in the intake air. DME fuel property information is shown in Table 5.1 [212]. DME has a high cetane number, making it an excellent compression ignition engine fuel [76, 83].

Table 5.1: Properties of dimethyl ether (DME) [212]

Property	DME
Chemical formula	CH ₃ OCH ₃
Molecular weight	46
Oxygen content—mass %	34.8
Stoichiometric air fuel ratio—kg/kg	9.1
Lower heating value—kJ/kg	28,800
Liquid density—g/ml@15°C	0.668
Boiling point—°C	-24.9
Viscosity—kg/m-s@25°C kg/m-s	est. 0.12–0.15
Vapor pressure@25°C—bar	5.1
Critical pressure—atm	52
Critical temperature—°C	127
Ignition temperature—°C	235

Hountalas and Papagiannakis developed a simulation model for a direct injection, dual fuel, diesel- natural gas engine [213]. Their data was compared to experimental data for diesel fuel only, and showed that the NO_x emissions for any of the diesel-natural gas blends was higher than for diesel over the BMEP (brake mean effective pressure) range [213]. Also, the data showed that the PM emissions could be reduced below that for diesel only, with increasing natural gas blends over 30% for the entire BMEP range [213].

Chen and coworkers performed experiments with DME and natural gas blends fumigated into a single cylinder Yanmar engine [214]. Through the significant combustion analysis performed, they showed the effect of increasing DME content in the blend on NO_x, thermal efficiency and total hydrocarbons [214]. Their research did not focus on the effect on soot emissions [214]. The data was presented so that one could understand the relationship between the DME concentration, natural gas concentration and the various emissions [214]. Conditions with the highest BMEP and brake thermal

efficiency were also the conditions with the highest total hydrocarbons and NO_x emissions [214].

The HCCI combustion process has more premixed heat release than the typical diesel combustion process, sometimes with a two stage heat release depending on the fuel used [215]. Therefore, the injection timing, fuel vaporization, and ignition timing are critical to occur in sequence to produce maximum engine power output, usually at top dead center (TDC). The ignition timing is specifically a function of the chain initiation and chain propagation reactions which begin the autoignition process, and are controlled through the heating of the fuel and air mixture. To that end, the ignition timing is a function of the fuel blend and in-cylinder conditions. When a gaseous fuel is used in the engine, the fuel vaporization process does not exist. Additionally, the mixture preparation of the fuel and air mixture is an important quality affecting the homogeneity of the combustion. Research has shown that HCCI can be effective to reduce emissions and improve efficiency within certain boundaries, broadly the ignition limit and the knocking limit of the fuel blend [214]. The goal of this research is to determine if the ignition quality of dimethyl ether (DME) or blends of DME fumigated into the engine, and then ignited by a diesel fuel pilot injection can produce the desired NO_x emissions reduction. Specifically, can the use of a diesel pilot injection of fuel to ignite a homogeneous mixture of DME and air and mixture of DME, Methane and air reduce NO_x emissions and particulate matter, while minimizing the typical hydrocarbon and CO increase associated with HCCI combustion? Researchers have used DME blends with other fuels to accelerate the low temperature reactions in the HCCI process, like propane and butane [216, 217]. Some experimental and modeling work with DME and Methane

or natural gas blends has also been performed [218, 219]. However, DME's use with Methane and a pilot injection of diesel fuel has not been demonstrated before.

The theoretical concepts of this research center around the low temperature reactions, the heat release rate, the ignition delay of the bulk fuel, and the NO_x mechanisms. Low temperature reactions are defined as reactions which occur below 600 K [220]. Martinez-Frias and coworkers have shown that the fraction of heat release from these reactions can be affected by thermally conditioning the intake charge within a 40 K window of the charge temperature at the beginning of the compression stroke (the temperature at BDC) [144]. These results were for an engine running at a specific compression ratio, speed, equivalence ratio, EGR and inlet pressure of air and fuel [144]. Therefore, it is difficult to give an exact temperature range for a specific engine, because it is a function of the compression ratio of the engine and other heat contributions to the fuel and air mixture. Heat release rate is defined as the amount of heat released by the chemically reacting system over time. Controlling the heat release rate is critical to managing the emissions and peak power output. Ignition delay of the bulk fuel is defined as the amount of time that it takes for the fuel to begin combustion measured from the start of injection of the fuel. Researchers define the start of injection as when the fuel first leaves the nozzle [221]. However, ignition delay means something different when talking about a gaseous fuel, especially when bringing it into the cylinder through the intake air system. Since intake air temperature, turbocharging and compression all add to the energy involved in the ignition process, a new definition of ignition delay may need to evolve as a part of this research. Some researchers suggest tracking the timing of mass

fraction burned 50% (MFB50) as a means to denote an endpoint to ignition [148, 222, 223].

NO_x producing mechanisms include the Zeldovich (thermal) NO, Fenimore (prompt) NO, nitrous oxide (N₂O) generated NO, and conversion of fuel nitrogen to NO [48]. Diesel combustion generates NO_x mostly from the Zeldovich mechanism, and some from the Fenimore mechanism due to CH formed in the flame front. However, NO is not typically generated due to fuel nitrogen conversion (as there is none) nor the nitrous oxide (N₂O) pathway. However, researchers are beginning to find that nitrous oxide (N₂O) is being emitted from HCCI engines, suggesting that its abundance shows this pathway is being used to create NO at the lower temperatures [224].

5.4 Design and Testing of the DME Gaseous Fueling System

The first part of the research involved demonstrating that a reduction in NO_x emissions could be produced through the induction of DME into the engine. This phase included developing the fuel system to handle DME induction. Hardware was added to the engine intake air system and upstream from the engine intake to provide mixing length for the fuel and air prior to entry into the cylinder via the intake air port. The DME fuel was dispersed and mixed with the boosted air using a custom built mixing manifold. A picture of the fuel aspiration manifold is shown in Figure 5.1. The manifold consisted of four Enerac Hastelloy filters placed on the radial of the manifold.



Figure 5.1: Custom intake air manifold aspiration system

The DME tank was fitted with tank heaters as shown in Figure 5.2, and pressure and temperature monitoring were added to the DME tank to maintain a constant pressure and temperature of the fuel delivery, as shown in Figure 5.3.

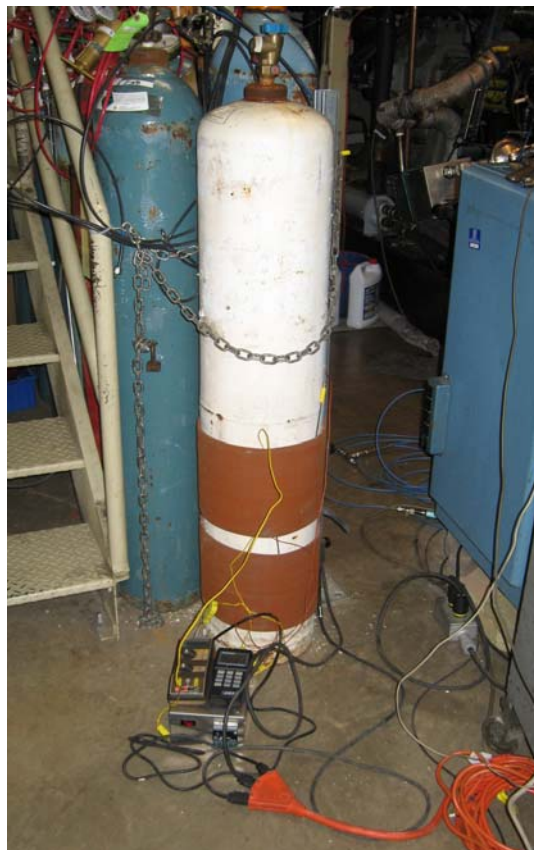


Figure 5.2: DME fuel tank with heaters

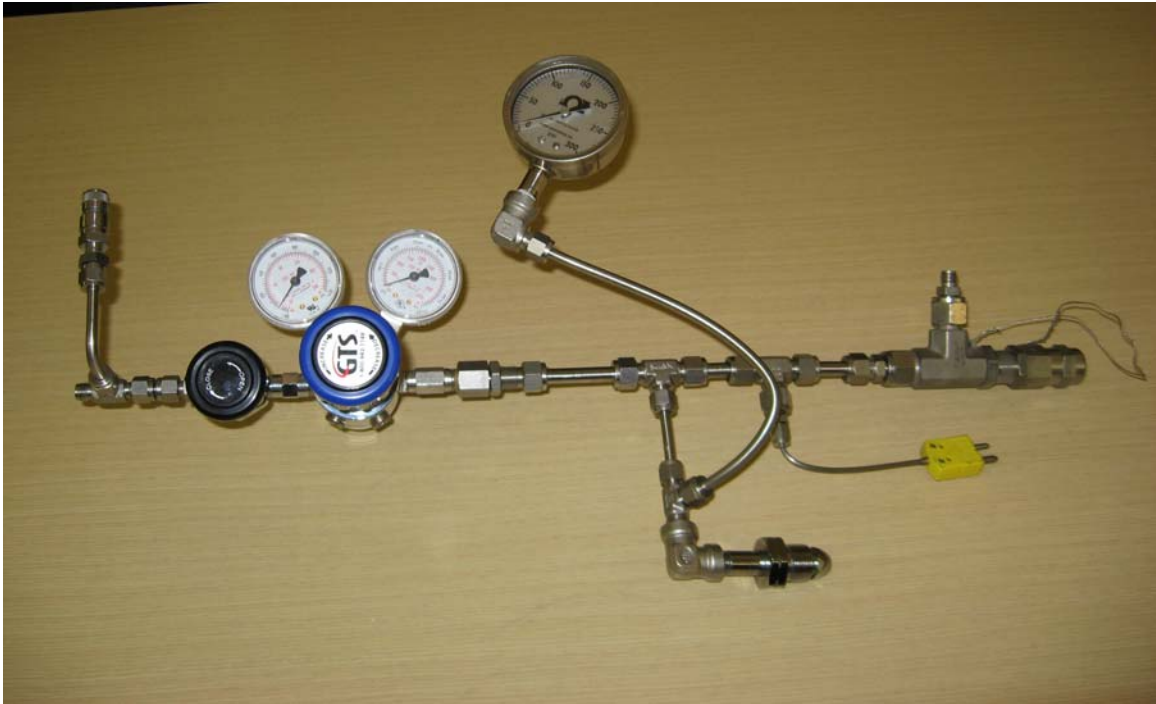


Figure 5.3: DME tank pressure and temperature monitoring system

Also, this stage included determining how much energy and therefore how much fuel would be required for a specific speed and load (mode) condition based on the mass air flow for that mode running on diesel. The Navistar 7.3L engine was set up to continue to inject the small pilot amount of diesel fuel that would be needed for idling the engine. The approach was to bring in a mixture of fuel and air on the intake stroke, metering the fuel with a Matheson flow meter. Depending on the flow rate required for the particular test, a different Matheson flow tube number was used. This mixture was compressed and would not ignite as it would in a typical HCCI combustion process. The only additional in-cylinder event occurring was the additional diesel fuel pilot and the associated diffusion burning. To prevent purely homogeneous ignition of the intake charge, the fuel and air mixtures in the intake charge were to be leaner than normal HCCI

mixtures. The combustion events were measured using a pressure transducer, and the heat release was determined through the use of a simple heat release equation assuming a constant gamma of 1.37 [11]. For further simplification, heat losses through the cylinder wall were ignored. Monitoring the combustion events via the pressure trace indicated when the knocking limit was reached at a particular speed and load condition.

5.5 Test Results from a Navistar 7.3L Heavy Duty Turbocharged Diesel Engine

A series of tests were conducted on a Navistar 7.3L turbocharged direct injection diesel engine with a modified fueling system permitting a homogeneous charge of DME fuel to be inducted into the intake air system. The fuel was introduced into the intake air system after the charge air cooler, but several feet prior to entering the intake air manifold to allow for mixing of the fuel and air. The test matrix comprised 2 speed and 4 load conditions comparing a normally operating diesel engine fueled by Ultra Low Sulfur Diesel (ULSD) (15ppm sulfur) with a mixed mode combustion engine operating with the same ULSD fuel and the inducted DME, as described in Table 5.2. Also, a series of tests were conducted at a set speed and load condition with varying concentrations of DME, as described below in Table 5.2. These speed and load conditions were picked because they represent the range between 2 and 3.5 bar IMEP (Indicated Mean Effective Pressure) where researchers have had the most success in achieving HCCI combustion [145]. IMEP is defined as the net work generated in the combustion chamber [225]. The DME was increased to a point where the amount of energy input would be equal to the amount of energy supplied by the directly injected diesel fuel.

Table 5.2: Description of Initial Engine Test Plan (ULSD= Ultra Low Sulfur Diesel; DME= Dimethyl Ether)

Engine Speed (rpm)	Engine Load (ft-lb)	Engine Combustion Mode	Fuel Type	DME Content (Flow meter scale)	DME Content (gm/s)
876	84	Diesel	ULSD	0	
876	100	Diesel	ULSD	0	
876	125	Diesel	ULSD	0	
876	150	Diesel	ULSD	0	
876	84	Mixed Mode	ULSD & DME	50mm	.7691
876	100	Mixed Mode	ULSD & DME	50mm	.7691
876	125	Mixed Mode	ULSD & DME	50mm	.7691
876	150	Mixed Mode	ULSD & DME	50mm	.7691
1000	84	Diesel	ULSD	0	
1000	100	Diesel	ULSD	0	
1000	125	Diesel	ULSD	0	
1000	150	Diesel	ULSD	0	
1000	84	Mixed Mode	ULSD & DME	50mm	.7691
1000	100	Mixed Mode	ULSD & DME	50mm	.7691
1000	125	Mixed Mode	ULSD & DME	50mm	.7691
1000	150	Mixed Mode	ULSD & DME	50mm	.7691
876	84	Mixed Mode	ULSD & DME	60mm	.9456
876	84	Mixed Mode	ULSD & DME	70mm	1.1301
876	84	Mixed Mode	ULSD & DME	80mm	1.3228
1000	150	Mixed Mode	ULSD & DME	70mm	1.1301
1000	150	Mixed Mode	ULSD & DME	80mm	1.3228
1000	150	Mixed Mode	ULSD & DME	90mm	1.5237

ULSD- Ultra Low Sulfur Diesel (15ppm)

Since the goal of this research is to reduce NO_x emissions and to improve fuel efficiency, gaseous emissions data and combustion pressure traces were collected. Figure 5.4 shows that through the induction of DME in the intake, NO_x emissions were reduced for both speed conditions versus the baseline, and were reduced as the load was increased in each speed condition. On further inspection, there was a significant decrease in the NO emission, shown in Figure 5.6, while the NO₂ emissions increased, as seen in

Figure 5.5 . Although not shown in this report, there was a significant increase in both CO and HC (hydrocarbon) emissions.

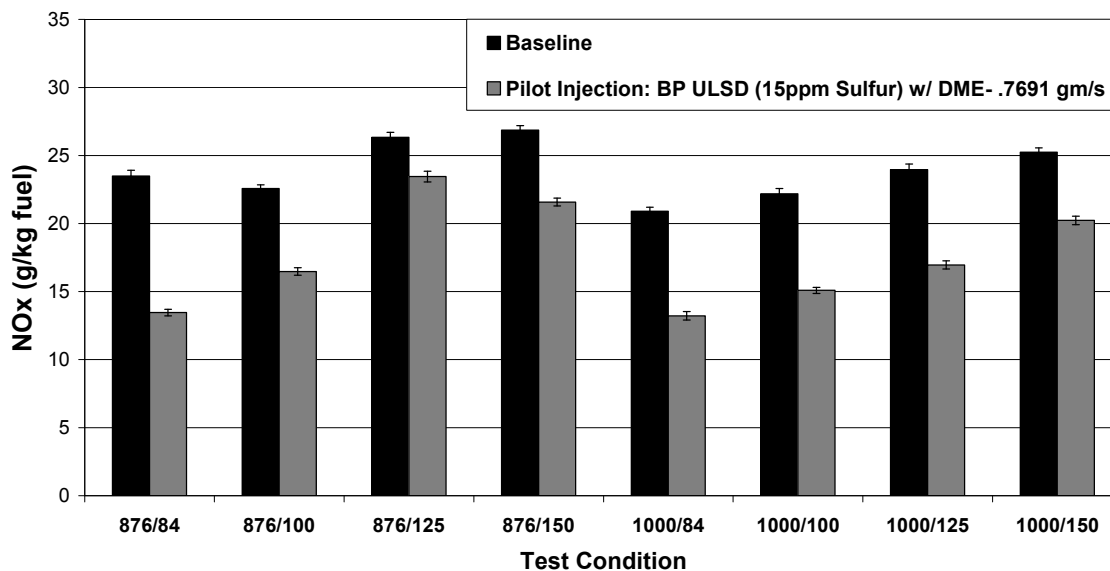


Figure 5.4: NOx emissions in gram NOx per kg fuel (Test Condition = Speed (rpm)/Load (ft-lbs)) ; Baseline is ULSD diesel fuel.

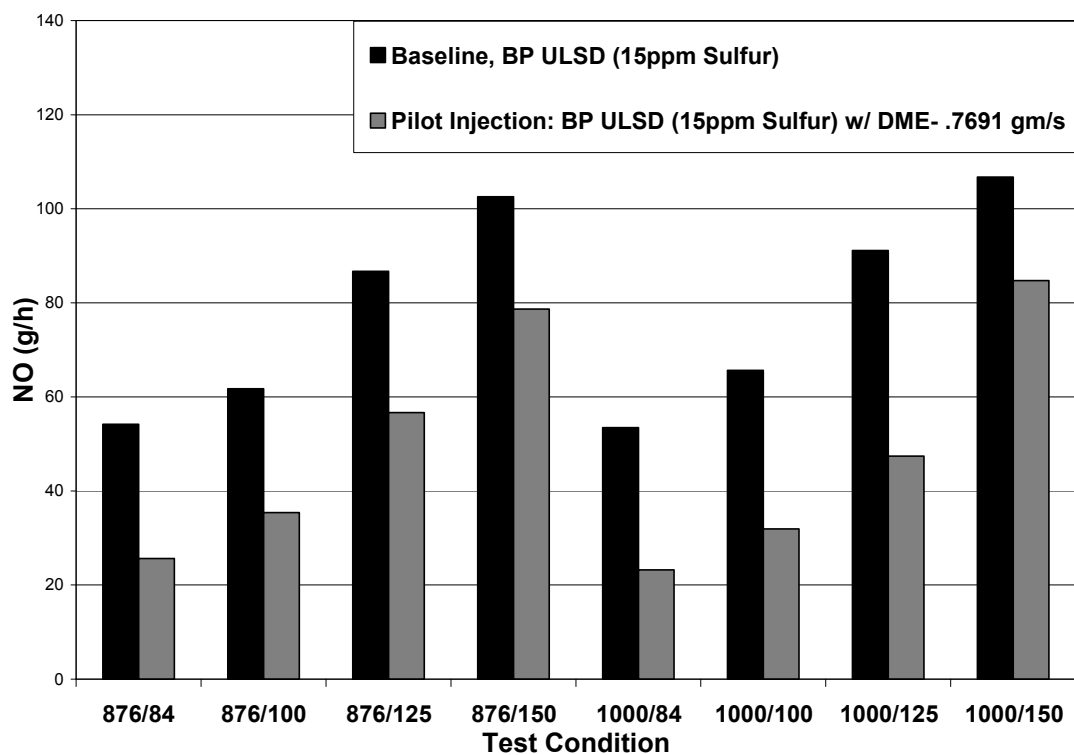


Figure 5.5: NO emissions (gram NO /hour) (Test Condition = Speed (rpm)/Load (ft-lbs)) ; Baseline is ULSD diesel fuel.

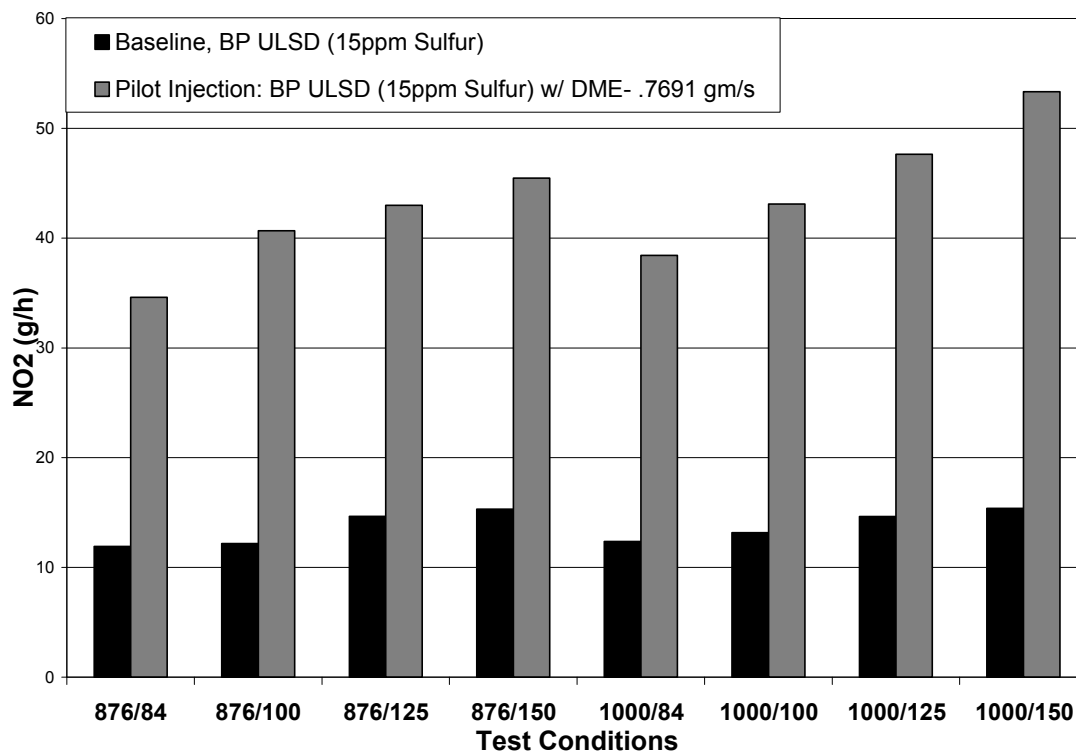


Figure 5.6: NO₂ emissions (gram NO₂ /hour) (Test Condition = Speed (rpm)/Load (ft-lbs)) ; Baseline is ULSD diesel fuel.

Figure 5.7 is a graph of the brake specific energy consumption. As can be seen, the engine was operating at a higher fuel/energy consumption rate (BSEC) over most test conditions. Although the goal of the test was to keep the speed, load and fuel energy content the same, this was not possible due to the engine control module (ECM). It seems that as the DME content was increased into the engine, the ECM began to dial back on the amount of diesel fuel injected as well as to adjust the fuel injection timing and injection pressure, possibly as a function of the fueling map of the engine. This is shown in Table 5.3 for the tests composed of holding speed and load constant and varying the DME concentration in the intake air. However, for all speed and load conditions, constant speed and load were maintained throughout the test.

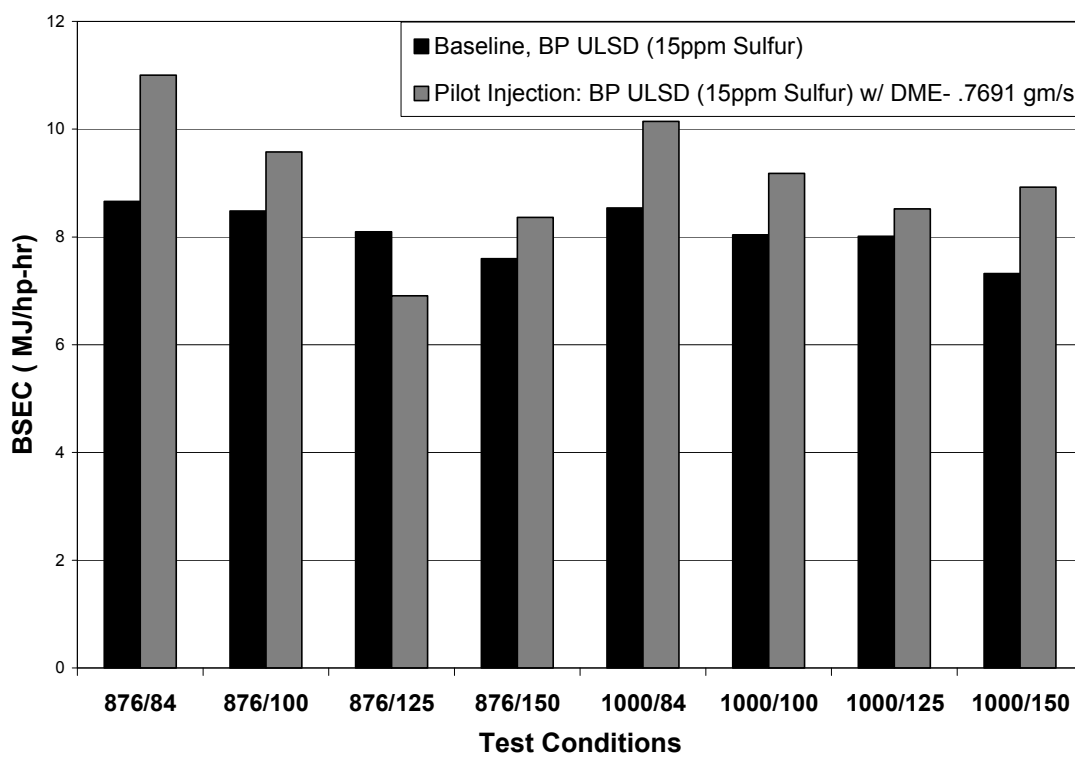


Figure 5.7: Brake Specific Energy Consumption (MJ/ hp-hr) ; Baseline is ULSD diesel fuel.

Table 5.3: Breakdown of fueling and injection conditions (Negative Dynamic Injection Timing indicates before TDC)

Speed (rpm)	Torque (ft-lbs)	Fuel-Diesel (g/s)	Fuel-Diesel (g/rev)	DME Flow (g/s)	DME Flow (g/rev)	Total Fuel Flow (g/s)	Vol Fuel Desired (Diesel)	Dynamic Injection Timing (Diesel)	Injection Control Pressure (Diesel)
873.8	84.380	0.7532	0.0517	0.0000	0.0000	0.7815	15.5500	-7.6461	3.5004
873.3	83.909	0.4739	0.0326	0.7691	0.0528	1.2434	9.9750	-7.6727	3.5066
873.8	84.041	0.6253	0.0429	0.9456	0.0649	1.5777	13.4750	-7.6539	3.4953
874.2	84.106	0.2967	0.0204	1.1301	0.0776	1.4466	7.5875	-7.6703	3.4979
873.45	84.139	0.2244	0.0154	1.3228	0.0909	1.5603	7.3750	-7.6594	3.5041
998.55	150.181	1.2954	0.0778	0.0000	0.0000	1.3439	25.2563	-8.3031	5.4516
998.75	150.150	1.1249	0.0676	0.7691	0.0462	1.8949	20.2938	-9.0023	4.2367
1011.45	150.899	0.8689	0.0515	1.1301	0.0670	1.9987	16.3875	-9.6109	3.7400
1010.85	150.890	0.7516	0.0446	1.3228	0.0785	2.0748	15.6656	-9.5656	3.6326
1011.25	150.965	0.7511	0.0446	1.5237	0.0904	2.2740	15.5719	-9.5625	3.6303

The following figures, Figure 5.8 and Figure 5.9 , show a comparison in the heat release for two speed and load conditions, specifically 876 rpm and 84ft-lb torque, and 1000 rpm and 150 ft-lb torque. A baseline diesel heat release curve is plotted to contrast the change in the heat release curves as the DME concentration being inducted is increased. As can be seen in both cases, heat release rate decreases during the combustion process, with increasing heat loss in the chamber to the cylinder gases either before the main heat release or between the primary and secondary heat release. Some heat release curves show the typical two stage heat release as shown in some HCCI studies [220]. The negative temperature regime is to be expected between the cool flame and hot flame heat release [140]. However, in this engine configuration, there are two pulses of fuel delivered at 876 rpm. After studying the fuel injection timing, the likely cause of the significant negative heat release is the diesel fuel vaporization.

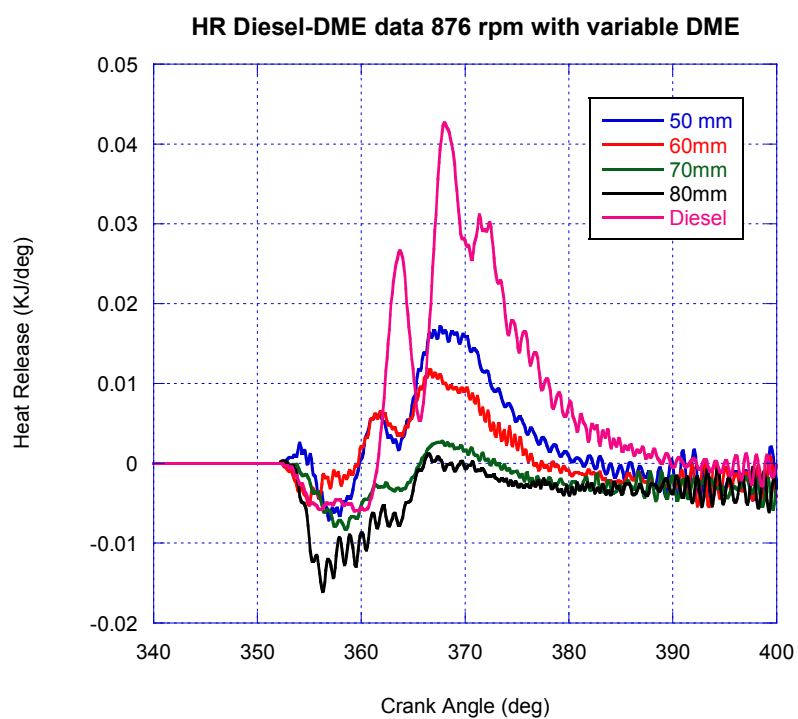


Figure 5.8: Heat Release data for 876 rpm and 84 ft-lb torque with increasing DME concentration in comparison to the baseline diesel operation.

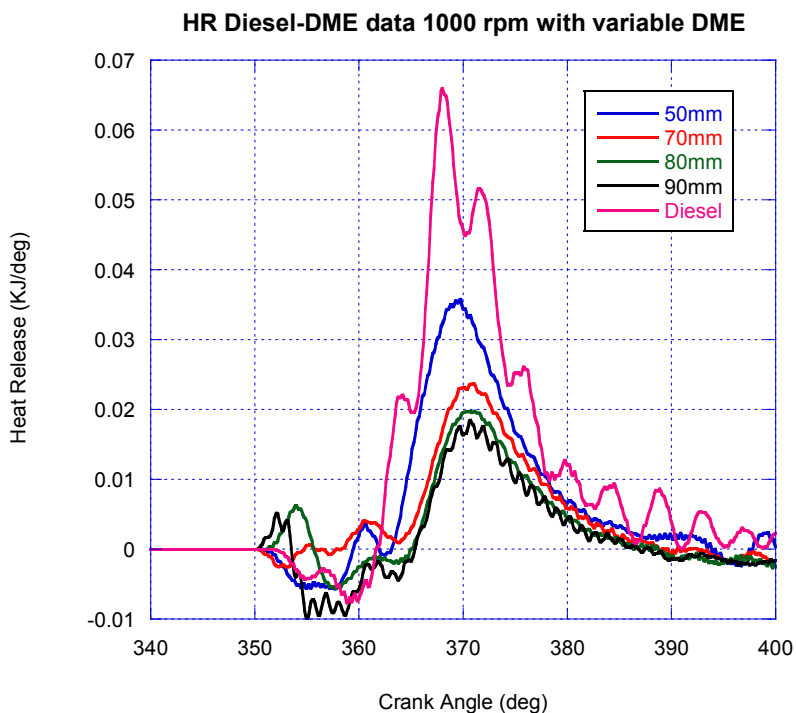


Figure 5.9: Heat Release data for 1000 rpm and 150 ft-lb torque with increasing DME concentration in comparison to the baseline diesel operation

The graphs suggest to further inspect the combustion flame temperatures and pressure traces for each test condition from the current data set, and to continue with further testing to separate the fuel pulse vs. the DME fueling. Chemkin analysis can aid in the explanation of the heat release rate, kinetics of the process, and change in NO_x emissions production. Specifically, it is important to know how the mixed mode process is changing the NO_x pathway, and if N₂O is produced or acting as an intermediate.

5.6 DDC 2.5L Light Duty Turbocharged Diesel Engine Tests

This research involves a second set of tests to explore the ignition quality of DME in an engine that will allow for control of injection pulse and timing control. The engine used for these experiments is a Detroit Diesel Corporation 2.5L light duty turbocharged diesel engine. The diesel fuel used is a British Petroleum 15 ppm sulfur ultra low sulfur diesel fuel, listed as BP15 on the figures for the results. When the DME is introduced, it represents the % energy equivalent substitution for the diesel fuel in combination with the rest of the fuel being BP15. For example, BP15 25% DME represents BP15 with 25% energy equivalent DME. The following section gives an overview of the experiments involved in this research.

The second set of experiments involve setting the engine into a single pulse injection mode and spanning DME concentrations to study the effect of the DME on the gaseous and particulate matter emissions for a particular speed and load condition.

For the third set of experiments, thermal conditioning of the intake charge is altered. An intake air heater is installed in the intake air system of the DDC 2.5L engine. The goal of using intake air heating is to observe the effect of this change on the ignition timing and combustion of the charge. Gaseous and particulate matter emissions are collected.

A fourth set of experiments involve modifying the ignition quality of the system by adjusting the cetane number to further reduce NO_x emissions and improve efficiency. The fuel brought into the intake is a combination of DME and Methane. Again, there is a pilot injection of diesel fuel. Gaseous and particulate matter emissions are collected.

5.7 Description of Experimental Set-up

The engine tests were performed in a DDC 2.5L engine with a modified intake air system which was designed to allow for intake air heating. The intake air heating will be used to study the ignition behavior of the fuel. Also, the intake air system was modified to host a series of ports for the gaseous fuel blends to be input into the system.

Figure 5.10 shows the layout of the intake air heaters before installation of the DDC 2.5L engine. The two Sylvania 20 Watt air heaters were located in parallel with the intake air flow.



Figure 5.10: Layout of intake air heating system before installation on the DDC 2.5L engine stand

The standard fuel injection strategy is comprised of a pre-injection followed by a main injection to reduce emissions and engine noise. For these tests, the engine was

commanded to provide a single pulse injection mode. The experimental tests were performed at: 1800 rpm, 61 ft-lbs torque, and a start of fuel injection timing of 7° BTDC.

5.8 Results from a DDC 2.5L Turbo Diesel Engine

The following sections are the results for the three sets of experiments described previously. Each experiment will be described with the gaseous and particulate matter emissions following.

5.8.1 Increasing Dimethyl Ether Concentrations in Intake Air

The second set of experiments involved setting the engine into a single pulse injection mode and spanning DME concentrations to study the effect of the DME on the NO_x emissions for a particular speed and load condition. The concentrations of DME are represented as the percent energy equivalent substitution by DME that replaced the diesel fuel energy, based on the calorific value of the fuels. Gaseous and particulate matter emissions were collected.

Figure 5.11 shows the NO_x (g/kg fuel) for mixed mode combustion at 1800 rpm and 61 ft-lb torque with increasing DME concentration fumigated in the intake air. NO_x emissions decrease slightly per gram of fuel, approximately 10%, but there is no decrease observed with increasing DME fumigated fuel.

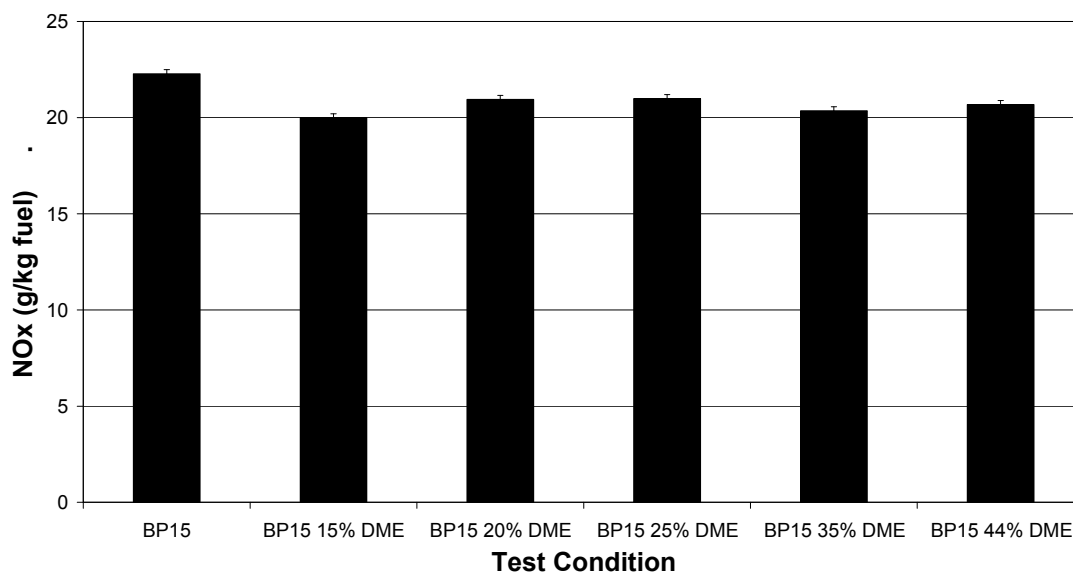


Figure 5.11: NO_x (g/kg fuel) for mixed mode combustion at 1800 rpm and 61 ft-lb torque with increasing DME concentration fumigated in the intake air

Figure 5.12 shows NO_x (g/kWh) for mixed mode combustion at 1800 rpm and 61 ft-lb torque with increasing DME concentration fumigated in the intake air. On the basis of power, a greater impact in NO_x emissions reduction is observed than for the conventional diesel BP15.

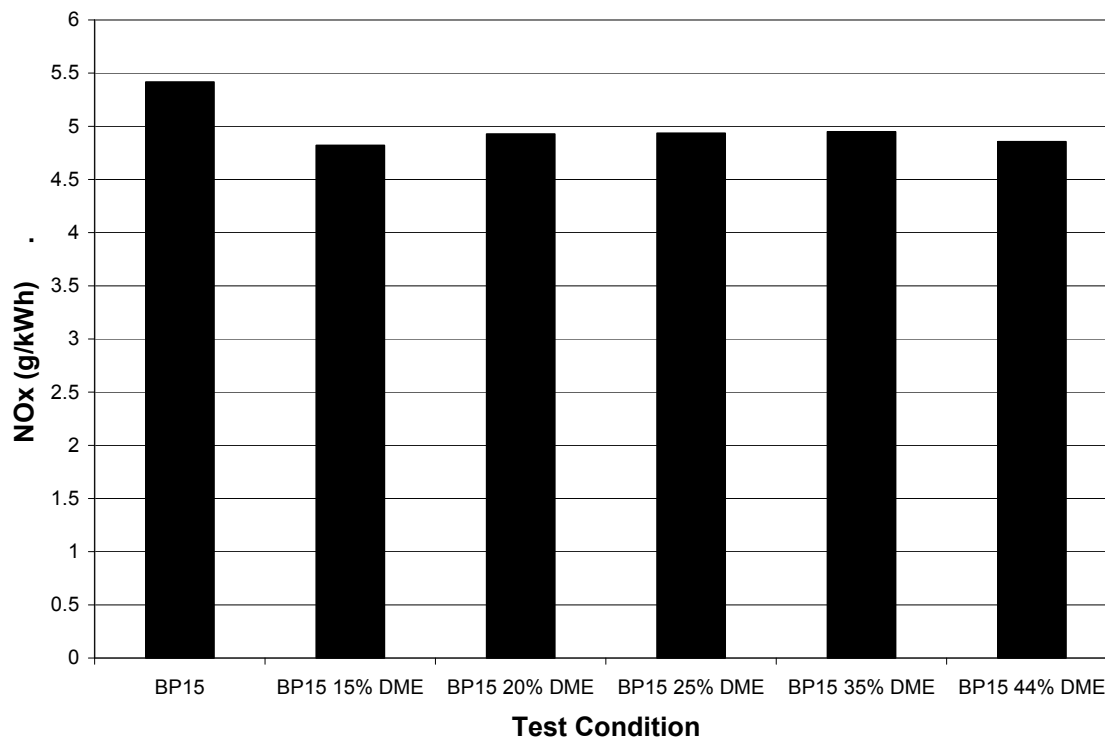


Figure 5.12: NO_x (g/kWh) for mixed mode combustion at 1800 rpm and 61 ft-lb torque with increasing DME concentration fumigated in the intake air

Figure 5.13 shows the NO (g/kg fuel) for mixed mode combustion at 1800 rpm and 61 ft-lb torque with increasing DME concentration fumigated in the intake air. As is seen in the figure, for a DME concentration of 15% energy equivalent, an almost 50% percent reduction in NO emissions is observed. As the DME % is increased, the NO emissions begin to increase.

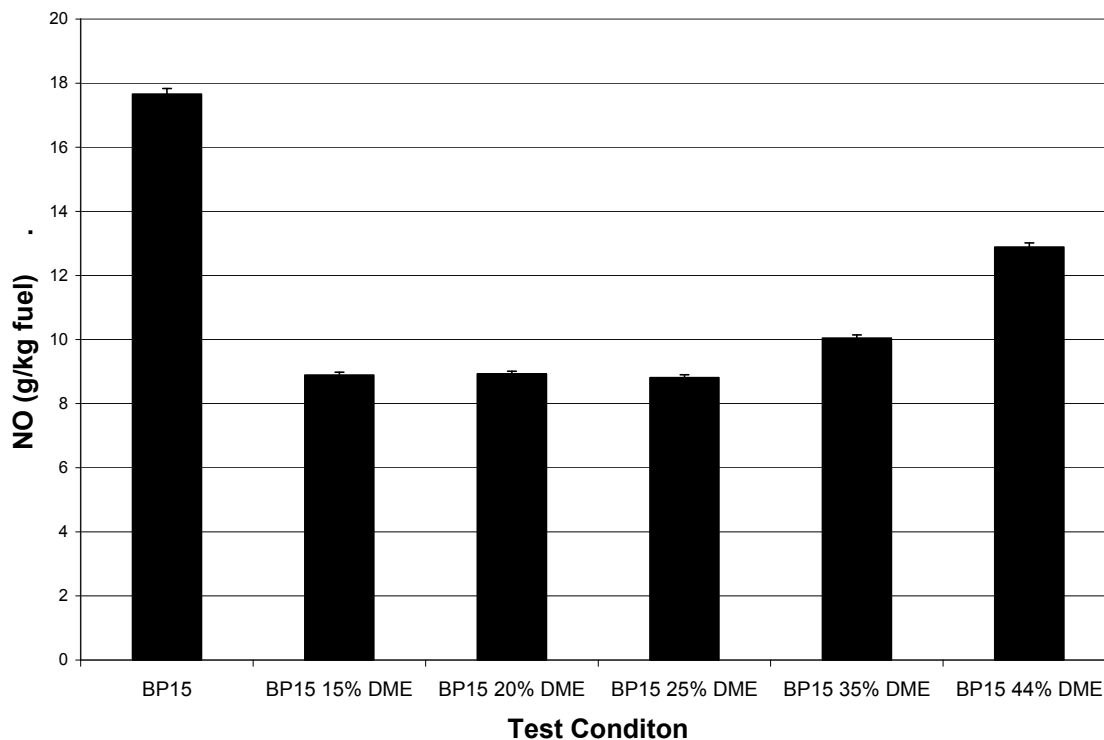


Figure 5.13: NO (g/kg fuel) for mixed mode combustion at 1800 rpm and 61 ft-lb torque with increasing DME concentration fumigated in the intake air

Figure 5.14 shows the NO_2 (g/kg fuel) for mixed mode combustion at 1800 rpm and 61 ft-lb torque with increasing DME concentration fumigated in the intake air. As is seen in the figure, for a DME concentration of 15% energy equivalent, an almost 50% percent increase in NO_2 emissions is observed. As the DME % is increased, the NO_2 emissions begin to decrease.

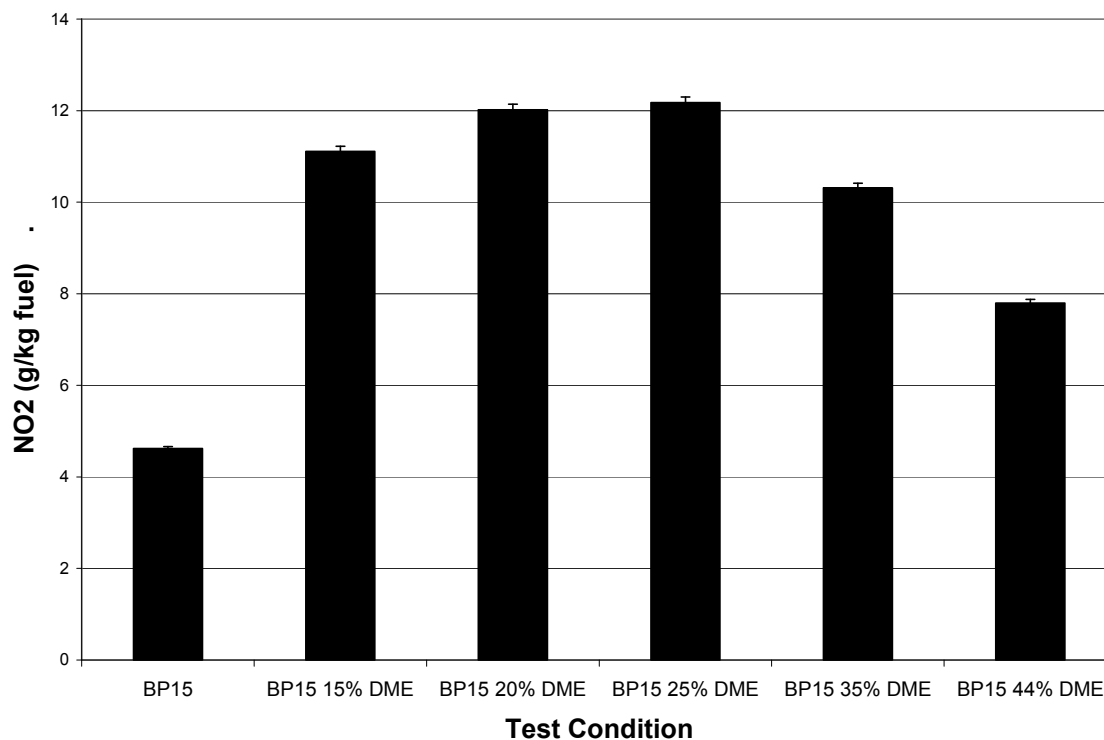


Figure 5.14: NO₂ (g/kg fuel) for mixed mode combustion at 1800 rpm and 61 ft-lb torque with increasing DME concentration fumigated in the intake air

The Nicolet Magma 500 FTIR was used to collect N₂O data for the 15% DME and 20% DME Mixed Mode Combustion data points. No N₂O was observed with these two concentrations, so the collection of this data was discontinued.

Figure 5.15 shows the Brake Specific Fuel Consumption (BSFC) (g/kWh) for mixed mode combustion at 1800 rpm and 61 ft-lb torque with increasing DME concentration fumigated in the intake air. Approximately the same amount of fuel mass was required to maintain the engine speed and load.

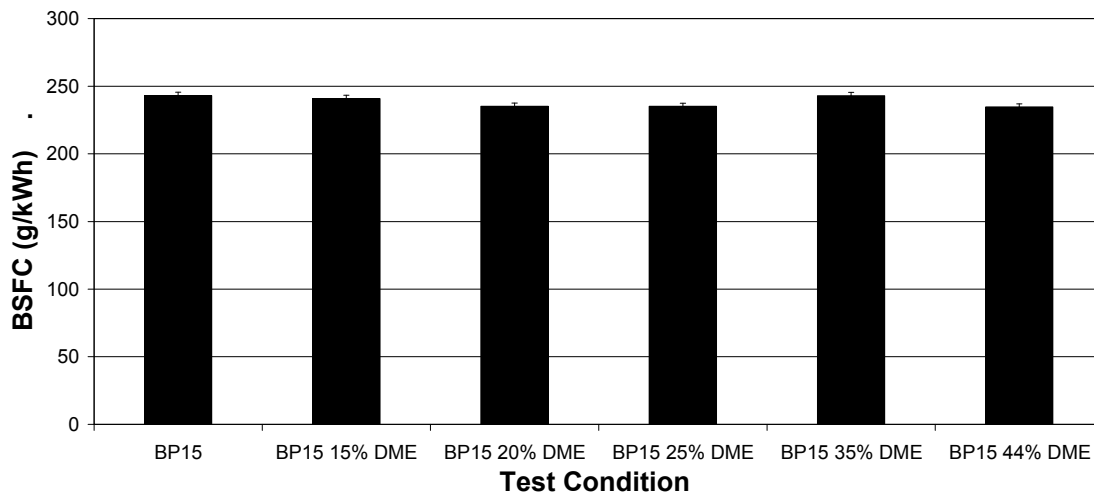


Figure 5.15: Brake Specific Fuel Consumption (g/kWh) for mixed mode combustion at 1800 rpm and 61 ft-lb torque with increasing DME concentration fumigated in the intake air

Figure 5.16 shows the Brake Specific Energy Consumption (BSEC) (MJ/kWh) for mixed mode combustion at 1800 rpm and 61 ft-lb torque with increasing DME concentration fumigated in the intake air. On an energy basis, as the percent of DME energy was increased, less energy was required to produce the same amount of power. At the 44% DME energy equivalent, 22.8% less energy was required to maintain the same power output from the engine.

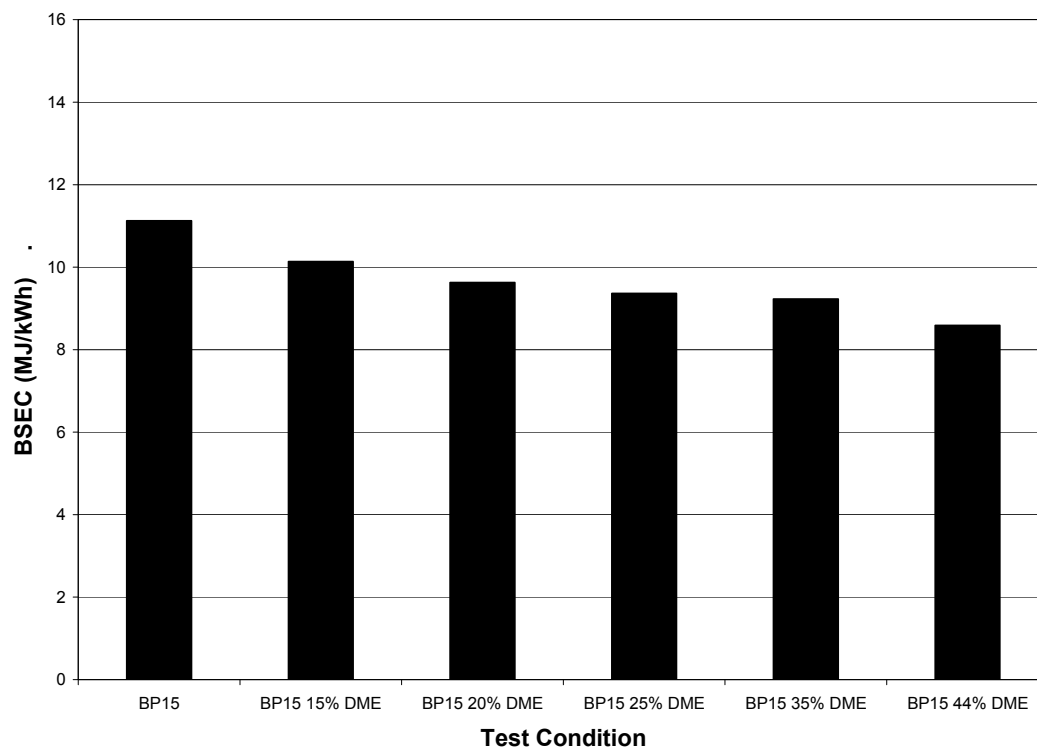


Figure 5.16: Brake Specific Energy Consumption (MJ/kWh) for mixed mode combustion at 1800 rpm and 61 ft-lb torque with increasing DME concentration fumigated in the intake air

Figure 5.17 shows the CO (g/kg fuel) for mixed mode combustion at 1800 rpm and 61 ft-lb torque with increasing DME concentration fumigated in the intake air. As is seen in the figure, with any blend concentration of DME, CO increases over the normal diesel fuel. The maximum CO is measured at 25% DME concentration, with CO decreasing from there whether the blend concentration is increased or decreased.

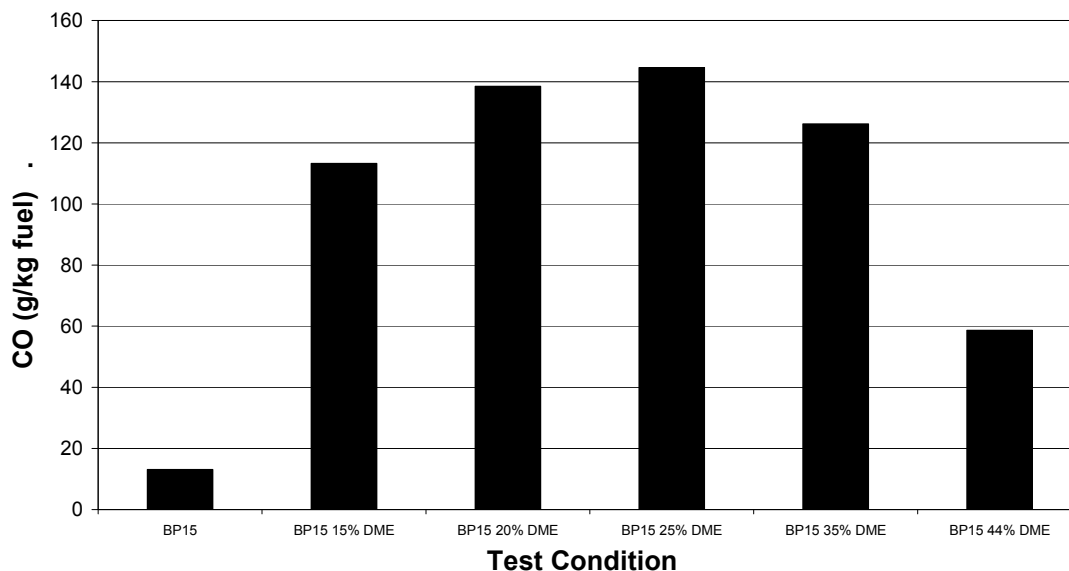


Figure 5.17: CO (g/kg fuel) for mixed mode combustion at 1800 rpm and 61 ft-lb torque with increasing DME concentration fumigated in the intake air

Figure 5.18 shows the Total Hydrocarbons (g/kg fuel) for mixed mode combustion at 1800 rpm and 61 ft-lb torque with increasing DME concentration fumigated in the intake air. The hydrocarbons increase with increasing percent DME concentration.

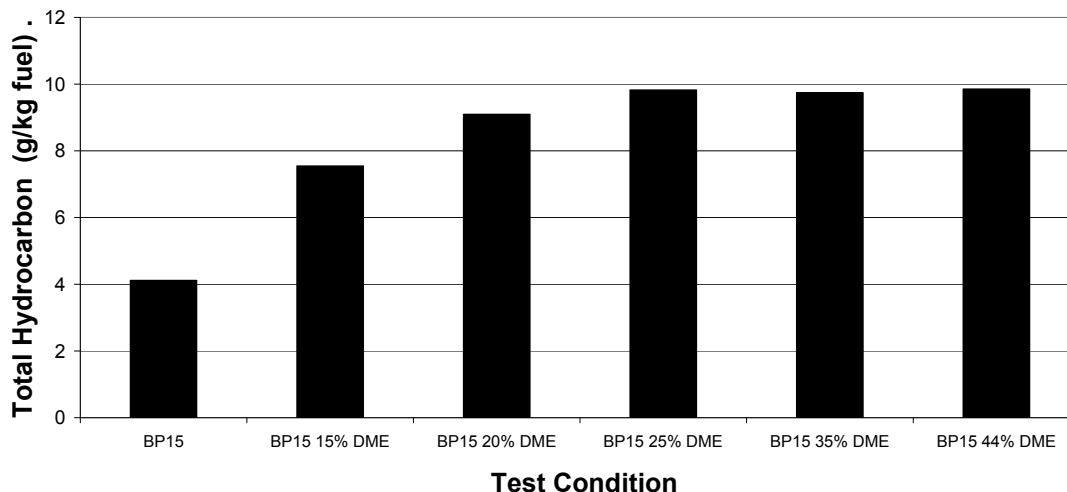


Figure 5.18: Total Hydrocarbons (g/kg fuel) for mixed mode combustion at 1800 rpm and 61 ft-lb torque with increasing DME concentration fumigated in the intake air

Figure 5.19 shows the data from the GC that was collected on the FID. The gases that were calibrated on the GC are shown and quantified. As can be seen, with increasing DME concentration, the amount of DME found in the exhaust gases increase. Also, the Methane concentration is seen to increase. THC is the total hydrocarbons of all those measured from the GC found in the exhaust gas. While not easily shown in this figure, but observed in the data is that the small concentrations of light hydrocarbons other than Methane and DME decrease to zero when using the fumigated DME.

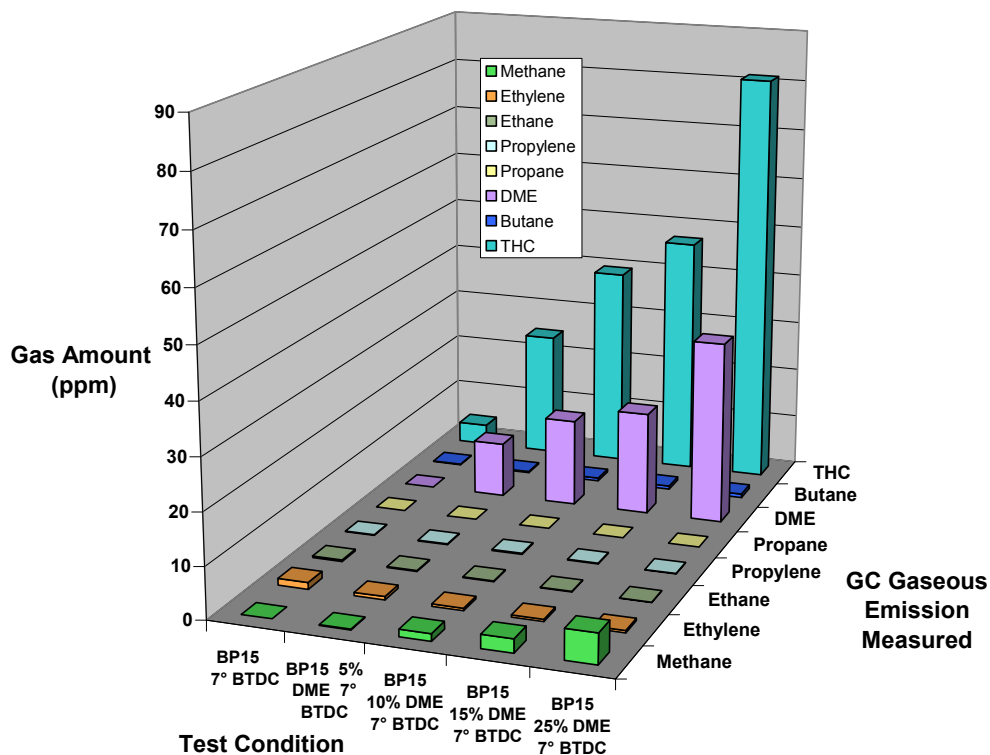


Figure 5.19: GC Data: BP15 in comparison to mixed mode combustion with increasing energy equivalent percent DME concentration at 7° BTDC

Figure 5.20 shows the CO₂ (g/kg fuel) for mixed mode combustion at 1800 rpm and 61 ft-lb torque with increasing DME concentration fumigated in the intake air. An approximately 5% reduction of CO₂ is observed for some DME blend concentrations, but the trend is not consistent.

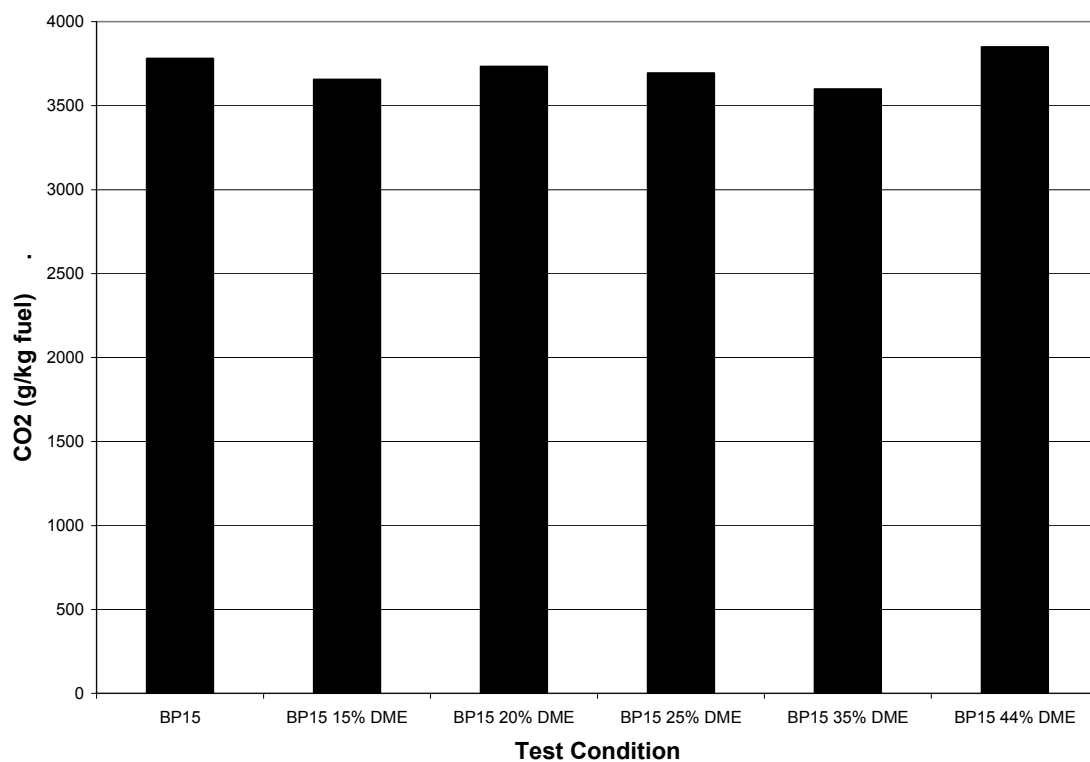


Figure 5.20: CO₂ (g/kg fuel) for mixed mode combustion at 1800 rpm and 61 ft-lb torque with increasing DME concentration fumigated in the intake air

Figure 5.21 shows Methane (ppm) for mixed mode combustion at 1800 rpm and 61 ft-lb torque with increasing DME concentration fumigated in the intake air. Methane is a maximum at the 25% DME concentration.

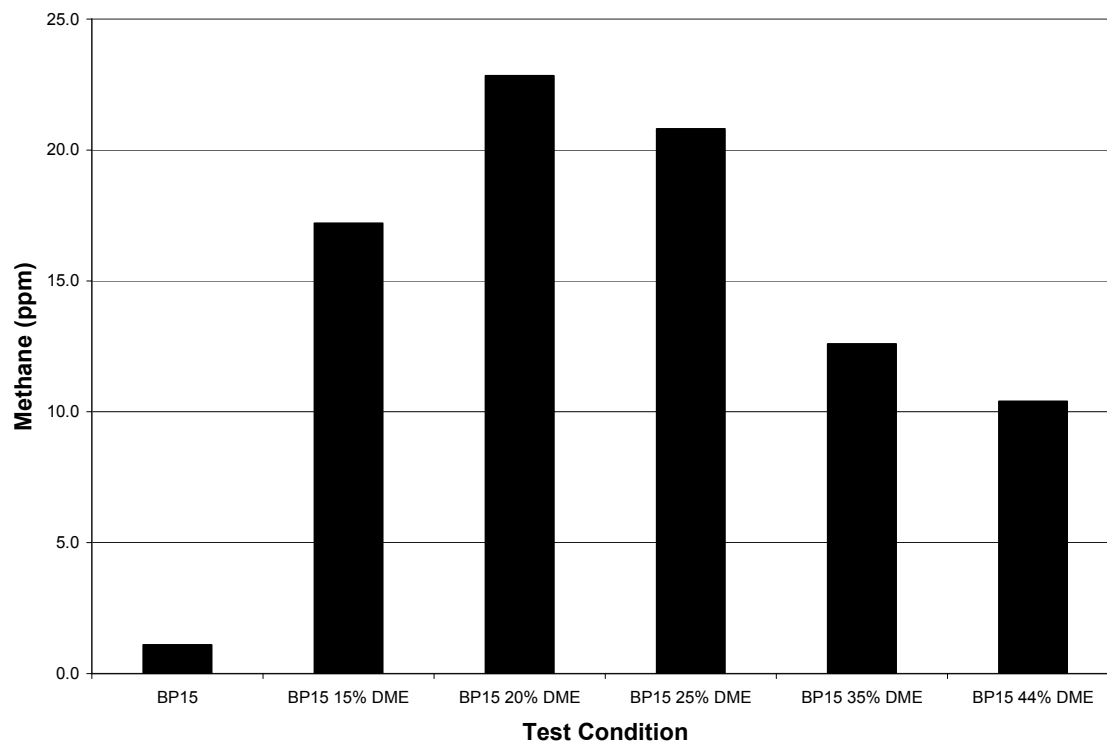


Figure 5.21: Methane (ppm) for mixed mode combustion at 1800 rpm and 61 ft-lb torque with increasing DME concentration fumigated in the intake air

Figure 5.22 shows Exhaust Temperatures ($^{\circ}\text{C}$) for mixed mode combustion at 1800 rpm and 61 ft-lb torque with increasing DME concentration fumigated in the intake air. The exhaust temperature is the same for each test condition.

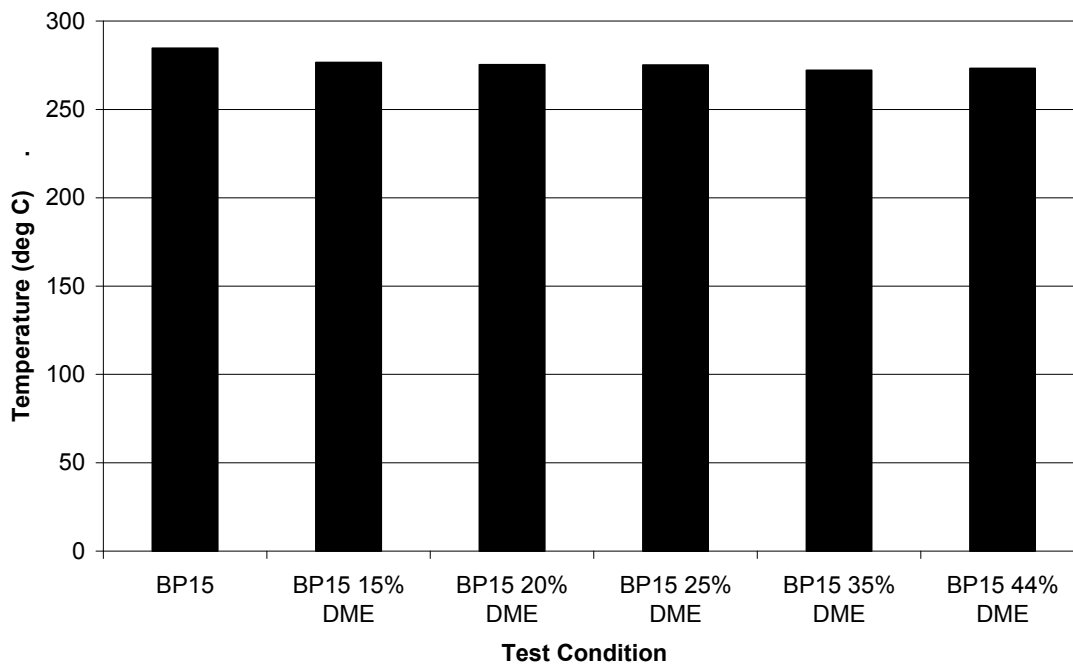


Figure 5.22: Exhaust Temperatures (°C) for mixed mode combustion at 1800 rpm and 61 ft-lb torque with increasing DME concentration fumigated in the intake air

Figure 5.23 shows Cylinder Pressure trace data for BP15 in comparison to mixed mode combustion with increasing energy equivalent percent DME concentration at 7° BTDC. The BP15 diesel pressure trace shows the distinction between the premixed and the diffusion burn parts of the process. As the DME concentration is increased, the start of combustion comes earlier and with it is premixed burning. The premixed phase and the diffusion phase merge. In addition, the pressure increases with increasing DME concentration.

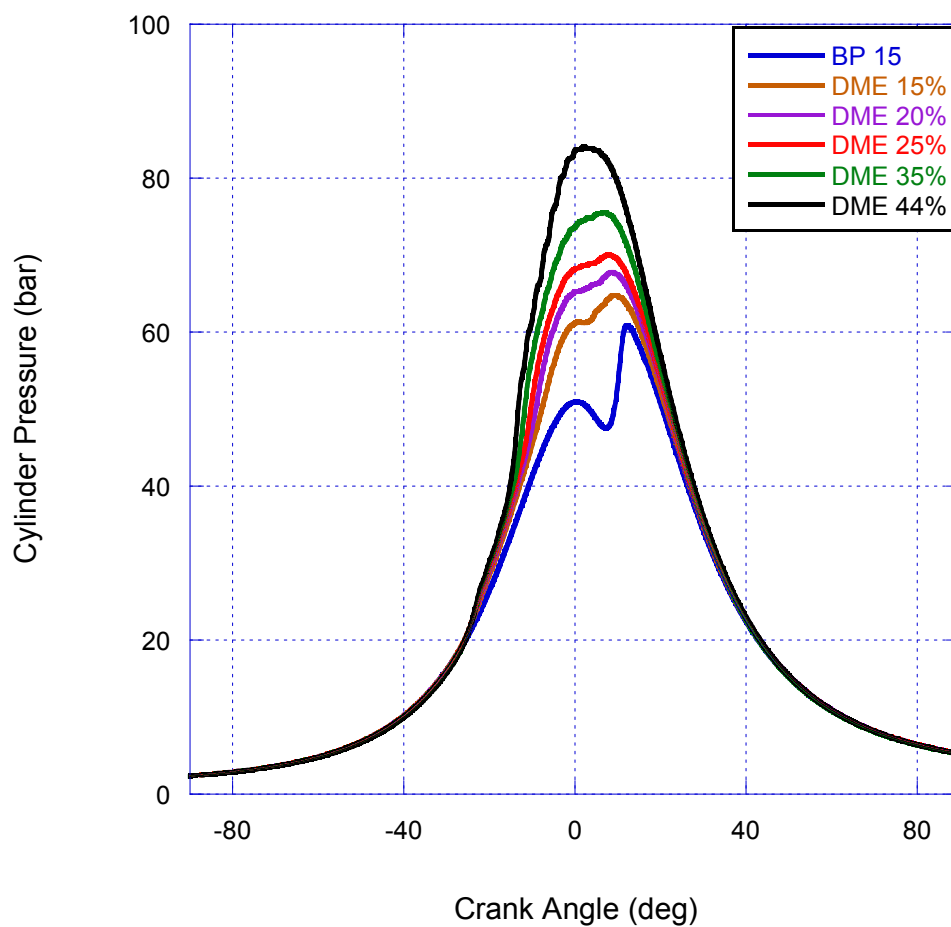


Figure 5.23: Cylinder Pressure Traces (bar) for BP15 in comparison to mixed mode combustion with increasing energy equivalent percent DME concentration at 7° BTDC

Figure 5.24 shows heat release rate (J/deg) for BP15 in comparison to mixed mode combustion with increasing energy equivalent percent DME concentration at 7° BTDC. DME exhibits a two peak heat release, the first a low temperature heat release (LTHR) and the second a high temperature heat release (HTHR). With increasing DME concentration, the LTHR peak increases and maintains the same combustion phasing.

However, as the DME concentration is increased, the HTHR peak increases and advances closer to the LTHR peak. In addition, the heat release from the diesel fuel is decreased with increasing DME concentration and maintains the same combustion phasing.

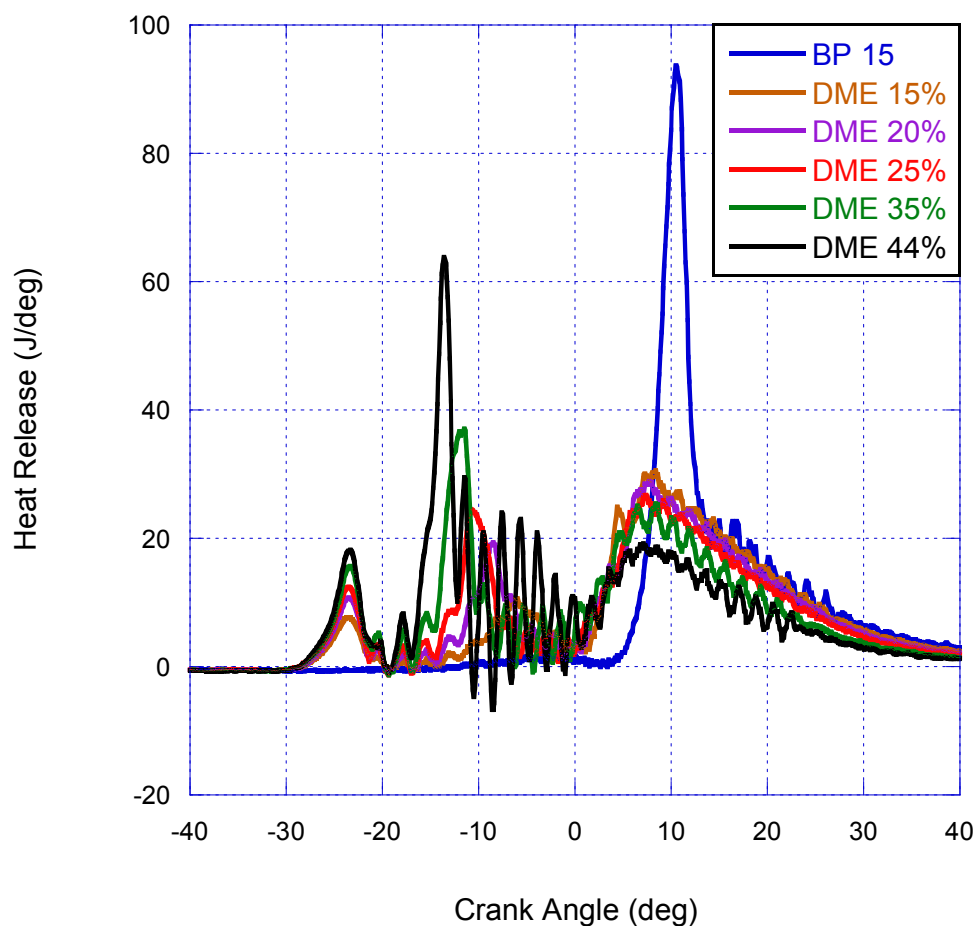


Figure 5.24: Heat Release Rate (J/deg) for BP15 in comparison to mixed mode combustion with increasing energy equivalent percent DME concentration at 7° BTDC

Figure 5.25 shows bulk cylinder temperature (K) for BP15 in comparison to mixed mode combustion with increasing energy equivalent percent DME concentration at 7° BTDC. With increasing DME concentration, the bulk temperature occurs earlier and an overall increase in bulk temperature occurs.

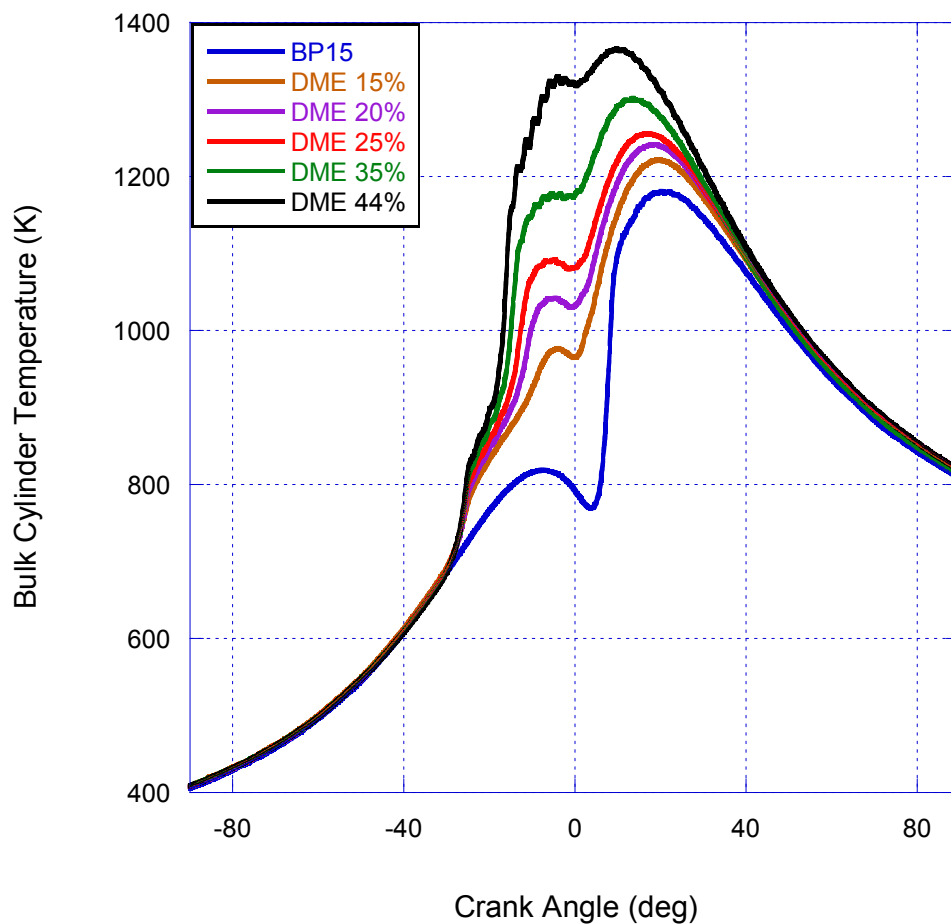


Figure 5.25: Bulk Cylinder Temperature (K) for BP15 in comparison to mixed mode combustion with increasing energy equivalent percent DME concentration at 7° BTDC

The following figures show the results of fixing DME concentration at 25% energy equivalent while changing in injection timing. All results are shown in comparison to diesel fuel (BP15) at 7° BTDC.

Figure 5.26 shows NO_x (g/kg fuel) for mixed mode combustion at 1800 rpm and 61 ft-lb torque with 25% energy equivalent DME concentration fumigated in the intake air at various injection timing. As the injection timing is retarded, the NO_x emissions decrease. The decrease in the NO_x emissions as the injection timing is retarded would be expected since there would be less time for the production of thermal NO until the exhaust valve opens and quenches the reactions.

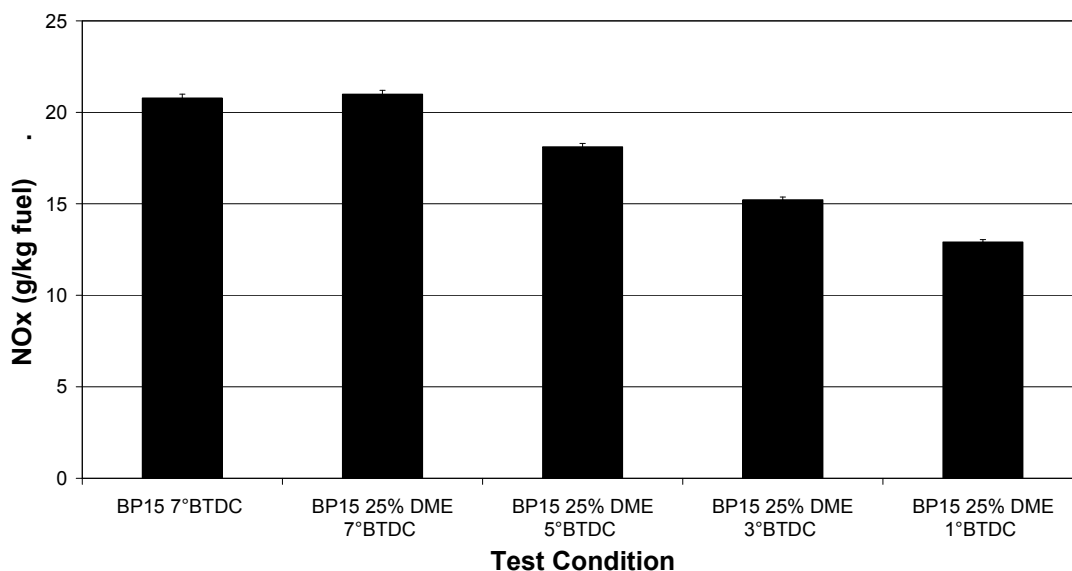


Figure 5.26: NO_x (g/kg fuel) for mixed mode combustion at 1800 rpm and 61 ft-lb torque with 25% energy equivalent DME concentration fumigated in the intake air at various injection timings

Figure 5.27 shows NO_x (g/kWh) for mixed mode combustion at 1800 rpm and 61 ft-lb torque with 25% energy equivalent DME concentration fumigated in the intake air at various injection timings. As the injection timing is retarded, the NO_x emissions decrease. For the same power output, NO_x emissions were reduced by almost 50% by injection of the diesel fuel at 1° BTDC.

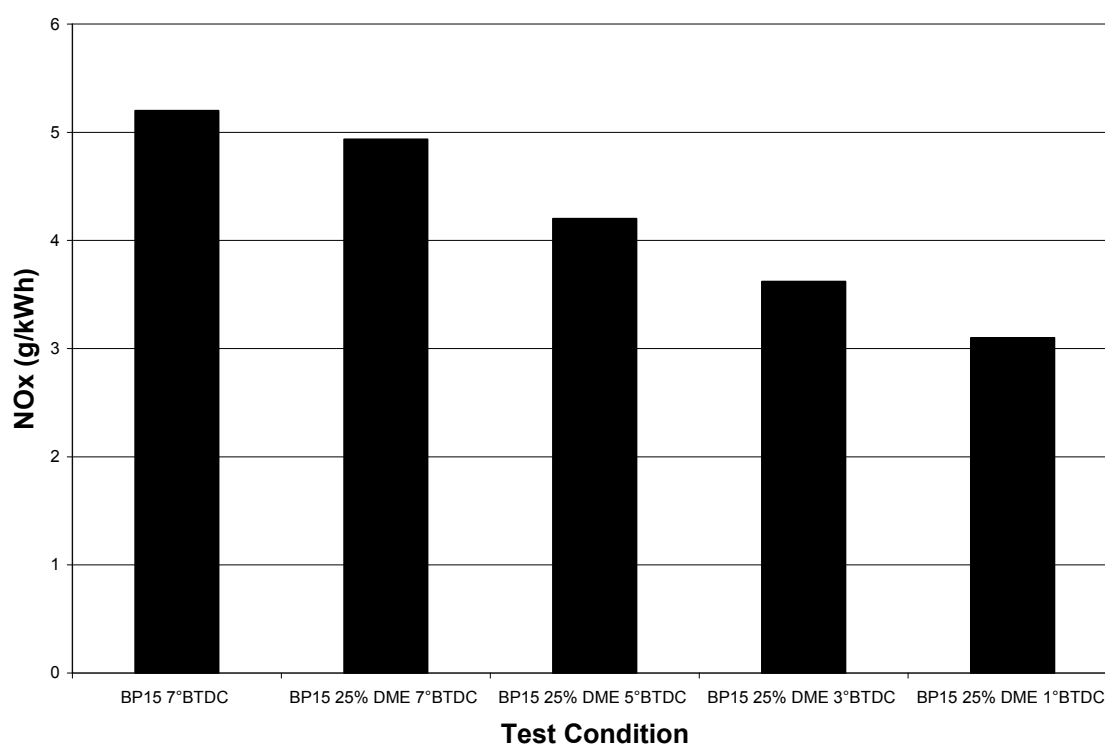


Figure 5.27: NO_x (g/kWh) for mixed mode combustion at 1800 rpm and 61 ft-lb torque with 25% energy equivalent DME concentration fumigated in the intake air at various injection timings

Figure 5.28 shows NO (g/kg fuel) for mixed mode combustion at 1800 rpm and 61 ft-lb torque with 25% energy equivalent DME concentration fumigated in the intake air at various injection timings. As the injection timing is retarded, the NO emissions

decrease. For the same power output, NO emissions were reduced by over 80% by injection of the diesel fuel at 1° BTDC.

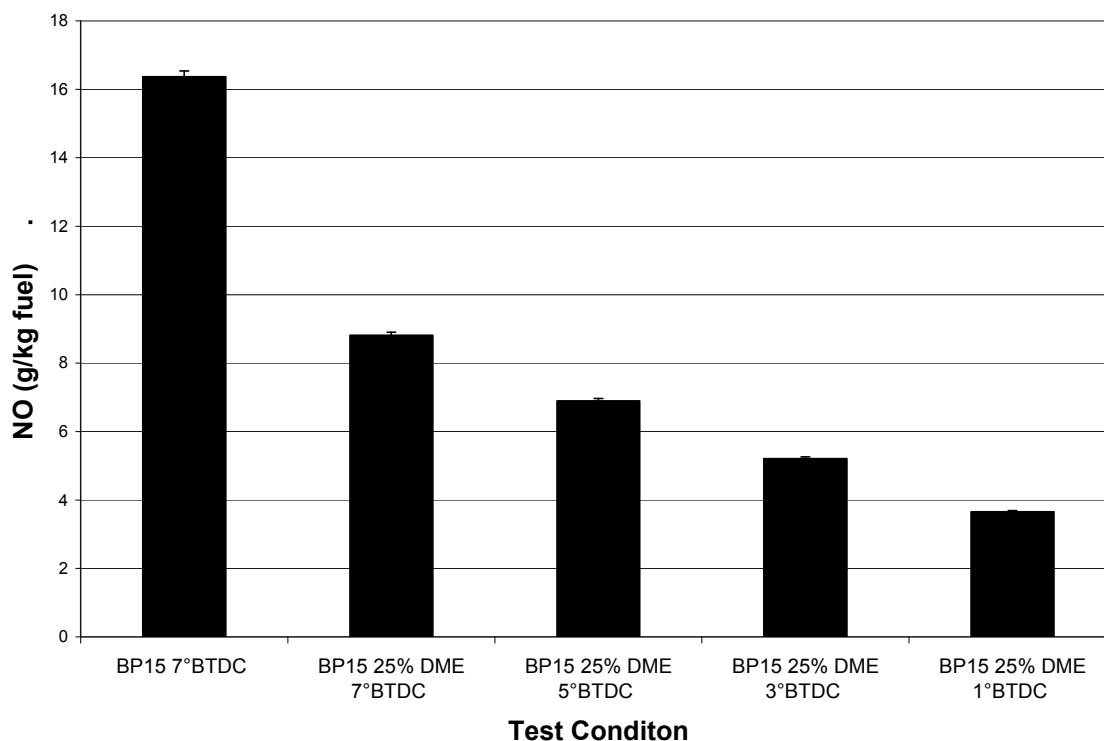


Figure 5.28: NO (g/kg fuel) for mixed mode combustion at 1800 rpm and 61 ft-lb torque with 25% energy equivalent DME concentration fumigated in the intake air at various injection timings

Figure 5.29 shows NO₂ (g/kg fuel) for mixed mode combustion at 1800 rpm and 61 ft-lb torque with 25% energy equivalent DME concentration fumigated in the intake air at various injection timings. While NO₂ emissions increase with DME concentration, they decrease as the injection timing is retarded.

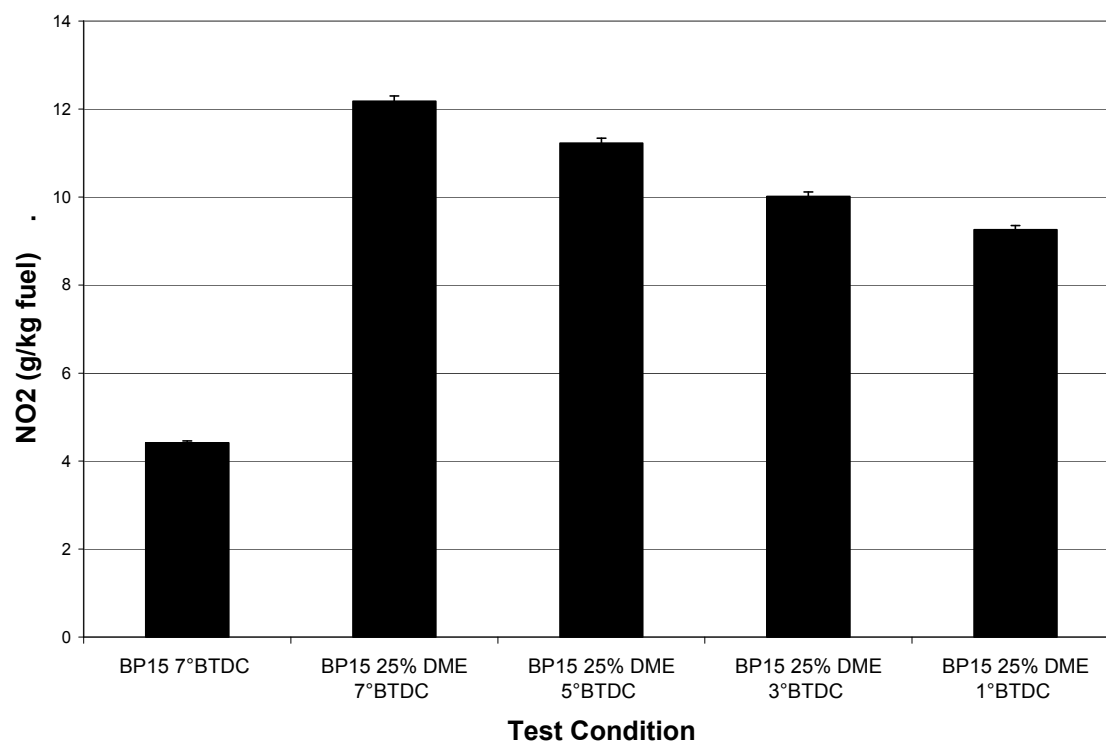


Figure 5.29: NO₂ (g/kg fuel) for mixed mode combustion at 1800 rpm and 61 ft-lb torque with 25% energy equivalent DME concentration fumigated in the intake air at various injection timings

Figure 5.30 shows Methane (ppm) for mixed mode combustion at 1800 rpm and 61 ft-lb torque with 25% energy equivalent DME concentration fumigated in the intake air at various injection timings. Methane emissions increase when injection timing is retarded.

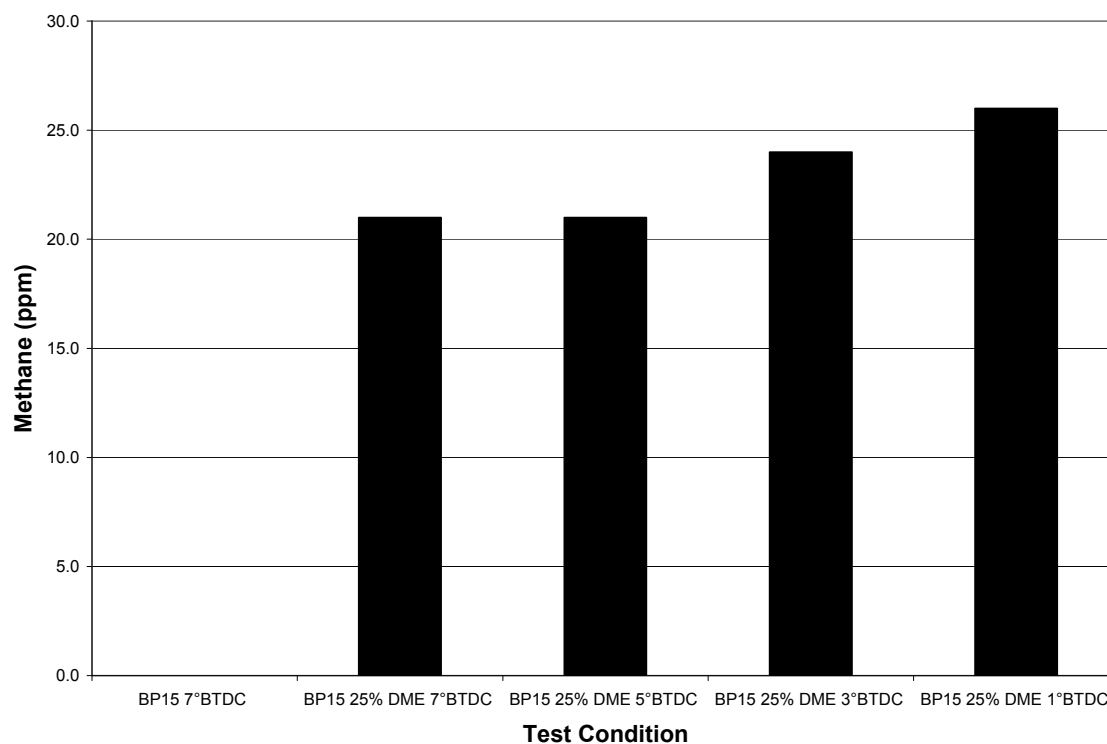


Figure 5.30: Methane (ppm) for mixed mode combustion at 1800 rpm and 61 ft-lb torque with 25% energy equivalent DME concentration fumigated in the intake air at various injection timings

Figure 5.31 shows GC data for 25% energy equivalent DME concentration at varying pilot injection timing: 7°, 5°, 3° BTDC. As the injection timing is retarded and injection begins later, the Methane concentration in the exhaust increases, while the DME concentration stays roughly the same.

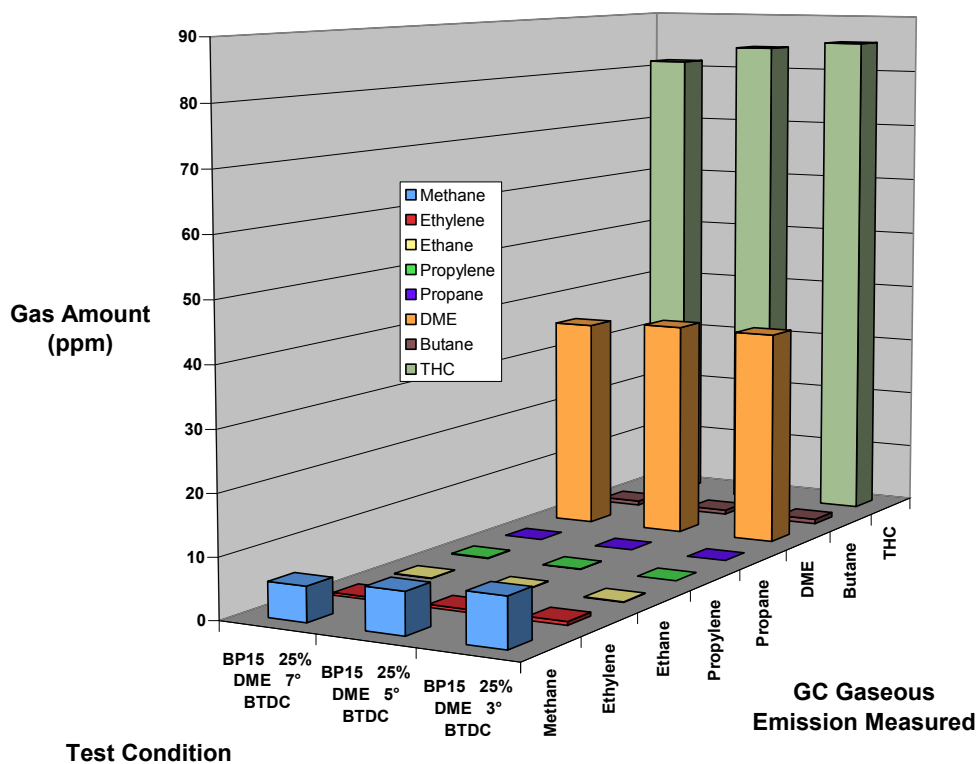


Figure 5.31: GC Data: 25% energy equivalent DME concentration at varying pilot injection timings: 7°, 5°, 3° BTDC

Figure 5.32 shows Brake Specific Fuel Consumption (g/kWh) for mixed mode combustion at 1800 rpm and 61 ft-lb torque with 25% energy equivalent DME concentration fumigated in the intake air at various injection timings. Besides a slight decrease in fuel consumption when using DME, there is no apparent change in fuel consumption with change in injection timing.

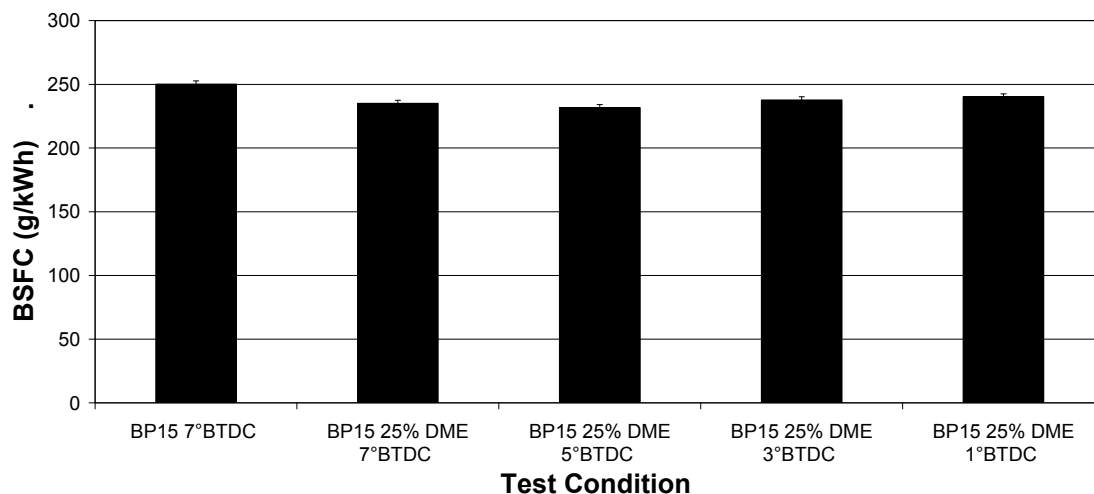


Figure 5.32: Brake Specific Fuel Consumption (g/kWh) for mixed mode combustion at 1800 rpm and 61 ft-lb torque with 25% energy equivalent DME concentration fumigated in the intake air at various injection timings

Figure 5.33 shows Brake Specific Energy Consumption (MJ/kWh) for mixed mode combustion at 1800 rpm and 61 ft-lb torque with 25% energy equivalent DME concentration fumigated in the intake air at various injection timings. Besides a 15% decrease in energy consumption when using DME, there is no apparent change in fuel consumption with change in injection timing.

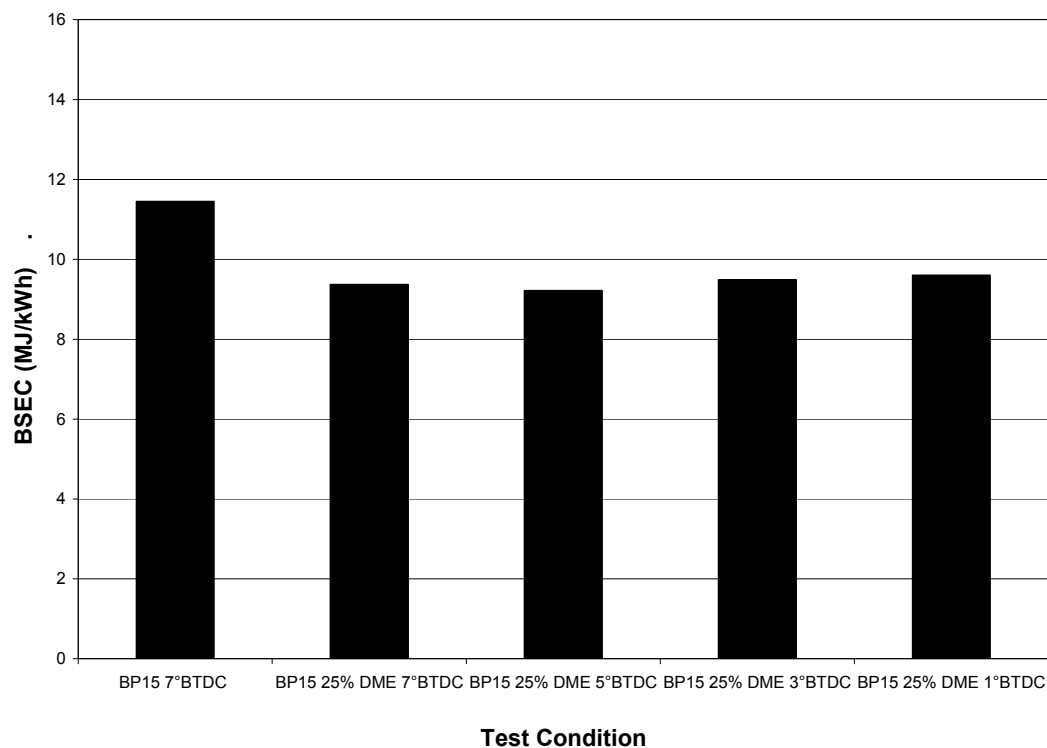


Figure 5.33: Brake Specific Energy Consumption (MJ/kWh) for mixed mode combustion at 1800 rpm and 61 ft-lb torque with 25% energy equivalent DME concentration fumigated in the intake air at various injection timings

Figure 5.34 shows Fuel Consumption (g/hr) for mixed mode combustion at 1800 rpm and 61 ft-lb torque with 25% energy equivalent DME concentration fumigated in the intake air at various injection timings. At 5° BTDC, a minimum fuel consumption is observed, about a 5% decrease when DME is fumigated. As the injection timing retarded, the fuel consumption increases back to the same level as diesel fuel.

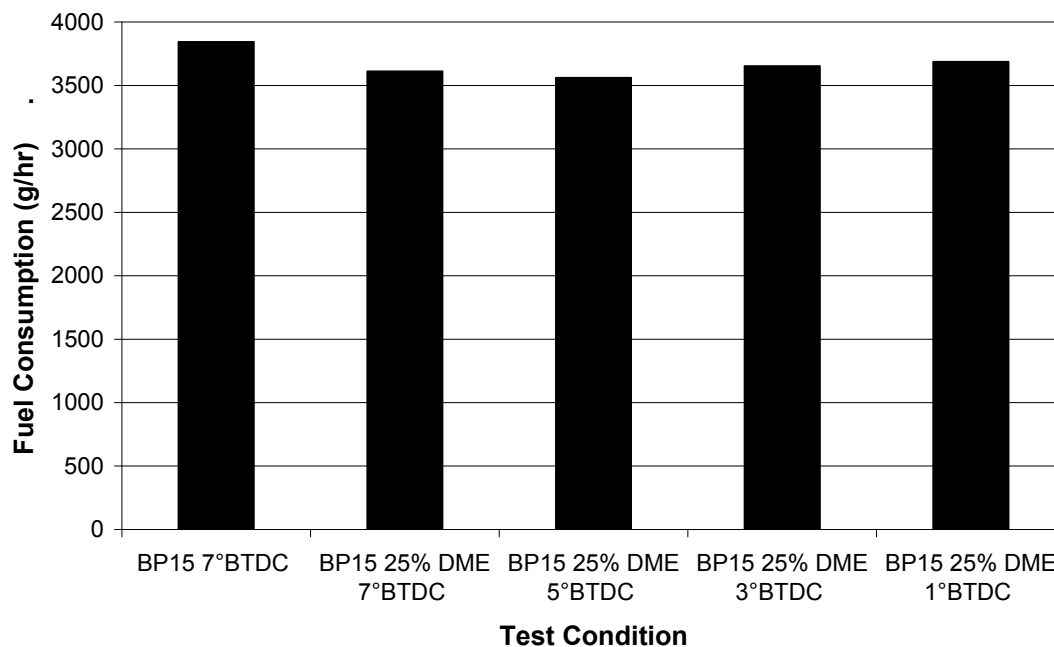


Figure 5.34: Fuel Consumption (g/hr) for mixed mode combustion at 1800 rpm and 61 ft-lb torque with 25% energy equivalent DME concentration fumigated in the intake air at various injection timings

Figure 5.35 shows Cylinder Pressure (bar) for mixed mode combustion at 1800 rpm and 61 ft-lb torque with 25% energy equivalent DME concentration fumigated in the intake air at various injection timings. As the timing is retarded, the crank angle degree of peak pressure shifts while the magnitude of peak pressure remains the same.

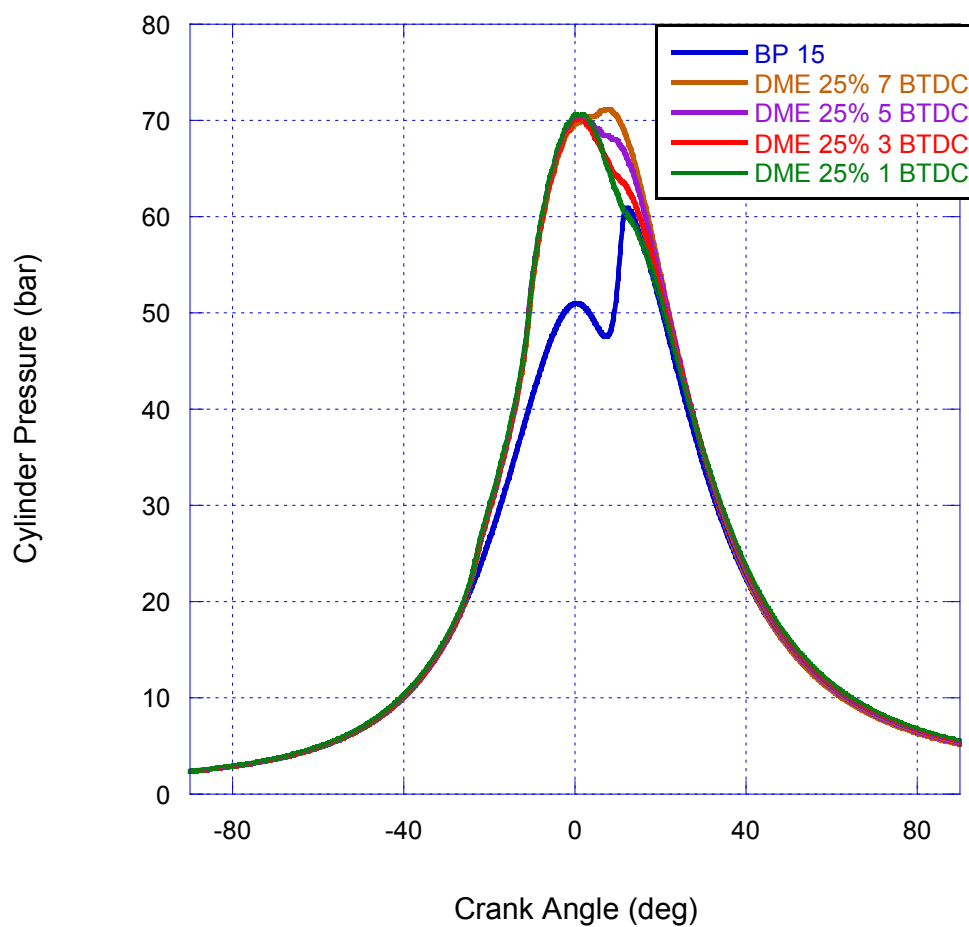


Figure 5.35: Cylinder Pressure (bar) for mixed mode combustion at 1800 rpm and 61 ft-lb torque with 25% energy equivalent DME concentration fumigated in the intake air at various injection timings

Figure 5.36 shows heat release rate (J/deg) for mixed mode combustion at 1800 rpm and 61 ft-lb torque with 25% energy equivalent DME concentration fumigated in the intake air at various injection timings. As the timing is retarded, the crank angle degree phasing of LTHR and HTHR remains the same despite the diesel pilot injection. Thus,

the DME portion is independent of the diesel portion. The timing of the diesel fuel heat release adjusts with the change in injection timing. Also, as the timing is retarded, it appears that the heat release from the diesel fuel portion increases.

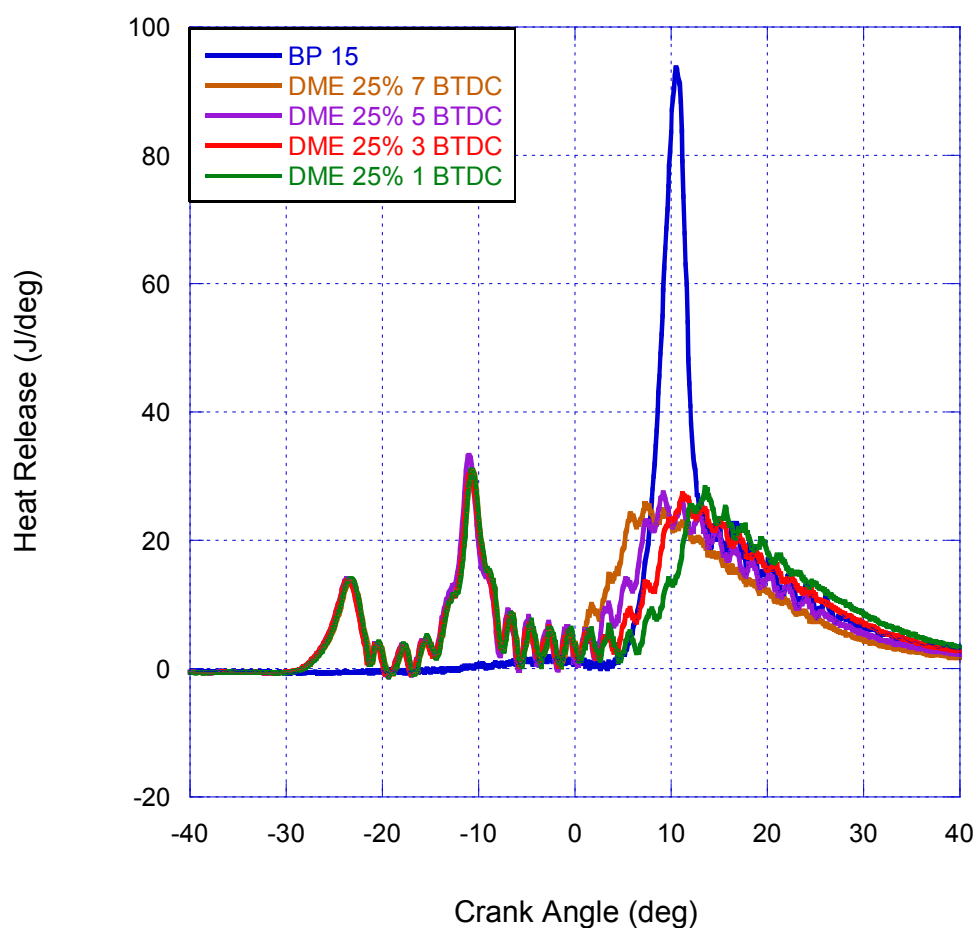


Figure 5.36: Heat Release Rate (J/deg) for mixed mode combustion at 1800 rpm and 61 ft-lb torque with 25% energy equivalent DME concentration fumigated in the intake air at various injection timings

Figure 5.37 shows bulk cylinder temperature (K) for mixed mode combustion at 1800 rpm and 61 ft-lb torque with 25% energy equivalent DME concentration fumigated in the intake air at various injection timings. As the timing is retarded, the bulk temperature as a result of the LTHR and HTHR peak appears to be same. There is a delay and a reduction in the high temperature peak as a result of the retarding of the injection timing and the diesel fuel impact on the combustion process.

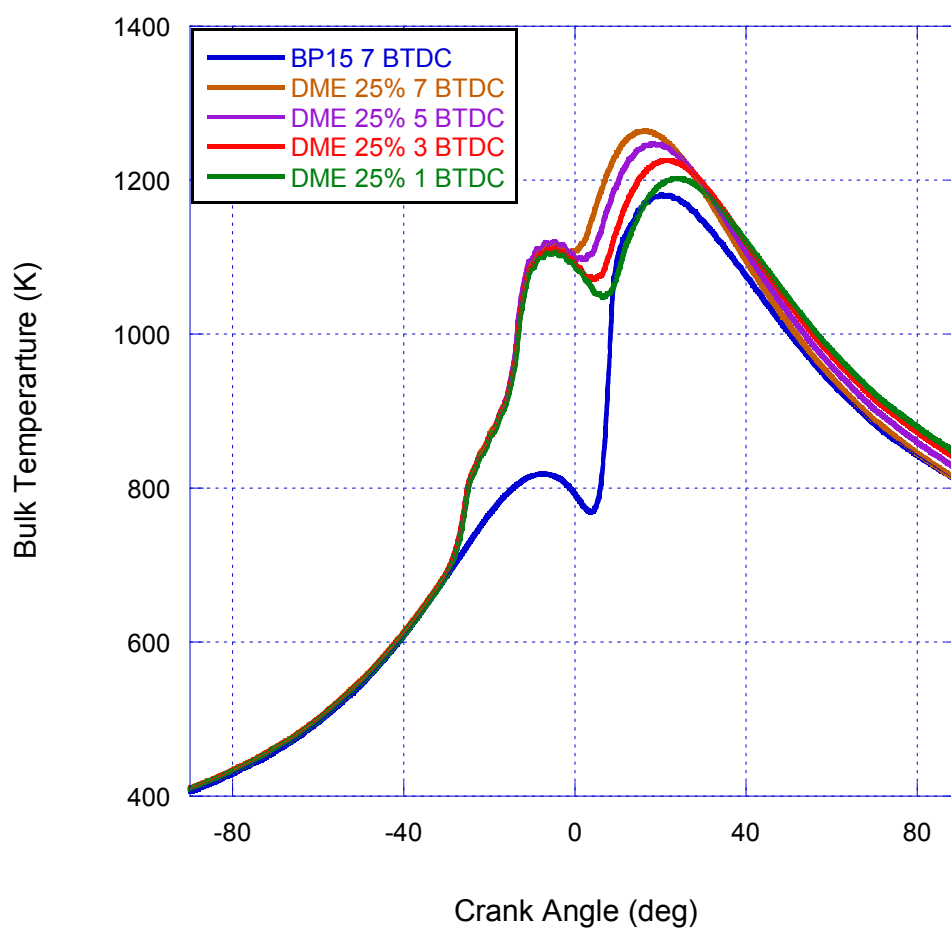


Figure 5.37: Bulk Cylinder Temperature (K) for mixed mode combustion at 1800 rpm and 61 ft-lb torque with 25% energy equivalent DME concentration fumigated in the intake air at various injection timings

5.8.1.1 Sierra Instruments BG-2 Gravimetric Particulate Matter Data

Exploratory observations were made with the BG-2 on the particulate matter (PM) change associated with the mixed mode combustion process. The following photographs show an observed change in the darkness of the filters. Darkness of the filter is related to particulate mass concentration. Again, the engine speed was 1800 rpm and the load was 61 ft-lbs torque for all data collected in these pictures.

An overview of the PM emissions for BP-15 is shown in Figure 5.38 with changing injection timing. The earlier that the fuel injection occurred, the darker the PM was on the filter.

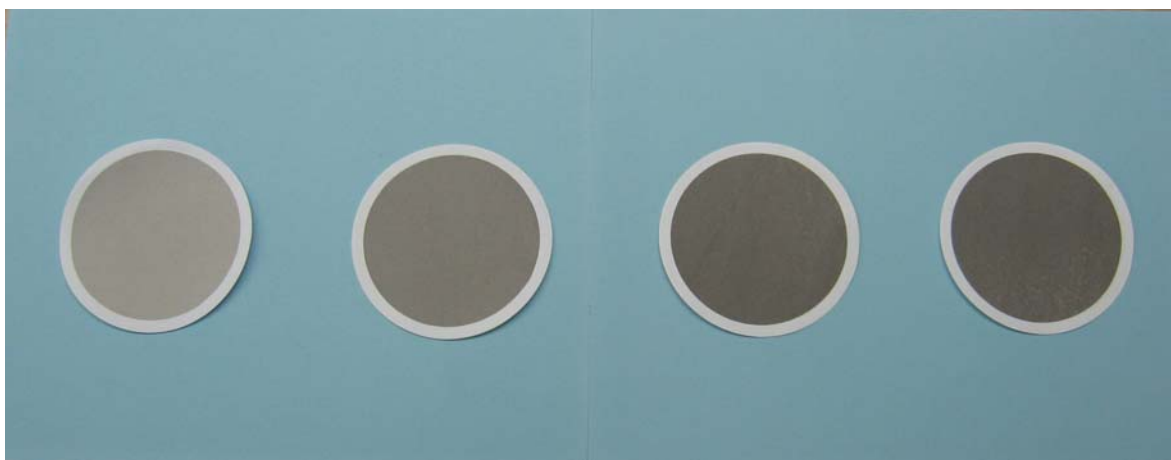


Figure 5.38: BP-15 1800 rpm 61 ft-lbs: 3°, 5°, 7°, 9° BTDC (left to right)

Figure 5.39 shows BP-15 with 25% energy equivalent DME: 1°, 3°, 7° BTDC (left to right). Based on the darkness only, it appears that the particulate matter mass is the same as the injection timing is advanced.



Figure 5.39: BP-15 with 25% energy equivalent DME: 1°, 3°, 7° BTDC (left to right)

Figure 5.40 shows BP-15 with 40% energy equivalent DME: 2°, 3°, 5°, 7° BTDC (left to right). Based on the darkness only, it appears that the particulate matter mass is the same as the injection timing is advanced. Also, comparing the 25% energy equivalent and the 40% energy equivalent, it appears that the particulate matter is the same regardless of DME energy equivalent.



Figure 5.40: BP-15 with 40% energy equivalent DME: 2°, 3°, 5°, 7° BTDC (left to right)

Figure 5.41 shows BP-15 with 40% energy equivalent DME: 7° BTDC (left) and BP-15 with 50% energy equivalent DME: 7° BTDC (right). Based on the darkness only, it appears that the particulate matter mass is decreasing in darkness as DME energy equivalent is increased from 40% to 50 % for the fixed injection timing. As is seen in the 50% energy equivalent DME: 7° BTDC (right), the filter appears to be somewhat gray, which indicates less mass on the filter.

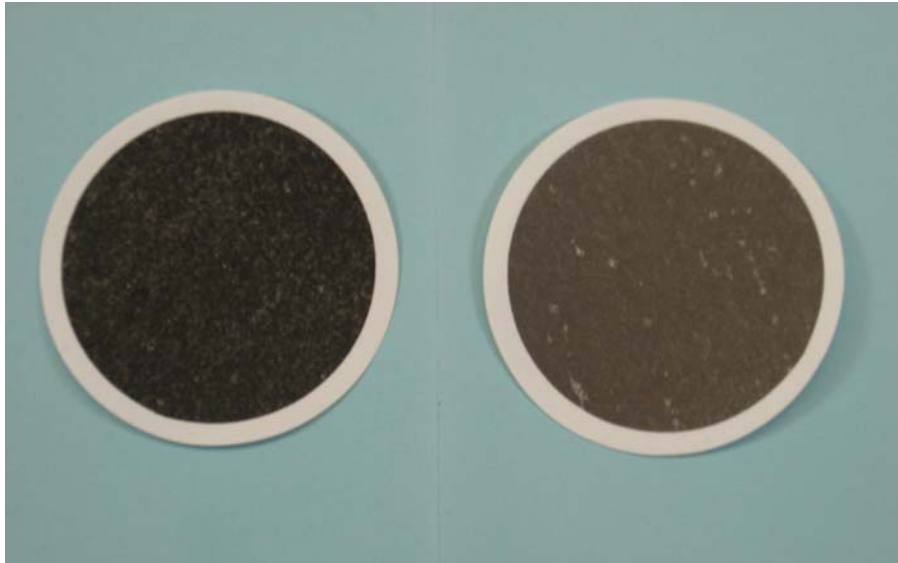


Figure 5.41: BP-15 with 40% energy equivalent DME: 7° BTDC (left)
BP-15 with 50% energy equivalent DME: 7° BTDC (right)

Figure 5.42 shows BP-15 1800 rpm 61 ft-lbs: 3° BTDC (top left), 7° BTDC (bottom left) and BP-15 with 25% energy equivalent DME : 3° BTDC (top right), 7° BTDC (bottom right). Based on the darkness only, it appears that the particulate matter for both BP-15 with 25% energy equivalent DME : 3° BTDC (top right), 7° BTDC (bottom right) are similar in mass, yet with retarded injection timing the filter is not as dark. In comparison, the BP-15 1800 rpm 61 ft-lbs: 3° BTDC (top left), 7° BTDC (bottom left) shows dramatic changes in darkness depending on the injection timing with the change in darkness indicating more particulate matter mass as the injection timing is retarded.

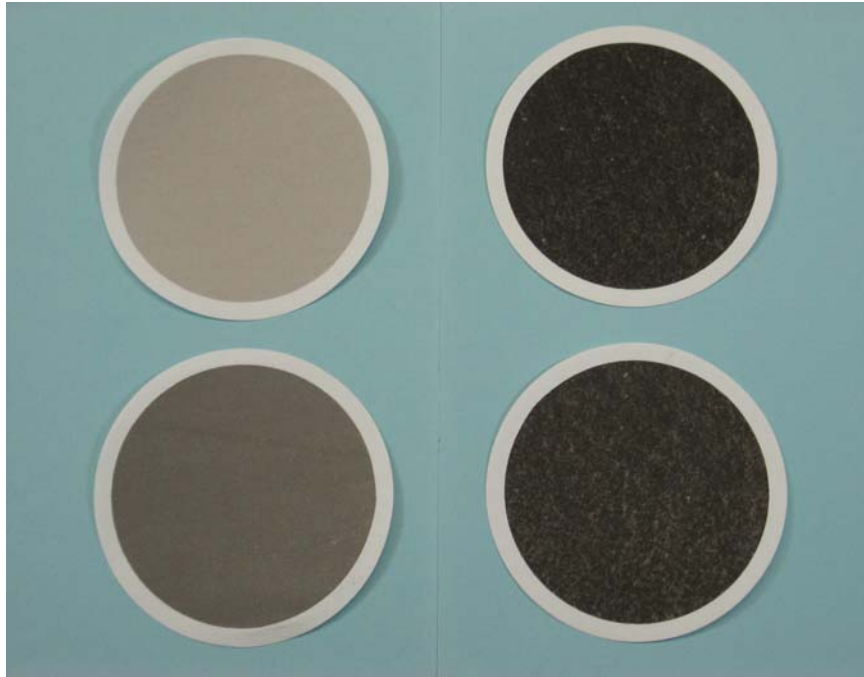


Figure 5.42: BP-15 1800 rpm 61 ft-lbs torque: 3° BTDC (top left), 7° BTDC (bottom left); BP-15 with 25% energy equivalent DME : 3° BTDC (top right), 7° BTDC (bottom right)

5.8.1.2 Tapered Element Oscillating Microbalance (TEOM) and Scanning Mobility Particle Sizer (SMPS) Data

The following section presents data taken from the TEOM and the SMPS.

Figure 5.43 shows TEOM data for mixed mode combustion at 1800 rpm and 61 ft-lb torque with increasing DME concentration fumigated in the intake air. As is seen in the figure, the mass of PM increases with increasing DME concentration.

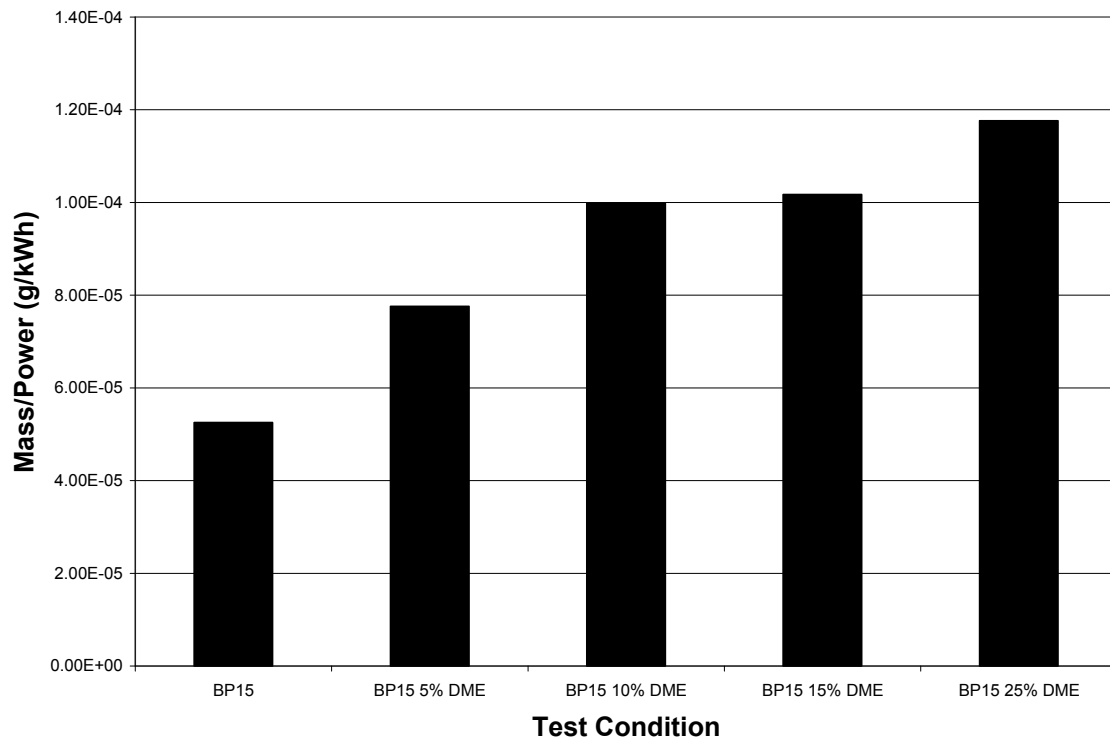


Figure 5.43: TEOM data for mixed mode combustion at 1800 rpm and 61 ft-lb torque with increasing DME concentration fumigated in the intake air

Figure 5.44 shows TEOM data for mixed mode combustion at 1800 rpm and 61 ft-lb torque with 25% energy equivalent DME concentration fumigated in the intake air at various fuel injection timings. As is shown in the figure, the maximum PM emissions appears at 5°BTDC, and declines with advanced and retarded injection timing from this point. BP15 gave the lowest PM per power output from the engine.

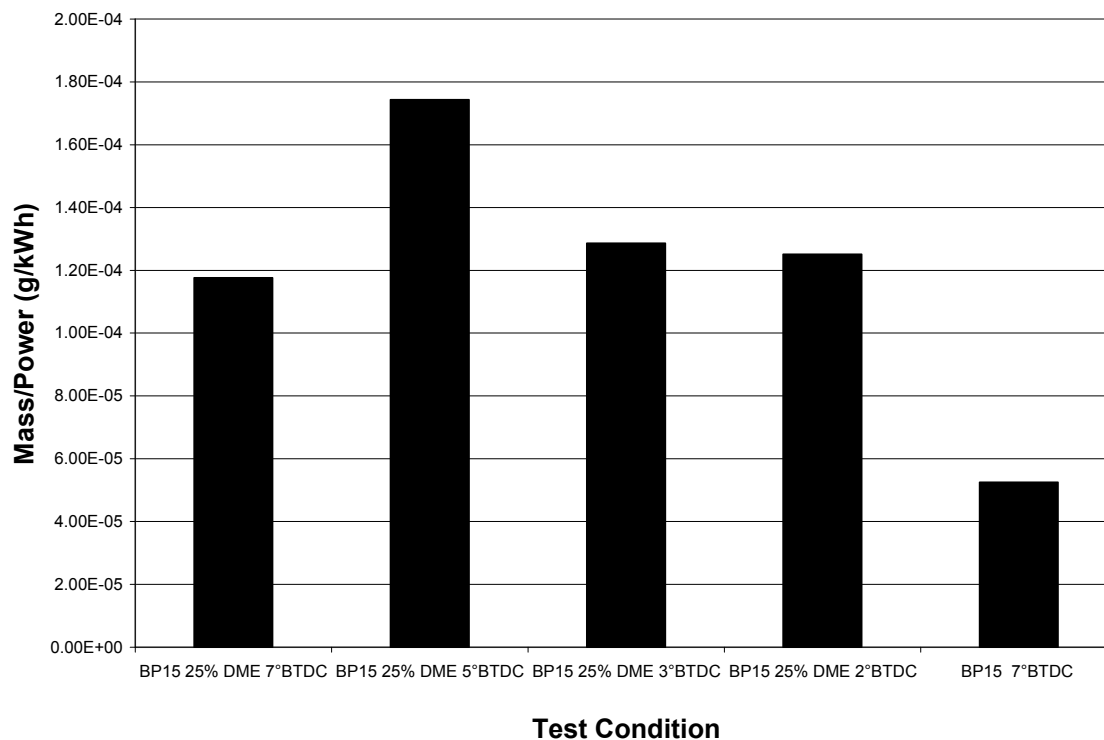


Figure 5.44: TEOM data for mixed mode combustion at 1800 rpm and 61 ft-lb torque with 25% energy equivalent DME concentration fumigated in the intake air at various fuel injection timings

Figure 5.45 shows SMPS data for BP-15 at 1800 rpm and 61 ft-lbs, comparing the particle size distribution with the Thermal Denuder at 40°C and 350°C. As the temperature is increased, the hydrocarbons are volatilized from the soot. Therefore, a shift in the distribution curve is observed which reflects that roughly 1/3 of the particles have been removed by the thermal denuder. The distributions are monomodal.

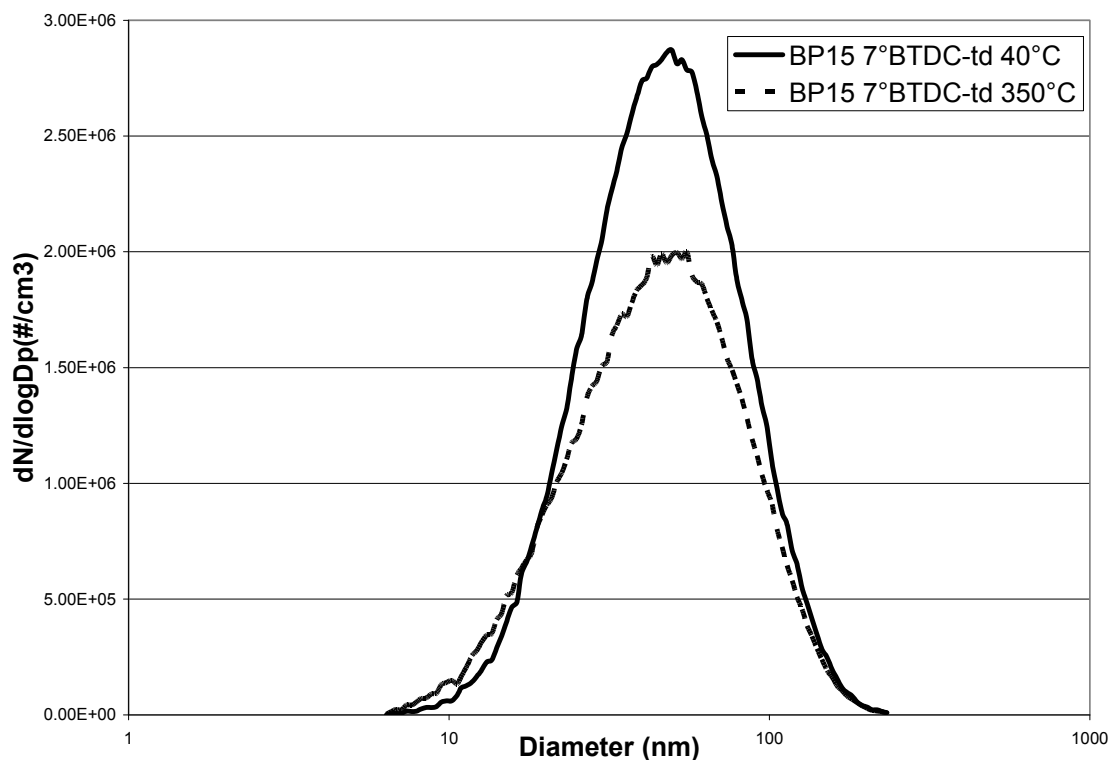


Figure 5.45: SMPS Data: BP-15 1800vrpm 61 ft-lbs comparing with the Thermal Denuder at 40°C and 350°C

Figure 5.46 shows SMPS data for BP-15 at 1800 rpm and 61 ft-lbs compared with the particle size distribution with the Thermal Denuder at 40°C and 350°C and for BP-15 with 25% energy equivalent DME addition at 1800 rpm and 61 ft-lbs compared with the particle size distribution with the Thermal Denuder at 40°C and 350°C. Both fuels and thermal denuder conditions show a monomodal distribution. This figure shows a reduction of solid and condensed particle concentrations and a shift toward larger remaining particles for DME. Also, the curves that were collected for the fumigated DME did not completely finish at the zero axis, indicating that more particles at the higher size range exist.

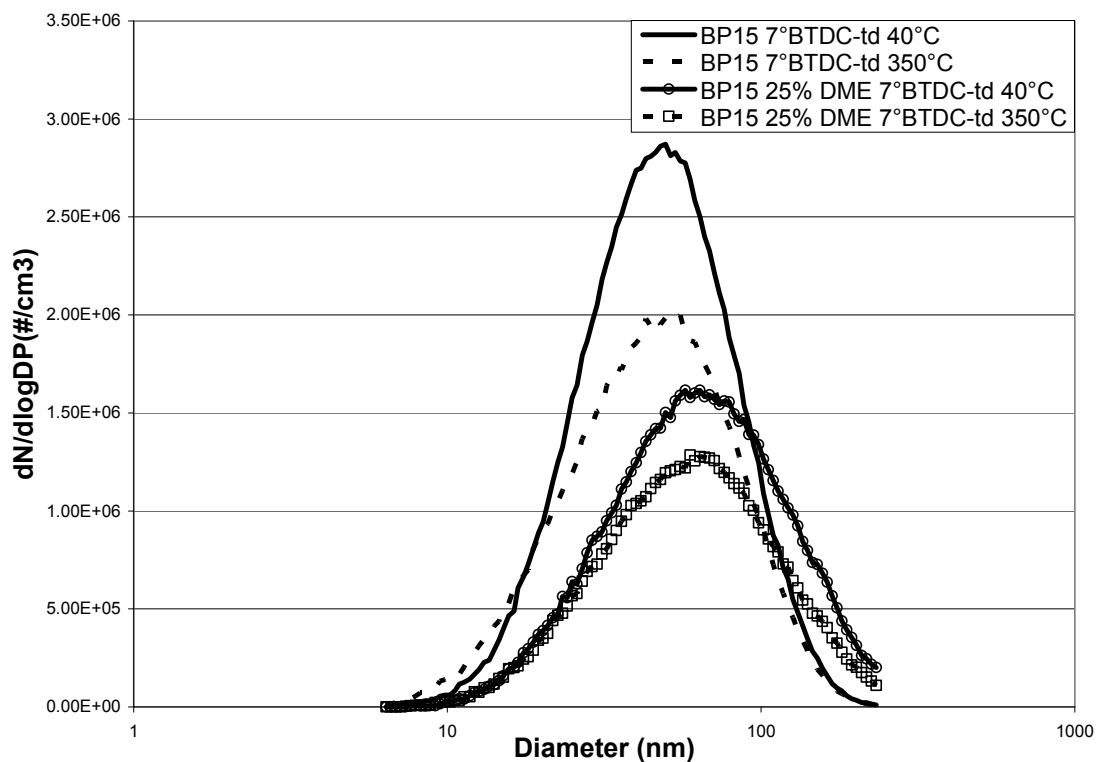


Figure 5.46: SMPS Data: BP-15 1800 rpm 61 ft-lbs comparing with the Thermal Denuder at 40°C and 350°C and SMPS Data: BP-15 with 25% energy equivalent DME 1800rpm 61 ft-lbs comparing with the Thermal Denuder at 40°C and 350°C

Figure 5.47 shows SMPS data for BP-15 with 25% energy equivalent DME at 1800 rpm and 61 ft-lbs compared with the Thermal Denuder at 40°C and 350°C at 7° BTDC and data for BP-15 with 25% energy equivalent DME at 1800 rpm and 61 ft-lbs compared with the Thermal Denuder at 40°C and 350°C at 3° BTDC. As the injection timing is retarded, a 25% increase of the solid and condensed particle concentrations is observed.

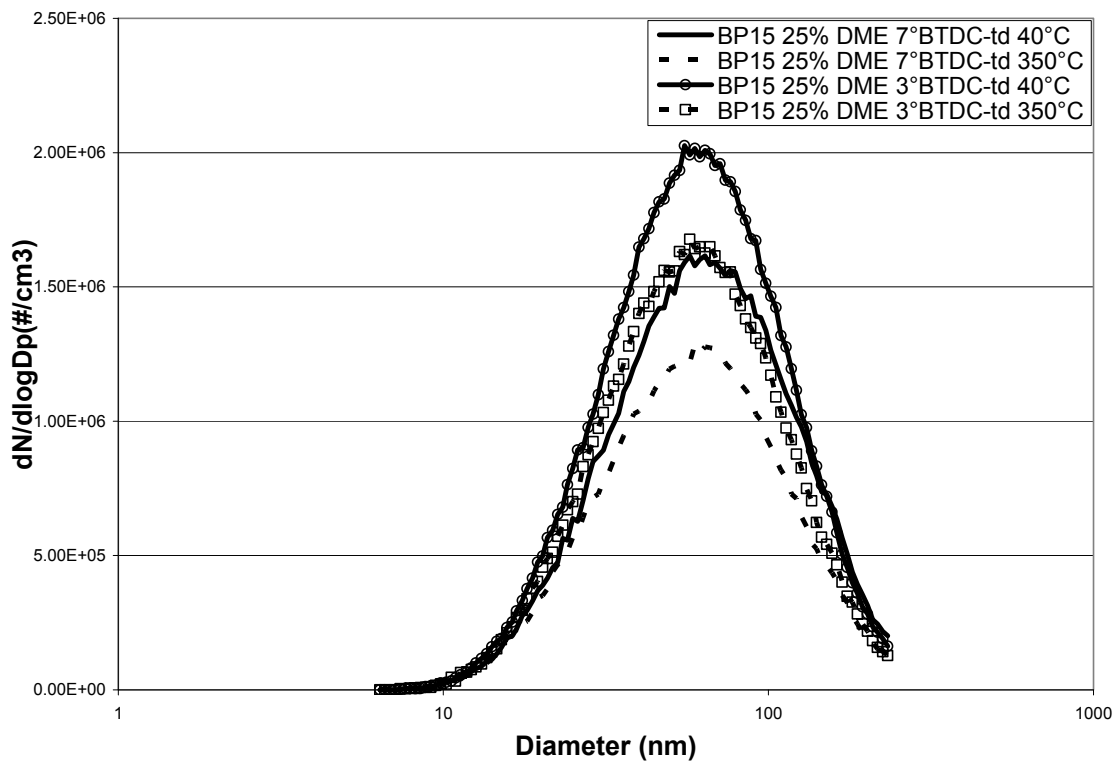


Figure 5.47: SMPS Data: BP-15 with 25% energy equivalent DME 1800 rpm 61 ft-lbs comparing with the Thermal Denuder at 40°C and 350°C at 7° BTDC and SMPS Data: BP-15 with 25% energy equivalent DME 1800 rpm 61 ft-lbs comparing with the Thermal Denuder at 40°C and 350°C at 3° BTDC

5.8.2 Impact of Intake Air Heating

For the third set of experiments, thermal conditioning of the intake charge was altered. An intake air heater was installed in the intake air system of the DDC 2.5L engine. The goal of using intake air heating was to observe the effect of this change on the ignition timing and combustion of the charge. Gaseous and particulate matter emissions were collected.

Figure 5.48 shows NO_x (g/kg fuel) for mixed mode combustion at 1800 rpm and 61 ft-lb torque with 25% energy equivalent DME concentration fumigated in the intake air at various intake air temperatures compared to BP15, all at 3° BTDC fuel injection timing. As the intake air temperature increases, the amount of NO_x emissions increases for the 25% DME mixed mode combustion. However, at the highest temperature, 80°C, for the 25% DME mixed mode combustion, the amount of NO_x emissions is over 10% less than that with BP15 diesel fuel for 70°C.

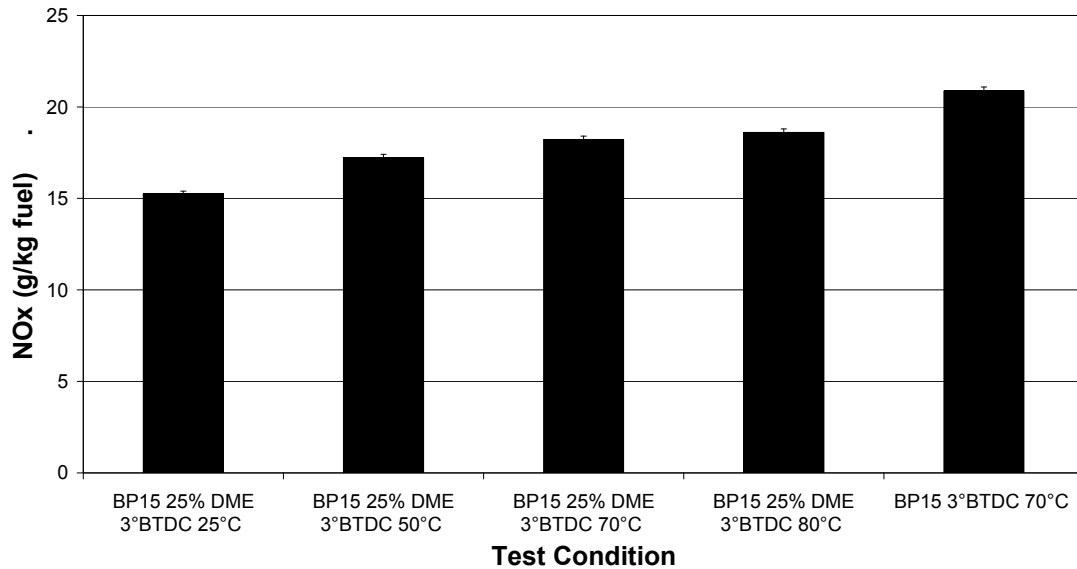


Figure 5.48: NOx (g/kg fuel) for mixed mode combustion at 1800 rpm and 61 ft-lb torque with 25% energy equivalent DME concentration fumigated in the intake air at various intake air temperatures compared to BP15, all at 3° BTDC fuel injection timing

Figure 5.49 shows NOx (g/kWh) for Mixed mode combustion at 1800 rpm and 61 ft-lb Torque with 25% energy equivalent DME concentration fumigated in the intake air at various intake air temperatures compared to BP15, all at 3° BTDC fuel injection timing. On a power basis, as the intake air temperature increases, the amount of NOx emissions increase for the 25% DME Mixed mode combustion. However, at the highest temperature, the amount of NOx emissions is almost 20% less than that with BP15 diesel fuel.

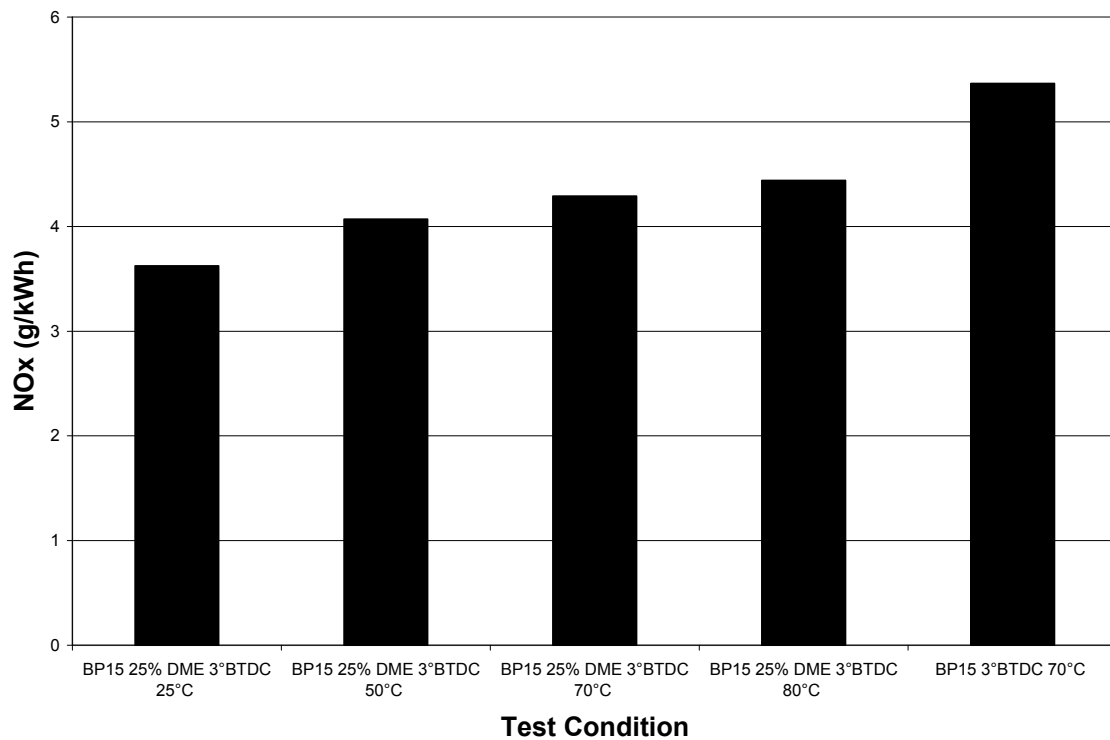


Figure 5.49: NOx (g/kWh) for mixed mode combustion at 1800 rpm and 61 ft-lb torque with 25% energy equivalent DME concentration fumigated in the intake air at various intake air temperatures compared to BP15, all at 3° BTDC fuel injection timing

Figure 5.50 shows NO (g/kg fuel) for mixed mode combustion at 1800 rpm and 61 ft-lb torque with 25% energy equivalent DME concentration fumigated in the intake air at various intake air temperatures compared to BP15, all at 3° BTDC fuel injection timing. As the intake air temperature increases, the amount of NO emissions increase for the 25% DME Mixed mode combustion. However, at the highest temperature, the amount of NO emissions is 50% less than that with BP15 diesel fuel. At the intake air temperature of 70 °C, the amount of NO emissions has been reduced by more than 50% with the 25% DME energy equivalent Mixed mode combustion over the BP15 diesel fuel.

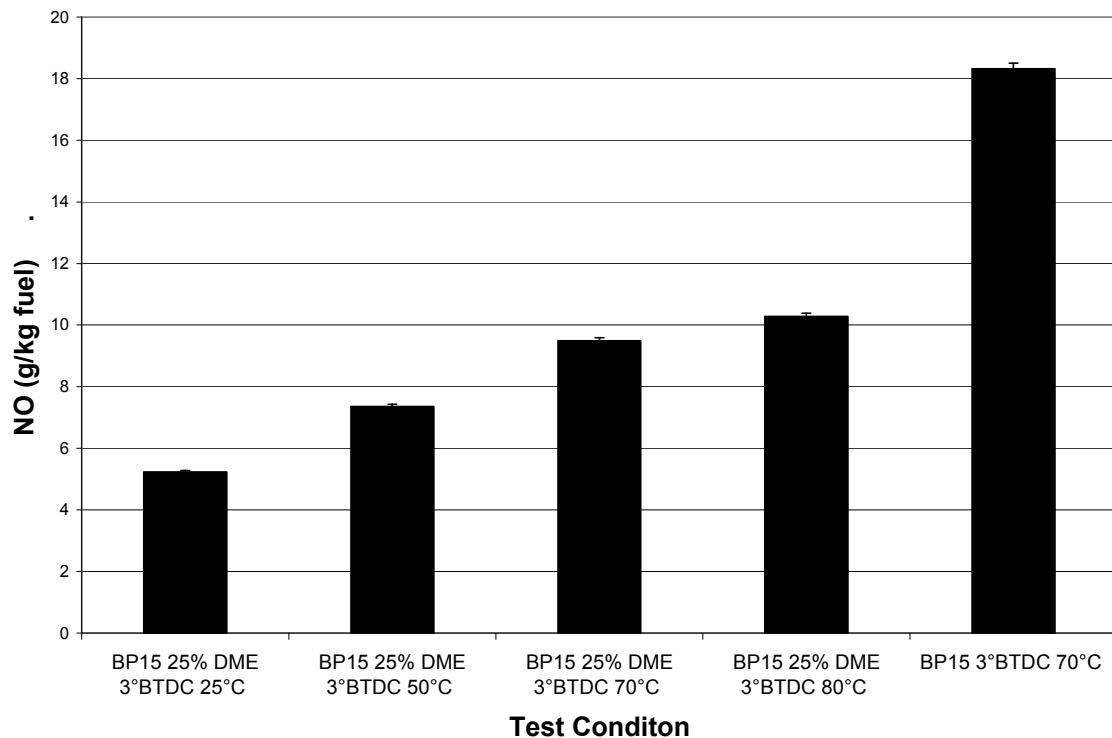


Figure 5.50: NO (g/kg fuel) for mixed mode combustion at 1800 rpm and 61 ft-lb torque with 25% energy equivalent DME concentration fumigated in the intake air at various intake air temperatures compared to BP15, all at 3° BTDC fuel injection timing

Figure 5.51 shows NO₂ (g/kg fuel) for mixed mode combustion at 1800 rpm and 61 ft-lb torque with 25% energy equivalent DME concentration fumigated in the intake air at various intake air temperatures compared to BP15, all at 3° BTDC fuel injection timing. As the intake air temperature increases, the amount of NO₂ emissions increase for the 25% DME Mixed mode combustion. However, at the highest temperature, the amount of NO₂ emissions is 4 times more than with BP15 diesel fuel.

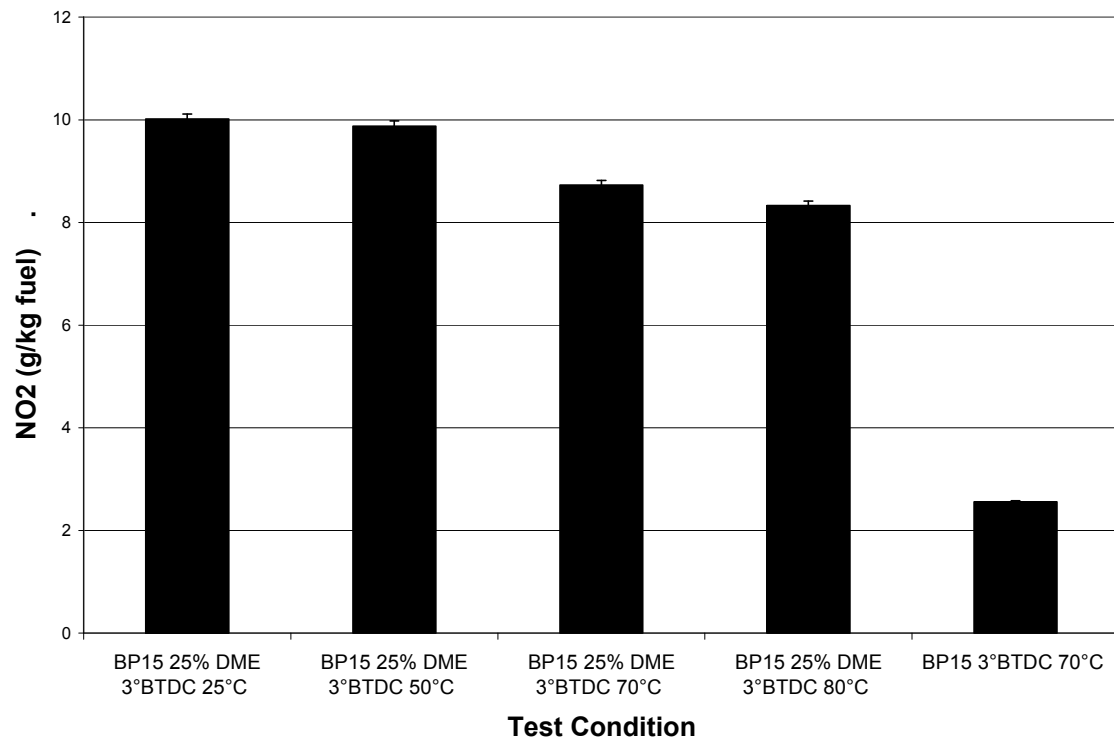


Figure 5.51: NO₂ (g/kg fuel) for mixed mode combustion at 1800 rpm and 61 ft-lb torque with 25% energy equivalent DME concentration fumigated in the intake air at various intake air temperatures compared to BP15, all at 3° BTDC fuel injection timing

Figure 5.52 shows Brake Specific Fuel Consumption (BSFC) (g/kWh) for mixed mode combustion at 1800 rpm and 61 ft-lb torque with 25% energy equivalent DME concentration fumigated in the intake air at various intake air temperatures compared to BP15, all at 3° BTDC fuel injection timing. At the same power, the grams of fuel required was less for the 25% DME mixed mode combustion than with BP15 diesel fuel alone.

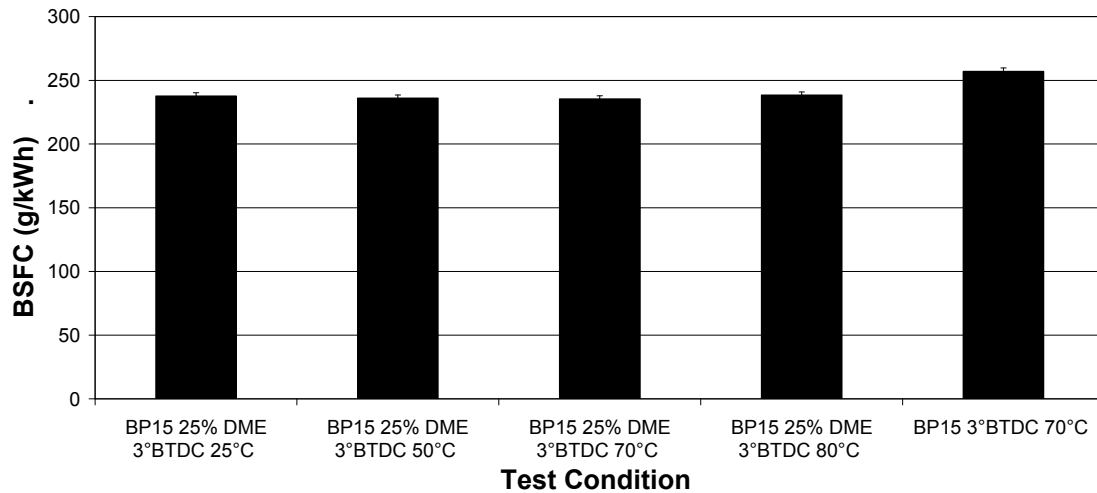


Figure 5.52: Brake Specific Fuel Consumption (g/kWh) for mixed mode combustion at 1800 rpm and 61 ft-lb torque with 25% energy equivalent DME concentration fumigated in the intake air at various intake air temperatures compared to BP15, all at 3° BTDC fuel injection timing

Figure 5.53 shows Brake Specific Energy Consumption (BSEC) (MJ/kWh) for mixed mode combustion at 1800 rpm and 61 ft-lb torque with 25% energy equivalent DME concentration fumigated in the intake air at various intake air temperatures compared to BP15, all at 3° BTDC fuel injection timing. At the same power, the energy of fuel required was less for the 25% DME mixed mode combustion than with BP15 diesel fuel alone.

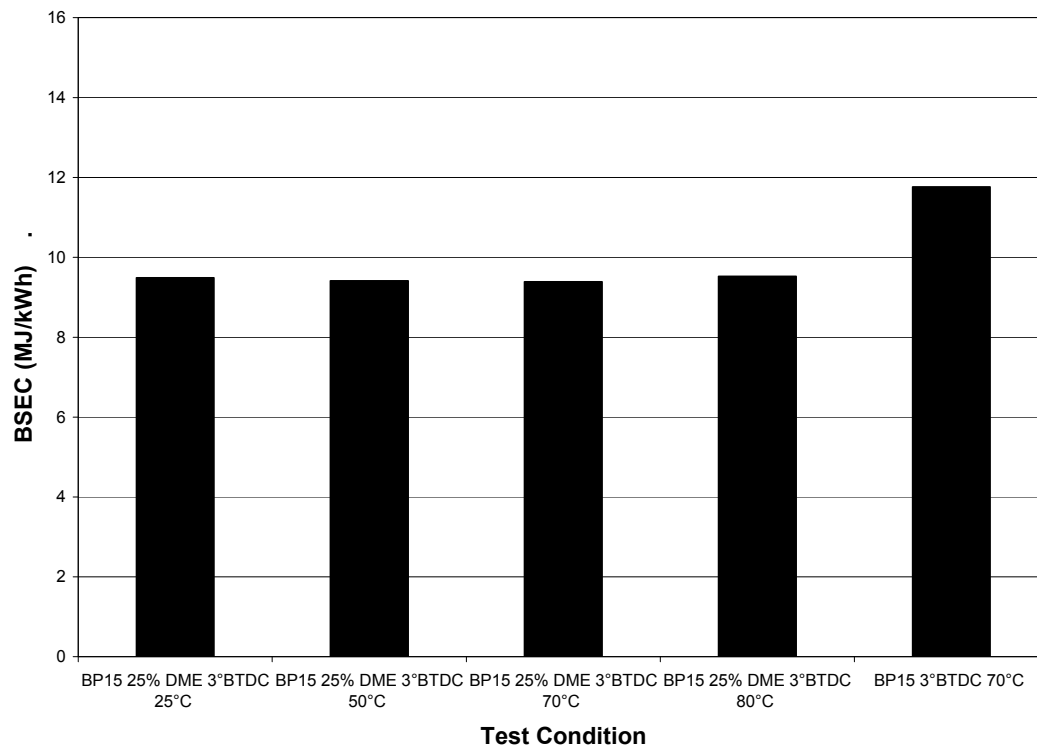


Figure 5.53: Brake Specific Energy Consumption (MJ/kWh) for mixed mode combustion at 1800 rpm and 61 ft-lb torque with 25% energy equivalent DME concentration fumigated in the intake air at various intake air temperatures compared to BP15, all at 3° BTDC fuel injection timing

Figure 5.54 shows CO (g/kg fuel) for mixed mode combustion at 1800 rpm and 61 ft-lb torque with 25% energy equivalent DME concentration fumigated in the intake air at various intake air temperatures compared to BP15, all at 3° BTDC fuel injection timing. As shown in the figure, the amount of CO was higher with the 25% DME mixed mode combustion than with BP15 diesel fuel alone. As the intake temperature was increased, the amount of CO decreased. For the BP15 diesel fuel, the CO emissions were only 10% of what the same CO emissions with the 25% DME mixed mode combustion.

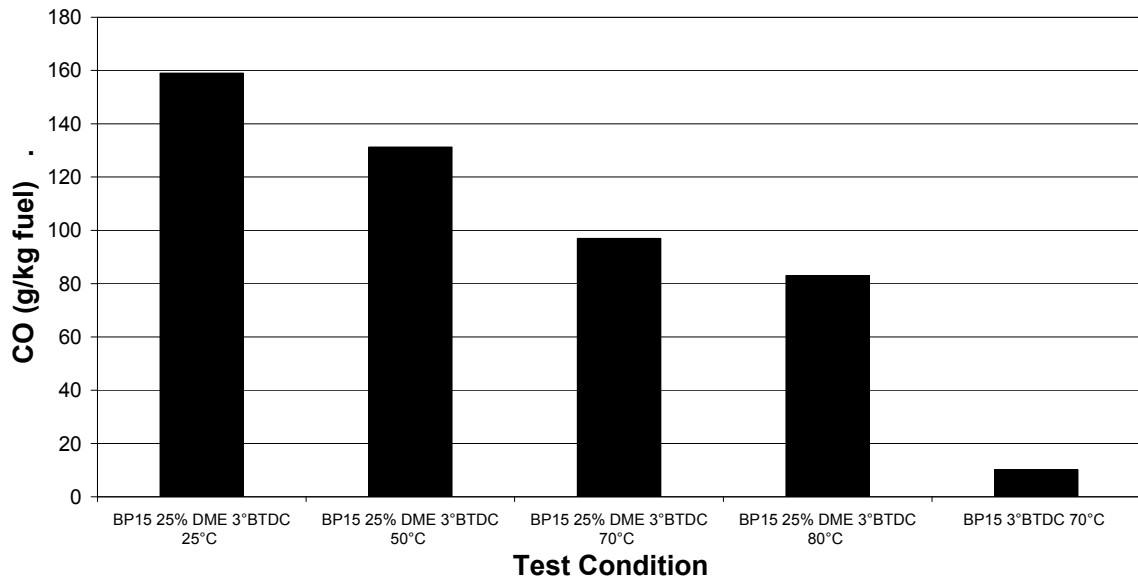


Figure 5.54: CO (g/kg fuel) for mixed mode combustion at 1800 rpm and 61 ft-lb torque with 25% energy equivalent DME concentration fumigated in the intake air at various intake air temperatures compared to BP15, all at 3° BTDC fuel injection timing

Figure 5.55 shows CO₂ (g/kg fuel) for mixed mode combustion at 1800 rpm and 61 ft-lb torque with 25% energy equivalent DME concentration fumigated in the intake air at various intake air temperatures compared to BP15, all at 3° BTDC fuel injection timing. As the intake air temperature was increased, the CO₂ emissions increased for the 25% DME mixed mode combustion. Because of the intake air heating, the density of the air changes, and thus less mass of air is present in the intake air as it is drawn into the engine. This results in less oxygen and nitrogen available in the combustion process, and thus a greater amount of CO₂ because of the change in the mass flow rate of the reactants.

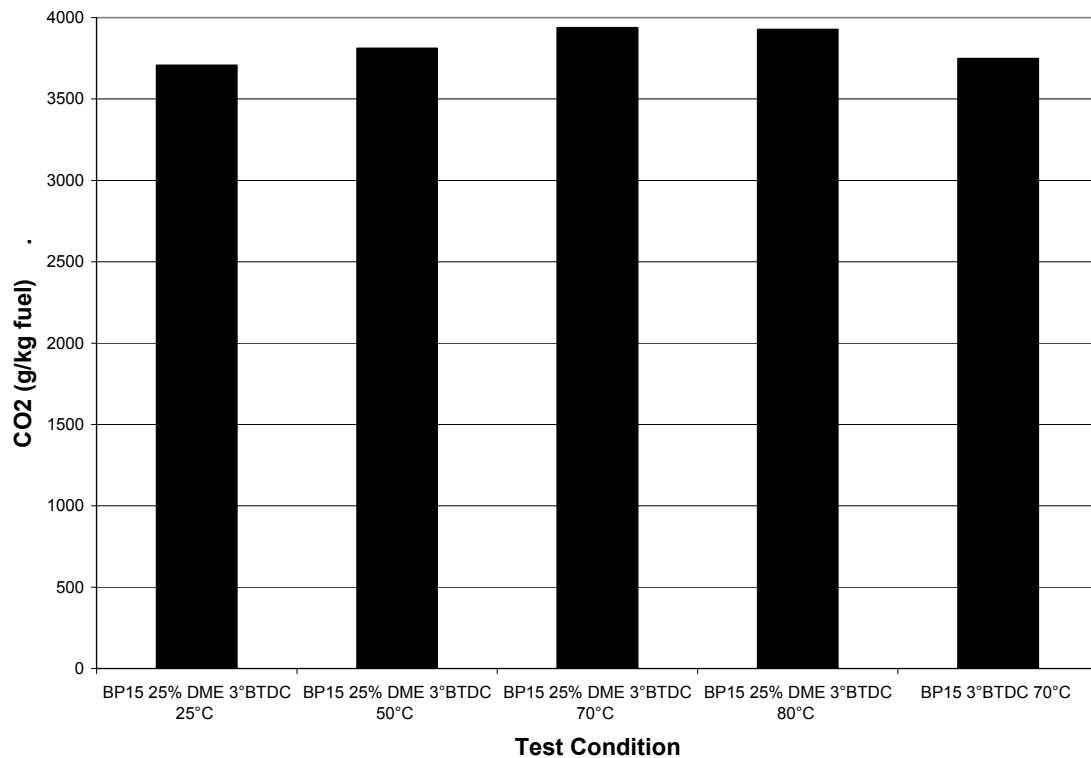


Figure 5.55: CO₂ (g/kg fuel) for mixed mode combustion at 1800 rpm and 61 ft-lb torque with 25% energy equivalent DME concentration fumigated in the intake air at various intake air temperatures compared to BP15, all at 3° BTDC fuel injection timing

Figure 5.56 shows Methane (ppm) for mixed mode combustion at 1800 rpm and 61 ft-lb torque with 25% energy equivalent DME concentration fumigated in the intake air at various intake air temperatures compared to BP15, all at 3° BTDC fuel injection timing. As the intake air temperature increased, the Methane decreased for the 25% DME mixed mode combustion. However, there was still 10ppm of Methane for the 25% DME mixed mode combustion at 70 °C temperature while only 2 ppm with the BP15 diesel alone.

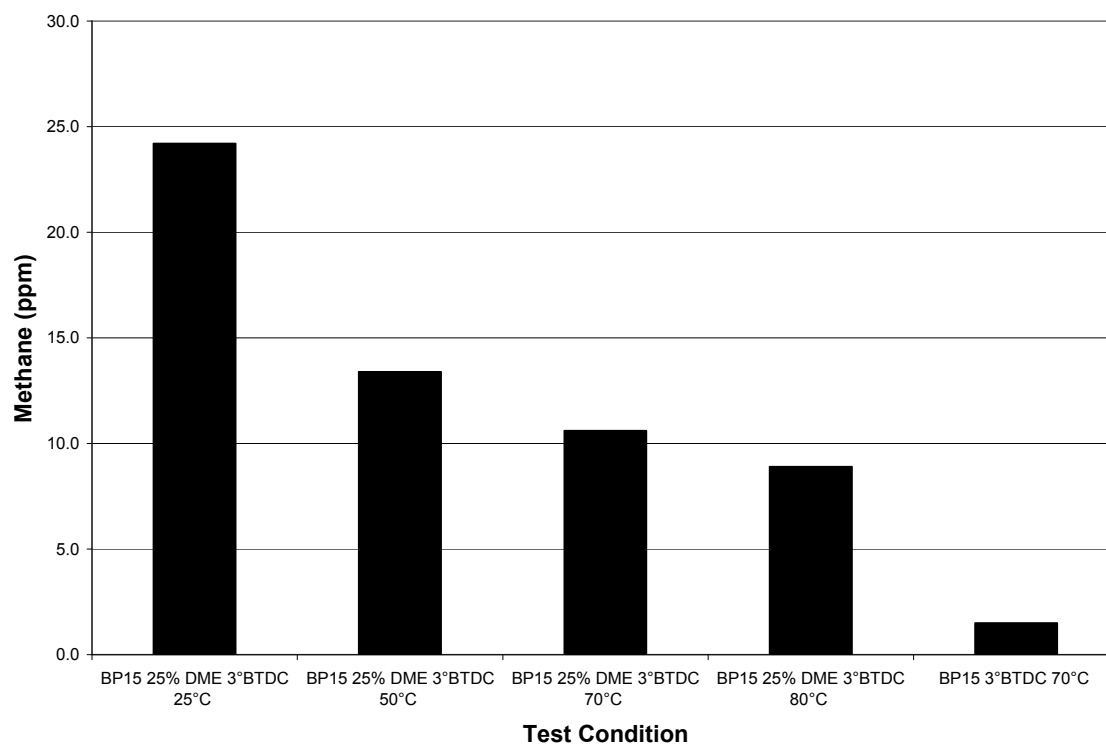


Figure 5.56: Methane (ppm) for mixed mode combustion at 1800 rpm and 61 ft-lb torque with 25% energy equivalent DME concentration fumigated in the intake air at various intake air temperatures compared to BP15, all at 3° BTDC fuel injection timing

Figure 5.57 shows Total Hydrocarbons (g/kg fuel) for mixed mode combustion at 1800 rpm and 61 ft-lb torque with 25% energy equivalent DME concentration fumigated in the intake air at various intake air temperatures compared to BP15, all at 3° BTDC fuel injection timing. As the intake air temperature increased, the amount of hydrocarbons decreased.

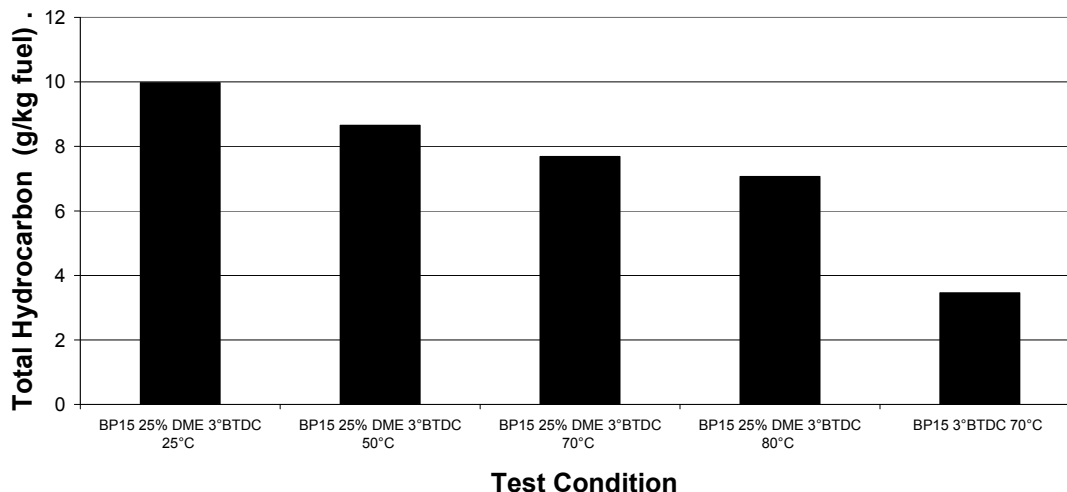


Figure 5.57: Total Hydrocarbons (g/kg fuel) for mixed mode combustion at 1800 rpm and 61 ft-lb torque with 25% energy equivalent DME concentration fumigated in the intake air at various intake air temperatures compared to BP15, all at 3° BTDC fuel injection timing

Figure 5.58 shows Exhaust Temperature (°C) for mixed mode combustion at 1800 rpm and 61 ft-lb torque with 25% energy equivalent DME concentration fumigated in the intake air at various intake air temperatures compared to BP15, all at 3° BTDC fuel injection timing. The temperatures are showing at the top of each bar on the graph. As the intake air temperature increases, the exhaust temperature increases. However, the exhaust temperature does not increase by the same amount that the intake air temperature was elevated to.

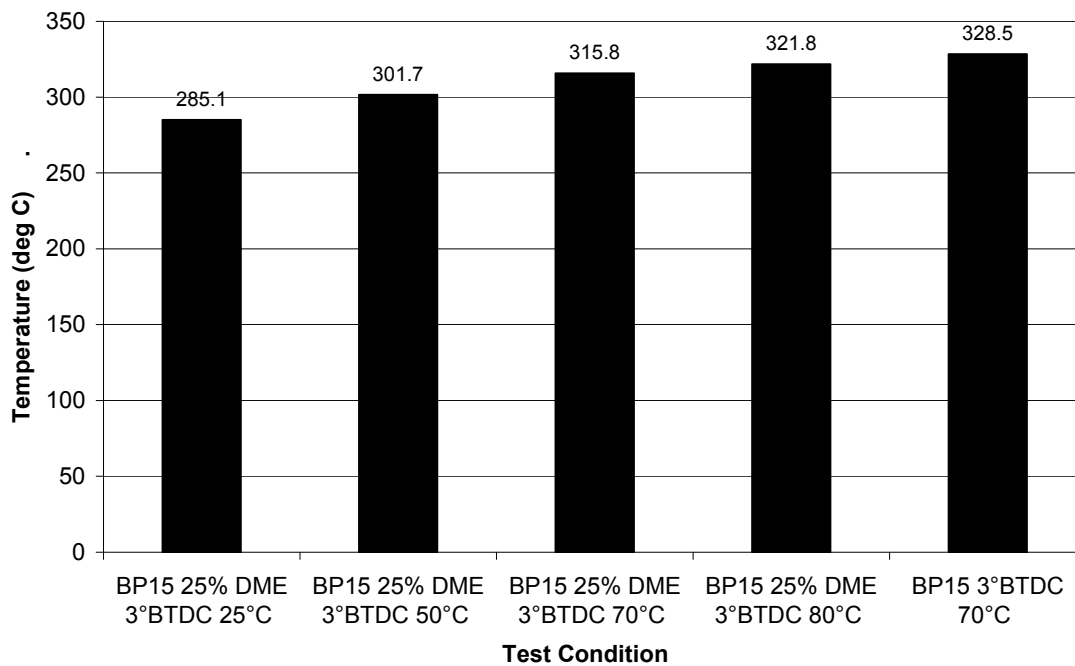


Figure 5.58: Exhaust Temperature ($^{\circ}\text{C}$) for mixed mode combustion at 1800 rpm and 61 ft-lb torque with 25% energy equivalent DME concentration fumigated in the intake air at various intake air temperatures compared to BP15, all at 3° BTDC fuel injection timing

Figure 5.59 shows the GC Data for BP15 in comparison to mixed mode combustion with 25% energy equivalent DME concentration at 3° BTDC with increasing temperature. As is seen in the figure, as the temperature increases when using DME, the concentration of Methane and DME begin to decrease, which results in an overall decrease in the total hydrocarbon emissions. The figure shows a comparison to the BP15 with increasing temperature. What is also shown with the BP15 increasing temperature is that the small amounts of ethylene and other gases also decrease with increasing temperature. What is also shown more clearly in this figure is the amount of butane that

is observed when using DME, although small in comparison to the Methane and DME observed.

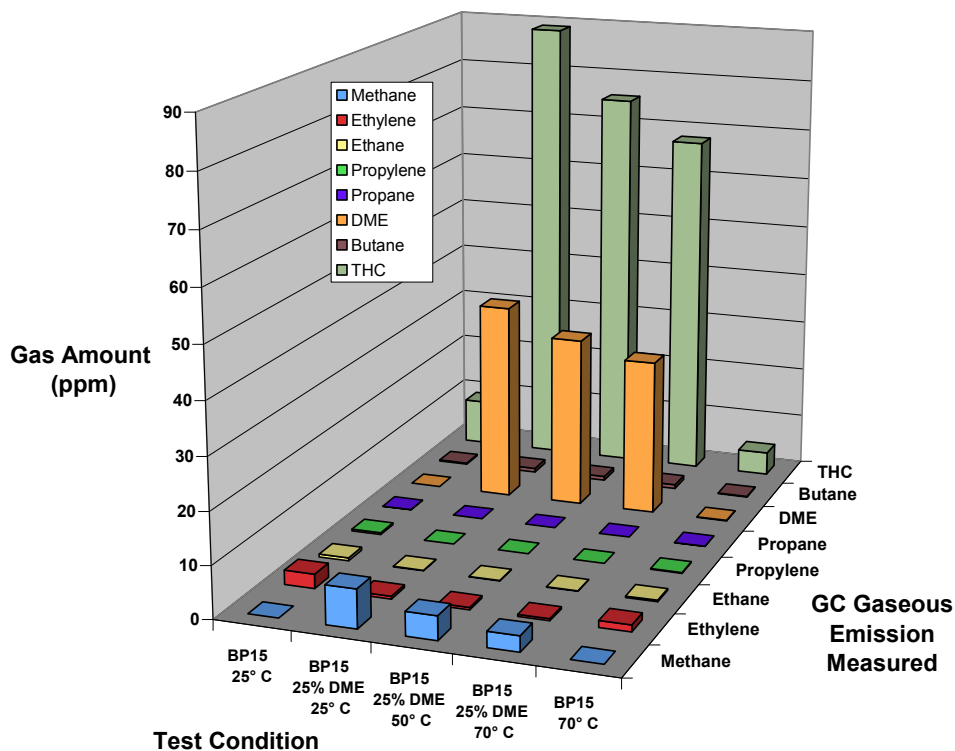


Figure 5.59: GC Data: BP15 in comparison to mixed mode combustion with 25% energy equivalent DME concentration at 3° BTDC with increasing temperature

Figure 5.60 shows Cylinder Pressure (bar) for mixed mode combustion at 1800 rpm and 61 ft-lb torque with 25% energy equivalent DME concentration fumigated in the intake air at various intake air temperatures compared to BP15, all at 3° BTDC fuel injection timing. With increasing intake air temperature, the peak pressure for the 25% DME mixed mode combustion increases slightly but maintains the same shape and peak pressure.

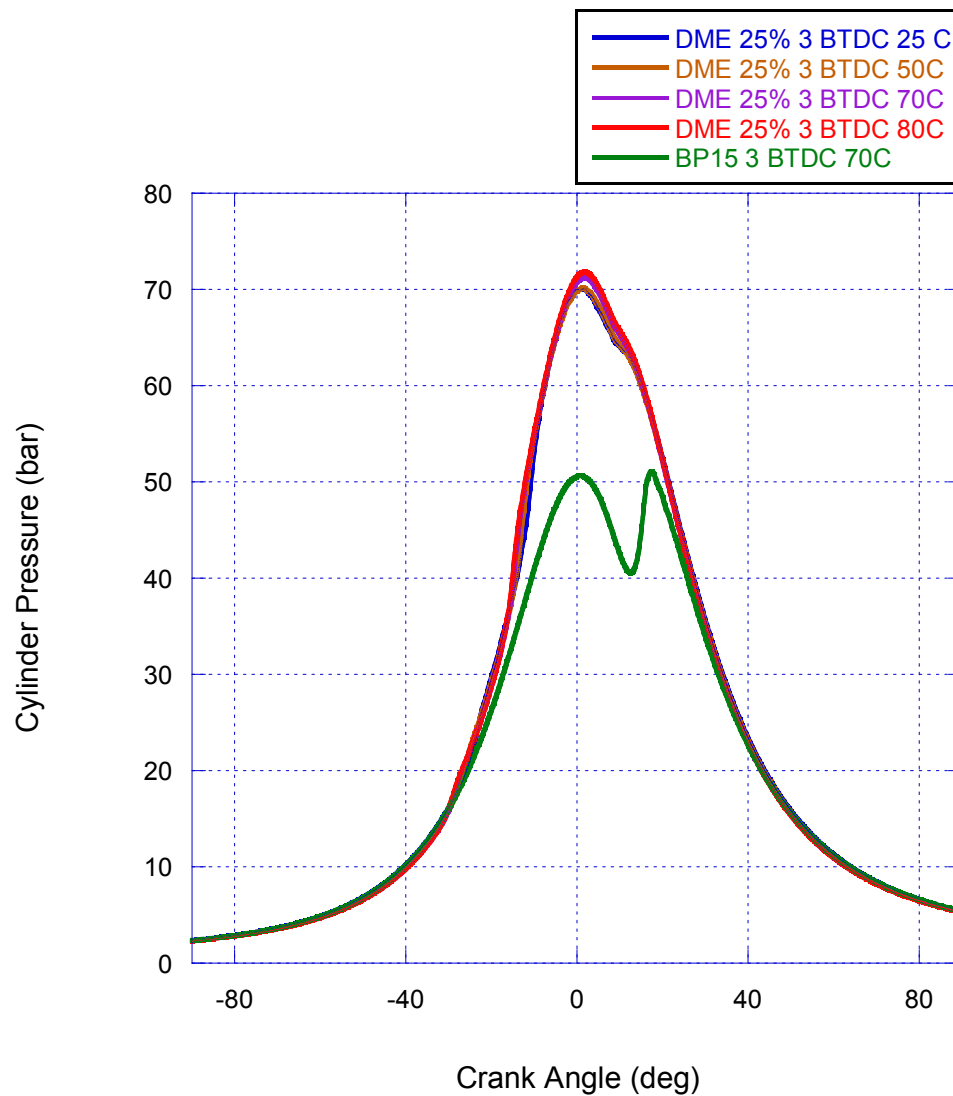


Figure 5.60: Cylinder Pressure (bar) for mixed mode combustion at 1800 rpm and 61 ft-lb torque with 25% energy equivalent DME concentration fumigated in the intake air at various intake air temperatures compared to BP15, all at 3° BTDC fuel injection timing

Figure 5.61 shows heat release rate (J/deg) for mixed mode combustion at 1800 rpm and 61 ft-lb torque with 25% energy equivalent DME concentration fumigated in the intake air at various intake air temperatures compared to BP15, all at 3° BTDC fuel injection timing. With increasing intake air temperature, the LTHR and the HTHR are

advanced. The peak of the LTHR decreases and the peak of the HTHR increases with increasing intake air temperature. However, the combustion phasing and shape of the heat release for the BP15 diesel fuel remains constant.

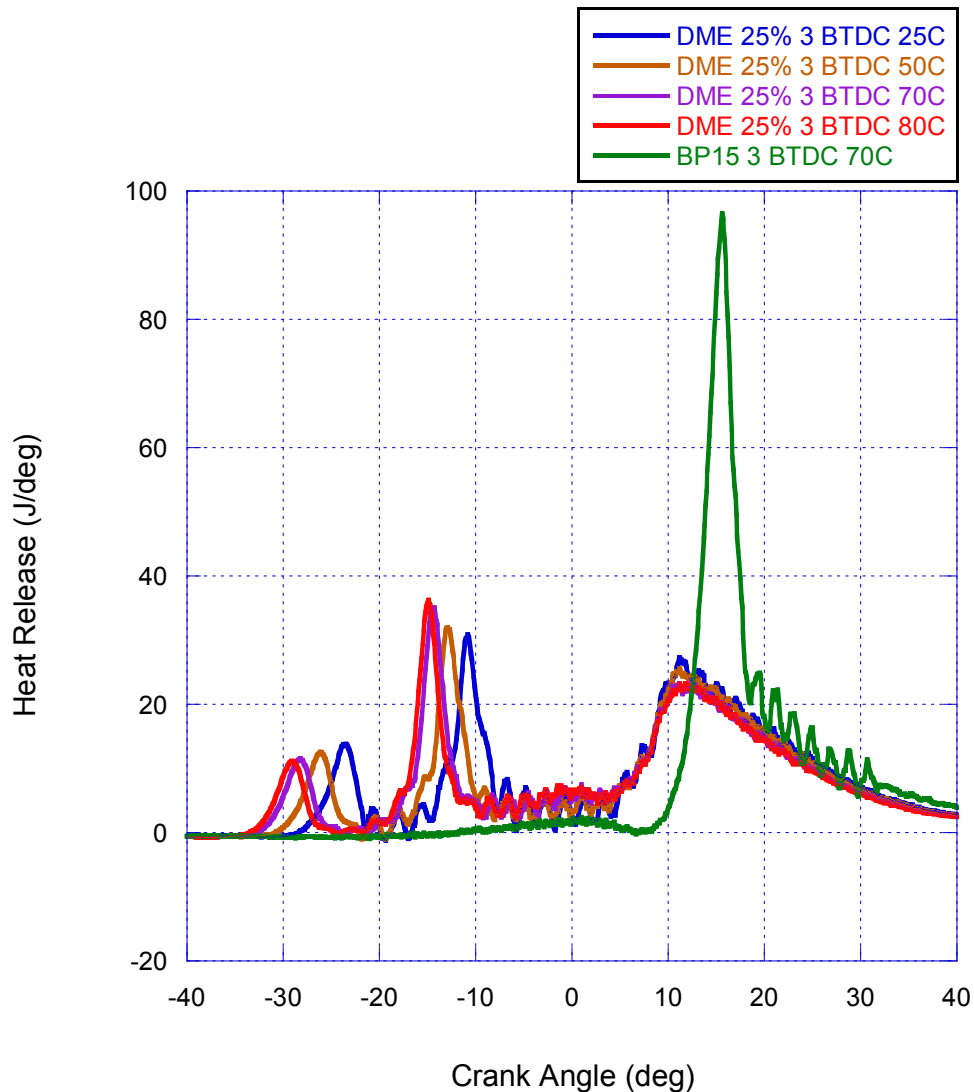


Figure 5.61: Heat Release Rate (J/deg) for mixed mode combustion at 1800 rpm and 61 ft-lb torque with 25% energy equivalent DME concentration fumigated in the intake air at various intake air temperatures compared to BP15, all at 3° BTDC fuel injection timing

Figure 5.62 shows bulk cylinder temperature (K) for mixed mode combustion at 1800 rpm and 61 ft-lb torque with 25% energy equivalent DME concentration fumigated in the intake air at various intake air temperatures compared to BP15, all at 3° BTDC fuel injection timing. With increasing intake air temperature the bulk cylinder temperature increases.

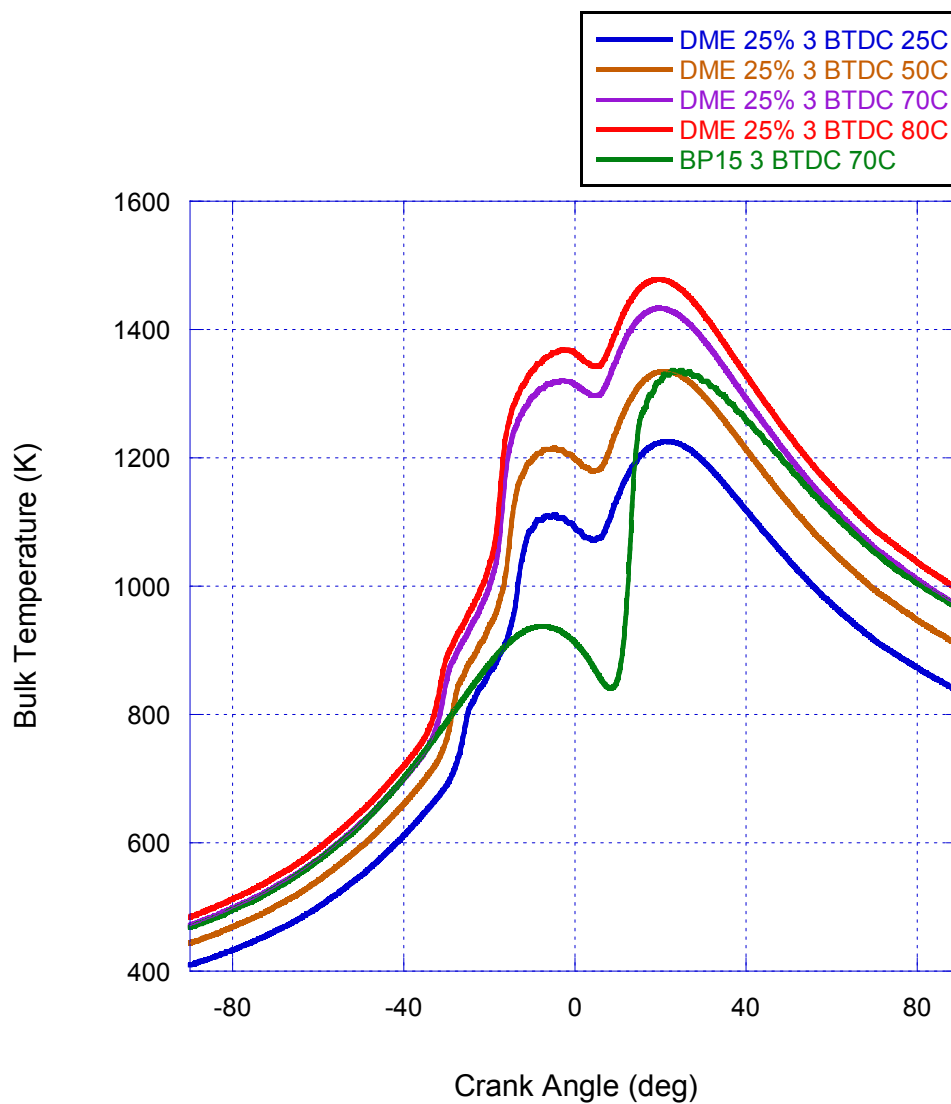


Figure 5.62: Bulk Temperature (K) for mixed mode combustion at 1800 rpm and 61 ft-lb torque with 25% energy equivalent DME concentration fumigated in the intake air at various intake air temperatures compared to BP15, all at 3° BTDC fuel injection timing

Figure 5.63 shows TEOM data for mixed mode combustion at 1800 rpm and 61 ft-lb torque with 25% energy equivalent DME concentration fumigated with increasing intake air temperature. As intake air temperature increase for the 25% DME mixed mode combustion, the mass of particulate increases per power output.

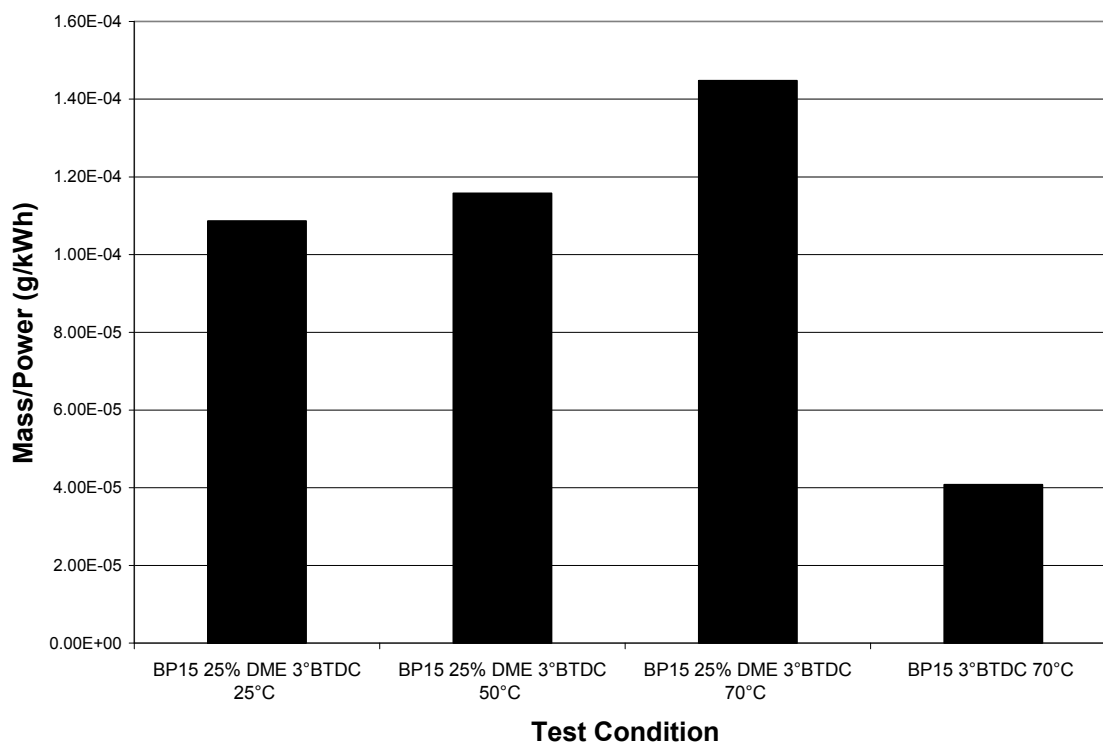


Figure 5.63: TEOM data for mixed mode combustion at 1800 rpm and 61 ft-lb torque with 25% energy equivalent DME concentration fumigated with increasing intake air temperature

Figure 5.64 shows SMPS Data for BP-15 with 25% energy equivalent DME at 1800 rpm and 61 ft-lbs compared with the Thermal Denuder at 40°C and 350°C at 3° BTDC with an Intake Air Temperature of 25°C and SMPS Data for BP-15 with 25% energy equivalent DME at 1800 rpm and 61 ft-lbs compared with the Thermal Denuder at 40°C and 350°C at 3° BTDC with Intake Air Temperature at 70°C. This data is also

compared to the BP15 conventional diesel at the same injection timing (red and blue lines in the figure) with an Intake Air Temperature of 25°C. As the intake air temperature increases for the 25% DME mixed mode combustion, the number density of condensed particles in this size range increases, but the number of solid particles remains approximately the same with a shift towards larger particles. Also, as indicated in the curve trends with increase intake air temperature, the peak maximum shifts towards larger particles. In comparison to the BP15 conventional diesel, the 25% DME mixed mode combustion has 2/3 more solid particles.

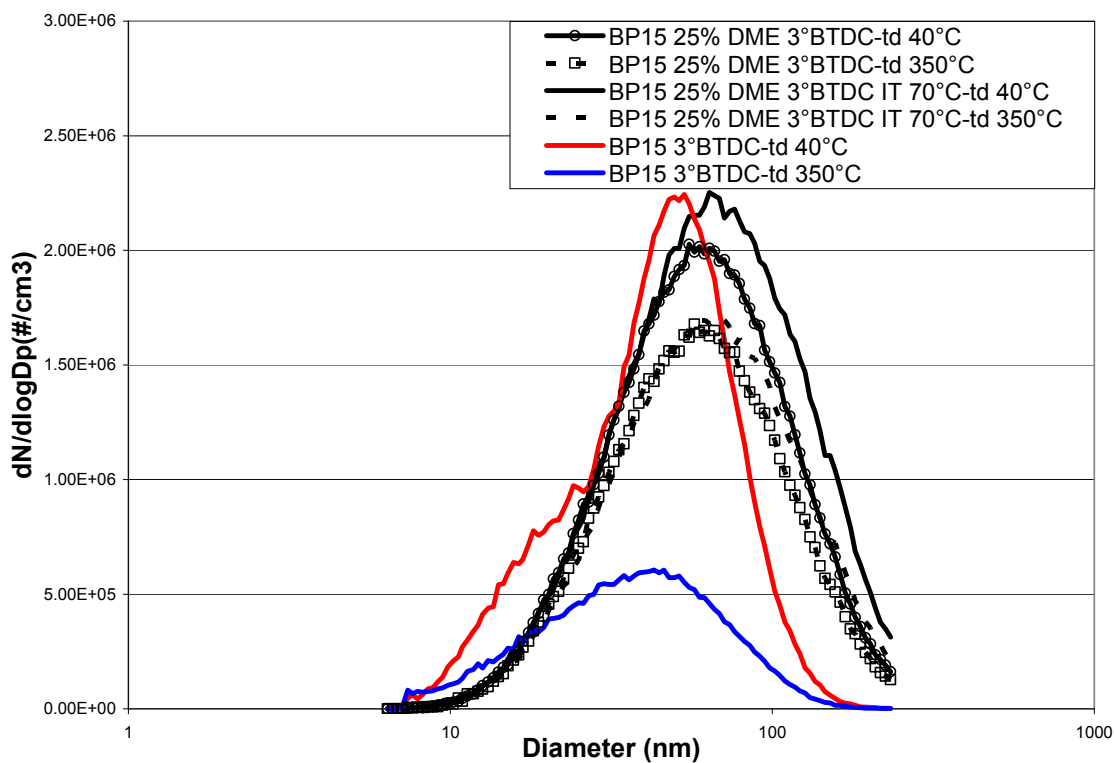


Figure 5.64: SMPS Data: BP-15 with 25% energy equivalent DME at 1800 rpm and 61 ft-lbs compared with the Thermal Denuder at 40°C and 350°C at 3° BTDC with an Intake Air Temperature of 25°C and SMPS Data for BP-15 with 25% energy equivalent DME at 1800 rpm and 61 ft-lbs compared with the Thermal Denuder at 40°C and 350°C at 3° BTDC with Intake Air Temperature at 70°C

5.8.3 Impact of Change in Cetane Number of the Fumigated Fuel

A fourth set of experiments involved modifying the ignition quality of the system by adjusting the cetane number of the fumigated fuel to further reduce NO_x emissions and improve efficiency. The fuel brought into the intake was a combination of DME and Methane. Again, there was a pilot injection of diesel fuel. Gaseous and particulate matter emissions were collected.

Figure 5.65 shows NO_x (g/kg fuel) for mixed mode combustion at 1800 rpm and 61 ft-lb torque with 25% DME energy equivalent with and without 5 SLPM (6.5% energy equivalent) Methane fumigated in the intake air at various intake air temperatures compared to BP15, at 7 and 1 ° BTDC fuel injection timing. There was no change in NO_x emissions with the addition of Methane in the intake air. NO_x emissions were reduced when the injection timing was retarded, but increased with increasing intake air temperature.

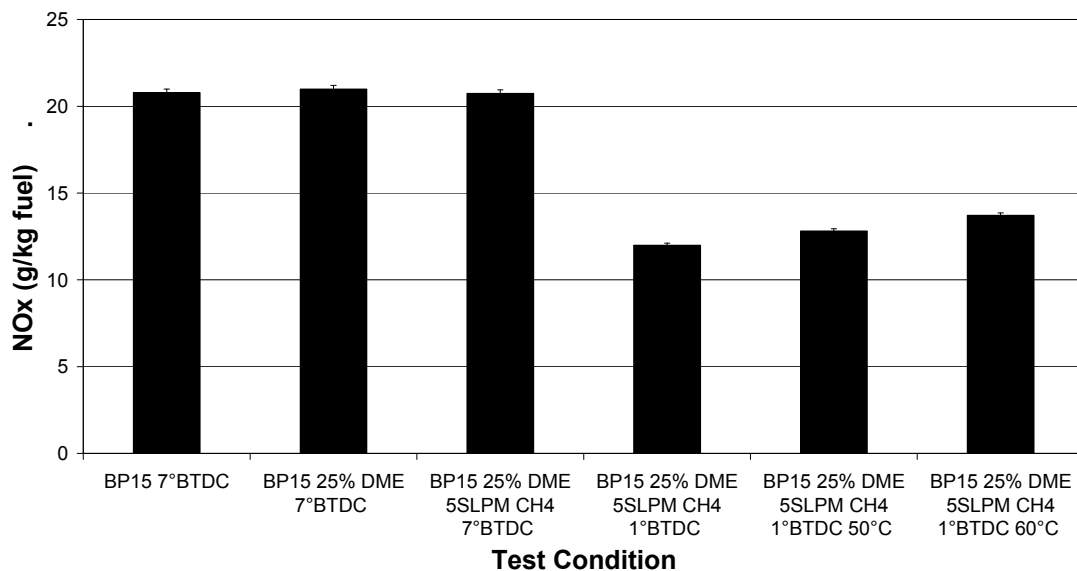


Figure 5.65: NOx (g/kg fuel) for mixed mode combustion at 1800 rpm and 61 ft-lb torque with 25% DME energy equivalent with and without 5 SLPM (6.5% energy equivalent) Methane fumigated in the intake air at various intake air temperatures compared to BP15, at 7 and 1 ° BTDC fuel injection timing

Figure 5.66 shows NOx (g/kWh) for mixed mode combustion at 1800 rpm and 61 ft-lb torque with 25% DME energy equivalent with and without % SLPM Methane fumigated in the intake air at various intake air temperatures compared to BP15, at 7 and 1 ° BTDC fuel injection timing. With the addition of 25% DME, on a power basis, the NOx emissions were reduced by approximately 10%. When Methane was added to the intake air, another 5% NOx was reduced based on power output. NOx emissions were reduced when the injection timing was retarded, but increased with increasing intake air temperature.

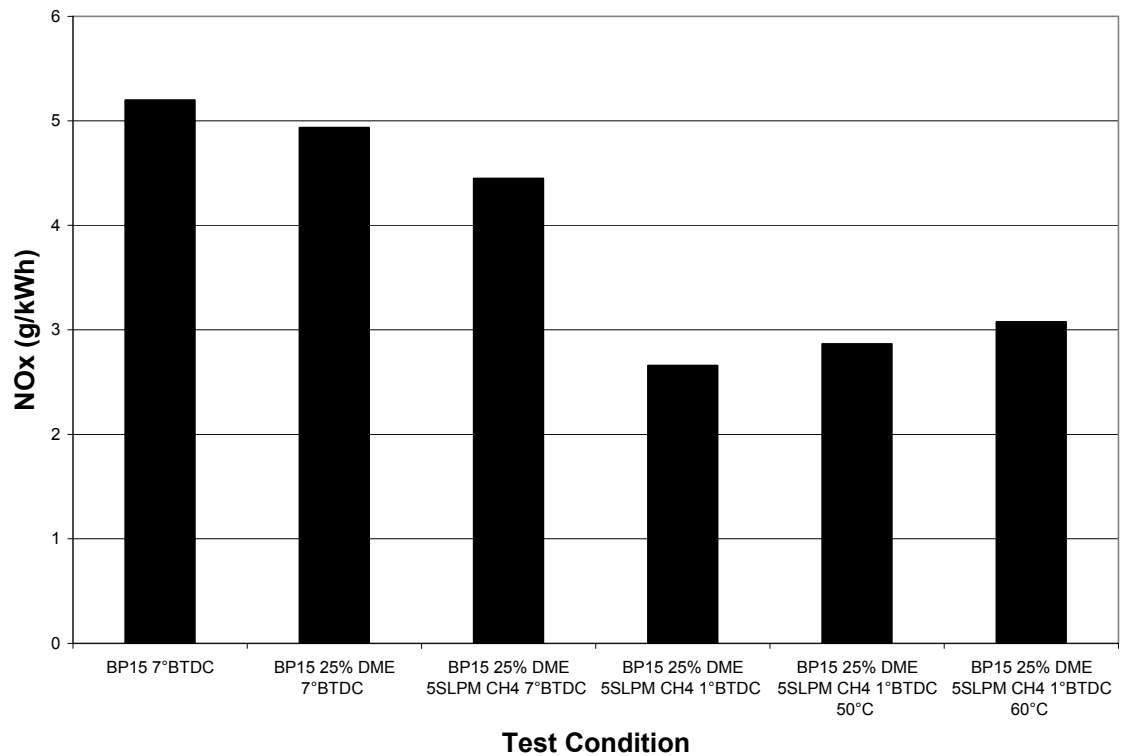


Figure 5.66: NO_x (g/kWh) for mixed mode combustion at 1800 rpm and 61 ft-lb torque with 25% DME energy equivalent with and without 5 SLPM (6.5% energy equivalent) Methane fumigated in the intake air at various intake air temperatures compared to BP15, at 7 and 1 ° BTDC fuel injection timing

Figure 5.67 shows NO (g/kg fuel) for mixed mode combustion at 1800 rpm and 61 ft-lb torque with 25% DME energy equivalent with and without 5 SLPM (6.5% energy equivalent) Methane fumigated in the intake air at various intake air temperatures compared to BP15, at 7 and 1 ° BTDC fuel injection timing. As is shown in the figure, the 25% DME mixed mode combustion achieves a 50% reduction in NO emissions on a fuel basis. However, when including Methane in the fumigation gases, this decrease is reduced to 35%. NO is further reduced by retarding injection timing, but increase with increasing intake air temperature.

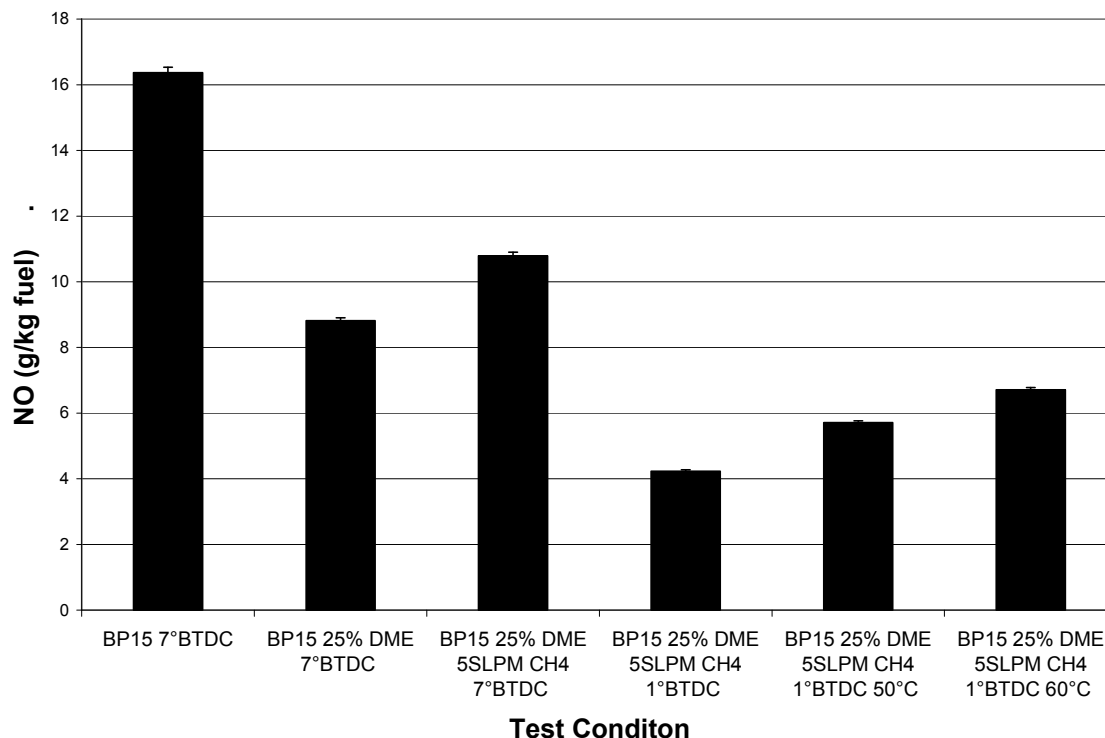


Figure 5.67: NO (g/kg fuel) for mixed mode combustion at 1800 rpm and 61 ft-lb torque with 25% DME energy equivalent with and without 5 SLPM (6.5% energy equivalent) Methane fumigated in the intake air at various intake air temperatures compared to BP15, at 7 and 1 ° BTDC fuel injection timing

Figure 5.68 shows NO₂ (g/kg fuel) for mixed mode combustion at 1800 rpm and 61 ft-lb torque with 25% DME energy equivalent with and without 5 SLPM (6.5% energy equivalent) Methane fumigated in the intake air at various intake air temperatures compared to BP15, at 7 and 1 ° BTDC fuel injection timing. NO₂ emissions increase by 175% over the BP15 diesel fuel with the addition of 25% DME mixed mode combustion, and that is reduced to 125% with the addition of Methane into the fumigated fuels. The NO₂ is further reduced when the injection timing is retarded, but there is very little effect on NO₂ with increasing intake air temperature.

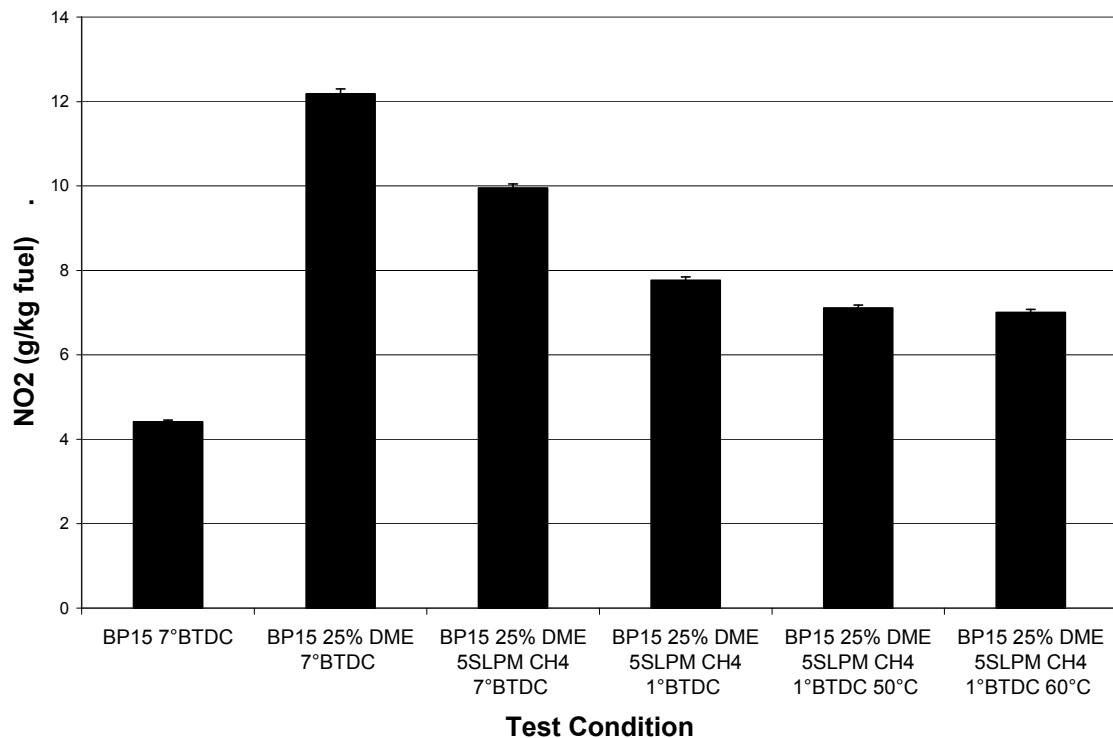


Figure 5.68: NO₂ (g/kg fuel) for mixed mode combustion at 1800 rpm and 61 ft-lb torque with 25% DME energy equivalent with and without 5 SLPM (6.5% energy equivalent) Methane fumigated in the intake air at various intake air temperatures compared to BP15, at 7 and 1 ° BTDC fuel injection timing

Figure 5.69 shows Brake Specific Fuel Consumption (BSFC) (g/kWh) for mixed mode combustion at 1800 rpm and 61 ft-lb torque with 25% DME energy equivalent with and without 5 SLPM (6.5% energy equivalent) Methane fumigated in the intake air at various intake air temperatures compared to BP15, at 7 and 1 ° BTDC fuel injection timing. On a power basis, there is less mass of fuel required for the 25% DME mixed mode combustion and with Methane. However, as injection timing is retarded and intake air temperature is increased, no change in fuel consumption is observed.

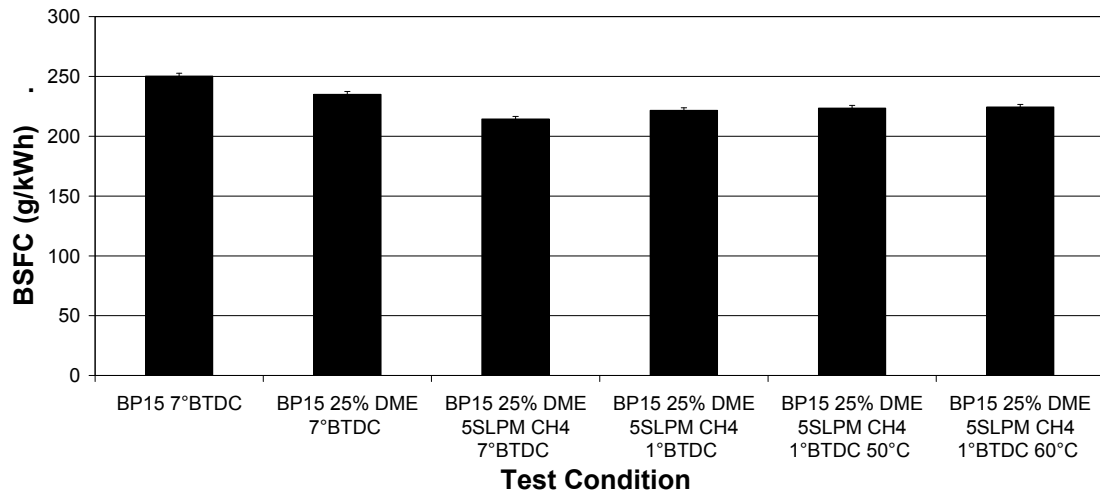


Figure 5.69: Brake Specific Fuel Consumption (g/kWh) for mixed mode combustion at 1800 rpm and 61 ft-lb torque with 25% DME energy equivalent with and without 5 SLPM (6.5% energy equivalent) Methane fumigated in the intake air at various intake air temperatures compared to BP15, at 7 and 1 ° BTDC fuel injection timing

Figure 5.70 shows Brake Specific Energy Consumption (BSEC) (MJ/kWh) for mixed mode combustion at 1800 rpm and 61 ft-lb torque with 25% DME energy equivalent with and without 5 SLPM (6.5% energy equivalent) Methane fumigated in the intake air at various intake air temperatures compared to BP15, at 7 and 1 ° BTDC fuel injection timing. On a power basis, there is less fuel energy required for the 25% DME mixed mode combustion and with Methane. However, as injection timing is retarded and intake air temperature is increased, no change in fuel consumption is observed.

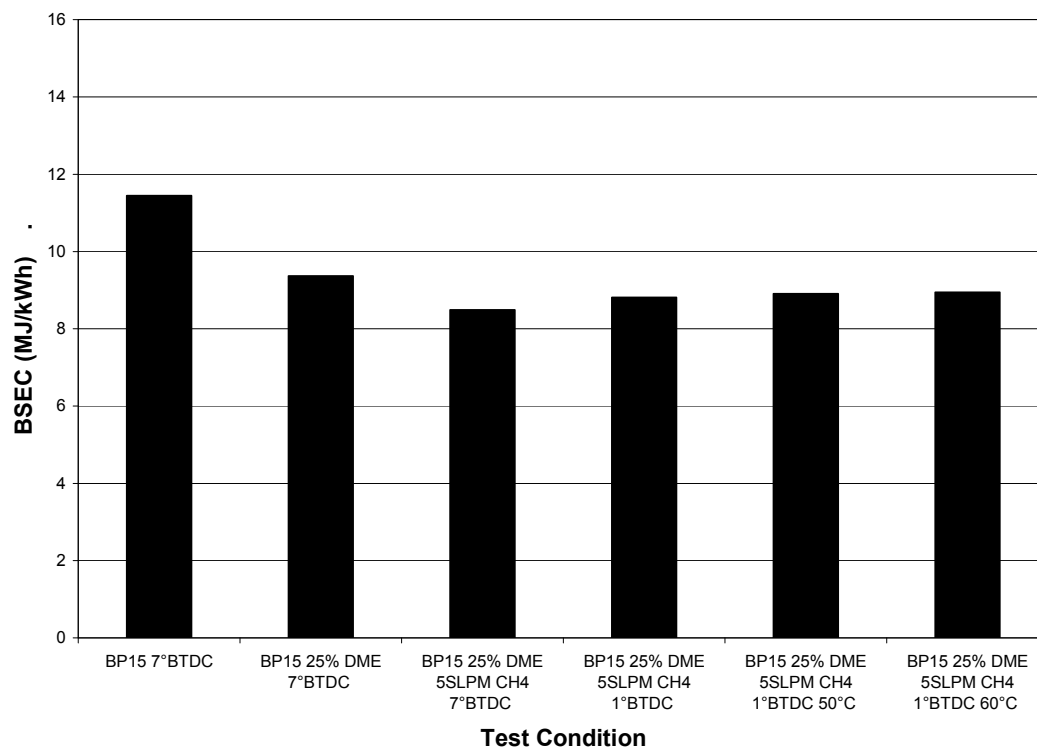


Figure 5.70: Brake Specific Energy Consumption (MJ/kWh) for mixed mode combustion at 1800 rpm and 61 ft-lb torque with 25% DME energy equivalent with and without 5 SLPM (6.5% energy equivalent) Methane fumigated in the intake air at various intake air temperatures compared to BP15, at 7 and 1 ° BTDC fuel injection timing

Figure 5.71 shows CO (g/kg fuel) for mixed mode combustion at 1800 rpm and 61 ft-lb torque with 25% DME energy equivalent with and without 5 SLPM (6.5% energy equivalent) Methane fumigated in the intake air at various intake air temperatures compared to BP15, at 7 and 1 ° BTDC fuel injection timing. As seen in the figure, adding the Methane to the fumigated DME reduced the CO emissions. When the injection timing was retarded, the CO emissions were increased. Intake air heating made the biggest impact on CO emissions by reducing it by over 50% from the unheated case.

However, the CO emissions from all of these cases were still 6 to 10 times the amount in comparison to BP15 diesel fuel.

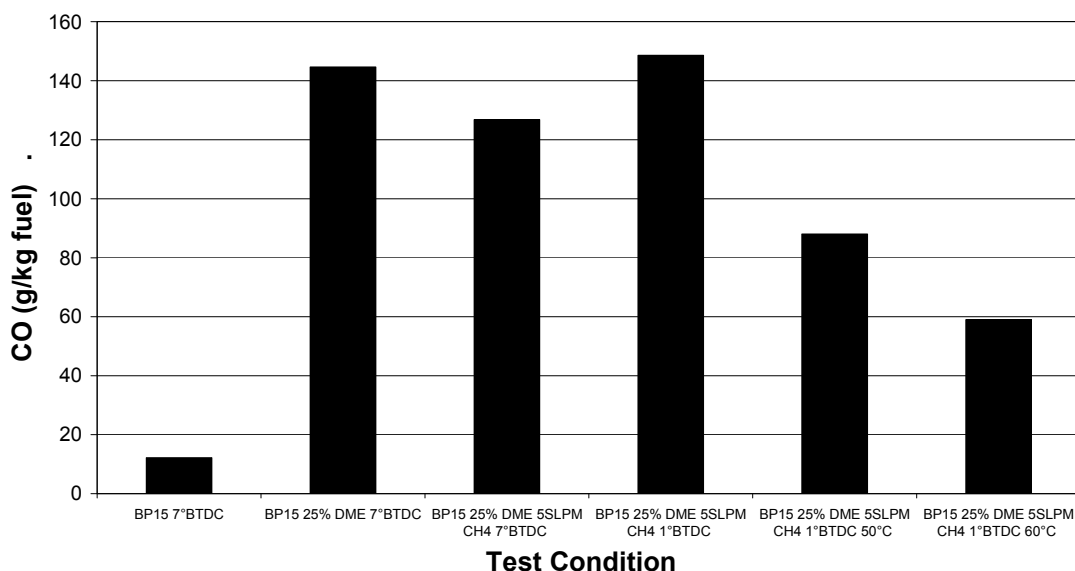


Figure 5.71: CO (g/kg fuel) for mixed mode combustion at 1800 rpm and 61 ft-lb torque with 25% DME energy equivalent with and without 5 SLPM (6.5% energy equivalent) Methane fumigated in the intake air at various intake air temperatures compared to BP15, at 7 and 1 ° BTDC fuel injection timing

Figure 5.72 shows Total Hydrocarbons (g/kg fuel) for mixed mode combustion at 1800 rpm and 61 ft-lb torque with 25% DME energy equivalent with and without 5 SLPM (6.5% energy equivalent) Methane fumigated in the intake air at various intake air temperatures compared to BP15, at 7 and 1 ° BTDC fuel injection timing. As seen in the figure, adding the Methane to the fumigated DME increased the hydrocarbon emissions. When the injection timing was retarded, the hydrocarbon emissions were increased. Intake air heating made some impact on hydrocarbon emissions, but was still 20% more than the case with 25% DME mixed mode combustion. However, the hydrocarbon

emissions from all of these cases were still 1.5 to 3 times the amount in comparison to BP15 diesel fuel.

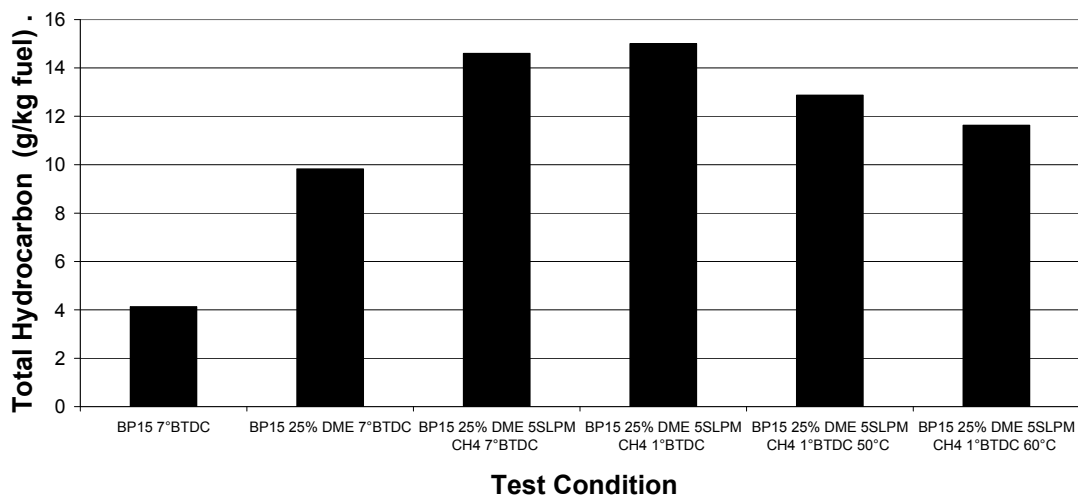


Figure 5.72: Total Hydrocarbons (g/kg fuel) for mixed mode combustion at 1800 rpm and 61 ft-lb torque with 25% DME energy equivalent with and without 5 SLPM (6.5% energy equivalent) Methane fumigated in the intake air at various intake air temperatures compared to BP15, at 7 and 1 ° BTDC fuel injection timing

Figure 5.73 shows CO₂ (g/kg fuel) for mixed mode combustion at 1800 rpm and 61 ft-lb torque with 25% DME energy equivalent with and without 5 SLPM (6.5% energy equivalent) Methane fumigated in the intake air at various intake air temperatures compared to BP15, at 7 and 1 ° BTDC fuel injection timing. As seen in the figure, adding the Methane to the fumigated DME increased the CO₂ emissions. When the injection timing was retarded, the CO₂ emissions were decreased. When the intake air was heated, the CO₂ emissions increased. However, the CO₂ emissions from all of these cases were higher in comparison to BP15 diesel fuel. Because of the intake air heating, the density of the air changes, and thus less mass of air is present in the intake air as it is

drawn into the engine. This results in less oxygen and nitrogen available in the combustion process, and thus a greater amount of CO₂ because of the change in the mass flow rate of the reactants.

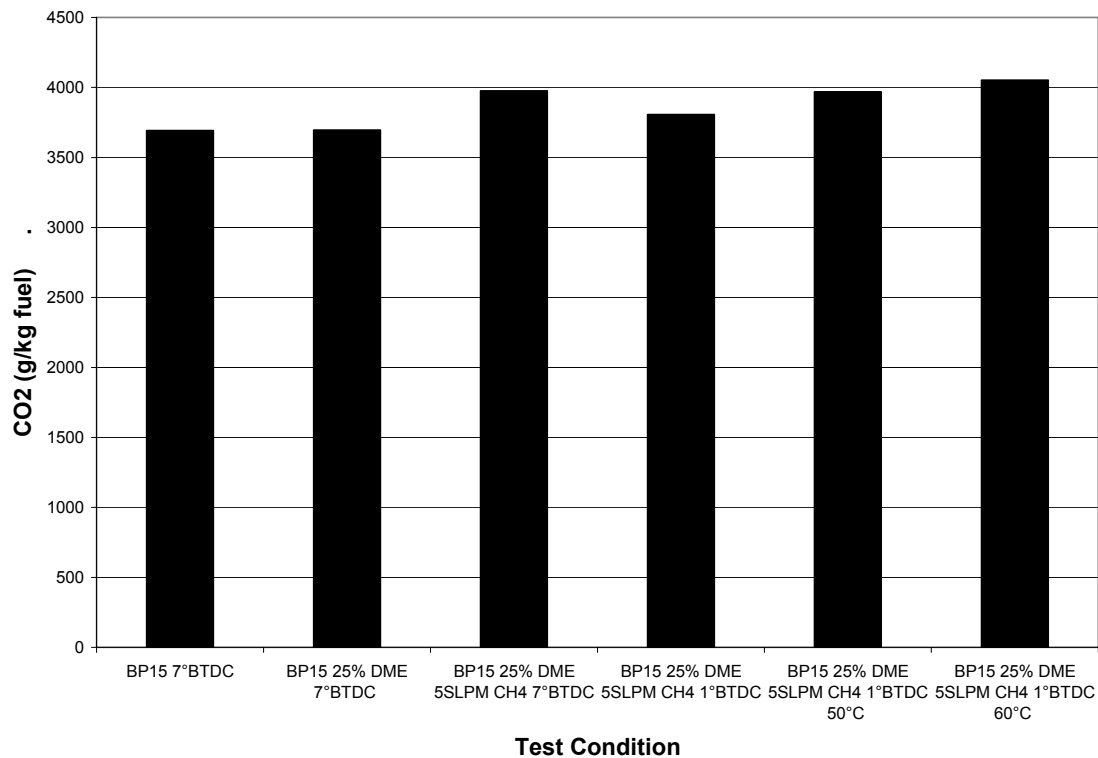


Figure 5.73: CO₂ (g/kg fuel) for mixed mode combustion at 1800 rpm and 61 ft-lb torque with 25% DME energy equivalent with and without 5 SLPM (6.5% energy equivalent) Methane fumigated in the intake air at various intake air temperatures compared to BP15, at 7 and 1 ° BTDC fuel injection timing

Figure 5.74 shows Methane (ppm) for mixed mode combustion at 1800 rpm and 61 ft-lb torque with 25% DME energy equivalent with and without 5 SLPM (6.5% energy equivalent) Methane fumigated in the intake air at various intake air temperatures compared to BP15, at 7 and 1 ° BTDC fuel injection timing. As shown in the figure, Methane emissions increased in the exhaust gas for all cases but the BP15 diesel fuel

case. While a little Methane was being formed for the 25% DME mixed mode combustion case, for the cases where Methane was being added to the fumigated fuel blend, the highest amounts were found in the exhaust by a factor of 6 to 8 times.

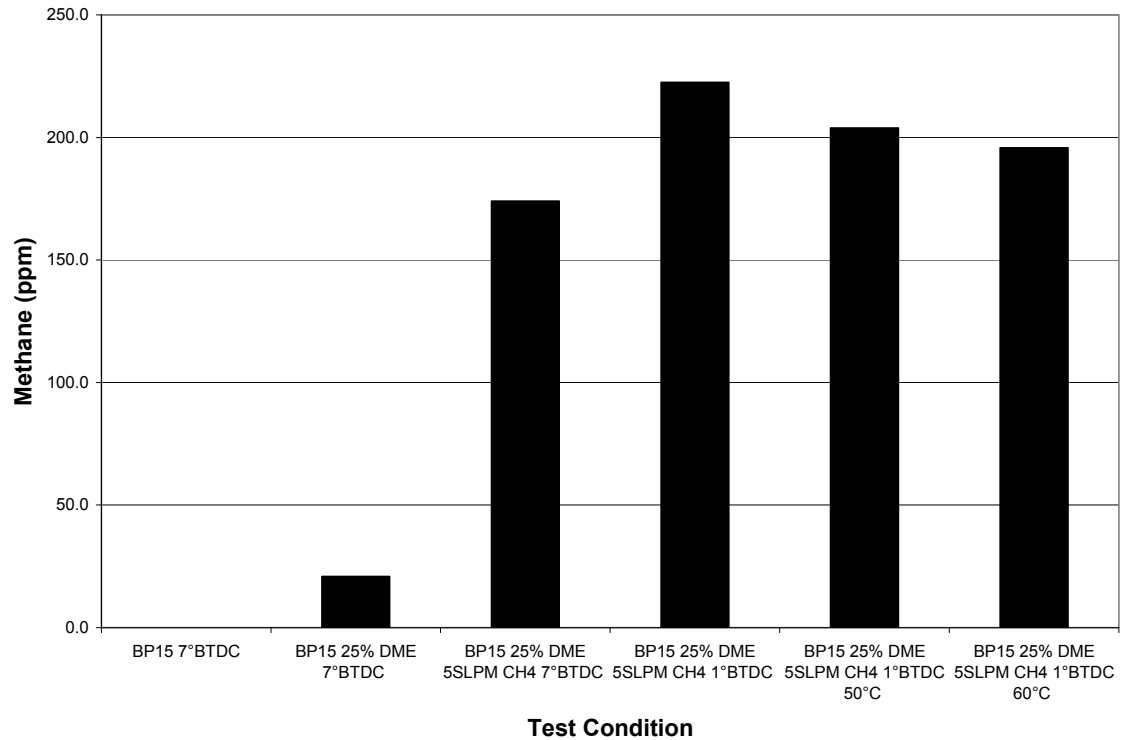


Figure 5.74: Methane (ppm) for mixed mode combustion at 1800 rpm and 61 ft-lb torque with 25% DME energy equivalent with and without 5 SLPM (6.5% energy equivalent) Methane fumigated in the intake air at various intake air temperatures compared to BP15, at 7 and 1 ° BTDC fuel injection timing

Figure 5.75 shows Exhaust Temperature (°C) for mixed mode combustion at 1800 rpm and 61 ft-lb torque with 25% DME energy equivalent with and without 5 SLPM (6.5% energy equivalent) Methane fumigated in the intake air at various intake air temperatures compared to BP15, at 7 and 1 ° BTDC fuel injection timing. Exhaust

temperature is fairly constant for this set of test conditions, except in the cases where the intake air temperature was increased.

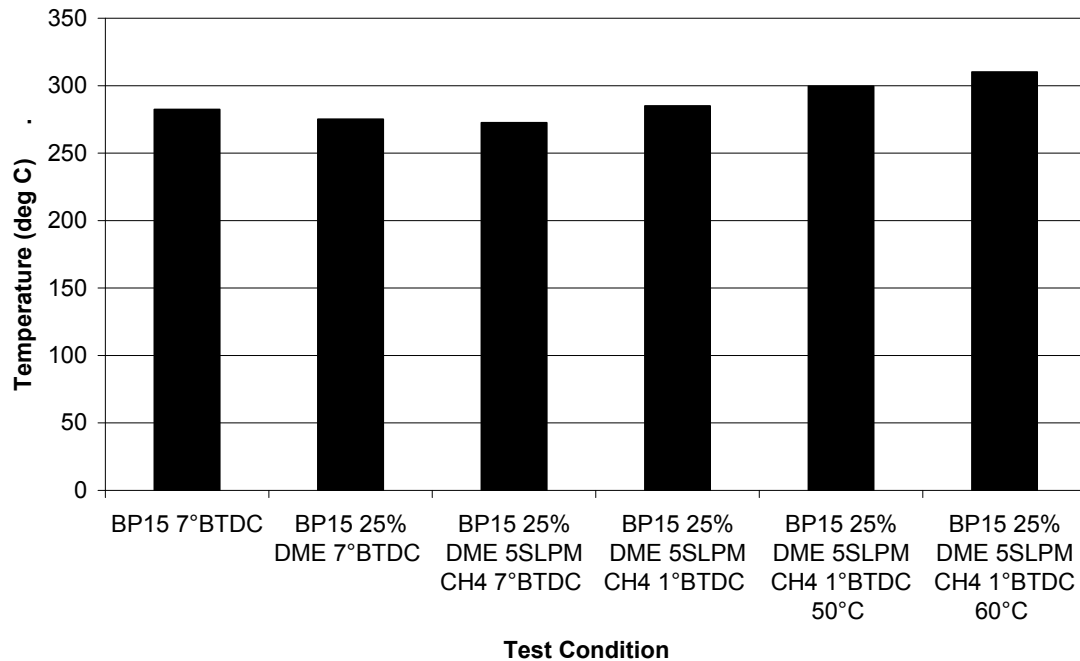


Figure 5.75: Exhaust Temperature (°C) for mixed mode combustion at 1800 rpm and 61 ft-lb torque with 25% DME energy equivalent with and without 5 SLPM (6.5% energy equivalent) Methane fumigated in the intake air at various intake air temperatures compared to BP15, at 7 and 1 ° BTDC fuel injection timing

Figure 5.76 shows GC Data for BP15 in comparison to mixed mode combustion with 25% energy equivalent DME concentration and with 25% energy equivalent DME concentration at various injection timing and with increasing temperature. When the engine is operated with DME and with a Methane blend fumigated in the intake, more Methane is observed in the exhaust in comparison to the same DME concentration without the Methane fumigated in the intake air. Retarding the injection timing towards

TDC yields an increase in Methane emissions regardless of the Methane fumigation in the intake air. Increasing the intake air temperature seems to have more effect on the DME and Methane emissions than a change in injection timing.

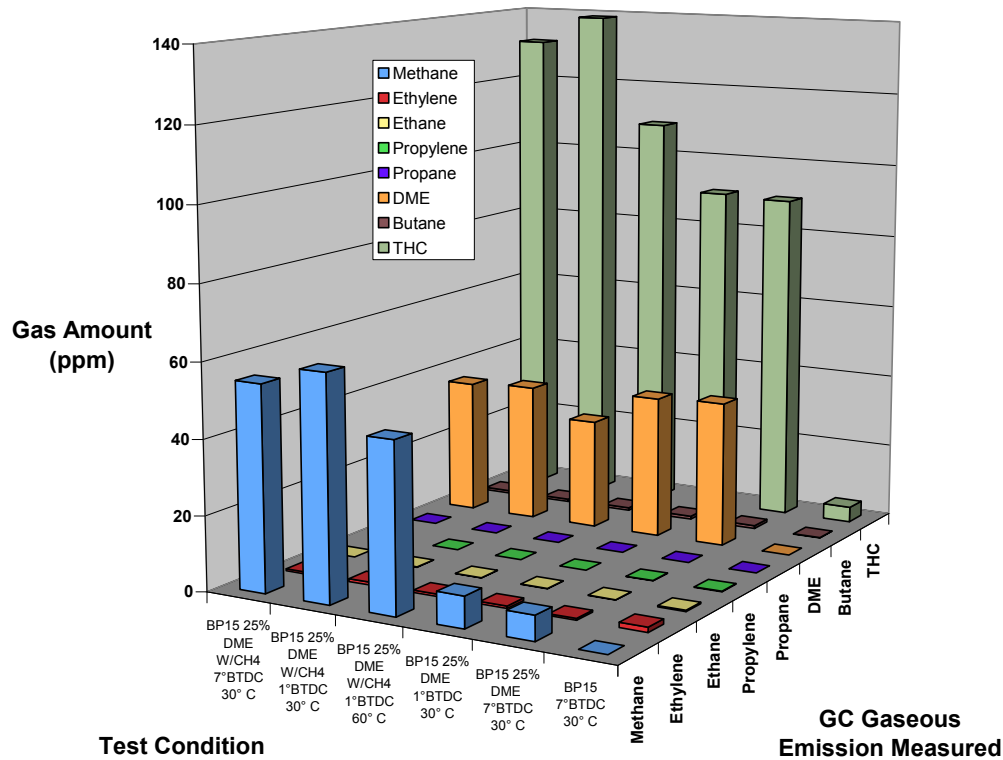


Figure 5.76: GC Data: BP15 in comparison to mixed mode combustion with 25% energy equivalent DME concentration and with 25% energy equivalent DME concentration at various injection timing and with increasing temperature

Figure 5.77 shows Cylinder Pressure (bar) for mixed mode combustion at 1800 rpm and 61 ft-lb torque with 25% DME energy equivalent with and without 5 SLPM (6.5% energy equivalent) Methane fumigated in the intake air at various intake air temperatures compared to BP15, at 7 and 1 ° BTDC fuel injection timing. As shown previously, with the addition of the 25% DME energy equivalent, the pressure trace shows a change from a distinct premixed and diffusion controlled phase of combustion to

a mostly premixed phase of combustion. With the addition of Methane to the DME, the pressure increases. A shift in the injection timing of the diesel fuel causes a shift in the combustion phasing of the peak pressure. Heating the intake air with this fuel scheme causes an increase in the peak pressure from the base condition by about 3 bar.

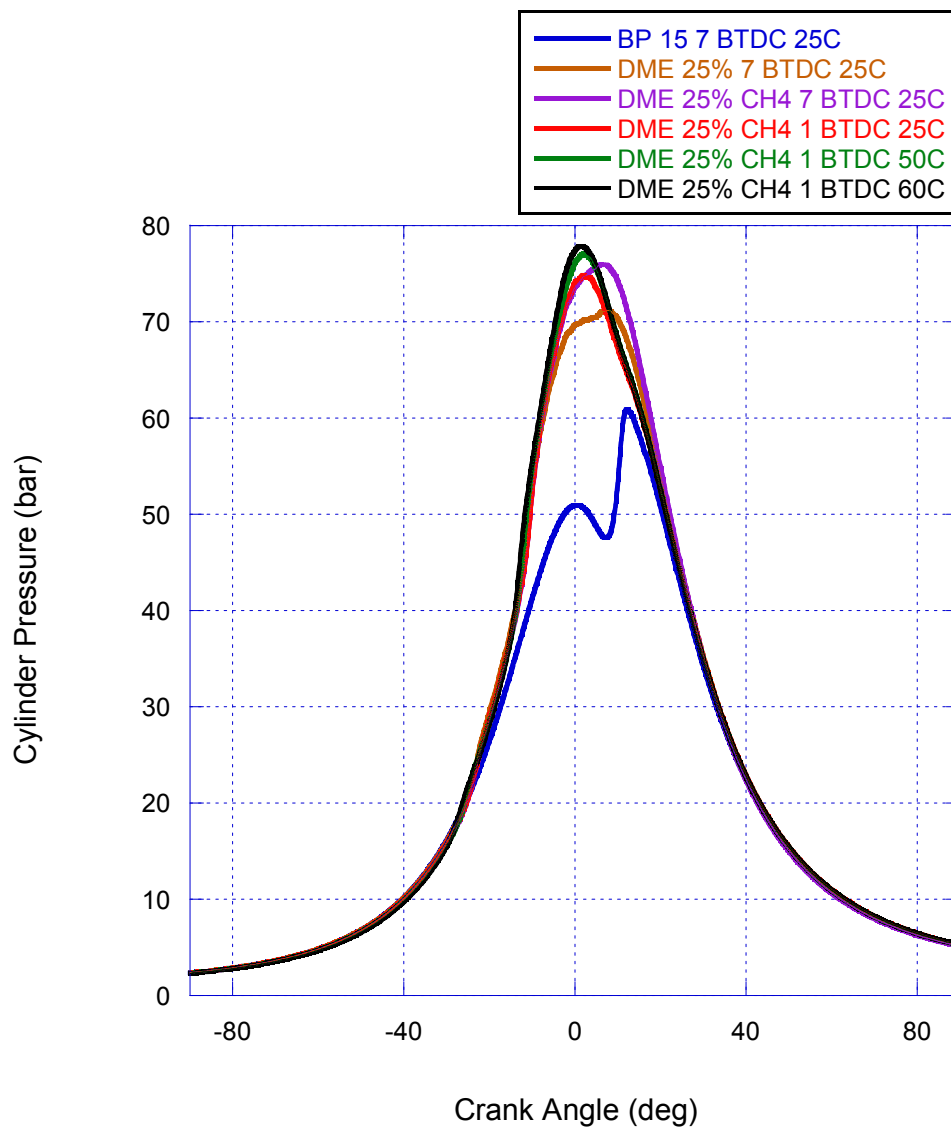


Figure 5.77: Cylinder Pressure (bar) for mixed mode combustion at 1800 rpm and 61 ft-lb torque with 25% DME energy equivalent with and without 5 SLPM (6.5% energy equivalent) Methane fumigated in the intake air at various intake air temperatures compared to BP15, at 7 and 1 ° BTDC fuel injection timing

Figure 5.78 shows heat release rate (J/deg) for mixed mode combustion at 1800 rpm and 61 ft-lb torque with 25% DME energy equivalent with and without 5 SLPM (6.5% energy equivalent) Methane fumigated in the intake air at various intake air temperatures compared to BP15, at 7 and 1 ° BTDC fuel injection timing. With the addition of Methane with DME into the intake air, the LTHR and the HTHR seem unaffected, but there is a decrease in the heat release from the diesel portion of the combustion. A shift in the injection timing of the diesel fuel causes an increase in the HTHR portion and the diesel fuel portion to be retarded. When using intake air heating, the LTHR and HTHR occur earlier in the combustion phasing while the combustion phasing and magnitude of the diesel combustion are the same in comparison for the cases of the three temperatures (25°C, 50°C, and 60°C). For the cases where no temperature is indicated, it should be assumed that this is the 25°C case. The LTHR is reduced, and the HTHR portion is increased as the intake air is heated.

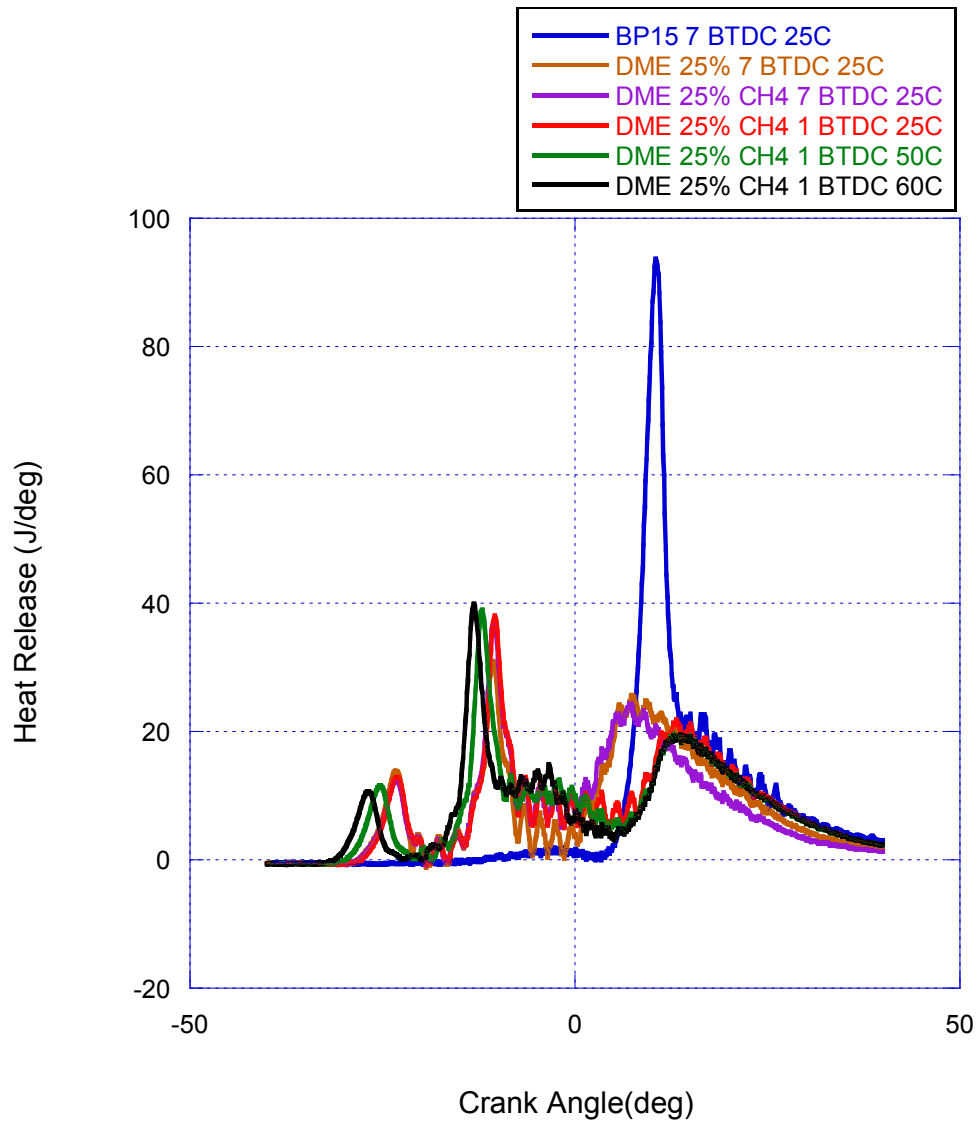


Figure 5.78: Heat Release Rate (J/deg) for mixed mode combustion at 1800 rpm and 61 ft-lb torque with 25% DME energy equivalent with and without 5 SLPM (6.5% energy equivalent) Methane fumigated in the intake air at various intake air temperatures compared to BP15, at 7 and 1 ° BTDC fuel injection timing

Figure 5.79 shows bulk cylinder temperature (K) for mixed mode combustion at 1800 rpm and 61 ft-lb torque with 25% DME energy equivalent with and without 5 SLPM (6.5% energy equivalent) Methane fumigated in the intake air at various intake air temperatures compared to BP15, at 7 and 1 ° BTDC fuel injection timing. As shown in

the figure, the Methane portion of the fumigated fuel increases the bulk temperature and advances the combustion phasing. With the retarding of the injection timing, the peak bulk temperature decreases, while the heat from the HTHR portion increases the bulk temperature. Increasing the intake air temperature serves to advance the LTHR peak and to increase both the HTHR peak and the main diesel fuel peak temperatures.

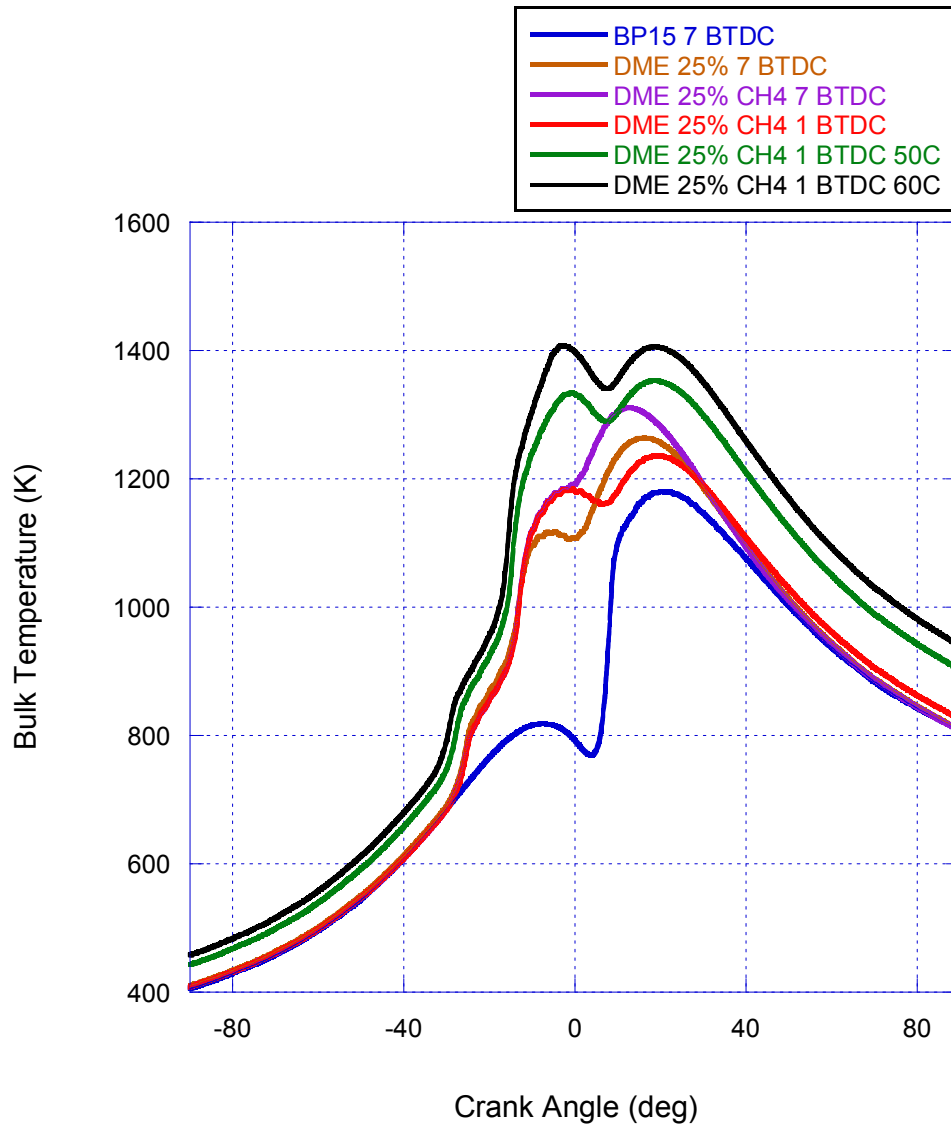


Figure 5.79: Bulk Temperature (K) for mixed mode combustion at 1800 rpm and 61 ft-lb torque with 25% DME energy equivalent with and without 5 SLPM (6.5% energy equivalent) Methane fumigated in the intake air at various intake air temperatures compared to BP15, at 7 and 1 ° BTDC fuel injection timing

5.9 Discussion

The following sections discuss the data from the experiments described in this chapter. Each of the three sets of experiments were analyzed and results were separately shown. In this section, the key observations of these research studies will be discussed.

These include:

- Reaction kinetics for DME that lead to the heat release
- Explanation for reduction in NO emissions and increase in NO₂ emissions
- Effect of injection timing and addition of heated intake air temperature
- Influence of HTHR on NO and main diesel combustion
- Observed hydrocarbons in the exhaust species
- Effect of Methane addition
- Effect of mixed mode combustion on particulate matter

5.9.1 DME Ignition and Reaction Kinetics

Pfahl and coworkers were able to measure the self-ignition behavior of diesel-relevant fuels as homogeneous mixtures using a high pressure shock tube [13]. Of the fuels they investigated, DME was also investigated in the temperature range of 650-1300K. They showed that DME exhibited a two step self ignition: a cool flame process at lower temperatures, followed by a negative temperature coefficient (NTC) region and a second detonation-like process [13].

Previously, many researchers have elucidated the reaction kinetics of dimethyl ether [23, 24, 26, 226, 227]. The oxidation chemistry is important in helping to understand what is happening in this mixed mode combustion process, and in other diesel engine applications. Figure 5.80 shows the overall reaction scheme for dimethyl ether oxidation [24]. Curran and coworkers studied dimethyl ether oxidation in a variable pressure flow reactor over the temperature range of 550-850K, in the pressure range of 12-18 atm, and at equivalence ratios of $0.7 \leq \phi \leq 4.2$ [24]. Curran and coworkers also performed studies in a jet stirred reactor at 1 and 10 atm, $0.2 \leq \phi \leq 2.5$, and 800-1300K [23]. Dagaut and coworkers studies the oxidation and ignition of DME from 500-1100 K in a fused silica jet stirred reactor at 10 atm, and $0.2 \leq \phi \leq 1$ [228].

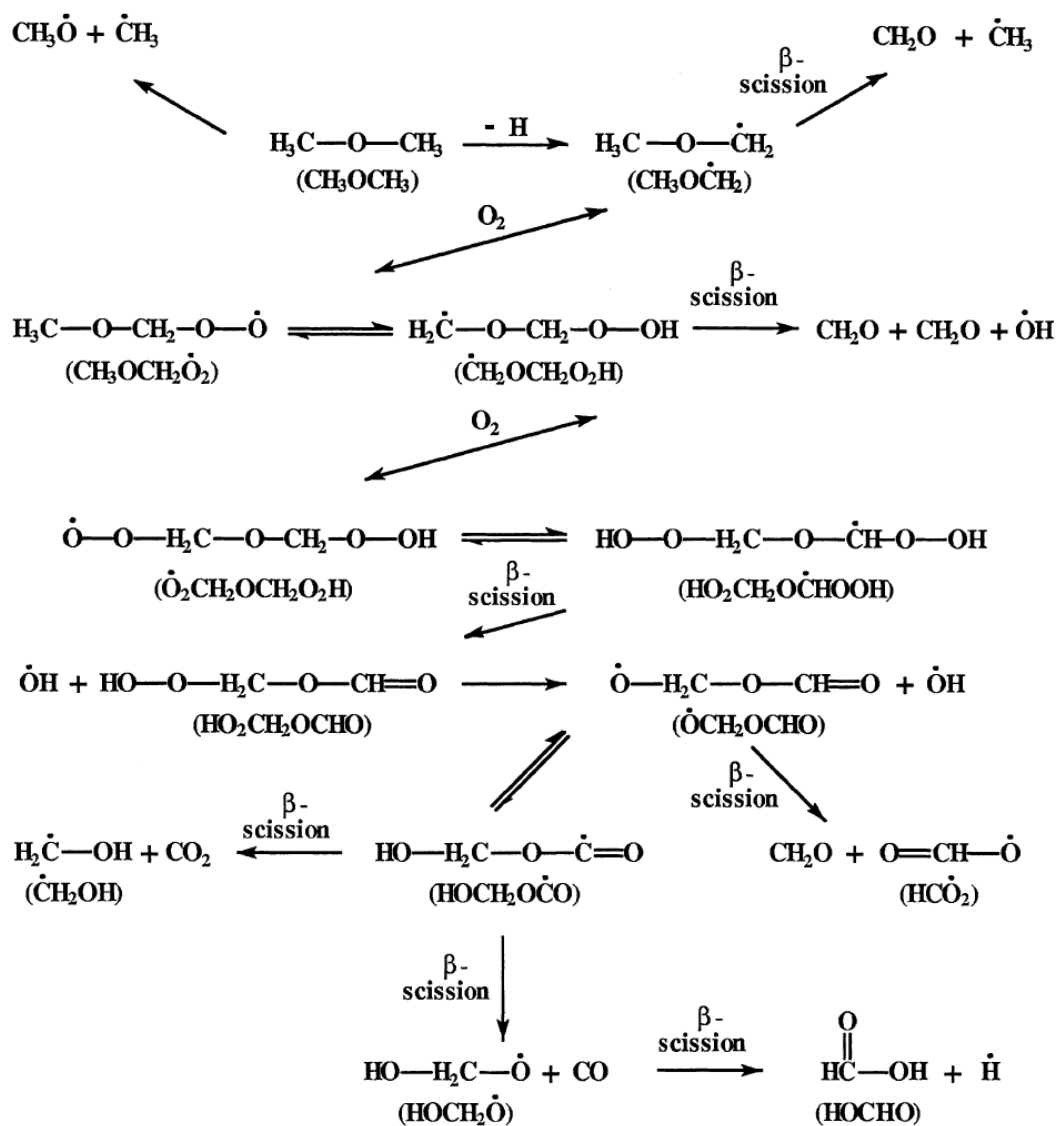


Figure 5.80: Overall reaction scheme for dimethyl ether oxidation [24]

Both Curran and Dagaut's research propose that the fuel initiation reactions occur by thermal decomposition of the fuel and reactions with O_2 . Both researchers discuss the methoxymethyl radical (CH_3OCH_2) formed by H-atom abstraction on DME. From this reaction, the methoxymethyl radical further decomposes forming formaldehyde and CH_3 , and reacts with O_2 , HO_2 , and CH_3 . The formation of the methoxymethylperoxy radical

(CH₃OCH₂OO—simplified as RO₂) were included in Dagaut's set of reactions, as well as a degradation reaction involving internal H-atom transfer yielding CH₂OCH₂OOH—simplified at QO₂H, self reactions and reactions with HO₂, DME and formaldehyde [228]. A kinetic analysis involving a sensitivity analysis and reaction paths analysis was used to interpret the results of Dagaut's work. It was found that in the cool flame regions, the route $R + O_2 \rightarrow RO_2 \rightarrow QO_2H (+O_2) \rightarrow OQ'O + 2OH$ dominates (R here is CH₃OCH₂). The competition between the propagation and branching paths for QO₂H is responsible in his model for the observed NTC. Above a particular temperature that restarts the reactions in the second stage, the decomposition of R is favored and the formation of RO₂ becomes negligible [228].

While there has been much research into the reaction rates and pathways of DME ignition and oxidation, it is difficult to determine the appropriate reactions and radicals involved in this current research with DME and NO_x mechanisms for an appropriate discussion. However, the work previously reported gives insight and an appropriate set of reactions for a model to be created.

5.9.2 Explanation for shift in NO to NO₂ emissions

According to work performed by Hori and coworkers, there is an effect of low concentrations of fuels on the conversion of NO to NO₂ [40, 229]. In their research, they show that the effectiveness of promoting the conversion depends on the type of fuel. They studied 7 different types of fuel, from H₂ and CH₄, to longer chain hydrocarbons like i-C₄H₁₀ and n-C₄H₁₀ [40]. Their work showed that the effectiveness increased with

increasing carbon chain length. Hori and coworkers went on to propose chemical kinetic reactions to explain the conversion of NO to NO₂ [40]. This conversion is indicated to proceed mainly through the NO + HO₂ → NO₂ + OH route. Therefore, if HO₂ is available in high quantities, the conversion is more effective [40]. In their conclusions, they also state that the temperature range of the conversion is important, but did not address which ranges. Also, they indicate that a C₃H₆ molecule would have a low conversion [40].

In Hori and coworkers later research, experiments and kinetic models were performed to further investigate the role of hydrocarbons in the NO to NO₂ conversion [229]. Five hydrocarbons were examined individually: methane, ethylene, ethane, propene, and propane. The results indicated that ethylene and propane are more effective than Methane to oxidize the NO. Highest effectiveness comes as a result of hydrocarbons that produce reactive radicals like OH and O atoms, that promote oxidation and lead to the HO₂ production. If the hydrocarbon produces radicals, like methyl and allyl, which reduce the oxidation by O₂, this tends to reduce the NO₂ to NO through the reaction $R + NO_2 \rightarrow RO + NO$ (R= CH₃ or aC₃H₅). Propane showed the greatest NO to NO₂ conversion at the lowest temperature and had the widest temperature range. Ethylene was also found to have similar effectiveness as propane. Methane and ethane were less effective.

Hori and coworkers research also showed that the effectiveness of the hydrocarbon is also dependent on the temperature range. While hydrocarbon consumption was accelerated when the reaction temperature increased, the reduction in NO₂ to NO was observed for longer residence times at the higher temperatures [229].

Hori and coworkers research helps to explain the shift in NO_2 to NO emissions seen in this research. In the decomposition of DME, HO_2 radicals are formed to propagate the reactions. In the series of DME reactions, methyl radicals are produced, which provide for the reaction route that shifts the NO_2 to NO . However, when the small quantity of Methane was introduced with the fumigated DME, this provided an additional pool of methyl radicals to the fumigated hot gases, which provided for some of the NO_2 to shift back to NO , and for the reaction route of $\text{CH}_3 + \text{HO}_2 \rightarrow \text{CH}_4 + \text{O}_2$, as described by Curran and coworkers occurring at approximately 750K [24]. As shown in the mixed mode combustion results with DME and without Methane, there was a small amount of Methane being formed, indicating that this reaction route must have been occurring.

Dagaut and coworkers published some research about the low temperature oxidation of DME and its mutual sensitization with NO [26]. They showed that at temperatures below 600K, the oxidation of DME was inhibited by NO , but above 600K NO enhances the oxidation of DME in the cool flame regime and yields methylformate and an additional HO_2 , which further provides the radicals to oxidize the NO to NO_2 . The study showed that below 616K, the NO inhibits the oxidation of DME due to the removal of the methoxymethyl peroxy ($\text{CH}_3\text{OCH}_2\text{O}_2$) radical by reaction with NO , reducing the production of OH radicals and slowing the cool flame oxidation [26]. Above about 620K, the oxidation of DME and NO is due to the additional production of $\text{CH}_3\text{OCH}_2\text{O}$ (also referred to as R) and OH which promote the oxidation in the following reactions: $\text{RO}_2 + \text{NO} \rightarrow \text{RO} + \text{NO}_2$ and $\text{HO}_2 + \text{NO} \rightarrow \text{OH} + \text{NO}_2$ [26].

5.9.3 Chemkin Modeling of DME HCCI

To determine if the HO₂ species was available in significant quantities, a model of a single cylinder from the DDC 2.5L engine was configured in Chemkin 4.1 to model the HCCI process of the DME combustion and ignition. Chemkin is a fortran library that was designed to aid in modeling the chemical kinetics of a reacting system [230]. As shown in the previous heat release plots for the mixed mode combustion, the DME combustion is occurring as a homogeneous charge prior to the diesel pilot fuel injection. Thus, an HCCI zero dimensional model will provide relevant kinetic information about the combustion. The high temperature and low temperature reaction mechanisms from Lawrence Livermore National Laboratory were used for the thermodynamic and reaction mechanism inputs [24, 25]. The system was assumed to be adiabatic with no heat loss and no wall heat transfer. The Chemkin model was programmed to start at the point that the intake valve closes, with an engine speed of 1800 rpm, and cycle through 1 crank revolution. The actual fuel and air for the testing was used to compute the mass fractions for the reaction species inputs, air and DME. Initial conditions were assumed to be 25 °C and 1 bar.

Figure 2.13 shows the fuel decomposition and select species pool of interest for the 25% energy equivalent DME HCCI. As shown, the HO₂ species is made available from the DME decomposition and heat generated by the reaction and the compression. As the DME decomposition reaches completion, the amount of HO₂ production drops off, and the H₂O₂ species increases and plateaus. As shown in this model, not all of the DME is reacted through the compression of the fuel.

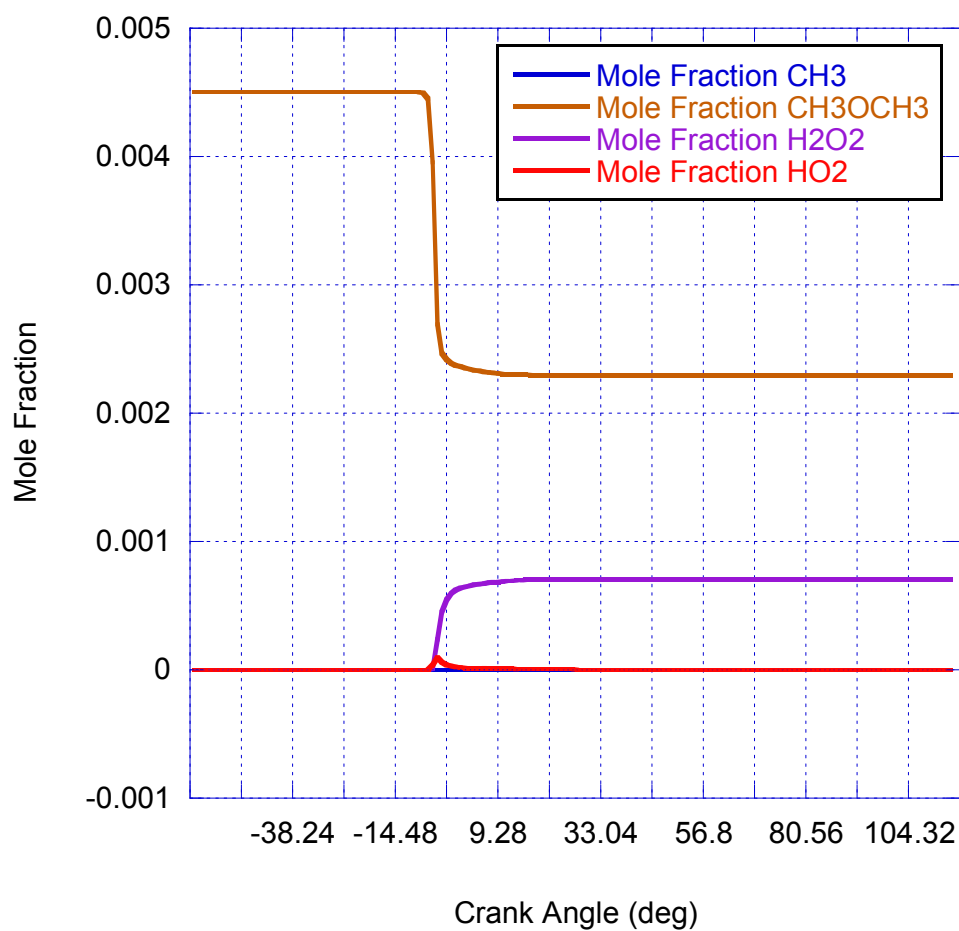


Figure 5.81: Chemkin simulation of 25% energy equivalent DME HCCI, A/F ratio of 138.1 and $\Phi = .065$, with various species (Initial Temperature 25 °C, Pressure 1 atm, Heat Loss 0.0 cal/sec)

Figure 5.82 shows the Chemkin model of 25% energy equivalent DME HCCI with HO₂ in comparison to other species of interest. In comparison, the production of HO₂ far exceeds the production of the other species, thus making the NO to NO₂ conversion possible. The Chemkin model confirms that HO₂ is available at the time

when NO would be produced from the diesel fuel portion of the combustion, as the injection of the diesel fuel occurs at -7° BTDC.

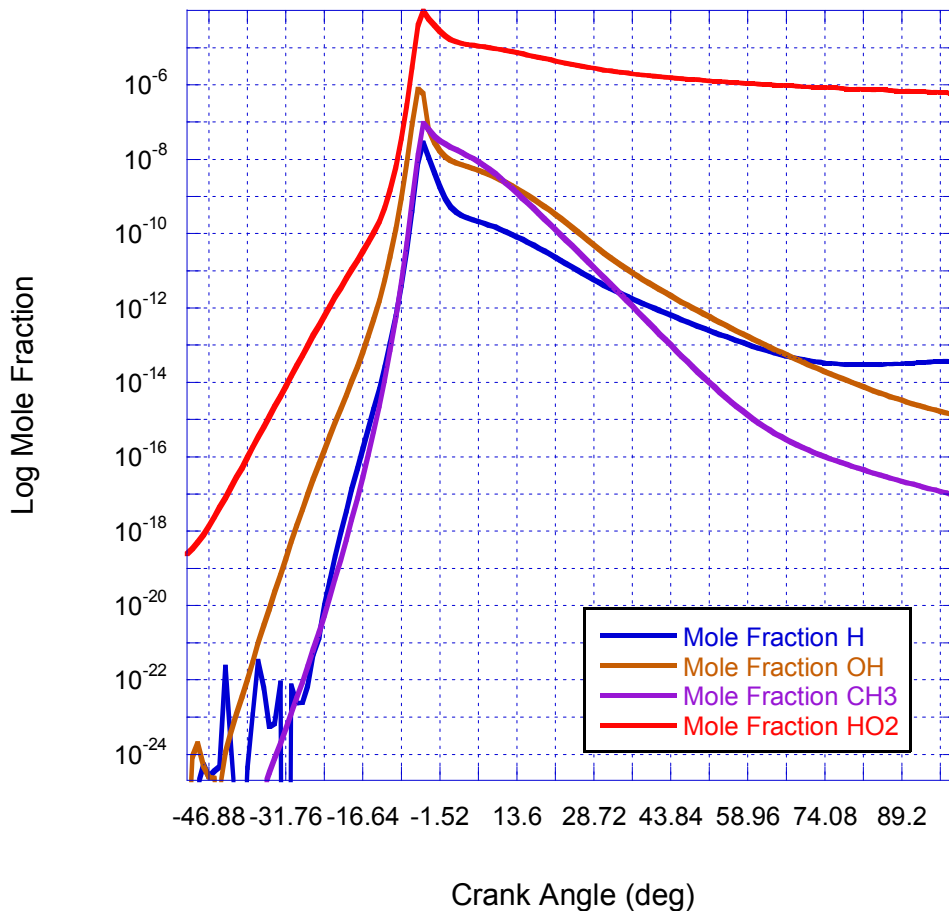


Figure 5.82: Chemkin model of 25% energy equivalent DME HCCI, A/F ratio of 138.1 and $\Phi = .065$, with HO₂ in comparison to other species (Initial Temperature 25 °C, Pressure 1 atm, Heat Loss 0.0 cal/sec)

Figure 5.83 shows that the HO_2 increases with increasing concentration of DME in the homogeneous charge. As shown, the increase is smaller between the 35% and 44% energy equivalent DME and than the 25% and 35% energy equivalent DME.

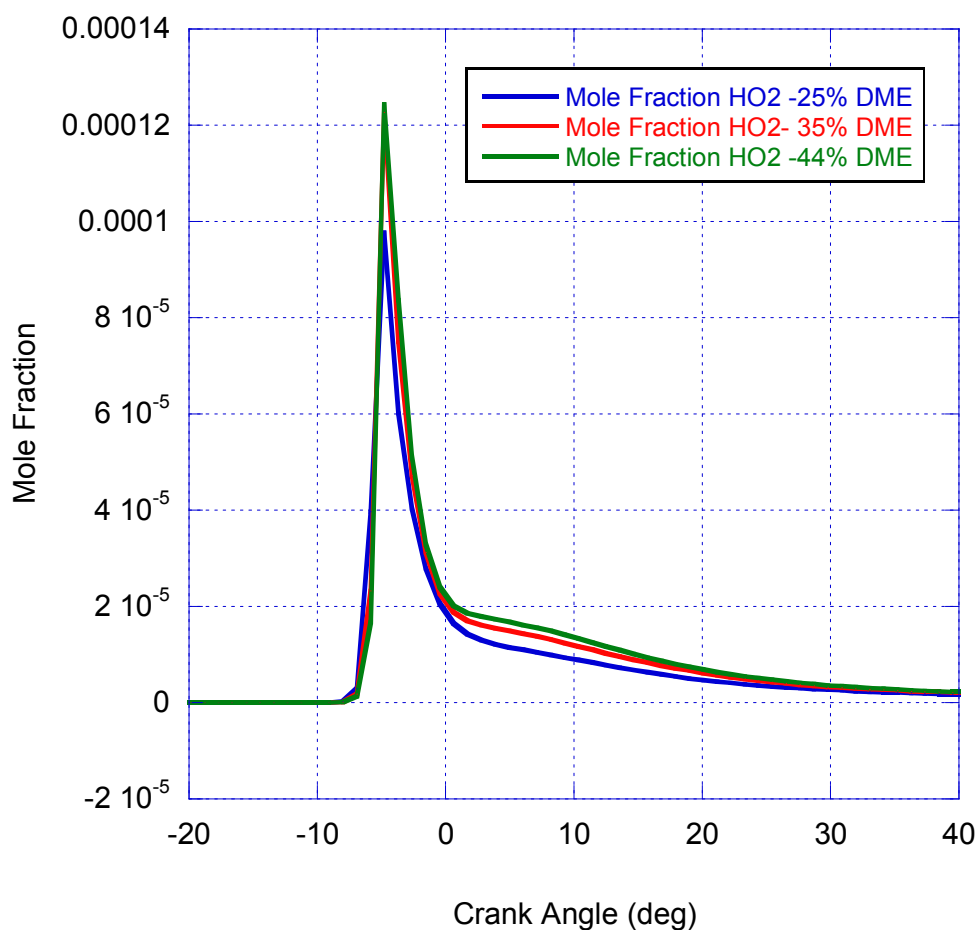


Figure 5.83: Chemkin model of 25% (A/F ratio of 138.1 and $\Phi = .065$), 35% (A/F ratio of 101.3 and $\Phi = .088$), and 44% (A/F ratio of 89.3 and $\Phi = .100$) energy equivalent DME HCCI showing increasing HO_2 species (Initial Temperature 25 °C, Pressure 1 atm, Heat Loss 0.0 cal/sec)

5.9.4 Injection Timing and Heated Intake Air Effect

In Figure 5.36, the injection timing of the diesel fuel is shown to only affect the ignition timing of the diesel fuel, with no apparent impact on the DME ignition. While it would be expected that the heat release from the diesel fuel portion would be lower when using the DME in a mixed mode combustion configuration because the amount of fuel being injected is less, it is unclear from the heat release and bulk temperature curves if the HTHR portion of the DME ignition contributes to a faster vaporization and additional heat release from the diesel fuel portion.

With retarded injection timing, the NO_x emissions decrease with a decrease in the NO and NO₂ emissions. One could conclude that with the retarded timing, there is less time for thermal NO formation and also less time for the light hydrocarbon species to reach the NO and react to form NO₂. With the retarded injection timing, the peak pressure finishes later, and the bulk temperature is lower for the diesel fuel portion of the heat release. As seen in Figure 5.35, the advanced injection timing pressure curve has a secondary peak, which merges into one peak as the injection timing is retarded. Also, the heat release is retarded in the same manner that the injection timing is retarded. The heat release rate is slightly higher with the retarded timing: 18J/deg for 7° BTDC versus 25 J/deg for 1° BTDC.

In the testing with the heated intake air system, an advance of the DME LTHR and HTHR was observed. With increasing intake air temperature, the LTHR portion decreases slightly, and the HTHR portion increases slightly. However, the temperature did not impact the timing of the diesel fuel ignition nor the magnitude. With increasing

intake air temperature, the bulk temperature increased. This resulted in an increase in the NO_x emissions, with an increase in NO and a decrease in NO₂. CO, Methane and total hydrocarbons were lower as the intake air was heated. Also, there was less DME present in the exhaust gas, so the heating allowed for greater combustion efficiency of the DME. The TEOM and SMPS data, Figures 5.63 and 5.64, showed that the intake air heating produced an increase in the total PM mass, and an increase in the number of particles observed in the accumulation mode.

5.9.5 Influence of High Temperature Heat Release from DME

As shown in Figures 5.13 and 5.24, with increasing DME concentration the NO emissions increase, with the high temperature heat release (HTHR) peak increasing and advancing towards the low temperature heat release (LTHR) peak. A similar trend is seen within the DME/Air HCCI work performed by Iida and Igarashi in a single cylinder Yanmar engine [231].

In Iida and coworkers' research, they measured a reduction in NO_x emissions in comparison to diesel fuel [231]. While NO_x increased with equivalence ratio with diesel fuel, from 100 to almost 250 ppm from their single cylinder Yanmar engine running at 800rpm, for DME HCCI, the NO_x were less than 50ppm [231]. However, the data does not reflect whether the NO_x increase is due to NO or NO₂. This research reflects a different trend with respect to NO_x emissions, and further elucidates the data presented by Iida and coworkers. In this research, while the NO_x emissions are still lower for the DME in a mixed mode combustion configuration, as the DME concentration is raised

beyond 25% energy equivalent, the amount of NO begins to increase and the NO₂ decreases. The magnitude of the HTHR peak at the 44% DME energy equivalent begins to approach the same magnitude of the diesel fuel heat release peak when running normal BP15 diesel, indicating that possibly the thermal NO mechanism is contributing more than the NO₂ pathways.

5.9.6 Hydrocarbons in Exhaust Species

As is seen with HCCI engines, hydrocarbon species in the exhaust system increase. In the case of this research, hydrocarbon species were seen to increase over normal diesel operation.

Total hydrocarbon species were collected with the AVL CEB II, and light hydrocarbon species were collected with a gas chromatograph. As shown in this research and expressed in the literature, light hydrocarbon species are present in exhaust when diesel fuel is used. In this mixed mode combustion configuration research with the DME and then with the DME/Methane blend, both species showed up in the GC results as unreacted species or species that were formed in the combustion process and frozen upon the exhaust stroke. However, other light hydrocarbons that would show up in the BP15 diesel fuel traces appeared but in much lower quantities in the mixed mode combustion configuration.

Based on the research by Hori and coworkers [40, 229], one could conclude that the light hydrocarbons that were present in the early part of the diesel spray vaporization and before its ignition, and in the gas phase oxidation around the diesel spray flame, were

able to participate in the low temperature combustion of the DME fuel and were involved in the NO to NO₂ conversion. It could be concluded that the light hydrocarbons from the diesel fuel spray were consumed in the reaction to produce the NO₂, and then the other hydrocarbons that were collected and show peaks in the GC must be from the DME fueling, which were mostly DME and Methane. The Methane contribution was higher when the mixed mode combustion configuration was fumigated with Methane. One could make this assertion because in all work with DME, very little if any of the light hydrocarbons show up in the GC traces, while with normal diesel operation they appear.

While most of the light hydrocarbon species from the combustion process for each test condition could be quantified, there were some species that appeared at various retention times that are unknowns. Figure 5.84 shows a GC trace for 25% DME energy equivalent mixed mode combustion at 7° BTDC. As is shown in this figure, there are two unidentified peaks. The first is located at 26.5 minutes and falling between dimethyl ether and the butane. The other peak is located at 29.5 minutes. It is unclear what either of these peaks may be. However, with this particular GC set up, the higher molecular weight molecules take a longer time to show up in the trace, so it would be possible to conclude that the first peak at 26.5 minutes has a molecular weight between 46 (DME) and 58 (Butane). It has been suggested that this peak may be butylene. The second peak is more difficult to determine, but it would have a molecular weight higher than 58.

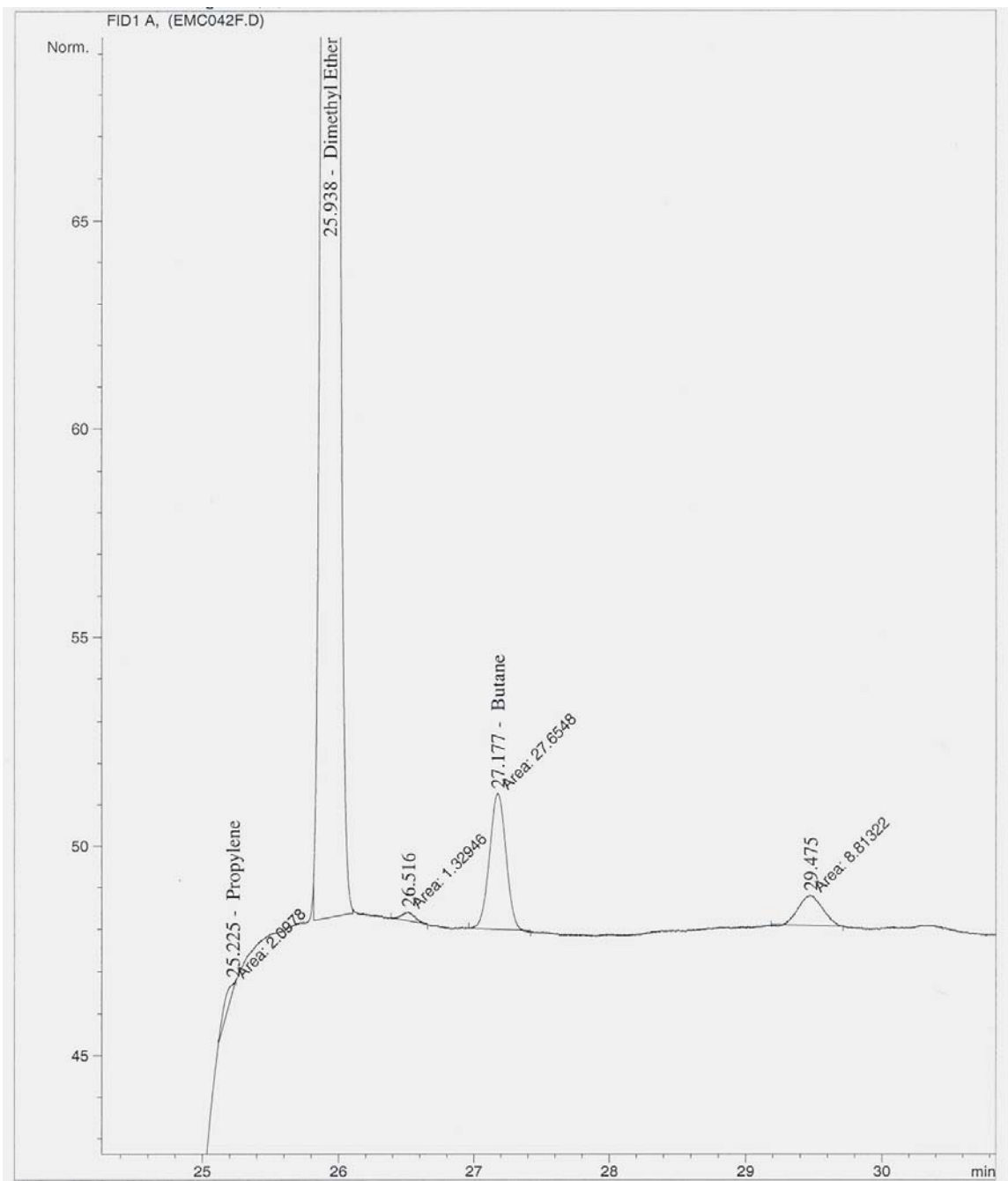


Figure 5.84: GC Trace for 25% DME energy equivalent mixed mode combustion at 7° BTDC: FID trace in the later retention time (x-axis) region at 225°C

5.9.7 Effect of Methane Addition

Based on the data collected for the DME/Methane blends, it appears that the Methane served to increase the pressure and bulk temperature from the combustion process, and reduced the heat release from the diesel fuel portion. This led to lower NO_x per power output, with higher NO and lower NO₂ in comparison to the use of just DME as the fumigated fuel. While the Methane addition seemed to make a slight impact on the combustion of DME and resulted in 2-3ppm less in the exhaust, there were overall higher hydrocarbon emissions, mainly of unreacted Methane. The additional pressure and bulk temperature in the exhaust system provided more conversion of the CO to CO₂, in comparison to a system with just DME.

According to research by Hori and coworkers, the Methane reactions in a low temperature environment would not support the reaction of NO to NO₂ as effectively as some other hydrocarbons[229]. This is due to the slow oxidation of Methane that produces a limited amount of HO₂, and the role of the methyl radicals in reducing NO₂ via this reaction: $\text{CH}_3 + \text{NO}_2 \rightarrow \text{CH}_3\text{O} + \text{NO}$ [229]. Thus, as seen in this research, the addition of a small amount of Methane to the fumigated fuel provided a larger pool of methyl radicals, as compared to the fumigation of DME alone, and resulted in an increase in the NO emissions in the exhaust gases as a result of the faster reaction of the NO₂ reduction to NO [229]. This is also seen and supported in the work by Amano and Dryer, as the oxidation of Methane more readily occurs via the $\text{CH}_3 + \text{NO}_2 \rightarrow \text{CH}_3\text{O} + \text{NO}$ reaction [232].

Combustion characteristics of a natural gas/DME mixture were studied numerically in a HCCI engine configuration [219]. This data was compared to experimental data collected by Chen and coworkers [214]. Kong confirmed that the low temperature heat release is more pronounced as the amount of DME increases within the natural gas/DME blend. His model also shows that as the natural gas and the DME concentration is increased, the amount of NO_x emissions is decreased, confirming and comparing to the work by Chen and coworkers [219]. While it is important to note this work, and to note that Kong has provided temporal histories of combustion intermediate species, a direct comparison to the Methane and DME blend work cannot be made. Kong's work does provide insight into the intermediate species from his model which would also be acting in this research [219]. Kong indicates that during the early chemical reactions, the concentrations of H₂O₂ and HO₂ increase rapidly before the first stage of ignition, with a small amount of OH forming. The species of H₂O₂ and HO₂ are associated with the low temperature heat release. As the compression continues and the intake air temperature rises, the temperature accelerates the decomposition of the H₂O₂ into OH radicals [219]. During the second stage of ignition, the concentration of H₂O₂ decreases as OH is formed. The decomposition of the H₂O₂ at about 1000K and the consumption of the remaining fuel results in ignition in Kong's calculations [219].

5.9.8 Effect of Mixed Mode Combustion on particulate matter

Particulate Matter (PM) data from a TEOM and from an SMPS was collected in the experiments for this research. Total PM data was collected with the TEOM. With the

SMPS data, particles in the size range of approximately 6nm to 250nm were collected.

Some BG-2 filters were collected to get an indication of the PM composition.

Total PM increased with increasing DME concentration, and was higher with DME in a mixed mode combustion configuration than with BP15 diesel fuel. Total PM also increased with retarded injection timing with the DME in a mixed mode combustion configuration. Also, Total PM increased with increasing intake air temperature with the DME in a mixed mode combustion configuration and was higher than with BP15 diesel fuel.

SMPS data showed that with the DME in a mixed mode combustion configuration the number of particles in the size range was reduced. Coupled with the TEOM data, this suggests that more large coarse particles were created with the DME in a mixed mode combustion configuration.

BG-2 filters were collected and digital pictures were presented. The BG-2 filters suggest that the PM with the DME in a mixed mode combustion configuration have more mass than with the conventional BP15 diesel fuel regardless of injection timing. Total hydrocarbon data shows that with the DME in a mixed mode combustion configuration, hydrocarbons are increased. Since the total amount of light hydrocarbons from the GC could not be completely quantified, it is unclear what the total is. However, from what was quantified, the GC showed approximately 30% of the hydrocarbons that were collected by the AVL CEB II in ppm. Therefore, there may have been some heavier hydrocarbons agglomerating on the PM.

The increase in PM with the DME in a mixed mode combustion configuration may be the result of the increased heating in the cylinder providing for a wider zone for

PM agglomeration and for a sustained time period. There were higher rates of PM formation. This was due to more soot precursors in and around the spray flame as a result of the shift in stoichiometry in the diesel spray flame due to DME competing for O₂ to oxidize. However, it is unclear whether all of the DME is being completely consumed, or if some of this is participating in the PM agglomeration. Further study of the PM through Soxhlet extraction of the BG-2 filters would provide an indication of the amount of hydrocarbons and other materials that have condensed on the PM in the combustion zone versus the purely soot portion.

5.10 Conclusions

For this research, a DDC 2.5L light duty turbocharged diesel was operated at 1800 rpm and 61 ft-lbs of torque, a BMEP of approximately 4.1. The engine was set to operate with a gaseous fuel fumigated in the intake air system, and with a single pulse injection of BP15 diesel fuel which was controlled for the entire set of research. All research data points were compared to the same fuel injection scheme with the normal BP15 diesel operation.

In the first set of experiments, DME concentration was spanned from 15% up to 44% on an energy equivalent basis. It was found that the lowest NO_x emissions, and more specifically the lowest NO and highest NO₂ was at a 25% DME energy equivalent for a diesel pilot injection timing of 7° BTDC. For all DME concentrations, NO_x was reduced by approximately 20% on a brake specific power basis. For the 25% concentration, NO was 50% lower, and NO₂ was over 140% higher in comparison to the

baseline diesel case. As the bulk cylinder temperature increased above about 1100K in the second stage of the DME heat release, the NO to NO₂ conversion subsided, and additional heating increased the thermal NO contribution. Chemkin modeling of a HCCI system with DME showed an increase in the HO₂ concentration with increasing DME concentration. As the HO₂ decreased, H₂O₂ increased, indicating temperature favoring the production of hydrogen peroxide. Based on these results, the rest of the experiments were performed at this 25% DME concentration test condition as the baseline mixed mode combustion configuration.

The second set of experiments involved spanning the fuel injection timing of the BP15 diesel fuel pilot. NO_x emissions decreased with retarded injection timing, up to 40% in comparison to BP15 diesel emissions. Both NO and NO₂ emissions decreased. While the bulk temperature was kept between 1000K and 1100K for a longer residence time, the late injection timing of the diesel fuel relative to the 2nd stage heat release (HTHR) of the DME did not provide additional conversion of NO to NO₂. It is unclear if the temperature was too high for this conversion to occur, or if the availability of hydrocarbon species to produce the HO₂ radicals and aid in the NO to NO₂ conversion was lacking as a result of the late timing. However, the late timing resulted in lower overall NO_x emissions, and may be only the result of less time for thermal NO formation from the diesel fuel spray heat release.

The third study utilized intake air heating to study its impact on the ignition and combustion of DME, and on the NO_x emissions. For all increases in the intake air temperature, the NO_x increased. The NO increased, but was still 50% less in comparison to the BP15 baseline diesel fuel. NO₂ emissions were also decreasing with increasing

intake air temperature. With the increase in intake air temperature, the bulk temperature associated with the 2nd stage heat release (HTHR) was above 1200K. Therefore, the heating of the air may have been too high to effectively convert NO to NO₂, shortening this phase, and yet providing a longer time for thermal NO production. The GC data showed that with the increase in intake air heating, the small amount of DME that was present was decreasing and the amount of Methane that was being produced from the available methyl radicals was also decreasing. However, there was no significant increase in the NO₂ emissions. Again, this may indicate that a threshold temperature was reached where the NO to NO₂ conversion was not effective.

The final set of experiments involved fumigating the DME mixed mode combustion configuration with a small amount of Methane, 5 SLPM (6.5% energy equivalent), as well as taking an exploratory set of data on the effect of injection timing and intake air heating. With this small addition of Methane, a 5 % reduction in NO_x emissions was observed over the DME mixed mode combustion configuration. NO emissions increased, while the NO₂ emissions decreased. As discussed previously, Methane is not considered as an effective hydrocarbon for the NO to NO₂ conversion, so the results of the NO and NO₂ seem reasonable in comparison to DME. The NO_x reduction trend with injection timing of the diesel fuel pilot and the NO_x increase with the intake air heating follow the same pattern as seen with the DME mixed mode combustion configuration presented before. It was clear from the pressure trace and heat release that the Methane was contributing to combustion process. While pressure was higher when using the Methane in comparison to the DME mixed mode combustion configuration, there was a suppression of the diesel fuel heat release.

While the results and discussion of this research provide some interesting insight into a DME mixed mode combustion configuration, there are many questions that arise from the research. Those will be presented and discussed in Chapter 6.

Chapter 6

Summary, Conclusions, and Suggestions for Future Work

6.1 Summary

Before stating conclusions deduced from the experimental data, the motivation and objectives of this research will be restated. The motivation for this research was to study strategies that could be used to reduce NO_x emissions from compression ignition engines to meet current and future US EPA emissions regulations. There were two strategies that were studied:

1. Modifying the chemical structure of the fuel, specifically reducing the iodine value and thus saturation of methyl esters of biodiesel, to reduce the NO_x emissions produced at the spray flame
2. Using a mixed mode combustion system to modify the combustion process

6.2 Observations and Conclusions

Based on the results presented in Chapters 4 and 5 for each of the NO_x reduction strategies, the following observations and conclusions can be made.

6.2.1 NO_x Reduction through fuel modification: Hydrogenated Biodiesel

Observations:

1. The 20% soy-based biodiesel blend showed increases in NO_x emissions across the 4 engine modes.
2. The 40% soy-based biodiesel blend and both hydrogenated biodiesel blends showed NO_x reductions for all 4 engine modes, and in all cases below the emissions levels for the conventional ULSD fuel.
3. The pressure, heat release rate, needle lift and bulk cylinder temperature figures are all very similar for each fuel tested. There was no correlation that could be made from minor changes in these figures to the amount of NO_x emissions reduced.
4. If a higher adiabatic flame temperature indicates an increase in the NO_x emissions as a result of the number of double bonds in the biodiesel fuel, then a decrease in those double bounds would lead to a decrease in the NO_x emissions. This data and the adiabatic flame temperature calculation support this conclusion.
5. Fuel injection pressure increased as the needle lifted higher to deliver the required fuel in the same timing. This increase in fuel injection pressure and its affect on NO_x emissions is unknown.
6. It may also be possible that the chemistry of the fuel affects the physical properties of the fuel as it is delivered into the cylinder. Specifically, that the higher density and lower volatility both produce a longer vaporization and a larger droplet spray field zone, thus causing higher NO_x emissions. However, the

density of the B100 and H100 are similar, which does not explain the reduction in NO_x result for the H20 and H40 fuel blends. The boiling range information for the neat fuels shows that the volatility of the biodiesel fuels are similar, and with higher volatility than the BP 15 diesel fuel. Thus, the higher volatility and shorter vaporization would lead to lower NO_x emissions. Heat Release data showed similar vaporization, and yet lower NO_x emissions with the H20 fuel.

7. Similar NO_x results were shown with single vs. double injection of fuel.

Conclusions:

Based on the discussion regarding the theories for the biodiesel NO_x effect, the results seen in the NO_x emission data would have to be explained by the increase in adiabatic flame temperature for the soy-based biodiesel and the Prompt NO_x effect as a result of the change in the biodiesel fuel properties between the soy-based biodiesel and the hydrogenated biodiesel. Also, the use of a neat fuel in the experiments would have provided for a greater difference in the NO_x data, thus indicating the actual impact of the change in the chemistry of the hydrogenated biodiesel fuel.

6.2.2 NO_x Reduction through Mixed Mode Combustion

First Set of Experiments: DME concentration spanned from 15% up to 44% on an energy equivalent basis

1. It was found that the lowest NO_x emissions, and more specifically the lowest NO and highest NO₂ was at a 25% DME energy equivalent for a diesel pilot injection timing of 7° BTDC.

2. For all DME concentrations, NO_x was reduced by approximately 20% on a power basis.
3. For the 25% DME energy equivalent concentration, NO was the 50% lower and NO₂ was over 140% higher in comparison to the baseline diesel case.
4. As was shown in the bulk temperature information, as the temperature increased above about 1100K in the HTHR of the DME heat release, the NO to NO₂ conversion subsided, and additional heating increased the thermal NO contribution.
5. Chemkin modeling of a HCCI system with DME showed an increase in the HO₂ concentration with increasing DME concentration. As the HO₂ decreased, H₂O₂ increased, indicating temperature favoring the production of hydrogen peroxide.

Conclusions:

In this system, greater utilization of DME did not produce a higher NO_x reduction because of the increasing cylinder pressure driving up the adiabatic flame temperature of the fuels in the system and thus increasing the NO emissions. While the DME concentration in the intake increasing, the NO_x were the same, but a greater amount of NO was converted to NO₂ because of the increasing HO₂ concentration available.

Second Set of Experiments: Spanning the fuel injection timing of the BP15 diesel fuel pilot injection

1. NO_x emissions decreased with retarded injection timing, up to 40% in comparison to BP15 diesel emissions. Both NO and NO₂ emissions decreased.
2. While the bulk temperature was kept between 1000K and 1100K for a longer residence time, the late injection timing of the diesel fuel injection and heat release did not provide additional conversion of NO to NO₂. It is unclear if the temperature was too high for this conversion to occur, or if the availability of hydrocarbon species to produce the HO₂ radicals and aid in the NO to NO₂ conversion was lacking as a result of the late timing.
3. The late timing resulted in lower overall NO_x emissions, and may be only the result of less time for the thermal NO from the diesel fuel spray heat release.

Conclusions:

Earlier injection timing provides more time for NO to NO₂ conversion but with higher overall NO_x emissions.

Third Set of Experiments: Utilized intake air heating to study the impact on the ignition and combustion of DME, and on the NO_x emissions

1. For all increases in the intake air temperature, the NO_x increased. The NO increased, but was still 50% less in comparison to the BP15 diesel fuel.
2. NO₂ emissions were also decreasing with increasing intake air temperature.

3. With the increase in intake air temperature, the bulk temperature associated with the DME HTHR was above 1200K. Therefore, the heating of the air may have been too high to effectively convert NO to NO₂, shortening this phase, and yet providing a longer time for thermal NO production.
4. The GC measurement of exhaust composition showed that with the increase in intake air heating, the small amount of DME that was present was decreasing and the amount of methane that was being produced from the available methyl radicals was also decreasing.

Conclusions:

Earlier retarded ignition of the DME would require cooling the intake air, thus providing more time for HO₂ production and NO to NO₂ conversion.

Fourth Set of Experiments: Fumigation of the DME Mixed Mode Combustion configuration with a small amount of methane, 5 SLPM (6.5% energy equivalent), as well as taking an exploratory set of data on the effect of injection timing and intake air heating

1. With this small addition of methane, a 5 % reduction in NO_x emissions was observed over the DME Mixed Mode Combustion configuration.
2. NO emissions increased, while the NO₂ emissions decreased.
3. The NO_x reduction trend with injection timing of the diesel fuel pilot and the NO_x increase with the intake air heating follow the same pattern as seen with

the DME Mixed Mode Combustion configuration: as timing is retarded, NO_x decreases and as intake air is heated, NO_x increases.

4. It was clear from the pressure and heat release rate figures that the methane was contributing to combustion process. While pressure was higher when using the methane in comparison to the DME Mixed Mode Combustion configuration, there was a suppression of the diesel fuel heat release.

Conclusions:

The presence of the methane, and therefore the methyl radical in the presence of NO₂ provided for the reaction $\text{CH}_3 + \text{NO}_2 \rightarrow \text{CH}_3\text{O} + \text{NO}$, and thus the oxidation and utilization of methane to occur in the system.

6.3 Suggestions for Future Work

Upon examination of the results and conclusions, it is apparent that this research could be extended to gain further insight. The suggestions for further work will be discussed by the strategy that was researched.

6.3.1 NO_x Reduction through fuel modification: Hydrogenated Biodiesel

While the research aimed to demonstrate that the hydrogenated biodiesel fuel could reduce NO_x emissions, there were some theories that were not addressed and some questions that deserve further research.

1. Comparison of the hydrogenated biodiesel fuel to other researchers' data should be pursued if possible. However, performing further experiments with the hydrogenated biodiesel fuel with modifications of fuel injection parameters, engine turbocharger and EGR parameters may yield more explanation of why this particular engine is yielding lower NO_x emissions while other researchers are showing neutral or increase NO_x emissions with methyl oleate.
2. A study of the effect of fuel injection pressure could be completed, with holding the injection timing constant and observing the change in exhaust emissions based on changes in injection pressure of the fuel spray.
3. The work by Boulanger and coworkers suggests that isolating the physical properties of the methyl esters can provide insight through experimentation and modeling of the physics of the process [204]. Specifically, comparing methyl oleate and methyl linoleate would explain what is found with changes in biodiesel chemical composition.
4. Experimental work in spray break up and droplet vaporization time scales would be useful to explain the onset of ignition for different methyl esters.
5. Imaging of biodiesel fuel spray, plume size and thermal mapping similar to the work by Dec [15, 29, 233] would be useful to determine if the burning of the biodiesel is creating a reduced area for NO_x production in relation to the temperature of the flame zone.

6.3.2 NO_x Reduction through Mixed Mode Combustion

While the research aimed to demonstrate a mixed mode combustion system with as much NO_x reduction as possible, there are observations that suggest further research.

1. After reviewing the diesel pilot injection data, it appears that advancing the pilot diesel to 9 ° BTDC or earlier may have allowed for a higher DME content to be used, and thus reduced the heat release from the HTHR DME as a result of the diesel fuel pilot vaporization. This may delay the onset of H₂O₂ production, and increase the HO₂ radical for greater NO to NO₂ conversion.
2. There are other methods that would essentially reduce the fast heat release of HTHR DME ignition, prolonging the low temperature combustion and conversion of the NO to NO₂. This might include the use of EGR or some gaseous fuel that slows the kinetics of the second stage heat release. Also, liquid fuels that would form light hydrocarbons through pyrolysis would be of interest since those components would potentially be involved in the low temperature combustion in the reactions outside of the fuel spray.
3. Based on the work by Hori [40, 229], the suggestion that propane and ethane would produce more conversion of NO to NO₂ in the low temperature combustion would be of interest to study in combination with DME. The radical contribution of the propane may increase the temperature range for the conversion, and produce a greater result.

4. Use of a motored engine would provide a means to study the partial oxidation products in the exhaust through adjustment of the compression ratio and quenching of the exhaust after partial combustion [234]. This would help explain the types of gaseous hydrocarbons in the exhaust in this mixed mode combustion process.
5. Some further work into understanding the increase in particulate matter mass is suggested by this data. While much research into DME shows that this and many other oxygenates reduce particulate matter emissions, it is unclear why this mixed mode combustion process would be producing more particulate matter.
6. To assist in elucidating what occurs in the HCCI combustion process of DME and DME /methane blend, a series of models could be developed with Chemkin. The chemical mechanisms for methane combustion have been available for some time, and the mechanisms for DME combustion have been developed by several groups [23, 235]. It seems that the mechanisms developed by Lawrence Livermore National Laboratory are the most common set in use [23, 142]. These could be incorporated with NO_x mechanisms (if not already available in the DME and methane mechanisms) so that the model can yield NO and NO₂ predictions. It would be important to consider the work by Hori and Dagaut in the NO_x modeling mechanisms selection[26, 229]. Researchers have shown that simple zero dimensional kinetic models are sufficient to predict the combustion process in an HCCI engine, since the heat release is a global non-propagating autoignition process [142]. In the case of a pilot injection of fuel, the modeling becomes more difficult as CFD code would be required to completely model the system.

7. Using combustion video of the engine combustion process may provide more significant indication of what is occurring during the process. While flame luminosity in the infrared and normal light would show the diesel flame ignition, the DME cool flame would be best observed by ultraviolet light. Thus, a camera and filters capable of both would provide the best inspection and evidence of continued experimentation with DME in a mixed mode combustion process.

Bibliography

1. EPA. *Final Emission Standards for 2004 and Later Model Year Highway Heavy-Duty Vehicles and Engines (EPA 420-F-00-026)*. 2000 [cited].
2. Demirbas, A., *Biodiesel Impacts on Compression Ignition Engine (CIE): Analysis of Air Pollution Issues Relating to Exhaust Emissions*. *Energy Sources*, 2005(27): p. 459-558.
3. Ross, R., *Air Pollution and Industry*. 1972, New York, New York: Van Nostrand Reinhold Company.
4. Wark, K., Warner, C., Davis, W., *Air Pollution: Its Origin and Control*. 1998, Menlo Park, CA: Addison Wesley Longman, Inc.
5. WHO, *Diesel Fuel and Exhaust Emissions*. 1st ed. 1996, Stuttgart, Germany: World Health Organization, Wissenschaftliche Verlagsgesellschaft. 389.
6. Stone, R., *Introduction to Internal Combustion Engines; 2nd edition*. 2nd ed. 1992, Warrendale, PA: Society of Automotive Engineers.
7. Blakeman, P.G., Chiffey, A.F., Phillips, P.R., Twigg, M.V., Walker, A.P., *Developments in diesel emission aftertreatment technology*. Society of Automotive Engineers, 2003(2003-01-3753E).
8. EPA. *Heavy-Duty Engine and Vehicle Standards and Highway Fuel Sulfur Control Requirements (EPA420-F-00-057)*. 2000 [cited].
9. EPA. *Proposed Heavy-Duty Engine and Vehicle Standards and Highway Diesel Fuel Sulfur Control Requirements (EPA420-F-00-022)*. 2000 [cited].
10. EPA. *Clean Diesel Trucks, Buses, and Fuel: Heavy-Duty Engine and Vehicle Standards and Highway Diesel Fuel Sulfur Control Requirements (the "2007 Heavy-Duty Highway Rule")*. 2001 [cited].
11. Heywood, J.B., *Internal Combustion Engine Fundamentals*. 1988, New York: McGraw-Hill.
12. Glassman, I., *Combustion*. 2nd ed. 1996, Orlando, FL.: Academic Press.
13. Pfahl, U., Fieweger, K., Adomett, G., *Self-Ignition of Diesel-Relevant Hydrocarbon-Air Mixtures under Engine Conditions*. International Symposium on Combustion (26th), 1996: p. 781 - 789.

14. Higgins, B., Siebers, D., *Diesel-Spray Ignition and Premixed-Burn Behavior*. Society of Automotive Engineers, 2000(2000-01-0940).
15. Dec, J., Espey, C., *Chemiluminescence Imaging of Autoignition in a DI Diesel Engine*. Society of Automotive Engineers, 1998(982685).
16. Curran, H., Gaffuri, P., Pitz, W., Westbrook, C., *A Comprehensive Modeling Study of n-Heptane Oxidation*. Combustion and Flame, 1998. **114**: p. 149-177.
17. Westbrook, C., *Chemical Kinetics of Hydrocarbon Ignition in Practical Combustion Systems*. International Symposium on Combustion (28th), 2000. **28**: p. 1563-1577.
18. Curran, H., Gaffuri, P., Pitz, W., Westbrook, C., *A Comprehensive Modeling Study of iso-Octane Oxidation*. Combustion and Flame, 2002. **129**: p. 253-280.
19. Flynn, P., Durrett, R., Hunter, G., Loye, A., Akinyemi, O., Dec, J., Westbrook, C., *Diesel Combustion: An Integrated View Combining Laser Diagnostics, Chemical Kinetics, and Empirical Validation*. Society of Automotive Engineers, 1999(1999-01-0509).
20. Tanaka, S., Ayala, F., Keck, J., Heywood, J., *Two-stage ignition in HCCI combustion and HCCI control by fuels and additives*. Combustion and Flame, 2003. **132**: p. 219-239.
21. Nash, J.J., Francisco, J.S., *Unimolecular Decomposition Pathways of Dimethyl Ether: An Ab Initio Study*. J. Phys. Chem. A, 1998. **102**(1): p. 236-241.
22. Maricq, M.M., Szente, J.J., Hybl, J.D., *Kinetic Studies of the Oxidation of Dimethyl Ether and Its Chain Reaction with Cl₂*. J. Phys. Chem. A, 1997. **101**(28): p. 5155-5167.
23. Curran, H., Pitz, W., Westbrook, C., Dagaut, P., Boettner, J-C., Cathonnet, M., *A Wide Range Modeling Study of Dimethyl Ether Oxidation*. Inter. Journal of Chemical Kinetics, 1998. **30**(3): p. 229-241.
24. Curran, H., Fischer, S., Dryer, F., *The Reaction Kinetics of Dimethyl Ether. II: Low-Temperature Oxidation in Flow Reactors*. International Journal of Chemical Kinetics, 2000. **32**(12): p. 741-769.
25. Fischer, S., Dryer, F., Curran, H., *The Reaction Kinetics of Dimethyl Ether. I: High-Temperature Pyrolysis and Oxidation in Flow Reactors*. Int. Journal of Chemical Kinetics, 2000. **32**: p. 713 - 740.
26. Dagaut, P., Luche, J., Cathonnet, M., *The Low Temperature Oxidation of DME and Mutual Sensitization of the Oxidation of DME and Nitric Oxide*:

- Experimental and Detailed Kinetic Modeling*. Combust. Sci. and Tech., 2001. **165**: p. 61 - 84.
27. Obert, E., *Internal Combustion Engines: Analysis and Practice*. 2nd ed. 1950, Scranton, PA: International Textbook Company.
 28. Chiu, W., Shahed, S., Lyn, W., *A Transient Spray Model for Diesel Combustion*. Society of Automotive Engineers- Transactions, 1976. **85**(760128): p. 502-512.
 29. Dec, J., *A Conceptual Model of DI Diesel Combustion Based on Laser-Sheet Imaging*. Society of Automotive Engineers, 1997(970873): p. 1 - 30.
 30. Fenimore, C., *Formation of Nitric Oxide in Premixed Hydrocarbon Flames*. International Symposium on Combustion (13th), 1970: p. 373-380.
 31. Turns, S., *An Introduction to Combustion: Concepts and Applications*. 1996, New York: McGraw-Hill, Inc.
 32. Bowman, C., *Control of Combustion-Generated Nitrogen Oxide Emissions: Technology Driven by Regulations*. International Symposium on Combustion (24th), 1992: p. 859-878.
 33. Miller, J., Bowman, C., *Mechanism and Modeling of Nitrogen Chemistry in Combustion*. Prog. Energy and Combust. Sci., 1989. **15**(4): p. 287-338.
 34. Challen, B., Baranescu, R., *Diesel Engine Reference Book*. 2nd ed. 1999, Warrendale, PA: Society of Automotive Engineers.
 35. Merryman, E., Levy, A., *Nitrogen Oxide Formation in Flames: The roles of NO₂ and fuel nitrogen*. International Symposium on Combustion (15th), 1975: p. 1073-1083.
 36. Cernansky, N., Sawyer, R., *NO and NO₂ formation in a turbulent hydrocarbon/air diffusion flame*. International Symposium on Combustion (15th), 1975: p. 1039-1050.
 37. Hilliard, J., Wheeler, R., *Nitrogen Dioxide in Engine Exhaust*. Society of Automotive Engineers Transactions, 1979. **88**(790691).
 38. Hori, M., Matsunaga, N. *Conversion of NO to NO₂ by the mixing of combustion of air containing low-level hydrocarbons*. in *Proceedings of the 3rd ASME/JSME Thermal Engineering Joint Conference*. 1991. Reno, NV.
 39. Hori, N., Matsunaga, N., Marinov, N., Pitz, W., Westbrook, C., *An experimental and kinetic calculation of the promotion effect of hydrocarbons on the NO-NO₂ conversion in a flow reactor*. International Symposium on Combustion (27th), 1998: p. 389-396.

40. Hori, M., Matsunaga, N., Malte, P., Marinov, N., *The effect of low-concentration fuels on the conversion of nitric oxide to nitrogen dioxide*. International Symposium on Combustion (24th), 1992: p. 909-916.
41. Meunier, P., Costa, M., Carvalho, M., *The formation and destruction of NO in turbulent propane diffusion flames*. Fuel, 1998. 77(15): p. 1705-1714.
42. Cheng, A., Upatnieks, A., Mueller, C., *Investigation of the impact of biodiesel fuelling on NOx emissions using an optical direct injection diesel engine*. Int. J. Engine Research, 2006. 7(4): p. 297-347.
43. Upatnieks, A., Mueller, C., *Clean, Controlled DI Diesel Combustion Using Dilute, Cool Charge Gas and a Short-Ignition-Delay, Oxygenated Fuel*. Society of Automotive Engineers, 2005(2005-01-0363).
44. Upatnieks, A., Mueller, C., Martin, G., *The Influence of Charge-Gas Dilution and Temperature on DI Diesel Combustion Processes Using Short-Ignition-Delay, Oxygenated Fuel*. Society of Automotive Engineers, 2005(2005-01-2088).
45. ISO, *ISO/DIS 8178-2.2 Reciprocating internal combustion engines- Exhaust emission measurement Part 2: Measurement of gaseous and particulate emissions at site, in International Organization for Standardization Draft International Standard*. 1995, International Organization for Standardization.
46. Johnson, J., Bagley, S., Gratz, L., Leedy, D., *A Review of Diesel Particulate Control Technology and Emissions Effects- 1992 Horning Memorial Award Lecture*. Society of Automotive Engineers, 1994.
47. Richter, H., and Howard, J., *Formation of Polycyclic Aromatic Hydrocarbons and Their Growth to Soot-- A Review of Chemical Reaction Pathways*. Prog. Energy and Combust. Sci., 2000(26): p. 565-608.
48. Warnatz, J., Maas, U., and Dibble, R.W., *Combustion: Physical and Chemical Fundamentals, Modeling and Simulation, Experiments, Pollutant Formation*. 1996, Berlin: Springer-Verlag.
49. Edgar, B., *Dimethyl Ether and Other Oxygenated Fuels for Low Emission Diesel Engine Combustion*, in *Mechanical Engineering*. 1997, University of California-Berkley: Berkley, CA. p. 227.
50. Eastwood, P., *Critical Topics in Exhaust Gas Aftertreatment*. 2000, Baldock, Hertfordshire, England: Research Studies Press LTD.
51. Morris, J.D., Wallace, G.M., *Evaluation of Impact of a Multifunctional Additive Package on European Diesel Passenger Car Emission Performance*. Society of Automotive Engineers, 1990.

52. Schmidt, D., Wong, V., Green, W., Weiss, M., Heywood, J., *Review and Assessment of Fuel Effects and Research Needs in Clean Diesel Technology*. ASME Spring Technical Conference, 2001. **36-1**: p. 23-37.
53. EPA. *A Comprehensive Analysis of Biodiesel Impacts on Exhaust Emissions (EPA420-P-02-001)*. 2002 [cited].
54. Hess, H., *The Impact of Oxygenated Fuels on Diesel Combustion and Emissions*, in *Energy & Geo-Environmental Engineering*. 2002, Pennsylvania State University: University Park, PA.
55. Truex, T., *Interaction of Sulfur with Automotive Catalysts and the Impact on Vehicle Emissions- A Review*. Society of Automotive Engineers, 1999(1999-01-1543).
56. Baranescu, R., *Influence of Fuel Sulfur on Diesel Particulate Emissions*. Society of Automotive Engineers, 1998.
57. Fleisch, T., McCarthy, C., Basu, A., Udovich, C., Charbonneau, P., Slodowske, W., Mikkelsen, S., McCandless, J., *A New Clean Diesel Technology: Demonstration of ULEV Emissions on a Mavistar Diesel Engine Fueled with Dimethyl Ether*. Society of Automotive Engineers, Inc., 1995(950061): p. 42 - 53.
58. Wakai, K., Nishis K., Yoshizaki T., Hiroyasu H., *Ignition Delays of DME and Diesel Fuel Sprays Injected by a D.I. Diesel Injector*. Society of Automotive Engineers, Inc., 1999(1999-01-3600).
59. Verbeek, R., Van der Weide, J., *Global Assessment of Dimethyl-Ether: Comparison with Other Fuels*. Society of Automotive Engineers, Inc., 1997(971607): p. 1 - 12.
60. Phillips, J.G., Reader, G. T., *The Use of DME as a Transportation fuel - A Canadian Perspective*. ASME Fall Technical Conference, 1998. **31-3**: p. 65-71.
61. Sorenson, S.C., Mikkelsen S., *Performance and Emissions of a DI Diesel Engine Fuelled with Neat Dimethyl Ether*. Society of Automotive Engineers, 1995.
62. Kapus, P.E., Cartellieri, W.P, *ULEV Potential of a Car Engine Operated on Dimethyl Ether*. Society of Automotive Engineers, 1995.
63. Tijm, P., Waller, F., Toseland, B., and Peng, X. '*Liquid Phase Di-Methyl EtherTM, A promising New Diesel Fuel*'. in *Energy Frontiers International Conference, Alaska*. 1997.

64. Hansen, J., Voss, B., Joensen, F., Siguroardottir, I., *Large Scale Manufacture of Dimethyl Ether - a New Alternative Diesel Fuel from natural Gas*. Society of Automotive Engineers, Inc., 1995(950063): p. 70 - 79.
65. McMurry, J., *Organic Chemistry, 4th ed.* 1995, Pacific Grove, CA: Brooks/Cole Publishing Company.
66. Marchionna, M., Patrini, R., Giavazzi, F., Pecci, G. *Linear Ethers as High Quality Components for Reformulated Diesel Fuels*. in *Symposium on Removal of Aromatics, Sulfur and Olefins from Gasoline and Diesel presented at the 212th National Meeting (Aug 25-29), American Chemical Society*. 1996. Orlando, FL.
67. Good, D., Francisco, J., *Atmospheric Chemistry of Alternative Fuels and Alternative Chlorofluorocarbons*. Chemical Review, 2003. **103**: p. 4999-5023.
68. Riesenber, K.O., Faupel, W., Blaich, B., Stumpp, G., Ungerer, G., Polach, W., Leonard, R., Schneider, V., Ritter, E., Tschoke, H., Dieter, W., Warga, W., Kaczynski, B., Bauer, H., *Diesel Fuel Injection*. 1st ed. 1994, Stuttgart, Germany: Robert Bosch.
69. Kapus, P., Ofner, H., *Development of Fuel Injection Equipment and Combustion Systems for DI Diesels operated on Dimethyl Ether*. Society of Automotive Engineers, 1995.
70. Ofner, H., Gill, D.W., Krotscheck, C., *DME as Fuel for CI engines - A New Technology and its Environmental Potential*. Society of Automotive Engineers, 1998.
71. Glensvig, M., Sorenson, S.C., Abata, D. L., *An Investigation of the Injection Characteristics of Dimethyl Ether*. ASME Fall Technical Conference, 1997. **29-3**: p. 77-84.
72. Barbour, R.H., Elliott, N.G., Rickeard, D.J., *Understanding Diesel Lubricity*. Society of Automotive Engineers, 2000.
73. Anastopoulos, G., Lois, E., Serdari, A., Zankos, F., Stournas, S., Kalligeros, S., *Lubrication Properties of Low-Sulfur Diesel Fuels in the Presence of Specific Types of Fatty Acid Derivatives*. Energy & Fuels, 2001. **15**: p. 106-112.
74. Nielsen, K., Sorenson, S., *Lubricity Additive and Wear with DME in Diesel Injection Pumps*. American Society of Mechanical Engineers, ICE Fall Technical Conference, 1999. **33-1**(99-ICE-217): p. 145-153.
75. Nikanjam, N., *Diesel Fuel Lubricity: On the Path to Specifications*. Society of Automotive Engineers, 1999(1999-01-1479).

76. Chapman, E., Boehman, A. Tijm, P.J.A., Waller, F., *Emissions Characteristics of a Navistar 7.3L Turbodiesel Fueled with Blends of Dimethyl Ether and Diesel Fuel*. Society of Automotive Engineers 2001 Transactions- Journal of Fuels & Lubricants, 2001. **110**(Section 4): p. 2166-2175.
77. Bechtold, R., *Alternative Fuels Guidebook: Properties, Storage, Dispensing, and Vehicle Facility Modifications*. 1997, Warrendale, PA: Society of Automotive Engineers.
78. Nabi, M.N., Minami, M., Ogawa, H., and Miyamoto, N., *Ultra Low Emission and High Performance Diesel Combustion with Highly Oxygenated Fuel*. Society of Automotive Engineers, 2000.
79. Kajitani, S., Chen, Z., Konno, M., Rhee, K., *Engine Performance and Exhaust Characteristics of Direct-Injection Diesel Engine Operated with DME*. Society of Automotive Engineers, Inc., 1997(972973).
80. Ikeda, M., Mikami, M., Kojima, N., *Exhaust Emission Characteristics of DME/Diesel Fuel Engine*. Society of Automotive Engineers, Inc., 2000(2000-01-2006).
81. Chen, Z., Kajitani, S., Minegisi, K., Oguma, M., *Engine Performance and Exhaust Gas Characteristics of a Compression Ignition Engine Operated with DME blended Gas Oil Fuel*. Society of Automotive Engineers, 1998(982538).
82. Chapman, E., Boehman, A., Tijm, P., Waller, F., *Emission Characteristics of a Navistar 7.3L Turbodiesel Fueled with Blends of Dimethyl Ether and Diesel Fuel*. Society of Automotive Engineers, Inc., 2001(2001-01-3626).
83. Chapman, E., *Emission Characteristics of a Navistar 7.3L Turbodiesel operated with blends of dimethyl ether (DME) and diesel fuel*, in *Energy and Geo-Environmental Engineering, Fuel Science*. 2002, Pennsylvania State University: University Park, PA. p. 185.
84. McCandless, J., Li, Shurong, *Development of a Novel Fuel Injection System (NFIS) for Dimethyl Ether – and Other Clean Alternative Fuels*. Society of Automotive Engineers, 1997.
85. Rouhi, A.M., *Amoco, Haldor Topsoe Develop Dimethyl Ether as Alternative Diesel Fuel*, in *C&EN*. 1995. p. 37-39.
86. Bunting, B., *Combustion, Control, and Fuel Effects in a Spark Assisted HCCI Engine Equipped with Variable Valve Timing*. Society of Automotive Engineers, Inc., 2006(2006-01-0872).

87. Frye, C., Boehman, A., Tijm, P.J.A., *Comparison of CO and NO Emissions from Propane, n-Butane, and Dimethyl Ether Premixed Flames*. Energy & Fuels, 1999. **13**(3): p. 650-654.
88. Mintz, M., Wang, M., Vyas, A., *Fuel-Cycle energy and Emissions Effects of Tripled Fuel-Economy Vehicles*. Transportation Research Record, 1998. **1641**(Paper No. 98-1406): p. 115-122.
89. Mintz, M., Vyas, A., Wang, M., Stodolsky, F., Cuenca, R., Gaines, L., *From Here to Efficiency*. Transportation Research Record, 2000. **1738**(Paper No. 00-1259).
90. Mintz, M., Wang, M., Vyas, A., *Fuel-Cycle Energy and Emissions Impacts of Propulsion System/Fuel Alternatives for Tripled Fuel-Economy Vehicles*. Society of Automotive Engineers, 1999(1999-01-1118).
91. Stork, K., Singh, M., Wang, M., Vyas, A., *Assessment of Capital Requirement for Alternative Fuels Infrastructure Under the Partnership for a New Generation of Vehicle Program*. Transportation Research Record, 1998. **1641**(Paper No. 98-141): p. 123-129.
92. Saricks, C., Rote, D., Stodolsky, F., Eberhardt, J., *Alternatives to Diesel Fuel in California: Fuel-Cycle Energy and Emission Effects of Possible Replacements due to the Toxic Air Contaminant Diesel Particulate Decision*. Transportation Research Record, 2000. **1738**(Paper No. 00-0513): p. 86-93.
93. Hatta, H. *DME Transportation by Deep-Sea Tankers*. in *DME 1 Conference*. 2004. Paris, France: International DME Association.
94. Matsuda, T. *DME R&D in Japan*. in *5th International DME Association Workshop*. 2002. Rome, Italy: International DME Association.
95. Graboski, M.S., and McCormick, R.L., *Combustion of Fat and Vegetable Oil Derived Fuels in Diesel Engines*. Prog. Energy and Combust. Sci., 1998. **24**(2): p. 125-164.
96. Suppes, G., Rui, Y., Regehr, E., *Hydrophilic Diesel Fuels- Ignition Delay Times of Several Different Fuel Blends*. Society of Automotive Engineers, 1997(971686).
97. Duffield, J., Shapouri, H., Grabowski, M., McCormick, R., Wilson, R., *U.S. Biodiesel Development: New Market for Conventional and Genetically Modified Agricultural Products*. 1998, Economic Research Service/USDA: Washington, DC.

98. Sharp, C., Howell, S., Jobe, J., *The Effect of Biodiesel Fuels on Transient Emissions from Modern Diesel Engines, Part I Regulated Emissions and Performance*. Society of Automotive Engineers, 2000(2000-01-1967).
99. McCormick, R., Graboski, M., Alleman, T., Herring, A., Tyson, S., *Impact of Biodiesel Source Material and Chemical Structure on Emissions of Criteria Pollutants from a Heavy-Duty Engine*. Environ. Sci. Tech., 2001. **35**(9): p. 1742-1747.
100. Kinney, A., Clemente, T., *Modifying soybean oil for enhanced performance in biodiesel blends*. Fuel Processing Technology, 2005. **86**: p. 1137-1147.
101. Knothe, G., Matheaus, A., Ryann III, T., *Cetane numbers of branched and straight-chain fatty esters determined in an ignition quality tester*. Fuel, 2003. **82**: p. 971-975.
102. Knothe, G., *Dependence of biodiesel fuel properties on the structure of fatty acid alkyl esters*. Fuel Processing Technology, 2005. **86**: p. 1059-1070.
103. Lapuerta, M., Armas, O., Rodriguez-Fernandez, J., *Effect of biodiesel fuels on diesel engine emissions*. Progress in Energy and Combustion Science, 2008. **34**: p. 198-223.
104. McCormick, R., Williams, A., Ireland, J., Brimhall, M., Hayes, R., *Effects of Biodiesel Blends on Vehicle Emissions: Fiscal Year 2006 Annual Operating Plan Milestone 10.4 (NREL/MP-540-40554)*. 2006, National Renewable Energy Laboratory: Golden, CO.
105. Knothe, G., Sharp, C., Ryan, T., *Exhaust Emissions of Biodiesel, Petrodiesel, Neat Methyl Esters, and Alkanes in a New Technology Engine*. Energy & Fuels, 2006. **20**: p. 403-408.
106. Sharp, C., Ryan III, T., Knothe, G., *Heavy-Duty Diesel Engine Emissions Tests Using Special Biodiesel Fuels*. Society of Automotive Engineers, Inc., 2005(2005-01-3671).
107. Dec, J., *PLIF imaging of NO formation in a DI diesel engine*. Society of Automotive Engineers, 1998(980147).
108. Lapuerta, M., Aramas, O., Ballesteros, R., *Diesel particulate emissions from biofuels derived from Spanish vegetable oils*. Society of Automotive Engineers, 2002(2002-01-1657).
109. Nabi, N., Shahadat, Z., Rhaman, S., Alam Beg, M., *Behavior of diesel combustion and exhaust emission with neat diesel fuel and diesel-biodiesel blends*. Society of Automotive Engineers, 2004(2004-01-3034).

110. Ban-Weiss, G., Chen, J., Buchholz, B., Dibble, R., *A numerical investigation into the anomalous slight NO_x increase when burning biodiesel: a new (old) theory*. Fuel Processing Technology, 2007. **88**: p. 659-667.
111. Nabi, M., Akhter, M., Shahadat, M., *Improvement of engine emission with conventional diesel fuel and diesel-biodiesel blends*. Bioresource Technology, 2006. **97**: p. 372-378.
112. Monyem, A., Van Gerpen, J., Canakci, J., *The Effect of Timing and Oxidation on Emissions from Biodiesel-Fueled Engines*. American Society of Agricultural Engineers, 2001. **44**(1): p. 35-42.
113. Musculus, M., *On the Correlation between NO_x Emissions and the Diesel Premixed Burn*. Society of Automotive Engineers, 2004(2004-01-1401).
114. Musculus, M., *Measurements of the Influence of Soot Radiation on In-Cylinder Temperatures and Exhaust NO_x in a Heavy Duty DI Diesel Engine*. Society of Automotive Engineers, Inc., 2005(2005-01-0925).
115. McCormick, R., Alvarez, J., Grabowski, M., *NO_x Solutions for Biodiesel: Final Report Report 6 in a series of 6 (NREL/SR-510-31465)*. 2003, National Renewable Energy Laboratory: Golden, CO.
116. Szybist, J., Song, J., Alam, M., Boehman, A., *Biodiesel combustion, emissions and emission control*. Fuel Processing Technology, 2007. **88**: p. 679-691.
117. Tat, M., *Investigation of oxides of nitrogen emissions from biodiesel-fueled engines*, in *Department of Mechanical Engineering*. 2003, Iowa State University: Ames, IA.
118. Boehman, A., Morris, D., Szybist, J., Esesn, E., *The Impact of the Bulk Modulus of Diesel Fuels on Fuel Injection Timing*. Energy & Fuels, 2004. **18** p. 1877 - 1882.
119. Szybist, J.P., Boehman, A.L., Taylor, J.D., McCormick, R.L., *Evaluation of Formulation Strategies to Eliminate the Biodiesel NO_x Effect*. Fuel Processing Technology, 2005. **86**(10): p. 1109-1126.
120. Szybist, J., Kirby, S., Boehman, A., *NO_x Emissions of Alternative Diesel Fuels: A Comparative Analysis of Biodiesel and FT Diesel*. Energy & Fuels, 2005. **19**: p. 1484-1492.
121. Zhang, Y., Boehman, A., *Impact of Biodiesel on NO_x Emissions in a Common Rail Direct Injection Diesel Engine*. Energy & Fuels, 2007. **21**: p. 2003-2012.

122. Choi, C., Bower, G., Reitz, R., *Effects of Biodiesel Blended Fuels and Multiple Injections on D.I. Diesel Engines*. Society of Automotive Engineers, 1997(970218).
123. Zhang, L., *A Study of Pilot Injection in a DI Diesel Engine*. Society of Automotive Engineers, Inc., 1999(1999-01-3493).
124. Senatore, A., Cardone, M., Buono, D., Rocco, V., Allocca, L., Vitolo, S., *Performance and Emissions Optimization of a CR Diesel Engine Fuelled with Biodiesel*. Society of Automotive Engineers, Inc., 2006(2006-01-0235).
125. Choi, C., Reitz, R., *A numerical analysis of the emissions characteristics of biodiesel blended fuels*. J. Engng for Gas Turb. and Power, 1999. **121**: p. 31-38.
126. Schmidt, K., Van Gerpen, J., *The effect of biodiesel fuel composition on diesel combustion and emissions*. Society of Automotive Engineers, 1996(961086).
127. Iida, N., Suzuki, Y., Sato, G., Sawada, T., *Effect of intake oxygen concentration on the characteristics of particulate emissions from a D.I. diesel engine*. Society of Automotive Engineers, 1986(861233).
128. Song, J., Zello, V., Boehman, A., *Comparison of the impact of intake oxygen enrichment and fuel oxygenation on diesel combustion and emissions*. Energy & Fuels, 2004. **18**: p. 1282-1290.
129. Lapuerta, M., Aramas, O., Ballesteros, R., Fernandez, J., *Diesel emissions from biofuels derived from Spanish potential vegetable oils*. Fuel, 2005. **84**(773-780).
130. Yuan, W., Hansen, A., Tat, M., Van Gerpen, J., Tan, Z., *Spray, Ignition, and Combustion Modeling of Biodiesel Fuels for Investigating NOx Emissions*. Transactions of the ASAE, 2005. **48**(3): p. 933-939.
131. Lapuerta, M., Hernandez, J., Gimenez, F., *Evaluation of exhaust gas recirculation as a technique for reducing diesel engine NOx emissions*. Proc. Instn. Mech. Engr. Part D, 2000. **214**: p. 85-93.
132. Dickey, D., Ryan T., Matheaus, A., *NOx Control in Heavy-Duty Diesel Engines--Wha is the Limit?* Society of Automotive Engineers, Inc., 1998(980174).
133. Lapuerta, M., Armas, O., Hernandez, J., *Effect of the Injection Parameters of a Common Rail Injection System on Diesel Combustion Through Thermodynamic Diagnosis*. Society of Automotive Engineers, 1999(1999-01-0194).
134. Neely, S., S., Huang, Y., Leet, J., Stewart, D., *New Diesel Emission Control Strategy to Meet S Tier 2 Emissions Regulations*. Society of Automotive Engineers, 2005(2005-01-1091).

135. Hardy, W.L., Reitz, R.D., *A Study of the Effects of High EGR, High Equivalence Ratio, and Mixing Time on Emissions Levels in a Heavy-Duty Diesel Engine for PCCI Combustion*. Society of Automotive Engineers, Inc., 2006(2006-01-0026).
136. Stanglmaier, R., Roberts, C., *Homogeneous Charge Compression Ignition (HCCI): Benefits, Compromises, and Future Engine Applications*. Society of Automotive Engineers, 1999(1999-01-3682).
137. DOE, *Homogeneous Charge Compression Ignition (HCCI) Technology*. 2001, U.S. Department of Energy, Energy Efficiency and Renewable Energy, Office of Transportation Technologies: Washington, D.C.
138. Furutani, M., Ohta, Y., Komatsu, K., *Onset Behavior of Low-Temperature Flames Caused by Piston Compression*. JSAE Review, 1993. **14**(2): p. 12-18.
139. Pucher, G., Gardiner, D., Bardon, M., Battista, V., *Alternative Combustion Systems for Piston Engines Involving Homogeneous Charge Compression Ignition Concepts- A Review of Studies using Methanol, Gasoline, and Diesel Fuel*. Society of Automotive Engineers, 1996(962063).
140. Lee, K., Lee, C., Ryu, J., Kim, H., *An Experimental Study on the Two-State Combustion Characteristics of a Direct-Injection Type HCCI Engine*. Energy & Fuels, 2005. **19**: p. 393-402.
141. Milovanovic, N., Chen, R., *A Review of Experimental and Simulation Studies on Controlled Auto-Ignition Combustion*. Society of Automotive Engineers, 2001(2001-01-1890).
142. Flowers, D., Aceves, S., Westbrook, C., Smith, J., Dibble, *Detailed Chemical Kinetic Simulation of Natural Gas HCCI Combustion: Gas Composition Effects and Investigation of Control Strategies*. Journal of Engineering for Gas Turbines and Power, 2001. **123**: p. 433-439.
143. Christensen, M., Johansson, B., AmnJus, P., Mauss, F., *Supercharged Homogeneous Charge Compression Ignition*. Society of Automotive Engineers, 1998(980787).
144. Martinez-Frias, A., S., Flowers, D., Smith, R., Dibble, R., *Thermal Charge Conditioning for Optimal HCCI Engine Operation*. Journal of Energy Resources Technology-Transactions of the ASME, 2002. **124**: p. 67 - 74.
145. Ryan, T., Matheaus, A. *Fuel Requirements for HCCI Engine Operation*. in *8th Annual Diesel Engine Emissions Reduction (DEER) Meeting, Aug. 25-29. 2002*. San Diego, CA.

146. Sun, Y., Reitz, R., *Modeling Diesel Engine NO_x and Soot Reductgion with Optimized Two-Stage Combustion*. Society of Automotive Engineers, Inc., 2006(2006-01-0027).
147. Ryan, T., Matheaus, A., *Fuel Requirements for HCCI Engine Operation*. Society of Automotive Engineers, 2003(2003-01-1813).
148. Szybist, J., Bunting, B., *Cetane Number and Engine Speed Effects on Diesel HCCI Performance and Emissions*. Society of Automotive Engineers, 2005(2005-01-3723).
149. Stanglmaier, R., Ryan, T., Souder, J., *HCCI Operation of a Dual-Fuel Natural Gas Engine for Improved Fuel Efficiency and Ultra-Low NO_x Emissions at Low to Moderate Engine Loads*. Society of Automotive Engineers, 2001(2001-01-1897).
150. Park, T., Atkinson, R., Clark, N., Traver, M., Atkinson, C., *Operation of a Compression Ignition Engine with a HEUI Injection System on Natural Gas with Diesel Pilot Injection*. Society of Automotive Engineers, 1999(1999-01-3522).
151. Karim, G., *Combustion in Gas Fueled Compression: Ignition Engines of the Dual Fuel Type*. Journal of Engineering for Gas Turbines and Power, 2003. **125**(3): p. 827 - 836.
152. Liu, Z., Karim, G. *Examination of Combustion Characteristics in Dual Fuel Engines*. in *ASME Proceedings of the 7th AIAA/ASME Joint Thermophysics and Heat Transfer Conference*. 1998. Albuquerque, New Mexico.
153. Poonia, M., Ramesh, A., aur, R., *Experimental Investigation of the Factors Affecting the Performance of a LPG- Diesel Dual Fuel Engine*. Society of Automotive Engineers, 1999(1999-01-1123).
154. Nazar, J., Ramesh, A., Nagalingam, B., *Studies on Dual Fuel Operatioin of Karanja Oil and Its Bio-Diesel with LPG as the Inducted Fuel*. Society of Automotive Engineers, 2006(2006-01-0237).
155. Hardenburg, H., Hase,F., *An Empirical Formula for Computing the Pressure Rise Delay of a Fuel from its Cetane Number and from the Relevant Parameters of Direct-Injection Diesel Engines*. Society of Automotive Engineers Transactions, 1979. **88**(790493).
156. Prakash, G., Ramesh, A., Shaik, S., *An approach for estimation of ignition delay ina dual fuel engine*. Society of Automotive Engineers, 1999(1999-01-0232).

157. Garnier, C., Bilcan, A., Le Corre, O., Rahmouni, C., *Characteristics of a Syngas-Diesel Fuelled CI Engine*. Society of Automotive Engineers, 2005(2005-01-1731).
158. Khair, M., *Diesel Engine Technology*. Society of Automotive Engineers Seminar Series. 1998, Warrendale, PA: Society of Automotive Engineers.
159. Khair, M., Lemaire, J., Fischer, S., *Integration of Exhaust Gas Recirculation, Selective Catalytic Reduction, Diesel Particulate Filters, and Fuel-Borne Catalyst for NOx/PM Reduction*. Society of Automotive Engineers, 2000(2001-01-1933).
160. Scarnegie, B., Miller, W., Ballmert, B., Doelling, W., Fischer, S., *Recent DPF/SCR Results Targeting US2007 and Euro 4/5 HD Emissions*. Society of Automotive Engineers, 2003(2003-01-0774).
161. Miller, W., Klein, J., Mueller, R., Doelling, W., Zuerbig, J., *The Development of Urea-SCR Technology for US Heavy Duty Trucks*. Society of Automotive Engineers, 2000(2000-01-0190).
162. Khair, M., Lemaire, J., Fischer, S., *Achieving Heavy-Duty Diesel NOx/PM Levels Below the EPA 2002 Standards--An Integrated Solution*. Society of Automotive Engineers, Inc., 2000(2000-01-0187).
163. Cho, S., *Properly Apply Selective Catalytic Reduction for NOx Removal*. Chemical Engineering Progress, 1994(January): p. 39-45.
164. Johnson, T., *Diesel Emission Control in Review*. Society of Automotive Engineers, 2007(2007-01-0233).
165. Twigg, M., *Progress and future challenges in controlling automotive exhaust gas emissions*. Applied Catalysis B: Environmental, 2007. **70**: p. 2-15.
166. Twigg, M., *Development of platinum catalysts and their use in the control of vehicle exhaust emissions*. Transactions of the Institutions of Mining and Metallurgy, Section B: Applied Earth Science, 2005. **114**(3): p. B158-B172.
167. Tennison, P., Lambert, C., Levin, M., *NOx Control Development with Urea SCR on a Diesel Passenger Car*. Society of Automotive Engineers, 2004(2004-01-1291).
168. Ogunwumi, S., Fox, R., Patil, M., He, L., *In-Situ NH₃ Generation for SCR NOx Applications*. Society of Automotive Engineers, 2002(2002-01-2872).
169. Allanson, R., Walker, A., Blakeman, P., Cooper, B., Hess, H., Silcock, P., *Optimizing the Low Temperature Performance and Regeneration Efficiency of the*

- Continuously regenerating Diesel Particulate Filter (Cr-Dpf) System*. Society of Automotive Engineers, 2002(2002-01-0428).
170. Webpage. www.nett.ca/faq_diesel.html. 2004 [cited].
 171. Heck, R., Farrauto, R., *Catalytic Air pollution Control: Commercial Technology*. 2002, New York, New York: John Wiley & Sons, Inc.
 172. Webpage. www.detroitdiesel.com. 2004 [cited].
 173. Grob, R., *Modern Practice of Gas Chromatography*. 1995, New York, New York: John Wiley & Sons, Inc.
 174. Baugh, P., *Gas Chromatography: A Practical Approach*. 1993, Oxford, England: Oxford University Press.
 175. Barry, E., Grob, R., *Columns for Gas Chromatography*. 2007, Hoboken, NJ: John Wiley & Sons, Inc. .
 176. *Sierra Instruments BG-1 Micro Dilution Test Stand Instruction Manual*. 1995, Sierra Instruments, Inc.: Monterey, CA.
 177. AVL, *AVL Indimodul 621 Indicom 1.3: Product Guide I and II*. 2003, Graz, Austria: AVL List GmbH.
 178. Chapman, E., Hile, M., Pague, M., Song, J., Boehman, A., *Eliminating the NOx Emissions Increase Associated with Biodiesel*. American Chemical Society, Division of Fuel Chemistry, 2003. **48**(2): p. 639-640.
 179. Chapman, E., Boehman, A., *Emissions Characteristics of a Light Duty Diesel Engine Fueled with a Hydrogenated Biodiesel Fuel*. American Chemical Society, Division of Fuel Chemistry, 2006. **51**(1): p. 31-32.
 180. EMA, *Technical Statement on the Use of Biodiesel Fuel in Compression Ignition Engines* (www.enginemanufacturers.org). 2003, Engine Manufacturers Association: Chicago, IL.
 181. NREL, *Biodiesel Handling and Use Guidelines, 3rd edition (DOE/GO-102006-2358)*. 2006, National Renewable Energy Laboratory: Golden, CO.
 182. McCormick, R., Alleman, T., Ratcliff, M., Moens, L., Lawrence, R., *Survey of the Quality and Stability of Biodiesel and Biodiesel Blends in the United States in 2004 (NREL/TP-540-38836)*. 2005, National Renewable Energy Laboratory: Golden, CO.

183. McCormick, R., Alleman, T., Waynick, J., Westbrook, S., Porter, S., *Stability of Biodiesel and Biodiesel Blends: Interim Report*. 2006, National Renewable Energy Laboratory: Golden, CO.
184. Knothe, G., Gerpen, J., Krahl, J., *The Biodiesel Handbook*. 2005, Urbana, IL: AOCS Press.
185. Ma, F., Hanna, M., *Biodiesel production: a review*. *Bioresources Technology*, 1999. **70**: p. 1-15.
186. O'Brien, R., Farr, W., Wan, P., *Introduction to Fats and Oils Technology*. 2000, Champaign, IL: AOCS Press.
187. Achenbach, S., *Personal Communication about the Hydrogenation Process at Twin River Technologies, Cincinnati, OH.*, E. Chapman, Editor. 2006: State College, PA.
188. ASTM, *Test Method D6890-07a Standard Test Method for Determination of Ignition Delay and Derived Cetane Number (DCN) of Diesel Fuel Oils by Combustion in a Constant Volume Chamber*, in *ASTM Book of Standards*. 2007, American Society of Testing and Materials: West Conshohocken, PA.
189. Knothe, G., Bagby, M., Ryan, T., *Precombustion of Fatty Acids and Esters of Biodiesel. A Possible Explanation for Differing Cetane Numbers*. *Journal of American Oil Chemical Society*, 1998. **75**(8): p. 1007-1013.
190. Haas, M., *Report of Biodiesel Sample Coupons Analysis*. 2004, USDA: Philadelphia, PA.
191. ASTM, *Test Method D2500-99 Standard Test Method for Cloud Point of Petroleum Products*, in *ASTM Book of Standards*. 1999, American Society of Testing and Materials: West Conshohocken, PA.
192. ASTM, *Test Method D97-96a Standard Test Method for Pour Point of Petroleum Products*, in *ASTM Book of Standards*. 1996, American Society of Testing and Materials: West Conshohocken, PA.
193. Kazancev, K., Makareviciene, V., Paulauskas, V., Janulis, P., *Cold Flow properties of fuel mixtures containing biodiesel derived from animal fatty waste*. *European Journal of Lipid Science and Technology*, 2006. **108**(2006): p. 753-758.
194. Moser, B., Haas, M., Winkler, J., Jackson, M., Erhan, S., List, G., *Evaluation of partially hydrogenated methyl esters of soybean oil as biodiesel*. *European Journal of Lipid Science and Technology*, 2007. **109**(2007): p. 17-24.

195. ASTM, *Test Method D446-07 Standard Specifications and Operating Instructions for Glass Capillary Kinematic Viscometers*, in *ASTM Book of Standards*. 2007, American Society of Testing and Materials: West Conshohocken, PA.
196. ASTM, *Test Method D445-06*, in *ASTM Book of Standards*. 2006, American Society of Testing and Materials: West Conshohocken, PA.
197. Knothe, G., Steidley, K., *Kinematic viscosity of biodiesel fuel components and related compounds. Influence of compound structure and comparison to petrodiesel fuel components*. *Fuel*, 2005. **84**: p. 1059-1065.
198. ASTM, *Test Method D5865-07 Standard Test method for Gross Calorific Value of Coal and Coke*, in *ASTM Book of Standards*. 2007, American Society of Testing and Materials: West Conshohocken, PA.
199. ASTM, *Test Method D2887-06a Standard Test Method for Boiling Range Distribution of Petroleum Fractions by Gas Chromatography*, in *ASTM Book of Standards*. 2007, American Society of Testing and Materials: West Conshohocken, PA.
200. Choi, C.Y., Reitz, R.D., *An Experimental Study on the effects of Oxygenated Fuel Blends and Multiple Injection Strategies on DI Diesel Engine Emissions*. *Fuel*, 1999. **78**(11): p. 1303-1317.
201. Zhang, Y., Boehman, A., *Effects of Biodiesel on engine Performance and NO_x Emissions in a Common Rail Diesel Engine*, in *Energy & Geo-Environmental Engineering*. 2006, Pennsylvania State University: University Park, PA.
202. Olikara, C., Borman, G., *A Computer Program Calculating Properties of Equilibrium Combustion Products with Some Applications to I.C. Engines*. Society of Automotive Engineers, Inc., 1975(750468).
203. Zhang, Y., *Effect of Biodiesel on Engine Performance and NO_x Emissions in a Common Rail Diesel Engine*, in *Energy & Geo-Environmental Engineering*. 2006, Pennsylvania State University: University Park, PA.
204. Boulanger, J., Neill, S., Liu, F., Smallwood, G., *Investigating renewable fuel combustion I: comparative simulations of a diesel engine fueled with n-C12 alkane and n-C18 fatty acid-derived liquid-property fuel*. *International Journal of Environmental Studies*, 2007. **64**(4): p. 401-418.
205. Carlucci, P., Ficarella, A., LaForgia, D., *Effects on combustion and emissions of early and pilot fuel injections in diesel engines*. *International Journal of Engine Research*, 2005. **6**(1): p. 43-60.

206. Tennison, P., Reitz, R., *An Experimental Investigation of the Effects of Common-Rail Injection System Parameters on Emissions and Performance in a High-Speed Direct Injection Diesel Engine*. Journal of Engineering for Gas Turbines and Power, 2001. **123**: p. 167-174.
207. Tat, M., Wang, P., Van Gerpen, J., *Exhaust Emissions from an Engine Fueled with Biodiesel from High-Oleic Soybeans*. J. Am Oil Chem Soc, 2007. **84**: p. 865-869.
208. *New fuel: The Lawnmower's tale*. Economist, 1995. **33**(7905): p. 79-82.
209. Sorenson, S.C., *Dimethyl Ether in Diesel Engines: Progress and Perspectives*. Journal of Engineering for Gas Turbines and Power, ASME, 2001. **123**: p. 652-658.
210. Liu, S., Clemente, E., Hu, T., Lu, S., Zhu, C., *Combustion Characteristics of a DME HCCI Engine*. Transactions of the CSICE (Chinese Society for Internal Combustion Engines), 2005. **23**(3): p. 207-212.
211. Sahnashi, W., Azetsu, A., Oikawa, C., *Effects of N₂ and CO₂ mixing on ignition and combustion in a homogeneous charge compression ignition engine operate on dimethyl ether*. International Journal of Engine Research, 2005. **6**: p. 423-431.
212. Sorenson, S., *Dimethyl Ether in Diesel Engines: Progress and Perspectives*. Journal of Engineering for Gas Turbines and Power, 2001. **123 No. 3**: p. 652 - 658.
213. Hountalas, D., Papagiannakis, R., *Development of a Simulation Model for Direct Injection Dual Fuel Diesel-Natural Gas Engines*. Society of Automotive Engineers, 2000(2000-01-0286).
214. Chen, Z., Konno, M., Oguma, M., Yanai, T., *Experimental Study of CI Natural-Gas/DME Homogeneous Charge Engine*. Society of Automotive Engineers, 2000(2000-01-0329).
215. Christensen, M., Hultqvist, A., Johansson, B., *Demonstrating the Multi Fuel Capability of a Homogeneous Charge Compression Ignition Engine with Variable Compression Ratio*. Society of Automotive Engineers, 1999(1999-01-3679).
216. Aceves, S., Flowers, D., Martinez-Frias, J., Smith, J., Westbrook, C., Pitz, W., Dibble, R., Wright, J., Akinyemi, W., Hessel, R., *A Sequential Fluid-Mechanic Chemical-Kinetic Model of Propane HCCI Combustion*. Society of Automotive Engineers, 2001(2001-01-1027).
217. Ogawa, H., Miyamoto, N., Kaneko, N., Ando, H., *Combustion Control and Operating Range Expansion in an HCCI Engine with Selective Use of Fuels with*

- Different Low-Temperature Oxidation Characteristics*. Society of Automotive Engineers, 2003(2003-01-1827).
218. Amano, T., Dryer, F. L., *Effect of DME, NOx, And Ethane or CH4 Oxidation : High Pressure, Intermediate - Temperature Experiments And Modelling*. Twenty Seventh International Combustion Symposium Proceedings, 1998: p. 397-404.
 219. Kong, S., *A study of natural gas/DME combustion in HCCI engine using CFD with detailed chemical kinetics*. Fuel, 2007. **86**: p. 1483-1489.
 220. Zhao, F., Asmus, T., Assanis, D., Dec., J., Eng, J., Najt, P., ed. *Homogeneous Charge Compression Ignition (HCCI) Engines: Key Research and Development Issues (PT-94)*. 2003, Society of Automotive Engineers: Warrendale, PA.
 221. Hsu, B., *Practical Diesel-Engine Combustion Analysis*. 2002, Warrendale, PA: Society of Automotive Engineers, Inc.
 222. Lewis, S., Storey, J., Bunting, B., Szybist, J., *Partial Oxidation Products and other Hydrocarbon Species in Diesel HCCI Exhaust*. Society of Automotive Engineers, 2005(2005-01-3737).
 223. Szybist, J., Bunting, B., *Fuel Composition Impacts on Processes in Compression Ignition Engines*, in *Energy and Gep-Environmental Engineering*. 2005, Pennsylvania State University: University Park. p. 179.
 224. Amneus, P., Mauss, F., Kraft, M., Vressner, A., Johansson, B., *NOx and N2O formation in HCCI engines*. Society of Automotive Engineers, 2005(2005-01-0126).
 225. Pulkrabek, W., *Engineering Fundamentals of Internal Combustion Engine*. 1997, Upper Saddle River, New Jersey: Prentice Hall.
 226. Dagaut, P., Daly, C.,, *The Oxidation and Ignition of Dimethyl Ether from Low to High Temperature (500 – 1600 K) : Experiments and Kinetic Modelling*. International Combustion Symposium (27th), 1998: p. 361-369.
 227. Rosado-Reyes, C., Francisco, J., Szente, J., Maricq, M., Ostergaard, L., *Dimethyl Ether Oxidation at Elevated Temperature (295-600K)*. J.Phys. Chem. A, 2005. **109**: p. 10940-10953.
 228. Dagaut, P., Daly, C., Simmie, J., Cathonnet, M. *The Oxidation and Ignition of Dimethylether From Low to High Temperature (500-1600 K): Experiments and Kinetic Modeling*. in *International Combustion Symposium (27th)*. 1998: Combustion Institute.

229. Hori, M., Matsunaga, N., Marinov, N., Pitz, W., Westbrook, C., *An Experimental and Kinetic Calculation of the Promotiion Effect of Hydrocarbons on the NO-NO₂ Conversion in a Flow Reactor*. International Symposium on Combustion (27th), 1998: p. 389-396.
230. Kee, R., Rupley, F., Miller, J., *Chemkin-II: A Fortran Chemical Kinetics Package for the Analysis of Gas Phase Chemical Kinetics*. SANDIA REPORT - reprinted 1994 (Supersedes SAND89-8009, September 1989), 1994. **SAND89-8009B - UC-706**: p. 127.
231. Iida, N., Igarashi, T., *Auto-ignition and Combustion of n-Butane and DME/Air Mixtures in a Homogeneous Charge Compression Ignition Engine*. Society of Automotive Engineers, 2000(2000-01-1832).
232. Amano, T., Dryer, F. *Effect of Dimethyl Ether, NO_x, and Ethane on CH₄ Oxidation: High Pressure, Intermediate-temperature Experiments and Modeling*. in *International Symposium on Combustion (27th)*. 1998: The Combustion Institute.
233. Dec, J., *Diesel combustion and emissions formation using multiple 2-D imaging diagnostics*. Proceedings - Diesel Engine Emissions Reduction Workshop July 1997, 1997(CONF - 970799): p. 269 - 273.
234. Szybist, J., Boehman, A., Haworth, D., Koga, H., *Premixed ignition behavior of alternative diesel fuel-relevant compounds in a motored engine environment*. *Combustion and Flame*, 2007. **149**: p. 112-128.
235. Frenklach, M., Wang, H., Goldenberg, M., Smith, G., Golden, D., Bowman, C., Hanson, C., Gardiner, W., Lissianski, V., *GRI-Mech-- An Optimized Detailed Chemical Reaction Mechanism for Methane Combustion*. GRI Topical Report NO. GRI-95/0058, 1995.

Appendix A

TEOM Instrument File Configuration and User Configuration

A.1 Instrument File Configuration

Slot	Primary Description	Secondary Description	Value
0	Files	Conversion File	1105
1	Files	User Config File	1105A
2	Screens	Instrument Title	Series 1105 TEOM Monitor
3	Screens	Screen Divisions	5
4	Hardware	Calib Constant (K0)	14051
5	Hardware	MR/MC/TM Cycles (sec)	0.4194304
6	Hardware	An/Di Cycle (sec)	0.1048576
7	Country	Language	English
8	Country	Print Code: Compress	015
9	Country	Print Code: Next Page	012
10	Clipping	Time Window (sec)	5
11	Clipping	In-Clip (0.0-0.5)	0.02
12	Clipping	Out-Clip (0.0-0.5)	0.02
13	Default	Resistance	51100
14	Temp/Flow Constants	Low Reference	0
15	Temp/Flow Constants	High Resistance	6
16	Temp/Flow Constants	T-Constant 1	8.267E-04
17	Temp/Flow Constants	T-Constant 2	2.090E-04
18	Temp/Flow Constants	T-Constant 3	8.090E-08
19	Temp/Flow Constants	Flow Rate Constant	Flow Rate 1.00
20	Counter Board	Board Type	1
21	Counter Board	Base Address	768
22	Analog-In Board	Board Type	5
23	Analog-In Board	Channels	15
24	Analog-In Board	Base Address	784
25	Analog-Out Board	Board Type	5
26	Analog-Out Board	Channels	8
27	Analog-Out Board	Base Address	784
28	Digital-In Board	Board Type	0
29	Digital-In Board	Channels	0

30	Digital-In Board	Base Address	0
31	Digital-Out Board	Board Type	5
32	Digital-Out Board	Channels	8
33	Digital-Out Board	Base Address	784
34	Readings per Analog Input		12
35	Short Numerical Display		120
36	Numerical Display Window	01: Row 1L	83
37	Numerical Display Window	02: Row 1M	84
38	Numerical Display Window	03: Row 1R	85
39	Numerical Display Window	04: Row 2L	116
40	Numerical Display Window	05: Row 2M	124
41	Numerical Display Window	06: Row 2R	119
42	Numerical Display Window	07: Row 3L	90
43	Numerical Display Window	08: Row 3M	88
44	Numerical Display Window	09: Row 3R	89
45	Numerical Display Window	10: Row 4L	120
46	Numerical Display Window	11: Row 4M	122
47	Numerical Display Window	12: Row 4R	123
48	Numerical Display Window	13: Row 5L	173
49	Numerical Display Window	14: Row 5M	174
50	Numerical Display Window	15: Row 5R	177
51	Numerical Display Window	16: Row 6L	117
52	Numerical Display Window	17: Row 6M	118
63	Numerical Display Window	18: Row 6R	0
54	Numerical Display Window	19: Row 7L	0
55	Numerical Display Window	20: Row 7M	0
56	Numerical Display Window	21: Row 7R	0
57	Numerical Display Window	22: Row 8L	0
58	Numerical Display Window	23: Row 8M	0
59	Numerical Display Window	24: Row 8R	0
60	AK Protocol	Station Number	052
61	AK Protocol	Channel Number	075048
62	AK Protocol	Append Codes	013010
63	AK Protocol	Baud Rate	9600
64	AK Protocol	Data Bits	8
65	AK Protocol	Stop Bits	1
66	AK Protocol	Parity	0
67	AK Protocol	Handshaking	0
68	AK Protocol	Serial Port	2
69	Pres. Comp.	(Yes=1/No=0)?	0
70	Bypass(1)/Purge(0) Status		0
71	Warm-Up: Filter Change(secs)		60
72	Warm-Up: Initial Delay(secs)		900
73	Collection Data Delay(secs)		120
74	Robitrol Delay		0

A.2 User File Configuration

Slot	Primary Description	Secondary Description	Value
0	X-Axis	X-Axis Span (min)	6
1	X-Axis	X-Axis Format (code)	0
2	On-Line Printing	Printing Interval (sec)	-300
3	On-Line Printing	Mode (0:no 1:Prt 2:Plt)	0
4	On-Line Storage	Disk Drive (A-Z)	6
5	On-Line Storage	Subdirectory (name)	ELANA
6	On-Line Storage	Storage Interval (sec)	10
7	On-Line Storage	Store Data (0:No 1:Yes)	1
8	Y-Axis	Default Left (0-10)	6
9	Y-Axis	Default Right (0-10)	7
10	Averaging	TM Calc (0:Ave 1:Exp)	0
11	Averaging	TM Time Window (sec)	10
12	Averaging	MR/MC Time Window (sec)	10
13	Settings	Sample Flow Rate	3
14	Settings	Housing Temperature	50
15	Settings	Air Tube Temperature	50
16	Settings	Horiba MDT	0
17	Settings	Horiba MDT	0
18	Settings	External Tube Temp	50
19	Flow Cont	STP Temperature	25
20	Transform	Clip Data (0:No 1: Yes)	0
21	Transform	MR Conversion Factor	1
22	Transform	MC Conversion Factor	1
23	Transform	TM Conversioni Factor	1
24	Printing	Contents of Column 01	83
25	Printing	Contents of Column 02	84
26	Printing	Contents of Column 03	85
27	Printing	Contents of Column 04	88
28	Printing	Contents of Column 05	89
29	Printing	Contents of Column 06	122
30	Printing	Contents of Column 07	177
31	Printing	Contents of Column 08	0
32	Disk Storage	Contents of Column 01	83
33	Disk Storage	Contents of Column 02	84
34	Disk Storage	Contents of Column 03	85
35	Disk Storage	Contents of Column 04	88
36	Disk Storage	Contents of Column 05	122
37	Disk Storage	Contents of Column 06	177
38	Disk Storage	Contents of Column 07	0
39	Disk Storage	Contents of Column 08	0
40	Analog Output	Chan 1: Contents	83
41	Analog Output	Chan 1: Minimum Point	-2.50E-07
42	Analog Output	Chan 1: Maximum Point	1.00E-06

43	Analog Output	Chan 2: Contents	84
44	Analog Output	Chan 2: Minimum Point	-2.50E+00
45	Analog Output	Chan 2: Maximum Point	22.5
46	Analog Output	Chan 3: Contents	85
47	Analog Output	Chan 3: Minimum Point	0.00E+00
48	Analog Output	Chan 3: Maximum Point	1.00E-04
49	Serial Output Contents		83
50	Key Assign	F1: Contents Units	-116 C
51	Key Assign	F1: Mimum Point	49.8
52	Key Assign	F1: Step	0.1
63	Key Assign	F2: Contents Units	-117 C
54	Key Assign	F2: Mimum Point	49.8
55	Key Assign	F2: Step	0.1
56	Key Assign	F3: Contents Units	-118 C
57	Key Assign	F3: Mimum Point	49.8
58	Key Assign	F3: Step	0.1
59	Key Assign	F4: Contents Units	-119 C
60	Key Assign	F4: Mimum Point	44.8
61	Key Assign	F4: Step	0.1
62	Key Assign	F5: Contents Units	83 g/s
63	Key Assign	F5: Mimum Point	-2.50E-07
64	Key Assign	F5: Step	2.50E-07
65	Key Assign	F6: Contents Units	84 mg/m ³
66	Key Assign	F6: Mimum Point	-2.50E-07
67	Key Assign	F6: Step	2.50E+00
68	Key Assign	F7: Contents Units	85 gms
69	Key Assign	F7: Mimum Point	0.00E+00
70	Key Assign	F7: Step	2.00E-05
71	Key Assign	F8: Contents Units	88 Hz
72	Key Assign	F8: Mimum Point	200
73	Key Assign	F8: Step	20
74	Key Assign	F9: Contents Units	89 SD
75	Key Assign	F9: Mimum Point	0.00E+00
76	Key Assign	F9: Step	1.00E+06
77	Key Assign	F10: Contents Units	-122 in. HG
78	Key Assign	F10: Mimum Point	0
79	Key Assign	F10: Step	5

Appendix B

Biodiesel and Ultra Low Sulfur Diesel Fuel Specification Reports

B.1 Biodiesel Fuel Specification

Composition of Penn State B100 samples- Area % by GCMS						
	Sigma					
FAME	Soy oil	AGP #1	AGP #2			
16:0	10.2	10.7	10.6			
18:0	3.93	4.5	4.5			
18:1	20.62	22.6	22.8			
18:2	54.3	52.3	52.2			
18:3	8.36	7.4	6.8			
20:0	0.33	0.3	0.3			

Data provided on normal biodiesel samples from Mike Haas at the USDA.

Sample 1 is from the barrel of fuel used in testing. Sample 2 is from a barrel from the sample batch for comparison.



The "Gold Standard" of Biodiesel

SOYGOLD

A BQ-9000 Accredited Producer

June 21, 2006

Property	ASTM Method	Units	ASTM D-6751-06^{E1} Standards	SoyGold Standard Ranges
Flash Point	D93	Degrees °C	130 min.	162-174
Water & Sediment	D2709	% vol.	0.050 max.	0.005-0.04
Kinematic Viscosity, 40 °C	D445	mm ² /sec.	1.9 – 6.0	4.062-4.141
Sulfated Ash	D874	% mass	0.020 max.	0.003-0.010
Total Sulfur	D5453	% mass	0.05 max.	0.0002-0.0005
S15 Grade		PPM	15 max.	2-5
S 500 Grade		PPM	500 max.	2-5
Copper Strip Corrosion	D130		No. 3 max.	1A
Cetane	D613		47 min.	48.4-49.7
Cloud Point	D2500	Degrees °C Degrees °F	Report Report	0.0-2.2 32.0-35.6
Carbon Residue 100% sample	D4530	% mass	0.050 max.	0.008-0.010
Acid Number	D664	mg KOH/gm	0.50 max.	0.08-0.20
Free Glycerine	D6584	% mass	0.020 max.	0.001-0.01
Total Glycerine	D6584	% mass	0.240 max.	0.050-0.15
Phosphorus Content	D4951	% mass	0.001 max.	0.0002-0.0005
Distillation Temperature, Atmospheric Equivalent Temperature, 90% Recovered	D1160	Degrees °C Degrees ° F	360 max. 680 max.	350 662
Sodium and Potassium, Combined	UOP391	ppm	5ppm max	<2



The "Gold Standard" of Biodiesel

SOYGOLD

A BQ-9000 Accredited Producer

June 21, 2006

Property	ASTM Method	Units	Non-ASTM Standards	SoyGold Standard Ranges
Specific Gravity Density@60°F	D4052	Sp. Gr. Pounds/Gallon API° Lbs/ Cu. Ft	Report	0.8843 7.3695 28.56 55.1578
Soap		PPM	Report	ND
Rancimat@110 ° C	EN14112	Hours	3.0	3.0-6.0
NACE Corrosion@72°F	TM0172-2001		B+ min.	A-B++
HAZE RATING @60° F	D4176		2	2
Voluntary Filtration Method	D6217 Modified (B)	Seconds	360 max.	20-200
METALS/OTHER*	ICP			
Ca + Mg		PPM	5	<0.50
Cu-Copper		PPM	Report	<0.10
Na-Sodium		PPM	Report	<1.00
Ca-Calcium		PPM	Report	<0.15
Mg Magnesium		PPM	Report	<0.15
P-Phosphorous		PPM	Report	<1.60
Fe-Iron		PPM	Report	<0.20
Ni-Nickel		PPM	Report	<0.30
K-Potassium		PPM	Report	<1.00

*- Metals-Less than 0.05 PPM reported As "ND" (Non-Detect)



SERGEANT BLUFF, IOWA
METHYL ESTER PLANT

Certificate of Analysis

Load Order 890-7584

Shipping date 5/8/2006 Rail/ Truck # CPT 137/T388

Customer AG Environmental Products Attn

Street 12700 West Dodge Road P O Box 2047

City Omaha State NE Zip code 68103-2047

Customer PO:

Schedule PO:

Product ID 99600 Product name SOYGOLD SoyDiesel

Lot number B605-06b (CB050806)

Total glycerin 0.096 %

Free glycerin 0.011 %

Acid Number 0.15 mg KOH/gram

Moisture 0.0267 %

Methanol 0.058 %

Soap 0 ppm

Additive None

Prepared by: Becky Still

Becky Still

AG Processing Inc. Methyl Ester Plant

Monday, May 08, 2006

B.2 Hydrogenated Biodiesel Fuel Specification

RBHD Soybean Ester Release

Lot Number ED60706-2

Analysis	Specification	Result
% FFA	0.10% max	0.05
% 440nm	90 % min	99.434
Transmittance 550nm	95 % min	99.773
% C 12	1.0 % max	0
% C 14	1.0 % max	0.07
% C 16	8.5 - 13.5%	11.0
% C 18	80 - 92%	88.07
PV	85 ppm max	NF
CV	200 ppm max	74
% Glycerine	150 ppm max	121
% Glycerides	500 ppm max	0
% Moisture	0.1 % max	NF

Approval Status

This Batch is: accepted / redistilled / blended
(circle one)

Approved by: 

(Distillation Technician)

Acid Summary Report
4/6/068:55 PM

Sample Code: ED60406-2

Analyst: WB

Data File: C:\HPCHEM\2\DATA\04042006\APR6F001.D

Instrument: US00009973

Acquisition Method: FACB.M

Acquisition Date: 4/6/06 20:40

Fatty Acid Chainlength Distribution

C12 ME: 0.00	C16=1 ME: 0.14
C14 ME: 0.07	C17=1 ME: 0.07
C16 ME: 10.86	Total C18=1 ME: 68.76
C17 ME: 0.09	Total C18=2 ME: 18.44
C18 ME: 0.00	Total C18=3 ME: 0.87
C20 ME: 0.30	C20=1 ME: 0.32
C21 ME: 0.00	C22=1 ME: 0.00
C22 ME: 0.07	C24=1 ME: 0.00
C23 ME: 0.00	
C24 ME: 0.00	

Summary Report

Total C16:	11.00
Total C18:	88.07
Total C22:	0.07

% Total Saturated Fatty Acid: 11.40

% Total Acid:	100.00
% Total Unknown:	0.00

Iodine value:	93.8
Total Area:	20436

Analytical Report
 Method: Fatty Acid Composition
 Sample: ED60406-2

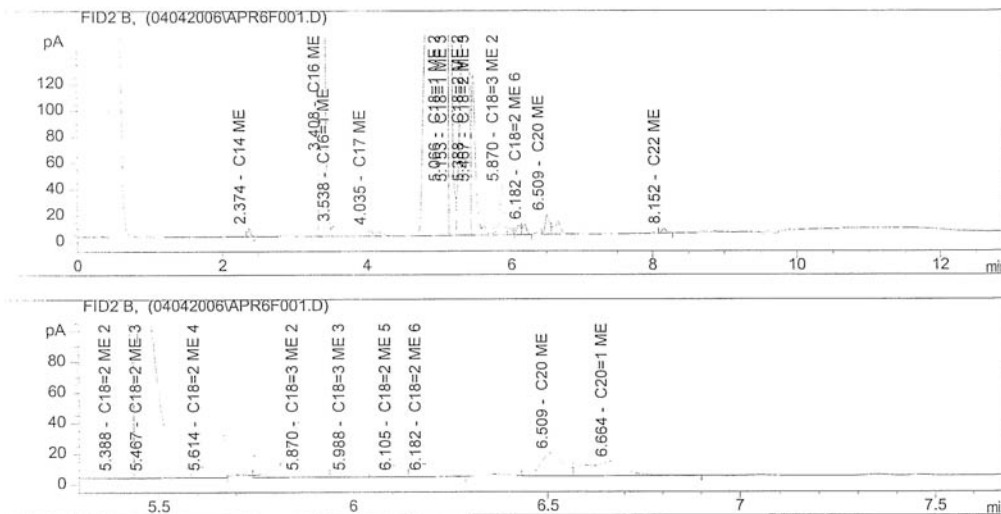
Page 1 of 2
 Method #: OMGC-03-0197
 Analyst:WB

Injected On:4/6/06 8:4->4/6/06 8:40:5-> Aquisition Method: FACB.M

Raw Data File:C:\HPCHEM\2\DATA\04042006\APR6F001.D
 Sequence:C:\HPCHEM\2\SEQUENCE\OMEGA3B.S

Vial #: 1.000

Method Last Modified:4/6/06 5:02:19 AM



#	Meas. Ret.	Exp. Ret.	Area	Compound Name	Area %
1	0.000	1.566	0.0	C12 ME	0.000
2	2.374	2.376	15.3	C14 ME	0.075
3	3.408	3.450	2219.9	C16 ME	10.863
4	3.538	3.542	28.0	C16=1 ME	0.137
5	4.035	4.012	19.3	C17 ME	0.095
6	4.190	4.150	14.7	C17=1 ME	0.072
7	0.000	4.800	0.0	C18 ME	0.000
8	0.000	4.980	0.0	C18=1 ME 1	0.000
9	5.066	5.102	11812.1	C18=1 ME 2	57.801
10	5.153	5.135	2240.1	C18=1 ME 3	10.962
11	0.000	5.175	0.0	C18=1 ME 4	0.000
12	0.000	5.235	0.0	C18=1 ME 5	0.000
13	0.000	5.300	0.0	C18=2 ME 1	0.000
14	5.388	5.350	3213.8	C18=2 ME 2	15.726
15	5.467	5.470	463.4	C18=2 ME 3	2.267
16	5.614	5.640	26.7	C18=2 ME 4	0.131
17	0.000	5.760	0.0	C18=3 ME 1	0.000
18	5.870	5.874	157.2	C18=3 ME 2	0.769
19	5.988	5.988	20.5	C18=3 ME 3	0.100
20	6.105	6.090	29.3	C18=2 ME 5	0.144

C:\HPCHEM\2\DATA\04042006\ ->

Page 2 of 2

Analytical Report					
#	Meas. Ret.	Exp. Ret.	Area	Compound Name	Area %
21	6.182	6.180	34.4	C18=2 ME 6	0.168
22	0.000	6.189	0.0	C18=2 ME 7	0.000
23	6.509	6.507	61.8	C20 ME	0.302
24	0.000	6.620	0.0	C18=2 ME 8	0.000
25	6.664	6.670	65.3	C20=1 ME	0.320
26	0.000	7.342	0.0	C21 ME	0.000
27	8.152	8.200	14.0	C22 ME	0.068
28	0.000	8.940	0.0	C22=1 ME	0.000
29	0.000	9.150	0.0	C23 ME	0.000
30	0.000	9.814	0.0	C24 ME	0.000

Total Area:		Area Sum			

		20436			

C:\HPCHEM\2\DATA\04042006\ ->

B.3 BP 15 Ultra Low Sulfur Diesel Fuel Certificate of Analysis

Certificate of Analysis

Conoco BP-15 Diesel Fuel

Issue date: July 18, 2002

RE: Conoco BP-15 Diesel Fuel 21071-70

TEST	TEST METHOD	SPECIFICATION	RESULT
Cetane Index (calculated)	ASTM D-976	report	48.8
Cetane Number (engine rating)	ASTM D-613	report	49.7
Corrosion, Cu Strip, 3hr. @ 122°F	ASTM D-130	report	1a
Distillation, degrees F	ASTM D-86		
IBP		report	330.3
T50		report	500.7
FBP		report	653.9
Dspecific Gravity @60°F	ASTM D-4052	report	.8374
Polycyclic aromatic hydrocarbon Content, GC-SFC, wt%		report	6.9
Carbon residue	ASTM D-524	report %	0.04
Flash point Pensky Martin °F	ASTM D-93	report	147
Viscosity at 40°C cSt	ASTM D-445	report	2.5
Pour point °F	ASTM D-97	report	-0.4
Cloud point °F	ASTM D-5773	report	10.4
Sulfur, Total	ASTM D-2622	<15 ppm W	13 ppm W
Lubricity, Boccle Pass		Report	4200
Lubricity, Boccle Fail		Report	4500

VITA

Elana M. Chapman

EDUCATION

Ph.D. in Fuel Science, Spring 2008.

M.S. in Mechanical Engineering, Spring 2008.

M.S. in Fuel Science, August 2002.

Pennsylvania State University, University Park, PA.

Bachelor of Science in Mechanical Engineering, University of Dayton, Dayton, OH, May 1992.

RESEARCH PUBLICATIONS

Flynn, P., Chapman, E., Boehman, A. "Destruction of Nitric Oxide via Selective NO_x Recirculation During Lean Combustion: A Comparison of Various Engines and Fuels" (Technical Paper No. 2006-01-3369) Society of Automotive Engineers, 2006.

Chapman, E., Boehman, A. "Emissions Characteristics of a Light Duty Diesel Engine Fueled with a Hydrogenated Biodiesel Fuel" American Chemical Society, Fuel Chemistry, Pre-Print, 2006, Vol. 51 No. 1 PGS. 31-32, 231st ACS National Meeting, Atlanta, GA, March 26-30, 2006.

Chapman, E., Pflumm, S., Kung, E., Acharya, R., Saxon, J., Feldman, B., Herrold, B., Wilson, K., Safabakhsh, P., Shirk, M., Caserta, J., Boehman, A., Haworth, D., Koga, H., Tadros, T., Maglast, D., Blackman, L., "Penn State FutureTruck Hybrid Electric Vehicle: Light-Duty Diesel Exhaust Emission Control System to meet ULEV Emissions Standard." (Technical Paper No. 2005-01-3877) Society of Automotive Engineers, 2005.

Wain, K., Perez, J., Chapman, E., Boehman, A. "Alternative and low sulfur fuel options: Boundary lubrication performance and potential problems", Tribology International, v38,n3, March 2005, pgs.313-319.

Eirich, J., Chapman, E., Glunt, H., Klinikowski, D., Boehman, A., Hansel, J., Heydorn, E., "Development of a Dimethyl Ether (DME)-Fueled Shuttle Bus." (Technical Paper No. 2003-01-0756), Society of Automotive Engineers 2003 Transactions- Journal of Fuels & Lubricants, (112), Section 4, pgs. 348-360.

Chapman, E., Hile, M., Pague, M., Song, J., Boehman, A., "Eliminating the NO_x Emissions Increase Associated with Biodiesel", Am. Chem. Soc. Div. Fuel Chem. Prepr., 2003, Vol. 48, No. 67, 226th ACS National Meeting, New York, NY, September 7-11, 2003.

Chapman, E., Bhide, S., Boehman, A., Boehman, L., Waller, F., "Engine Performance and Emissions from fuel blends of Dimethyl Ether (DME) and diesel fuel". Proceedings in AIChE Spring National Meeting, Session 141- Oxygenated Fuels, 2002. New Orleans, LA, March 10-14, 2002.

Bhide, S., Chapman, E., Stefanik, J., Glunt, H., Boehman, L., Boehman, A., Waller, F., "Development of a Dimethyl Ether-Fueled Shuttle Bus". Am. Chem Soc. Fuel Chemistry Division Preprints, 2002, 47(2), pgs. 562-563.

Chapman, E., Boehman, A. Tijm, P.J.A., Waller, F., "Emissions Characteristics of a Navistar 7.3L Turbodiesel Fueled with Blends of Dimethyl Ether and Diesel Fuel." (Technical Paper No. 2001-01-3626), Society of Automotive Engineers 2001 Transactions- Journal of Fuels & Lubricants, (110) Section 4, pgs. 2166-2175.

Chapman, E., Bhide, S., Boehman, A., Tijm, P.J.A., Waller, F.J., "Emission Characteristics of a Navistar 7.3L Turbodiesel Fueled with Blends of Oxygenates and Diesel." (Technical Paper No. 2000-01-2887) Society of Automotive Engineers, 2000.

Appendix A-2.2 MS Thesis in Mechanical Engineering by Bryan Nese

Bryan Nese
Direct 202.220.4256
bnese@kenyon.com

1500 K Street, N.W.
Washington, D.C. 20005

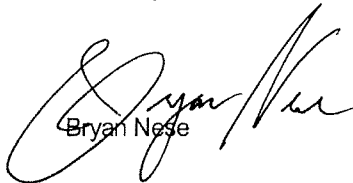
January 15, 2009

National Energy Technology Laboratory
U.S. Department of Energy
626 Cochrans Mill Road
P.O. Box 10940
Pittsburgh, PA 15236-0940

Dear U.S. Department of Energy:

I hereby grant the U.S. Department of Energy permission to use my thesis in the Final Technical Report for Award Number DE-FC26-04NT42233, "Hydrogen-Assisted IC Engine Combustion as a Route to Hydrogen Implementation." My thesis was written with support of the U.S. Department of Energy under this award and copyright for the thesis lies with me.

Sincerely,


Bryan Nese

CHAPTER 1

INTRODUCTION AND MOTIVATION

1.1 Motivation

A current issue of energy concern is the world-wide shortage of petroleum-derived fossil fuels. Given our heavy dependence on this precious resource, it is not surprising that a major priority for industries and governments has been to research alternative fuels and to improve energy efficiency. Internal combustion engines for transportation vehicles are no exception, and a large amount of effort has been concentrated on the search for alternative, renewable fuels as well as more efficient combustion processes.

One alternative to petroleum-derived hydrocarbon fuels is hydrogen. Although consideration of hydrogen as a transport fuel is not new, there has been renewed interest in recent years because of its potential for near-unlimited availability and significantly lower levels of hazardous emissions (**Error! Not a valid link.**).

With regard to new combustion processes, homogeneous-charge compression-ignition (HCCI) engines have been the focus of considerable research in the past several years. Attractive aspects of this technology include lower harmful oxides of nitrogen (NO_x) and particulate matter emissions and high thermal efficiency. Drawbacks to HCCI include the lack of control over ignition timing often encountered. This is an important issue due to

the role this plays both on the engine's thermal efficiency as well as emissions. As a result, restrictions are often placed on parameters such as equivalence ratio, intake temperature, and compression ratio in order to achieve favorable ignition times. An additional disadvantage to HCCI is the typically high levels of hazardous hydrocarbon emissions such as carbon monoxide (CO) and other unburned hydrocarbons (UHC) **(Error! Not a valid link.)**.

Although much research effort has been devoted to the topics of hydrogen and HCCI individually, significantly less attention has been given to the study of their combined effects. The use of hydrogen fuel in HCCI would, in theory, reduce the UHC and CO emissions to nearly zero, as the absence of carbon molecules in the fuel would effectively eliminate all carbon-based molecules from the combustion process.¹ This fact makes hydrogen a very attractive fuel choice for HCCI, a combustion process typically associated with high CO/UHC emissions.

In spite of these attractive features, a major problem arises in the difficulty with which pure hydrogen ignites via compression. This often necessitates the increase of intake temperatures or compression ratios to unreasonably high values. An additional drawback is the steep rate of pressure rise when hydrogen is compression-ignited.

¹ In reality, this of course is not the case, as slight amounts of hydrocarbons from the oil in the engine cylinder would still yield small amounts of UHC.

1.2 This Thesis

In this thesis, a computational approach is applied to investigate autoignition and NO_x emissions for hydrogen-hydrocarbon fuel blends with air or air-EGR blends. It is hypothesized that ignition timing might be controlled via a pilot injection of diesel fuel into a premixed hydrogen/air/EGR mixture.

Two levels of modeling are applied: a zero-dimensional time-dependant reactor model, and a three-dimensional time-dependant computational fluid dynamics (CFD) model. Because thermochemistry plays a crucial role in HCCI autoignition and NO_x emissions, significant effort has been devoted to selection and validation of the chemical mechanisms for representative single-component hydrocarbon fuels and for NO_x formation.

The remainder of this thesis is organized as follows.

In Chapter 2, a review of selected topics relevant to this thesis is presented. Topics include general and diesel-based HCCI, hydrogen as an alternative to petroleum-derived fuels, NO_x emissions, and numerical modeling.

Chapter 3 provides more detailed information on each of the two modeling tools used in this thesis: CHEMKIN and ACFluX. The chemical mechanisms considered for future use with each of these numerical codes are introduced and compared here. In addition,

the process by which these mechanisms were combined and modified is discussed and their accuracy confirmed.

Chapter 4 details the zero-dimensional modeling of homogeneous n-heptane/air mixtures using CHEMKIN. The chapter contains a description of the setup for this study as well as a discussion of the results, with particular attention given to the effects of various thermochemical parameters on ignition timing and NO_x/CO emissions.

In Chapter 5, an additional zero-dimensional study of homogeneous iso-octane/air/EGR mixtures is presented. This study is an attempt to replicate a similar study conducted by **Error! Not a valid link.**) in which predicted NO₂ levels exceeded those of NO.

Chapter 6 outlines the three-dimensional time-dependant CFD study used to explore the effects of turbulence, inhomogeneities, and pilot injection on ignition timing and NO_x/CO emissions. A comparison of the zero- and three-dimensional models is made, and the results of the CFD study are presented in contrast to those obtained from CHEMKIN. Emphasis is placed on the control of ignition timing by varying the spray injection parameters.

Finally, Chapter 7 summarizes the key findings of these studies and their significance. In addition, suggestions for future work are made and discussed.

CHAPTER 2

LITERATURE REVIEW

The relevant literature on hydrogen as a transportation fuel, HCCI engines, and numerical simulation of HCCI combustion is reviewed.

2.1 Hydrogen as a Transportation Fuel

There are several advantages to the use of hydrogen as a transportation fuel over conventional fossil fuels. Per unit mass, hydrogen stores about 2.6 times the amount of energy as gasoline. While the gas tank in a typical automobile holds approximately 15 gallons or 90 pounds of gasoline when full, a hydrogen tank containing the same amount of energy would weight just 34 pounds (Romm 2004).

These facts tend to be misleading, and although hydrogen does hold more energy per unit mass than gasoline, it has a low volumetric energy density. Hydrogen needs about 4 times the amount of space as gasoline to contain the same amount of energy (Romm 2004). In the above example, the 34 pound hydrogen tank would occupy a space of 60 gallons. This presents one of the major hurdles in the conversion to a hydrogen fuel economy: Much larger volumes of hydrogen are needed to achieve the same distances as conventional automobile engines (Cooper 2005). Suggested methods of addressing this issue relate to storing hydrogen in various other chemicals, such as ammonia, and releasing pure hydrogen using a chemical catalyst, cryogenic compression, or the use of metal hydrides (Cooper 2005). Metal hydrides are compounds which can be either liquid

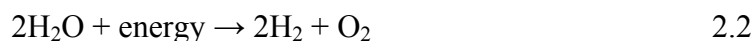
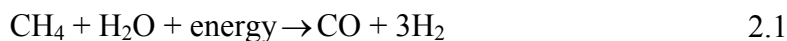
or solids, considered to be easily adaptable to fueling scenarios and which have the ability to store and release hydrogen. A drawback to this method is their high cost and large weight (Cooper 2005).

An additional benefit to hydrogen as a transportation fuel is the lack of harmful products after combustion. The only chemical product of complete combustion of hydrogen and oxygen is water; no CO or UHC is emitted as is the case with carbon-based fuels such as gasoline (Turns 2000). In spite of this, emissions of nitrogen oxides are notably higher with hydrogen (Wong and Karim 2000).

2.1.1 Hydrogen Production

As the world's most common chemical element, it would seem that hydrogen would be both an abundant and accessible resource. In reality, hydrogen almost never occurs naturally in its diatomic state (Sperling and Ogden 2004), necessitating its production, often by costly or thermally inefficient processes. One of the most common methods involves the combination of natural gas with steam over a catalyst (reaction given in Eq. 2.1). Less effective methods include the electrolysis of water (Eq. 2.2) and the partial oxidation of various hydrocarbons with air. These high-temperature reactions convert the hydrocarbons to a gas which can be further processed into pure hydrogen (Ogden 2004). These reactions require significant amounts of energy however, and it is estimated that nearly 95% of hydrogen is currently produced by burning fossil fuels. In accordance with the second law of thermodynamics, studies have suggested that current

methods consume as much or more fossil fuel than the hydrogen saves (Sperling and Ogden 2004). For this reason, many in this field consider hydrogen to be an energy carrier rather than a true energy source (Ogden 2004).



Additional possibilities for hydrogen production include the water-gas-shift reaction, given as,



which can occur at relatively low temperatures (~ 400 K). In this reaction, the water vapor is stripped of its oxygen atom (Turns 2000). Additional studies have found that certain types of algae produce hydrogen via a form of photosynthesis when deprived of sulfur (McAlister 2003).

2.1.2 Fuel Cells versus Internal Combustion Engines

An additional benefit to hydrogen is versatility, as it has applications in both internal combustion engines (ICEs) as well as fuel cells. While hydrogen used in ICEs in much the same way as traditional fossil fuels, fuel cells which run on hydrogen convert

chemical energy contained in the molecules to electricity. Similar to ICEs, fuel cells using hydrogen are also plagued by its low energy density, and therefore suffer similar problems with fuel tank size and storage. Unlike ICEs, fuel cells have the potential for much greater efficiency. Also unlike ICEs, however, the components used in the creation of fuel cells are extremely expensive and thus not yet practical for wide use (Romm 2004). Additionally, much of the research by automotive manufacturers currently focuses on light load fuel cell vehicles (Weiss et al. 2003).

2.2 HCCI Engines

The concept of HCCI engines (sometimes referred to as “controlled auto-ignition” engines) is a relatively new focus for combustion research and development. The process can best be described as a hybrid combustion process which combines various aspects of traditional spark-ignition (SI) and diesel engines. The incoming fuel-air mixture is premixed, which leads to reduced pollutant emissions. The mixture is ignited via compression, which leads to an increase in efficiency.

In a typical HCCI engine process, a premixed homogeneous mixture (charge) of air and fuel is taken into the cylinder well before top dead center (TDC) and compressed to a point at which it auto-ignites. This is achieved without any flame propagation and with reactions occurring at multiple points simultaneously (Kim and Lee 2005). Typically, this process is very air rich (or fuel lean), resulting in lower in-cylinder temperatures and

pressures than other combustion processes. The low NO_x emissions associated with HCCI are a direct consequence of this fact.

The ignition for the ideally homogenous case of HCCI is controlled primarily by chemical kinetics. This requires that the fuel chemistry be handled carefully and in great detail. Extensive research has been conducted on the development of chemical mechanisms. These mechanisms can vary in size from fewer than one hundred chemical reactions (Patel et al. 2004) to several thousand (Curran et al. 2002).

In most cases, HCCI deviates from this ideal model, and small inhomogeneities exist within the charge. This is most apparent in cases in which the fuel is introduced as a liquid.

The premixed nature of the charge is similar to that of most gasoline-based engines currently in use and allows for reduced emissions of nitric oxides and other harmful particulate matter. Since the charge is ignited via compression using high compression ratios, fuel efficiency comparable to diesel engines can be achieved.

2.2.1 Diesel-Based HCCI Engines

While much of the initial research on HCCI focuses on gasoline-based variations, the past decade has seen much interest in exploring the possibilities of a diesel-based alternative (Zhao et al. 2003). Many of the advantages to diesel-based HCCI are most relevant to the

trucking industry, which uses diesel engines almost exclusively. A shift to HCCI for this sector would be more likely if these heavy load vehicles could continue using the same fuel. At these heavy load conditions, issues with controlling the combustion timing become even more of a detriment. This requires the use of a more traditional combustion process at certain times during operation in order to maintain efficiency (Epping et al. 2002). Such a dual-mode system is more conveniently implemented using diesel-based HCCI than with other variations.

Two major drawbacks exist with diesel-based HCCI. Complications often arise with the proper vaporization of fuel, which requires temperatures higher than typically observed with HCCI. This makes the formation of a premixed charge difficult. Also, diesel fuel is known for its rapid auto-ignition at temperatures greater than 800 K (Kelly-Zion and Dec 2000). This becomes an additional factor adding to HCCI's lack of ignition timing control.

Diesel-based HCCI can be divided in three basic classifications: premixed, early direct-injection, and late direct-injection (Zhao et al. 2003).

In the premixed group, the fuel/air charge is homogeneously mixed prior to intake. An issue of concern here is the complete vaporization of the liquid fuel. To properly vaporize and premix with the remaining in-cylinder gases, temperatures much greater than that of the intake conditions are sometimes required. An additional concern is the problem of knocking at higher loads, creating even more difficulty in controlling the

combustion timing. This in turn can lead to increased hydrocarbon emissions and unfavorable thermal efficiencies (Suzuki et al. 1998). While some proposed solutions, such as injecting small amounts of additional fuel such as iso-octane (Suzuki et al. 1997) or methyl-tert-butyl ether (Suzuki et al. 1998) have been shown to offer slightly greater control over the combustion phasing of premixed HCCI, these serious issues make the practicality of this classification highly questionable in the absence of alternative means for premixing.

Early direct-injection, as its name implies, is categorized by the injection of fuel at a time significantly earlier than TDC. The injection of the fuel during the compression phase aids in the vaporization of the fuel as a result of higher in-cylinder temperatures. The injection occurs sufficiently early enough so that the charge may become nearly premixed by the time combustion occurs. This method uses lower intake temperatures, thus helping to prevent premature ignition, and is more compatible with currently used diesel engines (Epping et al. 2002).

In the third classification, late direct-injection, fuel is injected much later than in traditional direct-injection diesels. Typically, the injection timings are close to TDC and occur with large amounts of swirl to promote mixing and EGR to delay auto-ignition (Zhao et al. 2003). This method offers the advantage of improved control over ignition timing. One of the most successful implementations of late direct-injection is a technique developed by Nissan Motor Company called modulated kinetics (MK). This method was outlined by Kimura et al. 1999) and Mase et al. 1998).

An additional means to improve timing control in diesel-based HCCI engines is the addition of water in the fuel/air mixture (Nishijima et al. 2002).

2.2.2 Hydrogen in Diesel and HCCI Engines

The use of pure hydrogen in HCCI engines has been successfully achieved, although the success is limited at best. The use of hydrogen as the sole fuel in HCCI has been shown to further contribute to the problems of premature ignition. Experiments conducted by Tang et al. (2002) have shown there to be a significant reduction in the torque and power output when operated under production conditions compared to those of currently used diesel engines.

2.2.3 Current Issues in Diesel-Based HCCI

While significant research effort is devoted to HCCI engines, much work is still required to sufficiently optimize the combustion process for use in the automotive sector.

Significant performance issues associated with the HCCI combustion processes are in need of resolution. These include the control of ignition timing, emissions of carbon monoxide, unburned hydrocarbons, and other harmful pollutants, as well as optimal operation at a wider range of load-speeds (Zhang and Haworth 2004). In addition, the effects of turbulence on the combustion process have become an important concern. The

influence of factors which cause the system to deviate from the homogeneous case have been shown to have a strong effect on the combustion process (Haworth 2005). Even slight variations in species concentrations, temperature, or pressure can lead to drastic changes in the combustion regime. Both numerical and experimental research is needed in order to sufficiently understand and predict the effects caused by even subtle changes.

Finally, many components of HCCI engines used in laboratory settings are expensive and custom made. In order to effectively enter the automotive market, these components will need to be replaced or modified so as to be more favorable to mass production (Zhao et al. 2003).

2.3 NO_x Emissions in Diesel-Based HCCI Engines

An area of concern in the design of any combustion system is the amount of harmful emissions released as a result of the process. In HCCI engines, harmful products include carbon monoxide (CO), unburned hydrocarbons (UHC), oxides of nitrogen (NO_x), and particulate matter (PM). Of these, significant effort is devoted to the reduction of NO_x levels in automobile engines. Both NO and NO₂ are strong contributors to the production of ground-level ozone. All of the above are known to be extremely damaging to lung tissue, causing inflammation, reduced lung function, respiratory illnesses, as well as aggravate existing conditions such as asthma (Mitchell 2001).

One of the most attractive features of HCCI combustion is the potential for reduced NO_x emissions. Conventional diesel or SI engines achieve ignition through the propagation of a flame, leading to higher in-cylinder temperatures (Amnès et al. 2005). At such temperatures, nitrogen atoms begin to break down and combine with oxygen and hydrocarbon radicals, leading to increased amounts of NO and NO_2 (Amnès et al. 2005). Although numerous chemical pathways for NO_x formation have been proposed, it is generally accepted that the Zeldovich or “thermal” mechanism is in many cases the primary source (Turns 2000). As this pathway is highly temperature dependant, a reduction in combustion temperatures can lead to a significant decrease in the amount of NO_x created. It has been proposed that the effects of this group of chemical reactions can be considered negligible at temperatures below 1800-1900 K (Turns 2000). Since HCCI combustion processes normally run very fuel lean and without any flame propagation, the in-cylinder temperatures typically fall below this range and thermal NO_x is no longer the most important NO_x pathway. However, other pathways generally considered negligible due to the effect of thermal NO_x are especially important in HCCI.

2.4 Detailed Chemistry HCCI Engine Modeling

Chemical kinetics is one of the dominant factors controlling ideal HCCI combustion. As a result, the simulation of the fuel oxidation should be handled with care and in great detail. Throughout this thesis, two methods of numerical modeling were used, both of which approximate the complex effects of chemical kinetics on the combustion process. The first was a zero-dimensional HCCI engine model included as part of the CHEMKIN

4.0 software package (Reaction Design 2005). The second was a detailed three-dimensional computational fluid dynamics (CFD) model developed for the General Motors Company by Penn State researchers (Haworth 2005).

2.4.1 Zero-Dimensional Modeling

Reaction Design's CHEMKIN chemical kinetics software was used for the numerous zero-dimensional tests discussed in this thesis. The software package contains a built-in zero-dimensional closed-system IC engine model which simulates the auto-ignition of fuel-air mixtures via compression. The program is designed to focus primarily on the chemical reactions' impact on global engine parameters such as temperature and pressure in addition to the detailed chemistry of fuel oxidation. A shortcoming of this model is its lack of ability to account for three-dimensional effects. Additionally, the initial species are assumed to be premixed and remain perfectly homogeneous throughout the compression. The model is a fixed-mass system, and cannot simulate valve opening/closing or fuel injection.

The major advantage to this model is its speed. Highly detailed chemical mechanisms, such as those provided by Lawrence Livermore National Labs [Curran et al. (1998), Curran et al. (2002), and Westbrook et al. (2002)], sometimes contain well over a thousand chemical species and several thousand reactions. Even extremely large chemical kinetics files such as these may be run with relative ease and favorable computational times using CHEMKIN.

While speed is strength for many zero-dimensional models, accuracy and functionality often suffer as a result. Such models operate very well for many simple cases, but are inherently limited in their capabilities and flexibility. For instance, although CHEMKIN does contain a heat transfer model, it is minimal and does not allow for a great deal of customization. Because the model is a fixed-mass system, the true intake and exhaust processes cannot be modeled. Other scenarios such as fuel injection and spark ignition also cannot be modeled using most zero-dimensional codes. In spite of their disadvantages, they remain excellent tools for the numerical approximation of simple processes and for the observation of trends in parametric studies. A significant portion of the data presented in this thesis was obtained using the CHEMKIN software package.

2.4.2 CFD Modeling

Although the primary controlling mechanism of an ideal HCCI case is the thermochemistry, more practical cases necessitate the use of more robust physical models. To explore the impact of turbulence, swirl, and inhomogeneities, a three-dimensional model is required. The effects of turbulence on the combustion chemistry, or turbulence/chemistry interactions (TCI), play an important role in both the combustion process and emissions (Zhang et al. 2005).

Previous studies have shown that in cases with low in-cylinder swirl, TCI has little effect on ignition timing, but does a significant effect on emissions. As the swirl level increases

and the charge becomes increasingly inhomogeneous, TCI becomes an important factor on both ignition timing and emissions (Zhang et al. 2005). TCI has even been suggested as a major contributor to cases in which the level of NO₂ in the exhaust is greater than the level of NO (Amnès et al. 2005).

Using a CFD model, it is possible to simulate many scenarios which less extensive models cannot address. The effect of piston head or wall geometry on the fluid dynamics in the cylinder can be accounted for in CFD. More complex cases such as fuel injection and intake/exhaust can also be simulated.

Although many models are finite-volume (FV) based, some CFD models also have the potential to make use of probability density functions to describe the distribution of various quantities (Zhang et al. 2005). Such a method allows for additional accuracy in complex computational analyses. A probability density function (PDF) method assumes that certain variables in the computational domain randomly fluctuate as a function of their spatial locations. Each cell or node has a specified probability to have a certain amount of each variable. These functions typically remain constant throughout the model. Using a PDF method, spatial variations of these variables are modeled with a reasonably light computational effort (Zhang et al. 2005).

The primary drawback to using CFD models is the high computational cost often required. Codes of this nature can take several hours or days for a single run, making large parametric studies a lengthy and unreasonable process.

2.5 Present Work

This thesis explores a varied range of engine and fuel parameters under HCCI conditions in an effort to gain a better understanding of this combustion process. Particular focus is given to the effect the variation of parameters such as thermochemical conditions, EGR levels, air/fuel ratios, and fuel types have on ignition timing and emissions. The key role of chemical kinetics in HCCI combustion necessitates the careful comparison of chemical mechanisms, and a significant portion of the present work involves the testing, comparison, and validation of these mechanisms.

The studies employ both zero- and three-dimensional models time-dependant models. Homogeneous fuel/air mixtures are considered as well as the direct in-cylinder late injection of fuel.

CHAPTER 3

COMPUTATIONAL TOOLS

The numerical simulation tools that have been used for this research are introduced in this chapter. These fall into two categories: zero-dimensional modeling and three-dimensional CFD.

3.1 Zero-Dimensional Modeling: CHEMKIN

Chemical kinetics is a dominant factor in controlling an ideal HCCI combustion process. Accordingly, the selection of appropriate chemical kinetics models is an important endeavor. CHEMKIN is a chemical kinetics program created by Sandia National Laboratory which handles the complex chemical and thermodynamic considerations associated with various combustion processes. This collection of software is one of the most widely used, and is well-suited to the tasks required in this study. In this thesis, a commercial version [version 4.0, (Reaction Design 2005)] was used. The program collects data from various input files used to describe the chemical reaction sets and thermodynamic properties. The user is prompted for additional information including thermochemical conditions, global engine parameters, and other variables relevant to numerical modeling (such as time step or convergence criterion). This information is used to simulate the effects of chemical kinetics on the combustion process as the reactor volume changes with time.

3.1.1 IC Engine Model

CHEMKIN 4.0 includes a pre-programmed zero-dimensional internal combustion engine model (ICE), which was used to simulate the combustion process. This model is a zero-dimensional, fixed-mass, homogeneous, time-varying system and was previously known as “Aurora” in earlier versions of the code. Flame propagation is not addressed in this model. Global engine parameters such as compression ratio, displacement volume, and intake/exhaust valve opening/closing are specified by the user. Intake conditions, such as temperature, pressure, and species mole fractions, are also user-specified.

The major benefit to this model is its speed. This allows for numerous cases to be run quickly with relatively little computational effort. A major factor influencing the model’s speed is the size of the chemical mechanism (or gas-phase kinetics) file, with larger mechanisms corresponding to longer run times. Typical mechanisms can range from a few dozen species to several thousand, and the time required for a typical run can range from a few seconds to a several hours. In most cases, the run times are relatively short, making CHEMKIN an ideal tool for the parametric studies conducted in this thesis.

3.1.1.1 Heat Transfer in the ICE Model

CHEMKIN’s ICE model includes a skeletal convective heat transfer model of the form in Eq. 3.1,

$$Q_{conv} = hA(T - T_{wall}), \quad 3.1$$

where A is the surface area of the cylinder wall, T_{wall} is the temperature of the cylinder, T is the temperature of the in-cylinder gases, and h is the convective heat transfer coefficient. The value of h is based on the Nusselt number relation in Eq. 3.2,

$$Nu_h \equiv \frac{hD}{k} = a Re^b Pr^c. \quad 3.2$$

where D is the engine bore, k is the thermal conductivity of the cylinder gases, Re and Pr are the Reynolds and Prandtl numbers respectively, and a , b , and c are user-specified constants. The Reynolds number is given by in Eq. 3.3 ,

$$Re = \frac{D w \rho}{\mu}, \quad 3.3$$

where w is the average in-cylinder gas velocity, and ρ and μ are the gas density and viscosity respectively.

Two options for approximating heat loss during the combustion process are available. The first is to specify the wall heat flux, Q_{conv} , the rate at which heat is dissipated during the simulation. This heat flux may be given a constant value or calculated at each time step using a user-defined function.

A second option involves the specification of the engine bore, a constant wall temperature, Prandtl number, and coefficients a , b , and c . The wall heat flux is then calculated using Eqs. 3.1, 3.2, and Eq. 3.3 at each computational step. Additional flexibility in this convection scheme allows the user to calculate the average in-cylinder gas velocity using the Woschni Correlation (Heywood 1988) in order to obtain a more accurate Reynolds number. This correlation, given by Eq. 3.4, is,

$$w = \left(C_{11} + C_{12} \frac{v_{swirl}}{S_p} \right) S_p + C_2 \frac{V_d T_i}{P_i V_i} (p - p_m), \quad 3.4$$

where v_{swirl} is the swirl velocity, S_p is the mean piston speed, V_d is the volume displaced, T_i , p_i , and V_i are the temperature, pressure, and volume of the working-fluid at some initial reference state, and p and p_m are the instantaneous pressure and motored pressure respectively (Heywood 1988). C_{11} , C_{12} , and C_2 are constants determined by the flow regime.

3.1.1.2 Limitations of the ICE Model

The simple nature of CHEMKIN's ICE model leads to several inaccuracies. Perhaps most significant is the neglect of fluid dynamics and other multi-dimensional considerations. Effects such as turbulence, inhomogeneities, and swirl have been shown to have a strong influence on the oxidation of the fuel, and several studies have been

devoted to turbulence/chemistry interactions (Zhang et al. 2005). Additional problems arise from the assumption that the reactor is perfectly homogeneous at all times. For an ideal case of HCCI, this is a decent approximation. Large inaccuracies, however, can occur as the case deviates from this ideal, as is often observed. The exclusion of these considerations has been shown to result in earlier ignition times and steeper rates of pressure rise when compared to more detailed 3-D models or experimental data. As a fixed-mass system, additional restrictions are imposed on the capabilities of the model. CHEMKIN's engine model is unable to model fuel injection or true intake/exhaust conditions. And while heat loss is addressed with a bare-bones convective scheme, other important modes of heat transfer such as radiation are neglected, leading to great peak temperatures and earlier ignition.

In spite of these noted shortcomings, the CHEMKIN model has been an extremely useful tool throughout this study. Its speed is by far its greatest asset, allowing a large amount of data to be collected in a short amount of time. While the accuracy of the results may be slightly lacking, the most important controlling factor of ideal HCCI combustion, the chemical kinetics, is adequately addressed. So long as the chemistry of this process is properly handled, such a model may be considered an effective tool for the observation of trends in collected data.

3.1.2 Thermochemical Mechanisms

Perhaps the most important requirement for the use of CHEMKIN is the gas-phase kinetics file, an input file containing information about various chemical elements and the ways in which they react with one another. The file first defines the elements used, then the molecules (referred to as “species”) derived from these elements, and finally a list of global chemical reactions. In addition to defining how the species interact and exchange elements, this file defines each reaction’s rate coefficients and their temperature dependence.

The creation of a chemical mechanism is a tedious undertaking, and entire research projects are devoted solely to their design. An attempt to independently fabricate a mechanism is well beyond the scope of this research, and it became necessary to rely on those which are available to the public.

Numerous reliable gas-phase kinetics files are readily available. These mechanisms are often unique to a particular fuel and specific range of thermodynamic conditions, and may not be as effective (or even usable at all) in cases which involve other fuel types or that operate outside of this range. The files can contain fewer than thirty chemical species (Patel et al. 2004) or as many as several thousand (Curran et al. 2002). The size of the mechanism files directly affects the time required of the computational model, with larger files requiring longer run times.

An additional component required for nearly all CHEMKIN modules is a thermodynamic file. While the gas-phase kinetics file names each chemical species, the names are completely arbitrary. It is in the thermodynamics file that the names are given meaning. Here, the elements that make up each species as well as its state (gas, liquid, or solid) and any electrical charge it may have are defined. This file also describes how each species behaves based on the assumption that the various standard-state properties are functions of temperature. A set of fourteen coefficients are provided which are used in polynomial curve fits to describe how temperature influences these properties. A range of temperatures for which the polynomial fits are valid are provided at the top of the file. By using the heading "THERM," the thermodynamic file may be included in the gas-phase kinetics file instead of a separate document.

Throughout the course of this research, it became necessary to combine mechanisms in order to model certain cases. Many fuels such as n-heptane (C_7H_{16}) or iso-octane (C_8H_{18}) have numerous mechanisms of various sizes available. However, most of them contain little or no nitrogen chemistry. In these cases, nitrogen is treated as an inert gas, and does not dissociate into other species, making it impossible to model NO_x formation and emissions. In order to address this issue, a base mechanism was selected and the nitrogen chemistry of another mechanism added to it. It was important for the new mechanism to be created in this way (as opposed to adding the fuel chemistry to the entire nitrogen chemistry mechanism) so that the oxidation of the fuel in question was correctly preserved.

The creation of a combined thermodynamic property file (or “thermo file”) is a much easier process compared to that of a combined gas-phase kinetics file. One need only recall the species added to the original base mechanism and simply add the corresponding thermodynamic properties from the nitrogen thermo file to the base thermo file. As with the chemical mechanism formation, it is generally a good idea to keep the thermo information of the base file when duplicate species information is encountered.

A summary of the mechanism combination process is presented below.

1. Select a base mechanism containing the oxidation chemistry for the desired fuel and a secondary mechanism containing the additional chemistry to be added to the base.
2. Copy only the reactions involving the new chemistry (i.e. the nitrogen species) from the secondary mechanism and insert them into the base.
3. Be sure that all species are named in caps everywhere in both the gas-phase kinetics file and the thermodynamic file. This ensures conformity not only among various other mechanisms, but also with case-sensitive CFD codes.
4. Add species not contained in the base mechanism but which are contained in the secondary mechanism to the base mechanism species list.
5. Copy the species added above from the thermodynamics file of the secondary mechanism into the base thermodynamic file.
6. Search for any duplicate reactions in the gas-phase kinetics file, and remove those which were copied from the secondary mechanism.
7. Compare the new mechanism to the original base under the same operating conditions using a numerical model and observe the plots for temperature and pressure. If these remain unaltered in any significant way, then the new mechanism can be considered reliable and ready for use.

3.1.2.1 Comparison of Ignition Timing

The first step in the creation of a new mechanism is to select an existing one to serve as the “base.” This base should be a previously designed mechanism specific to the desired fuel which has been deemed reliable. In this study, largely concerned with the modeling of n-heptane, several mechanisms were considered. The bulk of these came from either the University of Wisconsin’s Engine Research Center (UW-ERC) or Lawrence Livermore National Laboratories (LLNL). Table 3-1 contains a list of these mechanisms and information on their respective sizes.

Table 3-1: List of n-heptane mechanism properties and references.

<i>Mechanism</i>	<i>Species</i>	<i>Reactions</i>	<i>Run Time (seconds)²</i>
UW-ERC (Patel et al. 2004)	29	52	6
UW-ERC (Patel et al. 2004)	40	165	9
LLNL (Seiser et al. 2000)	159	770	65
LLNL (Curran et al. 2002)	561	2539	288
LLNL (Curran et al. 2002)	1034	4236	960

Figure 3-1 is a comparison of the temperature profiles of these mechanisms under the operating conditions given in Table 3-2. These conditions were chosen to mirror those presented in a study conducted by Zhang et al. (2004).

² These approximate run times correspond to a computation through a single engine cycle on the Cambrian PC (cambrian.perc.psu.edu), a Linux-based 2.0 GHz Intel system. Each of these mechanisms was tested using CHEMKIN 4.0 under the operating conditions specified in Table 3-1.

Table 3-2: Thermochemical conditions and global engine parameters used for n-heptane mechanism comparison tests.

Compression Ratio:	15:1
Cylinder Displacement Volume:	1600 cm ³
Conn. Rod to Crank Angle Ratio:	3.7143
Bore:	12.065 cm
Stroke:	14.0 cm
Speed:	1000 rpm
Starting Crank Angle:	-146 deg ATDC
Ending Crank Angle:	141 deg ATDC
Intake Temperature:	300 K
Intake Pressure:	100 kPa
Heat Transfer Model:	adiabatic
Fuel:	n-heptane
Equivalence Ratio:	0.3731

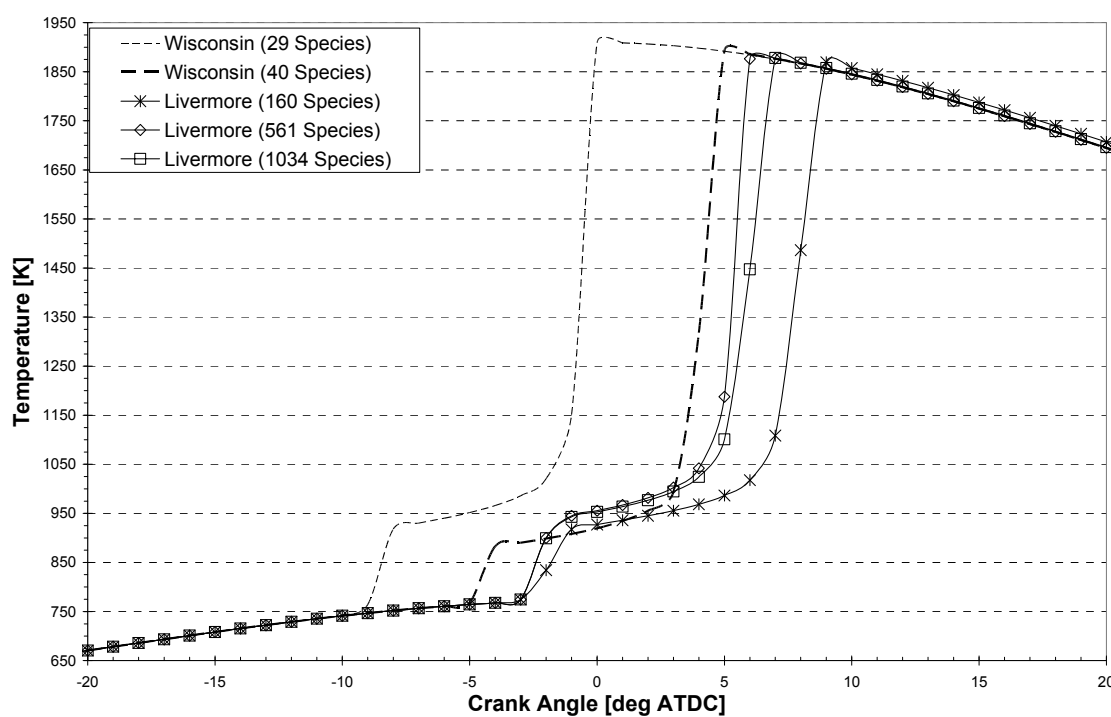


Figure 3-1: Comparison of various n-heptane mechanisms under the operating conditions in Table 3-2.

There are significant differences among the various oxidation mechanisms. While the peak temperatures are similar, ignition timing varies by as much as ten crank angle degrees (CAD). These variations become even more pronounced in higher temperature regimes.

Figure 3-2 suggests that the 40-species mechanism from the University of Wisconsin's Engine Research Center conforms better to the much larger Livermore mechanisms [(Seiser et al. 2000) and (Curran et al. 2002)], particularly to the smallest of these. Since the large size of the Livermore mechanisms makes them impracticable for later use in CFD, the 40-species UW-ERC mechanism has been adopted as the base n-heptane mechanism. The small size would allow for favorable run times, particularly in CFD, while the compatibility to the larger Livermore mechanisms suggests an accurate modeling of the fuel oxidation.

3.1.2.2 Comparison to Hydrogen Mechanism

As the combustion of hydrogen plays a crucial role in this study, it was necessary to compare the UW-40 mechanism to an established hydrogen/air mechanism to ensure compatibility in that regard. Using the conditions in Table Table 3-3, the UW-40 mechanism was compared with a H₂/O₂ mechanism from Lawrence Livermore National Laboratories (Connaire et al. 2004). The results of this comparison are presented in Figure 3-3.

Table 3-3: Thermochemical conditions and global engine parameters used for hydrogen mechanism comparison tests.

Compression Ratio:	18.7:1
Cylinder Displacement Volume:	1600 cm ³
Conn. Rod to Crank Angle Ratio:	3.7143
Speed:	1400 rpm
Starting Crank Angle:	180 deg ATDC
Ending Crank Angle:	450 deg ATDC
Intake Temperature:	355 K
Intake Pressure:	101.325 kPa
Heat Transfer Model:	adiabatic
Fuel:	hydrogen
Equivalence Ratio:	0.3731

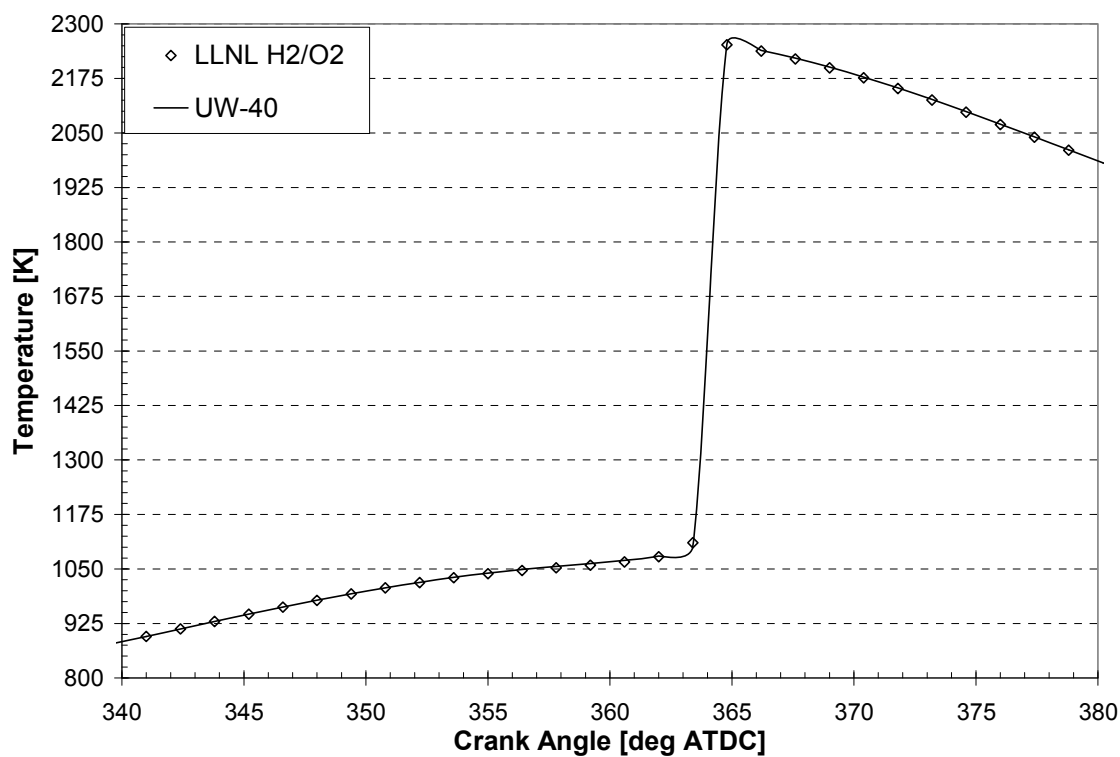


Figure 3-3: Comparison of the 40 species UW mechanisms with Livermore H₂/O₂ mechanism for hydrogen auto-ignition.

The global engine parameters and other thermochemical conditions were slightly modified from those of the other tests presented in this chapter. This was done to

promote the auto-ignition of hydrogen as means for an accurate basis of comparison. The results verify that the UW-40 mechanism is indeed well-suited for the oxidation of hydrogen.

3.1.2.3 Comparison of NO_x Emissions Using Hybrid Mechanisms

The nitrogen chemistry of one of three other mechanisms was added to the UW-ERC mechanism. The first two came from the Gas Research Institute, GRI-Mech versions 2.11 (Bowman et al. 2005) and 3.0 (Smith et al. 2005). The third was taken from research conducted by Glarborg et al. (1998). A comparison of these mechanisms is shown in Table 3-4.

Table 3-4: Basic properties of the hybrid n-heptane mechanisms.

<i>Hybrid Mechanism</i>	<i>Base Mechanism</i>	<i>NO_x Mechanism</i>	<i>Total Species</i>	<i>Total Reactions</i>
UW40_GRI2.11	40 Species UW	GRI-Mech 2.11	60	267
UW40_GRI3.0	40 Species UW	GRI-Mech 3.0	69	271
UW40_Glarborg	40 Species UW	Glarborg	71	375

The resulting three mechanisms were compared using CHEMKIN, and the corresponding difference in NO_x levels are shown in Figure 3-4.

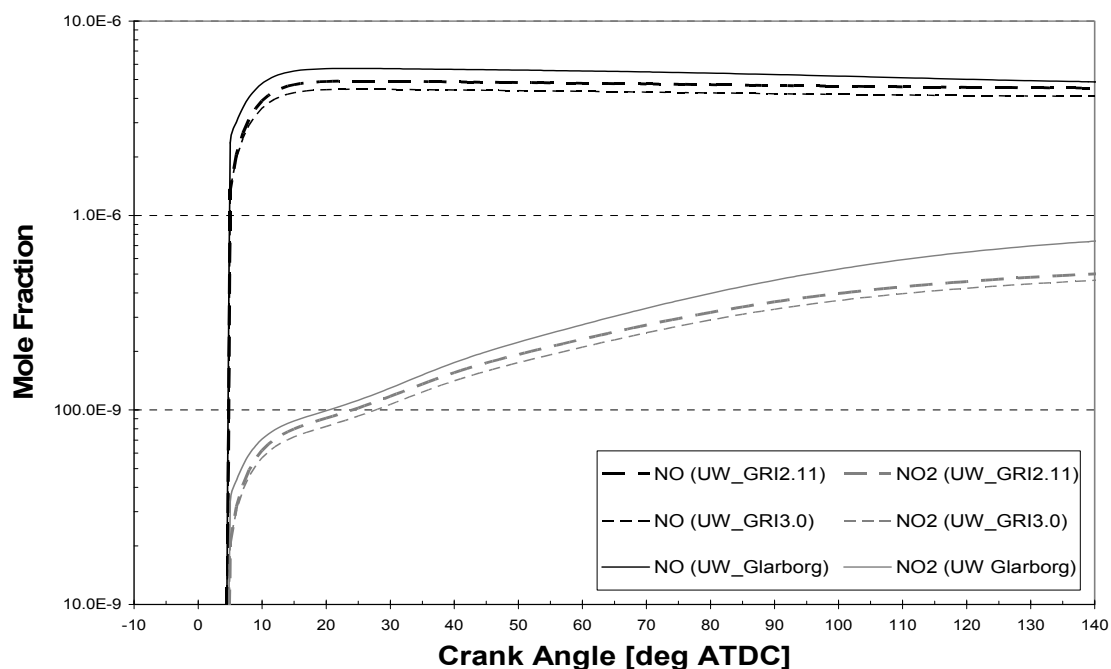


Figure 3-4: Comparison of NO_x emissions of hybrid n-heptane mechanisms under the operating conditions given in Table 3-2.

It is apparent from the figure above that the three mechanisms are somewhat similar, although version 2.11 of GRI-Mech was selected for use in this research. The primary reason for its selection was its favorable size. Made up of only 20 chemical species, when combined with the base n-heptane mechanism it is the smallest of the three hybrids. Although this will not significantly affect the 0-D testing, a smaller mechanism will noticeably impact CFD, where even a slightly smaller mechanism can have a profound effect on the time required for each simulation. An additional reason for selecting GRI-Mech 2.11 is that this set of nitrogen chemistry seems to produce results which fall neatly in between those produced by the other two mechanisms. It was determined that this middle value would be the best choice for the modeling of the nitrogen chemistry.

3.1.2.4 Validation of Hybrid Mechanism

Before using a hybrid mechanism in further studies, it is desirable to ensure that the addition of additional species and reactions did not alter the chemistry of the base mechanism. The base mechanisms before and after the additional chemistry was added were compared, with the results shown in Figure 3-5. The operating conditions for this case are once again those in Table 3-2.

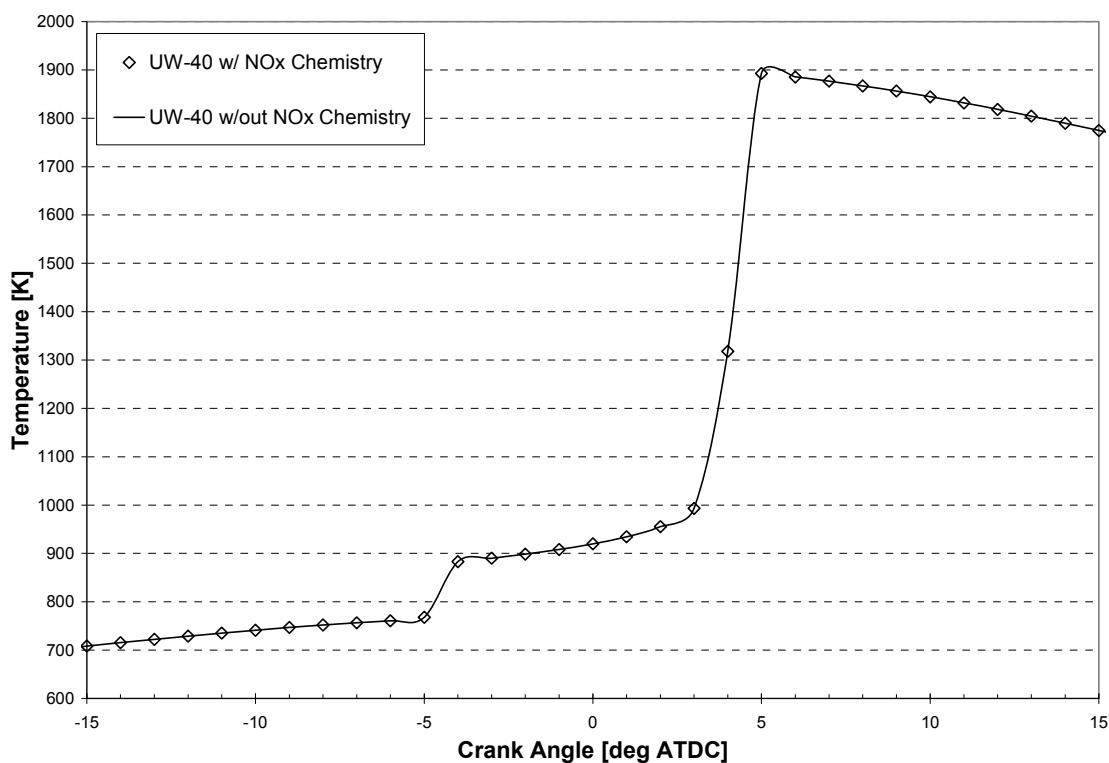


Figure 3-5: Comparison of the 40 species UW mechanisms before and after addition of nitrogen chemistry of GRI-Mech version 2.11.

The figure above verifies that the additional nitrogen chemistry did not significantly alter the base mechanism, justifying the use of the hybrid mechanism for additional testing.

3.2 Three-Dimensional CFD: ACFluX

To account for the effects of fluid dynamics, a more detailed computational tool becomes necessary. Since conditions such as turbulence and swirl are inherently multi-dimensional in nature, an appropriate model must, in addition to chemical kinetics, be able to handle calculations in spatial variations as well as time.

The primary tool employed for this task was ACFluX (Haworth 2005), a three-dimensional time-varying finite volume code capable of complex CFD modeling. This code is able to simulate additional aspects of an actual engine such as fuel injection and valve opening/closing. The code makes employ gas-phase kinetics and thermodynamic files in a similar format to those used with CHEMKIN to model chemical kinetics.

3.2.1 Basic Numerical Algorithm

Finite volume (FV) codes break down the physical space into tiny pieces with constant properties throughout. A collection of these volumes is referred to as a “mesh” or “computational domain.” A mesh which contains a large number of volumes is said to be fine. While finer meshes are generally more accurate, they are also more computational intense. ACFluX is provided with information as to the makeup of meshes via user-created input files. Within this computation domain, the governing equations for turbulent flow, species concentration and energy are simultaneously solved using a FV method.

3.2.2 Physical Models

The code employs numerical models used to simulate various physical processes such as heat loss, mixing, or fuel injection. Several of these are briefly described here.

The heat transfer model employed by ACFluX is a convective scheme similar to that of CHEMKIN. Although this convective scheme offers slightly greater flexibility, the calculations are fundamentally the same, and are based on either a constant wall temperature or a specified heat flux. Heat transfer is especially important in any multi-dimensional engine model, as any heat loss through the cylinder will lead to temperature gradients within the combustion chamber. These inhomogeneities in temperature can have an important effect on chemical kinetics as well as fluid dynamics.

ACFluX also contains a two-phase flow model for fuel injection. This spray model attempts to simulate droplets of liquid fuel as they are injected into the cylinder and vaporize to a gas. Collisions between droplets and the hydrodynamic effect of their introduction into the system are predicted using additional numerical models. The location of the spray nozzle, the fuel type, fuel mass droplet velocity, particle density, and injection timing can all be customized. Although relatively little is understood about fuel atomization and droplet collisions, current research suggests that a better understanding of these physical processes will have a drastic impact on engine design (Drake and Haworth 2006).

The turbulence model used in ACFluX is a standard k-epsilon flow model. The partial differential equations used to mathematically describe turbulence are solved using Reynolds-averaged simulation (RAS), a reliable method employed in CFD for nearly 30 years (Drake and Haworth 2006).

The importance of turbulence/chemistry interactions has been well established in recent studies (Zhang et al. 2005). These effects are often handled using probability density functions. A probability density function (PDF) method assumes that certain variables in the computational domain fluctuate as a function of their spatial locations. Each volume in the mesh has a specified probability to have a given value for each variable. These functions typically remain constant throughout the model. Using a PDF method, spatial variations of these variables are modeled with a reasonably light computational effort (Zhang et al. 2005).

CHAPTER 4

HOMOGENEOUS AUTOIGNITION OF N-HEPTANE-H₂/AIR MIXTURES

Two series of zero-dimensional tests were conducted. In the first, all thermochemical conditions and global engine parameters were held constant while the equivalence ratio and fuel composition (the % of H₂ in the C₇H₁₆/H₂ fuel mixture) were varied. In the second series, the ignition timing was fixed, first at approximately top dead center (TDC), then at approximately 4° before top dead center (BTDC). The desired ignition time was achieved for each case by varying the inlet temperature. In all cases in this chapter, the fuel was an n-heptane/hydrogen blend. Unless otherwise noted, all cases were run adiabatically. The UW40_GRI2.11 hybrid n-heptane/NO_x mechanism described in Section 3.1.2.3 was used for all cases. The results presented here focus on ignition timing and emissions.

4.1 Thermochemical Conditions

The parameters used in the CHEMKIN ICE model are discussed in this section.

4.1.1 Engine Operating Conditions

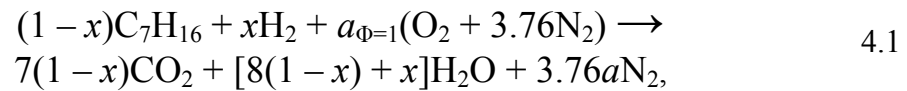
Global engine parameters and initial thermochemical conditions were modeled after those specified in Zhang et al. (2005). Table 4-1 summarizes the conditions used in the first series of tests.

Table 4-1: Conditions used for the first series of CHEMKIN tests.

Engine Cylinder Displacement Volume:	611.74 cm ³
Compression Ratio:	16.55
Engine Speed:	1 800.0 rpm
Inlet Pressure:	100.0 kPa
Inlet Temperature:	380.0 K
Exhaust Gas Recirculation (EGR):	0%
Conn. Rod/Crank Radius Ratio:	10 000.0
Inlet Valve Close:	-146.0 deg ATDC
Exhaust Valve Open:	141.0 deg ATDC

4.1.2 Stoichiometry

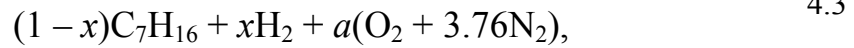
The global reaction corresponding to complete combustion of a stoichiometric C₇H₁₆-H₂/air mixture can be written on a per-unit-mole-of-fuel basis as,



where x is the number of moles of H₂ per mole of fuel mixture ($0 \leq x \leq 1$). An oxygen balance yields,

$$a_{\phi=1} = 7(1-x) + 4(1-x) + \frac{1}{2}x = 11 - \frac{21}{2}x. \quad 4.2$$

For nonunity equivalence ratios, the left-hand side of Eq. 4.1 can be written as,



where,

$$a = \frac{a_{\Phi=1}}{\Phi} = \frac{11 - 10.5x}{\Phi}. \quad 4.4$$

For reference, key thermochemical properties of H_2 and C_7H_{16} are provided in Table 4-2.

Table 4-2: Fuel thermochemical properties (Turns 2000).

Molecular Weight of H_2 (MW_{H_2}):	2.016	kg/kmol
Molecular Weight of C_7H_{16} ($MW_{\text{C}_7\text{H}_{16}}$):	100.203	kg/kmol
Lower Heating Value of H_2 (LHV_{H_2}):	120.500	MJ/kg
Lower Heating Value of C_7H_{16} ($LHV_{\text{C}_7\text{H}_{16}}$):	44.926	MJ/kg

4.2 Parametric Study: Fixed Initial Conditions

In the first series of tests, the equivalence ratio, Φ , was varied from $\Phi = 0.20$ to $\Phi = 1.00$.

The amount of hydrogen contained in the fuel on a molar basis, x , was varied from $x = 0.00$ to $x = 0.95$ for each equivalence ratio. Unless otherwise noted, all tests were run using the thermochemical conditions specified in Table 4-1.

4.2.1 Effect on Temperature and Ignition Delay

Figure 4-1 shows that peak temperatures increase with increasing hydrogen content in the fuel and with increasing equivalence ratio. The peak temperature is more sensitive to

changes in the equivalence ratio than to changes in hydrogen fuel concentration. This suggests that a given Φ , fuel composition should have a relatively small effect on NO_x emissions, except perhaps at very low equivalence ratios where peak temperatures are close to the 1700 – 1800 K thermal NO threshold.

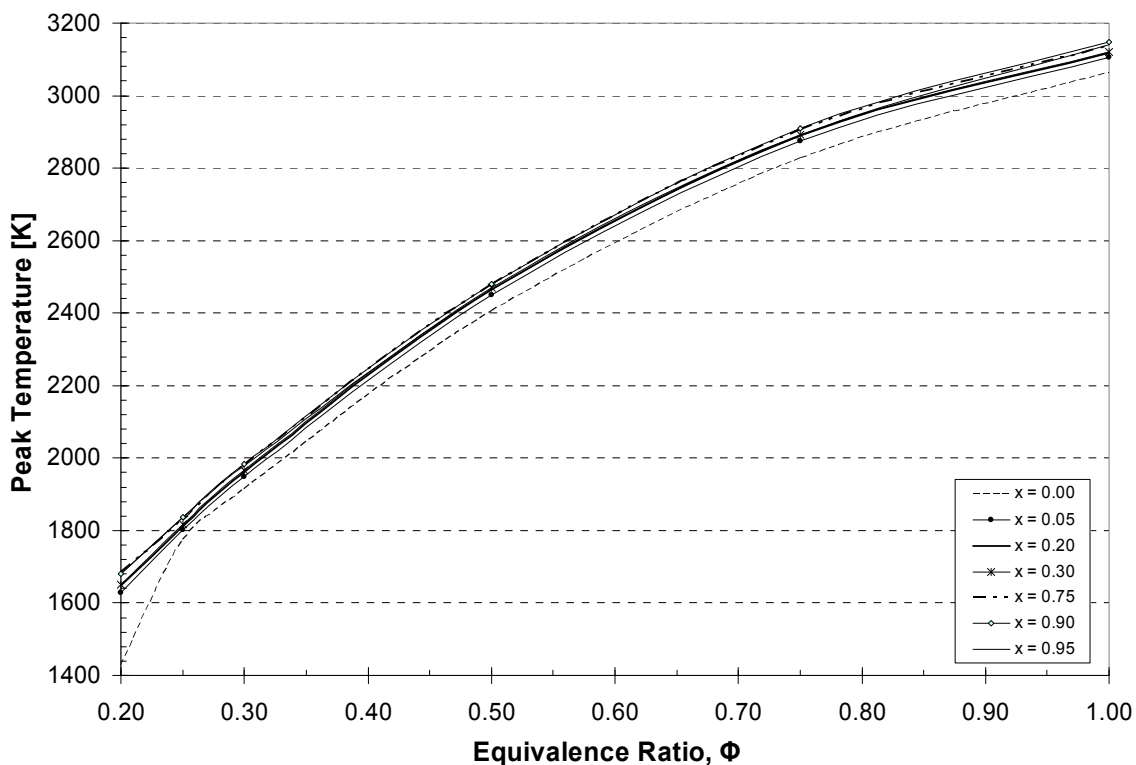


Figure 4-1: Effect of equivalence ratio, Φ , and hydrogen fuel concentration, x , on peak temperature.

In spite of the increase in peak temperature with increasing hydrogen content, ignition delay increases with increasing hydrogen content (Figure 4-2), especially at very high H_2 levels (90% - 95%). Note that the ignition timings in Figure 4-2 all correspond to

overadvanced ignition compared to what would be desirable in a practical engine for diesel-based HCCI.

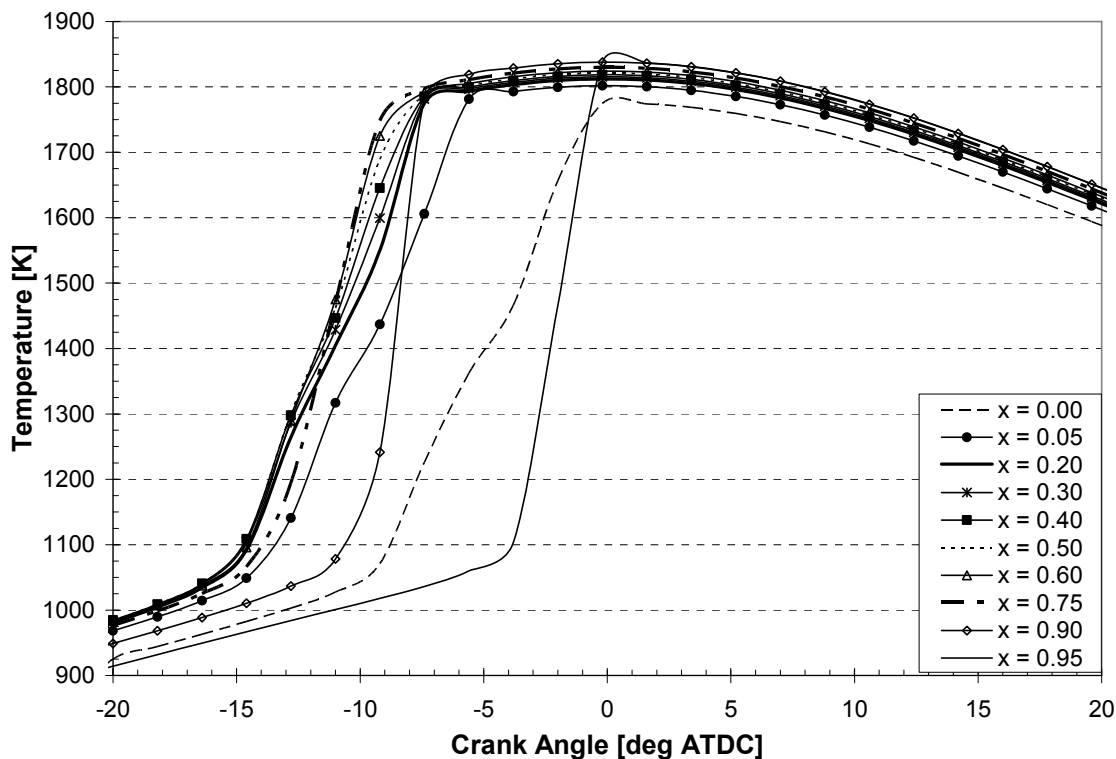


Figure 4-2: Effect of fuel composition on ignition timing for $\Phi = 0.25$.

4.2.2 Effect on Emissions

Figure 4-3 shows UHC emissions for $\Phi = 0.25$ with variations in hydrogen fraction (x). The values shown are mole fractions at 141° ATDC (exhaust valve opening). By that time, the mole fractions are essentially frozen. As expected, the amount of UHC decreases as the amount of hydrogen contained in the fuel increases. The reduction increases rapidly for mixtures containing greater than 75% hydrogen.

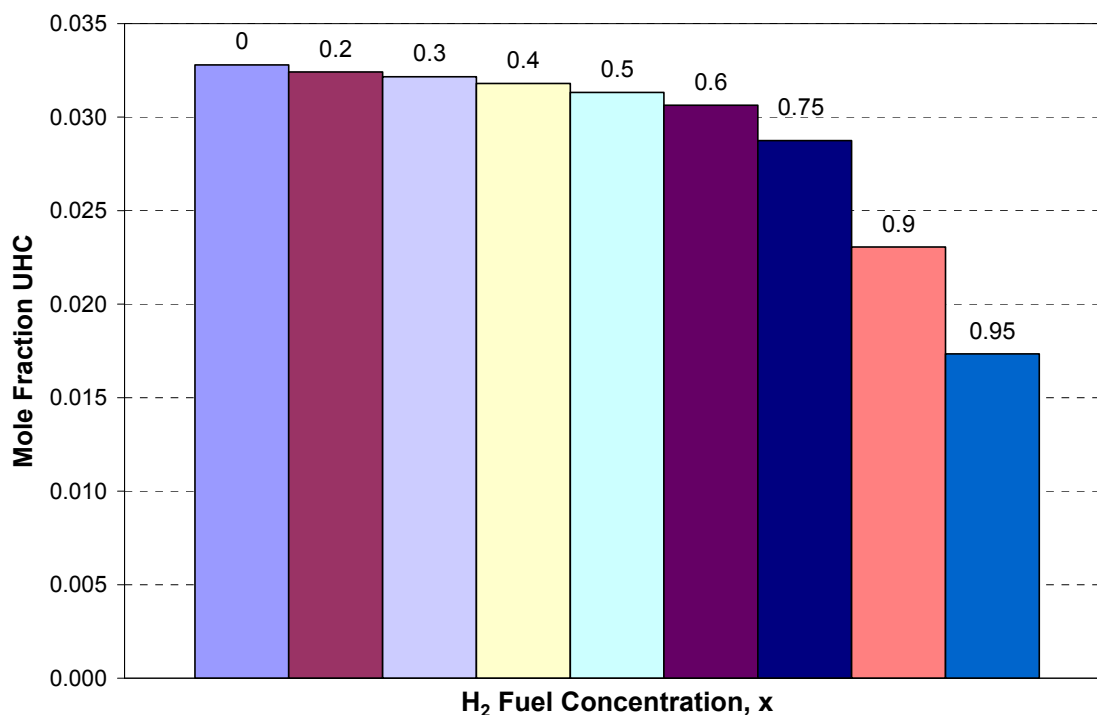


Figure 4-3: UHC emissions versus H₂ fuel content, x , for $\Phi = 0.25$.

Figure 4-4 shows emissions of CO, NO, and NO₂ with variations in H₂ content at $\Phi = 0.25$. The CO trend follows that for UHC while NO and NO₂ increase slightly with increasing x . This probably is a result of the higher in-cylinder temperatures for higher x (Figure 4-1). The operating conditions are those of Table 4-1.

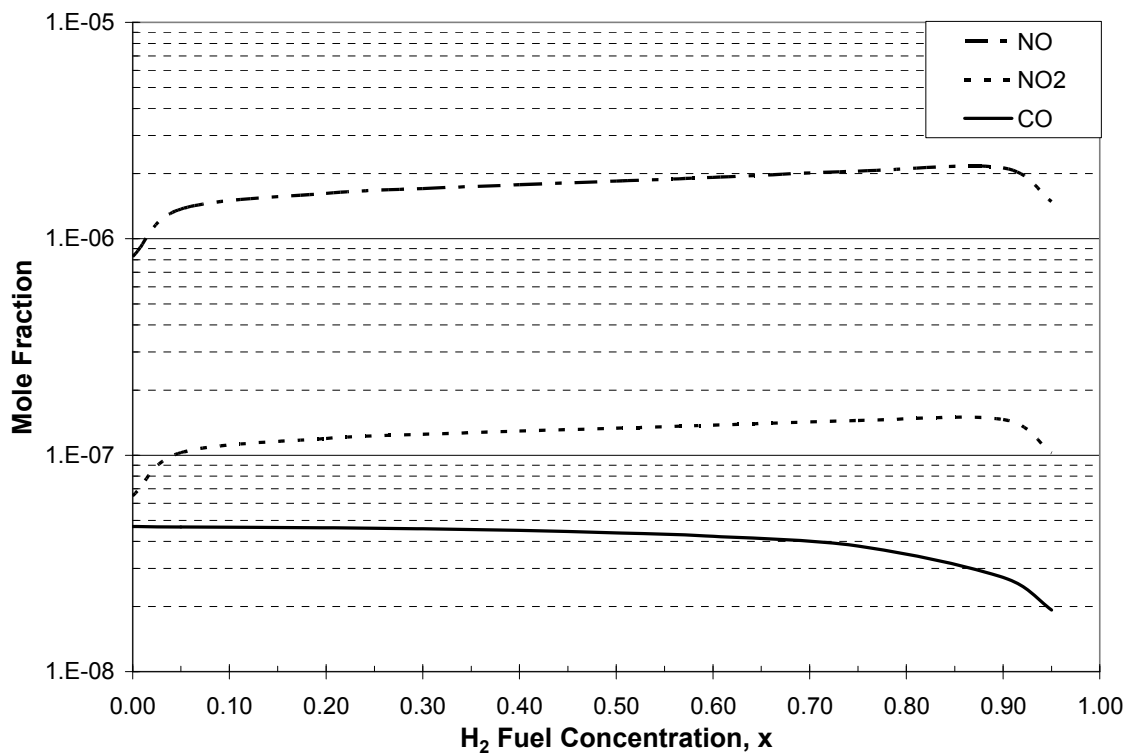


Figure 4-4: Emission trends for various hydrogen fuel concentrations at $\Phi = 0.25$.

In general, it has been found that emissions vary weakly with x for fixed Φ (as shown in Figures 4-3 and 4-4 for $\Phi = 0.25$), except at very high or very low x .

The variations in emissions with equivalence ratio are more dramatic. Figures 4-5 and 4-6 show NO and NO₂ emissions, respectively, as functions of Φ and x .

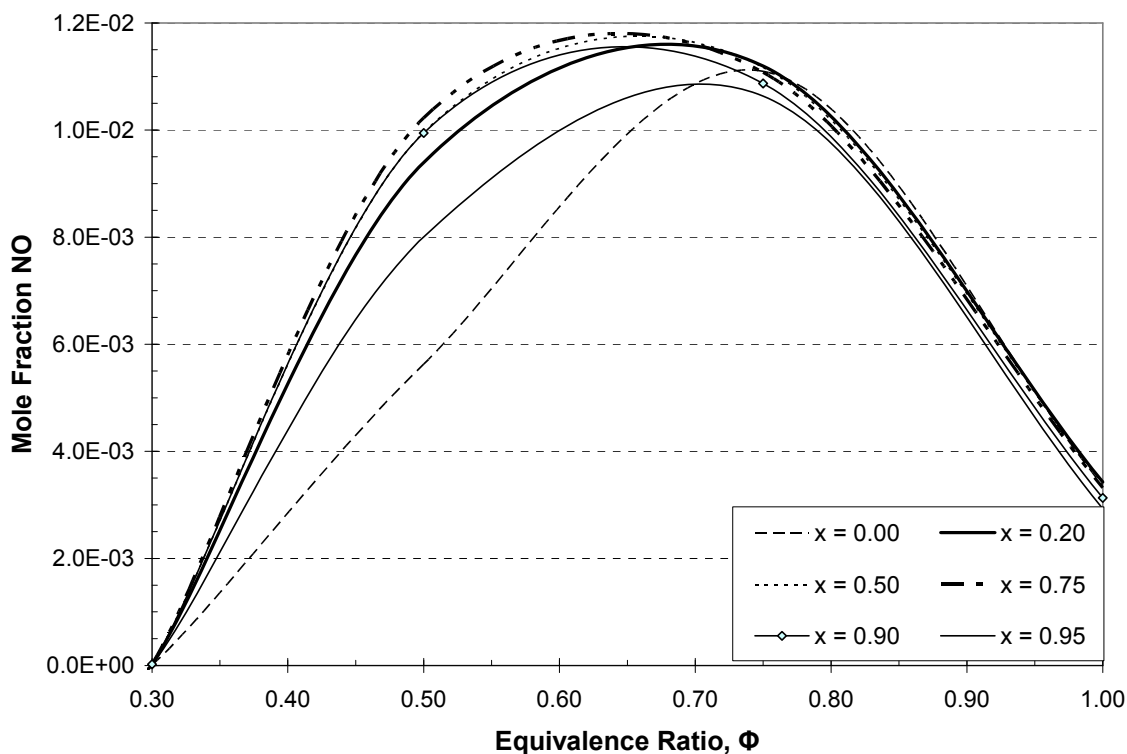


Figure 4-5: Effect of equivalence ratio and hydrogen fuel concentration on NO emissions.

In Figure 4-5, the NO level varies in a parabolic fashion with Φ , with the peak occurring at an equivalence ratio of approximately 0.75. A similar trend is observed for the NO_2 emissions in Figure 4-6. Both NO and NO_2 peak at intermediate equivalence ratios ($\Phi \approx 0.5$ for NO_2 , $\Phi \approx 0.75$ for NO). This is clearly a chemical effect rather than a thermal effect, since temperature increases monotonically with the equivalence ratio (Figure 4-1).

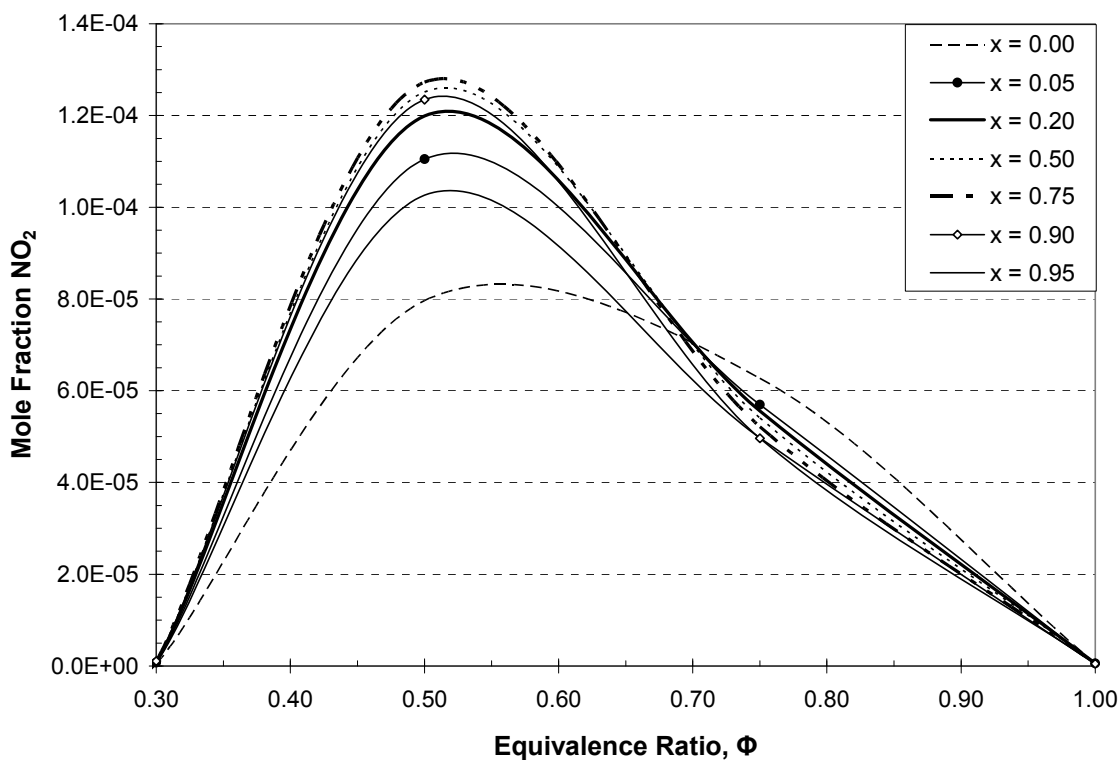


Figure 4-6: Effect of equivalence ratio and hydrogen fuel concentration on NO₂ emissions.

The difference in Φ for peak emissions of NO versus NO₂ may be related to the unusual emissions results described by Amnès et al. (2005), where the NO₂ levels surpassed the NO levels in some cases. The computed NO₂/NO ratios for a range of equivalence ratios and fuel compositions are plotted in Figure 4-7.

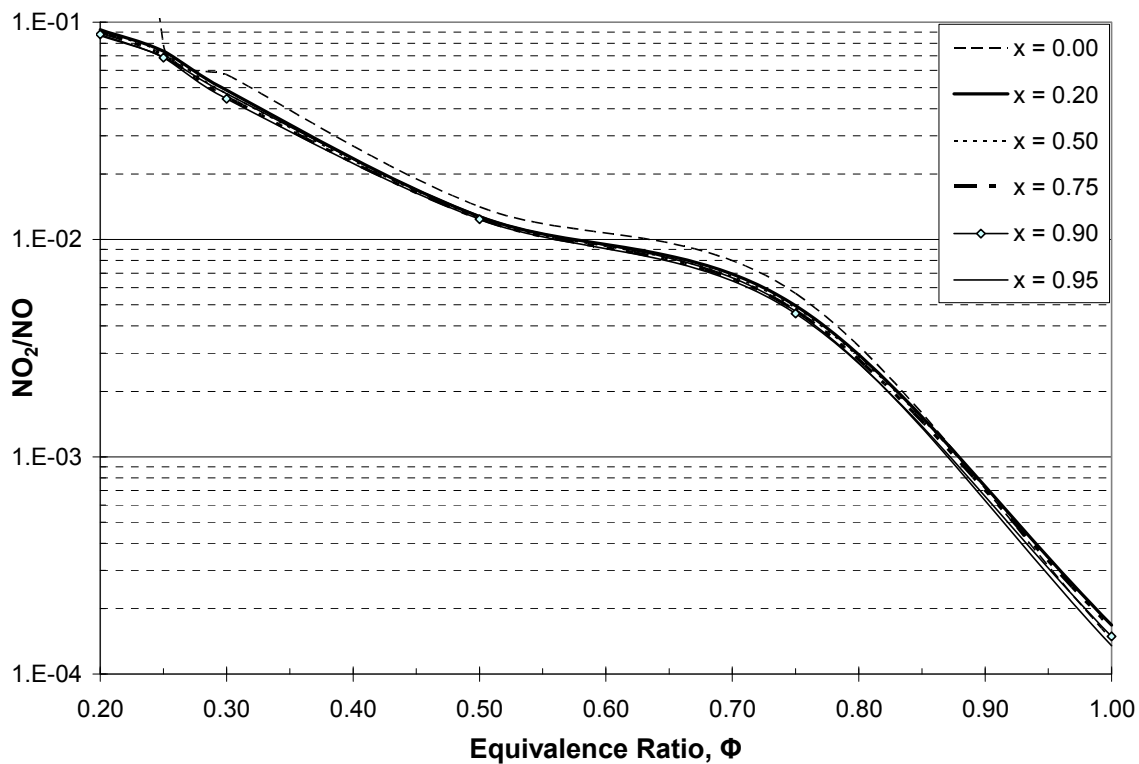


Figure 4-7: Effect of equivalence ratio and hydrogen fuel concentration on NO_2/NO ratio.

Figure 4-7 shows that the hydrogen fuel concentration does not have a significant impact on the NO_2/NO levels. The figure also shows that levels of NO relative to NO_2 increase as the equivalence ratio increases. This is likely the result of higher peak temperatures leading to greater NO production via the Zeldovich mechanism (Turns 2000).

A trend similar to that noted for NO_x emissions was observed for CO emissions (Figure 4-8), with a peak occurring at $\Phi \approx 0.75$.

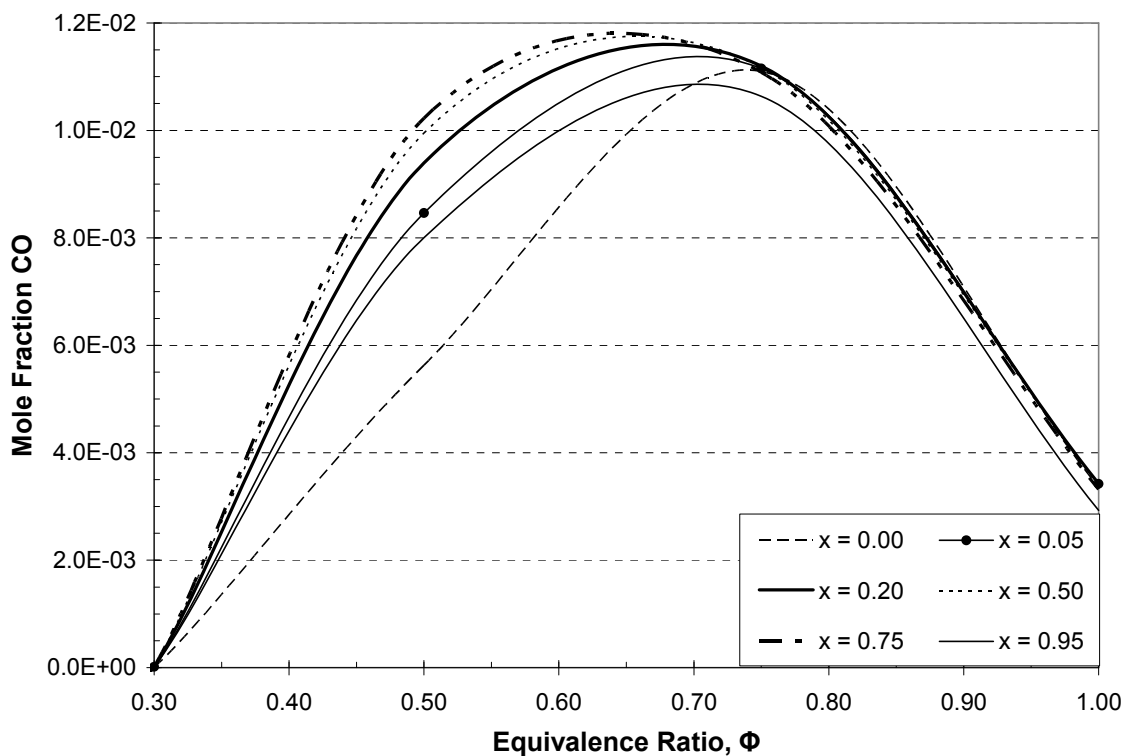


Figure 4-8: Effect of equivalence ratio and hydrogen fuel concentration on CO emissions.

4.3 Parametric Study: Fixed Ignition Timing

In the next series of tests, the ignition timing for each case was held at top-dead-center (TDC) by changing the intake temperature (Table 4-3 and Figure 4-9). For this study, “ignition” is defined as occurring at the onset of the maximum rate of temperature rise (at times almost vertical) on a temperature vs. crank angle graph. The remaining thermochemical properties and engine parameters were the same as those used in Section 4.2 (Table 4-1).

Table 4-3: Inlet temperatures [K] for the TDC fixed ignition timing tests.

Φ	H_2 Fuel Concentration, x									
	0.00	0.05	0.20	0.30	0.40	0.50	0.60	0.75	0.90	0.95
0.20	375	350	343	342	340	340	340	340	345	355
0.25	375	351	344	344	344	342	342	342	348	356
0.30	377	352	347	346	344	344	344	344	348	356
0.50	382	359	350	352	352	352	352	352	354	360

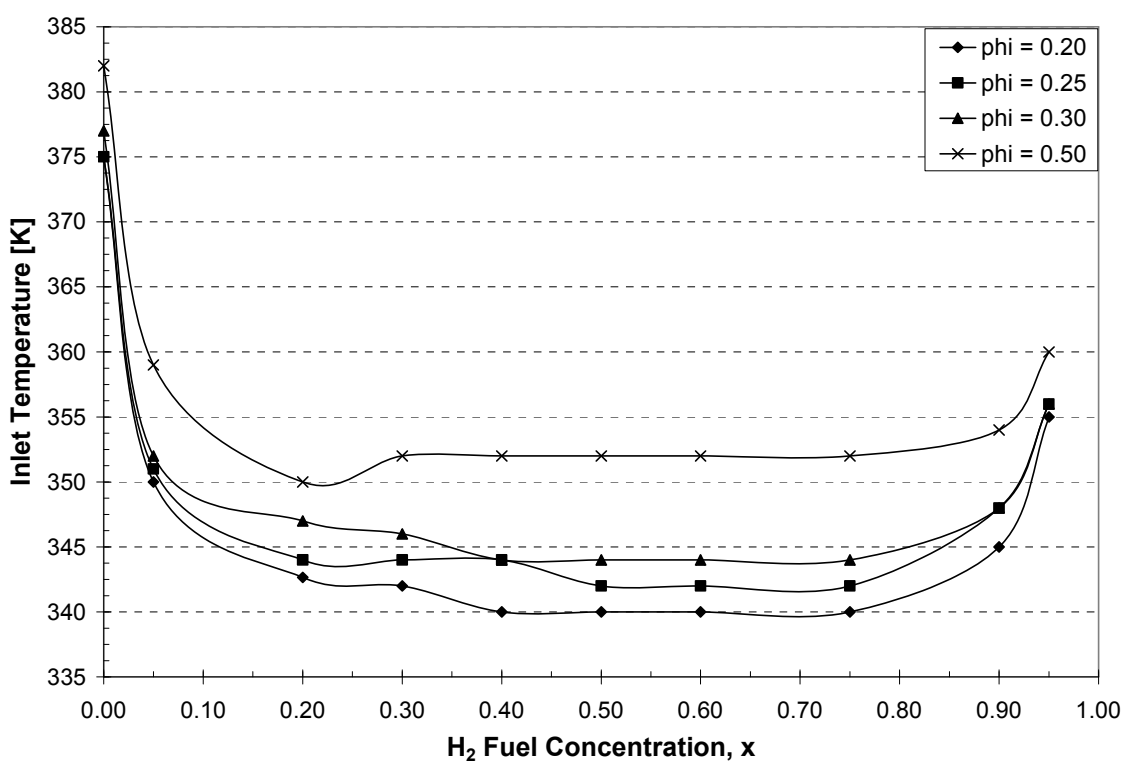


Figure 4-9: Graphical representation of Table 4-3: inlet temperatures used for the fixed ignition timing tests.

In this series, combustion took place at extremely low temperatures (Figure 4-10), much lower than would be used in a practical HCCI engine. In general, temperatures should be greater than 1500 K to ensure complete CO to CO₂ conversion (De Zilwa and Steeper

2006), and significant unconsumed fuel may remain for very low temperatures. For the cases presented here, at least 90% of the fuel was consumed. As a consequence of extremely low in-cylinder temperatures, the NO_x emissions are very low while UHC and CO are high. While these marginal cases are of little direct practical interest for HCCI engines, they are of interest as we move towards control of HCCI using pilot injection and other means.

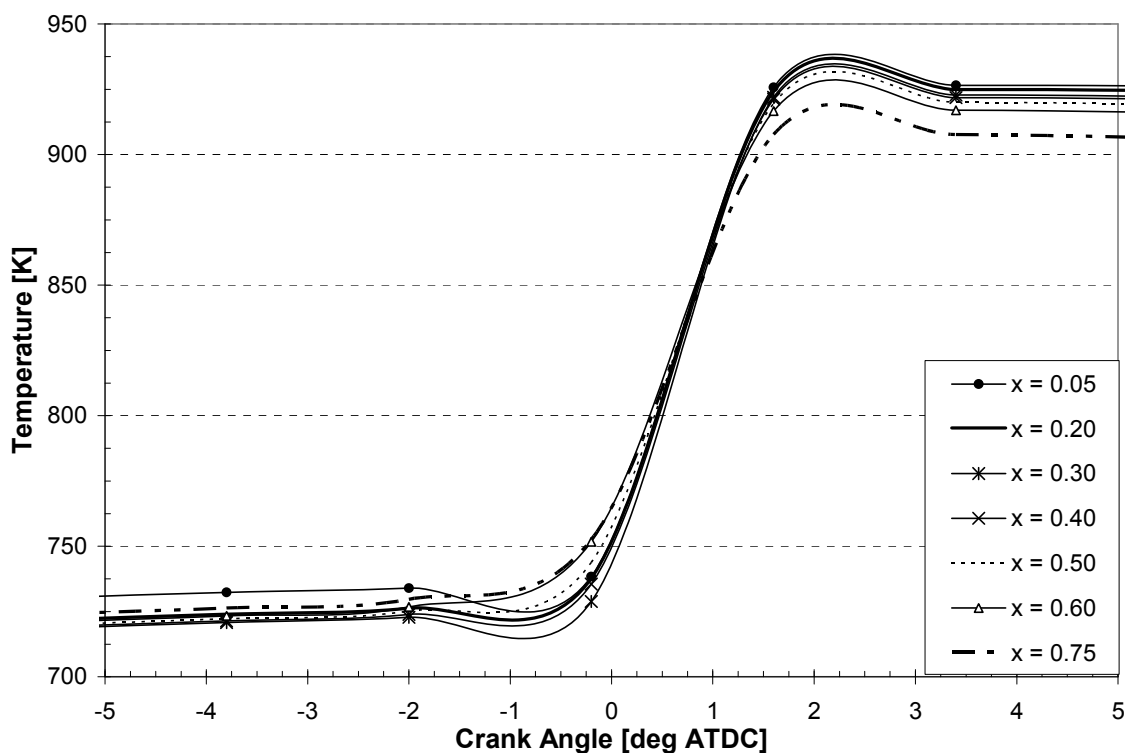


Figure 4-10: Temperature profiles for TDC fixed ignition timing ($\Phi = 0.50$).

Figure 4-11 compares the peak temperatures as the equivalence ratio and fuel composition are varied.

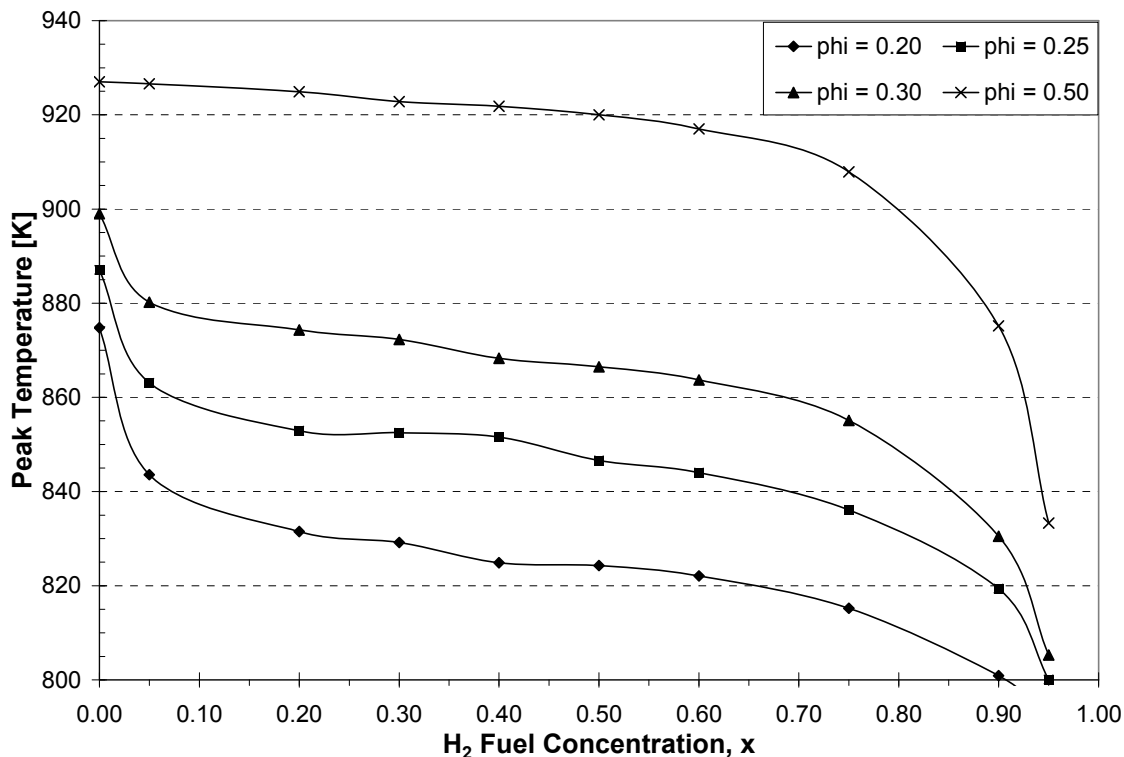


Figure 4-11: Effect of H₂ fuel concentration, x , on peak temperature for various Φ for the TDC fixed ignition timing simulations.

In this case (fixed ignition timing), the peak temperature decreases with increasing hydrogen content at a fixed equivalence ratio. That is because intake temperature was decreased with increasing hydrogen content for the range of x shown in Figure 4-11 to maintain fixed ignition timing. This decrease has caused the lower peak temperatures shown in Figure 4-11.

The CO emissions for fixed ignition timing follow trends similar to those observed earlier for fixed initial conditions. Figure 4-12 shows that the fuel composition affects CO emissions primarily at very high or very low hydrogen concentrations.

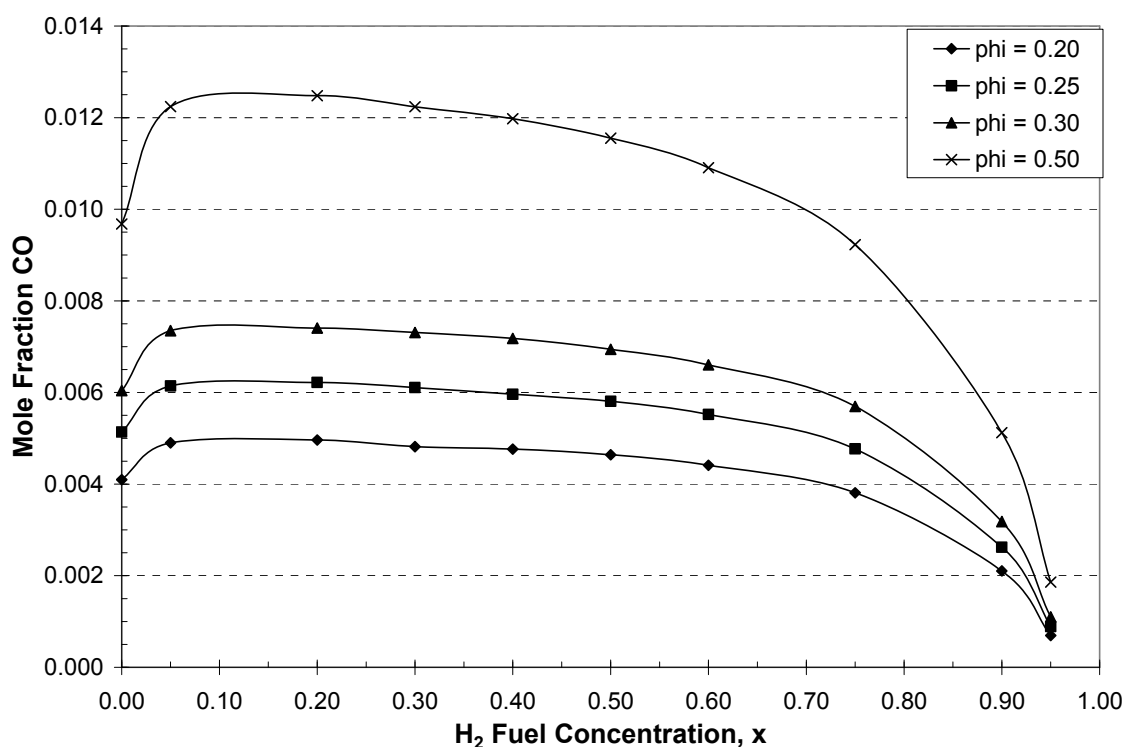


Figure 4-12: Effect of H₂ fuel concentration, x , on CO emissions for various Φ for TDC fixed ignition timing.

Since the peak in-cylinder temperatures for the cases discussed in this section have thus far been very low, and therefore not representative of an actual HCCI engine, it was next desired to fix the ignition timing under conditions matching those of more practical HCCI processes. Here, the ignition timing was fixed at approximately 4° BTDC (Figure 4-13) and peak temperatures fell mostly within the 1500 – 1700 K range (Figure 4-14). A new set of engine operating parameters and thermochemical conditions (Table 4-4) was used, along with a new set of inlet temperatures (Table 4-5).

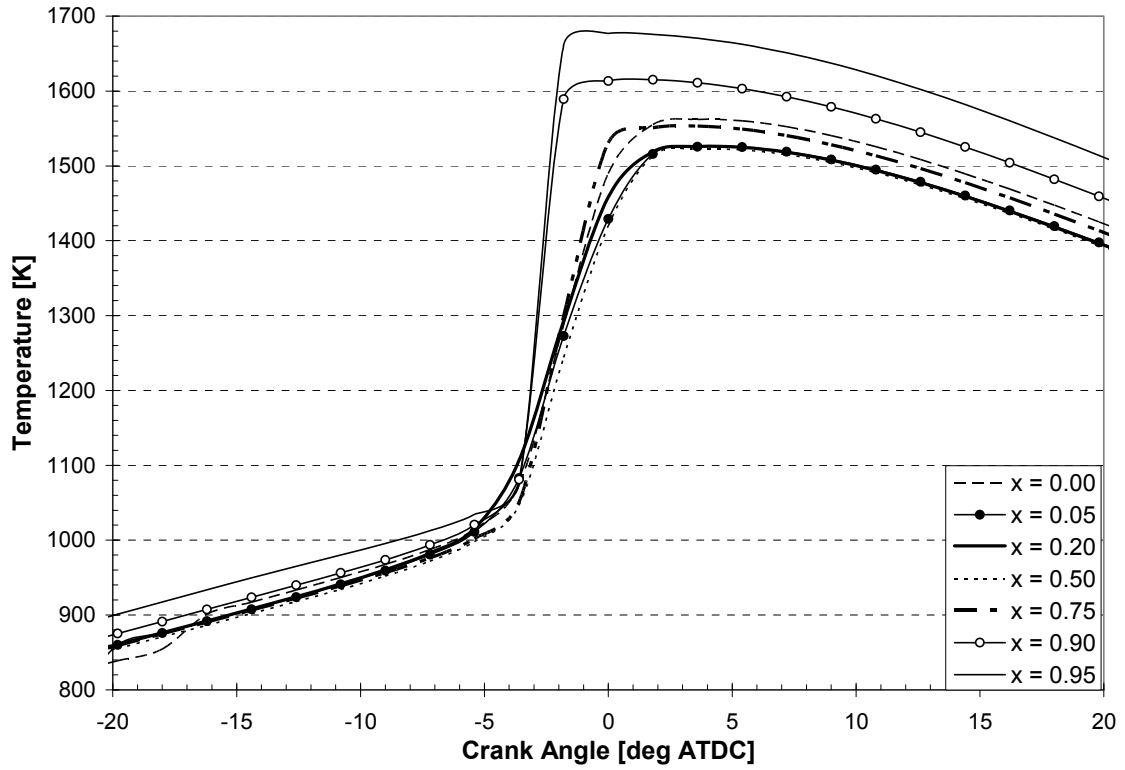


Figure 4-13: Temperature profiles for 4° BTDC fixed ignition timing ($\Phi = 0.20$).

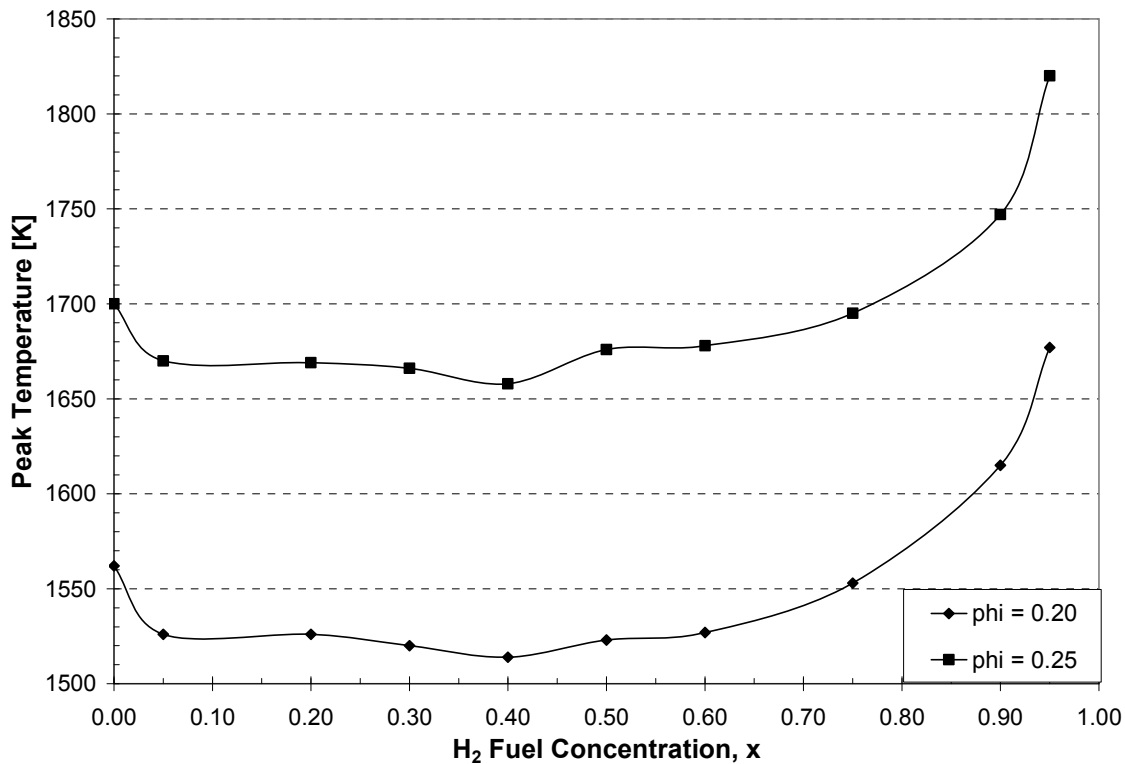


Figure 4-14 Effect of H₂ fuel concentration, x , on peak temperature for various Φ for the 4° BTDC fixed ignition timing simulations.

Table 4-4: Conditions used for second set of constant ignition timing simulations.

Engine Cylinder Displacement Volume:	611.74 cm ³
Compression Ratio:	15.0
Engine Speed:	1 800.0 rpm
Inlet Pressure:	101.325 kPa
Inlet Temperature:	variable (Table 4-5)
Exhaust Gas Recirculation (EGR):	0%
Conn. Rod/Crank Radius Ratio:	10 000.0
Inlet Valve Close:	-180.0 deg ATDC
Exhaust Valve Open:	135.0 deg ATDC

Table 4-5: Inlet temperatures [K] for the 4° BTDC fixed ignition timing tests.

Φ	<i>H₂ Fuel Concentration, x</i>									
	<i>0.00</i>	<i>0.05</i>	<i>0.20</i>	<i>0.30</i>	<i>0.40</i>	<i>0.50</i>	<i>0.60</i>	<i>0.75</i>	<i>0.90</i>	<i>0.95</i>
<i>0.20</i>	357	342	340	338	336	335	337	341	355	375
<i>0.25</i>	348	332	330	328	325	330	330	334	348	373

A comparison of Table 4-3 with Table 4-5 reveals that each of the fixed ignition timing series of tests both show decreasing inlet temperatures from $0.00 \leq x \leq 0.50$, then increasing inlet temperatures shortly afterwards. However, while the peak temperatures of the TDC ignition tests (Figure 4-11) are consistent with this, the peak temperatures for the 4° BTDC ignition tests (Figure 4-14) are not. The peak temperatures in Figure 4-11 continue to decrease with increasing x in spite of an increasing inlet temperature at higher H₂ fuel concentrations. The peak temperatures in Figure 4-14 begin to increase at $x > 0.50$ in correlation with increasing inlet temperatures at these x values.

The CO emissions for the 4° BTDC fixed ignition timing tests (not shown) were negligible compared (less than 10 ppm in all cases) to those from the TDC fixed ignition timing tests. However, UHC emissions were significant for $\Phi = 0.20$ (Figure 4-15). This is likely due to the low burned gas temperatures observed after combustion that fail to consume these unburned particles during the expansion stroke. The likelihood of this is further supported by the fact that UHC emissions are well below 0 ppm in all cases for $\Phi = 0.25$, where the burned gas temperatures are significantly greater.

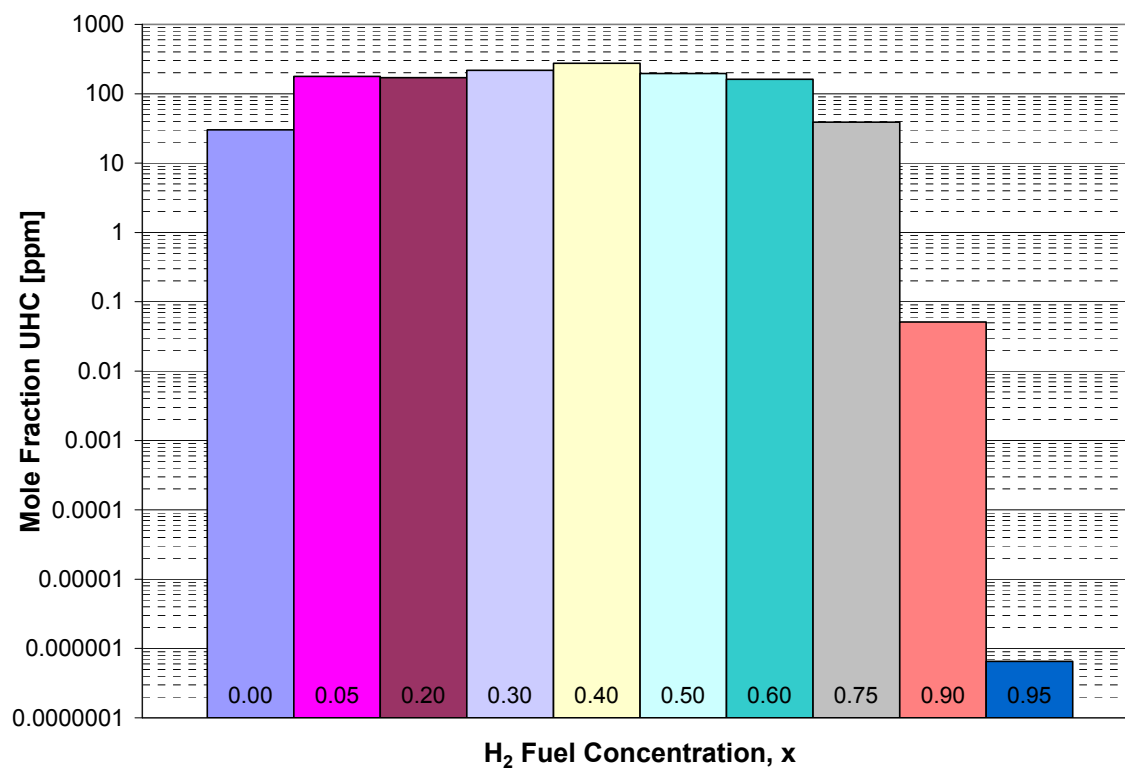


Figure 4-15: Effect of H₂ fuel concentration, x , on UHC emissions for $\Phi = 0.20$ for 4° BTDC fixed ignition timing.

CHAPTER 5

HOMOGENEOUS AUTOIGNITION OF ISO-OCTANE/AIR-EGR MIXTURES: A STUDY OF NO_x EMISSIONS

A second series of homogenous autoignition simulations was conducted to explore the effects of zero-dimensional modeling parameters on NO_x emissions. For conventional SI or diesel combustion process, the NO/NO₂ ratio is typically much greater than unity. Amnès et al. (2005) and others have shown that NO/NO₂ ratios can be significantly lower than unity for HCCI engines. Iso-octane was selected as the fuel here to more closely match the operating conditions in the Amnès et al. study.

5.1 Engine and Operating Conditions

The global engine parameters are based on a Volvo TD100-series engine (Maigaard et al. 2000) and are given in Table 5-1.

Table 5-1: Input parameters used for iso-octane CHEMKIN tests.

Engine Cylinder Displacement Volume:	1 600.0 cm ³
Bore:	12.065 cm
Crank Radius:	7.000 cm
Connecting Rod:	26.000 cm
Compression Ratio:	15.0 : 1
Engine Speed:	1 000 rpm
Intake Pressure:	100 000 Pa
Intake Temperature:	variable
Equivalence Ratio:	0.35
Exhaust Gas Recirculation (EGR):	0.00 - 6.20%
Intake Valve Close:	-146.0 deg ATDC
Exhaust Valve Open:	141.0 deg ATDC
Heat Transfer Model:	convective scheme (section 5.4)

5.2 Chemical Mechanism

The base chemical mechanism used is a primary reference fuel (PRF) mechanism for n-heptane/iso-octane oxidation developed by Lawrence Livermore National Laboratory (Curran et al. 2002). The mechanism contains 1024 species in 3246 reactions. The nitrogen chemistry of GRI-Mech 2.11 (Bowman et al. 2005) was added to this following the approach used in Section 3.1.2.4, resulting in a hybrid mechanism totaling 1052 species and 4338 reactions. Figure 5-1 verifies that the autoignition characteristics of the hybrid PRF_GRI2.11 mechanism remain indistinguishable from those of the base mechanism. The thermochemical conditions for the mechanism validation test are similar to those given in Table 5-1, with an intake temperature of 410 K and an equivalence ratio of $\Phi = 0.3721$. Unlike n-heptane, iso-octane undergoes a single-stage ignition, and allows for the realization of practical ignition timings with relative ease.

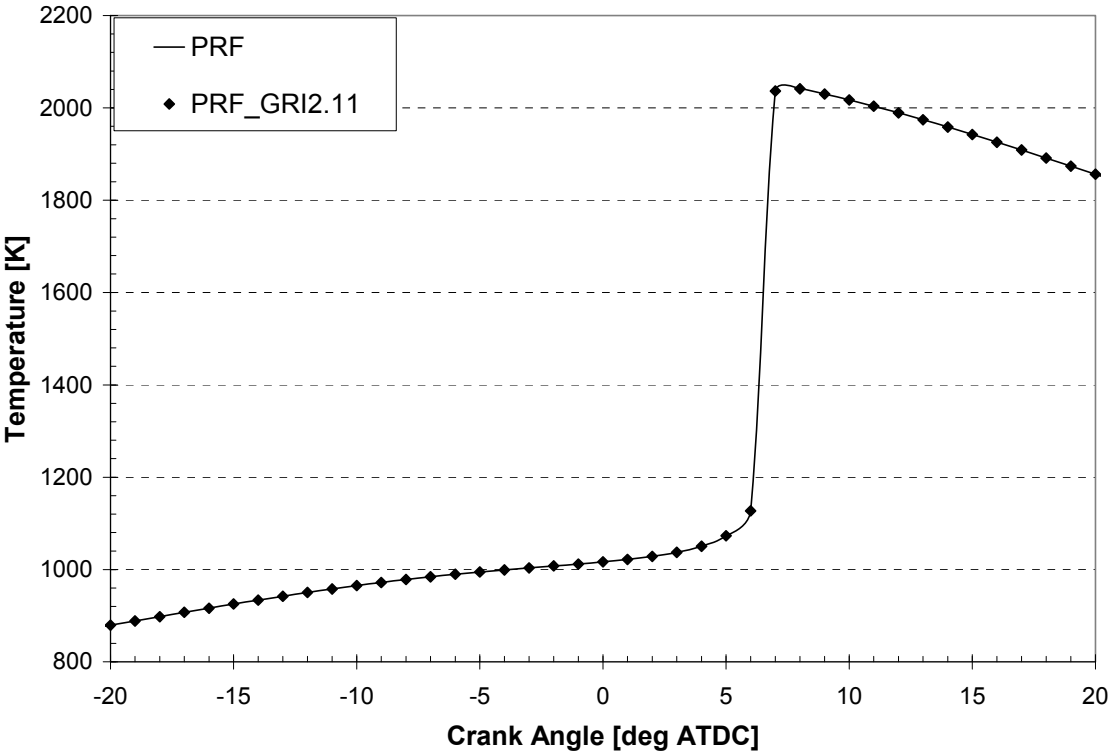


Figure 5-1: Comparison of base PRF mechanism with hybrid PRF_GRI2.11 mechanism.

5.3 Exhaust Gas Recirculation

An additional parameter addressed in this series of tests is the use of exhaust gas recirculation (EGR). This involves a specified quantity of the species contained in the exhaust of a combustion process being redirected to the intake of the next engine cycle. The amount is usually given as a percentage of the total intake mixture. In this study EGR is specified on a percent molar basis. EGR is used as a means to lower combustion temperatures and/or delay ignition timing, as the addition of these (mostly inert) species

inhibits the oxidation of the hydrocarbon fuel. In practical engine applications, the exhaust gas is sometimes cooled before blending with the new air/fuel mixture.

Although CHEMKIN does not have a direct method of implementing EGR, the simulation of this process is relatively straightforward. Adding a portion of the species from the end of one simulated cycle to the initial conditions of the next cycle is one approach. The challenge lies in determining the exact amount of each species. An iterative scheme must be employed to properly predict EGR concentrations, since the addition of new species to the initial composition will alter the combustion process, resulting in new concentrations of products. The temperature at which to introduce EGR must also be specified. This process by which EGR was modeled is summarized below.

1. Run a simulation without EGR.
2. Copy the species mole fractions (exhaust gas composition) from the final time step of the output of this run.
3. Multiply each of the initial fuel/air species mole fractions by one minus the desired molar percent of EGR. Note that this is done only once, as the new fuel air species mole fractions will not change from iteration to iteration.
4. Multiply each of the EGR species mole fractions from step two by the desired percent EGR.
5. Use the new mole fractions obtained from steps three and four as the initial species concentrations for a new simulation. Note that this effectively corresponds to cooling the EGR to the intake temperature.

6. Copy the species mole fractions from the final time step of the new run and compare them with the mole fractions of the previous run. If a change of less than five percent is observed in all of the species, the iteration is complete and these species concentrations may be used as the actual EGR values. If this is not the case, additional iterations are necessary. Repeat steps four through six using new species mole fractions.

Four to six iterations are typically needed for convergence. A new set of iterations is necessary for each set of operating conditions.

5.4 Heat Transfer Model

Eq. 3.2 with $a = 0.035$, $b = 0.8$, and $c = 0.0$ (Amnès et al. 2005) is used to compute wall heat transfer:

$$Nu_h \equiv \frac{hD}{k} = 0.035 Re^{0.8} Pr^{0.0}. \quad 5.1$$

The heat transfer model is further specified by the approach used to calculate the average in-cylinder gas velocity, w , used in calculating the Reynolds number. This is accomplished via the Woschni correlation (Section 3.1.1.1). The constants used in Eq. 3.2 and Eq. 3.4 are listed in Table 5-2 and are based on those provided by Amnès et

al. (2005). Note that the values for C_{11} , C_{12} , and C_2 are reduced from typical values [such as those presented in (Heywood 1988)] to match with those used in the Amnès study.

Table 5-2: Table of heat transfer constants used for iso-octane calculations.

a :	0.035
b :	0.800
c :	0.000
C_{11} :	0.760
C_{12} :	0.103
C_2 :	0.000108
Swirl Ratio:	0.010
T_w :	450.0 K

The values of the model constants in Table 5-2 have a strong influence on the heat loss during combustion, and often are adjusted to match numerical results with experimental data. An example of the effect of the coefficient a is shown in Figure 5-2.

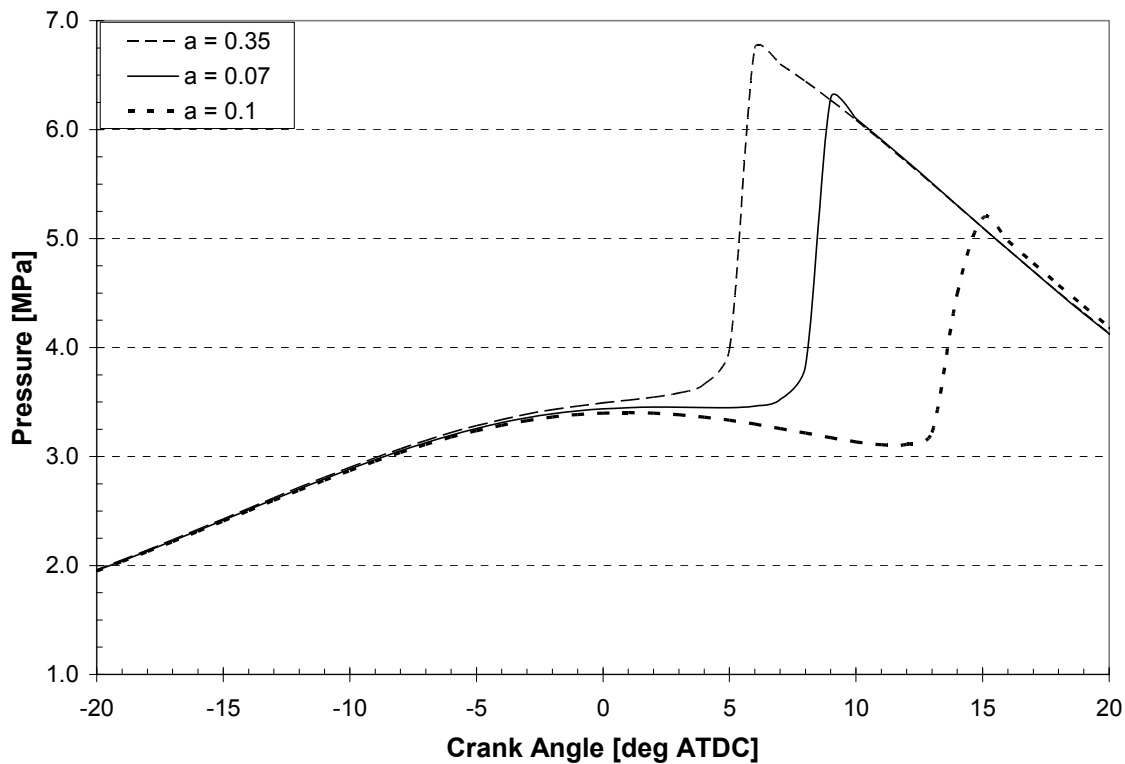


Figure 5-2: Effect of convection heat transfer coefficient, a , on combustion.

5.5 Parametric Study

The purpose of this study was to explore the variation of the NO/NO₂ ratio with intake temperature. Using the conditions specified in Table 5-1, 0.00% EGR, and varying the intake temperature from 407 K – 415 K, a range of NO/NO₂ ratios was captured (Figure 5-3).

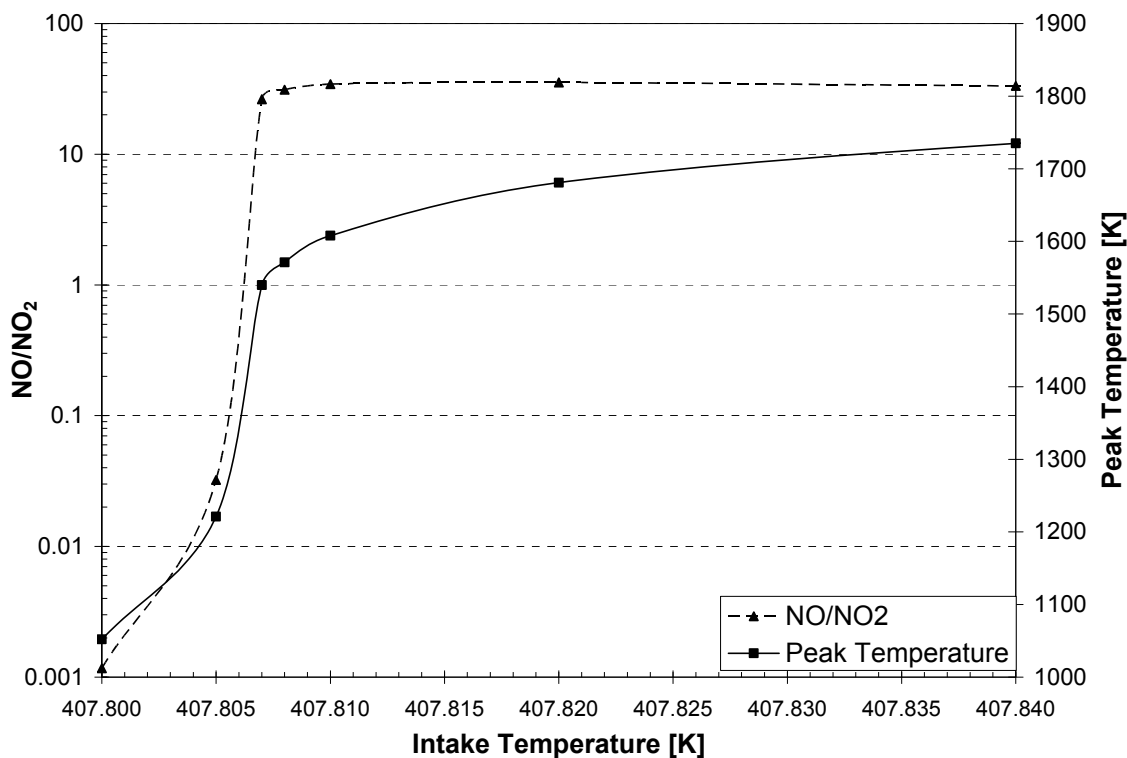


Figure 5-3: Effect of intake temperature on NO/NO₂ ratio and peak temperature.

It is apparent from this figure that even small variations of intake temperature have a profound effect on the combustion process. Computed NO₂ exceeds NO at conditions corresponding to very low peak temperatures, below the 1500 K mark considered to be the cutoff for complete CO to CO₂ conversion (Turns 2000). The case having an intake temperature of 407.807 K (the third data point in Figure 5.3) was run again using 6.20% EGR. This was done in an attempt to reduce the NO/NO₂ ratio while maintaining peak temperatures above 1500 K. While the results of this case (not shown) did confirm a decrease in the NO/NO₂ ratio, the ratio still remained above unity.

Additional cases were run to explore the sensitivity of the NO/NO₂ ratio to variations in engine operating conditions. A case with an equivalence ratio of $\Phi = 0.3817$, intake temperature of 415 K, cylinder wall temperature of 500 K, and 6.20% EGR showed comparable peak temperatures and ignition timings to those in the Amnès et al. (2005) study. Table 5-3 compares the approximate values from figures in this study with those captured using the CHEMKIN model.

Table 5-3: Comparison of CHEMKIN model with Amnès et al. (2005) study.

<i>Quantity</i>	<i>Amnès et al.</i>	<i>CHEMKIN</i>
Peak Temperature [K]	1975	1957
Ignition Timing [deg ATDC]	10	10
NO emissions [ppm]	3	9.32
NO ₂ emissions [ppm]	14	0.37

Despite an agreement among ignition timing and peak temperature, NO_x emissions values are significantly different between the two cases. Three-dimensional effects such as turbulence and in-cylinder temperature inhomogeneities not captured by the zero-dimensional model may be the cause of this discrepancy (Amnès et al. 2005). Another possibly was discussed by Bandaru and Turns (2000) in their study on turbulent jet flames. Here, it was discovered that the rapid addition of cold air to combustion products can result in the promotion of high NO₂/NO_x ratios. Cold air coupled with large amounts of mixing can lead to an increased production of HO₂, a strong promoter of the NO to NO₂ conversion pathway,



This process is further enhanced when UHC or trace amounts of fuel molecules are present (Bandaru and Turns 2000). This is the result of complex fluid dynamics that may occur during the exhaust process, and would not be captured with a zero-dimensional model.

CHAPTER 6

CFD OF H₂/AIR MIXTURES WITH N-HEPTANE PILOT INJECTION

In this chapter, the three-dimensional CFD model AC-FluX was utilized to explore the control of ignition timing of hydrogen/air mixtures via the pilot-injection of a small amount of surrogate diesel fuel (n-heptane).

6.1 Engine Configuration and Operating Conditions

AC-FluX operates by drawing information from several user-edited input files. These text files cover a wide breadth of information relating to engine parameters, thermochemical conditions, spray/valve conditions, physical model options, as well as controlling numerical parameters such as time step size and output printing. Two principle types of output were used: animation files and global output files. The global output (or global diagnostics) files contain in-cylinder averaged values for various quantities including temperature, pressure, and species mole fractions, and is similar to output files obtained from CHEMKIN. The much larger animation files, however, contain information for these same parameters in each of the three spatial dimensions for every time step. The data used to generate the majority of the plots in this chapter was obtained from global output files.

6.1.1 Engine Configuration

The engine geometry represents a generic bowl-in-piston diesel engine, including a top-ring-land crevice (Figure 6-1). The engine model does not include valves. Fuel is injected using an eight-hole diesel injector; hence a 45° sector model has been used to reduce computational time. There is no swirl. The fuel injector position and orientation can be seen in Figure 6-1. Global engine parameters are summarized in Table 6-1. These parameters are based on a Volvo TD100-series diesel engine (Maigaard et al. 2000), although the engine bore and stroke have been modified slightly to maintain the correct compression ratio.

Table 6-1: Global engine parameters for the CFD engine model.

Engine Cylinder Displacement Volume:	1597.42 cm ³
Stroke:	27.50 cm
Bore:	8.60 cm
Connecting Rod:	26.00 cm
Clearance:	1.25 cm
Compression Ratio:	18.7 : 1
Engine Speed:	1 400 rpm
Intake Valve Close:	180 deg ATDC
Exhaust Valve Open:	495 deg ATDC

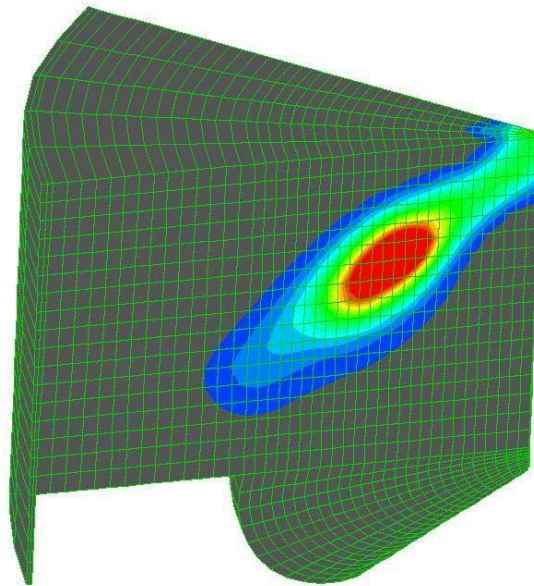


Figure 6-1: Sector mesh used in CFD tests detailing injection from upper right corner.

6.1.2 Thermochemical Conditions

The thermochemical conditions for the CFD tests were selected such that the homogeneous hydrogen/air mixture would be close to, but short of, the point of auto-ignition in the absence of fuel injection. CHEMKIN was used to scope out these conditions by varying the inlet temperatures for each equivalence ratio. The inlet temperature values were selected based on the percentage of hydrogen fuel consumed. The first and third series of tests used inlet temperatures that corresponded to a hydrogen consumption of approximately 3 – 5%, while the second series used inlet temperatures that corresponded to a hydrogen consumption of less than 1%. The results of this scoping study are presented in Tables 6-2 and 6-3. In each of these tables, bold values represent those selected for the CFD runs. Cells marked with a † correspond to values for the first

and third series of simulations, while those marked with a ‡ correspond to those used for the second series. For example, an inlet temperature of 355 K was used for the first series at an equivalence ratio of 0.20.

Table 6-2: Peak temperatures obtained from the CHEMKIN scoping study.

Inlet Temperature [K]	Peak Temperature [K]				
	$\phi = 0.20$	$\phi = 0.25$	$\phi = 0.30$	$\phi = 0.35$	$\phi = 0.40$
340	1013	1014	1015	1017	1018
341				1020	1021 [‡]
342			1021	1022 [‡]	1024
343		1022	1024 [‡]	1025	
344	1023	1025 [‡]	1026	1028	
345	1026 [‡]	1027	1029	1031	1033
346	1028				
347					1040
348					1044 [†]
349	1037			1044 [†]	
350	1039	1042	1044	1048	2269
351			1048 [†]	2099	
352		1048 [†]	1052		
355	1054 [†]	1819	2038		
357	1062				

Table 6-3: Percentage of fuel consumed obtained from the CHEMKIN scoping study.

Inlet Temperature [K]	Fuel Consumed [% by moles]				
	$\phi = 0.20$	$\phi = 0.25$	$\phi = 0.30$	$\phi = 0.35$	$\phi = 0.40$
340	0.43%	0.49%	0.57%	0.65%	0.74%
341				0.75%	0.86% [‡]
342			0.75%	0.87% [‡]	1.01%
343		0.73%	0.86% [‡]	1.02%	
344	0.71%	0.84% [‡]	1.00%	1.20%	
345	0.81% [‡]	0.97%	1.17%	1.43%	1.77%
346	0.93%				
347					2.92%
348					4.23% [†]
349	1.46%			3.66% [†]	
350	1.72%	2.28%	3.21%	5.67%	100%
351			4.39% [†]	100%	
352		3.62% [†]	7.10%		
355	5.06% [†]	100%	100%		
357	14.62%				

Table 6-4 specifies additional thermochemical conditions utilized for the CFD study. Equivalence ratios were chosen to be representative of practical HCCI values, and the inlet temperatures were selected according to the process described above. The heat transfer model employed used standard wall functions (Section 3.1.1.1) with a specified constant cylinder wall temperature. The heat transfer model used for the CHEMKIN simulations was identical to that described in Section 5.4, with a constant wall temperature of 450 K.

Table 6-4: Thermochemical conditions used with the CFD model.

Fuel:	H ₂ /C ₇ H ₁₆
Chemical Mechanism:	Hybrid UW40_GRI2.11 Mech
Equivalence Ratio, Φ :	0.20 – 0.40
Inlet Pressure, p_i :	101 325 Pa
Inlet Temperature, T_i :	340 – 355 K
Cylinder Wall Temperature, T_w :	450 K
Mass of C ₇ H ₁₆ Injected, m :	1.49 - 2.98 mg
Start of Injection, SOI:	330 – 355 deg ATDC
Injection Duration, τ :	5, 10, and 15 CAD

6.2 CFD versus Zero-Dimensional Model

To verify thermochemical consistency between the zero- and three-dimensional models, adiabatic autoignition was simulated using both models for identical thermochemical conditions (no pilot injection in the CFD). For initially homogeneous reactants and adiabatic walls, results from 3D CFD should be very close to those obtained using a 0D adiabatic model. There will be small differences because of flow effects on the CFD energy (enthalpy) equation.

In Figure 6-2, the results of the zero-dimensional CHEMKIN model are compared with those from the more detailed CFD code. The case shown here is for an equivalence ratio of $\Phi = 0.25$, inlet temperature of 352 K, and other conditions as specified in Table 6-1.

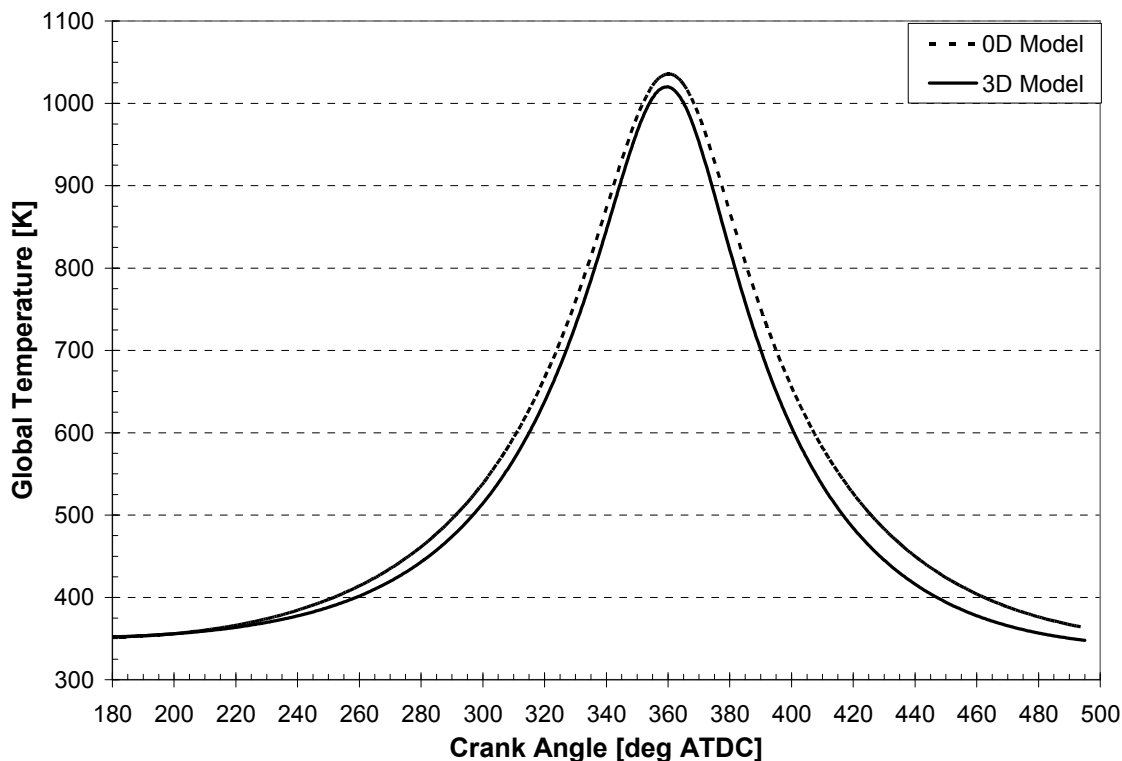


Figure 6-2: Comparison of 0D and 3D models for $\Phi = 0.25$.

Figure 6-2 shows that the hydrogen/air mixture did not auto-ignite, as desired, and results from the two models are very close (peak temperatures differ by ~ 16 K), with those from the 0D model being slightly higher.

6.3 Premixed Reactants versus Fuel Injection

Late direct in-cylinder injection of a small amount of liquid n-heptane can lead to global autoignition of a mixture that otherwise would not ignite. When the n-heptane is premixed with the hydrogen/air charge, ignition does not occur under the conditions shown in Figures 6-3 and 6-4; moreover, the n-heptane/ H_2 fuel behaves the same as pure

H₂ fuel for these conditions (Figure 6-4). However, when the same amount of n-heptane (2.98 mg) is injected at 340° ATDC, ignition does occur (Figure 6-3).

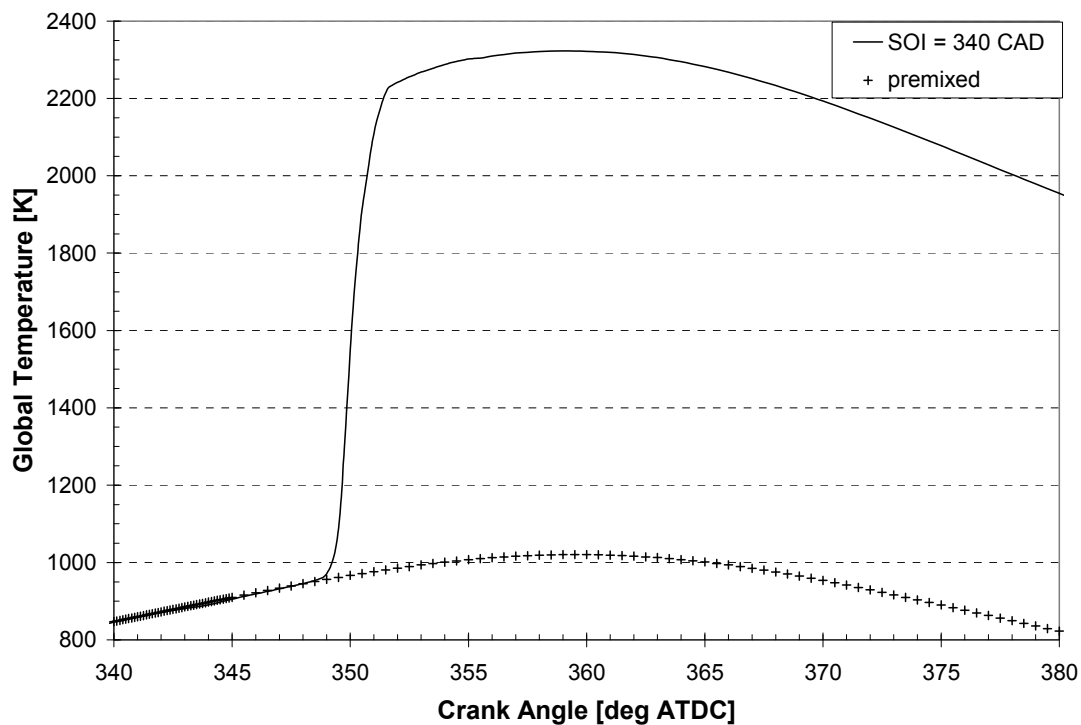


Figure 6-3: Comparison of premixed reactants versus fuel injection for the same total quantity of C₇H₁₆ and H₂ fuels. For the case of direct injection, SOI = 340 CAD, $\tau = 10$ CAD.

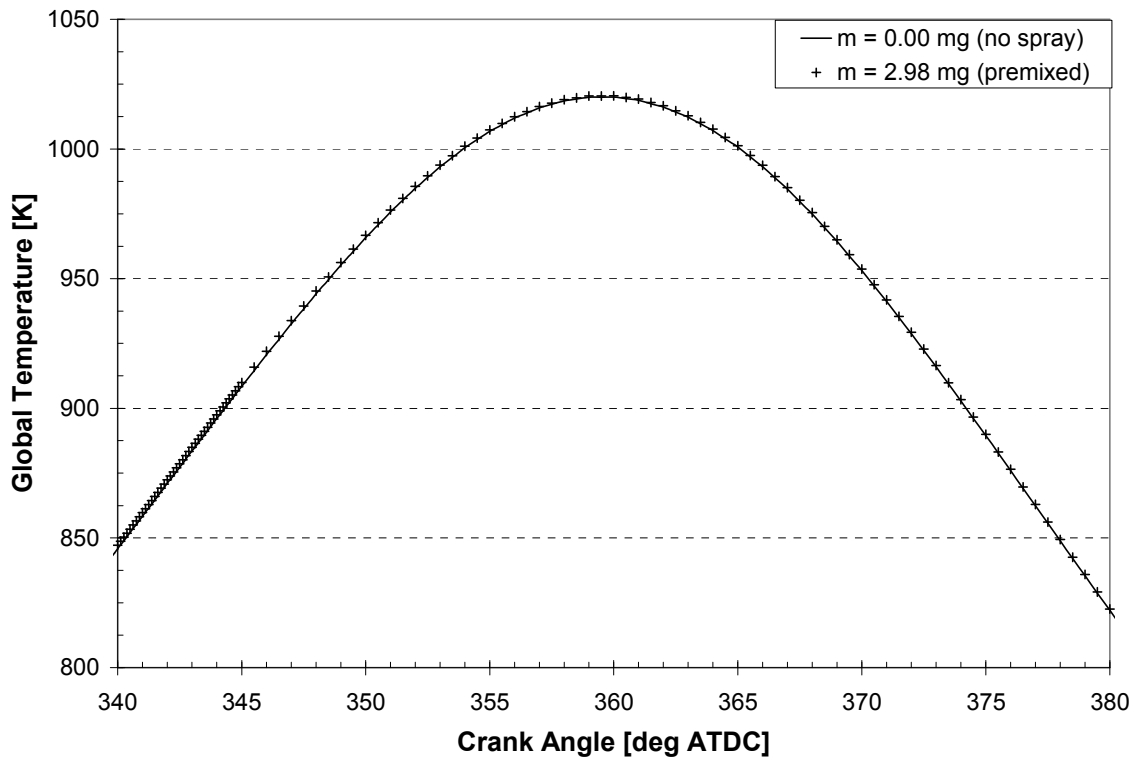


Figure 6-4: CFD comparison of premixed case and pure H₂/air case for $\Phi = 0.25$.

The cases presented here included both the n-heptane fuel and the hydrogen in calculating the value of the equivalence ratios. However, these values did not differ from those calculated using only the hydrogen, as the amount of n-heptane injected was very small (less than one part-per-billion in all cases).

6.4 Control of Ignition Timing Using Pilot Injection

With the models thus verified, we next explore the potential control of a diesel-based HCCI combustion process of H₂/air mixtures via late direct injection of a small amount of liquid n-heptane. Variations in start of injection (SOI), injection duration (τ), mass of

fuel injected (m), and the proximity of the H₂/air mixture to autoignition in the absence of injection were considered. All results below were for cases of an equivalence ratio of $\Phi = 0.25$, unless otherwise noted. This value was chosen to match those of a practical HCCI engine, and results obtained at this value were typical of those at other equivalence ratios (not shown). It was found that the ignition timing varied little as the equivalence ratio was changed.

Inlet temperature (T_i) Set A (Table 6-5) was used for Sections 6.4.1 and 6.4.2, with values of T_i corresponding to a 3 – 5% (by moles) consumption of hydrogen in the absence of fuel injection (Table 6-3). In Section 6.4.3, inlet temperature Set B was used, with values corresponding to less than 1% consumption of hydrogen (further from autoignition in the absence of pilot injection).

Table 6-5: Inlet temperatures and corresponding fuel consumption.

		<i>Inlet Temperature, T_i [K]</i>	<i>% H₂ Fuel Consumed</i>
$\Phi = 0.20$	Set A	355	5.06%
	Set B	345	0.81%
$\Phi = 0.25$	Set A	352	3.62%
	Set B	344	0.84%
$\Phi = 0.30$	Set A	351	4.39%
	Set B	343	0.86%
$\Phi = 0.35$	Set A	349	3.66%
	Set B	342	0.87%
$\Phi = 0.40$	Set A	348	4.23%
	Set B	341	0.86%

6.4.1 Variation of Start of Injection, SOI

The first parameter explored was the timing of the pilot injection. Cases were limited to late direct-injection, similar to those described in Section 2.2.1. Figure 6-5 shows the effect of three different SOI times on computed global in-cylinder temperatures.

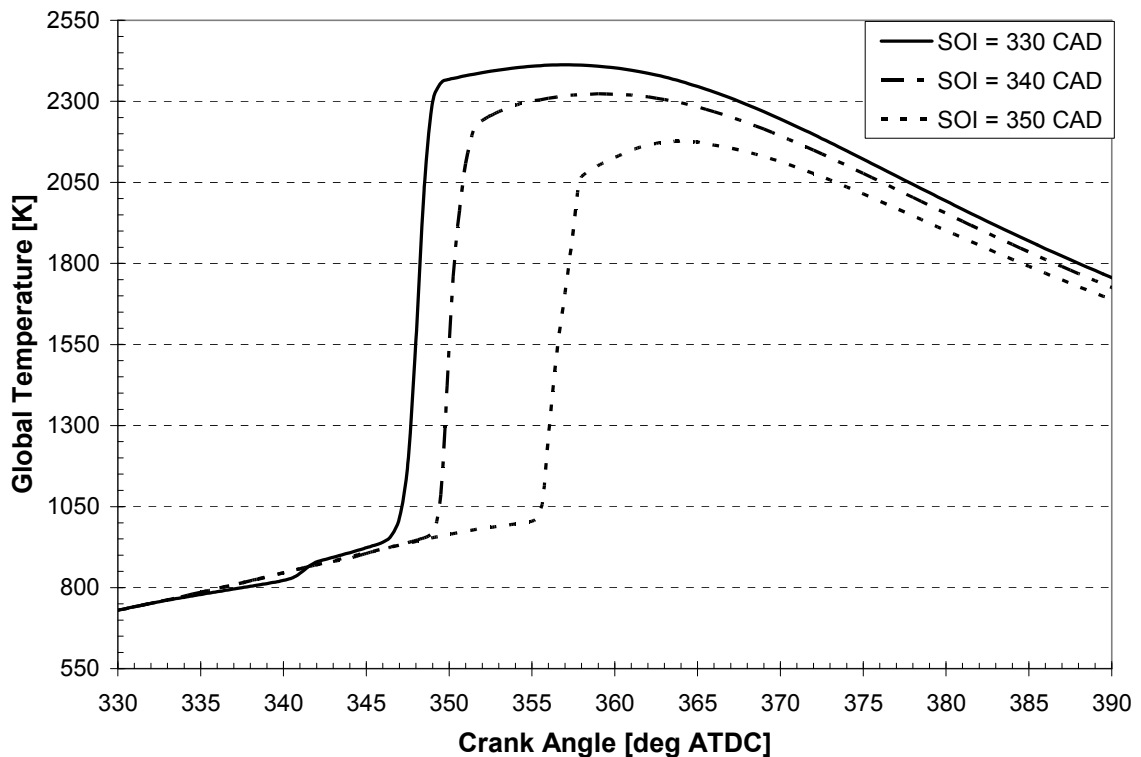


Figure 6-5: Effect of SOI on ignition timing for $\tau = 10$ CAD, $m = 2.98$ mg, and $\Phi = 0.25$.

Ignition occurs approximately 15 CAD after SOI for SOI = 330 CAD, 10 CAD after SOI for SOI = 340 CAD, and 5 CAD after SOI for SOI = 350 CAD. For SOI = 355 CAD (not shown), ignition did not occur. The steady decrease in ignition delay as SOI is retarded is most likely a direct consequence of the increased temperature and pressure conditions in the cylinder at later crank angles. The strong influence that SOI has on combustion

timing suggests that this parameter may be an effective means to control ignition timing in HCCI engines with pilot injection.

Variations in SOI also influence the rate of pressure rise (Figure 6-6).

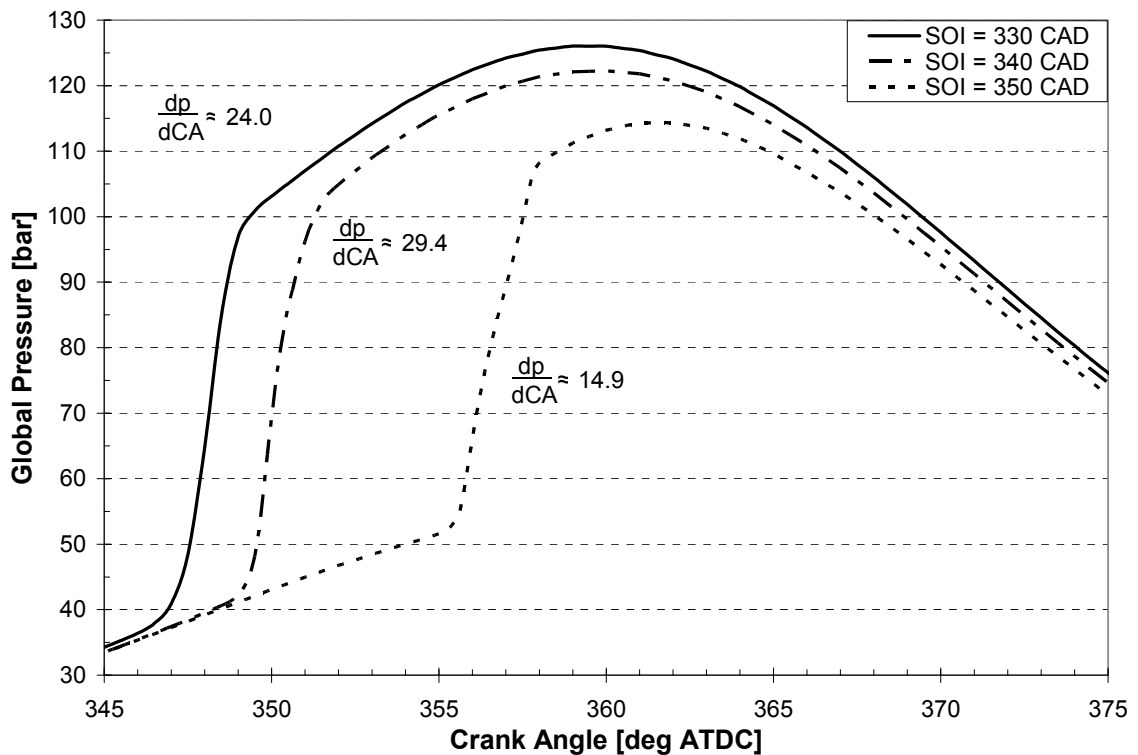


Figure 6-6: Effect of SOI on global in-cylinder pressure for $\tau = 10$ CAD, $m = 2.98$ mg, and $\Phi = 0.25$.

While these pressure gradients do not correspond to those desired in a practical HCCI engine (“knocking” in the engine occurs when the rate of pressure rise reaches 8 – 12 bar), it is interesting to note that the smallest value occurs when ignition is timed close to TDC.

6.4.2 Variation of Mass of Liquid Fuel Injected, m

A second method that was explored to control combustion phasing was to vary the amount of liquid fuel injected. Figure 6-7 compares the results of two different masses of n-heptane for the same overall equivalence ratio ($\Phi = 0.25$).

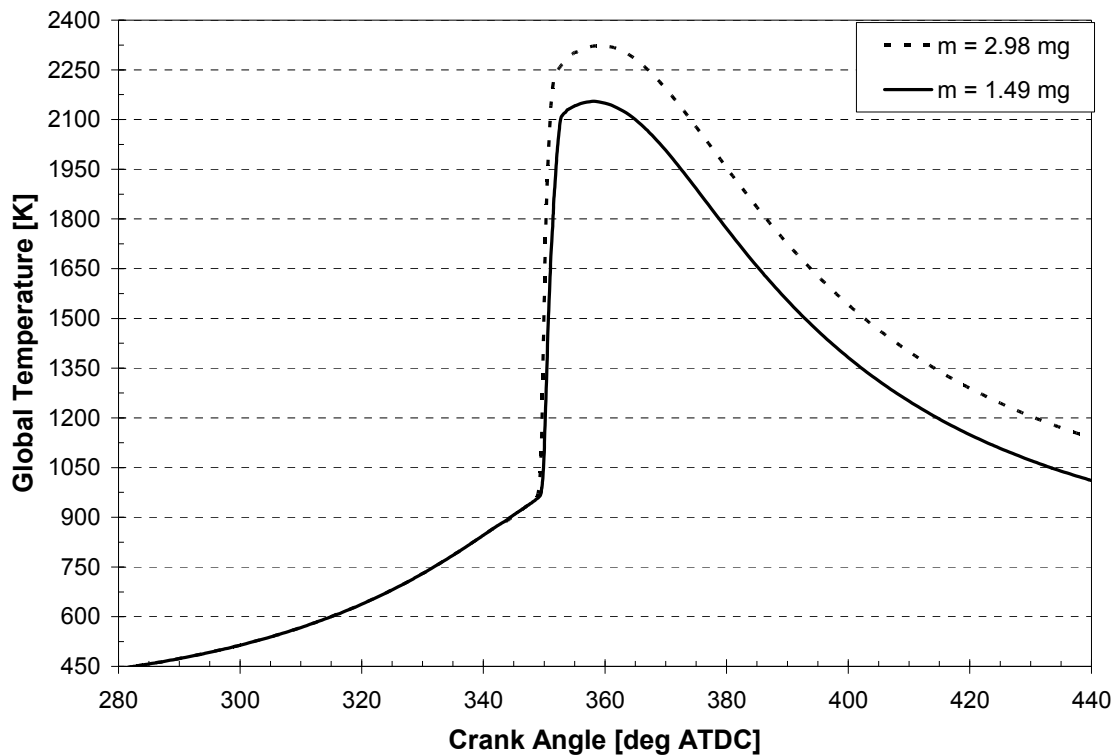


Figure 6-7: Effect of m on temperature profile (SOI = 340 CAD, $\tau = 10$ CAD).

Peak temperature is higher for the higher injected fuel quantity, although the effect on ignition timing appears to be small. A closer look (Figure 6-8) reveals a delay in ignition timing of approximately one crank angle degree along with a peak temperature reduction of approximately 200 K, with the reduced quantity of fuel injected. A lower rate of

temperature rise is also observed; controlling the maximum rate of pressure rise is an important consideration in HCCI engines.

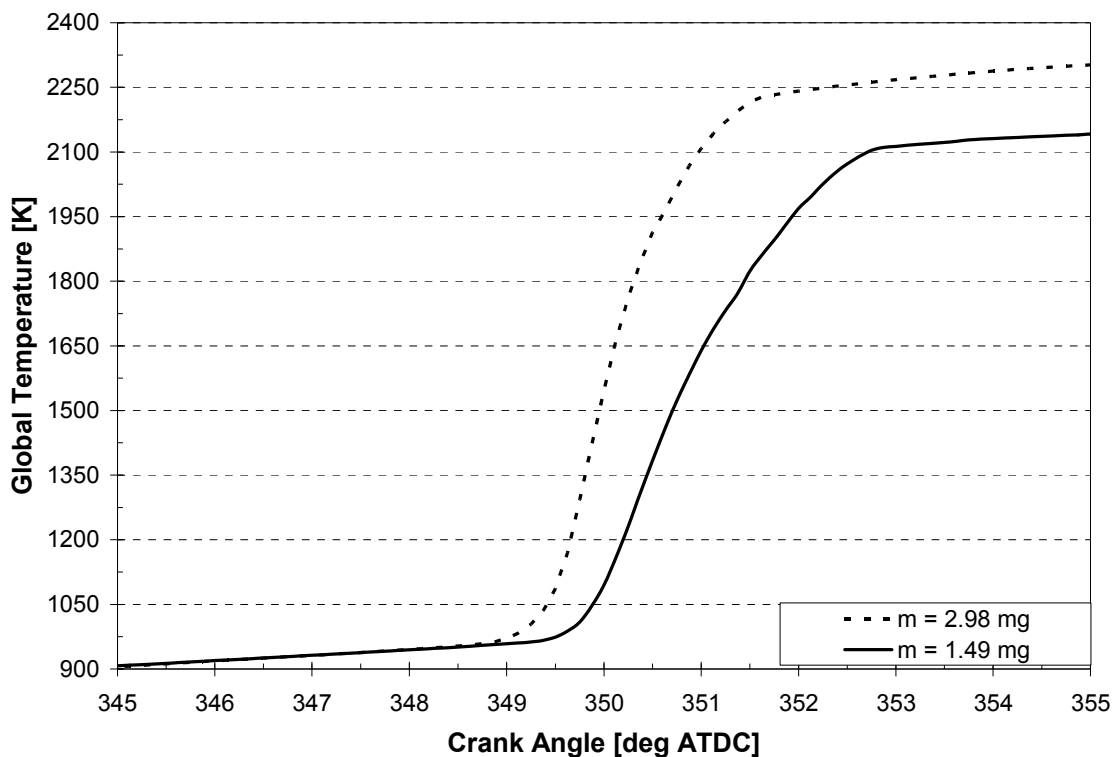


Figure 6-8: Expanded view of Figure 6-7 during autoignition.

6.4.3 Variation of Proximity to Autoignition of the Homogeneous H₂/Air Mixture

Inlet temperatures corresponding to 3 – 5% hydrogen consumption in the absence of pilot injection were utilized in Sections 6.4.1 and 6.4.2. Here, the inlet temperatures of the H₂/air mixtures were decreased such that less than one percent of the hydrogen fuel was consumed during compression in the absence of pilot injection. In Figure 6-9, two cases are compared for SOI = 330 CAD, and in Figure 6-10, two cases are compared for SOI =

350 CAD. Both cases have an injection duration of $\tau = 10$ CAD and an injected fuel mass of $m = 2.98$ mg.

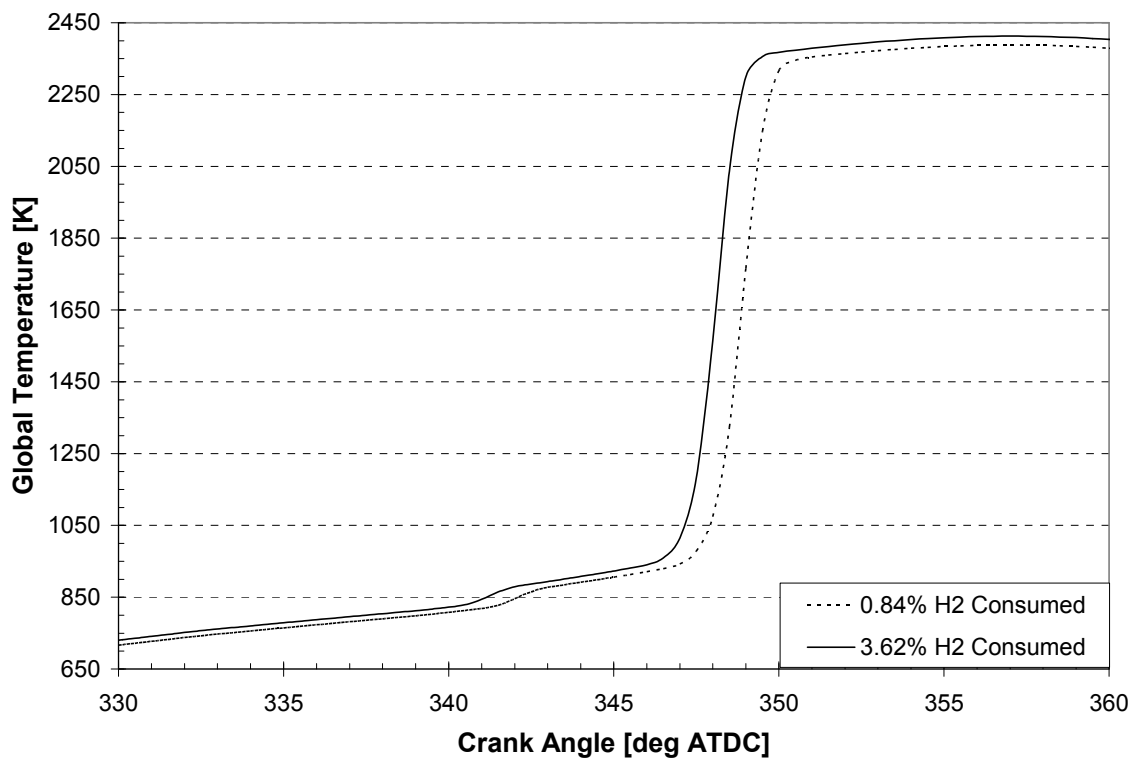


Figure 6-9: Comparison of H₂ fuel consumed for SOI = 330 CAD and $\Phi = 0.25$.

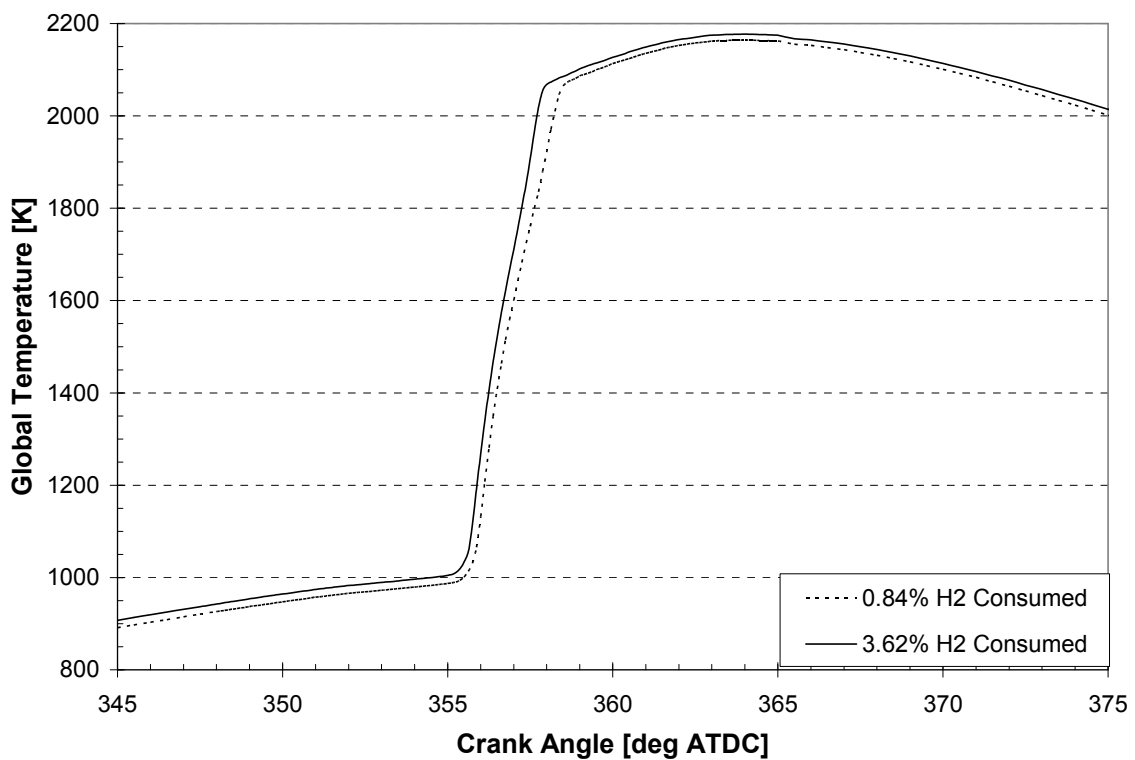


Figure 6-10: Comparison of H₂ fuel consumed for SOI = 350 CAD and $\Phi = 0.25$.

In both cases, a small delay in ignition timing and decrease in peak temperature are noted with the lower values of inlet temperature. This is most likely the result of a decrease in inlet temperature of 8 K between the two cases (Table 6-5), and it is safe to assume that changing the fuel consumed in the homogeneous mixture has a negligible effect on the combustion timing.

6.5 Emissions

Emissions of NO and NO₂ are shown in Figures 6-11 and 6-12, respectively. As expected, values of both NO and NO₂ decrease as the injection timing is advanced due to lower in-cylinder temperatures.

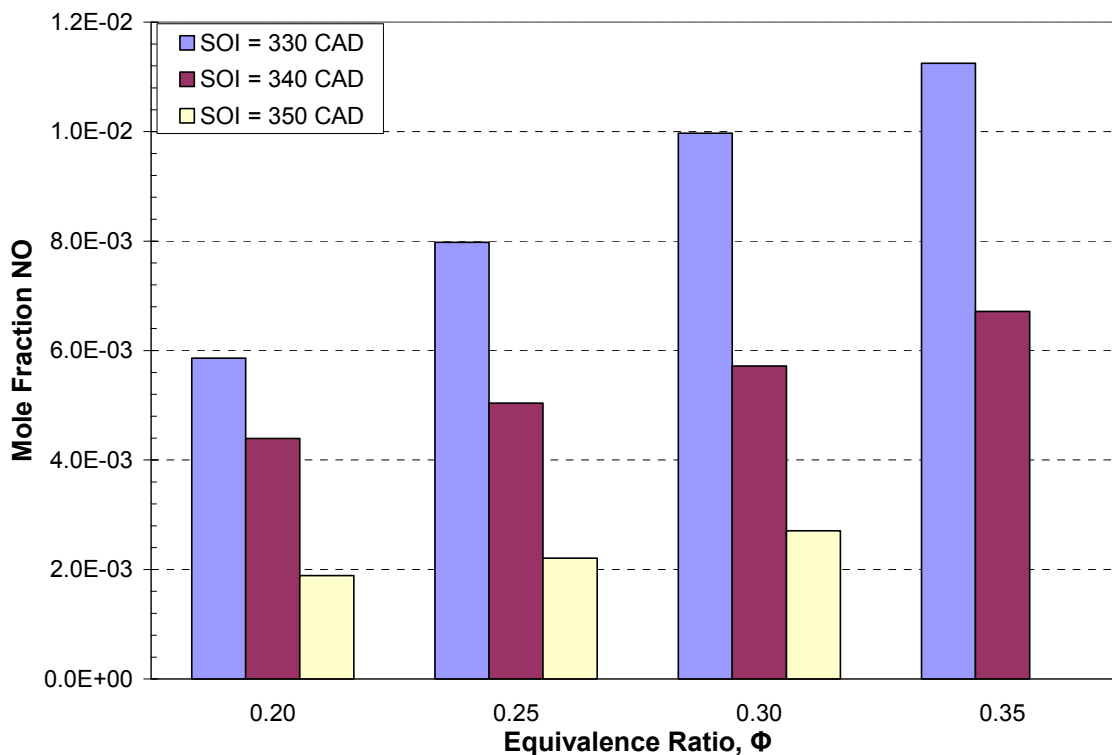


Figure 6-11: Effect of injection timing, SOI, on NO emissions for various Φ ($\tau = 10$ CAD and $m = 2.98$ mg).

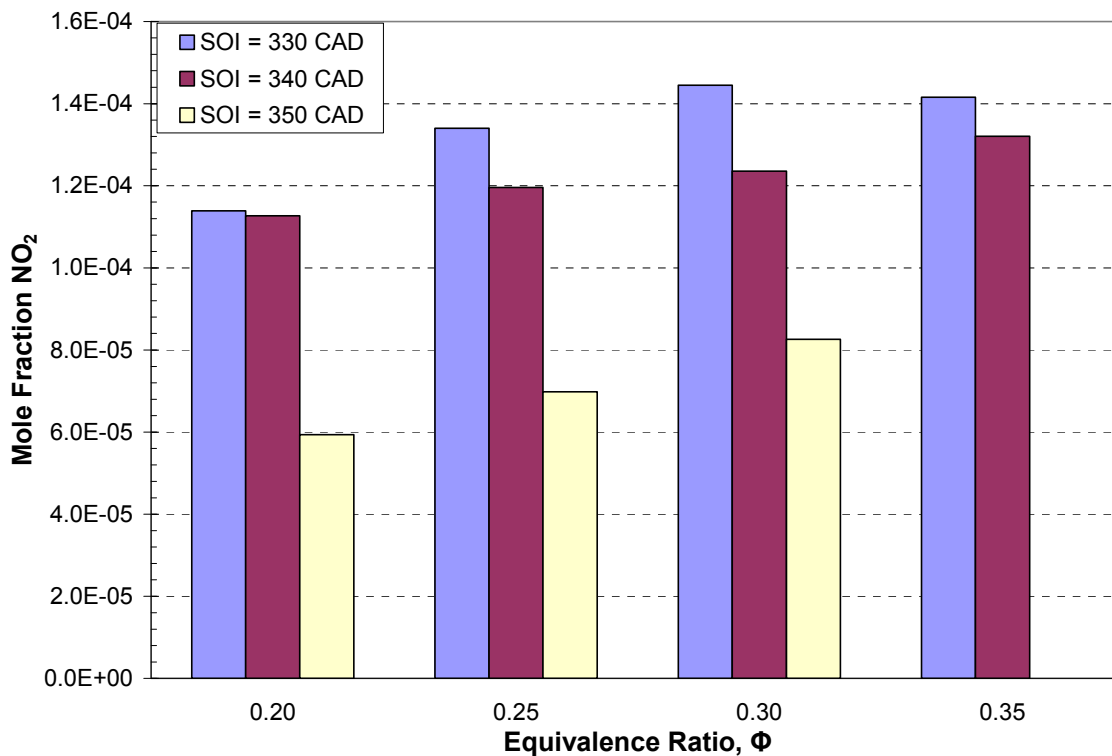


Figure 6-12: Effect of injection timing, SOI, on NO_2 emissions for various Φ ($\tau = 10$ CAD and $m = 2.98$ mg).

The most interesting emissions results are those of CO (Figure 6-13). Here, drastically greater CO levels are noted at SOI = 350 CAD. In this case, ignition occurs at approximately 5° BTDC. Liquid n-heptane continues to be injected as combustion occurs. The high CO emissions may be the result of the chemistry occurring under these temperature/pressure conditions.

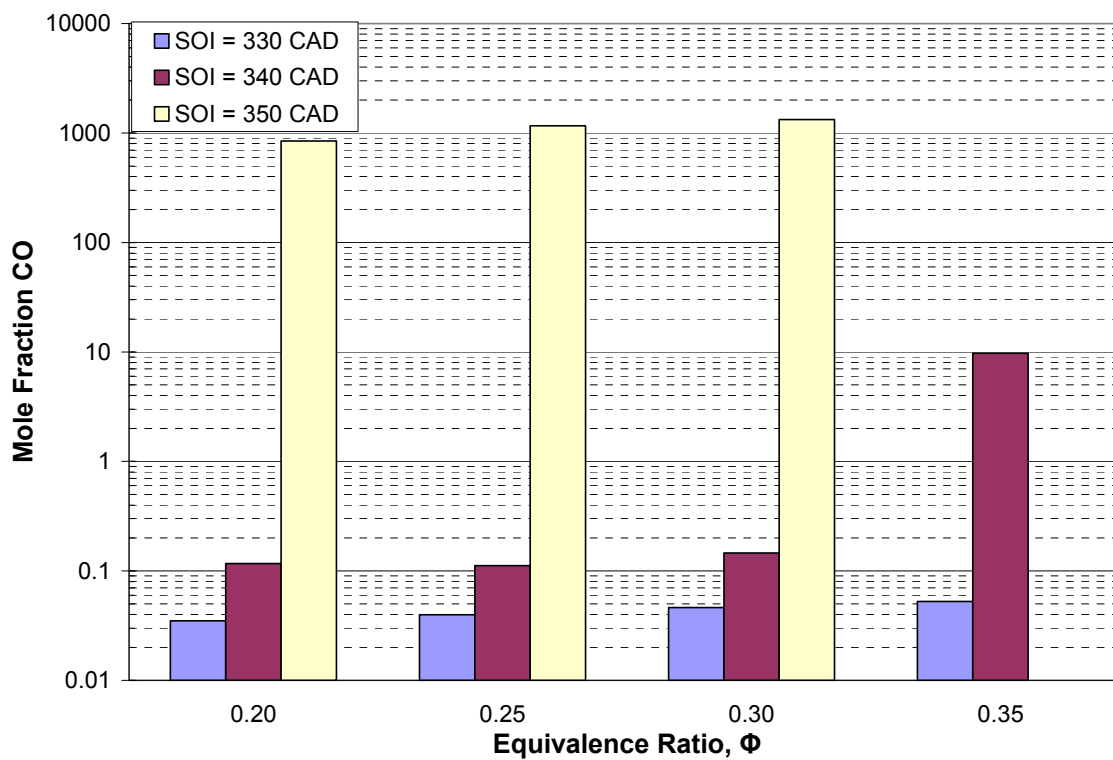


Figure 6-13: Effect of injection timing, SOI, on CO emissions for various Φ ($\tau = 10$ CAD and $m = 2.98$ mg).